

# Effective Lockdown and Role of Hospital-Based COVID-19 Transmission in Some Indian States: An Outbreak Risk Analysis

Tridip Sardar<sup>1</sup> and Sourav Rana<sup>2,\*</sup>

Several reports in India indicate hospitals and quarantined centers are COVID-19 hotspots. To study the transmission occurring from the hospitals and as well as from the community, we developed a mechanistic model with a lockdown effect. Using daily COVID-19 cases data from six states and overall India, we estimated several important parameters of our model. Moreover, we provided an estimation of the effective ( $R_T$ ), the basic ( $R_0$ ), the community ( $R_C$ ), and the hospital ( $R_H$ ) reproduction numbers. We forecast COVID-19 notified cases from May 3, 2020, till May 20, 2020, under five different lockdown scenarios in the seven locations. Our analysis suggests that 65% to 99% of the new COVID-19 cases are currently asymptomatic in those locations. Besides, about 1–16% of the total COVID-19 transmission are currently occurring from hospital-based contact and these percentage can increase up to 69% in some locations. Furthermore, the hospital-based transmission rate ( $\beta_2$ ) has significant positive (0.65 to 0.8) and negative (-0.58 to -0.23) correlation with  $R_0$  and the effectiveness of lockdown, respectively. Therefore, a much larger COVID-19 outbreak may trigger from the hospital-based transmission. In most of the locations, model forecast from May 3, 2020, till May 20, 2020, indicates a two-times increase in cumulative cases in comparison to total observed cases up to April 29, 2020. Based on our results, we proposed a containment policy that may reduce the threat of a larger COVID-19 outbreak in the future.

**KEY WORDS:** COVID-19; effective lockdown policy; ensemble model forecast; hospital-based transmission; outbreak risk analysis

## 1. INTRODUCTION

Coronavirus disease of 2019 (COVID-19) was first observed in Wuhan, China and rapidly spread across the globe in a short duration (Wang et al., 2020). World Health Organization (WHO) declared COVID-19 as pandemic after assessing its various

characteristics (WHO, 2020b). As of April 29, 2020, over 3 million cases and over 200,000 deaths due to COVID-19 have been reported across the globe (COVID-19 Tracker [CT], 2020a). In India, the first confirmed case of COVID-19 was reported on January 30, 2020 (WHO, 2020a), a student from Kerala studying in a university in Wuhan (India Today, 2020d)]. As of April 29, 2020, 33,065 confirmed cases and 1,079 deaths due to COVID-19 have been reported in India (CT, 2020b).

According to a daily monitoring report published by WHO, 22,073 healthcare workers across 52 countries have been tested positive for COVID-19 (WHO, 2020c). The report also noted that the number provided may be an underestimation as there is no

<sup>1</sup>Department of Mathematics, Dinabandhu Andrews College, Kolkata, West Bengal, India.

<sup>2</sup>Department of Statistics, Visva-Bharati University, Santiniketan, West Bengal, India.

\*Address correspondence to Sourav Rana, Department of Statistics, Visva-Bharati University, Santiniketan, 731235, West Bengal, India; sourav.rana@visva-bharati.ac.in.

systematic reporting of infections among the health-care workers (WHO, 2020c). Some recent reports from different states of India indicate that a high percentage of COVID-19 transmission is currently occurring due to hospital-based contacts (Economic Times [ET], 2020a; India Today, 2020a; New Delhi Television Ltd [NDTV], 2020a; The Hindu [TH], 2020); The Print (TP, 2020);). The doctors, nurses, and other health workers are most vulnerable as they are in close proximity with COVID-19 patients (ET, 2020a; India Today, 2020a; NDTV, 2020a, 2020b; TP, 2020). Close relatives of notified COVID-19 patients in quarantine centers may also be at risk of getting infection. In addition, the journalists who are continuously visiting hospitals and quarantine centers to get updated reports on COVID-19 may also be at risk of getting infected (India TV, 2020); Scroll.in (SI, 2020). Therefore, a significant percentage of susceptible population in the community may be exposed to COVID-19 infection occurring from the contacts with patients in hospitals and quarantine centers.

Currently there is no vaccine and effective medicine available for COVID-19 in India. Therefore, to break the transmission chain of COVID-19, the government had implemented a full nationwide lockdown (home-quarantined the community) starting from March 25 to April 14, 2020. However, in a large country like India with such diverse and huge population, lockdown all over the nation may not be a very feasible and effective solution. Moreover, a lockdown already has a huge impact on the Indian economy, especially on the short-scale industries (ET, 2020d; India Today, 2020b). To partially overcome this economic crisis as well reducing COVID-19 transmission, Government has proposed some amendments (known as cluster containment strategy) on the lockdown rules from April 20, 2020 (ET, 2020c; Financial Express [FE], 2020b). In these revised rules, the government has provided some relaxation in current rules by dividing different districts of the various states into three zones, namely red (hotspot), orange (limited human movement), and green (economic activity) depending on the number of COVID-19 cases (Business Today, 2020; ET, 2020c; FE, 2020b). However, question remains whether this cluster containment strategy might be successful in reducing COVID-19 transmission or not? If not, then what could be other alternative solutions to reduce COVID-19 transmission? These question can only be answered by studying the dynamics and prediction of a mechanistic mathematical model for COVID-19 transmission and testing the results in real situation

(Moghadas et al., 2020; Tang et al., 2020; Sardar et al., 2020b, 2020a)

In this article, we formulated a mechanistic model on COVID-19 with community as well as hospital-based transmission to study the lockdown effect. We assumed that patients from the hospitals and quarantine centers can only be in contact with a small fraction of the susceptible population from the community. Furthermore, we assume different transmission rates for the community and the hospital-based infection. In the mechanistic model, we have incorporated the lockdown effect through home quarantine of a certain percentage of susceptible population from the community. Using the daily notified COVID-19 cases from six states (Maharashtra, Delhi, Madhya Pradesh, Rajasthan, Gujarat, and Uttar Pradesh) and overall India, we estimated several important parameters of the mechanistic model. Furthermore, we estimated the basic ( $R_0$ ), the community ( $R_C$ ), and the hospital ( $R_H$ ) reproduction numbers for the seven locations under study. To obtain a reliable forecast of future COVID-19 notified cases in the above-mentioned locations, we used a hybrid statistical model that can efficiently capture fluctuations in the daily time series data. A Bayesian model averaging technique based on DRAM algorithm is used to ensemble our mechanistic mathematical model with the hybrid statistical model. Using the ensemble model, we forecast COVID-19 notified cases (daily and cumulative) from May 3 to May 20, 2020, under five different lockdown scenarios in the seven locations. To determine an effective lockdown policy, we carried out a global sensitivity analysis of four epidemiologically measurable and controllable parameters on the lockdown effect (number of cases reduction) and as well as on  $R_0$ .

## 2. METHOD

The mechanistic model we developed in this article is an extension of an SEIR model with additional asymptomatic, hospitalized, and notified and lockdown population (see Fig. 1 and Supporting Information Eqn S1 and S2). We assumed that hospitalized and notified infected population can only be in contact with a small fraction ( $\rho$ ) of the susceptible population from the community (see Fig 1 and Table I). Recently, Lee et al. (2020) showed that the viral load in the symptomatic and the asymptotically infected are similar. Therefore, we assumed that they transmit the disease at the same rate  $\beta_1$  (see Fig. 1 and Table I). We also assumed different

**Table I.** Parameters with Their Respective Epidemiological Information for the Mechanistic ODE Model (see Fig. 1 and Supporting Information) for COVID-19

Parameters	Biological Meaning	Value/Ranges	Reference
$\Pi = \mu \times N(0)$	Recruitment rate of human population	Differs over states	-
$\frac{1}{\mu}$	Average life expectancy at birth	Differs over states	Niti Aayog (2020)
$\beta_1$	Average transmission rate of a symptomatic and asymptomatic COVID-19 infected	(0–500) days	Estimated
$\beta_2$	Average transmission rate of a notified & hospitalized COVID-19 infected	(0–500) days	Estimated
$\rho$	Fraction of the susceptible population that are exposed to hospital-based transmission	0–0.2	Estimated
$\frac{1}{\sigma}$	COVID-19 incubation period	(1–14) days	Estimated
$k$	Fraction of the COVID-19 exposed population that become symptomatic infected	0–1	Estimated
$\gamma_1$	Average recovery rate of symptomatic infection	$(\gamma_3 - 1)\text{day}^{-1}$	Estimated
$\gamma_2$	Average recovery rate of asymptomatic infection	$(\gamma_3 - 1)\text{day}^{-1}$	Estimated
$\tau$	Average hospitalization rate for the COVID-19 symptomatic individuals	$(0-1)\text{day}^{-1}$	Estimated
$\delta$	Average death rate due to COVID-19 infection in hospital	Differs over states	CT (2020b)
$\gamma_3$	Average recovery rate of the notified & hospitalized populations	Differs over states	CT (2020)
$l$	Average lockdown rate	$(0-0.9)\text{day}^{-1}$	Estimated
$\frac{1}{\omega}$	Current lockdown period in India	40 days	TOI (2020); FE (2020a)

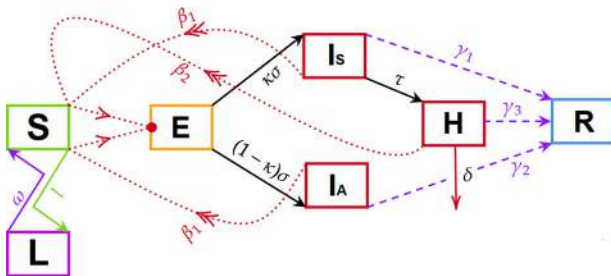


**Fig 1.** A Flow diagram of the mechanistic ODE model with hospital-based COVID-19 transmission and lockdown effect. Different class of population shown in this figure are S: Susceptible population; E: Exposed population;  $I_S$ : COVID-19 symptomatic infected population;  $I_A$ : COVID-19 asymptomatic infected population; H: Notified & Hospital individuals suffering from COVID-19 infection; R: COVID-19 recovered population; and L: Home quarantined susceptible population during lockdown, respectively. Two arrows from  $I_S$ ,  $I_A$ , and H to S represent that susceptible population can get infection in contact with these populations ( $I_S$ ,  $I_A$ , and H), whereas a single arrow from S to E represents the flow of new infection from susceptible to the exposed class. Epidemiological information of the parameters shown in this figure are provided in Table I.

transmission rates ( $\beta_1$  and  $\beta_2$ , respectively) for community and hospital-based infection. As it is very difficult to detect asymptotically infected in the community therefore, we assumed that only a fraction of symptomatically infected population was being noti-

fied and hospitalized by COVID-19 testing at a rate,  $\tau$  (see Fig. 1 and Table I). The disease related deaths are considered only for the notified and hospitalized population at a rate  $\delta$ . We incorporated lockdown effect in our model (see Fig. 1 and Supporting Information Eqn S2) by home quarantined a fraction of susceptible population at a rate  $l$ . We also assumed that after the current lockdown period ( $\frac{1}{\omega} = 40$  days) the home quarantined individuals will return to the general susceptible population (see Fig. 1 and Supporting Information Eqn S2) that is, this class of individuals do not contribute in disease transmission. A flow diagram and the information on our mechanistic ODE model parameters are provided in Fig. 1 and Table I, respectively.

The mechanistic ODE model (see Fig. 1 and Supporting Information Eqn S1 and S2) we are using for this study may be efficient in capturing overall trend of the time-series data and the transmission dynamics of COVID-19. However, as solution of the ODE model is always smooth therefore, our mechanistic model may not be able to capture fluctuations occurring in the daily time-series data. Several complex factors like lockdown, symptomatic, asymptomatic,

hospital transmission, awareness, rapid testing, preventive measures, and so on may influence the variations in daily COVID-19 time-series data. Therefore, it is an extremely challenging job to fit and long-term forecast using this daily time-series data. To resolve this issue, we considered a hybrid statistical model, which is a combination of five forecasting models namely, auto-regressive integrated moving Average model (ARIMA); exponential smoothing state space model (ETS); theta method model (THETAM); exponential smoothing state space model with box-cox transformation, ARMA errors, trend and seasonal components (TBATS); and neural network time series forecasts (NNETAR). Finally, the hybrid statistical model and the mechanistic ODE model (see Fig. 1 and Supporting Information Eqn S1 and S2) are combined together by a post-processing Bayesian model averaging (BMA) technique, which we discussed later in the article.

We used daily confirmed COVID-19 cases from Maharashtra (MH), Delhi (DL), Madhya Pradesh (MP), Rajasthan (RJ), Gujarat (GJ), Uttar Pradesh (UP) and overall India (IND) for the time period March 14–April 14, 2020 (MH), March 14–April 18, 2020 (DL), March 20–April 17, 2020 (MP), March–April 18, 2020 (RJ), March 19–April 16, 2020 (GJ), March 14–April 18, 2020 (UP), and March 2–April 19, 2020 (IND) for our study. As of April 29, 2020, these referred six states contribute to 74% of the total COVID-19 notified cases in India (CT, 2020b). Confirmed daily COVID-19 cases from the mentioned seven locations are collected from CT (2020b). State-wise population data are taken from The Unique Identification Authority of India (UIDAI) (2020).

We estimated several epidemiologically important parameters (see Table I) by calibrating our mathematical model (see Fig. 1 and Supporting Information Eqn S1 and S2) to the daily notified COVID-19 cases from the seven locations. As some initial conditions of our mathematical model (see Fig. 1 and Supporting Information Eqn S1 and S2) are also unknown therefore, we prefer to estimate these initial conditions from the data (see Supporting Information Table S1). In lockdown 1.0, the Indian government implemented a 21 days nationwide full lockdown (home quarantined the community) starting from March 25–April 14, 2020 (ET, 2020b) and then extend the lockdown period up to May 2, 2020 (lockdown 2.0) (Times of India [TOI], 2020); FE, 2020a). Therefore, the daily COVID-19 time series data contain the effect of with and without lockdown scenario,

therefore, we prefer to use a combination of two mathematical models (without and with lockdown) for calibration. An elaboration on the combination technique of the mathematical models without and with lockdown is provided below:

- We first use the mechanistic model without lockdown (see Eqn S1 in Supporting Information) starting from the first date of the daily COVID-19 data up to end of March 24, 2020 for the seven locations MH, DL, MP, RJ, GJ, UP, and IND, respectively.
- Using values of the state variables of the model without lockdown (see Eqn S1 in Supporting Information method) onset of March 24, 2020 as initial condition, we run the mechanistic model with lockdown (see Fig. 1 and Model S2 in Supporting Information) up to the end date of the daily COVID-19 data for the mentioned seven locations.

The nonlinear least square function “lsqnonlin” in the MATLAB-based optimization toolbox is called to fit the simulated and observed daily COVID-19 notified cases in the seven locations mentioned earlier. Bayesian-based “DRAM” algorithm (Haario et al., 2006) is used to sample the epidemiologically unknown parameters and initial conditions (see Table II and Table S1 in Supporting Information) of the mathematical models combination without and with lockdown (see Fig. 1 and Supporting Information Eqn S1 and S2). The details on mechanistic model fitting are provided in Sardar and Saha (2017).

Calibration of the hybrid statistical model for the mentioned seven states is done using the R package “forecastHybrid” (Shaub & Ellis, 2020). First, we fitted the individual models ARIMA, ETS, THETAM, TBATS, and NNETAR by calling the functions “auto.arima,” “ets,” “thetam,” “tbats,” and “nneta,” respectively. The results generated from each of the above models are combined with equal weights to determine the hybrid statistical model. Equal weight among the five individual models is taken as it generates a robust result (see Table S3 in Supporting Information) for the hybrid statistical model (Lemke & Gabrys, 2010).

Post-processing Bayesian model averaging technique for combining the mechanistic model (see Fig. 1 and Supporting Information S1 and S2) and the hybrid statistical model is based on “DRAM” algorithm (Haario et al., 2006). Let  $Y^{ODE} = \{y_j^{ODE}\}_{j=1}^n$  and  $Y^{HBD} = \{y_j^{HBD}\}_{j=1}^n$  be  $n$  simulated

**Table II.** Estimated Parameters of the Mechanistic ODE Model Combinations (see Fig. 1 and Supporting Information). Respective Subscripts are MH: Maharashtra, DL: Delhi, MP: Madhya Pradesh, RJ: Rajasthan, GJ: Gujarat, UP: Uttar Pradesh, and IND: India. All Data are Given in the Format Estimate (95% CI)

Region	$\beta_1$	$\beta_2$	$\rho \times 100$	$\sigma$	$k$	$\gamma_1$	$\tau \times 100$	$\gamma_2$	$l \times 100$
MH	2.03 (1.05–2.75)	21.6 (2.6–54.7)	7.98 (0.24–9.78)	0.163 (0.073–0.196)	0.118 (0.03–0.165)	0.963 (0.144–0.974)	5.05 (2.76–85.3)	0.863 (0.341–0.991)	61.5 (2.51–97.3)
DL	1.83 (0.557–3.54)	220.2 (12.97–488.8)	7.66 (0.25–9.67)	0.211 (0.075–0.748)	0.039 (0.002–0.039)	0.96 (0.321–0.987)	8.5 (3.8–96.3)	0.764 (0.328–0.988)	70.8 (13.1–87.8)
MP	1.45 (1.04–2.91)	42.1 (25.4–486)	5.88 (0.24–9.72)	0.194 (0.073–0.242)	0.014 (0.002–0.098)	0.827 (0.141–0.980)	14 (3.52–92.2)	0.585 (0.21–0.978)	34.8 (12.7–88.6)
RJ	1.16 (0.557–2.74)	325.6 (3.71–484)	1.33 (0.07–9.56)	0.937 (0.148–0.949)	0.0011 (0.001–0.003)	0.337 (0.253–0.988)	23.2 (4.66–96.3)	0.814 (0.244–0.978)	21 (10.6–81.2)
GJ	0.90 (0.53–2.10)	186.3 (9.64–490)	2.32 (0.21–9.20)	0.54 (0.101–0.94)	0.028 (0.01–0.092)	0.84 (0.15–0.98)	14 (4.02–76.2)	0.52 (0.202–0.98)	11.4 (2.31–32.2)
UP	0.53 (0.52–1.92)	242 (8.23–353)	4.29 (0.1–9.51)	0.66 (0.078–0.71)	0.12 (0.077–0.95)	0.78 (0.19–0.988)	2.38 (0.2–5)	0.408 (0.218–0.982)	48.9 (12.3–87.6)
IND	2.25 (1.29–3.24)	499 (494–499.8)	8.99 (0.32–9.70)	0.098 (0.072–0.15)	0.35 (0.07–0.96)	0.72 (0.38–0.99)	0.23 (0.03–0.53)	0.995 (0.25–0.9959)	76.6 (35.5–89.2)

observations from our mechanistic ODE model and the hybrid statistical model, respectively, and let  $\hat{Y} = \{y_j^{obs}\}_{j=1}^n$  be  $n$  observation from the data. Then

$$Y^E = \omega_1 Y^{ODE} + \omega_2 Y^{HBD}, \quad (1)$$

is our ensemble model, where the weights  $\omega_1$  and  $\omega_2$  satisfy the constraints

$$\Delta = \{\omega_1, \omega_2 \geq 0 : \omega_1 + \omega_2 = 1\}.$$

We assume  $\omega_1$  and  $\omega_2$  follows Gaussian proposal distribution. Then the error sum of square function (Haario et al., 2006) is defined as:

$$SS(\tilde{\theta}) = \sum_{i=1}^n (\hat{Y} - Y^E(\tilde{\theta}))^2$$

Posterior distribution of the weights  $\tilde{\theta} = (\tilde{\omega}_1, \tilde{\omega}_2)$  for the ensemble model (1) is generated using Bayesian-based “DRAM” algorithm (Haario et al., 2006) (see Table S2 and Fig. S23–S29 in Supporting Information).

To save the countries short-scale industries and the agricultural sectors, the Indian government has proposed some amendments on current lockdown rules from April 20, 2020 (ET, 2020c; FE, 2020b). In these revised rules, Government has provided some relaxation in current rules by dividing different districts of the various states into three red (hotspot), orange (limited human movement), and green (economic activity) zones depending on the number of COVID-19 cases (BT, 2020; ET, 2020c; FE, 2020b). Implementation of these new rules in our mechanistic models combination (see Fig. 1 and Supporting Information Eqn S1 and S2) are based on the following assumptions:

- Lockdown rule will be relaxed from April 20, 2020 in those states where the current estimate of the lockdown rate (see Table II) is higher than a threshold value. This relaxation in lockdown is based on the fact that locations where lockdown are strictly implemented before April 20, 2020 are likely to have more impact on the economic growth.
- Lockdown rule will be more intensive from April 20, 2020 in those states where the current estimate of the lockdown rate (see Table II) is below a threshold value. This assumption is made because locations where lockdown is not implemented properly before April 20, 2020 are likely to have more red (hotspot) zones.

- Note that 50% lockdown success is taken as the threshold value for our study. Here, 50% lockdown success in Delhi means that 50% of the susceptible population in this state is successfully home-quarantined during the period March 25–April 20, 2020.
- Insensitivity and relaxation in lockdown are measured in a same scale namely 10%, 20%, and 30% increment or decrement on the current estimate of lockdown rate (see Table II).

Following the above assumptions and using our ensemble model (1), we provided a forecast of notified COVID-19 cases (daily and cumulative) for the seven locations during May 3–May 20, 2020. As COVID-19 notified cases are continuously rising in the mentioned seven locations therefore, it is more likely that lockdown period will be extended beyond May 3, 2020. Therefore, forecast using the ensemble model (1) during the mentioned time duration in those seven locations are based on the following scenarios:

(A1) Using our mechanistic models combination (see Fig. 1 and Supporting Information Eqn S1 and S2) and the current estimate of the lockdown rates (see Table II), we forecast notified COVID-19 cases up to May 20, 2020. This forecast is combined together with the results obtain from the hybrid statistical model by using our ensemble model (1).

(A2) Using our mechanistic models combination (see Fig. 1 and Supporting Information Eqn S1 and S2) and the current estimate of the lockdown rates (see Table II), we forecast notified COVID-19 cases up to April 20, 2020. From April 21–May 20, 2020, forecast are made using 10% increment or decrement (depending on the state) in the estimate of current lockdown rate.

This forecast is combined together with the results obtain from the hybrid statistical model by using our ensemble model (1).

(A3) We followed same procedure as scenario (A2) with 20% increment or decrement (depending on the state) in the estimate of current lockdown rate from April 21–May 20, 2020 to obtain the forecast for the mentioned time duration.

(A4) In this case also, we followed same procedure as scenario (A2) with 30% increment

or decrement (depending on the state) in the estimate of current lockdown rate from April 21–May 20, 2020 to obtain the forecast for the mentioned time duration.

(A5) We followed same procedure as the scenario (A1) up to May 2, 2020. Forecast for the time period May 3–May 20, 2020 are made with no lockdown.

As, we assumed that lockdown individuals do not mixed with the general population therefore, the basic reproduction number ( $R_0$ ) with and without lockdown (see Fig. 1 and Supporting Information Eqn S1 and S2) are equal (Van den Driessche & Watmough, 2002):

$$R_0 = \frac{\beta_1 k \sigma}{(\mu + \sigma)(\gamma_1 + \mu + \tau)} + \frac{\beta_1 (1 - k) \sigma}{(\mu + \gamma_2)(\mu + \sigma)} + \frac{\beta_2 k \rho \sigma \tau}{(\mu + \sigma)(\delta + \gamma_3 + \mu)(\gamma_1 + \mu + \tau)}$$

In the expression of  $R_0$ , sum of first two term indicate the community infection occurring from symptomatically and asymptotically infected population. The third term in  $R_0$  specifies the hospital-based COVID-19 transmission. To distinguish the community and hospital-based COVID-19 transmission, we defined the community reproduction number ( $R_C$ ), and the hospital reproduction number ( $R_H$ ) as follows:

$$R_C = \frac{\beta_1 k \sigma}{(\mu + \sigma)(\gamma_1 + \mu + \tau)} + \frac{\beta_1 (1 - k) \sigma}{(\mu + \gamma_2)(\mu + \sigma)}$$

and

$$R_H = \frac{\beta_2 k \rho \sigma \tau}{(\mu + \sigma)(\delta + \gamma_3 + \mu)(\gamma_1 + \mu + \tau)}$$

Using estimated values of epidemiologically unknown parameters (see Table II), we estimated  $R_0$ ,  $R_C$ , and  $R_H$  for the mentioned seven locations.

The effective reproductive number ( $R_T$ ) indicates the average number of secondary cases produced per infected person in a population made up of both susceptible and nonsusceptible hosts (Rothman et al., 2008).  $R_T$  provides information about the severity of a disease over different time points and plays a vital role in control measures (Sardar et al., 2015). For example,  $R_T > 1$  signifies that number of new incidences has an increasing trend, whereas  $R_T = 1$  implies the disease become endemic in the population, and  $R_T < 1$  signifies that number of new cases will have a decreasing trend. We estimated  $R_T$  using our ensemble model (1) projected COVID-19 new

cases data under two lockdown scenarios (A1 and A5) during the period April 21–May 20, 2020 by using the following equation derived from the renewal equation of a birth process (Pinho et al., 2010; Sardar et al., 2015):

$$R_T = \frac{b(t)}{\int_{a=0}^{\infty} b(t-a)g(a) da}, \quad (2)$$

where, the term  $b(t)$  corresponds to the number of new cases at the  $t$ th day and the term  $g()$  is the generation interval distribution for a disease. We derive the expression of the generation interval distribution  $g(t)$  from the COVID-19 mechanistic model (see Fig. 1 and Eqn S2 in Supporting Information) by applying the method discussed in (Pinho et al, 2010; Wallinga and Lipsitch, 2007). The rates of leaving the exposed and infectious compartments are indicated by  $b_1, b_2, b_3$  and  $b_4$ . These quantities are constant and extracted from our model (see Fig. 1 and Eq S2 in Supporting Information) as  $b_1 = \mu + \sigma$ ,  $b_2 = \mu + \gamma_1 + \tau$ ,  $b_3 = \mu + \gamma_2$ , and  $b_4 = \mu + \gamma_3 + \delta$ . Moreover, the generation interval distribution is the convolution of four exponential distributions with a mean  $M = \frac{1}{b_1} + \frac{1}{b_2} + \frac{1}{b_3} + \frac{1}{b_4}$ . Following (Akkouchi, 2008; Pinho et al., 2010), the expression for the convolution is provided below:

$$g(t) = \sum_{i=1}^4 \frac{b_1 b_2 b_3 b_4 \exp(-b_i t)}{\prod_{j=1, j \neq i}^4 (b_j - b_i)} \quad (3)$$

with  $t \geq 0$ . The validity of the above relation (3) holds for a minimum threshold value of the force of infection  $\Lambda$ , defined as  $\Lambda > \min(-b_1, -b_2, -b_3, -b_4)$  (Pinho et al., 2010; Wallinga & Lipsitch, 2007).

Constructing an effective policy on future lockdown in a region will require some relation between effect of lockdown (number of COVID-19 case reduction) with some important epidemiologically measurable and controllable parameters. Our mechanistic ODE model (see Fig. 1 and Supporting Information Eqn S2) has several important parameters and among them measurable and controllable parameters are  $\beta_2$ : average rate of transmission occurring from hospitalized and notified contacts (it can be controllable by following WHO guidelines);  $\rho$ : fraction of susceptible population from the community that are exposed to notified and hospitalized contacts (it also can be minimized by following proper guidelines from WHO);  $\kappa$ : fraction of infected that are symptomatic (rapid COVID-19 test-

ing can provide an accurate estimate);  $\tau$ : notification and hospitalization rate of symptomatic infected population (it also depend on number of COVID-19 testing). We perform a global sensitivity analysis (Marino et al., 2008) to determine the effect of these parameters on the lockdown effect and on the basic reproduction number ( $R_0$ ), respectively. The effect of lockdown is measured in terms of differences in the total number of COVID-19 cases that occurred during May 3–May 20, 2020 under the lockdown scenarios (A1) and (A5), respectively. We draw 500 samples from the biologically feasible ranges of the mentioned four parameters (see Table I) using Latin hypercube sampling (LHS) technique. Other epidemiologically known and unknown parameters during simulation of the mechanistic model are taken from Table I and Table II, respectively. Partial rank correlation coefficients (PRCC) and its corresponding  $p$ -value are evaluated to determine the effect of these mentioned four parameters on the lockdown effect and the basic reproduction number ( $R_0$ ), respectively.

### 3. RESULTS AND DISCUSSION

Testing of the three models (the mechanistic ODE model, the hybrid statistical model, and the ensemble model) on daily notified COVID-19 cases from MH, DL), MP, RJ, GJ, UP, and IND are presented in Fig. 2. Based on the performance on testing data from the seven locations, we estimated the weights ( $w_1$  and  $w_2$ ) for our ensemble model (1) (see Table S2 in Supporting Information). Our result suggest that the mechanistic ODE model (see Fig. 1 and Supporting Information Eqn S1 and S2) displayed a better performance in RJ, UP, and IND compared to the hybrid statistical model (see Table S2 in Supporting Information). For rest of the locations (MH, DL, MP, and GJ), the hybrid statistical model has performed better than the mechanistic ODE model in terms of capturing the trend of the time-series data (Table S2 in Supporting Information). The ensemble model (1), which is derived from a combination of the mechanistic ODE and the hybrid statistical model respectively, has provided a robust result in all of these mentioned seven locations in terms of capturing time-series data trend (see Fig. 2).

The estimates of different parameters of the mechanistic ODE model (Fig. 1 and Supporting Information Eqn S1 and S2) suggests that currently in the seven locations (MH, DL, MP, RJ, GJ, UP, and IND) the community infection is mainly dominated

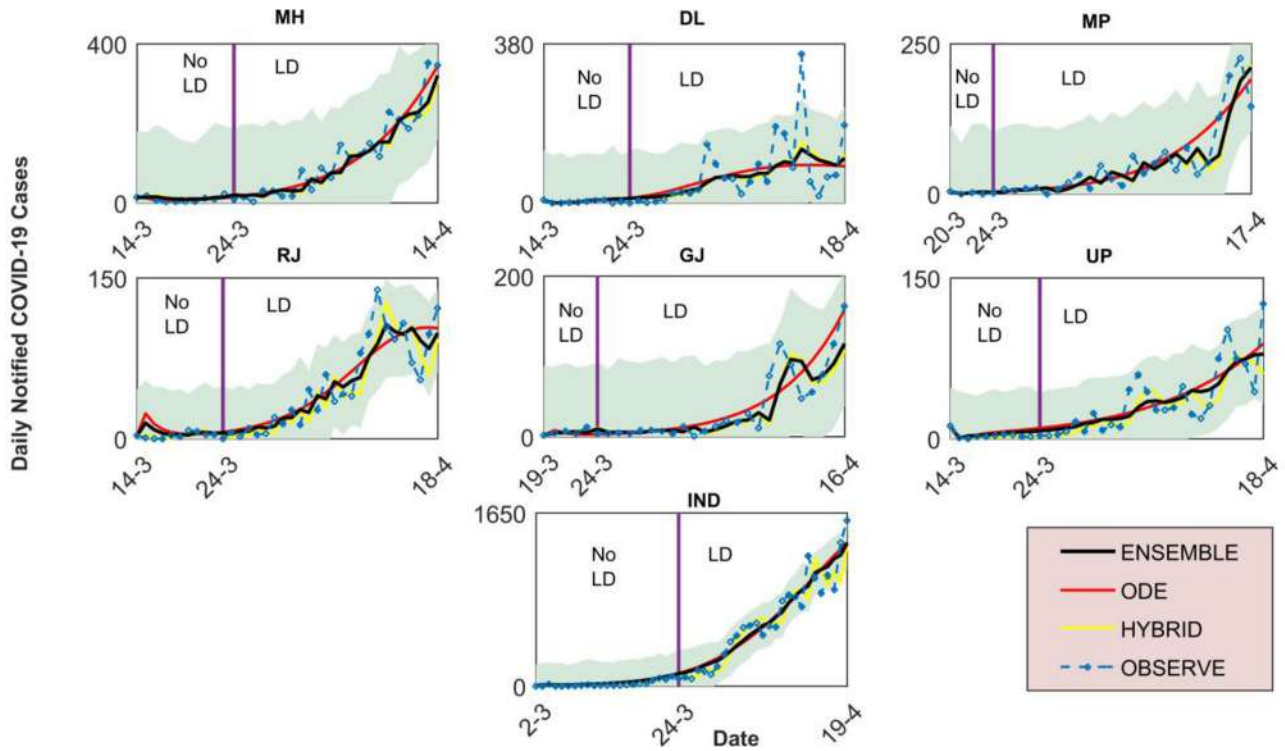


**Fig 2.** Combination of mechanistic ODE models (Fig. 1 and Supporting Information), Hybrid statistical model, and Ensemble model (1) fitting to the daily notified COVID-19 cases form six different states and overall India. Respective subscripts are MH : Maharashtra, DL : Delhi, MP : Madhya Pradesh, RJ : Rajasthan, GJ : Gujarat, UP : Uttar Pradesh, and IND : India. Here, LD indicate the period after the lockdown implementation in overall India started at 25/03/2020 and No LD specifies the period before lockdown. Lockdown effect is considered only for the mechanistic ODE model (Fig. 1 and Supporting Information) and consequently in the ensemble model (1). Shaded area specifies the 95% confidence region.

by contribution from the asymptotically infected population (Table II). Among the seven locations, the lowest percentage of symptomatic infection in the community is found in RJ (about 0.1%) and the highest percentage is found in IND (about 35%) (Table II). Our estimates suggest that currently in the seven locations, the notification and hospitalization rate of symptomatically infected population is about 0.2–23 % (Table II). Therefore, most of the COVID-19 infections in the seven mentioned locations are currently undetected. Our result agrees with the recent report by the Indian Council of Medical Research (ICMR) (India Today, 2020c). Our estimates of the lockdown rate for the mentioned seven locations, suggest that lockdown is properly implemented in the two metro cities DL and MH. Also, in overall India (IND) lockdown is properly implemented. In these three locations (MH, DL, and IND), about 61–77% of the total susceptible population may be successfully home quarantined during the present lockdown period (Table II). However, for rest of the lo-

cations, our results suggest that lockdown may not be successful as about 11–49% of the total susceptible population may be isolated (home quarantined) during the current lockdown period in MP, RJ, GJ, and UP, respectively (Table II). In the seven locations, we found that about 1–9% of the total susceptible populations may be exposed to hospital (notified and hospitalized population) related contacts (Table II). Considering the fact that estimates of the average hospital-based transmission rates for the seven locations are very high (Table II), therefore, a significant amount of COVID-19 infection in these seven locations may be currently occurring due to notified and hospitalized infected related contacts. These findings can be further justified by analyzing the estimates of the basic ( $R_0$ ), community ( $R_C$ ) and hospitalized ( $R_H$ ) reproduction numbers for the mentioned seven locations (see Table III). Except for the RJ, in the remaining six locations, we found that about 1–16% of the total COVID-19 transmission currently occurring is from notified and hospitalized infected



**Table III.** Estimates of the Basic, the Community and the Hospital Reproduction Numbers. The Epidemiologically Known and Unknown Parameters of the Mechanistic ODE model (see Fig. 1 and Supporting Information) During the Estimation of the Different Reproduction Numbers are Taken from Table I and Table II, Respectively. Respective Subscripts MH, DL, MP, RJ, GJ, UP, and IND are same as Table II. All Data are Given in the Format Estimate (95% CI)

Region	$R_0$	$R_C$	% $R_0$	$R_H$	% $R_0$
MH	2.371 (2.095–4.005)	2.309 (1.542–3.894)	97.37 (55.46–99.93)	0.0623 (0.0019–1.254)	2.63 (0.1–44.54)
DL	2.54 (1.37–5.52)	2.37 (0.934–5.49)	93.46 (56.91–99.95)	0.1658 (0.0016–0.8236)	6.53 (0.048–43.09)
MP	2.497 (2.21–6.11)	2.467 (1.68–5.63)	98.82 (49.22–99.81)	0.0296 (0.0062–2.045)	1.18 (0.19–50.78)
RJ	1.43 (1.42–3.78)	1.42 (1.405–3.76)	99.46 (94.40–100)	0.01 (0–0.068)	0.54 (0–3.66)
GJ	1.835 (1.51–4.86)	1.706 (0.895–3.72)	93.02 (31.4–99.56)	0.128 (0.0083–2.68)	6.98 (0.43–68.60)
UP	1.46 (1.35–3.14)	1.22 (0.787–2.88)	84 (39.21–99.96)	0.233 (0.001–1.47)	16 (0.039–60.79)
IND	2.81 (2.15–4.94)	2.56 (1.92–4.86)	91.28 (84.63–99.84)	0.245 (0.0048–0.388)	8.72 (0.16–15.37)

related contacts (see Table III). These figures can be increased up to 69% if proper measures are not taken in MH, DL, MP, GJ, UP, and IND, respectively, (see Table III). This is a worrisome situation as higher value of the hospital-based transmission rate in these six locations (Table II) indicates that there may be super-spreading incidents occurring from hospital-based contacts. In RJ, low contribution of  $R_H$  on  $R_0$  (see Table III) may be due to existence of low percentage of the symptomatically infected population in the community (Table II) and that leads to low percentage of notified and hospitalized COVID-19 cases.

For further investigation on super-spreading events, we carried a global uncertainty and sensitivity analysis of some epidemiologically measurable and controllable parameters from our mechanistic ODE model (Fig. 1 and Supporting Information Eqn S1 and S2) namely,  $\beta_2$  : average rate of transmission occurring from notified and hospitalized based contact (it can be controllable following the WHO guidelines (Europe World Health Organization [EWHO], 2020),  $\rho$  : fraction of susceptible population that are exposed to hospital-based contact (it can be reduced by following proper guidelines from the WHO (EWHO, 2020),  $\kappa$  : fraction of the newly infected that are symptomatic (Rapid COVID-19 testing can provide an accurate estimate),  $\tau$  : hospitalization and notification rate of symptomatic infected population (it also depend on number of COVID-19 testing) on the basic reproduction number ( $R_0$ ). Partial rank correlation coefficients (PRCC) and its corresponding  $p$ -

value suggested that all these four parameters have significant positive correlation with  $R_0$  (see Fig. 6 and Fig. S17 to Fig. S22 in Supporting Information). Furthermore, high positive correlation of  $\rho$  on  $R_0$  indicate that small increase in the percentage of susceptible population from the community that are exposed hospital-based transmission will lead to significant increase in COVID-19 infection. Considering the fact that estimated value of  $\beta_2$  (see Table II) in the seven locations are very high (much higher than community transmission rate), therefore, a small increase in  $\rho$  may leads to a larger COVID-19 outbreak in those seven locations. Therefore, until and otherwise any preventive measures are taken in these locations, a larger COVID-19 outbreak may trigger from hospitals and quarantine centers.

Using the ensemble model (1), we forecast daily as well as total COVID-19 cases under five different lockdown scenarios in the mentioned seven locations, from May 3–May 20, 2020, (see Fig. 3, Table IV and Fig. S1 to Fig. S6 in Supporting Information). Spatial distribution of the projected COVID-19 cases under different lockdown scenarios in the six states of India during the mentioned projection period are provided in Fig. 4 and Fig. S7–S10 in Supporting Information. Comparing the projected total COVID-19 cases during May 3–20, 2020, (see Table IV) with the total observed cases (CT, 2020b) during March 2–April 29, 2020, we found about double increase in the total cases in MH, MP, GJ, UP, and IND, respectively. In summary, our forecast result suggest that in the coming two weeks a significant

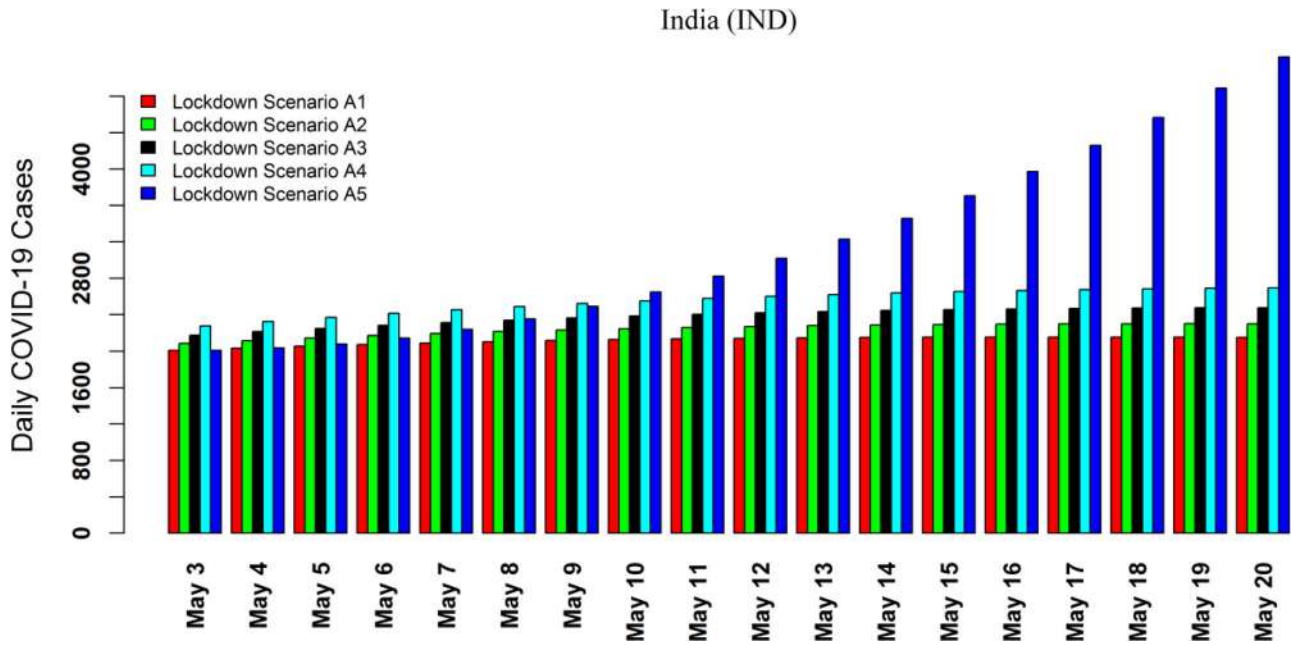


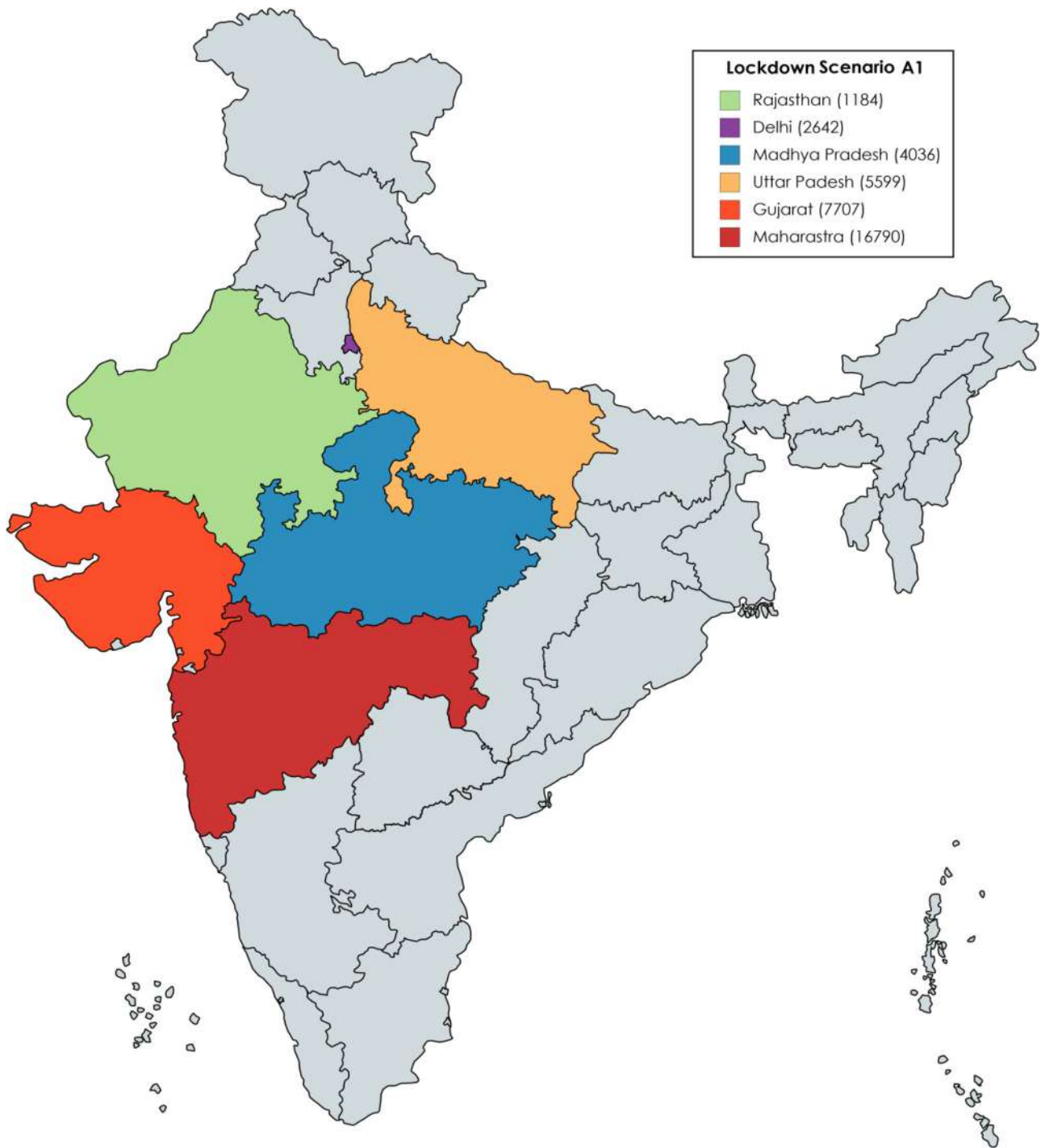
**Fig 3.** Ensemble model (1) forecast for the daily notified COVID-19 cases in India during May 3–May 20, 2020 under five different lockdown scenarios. Under lockdown scenarios (A2)–(A4), projections are made with 10%, 20%, and 30% decrement in the current estimate of the lockdown rate, respectively (see Table II). In lockdown scenario (A1), projections are made with current estimated lockdown rate (see Table II). Finally, in the lockdown scenario (A5), projections are made with no lockdown during May 3–May 20, 2020.

increase in cases may be observed in most of these locations.

Estimation of the effective reproduction number ( $R_T$ ) under two lockdown scenarios (A1 and A5) for the seven locations during the period April 21–May 20, 2020 (see Fig. 5 and Fig. S11 to Fig. S16 in Supporting Information) suggest that except for RJ, all other six locations the cases will increase with or without lockdown ( $R_T > 1$ ). However, in RJ, values of  $R_T$  were found to be below unity under lockdown scenario (A1) and found to be greater than unity (After May 18, 2020) under lockdown scenario (A5) (see Fig. S14 in Supporting Information). Therefore, if the current lockdown rate is maintained after April 21, 2020 then COVID-19 cases in RJ may gradually decrease in the coming days.

To determine which epidemiologically measurable and controllable parameters are most influencing, we carried out a global uncertainty analysis of  $\beta_2$ ,  $\rho$ ,  $\kappa$ , and  $\tau$  on the lockdown effect. The lockdown effect is measured in terms of differences in the total number of COVID-19 cases during May 3–May 20, 2020, in the seven locations under the lockdown scenarios (A1) and (A5), respectively (see Section 2 for details). For MH, PRCC and its corresponding  $p$ -value suggested that all these four pa-

rameters have significant influence on the lockdown effect (see Fig. S17 in Supporting Information). Furthermore, significant negative correlation of  $\beta_2$ , and  $\rho$  with the lockdown effect (see Fig. S17 in Supporting Information) suggested that only home quarantined the community may not be sufficient to reduce COVID-19 transmission in MH. Government and the policymakers may also have to focus on reducing the transmission occurring from hospital premises based on the guidelines from the WHO (EWHO, 2020). For DL, PRCC and its corresponding  $p$ -value suggested that  $\beta_2$ ,  $\rho$ , and  $\kappa$  are the main parameters that are influencing the lockdown effect (see Fig. S18 in Supporting Information). Moreover, significant negative correlation of  $\beta_2$  and  $\rho$  with the lockdown effect and as well as significant positive correlation of  $\kappa$  with the lockdown effect (see Fig. S18 in Supporting Information) implies that an effective lockdown policy in DL may be a combination of lockdown in the community, contact tracing of COVID-19 cases, and with some effort in reducing hospital-based transmission following WHO guidelines (EWHO, 2020). For MP, PRCC and its corresponding  $p$ -value suggested that  $\kappa$  and  $\tau$  have high positive correlation with the lockdown effect (see Fig. S19 in Supporting Information). Furthermore,



Created with mapchart.net ©

**Fig 4.** Spatial distribution of total number of COVID-19 cases during May 3, 2020 till May 20, 2020 in the six states namely, Maharashtra (MH), Delhi (DL), Madhya Pradesh (MP), Rajasthan (RJ), Gujarat (GJ), and Uttar Pradesh (UP), under the lockdown scenario (A1). We used the following color clustering of the cases: Green (1,000–1,500), Purple (1,501–3,000), Blue (3,001–5,000), Yellow (5,001–7,000), Orange (7,001–12,000), and Red (12,001–24,000).

**Table IV.** Ensemble Model (1) Forecast of the Total Notified COVID-19 Cases During May 3–May 20, 2020. Respective Subscripts MH, DL, MP, RJ, GJ, UP, and IND are same as Table II. Regions Where, Current Lockdown Rate ( $\downarrow$ ) implies the Ensemble Model (1) Projections for the Scenarios (A2) to (A4) with 10%, 20% and 30% Decrement in the Current Estimate of Lockdown Rate (see Table II) during the Mentioned Period, whereas Current Lockdown Rate ( $\uparrow$ ) Implies the Ensemble Model (1) Projections for the Scenarios (A2) to (A4) with 10%, 20% and 30% Increment in the Current Estimate of Lockdown Rate (see Table II) During the Mentioned Period.

Scenario (A1) Implies the Ensemble Model (1) Forecast with the Current Estimate of the Lockdown Rate (see Table II) During May 3–May 20, 2020. Finally, Scenario (A5) Implies the Ensemble Model (1) Forecast with no Lockdown During May 3–May 20, 2020. All Data are Provided in the Format Estimate (95% CI)

Region	Current lockdown rate	Scenario A1	Scenario A2	Scenario A3	Scenario A4	Scenario A5
MH	$\downarrow$	16,790 (16,056–18,727)	17,410 (16,499–19,812)	18,147 (17,026–21,101)	19,036 (17,662–22,656)	23,000 (20,499–29,596)
DL	$\downarrow$	2,642 (1,791–3,294)	1,840 (1,337–3,297)	2,693 (1,901–3,300)	2,729 (1,979–3,304)	2,886 (2,319–3,320)
MP	$\uparrow$	4,036 (3,599–4,578)	3,924 (3,531–4,410)	3,825 (3,472–4,263)	3,738 (3,419–4,134)	5,058 (4,216–6,101)
RJ	$\uparrow$	1,184 (654–1,624)	1,156 (611–1,608)	1,133 (576–1,595)	1,114 (547–1,585)	1318 (858–1,699)
GJ	$\uparrow$	7,707 (7,689–12,589)	7,444 (7,427–11,991)	7,206 (7,191–11,451)	6,990 (6,976–10,961)	9,337 (9,316–16,292)
UP	$\uparrow$	5,599 (3,656–6,478)	5,383 (3,564–6,206)	5,184 (3,479–5,954)	4,999 (3,401–5,722)	7,217 (4,343–8,517)
IND	$\downarrow$	38,134 (36,550–45,296)	40,278 (38,877–46,612)	42,824 (41,640–48,174)	45,896 (44,975–50,059)	57,159 (56,971–57,201)

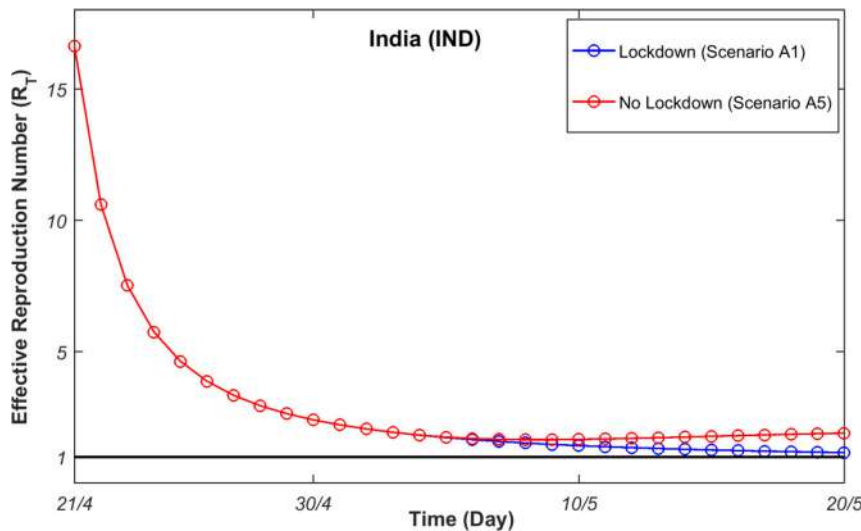
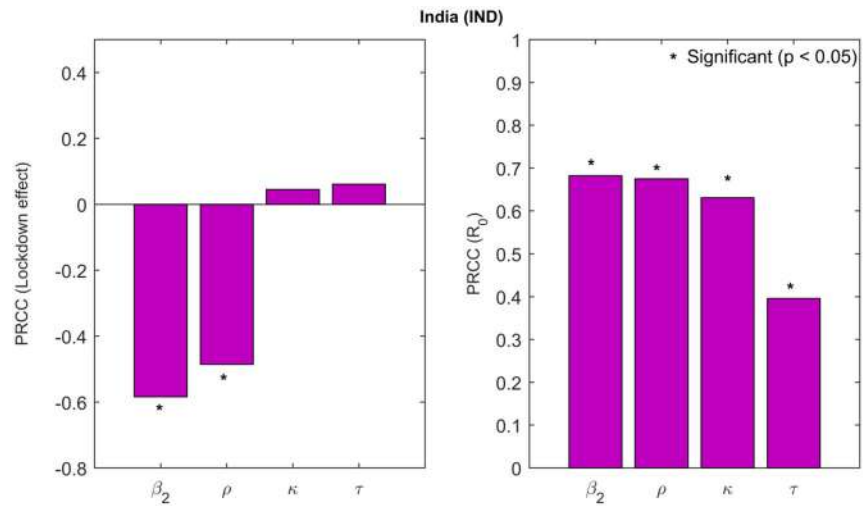


**Fig 5.** Effective reproduction number ( $R_T$ ) under two lockdown scenarios (A1 and A5) for the period April 21–May 20, 2020 for India.

$\rho$  has significant negative correlation with the lockdown effect (see Fig. S19 in Supporting Information). Therefore, an effective lockdown policy in MP may be a strict implementation of lockdown in the red and orange zones, rapid COVID-19 testing in the community and reducing hospital-based transmission by following guidelines from WHO (EWHO, 2020). For RJ, PRCC and its corresponding  $p$ -value suggested that only  $\kappa$  has a significant positive correlation with the lockdown effect (see Fig. S20 in Supporting In-

formation). No significant correlation with hospital-based parameters may be due to existence of low percentage of the symptomatically infected population in the community (see Table II) and that leads to low percentage of notified and hospitalized based COVID-19 transmission. Therefore, RJ Government may focus more on contact tracing in the community with relaxation given in the Green and Orange zones to increase the percentage of symptomatically infected in the community. For GJ, PRCC and its cor-

**Fig 6.** Effect of uncertainty of four epidemiologically measurable and controllable parameters of the mechanistic ODE model (see Fig. 1, Table I and method section) on the effect of lockdown and the basic reproduction number ( $R_0$ ). Lockdown effect is measured in terms of the differences in total number of COVID-19 cases occurred during May 3–May 20, 2020 in India under the lockdown scenarios (A1) and (A5), respectively (see method section). Effect of Uncertainty of these four parameters on the two mentioned responses are measured using Partial Rank Correlation Coefficients (PRCC). 500 samples for each parameter were drawn using Latin hypercube sampling techniques (LHS) from their respective ranges provided in Table I.



responding  $p$ -value suggested that all these four parameters have significant influence on the lockdown effect (see Fig. S21 in Supporting Information). Furthermore, significant negative correlation of  $\beta_2$ , and  $\rho$  with the lockdown effect (see Fig. S21 in Supporting Information) indicate that only home quarantining the community may not be sufficient to reduce COVID-19 transmission in GJ. Government of GJ and policymakers may also have to focus on reducing the transmission occurring from hospital premises based on the guidelines from the WHO (EWHO, 2020). For UP, PRCC and its corresponding  $p$ -value suggested that  $\beta_2$ ,  $\rho$ , and  $\kappa$  are the main parameters that are influencing the lockdown effect (see Fig. S22 in Supporting Information). Moreover, significant negative correlation of  $\beta_2$  and  $\rho$  with the lockdown effect and as well as significant positive correlation of  $\kappa$  with the lockdown effect (see Fig. S22 in Supporting Information) implies that an effective lockdown policy in UP may be a combination of lockdown (relaxation in Green zone), contact tracing in community with effort in reducing hospital-based transmission following the WHO guidelines (EWHO, 2020). Finally for IND, PRCC and its corresponding  $p$ -value suggested that  $\beta_2$  and  $\rho$  are the main parameters that are most influencing the lockdown effect (see Fig. 6). Therefore, only home quarantining the community may not be sufficient to reduce COVID-19 transmission in IND. Government of IND and the policymakers may also have to focus on reducing the transmission occurring from hospital premises based on the guidelines from the WHO (EWHO, 2020).

#### 4. CONCLUSION

Our analysis of the mechanistic model with hospital-based COVID-19 transmission suggest that most of the new infections occurring in India as well most of the states are currently undetected. Furthermore, a global sensitivity analysis of two epidemiologically controllable parameters from the hospital-based transmission on the basic reproduction number ( $R_0$ ), indicate that if appropriate preventive measures are not taken immediately, a much larger COVID-19 outbreak may trigger due to the transmission occurring from the hospitalized and notified based contacts. Moreover, our ensemble forecast model (1) predicted a substantial percentage of increase in the COVID-19 notified cases during May 3–May 20, 2020, (see Table IV) in most of these locations. In RJ, trend of the forecast data (see Fig. S4 in Supporting Information) during May 3–May 20, 2020, is showing a decreasing trend. This may be due to low number of hospitalized and reported cases in this state (see Table II). However, cases may rise in RJ if relaxation in lockdown is applied. Furthermore, trend of the forecast data in IND (see Fig. 3) during May 3–May 20, 2020 indicates the fact that reaching the peak of the COVID-19 epidemic curve may be a long way ahead for India. Finally, based on our results of global sensitivity analysis of the four important epidemiologically measurable and controllable parameters on the lockdown effect, we are suggesting the following policy that may reduce the threat of a larger COVID-19 outbreak in the coming days.

#### 4.1. Effective Lockdown Policy

Dividing different states into three clusters (red, orange, and green) with extensive lockdown in red zones and providing relaxation in orange and green zones of a state will increase the percentage of symptomatically infection in these two zones (orange, and green). From our sensitivity analysis results, the lockdown will be effective in those locations where higher percentage of symptomatic infection exist in the population. Therefore, the government has to shift some orange or green zones under the red zones or move some red zones under the orange or green zones depending upon the percentage of symptomatic infection of those locations. However, from time-to-time COVID-19 testing is needed in these zones to get better result out of this cluster lockdown policy. Furthermore, COVID-19 testing will increase the number of notified and hospitalized cases over the states. Also from our results, lockdown effectiveness has a negative correlation with the hospital-based transmission rate ( $\beta_2$ ) and fraction of the susceptible population that is exposed to hospital-based contact ( $\rho$ ). Therefore, reducing these two parameters will increase the effectiveness of the lockdown in those seven locations. To reduce the hospitalized and notified based contacts, an efficient disaster management team is required. They will continuously monitor the situations in different hospitals and quarantine centers across India. This team must ensure that proper safety measures are being followed based on the guidelines provided by ICMR and WHO (WHO, 2020a).

There are few limitations of this current study and may be improved in future. We assumed that home quarantined population do not mix with the infected individuals from the community. This is a very crude approximation because in such a huge country like India with such a dense population there is always a possibility that a certain percentage of population under the lockdown can get infection from the community. In addition to this fact, there is a possibility of cross infection within the home quarantined population. This assumption will lead to more compartments (exposed under lockdown, symptomatic under lockdown, and asymptomatic under lockdown) and thus make our model more complex. Moreover, currently there is little evidence of air-borne transmission of COVID-19 in some regions (Morawska & Milton, 2020). However, this alternative air-borne transmission route is not considered in our model. Adding all these components in our mechanistic model may produce some rich dy-

namical properties like backward bifurcation, hopf-bifurcation, and so on. We shall explore these factors in our future studies.

#### ACKNOWLEDGEMENTS

Dr. Tridip Sardar acknowledges the Science & Engineering Research Board (SERB) major project grant (File No: EEQ/2019/000008 dt. 4/11/2019), Govt. of India.

The authors would like to thank the editor and anonymous reviewers for their valuable suggestions and constructive comments, which really helped to improve the presentation and quality of the paper.

#### CONFLICT OF INTERESTS

The authors declare that they have no conflicts of interest.

#### REFERENCES

- Akkouchi, M. (2008). On the convolution of exponential distributions. *Journal of the Chungcheong Mathematical Society*, 21(4), 501–510.
- Business Today. (2020, April 16). *Coronavirus lockdown India: Does your district fall in 'red zone' hotspots? Check out full list here*. Available at: <https://www.businesstoday.in/latest/trends/coronavirus-lockdown-20-does-your-district-fall-in-red-zone-check-out-full-list-here/story/401188.html>.
- COVID-19 Tracker. (2020a). *India COVID-19 Tracker*. Available at: <https://www.covid19world.org/> [Accessed on 2020-04-28].
- COVID-19 Tracker. (2020b). *India COVID-19 Tracker*. Available at: <https://www.covid19india.org> [Accessed on 2020-04-10].
- Economic Times. (2020a, April 8). *COVID-19 impact: Over 40 nurses test positive in Mumbai hospital*. Available at: <https://economictimes.indiatimes.com/news/politics-and-nation/two-private-hospitals-in-mumbai-sealed-after-staff-test-positive/articleshow/75009359.cms>
- Economic Times. (2020b). *India will be under complete lockdown for 21 days: Narendra Modi*. Available at: <https://economictimes.indiatimes.com/news/politics-and-nation/india-will-be-undercomplete-lockdown-starting-midnight-narendra-modi/articleshow/74796908.cms?from=mdr>
- Economic Times. (2020c). *Red, orange, green zones may come up during extended lockdown*. Available at: <https://economictimes.indiatimes.com/news/politics-and-nation/red-orange-green-zones-may-come-up-during-extended-lockdown/articleshow/75101054.cms?from=mdr>.
- Economic Times. (2020d). *World's biggest lockdown may have cost rs 7–8 lakh crore to Indian economy*. Available at: <https://economictimes.indiatimes.com/news/economy/finance/worlds-biggest-lockdown-may-have-cost-rs-7-8-lakh-crore-to-indian-economy/articleshow/75123004.cms?%20from=mdr>.
- Europe World Health Organization, (2020) *Health systems respond to COVID-19*. Available at: [http://www.euro.who.int/\\_data/assets/pdf\\_file/0006/437469/TG2-CreatingSurgeAcuteICUcapacity-eng.pdf](http://www.euro.who.int/_data/assets/pdf_file/0006/437469/TG2-CreatingSurgeAcuteICUcapacity-eng.pdf) [Accessed on 2020-04-30].
- Financial Express. (2020a). *Coronavirus lockdown 2.0: Till may 3 now, taking total to 40 days*. Available at:

- <https://www.financialexpress.com/india-news/coronavirus-lockdown-2-0-till-may-3-now-taking-total-to-40-days/1928585/>, published on: 2020-04-15
- Financial Express. (2020b). *COVID-19 lockdown relaxation: Full list of activities allowed from April 20; details*. Available at: <https://www.financialexpress.com/lifestyle/covid-19-lockdown-relaxation-full-list-of-activities-allowed-from-april-20-details/1933136/>, published on: 2020-04-19
- Haario, H., Laine, M., Mira, A., & Saksman, E. (2006). Dram: efficient adaptive MCMC. *Statistics and Computing*, 16(4), 339–354.
- India Today. (2020a). *Over 50 doctors, medical staff test positive for COVID-19; govt probing if they got infected from patients*. Available at: <https://www.indiatoday.in/india/story/over-50-doctors-medical-staff-test-positive-for-covid-19-govt-probing-if-they-got-infected-from-patients-1662917-2020-04-03>, published on: 2020-04-03.
- India Today. (2020b). *Coronavirus: 5 indian sectors that need urgent help as virus ravages economy*. Available at: <https://www.indiatoday.in/business/story/coronavirus-5-indian-sectors-that-need-urgent-help-as-virus-ravages-economy-1670099-2020-04-23>, published on: 2020-04-24.
- India Today. (2020c). *Coronavirus: 80% cases asymptomatic, but no need to revise testing criteria, says ICMR*. Available at: <https://www.indiatoday.in/india/story/80-of-coronavirus-cases-in-india-are-asymptomatic-icmr-1669073-2020-04-20>, published on: 2020-04-20.
- India Today. (2020d). *Coronavirus in India: Tracking country's first 50 COVID-19 cases; what numbers tell*. Available at: <https://www.indiatoday.in/india/story/coronavirus-in-india-tracking-country-s-first-50-covid-19-cases-what-numbers-tell-1654468-2020-03-12>, published on: 2020-03-12.
- India TV. (2020). *3 Delhi journalists test COVID-19 positive, says Arvind Kejriwal*. Available at: <https://www.indiatvnews.com/news/india/coronavirus-delhi-journalist-coronavirus-positive-covid-19-turn-arvind-kejriwal-612422>, published on: 2020-04-29
- Lee, S., Kim, T., Lee, E., Lee, C., Kim, H., Rhee, H., ... Kim, T. H. (2020). Clinical course and molecular viral shedding among asymptomatic and symptomatic patients with sars-cov-2 infection in a community treatment center in the republic of Korea. *JAMA Internal Medicine*, 180(11), 1447–1452.
- Lemke, C., & Gabrys, B. (2010). Meta-learning for time series forecasting and forecast combination. *Neurocomputing*, 73(10–12), 2006–2016.
- Marino, S., Hogue, IB., Ray, CJ., & Kirschner, DE. (2008). A methodology for performing global uncertainty and sensitivity analysis in systems biology. *Journal of Theoretical Biology*, 254(1), 178–196.
- Moghadas, SM., Shoukat, A., Fitzpatrick, MC., Wells, C. R., Sah, P., Pandey, A., ... Galvani, A. P. (2020). Projecting hospital utilization during the COVID-19 outbreaks in the United States. *Proceedings of the National Academy of Sciences*, 117(16), 9122–9126.
- Morawska, L., & Milton, DK. (2020). It is time to address airborne transmission of coronavirus disease 2019 (COVID-19). *Clinical Infectious Diseases*, 71(9), 2311–2313.
- New Delhi Television Ltd. (2020a). *20 doctors, medics isolated after surgeon tests COVID-19 positive at Aligarh Muslim University*. Available at: <https://www.ndtv.com/cities/20-doctors-medics-isolated-after-surgeon-tests-covid-19-positive-at-aligarh-muslim-un>, published on: 2020-04-23.
- New Delhi Television Ltd. (2020b). *90 health workers infected with COVID-19, total cases over 8,000 in India*. Available at: <https://www.ndtv.com/india-news/coronavirus-india-coronavirus-cases-in-india-cross-8-000-mark-34-dead-in-24-hours-2210282>, published on: 2020-04-12.
- Niti Aayog. (2020). *Life expectancy*. Available at: <https://niti.gov.in/content/life-expectancy> [Accessed on 2020-04-10].
- Pinho, STR., Ferreira, CP., Esteva, L., Barreto, FR., Morato e Silva, V., & Teixeira, M. (2010). Modelling the dynamics of dengue real epidemics. *Philosophical Transactions of the Royal Society A: Mathematical, Physical and Engineering Sciences*, 368(1933), 5679–5693.
- Rothman, KJ., Greenland, S., & Lash, TL. (2008). *Modern epidemiology*. Philadelphia, PA: Lippincott Williams & Wilkins.
- Sardar, T., Rana, S., Bhattacharya, S., Al-Khaled, K., & Chattopadhyay, J. (2015). A generic model for a single strain mosquito-transmitted disease with memory on the host and the vector. *Mathematical Biosciences*, 263, 18–36.
- Sardar, T., & Saha, B. (2017). Mathematical analysis of a power-law form time dependent vectorborne disease transmission model. *Mathematical Biosciences*, 288, 109–123.
- Sardar, T., Ghosh, I., Rodo, X., & Chattopadhyay, J. (2020a). A realistic two-strain model for mers-cov infection uncovers the high risk for epidemic propagation. *PLoS Neglected Tropical Diseases*, 14(2), <https://doi.org/10.1371/journal.pntd.0008065>.
- Sardar, T., Nadim, SS., Rana, S., & Chattopadhyay, J. (2020b). Assessment of lockdown effect in some states and overall India: A predictive mathematical study on COVID-19 outbreak. *Chaos, Solitons & Fractals*, 139, <https://doi.org/10.1016/j.chaos.2020.110078>
- Shaub, D., Ellis, P. (2020). *forecastHybrid: Convenient functions for ensemble time series forecasts*. Available at: <https://gitlab.com/dashaub/forecastHybrid>, <https://github.com/ellis/forecastHybrid>.
- Scroll.in. (2020). *COVID-19: Over 50 journalists in Mumbai test positive, says municipal corporation*. Available at: <https://scroll.in/latest/959732/covid-19-over-50-journalists-in-mumbai-test-positive-says-municipal-corporation>, published on: 2020-04-11.
- Tang, B., Wang, X., Li, Q., Bragazzi, NL., Tang, S., Xiao, Y., & Wu, J. (2020). Estimation of the transmission risk of the 2019-nCov and its implication for public health interventions. *Journal of Clinical Medicine*, 9(2), <https://doi.org/10.3390/jcm9020462>.
- Times of India. (2020). *Lockdown goes from 21 to 40 days, curbs may be conditionally eased in some non-hotspot areas from April 20*. Available at: <https://timesofindia.indiatimes.com/india/lockdown-goes-from-21-to-40-days-curbs-may-be-conditionally-eased-in-some-non-hotspot-areas-from-april-20/articleshow/75149611.cms>, published on: 2020-04-15
- The Hindu. (2020). *Why are hospitals hotbeds of COVID-19 transmission?* Available at: <https://www.thehindu.com/sci-tech/why-are-hospitals-hotbeds-of-covid-19-transmission/article31386208.ece>, published on: 2020-04-20.
- ThePrint. (2020). *89 health dept members, including doctors & IAS officers, test positive for COVID-19 in MP*. Available at: <https://theprint.in/health/89-health-dept-members-including-doctors-ias-officers-test-positive-for-covid-19-in-mp/403102/>, published on: 2020-04-16.
- The Unique Identification Authority of India. (2020). *State/UT wise aadhaar saturation*. Available at: <https://uidai.gov.in/images/state-wise-aadhaar-saturation.pdf> [Accessed on 2020-04-10].
- Van den Driessche, P., & Watmough, J. (2002). Reproduction numbers and sub-threshold endemic equilibria for compartmental models of disease transmission. *Mathematical Biosciences*, 180(1–2), 29–48.
- Wang, C., Horby, PW., Hayden, FG., & Gao, GF. (2020). A novel coronavirus outbreak of global health concern. *The Lancet*, 395(10223), 470–473.
- Wallinga, J., & Lipsitch, M. (2007). How generation intervals shape the relationship between growth rates and reproductive numbers. *Proceedings of the Royal Society B: Biological Sciences*, 274(1609), 599–604.
- World Health Organization. (2020a). *Coronavirus disease 2019 (COVID-19), situation report -10*. Available at:

<https://www.who.int/emergencies/diseases/novel-coronavirus-2019/situation-reports/> [Accessed on 2020-03-25].

World Health Organization. (2020b). *WHO Director-General's opening remarks at the media briefing on COVID-19 - 11 March 2020*. Available at: <https://www.who.int/director-general/speeches/detail/who-director-general-s-opening-remarks-at-the-media-briefing-on-covid-19-11-march-2020>, published on: 2020-03-11.

World Health Organization. (2020c). *WHO says over 22,000 healthcare workers across 52 countries infected by COVID-19*. <https://health.economictimes.indiatimes.com/news/industry/who-says-over-22000-healthcare-workers-across-52-countries-infected-by-covid-19/75107238>, published on: 2020-04-12.

## SUPPORTING INFORMATION

Additional supporting information may be found online in the Supporting Information section at the end of the article.

**Table S1:** Estimated uninformative initial conditions for the mechanistic ODE model combinations (S-1) & (S-2).

**Table S2:** Weight estimates for the mechanistic ODE model combinations (S-1) & (S-2) and the Hybrid statistical model (see main text), respectively.

**Table S3:** Goodness of fit (RMSE and MAE) of the Hybrid statistical model (see main text) for the test data from **MH, DL, MP, RJ, GJ, UP**, and **IND**, respectively. Respective subscripts **MH, DL, MP, RJ, GJ, UP**, and **IND** are same as Table S1.

**Fig. S1:** Ensemble model (see main text) forecast for the daily notified COVID-19 cases in Maharashtra during May 3, 2020 till May 20, 2020 under five different lockdown scenarios.

**Fig. S2:** Ensemble model (see main text) forecast for the daily notified COVID-19 cases in Delhi during May 3, 2020 till May 20, 2020 under five different lockdown scenarios.

**Fig. S3:** Ensemble model (see main text) forecast for the daily notified COVID-19 cases in Madhya Pradesh during May 3, 2020 till May 20, 2020 under five different lockdown scenarios.

**Fig. S4:** Ensemble model (see main text) forecast for the daily notified COVID-19 cases in Rajasthan during May 3, 2020 till May 20, 2020 under five different lockdown scenarios.

**Fig. S5:** Ensemble model (see main text) forecast for the daily notified COVID-19 cases in Gujarat during May 3, 2020 till May 20, 2020 under five different lockdown scenarios.

**Fig. S6:** Ensemble model (see main text) forecast for the daily notified COVID-19 cases in Uttar Pradesh during May 3, 2020 till May 20, 2020 under five different lockdown scenarios.

**Fig. S7:** Spatial distribution of total number of COVID-19 cases during May 3, 2020 till May 20, 2020 in the six states namely, Maharashtra (MH), Delhi (DL), Madhya Pradesh (MP), Rajasthan (RJ), Gujarat (GJ), and Uttar Pradesh (UP), under the lockdown scenario (A2). We used the following colour clustering of the cases: Green (1000 – 1500), Purple (1501 – 3000), Blue (3001 – 5000), Yellow (5001 – 7000), Orange (7001 – 12000), and Red (12001 – 24000).

**Fig. S8:** Spatial distribution of total number of COVID-19 cases during May 3, 2020 till May 20, 2020 in the six states namely, Maharashtra (MH), Delhi (DL), Madhya Pradesh (MP), Rajasthan (RJ), Gujarat (GJ), and Uttar Pradesh (UP), under the lockdown scenario (A3). Colour clustering of the cases are same as Fig. S7.

**Fig. S9:** Spatial distribution of total number of COVID-19 cases during May 3, 2020 till May 20, 2020 in the six states namely, Maharashtra (MH), Delhi (DL), Madhya Pradesh (MP), Rajasthan (RJ), Gujarat (GJ), and Uttar Pradesh (UP), under the lockdown scenario (A4). Colour clustering of the cases are same as Fig. S7.

**Fig. S10:** Spatial distribution of total number of COVID-19 cases during May 3, 2020 till May 20, 2020 in the six states namely, Maharashtra (MH), Delhi (DL), Madhya Pradesh (MP), Rajasthan (RJ), Gujarat (GJ), and Uttar Pradesh (UP), under the lockdown scenario (A5). Colour clustering of the cases are same as Fig. S7.

**Fig. S11:** Effective reproduction number (RT) under two lockdown scenarios (A1 & A5) for the period April 21, 2020 till May 20, 2020 for Maharashtra.

**Fig. S12:** Effective reproduction number (RT) under two lockdown scenarios (A1 & A5) for the period April 21, 2020 till May 20, 2020 for Delhi.

**Fig. S13:** Effective reproduction number (RT) under two lockdown scenarios (A1 & A5) for the period April 21, 2020 till May 20, 2020 for Madhya Pradesh.

**Fig. S14:** Effective reproduction number (RT) under two lockdown scenarios (A1 & A5) for the period April 21, 2020 till May 20, 2020 for Rajasthan.

**Fig. S15:** Effective reproduction number (RT) under two lockdown scenarios (A1 & A5) for the period April 21, 2020 till May 20, 2020 for Uttar Pradesh.

**Fig. S16:** Effective reproduction number (RT) under two lockdown scenarios (A1 & A5) for the period April 21, 2020 till May 20, 2020 for Gujarat.

**Fig. S17:** Effect of uncertainty of four epidemiologically measurable and controllable parameters of the mechanistic ODE model (see Table I and Fig.1 in the



main text) on the effect of lockdown and the basic reproduction number ( $R_0$ ).

**Fig. S18:** Effect of uncertainty of four epidemiologically measurable and controllable parameters of the mechanistic ODE model (see Table I and Fig.1 in the main text) on the effect of lockdown and the basic reproduction number ( $R_0$ ).

**Fig. S19:** Effect of uncertainty of four epidemiologically measurable and controllable parameters of the mechanistic ODE model (see Table I and Fig.1 in the main text) on the effect of lockdown and the basic reproduction number ( $R_0$ ).

**Fig. S20:** Effect of uncertainty of four epidemiologically measurable and controllable parameters of the mechanistic ODE model (see Table I and Fig.1 in the main text) on the effect of lockdown and the basic reproduction number ( $R_0$ ).

**Fig. S21:** Effect of uncertainty of four epidemiologically measurable and controllable parameters of the mechanistic ODE model (see Table I and Fig.1 in the main text) on the effect of lockdown and the basic reproduction number ( $R_0$ ).

**Fig. S22:** Effect of uncertainty of four epidemiologically measurable and controllable parameters of the mechanistic ODE model (see Table I and Fig.1 in the main text) on the effect of lockdown and the basic reproduction number ( $R_0$ ).

**Fig. S23:** Posterior distribution of the weights for the mechanistic ODE model combinations

(S-1) & (S-2) and the Hybrid statistical model (see main text), respectively for Maharashtra.

**Fig. S24:** Posterior distribution of the weights for the mechanistic ODE model combinations (S-1) & (S-2) and the Hybrid statistical model (see main text), respectively for Delhi.

**Fig. S25:** Posterior distribution of the weights for the mechanistic ODE model combinations (S-1) & (S-2) and the Hybrid statistical model (see main text), respectively for Madhya Pradesh.

**Fig. S26:** Posterior distribution of the weights for the mechanistic ODE model combinations (S-1) & (S-2) and the Hybrid statistical model (see main text), respectively for Rajasthan.

**Fig. S27:** Posterior distribution of the weights for the mechanistic ODE model combinations (S-1) & (S-2) and the Hybrid statistical model (see main text), respectively for Gujarat.

**Fig. S28:** Posterior distribution of the weights for the mechanistic ODE model combinations (S-1) & (S-2) and the Hybrid statistical model (see main text), respectively for Uttar Pradesh.

**Fig. S29:** Posterior distribution of the weights for the mechanistic ODE model combinations (S-1) & (S-2) and the Hybrid statistical model (see main text), respectively for India.



# Source details

[Feedback >](#) [Compare sources >](#)

## Risk Analysis

Scopus coverage years: from 1981 to Present

Publisher: Wiley-Blackwell

ISSN: 0272-4332 E-ISSN: 1539-6924

Subject area: [Engineering: Safety, Risk, Reliability and Quality](#) [Medicine: Physiology \(medical\)](#)

Source type: Journal

[View all documents >](#)

[Set document alert](#)

[Save to source list](#)

CiteScore 2022

7.8



SJR 2022

0.931



SNIP 2022

1.458





## Synthesis, Structure, Magnetic and Catalytic Competency of a Tetradentate (NNOO) Schiff Base Mediated Dimeric Copper(II) Complex

HABIBAR CHOWDHURY<sup>1</sup>, RAJESH BERA<sup>2</sup> and CHANDAN ADHIKARY<sup>3,\*</sup>

<sup>1</sup>Department of Chemistry, Kabi Nazrul College, Murarai, Birbhum-731219, India

<sup>2</sup>Department of Chemistry, Dinabandhu Andrews College, Kolkata-700084, India

<sup>3</sup>Department of Education, The University of Burdwan, Golapbag, Burdwan-713104, India

\*Corresponding author: E-mail: [cadhikary@edu.buruniv.ac.in](mailto:cadhikary@edu.buruniv.ac.in)

Received: 13 February 2021;

Accepted: 28 March 2021;

Published online: 5 June 2021;

AJC-20356

One dinuclear copper(II) complex  $\{\mu\text{-}[2,2'\text{-}\{\text{ethane-1,2-diy}l\text{bis}[(\text{azanylylidene})\text{methanylylidene}]\}\text{bis}(\text{phenolato})]\}\text{-}\{\mu\text{-}[2,2'\text{-}\{\text{ethane-1,2-diy}l\text{bis}[(\text{azanylylidene})\text{methanylylidene}]\}\text{bis}(\text{phenolato})]\}\text{dicopper(II)}$ ,  $[\text{Cu}_2(\text{salen})_2]$  (**1**) [ $\text{salen}^{2-} = [2,2'\text{-}\{\text{ethane-1,2-diy}l\text{bis}[(\text{azanylylidene})\text{methanylylidene}]\}\text{bis}(\text{phenolato})]$ ] has been isolated and characterized by X-ray diffraction analysis and spectroscopic studies. X-ray single crystal structure examination revealed that each Cu(II) center in the asymmetric unit of **1** adopts a distorted square planar geometry with a  $\text{CuN}_2\text{O}_2$  chromophore, where two asymmetric units are attached through congregation of Salen involving Cu-O bond to form dinuclear molecular unit  $[\text{Cu}_2(\text{salen})_2]$ . In crystalline state, these dinuclear entities in **1** are extended through C-H $\cdots\pi$  interactions and  $\pi\cdots\pi$  interactions displaying a 3D network structure. The variable-temperature magnetic susceptibility measurement asserted a dominant antiferromagnetic interaction between the copper(II) centers through Cu-O-Cu linkage in **1** with  $J = -1.46 \text{ cm}^{-1}$ . The catalytic efficacy of complex **1** was studied in a series of solvents for the oxidation of styrene and cyclooctene using *tert*-butyl-hydroperoxide (TBHP) as an active oxidant under mild conditions. The catalytic reaction mixture has been analyzed by gas chromatography and it displayed that the yield of the epoxidation and its selectivity is optimum in acetonitrile medium.

**Keywords:** Dimeric copper(II) complex, Tetradentate Schiff base, Structure, Magnetism, Catalytic competency.

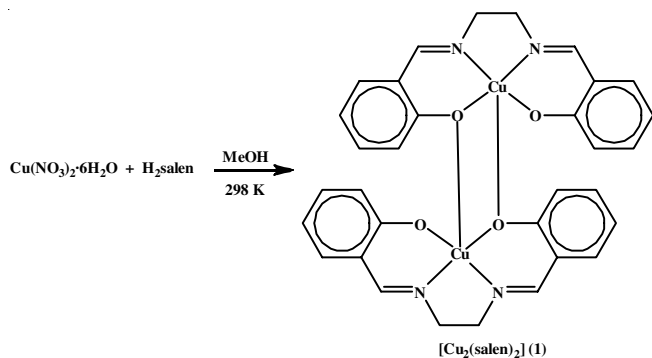
### INTRODUCTION

Metal-organic frameworks (MOFs) [1] constructed through strong metal-ligand covalent bonds [2] and multiple weak non-covalent forces [3] have drawn great attention of many research groups in isolation of different advanced functional materials [4-8]. Single-pot synthesis [9] is an efficient synthetic approach using judiciously chosen metal ions and organic in pre-assigned molar ratios to isolate such target materials. Copper(II), a  $3d^9$  ion, affords [10] a variety of geometries that may lead to significant differences in overall molecular and crystalline architectures and thereby different biological and catalytic activities [11,12].

Schiff bases [13] are the important organic ligands because of their straightforward synthesis, structural varieties, varied denticities and are moderate electron donors with easily-tunable electronic and steric effects [14]. Salen refers to a tetradentate

$\text{C}_2$ -symmetric ligand synthesized from salicylaldehyde and ethylenediamine, which are structurally related to the classical salen ligand, primarily *bis*-Schiff bases. The metal-free salen compound ( $\text{H}_2\text{salen}$  or  $\text{salenH}_2$ ) has two phenolic hydroxyl groups. The salen ligand is usually its conjugate base ( $\text{salen}^{2-}$ ), resulting from the loss of protons from those hydroxyl groups. Salen ligands are notable for coordinating a wide range of different metals, which they can often stabilize in various oxidation states [15]. Copper(II) Schiff base complexes find wide applicability in the field of catalysis, antimicrobial activities, antifungal and antiviral activities, synergistic action on insecticides, plant growth regulator, antitumor, cytotoxic activity, harmonic generation activity, *etc.* Schiff base copper(II) complexes can now be extensively used as active catalysts [16-28]. In the present endeavour, we have successfully isolated a neutral dinuclear complex,  $\{\mu\text{-}[2,2'\text{-}\{\text{ethane-1,2-diy}l\text{bis}[(\text{azanylylidene})\text{methanylylidene}]\}\text{bis}(\text{phenolato})]\}\text{-}\{\mu\text{-}[2,2'\text{-}\{\text{ethane-1,2-diy}l\text{bis}[(\text{azanylylidene})\text{methanylylidene}]\}\text{bis}(\text{phenolato})]\}\text{dicopper(II)}$ .

1,2-diylbis[(azanylylidene)methanylylidene]}bis(phenolato)]-dicopper(II), [Cu<sub>2</sub>(salen)<sub>2</sub>] (**1**) [salen<sup>2-</sup> = [2,2'-{ethane-1,2-diylbis[(azanylylidene)methanylylidene]}bis(phenolato)]. Structure of complex **1** has been resolved by X-ray diffraction measurements to define the exact coordination sphere. This work has addressed to the synthesis, characterization, magnetic property and catalytic efficacy has been justified by the oxidation of cyclooctene by employing *tert*-butyl-hydroperoxide (TBHP) as an efficient oxidant in different solvent media.



Scheme-I: Synthetic route for complex **1**

## EXPERIMENTAL

High purity salicylaldehyde (E. Merck, India), ethanediamine, cyclooctene and *tert*-BuOOH (70% aq.) (Aldrich, USA), copper(II) nitrate hexahydrate (E. Merck, India) were purchased and used as received. Schiff base, H<sub>2</sub>salen was synthesized by the condensation of 1:2 molar ratio of ethylenediamine and salicylaldehyde in dehydrated alcohol [29]. All other chemicals and solvents were of AR grade. The solvents were distilled and dried before use.

**Physical measurements:** Microanalysis (CHN) was performed in a Perkin-Elmer 240 elemental analyzer. IR spectra were recorded on a Bruker Alpha T200140 FT-IR spectrometer. Absorption spectra were studied on Shimadzu UV2100 UV-vis recording spectrophotometer. Magnetic measurement of **1** was performed with a Cryogenic SQUID S600 magnetometer operating between 2 and 300 K at an applied field of 1T. The magnetic data were corrected for the diamagnetism of the sample holder, measured in the same range of temperature field and the intrinsic diamagnetism of the samples was estimated through Pascal's constants.

**Synthesis of [Cu<sub>2</sub>(salen)<sub>2</sub>] (**1**):** A methanolic solution (5 mL) of H<sub>2</sub>salen (0.268 g, 1.00 mmol) was added dropwise to a solution of copper(II) nitrate hexahydrate (0.296 g, 1.00 mmol) in the same solvent (10 mL). The final deep blue solution was filtered and the supernatant liquid was kept undisturbed in open air for slow evaporation. After 3 days, a dark green crystalline product of complex **1** was isolated by filtration, washed with dehydrated alcohol and dried *in vacuo* over silica gel (**Scheme-I**). Yield: 0.462 g (70%). Elemental anal. calcd. (found) % for C<sub>32</sub>H<sub>28</sub>N<sub>4</sub>O<sub>4</sub>Cu<sub>2</sub> (**1**): C, 58.26 (58.50); H, 4.28 (4.36); N, 8.49 (9.12). IR (KBr, cm<sup>-1</sup>): ν(CH=N), 1620-1655; ν(C-O), 1332-1355. UV-Vis (λ<sub>max</sub>, nm; DMF): 266, 296, 388, 620; Λ<sub>M</sub> (DMF): 7 Ω<sup>-1</sup> cm<sup>2</sup> mol<sup>-1</sup>.

**X-ray data collection and structure refinement:** A single crystal of complex **1** suitable for X-ray analysis was selected from those obtained by slow evaporation of a methanol solution at room temperature. Diffraction data were collected on a Bruker SMART 1000 CCD diffractometer using graphite monochromated MoKα radiation (λ = 0.71073 Å) and were used to measure cell dimensions and diffraction intensities. Data were collected using the ω-θ scan technique in the range to a maximum 1.54° < θ < 25.24°. For data collection, data reduction and cell refinement the program SAINT-Plus [30] was used. The structure was solved by direct methods using SIR97 [31] and refined with version 2018/3 of SHELXL [32] using least squares minimization. A summary of the crystallographic data and structure determination parameters for complex **1** is shown in Table-1.

TABLE-1  
CRYSTALLOGRAPHIC DATA FOR COMPLEX **1**

Empirical formula	C <sub>32</sub> H <sub>28</sub> N <sub>4</sub> O <sub>4</sub> Cu <sub>2</sub>
Formula weight	659.66
Crystal system, space group	Monoclinic, C2/c
Temperature	293(2) K
Wavelength	0.71073 Å
Unit cell dimensions	a = 26.752(6) Å, b = 7.0118(15) Å, c = 14.772(3) Å, α = 90.00°, β = 97.423(3)°, γ = 90.00°
Volume	2747.7(10) Å <sup>3</sup>
Z, calculated density	4, 1.595 mg/cm <sup>3</sup>
Absorption coefficient	1.595 mm <sup>-1</sup>
F(000)	1352
Crystal size	0.23 × 0.16 × 0.09 mm <sup>3</sup>
Theta range	1.54 to 25.24 °
Limiting indices	-32 ≤ h ≤ 32, -8 ≤ k ≤ 8, -16 ≤ l ≤ 16
Reflections collected/unique	12859/2503 [R(int) = 0.049]
T <sub>max</sub> and T <sub>min</sub>	0.872 and 0.710
Data/restraints/parameters	2503/0/190
Goodness-of-fit on F <sup>2</sup>	1.064
Final R indices [I>2σ(I)]	R = 0.0329 and wR = 0.0869
R indices (all data)	R = 0.0386 and wR = 0.0917
Largest peak and hole	0.435 and -0.767
Weighting scheme:	R = Σ  F <sub>o</sub>   -  F <sub>c</sub>    / Σ F <sub>o</sub>  , wR = [Σw(F <sub>o</sub> <sup>2</sup> - F <sub>c</sub> <sup>2</sup> ) <sup>2</sup> / Σw(F <sub>o</sub> <sup>2</sup> ) <sup>2</sup> ] <sup>1/2</sup> , calcd. w = 1/[σ <sup>2</sup> (F <sub>o</sub> <sup>2</sup> ) + (0.0500P) <sup>2</sup> + 2.7518P] where P = (F <sub>o</sub> <sup>2</sup> + 2F <sub>c</sub> <sup>2</sup> )/3.

## RESULTS AND DISCUSSION

A new dinuclear copper(II) Schiff base complex {μ-[2,2'-{ethane-1,2-diylbis[(azanylylidene)methanylylidene]}bis(phenolato)]}-{μ-[2,2'-{ethane-1,2-diylbis[(azanylylidene)methanylylidene]}bis(phenolato)]}dicopper(II), [Cu<sub>2</sub>(salen)<sub>2</sub>] (**1**) [salen<sup>2-</sup> = [2,2'-{ethane-1,2-diylbis[(azanylylidene)methanylylidene]}bis(phenolato)] has been isolated using a one-pot reaction of a 1:1 molar ratio of Cu(NO<sub>3</sub>)<sub>2</sub>·6H<sub>2</sub>O and a tetradentate Schiff base (H<sub>2</sub>salen) in methanol at room temperature.

Complex **1** was characterized by microanalytical, spectroscopic and other physico-chemical results. The microanalytical data are in good conformity with the formulation of the complex. The air stable moisture insensitive compound is stable over a long period of time in powdery and crystalline state and soluble in MeOH, EtOH, MeCN, DMF and DMSO, but are insoluble

in water. In DMF solution, complex **1** behaves as non-electrolytes as reflected from their low conductivity value ( $7 \text{ ohm}^{-1} \text{ cm}^2 \text{ mol}^{-1}$ ).

**Spectral studies:** In IR spectrum, complex **1** shows a band in the range  $1655\text{--}1620 \text{ cm}^{-1}$  attributable due to azomethine group [33]. A sharp band in the range  $1355\text{--}1332 \text{ cm}^{-1}$  is assigned to  $\nu(\text{C-O})$ . A broad band around  $3460 \text{ cm}^{-1}$  due to  $\nu(\text{O-H})$  for free ligands was absent for complex, suggesting the coordination of Schiff base as a dianionic ligand. In the UV-vis spectrum, a low-intensity absorption band at  $620 \text{ nm}$  allocated to  $d\text{-}d$  transition, congruent with the square pyramidal ( $sp$ ) geometry of the copper(II) centers [34]. The absorption band observed at  $388 \text{ nm}$  may be attributed to the ligand to copper(II) charge transfer transition (LMCT). Additionally, two strong absorption bands in the region  $266$  and  $296 \text{ nm}$  may be assigned to a ligand based charge transfer transitions.

**Crystal structure of  $[\text{Cu}_2(\text{salen})_2]$  (**1**):** Single-crystal X-ray diffraction measurement of  $[\text{Cu}_2(\text{salen})_2]$  (**1**) reveals that the crystal belongs to the monoclinic system corresponding from the space group  $C2/c$ . Single crystal X-ray diffraction study of  $[\text{Cu}_2(\text{salen})_2]$  (**1**) was made to define the coordination sphere. An ORTEP diagram of asymmetric units, molecular unit and packing views of 2D sheet and 3D network structures of complex **1** are depicted in Figs. 1-4. Selected bond distances and angles relevant to the coordination spheres are presented in Table-2. Parameters of  $\text{C-H}\cdots\pi$  and  $\pi\cdots\pi$  interactions are given in Tables 3 and 4, respectively. X-ray structural analysis revealed that each Cu(II) center in asymmetric unit of complex **1** adopts a distorted square planar geometry with a  $\text{CuN}_2\text{O}_2$  chromophore coordinated by two N atoms (N1, N2) and two O atoms (O1, O2) of the tetradentate Schiff base ligand (salen) (Fig. 1). The coordination sites of the basal plane in square are occupied by (N1 and O2) and (N2 and O1) in *trans* position. Angles of *cisoid* and *transoid* are in  $[83.60(9)\text{--}94.79(8)^\circ]$  and  $[170.37(8)\text{--}171.10(8)^\circ]$  ranges, respectively (Table-2). These two asymmetric units are connected through congregation of salen ligand involving Cu-O bond to form dinuclear molecular unit  $[\text{Cu}_2(\text{salen})_2]$  (Fig. 2), where each Cu(II) center completes its penta-coordination in a distorted square pyramidal environment. The Cu $\cdots$ Cu separation in each dinuclear entity is  $3.207 \text{ \AA}$  and bond angle of Cu1-O1-Cu1<sup>i</sup> core is  $93.78(7)^\circ$  [symmetry code: (i)  $1/2-x, 1/2-y, -z$ ]. The primary bond distances of Cu-N and Cu-O are ranges from  $1.9168(17)\text{--}1.964(2) \text{ \AA}$ , while Cu1-O1<sup>i</sup>/Cu1<sup>i</sup>-O1 are comparatively larger [ $2.4212(18) \text{ \AA}$ ] indicating weaker in nature. In crystalline state, these dinuclear entities

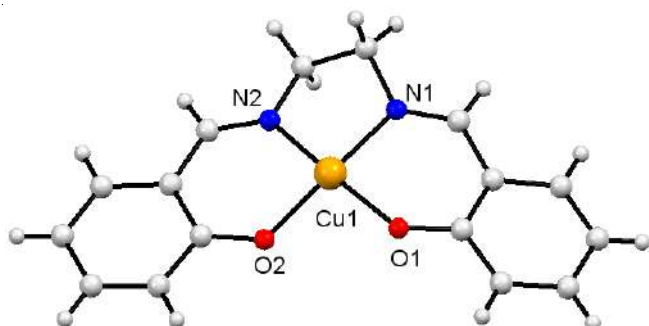


Fig. 1. Perspective view of the asymmetric unit of  $[\text{Cu}_2(\text{salen})_2]$  (**1**) with displacement ellipsoid drawn at the 50% probability level

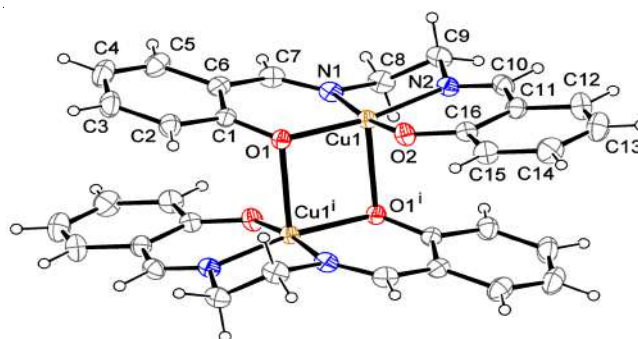


Fig. 2. An ORTEP diagram of dinuclear molecular unit of  $[\text{Cu}_2(\text{salen})_2]$  (**1**) with displacement ellipsoid drawn at the 40% probability level; symmetry code: (i)  $1/2-x, 1/2-y, -z$

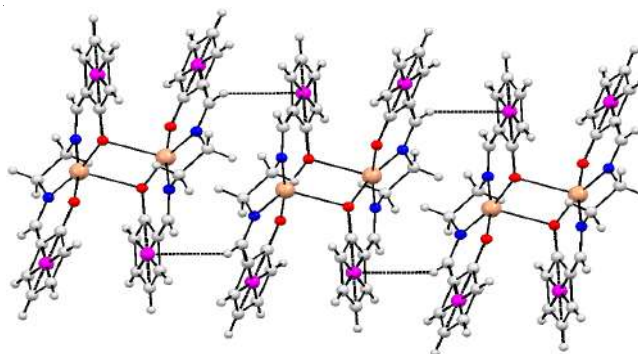


Fig. 3. Crystal packing view of 2D sheet structure in complex **1** through  $\text{C-H}\cdots\pi$  interactions viewed along crystallographic  $b$  axis

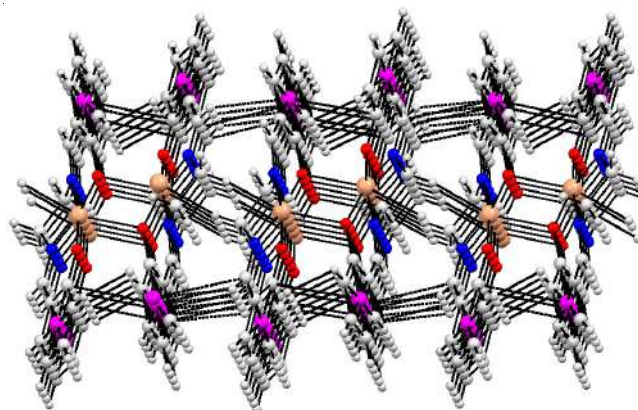


Fig. 4. 3D network structure of complex **1** involving both  $\text{C-H}\cdots\pi$  and  $\pi\cdots\pi$  interactions

TABLE-2  
SELECTED BOND DISTANCES ( $\text{\AA}$ )  
AND BOND ANGLES ( $^\circ$ ) FOR COMPLEX **1**

Bond distances ( $\text{\AA}$ )			
Cu1-N1	1.958(2)	Cu1-O2	1.9168(17)
Cu1-N2	1.964(2)	Cu1-O1 <sup>i</sup>	2.4212(18)
Cu1-O1	1.9488(16)	Cu1 <sup>i</sup> -O1	2.4212(18)
Bond angles ( $^\circ$ )			
N1-Cu1-N2	83.60(9)	N2-Cu1-O1 <sup>i</sup>	102.27(7)
N1-Cu1-O1	91.26(8)	O1-Cu1-O2	91.34(7)
N1-Cu1-O2	171.10(8)	O1-Cu1-O1 <sup>i</sup>	86.22(7)
N1-Cu1-O1 <sup>i</sup>	94.79(8)	O2-Cu1-O1 <sup>i</sup>	93.87(7)
N2-Cu1-O1	170.37(8)	Cu1-O1-Cu1 <sup>i</sup>	93.78(7)
N2-Cu1-O2	92.58(8)		

Symmetry code: (i)  $1/2-x, 1/2-y, -z$ .

in complex **1** are engaged through C-H... $\pi$  interactions [C10-H10...Cg(5): 2.94 Å, 135.00°; Cg(5) = C(1)→C(2)→C(3)→C(4)→C(5)→C(6)] (Table-3) to give 2D sheet structure (Fig. 3) viewed along crystallographic *b*-axis. These 2D sheet structure are further stabilized through  $\pi$ ... $\pi$  interaction [Cg(6)...Cg(6): 5.477(2)°; Cg(6) = C(11)→C(12)→C(13)→C(14)→C(15)→C(16)] (Table-4) to result a supramolecular 3D network structure (Fig. 4).

**Magnetic studies:** The temperature dependence of the molar magnetic susceptibility ( $\chi_M$ ) for complex **1** in the 5-300 K temperature range was measured with a superconducting quantum interference device (SQUID) magnetometer, under magnetic fields of 10 kG (Fig. 5). The  $\chi_M T$  value of 0.019 cm<sup>3</sup> mol<sup>-1</sup> at 300 K for complex **1** is higher than the value expected for an isolated magnetically uncoupled copper(II) ion ( $\chi_M T$  = 0.013 cm<sup>3</sup> mol<sup>-1</sup> for *g* = 2.0). Upon cooling the  $\chi_M$  value of complex **1** remains almost the same until about 65 K and then increases rapidly to reach a minimum of 0.13 cm<sup>3</sup> mol<sup>-1</sup> K at about 5 K. This clearly indicates that magnetic interaction between copper(II) ions through Cu-O-Cu linkage is antiferromagnetic in nature. To estimate the magnitude of the antiferromagnetic coupling the magnetic susceptibility data were fitted to the modified Bleaney-Bowers equation for two interacting copper (II) ions (*S* = 1/2) with the Hamiltonian in the form  $H = -J\hat{S}_1\cdot\hat{S}_2$ . The susceptibility equation for such a dimeric system can be written as follows in eqn. 1 [35-37]:

$$\chi = \frac{2Ng^2\beta^2}{kT} [3 + \exp(-J/kT)]^{-1}(1-\rho) + \frac{Ng^2\beta^2}{2kT}\rho \quad (1)$$

where *N*, *g*,  $\beta$  and  $\rho$  parameters in the equation bear their usual meaning. The best fit parameters were *J* = - 1.46 cm<sup>-1</sup>, *g* = 2.11 and *r* = 0.0005.

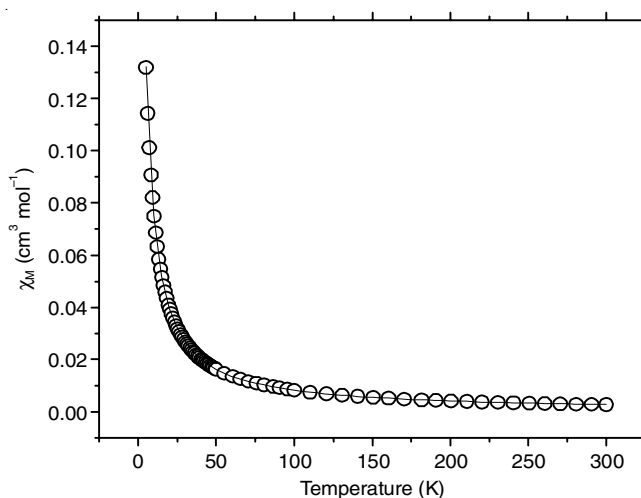


Fig. 5. Thermal dependence of  $\chi_M$  for complex **1**

**Catalytic activities of [Cu<sub>2</sub>(salen)<sub>2</sub>] (**1**):** The catalytic activity of complex **1** in the oxidation of styrene and cyclooctene in homogeneous medium is summarized in Table-5. The graphical representation of alkene conversion in the presence of complex **1** is shown in Fig. 6. Styrene was efficiently converted to 97% with epoxide selectivity of 54%. Along with this a considerable amount of benzaldehyde and benzoic acid are also formed. Copper(II) Schiff base complexes have been used as homogeneous catalysts in olefin oxidation reactions with different oxidizing agents in the recent past. Koner *et al.* [16] studied this reaction over a series of copper(II) Schiff base complexes, which gives styrene epoxide in 54-39% yield (selectivity 72-39%) under homogeneous conditions with *tert*-BuOOH. Recently, a diazido-bridged dinuclear copper(II) compound containing a tridentate Schiff base ligand shows 82% conversion of styrene with 60% epoxide selectivity [17].

TABLE-3  
C-H... $\pi$  INTERACTION PARAMETERS (Å, °) FOR COMPLEX **1**

C-H... $\pi$ interactions (Å, °)					
D-H...A	D-H	H...A	D...A	D-H...A	Symmetry code
C10-H10...Cg(5)	0.9300	2.94	3.676(3)	135	1/2-x, -1/2+y, 1/2-z
Cg(5) = C(1)→C(2)→C(3)→C(4)→C(5)→C(6)					

TABLE-4  
 $\pi$ ... $\pi$  INTERACTION PARAMETERS (Å, °) FOR COMPLEX **1**

$\pi$ ... $\pi$ interaction (Å, °)					
Ring-ring	Cg-Cg distance	Dihedral angle (i, j)	Perpendicular distances between baricenters (i, j)	Slippage	Symmetry code
Cg(6)-Cg(6)	5.477(2)	56.01	0.2485	4.541	-x, 1-y, -z
Cg(6) = C(11)→C(12)→C(13)→C(14)→C(15)→C(16)					

TABLE-5  
HOMOGENEOUS CATALYTIC OXIDATION OF OLEFINS CATALYZED BY COMPLEX **1** IN ACETONITRILE MEDIA

Substrate	Reaction time (h)	Conversion (wt.%)	Yield of products (%)	
			Epoxide	Others
Styrene	24	97	52	45 <sup>a</sup>
Cyclooctene	24	82	68	14 <sup>b</sup>

Reaction conditions: Cyclooctene (10 mmol); catalysts (0.005 mmol); *tert*-BuOOH (20 mmol); acetonitrile (8 mL); temperature (70 °C)

<sup>a</sup>Benzaldehyde and benzoic acid; <sup>b</sup>cyclooct-2-en-1-ol and cyclooct-2-en-1-one

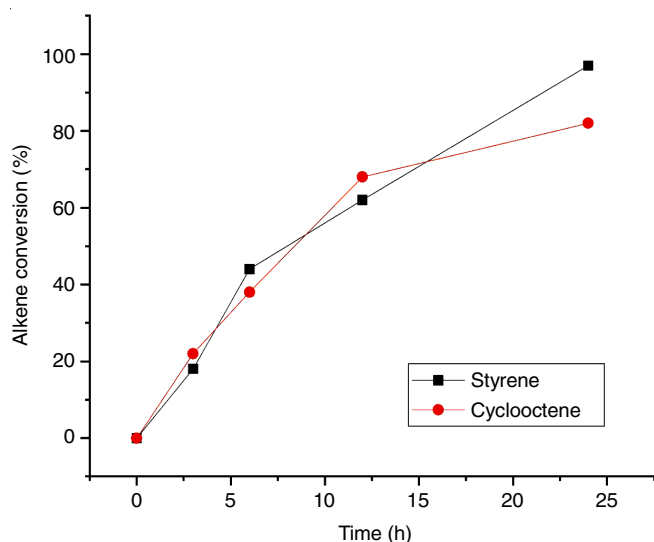


Fig. 6. Reaction profile for the oxidation of olefins with *tert*-BuOOH in presence of complex **1**

The catalytic efficacy of different azido-bridged Schiff base copper(II) complexes which gives styrene epoxide in 100-90% yield (selectivity 72-54%) was also studied under homogeneous condition using same oxidant [18,19]. Das *et al.* [20] have obtained a moderate yield of olefin epoxide using a copper(II) Schiff base complex as a catalyst in the presence of 2-methylpropanal using molecular oxygen as oxidant under homogeneous conditions [20]. A maximum yield of 15% of styrene epoxide has been achieved using iodosyl benzene as oxidant over Schiff base copper(II) complexes [21]. Rayati *et al.* [22] studied epoxidation of styrene over two copper(II) Schiff base

complexes under homogeneous conditions using *tert*-BuOOH, which shows over 95% conversion with epoxide selectivity 25%. Saha *et al.* [23] reported styrene epoxidation reaction over a copper(II) Schiff base complex, [Cu(HL<sup>1</sup>)(NO<sub>3</sub>)] (H<sub>2</sub>L<sup>1</sup> = 1-(*N*-ortho-hydroxyacetophenimine)ethane-2-ol), which shows 86% conversion with 100% epoxide selectivity [23].

The results of reported epoxidation reactions of styrene using *tert*-BuOOH as oxidant over copper(II) Schiff base complexes under homogeneous conditions are collated in Table-6. Cyclooctene was converted in good yield (conversion 82%) to their oxides, with high epoxide selectivity (83%) when reacted with *tert*-BuOOH. In addition, a small amount of cyclooctane-1,2-diol was also formed. We have earlier studied the oxidation reactions of a variety of olefins over copper(II) Schiff base complexes, which exhibit excellent catalytic activity with *tert*-BuOOH in different solvent media, where cyclooctene has been converted to its epoxide (conversion 76-75%, selectivity 63-56%) in acetonitrile media [16]. Likewise, the epoxidation of cyclooctene using a single end-on azido bridged 1D chain Schiff base copper(II) complex as catalyst is also reported [24], where the highest conversion occurred also in acetonitrile conversion 86%, selectivity 81%) with *tert*-BuOOH as oxidant. We have successfully converted cyclooctene to cyclooctene oxide by some azido-bridged Schiff base copper(II) complexes (conversion 96-85%, selectivity 76-72%) in recent past [18,19]. In our very recent attempt, we converted cyclooctene with 86% epoxide yield using a neutral nitrate bridged coordination polymer of copper(II) containing a tridentate Schiff base as catalyst [25]. Rayati *et al.* [22] studied the oxidation of cyclooctene with *tert*-BuOOH in the presence of electron-rich salen type Schiff base copper(II) complexes, where the highest con-

TABLE-6  
COMPARISON OF CATALYTIC EFFICACY OF THE COMPLEX **1** WITH OTHER REPORTED COPPER(II) CATALYSTS FOR THE OXIDATION OF STYRENE AND CYCLOOCTENE WITH *tert*-BUOOH IN CH<sub>3</sub>CN MEDIUM

Complexes	Conversion (%)		Ref.
	Styrene	Cyclooctene	
[Cu(L <sup>1</sup> )(H <sub>2</sub> O)](ClO <sub>4</sub> )	86	75	[16]
[Cu(L <sup>2</sup> )]	75	75	[16]
[Cu(L <sup>3</sup> )]	99	76	[16]
[Cu <sub>2</sub> (L <sup>4</sup> ) <sub>2</sub> (μ <sub>2</sub> -1,1-N <sub>3</sub> ) <sub>2</sub> ]	82	78	[17]
[CuL <sup>5</sup> (μ <sub>3</sub> -1,3-N <sub>3</sub> ) <sub>n</sub> ]	100	96	[18]
[Cu(L <sup>6</sup> )(N <sub>3</sub> )]	98	95	[19]
[Cu <sub>2</sub> (L <sup>7</sup> ) <sub>2</sub> (μ <sub>2</sub> -1,1-N <sub>3</sub> ) <sub>2</sub> ] [Cu(L <sup>8</sup> )(N <sub>3</sub> )]	96	90	[19]
[Cu(L <sup>8</sup> )(N <sub>3</sub> )]	90	85	[19]
[Cu{salnptn(3-OMe) <sub>2</sub> }]	97 <sup>a</sup>	70 <sup>b</sup>	[22]
[Cu(hnaphnptn)]	96 <sup>a</sup>	70 <sup>b</sup>	[22]
[Cu(HL <sup>9</sup> )(NO <sub>3</sub> )]	98	–	[23]
CuL <sup>10</sup> (μ-1,1-N <sub>3</sub> ) <sub>n</sub>	–	86	[24]
[Cu(L <sup>11</sup> )(μ-ONO <sub>2</sub> ) <sub>n</sub> ]	–	88	[25]
(CuL <sub>n</sub> , n = 1–4)	–	69	[26]
[Cu <sub>2</sub> (salen) <sub>2</sub> ] ( <b>1</b> )	97	82	This work

HL<sup>1</sup> = 1-(*N*-ortho-hydroxy-acetophenimine)-2-methyl-pyridine, H<sub>2</sub>L<sup>2</sup> = *N,N'*-(2-hydroxy-propane-1,3-diyl)-*bis*-salicylideneimine, H<sub>2</sub>L<sup>3</sup> = *N,N'*-(2,2-dimethyl-propane-1,3-diyl)-*bis*-salicylideneimine, L<sup>4</sup> = 2-[1-(aminoethylimino)ethyl]-phenoxo ion, HL<sup>5</sup> = 2-[1-(methylamino-ethylimino)-methyl]-phenol, HL<sup>6</sup> = 1-(*N*-5-methoxy-ortho-hydroxyacetophenimino)-2,2-dimethyl-aminoethane, HL<sup>7</sup> = 1-(*N*-ortho-hydroxyacetophenimine)-2,2'-diethyl-aminoethane, HL<sup>8</sup> = 1-(*N*-salicylideneimino)-2-(*N,N*-diethyl)-aminoethane, H<sub>2</sub>{salnptn(3-OMe)<sub>2</sub>} = Schiff-base derived by the condensation of 2,2'-dimethylpropandiamine and 2-hydroxy-3-methoxybenzaldehyde, H<sub>2</sub>{hnaphnptn} = Schiff-base derived by the condensation of 2,2'-dimethylpropandiamine and 2-hydroxy-1-naphthaldehyde, H<sub>2</sub>L<sup>9</sup> = 1-(*N*-ortho-hydroxyacetophenimine)-ethane-2-ol, HL<sup>10</sup> = 1-(*N*-ortho-hydroxyacetophenimine)-2-(*N*-ethyl)aminoethane, HL<sup>11</sup> = 4-methoxy-2-[1-(methylaminoethylimino)methyl]-phenol, Schiff-base derived from the condensation of meso-1,2-diphenyl-1,2-ethylenediamine with various salicylaldehyde derivatives (*x*-salicylaldehyde for H<sub>2</sub>L<sub>n</sub>, *x* = H (*n* = 1), 5-Br (*n* = 2), 5-Br-3-NO<sub>2</sub> (*n* = 3) and 2-hydroxyacetophenone (*n* = 4); <sup>a</sup>For 6 h, <sup>b</sup>For 8 h

ersion was 70% after 8 h in acetonitrile media and epoxide selectivity was 100% [22]. Abbasi *et al.* [26] demonstrated the epoxidation of cyclooctene over a series of mononuclear and dinuclear salen type copper(II) Schiff base complexes using *tert*-BuOOH, where the highest conversion goes to 85% with maximum 67% epoxide selectivity. Along with the epoxide, the allylic oxidation product cyclooct-2-en-1-ol and cyclooct-2-en-1-one were also obtained.

However, in present study, the conversion of cyclooctene by complex **1** displayed favourable epoxide selectivity. We studied some control experiments by varying the solvents, temperature and the ratio of the oxidant to optimize the catalytic reaction. Solvent polarity plays an important role for oxidation reaction. The best performance of the catalyst was observed in acetonitrile media. Due to the optimum polarity of acetonitrile, it can dissolve both olefin and *tert*-BuOOH, which might be facilitating the highest catalytic activity. A graphical representation of the relative efficacy of the catalyst **1** for the oxidation of alkenes in different solvents is shown in Fig. 7. The efficiency of catalyst followed the order: acetonitrile > acetone > chloroform > dichloromethane (Table-7). We acquainted the reactions by varying the temperature from room temperature to 75 °C for cyclooctene in acetonitrile to determine the optimum reaction temperature (Fig. 8). The reaction profile clearly evidenced that an optimum temperature of 65-70 °C is needed to activate the catalyst. Control experiments without using catalyst failed to produce the desired product (Table-8). The conversion of cyclooctene was only 4% in the absence of the catalyst. Simple copper nitrate was compared with catalyst **1** to glimpse the structural effect. Although the conversion was good (67%), it showed poor epoxide selectivity (54%). The copper(II) binds the peroxy-group on treatment with peroxides [27] to form the pre-catalyst containing  $L_nCu-OOH$  (where L= ligand), which are capable of transferring the oxo-functionality to the organic substrates to produce the oxidized products [28]. It is our assumption that a similar kind of mechanism may be workable in this present case too. The coordination environment

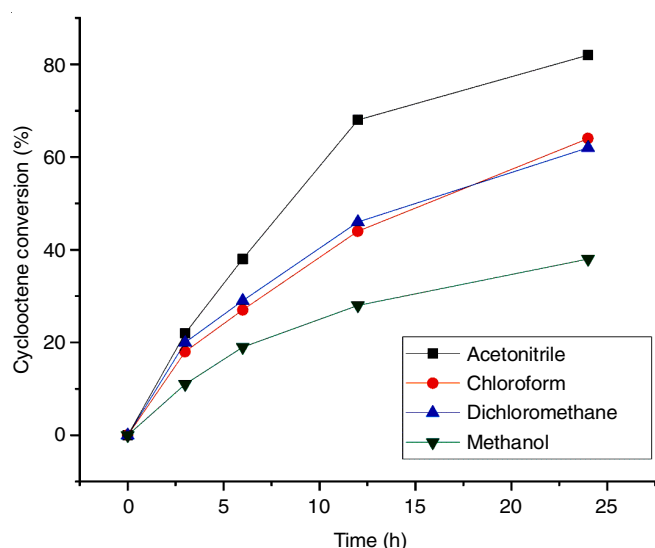


Fig. 7. Reaction profile for the oxidation of cyclooctene with *tert*-BuOOH in different solvents over complex **1**

Solvent	Reaction time (h)	Conversion (wt.%)	Yield of products (%)	
			Epoxide	Others <sup>a</sup>
CH <sub>3</sub> CN	24	82	68	14
CHCl <sub>3</sub>	24	64	47	17
CH <sub>2</sub> Cl <sub>2</sub>	24	62	46	16
CH <sub>3</sub> OH	24	38	24	14

Reaction conditions: Cyclooctene (10 mmol); catalysts (0.005 mmol); *tert*-BuOOH (20 mmol); acetonitrile (8 mL); <sup>a</sup>Cyclooct-2-en-1-ol and cyclooct-2-en-1-one.

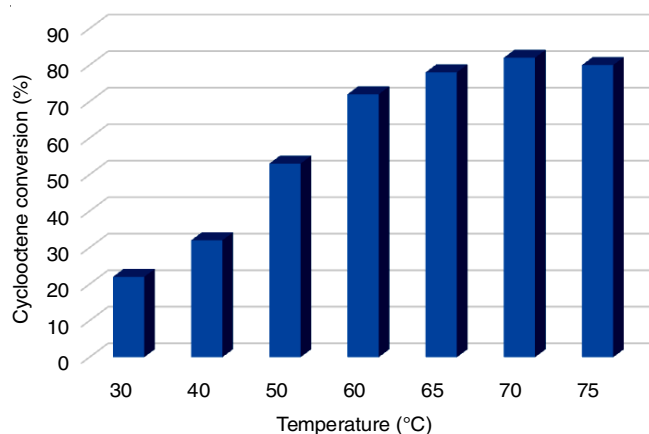


Fig. 8. Comparison of catalytic efficacy of complex **1** at different temperatures

Run	Catalyst	Conversion (wt%)	Yield of epoxide (%)
1	No catalyst	5	5
2	Cu(NO <sub>3</sub> ) <sub>2</sub>	67	36
3	[Cu <sub>2</sub> (salen) <sub>2</sub> ] ( <b>1</b> )	82	68

Reaction conditions: Cyclooctene (10 mmol); catalyst (0.005 mmol); *tert*-BuOOH (20 mmol); CH<sub>3</sub>CN (8 mL).

around copper(II) is easily cognizable for an external ligand. As a result, *tert*-BuOOH occupies enough space to bind copper in the intermediate stages of the catalytic cycle.

## Conclusion

In summary, a one neutral dimeric copper(II) complex  $\{\mu-[2,2'-\{\text{ethane-1,2-diylbis}[(\text{azanylylidene})\text{methanylylidene}]]\text{-bis(phenolato)}]\}-\{\mu-[2,2'-\{\text{ethane-1,2-diylbis}[(\text{azanylylidene})\text{methanylylidene}]]\text{bis(phenolato)}]\}\text{dicopper(II)}$  (**1**) with a tetradentate Schiff base (NNOO) has been synthesized and characterized by X-ray diffraction analysis and spectroscopic studies. X-ray single crystal structure examination indicated that the dimeric structure is embodied through congregation of a tetradentate Schiff base (salen) with (NNOO) donor sets with Cu...Cu separation 3.207 Å. A 3D network structure architects involving dimeric units through C-H... $\pi$  and  $\pi$ ... $\pi$  interactions in the crystalline state. The variable-temperature magnetic susceptibility measurement revealed an antiferromagnetic interaction between the copper(II) centers. The catalytic competency



of complex **1** was studied in a series of solvents for the oxidation of styrene and cyclooctene using *tert*-butyl-hydroperoxide (TBHP) as an efficient oxidant under mild conditions. The catalytic reaction mixture has been analyzed by gas chromatography and it displayed that the yield of the oxidation and its selectivity is maximum in acetonitrile medium.

### Supplementary material

Crystallographic data for the structural analysis has been deposited with the Cambridge Crystallographic Data Centre No. 1551353 for complex **1**. Copy of the data can be obtained free of charge from the Director, CCDC, 12 Union Road, Cambridge CB2 1EZ, UK (fax: +44(0) 1223-336033; or e-mail: deposit@ccdc.cam.ac.uk or <http://www.ccdc.cam.ac.uk>).

### ACKNOWLEDGEMENTS

The work is financially supported by the Department of Science and Technology, Government of India, by a grant (SR/S1/IC-0013/2010).

### CONFLICT OF INTEREST

The authors declare that there is no conflict of interests regarding the publication of this article.

### REFERENCES

- R. Ricco, C. Pfeiffer, K. Sumida, C.J. Sumbly, P. Falcaro, S. Furukawa, N.R. Champness and C.J. Doonan, *CrystEngComm*, **18**, 6532 (2016); <https://doi.org/10.1039/C6CE01030J>
- M.L. Neidig, D.L. Clark and R.L. Martin, *Coord. Chem. Rev.*, **257**, 394 (2013); <https://doi.org/10.1016/j.ccr.2012.04.029>
- J. Reedijk, *Chem. Soc. Rev.*, **42**, 1776 (2013); <https://doi.org/10.1039/C2CS35239G>
- E.R.T. Tiekink and J. Zukerman-Schpector, The Importance of Pi-interactions in Crystal Engineering: Frontiers in Crystal Engineering, John Wiley & Sons: Chichester, UK, Ed. 1 (2012).
- R.R. Ozer and J.P. Hinestroza, *RSC Adv.*, **5**, 15198 (2015); <https://doi.org/10.1039/C4RA15161E>
- C.C. Corrêa, L.B. Lopes, L.H.R. dos Santos, R. Diniz, M.I. Yoshida, L.F.C. de Oliveira and F.C. Machad, *Inorg. Chim. Acta*, **367**, 187 (2011); <https://doi.org/10.1016/j.ica.2010.12.034>
- Z.N. Wang, X. Wang, S.Y. Wei, J.X. Wang, F.Y. Bai, Y.H. Xing and L.X. Sun, *New J. Chem.*, **39**, 4168 (2015); <https://doi.org/10.1039/C5NJ00173K>
- C. Mottillo and T. Friscic, *Chem. Commun.*, **51**, 8924 (2015); <https://doi.org/10.1039/C5CC01645B>
- E.-S.M. El-Sayed and D. Yuan, *Chem. Lett.*, **49**, 28 (2020); <https://doi.org/10.1246/cl.190731>
- M. Habib, T.K. Karmakar, G. Aromí, J. Ribas-Ariño, H.-K. Fun, S. Chantrapromma and S.K. Chandra, *Inorg. Chem.*, **47**, 4109 (2008); <https://doi.org/10.1021/ic701754u>
- S. Konar, S. Dalai, J. Ribas, M.G.B. Drew, E. Zangrando and N.R. Chaudhuri, *Inorg. Chim. Acta*, **357**, 4208 (2004); <https://doi.org/10.1016/j.ica.2004.05.035>
- M. Du, Q. Wang, Y. Wang, X.-J. Zhao and J. Ribas, *J. Solid State Chem.*, **179**, 3926 (2006); <https://doi.org/10.1016/j.jssc.2006.08.039>
- P.A. Vigato and S. Tamburini, *Coord. Chem. Rev.*, **252**, 1871 (2008); <https://doi.org/10.1016/j.ccr.2007.10.030>
- F.A. Mautner, M. Mikuriya, H. Ishida, H. Sakiyama, F.R. Louka, J.W. Humphrey and S.S. Massoud, *Inorg. Chim. Acta*, **362**, 4073 (2009); <https://doi.org/10.1016/j.ica.2009.05.066>
- S. Shaw and J.D. White, *Chem. Rev.*, **119**, 9381 (2019); <https://doi.org/10.1021/acs.chemrev.9b00074>
- C. Adhikary, R. Bera, B. Dutta, S. Jana, G. Bocelli, A. Cantoni, S. Chaudhuri and S. Koner, *Polyhedron*, **27**, 1556 (2008); <https://doi.org/10.1016/j.poly.2008.01.030>
- H. Chowdhury, R. Bera, C. Rizzoli and C. Adhikary, *J. Coord. Chem.*, **73**, 3062 (2020); <https://doi.org/10.1080/00958972.2020.1836360>
- S. Banerjee, C. Adhikary, C. Rizzoli and R. Pal, *Inorg. Chim. Acta*, **409**, 202 (2014); <https://doi.org/10.1016/j.ica.2013.09.032>
- C. Adhikary, S. Banerjee, J. Chakraborty and S. Ianelli, *Polyhedron*, **65**, 48 (2013); <https://doi.org/10.1016/j.poly.2013.08.019>
- G. Das, R. Shukla, S. Mandal, R. Singh, P.K. Bharadwaj, J. van Hall and K.H. Whitmire, *Inorg. Chem.*, **36**, 323 (1997); <https://doi.org/10.1021/ic9510371>
- S. Zolezzi, E. Spodine and A. Decinti, *Polyhedron*, **22**, 1653 (2003); [https://doi.org/10.1016/S0277-5387\(03\)00326-7](https://doi.org/10.1016/S0277-5387(03)00326-7)
- S. Rayati, S. Zakavi, M. Koliaei, A. Wojtczak and A. Kozakiewicz, *Inorg. Chem. Commun.*, **13**, 203 (2010); <https://doi.org/10.1016/j.inoche.2009.11.016>
- D. Saha, T. Maity, T. Dey and S. Koner, *Polyhedron*, **35**, 55 (2012); <https://doi.org/10.1016/j.poly.2011.12.039>
- R. Bera, C. Adhikary, S. Ianelli, S. Chaudhuri and S. Koner, *Polyhedron*, **29**, 2166 (2010); <https://doi.org/10.1016/j.poly.2010.04.012>
- H. Chowdhury, R. Bera, C. Rizzoli and C. Adhikary, *Transition Met. Chem.*, **45**, 605 (2020); <https://doi.org/10.1007/s11243-020-00415-7>
- Z. Abbas, M. Behzad, A. Ghaffari, H.A. Rudbari and G. Bruno, *Inorg. Chim. Acta*, **414**, 78 (2014); <https://doi.org/10.1016/j.ica.2014.01.047>
- T. Osako, S. Nagatomo, Y. Tachi, T. Kitagawa and S. Itoh, *Angew. Chem. Int. Ed. Engl.*, **41**, 4325 (2002); [https://doi.org/10.1002/1521-3773\(20021115\)41:22<4325::AID-ANIE4325>3.0.CO;2-Y](https://doi.org/10.1002/1521-3773(20021115)41:22<4325::AID-ANIE4325>3.0.CO;2-Y)
- S.T. Prigge, B.A. Eipper, R.E. Mains and L.M. Amzel, *Science*, **304**, 864 (2004); <https://doi.org/10.1126/science.1094583>
- M.M. Bhadbhade and D. Srinivas, *Inorg. Chem.*, **32**, 6122 (1993); <https://doi.org/10.1021/ic00078a037>
- Bruker APEX2, (Version 2008.1-0), SAINT (Version 7.51A) and SADABS (Version 2007/4) Bruker AXS Inc: Madison, Wisconsin, USA (2008).
- A. Altomare, M.C. Burla, M. Camalli, G.L. Casciarano, C. Giacovazzo, A. Guagliardi, A.G.G. Moliterni, G. Polidori and R. Spagna, *J. Appl. Cryst.*, **32**, 115 (1999); <https://doi.org/10.1107/S0021889898007717>
- G.M. Sheldrick, *Acta Cryst.*, **C71**, 3 (2015); <https://doi.org/10.1107/S2053229614024218>
- K. Nakamoto, Infrared and Raman Spectra of Inorganic and Coordination Compounds, Part A and B, Wiley: New York, Ed. 5 (1997).
- A.B.P. Lever, Inorganic Electronic Spectroscopy, Elsevier: New York, Ed. 2 (1984).
- A. Escuer, M.A.S. Goher, F.A. Mautner and R. Vicente, *Inorg. Chem.*, **39**, 2107 (2000); <https://doi.org/10.1021/ic991135c>
- E. Ruiz, S. Alvarez and P. Alemany, *Chem. Commun.*, 2767 (1998); <https://doi.org/10.1039/a807973k>
- C.P. Landee and M.M. Turnbull, *J. Coord. Chem.*, **67**, 375 (2014); <https://doi.org/10.1080/00958972.2014.889294>



## Source details

[Feedback >](#) [Compare sources >](#)

### Asian Journal of Chemistry

Scopus coverage years: from 1996 to Present

Publisher: Asian Publication Corporation

ISSN: 0970-7077

Subject area: [Chemistry: General Chemistry](#)

Source type: Journal

[View all documents >](#)[Set document alert](#)[Save to source list](#)

CiteScore 2022

0.9



SJR 2022

0.149



SNIP 2022

0.223





# Coordination of reduced Schiff base anion to Pd(II): Synthesis, characterization, DFT calculation and catecholase activity

Madhusudan Shit<sup>a,b,\*</sup>

<sup>a</sup> Department of Chemistry, Dinabandhu Andrews College, 54, Raja S. C. Mallick Road, Kolkata, 700084, West Bengal, India

<sup>b</sup> Department of Chemistry, Ramakrishna Mission Residential College, Narendrapur, Kolkata, 700103, West Bengal, India

## ARTICLE INFO

### Keywords:

Reduced Schiff base  
Crystal structure  
DFT calculation  
Catecholase activity

## ABSTRACT

The article reports the synthesis and characterization of a new palladium(II) complex of type  $[(L_{NNN}^1)PdCl]$  (**1**) where  $L_{NNN}^1$  is a mono anionic Schiff's base having a imine bond in reduced state. The  $L_{NNN}^1$  is generated from a tridentate NNN donor ligand ( $L_{NNN}$ ) through in-situ reduction using sodium borohydride, where  $L_{NNN}$  is [(E)-N-(phenyl(pyridine-2-yl)methylene)quinoline-8-amine)]. **1** is characterized by the single crystal X-ray diffraction study, IR, mass and UV-Vis spectroscopy. The X-ray bond parameter authenticates the imine bond of the coordinated Schiff's base anion is in reduced state. **1** exhibits catalytic activity towards the oxidation of 3,5-ditertiarybutyl catechol (3,5-DTBC) with turnover number ( $K_{cat}$ ) = 135.6 h<sup>-1</sup>. The catalytic oxidation of 3,5-DTBC is authenticated by the UV-Vis, mass and EPR spectroscopy. An isotropic EPR signal with  $g = 2.011$  of a solution containing **1** and 3,5-DTBC authenticating the generation of organic radical during the oxidation process. Cyclic voltammogram of **1** displays an irreversible anodic wave at +0.22 V may be due to the oxidation of N<sup>-</sup> to N<sup>•-</sup>. The atomic spin density of **1**<sup>+</sup> obtained from DFT calculation is also supporting the N-centre oxidation process.

## 1. Introduction

Schiff base ligands are versatile in nature and form variable complexes with almost all transition metal ions [1,2]. Many scientific reports highlighting the catalytic activities of transition metal Schiff base complexes both in homogeneous and heterogeneous medium were known to literature [3–6]. The activities of these complexes were widespread to chemical, biochemical, industrial, clinical and analytical field [7,8]. However, the Schiff's bases having imine reduced fragment are more effective for coordination to metal ion compared to corresponding Schiff base analogue because of greater stability, flexible conformationality and adaptability of the former to provide a flexible backbone. Therefore, researchers are focused to synthesize new coordination complexes with imine reduced Schiff base anions [9,10]. Coordination complexes of palladium(II) with Schiff bases have enormous catalytic reactivity towards polymerisation of ethylene, Suzuki-Miyara cross coupling reaction, Heck reaction, oxidation, epoxidation, C–H bond activation reaction [11,12]. For this reason, researchers are interested to explore the catalytic activities of new type of palladium complexes with Schiff base or reduced Schiff base ligands. In this work, synthesis and catecholase activity of a new palladium(II) complex containing an imine reduced Schiff base of the type  $[(L_{NNN}^1)PdCl]$  (**1**) is reported. The synthetic route of the **1**

is given in Chart S1. The catecholase activities of Mn(II), Fe(III), Co(III), Ni(II), Cu(II) and Zn(II) complexes were reported earlier [13–24] but the catecholase activity of transitional metal complexes with reduced Schiff's base are only very few [25–27]. It is worth mentioning that the catecholase activity of Pd(II) complex is not known till now. Therefore, the catecholase activity of **1** gives a quill to the palladium(II) chemistry towards catalytic activities. The article is presenting synthesis, characterization, molecular and electronic structures and catecholase activity of **1**. These are authenticated by X-ray crystallography, UV-vis, mass, EPR spectroscopy, cyclic voltammetry and DFT calculation.

## 2. Experimental section

### 2.1. Materials and physical measurements

8-aminoquinoline (8AQ), 2-benzoylpyridine (bpy) and palladium chloride were purchased from commercial suppliers and used without further purification. The ligand [(E)-N-(phenyl(pyridine-2-yl)methylene)quinoline-8-amine] was prepared by the reported procedure [28]. Spectroscopic-grade solvents were used for spectroscopic and electrochemical measurements. The C, H and N content of the compound were obtained from a PerkinElmer 2400 Series II elemental analyzer. The

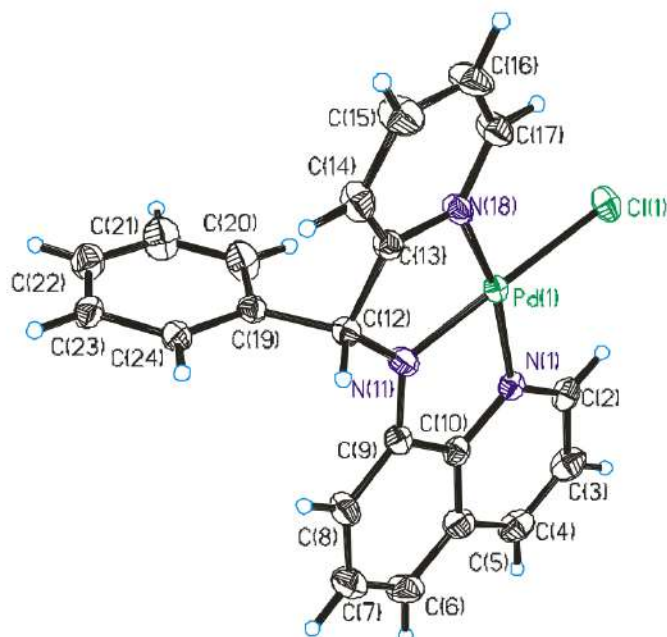
\* Department of Chemistry, Dinabandhu Andrews College, 54, Raja S. C. Mallick Road, Kolkata, 700084, West Bengal, India.

E-mail address: [madhusudanshit@gmail.com](mailto:madhusudanshit@gmail.com).

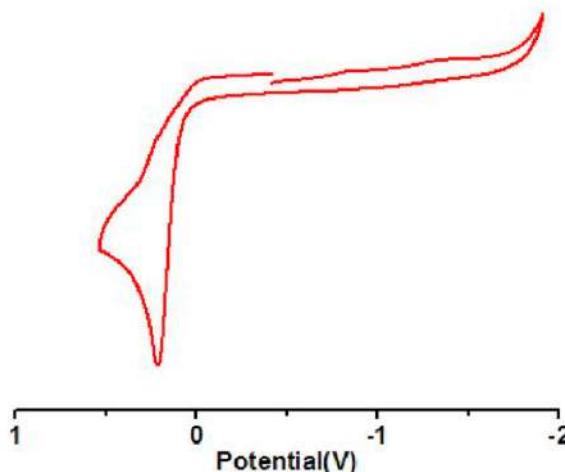
**Table 1**  
Crystallographic data of **1**.

Formula	C <sub>21</sub> H <sub>16</sub> ClN <sub>3</sub> Pd	T (K)	294(2)
Fw	452.22	2θ	50.00
crystal system	monoclinic	ρ calcd (g.cm <sup>-3</sup> )	1.605
crystal colour	red	refl. collected	21820
space group	P2 <sub>1</sub> /c	unique refl.	3179
a (Å)	15.380(11)	reflection [I > 2σ(I)]	2964
b (Å)	11.8341 (8)	F(000)	904
c (Å)	10.2369(7)	no. of params/restr.	235/0
α (deg)	90	λ (Å)/μ(mm <sup>-1</sup> )	0.71073/1.174
β (deg)	102.062(3)	R1 <sup>a</sup> [I > 2σ(I)]/GOF <sup>b</sup>	0.0561/1.258
γ (deg)	90	wR2 <sup>c</sup> [I > 2σ(I)]	0.1431
V (Å <sup>3</sup> )	1822.1(2)	residual density (eÅ <sup>-3</sup> )	1.534
Z	4		

Observation criterion: <sup>a</sup>R1 =  $\sum ||F_o| - |F_c|| / \sum |F_o|$ , <sup>b</sup>GOF =  $\{\sum [w(F_o^2 - F_c^2)^2] / (n-p)\}^{1/2}$ , <sup>c</sup>wR2 =  $[\sum [w(F_o^2 - F_c^2)^2] / \sum w(F_o^2)]^{1/2}$  where  $w = 1/[\sigma^2(F_o^2) + (ap)^2 + bP]$ ,  $P = (F_o^2 + 2F_c^2) / 3$ .

**Fig. 1.** Molecular geometry of **1** in crystals (30% thermal ellipsoid, H atoms are omitted for clarity).**Table 2**  
The selected experimental and calculated bond parameter of **1**.

Exp	Cal	
Bonds/Angles	Length(Å)/Deg(°)	
Pd(1)–N(1)	2.031(6)	2.056
Pd(1)–N(11)	1.921(6)	1.980
Pd(1)–N(18)	2.035(6)	2.058
Pd(1)–Cl(1)	2.330(2)	2.382
N(1)–C(10)	1.393(10)	1.375
C(9)–C(10)	1.422(11)	1.443
C(9)–N(11)	1.347(10)	1.359
N(11)–C(12)	1.482(10)	1.448
C(12)–C(13)	1.520(10)	1.533
C(13)–N(18)	1.350(9)	1.357
N(1)–Pd(1)–N(18)	163.7(3)	162.7
N(11)–Pd(1)–Cl(1)	178.7(2)	179.25
N(1)–Pd(1)–Cl(1)	97.69(19)	98.4
N(1)–Pd(1)–N(11)	82.3(3)	81.73
N(11)–Pd(1)–N(18)	81.9(3)	81.33
N(18)–Pd(1)–Cl(1)	98.01(18)	98.5

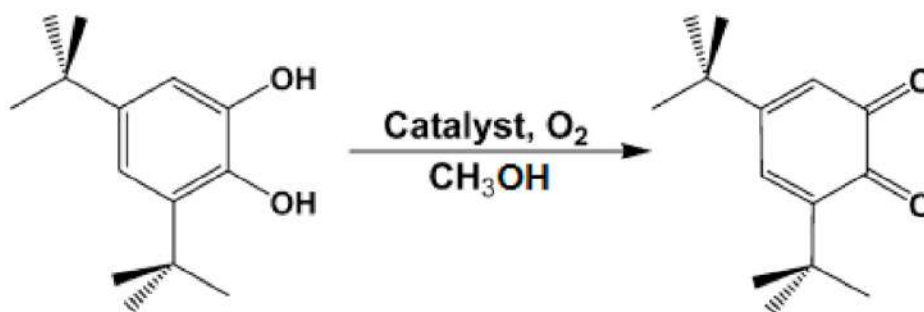
**Fig. 2.** Cyclic voltammogram of complex in CH<sub>2</sub>Cl<sub>2</sub> (0.20 M [N(n-Bu)<sub>4</sub>]PF<sub>6</sub>) at 295 K.

elemental analysis was performed after evaporating the solvents under high vacuum. Infrared spectrum of the sample was measured from 4000 to 400 cm<sup>-1</sup> with KBr pellet at 295 K on a PerkinElmer Spectrum RX 1 Fourier transform infrared (FT-IR) spectrophotometer. Electrospray ionization (ESI) mass spectra were obtained from LCMS 2020 mass spectrometer. Electronic absorption spectra and catecholase activity were studied with a PerkinElmer Lambda 750 spectrophotometer in the range of 3300–175 nm. The electro-analytical instrument, BASi Epsilon-EC for cyclic voltammetric experiments in dichloromethane containing 0.2 M tetrabutylammoniumhexafluorophosphate as supporting electrolyte was used. The BASi platinum working electrode, platinum auxiliary electrode, Ag/AgCl reference electrodes were used for the measurements. The redox potential data were referenced to ferrocene/ferrocene, Fc<sup>+</sup>/Fc, couple. X-band EPR spectra were recorded on a Magnetech GmbH MiniScope MS400 spectrometer (equipped with temperature controller TC H03, Magnetech, Berlin, Germany), where the microwave frequency was measured with an FC400 frequency counter.

## 2.2. Synthesis

### 2.2.1. [(L<sub>NN</sub>)Pd<sup>II</sup>Cl] (**1**)

8-aminoquinoline (8AQ) (36 mg, 0.25 mmol) and 2-benzoylpyridine (bpy) (46 mg, 0.25 mmol) were taken in a round bottom flask. The solids are blended with a glass rod to mix uniformly and heated at 40 °C to melt and then refluxed with a mixture of solvent (20 ml CH<sub>3</sub>CN and 5 ml CH<sub>3</sub>OH). After that sodium borohydride (20 mg, 0.50 mmol) was added portion wise and stir for 30 minutes. The reaction mixture was allowed to stand for few minutes to ensure the complete reduction of the ligand and allow to decomposing excess NaBH<sub>4</sub> if present in solution by reaction with solvent CH<sub>3</sub>OH. After that, the solution was filtered to get the clear solution. Finally, PdCl<sub>2</sub> (44.5 mg, 0.25 mmol) in 20 ml CH<sub>3</sub>CN was added to the resulting filtrate and refluxed for another 10 minutes. The solution turns to deep red colour. Then, the solution was cooled to room temperature and filtered. The filtrate was allowed to evaporate slowly in air. After 3–4 days, deep red crystals of **1** was separated out, which were collected upon filtration and dried in air. Yield: 68 mg (~60% with respect to palladium). Mass spectral data [electrospray ionization (ESI) positive ion, CH<sub>3</sub>OH]: *m/z* 451 for [1]<sup>+</sup>. Elemental Analysis: Anal. Calcd for C<sub>21</sub>H<sub>16</sub>ClN<sub>3</sub>Pd: C, 55.77; H, 3.57; N, 9.29; Found: C, 54.22; H, 3.35; N, 8.87. <sup>1</sup>H NMR (CDCl<sub>3</sub>, 300 MHz, 300 K): δ 9.01 (s, 1H), 7.73 (d, 1H), 7.72 (d, 1H), 7.70 (d, 2H), 7.69–7.51 (multiplet, 5H), 7.55–7.50 (multiplet, 4H), 6.82 (d, 1H), 6.98 (t, 1H) ppm. IR/cm<sup>-1</sup> (KBr): ν 3436(br), 2924(s), 1569(s), 1503(m), 1467(m), 1384(s), 809(s), 732(s), 703(m).



Scheme 1. Catalytic Oxidation of 3,5-DTBC to 3,5-DTBQ in methanol in presence of air.

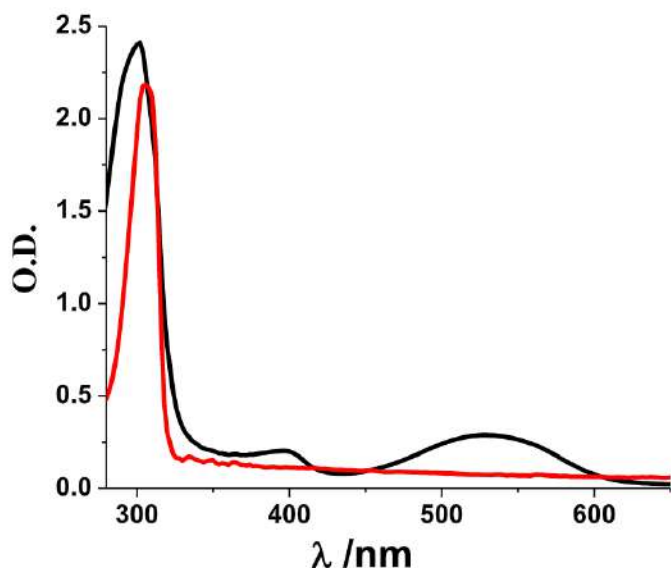


Fig. 3. UV-Vis spectra of 3,5-DTBC (red) and mixture of 3,5-DTBC and **1** (black) in methanol solution at room temperature. (For interpretation of the references to colour in this figure legend, the reader is referred to the Web version of this article.)

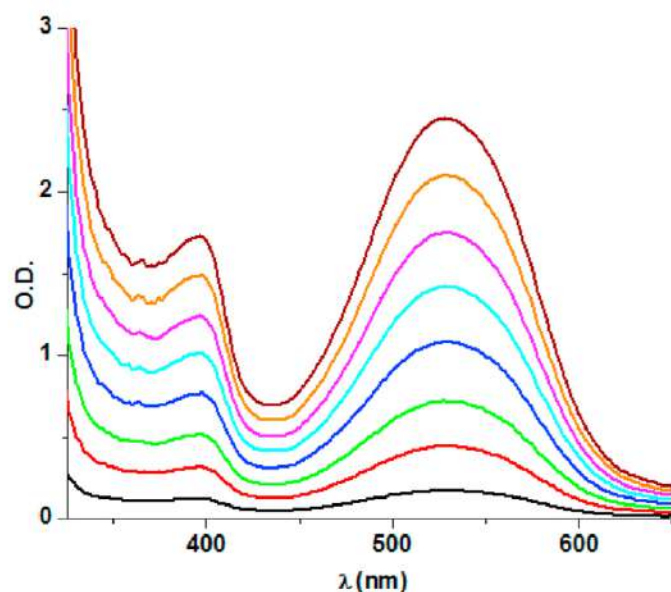


Fig. 4. Change of UV-vis spectra during Pd(II) mediated catalytic oxidation of 3,5-DTBC to 3,5-DTBQ in air-saturated methanol. First run was taken after 5 min and time interval between the successive run is 10 min.

#### 2.2.2. Single crystal X-ray structure determinations of the complex (CCDC No 2082144)

Red single crystal of **1** was picked up with nylon loops and mounted on a Bruker AXS Enraf-Nonius Kappa CCD diffractometer equipped with a Mo K $\alpha$  target rotating-anode X-ray source and a graphite monochromator (Mo K $\alpha$ ,  $\lambda = 0.71073$  Å). Final cell constants were obtained from least-squares fits of all measured reflections. Intensity data were corrected for absorption using intensities of redundant reflections. The structure was readily solved by direct methods and subsequent difference Fourier techniques. The Siemens SHELXS-97 [29] software package was used for solution, and SHELXL-97 [30] was used for the refinement and XS. Ver. 2013/1 [31], XT. Ver. 2014/4 [32] and XL. Ver. 2014/7 [33] was used for the structure solution and refinement. All non hydrogen atoms were refined anisotropically. Hydrogen atoms were placed at the calculated positions and refined as riding atoms with isotropic displacement parameters.

#### 2.2.3. Catecholase activity study

Catalytic activity of **1** towards oxidation of 3,5-DTBC was studied by measurement of UV-vis spectroscopy of **1**, 3,5-DTBC and mixture of the solution containing **1** and 3,5-DTBC. The activity was studied in the range of 250 nm–800 nm by mixing  $1 \times 10^{-4}$  M solution of **1** to the  $50 \times 10^{-4}$  M 3,5-DTBC in methanol under atmospheric condition at room temperature. Progress of the reaction was monitored with respect to time at the wavelength 398 nm in methanol solution for 2 h. Details of the solutions preparation and corresponding calculations are given in SI.

#### 2.2.4. Density functional theory (DFT) calculations

All calculations were done with the Gaussian 03W [34] program package supported by GaussView 4.1. The DFT [35] calculations were performed at the level of Becke three parameter hybrid functional with the nonlocal correlation functional of Lee–Yang–Parr (B3LYP) [36–39]. Gas-phase geometry of **1** was optimized with singlet spin state, while **1**<sup>+</sup> was optimized with doublet spin state, using Pulay's Direct Inversion [40–42] in the Iterative Subspace (DIIS), "tight" convergent self-consistent field procedure [43] ignoring symmetry. All the calculations were performed with a LANL2DZ basis set [44], along with the corresponding effective core potential (ECP) for palladium, 6-31+G\* (d,p) [45–47] basis set for C, O, N atoms and 6-31G [48] for H atoms.

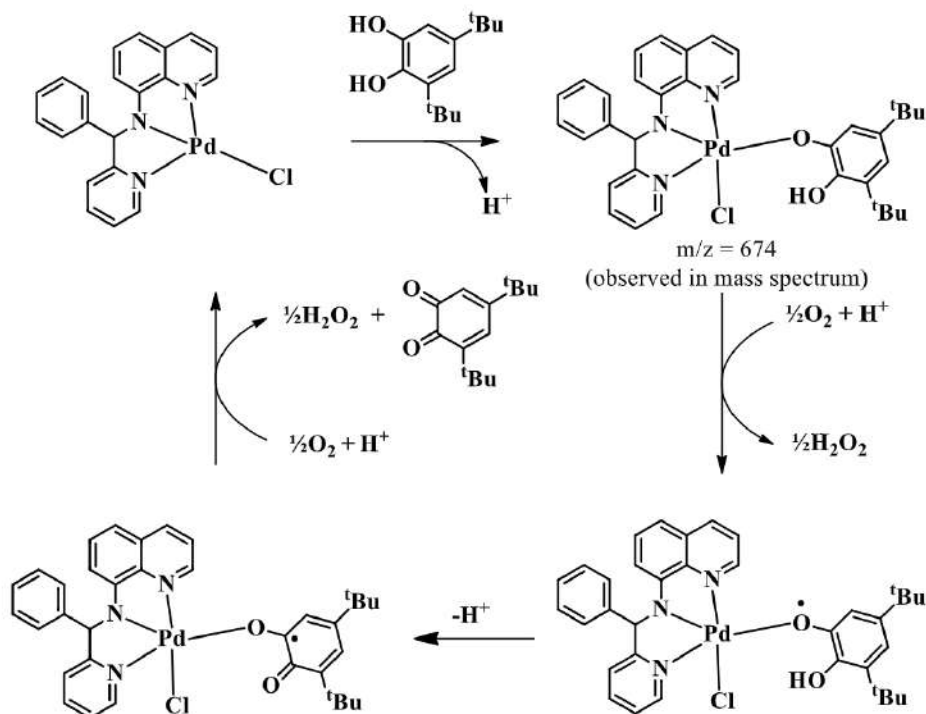
### 3. Results and discussion

#### 3.1. Synthesis and characterization

The reaction of PdCl<sub>2</sub> with L<sub>NNN</sub><sup>1-</sup> in a mixed solvent of CH<sub>3</sub>CN and CH<sub>3</sub>OH affords **1** in good yields. A detail of the synthesis is outlined in the experimental section. The IR spectrum of **1** is given in Fig. S1.

#### 3.2. X-ray crystallography

Complex **1** crystallizes in P2<sub>1</sub>/c space group. The crystallographic data of **1** is summarized in Table 1. The molecular structure of **1** in



Scheme 2. Plausible mechanism of the oxidation of 3,5-DTBC to 3,5-DTBQ.

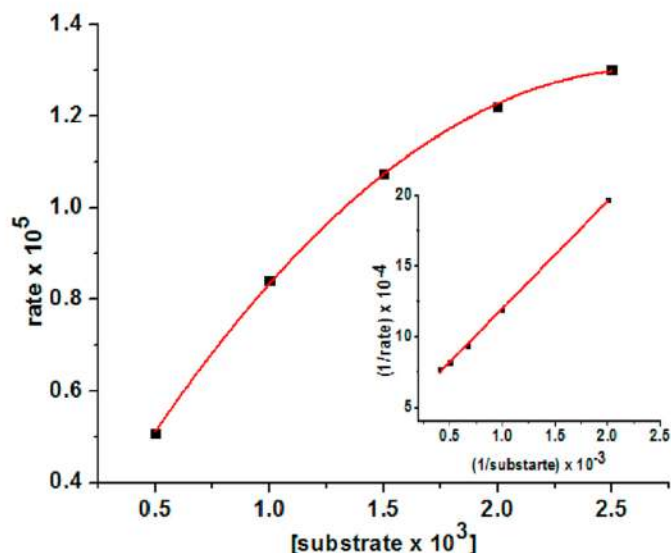


Fig. 5. Plot of rate vs [3,5-DTBC] for oxidation of 3,5-DTBC by complex 1.

crystals and the atom labelling scheme is illustrated in Fig. 1. The selected bond parameters are summarized in Table 2. The tridentate NNN donor ligand and a chloride ion are coordinated to the palladium(II) in a square planer fashion.

The N(1)-Pd(1)-N(18) and N(11)-Pd(1)-Cl(1) bond angles are 163.7 and 178.7 Deg( $^{\circ}$ ) makes the molecule distorted square planer geometry. The Pd(1)-N(1) and Pd(1)-N(18) bond lengths are 2.031(6) Å and 2.035(6) Å are comparable whereas Pd(1)-N(11) bond length is 1.921(6) Å, considerably smaller than the other two Pd-N bond lengths. Bond matrices indicate that N(1) and N(18) atoms are coordinated as neutral donor site and these are well correlated with the reported neutral-N donor towards palladium(II) [49,50]. The Pd(1)-N(11) bond length is smaller due to the coordination of anionic-N to the Pd(II). Generally,

Table 3

Comparison of  $K_{cat}$  value for the oxidation of 3,5-DTBC to 3,5-DTBQ by different reduced Schiff's base complexes.

Complex	Metal ion present	$K_{cat}$ (l $^{-1}$ s $^{-1}$ )(Solvent)	Reference
[Ni <sub>2</sub> (L <sup>1</sup> ) <sub>2</sub> (NCS) <sub>2</sub> ]	Ni(II)	64.1, CH <sub>3</sub> CN	[25]
[Ni <sub>2</sub> (L <sup>2</sup> ) <sub>2</sub> (NCS) <sub>2</sub> ]	Ni(II)	51.1, CH <sub>3</sub> CN	[25]
[Ni <sub>2</sub> (L <sup>3</sup> ) <sub>2</sub> (NCS) <sub>2</sub> ]	Ni(II)	81.7, CH <sub>3</sub> CN	[25]
[Cu <sub>2</sub> (Scp11) <sub>2</sub> (MeOH) <sub>2</sub> ]	Cu(II)	850, DMF	[27]
[Cu <sub>2</sub> (ClScp11) <sub>2</sub> (DMF)·(H <sub>2</sub> O)·MeCN	Cu(II)	694, DMF	[27]
[Cu <sub>2</sub> (MeScp11) <sub>2</sub> (MeOH) <sub>2</sub> ·2MeOH	Cu(II)	1003, DMF	[27]
[Ni <sub>2</sub> L <sub>2</sub> (PhCOO)(H <sub>2</sub> O) <sub>2</sub> ]ClO <sub>4</sub>	Ni(II)	167.64, CH <sub>3</sub> OH	[26]
[(L <sup>1</sup> ) <sub>NN</sub> PdCl]	Pd(II)	135.6, CH <sub>3</sub> OH	Present work

imine bond lengths (-C=N) are appeared in the range 1.28–1.31 Å as reported earlier [49,50] but in **1**, the N(11)-C(12) bond length is 1.482(10) Å, larger than the reported imine (C=N) bond lengths. This bond parameter authenticates the reduction of the imine bond of Schiff's base in **1**. The Pd-Cl bond length, 2.330(2) Å, is greater than the other Pd-Cl bonds (2.27 Å to 2.29 Å) reported in literature [51,52]. This is due to greater  $\pi$  bonding effect of N $^{-}$  compared to neutral N atom present in the trans position of Cl atom.

### 3.3. Electrochemical studies

The redox activity of **1** was investigated by cyclic voltammetry in CH<sub>2</sub>Cl<sub>2</sub> at 295 K. The cyclic voltammogram is shown in Fig. 2. **1** displays only an irreversible anodic peak at 0.22 V with referenced to ferrocene/ferrocene (Fc $^{+}$ /Fc) couple due to oxidation at the amine-N of the ligand fragment. The oxidation may be assigned to N $^{-}$ /N $^{+}$  redox couple which is also supported by the atomic spin density on N atom obtained from DFT calculation on **1** $^{+}$ .

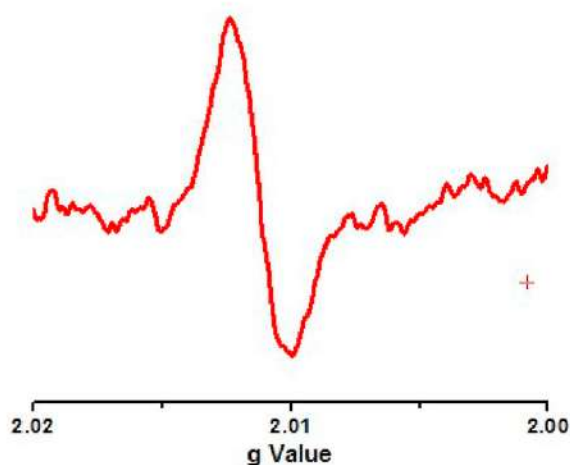


Fig. 6. X-band EPR spectra of mixture of **1** and 3,5-DTBC in  $\text{CH}_2\text{Cl}_2$  solution at 298 K.

### 3.4. Study of oxidation of 3,5-di-tertiarybutylcatechol(3,5-DTBC)

The oxidation of 3,5-DTBC to 3,5-DTBQ was investigated in presence of **1**. On exposure to air for long time catechol is oxidized to benzoquinone but 3,5-DTBC which is more stable in air as well in solution and resist the oxidation. For this reason 3,5-DTBC is used as a standard substrate to study the catecholase activity of **1** as depicted in Scheme 1. Generally, 3,5-DTBQ is highly stable in solution and exhibits an absorption maximum at 401 nm in methanol [53]. The catalytic activity was measured in a solution of  $1 \times 10^{-4}$  M metal complex and  $50 \times 10^{-4}$  M 3,5-DTBC in  $\text{CH}_3\text{OH}$ .

The change in UV-vis spectra were recorded on a PerkinElmer Lambda 750 spectrophotometer in the range of 800-250 nm. The solution gives a new absorption band at 398 nm which is not absorb either by **1** or 3,5-DTBC in methanol solution as depicted in Fig. 3. During the oxidation process intensity of the absorption band at 398 nm is gradually increases with time as illustrated in Fig. 4. The absorption band at 398 nm supports the oxidation of 3,5-DTBC to 3,5-DTBQ in presence of **1**. 3,5-DTBC first coordinate to the Pd centre and then in presence of oxygen it gets 1e oxidation to the benzosemiquinone anion radical then oxidized further by 1e to benzoquinone. The coordination of 3,5-DTBC to the Pd centre and formation of 3,5-DTBQ confirmed by mass spectra of the solution containing **1** and 3,5-DTBC in methanol. The mass appear at  $m/z$  674 (Fig. S4) and  $m/z$  221 (Fig. S4) confirms the substrate catalyst binding and formation of 3,5-DTBQ as product in the oxidation process. Generation of the benzosemiquinonate anion radical as an intermediate was

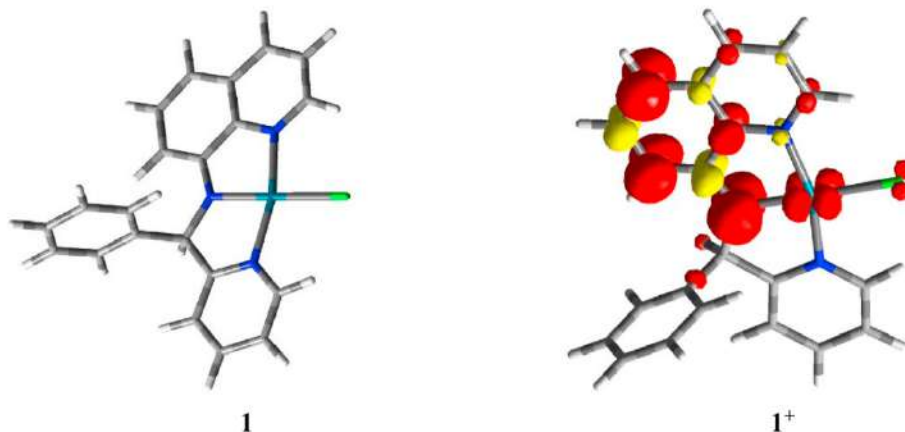


Fig. 7. Gas phase optimized geometry of **1** and atomic spin density plots of  $1^+$  obtained from DFT calculations in doublet state (Mulliken spin densities): Pd, 0.088; N(11), 0.486; C(8), 0.31.

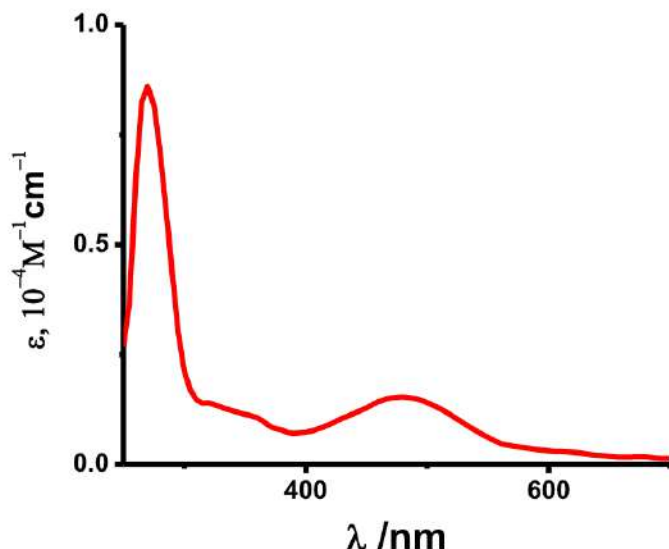


Fig. 8. UV-vis absorption spectra of **1** in  $\text{CH}_2\text{Cl}_2$  at 295 K.

Table 4

Possible transitions obtained from DFT calculation of **1**.

Complex	$\lambda_{\text{max}}$ (nm) ( $\epsilon$ , $10^4 \text{ M}^{-1} \text{ cm}^{-1}$ )	Transitions obtained from DFT calculation
<b>1</b>	480 (0.15)	HOMO $\rightarrow$ (LUMO+1), HOMO $\rightarrow$ (LUMO+2)
	362(0.10)	HOMO $\rightarrow$ (LUMO+4)
	315(0.13)	(HOMO-3) $\rightarrow$ LUMO
	270(.85)	(HOMO-1) $\rightarrow$ (LUMO+2)

confirmed by the EPR spectra. The plausible mechanism of the oxidation of 3,5-DTBC to 3,5-DTBQ is given in the Scheme 2. During the oxidation of 3,5-DTBC, hydrogen peroxide is generated as byproduct and was detected by the reported iodometric method [54]. The spectrum shown three absorption bands at 438, 353 and 290 nm (Fig. S6) indicating the presence of both  $\text{I}_2$  and  $\text{I}_3^-$  in solution. The spectrum is well corroborates with the UV-Vis spectrum of  $\text{I}_2$  in methanol solution reported earlier [55]. The detail procedure for detection of hydrogen peroxide is given in the SI.

The kinetics of oxidation of 3,5-DTBC was performed to evaluate the catalytic efficiency of **1**. The reaction rates were measured by using complex concentration  $1 \times 10^{-5}$  M and varying concentration of substrate from  $5 \times 10^{-4}$  M to  $25 \times 10^{-4}$  M and then rate vs. concentration was plotted. The rate constant vs. substrate concentration profile is given in Fig. 5,

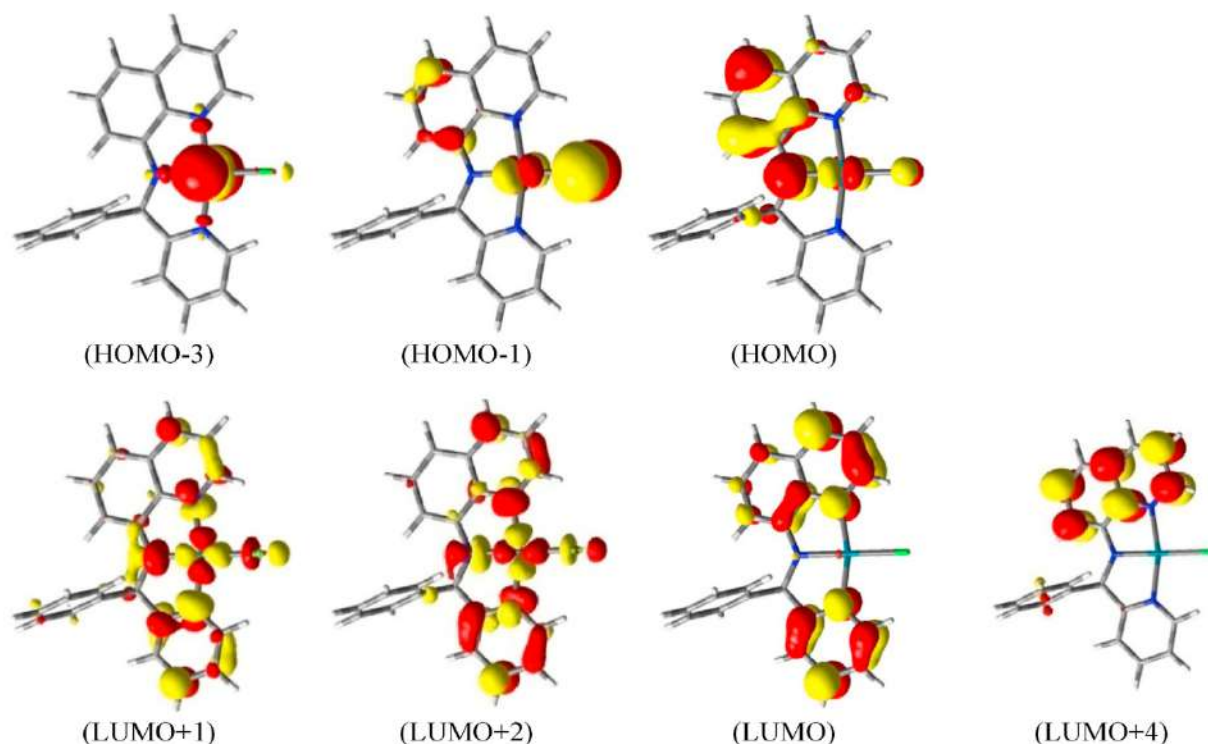


Fig. 9. Frontier molecular orbitals of **1**.

that discloses the nature of kinetics.

The nature of kinetics is first order with respect to substrate concentration obeying the Michaelis-Menten model as per the equation given below.

$$V = \frac{V_{\max}[S]}{K_M + [S]}$$

Where,  $V$  is rate of the reaction,  $K_M$  is denoted as Michaelis-Menten constant,  $V_{\max}$  is the maximum velocity of the reaction and  $[S]$  is concentration of the substrate. The kinetic parameters were determined from Michaelis-Menten equation as  $V_{\max}(\text{M min}^{-1}) = 2.26 \times 10^{-5}$ ;  $K_M = 17.13 \times 10^{-4}$  [Std. Error for  $V_{\max}(\text{M min}^{-1}) = 0.077 \times 10^{-5}$ ; Std. Error for  $K_M(\text{M}) = 0.3 \times 10^{-4}$ ]. The turnover number ( $k_{\text{cat}}$ ) was determined as  $135.6 \pm 4.6 \text{ h}^{-1}$ . The catecholase activities of some metal complexes with reduced Schiff's base have been depicted in Table 3. By comparing the Turn over number ( $K_{\text{cat}}$ ) of these reported complexes, it is worth mentioning that the **1** is an active catalyst towards the catechol oxidation.

### 3.5. EPR spectroscopy

X-band EPR spectroscopy was studied to established the generation of organic radical as an intermediate of the oxidation process. For this purpose, EPR spectra were performed with 3,5-DTBC and **1** in dichloromethane solution at 298 K, but both are found to be EPR silent.

But, when these two compound is mixed together in which concentration of 3,5-DTBC is 100 times greater than **1**, then an isotropic EPR signal with  $g = 2.011$  was obtained as depicted in Fig. 6. The EPR signal strongly supports the formation of *o*-benzosemiquinonate anion radical as an intermediate in the oxidation process.

### 3.6. DFT calculations

DFT calculations were employed to elucidate the electronic structures of **1** and  $1^+$ . The gas phase geometry of **1** was optimized with singlet

whereas  $1^+$  was optimized with doublet spin state. The optimized geometry of **1** is given in Fig. 7. The calculated bond parameters are summarized in Table 2. The calculated bond length of C(12)–C(13) is 1.533 Å similar to the experimental bond length 1.520(10) Å. Calculated bond length of N(11)–C(12) bond length is 1.448 Å very close to experimental bond length 1.482(10) Å. Mulliken spin population analysis shows that, in  $1^+$  48% spin is localized on N(11) and 31% spin localized on C(8) atom as depicted in Fig. 7. This parameter indicates the N-centre oxidation occurs in the reduced Schiff base anion. The feature correlates with the oxidation of  $\text{N}^-$  to  $\text{N}^{\bullet-}$ . Thus,  $1^+$  is defined as aldimine anion radical complex of palladium (II) [56].

### 3.7. Electronic spectra

The UV-vis/NIR absorption spectrum of the complex was recorded in  $\text{CH}_2\text{Cl}_2$  at 295 K. The spectrum is illustrated in Fig. 8. **1** absorbs at 480 nm due to ligand to ligand (LLCT) charge transfer transition.

This transition is assigned as HOMO to LUMO+1 and HOMO to LUMO+2 transitions. The electronic transition at 362 nm is also ligand to ligand charge transfer transition. The complex also absorbs at 362, 315 and 270 nm and details of the transitions are summarized in Table 4 and their corresponding frontier molecular orbitals are given in Fig. 9 obtained from TD-DFT calculations. The transition at 315 and 270 nm is assigned as metal to ligand charge transfer transition (MLCT).

## 4. Conclusions

In this article, synthesis, characterization and catecholase activity of a new palladium(II) complex containing an imine reduced Schiff base of the type  $[(\text{L}_{\text{NN}}^1)\text{Pd}^{\text{II}}\text{Cl}]$  (**1**) is reported. **1** is characterised by different spectroscopic techniques like single crystal X-ray crystallography, IR, UV-Vis, mass spectroscopy and cyclic voltammetry. DFT calculation was performed on **1** to correlates the theoretical bond length and bond angles to the experimental parameters. Molecular and electronic states of **1** were elucidated which correlates well with the theoretical data obtained from DFT calculation on **1** and  $1^+$ . **1** exhibits catecholase activity, which is



confirmed by UV-Vis, mass and EPR spectroscopic study. All of these experimental observation show good conformity with the theoretical data obtained from DFT calculations. Therefore, the article reports a concise study of synthesis, characterization and the catalytic activity of a new palladium(II) complex.

### Declaration of Competing interest

There are no conflicts of interest to declare.

### Acknowledgements

I gratefully acknowledged Dr. Prasanta Ghosh, Dr. Suvendu Maity and Dr. Sachinath Bera of Ramakrishna Mission Residential College, Narendrapur, Kolkata-103, West Bengal, India, for their valuable suggestion.

### Appendix A. Supplementary data

Supplementary data to this article can be found online at <https://doi.org/10.1016/j.jics.2021.100186>.

### References

- [1] Omidi S, Kakanejadifard A. A review on biological activities of Schiff base, hydrazone, and oxime derivatives of curcumin. *RSC Adv.* 2020;10:30186–202. <https://doi.org/10.1039/D0RA05720G>.
- [2] Borase JN, Mahale RG, Rajput SS, Shirsath DS. *SN Appl. Sci.* 2021;3:197. <https://doi.org/10.1007/s42452-021-04144-z>.
- [3] Glaser F, Wenger OS. Recent progress in the development of transition-metal based photoredox catalysts. *Coord. Chem. Rev.* 2020;405:213129–42. <https://doi.org/10.1016/j.ccr.2019.213129>.
- [4] Burke JE, Khoury EA, Koskay GJ, LeWarne CJ, Reeson EA, L Sandquist K, Oshin KD, Zeller M. Using transition-metal complexes as catalysts for radical addition reactions: a laboratory experiment demonstrating the important role of catalysts in an organic transformation reaction. *J. Chem. Educ.* 2019;96:1236–44. <https://doi.org/10.1021/acs.jchemed.8b00721>.
- [5] Zoubi W Al, Ko YG. Schiff base complexes and their versatile applications as catalysts in oxidation of organic compounds: part I. *Appl. Organomet. Chem.* 2017;31:1–12. <https://doi.org/10.1002/aoc.3574>.
- [6] Sutar AK, C Gupta K. Catalytic activities of Schiff base transition metal complexes. *Coord. Chem. Rev.* 2008;252:1420–50. <https://doi.org/10.1016/j.ccr.2007.09.005>.
- [7] Dong YW, Fan RQ, Chen W, Zhang HJ, Song Y, Du X, Wang P, Wei LG, Yong YL. Different conjugated system Zn(II) schiff base complexes: supramolecular structure, luminescent properties and application in PMMA-doped hybrid material. *Dalton Trans.* 2017;46:1266–76. <https://doi.org/10.1039/C6DT04159K>.
- [8] Low ML, Maigre L, Tahir MIM, T Tiekink ER, Dorlet P, Guillot R, Ravoo F, Rosli R, Pages JM, Policar C, Delsuc N, Crouse KA. New insight into the structural, electrochemical and biological aspects of macrocyclic Cu(II) complexes derived from S-substituted dithiocarbamate schiff bases. *Eur. J. Med. Chem.* 2016;120:1–12. <https://doi.org/10.1016/j.ejmech.2016.04.027>.
- [9] Sreenivasulu B. Schiff Base and Reduced Schiff Base Ligands, Supramolecular Chemistry: from Molecules to Nanomaterials. 2012. <https://doi.org/10.1002/9780470661345.smc051>.
- [10] Biswas A, Drew MGB, Gomez-Garcia CJ, Ghosh A. Use of a reduced schiff-base ligand to prepare novel chloro-bridged chains of rare Cu(II) trinuclear complexes with mixed azido/oxo and chloro/oxo bridges. *Inorg. Chem.* 2010;49:8155–63. <https://doi.org/10.1021/ic101183n>.
- [11] Dubey P, Gupta S, Singh AK. Complexes of Pd(II), η<sup>6</sup>-C<sub>6</sub>H<sub>6</sub>Ru(II), and η<sup>5</sup>-cp<sup>\*</sup>Rh(III) with chalcogenated schiff bases of anthracene-9-carbaldehyde and base-free catalytic transfer hydrogenation of aldehydes/ketones and N-alkylation of amines. *Organometallics* 2019;38:944–61. <https://doi.org/10.1021/acs.organomet.8b00908>.
- [12] Faghiz Z, Neshat A, Wojtczak A, Faghiz Z, Mohammadi Z, Varestan S. Palladium (II) complexes based on Schiff base ligands derived from ortho-vanillin; synthesis, characterization and cytotoxic. *Inorg. Chim. Acta.* 2018;471:404–12. <https://doi.org/10.1016/j.ica.2017.11.025>.
- [13] Chakraborty P, Majumder I, Banu KS, Ghosh B, Kara H, Zangrando E, Das D. Mn(II) complexes of different nuclearity: synthesis, characterization and catecholase-like activity. *Dalton Trans.* 2015;45:742–52. <https://doi.org/10.1039/C5DT03659C>.
- [14] Magherusan AM, Nelis DN, Twamley B, McDonald AR. Catechol oxidase activity of comparable dimanganese and dicopper complexes. *Dalton Trans.* 2018;47:15555–64. <https://doi.org/10.1039/c8dt01378k>.
- [15] Pal CK, Mahato S, Yadav HR, Shit M, Choudhury AR, Biswas B. Bio-mimetic of catecholase and phosphatase activity by a tetra-iron(III). *Cluster* 2019;174:114156. <https://doi.org/10.1016/j.poly.2019.114156>.
- [16] Chatterjee A, Kaur G, Joshi M, Choudhury AR, Ghosh R. pH dependent catecholase activity of Fe(II) complexes of type [Fe(L)]X<sub>2</sub> [L = N-(phenyl-pyridin-2-yl-methylene)-ethane-1,2-diamine; X = ClO<sub>4</sub> (1), PF<sub>6</sub> (2)]: role of counter anion on turnover number. *Inorg. Chim. Acta.* 2020;513:119933. <https://doi.org/10.1016/j.ica.2020.119933>.
- [17] Mohan N, Sreejith SS, Kurup MRP. Investigation on catecholase activity of salen Co(III) octahedral Complexes. *Polyhedron* 2019;173:114129. <https://doi.org/10.1016/j.poly.2019.114129>.
- [18] Dey SK, Mukherjee Arindam. The synthesis, characterization and catecholase activity of dinuclear cobalt(II/III) complexes of an O-donor rich Schiff base ligand. *New J. Chem.* 2014;38:4985. <https://doi.org/10.1039/c4nj00715h>.
- [19] Shit M, Maity S, Bera S, K Mudi P, Biswas B, Weyhermüller T, Ghosh P. Nickel(ii) di-aqua complex containing a water cluster: synthesis, X-ray structure and catecholase activity. *New J. Chem.* 2021;45:2221–7. <https://doi.org/10.1039/D0NJ05238H>.
- [20] Mondal M, Ghosh S, Maity S, Giri S, Ghosh A. In situ transformation of a tridentate to a tetradentate unsymmetric Schiff base ligand via deaminative coupling in Ni(II) complexes: crystal structures, magnetic properties and catecholase activity study. *Inorg. Chem. Front.* 2020;7:247–59. <https://doi.org/10.1039/C9QI00975B>.
- [21] Mukherjee J, Mukherjee R. Catecholase activity of dinuclear copper(II) complexes with variable endogenous and exogenous bridge. *Inorg. Chim. Acta.* 2002;337:429–38. [https://doi.org/10.1016/S0020-1693\(02\)01106-4](https://doi.org/10.1016/S0020-1693(02)01106-4).
- [22] Neves A, Rossi LM, Bortoluzzi AJ, Szpoganicz B, Wieszicki C, Schwingel E. Catecholase activity of a Series of dicopper(II) complexes with variable Cu-OH(phenol) moieties. *Inorg. Chem.* 2002;41:1788–94. <https://doi.org/10.1021/ic101708u>.
- [23] Rakshit T, Mandal B, Alenezi KM, Ganguly R, Mandal D. Synthesis, structure, luminescent properties and catecholase activity of Zn(II) complex with N, O chelating agent. *J. Mol. Struct.* 2021;1227:129544. <https://doi.org/10.1016/j.jmolstruc.2020.129544>.
- [24] Das S, Sahu A, Joshi M, Paul S, Shit M, Choudhury AR, Biswas B. Ligand-Centered radical activity by a zinc-schiff-base complex towards catechol oxidation. *ChemistrySelect* 2018;3:10774–81. <https://doi.org/10.1002/slct.201801084>.
- [25] Biswas A, Das LK, Drew MGB, Aromi G, Gamez P, Ghosh A. Synthesis, crystal structures, magnetic properties and catecholase activity of double phenoxido-bridged penta-coordinated dinuclear nickel(II) complexes derived from reduced schiff-base ligands: mechanistic inference of catecholase activity. *Inorg. Chem.* 2012;51:7993–8001. <https://doi.org/10.1021/ic202748m>.
- [26] Mondal M, Guha PM, Giri S, Ghosh A. Deactivation of catecholase-like activity of a dinuclear Ni(II) complex by incorporation of an additional Ni(II). *J. Mol. Catal. Chem.* 2016;424:54–64. <http://doi:10.1016/j.molcata.2016.08.012>.
- [27] Sreenivasulu B, Zhao F, Gao S, Vittal JJ. Synthesis, structures and catecholase activity of a new Series of dicopper(II) complexes of reduced schiff base ligands. *Eur. J. Inorg. Chem.* 2006;13:2656–70. <https://doi.org/10.1002/ejic.200600022>.
- [28] Sun W-H, Wang K, Wedeking K, Zhang D, Zhang S, Cai J, Li Y. Synthesis, characterization, and ethylene oligomerization of nickel complexes bearing N-(Pyridin-2-yl)methylenequinolin-8-amine derivatives. *Organometallics* 2007;26:4781–90. <https://doi.org/10.1021/om700440v>.
- [29] Shelldrick GM. SHELXS97. Göttingen, Germany: Universität Göttingen; 1997.
- [30] Shelldrick GM. SHELXL97. Göttingen, Germany: Universität Göttingen; 1997.
- [31] XS Shelldrick GM. Göttingen, Germany: Georg-August-Universität Göttingen; 2013. Version 2013/1.
- [32] Shelldrick GM. SHELXT - integrated space-group and crystal-structure determination. *Acta Crystallogr.* 2015;A71:3–8. <https://doi.org/10.1107/S2053273314026370>.
- [33] Shelldrick GM. Crystal structure refinement with SHELXL. *Acta Crystallogr.* 2015; C71:3–8. <https://doi.org/10.1107/S2053229614024218>.
- [34] Pal S, Choudhury B, Patra M, Maji M, Biswas B. Ligand centered radical pathway in catechol oxidase activity with a trinuclear zinc-based model: synthesis, structural characterization and luminescence properties. *Spectrochim. Acta. Mol. Biomol. Spectrosc.* 2015;144:148–54. <https://doi.org/10.1016/j.saa.2015.02.046>.
- [35] Frisch MJ, Trucks GW, Schlegel HB, Scuseria GE, Robb MA, Cheeseman JR, Montgomery JA, Vreven T, Kudin KN, Burant JC, Millam JM, Iyengar SS, Tomasi J, Barone V, Mennucci B, Cossi M, Scalmani G, Rega N, Petersson GA, Nakatsuji H, Hada M, Ehara M, Toyota K, Fukuda R, Hasegawa J, Ishida M, Nakajima T, Honda Y, Kitao O, Nakai H, Klene M, Li X, Knox JE, Hratchian HP, Cross JB, Bakken V, Adamo C, Jaramillo J, Gomperts R, Stratmann RE, Yazyev O, Austin JA, Cammi R, Pomelli C, Ochterski JW, Ayala PY, Morokuma K, Voth GA, Salvador P, Dannenberg JJ, Zakrzewski JG, Dapprich S, Daniels AD, Strain MC, Farkas O, Malick DK, Rabuck AD, Raghavachari K, Foresman JB, Ortiz JV, Cui Q, Baboul AG, Clifford S, Cioslowski J, Stefanov BB, Liu G, Liashenko A, Piskorz P, Komaromi I, Martin RL, Fox DJ, Keith T, Al-Laham MA, Peng CY, Nanayakkara A, Challacombe M, Gill PMW, Johnson B, Chen W, Wong MW, Gonzalez C, Pople JA. GAUSSIAN 03 (Revision E.01). Wallingford, CT: Gaussian, Inc.; 2004.
- [36] Parr RG, Yang W. Density Functional Theory of Atoms and Molecules. Oxford, UK: Oxford University Press; 1989.
- [37] Salahub DR, Zerner MC. The challenge of d and f Electrons. In: *ACS Symposium Series* 394, American Chemical Society, Washington, DC; 1989.
- [38] Kohn W, Sham LJ. Self-consistent equations including exchange and correlation effects. *Phys. Rev.* 1965;140:A1133–8. <https://doi.org/10.1103/PhysRev.140.A1133>.
- [39] Hohenberg P, Kohn W. Inhomogeneous electron gas. *Phys. Rev.* 1964;136:B864–71.
- [40] Becke AD. Density-functional thermochemistry. III. The role of exact exchange. *J. Chem. Phys.* 1993;98:5648–52. <https://doi.org/10.1063/1.464913>.
- [41] Miehlich B, Savin A, Stoll H, Preuss H. *Chem. Phys. Lett.* 1989;157:200–5.
- [42] Lee C, Yang W, Parr RG. Development of the Colle-Salvetti correlation-energy formula into a functional of the electron density. *Phys. Rev. B Condens. Matter* 1988;37:785–9. <https://doi.org/10.1103/PhysRevB.37.785>.
- [43] Pulay PJ. Improved SCF convergence acceleration. *Comput. Chem.* 1982;3:556–60. <https://doi.org/10.1002/jcc.540030413>.

- [44] Schlegel HB, McDouall JJ. In: Ogretrir C, Csizmadia IG, editors. *Computational Advances in Organic Chemistry*. The Netherlands: Kluwer Academic; 1991. p. 167–85.
- [45] Hay PJ, Wadt WR. Ab initio effective core potentials for molecular calculations. Potentials for the transition metal atoms Sc to Hg. *J. Chem. Phys.* 1985;82:270–83. <https://doi.org/10.1063/1.448799>.
- [46] Wadt WR, Hay PJ. Ab initio effective core potentials for molecular calculations. Potentials for main group elements Na to Bi. *J. Chem. Phys.* 1985;82:284–98. <https://doi.org/10.1063/1.448800>.
- [47] Hay PJ, Wadt WR. Ab initio effective core potentials for molecular calculations. Potentials for K to Au including the outermost core orbitals. *J. Chem. Phys.* 1985; 82:299–310. <https://doi.org/10.1063/1.448975>.
- [48] Hehre WJ, Ditchfield R, Pople JA. Self-consistent molecular orbital methods. XII. Further extensions of Gaussian-type basis sets for use in molecular orbital studies of organic molecules. *J. Chem. Phys.* 1972;56:2257–61. <https://doi.org/10.1063/1.1677527>.
- [49] Ali MA, Mirza AH, Keng STW. Palladium(II) and platinum(II) complexes of Schiff bases derived from 2,6-diacetylpyridine and S-methyldithiocarbamate and the X-ray crystal structure of the [Pd(mdapmsme)Cl] complex. *Transit. Met. Chem.* 2003;28: 241–5. <https://doi.org/10.1023/A:1022960632103>.
- [50] S. Kumari, K. Maddipoti, B. Das, S. Ray, Palladium–Schiff base complexes encapsulated in zeolite-Y host: functionality controlled by the structure of a guest complex, *Inorg. Chem.* 58(2019)1527–1540, DOI: 10.1021/acs.inorgchem.8b03031.
- [51] Zhang L-M, Li H-Y, Li H-X, Young DJ, Wang Y, Lang J-P. Palladium(II) chloride complexes of N,N'-Disubstituted imidazole-2- thiones: syntheses, structures, and catalytic performances in Suzuki–Miyaura and sonogashira coupling reactions. *Inorg. Chem.* 2017;56:11230–43. <https://doi.org/10.1021/acs.inorgchem.7b01616>.
- [52] Tsutsumi K, Itagaki K, Nomura K. Synthesis and structural analysis of palladium(II) complexes containing neutral or anionic C2-symmetric bis(oxazoline) ligands: effects of substituents in the 5-position. *ACS Omega* 2017;2:3886–900. <https://doi.org/10.1021/acsomega.7b00457>.
- [53] Cai L-Z, Chen W-T, Wang M-S, Guo G-C, Huang J-S. Syntheses, structures and luminescent properties of four new 1D lanthanide complexes with 2-thiophene-acetic acid ligand. *Inorg. Chem. Commun.* 2004;7:611–3. <https://doi.org/10.1016/j.inoche.2004.02.015>.
- [54] Monzani E, Quinti L, Perotti A, Casella L, Gullotti M, Randaccio L, Geremia S, Nardin G, Faleschini P, Tabbi G. Tyrosinase models. Synthesis, structure, catechol oxidase activity and phenol monooxygenase activity of a dinuclear copper complex derived from a triamino pentabenzimidazole ligand. *Inorg. Chem.* 1998;37:553–62. <https://doi.org/10.1021/ic970996n>.
- [55] Swamy P, Naresh M, Reddy MM, Srujana K, Durgaiha C, Prabhakar S, Narender N. Hypoiodous acid-catalyzed regioselective geminal addition of methanol to vinylarenes: synthesis of anti-markovnikov methyl acetals. *RSC Adv.* 2015:1–5. <https://doi.org/10.1039/C5RA16826K>.
- [56] Shit M, Bera S, Maity S, Weyhermüller T, Ghosh P. Coordination of o-benzosemiquinonate, o-iminobenzosemiquinonate and aldimine anion radicals to oxidovanadium(IV). *New J. Chem.* 2017;41:4564–72. <https://doi.org/10.1039/C7NJ00186J>.



## Source details

[Feedback >](#) [Compare sources >](#)

### Journal of the Indian Chemical Society

Scopus coverage years: from 1973 to 1985, from 1987 to 1991, from 1996 to Present

Publisher: Elsevier

ISSN: **0019-4522**

Subject area: [Pharmacology, Toxicology and Pharmaceutics: Drug Discovery](#) [Chemistry: Physical and Theoretical Chemistry](#) [Chemistry: Inorganic Chemistry](#)  
[Chemistry: Organic Chemistry](#) [Chemistry: Electrochemistry](#)

Source type: Journal

[View all documents >](#)[Set document alert](#)[Save to source list](#)

CiteScore 2022

1.3



SJR 2022

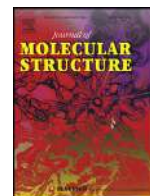
0.242



SNIP 2022

0.371





# Solvent induced distortion in a square planar copper(II) complex containing an azo-functionalized Schiff base: Synthesis, crystal structure, *in-vitro* fungicidal and anti-proliferative, and catecholase activity

Subham Mukherjee<sup>a</sup>, Chanchal Kumar Pal<sup>a</sup>, Muddukrishnaiah Kotakonda<sup>b</sup>, Mayank Joshi<sup>c</sup>, Madhusudan Shit<sup>d</sup>, Prasanta Ghosh<sup>e</sup>, Angshuman Roy Choudhury<sup>c</sup>, Bhaskar Biswas<sup>a,\*</sup>

<sup>a</sup> Department of Chemistry, University of North Bengal, Darjeeling-734013, India

<sup>b</sup> Department of Technology, Anna University, Chennai 600025, India

<sup>c</sup> Department of Chemical Sciences, Indian Institute of Science Education and Research, Mohali, Sector 81, Knowledge City, S. A. S. Nagar, Manauli PO, Mohali, Punjab 140306, India

<sup>d</sup> Department of Chemistry, Dinabandhu Andrews College, Kolkata 700084, India

<sup>e</sup> Department of Chemistry, Ramakrishna Mission Residential College, Kolkata 700103, India

## ARTICLE INFO

### Article history:

Received 19 April 2021

Revised 12 June 2021

Accepted 5 July 2021

Available online 10 July 2021

### Keywords:

Copper(II)

Electrochemical analysis

Catechol oxidation activity

Schiff base

X-ray structure

Antifungal property

Antiproliferative activity

## ABSTRACT

This research work reports the synthesis, single crystal X-ray structure, catechol oxidation, fungicidal and antiproliferative activity of a newly synthesized copper(II) complex,  $[\text{Cu}(\text{L})_2]\text{H}_2\text{O} \cdot \text{CH}_3\text{OH}$  (**1**) containing an azo-functionalized Schiff base, HL = 2-methoxy-6-((Z)-((4-((E)-phenyldiazenyl)phenyl)imino)methyl)phenol. The crystal structure analysis reveals that the Cu(II) centre exists in a highly distorted square planar geometry. The crystallize water and methanol form a strong intermolecular association through H-bonding. More importantly, the H atoms of the lattice water interact with the O atoms of ligand units leading to 5- and 6-membered cycles through the H-bonding network and distort the square planar geometry. The copper(II) complex has emerged as a bioinspired catalyst in the oxidative transformation of 3,5-di-*tert*-butylcatechol (DTBC) to *o*-benzoquinone in methanol with a high turnover number,  $4.75 \times 10^2 \text{ h}^{-1}$ . Electrochemical analysis of the copper(II) complex in presence of DTBC recommends the generation of catechol/*o*-benzosemiquinone redox couple in the course of oxidation. The EPR spectral analysis of **1** in presence of DTBC was found silent and suggested the antiferromagnetic interaction between copper centre and benzosemiquinone species. The copper(II) complex turns out to be a potential fungicidal agent against clinical *candida albicans* and scanning electron microscope studies confirm the destruction of the fungal cell membrane with the deposition of copper. The  $\text{IC}_{50}$  value of the copper complex was determined as 15  $\mu\text{g}/\text{mL}$  which suggests the excellent antiproliferative potency of the synthetic compound against the breast cancer cell lines, MCF-7.

© 2021 Elsevier B.V. All rights reserved.

## 1. Introduction

Nowadays, azo-functionalised Schiff bases grab special attention for their unique and versatile structural and functional properties [1-3]. Generally, azo-functionalised compounds are widely used in dye and pigment industries [4,5]. Besides that azo compounds exhibit remarkable importance in the medicinal and pharmaceutical field including biological sciences [6-8]. These compounds show

important electronic reversibility in photo-isomerisation processes and they are employed to a greater extent in the development of functional materials, optical computing, and coordination compounds [9-12]. Azo-functionalized Schiff bases form stable coordination compounds with interesting structural and functional properties [13]. amongst the various coordination compounds, copper(II) complexes have been paid substantial attention for their stability in an aerobic environment, good reactivity in solutions and the interesting flexible geometry [14-20]. Being a d9 system, copper(II) ion undergoes Jahn-Teller distortion and imposes a dis-

\* Corresponding author.

E-mail address: [bhaskarbiswas@nbu.ac.in](mailto:bhaskarbiswas@nbu.ac.in) (B. Biswas).

tortion in coordination geometries which facilitates the catalytic routes for different organic transformations [21–23].

The copper complexes mediated catalytic transformation of organic substrates in molecular oxygen environment increase exponentially using oxygen a sink of electrons (oxidase activity) as well incorporating oxygen atoms the product (oxygenase activity) or both [24–27]. In the biological world, copper ions in the coordination of various bio-ligands exist in the functional core of different metalloproteins [28–30]. At present different scientific groups are actively engrossed in the catalytic oxidations of organic substrates based on synthetic copper(II) based coordination compounds [31–34]. In light of a better understanding of metalloenzymes mediated biological oxidation and the emergence of novel antibiotics with potential resistance, it is of great importance to design novel antibiotics, which would destroy the lipid layer as well as the cell membrane of the pathogen with high selectivity [35,36]. In this perspective, copper-based coordination compounds hold a great promise to provide future alternatives to the existed antibiotics [37,38]. In the context of newly designed copper(II) complexes with high catalytic activities and potential therapeutic values, this research study describes the synthesis, structural characterization and catalytic catecholase activity of a newly synthesized square planar copper(II)-Schiff base complex. The fungicidal property against *candida albicans* and the antitumor activity towards the breast cancer MCF-7 cell lines has also been delineated.

## 2. Experimental

### 2.1. Preparation of the SCHIFF base and copper(II) complex

#### (a) Chemicals, solvents and starting materials

Highly pure 2-hydroxy-3-methoxybenzaldehyde (Alfa Aesar, UK), aniline (Merck, India), copper acetate monohydrate (Thomas Baker, India) and other reagents were purchased from respective suppliers. All the reagents and chemicals were of analytical grade. The solvents of spectroscopic grade were used to study the bio-inspired oxidation of catechol.

#### (b) Synthesis of the Schiff base and copper(II) complex

4-aminoazobenzene was prepared by using a previously reported well-established synthetic procedure [39]. 2-hydroxy-3-methoxy benzaldehyde (1.52 g, 10 mmol) was condensed with 4-aminoazobenzene (1.97 g, 10 mmol) under reflux for 8 hr in EtOH. The Schiff base was extracted as a reddish-orange crystalline product and dried in a vacuum desiccator.

Then, the yellowish brown coloured gummy product was extracted and stored *in vacuo* over  $\text{CaCl}_2$  for use. Yield: 0.317 g (~90.8%). Anal. Calc. for  $\text{C}_{20}\text{H}_{17}\text{N}_3\text{O}_2$  (HL): C, 72.49; H, 5.17; N, 12.68; Found: C, 72.53; H, 5.20; N, 12.75. IR (KBr,  $\text{cm}^{-1}$ ; Fig. S1): 3446 ( $\nu_{\text{OH}_2}$ ), 1618, 1593 ( $\nu_{\text{C}=\text{N}}$ ), 1468 ( $\nu_{\text{N}=\text{N}}$ ), 1260 ( $\nu_{\text{Ph-O}}$ ); UV-Vis ( $\lambda_{\text{max}}$ , nm; Fig. S2): 224, 356;  $^1\text{H}$  NMR ( $\delta$  ppm, 400 Mz,  $\text{CDCl}_3$ ; Fig. S3)  $\delta$  = 12.90 (s, 1H), 9.06 (s, 1H), 6.91–8.04 (Ar-H, 12H), 3.88 (s, 3H) ppm.  $^{13}\text{C}$  NMR (400 MHz,  $\text{CDCl}_3$ ; Fig. S4): 206.9, 192.4 (C=N=N-C); 164.90 (HC=N); 153.31, 152.91, 151.31, 150.84 (Ar-OH); 148.85, 143.27 (Ar-N=C); 131.98, 129.94, 125.60, 124.42, 123.0, 122.94, 120.57, 119.78, 118.0, 116.40, 113.84 (Ar-C); 56.50, 40.55, 39.93, 31.10 ( $-\text{OCH}_3$ ).

The copper(II) complex containing azo-functionalized Schiff base was synthesized through the reaction of  $\text{Cu}(\text{OAc})_2$  (0.199 g, 1 mmol) with HL (0.69 g, 2 mmol) in MeOH-DCM solvent mixture. The reaction solution turned instantly to deep brown upon dropwise addition of  $\text{Cu}(\text{OAc})_2$  to HL and the total solution was stirring for 30 mins. The resultant solution was filtered and kept for slow evaporation. After a week, a green crystalline product of the copper complex was separated. The compound was dried over silica gel.

Yield of **1**: 0.775 g (~86.4%) Anal. calc. for  $\text{C}_{41}\text{H}_{38}\text{N}_6\text{O}_6\text{Cu}$  (**1**): C, 63.60; H, 4.95; N, 10.85; Found: C, 63.65; H, 4.91; N, 10.89. IR (KBr pellet,  $\text{cm}^{-1}$ ; Fig. S5): 3379 ( $\nu_{\text{OH}}$ ), 1616, 1581 ( $\nu_{\text{C}=\text{N}}$ ), 1437 ( $\nu_{\text{N}=\text{N}}$ ), 1252 ( $\nu_{\text{Ph-O}}$ ); UV-Vis ( $1 \times 10^{-4}$  M,  $\lambda_{\text{max}}$ (abs), nm, MeOH; Fig. S2): 230, 346.

### 2.2. Physical measurements

FTIR-8400S SHIMADZU spectrometer (Shimadzu, Kyoto, Japan) was employed to record IR spectra (KBr) of Schiff base and **1** ranging 400–3600  $\text{cm}^{-1}$ .  $^1\text{H}$  and  $^{13}\text{C}$  NMR spectra of the ligand (HL) were obtained on a Bruker Advance 400 MHz spectrometer (Bruker, Massachusetts, USA) in  $\text{CDCl}_3$  at 298 K. Steady-state absorption and other spectral data were obtained on a JASCO V-730 UV-Vis spectrophotometer (Jasco, Tokyo, Japan). A Perkin Elmer 2400 CHN microanalyser (Perkin Elmer, Waltham, USA) was used to perform the elemental analysis. X-band EPR spectra were recorded on a Magnetech GmbH MiniScope MS400 spectrometer (equipped with temperature controller TC H03, Magnetech, Berlin, Germany), where the microwave frequency was measured with an FC400 frequency counter. The electroanalytical instrument, BASi Epsilon-EC was employed for recording the cyclic voltammograms in  $\text{CH}_2\text{Cl}_2$  solutions. The BASi platinum working electrode, platinum auxiliary electrode, Ag/AgCl reference electrode were used for the measurements. Field emission scanning microscopy images of the fungal species in presence and absence of the copper complex was recorded with JSM-IT800 FESEM, Japan.

### 2.3. Crystal structure determination and refinement

X-ray diffraction data of **1** were collected using a Rigaku XtaLAB Mini diffractometer equipped with Mercury 375R ( $2 \times 2$  bin mode) CCD detector. The data were collected with a graphite monochromated Mo-K $\alpha$  radiation ( $\lambda=0.71073$  Å) at 150 K using  $\omega$  scans. The data were reduced using CrysAlisPro 1.171.39.7f [40] and the space group determination was done using Olex2. The structure was resolved by the dual space method using SHELXT-2015 [41] and refined by full-matrix least-squares procedures using the SHELXL-2015 [42] software package through the OLEX2 suite [43]. The observed  $R_{\text{int}}$  is high as the crystals of the copper(II) complex weren't diffracted to a great extent. Further, as a d-block metal, copper absorbs x-ray sometimes leading to additional residual density around copper. This fact accounts for the presence of residual density around the copper ion in this structure.

### 2.4. Catecholase activity of the copper(II) complex (**1**)

The catecholase activity was examined by the treatment of  $1 \times 10^{-4}$  M solution of Cu(II) complex with  $1 \times 10^{-3}$  M of 3,5-di-*tert*-butylcatechol (DTBC) in methanol under an aerobic atmosphere. absorbance vs. wavelength (wavelength scans) of the solution was monitored through a spectrophotometer at a regular time interval of 8 minutes for ~1.6 h in the wavelength range from 300–600 nm [44–45]. All the experiments were performed under aerobic conditions at room temperature.

Kinetic experiments were also performed with a spectrophotometer to determine the efficiency of catalytic oxidation of DTBC by the Cu(II) complex in MeOH [44–45]. The kinetics of catalytic transformation of DTBC was performed following the initial rate method. The catalytic oxidation was monitored as a function of time on the growth of the o-quinone species at 398 nm [46]. 0.04 mL of the solution of copper complex with a constant concentration of  $1 \times 10^{-3}$  M was added to 2 mL solution of DTBC of a particular concentration (varying its concentration from  $1 \times 10^{-3}$  M to  $1 \times 10^{-2}$  M) to achieve the ultimate concentration as  $1 \times 10^{-3}$  M. The conversion of DTBC to 3,5-di-*tert*-o-

butylquinone was monitored with time at a wavelength 398 nm (time scan) in MeOH [44–47]. To determine the dependence of rate on substrate concentration, kinetic analyses were performed in triplicate.

The involvement of aerobic oxygen in the oxidation of DTBC was examined by the presence of hydrogen peroxide following a reported procedure [47]. In the oxidation of DTBC in MeOH, H<sub>2</sub>SO<sub>4</sub> was added to reach pH 2 of the solution. After a certain time, the water of equal volume was further supplied to stop the oxidation. The o-quinone species were isolated using DCM as an extractant. 10 % KI solution (1 mL) and 3% ammonium molybdate solution were added to the aqueous layer. The development of I<sub>3</sub><sup>-</sup> was monitored through a spectrophotometer to examine the formation of I<sub>3</sub><sup>-</sup> band ( $\lambda_{\text{max}} = 353 \text{ nm}$ ) which reveals the production of hydrogen peroxide in the course of catalytic oxidation.

### Fungicidal susceptibility studies

The fungicidal activity of the copper complex was performed against clinical *Candida albicans*.

#### 2.5.1. Clinical cultures and culture media

The fungicidal property of the copper complex was tested against clinical *Candida albicans*. The microbial cultures were procured from the government medical college from Tiruchirappalli, Tamil Nadu. Muller-Hinton agar media of Himedia Pvt., India was used for the media. The fungicidal activity was evaluated employing the Himedia zone reader.

#### 2.5.2. Inoculum preparation

A 100 $\mu\text{L}$  of clinical *C. albicans* organisms was inoculated in 5.0 mL of sterile nutrient broth (NB) media, PDB (Potato dextrose broth) and incubated at 37 °C for 24 h. 200 $\mu\text{L}$  of the fresh culture of the *C. albicans* was dispensed into 30 mL sterile nutrient broth and incubated 24 h to standardize the culture to 10<sup>8</sup> CFU/ml (colony forming units).

#### 2.5.3. Agar well diffusion method (Kirby-Bauer method)

The fungicidal activity of the copper complex and a standard marketed drug (Fluconazole-100 mg/2 mL) was studied initially by using the agar well plate method. *C. albicans* inoculum was prepared by using sterile nutrient broth media. Mueller Hinton agar double strength media were made by autoclaving 0.760 g in 100 mL. Standardized inoculum inoculate the test microorganisms on the Mueller Hinton agar plates by using sterile cotton swabs. Four 8 mm diameter agar wells were prepared using sterile cork-borer, and copper complex 0.1 mL (50 mg/mL) and 0.1 mL Fluconazole (10 mg/mL) were placed on agar well using micropipette under aseptic conditions. Sterile water was used as a negative control. Agar plates were incubated for 30 min at the refrigerator to diffuse the formulation into the agar, and finally, plates were incubated at 37°C for 24 h. Antifungal activity was evaluated by using the Himedia zone reader.

Preparation of stock solutions for MIC was done following the equation 1.

Weight of the powder (mg) =

$$\frac{\text{Volume of solution (mL)} \times \text{Concentration (mg/L)}}{\text{The potency of powder (mg/g)}} \quad (1)$$

#### 2.5.3. Determination of minimum inhibitory concentration (MIC) for copper complex against clinical *C. albicans*

The method of micro-dilution was used to establish the antibacterial potential of the copper complex and respective controls. A spectrophotometer (OD<sub>595</sub> = 0.22) equivalent to 10<sup>8</sup> CFU/mL used to fix the bacterial cultures to 0.22 optical density at 595 nm. Different concentrations of copper complex (100, 50, 25, 12.5,

6.25 mg/mL) and the standard drug, fluconazole (50, 25, 12.5, 6.25, 3.125, 1.5625 mg/mL) were added to the respective controls in 2.0 mL MIC tubes. 10<sup>8</sup> CFU/ml 100  $\mu\text{L}$  of the tested were added into each MIC test tube. MIC tubes were incubated overnight at 37 °C for 24 h.

#### 2.5.4. Antifungal activity of copper(II) complex using scanning electronic microscope

To examine the mode of action of copper(II) complex on the fungal species, fungi cultures were obtained from MIC samples and centrifuged. Thereafter, the fungi cells were collected and sputter-coated with a thin layer of gold-palladium. The coated fungal cells were fixed on a glass coverslip and observed under a scanning electron microscope.

### 2.6. Antiproliferative activity of the copper complex

#### 2.6.1. Chemical and reagents for antitumor activity

Dulbecco's Modified Eagle's Medium (DMEM), streptomycin, penicillin-G, L-glutamine, phosphate-buffered saline, (3-[4,5-dimethylthiazol-2-yl]-2,5-diphenyltetrazolium bromide; MTT), ethylene diamine tetraacetic acid (EDTA), ethanol, and dimethyl sulfoxide (DMSO) were purchased from Sigma Aldrich Chemicals Pvt. Ltd (India). All other chemicals were of analytical grade and purchased from Himedia Laboratories Pvt. Ltd. India.

#### 2.6.2. Cell culture maintenance

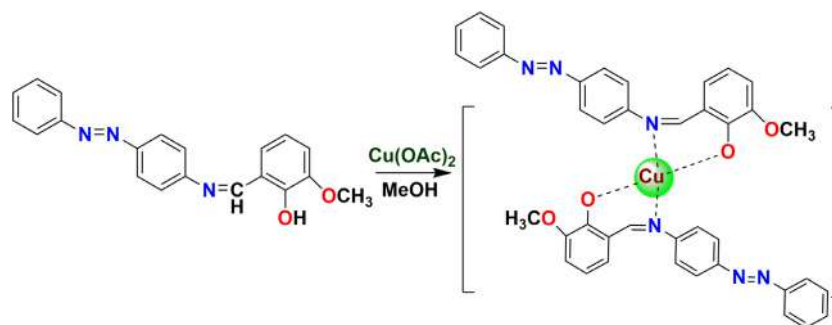
Human breast cancer MCF-7 cell lines were procured from the cell repository of the National Centre for Cell Sciences (NCCS), Pune, India. DMEM was used for maintaining the cell line which was supplemented with 10% fetal Bovine Serum (FBS). The penicillin (100  $\mu\text{g/mL}$ ), and streptomycin (100  $\mu\text{g/mL}$ ) was added to the medium to prevent the microbial contamination. The medium constituting the cell lines was maintained in a humidified environment with 5% CO<sub>2</sub> at 37 °C.

#### 2.6.3. MTT assay

The cytotoxicity of the copper complex on the breast cancer cell lines, MCF-7 was determined through 3-[4,5-dimethylthiazol-2-yl]-2,5-diphenyltetrazolium bromide (MTT) assay employing the method reported by Mosmann *et al* (1983).

50 mg of MTT dye was dissolved in 10 mL of PBS. After vortexing for 1 min, it was filtered through 0.45 microfilters. The bottle was wrapped with aluminium foil to prevent light, as MTT was light-sensitive. The preparation was stored at 4 °C.

Cell viability assay for MCF-7 viable cells was harvested and counted using a hemocytometer and diluted in DMEM medium to reach a density of 1  $\times$  10<sup>4</sup> cells/mL which were seeded in 96 well plates for each well and incubated for 24 h to allow attachment. After MCF-7 cells treated with control and the containing different concentrations of copper complex 5 to 30  $\mu\text{g/mL}$  were applied to each well. MCF-7 cells were incubated at 37 °C in a humidified 95% air and 5% CO<sub>2</sub> incubator for 24 h. After incubation, the drug-containing cells wash with a fresh culture medium and the MTT (5 mg/mL in PBS) dye was added to each well, followed by incubated for another 4 h at 37 °C. The purple precipitated formazan formed was dissolved in 100  $\mu\text{L}$  of concentrated DMSO and the cell viability was absorbance and measured 540 nm using a multi-well plate reader. The results were expressed at the percentage of stable cells to the control. The half-maximal inhibitory concentration (IC<sub>50</sub>) values were calculated and the optimum doses were analysed at the different periods.



**Scheme 1.** Synthetic route for the copper(II) complex.

$$\text{Inhibitory of call proliferation(\%)} = \frac{\text{Mean absorbance of the control} - \text{Mean absorbance of the sample}}{\text{Mean absorbance of the control}} \times 10$$

The  $IC_{50}$  values were determined from the dose-responsive curve of the copper complex. All experiments were performed at least three times in triplicate. The values are expressed as mean  $\pm$  SD. The statistical comparisons were performed by one-way analysis of variance (ANOVA) followed by Duncan's Multiple Range Test (DMRT), using SPSS version 12.0 for windows (SPSS Inc. Chicago; <http://www.spss.com>). The values are considered statistically significant if the p-value was less than 0.05.

### 3. Results and discussion

#### 3.1. Design, synthesis and formulation of the Schiff base (HL) and copper(II) complex (1)

The azo-functionalized Schiff base (HL) was synthesized by a reaction between 4-aminoazobenzene and 2-hydroxy-3-methoxybenzaldehyde under refluxing conditions. The copper(II)-Schiff base complex was synthesized by reacting copper(II) acetate with HL in 1:2 mole ratio in a methanol medium. The synthetic procedure is shown in Scheme 1. Attempts were also made to develop the different structural composition of the copper(II)-Schiff base complex, perhaps we were unsuccessful to produce the different structure. Both the Schiff base and the copper(II) complex are soluble in polar solvents like methanol, ethanol, acetonitrile, chloroform etc.

#### 3.2. Description of crystal structure and non-covalent interactions

The crystal structural analysis reveals that the copper complex crystallizes in a monoclinic system with a  $P2_1/c$  space group. The ORTEP diagram of the Cu(II) complex is displayed in Fig. 1. The crystallographic refinement parameter is summarized in Table 1 and bond angles, and bond distances are given in Table 2. The azo-functionalized Schiff base contains three donor centres in association with an azo group, however, during coordination two donor centres of one ligand unit coordinate with the copper(II) centre ion as a bidentate chelator. The copper(II) complex adopts two units of coordinated Schiff base and exists in a highly distorted square planar coordination geometry. The deviation of copper(II) centric average bond angles ( $\angle L-M-L$ , 94.23) from the tetrahedral geometry is found larger while the average bond angles around copper(II) centre ( $\angle L-M-L$ , 94.23) are closer to the average value of an ideal square planar geometry (Table 2). Therefore, bond angle measurements around the copper centre support the existence of a square planar geometry.

To understand the cause of distortion, the effect of solvate molecules and the presence of noncovalent interactions in the

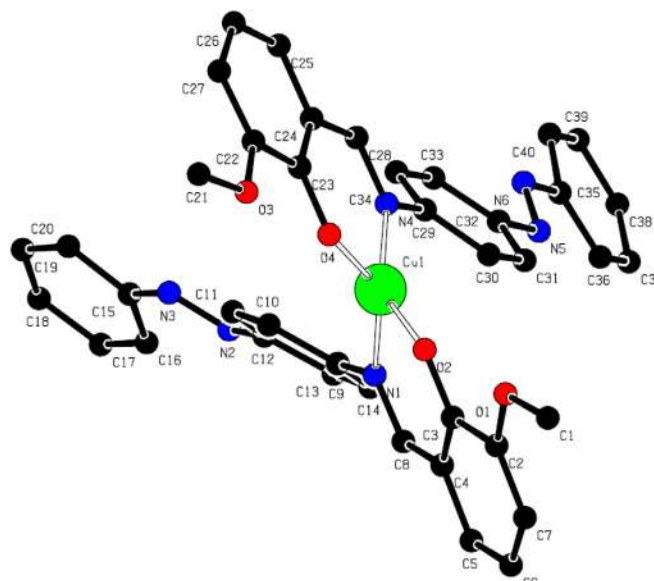


**Fig. 1.** Ball and stick drawing of the copper(II) complex with 30% probability. The hydrogen atoms and the solvent molecules are removed for clarity.

**Table 1**  
Crystallographic data and structure refinement parameters for 1.

Parameters	1
Empirical formula	$C_{41}H_{38}N_6O_6Cu$
Formula weight	774.31
Temperature (K)	150
Crystal system	Monoclinic
Space group	$P2_1/c$
a (Å)	16.104(2)
b (Å)	18.584(2)
c (Å)	13.265(2)
Volume (Å <sup>3</sup> )	3748.4(9)
Z	4
$\rho$ (gcm <sup>-3</sup> )	1.3721
$\mu$ (mm <sup>-1</sup> )	0.639
F (000)	1612
$R_{int}$	0.181
$\theta$ ranges (°)	2.6–25
Number of unique reflections	6579
Total number of reflections	32,338
Final R indices	0.0750, 0.2230
Largest peak and hole (eÅ <sup>-3</sup> )	1.00, -0.63

crystalline architectures of the copper complex were examined. It was observed that the crystallized water and methanol form a very strong intermolecular H-bonding network with the copper complex ranging from 1.91 Å to 2.11 Å (Fig. S6). Investigation of the self-assembly of the copper complex exhibits that methanol-

**Table 2**  
Bond angles and bond distances value of Cu(II) complex.

Bond distances (Å)			
Cu1 -O2	1.894(3)	Cu1 - O4	1.890(3)
Cu1 -N1	1.985(3)	Cu1 - N4	1.978(3)
Bond angles (°)			
∠O2-Cu1-O4	88.79(13)	∠O4-Cu1-N1	145.64(14)
∠O2-Cu1-N1	93.17(14)	∠O4-Cu1-N4	94.78(13)
∠O2 -Cu1-N4	150.08(14)	∠N1-Cu1-N4	100.19(14)

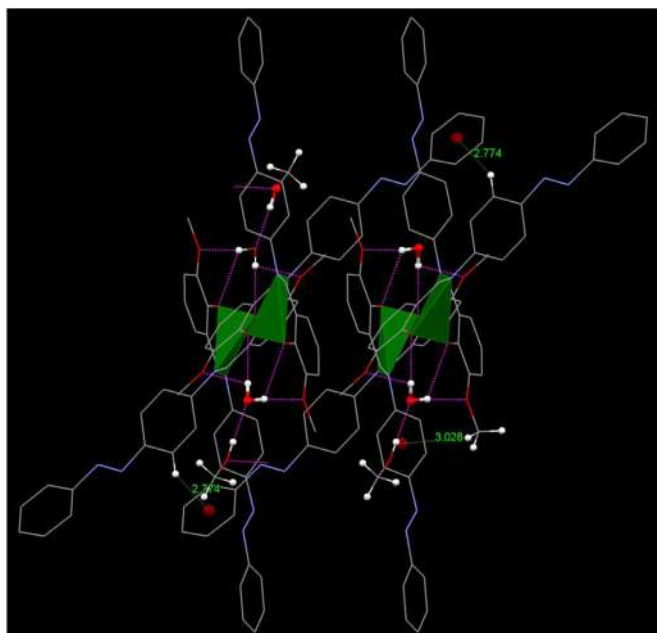
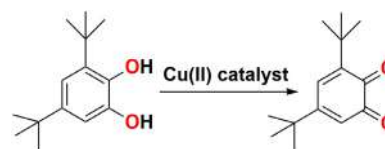


**Fig. 2.** OH (pink dash lines) and C-H... $\pi$  (green dashed lines) mediated formation of a supramolecular architecture for the copper(II) complex. (For interpretation of the references to colour in this figure legend, the reader is referred to the web version of this article.)

OH(H6A) acts as an acceptor towards the oxygen of water (O5) while the O5 atom behaves as a donor to develop a strong intermolecular association between the crystallized water and methanol molecules (Fig. S6). Furthermore, the hydrogen atoms of water (H5A and H5B) play a key role in causing a high distortion in the molecules. Two H-atoms of water strongly hold two units of azo-functionalized Schiff base separately through the strong intermolecular network (H5A...O3, 2.14 Å; H5A...O4, 2.45 Å; H5B...O1, 2.45 Å; H5B...O2, 2.11 Å, Fig. 2, Table S1). More captivatingly, the Hs of O5 in the crystallized water form two 5-member cyclic rings with the phenoxo-O and methoxy-O of the ligand units and as a result a 6-member cycle is also formed with the copper centre coordinated by the phenoxo-O (Fig. 2). This intermolecular H-bonded network amongst the crystallize solvate molecules and ligand units account for the cause of high distortion in the chelating ligands during coordination. It is further documented that for the involvement of strong intermolecular H-bonding in ligand units, the methoxy-O didn't coordinate with the copper centre.

A close look at the nature of non-covalent interactions suggests that the mononuclear copper(II) complex interacts with another complex unit through strong O...H and C-H... $\pi$  and seems to be a complex dimer (Fig. 2, Table S2). This complex dimer is further extended and stabilized through the intermolecular C-H... $\pi$  interactions between the azo-linked phenyl-C-H and the terminal centroid of the azo-linked phenyl ring. The H of the methyl group adds more stabilization energy to the complex dimer through another



**Scheme 2.** Catalytic oxidation of DTBC to DTBQ.

set of C-H... $\pi$  interactions in the crystalline phase (Fig. 2, Table S2).

The Hirshfeld surface analysis of the copper(II) complex over a definite  $d_{\text{norm}}$  was calculated with Crystal Explorer software. The surface volume and area are calculated as 963.85 Å<sup>3</sup> and 687.91 Å<sup>2</sup>. The red highlighted spots indicate the  $d_{\text{norm}}$  area and present close non-covalent interactions in the copper complex with its surrounding molecules (Fig. S7). The contribution of each element in the non-covalent interactions is given in Table S3. The blue area in  $d_{\text{norm}}$  cites important C-H... $\pi$  interactions between the azo-linked phenyl centroid with the H of C-attached to phenyl and methyl groups. The white denotes no interaction. The interactions in the copper(II) complex is displayed in Fingerprint plots (Fig. S8).

### 3.3. Solution property of the Schiff base and copper(II) complex

The Schiff base exhibit characteristic electronic transitions at 224 and 356 nm while the copper(II) complex displayed the electronic bands at 230 and 346 nm in methanol at room temperature. The electronic bands at 224 and 365 nm in the Schiff base are assignable to the presence of  $\pi \rightarrow \pi^*$  and charge transfer (CT) transitions respectively. The lower energetic electronic band at 346 nm gets blue-shifted in the complex and is attributed to the CT band from  $\text{PhO}^- \rightarrow \text{Cu(II)}$  centre exhibited electronic bands at 238, 283 and 400 nm. The electronic spectra are displayed in Fig. S2. The appearance of the characteristic electronic bands for the Schiff base and copper complex are in good agreement with the previously reported values of electronic transitions [48,49]. The high resolution mass spectrum was recorded in methanol at room temperature to reveal the purity and homogeneity of copper complex in solution. The spectrum is displayed in Fig. S9. The mass spectrum shows a characteristic peak at 723.21  $m/z$  which ensures the existence of the tetracoordinate copper(II) complex with its structural integrity and suggests the homogeneity of the compound in MeOH.

### 3.4. Catecholase activity of the copper(II) complex (1)

The catecholase activity of the copper(II) complex has been examined by considering 3,5-di-*tert*-butyl catechol (DTBC) as a model substrate. DTBC contains two bulky *t*-butyl substituents at the phenyl ring and helps to lower down the quinone-catechol reduction potential. The low quinone-catechol reduction potential facilitates the oxidation of catechol to the corresponding *o*-quinone, DTBQ under ambient reaction conditions (Scheme 2). It is well documented that DTBQ is quite stable in solution and displays a characteristic absorption peak at 401 nm in methanol [50].

The nature of changes of the spectral bands during the catalytic oxidation was monitored with a UV-Vis spectrophotometer for a period of 1.6 h (Fig. 3). The copper complex displays a characteristic electronic transition at 346 nm. Upon addition of the Cu(II) complex to the solution of DTBC, a new electronic band at 398 nm was started to develop with increasing absorbance (Fig. 3). The rise of the optical band at 398 nm is a definite sign of the oxidation of DTBC in MeOH [51,52]. The appearance of this new electronic band at 398 nm in the spectrophotometric scan is assignable to the production of the *o*-benzoquinone species in MeOH.



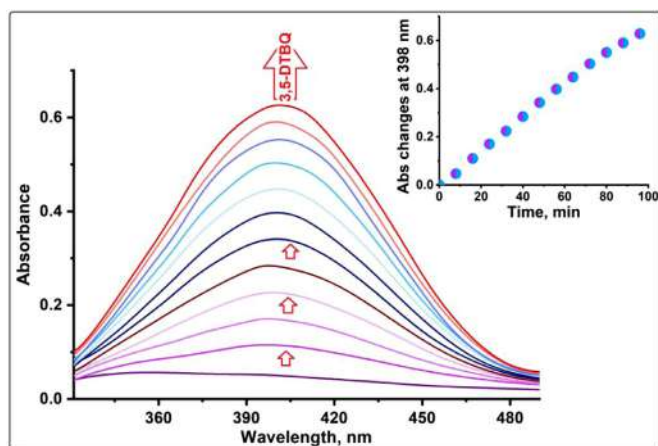


**Fig. 3.** Rise of a new electronic band at 398 nm upon addition of copper complex **1** to DTBC in MeOH with a time interval of 8 mins. Inset: Time vs absorbance plot at 398 nm.

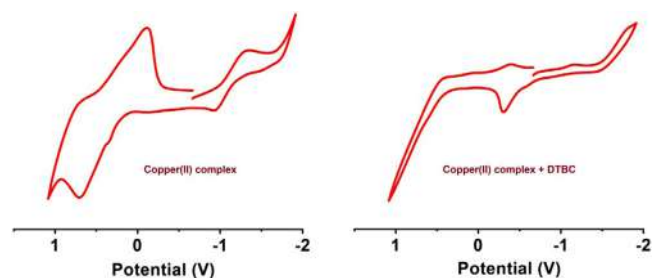


**Fig. 4.** Left: Cyclic voltammogram of the copper(II) complex **1** in  $\text{CH}_2\text{Cl}_2$ ; Right: Cyclic voltammogram of copper(II) complex **1** in presence of DTBC under molecular oxygen atmosphere in  $\text{CH}_2\text{Cl}_2$ .

The kinetics for the catalytic oxidation of DTBC was studied to determine the catalytic performance of the copper(II) complex. The kinetic parameter of the catalytic oxidation of DTBC was evaluated employing the method of the initial rate. The growth of o-benzoquinone was monitored as a function of time with respect to 398 nm (Fig. S10) [53]. The nature of oxidation kinetics was examined by plotting the rate constants vs. concentration of DTBC and shown in Fig. S10. The first order saturation kinetics of the oxidation reaction seems to be suitable in the Michaelis–Menten model and can be expressed as the Eq. (2):

$$V = \frac{V_{\max} [S]}{K_M + [S]} \quad (2)$$

Where,  $V$  indicates the rate of oxidation reaction,  $K_M$  denotes the Michaelis–Menten constant,  $V_{\max}$  presents the maximum velocity of the reaction, and  $[S]$  is the concentration of the DTBC.

The values of kinetics parameters were determined from Michaelis–Menten equation as  $V_{\max} (\text{MS}^{-1}) = 1.32 \times 10^{-4}$ ;  $K_M = 4.52 \times 10^{-3}$  [Std. Error for  $V_{\max} (\text{MS}^{-1}) = 7.79 \times 10^{-5}$ ; Std. Error for  $K_M (\text{M}) = 4.53 \times 10^{-4}$ ]. The catalytic efficiency for the catalytic oxidation of DTBC was determined as  $k_{\text{cat}}/K_M = 1.05 \times 10^5$ .

The redox activities of the copper complex and its activities toward the biomimetics of the catecholase activities were studied by electrochemical analysis in  $\text{CH}_2\text{Cl}_2$  at 295 K. The redox behaviour of the copper complex was recorded using ferrocenium/ferrocene ( $\text{Fc}^+/\text{Fc}$ ) reference under aerobic atmosphere. The cyclic voltammograms are illustrated in Fig. 4. The copper(II) complex exhibits a quasi-reversible cathodic wave at  $-1.13$  V due to  $\text{Cu}^{2+}/\text{Cu}^+$  redox species in solution. The anodic peak appears at  $+0.70$  V due to phenoxide/phenoxide anion radical ( $\text{O}^-/\text{O}\bullet^-$ ) redox couple and

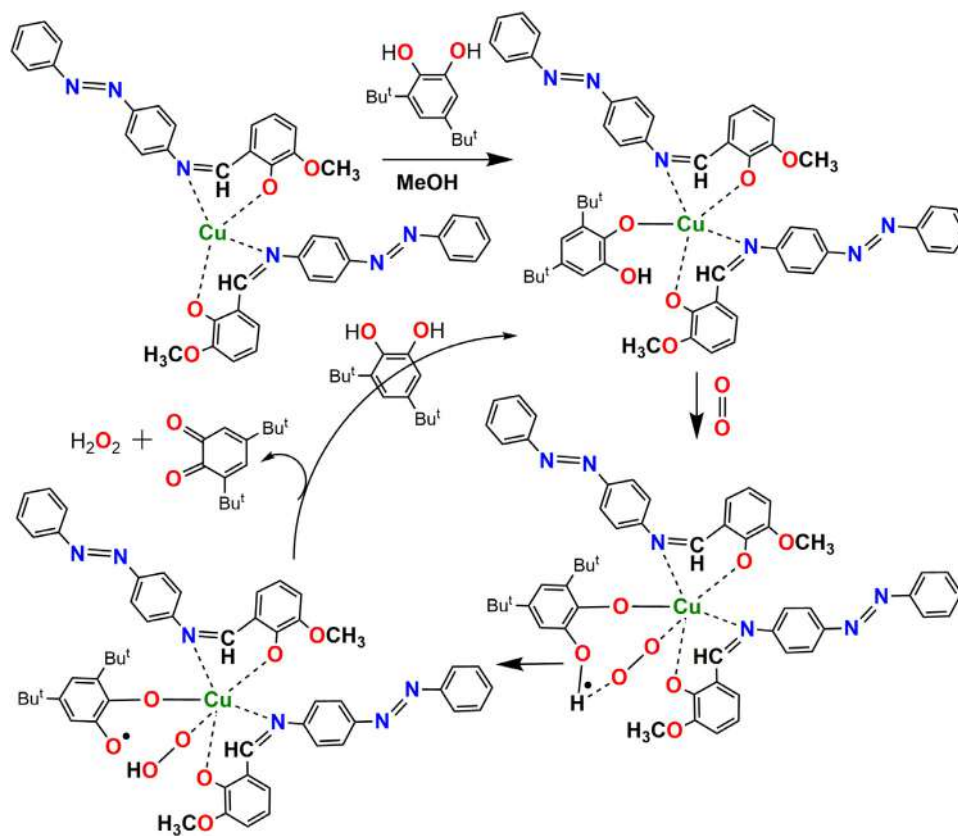
**Table 3**  
Comparison of  $k_{\text{cat}}$  ( $\text{h}^{-1}$ ) values for catalytic oxidation of DTBC by reported copper(II) compounds and **1**.

Complex	$k_{\text{cat}}$ ( $\text{h}^{-1}$ )(Solvent)	CCDC No	Ref
$[\text{Cu}(\text{dpa})_2\text{NCS}]_2$	4788 ( $\text{CH}_3\text{OH}$ )	1456703	[51]
$[\text{Cu}(\text{dpa})_2(\text{NCS})_2](\text{ClO}_4)_2$			
$[\text{Cu}_2(\text{L}^1\text{SSL}^1)](\text{BF}_4)_4$	$6.90 \times 10^3$ ( $\text{CH}_3\text{CN}$ )	-	[52]
$[\text{Cu}(\text{phen})(\text{OH}_2)_2(\text{NO}_3)](\text{NO}_3)$	$3.91 \times 10^3$ ( $\text{CH}_3\text{OH}$ )	1061531	[53]
$[\text{Cu}(2,2\text{-bpy})\text{Cl}_2]$	$2.08 \times 10^3$ ( $\text{CH}_3\text{OH}$ )	1524681	[45c]
$[\text{Cu}(2,2\text{-bpy})_2(\text{OAc})]^+$	$1.83 \times 10^3$ ( $\text{CH}_3\text{OH}$ )	1513638	[54]
$[\text{Cu}(\text{L})_2]$	$4.75 \times 10^2$ ( $\text{CH}_3\text{OH}$ )	2046277	This work

the peak at  $-0.11$  V is for the deposition of copper. The catecholase activity was authenticated by the change in cyclic voltammograms of the copper complex in presence of DTBC in  $\text{CH}_2\text{Cl}_2$  at 295 K. Cyclic voltammograms of the copper complex in presence of DTBC produces an anodic peak at  $-0.30$  V perhaps the cathodic wave of  $\text{Cu}^{2+}/\text{Cu}^+$  couple was disappeared. This peak is a definite sign of the oxidation of DTBC. Therefore, this peak is assignable to cat/sq redox couple (cat = catechol, sq = o-benzoquinone and isq = o-iminobenzoquinone). The disappearance of  $\text{Cu}^{2+}/\text{Cu}^+$  peak indicates the involvement of  $\text{Cu}^{2+}$  in the oxidation processes. This metal-mediated oxidation of DTBC was also authenticated by the EPR spectral analysis. The copper complex gives a four-line hyperfine structure at  $g = 2.13$  due to  $^{63,65}\text{Cu}$  in  $\text{CH}_2\text{Cl}_2$  at 295 K (Fig. S11). However, in the presence of DTBC, the metal complex becomes EPR silent (Fig. S12). This is due to the antiferromagnetic coupling between the copper centre and semiquinone species. These experiments strongly support the metal-mediated oxidation of DTBC. Further, the fate of molecular oxygen in the oxidation of DTBC was examined through the production of hydrogen peroxide in solution [37,38]: An electronic band at  $\lambda_{\text{max}}$  353 nm confirmed the development of hydrogen peroxide in the course of catalytic oxidation and thereby, ensured the transformation of molecular oxygen to  $\text{H}_2\text{O}_2$  in the catalytic oxidation of DTBC. Furthermore, the retention of structural identity of the copper(II) complex was confirmed in the catalytic oxidation of DTBC by measuring the UV–vis spectrum of the solution after separating the oxidation product. The solution containing the copper complex as catalyst produces similar kind of electronic bands at 233 and 350 nm (Fig. S13) as like the electronic bands of the original copper complex displayed in methanol and ensures the retention of structural identity in catalytic oxidation of DTBC. Therefore, based on the experimental outcomes, a plausible mechanistic cycle for the catalytic oxidation of DTBC may be proposed according to the following scheme 3. A comparison of catalytic oxidation of DTBC by this Cu(II) complex with some other reported Cu(II) complexes is furnished in Table 3 [51–54].

### 3.6. Fungicidal activity of the Cu(II)-Schiff base complex

The fungicidal activity of the copper complex was assessed with a well diffusion method against the fungi *candida albicans*. The results of the inhibition zone diameters are shown in Table S4. The antifungal efficiency for the Cu(II) complex was determined by calculating MIC on *candida albicans*. The minimum inhibitory concentration (MIC) value was estimated as 230  $\mu\text{g}/\text{mL}$  for the copper(II) complex. Scientific literature suggest that the Cu(II) complex is quite competent to inhibit the growth of *candida albicans*. Under a similar experimental condition, the standard fluconazole shows the MIC value of 6.25  $\mu\text{g}/\text{mL}$  (Table S5). The MIC value suggests a good fungicidal potency for the inhibition of the growth of *c. albicans* fungal species under experimental conditions. To understand the origin of fungicidal activity of the copper(II) complex, field emission scanning electron microscopy (FESEM) image



**Scheme 3.** Plausible mechanistic cycle for catecholase activity of the copper complex.

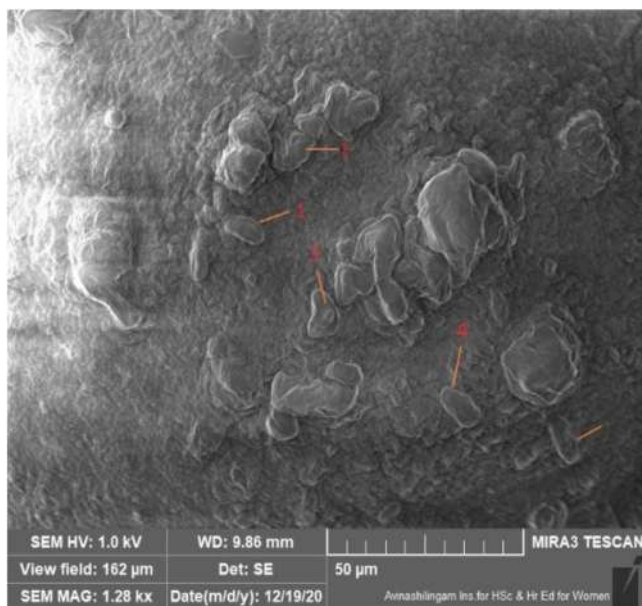


**Fig. 5.** Morphological changes in *candida albicans* upon treated with the Cu(II) complex.

was recorded for the *candida albicans* upon treatment with copper(II) complex. The recorded SEM micrographs of *candida albicans* cells are shown in Fig. 5. Commonly, the *candida albicans* fungal species was found as nearly spherical-shaped cell morphology with smooth and intact cell walls. It is well observed that the number of *candida albicans* was remarkably decreased, and clustered. The

cell walls of the fungal species *candida albicans* became damaged and shrank upon the interaction of the Cu(II) complex with the fungi [55,56]. Most captivatingly, the presence of elemental copper was detected on the cell wall of *candida albicans* through the energy dispersive X-ray spectroscopy (Fig. S14) and is shown as the orange coloured mark in Fig. 5. Truly, the presence of elemental copper on cell wall is a remarkable phenomenon to report and in very limited cases, such type of observation was noted.

### 3.7. Antiproliferative activity of the Cu(II)-Schiff base complex

MTT assay was employed to determine the cytotoxic effect of the copper(II) complex on MCF-7 cell lines. The breast cancer cell lines, MCF-7 were treated with the copper(II) complex in a dose dependant manner varying the concentration 5 to 30  $\mu\text{g}$  per ml for 24 h. The results are expressed as a percentage of the control value in presenting as a cell cytotoxicity ratio for MCF-7 cells and displayed in Fig. 6. The  $\text{IC}_{50}$  value for the copper complex was determined as 15  $\mu\text{g}/\text{mL}$  against MCF-7 cells for 24 h. It is well documented that (3-[4,5-dimethylthiazol-2-yl]-2,5-diphenyltetrazolium bromide is a water soluble tetrazolium salt yielding a yellowish solution when prepared in media. The yellow coloured MTT is reduced by mitochondrial dehydrogenase of viable cells yielding a measurable purple formation product. The viable cells consist of NADPH-dependant reductase and reduce the MTT reagent to formazon with the development of deep purple formazon species. Thereafter, the absorbance of formazon solution was measured by plate reader to examine the cytotoxic effects of the copper complex. The induced morphological changes in MCF-7 cells by Cu(II) complex (Fig. 7) leads to the shrinkage, detachment and membrane blebbing which suggests the high anti-proliferative potency of the copper complex.

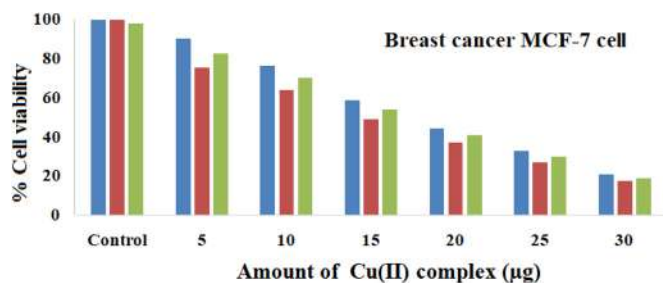


Fig. 6. Cellular viability of breast cancer cell lines, MCF-7 cells treated with copper(II) complex in a dose dependent manner for 24 h employing MTT assay.

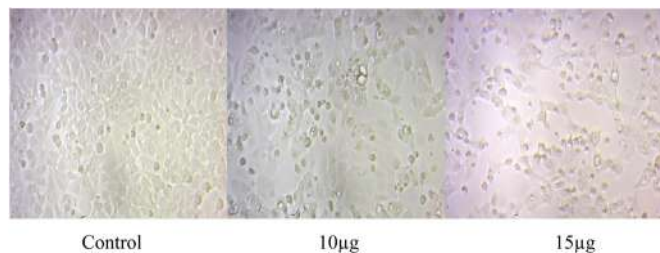


Fig. 7. Photomicrograph (40 ×) represents morphological changes in MCF-7 cells such as shrinkage, detachment, membrane blebbing and distorted shape induced by Cu(II) complex (10 and 15 µg/mL for 24 h) as compared with control. Control cells showed normal intact cell morphology and their images were captured by light microscope. (For interpretation of the references to colour in this figure legend, the reader is referred to the web version of this article.)

In true sense, the introduction of the azo-functionalized copper(II)-Schiff base complex helps to develop reactive oxygen species (ROS) in the lipid peroxidase in MCF-7 cells. Consequently, the redox active copper complex generates more reactive free radicals which involve in the destruction of membrane lipid of MCF-7 cells. This phenomenon accounts for the detachment and shrinkage of the normal cells and increases the apoptosis of MCF-7 cells. This observation is also supported by previously reported anti-tumour activities induced by copper complexes [55,56].

#### 4. Conclusions

This research work deals with the synthesis, crystal structure, bio-mimics of catecholase, antifungal and antitumor activity of a newly designed copper(II) complex containing an azo-functionalized Schiff base. The copper(II) centre adopts a distorted square planar geometry. The strong association of lattice water with the ligand units through very strong intermolecular H-bonding interaction induces a large distortion in the square planar complex. The copper(II) complex exhibits a good catalytic activity with a high turnover number,  $4.75 \times 10^2 \text{ h}^{-1}$  towards the catalytic oxidation of DTBC in methanol. Electrochemical, EPR and spectrophotometric spectral studies of the copper(II) complex in presence of DTBC suggest the copper(II) mediation catalytic oxidation of DTBC. The copper(II) complex turns out to be a potential fungicidal agent against clinical *Candida albicans* and scanning electron microscope studies confirm the destruction of the fungal cell membrane with the deposition of copper. In vitro study of cytotoxicity of the copper complex towards the breast cancer, MCF-7 cell lines account for its excellent antiproliferative potency at  $IC_{50}$  value, 15 µg/mL for 24 h. The synthesis of azo-functionalized Schiff base and its copper(II) complex will certainly enrich the molecular library having solvent-induced distortion in copper(II) complex with important catalytic and biological activities

#### Declaration of Competing Interest

The authors declare that they have no known competing financial interests or personal relationships that could have appeared to influence the work reported in this paper.

#### CRediT authorship contribution statement

**Subham Mukherjee:** Conceptualization, Formal analysis, Methodology, Investigation. **Chanchal Kumar Pal:** Formal analysis, Methodology, Investigation. **Muddukrishnaiah Kotakonda:** Formal analysis, Methodology, Investigation, Validation. **Mayank Joshi:** Formal analysis, Validation. **Madhusudan Shit:** Formal analysis, Methodology, Investigation. **Prasanta Ghosh:** Formal analysis, Visualization. **Angshuman Roy Choudhury:** Software, Validation. **Bhaskar Biswas:** Conceptualization, Writing – review & editing, Supervision.

#### Acknowledgements

BB thanks Science and Engineering Research Board (SERB), India for financial support under Empowerment and Equity Opportunities for Excellence in Science (EEQ/2020/000079). The authors sincerely acknowledge the Department of Technology of Anna University, Chennai, India for supporting the measurement of biological activities.

#### Supplementary materials

Supplementary material associated with this article can be found, in the online version, at doi:10.1016/j.molstruc.2021.131057.

#### References

- [1] S. Roy, M. Böhme, S.P. Dash, M. Mohanty, A. Buchholz, S. Majumder, W. Plass, S. Kulanthavel, I. Banerjee, H. Reuter, W. Kaminsky, R. Dinda, *Inorg. Chem.* 57 (2018) 5767–5781.
- [2] W.A. Zoubi, Y.G. Ko, *Appl. Organomet. Chem.* 31 (2017) e3574.
- [3] A. Shili, A. Ayadi, S. Taboukhat, N. Zouari, B. Sahaoui, *Conceptualisation, A. El-Ghayoury, J. Mol. Struct.* 1222 (2020) 128933.
- [4] King-Thom Chung, *J. Environ. Sci. Health, part C* 34 (2016) 233–261.
- [5] H. Zollinger, *Color Chemistry, Syntheses, Properties and Applications of Organic Dyes and Pigments*, 3rd edition, Wiley-VCH, Weinheim, Germany, 2003.
- [6] N.M. Aljamali, *Biochem. Anal. Biochem.* 4 (2015) 1000169.
- [7] V.M. Dembitsky, T.A. Glorizova, V.V. Poroikov, *Nat. Prod. Bioprospect.* 7 (2017) 151–169.
- [8] S. Concilio, L. Sessa, A.M. Petrone, A. Porta, R. Diana, P. Iannelli, S. Piotto, *Molecules* 22 (6) (2017) 875.
- [9] H. Nishihara, *Coord. Chem. Rev.* 249 (2005) 1468–1475.
- [10] H.A. Wegner, *Angew. Chem. Int. Ed.* 51 (2012) 4787.
- [11] H. Koshima, N. Ojima, H. Uchimoto, *J. Am. Chem. Soc.* 131 (2009) 6890.
- [12] G. Heitmann, C. Schütt, R. Herges, *Eur. J. Org. Chem.* 22 (2016) 3817.
- [13] A.D. Garnovskii, E.V. Sennikova, B.I. Kharisov, *The Open Inorg. Chem. J.* 3 (2009) 1–20.
- [14] J. Valentová, S. Varényi, P. Herich, P. Baran, A. Bilková, J. Kozířek, L. Habala, *Inorg. Chim. Acta* 480 (2018) 16.
- [15] S. Al-Saeedi, L.H. Abdel-Rahman, A.M. Abu-Dief, S.M. Abdel-Fatah, T.M. Alotaibi, A.M. Alsahme, *Catalysts* 8 (2018) 452.
- [16] E.L. De Araújo, H. Franciane, G. Barbosa, E.R. Dockal, É. Tadeu, G. Cavalheiro, *Int. J. Biol. Macromol.* 95 (2016) 168.
- [17] W.J. Lian, X.T. Wang, C.Z. Xie, H. Tian, X.Q. Song, H.T. Pan, X. Qiao, J.Y. Xu, *Dalton Trans* 45 (2016) 9073.
- [18] L.H. Abdel-Rahman, M.S.S. Adam, A.M. Abu-Dief, H. Moustafa, M.T. Basha, A.S. Aboraia, B.S. Al-Farhan, H. El-Sayed Ahmed, *Appl. Organometal. Chem.* 32 (2018) e4527.
- [19] B. Iftikhar, et al., *J. Mol. Struct.* 1155 (2018) 337–348.
- [20] E. Akila, M. Usharani, S. Vimala, R. Rajavel, *Chem. Sci. Rev. Lett.* 1 (2012) 181–194.
- [21] S.E. Allen, R.R. Walvoord, R. Padilla-Salinas, M.C. Kozłowski, *Chem. Rev.* 113 (2013) 6234–6458.
- [22] X. Liu, N. Nvoa, C. Manzur, S. Celedón, D. Carrillo, J. Hamon, *Coord. Chem. Rev.* 357 (2018) 144–172.
- [23] P. Capdevielle, M. Maumy, *Tetrahedron* 57 (2001) 379.
- [24] P.K. Mudi, R.K. Mahato, M. Joshi, M. Shit, A.R. Choudhury, H.S. Das, B. Biswas, *J. Appl. Organometal. Chem.* 35 (2021) e6211.

- [25] (a) S. Mukherjee, S. Roy, S. Mukherjee, B. Biswas, *J. Mol. Struct.* 1217 (2020) 128348; (b) A. Sánchez-Ferrer, J.N. Rodríguez-López, V. García-Cañovas, F.G. Carmona, *Biochim. Biophys. Acta* 1 (1995) 1247.
- [26] C. Gerdemann, C. Eicken, B. Krebs, *Acc. Chem. Res.* 35 (2002) 183.
- [27] (a) F. Fusetti, K.H. Schrotter, R.A. Steiner, P.I. van Noort, T. Pijning, H.J. Rozeboom, K.H. Kalk, M.R. Egmond, B.W. Dijkstra, *Structure* 10 (2002) 259; (b) R.A. Steiner, I.M. Kooter, B.W. Dijkstra, *Biochem* 41 (2002) 7955; (c) I.M. Kooter, R.A. Steiner, B.W. Dijkstra, P.I. van Noort, M.R. Egmond, M. Huber, *Eur. J. Biochem.* 269 (2002) 2971.
- [28] E.I. Solomon, D.E. Heppner, E.M. Johnston, J.W. Ginsbach, J. Cirera, M. Qayyum, M.T. Kieber-Emmons, C.H. Kjaergaard, R.G. Hadt, L. Tian, *Chem. Rev.* 114 (2014) 3659.
- [29] E.I. Solomon, M.J. Baldwin, M.D. Lowery, *Chem. Rev.* 92 (1992) 521.
- [30] (a) E.I. Solomon, B.L. Hemming, D.E. Root, *Electronic Structures of Active Sites in Copper Proteins: Coupled Binuclear and Trinuclear Cluster Sites in Bioinorganic chemistry of Copper*, (K.D. Karlin, Z. Tyeklar), Chapman & Hall Publishing House, New York, USA, (1993) doi:10.1007/978-94-011-6875-5.; (b) C. Mukherjee, U. Pieper, E. Bothe, V. Bachler, E. Bill, T. Weyhermüller, P. Chaudhuri, *Inorg. Chem.* 47 (2008) 8943.
- [31] T. Punniyamurthy, S. Velusamy, J. Iqbal, *Chem. Rev.* 105 (2005) 2329.
- [32] T. Punniyamurthy, L. Rout, *Coord. Chem. Rev.* 252 (2008) 134.
- [33] K. Selmezi, M. Réglier, M. Giorgi, G. Speier, *Coord. Chem. Rev.* (2003) 19 2003.
- [34] P.J. Walsh, M.C. Kozlowski, *Fundamentals of Asymmetric Catalysis*, University Science Books, Sausalito, CA, 2009 Chapter 8.
- [35] S. Mahato, N. Meheta, K. Muddukrishnaiah, M. Joshi, M. Shit, A.Roy Choudhury, B. Biswas, *Polyhedron* 194 (2020) 114933.
- [36] C. Duncan, A.R. White, *Metallomics* 4 (2012) 127.
- [37] J. Zhang, D. Duan, J. Xu, J. Fang, *ACS Appl. Mat. Interfac.* 10 (2018) 33010.
- [38] K.Y. Djoko, M.M. Goytia, P.S. Donnelly, M.A. Schembri, W.M. Shafer, A.G. McEwan, *Antimicrob. Agents Chemother.* 59 (2015) 6444.
- [39] B.S. Furniss, A.J. Hannaford, P.W.G. Smith, A.R. Tatchell, *Vogel's Textbook of Practical Organic Chemistry*, 1989, p. 952. Fifth Edition.
- [40] *CrysAlisPro 1.171.39.35c* Rigaku Oxford Diffraction, Rigaku Corporation, Tokyo, Japan, 2017.
- [41] G.M. Sheldrick, *SHELXT- Integrated space-group and crystal-structure determination*, *Acta Cryst.* A71 (2015) 3.
- [42] G.M. Sheldrick, *Crystal structure refinement with SHELXL*, *Acta Cryst.* C71 (2015) 3.
- [43] O.V. Dolomanov, L.J. Bourhis, R.J. Gildea, J.A.K. Howard, H. Puschmann, *J. Appl. Cryst.* 42 (2009) 339.
- [44] (a) L.I. Simandi, S. Nemeth, N. Rumlis, *J. Mol. Catal.* 42 (1987) 357; (b) Z. Szeverenyi, E.R. Mileava, L.I. Simandi, *J. Mol. Catal.* 67 (1991) 251; (c) G.C. Paul, K. Das, S. Maity, S. Begum, H.K. Srivastava, C. Mukherjee, *Inorg. Chem.* 58 (2019) 1782; (d) F. Benedini, G. Galliani, M. Nali, B. Rindone, S. Tollari, *J. Chem. Soc. Perkin Trans. 2* (1985) 1963.
- [45] (a) N.C. Jana, M. Patra, P. Brandão, A. Panja, *Inorg. Chim. Acta.* 490 (2019) 163; (b) S. Thakur, S. Banerjee, S. Das, S. Chattopadhyay, *New J. Chem.* 43 (2019) 18747; (c) M. Garai, D. Dey, H.R. Yadav, A.R. Choudhury, M. Maji, B. Biswas, *ChemistrySelect* 2 (2017) 11040; (d) A. De, M. Garai, H.R. Yadav, A.R. Choudhury, B. Biswas, *Appl. Organomet. Chem.* 31 (2017) e3551.
- [46] C.K. Pal, S. Mahato, H.R. Yadav, M. Shit, A.R. Choudhury, B. Biswas, *Polyhedron* 174 (2019) 114156.
- [47] (a) B. Chowdhury, M. Maji, B. Biswas, *J. Chem. Sci.* 129 (2017) 1627–1637; (b) A. De, D. Dey, H.R. Yadav, M. Maji, V. Rane, R.M. kadam, A.R. Choudhury, B. Biswas, *J. Chem. Sci.* 128 (2016) 1775–1782.
- [48] (a) S. Khan, S. Herrero, R. Gonzalez-Prieto, M.G.B. Drew, S. Banerjee, S. Chattopadhyay, *New J. Chem.* 42 (2018) 13512; (b) T.M. Rajendiran, *Transit. Met. Chem.* 28 (2003) 447.
- [49] A.S. Smirnov, L.M.D.R.S. Martins, D.N. Nikolaev, R.A. Manzhos, V.V. Gurzhiy, A.G. Krivenko, K.O. Nikolaenko, A.V. Belyakov, A.V. Garabadzhiua, P.B. Davydovich, *New J. Chem.* 43 (2019) 188.
- [50] L.Z. Cai, W.T. Chen, M.S. Wang, G.C. Guo, J.S. Huang, *Inorg. Chem. Commun.* 7 (2004) 611–613.
- [51] A. De, D. Dey, H.R. Yadav, M. Maji, V. Rane, R.M. kadam, A.R. Choudhury, B. Biswas, *J. Chem. Sci.* 128 (2016) 1775–1782.
- [52] E.C.M. Ording-Wenker, M.A. Siegler, M. Lutz, E. Bouwman, *Dalton Tran.* 44 (2015) 12196.
- [53] D. Dey, S. Das, H.R. Yadav, A. Ranjani, L. Gyathri, S. Roy, P.S. Guin, D. Dhanasekaran, A.R. Choudhury, M.A. Akbarsha, B. Biswas, *Polyhedron* 106 (2016) 106–114.
- [54] P.K. Mudi, N. Bandopadhyay, M. Joshi, M. Shit, S. Paul, A.R. Choudhury, B. Biswas, *Inorg. Chim. Acta* 505 (2020) 119468.
- [55] A. Reyes-Jara, N. Cordero, J. Aguirre, M. Troncoso, G. Figueroa, *Front. Microbiol.* 7 (2016) 626.
- [56] H. Li, et al., Enhancing the antimicrobial activity of natural extraction using the synthetic ultra small metal nanoparticles. *Sci. Rep.* 5 (2019).



## Source details

[Feedback >](#) [Compare sources >](#)

### Journal of Molecular Structure

Scopus coverage years: from 1967 to Present

Publisher: Elsevier

ISSN: 0022-2860

Subject area: [Chemistry: Inorganic Chemistry](#) [Chemistry: Analytical Chemistry](#) [Chemistry: Spectroscopy](#) [Chemistry: Organic Chemistry](#)

Source type: Journal

[View all documents >](#)[Set document alert](#)[Save to source list](#)

CiteScore 2022

6.0



SJR 2022

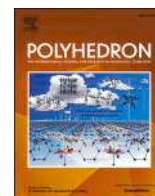
0.482



SNIP 2022

0.954

[CiteScore](#)[CiteScore rank & trend](#)[Scopus content coverage](#)



# A thiomethyl-substituted imidazolyl imine functionalized copper(II) complex: synthesis, structural characterization, phenoxazinone synthase mimics and biological activities

Nilaj Bandopadhyay<sup>a</sup>, Krishnendu Paramanik<sup>a</sup>, Prafulla Kumar Mudi<sup>a</sup>, Gayetri Sarkar<sup>a</sup>, Muddukrishnaiah Kotakonda<sup>b</sup>, Madhusudan Shit<sup>c</sup>, Bhaskar Biswas<sup>a,\*</sup>, Hari Sankar Das<sup>a,\*</sup>

<sup>a</sup> Department of Chemistry, University of North Bengal, Darjeeling 734013, India

<sup>b</sup> Faculty of Technology, Anna University, Chennai 600025, India

<sup>c</sup> Department of Chemistry, Dinabandhu Andrews College, Kolkata 700084, India

## ARTICLE INFO

### Keywords:

Copper(II)  
Schiff base  
X-ray structure  
Phenoxazinone synthase activity  
Cytotoxicity

## ABSTRACT

A *cis*-dichloro copper(II) complex with a novel tridentate thiomethyl substituted imidazole based Schiff base ligand L, obtained from 2-methylthioaniline and 2-imidazolecarboxaldehyde, has been synthesized and characterized by spectroscopic methods and X-ray crystallography. The crystal structure of the complex shows a distorted square-pyramidal environment around the copper(II) centre, coordinated by the tridentate ligand L and two *cis*-chloride ligands (one axial and another equatorial). The supramolecular framework, connected through several intermolecular noncovalent interactions in the crystal structure, has been investigated in detail. The complex effectively shows phenoxazinone synthase-like activity (aerial oxidation of 2-aminophenol to 2-aminophenoxazine-3-one) under ambient conditions with a high turnover number of  $1.92 \times 10^4 \text{ h}^{-1}$ . Further, the antimicrobial activity of the copper(II) complex was examined against *E. coli*, *Staphylococcus aureus* and *K. pneumoniae* clinical microbial cultures, which imply its significant bactericidal property compared to the standard antibiotic agent *ciprofloxacin*. In addition, the anticancer activity of the copper(II) complex was tested against the human colorectal adenocarcinoma (HT-29) cancerous cell line and it shows notable activity with an  $\text{IC}_{50}$  value of  $125 \mu\text{g mL}^{-1}$ .

## 1. Introduction

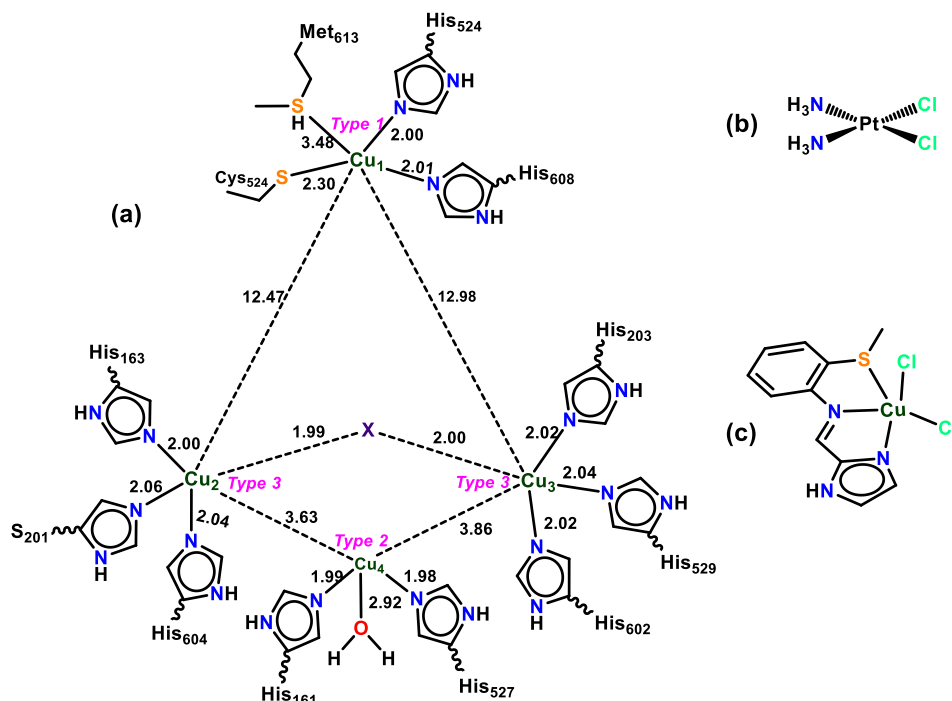
The combination of a copper ion and a protein-bound imidazole-based histidine ligand, present in the active site of many metalloproteins, plays crucial roles in several important biological functions, such as oxygen transport [1,2], electron transport [3–5] and substrate oxidation [5–9]. The phenoxazinone synthase (PHS) is an important naturally occurring pentacopper containing oxidase enzyme (Scheme 1a), found in the bacterium *Streptomyces antibiotus*. The metalloenzyme activates dioxygen and facilitates the catalytic oxidation of substituted 2-aminophenol (2-AP) to yield the 2-aminophenoxazinone (APX) heterocyclic chromophore [10]. The formation of APX is highly important and takes place in the penultimate step of the biosynthesis of actinomycin D, a strong antineoplastic agent which exhibits significant antibacterial and antitumor activities [11]. Actinomycin D is widely used clinically to treat the gestational trophoblastic disease and many tumors,

such as Wilms and Ewing tumors, testicular cancer, sarcomas, etc. A literature survey shows that the phenoxazinone compound binds with DNA by intercalation between adjacent G-C base pairs of the double helix, thereby inhibiting the DNA directed RNA synthesis [12–14].

PHS was first structurally characterized from the *Streptomyces antibiotus* bacteria by James P. Allen and Wilson A. Francisco, and mediates the six-electron oxidation of two 2-aminophenol to the phenoxazinone chromophore using molecular oxygen as the oxidant [15,16]. It is also documented that PHS holds two distinct oligomeric units, a dimer and a hexamer [16]. Only the hexamer predominantly produces actinomycin, which contains a total of 5 Cu atoms having mononuclear one type-1 (blue), two type-2 (normal) and one binuclear type-3 copper-binding motifs bridged by a ligand, that can be a  $\text{OH}^-$  or a halide ion or even a neutral water molecule (Scheme 1a) [10]. PHS activity has earned great attention in recent years, with studies to mimic its enzymatic process and develop model complexes for improved catalytic activity. As a

\* Corresponding authors.

E-mail addresses: [bhaskarbiswas@nbu.ac.in](mailto:bhaskarbiswas@nbu.ac.in) (B. Biswas), [harisankardas@nbu.ac.in](mailto:harisankardas@nbu.ac.in), [idasitk@gmail.com](mailto:idasitk@gmail.com) (H. Sankar Das).



**Scheme 1.** (a) Schematic diagram of the active site of the phenoxazinone synthase enzyme along with the metal–ligand and metal–metal distances. The fifth type 2 copper unit is not shown in this scheme, which is located at a distance of 25 Å from the type 1 blue copper. (b) The structure of cisplatin. (c) The structure of the mononuclear copper complex **1** described in this work.

result, several metal catalysts have developed and it has been found that not only multimetallic systems, but also mononuclear metal complexes could effectively catalyze the aerial oxidation of the model substrate 2-AP to APX [16–27]. Therefore, considering the importance of phenoxazinone synthase activity, a naturally occurring bioinspired oxidative coupling reaction, we have designed a biologically important (phenoxazinone synthase, azurin) [16,28] thiomethyl-substituted imidazole-based Schiff base ligand, 1-(1H-imidazol-2-yl)-N-(2-(methylthio)phenyl)methanimine (**L**), coordinated mononuclear copper(II) complex of the type  $\text{CuLCl}_2 \cdot \text{H}_2\text{O}$ , **1** (Scheme 1c). Complex **1** shows impressive catalytic activity towards the transformation of 2-AP to APX in air.

Coordinated complexes of copper can induce the hydrolysis or oxidative cleavage of DNA [29,30]. Therefore, many complexes have been studied and show promising anticancer activity as well as low toxicity [31–36]. Although expensive, the drug cisplatin (Scheme 1b) is the best metal-based chemotherapeutic drug and is widely used for the treatment of various cancers [37]. However, it suffers from common problems, like multi-drug resistance, serious toxicity and other side effects [38,39]. Hence, the design of new metal-based cost-effective therapeutic drugs with low toxicity, better efficacy and that are more target-specific than cisplatin is highly important [40]. The N-heterocyclic imidazole moiety is also known to show notable anticancer activity [21]. The present complex **1** has two labile chloride ligands, similar to cisplatin, and the presence of imidazole in the backbone prompted us to investigate its anticancer and antibacterial properties. Herein, along with the PHS activity, we have also reported the antibacterial activity of **1** against *E. coli*, *Staphylococcus aureus* and *K. pneumoniae*, as well as its anticancer activity against the HT-29 cell line.

## 2. Experimental

### 2.1. Materials and methods

Highly pure 2-(methylthio)aniline was purchased from TCI, Japan, imidazole-2-carboxaldehyde from Sigma Aldrich, USA, copper(II) chloride dihydrate from Sigma Aldrich, USA and 2-aminophenol from Avra,

India. Analytical grade chemicals and solvents were used in this study.

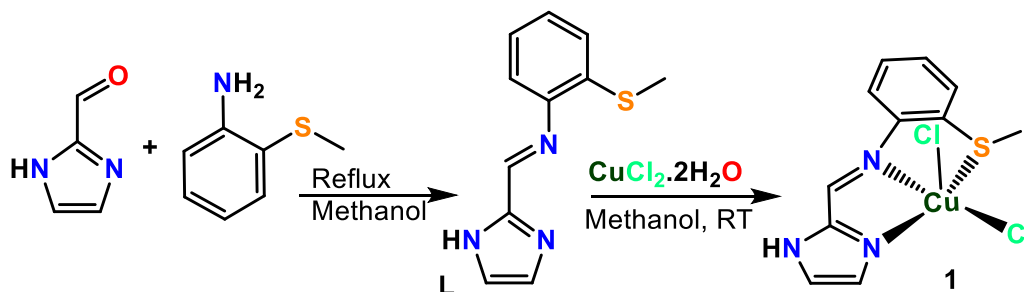
The C, H, N contents were determined with a micro analyser (Perkin Elmer 2400 CHN, Waltham, USA). The NMR spectral analyses were measured on an NMR spectrometer (Bruker Avance 400 MHz, Massachusetts, USA). The FT-IR spectra were recorded on a spectrometer (FTIR-8400S SHIMADZU, Shimadzu, Kyoto, Japan) with KBr pellets. Electronic absorption spectra were recorded with a UV–Vis spectrophotometer (HITACHI U-2910, Tokyo, Japan). Electrospray ionization (ESI) mass spectra were performed on a Q-tof-micro quadrupole mass spectrometer. The electrochemical analyses were recorded in a K-Lyte 1.2 potentiostat system (Kanopy, India). A three-electrode set-up (glassy-carbon working electrode, Pt counter electrode, Ag wire as pseudo-reference electrode) was used in 0.1 M  $\text{Bu}_4\text{NPF}_6$  solutions. The ferrocene/ferrocenium ( $\text{Fc}^0/\text{Fc}^+$ ) couple served as an internal standard.

### 2.2. Synthesis of the Schiff base ligand **L**

To a methanolic solution (25 mL) of imidazole-2-carboxaldehyde (0.384 g, 4 mmol), 2-methyl thioaniline (0.556 g, 4 mmol) was added dropwise under stirring conditions and then refluxed for 8 h. The progress of the course of the reaction was assessed by TLC. The reaction mixture was reduced to 5 mL under a reduced pressure, which precipitated an off-white solid. Thereafter, the product was dried in a vacuum. Yield: 0.787 g (~84%). Anal. calc. for  $\text{C}_{11}\text{H}_{11}\text{N}_3\text{S}$  (**L**): C, 60.80; H, 5.10; N, 19.34; Found C, 60.72; H, 5.02; N, 19.53%.  $^1\text{H}$  NMR (400 MHz,  $\text{DMSO}-d_6$ , 25 °C, Figure S1)  $\delta$ , ppm: = 8.26 (s, 1H,  $-\text{N}=\text{CH}$ ), 7.28–7.07 (s, 6H, Ar-H), 12.99 (s, 1H,  $-\text{NH}$ ), 2.50 (s, 3H;  $\text{CH}_3$ );  $^{13}\text{C}\{^1\text{H}\}$  NMR (75 MHz,  $\text{DMSO}-d_6$ , 25 °C, Figure S2)  $\delta$ , ppm: 151.01, 148.71, 145.15, 133.90, 131.32, 127.11, 125.70, 124.81, 121.16, 118.38, 14.37; IR (KBr,  $\text{cm}^{-1}$ ; Figure S3): 3480 ( $\nu_{\text{N-H}}$ ), 1622 ( $\nu_{\text{C=N}}$ ), 1642 ( $\nu_{\text{C-N,Imd}}$ ); UV–Vis ( $\lambda_{\text{max}}$ , nm; Figure S4): 272, 297, 358.

### 2.3. Synthesis of the copper(II) complex, $[\text{Cu}(\text{L})\text{Cl}_2] \cdot \text{H}_2\text{O}$ (**1**)

The ligand **L** (0.100 g, 0.46 mmol) was dissolved in 15 mL MeOH and left under stirring for 15 min. After that, copper(II) chloride dihydrate



Scheme 2. Preparation of L and its copper complex 1.

(0.0784 g, 0.46 mmol) dissolved in 5 mL MeOH was added dropwise to the ligand solution. The resultant mixture was stirred for another 4 h, then filtered off and kept in a column tube for slow evaporation. A dark green block-shaped crystalline compound was obtained after 4–5 days. Yield: 0.140 g (~78%). Anal. calc. for  $\text{C}_{11}\text{H}_{11}\text{N}_3\text{SCuCl}_2 \cdot \text{H}_2\text{O}$ : C, 34.12; H, 2.86; N, 10.85; found C, 34.37; H, 2.76; N, 10.61%. IR (KBr,  $\text{cm}^{-1}$ ; Figure S3): 3460 ( $\nu_{\text{N-H}}$ ), 1596 ( $\nu_{\text{C=N}}$ ), 1634 ( $\nu_{\text{C-N,Im}}$ ); UV-Vis ( $\lambda_{\text{max}}$ , nm; Fig. S4): 270, 290, 345, 415; ESI-MS ( $m/z$ ; Figure S5) calc. for  $\text{C}_{11}\text{H}_{11}\text{N}_3\text{SCu} [\text{M} - 2\text{Cl}]^+$  280.8360, found 280.8450 and calc. for  $\text{C}_{11}\text{H}_{11}\text{N}_3\text{SCuCl} [\text{M} - \text{Cl}]^+$  316.2860, found 316.2807.

#### 2.4. Crystal structure determination and refinement

A Rigaku XtaLABmini diffractometer was used to collect the X-ray diffraction data at 296.0(2) K for complex 1. A Mercury 375R ( $2 \times 2$  bin mode) CCD detector, equipped with the diffractometer, and graphite monochromated Mo-K $\alpha$  radiation ( $\lambda = 0.71073 \text{ \AA}$ ) were employed to collect the data using  $\omega$  scans. CrysAlisPro 1.171.39.7f [41] was screened to reduce the data and the space group was determined with Olex2 [42]. The structure of 1 was resolved by the dual space method using SHELXT-2015 [43] and refined by full-matrix least-squares procedures using the SHELXL-2015 [44] software package through the OLEX2 suite [42]. All hydrogen atoms were geometrically fixed. The molecular graphics, noncovalent bonds and packing figures were created by using ORTEP and mercury software.

#### 2.5. Phenoxazinone synthase-like activity of the copper(II) complex (1)

We have examined the phenoxazinone synthase-like catalytic activity of the copper(II) complex 1 by the treatment of a  $1 \times 10^{-4} \text{ M}$  copper (II) complex solution of 1 in MeOH with a  $1 \times 10^{-3} \text{ M}$  methanolic solution of the model substrate 2-aminophenol (2-AP) in methanol under aerobic conditions. The conversion of 2-AP to 2-aminophenoxazinone (APX) was monitored by scanning the UV-vis absorption spectra in the wavelength range from 300 to 800 nm for 1.5 h using a spectrophotometer [45–47].

Kinetic experiments were also carried out spectrophotometrically to understand the catalytic efficacy of 1 as well as the nature of the 2-AP oxidation to APX in MeOH at 298 K [48]. For this purpose, 100 mL of a  $1 \times 10^{-4} \text{ M}$  constant concentration of 1 was mixed with a 2 mL methanolic solution of 2-AP with a 10-fold order of concentration under aerobic conditions and the increase in absorption intensity at 435 nm was measured. The rate 2-AP oxidation catalyzed by 1 based on substrate concentration was calculated by the initial rate law in triplicate. The gram scale catalysis reaction was also performed by mixing 1.0 g 2-AP (9.2 mmol) and 5 mol percent of catalyst 1 (0.017 g, 0.46 mmol) in 30 mL methanol and stirring for 2 h under aerobic conditions. The product, PHX, was isolated in ~86% yield.  $^1\text{H}$  NMR data for APX, ( $\text{CDCl}_3$ , 400 MHz)  $\delta_{\text{H}}$ , ppm: 7.61 (m, 1H), 7.45(m, 3H), 6.46 (s, 1H), 6.37 (s, 1H), 6.25 (s, 1H).

To confirm the fate of the aerobic oxygen as the oxidant in the catalytic oxidative coupling reaction, the production of hydrogen peroxide

( $\text{H}_2\text{O}_2$ ) was assessed according to the reported literature, described elsewhere [45–47].

#### 2.6. Antibacterial activity

The antimicrobial properties of the copper complex 1 were examined with respect to a standard antibiotic, Ciprofloxacin, against a few clinical microbial cultures, namely *E. coli*, *Staphylococcus aureus* and *K. pneumonia*. The microbial cultures were procured from the microbiology lab Coimbatore, Tamil Nadu, India. The antibacterial efficiency was evaluated following a disc-diffusion method and the zone of inhibition was marked using a Himedia zone reader. Details of the inoculum preparation, sample dose, minimum inhibitory concentration estimation and morphological analysis are described in the Supporting Information file.

#### 2.7. Cytotoxicity

##### 2.7.1. MTT assay

The antiproliferative effect of the copper complex was evaluated against a human colorectal adenocarcinoma cell line (HT-29), which was procured from the cell repository of the National Centre for Cell Sciences (NCCS), Pune, India. The cell viability assay (MTT assay) was carried out to examine the efficacy of the synthetic complex in a dose-dependent manner. The half-maximal inhibitory concentration ( $\text{IC}_{50}$ ) was also determined to measure the effectiveness of the synthetic compound [49]. The necessary information on the cell maintenance and details of the MTT assay are provided in the Supporting Information file.

##### 2.7.2. Acridine orange/ethidium bromide (AO/EB) staining analysis

The apoptosis of HT-29 cells was assessed on a fluorescence microscope following the method reported by Baskic et al. [50]. A 200  $\mu\text{L}$  dye mixture was prepared by dissolving 100  $\mu\text{L}$  acridine orange and 100  $\mu\text{L}$  ethidium bromide in PBS. The HT-29 cells were seeded at  $5 \times 10^4$  cells/well in a 6 well plate and incubated for 24 h. Afterwards, the copper complex was added and the cells were kept for 24 h to observe the cell detachment. Then, the cells were washed with cold PBS, followed by staining with a 1:1 mixture of AO/EB at RT. Thereafter, the stained cells were observed with a 40X magnifications fluorescence microscope. The apoptotic cells were numbered and counted as a function of the total number of cells present in the field. Further details are given in the Supporting Information file.

### 3. Results and discussion

#### 3.1. Synthesis of the ligand L and the copper complex $[\text{Cu}(\text{L})\text{Cl}_2] \cdot \text{H}_2\text{O}$ (1)

The tridentate Schiff base ligand 1-(1H-imidazol-2-yl)-N-(2-(methylthio)phenyl)methanimine, L, was synthesized by refluxing of 2-methylthioaniline with imidazole carbaldehyde in methanol (Scheme 1). The copper(II) complex was synthesized by reacting  $\text{CuCl}_2 \cdot 2\text{H}_2\text{O}$  with L in



**Table 1**  
Crystallographic refinement parameters for complex **1**.

Parameters	1
CCDC	2,153,757
Empirical formula	C <sub>11</sub> H <sub>11</sub> Cl <sub>2</sub> CuN <sub>3</sub> S·H <sub>2</sub> O
Formula weight	369.74
Temperature (K)	296.0(2)
Crystal system	Orthorhombic
Space group	<i>Pbca</i>
a (Å)	16.9351(8)
b (Å)	9.9068(5)
c (Å)	17.5703(9)
Volume (Å <sup>3</sup> )	2947.8(3)
Z	8
ρ (g cm <sup>-3</sup> )	1.666
μ (mm <sup>-1</sup> )	1.979
F (000)	1496
R <sub>int</sub>	0.081
θ ranges (°)	2.6, 27.5
Number of unique reflections	3375
Total number of reflections	13,800
Final R indices (R <sub>1</sub> and wR <sub>2</sub> )	0.0472, 0.1393
Largest peak and hole (e Å <sup>-3</sup> )	-1.01, 0.60

methanol at room temperature (RT) and isolated as a green coloured crystalline hydrated complex, [Cu(L)Cl<sub>2</sub>].H<sub>2</sub>O, **1** (Scheme 2). Complex **1** is air-stable and well soluble in DMSO, methanol and ethanol. The ligand **L** and its copper(II) complex **1** were characterized by several analytical methods, including elemental analysis, NMR (Figures S1 and S2), IR (Figure S3), UV–Vis (Figure S4), mass spectroscopy (Figure S5) and

crystal structure analysis.

### 3.2. Description of the crystal structure of **1**

Crystal structure analysis revealed that complex **1** crystallized in an orthorhombic system with the *Pbca* space group (Table 1). The thermal ellipsoidal plots of **1** with the atom labelling scheme is displayed in Fig. 1a. The copper ion in the crystal structure of **1** is in a distorted square pyramidal environment, with the basal positions being occupied by the tridentate N,N,S-donor Schiff base ligand and by one chloride ion. The fifth position is occupied by the second chloride ion, suggesting the bivalent oxidation level of the copper ion. The distortion of the square pyramid is imposed by the chelating nature of the **L** ligand, steric repulsion between two bulky chloride ions, the bulky sulfur atom with two chloride ions, hydrogen bonding and Jahn–Teller distortion. Selected bond angles and bond lengths are recorded in Table S1. Some weak repulsions between the equatorial chloride atom and the imidazole nitrogen atom, and the axial chloride atom with the imidazole nitrogen and imine nitrogen atoms are also present in the structure, as evident from the corresponding copper-centric bond angle values (Table S1). The Cu(II) ion in **1** is slightly out of the square plane by 0.369 Å towards the axial chlorine atom. Bond-length analyses around the copper centre show a relatively long axial Cu–Cl bond length [Cu1–Cl2, 2.5118(9) Å] compared to the equatorial Cu–Cl bond length [Cu1–Cl1, 2.2293(10) Å], as observed in similar tridentate supporting ligand coordinated bis-chloro complexes [21,51–53]. This large extent of axial bond elongation can be explained by considering the second-order Jahn–Teller effect and hydrogen bonding of the axial chloride ligand with the water

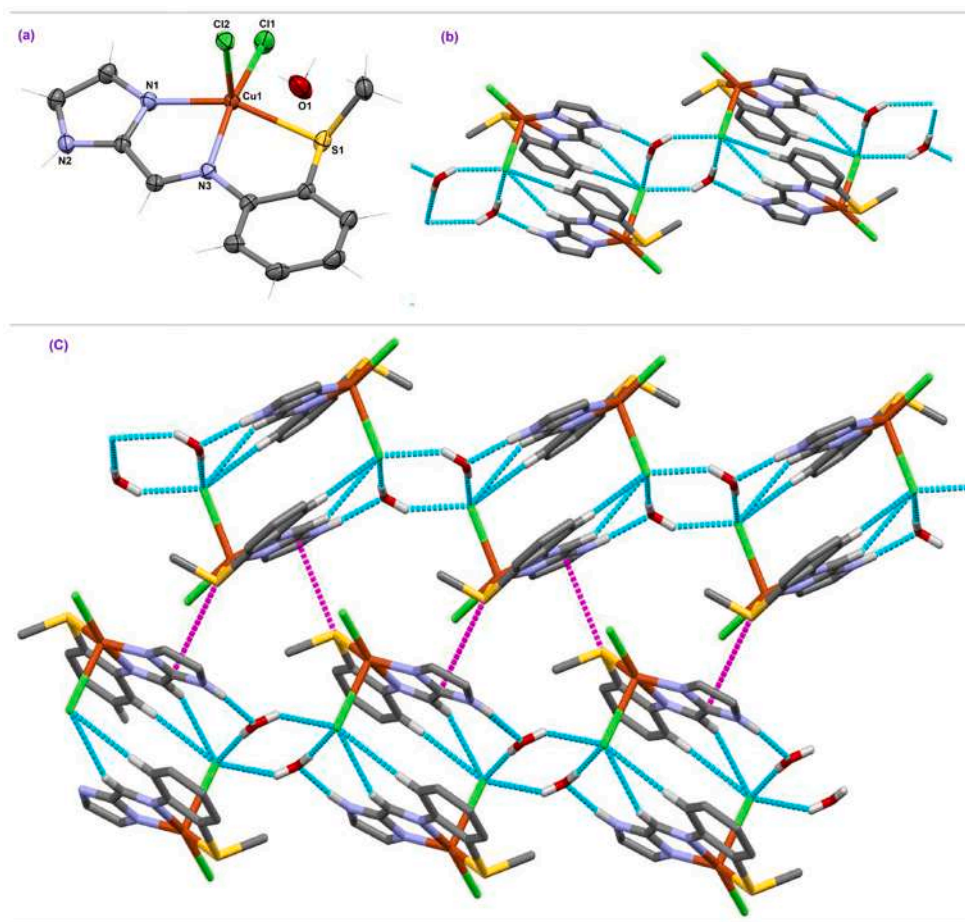


**Fig. 1.** a) ORTEP diagram of the asymmetric unit of **1** (30% thermal ellipsoid) with the atom labelling scheme; b) Construction of one-dimensional supramolecular frameworks of **1** through intermolecular N–H···O and C/N/O–H···Cl hydrogen bonds (cyan dotted); c) Formation of a 3D supramolecular framework of **1** through S···π interactions (pink dotted), including N–H···O, C/N/O–H···Cl interactions. ((Colour online.))

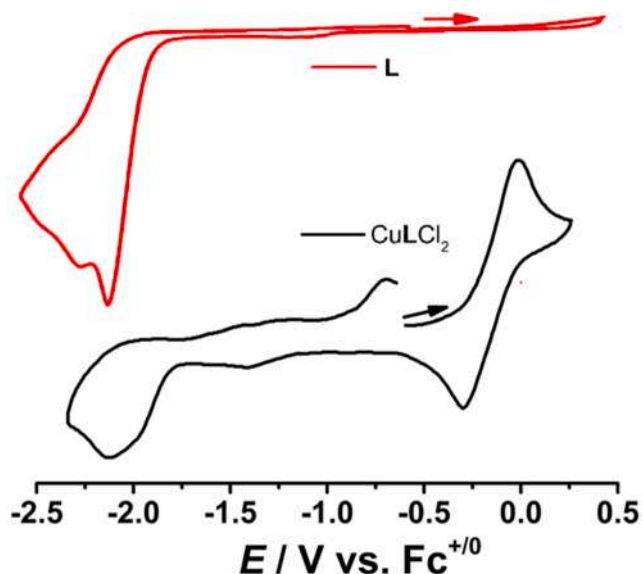


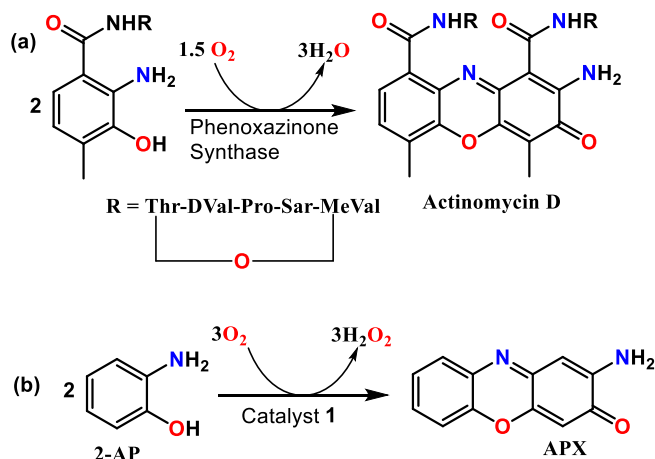
Fig. 2. Cyclic voltammogram of L (top) and 1 (bottom) in DCM/0.1 M TBAP at 298 K vs  $\text{Fc}^{+/0}$ .

molecule present in 1. The Cu–N<sub>imid</sub> bond length [Cu1–N1, 2.009(2) Å] is slightly shorter than the Cu–N<sub>imn</sub> [Cu1–N3, 2.027(2) Å] bond length, as expected, due to the greater  $\pi$ -accepting nature of the imidazole moiety compared to the imine moiety [54]. The Cu–S thioether bond length [Cu1–S1] is 2.3343(8) Å, similar to that seen for a 2-pyridyl-N-(2-methylthiophenyl)methyleneimine coordinated copper complex [21], but much shorter than the Cu–S thioether bond length observed in certain type 1 copper enzymes, especially PHS and azurin [17]. The two 5-membered chelate rings constructed by copper and the tridentate L ligand are not planar (torsion angles N1–C3–C4–N3 = 2.5(4)° and N3–C5–C10–S1 = –3.51°). A slight twisting occurs around the N3–C5 single bond (torsion angles C4–N3–C5–C6 = –13.6°, Table S2). The small deviations from coplanarity are assumed to be due to the presence of multiple intermolecular noncovalent interactions, which are noted in Table S3.

The formation of the supramolecular framework of 1 was assessed with the involvement of weak forces. The axial chloride ligand of the asymmetric unit of 1 interacts with another asymmetric unit via C–H...Cl intermolecular hydrogen bonding, leading to a molecular dimer. Each of the molecular dimers strongly interacts with lattice water molecules through short-distant hydrogen bonding [O1–H1A...Cl2, 2.33 Å, O1–H1B...Cl2, 2.37 Å, N2–H2...O1, 1.86 Å] and lead to a one-dimensional hydrogen-bonded polymeric framework (Fig. 1b). Meanwhile, a herringbone arrangement of the asymmetric units is also evident in the packing diagram of 1. The herringbone packing effect shows the development of a second 1D framework using the same type-hydrogen bonding. It is noteworthy that long-distant weak  $\pi$ ... $\pi$  interactions (~4.2 Å) between the aromatic centroids further stabilize the crystalline framework. The oppositely directed two 1D supramolecular frameworks stabilize a short-contact between the sulfur atom with an imidazole carbon atom [C...S, 3.45 Å], leading to a three-dimensional supramolecular framework (Fig. 1c).

### 3.3. Solution phase property of the ligand L and the copper(II) complex 1

The absorption spectra of the thiomethyl substituted imidazole-based Schiff base ligand L and complex 1 were recorded in methanol medium (MeOH) from 200 to 900 nm at RT (Figure S4). The ligand L shows intense  $\pi \rightarrow \pi^*$  and  $n \rightarrow \pi^*$  transition bands at 272, 297 and 358 nm, while its copper(II) complex 1 shows characteristic absorption bands at 270, 290, 345 and 415 nm (Fig. S4). The blue-shifted electronic



Scheme 3. (a) Phenoxazinone synthase (PHS) catalysed biological reaction; the formation of actinomycin D. (b) Model reaction for phenoxazinone synthase-like activity; aerial oxidative coupling of 2-aminophenol 2-AP to APX.

bands of L (270, 290 and 345 nm) in complex 1 are attributed to ligand centric electronic transitions, while the optical band at 415 nm is assignable to the d-d electronic transitions of the copper complex. Furthermore, the solution phase stability of the complex has been assessed by time-dependent UV–Vis measurement of 1 over a period of 72 hrs. The time-dependent absorption profile of complex 1 shows the unaltered band positions of the electronic transitions in Fig. S6 and confirms the solution phase stability of the copper complex.

### 3.4. Electrochemical properties

The capability of the copper(II) complex 1 to oxidize substrates including DNA and aminophenol prompted us to investigate its redox property using cyclic voltammetry. Complex 1 shows three redox processes in DMSO/0.1 m  $\text{Bu}_4\text{NPF}_6$  in a nitrogen atmosphere at room temperature (Fig. 2). The quasi-reversible redox process at a very low potential value of –0.15 V to the ferrocenium/ferrocene ( $\text{Fc}^+/\text{Fc}$ ) couple is likely to be a copper(II) centred reduction. The two completely irreversible redox processes at –1.97 and –2.13 V can be assigned to ligand centred reductions as the free ligand L shows two irreversible redox processes in this region, at –2.21 and –2.34 V (Fig. 2). Complex 1 acts as a strong oxidizing catalyst because it can accept electrons from a substrate easily at a very low redox potential (–0.15 V with respect to  $\text{Fc}^{+/0}$

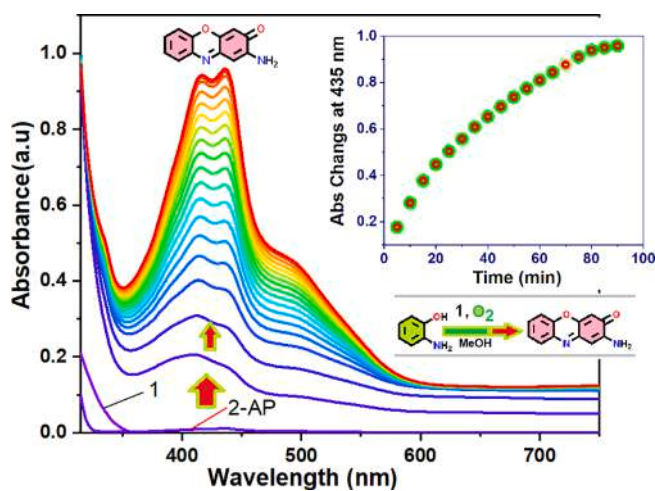


Fig. 3. Generation of a new electronic band at 435 nm after addition of complex 1 to 2-AP in MeOH with a time interval of 5 min. Inset: time vs. absorbance plot at 435 nm.

**Table 2**

Comparison of  $k_{\text{cat}}$  ( $\text{h}^{-1}$ ) values for reported copper(II) complex-mediated catalytic oxidation of 2-AP with that of complex **1**.

Complex	$k_{\text{cat}}$ ( $\text{h}^{-1}$ )(Solvent)	CCDC No	Ref
[Cu(L) <sub>2</sub> Cl <sub>2</sub> ] <sub>2</sub> ( <b>1</b> )	$2.31 \times 10^4$ (CH <sub>3</sub> OH)	2,046,275	[23]
[Cu(L) <sub>2</sub> (NO <sub>3</sub> ) <sub>2</sub> ] <sub>2</sub> ( <b>2</b> )	$6.3 \times 10^4$ (CH <sub>3</sub> OH)	2,046,276	[23]
[Cu( $\mu$ -Cl)(Phen)Cl]	$1.69 \times 10^4$ (CH <sub>3</sub> OH)	1,524,680	[55]
[Cu(bpy)Cl <sub>2</sub> ]	$5.40 \times 10^3$ (CH <sub>3</sub> OH)	1,524,681	[55]
[Cu(Phen) <sub>2</sub> (H <sub>2</sub> O)](NO <sub>3</sub> ) <sub>2</sub> ( <b>1</b> )	$1.43 \times 10^3$ (CH <sub>3</sub> OH)	1,012,512	[24]
[Cu(dpa) <sub>2</sub> (OAc)] <sup>+</sup>	$1.83 \times 10^3$ (EtOH)	1,513,638	[57]
[Cu(L <sup>b1</sup> )(Cl) <sub>2</sub> ]MeOH	6.264(CH <sub>3</sub> OH-H <sub>2</sub> O)	2,001,075	[21]
[Cu(L <sup>b2</sup> )(Cl) <sub>2</sub> ]H <sub>2</sub> O	7.668(CH <sub>3</sub> OH-H <sub>2</sub> O)	2,001,076	[21]
[Cu(L <sup>b3</sup> )(Cl) <sub>2</sub> ]	8.424(CH <sub>3</sub> OH-H <sub>2</sub> O)	2,001,077	[21]
[Cu(L)(Cl) <sub>2</sub> ]	$1.92 \times 10^4$ (CH <sub>3</sub> OH)	2,153,757	<i>This work</i>

**Note:** L<sup>2</sup> = (E)-4-chloro-2-((thiazol-2-ylimino)methyl)phenol; L<sup>3</sup> = (E)-4-bromo-2-((thiazol-2-ylimino)methyl)phenol; L<sup>b1</sup> = N-(pyridin-2-ylmethyl)quinolin-8-amine; L<sup>b2</sup> = N-(1-methylbenzimidazol-2-ylmethyl)quinolin-8-amine; L<sup>b3</sup> = N-(1-methylimidazol-2-ylmethyl)quinolin-8-amine; L = 1-(4-methoxybenzyl)-2-(4-methoxyphenyl)benzimidazole.

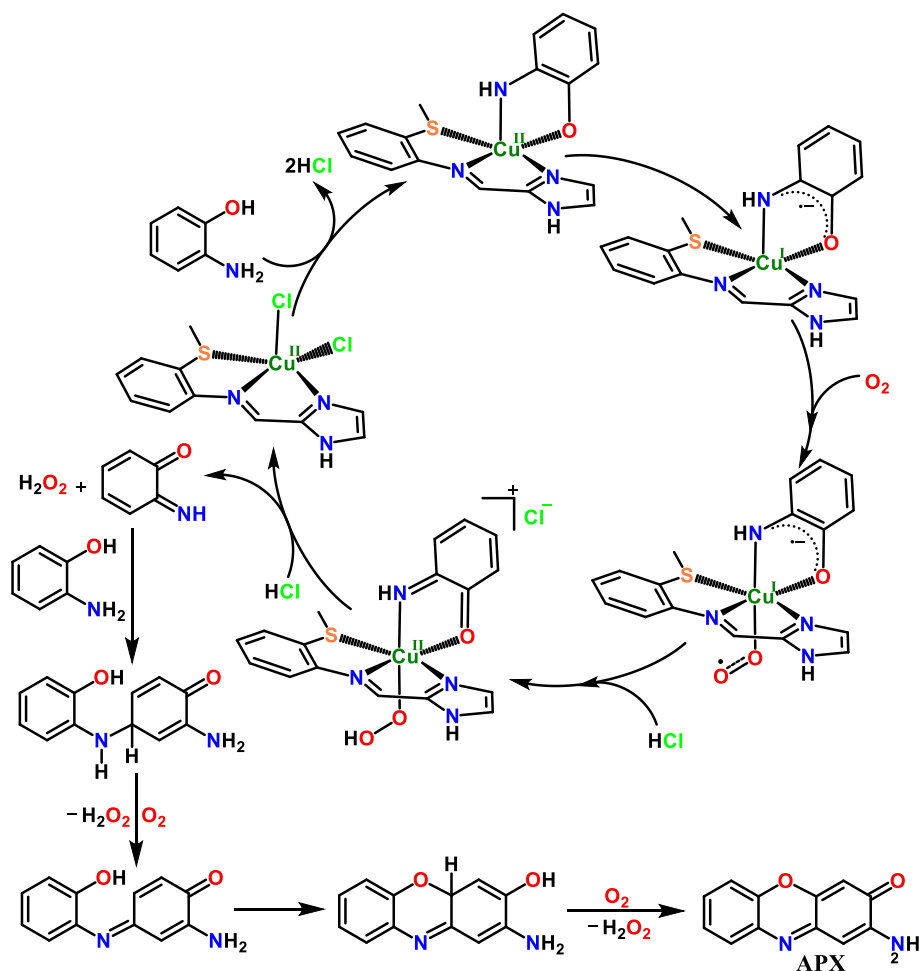
<sup>0</sup>).

### 3.5. Phenoxazinone synthase-like activity of complex **1** and kinetic studies

As a mimic for phenoxazinone activity, **1** was tested for the oxidative coupling of the model substrate 2-aminophenol (2-AP) to 2-amino-phenoxazine-3-one (APX) (Scheme 3). The catalytic oxidation of 2-AP to APX was measured by monitoring the UV-vis spectra of the reaction

mixture over 1.5 h. For this, 100  $\mu\text{L}$   $10^{-2}$  (M) 2-AP and 100  $\mu\text{L}$   $10^{-4}$  (M) catalyst **1** were mixed with 2 mL methanol in a UV-vis quartz cell and measured under aerobic conditions at RT, as reported previously [24–27]. The development of the characteristic bands for APX at 435 nm with a shoulder at 417 nm signify the aerobic oxidative dimerization of 2-AP (Fig. 3). The rate of gradual increase of the 435 nm absorption band proposes a pseudo-first-order type reaction for the formation of APX. In the absence of **1**, the catalytic oxidation did not show a significant growth of APX at 435 nm under identical conditions, which confirms the catalytic role of **1** (Figure S7). Further, when the catalytic oxidation was performed under anaerobic conditions, the intensity of the absorption band at 435 nm remained unchanged (Figure S8), implying that molecular dioxygen is essential for this oxidative transformation reaction. Additionally, we can scale up the catalytic oxidation of 2-AP to APX to the gram scale, resulting in  $\sim 86\%$  yield for APX.

Next, to understand the catalytic proficiency of complex **1**, kinetic studies were carried out with various substrate concentrations. For this purpose, the method of initial rate determination was followed by spectrophotometry at 435 nm for different concentrations of 2-AP as a function of time. The initial rate of the reaction follows the rate saturation kinetics, as portrayed in Figure S9. The kinetic parameters for the mediated oxidative coupling reaction of 2-AP by **1** were evaluated by applying the Michaelis–Menten kinetic model of enzymatic reactions [55–58], as listed in Table 2. A comparison of the kinetic parameters of 2-AP oxidation catalysed by **1** with other recently reported copper complexes were also made (Table 2) to examine the catalytic efficiency of **1** and it is observed that the present complex **1** shows prominent catalytic activity [24–26,55–57].



**Scheme 4.** Plausible catalytic pathway for the oxidative coupling of 2-AP catalysed by **1**.

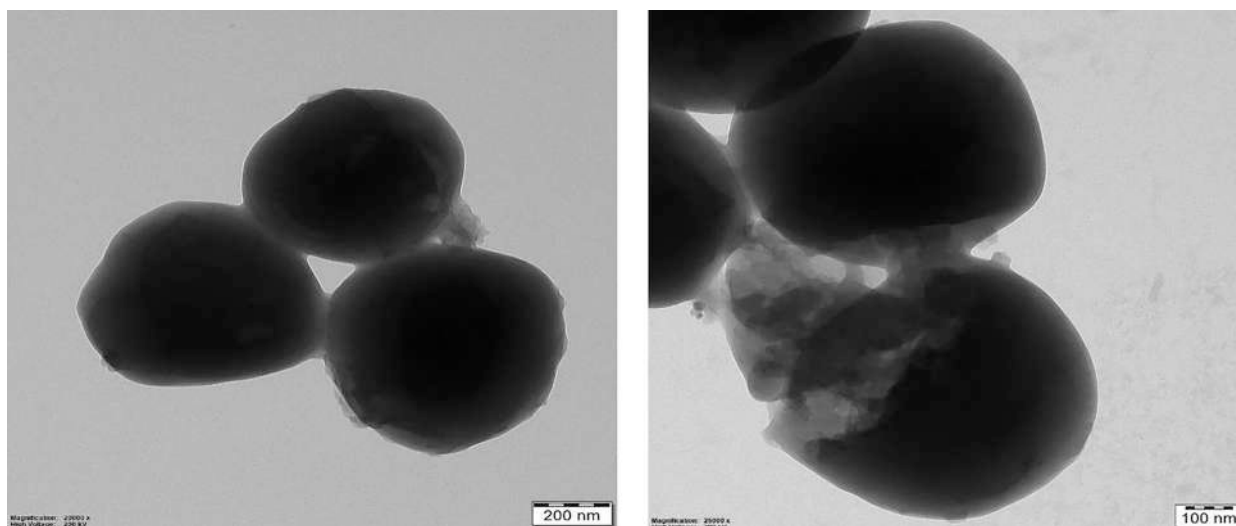
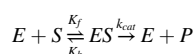


Fig. 4. (a) HR-TEM image of the control, *Staphylococcus aureus* (left); (b) copper complex treated *Staphylococcus aureus* (right).

For any enzyme (E), the catalysed conversion of a substrate (S) into a product (P) proceeds through the formation of an enzyme-substrate (ES) adduct and follows the equation:



where  $K_f$  = forward rate constant,  $K_b$  = backward rate constant and  $k_{cat}$  = catalytic rate constant.

The Michaelis–Menten equation:

$$V = \frac{V_{max}[S]}{K_M + [S]}$$

where  $V$  indicates the initial reaction rate,  $[S]$  is the concentration of substrate,  $K_M$  is the Michaelis–Menten constant ( $K_M = (K_b + k_{cat})/K_f$ ) and  $V_{max}$  presents the maximum reaction velocity. The kinetic parameters of the 2-AP oxidation catalysed by **1** were determined from the Michaelis–Menten approach as  $V_{max}$  ( $MS^{-1}$ ) =  $5.35 \times 10^{-4}$  and  $K_M = 1.46 \times 10^{-3}$  [Std. Error for  $V_{max}$  ( $MS^{-1}$ ) =  $9.43 \times 10^{-6}$ ; Std. Error for  $K_M$  (M) =  $7.08 \times 10^{-5}$ ]. The turnover number ( $k_{cat}$  in  $h^{-1}$ ) for catalyst **1** was calculated as  $1.92 \times 10^4 h^{-1}$ .

To find further insight into the underlying mechanism of this catalytic oxidation of 2-AP to APX, ESI-mass spectrometric studies of the reaction mixture of the copper(II) complex **1** with 2-AP was carried out in methanol. After mixing for 20 mins, the mass spectrum of the reaction mixture is shown in Figure S10. The base peak at  $m/z$  213.41 indicates the formation of APX. The characteristic peak that appeared at  $m/z$  280.0830 was assigned as the molecular ion peak of **1**. The formation of the adduct between complex **1** and the substrate 2-AP was ensured from the presence of another intense characteristic peak at 388.0798  $m/z$ ,  $[[Cu(L)+(2-AP)] + H]^+$ . This mass spectroscopic investigation gives some idea about the labile nature of **1** and its binding aspects with 2-AP. The participation of aerobic oxygen as an oxidant in the course of the 2-AP oxidation was also examined to understand the fate of  $O_2$  through the presence of hydrogen peroxide ( $H_2O_2$ ) in the course of the reaction. The conversion of  $O_2$  to  $H_2O_2$  was confirmed by treatment with KI, which led to the formation of  $I_3^-$ , as detected by the characteristic absorption band at 353 nm (Figure S11). [24,25] On the basis of the results and the reported literature, a possible mechanistic route for the catalytic oxidation of 2-AP to APX is shown in Scheme 4.

### 3.6. Antibacterial activity

The antibacterial properties of the copper complex **1** were measured

by the agar well diffusion method against clinical *E. coli*, *Staphylococcus aureus* and *K. pneumoniae*. The zone of inhibition diameters produced by **1** against these bacteria are shown in Figure S12 and are compared with a medically recommended commercially available standard antibiotic, ciprofloxacin (Table S4). The copper(II) complex **1** exhibits significant bactericidal efficiency against *E. coli* and *K. pneumoniae* with respect to ciprofloxacin. The lowest susceptibility to complex **1** was observed for *Staphylococcus aureus*, with relatively lower values compared to ciprofloxacin. The estimation of the minimum inhibitory concentration (MIC) of **1** was evaluated for *E. coli* as 25  $\mu g/mL$  (Figure S13, Table S5).

In this study, the geometry, electronic nature and labile nature of the copper(II) complex play an essential role in its biochemical function against the pathogenic bacteria, *E. coli*, *Staphylococcus aureus* and *K. pneumoniae*. The cisoid chloride ligands with long Cu - Cl distances make the complex labile in nature and helps to bind with amino acids and proteins in bacteria. On binding with microbial species, the electron-deficient nature (low reduction potential of  $-0.34$  V) of **1** oxidize the microbial species, resulting in inactivation of microbial growth. Such oxidative inhibition activity induced by transition metal complexes is evident in the literature [58–60]. The presence of the  $\pi$ -accepting electron-withdrawing group in complex **1** also plays a role in enhancing the inhibition activity.

To get some ideas about the morphological characteristics of the copper(II) complex treated bacteria, we recorded HR-TEM images of the bacteria before and after exposure to the copper complex. The obtained TEM micrographs of *Staphylococcus aureus* cells are shown in Fig. 4. As shown in Fig. 4a, untreated *Staphylococcus aureus* cells are typically smooth and elliptical in shape. On application of the Cu complex to the cells for 24 h, the cell morphology displays wrinkled damage (Fig. 4b).

### 3.7. Antiproliferative activity of the copper(II) complex

#### 3.7.1. MTT assay

The cytotoxicity of the copper(II) complex was assessed against a human colorectal adenocarcinoma cell line (HT-29) by a 3-(4,5-dimethylthiazol-2-yl)-2,5-diphenyltetrazolium bromide (MTT) assay in DMSO. The  $IC_{50}$  value was determined from a plot of the cell viability expressed in percentage versus the concentration of the copper complex **1** in  $\mu g/mL$  (Figure S14). The value of the concentration of copper complex **1** causing 50% cell destruction,  $IC_{50}$ , was determined from the MTT assay at 24 h as  $125 \pm 0.2 \mu g/mL$ .

#### 3.7.2. Fluorescent staining for apoptosis

A fluorescence staining experiment was performed by adopting

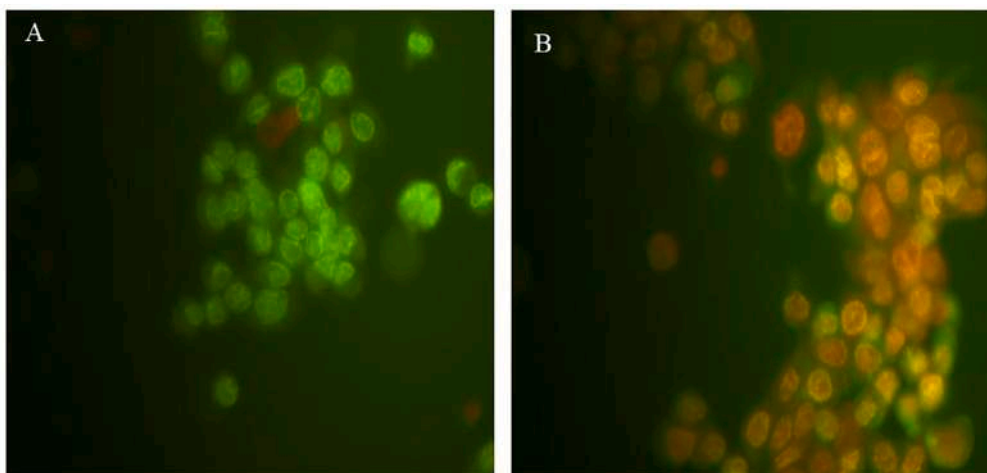


Fig. 5. Effect of copper complex induced apoptosis in HT-29 cells; (a) AO/EB staining of untreated HT-29 cell line and (b) copper complex 1 treated HT-29 cell line.

acridine orange/ethidium bromide (AO/EB) staining to highlight the morphological transformation of the HT-29 cell line. Literature reports suggest that cell apoptosis leads to dramatic morphological cellular transformations, including cell shrinkage, DNA fragmentation, nuclear condensation, membrane blebbing and fragmentation into apoptotic bodies, that can be detected by Dual AO/EB staining of the cell [61]. The morphological transformation of the HT-29 cell treated with the copper complex and control at 24 h was observed AO/EB staining and then analysed by fluorescence microscopy. Typically, normal living cells displayed a green coloured nucleus, while a yellow coloured nucleus with chromatin was indicative of early apoptotic condensed or fragmented forms of the cells. In contrast, late apoptotic chromatin condensed or fragmented nuclei showed an orange colour and necrotic cells appeared as uniformly red-stained cell nuclei (Fig. 5). Similar kinds of cancerous cell destruction were observed for mononuclear cobalt(III)-polypyridyl complexes having chloride ions in a cisoid orientation [62,63].

#### 4. Conclusion

Using a novel electron-deficient tridentate thiomethyl substituted imidazole-based Schiff base ligand, 1-(1*H*-imidazol-2-yl)-*N*-(2-(methylthio)phenyl)methanimine, we have reported here a mononuclear bischloro copper(II) complex, **1**, with a distorted square-pyramidal geometry, having two chloride ligands, one axial and another equatorial. A detailed structural investigation of **1** revealed that multiple intermolecular noncovalent interactions lead to a three-dimensional polymeric framework. The copper(II) complex **1** undergoes one copper(II) centred quasi-reversible reduction at very low potential (-0.15 V with respect to  $\text{Fc}^{+/0}$ ) along with two completely irreversible high potential L centred reductions. The catalytic activity of the redox-active copper(II) complex **1** towards aerial oxidation of 2-AP to 2-APX (bio-mimics of phenoxazinone synthase activity) was investigated and an excellent catalytic efficiency with a  $k_{\text{cat}}/K_{\text{M}}$  value of  $13.15 \times 10^6$  was found. Furthermore, complex **1** shows notable antibacterial activity against *E. coli* *Staphylococcus aureus* and *K. pneumonia* microorganisms as well as anticancer activity against the human colorectal adenocarcinoma HT-29 cancerous cell line, with an  $\text{IC}_{50}$  value of  $125 \mu\text{g mL}^{-1}$ . The morphological transformation of the *Staphylococcus aureus* and HT-29 cell line treated with complex **1** was assessed in a dose-dependent manner for 24 h. The presence of labile chlorides in **1** and its oxidizing nature probably facilitate the oxidative damage of the bacteria and DNA. To make system **1** a suitable bactericidal and cytotoxic agent, further steric and electronic tuning is currently underway in our laboratory.

#### Author Contributions

HSD and BB originated the idea of the work. NB and HSD planned the experiments. KP and GS carried out the electrochemistry experiments. PKM carried out a formal analysis. M. Kotakonda carried out the biological studies. M. Shit carried out the X-ray structural characterisation. HSD and BB supervised the work. NB, BB and HSD analysed the data and prepared the manuscript.

#### CRediT authorship contribution statement

**Nilaj Bandopadhyay**: Conceptualization, Formal analysis, Investigation, Methodology. **Krishnendu Paramanik**: Conceptualization, Formal analysis, Investigation, Methodology. **Prafulla Kumar Mudi**: Formal analysis, Investigation, Methodology. **Gayetri Sarkar**: Formal analysis, Investigation, Methodology, Validation. **Muddukrishnaiah Kotakonda**: Formal analysis, Investigation, Methodology. **Madhusudan Shit**: Formal analysis, Visualization. **Bhaskar Biswas**: Conceptualization, Supervision, Writing – review & editing. **Hari Sankar Das**: Conceptualization, Supervision, Writing – review & editing.

#### Declaration of Competing Interest

The authors declare that they have no known competing financial interests or personal relationships that could have appeared to influence the work reported in this paper.

#### Acknowledgement

HSD and BB sincerely thank the Science and Engineering Research Board (SERB), India for financial support under Empowerment and Equity Opportunities for Excellence in Science (EMEQ) scheme (EEQ/2019/000374 and EEQ/2020/000079).

#### Appendix A. Supplementary data

Supplementary data to this article can be found online at <https://doi.org/10.1016/j.poly.2022.115783>.

#### References

- [1] K.A. Magnus, H.T. That, J.E. Carpenter, *Chem. Rev.* 94 (1994) 727.
- [2] J. Reedijk, *Science* 308 (2005) 1876–1877A.
- [3] K. Sigfridsson, *Photosynthesis Res.* 57 (1998) 1–28.
- [4] H.B. Gray, J.R. Winkl, *Annu. Rev. Biochem.* 65 (1996) 537–561.

- [5] E.I. Solomon, D.E. Heppner, E.M. Johnston, J.W. Ginsbach, J. Cirera, M. Qayyum, M.T. Kieber-Emmons, C.H. Kjaergaard, R.G. Hadt, L. Tian, *Chem. Rev.* 114 (2014) 3659–3853.
- [6] K.J. Humphreys, L.M. Mirica, Y. Wang, J.P. Klinman, *J. Am. Chem. Soc.* 131 (2009) 4657–4663.
- [7] C. Gerdemann, C. Eicken, B. Krebs, *Acc. Chem. Res.* 35 (2002) 183.
- [8] I.M. Kooter, R.A. Steiner, B.W. Dijkstra, P.I. van Noort, M.R. Egmund, M. Huber, *Eur. J. Biochem.* 269 (2002) 2971.
- [9] R.L. Lieberman, D.B. Shrestha, P.E. Doan, B.M. Hoffman, T.L. Stemmler, A. C. Rosenzweig, *Proc. Natl. Acad. Sci.* 100 (2003) 3820.
- [10] A.W. Smith, A. Camara-Artigas, M. Wang, J.P. Allen, W.A. Francisco, *Biochem.* 45 (2006) 4378–4387.
- [11] T.M. Karpinski, A. Adamczak, *Pharmaceutics* 10 (2018) 54.
- [12] C. Avendaño, J.C. Menéndez, *Med. Chem. Anticancer Drugs* (2015) 133–195.
- [13] E. Frei, *Cancer Chemother. Rep.* 58 (1974) 49–54.
- [14] U. Hollstein, *Chem. Rev.* 74 (1974) 625–652.
- [15] C.E. Barry III, P.G. Nayar, T.P. Begley, *Biochemistry* 28 (1989) 6323–6333.
- [16] S.K. Dey, A. Mukherjee, *Coord. Chem. Rev.* 310 (2016) 80–115.
- [17] C. Mukherjee, T. Weyhermuller, E. Bothe, E. Rentschler, P. Chaudhuri, *Inorg. Chem.* 46 (2007) 9895–9905.
- [18] P. Mahapatra, S. Ghosh, S. Giri, V. Rane, R. Kadam, M.G.B. Drew, A. Ghosh, *Inorg. Chem.* 56 (2017) 5105–5121.
- [19] S. Ganguly, P. Kar, M. Chakraborty, K. Sarkar, A. Ghosh, *New J. Chem.* 43 (2019) 18780–18793.
- [20] N. Podder, S. Mandal, *New J. Chem.* 44 (2020) 12793–12805.
- [21] M. Garai, D. Dey, H.R. Yadav, A.R. Choudhury, N. Kole, B. Biswas, *Polyhedron* 129 (2017) 114–122.
- [22] A. Muley, K.S. Karumban, S. Kumbhakar, B. Giri, S. Maji, *New J. Chem.* 46 (2022) 521–532.
- [23] P.K. Mudi, R.K. Mahato, M. Joshi, M. Shit, A.R. Choudhury, H.S. Das, B. Biswas, *Appl. Organomet. Chem.* 35 (2021), e6211.
- [24] D. Dey, S. Das, H.R. Yadav, A. Ranjani, L. Gyathri, S. Roy, P.S. Guin, D. Dhanasekaran, A.R. Choudhury, M.A. Akbarsha, B. Biswas, *Polyhedron* 106 (2016) 106–114.
- [25] S. Mahato, N. Meheta, K. Muddukrishnaiah, M. Joshi, P. Ghosh, M. Shit, A. R. Choudhury, B. Biswas, *Appl. Organomet. Chem.* 34 (2020), e5935.
- [26] P.K. Mudi, N. Bandopadhyay, M. Joshi, M. Shit, S. Paul, A.R. Choudhury, B. Biswas, *Inorg. Chim. Acta* 505 (2020), 119468.
- [27] A. De, D. Dey, H.R. Yadav, M. Maji, V. Rane, R.M. kadam, A.R. Choudhury, B. Biswas, *J. Chem. Sci.* 128 (2016) 1775–1782.
- [28] D. Sequeira, P.V. Baptista, R. Valente, M.F.M. Piedade, M.H. Garcia, T.S. Morais, A. R. Fernandes, *Dalton Trans.* 50 (2021) 1845.
- [29] D.S. Kalinowski, C. Stefani, S. Toyokuni, T. Ganz, G.J. Anderson, N. V. Subramaniam, D. Trinder, J.K. Olynyk, A. Chua, P.J. Jansson, S. Sahni, D. J. Lane, A.M. Merlot, Z. Kovacevic, M.L. Huang, C.S. Lee, D.R. Richardson, *Biochim. Biophys. Acta* 1863 (2016) 727–748.
- [30] S. Yousuf, F. Arjm, S. Tabassum, *Polyhedron* 209 (2021), 115450.
- [31] S. Gama, F. Mendes, F. Marques, I.C. Santos, M.F. Carvalho, I. Correia, J.C. Pessoa, I. Santos, A. Paulo, *J. Inorg. Biochem.* 105 (2011) 637–644.
- [32] J. Shao, Q. Zhang, J. Wei, Z. Yuchi, P. Cao, S.Q. Li, S. Wang, J.Y. Xu, S. Yang, Y. Zhang, J.X. Wei, J. L. Tian *Dalton Trans.*, 50 (2021) 13387.
- [33] L.M. Balsa, V.F. Curotto, M.J. Lavecchia, G.A. Echeverría, O.E. Piro, J.G. Tojal, R. P. Diez, C.G. Baró, I.E. León, *Dalton Trans.* 50 (2021) 9812.
- [34] R.K. Mahato, A.K. Mahanty, S. Paul, V. Gopal, B. Perumalsamy, B. Perumalsamy, G. Balakrishnan, T. Ramasamy, D. Dharumadurai, B. Biswas, *J. Mol. Struct.* 1223 (2021), 129264.
- [35] S. Mahato, N. Meheta, K. Muddukrishnaiah, M. Joshi, M. Shit, A.R. Choudhury, B. Biswas, *Polyhedron* 194 (2021), 114933.
- [36] D. Dey, G. Kaur, A. Ranjani, L. Gyathri, P. Chakraborty, J. Adhikary, J. Pasan, D. Dhanasekaran, A.R. Choudhury, M.A. Akbarsha, N. Kole, B. Biswas, *Eur. J. Inorg. Chem.* (2014) 3350–3358.
- [37] B. Rosenberg, F. Charles, P. Ketting, *Cancer* 55 (1985) 2303.
- [38] A. Rana, J.M. Alex, M. Chauhan, G. Joshi, R. Kumar, *Med. Chem. Res.* 24 (2015) 903.
- [39] K. Saleem, W.A. Wani, A. Haque, M.N. Lone, M.-F. Hsieh, M.A. Jairajpuri, I. Ali, *Med. Chem.* 5 (2013) 135.
- [40] S. Banerjee, A.R. Chakravarty, *Acc. Chem. Res.* 48 (2015) 2075.
- [41] *CrysAlisPro 1.171.39.35c*, 2017, Rigaku Oxford Diffraction, Rigaku Corporation: Tokyo, Japan.
- [42] O.V. Dolomanov, L.J. Bourhis, R.J. Gildea, J.A.K. Howard, H. Puschmann, *J. Appl. Cryst.* 42 (2009) 339.
- [43] G.M. Sheldrick, *Acta Cryst. A* 71 (2015) 3.
- [44] G.M. Sheldrick, *Acta Cryst. C* 71 (2015) 3.
- [45] C.K. Pal, S. Mahato, H.R. Yadav, M. Shit, A.R. Choudhury, B. Biswas, *Polyhedron* 174 (2019), 114156.
- [46] A. De, M. Garai, H.R. Yadav, A.R. Choudhury, B. Biswas, *Appl. Organomet. Chem.* 31 (2017), e3551.
- [47] B. Chowdhury, B. Bhowmik, A. Sahu, M. Joshi, S. Paul, A.R. Choudhury, B. Biswas, *J. Chem. Sci.* 130 (2018) 161.
- [48] M. Garai, A. Das, M. Joshi, S. Paul, M. Shit, A. Roy Choudhury, B. Biswas, *Polyhedron* 156 (2018) 223–230.
- [49] F.D. Gonelimali, J. Lin, W. Miao, J. Xuan, F. Charles, M. Chen, S.R. Hatab, *Front. Microbiol.* 9 (2018) 1639.
- [50] D. Baskic, S. Popovic, P. Ristic, N.N. Arsenijevic, *Cell Biol. Int.* 30 (2006) 924.
- [51] S. Roy, P. Mitra, A.K. Patra, *Inorg. Chim. Acta* 370 (2011) 247–253.
- [52] E. Colacio, M. Ghazi, R. Kivekäs, J.M. Moreno, *Inorg. Chem.* 39 (2000) 2882–2890.
- [53] P.R. Vashi, H.M. Marques, *J. Inorg. Biochem.* 98 (2004) 1471.
- [54] L. Michaelis, M.L. Menten, *Biochem.* 49 (1913) 333–369.
- [55] M. Garai, D. Dey, H.R. Yadav, A.R. Choudhury, M. Maji, B. Biswas, *ChemistrySelect* 2 (2017) 11040.
- [56] S. Mukherjee, S. Roy, S. Mukherjee, B. Biswas, *J. Mol. Struct.* 1217 (2020), 128348.
- [57] B. Chowdhury, M. Maji, B. Biswas, *J. Chem. Sci.* 129 (2017) 1627–1637.
- [58] D. Dey, A. Al-Hunaiti, G. Vinothini, B. Perumalsamy, G. Balakrishnan, T. Ramasamy, D. Dharumadurai, B. Biswas, *J. Mol. Struct.* 1222 (2020), 128919.
- [59] S. Mukherjee, C.K. Pal, M. Kotakonda, M. Joshi, M. Shit, P. Ghosh, A.R. Choudhury, B. Biswas, *J. Mol. Struct.* 1245 (2021), 131057.
- [60] P.U. Maheswari, S. Roy, H. den Dulk, S. Barends, G. van Wezel, B. Kozlevcar, P. Gamez, J. Reedijk, *J. Am. Chem. Soc.* 128 (2006) 710–711.
- [61] Y. Zhang, X. Chen, C. Gueydan, J. Han, *Cell Res* 28 (2018) 9–21.
- [62] S. Das, J. Pasan, A. Ranjani, L. Gayathri, S. Saha, S. Chandraleka, D. Dhanasekaran, D.J. Pasan, M. Maji, M.A. Akbarsha, B. Biswas, *J. Chem. Sci.* 128 (2016) 1755–1764.
- [63] D. Dey, A. Basu Roy, C.-Y. Shen, H.-L. Tsai, A. Ranjani, L. Gayathri, S. Chandraleka, D. Dhanasekaran, M.A. Akbarsha, N. Kole, B. Biswas, *J. Chem. Sci.* 127 (2015) 649–661.



# Source details

[Feedback >](#) [Compare sources >](#)

## Polyhedron

Formerly known as: [Journal of Inorganic and Nuclear Chemistry](#)

Formerly known as: [Inorganic and Nuclear Chemistry Letters](#)

Scopus coverage years: from 1982 to Present

Publisher: Elsevier

ISSN: 0277-5387

Subject area: [Chemistry: Inorganic Chemistry](#) [Materials Science: Materials Chemistry](#) [Chemistry: Physical and Theoretical Chemistry](#)

Source type: Journal

[View all documents >](#)[Set document alert](#)[Save to source list](#)

CiteScore 2022

5.4



SJR 2022

0.400



SNIP 2022

0.635



# Instigating the *In Vitro* Anticancer Activity of New Pyridine–Thiazole-Based Co(III), Mn(II), and Ni(II) Complexes: Synthesis, Structure, DFT, Docking, and MD Simulation Studies

Pradip Bera,<sup>‡‡</sup> Abhishek Aher,<sup>‡‡</sup> Paula Brandao, Utsab Debnath, Varun Dewaker, Sunil Kr. Manna,<sup>\*</sup> Abhimanyu Jana, Chandana Pramanik, Basudev Mandal, and Pulakesh Bera<sup>\*</sup>



Cite This: <https://doi.org/10.1021/acs.jcim.1c01280>



Read Online

ACCESS |



Metrics & More

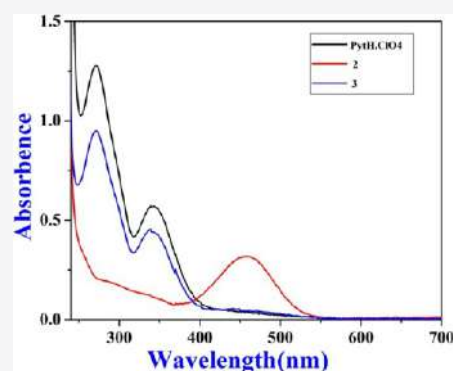


Article Recommendations



Supporting Information

**ABSTRACT:** The perchlorate salt of (4-(4-methoxy phenyl)-2-(2-(1-pyridine-2-yl)ethylidene)hydrazinyl)thiazole (**PytH·ClO<sub>4</sub>**) and its metal perchlorate derivatives, namely, [Co(**PytH**)<sub>2</sub>](ClO<sub>4</sub>) (1), [Mn(**PytH**)<sub>2</sub>](ClO<sub>4</sub>)<sub>2</sub> (2), and [Ni(**PytH**)<sub>2</sub>](ClO<sub>4</sub>)<sub>2</sub> (3), have been synthesized and characterized through single X-ray crystallography and spectroscopic methods. The ligand crystallizes in a space group *P2<sub>1</sub>/n* in a nearly planar structure. The overall geometry of the complex salts is described as a distorted octahedron with a MN<sub>6</sub> chromophore. The ligand (**PytH·ClO<sub>4</sub>**) behaves as a neutral *N,N,N*-tridentate donor toward the “soft” Mn(II) and Ni(II) centers, whereas the deprotonated ligand stabilizes the “hard” Co(III) center. The DNA binding constant (*K<sub>b</sub>*) values of **PytH·ClO<sub>4</sub>**, 1, 2, and 3 are determined using the UV–vis spectroscopic method, and the *K<sub>b</sub>* values are  $9.29 \times 10^5$ ,  $7.11 \times 10^5$ ,  $8.71 \times 10^5$ , and  $7.82 \times 10^5$  mol<sup>-1</sup>, respectively, indicating the intercalative mode of interactions with CT-DNA. All the derivatives show effective antiproliferative activity against U-937 human monocytic tumor cells with IC<sub>50</sub> values  $4.374 \pm 0.02$ ,  $5.583 \pm 0.12$ ,  $0.3976 \pm 0.05$ , and  $11.63 \pm 0.01$  μM for **PytH·ClO<sub>4</sub>**, 1, 2, and 3, respectively. The best apoptosis mode of cell death is shown by 2 followed by **PytH·ClO<sub>4</sub>** and 1 at an equivalent concentration of IC<sub>50</sub> values. The combined molecular docking and dynamics simulation study evaluates the binding energies of anticancer agents, providing groove binding property with DNA. The 20 ns molecular dynamics simulation study reveals the maximum DNA binding stability of 2 corroborating the experimental results. The new class of metal derivatives of pyridine–thiazole can be used for advanced cancer therapeutics.



## INTRODUCTION

The thiazole and pyridine-containing compounds have shown therapeutically potent biological activities, such as antimicrobial,<sup>1</sup> antitumor,<sup>1,2</sup> anti-inflammatory,<sup>3</sup> and hypoglycemic activities.<sup>4</sup> Such excellent activities are related to the structural aspects of N and S heterocycles. Thiazole is a well-known stable NS donor heterocyclic aromatic compound having a Bird's Index of aromaticity of 79.<sup>5</sup> The  $\pi$ -electron density makes C5 the site for electrophilic substitution and the C2 position as the site for nucleophilic substitution in thiazole. The aromatic behavior of thiazole was nicely explained by Erlenmeyer et al. based on the concept of isosterism, the lone pair of electrons on bivalent sulfur atoms being equivalent to the vinylene part of the pyridine structure.<sup>6</sup> Both the electron-accepting and -donating properties are inherited in the thiazole ring due to the presence of a –C=N bond and a –S– bond, respectively. This unique property of thiazole has been exploited to establish several new biochemical formulae in advanced biology. Different groups in thiazole rings in different positions lead to plenty of bioactive thiazole derivatives having a wide range of applications in biology and pharmacy.<sup>7–14</sup> On the other hand, pyridine ( $pK_a = 5.2$ ) provides N-terminal and

forms stable salts, which is often used as a solvent to neutralize the acid formed in the reaction.<sup>15</sup> Moreover, the metal directing property of pyridine makes it an important fluorophore in bioinorganic chemistry. Several high-profile proprietary drugs, namely, Nexium, Takepron, Singulair, and Actos, contain pyridine scaffolds.<sup>16</sup> The compounds containing both thiazole and pyridine moieties have been used in designing new ligands for therapeutics, notably for cancer treatment. The antitumor activity of the molecules increased many folds while bonded covalently to metal ions. The reason may be that the formation of a metal–organic framework added some more properties such as redox activities, unsaturated metal center, strain in the complex structure, planarity, lipophilicity, and so forth than the metal-free organic

Received: October 20, 2021



Table 1. Crystallographic Refinement Data of PytH·ClO<sub>4</sub>, 2, and 3<sup>a,b</sup>

parameter	PytH·ClO <sub>4</sub>	2	3
formula	C <sub>17</sub> H <sub>17</sub> N <sub>4</sub> O <sub>5</sub> , Cl O <sub>4</sub> ·H <sub>2</sub> O	C <sub>68</sub> H <sub>64</sub> Cl <sub>4</sub> Mn <sub>2</sub> N <sub>16</sub> O <sub>23</sub> S <sub>4</sub>	C <sub>34</sub> H <sub>32</sub> N <sub>8</sub> NiO <sub>8</sub> S <sub>2</sub> Cl <sub>2</sub>
CCDC no.	1530855	2010934	2010933
mol. wt.	442.87	1853.27	938.39
crystal system	monoclinic	triclinic	monoclinic
space group	<i>P</i> 2 <sub>1</sub> / <i>n</i>	<i>P</i> $\bar{1}$	<i>C</i> 2/ <i>c</i>
<i>T</i> (K)	150	150	150
<i>a</i> (Å)	7.1698(9)	16.543(2)	25.593(4)
<i>b</i> (Å)	13.9800(18)	16.603(2)	7.9388(14)
<i>c</i> (Å)	19.745(2)	18.807(3)	21.044(4)
$\alpha$ (°)	90	68.427(5)	90
$\beta$ (°)	100.208(4)	64.178(5)	111.345(6)
$\gamma$ (°)	90	60.352(5)	90
<i>V</i> (Å <sup>3</sup> )	1947.8(4)	3963.8(10)	3982.4(12)
<i>Z</i>	4	2	4
<i>D</i> <sub>calc</sub> (gm cm <sup>3</sup> )	1.510	1.553	1.565
<i>F</i> (000)	0.347	1900	1928
<i>h</i> , <i>k</i> , <i>l</i> (max)	9,17,25	19,19,22	34,10,28
<i>R</i> <sub>1</sub>	0.0394	0.0641(9311)	0.0534(3721)
<i>wR</i> <sub>2</sub>	0.1011	0.1741	0.1451
2 $\theta$	27.2	25.0	29.2

<sup>a</sup>*R*<sub>1</sub> =  $\sum(|F_o| - |F_c|) / \sum|F_o|$ . <sup>b</sup>*wR*<sub>2</sub> =  $\{\sum[w(F_o^2 - F_c^2)^2] / \sum[w(F_o^2)^2]\}^{1/2}$  and  $w = 1 / [\sigma^2(F_o^2) + (0.0265P)^2 + 0.4876P]$ , where  $P = (F_o^2 + 2F_c^2) / 3$ .

compounds. The conformation of the complex may facilitate the recruitment of biomolecules that are involved in various biological actions. However, in our study, we found that the planar aromatic group(s) such as benzene, naphthalene, and so forth attached in the metal–organic complexes stacks between base pairs of DNA and hence renders the intercalative property even after the formation of the metal complex. The antiproliferative activities of 2-pyridyl 2,3-thiazole derivatives were investigated against HL-60, MCF-7, HepG2, and NCI–H292 human tumor cell lines.<sup>17</sup> Pyridine and thiazole moieties anchored by the hydrazone unit were demonstrated for their remarkable cytotoxicity against macrophage cells such as J774A.1 (IC<sub>50</sub>: 11.65–30.35  $\mu$ M), HT-29 (IC<sub>50</sub>: 25.22–57.83  $\mu$ M), and Jurkat (IC<sub>50</sub>: 16.54–21.25  $\mu$ M).<sup>18</sup> Elshafly et al. (2016) synthesized several of 2,4 di-substituted pyridine thiazole compounds to investigate their anticancer activity against human breast cancer MCF-7 cells.<sup>19</sup> In search of new biopotent agents/ligands, the judicious combination of structural features of thiazole and pyridine through the hydrazone link has been considered in the present study. It has been reported that the contribution of hydrazine moieties has potential functions in improving biological properties.<sup>20–23</sup> Further, the ability of transition metal(s) to coordinate ligand(s) allows them to be active intermediates in several biochemical processes.<sup>24</sup> The transition elements such as iron, manganese, zinc, cobalt, and so forth have been usually modeled to study the structure–activity relationship in the biological system.<sup>25,26</sup> For example, Mn(II) of the amino-thiazole acetate derivative exhibits anticancer activity against human cervix adenocarcinoma and Hela cells.<sup>27</sup> Neelakantan et al. (2008) demonstrated the antimicrobial and antifungal activities of the Mn(II) complex of polydentate ligands containing the thiazole moiety.<sup>28</sup> Another transition metal, that is, Co(III), a key substituent in vitamin B<sub>12</sub>, is chosen as the central metal ion since its complexes often possess higher activities than cisplatin.<sup>29</sup> Ambika et al. (2019) reported the antiproliferative and antiangiogenic activities of the cobalt(III) complex of N, S donor against A549 and VERO cells.<sup>30</sup> Zhao

et al. (2019) reported the antiproliferative activity against several cancer cell lines by multinuclear Co(II) complexes of the pyridyl-imidazole ligand.<sup>31</sup> The cytotoxic activity of Co(II) and Ni(II) complexes of phenylthiazole against HL-60, NAML-6, and WM-115 cell lines was tested.<sup>32</sup> The octahedral Ni(II) thiazole complexes exhibited a significant role to damage the different cancer cell types.<sup>33</sup> All these qualified properties of thiazole and pyridine derivatives prompted us to initiate research on thiazole-anchored pyridinyl late transitional first-row metal derivatives. The present work reports on the synthesis and spectroscopic and structural characterization of a perchlorate salt of (4-(4-methoxy phenyl)-2-(2-(1-pyridine-2-yl) ethylidene)hydrazinyl)thiazole (PytH·ClO<sub>4</sub>) and its cobalt(III), manganese(II), and nickel(II) perchlorate derivatives. The *in vitro* antiproliferative activities of the new derivatives are investigated in histiocytic lymphoma (U-937) cells. The cell death mechanism (PARP cleavage), the cell viability of peripheral blood mononuclear cells (PBMCs), and the DNA binding experiments are performed. The theoretical interpretation of the experiments is shaded out by the molecular dynamics (MD) simulations and docking studies.

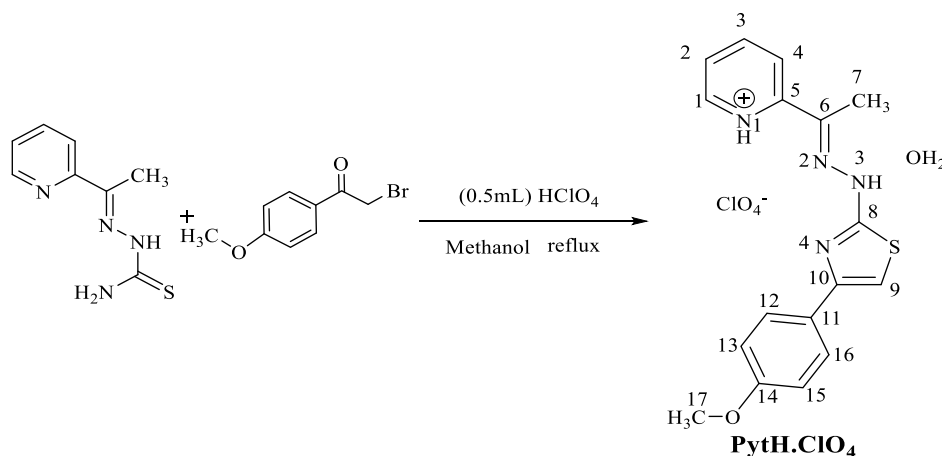
## EXPERIMENTAL SECTION

**Materials and Methods.** Thiosemicarbazide (99%), 2-acetyl pyridine (99%), 2-bromo-4-methoxyacetophenone, CT-DNA, and Tris–HCl buffer were procured from Aldrich Chemical Company. Nickel(II) perchlorate hexahydrate, cobalt(II) perchlorate hexahydrate, manganese(II) perchlorate hexahydrate, perchloric acid, and DMSO were obtained from Merck Chemical Company. All solvents (reagent grade) were obtained from commercial suppliers and used after distillation.

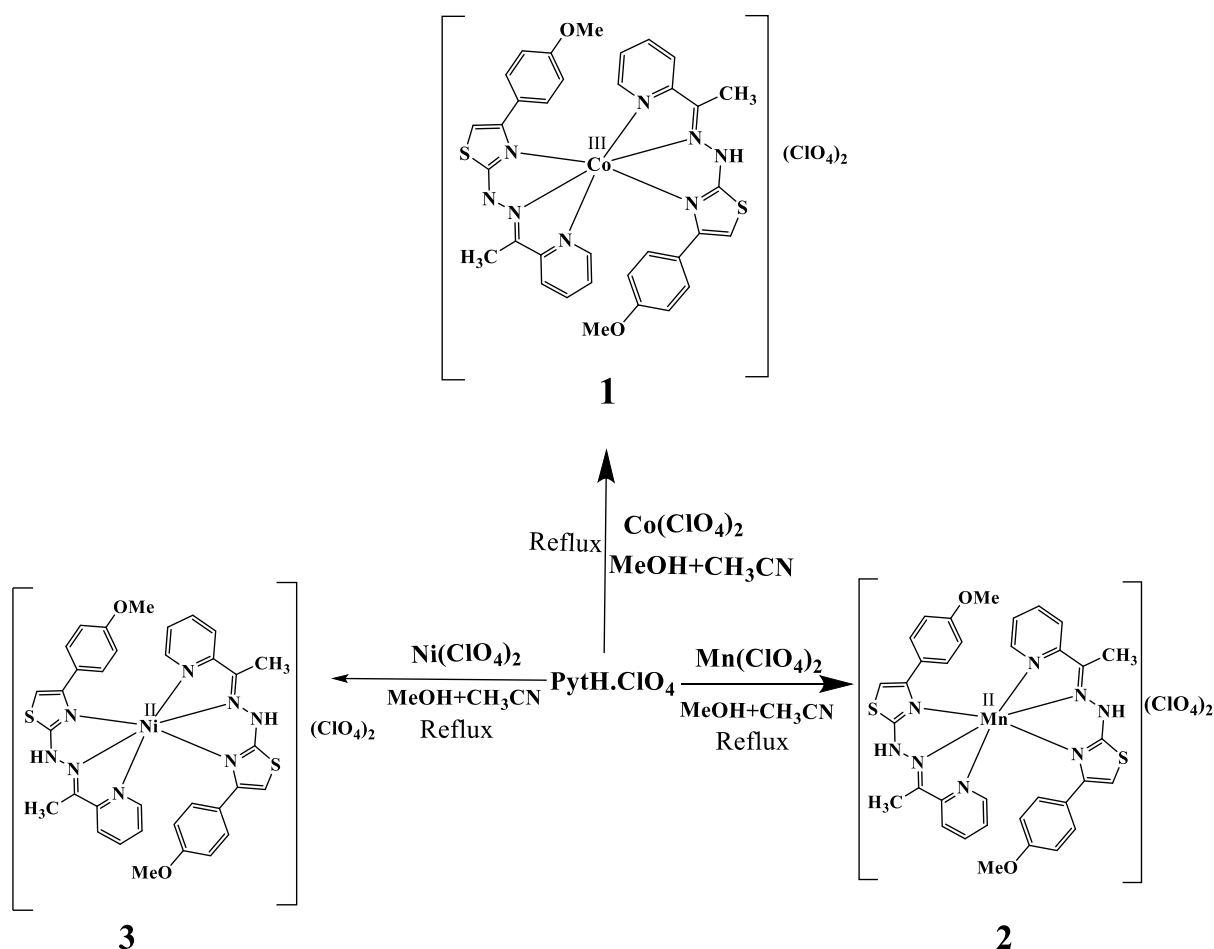
**Conductivity Measurement.** The molar conductance of a 10<sup>−3</sup> (M) solution of the compounds in a dry acetonitrile solution was measured at 30 °C using a Thermo Orion model 550A conductivity meter and a dip-type cell with the platinized electrode.

**Spectroscopic Methods.** A PerkinElmer Lambda 35 spectrophotometer with a wavelength range of 200–800 nm

Scheme 1. Outline of the Synthesis Procedure of the Ligand



Scheme 2. Outline of the Synthesis Procedure of the Metal Complexes



is used to evaluate the UV–vis absorption spectra of the ligand and complexes at room temperature. A PerkinElmer Fluorescence Spectrometer LS 45 is used in the present study at an excitation wavelength of 340 nm. The KBr-phase FT-IR spectra of the samples were recorded in the range of 4000–500  $\text{cm}^{-1}$  using a PerkinElmer Spectrum 2 spectrophotometer. The elemental analysis (C, H, N, and S) of both the ligand and complexes was performed using a FISON EA-1108 CHN analyzer. A CH Instrument electrochemical workstation model CHI630E is used for cyclic voltammetry (CV)

experiments at room temperature in acetonitrile solvent using tetra butyl ammonium perchlorate as the supporting electrolyte, where the conventional three-electrode assembly comprised a platinum working electrode, a platinum wire auxiliary electrode, and a Ag/AgCl reference electrode.

**X-ray Crystallography.** Single-crystal X-ray diffraction data for the ligand and complex were collected with monochromated Mo- $K\alpha$  radiation ( $\lambda = 0.71073 \text{ \AA}$ ) on a Bruker KAPPA APEX-II diffractometer equipped with a CCD area detector at low temperatures. Several scans in  $\varphi$  and  $\omega$  directions were

made to increase the number of redundant reflections and were averaged during the refinement cycles. Data processing for all the complexes was performed using the Bruker APEX-II suite. Reflections were then corrected for absorption, inter-frame scaling, and other systematic errors with SADABS.<sup>34</sup> All the structures were solved by the direct methods, and all non-hydrogen atoms were refined anisotropically by the full-matrix least-squares based on F2 using the SHELXL-97.<sup>35</sup> The hydrogen atoms were isotropically treated using a riding model with their isotropic displacement parameters depending on the parent atoms. A summary of the crystallographic data and refinement parameters is given in Table 1.

**Procedure for the Synthesis of Compounds (PytH·ClO<sub>4</sub>, 1, 2, and 3).** *Synthesis of [Co(Pyt)<sub>2</sub>]ClO<sub>4</sub> (1).* The synthesis of [Co(Pyt)<sub>2</sub>]ClO<sub>4</sub> (1) was carried out by refluxing the equimolar methanolic solution of Co(ClO<sub>4</sub>)<sub>2</sub>·6H<sub>2</sub>O and the bromo salt of (4-(4-methoxyphenyl)-2-(2-(1-(pyridine-2-yl)ethylidene)hydrazinyl)thiazole as reported earlier by us.<sup>40</sup>

*Synthesis of (4-(4-Methoxy phenyl)-2-(2-(1-pyridine-2-yl)ethylidene)hydrazinyl)thiazole Perchlorate (PytH·ClO<sub>4</sub>).* The methanolic solution of 2-bromo-4-methoxyacetophenone (10 mmol, 2.29 g) was added dropwise into the methanolic solution of 2-(1-(pyridine-2-yl)ethylidene)hydrazine-1-carbothioamide (10 mmol, 1.942 g) under constant stirring at room temperature.<sup>40</sup> After completing the addition, the reaction mixture was refluxed in the presence of 1 mL of perchloric acid (Caution! Explosive material must be handled with care) in a water bath temperature for 2 h. Deep orange single crystals were obtained after the slow evaporation of the resultant solution (Scheme 1). Yield: 2.984 g (71.75%). Anal. Calcd for C<sub>17</sub>H<sub>19</sub>N<sub>4</sub>OS·ClO<sub>4</sub>·H<sub>2</sub>O (%): C, 46.11; H, 4.32; N, 12.65. Found: C, 46.19; H, 4.38; N, 12.78; IR (KBr pellets, cm<sup>-1</sup>):  $\nu_{\text{N-H}}$  3446,  $\nu_{\text{C=N}}$  1606  $\nu_{\text{N-N}}$  1247,  $\nu_{\text{C=S}}$  825,  $\nu_{\text{Cl-O}}$ . <sup>1</sup>H NMR (CDCl<sub>3</sub>),  $\delta$  (in ppm) (Figure S1): 11.72 (s, 1H at N3), 8.70 (s, 1H at C1), 8.34 (s, 1H at C3), 8.49–8.56 (d, H at C2 and C4), 5.94 (s, 1H at C9), 7.19–7.25 and 7.26–7.26 (d, 2H at C12 & C16 and C13 & C15, <sup>3</sup>J<sub>12,16</sub> = <sup>3</sup>J<sub>13,15</sub> = 8.0 Hz); 4.65–4.73 (m, 3H at C17). <sup>13</sup>C NMR (CDCl<sub>3</sub>),  $\delta$  (in ppm) (Figure S2): 11.5 (s, C7), 53.6 (s, C17), 157.8 (s, C8), 167.6 (s, C10), 112.4 (s, C9), 101.2 (s, C14), 123.6 (d, C13 & C15), 125.6 (s, C11), 137.7 (s, C6), 147.7 (d, C2 & C4).

*Synthesis of [Mn(Pyth)<sub>2</sub>](ClO<sub>4</sub>)<sub>2</sub> (2).* A mixture of Mn(ClO<sub>4</sub>)<sub>2</sub>·6H<sub>2</sub>O (0.584 g, 2.0 mmol) and PytH·ClO<sub>4</sub> (0.774 g, 2.0 mmol) was stirred in solvent methanol–acetonitrile (1:1). The resulting mixture was heated in a water bath for 4 h. The color of the solution changed from yellow to orange. The reaction mixture was filtered and placed in a dry beaker for slow evaporation. Yellow transparent crystals were collected from the solution by filtration and washed with acetonitrile–methanol mixture (1:1) (Scheme 2). Yield: 75% (concerning metal salt). Anal. Calcd for C<sub>68</sub>H<sub>64</sub>Cl<sub>4</sub>Mn<sub>2</sub>N<sub>16</sub>O<sub>23</sub>S<sub>4</sub> (%) of C, 44.3; H, 3.48; N, 12.39; O, 18.75. Found: C, 44.03; H, 3.40; N, 12.58; O, 19.85%. IR (KBr pellets, cm<sup>-1</sup>): 3226 for  $\nu(\text{N-H})$ , 1611 for  $\nu(\text{C=N})$ , 1496 for  $\nu(\text{C=C})$ , 1248 for  $\nu(\text{C-O})$ , 1099 for  $\nu(\text{C-N})$ , 776 for  $\nu(\text{C=S})$  and 614 for  $\nu(\text{Cl-O})$ .

*Synthesis of the Complex [Ni(Pyth)<sub>2</sub>](ClO<sub>4</sub>)<sub>2</sub> (3).* A stoichiometric mixture of Ni(ClO<sub>4</sub>)<sub>2</sub>·6H<sub>2</sub>O (0.365 g, 1.0 mmol) and PytH·ClO<sub>4</sub> (0.42 g, 1.0 mmol) was dissolved in methanol and acetonitrile solution (1:1) (30 mL). The resulting wine-red color solution was heated for 3 h. The color of the solution changed from wine to deep red. Rod-shaped violet crystals were obtained by slow evaporation of the

red solution (Scheme 2). The crystals were separated and washed with methanol and dried in air. Yield: 0.27 g (65% based on metal salt). Elemental analyses (%) for C<sub>32</sub>H<sub>30</sub>N<sub>10</sub>Cl<sub>2</sub>NiO<sub>10</sub>S<sub>2</sub> are C, 42.31; H, 3.33; N, 15.42%. Found: C, 42.56; H, 3.41; N, 15.91%. IR frequencies (KBr pellets, in cm<sup>-1</sup>): 3470 for  $\nu(\text{N-H})$ , 1621 for  $\nu(\text{C=N})$ , 1496 for  $\nu(\text{C=C})$ , 1253 for  $\nu(\text{C-O})$ , 1089 for  $\nu(\text{C-N})$ , 786 for  $\nu(\text{C=S})$  and 614 for  $\nu(\text{Cl-O})$ .

**Bioassays.** *MTT Cell Viability Assay.* The newly synthesized compounds PytH·ClO<sub>4</sub> and 1–3 were screened for their *in vitro* cytotoxic activity against the human histiocytic lymphoma (U-937) cell line according to the previously reported method.<sup>41</sup> The cytotoxicity assay was performed, the percentage of cell death was plotted, and the IC<sub>50</sub> values were calculated using Graph Pad Prism 6.<sup>41</sup>

*Live and Dead Cell Assay.* U-937 cells were treated with each compound at a concentration of 10  $\mu\text{M}$  by incubating at 37 °C in a 5% CO<sub>2</sub> incubator overnight. The cells treated with 1  $\mu\text{M}$  doxorubicin were used as control. The next day, the cells were washed thrice with PBS, stained, and incubated with 5  $\mu\text{M}$  calcein-AM (4',5'-bis(*N,N*-bis(carboxymethyl)-aminomethyl)fluorescein acetoxyethyl ester) and propidium iodide to assess the live and dead cell population in the treated cells. Calcein-AM stains live cells (green), whereas propidium iodide stains dead cells (Red). The stained cells were observed under an Olympus IX73 Fluorescent Microscope.<sup>42,43</sup>

*LDH Release Assay.* LDH is a cytosolic enzyme, which is released into the culture supernatant upon induction of necrosis of cells. U-937 cells (2 × 10<sup>6</sup>) were taken per well of a six-well plate. After treatment, the culture supernatants were collected and assayed for LDH as described earlier.<sup>44</sup>

*PARP Cleavage by Western Blot.* U-937 cells (2 × 10<sup>6</sup>) seeded in six-well plate were treated with 5  $\mu\text{M}$  ligands PytH·ClO<sub>4</sub>, 1, 2, and 3, keeping untreated cells as control. However, cells treated with 1  $\mu\text{M}$  doxorubicin were used as a positive control for cell death. The treated cells along with control were incubated at 37 °C in a 5% CO<sub>2</sub> incubator for 24 h, and then cells were harvested by centrifugation at 14 000 rpm, 4 °C, for 5 min. The whole cell lysate was prepared by adding a whole cell extract (WCE) mixture [50 mM Tris–HCl buffer, pH 7.6 with a protease inhibitor cocktail (100:1), and 1% Triton X100] to the cell pellet and incubating on ice for 15 min, followed by a cycle of vortexing for 30 s and cooling for 45 s, which was repeated for 30 min. Finally, the cells were centrifuged at 14 000 rpm, 4 °C, for 10 min to collect the supernatant. The protein concentration in the supernatant was estimated with Bradford's protein estimation method as described previously. 100  $\mu\text{g}$  of whole cell lysate was used for western blot to probe for cleaved PARP cleavage and cleaved caspase 3. GAPDH was used as a loading control. The blots were visualized with a chemiluminescent substrate (femto LUCENT PLUS-HRP, G-Biosciences)<sup>44,45</sup> using UVITEC Chemidoc (Cambridge) and UVITEC Nine Alliance software.

*Isolation of PBMCs from Fresh Human Blood.* PBMCs were isolated from fresh human blood by the Ficoll-Paque (Histopaque-1077) density gradient centrifugation method. The blood was diluted with sterile phosphate buffer saline (PBS) 1:1, layered over histopaque-1077 (1.077 density), and centrifuged at 400×g at room temperature for 30 min. The PBMC layer, formed above the Ficoll layer, was aspirated and washed three times with PBS. The PBMCs were then suspended in DMEM for culture. The viability and purity of PBMCs were tested by the Trypan blue dye exclusion

method.<sup>46,47</sup> Almost 95% of cells were PBMCs and 98% of cells were viable.

**Effect of Compounds on PBMCs.** Isolated PBMCs were used to assess the cytotoxicity of the ligand and its derivatives on primary immune cells (PBMCs) using the MTT assay as aforementioned with slight modification. Briefly,  $5 \times 10^3$  PBMCs seeded in each well of a 96-well plate was treated at  $IC_{50}$  values and double the  $IC_{50}$  values of the compounds. These cells were incubated at 37 °C for 24 h, and then the MTT dye was added, followed by cell lysis with MTT lysis buffer. Following a day, absorbance at 595 nm using the Bio-Rad iMark Microplate Reader was taken and used to calculate percentage cell death.

**CT-DNA Binding Study by the UV-Vis Spectroscopic Method.** A stock solution of CT-DNA was prepared in 50 mM Tris-HCl/50 mM NaCl in H<sub>2</sub>O at pH 7.4 in the binding experiment. To exclude free protein in the CT DNA, the UV absorbance experiment was carried out in a buffer medium of CT DNA, and the ratio of absorbance found at 260 and 280 nm was ca.1.9:1, which suggests that the CT DNA was free from protein. The stock solution of DNA was stored at 4 °C and used within five days. The molar concentration of the stock solution was calculated using a molar absorption coefficient value of  $6600 \text{ M}^{-1} \text{ cm}^{-1}$  at 260 nm and adjusted to 5 mM concentration. The interaction of PytH·ClO<sub>4</sub> and 1–3 with CT DNA was monitored by a UV-vis spectroscopic titration method in 50 mM Tris-HCl buffer (pH 7.4) at room temperature. The complex solution was also prepared in the same medium. The concentration of the complex was fixed to 30 μM during titration. The change in the absorbance was recorded with the subsequent addition of an aliquot of 10 μL ( $14 \times 10^{-4} \text{ M}$ ) of CT DNA in the sample and reference cuvette. All the UV spectra were recorded after equilibration of the solution for 5 min. The experiment was continued until there was no significant change in absorbance for the last four successive additions.<sup>48,49</sup>

**Methods of Calculation. DFT Calculation.** The HOMO and LUMO orbitals are plotted using the X-ray coordinates of the complex, and the ground-state electronic structure of the complex is calculated using the DFT method<sup>36</sup> with the Orca 4.0 program. Becke's hybrid function<sup>37,38</sup> with the Lee–Yang–Parr (LYP) correlation function<sup>36</sup> was used throughout the study. The valence only SV (P) SV/J, the def2-SVP basis set, and the B3LYP/G effective one potential functional were used.<sup>39</sup> The energy calculations were performed using the self-consistent field "Opt" option of the Orca\_4\_0\_1\_2\_win64\_msmmpi81 program to ensure sufficient and well-converged values for the state energies.

**Molecular Docking.** Molecular docking was carried out using AUTODOCK 4.0 software as accomplished by the graphical user interface AUTODOCK TOOLS 4.0 (AD4.1\_bound.dat). The macrocyclic receptor was chosen as the three-dimensional X-ray crystal structure of DNA (entry 1bna in the Protein Data Bank).

The graphical user interface AUTODOCK TOOLS devoted to set up the protein–water molecule was deleted from the crystal of protein; only polar hydrogen was added, and computed Gasteiger charge was calculated as −13.98e, and non-polar hydrogen was merged to the carbon atom. Complex 3D structures were saved in the PDB format with the aid of the program MERCURY. The AUTODOCK TOOLS program was used to make docking input files. The grid box size for PytH·ClO<sub>4</sub>, 1, 2, and 3 was  $42 \times 48 \times 98$ ,  $42 \times 48 \times 90$ ,  $48 \times$

$48 \times 90$ , and  $44 \times 50 \times 90$ , respectively. The center grid box coordinates ( $x$ ,  $y$ , and  $z$ ) of DNA were 12.877, 21.214, and 7.035; 13.558, 20.331, and 16.571; 14.780, 20.976, and 8.807; and 12.604, 19.602, and 16.690 for evaluating the mode of binding. Both the receptor and compound are saved in the pdbqt format. Distance-dependent functions of the dielectric constant were used for the calculation of the energetic map. Ten runs are generated by using Lamarckian genetic algorithm searches. Default settings are used with a maximum number of  $2.5 \times 10^6$  energy evaluations, an initial population of 50 randomly placed individuals.<sup>46,50</sup> Final docking is run with autogrid4.exe and autodock4.exe functions to generate glg and dlg files, respectively. The graphical interaction pictures were found using discovery Studio software.

**MD Simulation.** NAMD is an open-source MD simulation package.<sup>51</sup> When it comes to MD simulations, NAMD has been designed with high-performance computing (HPC) scalability and GPU support. For analysis and visualization, it offers a powerful scripting engine in association with VMD 1.9.3.<sup>52</sup> The 3D structural coordinates of the systems generated through the docking study were used for the MD simulations. The preparation is done according to the tutorial and concerning literature.<sup>53</sup> The DNA, metal co-factor ( $\text{Mn}^{2+}$ ), and ligand under investigation were individually prepared, parameterized, and merged through the VMD 1.9.3. The parameterization of DNA was done through the CHARMM36 nucleic acid parameter file developed by Mackerell junior and co-workers. For metal co-factor ( $\text{Mn}^{2+}$ ), we have used the top\_ions\_won.str parameter file. It contains general models of several metals for mono-, di-, and trivalent cations. The ligand parameters were generated via the ParamChem web server (<https://cgenff.ParamChem.org/>).<sup>54</sup> This server generates the ligand's topology and parameters through the CGENFF approach. The merged system was used for the generation of a cubic water box having TIP3P as a water molecule along with 20 Å padding. The solvated system was neutralized by the ions Na<sup>+</sup> or Cl<sup>−</sup>. This ionized complex was subjected to 70 ps of minimization, followed by 20 ns MD simulations (NPT ensemble, pressure 1 atm, and temperature 310 K). In addition, non-bonded interactions were restricted to a distance of 12 Å. PME electrostatics and the Langevin piston were also used in on conditions. During the MD simulations, the trajectories were recorded at 2 ps intervals. The visualization and trajectories were analyzed in VMD 1.9.3 for root-mean-square deviation (RMSD), the radius of gyration, and energies.<sup>52</sup>

## RESULTS AND DISCUSSION

In an early report, the synthesis and structural characterization of the bromo salt of (4-(4-methoxy phenyl)-2-(2-(1-pyridine-2-yl)ethylidene)hydrazinyl)thiazole (PytH·Br) and its cobalt(III) complex  $[\text{Co}(\text{Pyt})_2]\text{ClO}_4$  (1) had been demonstrated for their in vitro antibacterial evaluation.<sup>40</sup> The present report involves the study of perchlorate salt of the pyridine–thiazole ligand (PytH·ClO<sub>4</sub>) and its Co(II), Mn(II), and Ni(II) complexes to screen their antitumor efficacy. The outline of the synthesis procedure of the ligand and metal complexes is shown in Schemes 1 and 2, respectively. The perchlorate derivatives under experiment are fairly soluble in water and stable up to 72 h in the experimental condition. PytH·ClO<sub>4</sub> and 1 are 1:1 electrolytes, whereas 2 and 3 are 1:2 electrolytes as envisaged by the conductance measurements. Very recently, we have also reported the synthesis and biological evaluation of

similar type pyridine–thiazole and pyrazine–thiazole ligands and their metal complexes.<sup>23,49,55</sup> The NNN donor 4-(2-(2-(phenyl(pyridine-2-yl)methylene)hydrazinyl)thiazole-4-yl)-benzotrile and its cobalt(II) complex exhibited the potential anticancer property following the apoptotic cell death mechanism in U-937 human monocytic cells having IC<sub>50</sub> values of  $12.76 \pm 0.75$  and  $12.83 \pm 1.37 \mu\text{M}$ , respectively.<sup>23</sup> To compare the antitumor efficacy of the substituents in the core structure, a perchlorate salt of (4-(4-methoxy phenyl)-2-(2-(1-pyridine-2-yl)ethylidene)hydrazinyl)thiazole and its Co(III), Mn(II), and Ni(II) complexes have been demonstrated. To shed light on the interactions at the molecular level, computational studies are also performed.

**Spectral Study.** <sup>1</sup>H NMR and <sup>13</sup>C NMR Spectroscopy Study of **PytH·ClO<sub>4</sub>**. The <sup>1</sup>H NMR experiment is performed in CDCl<sub>3</sub>. The signals obtained in the <sup>1</sup>H NMR spectrum of the ligand were in good agreement with the expected structure (Figure S1). The signal at  $\delta$  11.72 ppm can be assigned for acetyl pyridyl hydrazone (–NH) protons. The single peak observed at  $\delta$  8.70 ppm indicates the proton attached with the C1 atom. Another single peak found at  $\delta$  8.34 ppm is attributed to the proton at C3. The multiplet observed at  $\delta$  8.49–8.56 ppm may be due to the proton attached with C4 and C2. The peak at  $\delta$  5.94 ppm for a single proton may correspond to a proton attached to C9. Another doublet peak at  $\delta$  7.19–7.25 ppm counts two protons and can be the protons attached with C16 and C15. The doublet peak at  $\delta$  7.26–7.26 ppm also counts two protons that can be attached to C13 and C15 with a *J* value of 8.0 Hz. On the other hand, the multiplet signal in the region  $\delta$  4.65–4.73 ppm may be due to the presence of three methoxy protons attached with C17. The broad signal was found at  $\delta$  10.29 ppm due to the presence of water molecules in the unit lattice. The <sup>13</sup>C NMR spectrum of **PytH·ClO<sub>4</sub>** consists of 14 peaks in the region of aromatic carbon atoms except for the solvent peak at  $\delta$  76.6–77.3 ppm (Figure S2). The acetyl carbon C7 can be assigned to the peak at 11.5 ppm and the peak observed at 53.6 ppm due to the presence of methoxy carbon C17. Mostly, deshielded carbons C8 and C10 in the thiazole ring can be assigned to the peaks at  $\delta$  157.8 and 167.6 ppm, respectively. The peak was found at 112.4 ppm for another carbon C9 of thiazole.<sup>46</sup> The peaks at  $\delta$  101.2 ppm for C14 and 123.5 ppm can be assigned for two adjacent carbon atoms (C13 and C15) to the phenyl ring in **PytH·ClO<sub>4</sub>**. The peak was assigned at  $\delta$  125.6 ppm for C11. The azomethine carbon (C6) peaks are also expected in the aromatic carbon region to be assigned to the peaks at  $\delta$  137.7. The peak at  $\delta$  147.7 ppm can be assigned for two carbon atoms (C2 and C4) to the pyridine ring in **PytH·ClO<sub>4</sub>**.

**FT-IR Spectroscopy Studies of **PytH·ClO<sub>4</sub>**, 1, 2, and 3.** The FT-IR stretching frequencies of **PytH·ClO<sub>4</sub>**, 1, 2, and 3 are recorded in the frequency range at 4000–500 cm<sup>−1</sup> using the KBr plate and are shown in Figures S3–S6, respectively. The broad signals of **PytH·ClO<sub>4</sub>** at 3493 cm<sup>−1</sup> implied the presence of pyridyl hydrazone (–NH) bond in the ligand moiety. The peak at 3226 and 3470 cm<sup>−1</sup> for 2 and 3 indicates that the pyridyl hydrazone (–NH) bond of **PytH·ClO<sub>4</sub>** remains unchanged in complexation. Therefore, **PytH·ClO<sub>4</sub>** acts as a neutral ligand when bound with Mn(II) and Ni(II). The peak is observed in the range 1591–1621 cm<sup>−1</sup> for both ligand and complexes due to the vibration frequency of the C=N bond (azomethane). The other intense peaks at the 1453–1496 cm<sup>−1</sup> region were attributed to the aromatic C=C bond

stretching vibration in both **PytH·ClO<sub>4</sub>** and complexes.<sup>56,57</sup> The C=C bond stretching vibration of complexes is greater than the corresponding ligand's C=C bond stretching frequency by 53 cm<sup>−1</sup>, which is attributed to the increased rigidity in the ligand structure on complexation. The accomplished peak in the region 1248–1253 cm<sup>−1</sup> can be assigned to the stretching frequency C=N bond in the thiazole ring in the complexes. The peaks in the region at 1020–1099 cm<sup>−1</sup> assigned for the stretching frequency of methoxy C–O bonds, which remain unchanged during complexation. The stretching vibration of Cl–O in ClO<sub>4</sub><sup>−</sup> found at 614–619 cm<sup>−1</sup> in the compounds confirms the presence of ClO<sub>4</sub><sup>−</sup> in the ligand and complexes under discussion.<sup>58</sup>

**UV–Vis Spectroscopy of **PytH·ClO<sub>4</sub>**, 1, 2, and 3.** The electronic absorption spectra of the tested compounds are carried out in acetonitrile solution (10<sup>−5</sup> M) at room temperature (Figure 1), and the data are given in Table S1.

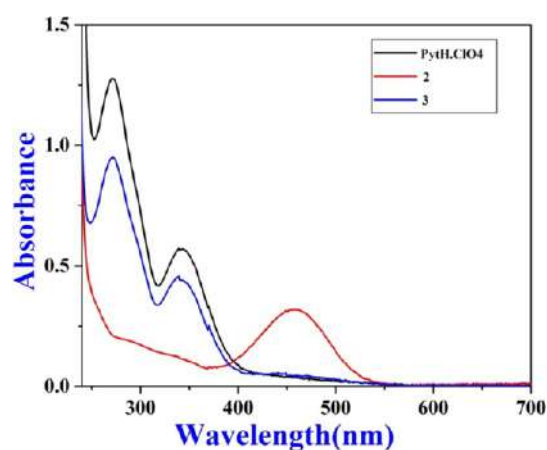


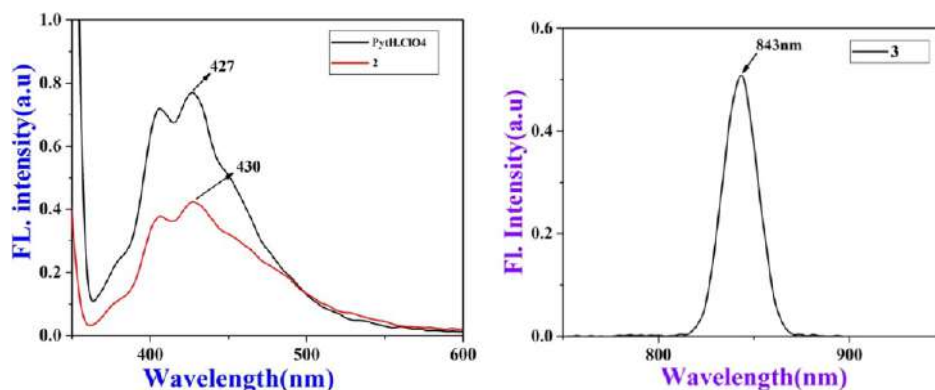
Figure 1. UV–vis absorption spectroscopy of **PytH·ClO<sub>4</sub>**, 2, and 3.

**PytH·ClO<sub>4</sub>** shows two intense absorption bands at 272 and 344 nm. The peak at 272 nm may be attributed to the intraligand spin allowed  $\pi \rightarrow \pi^*$  transition, whereas the peak at 344 nm can be assigned to the  $n \rightarrow \pi^*$  transition.<sup>59</sup> The electronic spectrum of 1 shows a weak d–d transition band at 470 nm, and ligand to metal charge-transfer transition (LMCT) is observed at 344 nm in an octahedral ligand field environment.<sup>60</sup> Complex 2 shows that only one broad intense absorbance band at 460 nm may be due to the overlap of all possible d–d transitions in the d<sup>5</sup> system (Figure 1). The absorption peak of 3 is similar to that of **PytH·ClO<sub>4</sub>** with little displacement. The broad peak at 270 and 338 nm may arise due to the  $n \rightarrow \pi^*$  transition and the  $\pi \rightarrow \pi^*$  transition, respectively.<sup>28</sup> To check the stability of the complexes, UV–vis spectra were evaluated at different times until 72 h, and no significant change in absorption peaks was found.

**Fluorescence Spectroscopy of **PytH·ClO<sub>4</sub>**, 2, and 3.** The fluorescence spectroscopy spectra of **PytH·ClO<sub>4</sub>** ( $\lambda_{\text{ex}} = 340$  nm), 2, and 3 ( $\lambda_{\text{ex}} = 420$  nm) were recorded in the CH<sub>3</sub>CN solution, as shown in Table 2. The fluorescence emission bands of **PytH·ClO<sub>4</sub>**, 2, and 3 are found at 427, 430, and 843 nm, respectively (Figure 2). The ligand **PytH·ClO<sub>4</sub>** and its Mn(II) complexes (2) exhibit a similar intense emission band. The spectral data of 2 shows that there is no remarkable change in fluorescence properties in the presence of ligand environments. However, 3 exhibits a remarkable change in

Table 2. Different Interaction Energies of PytH·ClO<sub>4</sub>, 1, 2, and 3 with CT-DNA Are Given in Kcal/mol

compound	estimated inhibition constant, $K_i$ ( $\mu\text{M}$ ) at $T = 298.15$	vdW + H bond + dissolving energy ( $\Delta G_{\text{vdW+hb+desolv}}$ )	electrostatic energy ( $\Delta G_{\text{elec}}$ )	total internal energy ( $\Delta G_{\text{total}}$ )	torsional free energy ( $\Delta G_{\text{tor}}$ )	unbound system's energy ( $\Delta G_{\text{unb}}$ )	binding free energy ( $\Delta G_{\text{binding}}$ )
PytH·ClO <sub>4</sub>	0.067	-11.27	-0.01	-1.55	+1.49	-1.55	-9.79
1	67.74	-6.92	+0.03	-2.66	+1.19	-2.66	-5.69
2	14.99	-7.66	-0.11	-2.87	+1.19	-2.87	-6.58
3	35.05	-6.95	-0.32	-2.84	+1.19	-2.84	-6.08

Figure 2. Fluorescence spectroscopy of PytH·ClO<sub>4</sub>, 2, and 3 at  $1 \times 10^{-5}$  (M) concentration.

fluorescence emission at a wavelength of 843 nm concerning the ligand. The better coordination of Ni(II) with ligand than Co(II) and Mn(II) is envisaged by the increase of fluorescence intensity in 3.<sup>61</sup> Thus, complex 3 can be used as a fluorophore in photochemical applications.

**Electrochemical Study.** A study of the electrochemical behavior of a metal complex has an immense role in exploring the chemical and electrochemical reactions and mechanisms involved in a molecule. The redox property of a bioactive compound can also give insight into its metabolic facts and biological activities. We studied the electrochemical behavior of the compounds since this category of compounds has a wide application in biology and chemistry. The CV of 1 shows three reduction peaks at -0.83, +0.56, and +0.85 V versus Ag/AgCl, saturated KCl, corresponding to the ligand reduction, Co(III) to Co(II) and Co(II) to Co(I) reduction, respectively. The predominant single oxidation peak at 0.93 V might be the combination of oxidation processes Co(I) → Co(II) and Co(II) → Co(III).<sup>49</sup> The CV of 2 in CH<sub>3</sub>CN (Figure 3) shows two reduction potential peaks at 0.32 V (a) and 0.78 V (b) versus Ag/AgCl in saturated KCl, which implies that Mn(II) is reduced to Mn(I) and then Mn(I) is reduced to Mn(0), respectively, while the reverse process of two oxidation potential peaks at 0.38 V (c) and 0.79 V (d) indicate Mn(0) → Mn(I) and Mn(I) → Mn(II) oxidation processes, respectively.

As shown in Figure 4, the CV of 3 in CH<sub>3</sub>CN shows two reduction potential peaks at -0.24 V (a) and 0.42 V (b) versus Ag/AgCl in saturated KCl. The first peak -0.24 V (a) implies the reduction of ligand moiety. The second peak 0.42 V (b) is attributed to the reduction of Ni(II) → Ni(0), while in the reverse process one, the oxidation potential peaks at 0.32 V (c) indicate the Ni(0) → Ni(II) oxidation reaction in the presence of ligand field environment. The oxidation and reduction processes are irreversible in the complexes. The Mn(II) complex (2) shows the lowest value of reduction potential ( $E_R = 0.32$  V) and is more susceptible to reduction than Co(III) and Ni(II) complexes. Therefore, it is quite reasonable to

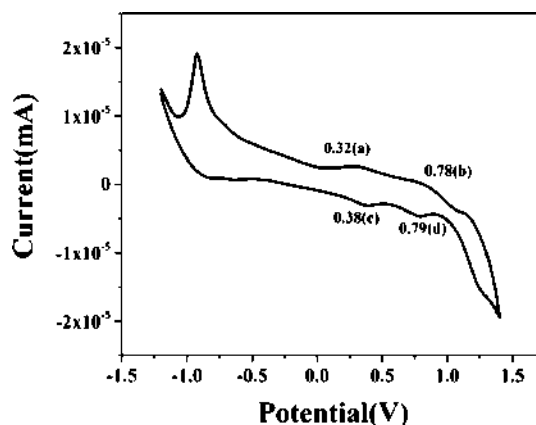
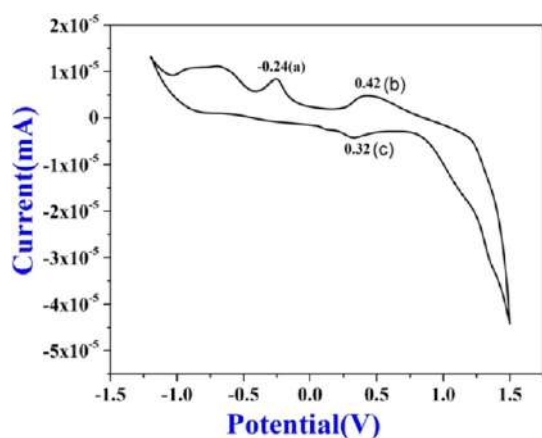


Figure 3. Cyclic voltammogram of 2 in an acetonitrile solvent containing tetrabutylammonium perchlorate as a supporting electrolyte at a scan rate of 20 mV/s.

conclude that the Mn(II) complex will be a biologically active redox species.

**X-ray Crystallography Study and DFT.** The detailed structural description of 1 was reported earlier by us.<sup>40</sup> The HOMO–LUMO energy calculation of 1 is given in Figure S7. The refinement X-ray crystallography pictures of PytH·ClO<sub>4</sub>, 2, and 3 are shown in Figures 5, 7, and 8, and the refinement X-ray crystallography data, bond distance, bond angle of PytH·ClO<sub>4</sub>, 2, and 3 are summarized in Tables 1 and S2 and S3. The space group of PytH·ClO<sub>4</sub> crystal is  $P2_1/n$  with a monoclinic crystal system (Figure 5a). The angles between the different planes C12–C11–C10 and C11–C10–N4, C10–N4–C8 and N4–C8–N3, C8–N3–N2 and N3–N2–C6, and N2–C6–C5 and C6–C5–N1 are 10.38, 0.52, 2.32, and 6.78° indicate that the molecule is nearly planar. The perchlorate (ClO<sub>4</sub><sup>-</sup>) and water molecules are placed in opposite directions concerning the ligand backbone. The delocalization of  $\pi$ -electron clouds of the thiazole ring is assigned from two



**Figure 4.** Cyclic voltammogram of **3** in acetonitrile containing tetrabutyl ammonium perchlorate as a supporting electrolyte at a scan rate of 20 mV/s.

sufficiently different bond distances, namely, C8–N4 (1.308 Å) and C10–N4 (1.398 Å). The ligand molecule crystallizes in a Z-isomeric form and stabilized through intermolecular H-bonding with N1–H1A···O12 of ClO<sub>4</sub><sup>−</sup> at distance 2.23 Å and N3–H3A···O100 of a water molecule at a distance 2.150 Å (Figure 6a). The corresponding H-bonds are given in Table S4. The presence of a larger ClO<sub>4</sub><sup>−</sup> anion in the asymmetric unit is preferred for crystallization as perchlorate salt of quaternary pyridinium ion rather than the neutral ligand molecule. The MO orbital picture of PytH·ClO<sub>4</sub> is shown in Figure 5b. The energy difference between HOMO and LUMO is 1.397 eV. The characteristic properties such as molecular planarity, high solubility, and small energy gap of HOMO and LUMO make the ligand a good candidate for biological study.

The asymmetric unit of **2** contains two molecules. The crystal system of **2** is triclinic with the space group  $P\bar{1}$ . Each manganese center is coordinated with two neutral ligands (PytH·ClO<sub>4</sub>) forming a rigid distorted octahedral geometry with a *mer* configuration (Figure 7). The primary valency of **2** is satisfied by two ClO<sub>4</sub><sup>−</sup> ions present outside of the

coordination zone confirming the +2 oxidation state of manganese. Each ligand acts as a neutral tridentate NNN donor and forms five-membered chelate rings with Mn(II) ions. Two axial bonds are nearly the same, for example, Mn–N1 (2.285 Å) and Mn–N4 (2.305 Å), and four equatorial bonds are also very close in values, for example, Mn–N2 (2.233 Å), Mn–N5 (2.241 Å), Mn–N6 (2.262 Å), and Mn–N8 (2.262 Å). All equatorial bond angles, namely, N2–Mn–N5 (106.0°), N5–Mn–N6 (140.9°), N6–Mn–N8 (70.6°), and N2–Mn–N8 (112.3°), deviate from the ideal bond angle. The angles N1–Mn–N2 (70.60), N1–Mn–N5 (105.0), N1–Mn–N6 (96.40), N1–Mn–N8 (81.20), N4–Mn–N2 (70.90), N4–Mn–N6 (122.50), N4–Mn–N8 (109.90), and N4–Mn–N5 (89.60) are not equivalent and are also deviated from 90° of an idealized octahedron, indicating a high level of distortion in the structure of **2** (Table S3). The complex (**2**) is stabilized through hydrogen bonding (Figure 8a),  $\pi\cdots\pi$ , and C–H··· $\pi$  stacking interactions (Figure 8c). Supramolecular associations of **2** are given bc directions in Figure 8b. The energy gap between the HOMO and LUMO is 1.712 eV, and the contribution to the HOMO and LUMO is mainly due to the Mn ion and perchlorate ion. However, the HOMO–LUMO in **1** is mainly formed by the metal ion and ligand moiety (Figure S7), and the corresponding energy gap (0.4217 eV) is lower than **2** or **3**. The lowest HOMO–LUMO energy difference of **1** is responsible for a favorable electronic property than any other complexes.

Complex **3** is a monoclinic crystal system with the space group  $C2/c$ . The perspective view of the complex molecule is given in Figure 9. The geometry of the complex is distorted octahedral with the NiN<sub>6</sub> chromophore where the ligands act as neutral tridentate NNN donors forming a tris complex with *mer* configuration. Two perchlorate ions are present outside of the coordination zone satisfying the +2 oxidation state of Ni(II). Ni(II) is coordinated by two pyridine nitrogen (N1 and N1i), two hydrazone nitrogen (N2 and N2i), and two thiazole nitrogen (N4 and N4i). The relative positions around Ni(II) within the pairs of pyridine nitrogen, hydrazone nitrogen, and thiazole nitrogen are *cis*, *trans*, and *cis*,

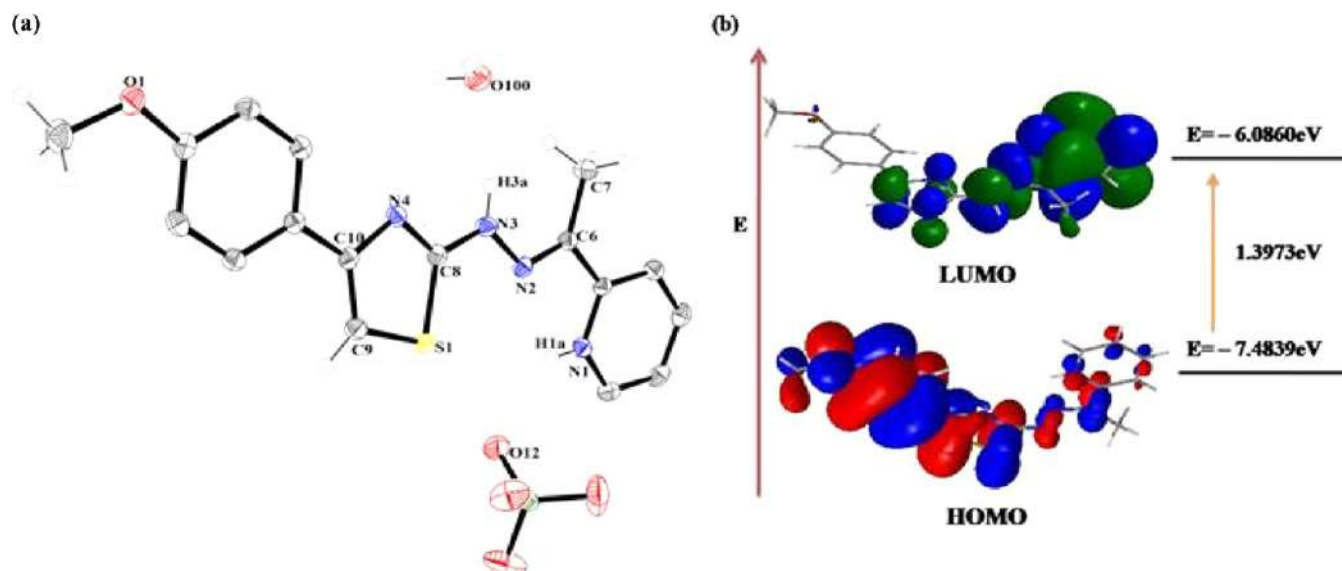


**Figure 5.** (a) Molecular structures of PytH·ClO<sub>4</sub>. Thermal ellipsoids are drawn at the 50% probability label. For the clarity of the structure, some hydrogen atoms have been omitted. (b) HOMO and LUMO energy-level diagrams of PytH·ClO<sub>4</sub>.

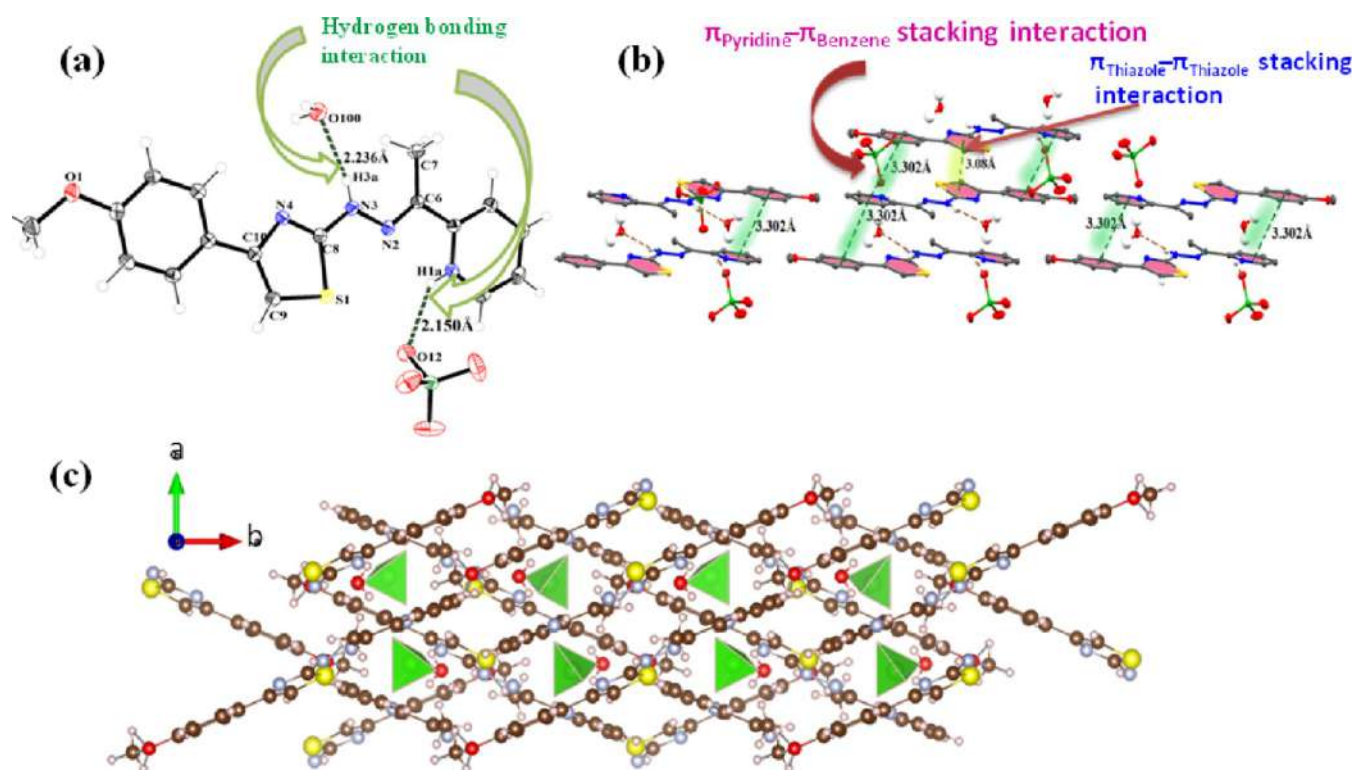


**Figure 6.** (a) Hydrogen bond and (b) different  $\pi$ - $\pi$  stacking interactions form supramolecular structures. (c) 2D framework in crystallographic  $ab$  plane in  $\text{PytH}\cdot\text{ClO}_4$ , where perchlorate ions are shown as green colored polyhedrons.

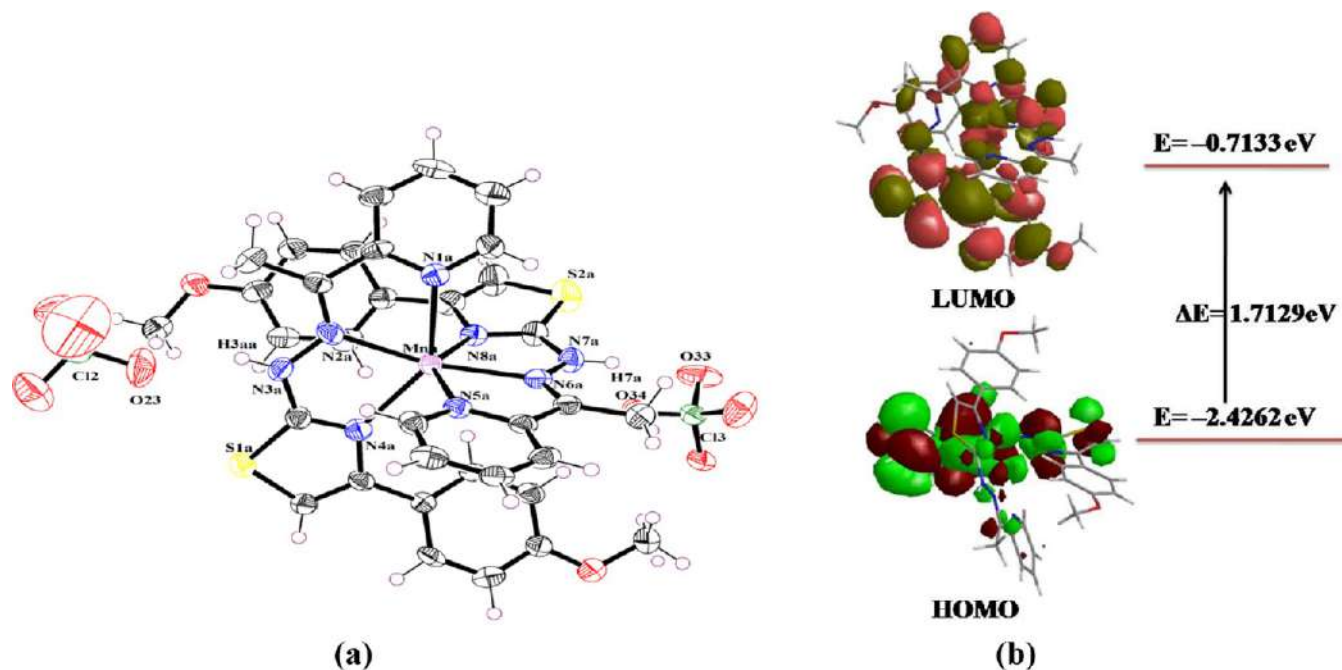


**Figure 7.** (a) Molecular structure of **2** showing the atom numbering scheme. Ellipsoids are drawn at the 50% probability level. (b) HOMO and LUMO energy-level diagrams of **2**.

respectively. The Ni–N1 (pyridine), Ni–N2 (hydrazone), and Ni–N4 (thiazole) bond distances are 2.092(2), 2.021(3), and 2.172(2) Å, respectively, which are close to the values reported earlier.<sup>60</sup> The bite angles formed by similar donor atoms of ligands have the same value [N1–Ni–N2 and N1i–Ni–N2i is 76.94 (10) and N2–Ni–N4i and N2i–Ni–N4 is 105.17 (10)]. The symmetrical biting angles reveal the symmetric

arrangements of ligands in the *bis* chelate complex. Complex (**3**) is stabilized by H-bonding. As shown in Figure 10a, boat-like intermolecular 3D hydrogen bondings are observed in **3** between counter anion ( $\text{ClO}_4^-$ ) and crystal water. Supramolecular association of **3** in  $ab$  directions and  $ac$  direction are shown in Figure 10b,c, respectively. The orbital picture of **3** shows that both ligand and metal orbitals are



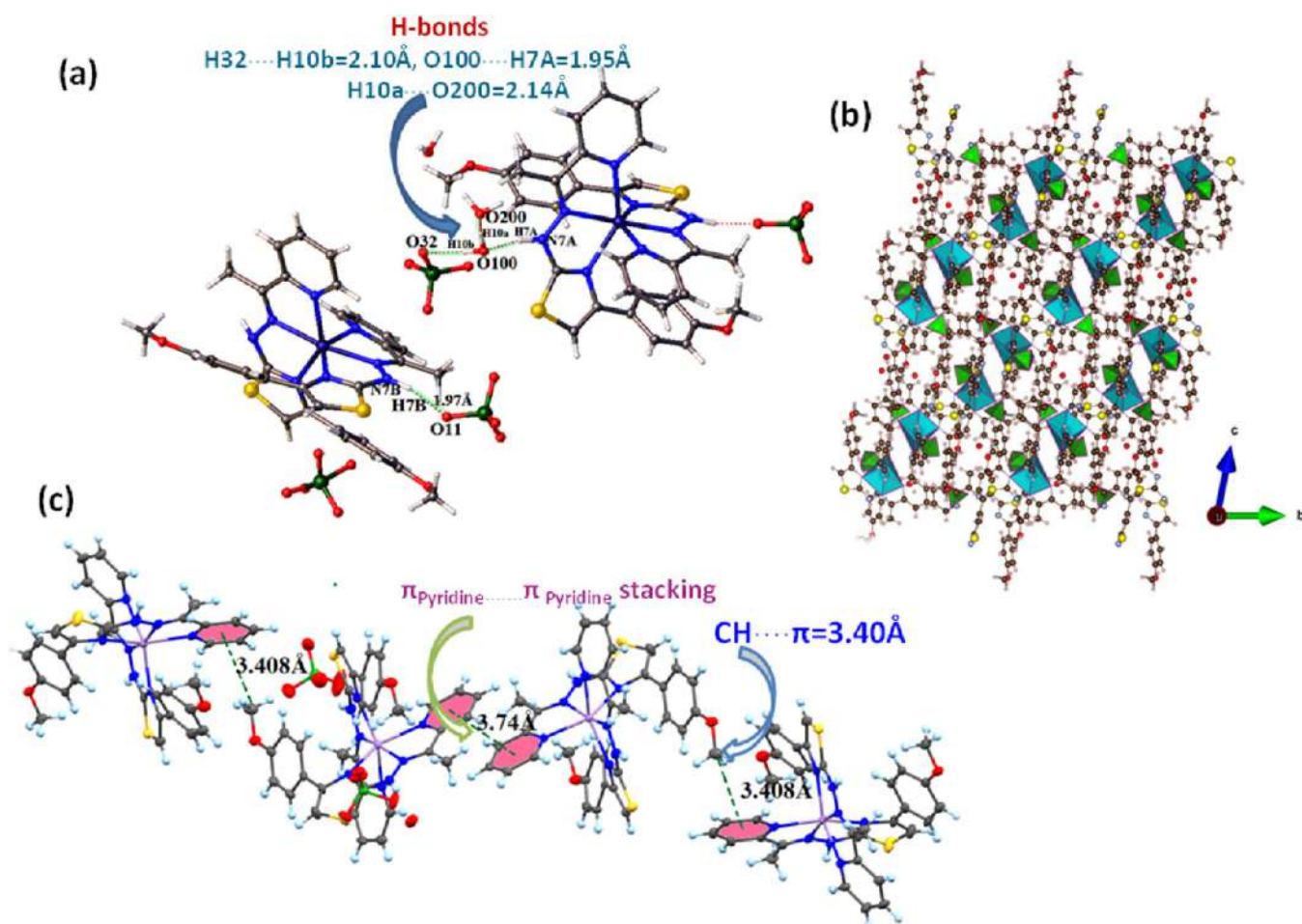


**Figure 8.** (a) Hydrogen bonding in **2**, counter anion ( $\text{ClO}_4^-$ ), and crystal water. (b) Supramolecular association of **2** in the bc direction. (c)  $\pi_{\text{pyridine}} \cdots \pi_{\text{pyridine}}$  stacking and C–H... $\pi_{\text{pyridine}}$  stacking interactions.

participating in HOMO and LUMO orbital formation. The calculated energy gap between HOMO and LUMO is 2.656 eV.

**Biological Activity.** *DNA Binding Study of PytH·ClO<sub>4</sub>, 1, 2, and 3 with CT-DNA.* UV–vis spectroscopy is a common useful method to study the interaction properties of the synthesized compound with DNA (CT-DNA). The shifts (red or blue) of absorption peak wavelength during titration indicated the structural change of DNA in the presence of drug molecules.<sup>62</sup> In our experiment, the absorbance peaks were observed at 270 nm ( $\pi \rightarrow \pi^*$ ) and 413 nm ( $n \rightarrow \pi^*$ ) (for PytH·ClO<sub>4</sub>), 485 nm (d–d transition) (for **1**), 272 and 353 nm (for **2**), and 265 and 486 nm (for **3**) in the absence of CT-DNA. The intensity of the absorbance peak of PytH·ClO<sub>4</sub> increased at 270 and 413 nm with the gradual addition of CT-DNA. The absorbance band intensity of **1**, **2**, and **3** decreased with the addition of CT-DNA. The position of these absorption bands of all compounds shifted slightly to a longer wavelength (3–10 nm), which reveals that the tested compounds have substantial interaction with CT-DNA. As can be seen in Figure 11, the compounds showed a red shift which can be caused by the coupling  $\pi$  orbital of base pair of DNA with the  $\pi^*$  orbital of an external molecule and form  $\pi$ – $\pi^*$  conjugation.<sup>63,64</sup> The binding constant ( $K_b$ ) was calculated from the ratio of slope and intercept by plotting  $[\text{DNA}]/(\epsilon_b - \epsilon_f)$  versus  $[\text{DNA}]$  at a fixed wavelength by increasing the concentration of CT-DNA. The order of  $K_b$

values shown by the tested molecules is PytH·ClO<sub>4</sub> ( $K_b = 9.29 \times 10^5 \text{ mol}^{-1}$ ) > **2** ( $K_b = 8.71 \times 10^5 \text{ mol}^{-1}$ ) > **3** ( $K_b = 7.82 \times 10^5 \text{ mol}^{-1}$ ) > **1** ( $K_b = 7.11 \times 10^5 \text{ mol}^{-1}$ ) according to the equation  $[\text{DNA}]/(\epsilon_a - \epsilon_f) = [\text{DNA}]/(\epsilon_0 - \epsilon_f) + 1/K_b(\epsilon_0 - \epsilon_f)$ . Therefore, it can be concluded that the compounds under investigation behave as intercalators with CT-DNA.<sup>49,65</sup>

**Cytotoxic Activity of PytH·ClO<sub>4</sub>, 1, 2, and 3.** The MTT assay is used to investigate the *in vitro* cytotoxic activities of PytH·ClO<sub>4</sub>, **1**, **2**, and **3** against U-937 human histiocytic lymphoma cells for 72 h in triplicate. Based on the MTT assay results, it is found that compound PytH·ClO<sub>4</sub>, **1**, **2**, and **3** exhibited potent cell death activity as shown in Figure 12. The order of cytotoxicity is observed as **2** > PytH·ClO<sub>4</sub> > **1** > **3**. The Mn(II) complex (**2**) has shown the least IC<sub>50</sub> value ( $0.3976 \pm 0.05 \mu\text{M}$ ), making it most potent among the tested compounds. The data are transformed, normalized, and calculated using GraphPad Prism (Figure 12). PytH·ClO<sub>4</sub> (IC<sub>50</sub> value  $4.374 \pm 0.02 \mu\text{M}$ ) shows higher cytotoxicity than **1** (IC<sub>50</sub> value  $5.583 \pm 0.012 \mu\text{M}$ ) and **3** (IC<sub>50</sub> value  $11.63 \pm 0.01 \mu\text{M}$ ). The MTT assay indicates that both ligand PytH·ClO<sub>4</sub> and its Co(III) and Mn(II) complexes showing antiproliferative activity can be used as potent antitumor agents against the U-937 cancer cell line.

**Live and Dead Cell Assay.** Live and dead cell assay is performed to check the cell viability properties of the synthesized compounds against the U-937 cells. The principle for this assay is that the non-fluorescent calcein AM is

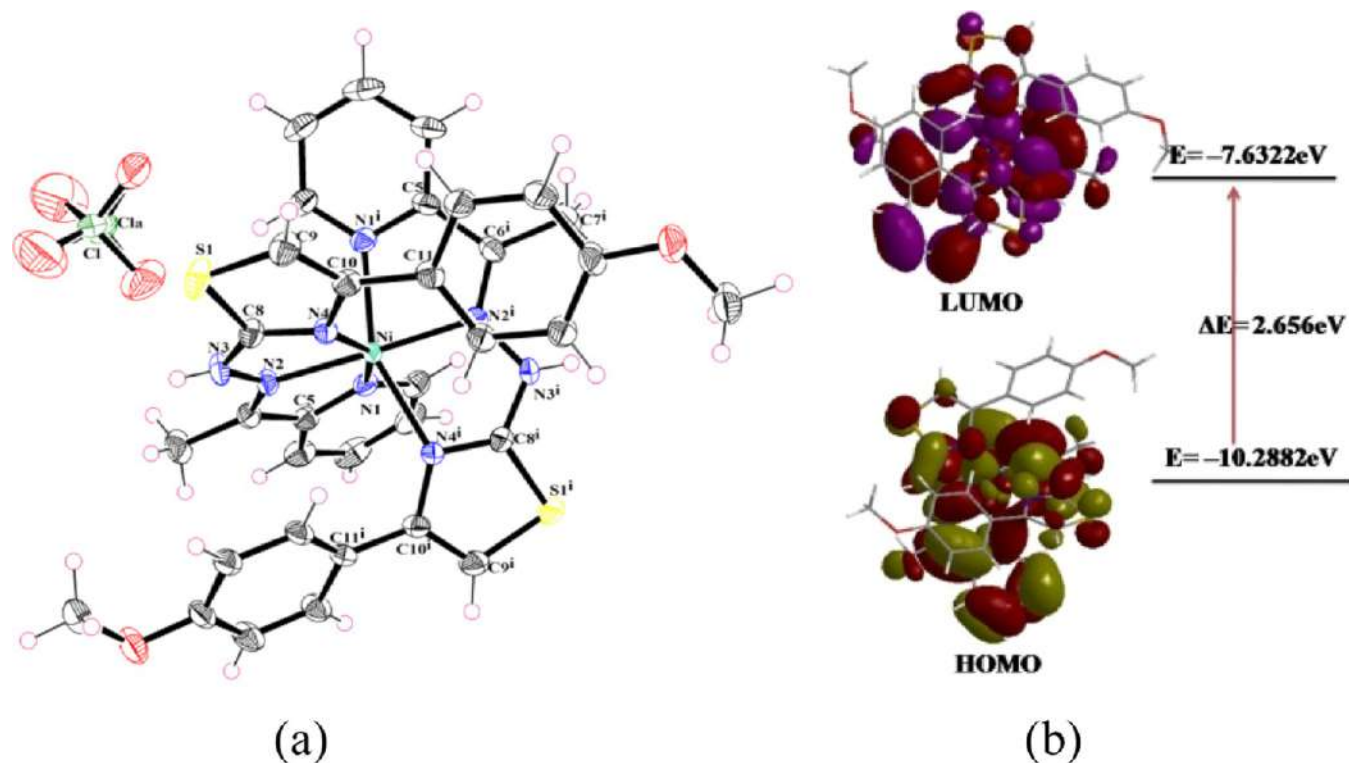


**Figure 9.** Molecular structure of **3** (a) showing the atom numbering scheme. Ellipsoids are drawn at the 50% probability level (a). HOMO and LUMO energy-level diagram of **3** (b).

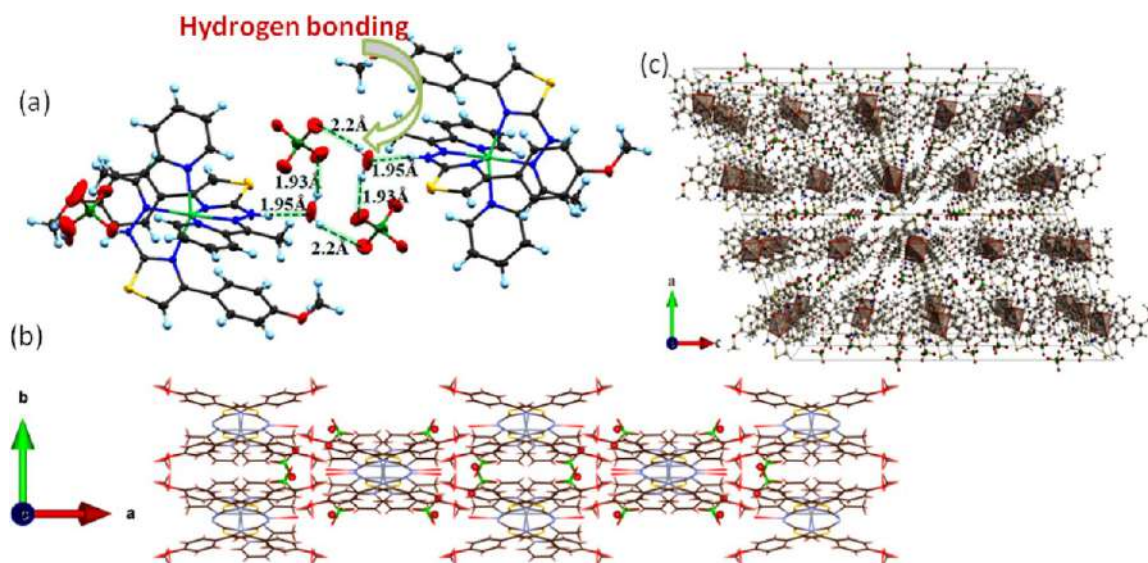


**Figure 10.** (a) Boat-like intermolecular 3D hydrogen bonding interactions in complex **3** between counter anion ( $\text{ClO}_4^-$ ) and crystal water. (b) Supramolecular association of **3** in *a*, *b* directions. (c) Supramolecular ( $2 \times 2 \times 2$  cells) structure of **3** in *a*, *c* directions.

converted to a green fluorescent calcein in live cells after acetoxymethyl ester hydrolysis by intracellular esterase. Propidium iodide, a membrane impermeant dye, binds to double-stranded DNA through intercalation after crossing the plasma membrane of dead cells. U-937 cells, treated with  $5 \mu\text{M}$   $\text{PytH} \cdot \text{ClO}_4$ , **1**, **2**, and **3** and  $2 \mu\text{M}$  doxorubicin, were incubated at  $37^\circ\text{C}$  in a  $5\%$   $\text{CO}_2$  incubator overnight. After incubation, the cells were centrifuged and washed thrice with PBS and stained with  $5 \mu\text{M}$  calcein-AM 4',5'-bis(*N,N*-bis-(carboxymethyl)aminomethyl)fluorescein acetoxymethyl ester along with propidium iodide to determine the live and dead

cell population in the treated cells. The green-stained cells indicated the presence of live cells, whereas propidium iodide-stained red cells indicated the dead cell population after treatment as shown in Figure 13A. The stained cells were observed under an Olympus IX73 Fluorescent Microscope.<sup>66,67</sup> As can be seen in Figure 13B, about 88.5% of cells are dead in the presence of  $\text{PytH} \cdot \text{ClO}_4$  and 80.5% of cells are dead by **2** at a  $5 \mu\text{M}$  concentration. The results are consistent with the data of the MTT assay. Henceforth, it could be concluded that  $\text{PytH} \cdot \text{ClO}_4$  and **2** (Mn-complex) exhibit more cell death than **1** and **3** against U-937.

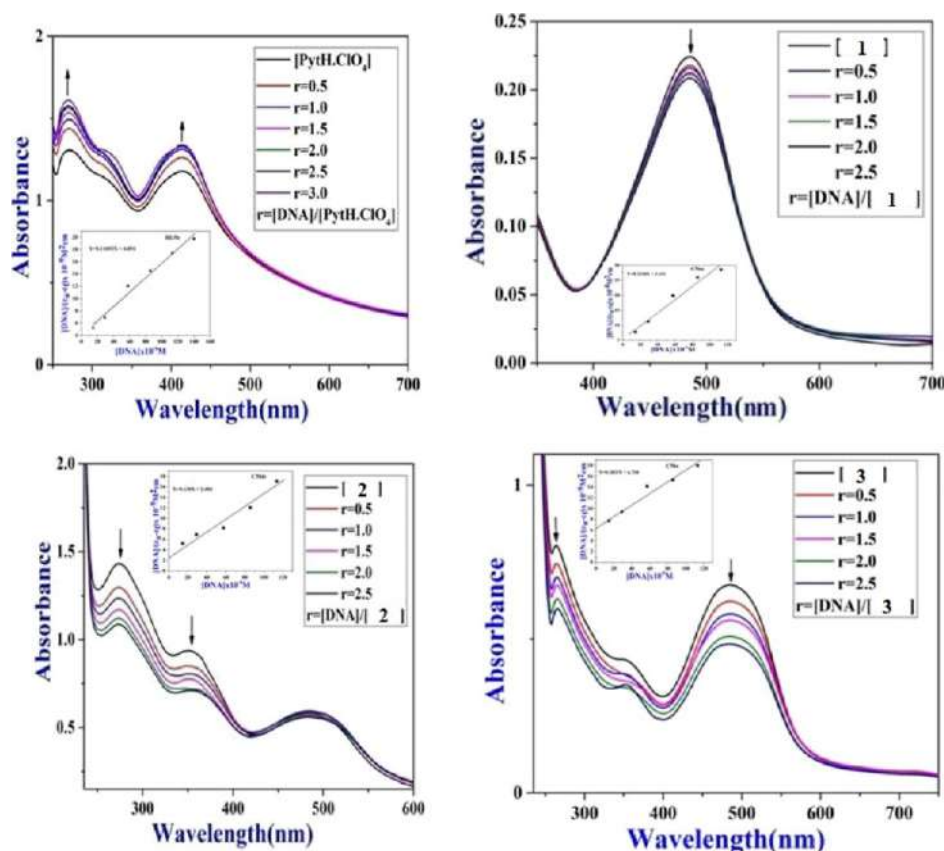


**Figure 11.** Absorption spectra of complex ( $[\text{complex}] = 29.4 \times 10^{-6} \text{ M}$ ) in the absence and presence of increasing amounts of CT-DNA at room temperature in 50 mM Tris-HCl/NaCl buffer (pH = 7.4). Inset: Plot of  $[\text{DNA}]/(\epsilon_b - \epsilon_t)$  vs  $[\text{DNA}]$  for absorption titration of CT-DNA with **Pyth**-**C10<sub>4</sub>** and **1**, **2**, and **3**.

**Lactate Dehydrogenase Release Assay.** Lactate dehydrogenase (LDH) release assay is a gold standard technique to distinguish apoptotic (programmed cell death) mode of cell death over the necrotic mode of cell death. The amount of LDH release is quantified at 6 h. LDH enzyme, a marker of cytoplasm leakage due to necrosis, is assayed to elucidate the physiological pathway, followed by compounds to elucidate their action on the cells. The compounds **1**, **2**, and **Pyth**-**C10<sub>4</sub>** did not release significant LDH at concentrations equivalent to the  $\text{IC}_{50}$  value and higher concentration (at a double concentration of  $\text{IC}_{50}$ ) (Figure 14). However, compound **3** released LDH at the  $\text{IC}_{50}$  and double  $\text{IC}_{50}$  values, indicating the necrotic mode of cell death.<sup>68,69</sup> Therefore, it is now safe to conclude that the compounds **Pyth**-**C10<sub>4</sub>**, **1**, and **2** exhibit the apoptotic mode of cell death, and **3** follows the necrotic mode of cell death. Further, the apoptosis mode of cell death is investigated by PARP and caspase 3 cleavages.

**PARP-1 Cleavage Activity of **Pyth**-**C10<sub>4</sub>**, **1**, **2**, and **3**.** Poly(ADP-ribose)polymerase (PARP) is a highly abundant nuclear enzyme involved in the DNA repair process. PARP synthesizes poly-ADP ribose from  $\text{NAD}^+$  in response to DNA damage. The activation of the apoptosis-specific family of proteases such as active caspases results in the cleavage of PARP. The cleavage produces a C-terminal 89 kDa fragment, which is detected by western blot. The whole cell lysates of U-937 cells treated with **Pyth**-**C10<sub>4</sub>**, **1**, **2**, and **3** at 40  $\mu\text{M}$  were probed for cleaved PARP and cleaved caspase 3 using western blot. The cells treated with **Pyth**-**C10<sub>4</sub>**, **1**, and **2** (except **3**) had shown a band of cleaved PARP and cleaved caspase 3,

confirming the apoptosis mode of cell death (Figure 15) among the tested compounds.<sup>70–73</sup> This result was also attested by the low level of LDH release by **Pyth**-**C10<sub>4</sub>**, **1**, and **2**. It is interesting to note that **3** has shown significant LDH release and does not show any sign of PARP cleavage. The above discussion revealed that compounds **Pyth**-**C10<sub>4</sub>**, **1**, and **2** show apoptosis mode of cell death, and they can be used as potent anticancer agents for future study.

**PBMC Viability Assay.** The cytotoxicity of **Pyth**-**C10<sub>4</sub>**, **1**, **2**, and **3** is checked on PBMCs using the MTT assay. These compounds were treated on PBMCs (PBMCs) and isolated from fresh human blood with  $\text{IC}_{50}$  values and twice  $\text{IC}_{50}$  values. Both **Pyth**-**C10<sub>4</sub>** and **2** showed no toxic effects to PBMCs compared to control (Figure 16). It can be concluded that **Pyth**-**C10<sub>4</sub>**, **1**, and **2** can be trailed as a potential antitumor agent against U-937 tumor cells, without affecting primary cells.

**Molecular Docking Study of **Pyth**-**C10<sub>4</sub>**, **1**, **2**, and **3** with DNA.** The docking studies of the synthesized ligand and its derivatives were performed with DNA using Auto Dock Tools.<sup>32</sup> The best affinity modes of docked compounds **Pyth**-**C10<sub>4</sub>**, **1**, **2**, and **3** with DNA are shown in Figures 17, S8, 18, and S9, respectively. The various types of interactions such as hydrogen bonding,  $\pi$ - $\pi$  stacking, cationic- $\pi$  interactions, and hydrophobic are present between docked compounds and base pairs of DNA. The free binding energies of **Pyth**-**C10<sub>4</sub>**, **1**, **2**, and **3** with DNA are  $-9.79$ ,  $-5.69$ ,  $-6.58$ , and  $-6.08$  Kcal/mol, respectively, and other binding parameters are given in Table 2.

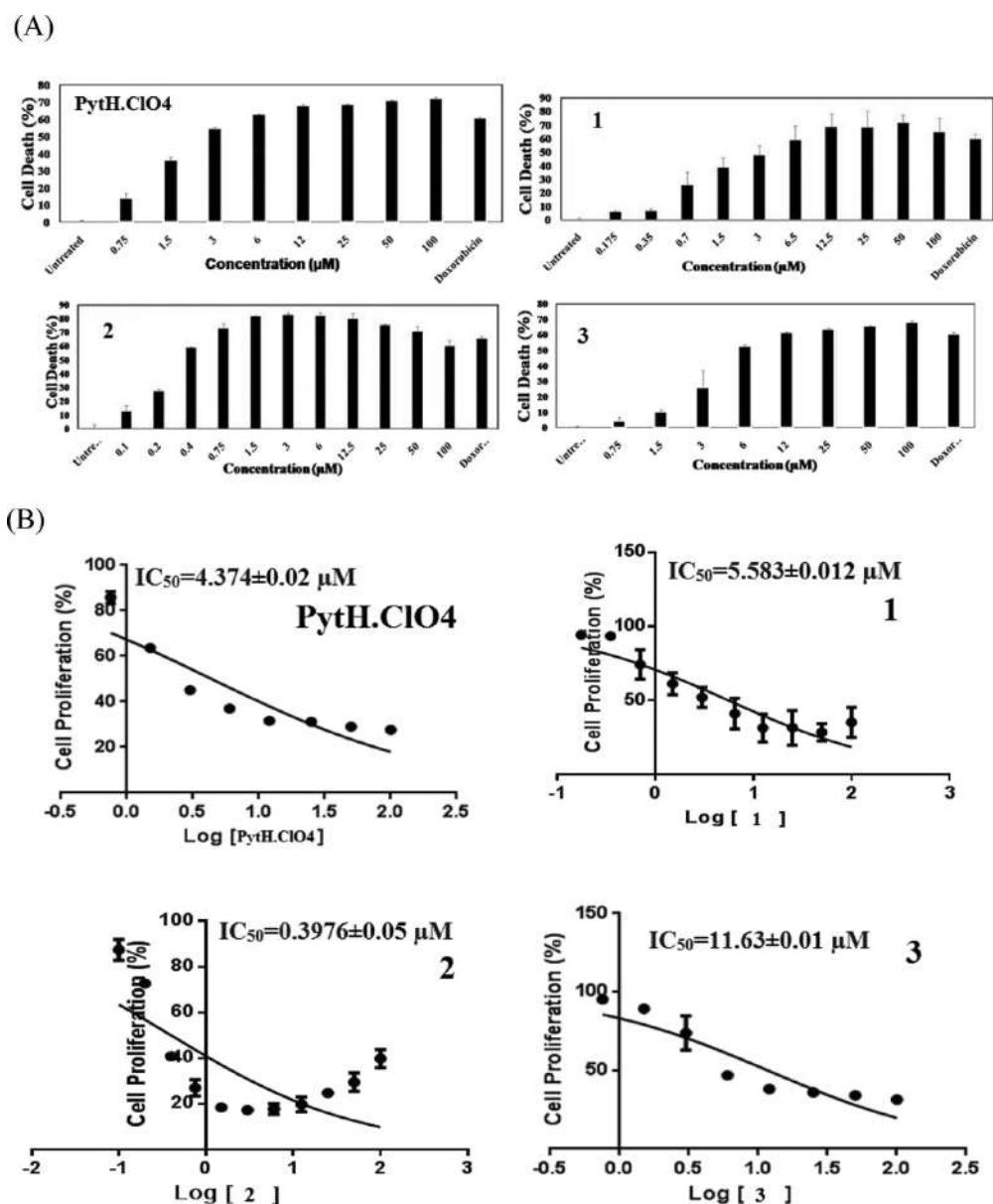


**Figure 12.** U-937 cells (5000 cells/well of a 96-well plate) are treated with different concentrations of ligand (PytH·ClO<sub>4</sub>) and its derivatives 1, 2, and 3 for 72 h in triplicate. The MTT cell viability was assayed. The mean cell death from triplicate samples is calculated in percentage, considering that the untreated cell death is 0% and is indicated in graph (A). U-937 cells were treated as shown above for 72 h with different concentrations of PytH·ClO<sub>4</sub>, 1, 2, and 3 and the MTT assay was carried out. The percentage of cell viability is plotted in the group (B). Data are transformed and normalized, and IC<sub>50</sub> values are calculated using GraphPad Prism.

PytH·ClO<sub>4</sub> interacted with Cyt9 through hydrogen bonding (PytH·ClO<sub>4</sub>)N···H-Cyt9 at a distance of 2.28 Å. The  $\pi$  (alkyl group of PytH·ClO<sub>4</sub>)– $\pi$  (DNA base pair) stacking interaction was observed between the acetyl group attached with pyridine of PytH·ClO<sub>4</sub> and pi-electron clouds of cytosine 9 (Cyt9). On the other hand, the base pair of Ade6 and Thy20 interacts with the methoxy group with  $\pi$  (alkyl group of PytH·ClO<sub>4</sub>)– $\pi$  (DNA base pair) stacking interaction with maintaining the distances of 4.74 and 3.21 Å, respectively. The C (thymine)–O (PytH·ClO<sub>4</sub>) charge–charge interaction with a distance of 3.62 Å also stabilized the ligand–DNA adduct as shown in Figure 17b,c. The interaction position shows that it acts as a major groove binder with DNA (Figure 17a), and the binding parameters implied that it also behaved as a good intercalator with a DNA base pair. The intercalating nature of PytH·ClO<sub>4</sub> is due to the molecular planarity, and suitable size is

susceptible to penetrate in the double-stranded DNA base pair, which may be the cause of higher binding energy of PytH·ClO<sub>4</sub> (–9.79 Kcal/mol).

The binding free energy of 1 is –5.69 Kcal/mol. The docking result of the complex 1 exhibits mainly  $\pi_{\text{Alkyl}(1)}$ – $\pi$  (DNA base pairs), the interaction between different base pairs of DNA with the methoxy group of the coordinated ligand moiety to stabilize the DNA–metal complexes shown in Figure S8. The C<sub>Thymine</sub>–O<sub>(PytH·ClO<sub>4</sub>)</sub> charge–charge interaction with a distance of 3.07 Å was also observed between 1 and DNA. No hydrogen bonding interactions are found between 1 and DNA. The docking study also reveals that complex 1 acts as a minor groove binder with double-stranded DNA. The docking parameter given in Table 2 shows that the incorporation of metal ions in the ligand reduces the binding free energy of

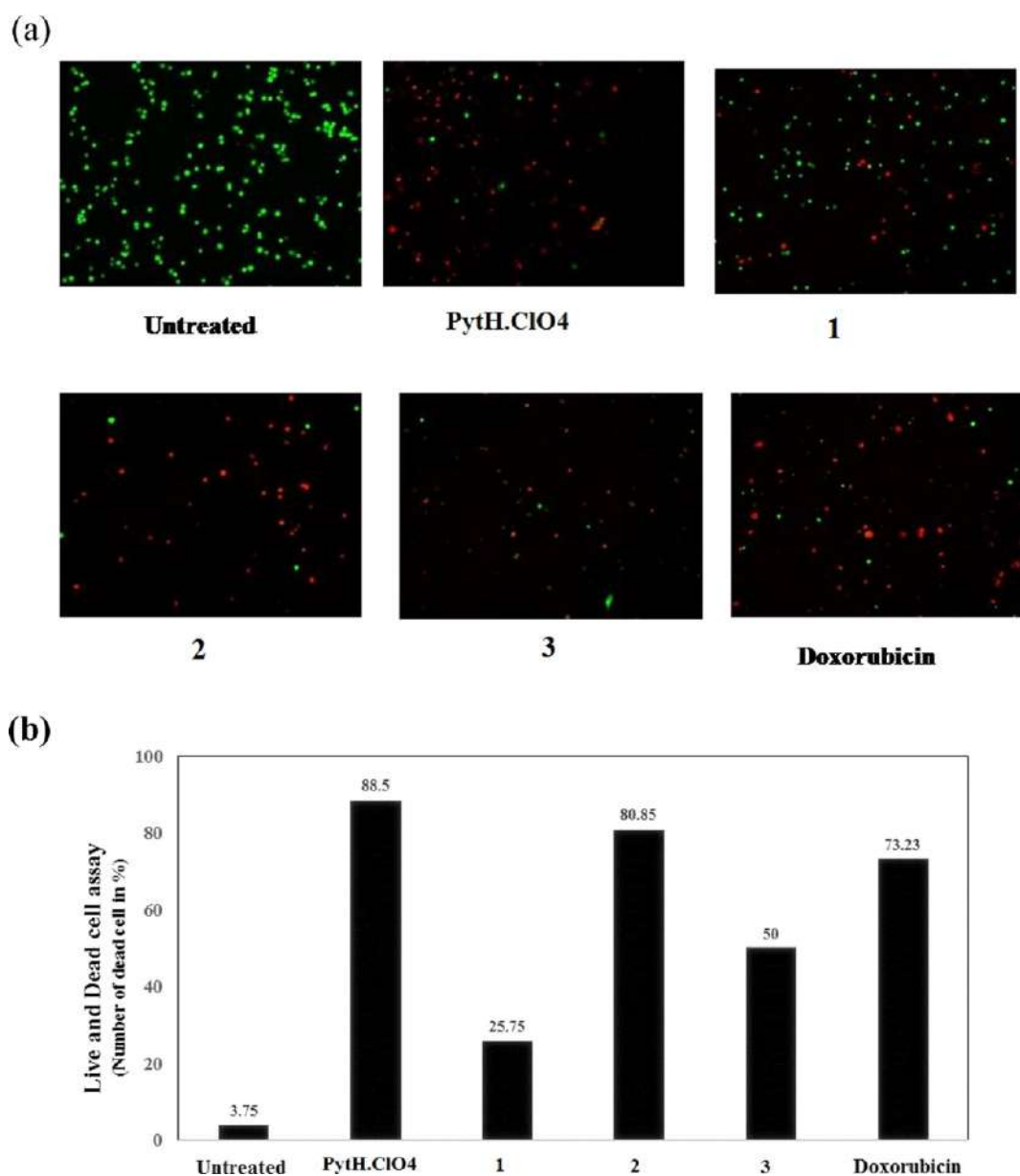


**Figure 13.** (A) Live and dead cell assay showing the effect of PytH.CIO<sub>4</sub> and its derivatives **1**, **2**, and **3** on the viability of U-937 cells at 5  $\mu$ M concentration with doxorubicin (2  $\mu$ M) as a positive control using a fluorescence microscope. (B) For the same data, the percentage of cell death is calculated and plotted as a bar graph.

metal complexes. The free energy of binding of **2** is  $-6.58$  Kcal/mol, and other parameters are given in Table 2. Complex **2** interacts with the base-paired DNA with various interactions; hydrogen bonding interactions are observed in the S-atom of the thiazole moiety with the H-atom attached with the Gua4 base pair at a distance of 2.11 Å. The  $\pi$  (DNA base pair)–alkyl group (coordinated ligand) was also observed between the methoxy group of the coordinating ligand and the  $\pi$ -electron cloud of Ade6, Gua22, and Cyt21 base pair of DNA shown in Figure 18. Another  $\pi$  (coordinated ligand)– $\sigma$  (CH<sub>3</sub> group of DNA base) and  $\pi$  (thiazole S)– $\pi$  (DNA base pair) stacking interaction are seen between the coordinated ligand and Ade5, Cyt23, and Gua4 with maintaining a distance of 3.36, 3.82, and 4.16 Å respectively. The most favorable dock position of **2** with DNA exhibits a major groove binder. The docking parameter shows that the number of interactions in **2** with DNA base pair is greater than **1** and **3**. The findings of docking results under

investigation attested to the results of the DNA binding and cytotoxicity study.

The estimated free binding energy of complex **3** is 6.08 Kcal/mol. Compound **3** interacts to the DNA base pairs mainly with hydrogen bonding,  $\pi$ –alkyl,  $\pi$ –anion, and charge–charge stacking interaction shown in Figure S9. The  $\pi$ -electron cloud of DNA base pairs of Gua4 holds with the CH<sub>3</sub>O– group of the coordinated ligand with a distance of 4.62 and 5.14 Å, respectively. The hydrogen bonding interaction observed between H-attached to Gua4 and methoxy-O of the coordinated ligand at a distance of 1.99 Å. The  $\pi$  (coordinated ligand)–anion (PO<sub>4</sub><sup>3-</sup>) interaction observed between the thiazole or benzene ring of coordinated ligands and O-atoms of PO<sub>4</sub><sup>3-</sup> attached to thiamin 7, adenine 6, and cytosine 21 shown in Figure S9. The  $\pi$  (DNA)–sulfur (thiazole moiety) interaction and charge–charge also contributes free binding energy. The number of DNA interactions of **3**

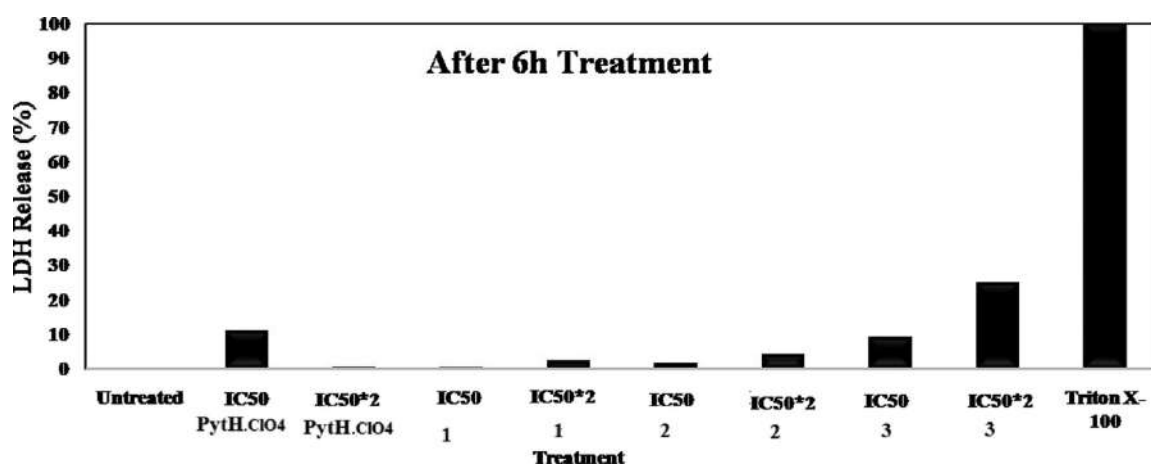


Figure 14. U-937 cells are treated with IC<sub>50</sub> and double IC<sub>50</sub> values of ligand PytH·ClO<sub>4</sub> and its derivatives 1, 2, and 3 for 6 h. LDH release is plotted as a percentage against Triton X-100, which is considered as 100% and untreated cells are considered as 0%.

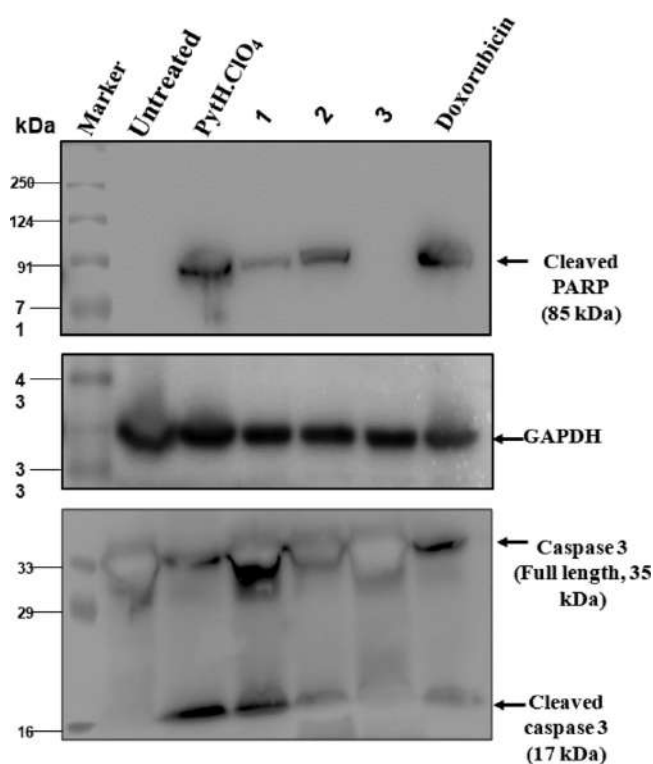


Figure 15. U-937 cells were treated with 5  $\mu$ M PytH·ClO<sub>4</sub> and its derivatives 1, 2, and 3. The whole cell lysate was probed for cleaved PARP-1, full-length caspase 3, and cleaved caspase 3 on western blot. The same blot was probed for GAPDH as a loading control. Cells treated with doxorubicin were considered as a positive control.

is higher than that of 1 but less than that of 2. This result also supports the order of Kb values obtained from the DNA binding experiment. The analysis of the docking result implies that the compounds can intercalate with DNA.<sup>33,55,65,74</sup>

**MD Study.** A docking study is carried out to find out probable binding interaction sites in between DNA and different guest molecules. Subsequently, to check the binding stability of guest–DNA adducts, an MD simulation study is performed for 20 ns. This study also gives information related to the comparison of the DNA binding stability of the ligand (PytH·ClO<sub>4</sub>) (metal free) with different metal-incorporated species (namely, metal complexes 1–3). The MD simulation

study shows that the DNA and ligand trajectories are not very much close to each other due to the absence of the ligand from the docking site. The radius of gyration confirms that these systems followed a harmonious swirl throughout the dynamics (please see the Supporting Information Videos). After MD simulation, the coordinates of the most important binding residues are changed for PytH·ClO<sub>4</sub> (Figure 19A). Interestingly, the ligand (PytH·ClO<sub>4</sub>) became unglued from the docked site after a 3.5 ns run of MD simulation and traveled in the solvent system. However, all the metal complexes (1–3) are almost stable in their docked positions as shown in Figure 19C,D for 2 and Figure S10 for 1 and 3. Moreover, two H-bond interactions with the adenine residues of the DNA structure and 2 increase the binding affinity. In addition, the 2-DNA system shows several  $\pi$ – $\pi$  static hydrophobic interactions with the aromatic adenine and guanine residues. As can be seen in the RMSD plot in Figure 19B,C, the metal complexes are more stable than the ligand. The RMSD plots of 1 and 3 are given in the Supporting Information (Figure S11). The maximum binding stability of 2 accounts for its good in vitro activity and DNA binding affinity. This study helps to conclude that the incorporation of metal into an organic small molecule persists planarity as a whole to the molecular system, which substantially improves the penetration of the molecule inside the DNA groove. In addition, a relative binding free energy study of 2 ( $-544.03 \pm 9.54$  Kcal/mol) is found in the MMPBSA methodology, which showed a strong affinity toward the DNA binding site in comparison to PytH·ClO<sub>4</sub> ( $+8.15 \pm 4.10$  Kcal/mol). Other metal complexes (i.e., 1 and 3) also exhibited a prominent binding free energy profile ( $-655.11 \pm 9.88$  Kcal/mol for 1 and  $-553.0659 \pm 7.7866$  Kcal/mol for 3). The difference in the binding free energies of metal-free ligands and metallated ligands is observed not due to over polarization but due to the probable presence of a higher electrostatic interaction of the divalent metal ions (Figures S12 and S13). This data proves the significant improvement in showing the antiproliferative activity of 2 concerning the parent ligand inherited from Mn<sup>2+</sup> present in the system.

Generally, an enhanced anticancer efficacy was observed when the ligand is attached to the metal center.<sup>17–19,75,76</sup> In the present study, a significant change in the anticancer property of the perchlorate salt of ligand (PytH·ClO<sub>4</sub>) is not observed in coordination with the metal ion. Notably, ligand

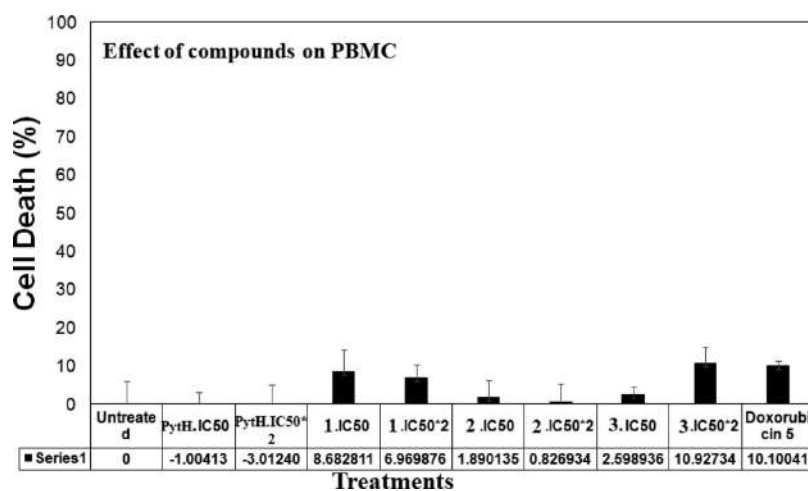


**Figure 16.** Effect of PytH·ClO<sub>4</sub> and its metal derivatives 1, 2, and 3 on PBMC. PBMCs seeded in triplicates were treated with IC<sub>50</sub> and with double the IC<sub>50</sub> values for 24 h. Cell death was calculated with the MTT assay.

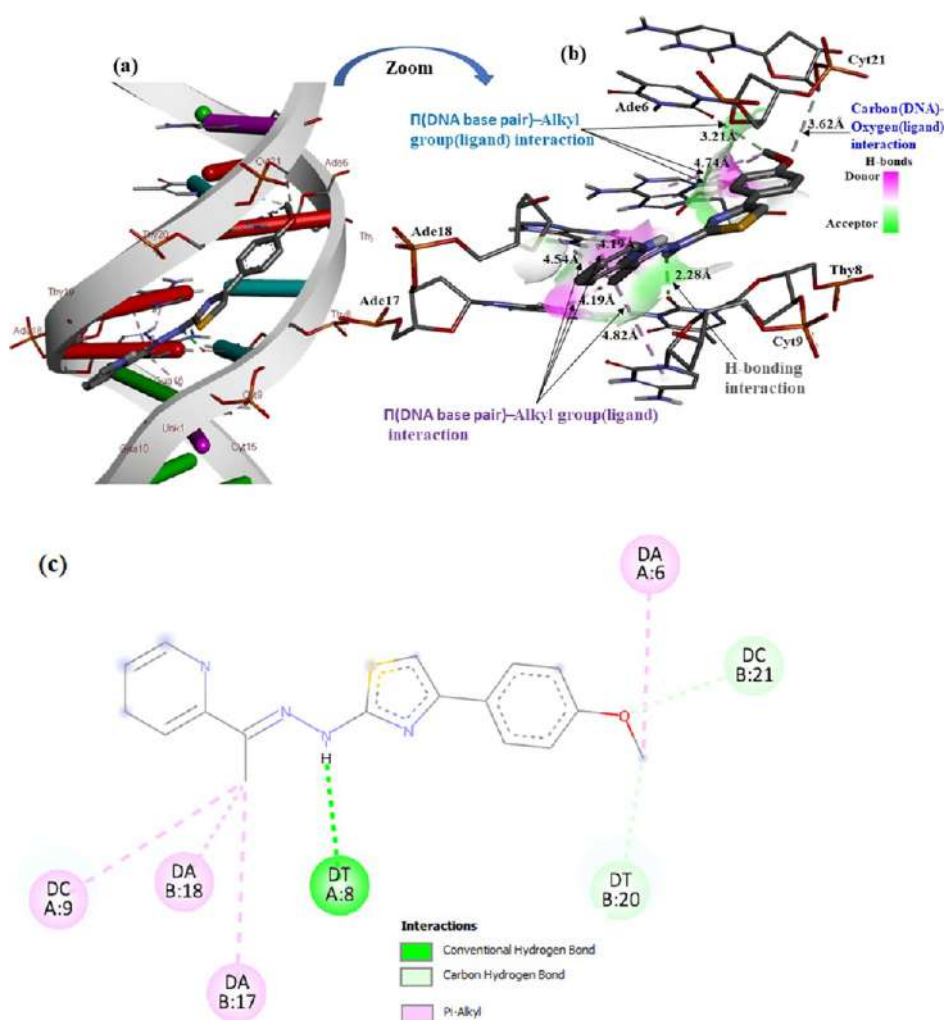


**Figure 17.** (a) Different interactions between PytH·ClO<sub>4</sub> and DNA and (b) zoom picture showing hydrogen bonding, hydrophobic,  $\pi$ - $\pi$ ,  $\pi$ -alkyl, cationic- $\pi$  carbon (DNA)-oxygen(ligand) interactions where DNA is shown on the surface and PytH·ClO<sub>4</sub> is shown in the ball stick model and (c) shows the 2d model of PytH·ClO<sub>4</sub> and DNA.

and its Mn(II) complex (2) showed the most promising anticancer activity. There is a straightforward parallel relationship between the experimental values of DNA binding study to that of the theoretical docking values, that is, PytH·ClO<sub>4</sub> ( $K_b =$

$9.29 \times 10^5 \text{ mol}^{-1}$ ;  $\Delta G_{\text{binding}} = -9.79 \text{ Kcal/mol}$ ) > 2 ( $K_b = 8.71 \times 10^5 \text{ mol}^{-1}$ ;  $\Delta G_{\text{binding}} = -6.58 \text{ Kcal/mol}$ ) > 3 ( $K_b = 7.82 \times 10^5 \text{ mol}^{-1}$ ;  $\Delta G_{\text{binding}} = -6.08 \text{ Kcal/mol}$ ) > 1 ( $K_b = 7.11 \times 10^5 \text{ mol}^{-1}$ ;  $\Delta G_{\text{binding}} = -5.69 \text{ Kcal/mol}$ ). However, the

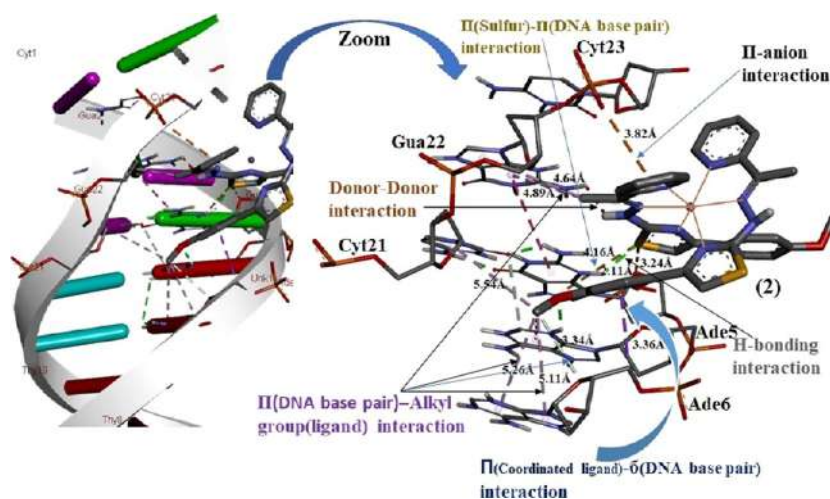


**Figure 18.** Various types of stacking interactions of **2** with DNA base pair, namely,  $\pi$  (thiazole/benzene)  $\cdots \sigma$  (O atom of  $\text{PO}_4^{4-}$  of Guanine19) and  $\sigma\text{N}7 \cdots \sigma$  (O atom of  $\text{PO}_4^{4-}$  of Guanine30). The DNA is shown on the surface, and the complex is shown in the ball stick model.

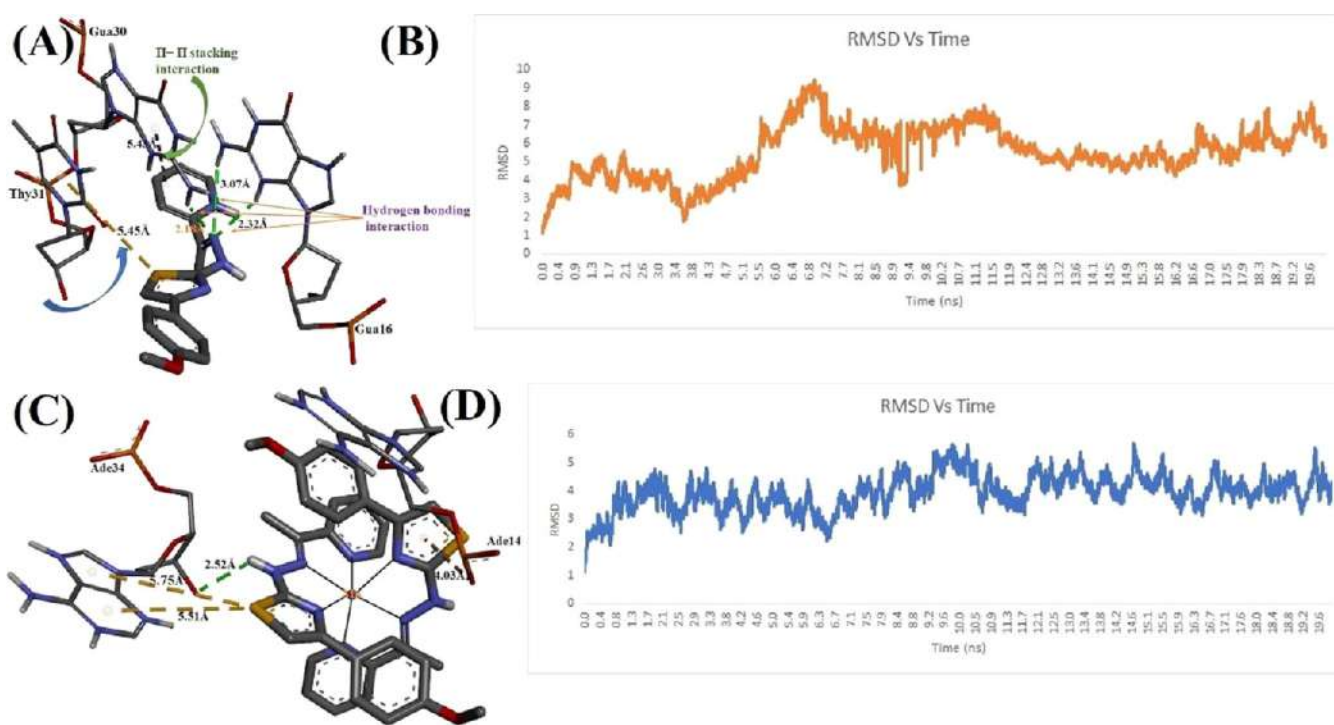


**Figure 19.** Results of MD simulation studies of  $\text{PytH}\cdot\text{ClO}_4$  and **2**. (A,C) indicate the binding conformation of  $\text{PytH}\cdot\text{ClO}_4$  and **2**, respectively. The green dotted lines indicate the H-bond interaction sites. (B,D) indicate the RMSD plot of  $\text{PytH}\cdot\text{ClO}_4$  and **2** concerning the MD simulation time (up to 20 ns).

cytotoxicity order varies from the trend; the order of cytotoxicity is observed as  $\mathbf{2} > \text{PytH}\cdot\text{ClO}_4 > \mathbf{1} > \mathbf{3}$ . However, the highest cytotoxicity of complex **2** is consistent with the  $K_b$  and  $\Delta G_{\text{binding}}$  value concerning the other metal complexes under investigation. The highest binding free energy value of  $\text{PytH}\cdot\text{ClO}_4$  ( $-9.79$  Kcal/mole) is expected for its planar structure having significant anticancer potential ( $\text{IC}_{50}$ :  $4.374 \pm 0.02$   $\mu\text{M}$ ) next to the Mn(II) complex ( $\text{IC}_{50}$ :  $0.3976 \pm 0.05$   $\mu\text{M}$ ). The order of anticancer efficacy among the metal complexes has come out with their binding free energy order. Additionally, the highest anticancer property of the Mn(II) complex (**2**) may be attributed to the preferable reduction potential profile undergoing facile reduction steps than any other compounds under discussion. It is worth mentioning that

the perchlorate compounds under experiment show better antitumor efficacy than the recently published compounds bearing the thiazole–pyrazole unit.<sup>18,19</sup>

## CONCLUSIONS

The thiazole and pyridine derivatives are a class of organic compounds showing excellent biological activity. A thiazolyl pyridinium perchlorate molecule ( $\text{PytH}\cdot\text{ClO}_4$ ) and its cobalt(III), manganese(II), and nickel(II) perchlorate complexes are synthesized and structurally characterized. The ligand  $\text{PytH}\cdot\text{ClO}_4$  having a rigid and quasi *e*-configuration forms distorted octahedral complexes with the composition  $[\text{Co}(\text{Pyt})_2]\text{ClO}_4$ ,  $[\text{Mn}(\text{PytH})_2](\text{ClO}_4)_2$ , and  $[\text{Ni}(\text{PytH})_2](\text{ClO}_4)_2$ . The asym-



metric unit of the Co(III) and Mn(II) complexes contains crystallographically independent twin  $[\text{Co}(\text{Pyt})_2]^+$  and  $[\text{Mn}(\text{PytH})_2]^{2+}$  entities, respectively. The coordination sites of the complex are occupied by two heterocyclic “N” atoms (one from pyridine and another from thiazole) and one hydrazinic “N” atom of each ligand forming five-membered cyclic rings. The ligands bind to metal through *mer* configuration. The compounds show prominent antiproliferative activity against human monocytic cells (U-937). Compound **2** and  $\text{PytH}\cdot\text{ClO}_4$  exhibit better activity with  $\text{IC}_{50}$  values  $0.3976 \pm 0.05 \mu\text{M}$  and  $4.374 \pm 0.02 \mu\text{M}$  than **1** ( $5.583 \pm 0.012 \mu\text{M}$ ) and **3** ( $11.63 \pm 0.01 \mu\text{M}$ ). Based on the result of LDH assay and PARP-1 cleavage activity, it is found that  $\text{PytH}\cdot\text{ClO}_4$  and **2** show the apoptosis mode of cell death, whereas **1** and **3** show the necrotic mode of cell death. The DNA binding experiment, docking, and MD simulation study reveal their most probable intercalating mode of binding to the base pair of DNA. The PBMC assay reveals the non-toxicity of  $\text{PytH}\cdot\text{ClO}_4$  and **2** toward normal blood cells. In conclusion, the pyridinium thiazole ligand and its metal derivatives emerge as potential antitumor activity, and new advanced research is needed to understand how the mechanism of action of these compounds against tumor cells occurs.

## DATA AND SOFTWARE AVAILABILITY

The study reported in this article has utilized the Orca 4.0 program for DFT calculation of the ground-state electronic structure of the complex. For docking study, the Cartesian coordinate of one PDB code was used, which is reported in the PDB database as primary data. The Cartesian coordinate of this PDB is freely available at <https://www.rcsb.org/>. After the docking study, the PDB was examined in discovery studio software for the 3D interaction diagram of the ligand binding site. The ligand docking in the protein was carried out using open-source software, namely, the AutoDock 4.0 version. The MD simulations were carried out using open-source packages VMD1.9.3 and NAMD2. The trajectories of MD simulations were analyzed in VMD1.9.3 using appropriate scripts provided in the NAMD tutorials/manual. Relative binding free energy was determined involving the open-source CaFE plugin in VMD1.9.3. The plots were generated using the MS Excel (version 2016) and open-source software Grace (version 5.1.25). The 3D figures were generated using the UCSF chimera. Inkscape, an open-source package, was used for figure processing. The animation files of trajectories were generated using the VMD1.9.3 movie plugin.

## ASSOCIATED CONTENT

### Supporting Information

The Supporting Information is available free of charge at <https://pubs.acs.org/doi/10.1021/acs.jcim.1c01280>.

Supporting Information has been provided along with the manuscript for the results and discussion. Due to the very large sizes, the “.dcd files” (trajectories) of MD simulations are not included in the Supporting Information They are available from the authors upon request (PDF)

### Accession Codes

CCDC 1530855, CSD 2010934, and 2010933 for the compounds  $\text{PytH}\cdot\text{ClO}_4$ , **2**, and **3**, respectively. Crystallographic data can be obtained free of charge on application to CCDC, 12 Union Road, Cambridge CB2 1EZ, UK, fax: (+44)

1223 336033, e-mail: [deposit@ccdc.cam.ac.uk](mailto:deposit@ccdc.cam.ac.uk). The computational structures are provided.

## AUTHOR INFORMATION

### Corresponding Authors

**Sunil Kr. Manna** – Centre for DNA Fingerprinting & Diagnostics (CDFD), Hyderabad, Telangana 500 039, India; Adjunct Faculty, Regional Centre for Biotechnology, Faridabad, Haryana 121001, India; Email: [manna@cdfd.org.in](mailto:manna@cdfd.org.in)

**Pulakesh Bera** – Post Graduate Department of Chemistry, Panskura Banamali College (Vidyasagar University), Midnapore (East), West Bengal 721152, India; [orcid.org/0000-0001-8566-0742](https://orcid.org/0000-0001-8566-0742); Email: [pulakeshbera68@gmail.com](mailto:pulakeshbera68@gmail.com)

### Authors

**Pradip Bera** – Post Graduate Department of Chemistry, Panskura Banamali College (Vidyasagar University), Midnapore (East), West Bengal 721152, India; Department of Chemistry, Kandi Raj College, Murshidabad, West Bengal 742137, India

**Abhishek Aher** – Centre for DNA Fingerprinting & Diagnostics (CDFD), Hyderabad, Telangana 500 039, India; Graduate Studies, Regional Centre for Biotechnology, Faridabad, Haryana 121001, India

**Paula Brandao** – Department of Chemistry, CICECO, University of Aveiro, Aveiro 3810-193, Portugal

**Utsab Debnath** – School of Health Science, University of Petroleum and Energy Studies, Dehradun 246007, India

**Varun Dewaker** – Medicinal & Process Chemistry Division, CSIR-Central Drug Research Institute, Lucknow 226031, India

**Abhimanyu Jana** – Post Graduate Department of Chemistry, Panskura Banamali College (Vidyasagar University), Midnapore (East), West Bengal 721152, India; Department of Chemistry, Indian Institute of Engineering Sciences and Technology, Shibpur, Howrah 711103, India

**Chandana Pramanik** – Post Graduate Department of Chemistry, Panskura Banamali College (Vidyasagar University), Midnapore (East), West Bengal 721152, India; Department of Chemistry, Dinabandhu Andrews College, Kolkata, West Bengal 700 084, India

**Basudev Mandal** – Post Graduate Department of Chemistry, Panskura Banamali College (Vidyasagar University), Midnapore (East), West Bengal 721152, India; Department of Chemistry, Shahid Matangini Hazra Govt. College for Women, Midnapore (East), West Bengal 721 649, India

Complete contact information is available at:

<https://pubs.acs.org/doi/10.1021/acs.jcim.1c01280>

### Author Contributions

††P.B. and A.A. contributed equally to this work.

### Notes

The authors declare no competing financial interest.

## ACKNOWLEDGMENTS

We gratefully acknowledge the Council for Scientific and Industrial Research (CSIR), Government of India, for financial support [grant no. 1(2858)/16/EMR-II]. Panskura Banamali College (Autonomous) acknowledges the grants received from the Department of Science and Technology (DST), Govt. of

India through FIST program (No.SR-FIST-COLLEGE-295-dt18/11/2015).

## REFERENCES

- (1) Gouhar, R. S. E.; Ewies, F.; El-Shehry, M. F.; El-Mahdy, E. M.; Shaheen, M. N. F. Synthesis and Reactions of Some New Quinazoline Derivatives for In Vitro Evaluation as Anticancer and Antimicrobial Agents: Synthesis and Anticancer Evaluation of Some New Quinazoline Derivatives. *Pharm. Chem.* **2018**, *10*, 42–54.
- (2) Mohareb, R. M.; Khalil, E. M.; Mayhoub, A. E.; Abdallah, A. E. M. Novel synthesis of pyran, thiophene, and pyridine derivatives incorporating thiazole ring and their antitumor evaluation. *J. Heterocycl. Chem.* **2020**, *57*, 1330–1343.
- (3) Pluta, K.; Morak-Młodowska, B.; Jeleń, M. Recent progress in biological activities of synthesized phenothiazines. *Eur. J. Med. Chem.* **2011**, *46*, 3179–3189.
- (4) Firake, S.; Bari, S. An Insight into Synthetic and Docking Approaches of Benzenesulfonamide Scaffold Revealing COX-2 Inhibitors. *Curr. Enzyme Inhib.* **2015**, *11*, 76–107.
- (5) Bird, C. W. A new aromaticity index and its application to five-membered ring heterocycles. *Tetrahedron* **1985**, *41*, 1409–1414.
- (6) Erlenmeyer, H.; Marbet, R. Zur Kenntnis des  $\alpha$ -[Thiazolyl-(5)]-pyrrolidins. *Helv. Chim. Acta* **1946**, *29*, 1946–1949.
- (7) Kashyap, S. J.; Garg, V. K.; Sharma, P. K.; Kumar, N.; Dudhe, R.; Gupta, J. K. Thiazoles: having diverse biological activities. *Med. Chem. Res.* **2012**, *21*, 2123–2132.
- (8) Gupta, R. R.; Kumar, M.; Gupta, V. *Heterocyclic Chemistry*; Springer-Verlag: Berlin, Heidelberg, New York, 1999; Vol. 2, p 416.
- (9) Breslow, R. On the Mechanism of Thiamine Action. IV.1 Evidence from Studies on Model Systems. *J. Am. Chem. Soc.* **1950**, *80*, 3719–3726.
- (10) Kathiravan, M. K.; Salake, A. B.; Chothe, A. S.; Dudhe, P. B.; Watode, R. P.; Mukta, M. S.; Gadhwane, S. The biology and chemistry of antifungal agents: A review. *Bioorg. Med. Chem.* **2012**, *20*, 5678–5698.
- (11) Bondock, S.; Naser, T.; Ammar, Y. A. Synthesis of some new 2-(3-pyridyl)-4,5-disubstituted thiazoles as potent antimicrobial agents. *Eur. J. Med. Chem.* **2013**, *62*, 270–279.
- (12) Karuvalam, R. P.; Haridas, K. R.; Nayak, S. K. K.; Guru Row, T. N.; Rajeev, P.; Rishikesan, R.; Kumari, N. S. Design, synthesis of some new (2-aminothiazol-4-yl)methyl ester derivatives as possible antimicrobial and antitubercular agents. *Eur. J. Med. Chem.* **2012**, *49*, 172–182.
- (13) Jiang, X.-Y.; Chen, T.-K.; Zhou, J.-T.; He, S.-Y.; Yang, H.-Y.; Chen, Y.; Qu, W.; Feng, F.; Sun, H.-P. Dual GSK-3 $\beta$ /AChE Inhibitors as a New Strategy for Multitargeting Anti-Alzheimer's Disease Drug Discovery. *Med. Chem. Lett.* **2018**, *9*, 171–176.
- (14) Sharma, R. N.; Xavier, F. P.; Vasu, K. K.; Chaturvedi, S. C.; Pancholi, S. S. Synthesis of 4-benzyl-1,3-thiazole derivatives as potential anti-inflammatory agents: An analogue-based drug design approach. *J. Enzyme Inhib. Med. Chem.* **2009**, *24*, 890–897.
- (15) Katritzky, A. R.; Ramsden, C. A.; Joule, J. A.; Zhdankin, V. V. *Handbook of Heterocyclic Chemistry*, 3rd ed.; Elsevier, 2010; pp 242–238.
- (16) Alford, P. E. Six-Membered Ring Systems. *Prog. Heterocycl. Chem.* **2011**, *23*, 329–369.
- (17) dos Santos Silva, T. D.; Bomfim, L. M.; da Cruz Rodrigues, A. C. B.; Dias, R. B.; Sales, C. B. S.; Rocha, C. A. G.; Soares, M. B. P.; Bezerra, D. P.; de Oliveira Cardoso, M. V.; Leite, A. C. L.; Militão, G. C. G. Anti-liver cancer activity in vitro and in vivo induced by 2-pyridyl 2,3-thiazole derivatives. *Toxicol. Appl. Pharmacol.* **2017**, *329*, 212–223.
- (18) dos Santos, T. A. R.; da Silva, A. C.; Gomes, P. A. T. d. M.; Espindola, J. W. P.; Cardoso, M. V. d. O.; Moreira, D. R. M.; Leite, A. C. L.; Pereira, V. R. A.; Leite, A. C. L.; Pereira, V. R. A. Antitumor and immunomodulatory activities of thiosemicarbazones and 1,3-Thiazoles in Jurkat and HT-29 cells. *Biomed. Pharmacother.* **2016**, *82*, 555–560.
- (19) Elshafly, H.; Bjelogrić, S.; Muller, C. D.; Todorović, T. R.; Rodić, M.; Marinković, A.; Filipović, N. R. Co(III) complex with (E)-2-(2-(pyridine-2-ylmethylene)hydrazinyl)-4-(4-tolyl)-1,3-thiazole: structure and activity against 2-D and 3-D cancer cell models. *J. Coord. Chem.* **2016**, *69*, 3354–3366.
- (20) Cardoso, M. V. d. O.; Siqueira, L. R. P. d.; Silva, E. B. d.; Costa, L. B.; Hernandez, M. Z.; Rabello, M. M.; Ferreira, R. S.; da Cruz, L. F.; Magalhães Moreira, D. R.; Pereira, V. R. A.; de Castro, M. C. A. B.; Bernhardt, P. V.; Leite, A. C. L. 2-Pyridyl thiazoles as novel anti-Trypanosoma cruzi agents: Structural design, synthesis and pharmacological evaluation. *Eur. J. Med. Chem.* **2014**, *86*, 48–59.
- (21) Ferrari, M. B.; Bisceglie, F.; Pelosi, G.; Tarasconi, P.; Albertini, R.; Dall'Aglio, P. P.; Pinelli, S.; Bergamo, A.; Sava, G. Synthesis, characterization and biological activity of copper complexes with pyridoxal thiosemicarbazone derivatives: X-ray crystal structure of three dimeric complexes. *J. Inorg. Biochem.* **2004**, *98*, 301–312.
- (22) Kaddouri, Y.; Abridgach, F.; Yousfi, E. B.; Kodadi, M. E.; Touzani, R. New thiazole, pyridine and pyrazole derivatives as antioxidant candidates: synthesis, DFT calculations and molecular docking study. *Heylton* **2020**, *6*, No. e03185.
- (23) Bera, P.; Aher, A.; Brandao, P.; Manna, S. K.; Bhattacharyya, I.; Pramanik, C.; Mandal, B.; Das, S.; Bera, P. Synthesis, structure elucidation and DFT study of a new thiazole–pyridine anchored NNN donor and its cobalt(II) complex: In-vitro antitumor activity against U937 cancer cells, DNA binding property and molecular docking study. *J. Mol. Struct.* **2021**, *1224*, 129015.
- (24) Ndagi, U.; Mhlongo, N.; Soliman, M. Metal complexes in cancer therapy— an update from a drug design perspective. *Drug Des., Dev. Ther.* **2017**, *11*, 599–616.
- (25) Warra, A. A. Transition metal complexes and their application in drugs and cosmetics-A Review. *Chem. Pharm. Res.* **2011**, *3*, 951–958.
- (26) Mwangi, S.; Timmons, J.; Ao, T.; Paul, M.; Macalintal, L.; Pescatore, A.; Cantor, A.; Dawson, K. A. Effect of manganese preconditioning and replacing inorganic manganese with organic manganese on the performance of male broiler chicks. *Poult. Sci.* **2019**, *98*, 2105–2113.
- (27) Alexandru, M.-G.; Velickovic, T.; Jitaru, I.; Grguric-Sipka, S.; Draghici, C. Synthesis, characterization and antitumor activity of Cu(II), Co(II), Zn(II) and Mn(II) complex compounds with aminothiazole acetate derivative. *Cent. Eur. J. Chem.* **2010**, *8*, 639–645.
- (28) Neelakantan, M. A.; Marriappan, S. S.; Dharmaraj, J.; Jayakumar, T.; Muthukumar, K. Spectral, XRD, SEM and biological activities of transition metal complexes of polydentate ligands containing thiazole moiety. *Spectrochim. Acta, Part A* **2008**, *71*, 628–635.
- (29) Munteanu, C. R.; Suntharalingam, K. Advances in cobalt complexes as anticancer agents. *Dalton Trans.* **2015**, *44*, 13796.
- (30) Ambika, S.; Manojkumar, Y.; Arunachalam, S.; Gowdhami, B.; Meenakshi Sundaram, K. K.; Solomon, R. V.; Venuvanalingam, P.; Akbarsha, M. A.; Sundararaman, M. Biomolecular Interaction, Anti-Cancer and Anti-Angiogenic Properties of Cobalt(III) Schiff Base Complexes. *Sci. Rep.* **2019**, *9*, 2721.
- (31) Zhao, Z.; Zhang, J.; Zhi, S.; Song, W.; Zhao, J. a. Novel binuclear and trinuclear metal (II) complexes: DNA interactions and in vitro anticancer activity through apoptosis. *J. Inorg. Biochem.* **2019**, *197*, 110696–110705.
- (32) Sobiesiak, M.; Muzioł, T.; Rozalski, M.; Krajewska, U.; Budzisz, E. Co(ii), Ni(ii) and Cu(ii) complexes with phenylthiazole and thiosemicarbazone-derived ligands: synthesis, structure and cytotoxic effects. *New J. Chem.* **2014**, *38*, 5349–5361.
- (33) Kalaivanan, C.; Sankarganesh, M.; Suvaikin, M. Y.; Karthi, G. B.; Gurusamy, S.; Subramanian, R.; Asha, R. N. Novel Cu(II) and Ni(II) complexes of nicotinamide based Mannich base: Synthesis, characterization, DFT calculation, DNA binding, molecular docking, antioxidant, antimicrobial activities. *J. Mol. Liq.* **2020**, *320*, 114423.
- (34) Sheldrick, G. M. SADABS; University of Göttingen: Germany, 1996.

- (35) Sheldrick, G. M. *SHELXL-97. Crystal Structure Refinement Program*; University of Göttingen, 1997.
- (36) Parr, R. G.; Yang, W. *Density Functional Theory of Atoms and Molecules*; Oxford University Press: Oxford, 1989.
- (37) Becke, A. D. Density-functional thermochemistry. III. The role of exact exchange. *J. Chem. Phys.* **1993**, *98*, 5648–5652.
- (38) Lee, C.; Yang, W.; Parr, R. G. Development of the Colle-Salvetti correlation-energy formula into a functional of the electron density. *Phys. Rev. B: Condens. Matter Mater. Phys.* **1998**, *37*, 785–789.
- (39) Becke, A. D. Density-functional thermochemistry-II. The effect of the Perdew–Wang generalized-gradient correlation correction. *J. Chem. Phys.* **1992**, *97*, 9173–9177.
- (40) Bera, P.; Brandão, P.; Mondal, G.; Jana, H.; Jana, A.; Santra, A.; Bera, P. Synthesis of a new pyridinyl thiazole ligand with hydrazone moiety and its cobalt(III) complex: X-ray crystallography, in vitro evaluation of the antibacterial activity. *Polyhedron* **2017**, *134*, 230–237.
- (41) Ou, K.; Mertsch, S.; Theodoropoulou, S.; Wu, J.; Liu, J.; Copland, D. A.; Scott, L. M.; Dick, A. D.; Schrader, S.; Liu, L. Müller Cells Stabilize Microvasculature through Hypoxic Preconditioning. *Cell. Physiol. Biochem.* **2019**, *52*, 668–680.
- (42) Cherif, H.; Bisson, D.; Jarzem, P.; Weber, M.; Ouellet, J.; Haglund, L. Curcumin and o-Vanillin Exhibit Evidence of Senolytic Activity in Human IVD Cells In Vitro. *J. Clin. Med.* **2019**, *8*, 433–452.
- (43) Blot, M. W.; Mahony, P. High-Efficiency Blotting of Proteins of Diverse Sizes Following Sodium Dodecyl Sulfate–Polyacrylamide Gel Electrophoresis. *Anal. Biochem.* **1997**, *247*, 185–192.
- (44) Galanski, M.; Arion, V.; Jakupec, M.; Keppler, B. Recent Developments in the Field of Tumor-Inhibiting Metal Complexes. *Curr. Pharm. Des.* **2003**, *9*, 2078–2089.
- (45) Mitra, I.; Mukherjee, S.; Reddy, B., V. P.; Misini, B.; Das, P.; Dasgupta, S.; Linert, W.; Moi, S. C.. Synthesis, biological evaluation, substitution behaviour and DFT study of Pd (II) complexes incorporating benzimidazole derivative. *New J. Chem.* **2018**, *42*, 2574–2589.
- (46) Yousef, T. A.; Abu El-Reash, G. M.; El Morshedy, R. M. Structural, spectral analysis and DNA studies of heterocyclic thiosemicarbazone ligand and its Cr (III), Fe (III), Co (II) Hg (II), and U (VI) complexes. *J. Mol. Struct.* **2013**, *1045*, 145–159.
- (47) Baul, T. S. B.; Kehie, P.; Duthie, A.; Guchait, N.; Raviprakash, N.; Mokhamatam, R. B.; Manna, S. K.; Armata, N.; Scopellite, M.; Wang, R.; Englert, U. Synthesis, photophysical properties and structures of organotin-Schiff bases utilizing aromatic amino acid from the chiral pool and evaluation of the biological perspective of a triphenyl tin compound. *J. Inorg. Biochem.* **2017**, *168*, 76–89.
- (48) You, Z.-L.; Cui, Y.-M.; Ma, Y.-P.; Wang, C.; Zhou, X.-S.; Li, K. Synthesis, characterization and urease inhibitory activity of oxovanadium(V) complexes with similar Schiff bases. *Inorg. Chem. Commun.* **2011**, *14*, 636–640.
- (49) Bera, P.; Aher, A.; Brandao, P.; Manna, S. K.; Mondal, G.; Jana, A.; Santra, A.; Jana, H.; Bera, P. Induced apoptosis against U937 cancer cells by Fe (II), Co (III) and Ni (II) complexes with a pyrazine-thiazole ligand: Synthesis, structure and biological evaluation. *Polyhedron* **2020**, *182*, 114503.
- (50) Brenchley, J. M.; Douek, D. C. Flow Cytometric Analysis of Human Antigen-Specific T-Cell Proliferation. *Methods Cell Biol.* **2004**, *75*, 481–496.
- (51) Phillips, J. C.; Braun, R.; Wang, W.; Gumbart, J.; Tajkhorshid, E.; Villa, E.; Chipot, C.; Skeel, R. D.; Kalé, L.; Schulten, K. Scalable Molecular Dynamics with NAMD. *J. Comput. Chem.* **2005**, *26*, 1781–1802.
- (52) Humphrey, W.; Dalke, A.; Schulten, K. VMD: Visual molecular dynamics. *J. Mol. Graphics* **1996**, *14*, 33–38.
- (53) Phillips, J.; Hardy, D.; Isgro, T.; Phillips, J.; Villa, E.; Yu, H.; Tanner, D.; Liu, Y.; Wu, Z.; Hardy, D. *NAMD Tutorial*, 2017; pp 1–120.
- (54) Vanommeslaeghe, K.; MacKerell, A. D. Automation of the CHARMM general force field (CGenFF) I: Bond perception and atom typing. *J. Chem. Inf. Model.* **2012**, *52*, 3144–3154.
- (55) Bera, P.; Aher, A.; Brandao, P.; Manna, S. K.; Bhattacharyya, I.; Mondal, G.; Jana, A.; Santra, A.; Bera, P. Anticancer activity, DNA Binding, and docking study of M(II) complexes (m = Zn, Cu, Ni) derived from a new pyrazine-thiazole ligand: Synthesis, structure and DFT. *New J. Chem.* **2021**, *45*, 11999–12015.
- (56) Solanki, A.; Patil, Y. P.; Kumar, S. B. Mononuclear five-coordinate cobalt(II) complexes with N4-coordinate pyrazole based ligand and pseudohalogens: Synthesis, structures, DNA and protein binding study. *J. Coord. Chem.* **2015**, *68*, 4017–4037.
- (57) Yousef, T. A.; Abu El-Reash, G. M.; Al-Jahdali, M.; El-Rakhawy, E.-B. R. Synthesis, spectral characterization and biological evaluation of Mn(II), Co(II), Ni(II), Cu(II), Zn(II) and Cd(II) complexes with thiosemicarbazone ending by pyrazole and pyridyl rings. *Spectrochim. Acta, Part A* **2014**, *129*, 163–172.
- (58) Sreeja, P. B.; Prathapachandra Kurup, M. R.; Kishore, A.; Jasmin, C. Spectral characterization, X-ray structure and biological investigations of copper(II) ternary complexes of 2-hydroxyacetophenone 4-hydroxybenzoic acid hydrazone and heterocyclic bases. *Polyhedron* **2004**, *23*, 575–581.
- (59) Arjmand, F.; Muddassir, M.; Khan, R. H. Chiral preference of l-tryptophan derived metal-based antitumor agent of late 3d-metal ions (Co(II), Cu(II) and Zn(II)) in comparison to d- and dl-tryptophan analogues: Their in vitro reactivity towards CT DNA, 5'-GMP and 5'-TMP. *Eur. J. Med. Chem.* **2010**, *45*, 3549–3557.
- (60) Sun, P. P.; Jian, F. F.; Wang, X. Synthesis, Crystal Structures and Fluorescence Properties of Ni (II) and Cu (II) Complexes with 1-(Furan-2-ylmethylene)-4-phenylthiosemicarbazone. *J. Chem. Crystallogr.* **2010**, *40*, 4–9.
- (61) Gulcan, M.; Karataş, Y.; Işik, S.; Öztürk, G.; Akbaş, E.; Şahin, E. Transition metal (II) complexes of a novel symmetrical benzothiazole-based ligand: synthesis, spectral/structural characterization and fluorescence properties. *J. Fluoresc.* **2014**, *24*, 1679–1686.
- (62) Tiwari, A. D.; Mishra, A. K.; Mishra, S. B.; Mamba, B. B.; Maji, B.; Bhattacharya, S. Synthesis and DNA binding studies of Ni(II), Co(II), Cu(II) and Zn(II) metal complexes of N1,N5-bis[pyridine-2-methylene]-thiocarbohydrazone Schiff-base ligand. *Spectrochim. Acta, Part A* **2011**, *79*, 1050–1056.
- (63) Pyle, A. M.; Rehmann, J. P.; Meshoyrer, R.; Kumar, C. V.; Turro, N. J.; Barton, J. K. Mixed-ligand complexes of ruthenium(II): factors governing binding to DNA. *J. Am. Chem. Soc.* **1989**, *111*, 3051–3058.
- (64) Zhou, C.-Y.; Zhao, J.; Wu, Y. B.; Yin, C. X.; Yang, P. Synthesis, characterization and studies on DNA-binding of a new Cu (II) complex with N1, N8-bis (1-methyl-4-nitropyrrole-2-carbonyl) triethylenetetramine. *J. Inorg. Biochem.* **2007**, *101*, 10–18.
- (65) Yilmaz, V. T.; Icsel, C.; Suyunova, F.; Aygun, M.; Cevatemre, B.; Ulukaya, E. Synthesis, structures, DNA/protein binding, molecular docking, anticancer activity and ROS generation of Ni(ii), Cu(ii) and Zn(ii) 5,5-diethylbarbiturate complexes with bis(2-pyridylmethyl)-amine and terpyridine. *New J. Chem.* **2017**, *41*, 8092–8106.
- (66) Rodríguez-Seguí, S. A.; Ortuño, M. J.; Ventura, F.; Martínez, E.; Samitier, J. Simplified microenvironments and reduced cell culture size influence the cell differentiation outcome in cellular microarrays. *J. Mater. Sci.: Mater. Med.* **2013**, *24*, 189–198.
- (67) Olsvik, P. A.; Berntssen, M. H. G.; Waagbø, R.; Hevrøy, E.; Søfteland, L. The mining chemical Polydadmac is cytotoxic but does not interfere with Cu-induced toxicity in Atlantic salmon hepatocytes. *Toxicol. in Vitro* **2015**, *30*, 492–505.
- (68) Chan, F. K.-M.; Shisler, J.; Bixby, J. G.; Felices, M.; Zheng, L.; Appel, M. J.; Orenstein, B.; Lenardo, M. J. A role for tumor necrosis factor receptor-2 and receptor-interacting protein in programmed necrosis and antiviral responses. *J. Biol. Chem.* **2003**, *278*, 5161–5162.
- (69) Cho, Y.; Challa, S.; Moquin, D.; Genga, R.; Ray, T. D.; Guildford, M.; Chan, F. K.-M. Phosphorylation-driven assembly of the RIP1-RIP3 complex regulates programmed necrosis and virus-induced inflammation. *Cell* **2009**, *137*, 1112–1123.
- (70) Holler, N.; Zaru, R.; Micheau, O.; Thome, M.; Attinger, A.; Valitutti, S.; Bodmer, J.-L.; Schneider, P.; Seed, B.; Tschopp, J. Fas triggers an alternative, caspase-8-independent cell death pathway

using the kinase RIP as effector molecule. *Nat. Immunol.* **2000**, *1*, 489–495.

(71) Chan, F. K. M.; Moriwaki, K.; Rosa, M. J. D. Detection of Necrosis by Release of Lactate Dehydrogenase Activity. *Methods Mol. Biol.* **2013**, *979*, 65.

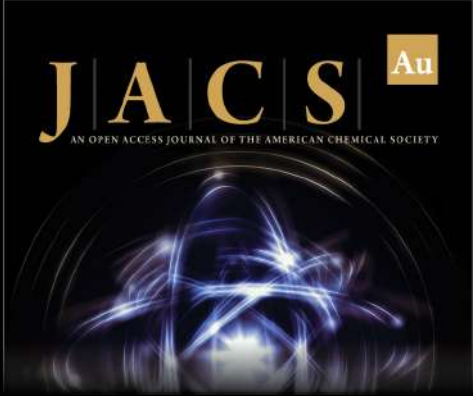
(72) Gobeil, S.; Boucher, C. C.; Nadeau, D.; Poirier, G. G. Characterization of the necrotic cleavage of poly (ADP-ribose) polymerase (PARP-1): implication of lysosomal proteases. *Cell Death Differ.* **2001**, *8*, 588–594.

(73) Aikin, R.; Rosenberg, L.; Paraskevas, S.; Maysinger, D. Inhibition of caspase-mediated PARP-1 cleavage results in increased necrosis in isolated islets of Langerhans. *J. Mol. Med.* **2004**, *82*, 389–397.


(74) Abumelha, H. M.; Alkhatib, F.; Alzahrani, S.; Abualnaja, M.; Alsaigh, S.; Alfaifi, M. Y.; Althagafi, I.; El-Metwaly, N. Synthesis, characterization, pharmaceutical models of Co(II), Ni(II) and Cu(II)-thiophen complexes: apoptosis, various theoretical studies and pharmacophore modelling. *J. Mol. Liq.* **2021**, *328*, 115483.


(75) Cavalcante, C. d. Q. O.; Arcanjo, D. d. S.; Silva, G. G. d.; Gatto, C. C.; Gatto, C. C. Solution and solid behavior of mono and binuclear zinc(II) and nickel(II) complexes with dithiocarbazates: X-ray analysis, mass spectrometry and cytotoxicity against cancer cell lines. *New J. Chem.* **2019**, *43*, 11209–11221.


(76) Shi, S.; Yu, S.; Quan, L.; Mansoor, M.; Chen, Z.; Hu, H.; Liu, D.; Liang, Y.; Liang, F. Synthesis and antitumor activities of transition metal complexes of a bis-Schiff base of 2-hydroxy-1-naphthalene-carboxaldehyde. *J. Inorg. Biochem.* **2020**, *210*, 111173.



**JACS Au**  
AN OPEN ACCESS JOURNAL OF THE AMERICAN CHEMICAL SOCIETY

 Editor-in-Chief  
**Prof. Christopher W. Jones**  
Georgia Institute of Technology, USA

**Open for Submissions** 

pubs.acs.org/jacsau  ACS Publications  
Most Trusted. Most Cited. Most Read.



# Source details

[Feedback >](#) [Compare sources >](#)

## Journal of Chemical Information and Modeling

Formerly known as: [Journal of Chemical Information and Computer Sciences](#)

Scopus coverage years: from 2005 to Present

Publisher: American Chemical Society

ISSN: 1549-9596 E-ISSN: 1549-960X

Subject area: [Social Sciences: Library and Information Sciences](#) [Computer Science: Computer Science Applications](#)

[Chemical Engineering: General Chemical Engineering](#) [Chemistry: General Chemistry](#)

Source type: Journal

[View all documents >](#)[Set document alert](#)[Save to source list](#)

CiteScore 2022

9.8



SJR 2022

1.357



SNIP 2022

1.379



# Roles of matrix metalloproteinases in development, immunology, and ovulation in fruit Fly (*Drosophila*)

Banani Bindhani<sup>1</sup>  | Sulagna Maity<sup>1</sup> | Ipsit Chakrabarti<sup>1</sup> | Samir Kumar Saha<sup>2</sup>

<sup>1</sup>Department of Zoology, Dinabandhu Andrews College (affiliated to University of Calcutta), Kolkata, West Bengal, India

<sup>2</sup>Department of Zoology, West Bengal State University, Barasat, Kolkata, West Bengal, India

## Correspondence

Banani Bindhani, Department of Zoology, Dinabandhu Andrews College (affiliated to University of Calcutta), Garia, Kolkata 700084, West Bengal, India.  
Email: [bindhanibanani@gmail.com](mailto:bindhanibanani@gmail.com)

## Abstract

Matrix metalloproteinase (MMP), a protease enzyme, participates in proteolytic cleavage of extracellular matrix proteins from *Drosophila* and mammals. But, recent studies have revealed other physiologically important roles of MMP in *Drosophila*. MMP contributes to cardioblast movement and distribution of collagen proteins during cardiogenesis in developing *Drosophila*. Tissue remodeling, especially tracheal development is also maintained by MMP. MMP regulates certain immunological functions in *Drosophila* such as wound repairing, plasmatocyte assemblage at the injured site of the basement membrane and glial response to axon degeneration in *Drosophila* nervous system. But, the contribution of MMP to tumor formation and metastasis in *Drosophila* has made it an interesting topic among researchers. Ovulation and egg laying are also found to be affected positively by MMP in *Drosophila*.

## KEYWORDS

*Drosophila*, immunological function, matrix metalloproteinase, metastasis, ovulation

## 1 | INTRODUCTION

Matrix metalloproteinases (MMP) or matrixins are calcium dependent zinc-containing metalloproteinases that are capable of cleaving any type of extracellular matrix (ECM) proteins (Verma & Hansch, 2007; Visse & Nagase, 2003). Apart from the removal of ECM molecules, MMP also takes part in several biological processes inside an organism. To give an idea, it plays a critical role in cell proliferation (Cui et al., 2017), cell migration (Amalinei et al., 2007), cell differentiation (Cui et al., 2017), host defense, cancer cell invasion (metastasis) (Nagase & Woessner, 1999; Verma

& Hansch, 2007). Two classes of MMP include secreted MMP and membrane-bound MMP (Page-McCaw et al., 2007; Ra & Parks, 2007).

Our review is aimed at the role of MMP in *Drosophila*. *Drosophila* (Fruit fly), being the most useful experimental Arthropod organism, is chosen preferably to perform genetic, biochemical, and immunological analysis of MMPs. Because of its small body size, easy availability, and an unexpected level of conservation among biological processes between flies and vertebrates (LaFever et al., 2017), *Drosophila* is favorite to many research workers. There are only two matrixins found in *Drosophila*, MMP1 and MMP2 (Llano et al., 2002; Page-McCaw et al., 2003). MMP1 is primarily a secreted collagenase cleaving collagen whereas MMP2 is primarily a membrane-bound gelatinase breaking down the gelatin (Llano et al., 2002; Page-McCaw et al., 2003; Steven & Page-McCaw, 2012). MMP2 is also glycosylphosphatidylinositol (GPI) anchored (Page-McCaw et al., 2003). Both MMPs have been shown to possess some common and some discrete functions. In this review, we present the basic structure of *Drosophila* MMP to give the readers an idea on how it is activated and how it works. Then, we are going to focus on some important functions of both the MMPs in *Drosophila* including developmental, immunological and reproductive roles and try to understand its effectiveness in the *Drosophila* body.

## 2 | STRUCTURE OF MMP

An MMP is composed of a propeptide, a catalytic metalloproteinase domain, a hinge region and a hemopexin domain (Nagase et al., 2006). Of them, the propeptide, catalytic and the hemopexin domain are greatly conserved (Glasheen et al., 2009). In *Drosophila melanogaster*, both MMPs (MMP1 and MMP2) have the same structure- propeptide domain, catalytic domain, hinge region and hemopexin domain (Figure 1) (Llano et al., 2002; Page-McCaw et al., 2003). A computer analysis on *Drosophila* genomic sequence revealed the similarity to the catalytic and hemopexin domain as in vertebrate MMPs (Llano et al., 2002). Propeptide domain: The propeptide domain actually acts negatively (Glasheen et al., 2009) and has three  $\alpha$  chains and connecting loops (Nagase et al., 2006). For MMP1 and MMP2, The region between helix 1 and helix 2, known as "bait region" (Murphy & Nagase, 2008; Nagase et al., 2006), is prone to extracellular proteases (Visse & Nagase, 2003). Proteolysis of this region plays a role in MMP activation. The  $\alpha$  helices are followed by a "cysteine switch" that contains cysteine residues interacting with the Zinc ion present at the catalytic site (Nagase et al., 2006). This causes the inactivation of the enzyme (Pro-MMP form). Degradation of Cys-Zn<sup>2+</sup> occurs when the enzyme is activated (Nagase et al., 2006).

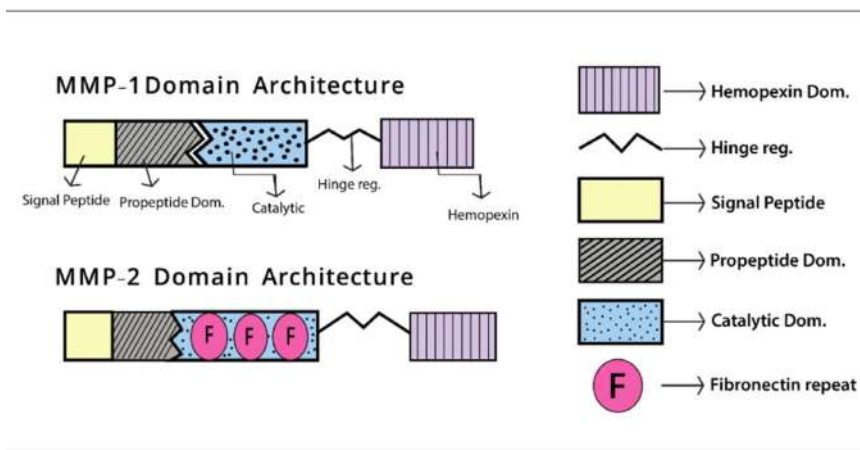


**FIGURE 1** Domain structure of MMP1 and MMP2.

**Catalytic domain:** MMP catalytic domain consists of five  $\beta$  pleated sheet, three  $\alpha$  helices and connecting loop (Nagase et al., 2006). It has one catalytic and one structural zinc ion. A conserved methionine has been found at this domain giving rise to a “Met-Turn” after zinc-binding motif (Bode et al., 1993). The catalytic domain has highly conserved sequence which contains three histidine residues (Cui et al., 2017; Nagase et al., 2006). MMP2, also identified as gelatinase A, comprises three repeats of fibronectin II motif in the catalytic metalloproteinase domain (Morgunova et al., 1999).

**Hinge region:** Hinge region, made up of proline (Amaliei et al., 2007; Maskos, 2005), acts as a linker between catalytic and hemopexin domain. This region allows domain flexibility and enzyme constancy (Maskos, 2005).

**Hemopexin domain:** The hemopexin domain consists of a four-bladed  $\beta$  propeller structure with a single disulfide bond between the first and fourth blade (Glasheen et al., 2009; Nagase et al., 2006). This domain is required for substrate recognition and specificity, denaturation of collagen triple helix and protein-protein interaction (Figures 2 and 3) (Chung et al., 2000; Patterson et al., 2001).

### 3 | DEVELOPMENT AND GROWTH OF HEART

*Drosophila* has an open circulatory system consisting of a simple tube like heart that controls hemolymph circulation (Demerec, 1950; Rotstein & Paululat, 2016). *Drosophila* is being used as a model organism in cardiac biology since it contains more than 80% homology with mice as shown by comparing the ontological profile of *Drosophila* cardiac

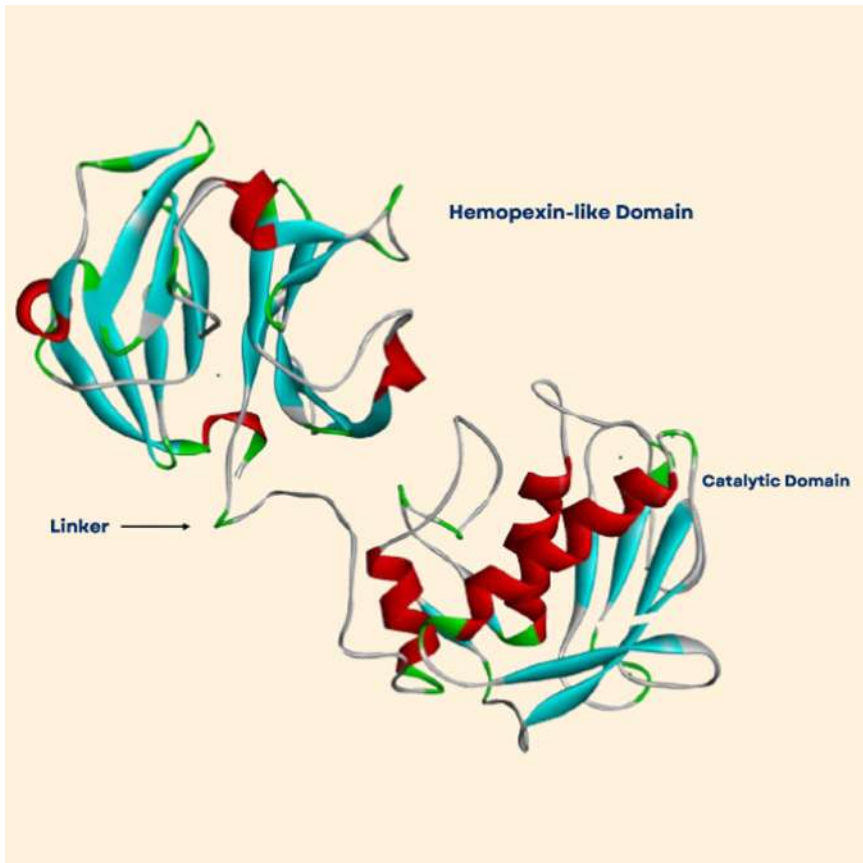


**FIGURE 2** 3D structure of MMP1. MMP, matrix metalloproteinase



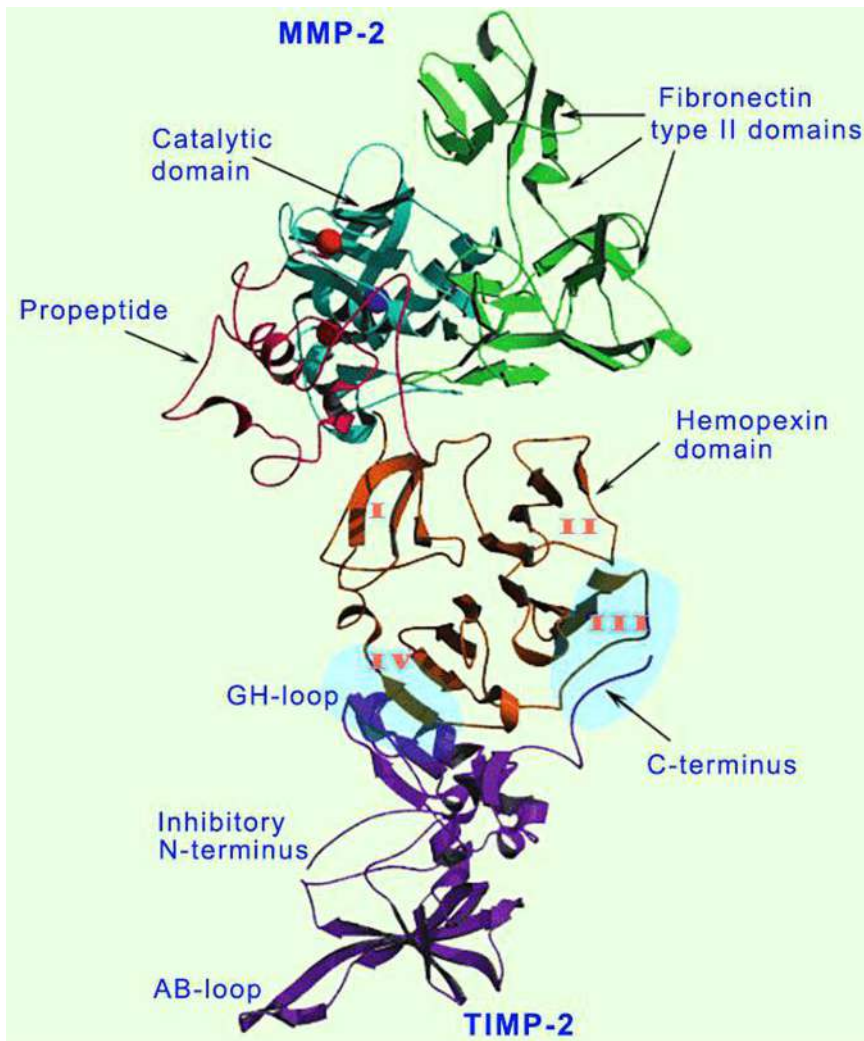


**FIGURE 3** 3D structure of MMP2. MMP, matrix metalloproteinase

proteome and mouse heart proteome (Cammarato et al., 2011). Expression of MMP1 and MMP2 in cardioblasts and their influence on collective cell migration (CCM) of cardioblasts have been shown experimentally (Raza et al., 2017). It was also demonstrated that the apical localization of signaling molecules such as Slit and Robo and receptors of ECM (integrin and dystroglycan) are regulated by MMP2 (Raza et al., 2017).

Both MMP1 and MMP2 are necessary to induce migration of cardioblasts during CCM because a crucial decrease in the motility of cardioblasts in *mmp1,2* double mutant and *mmp2* mutant has been reported (Raza et al., 2017). It was also observed that increased MMP2 level enhances ECM disruption (Raza et al., 2017). As pupa undergoes fat body disintegration, MMP2 plays a role in lysis of basement membrane to inhibit cell-ECM interaction and MMP1 is required to cleave E-cadherin molecule to disrupt cell-cell adhesion (Jia et al., 2014). MMP1 is the key factor to increase the luminal size by removing E-cadherin from the medial lumen. Embryos with *mmp1* mutation were reported to have a small lumen (Raza et al., 2017). MMP2, present at the cadherin expressing cardioblast leading-edge, protects the junctional domain by inhibition of Collagen IV based lumen development

(Raza et al., 2017). Embryo with *mmp2* mutation showed a failure of lumenogenesis due to unusual accumulation of Collagen IV around cardioblasts (Raza et al., 2017).

MMP2 also performs in the distribution of heart specific collagen, pericardin (Prc) protein (Hughes et al., 2020). In *mmp2* mutation or when MMP2 activity was reduced, an abnormally high concentration of Prc protein was observed in both cases (Hughes et al., 2020). Oppositely, overexpressed MMP2 showed a significant diminution of Prc network formation (Hughes et al., 2020). Viking (Vkg), a type of collagen IV, is found at the basal and medially located apical surface, not in the apical extensions (Raza et al., 2017). In *mmp2* and *mmp1,2* double mutants, Vkg is found to be expanded over the entire apical region (Figure 4) (Raza et al., 2017).

#### 4 | TISSUE REMODELING

The invertebrate trachea is made of a tubular network. Tracheal growth is regulated by expanding cell size without cell division (Beitel & Krasnow, 2000). Null mutants of MMP1 do not survive due to the lack of tracheae. In MMP1 mutation, the tracheal tube undergoes breakage and disruption after the first molt (Page-McCaw et al., 2003). Due to faulty tracheae, MMP1 mutants show behavior similar to hypoxia and sometimes, they die before metamorphosis (Beaucher et al., 2007; Page-McCaw et al., 2003). Another role of *Drosophila* MMP1 is to break a transmembrane adhesion factor ninjurin A (NinjA) and this cleavage plays a significant role in appropriate branching and formation of a mature tracheal system (Zhang et al., 2006). MMP2 mutation results in imperfect histolysis of the tissues that is involved in metamorphosis (Page-McCaw, 2008). A huge amount of MMP1 becomes expressed in autophagic tissues during metamorphosis (Lee et al., 2003). On the whole, MMP1 and MMP2- both are required for tissue remodeling. Additionally, both MMPs function in a cooperative mode and bring on *Drosophila* fat body cell dissociation in a distinct manner (Jia et al., 2014).

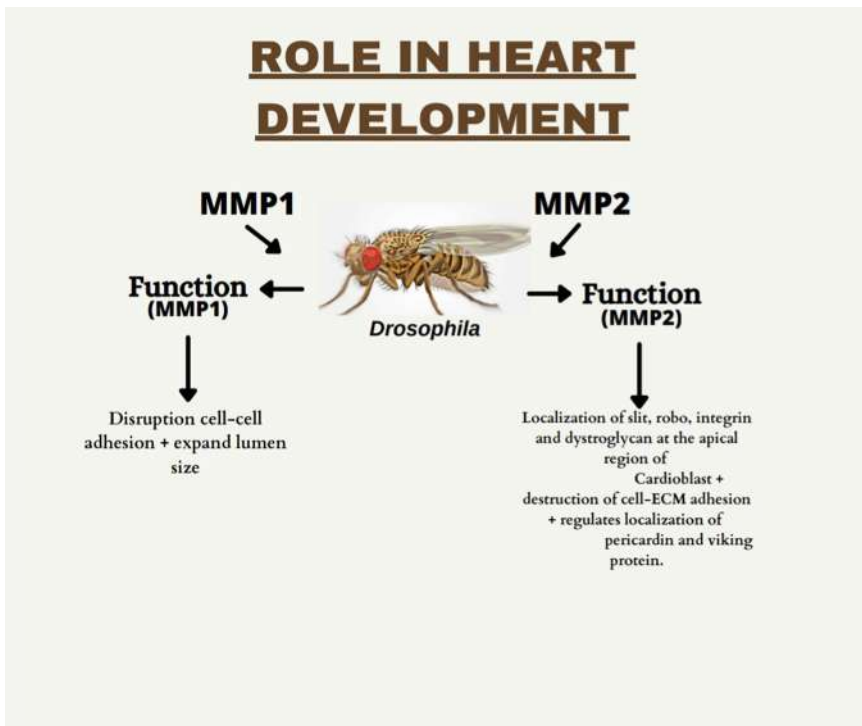


**FIGURE 4** Role of MMP in heart development.

## 5 | HEALING OF WOUND VIA EPITHELIALIZATION

Both MMPs are necessary for wound healing in *Drosophila* (Steven & Page-McCaw, 2012). Generally, wounds are healed about 86% of the wild types after 18 h of wounding. In MMP1 knocked down flies, wound did not heal in any of the tested flies by 18 h postwounding and the size of the wounded area expanded (Steven & Page-McCaw, 2012). MMP2 also participates in wound repairing since *mmp2* mutants were unable to close the wounds (Steven & Page-McCaw, 2012).

Catalytically inactive MMP1 (acting as a dominant negative) has shown that wounds continued to be open in 100% of the animals after 18 h of being wounded. This hinted that MMP1 catalytic activity is involved in epithelialization (Steven & Page-McCaw, 2012). Low expression of MMP1 was found in the unwounded epidermis. Steven and Page-McCaw (2012) also reported that the MMP1 level is increased in a gradient, being highest at the site of the wounded region. MMP1 is found to be performing assembly of collagen IV at the wound site, thereby maintaining the basement membrane. A study with Vkg-green fluorescent protein (GFP), wild types were shown to be lacking Vkg-GFP accumulation at the damaged edge after 1 h of wounding. But, a dramatic increase in Vkg-GFP was seen at that site by 5 h postwounding (Figure 5) (Steven & Page-McCaw, 2012).

## 6 | BASEMENT MEMBRANE DAMAGE AND ACCUMULATION OF PLASMATOCYTES AT DAMAGED SITE

Hemocytes are the circulating immune cells of *Drosophila* (Pham & Schneider, 2008). Of the three types of hemocytes, plasmatocytes are the most abundant, performing function that is analogous to that of mammalian macrophages (Diwanji & Bergmann, 2020; Gold & Bruckner, 2015). Phagocytic nature of *Drosophila* plasmatocyte

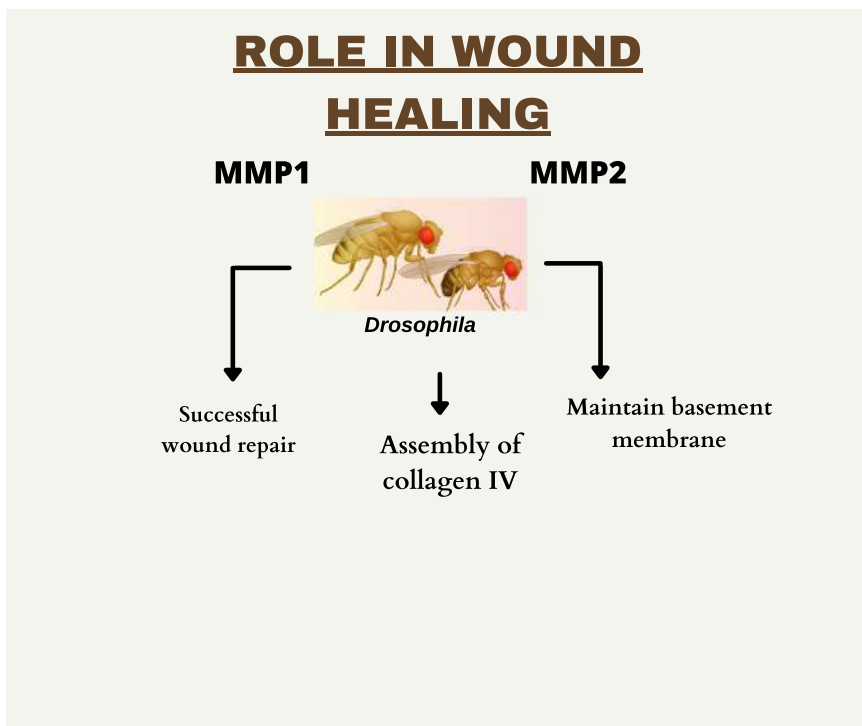


**FIGURE 5** Role of MMP in wound healing process. MMP, matrix metalloproteinase

has been demonstrated by Franc et al. (1999) and Ayyaz et al. (2015). Even though these hemocytes repair damaged tissue, they can promote pathological overproliferation of tissues on certain conditions (Gold & Bruckner, 2015). Fogarty et al. (2016) experimentally showed the correlation between hemocytes and *Drosophila* eye imaginal disc.

MMP2 is being reported to recruit plasmatocytes at the tumors and this is mediated by reactive oxygen species (ROS) and JNK (Diwanji & Bergmann, 2020). The *Drosophila* eye imaginal disc consists of columnar disc proper (DP) and peripodial epithelium (PE) (Atkins & Mardon, 2009). Though MMP2 is upregulated at PE in the overgrown tumor (immortal) disc, it is extensively accumulated at the basal side of the DP region where the basement membrane is injured (Diwanji & Bergmann, 2020). The absence of ROS and JNK in the overgrown tumor (immortal) disc leads to a striking shrinkage in the raised level of MMP2 (Diwanji & Bergmann, 2020). Overexpression of MMP1 showed no effect, but MMP2 damaged the basement membrane. Hemocytes were not found to be recruited to disc expressing MMP1 which has an intact basement membrane (Diwanji & Bergmann, 2020). Moreover, knockdown of MMP1 by RNA interference neither inhibited basement membrane degradation nor had any effect on hemocyte recruitment in the tumor disc (Diwanji & Bergmann, 2020). But, a rise in the number of hemocytes has been reported to be associated with the disc that contains damaged basement membrane due to MMP2 (Diwanji & Bergmann, 2020; Pastor-Pareja et al., 2008).

## 7 | TUMOR GROWTH AND INVASION

MMPs in mammals have been found to be responsible for several cancer cell stages like angiogenesis, proliferation and metastasis. Many studies are done on MMP to show its significance in cancer progression in both host cell and malignant cells. Similarly, *Drosophila* is also an ideal organism to perform research on cancer (Vidal & Cagan, 2006). Regulation of MMP1 by JNK (c-Jun N Terminal Kinase) signaling during cancer metastasis (Uhlírova & Bohmann, 2006) has already been reported.

In one study, the MMP effect was observed in two mutants, lethal giant larva (*lgl*) mutation and *brat* (brain tumor) mutation (Beaucher et al., 2007). The absence of either gene function gives rise to neoplastic brain tumor. MMP1 level was considerably high in the imaginal disc and brain of *lgl* mutants (Beaucher et al., 2007). But, this effect was totally opposite in *brat* mutant brains and eye-antennal disc, showing no change in MMP1 level (Beaucher et al., 2007). Deletion of MMP1 expression from *lgl* mutants lowers the metastatic ability of malignant cells (Beaucher et al., 2007). In contrast, the absence of MMP1 expression from *brat* mutants causes no effect. However, Beaucher et al. (2007) found a negligible level of MMP2 in both mutants. When ovaries of the wild type hosts were treated with *brat* mutant tissue, the ovaries were more likely to express high folds of MMP1 (Beaucher et al., 2007).

A study on a *Drosophila* model expressing Ras1 oncogene (Ras1<sup>v12</sup>) has shown an increased expression of MMP1 in hind gut epithelium which could be a possible factor for delamination of hind gut cells (Christofi & Apidianakis, 2013). It was reported that JNK promotes MMP1 production which is required for metastasis through hind gut cells (Uhlírova & Bohman, 2006; Weston & Davis, 2007). Inhibition of JNK signaling and MMP1 inactivation lessen the dissemination degree caused by Ras1<sup>v12</sup> (Christofi & Apidianakis, 2013).

Another study of MMP was based on *Drosophila* tumor suppressor, C-terminus Src Kinase (dCsk) (Vidal et al., 2010). Src family kinase regulates cell growth, cell cycle and migration (Thomas & Brugge, 1997). Mutation in Src leads to cancer progression (Ishizawa & Parsons, 2004). Removal of dCsk activity was found to increase Src activity leading to overproliferation (Vidal et al., 2006). Experiment with *Drosophila* imaginal epithelia showed that the absence of dCsk activity results in the loss of association between cell and its neighbor leading to unregulated cell movement (Vidal et al., 2010). A study on dCsk transcript by RNA interference using inverted repeats (dCsk-IR) showed that both the loss of a single copy of MMP1 and RNA interference of *mmp1* messenger RNA repress dCsk-IR mediated migration of boundary cell to the posterior compartment (Vidal et al., 2010). This indicates that

*Drosophila* MMP1 plays an important role in metastasis-like activity in boundary cells in the epithelial micro-environment (Figure 6) (Vidal et al., 2010).

## 8 | GLIAL RESPONSE TO AXON DEGENERATION AND REMOVAL OF DEGENERATED AXON

*Drosophila* is also chosen to observe the effect of MMP on expressing innate nerve immunity. Some morphologically similar pathways or reactions were seen between flies and mammals regarding the response of glial cells to injury (Awasaki et al., 2006; Macdonald et al., 2013). *Drosophila* and mammals also share some molecules required for recognition and engulfment of axon fragments such as Draper/MEGF-10 receptor, Syk tyrosine kinases and Rac-1 mediated cytoskeleton remodeling (Awasaki et al., 2006; Logan & Freeman, 2007; MacDonald et al., 2006).

MMP1 level was strongly enhanced in the accessory mesothoracic neuropil region of the ventral nerve cord when a unilateral wing was damaged (Purice et al., 2017). Also, overlapping of MMP1 signal was found with ensheathed glial membrane due to nerve lesion (Purice et al., 2017). A robust increase in MMP1 level caused by antennal nerve injury was also reported (Purice et al., 2017). Overall, MMP1 response is stimulated in the olfactory system after axotomy (Purice et al., 2017).

Since ensheathing glia expresses Draper (cell surface receptor) and causes its upregulation during nerve injury, a relationship between MMP1 and Draper was also observed (Purice et al., 2017). Depletion of the Draper receptor led to blockade of MMP1 secretion (Purice et al., 2017). Loss of MMP1 prevents enlargement of the glial membrane, as well as glial clearance of neuron axon debris, is also hindered (Purice et al., 2017). It was experimentally shown that MMP1 expression needs the stimulation of glial receptor, Draper (Purice et al., 2017). A high level of

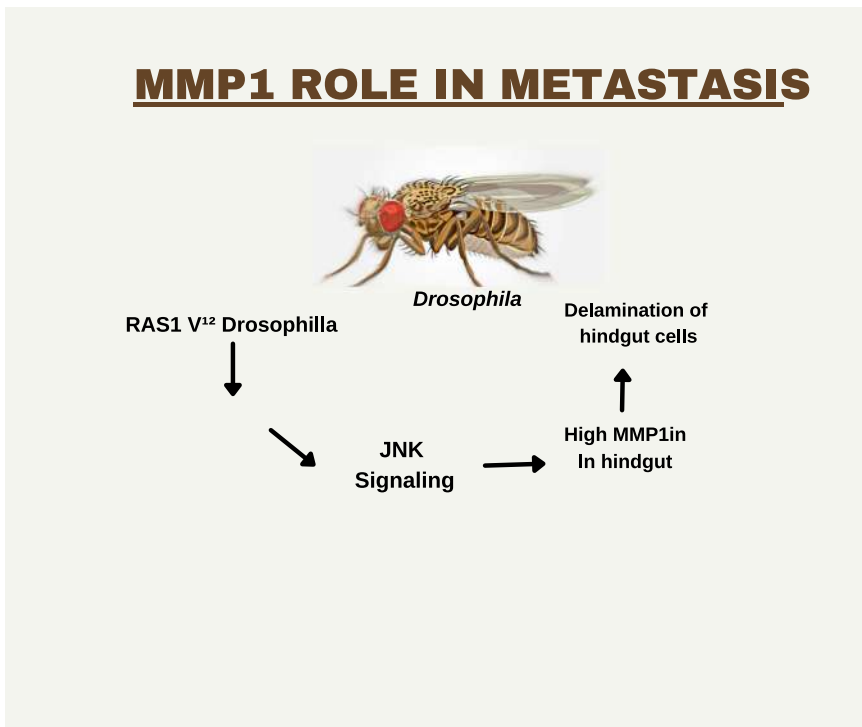


**FIGURE 6** Role of MMP in metastasis. MMP, matrix metalloproteinase

MMP1 was found to be accumulated in central region of antennal lobe 3 days after injury. However, it is still uncertain whether MMP2 has any role in the clearance of axon debris through the Draper pathway in the adult *Drosophila* brain (Figure 7) (Purice et al., 2017).

## 9 | MMP AS A VITAL FACTOR FOR OVULATION

A relationship between MMP2 activity and ovulation in *Drosophila* has been found in recent works. High activity was observed at the posterior end of one mature follicle and lesser activity in the secondary follicle (Deady et al., 2015). Also, high activity of anterior MMP disrupts the ECM that separates the oocyte from intact middle and anterior follicle cells (Deady et al., 2015). Overexpression of MMP2 in mature follicle cells results in rupturing of mature eggs and their release into the female abdominal cavity (Deady et al., 2015). Fewer follicles were shown to be ruptured when MMP1 was ectopically expressed (Deady et al., 2015).

Deady et al. (2015) did an in situ gelatinase assay to measure the localized activity of MMP in *Drosophila* follicles. This assay showed an elevated localized activity at the posterior side of one mature follicle whilst lower activity was reported in the second follicle (early ovulation stage). At late ovulation (eggs almost separated from follicles), gelatinase activity was found over the entire egg surface by Deady et al. (2015). This signifies the association of MMP activity with posterior follicle cell trimming and trimming is necessary for ovulation (Deady et al., 2015). Eggs pass into oviduct and the part of the follicular surface, which showed gelatinase activity, spread from posterior to anterior (Deady et al., 2015). MMP2, not MMP1, was found to be involved as the genetic requirement for ovulation (Deady et al., 2015). An experiment with MMP2 knockdown females hinted at blockade

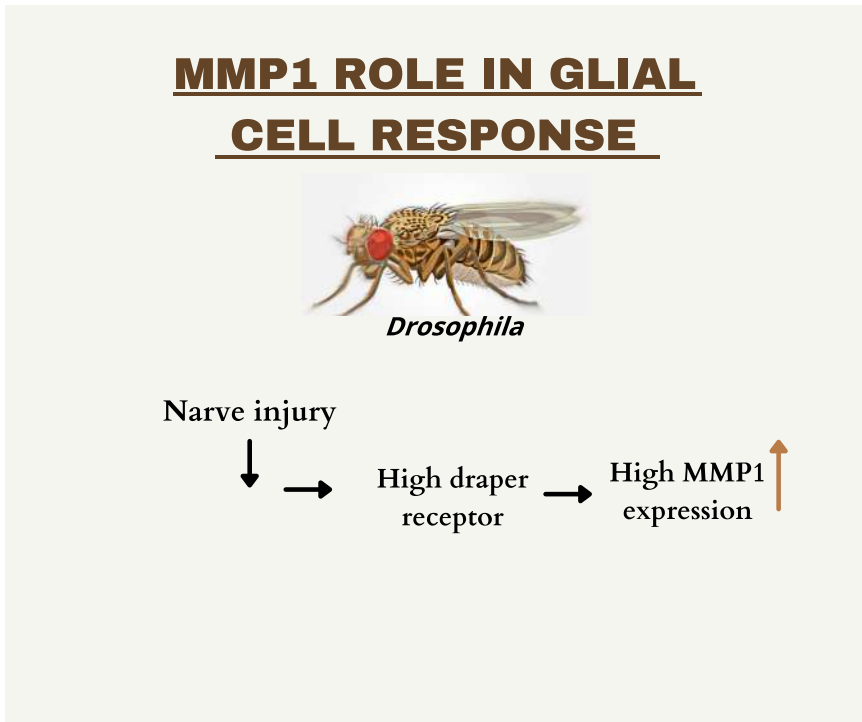


**FIGURE 7** MMP1 role in Glial cell response.

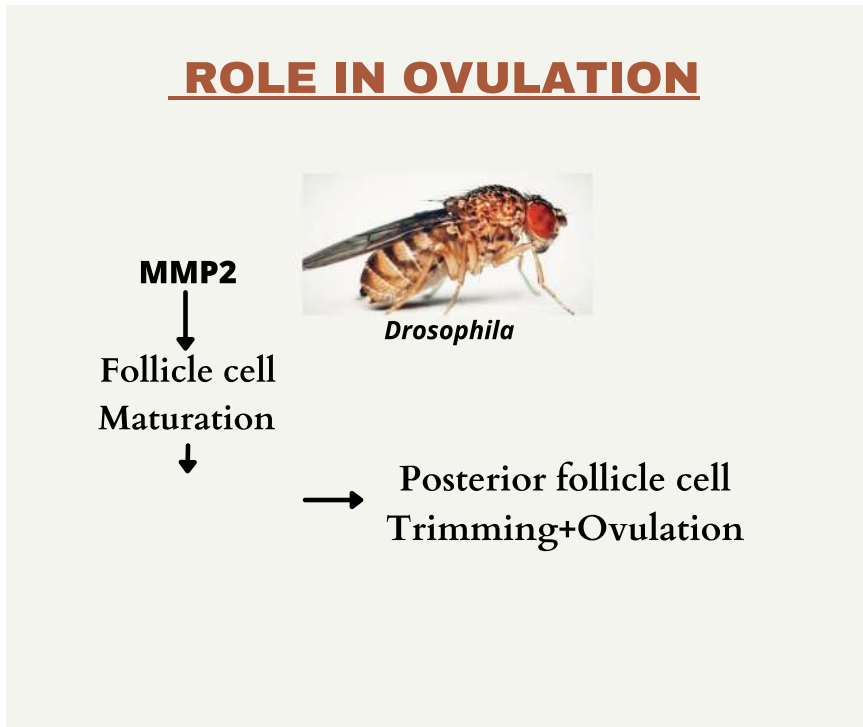


**FIGURE 8** MMP2 role in ovulation.

ovulation and a rise in average ovulation time (Deady et al., 2015). These female flies also showed defective egg laying (Figure 8) (Deady et al., 2015).

## 10 | FUTURE RESEARCH DIRECTION

*Drosophila* has emerged as a valuable model organism for studying biological processes. Some of the functions of *Drosophila* MMP are similar with that of the vertebrate MMP. Effect of *Drosophila* MMP to any nerve injury can help us to understand the effect of MMP in neurological disorders more deeply. Though mammalian MMP is involved in angiogenesis and cancer (Quintero-Fabian et al., 2019), more research is yet to be done on certain types of malignant cells. Also, there is a possible correlation between MMP2 and polycystic ovarian syndrome (Goldman & Shalev, 2004). Further experiments on *Drosophila* MMP would be useful to find how MMP can promote pathological conditions in vertebrates, especially in mammals. Therefore, we hope that the usage of *Drosophila* will have the access to the field of developing new medicines and therapies in near future.

### CONFLICT OF INTERESTS

The authors declare that there are no conflict of interests.

### ORCID

Banani Bindhani  <http://orcid.org/0000-0003-2204-8702>

## REFERENCES

- Amalinei, C., Caruntu, I. D., & Balan, R. A. (2007). Biology of metalloproteinases. *Romanian Journal of Morphology and Embryology*, 48, 323–334.
- Atkins, M., & Mardon, G. (2009). Signalling in the third dimension: The peripodial epithelium in eye disc development. *Developmental Dynamics*, 238, 2139–2148. <https://doi.org/10.1002/dvdy.22034>
- Awasaki, T., Tatsumi, R., Takahashi, K., Arai, K., Nakanishi, Y., Ueda, R., & Ito, K. (2006). Essential role of the apoptotic cell engulfment genes *Draper* and *ced-6* in programmed axon pruning during *Drosophila* metamorphosis. *Neuron*, 50, 855–867. <https://doi.org/10.1016/j.neuron.2006.04.027>
- Ayyaz, A., Li, H., & Jasper, H. (2015). Hemocytes control stem cell activity in *Drosophila* intestine. *Nature Cell Biology*, 17, 736–748. <https://doi.org/10.1038/ncb3174>
- Beaucher, M., Hersperger, E., Page-McCaw, A., & Shearn, A. (2007). Metastatic ability of *Drosophila* tumors depends on MMP activity. *Developmental Biology*, 303, 625–634. <https://doi.org/10.1016/j.ydbio.2006.12.001>
- Beitel, G. J., & Krasnow, M. A. (2000). Genetic control of epithelial tube size in the *Drosophila* tracheal system. *Development*, 127, 3271–3282.
- Bode, W., Gomis-Ruth, F. X., & Stockler, W. (1993). Astacins, serralysins, snake venom and matrix metalloproteinases exhibit identical zinc-binding environments (HEXXHXXGXXH and Met-turn) and topologies and should be grouped into a common family, the metzincins. *FEBS Lett*, 331, 134–140.
- Cammarato, A., Ahrens, C. H., Nakissa, A. N., Qeli, E., Rucker, J., Reedy, M. C., Zmasek, C. M., Gucek, M., Cole, R. N., Van Eyk, J. E., Bodmer, R., O'Rourke, B., Bernstein, S. I., & Foster, D. B. (2011). A mighty small heart: The Cardiac Proteome of Adult *Drosophila melanogaster*. *PLoS One*, 6, e18497. <https://doi.org/10.1371/journal.pone.0018497>
- Christofi, T., & Apidianakis, Y. (2013). Ras oncogenic *Drosophila* hindgut but not midgut cells use an inflammation like program to disseminate to distant site. *Gut Microbes*, 4, 54–59. <https://doi.org/10.4161/gmic.22429>
- Chung, L., Shimokawa, K., Dinakarandian, D., Grams, F., Fields, G. B., & Nagase, H. (2000). Identification of the <sup>189</sup>RWTNNF<sup>191</sup> region as a critical segment of matrix metalloproteinase 1 for the expression of collagenolytic activity. *Journal of Biological Chemistry*, 275, 29610–29617. <https://doi.org/10.1074/jbc.M004039200>
- Cui, N., Hu, M., & Khalil, R. A. (2017). Biochemical and biological attributes of matrix metalloproteinases. *Progress in Molecular Biology and Translational Science*, 147, 1–73. <https://doi.org/10.1016/bs.pmbts.2017.02.005>
- Deady, L. D., Shen, W., Mosure, S. A., Spradling, A. C., & Sun, J. (2015). Matrix metalloproteinase 2 is required for ovulation and corpus luteum formation in *Drosophila*. *PLoS Genetics*, 11, e1004989. <https://doi.org/10.1371/journal.pgen.1004989>
- Demerec, M., (Ed.). (1950). The internal anatomy and histology of the imago of *Drosophila melanogaster*. *Biology of Drosophila*. (Facsimile, 421–534). John Wiley & Sons.
- Diwanji, N., & Bergmann, A. (2020). Basement membrane damage by ROS and JNK mediated Mmp2 activation drives macrophage recruitment to overgrown tissue. *Nature Communications*, 11, 3631. <https://doi.org/10.1038/s41467-020-17399-8>
- Fogarty, C. E., Diwanji, N., Lindblad, J. L., Tare, M., Amcheslavsky, A., Makhijani, K., Bruckner, K., Fan, Y., & Bergmann, A. (2016). Extracellular reactive oxygen species drive apoptosis-induced proliferation via *Drosophila* macrophages. *Current Biology*, 26, 575–584.
- Franc, N. C., Heitzler, P., Ezekowitz, R. A., & White, K. (1999). Requirement of croquemort in phagocytosis of apoptotic cells in *Drosophila*. *Science*, 284, 1991–1994. <https://doi.org/10.1126/science.284.5422.1991>
- Glasheen, B. M., Kabra, A. T., & Page-McCaw, A. (2009). Distinct functions for the catalytic and hemopexin domains of a *Drosophila* matrix metalloproteinase. *Proceedings of the National Academy of Sciences of the United States of America*, 106, 2659–2664. <https://doi.org/10.1073/pnas.0804171106>
- Gold, K. S., & Bruckner, K. (2015). Macrophages and cellular immunity in *Drosophila melanogaster*. *Seminars in Immunology*, 27, 357–368. <https://doi.org/10.1016/j.smim.2016.03.010>
- Goldman, S., & Shalev, E. (2004). MMPs and TIMPs in ovarian physiology and pathophysiology. *Frontiers in Bioscience*, 9, 2474–2483. <https://doi.org/10.2741/1409>
- Hughes, C. J. R., Turner, S., Andrews, R. M., Vitkin, A., & Jacobs, J. R. (2020). Matrix metalloproteinase regulate ECM accumulation but not larval heart growth in *Drosophila melanogaster*. *Journal of Molecular and Cellular Cardiology*, 140, 42–55. <https://doi.org/10.1016/j.yjmcc.2020.02.008>
- Ishizawa, R., & Parsons, S. J. (2004). C-Src and cooperating partners in human cancer. *Cancer Cell*, 6, 209–214. <https://doi.org/10.1016/j.ccr.2004.09.001>
- Jia, Q., Liu, Y., Liu, H., & Li, S. (2014). MMP1 and MMP2 cooperatively induce *Drosophila* fat body cell dissociation with distinct roles. *Scientific Reports*, 4, 7535. <https://doi.org/10.1038/srep07535>
- LaFever, K. S., Wang, X., Page-McCaw, P., Bhave, G., & Page-McCaw, A. (2017). Both *Drosophila* matrix metalloproteinases have released and membrane tethered forms but have different substrates. *Scientific Reports*, 7, 44560. <https://doi.org/10.1038/srep44560>



- Lee, C. Y., Clough, E. A., Yellon, P., Teslovich, T. M., Stephan, D. A., & Baehrecke, E. H. (2003). Genome-wide analyses of steroid- and radiation-triggered programmed cell death in *Drosophila*. *Current Biology*, 13, 350–357.
- Llano, E., Adam, G., Pendas, A. M., Quesada, V., Sanchez, L. M., Santamaria, I., Noselli, S., & Lopez-Otin, C. (2002). Structural and enzymatic characterization of *Drosophila* Dm2-MMP, a membrane-bound matrix metalloproteinase with tissue-specific expression. *Journal of Biological Chemistry*, 277, 23321–23329. <https://doi.org/10.1074/jbc.M200121200>
- Logan, M. A., & Freeman, M. R. (2007). The scoop on the fly brain: Glial engulfment functions in *Drosophila*. *Neuron GliaBiology*, 3, 63–74. <https://doi.org/10.1017/S1740925X0700049X>
- MacDonald, J. M., Beach, M. G., Porpiglia, E., Sheehan, A. E., Watts, R. J., & Freeman, M. R. (2006). The *Drosophila* cell corpse engulfment receptor Draper mediates glial clearance of severed axons. *Neuron*, 50, 869–881. <https://doi.org/10.1016/j.neuron.2006.04.028>
- Macdonald, J. M., Doherty, J., Hackett, R., & Freeman, M. R. (2013). The c-Jun kinase signaling cascade promotes glial engulfment activity through activation of Draper and phagocytic function. *Cell Death and Differentiation*, 20, 1140–1148. <https://doi.org/10.1038/cdd.2013.30>
- Maskos, K. (2005). Crystal structures of MMPs in complex with physiological and pharmacological inhibitors. *Biochimie*, 87, 249–263.
- Morgunova, E., Tuuttila, A., Bergmann, U., Isupov, M., Lindqvist, Y., Schneider, G., & Tryggvason, K. (1999). Structure of human pro-matrix metalloproteinase-2: Activation mechanism revealed. *Science*, 284, 1667–1670. <https://doi.org/10.1126/science.284.5420.1667>
- Murphy, G., & Nagase, H. (2008). Progress in matrix metalloproteinase research. *Molecular Aspects of Medicine*, 29(5), 290–308. <https://doi.org/10.1016/j.mam.2008.05.002>
- Nagase, H., Visse, R., & Murphy, G. (2006). Structure and function of matrix metalloproteinases and TIMPs. *Cardiovascular Research*, 69, 562–573.
- Nagase, H., & Woessner, J. F. (1999). Matrix metalloproteinases. *The Journal of Biological Chemistry*, 274(31), 21491–21494. <https://doi.org/10.1074/jbc.274.31.21491>
- Page-McCaw, A. (2008). Remodeling the model organism: Matrix metalloproteinase functions in invertebrates. *Seminars in Cell and Developmental Biology*, 19, 14–23.
- Page-McCaw, A., Ewald, A. J., & Werb, Z. (2007). Matrix metalloproteinases and the regulation of tissue remodeling. *Nature Reviews Molecular Cell Biology*, 8, 221–233. <https://doi.org/10.1038/nrm2125>
- Page-McCaw, A., Serano, J., Sante, J. M., & Rubin, G. M. (2003). *Drosophila* matrix metalloproteinases are required for tissue remodeling, but not embryonic development. *Developmental Cell*, 4, 95–106.
- Pastor-Pareja, J. C., Wu, M., & Xu, T. (2008). An innate immune response of blood cells to tumors and tissue damage in *Drosophila*. *Dis. Model Mech*, 1, 144–154.
- Patterson, M. L., Atkinson, S. J., Knauper, V., & Murphy, G. (2001). Specific collagenolysis by gelatinase A, MMP-2, is determined by the hemopexin domain and not the fibronectin-like domain. *FEBS Letters*, 503, 158–162. [https://doi.org/10.1016/S0014-5793\(01\)02723-6](https://doi.org/10.1016/S0014-5793(01)02723-6)
- Pham, L. N., & Schneider, D. S. (2008). Evidence for specificity and memory in the insect innate immune response. *Insect Immunology*, 97–127. <https://doi.org/10.1016/B978-012373976-6.50007-0>
- Purice, M. D., Ray, A., Munzel, E. J., Pope, B. J., Park, D. J., Speese, S. D., & Logan, M. A. (2017). A novel *Drosophila* injury model reveals severed axons are cleared through a Draper/MMP1 signalling cascade. *eLife*, 6, e23611. <https://doi.org/10.7554/eLife.23611>
- Quintero-Fabian, S., Arreola, R., Becerril-Villanueva, E., Torres-Romero, J. C., Arana-Argaez, V., Lara-Riegos, J., Ramirez-Camacho, M. A., & Alvarez-Sanchez, M. E. (2019). Role of matrix metalloproteinases in angiogenesis and cancer. *Frontiers in Oncology*, 9, 1370. <https://doi.org/10.3389/fonc.2019.01370>
- Ra, H. J., & Parks, W. C. (2007). Control of matrix metalloproteinase catalytic activity. *Matrix Biology*, 26, 587–596.
- Raza, Q. S., Vanderploeg, J. L., & Jacobs, R. (2017). Matrix metalloproteinases are required for membrane motility and lumenogenesis during *Drosophila* heart development. *PLoS One*, 12, e0171905. <https://doi.org/10.1371/journal.pone.0171905>
- Rotstein, B., & Paululat, A. (2016). On the morphology of *Drosophila* heart. *J Cardiovasc Dev Dis*, 3, 15. <https://doi.org/10.3390/jcdd3020015>
- Steven, L. J., & Page-McCaw, A. (2012). A secreted MMP is required for reepithelialization during wound healing. *Molecular Biology of the Cell*, 23, 1068–1079. <https://doi.org/10.1091/mbc.E11-09-0745>
- Thomas, S. M., & Brugge, J. S. (1997). Cellular functions regulated by Src family kinases. *Annual Review of Cell and Developmental Biology*, 13, 513–609.
- Uhlirova, M., & Bohmann, D. (2006). JNK- and Fos-regulated Mmp1 expression cooperates with Ras to induce invasive tumors in *Drosophila*. *EMBO Journal*, 25, 5294–5304. <https://doi.org/10.1038/sj.emboj.7601401>
- Verma, R. P., & Hansch, C. (2007). Matrix metalloproteinases (MMPs): Chemical- biological functions and (Q)SARs. *Bioorganic and Medicinal Chemistry*, 15, 2223–2268. <https://doi.org/10.1016/j.bmc.2007.01.011>

- Vidal, M., & Cagan, R. L. (2006). *Drosophila* models for cancer research. *Current Opinion in Genetics & Development*, 16, 10–16. <https://doi.org/10.1016/j.gde.2005.12.004>
- Vidal, M., Larson, D. E., & Cagan, R. L. (2006). Csk deficient boundary cells are eliminated from normal *Drosophila* epithelia by exclusion, migration and apoptosis. *Developmental Cell*, 10, 33–44. <https://doi.org/10.1016/j.devcel.2005.11.007>
- Vidal, M., Salavaggione, L., Ylagan, L., Wilkins, M., Watson, M., Weilbaecher, K., & Cagan, R. (2010). A role of epithelial microenvironment at tumor boundaries: Evidence from *Drosophila* and human squamous cell carcinomas. *The American Journal of Pathology*, 176, 3007–3014. <https://doi.org/10.2353/ajpath.2010.090253>
- Visse, R., & Nagase, H. (2003). Matrix metalloproteinases and tissue inhibitors of metalloproteinases: Structure, function, and biochemistry. *Circulation Research*, 92, 827–839. <https://doi.org/10.1161/01.RES.0000070112.80711.3D>
- Weston, C. R., & Davis, R. J. (2007). The JNK signal transduction pathway. *Current Opinion in Cell Biology*, 19, 142–149.
- Zhang, S., Dailey, G. M., Kwan, E., Glasheen, B. M., Sroga, G. E., & Page-McCaw, A. (2006). An MMP liberates the Ninjurin A ectodomain to signal a loss of cell adhesion. *Genes and Development*, 20, 1899–1910. <https://doi.org/10.1101/gad.1426906>

## SUPPORTING INFORMATION

Additional supporting information may be found in the online version of the article at the publisher's website.

**How to cite this article:** Bindhani, B., Maity, S., Chakrabarti, I., & Saha, S. K. (2021). Roles of matrix metalloproteinases in development, immunology, and ovulation in fruit Fly (*Drosophila*). *Archives of Insect Biochemistry and Physiology*, e21849. <https://doi.org/10.1002/arch.21849>



## Source details

[Feedback >](#) [Compare sources >](#)

### Archives of Insect Biochemistry and Physiology

Scopus coverage years: from 1983 to Present

Publisher: Wiley-Blackwell

ISSN: 0739-4462 E-ISSN: 1520-6327

Subject area: [Agricultural and Biological Sciences: Insect Science](#) [Biochemistry, Genetics and Molecular Biology: Physiology](#)

[Biochemistry, Genetics and Molecular Biology: Biochemistry](#)

Source type: Journal

[View all documents >](#)[Set document alert](#)[Save to source list](#)

CiteScore 2022

3.8



SJR 2022

0.529



SNIP 2022

0.692

[CiteScore](#)[CiteScore rank & trend](#)[Scopus content coverage](#)

# Roles of matrix metalloproteinases in development, immunology, and ovulation in fruit Fly (*Drosophila*)

Banani Bindhani<sup>1</sup>  | Sulagna Maity<sup>1</sup> | Ipsit Chakrabarti<sup>1</sup> | Samir Kumar Saha<sup>2</sup>

<sup>1</sup>Department of Zoology, Dinabandhu Andrews College (affiliated to University of Calcutta), Kolkata, West Bengal, India

<sup>2</sup>Department of Zoology, West Bengal State University, Barasat, Kolkata, West Bengal, India

## Correspondence

Banani Bindhani, Department of Zoology, Dinabandhu Andrews College (affiliated to University of Calcutta), Garia, Kolkata 700084, West Bengal, India.  
Email: [bindhanibanani@gmail.com](mailto:bindhanibanani@gmail.com)

## Abstract

Matrix metalloproteinase (MMP), a protease enzyme, participates in proteolytic cleavage of extracellular matrix proteins from *Drosophila* and mammals. But, recent studies have revealed other physiologically important roles of MMP in *Drosophila*. MMP contributes to cardioblast movement and distribution of collagen proteins during cardiogenesis in developing *Drosophila*. Tissue remodeling, especially tracheal development is also maintained by MMP. MMP regulates certain immunological functions in *Drosophila* such as wound repairing, plasmatocyte assemblage at the injured site of the basement membrane and glial response to axon degeneration in *Drosophila* nervous system. But, the contribution of MMP to tumor formation and metastasis in *Drosophila* has made it an interesting topic among researchers. Ovulation and egg laying are also found to be affected positively by MMP in *Drosophila*.

## KEYWORDS

*Drosophila*, immunological function, matrix metalloproteinase, metastasis, ovulation

## 1 | INTRODUCTION

Matrix metalloproteinases (MMP) or matrixins are calcium dependent zinc-containing metalloproteinases that are capable of cleaving any type of extracellular matrix (ECM) proteins (Verma & Hansch, 2007; Visse & Nagase, 2003). Apart from the removal of ECM molecules, MMP also takes part in several biological processes inside an organism. To give an idea, it plays a critical role in cell proliferation (Cui et al., 2017), cell migration (Amalinei et al., 2007), cell differentiation (Cui et al., 2017), host defense, cancer cell invasion (metastasis) (Nagase & Woessner, 1999; Verma

& Hansch, 2007). Two classes of MMP include secreted MMP and membrane-bound MMP (Page-McCaw et al., 2007; Ra & Parks, 2007).

Our review is aimed at the role of MMP in *Drosophila*. *Drosophila* (Fruit fly), being the most useful experimental Arthropod organism, is chosen preferably to perform genetic, biochemical, and immunological analysis of MMPs. Because of its small body size, easy availability, and an unexpected level of conservation among biological processes between flies and vertebrates (LaFever et al., 2017), *Drosophila* is favorite to many research workers. There are only two matrixins found in *Drosophila*, MMP1 and MMP2 (Llano et al., 2002; Page-McCaw et al., 2003). MMP1 is primarily a secreted collagenase cleaving collagen whereas MMP2 is primarily a membrane-bound gelatinase breaking down the gelatin (Llano et al., 2002; Page-McCaw et al., 2003; Steven & Page-McCaw, 2012). MMP2 is also glycosylphosphatidylinositol (GPI) anchored (Page-McCaw et al., 2003). Both MMPs have been shown to possess some common and some discrete functions. In this review, we present the basic structure of *Drosophila* MMP to give the readers an idea on how it is activated and how it works. Then, we are going to focus on some important functions of both the MMPs in *Drosophila* including developmental, immunological and reproductive roles and try to understand its effectiveness in the *Drosophila* body.

## 2 | STRUCTURE OF MMP

An MMP is composed of a propeptide, a catalytic metalloproteinase domain, a hinge region and a hemopexin domain (Nagase et al., 2006). Of them, the propeptide, catalytic and the hemopexin domain are greatly conserved (Glasheen et al., 2009). In *Drosophila melanogaster*, both MMPs (MMP1 and MMP2) have the same structure- propeptide domain, catalytic domain, hinge region and hemopexin domain (Figure 1) (Llano et al., 2002; Page-McCaw et al., 2003). A computer analysis on *Drosophila* genomic sequence revealed the similarity to the catalytic and hemopexin domain as in vertebrate MMPs (Llano et al., 2002). Propeptide domain: The propeptide domain actually acts negatively (Glasheen et al., 2009) and has three  $\alpha$  chains and connecting loops (Nagase et al., 2006). For MMP1 and MMP2, The region between helix 1 and helix 2, known as "bait region" (Murphy & Nagase, 2008; Nagase et al., 2006), is prone to extracellular proteases (Visse & Nagase, 2003). Proteolysis of this region plays a role in MMP activation. The  $\alpha$  helices are followed by a "cysteine switch" that contains cysteine residues interacting with the Zinc ion present at the catalytic site (Nagase et al., 2006). This causes the inactivation of the enzyme (Pro-MMP form). Degradation of Cys-Zn<sup>2+</sup> occurs when the enzyme is activated (Nagase et al., 2006).

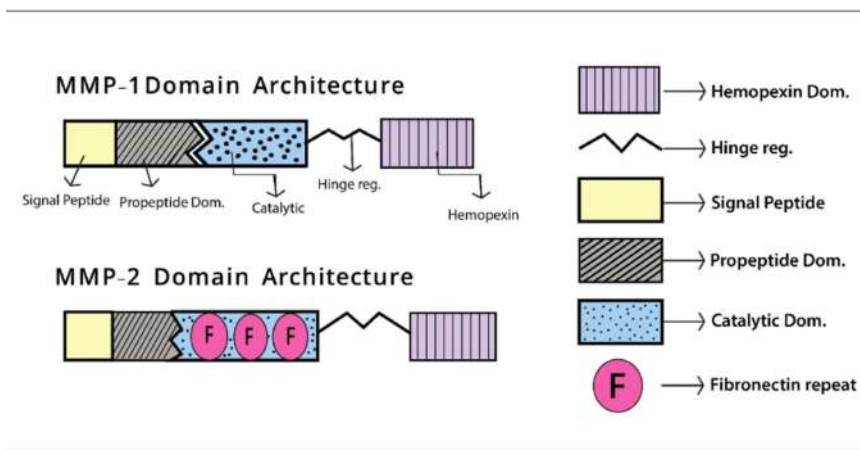


**FIGURE 1** Domain structure of MMP1 and MMP2.

**Catalytic domain:** MMP catalytic domain consists of five  $\beta$  pleated sheet, three  $\alpha$  helices and connecting loop (Nagase et al., 2006). It has one catalytic and one structural zinc ion. A conserved methionine has been found at this domain giving rise to a “Met-Turn” after zinc-binding motif (Bode et al., 1993). The catalytic domain has highly conserved sequence which contains three histidine residues (Cui et al., 2017; Nagase et al., 2006). MMP2, also identified as gelatinase A, comprises three repeats of fibronectin II motif in the catalytic metalloproteinase domain (Morgunova et al., 1999).

**Hinge region:** Hinge region, made up of proline (Amaliei et al., 2007; Maskos, 2005), acts as a linker between catalytic and hemopexin domain. This region allows domain flexibility and enzyme constancy (Maskos, 2005).

**Hemopexin domain:** The hemopexin domain consists of a four-bladed  $\beta$  propeller structure with a single disulfide bond between the first and fourth blade (Glasheen et al., 2009; Nagase et al., 2006). This domain is required for substrate recognition and specificity, denaturation of collagen triple helix and protein-protein interaction (Figures 2 and 3) (Chung et al., 2000; Patterson et al., 2001).

### 3 | DEVELOPMENT AND GROWTH OF HEART

*Drosophila* has an open circulatory system consisting of a simple tube like heart that controls hemolymph circulation (Demerec, 1950; Rotstein & Paululat, 2016). *Drosophila* is being used as a model organism in cardiac biology since it contains more than 80% homology with mice as shown by comparing the ontological profile of *Drosophila* cardiac

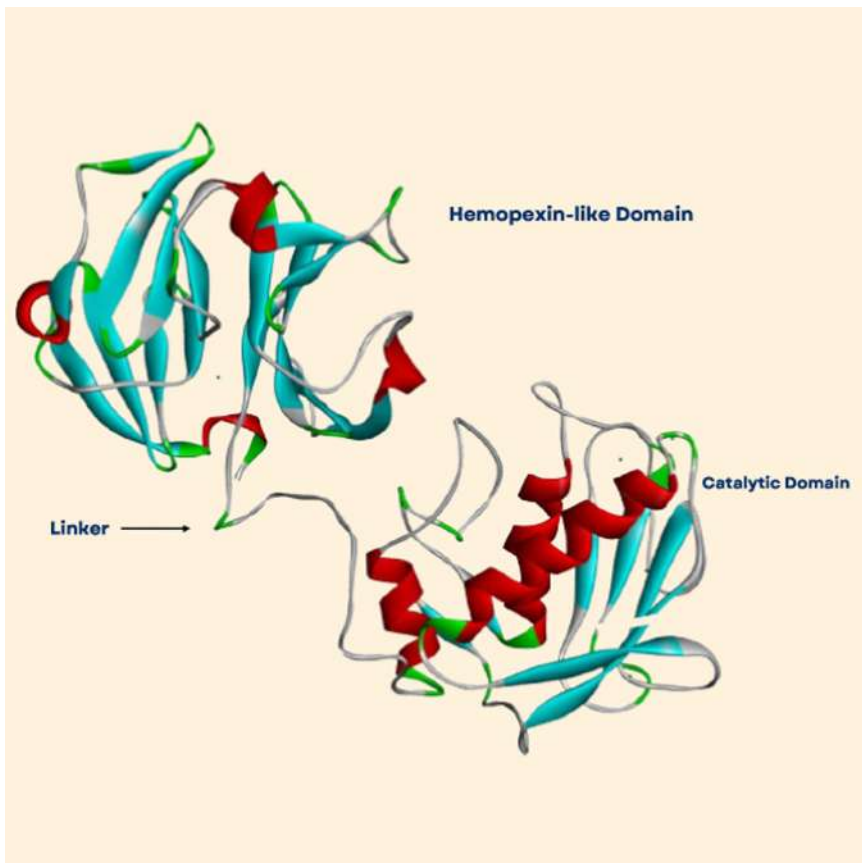


**FIGURE 2** 3D structure of MMP1. MMP, matrix metalloproteinase

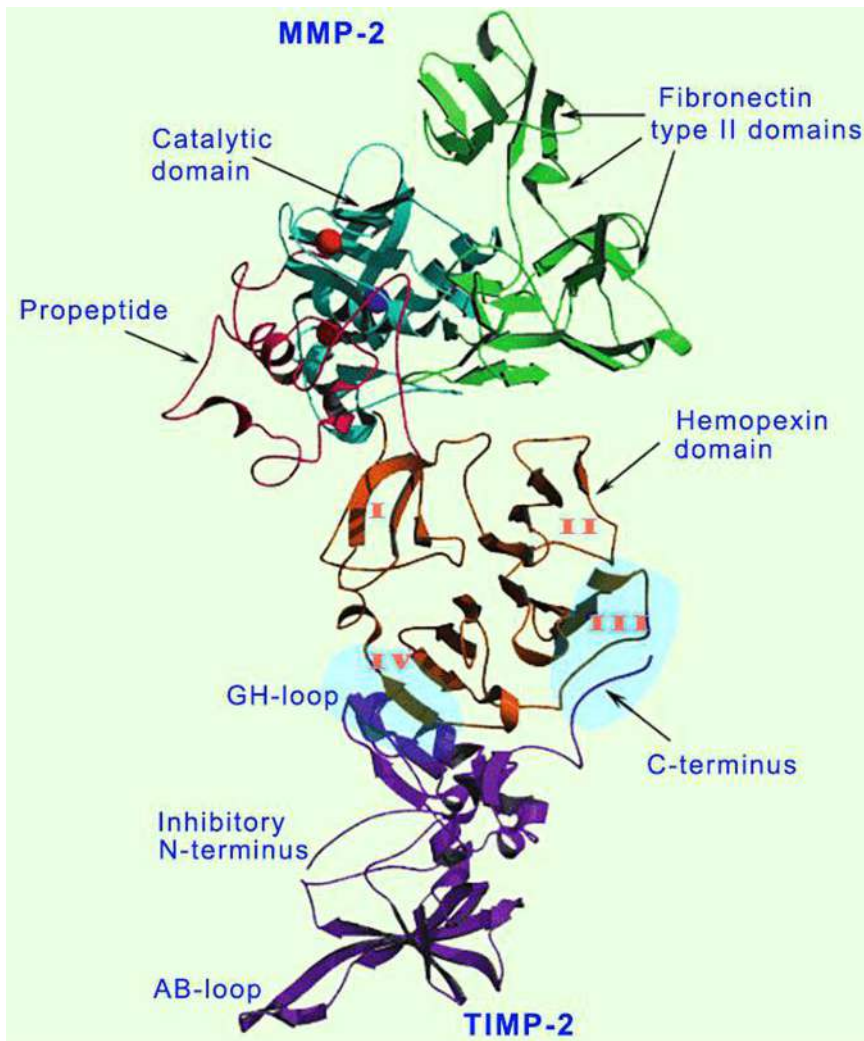


**FIGURE 3** 3D structure of MMP2. MMP, matrix metalloproteinase

proteome and mouse heart proteome (Cammarato et al., 2011). Expression of MMP1 and MMP2 in cardioblasts and their influence on collective cell migration (CCM) of cardioblasts have been shown experimentally (Raza et al., 2017). It was also demonstrated that the apical localization of signaling molecules such as Slit and Robo and receptors of ECM (integrin and dystroglycan) are regulated by MMP2 (Raza et al., 2017).

Both MMP1 and MMP2 are necessary to induce migration of cardioblasts during CCM because a crucial decrease in the motility of cardioblasts in *mmp1,2* double mutant and *mmp2* mutant has been reported (Raza et al., 2017). It was also observed that increased MMP2 level enhances ECM disruption (Raza et al., 2017). As pupa undergoes fat body disintegration, MMP2 plays a role in lysis of basement membrane to inhibit cell-ECM interaction and MMP1 is required to cleave E-cadherin molecule to disrupt cell-cell adhesion (Jia et al., 2014). MMP1 is the key factor to increase the luminal size by removing E-cadherin from the medial lumen. Embryos with *mmp1* mutation were reported to have a small lumen (Raza et al., 2017). MMP2, present at the cadherin expressing cardioblast leading-edge, protects the junctional domain by inhibition of Collagen IV based lumen development

(Raza et al., 2017). Embryo with *mmp2* mutation showed a failure of lumenogenesis due to unusual accumulation of Collagen IV around cardioblasts (Raza et al., 2017).

MMP2 also performs in the distribution of heart specific collagen, pericardin (Prc) protein (Hughes et al., 2020). In *mmp2* mutation or when MMP2 activity was reduced, an abnormally high concentration of Prc protein was observed in both cases (Hughes et al., 2020). Oppositely, overexpressed MMP2 showed a significant diminution of Prc network formation (Hughes et al., 2020). Viking (Vkg), a type of collagen IV, is found at the basal and medially located apical surface, not in the apical extensions (Raza et al., 2017). In *mmp2* and *mmp1,2* double mutants, Vkg is found to be expanded over the entire apical region (Figure 4) (Raza et al., 2017).

#### 4 | TISSUE REMODELING

The invertebrate trachea is made of a tubular network. Tracheal growth is regulated by expanding cell size without cell division (Beitel & Krasnow, 2000). Null mutants of MMP1 do not survive due to the lack of tracheae. In MMP1 mutation, the tracheal tube undergoes breakage and disruption after the first molt (Page-McCaw et al., 2003). Due to faulty tracheae, MMP1 mutants show behavior similar to hypoxia and sometimes, they die before metamorphosis (Beaucher et al., 2007; Page-McCaw et al., 2003). Another role of *Drosophila* MMP1 is to break a transmembrane adhesion factor ninjurin A (NinjA) and this cleavage plays a significant role in appropriate branching and formation of a mature tracheal system (Zhang et al., 2006). MMP2 mutation results in imperfect histolysis of the tissues that is involved in metamorphosis (Page-McCaw, 2008). A huge amount of MMP1 becomes expressed in autophagic tissues during metamorphosis (Lee et al., 2003). On the whole, MMP1 and MMP2- both are required for tissue remodeling. Additionally, both MMPs function in a cooperative mode and bring on *Drosophila* fat body cell dissociation in a distinct manner (Jia et al., 2014).

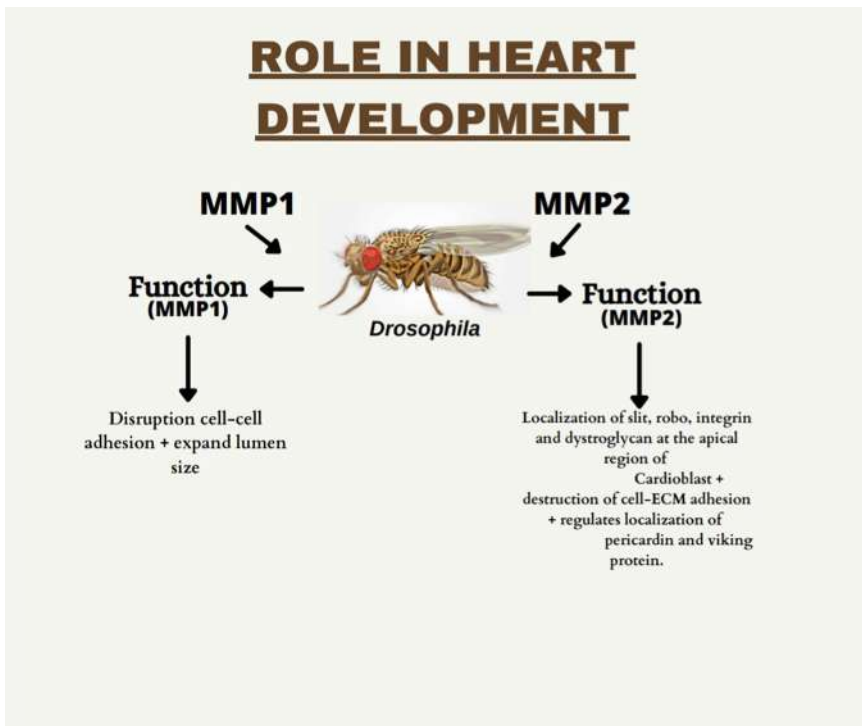


**FIGURE 4** Role of MMP in heart development.



## 5 | HEALING OF WOUND VIA EPITHELIALIZATION

Both MMPs are necessary for wound healing in *Drosophila* (Steven & Page-McCaw, 2012). Generally, wounds are healed about 86% of the wild types after 18 h of wounding. In MMP1 knocked down flies, wound did not heal in any of the tested flies by 18 h postwounding and the size of the wounded area expanded (Steven & Page-McCaw, 2012). MMP2 also participates in wound repairing since *mmp2* mutants were unable to close the wounds (Steven & Page-McCaw, 2012).

Catalytically inactive MMP1 (acting as a dominant negative) has shown that wounds continued to be open in 100% of the animals after 18 h of being wounded. This hinted that MMP1 catalytic activity is involved in epithelialization (Steven & Page-McCaw, 2012). Low expression of MMP1 was found in the unwounded epidermis. Steven and Page-McCaw (2012) also reported that the MMP1 level is increased in a gradient, being highest at the site of the wounded region. MMP1 is found to be performing assembly of collagen IV at the wound site, thereby maintaining the basement membrane. A study with Vkg-green fluorescent protein (GFP), wild types were shown to be lacking Vkg-GFP accumulation at the damaged edge after 1 h of wounding. But, a dramatic increase in Vkg-GFP was seen at that site by 5 h postwounding (Figure 5) (Steven & Page-McCaw, 2012).

## 6 | BASEMENT MEMBRANE DAMAGE AND ACCUMULATION OF PLASMATOCYTES AT DAMAGED SITE

Hemocytes are the circulating immune cells of *Drosophila* (Pham & Schneider, 2008). Of the three types of hemocytes, plasmatocytes are the most abundant, performing function that is analogous to that of mammalian macrophages (Diwanji & Bergmann, 2020; Gold & Bruckner, 2015). Phagocytic nature of *Drosophila* plasmatocyte

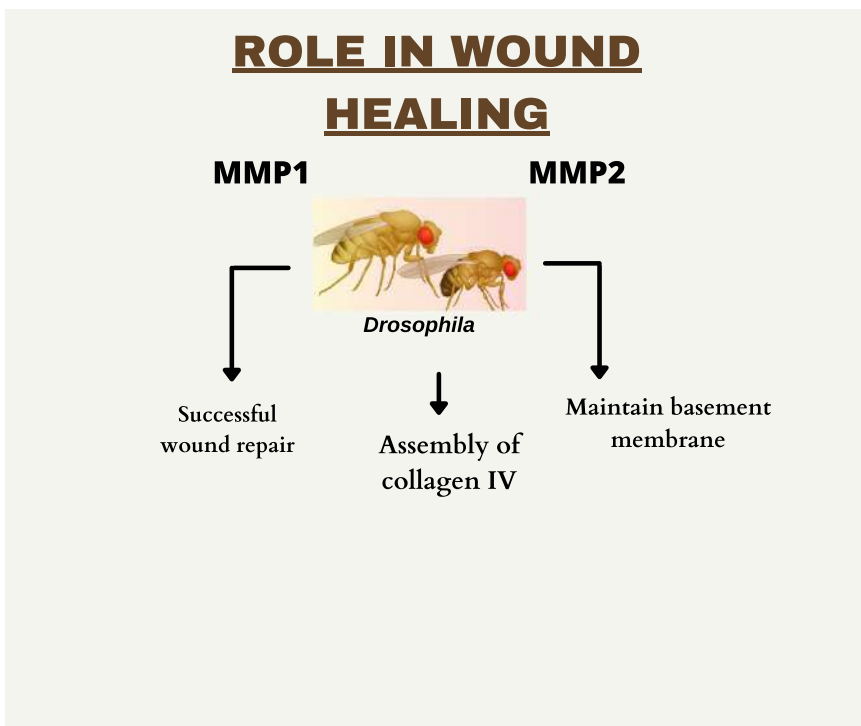


**FIGURE 5** Role of MMP in wound healing process. MMP, matrix metalloproteinase

has been demonstrated by Franc et al. (1999) and Ayyaz et al. (2015). Even though these hemocytes repair damaged tissue, they can promote pathological overproliferation of tissues on certain conditions (Gold & Bruckner, 2015). Fogarty et al. (2016) experimentally showed the correlation between hemocytes and *Drosophila* eye imaginal disc.

MMP2 is being reported to recruit plasmatocytes at the tumors and this is mediated by reactive oxygen species (ROS) and JNK (Diwanji & Bergmann, 2020). The *Drosophila* eye imaginal disc consists of columnar disc proper (DP) and peripodial epithelium (PE) (Atkins & Mardon, 2009). Though MMP2 is upregulated at PE in the overgrown tumor (immortal) disc, it is extensively accumulated at the basal side of the DP region where the basement membrane is injured (Diwanji & Bergmann, 2020). The absence of ROS and JNK in the overgrown tumor (immortal) disc leads to a striking shrinkage in the raised level of MMP2 (Diwanji & Bergmann, 2020). Overexpression of MMP1 showed no effect, but MMP2 damaged the basement membrane. Hemocytes were not found to be recruited to disc expressing MMP1 which has an intact basement membrane (Diwanji & Bergmann, 2020). Moreover, knockdown of MMP1 by RNA interference neither inhibited basement membrane degradation nor had any effect on hemocyte recruitment in the tumor disc (Diwanji & Bergmann, 2020). But, a rise in the number of hemocytes has been reported to be associated with the disc that contains damaged basement membrane due to MMP2 (Diwanji & Bergmann, 2020; Pastor-Pareja et al., 2008).

## 7 | TUMOR GROWTH AND INVASION

MMPs in mammals have been found to be responsible for several cancer cell stages like angiogenesis, proliferation and metastasis. Many studies are done on MMP to show its significance in cancer progression in both host cell and malignant cells. Similarly, *Drosophila* is also an ideal organism to perform research on cancer (Vidal & Cagan, 2006). Regulation of MMP1 by JNK (c-Jun N Terminal Kinase) signaling during cancer metastasis (Uhlirva & Bohmann, 2006) has already been reported.

In one study, the MMP effect was observed in two mutants, lethal giant larva (*lgl*) mutation and *brat* (brain tumor) mutation (Beaucher et al., 2007). The absence of either gene function gives rise to neoplastic brain tumor. MMP1 level was considerably high in the imaginal disc and brain of *lgl* mutants (Beaucher et al., 2007). But, this effect was totally opposite in *brat* mutant brains and eye-antennal disc, showing no change in MMP1 level (Beaucher et al., 2007). Deletion of MMP1 expression from *lgl* mutants lowers the metastatic ability of malignant cells (Beaucher et al., 2007). In contrast, the absence of MMP1 expression from *brat* mutants causes no effect. However, Beaucher et al. (2007) found a negligible level of MMP2 in both mutants. When ovaries of the wild type hosts were treated with *brat* mutant tissue, the ovaries were more likely to express high folds of MMP1 (Beaucher et al., 2007).

A study on a *Drosophila* model expressing Ras1 oncogene (Ras1<sup>v12</sup>) has shown an increased expression of MMP1 in hind gut epithelium which could be a possible factor for delamination of hind gut cells (Christofi & Apidianakis, 2013). It was reported that JNK promotes MMP1 production which is required for metastasis through hind gut cells (Uhlirva & Bohman, 2006; Weston & Davis, 2007). Inhibition of JNK signaling and MMP1 inactivation lessen the dissemination degree caused by Ras1<sup>v12</sup> (Christofi & Apidianakis, 2013).

Another study of MMP was based on *Drosophila* tumor suppressor, C-terminus Src Kinase (dCsk) (Vidal et al., 2010). Src family kinase regulates cell growth, cell cycle and migration (Thomas & Brugge, 1997). Mutation in Src leads to cancer progression (Ishizawar & Parsons, 2004). Removal of dCsk activity was found to increase Src activity leading to overproliferation (Vidal et al., 2006). Experiment with *Drosophila* imaginal epithelia showed that the absence of dCsk activity results in the loss of association between cell and its neighbor leading to unregulated cell movement (Vidal et al., 2010). A study on dCsk transcript by RNA interference using inverted repeats (dCsk-IR) showed that both the loss of a single copy of MMP1 and RNA interference of *mmp1* messenger RNA repress dCsk-IR mediated migration of boundary cell to the posterior compartment (Vidal et al., 2010). This indicates that

*Drosophila* MMP1 plays an important role in metastasis-like activity in boundary cells in the epithelial micro-environment (Figure 6) (Vidal et al., 2010).

## 8 | GLIAL RESPONSE TO AXON DEGENERATION AND REMOVAL OF DEGENERATED AXON

*Drosophila* is also chosen to observe the effect of MMP on expressing innate nerve immunity. Some morphologically similar pathways or reactions were seen between flies and mammals regarding the response of glial cells to injury (Awasaki et al., 2006; Macdonald et al., 2013). *Drosophila* and mammals also share some molecules required for recognition and engulfment of axon fragments such as Draper/MEGF-10 receptor, Syk tyrosine kinases and Rac-1 mediated cytoskeleton remodeling (Awasaki et al., 2006; Logan & Freeman, 2007; MacDonald et al., 2006).

MMP1 level was strongly enhanced in the accessory mesothoracic neuropil region of the ventral nerve cord when a unilateral wing was damaged (Purice et al., 2017). Also, overlapping of MMP1 signal was found with ensheathed glial membrane due to nerve lesion (Purice et al., 2017). A robust increase in MMP1 level caused by antennal nerve injury was also reported (Purice et al., 2017). Overall, MMP1 response is stimulated in the olfactory system after axotomy (Purice et al., 2017).

Since ensheathing glia expresses Draper (cell surface receptor) and causes its upregulation during nerve injury, a relationship between MMP1 and Draper was also observed (Purice et al., 2017). Depletion of the Draper receptor led to blockade of MMP1 secretion (Purice et al., 2017). Loss of MMP1 prevents enlargement of the glial membrane, as well as glial clearance of neuron axon debris, is also hindered (Purice et al., 2017). It was experimentally shown that MMP1 expression needs the stimulation of glial receptor, Draper (Purice et al., 2017). A high level of

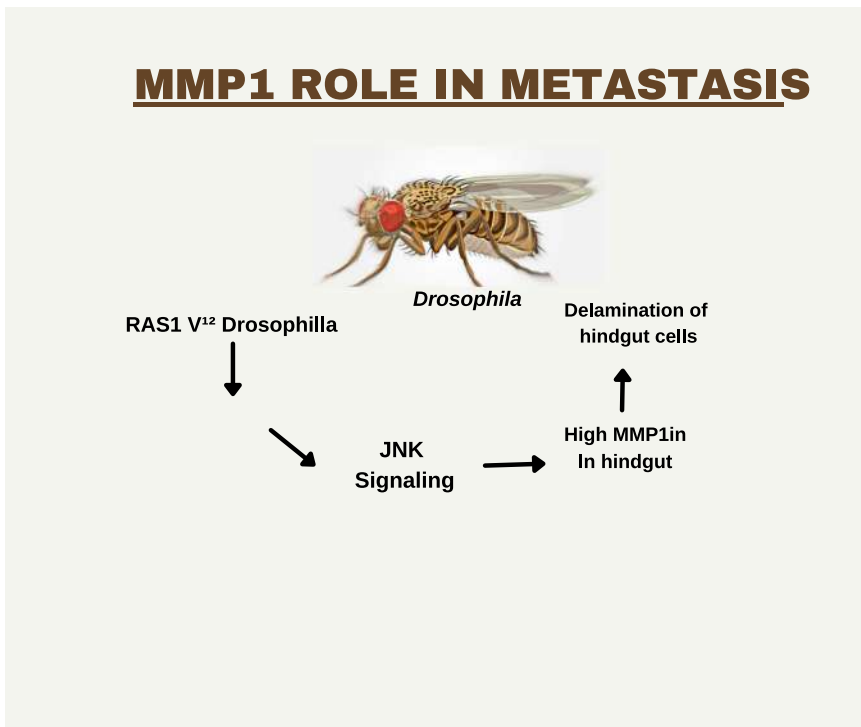


**FIGURE 6** Role of MMP in metastasis. MMP, matrix metalloproteinase

MMP1 was found to be accumulated in central region of antennal lobe 3 days after injury. However, it is still uncertain whether MMP2 has any role in the clearance of axon debris through the Draper pathway in the adult *Drosophila* brain (Figure 7) (Purice et al., 2017).

## 9 | MMP AS A VITAL FACTOR FOR OVULATION

A relationship between MMP2 activity and ovulation in *Drosophila* has been found in recent works. High activity was observed at the posterior end of one mature follicle and lesser activity in the secondary follicle (Deady et al., 2015). Also, high activity of anterior MMP disrupts the ECM that separates the oocyte from intact middle and anterior follicle cells (Deady et al., 2015). Overexpression of MMP2 in mature follicle cells results in rupturing of mature eggs and their release into the female abdominal cavity (Deady et al., 2015). Fewer follicles were shown to be ruptured when MMP1 was ectopically expressed (Deady et al., 2015).

Deady et al. (2015) did an in situ gelatinase assay to measure the localized activity of MMP in *Drosophila* follicles. This assay showed an elevated localized activity at the posterior side of one mature follicle whilst lower activity was reported in the second follicle (early ovulation stage). At late ovulation (eggs almost separated from follicles), gelatinase activity was found over the entire egg surface by Deady et al. (2015). This signifies the association of MMP activity with posterior follicle cell trimming and trimming is necessary for ovulation (Deady et al., 2015). Eggs pass into oviduct and the part of the follicular surface, which showed gelatinase activity, spread from posterior to anterior (Deady et al., 2015). MMP2, not MMP1, was found to be involved as the genetic requirement for ovulation (Deady et al., 2015). An experiment with MMP2 knockdown females hinted at blockade

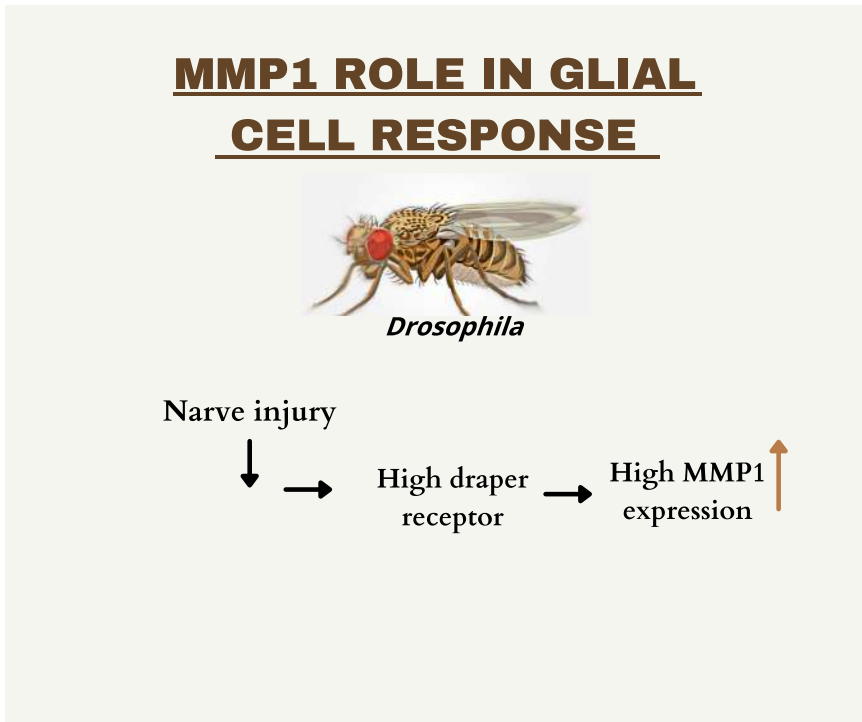


**FIGURE 7** MMP1 role in Glial cell response.

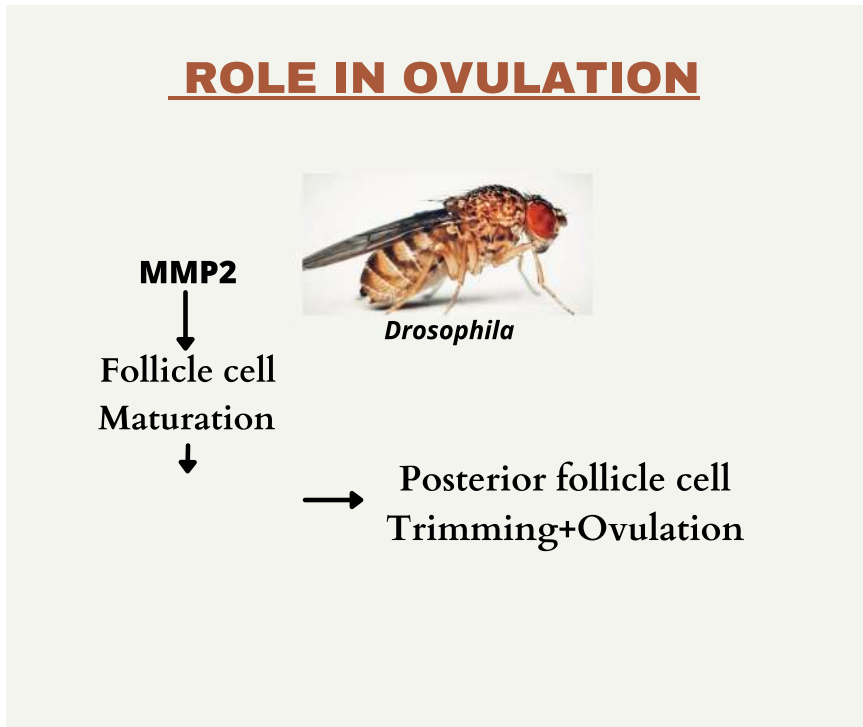


**FIGURE 8** MMP2 role in ovulation.

ovulation and a rise in average ovulation time (Deady et al., 2015). These female flies also showed defective egg laying (Figure 8) (Deady et al., 2015).

## 10 | FUTURE RESEARCH DIRECTION

*Drosophila* has emerged as a valuable model organism for studying biological processes. Some of the functions of *Drosophila* MMP are similar with that of the vertebrate MMP. Effect of *Drosophila* MMP to any nerve injury can help us to understand the effect of MMP in neurological disorders more deeply. Though mammalian MMP is involved in angiogenesis and cancer (Quintero-Fabian et al., 2019), more research is yet to be done on certain types of malignant cells. Also, there is a possible correlation between MMP2 and polycystic ovarian syndrome (Goldman & Shalev, 2004). Further experiments on *Drosophila* MMP would be useful to find how MMP can promote pathological conditions in vertebrates, especially in mammals. Therefore, we hope that the usage of *Drosophila* will have the access to the field of developing new medicines and therapies in near future.

### CONFLICT OF INTERESTS

The authors declare that there are no conflict of interests.

### ORCID

Banani Bindhani  <http://orcid.org/0000-0003-2204-8702>

## REFERENCES

- Amalinei, C., Caruntu, I. D., & Balan, R. A. (2007). Biology of metalloproteinases. *Romanian Journal of Morphology and Embryology*, 48, 323–334.
- Atkins, M., & Mardon, G. (2009). Signalling in the third dimension: The peripodial epithelium in eye disc development. *Developmental Dynamics*, 238, 2139–2148. <https://doi.org/10.1002/dvdy.22034>
- Awasaki, T., Tatsumi, R., Takahashi, K., Arai, K., Nakanishi, Y., Ueda, R., & Ito, K. (2006). Essential role of the apoptotic cell engulfment genes *Draper* and *ced-6* in programmed axon pruning during *Drosophila* metamorphosis. *Neuron*, 50, 855–867. <https://doi.org/10.1016/j.neuron.2006.04.027>
- Ayyaz, A., Li, H., & Jasper, H. (2015). Hemocytes control stem cell activity in *Drosophila* intestine. *Nature Cell Biology*, 17, 736–748. <https://doi.org/10.1038/ncb3174>
- Beaucher, M., Hersperger, E., Page-McCaw, A., & Shearn, A. (2007). Metastatic ability of *Drosophila* tumors depends on MMP activity. *Developmental Biology*, 303, 625–634. <https://doi.org/10.1016/j.ydbio.2006.12.001>
- Beitel, G. J., & Krasnow, M. A. (2000). Genetic control of epithelial tube size in the *Drosophila* tracheal system. *Development*, 127, 3271–3282.
- Bode, W., Gomis-Ruth, F. X., & Stockler, W. (1993). Astacins, serralysins, snake venom and matrix metalloproteinases exhibit identical zinc-binding environments (HEXXHXGXH and Met-turn) and topologies and should be grouped into a common family, the metzincins. *FEBS Lett*, 331, 134–140.
- Cammarato, A., Ahrens, C. H., Nakissa, A. N., Qeli, E., Rucker, J., Reedy, M. C., Zmasek, C. M., Gucek, M., Cole, R. N., Van Eyk, J. E., Bodmer, R., O'Rourke, B., Bernstein, S. I., & Foster, D. B. (2011). A mighty small heart: The Cardiac Proteome of Adult *Drosophila melanogaster*. *PLoS One*, 6, e18497. <https://doi.org/10.1371/journal.pone.0018497>
- Christofi, T., & Apidianakis, Y. (2013). Ras oncogenic *Drosophila* hindgut but not midgut cells use an inflammation like program to disseminate to distant site. *Gut Microbes*, 4, 54–59. <https://doi.org/10.4161/gmic.22429>
- Chung, L., Shimokawa, K., Dinakarandian, D., Grams, F., Fields, G. B., & Nagase, H. (2000). Identification of the <sup>189</sup>RWTNNFREY<sup>191</sup> region as a critical segment of matrix metalloproteinase 1 for the expression of collagenolytic activity. *Journal of Biological Chemistry*, 275, 29610–29617. <https://doi.org/10.1074/jbc.M004039200>
- Cui, N., Hu, M., & Khalil, R. A. (2017). Biochemical and biological attributes of matrix metalloproteinases. *Progress in Molecular Biology and Translational Science*, 147, 1–73. <https://doi.org/10.1016/bs.pmbts.2017.02.005>
- Deady, L. D., Shen, W., Mosure, S. A., Spradling, A. C., & Sun, J. (2015). Matrix metalloproteinase 2 is required for ovulation and corpus luteum formation in *Drosophila*. *PLoS Genetics*, 11, e1004989. <https://doi.org/10.1371/journal.pgen.1004989>
- Demerec, M., (Ed.). (1950). The internal anatomy and histology of the imago of *Drosophila melanogaster*. *Biology of Drosophila*. (Facsimile, 421–534). John Wiley & Sons.
- Diwanji, N., & Bergmann, A. (2020). Basement membrane damage by ROS and JNK mediated Mmp2 activation drives macrophage recruitment to overgrown tissue. *Nature Communications*, 11, 3631. <https://doi.org/10.1038/s41467-020-17399-8>
- Fogarty, C. E., Diwanji, N., Lindblad, J. L., Tare, M., Amcheslavsky, A., Makhijani, K., Bruckner, K., Fan, Y., & Bergmann, A. (2016). Extracellular reactive oxygen species drive apoptosis-induced proliferation via *Drosophila* macrophages. *Current Biology*, 26, 575–584.
- Franc, N. C., Heitzler, P., Ezekowitz, R. A., & White, K. (1999). Requirement of croquemort in phagocytosis of apoptotic cells in *Drosophila*. *Science*, 284, 1991–1994. <https://doi.org/10.1126/science.284.5422.1991>
- Glasheen, B. M., Kabra, A. T., & Page-McCaw, A. (2009). Distinct functions for the catalytic and hemopexin domains of a *Drosophila* matrix metalloproteinase. *Proceedings of the National Academy of Sciences of the United States of America*, 106, 2659–2664. <https://doi.org/10.1073/pnas.0804171106>
- Gold, K. S., & Bruckner, K. (2015). Macrophages and cellular immunity in *Drosophila melanogaster*. *Seminars in Immunology*, 27, 357–368. <https://doi.org/10.1016/j.smim.2016.03.010>
- Goldman, S., & Shalev, E. (2004). MMPs and TIMPs in ovarian physiology and pathophysiology. *Frontiers in Bioscience*, 9, 2474–2483. <https://doi.org/10.2741/1409>
- Hughes, C. J. R., Turner, S., Andrews, R. M., Vitkin, A., & Jacobs, J. R. (2020). Matrix metalloproteinase regulate ECM accumulation but not larval heart growth in *Drosophila melanogaster*. *Journal of Molecular and Cellular Cardiology*, 140, 42–55. <https://doi.org/10.1016/j.yjmcc.2020.02.008>
- Ishizawa, R., & Parsons, S. J. (2004). C-Src and cooperating partners in human cancer. *Cancer Cell*, 6, 209–214. <https://doi.org/10.1016/j.ccr.2004.09.001>
- Jia, Q., Liu, Y., Liu, H., & Li, S. (2014). MMP1 and MMP2 cooperatively induce *Drosophila* fat body cell dissociation with distinct roles. *Scientific Reports*, 4, 7535. <https://doi.org/10.1038/srep07535>
- LaFever, K. S., Wang, X., Page-McCaw, P., Bhave, G., & Page-McCaw, A. (2017). Both *Drosophila* matrix metalloproteinases have released and membrane tethered forms but have different substrates. *Scientific Reports*, 7, 44560. <https://doi.org/10.1038/srep44560>

- Lee, C. Y., Clough, E. A., Yellon, P., Teslovich, T. M., Stephan, D. A., & Baehrecke, E. H. (2003). Genome-wide analyses of steroid- and radiation-triggered programmed cell death in *Drosophila*. *Current Biology*, 13, 350–357.
- Llano, E., Adam, G., Pendas, A. M., Quesada, V., Sanchez, L. M., Santamaria, I., Noselli, S., & Lopez-Otin, C. (2002). Structural and enzymatic characterization of *Drosophila* Dm2-MMP, a membrane-bound matrix metalloproteinase with tissue-specific expression. *Journal of Biological Chemistry*, 277, 23321–23329. <https://doi.org/10.1074/jbc.M200121200>
- Logan, M. A., & Freeman, M. R. (2007). The scoop on the fly brain: Glial engulfment functions in *Drosophila*. *Neuron Glia Biology*, 3, 63–74. <https://doi.org/10.1017/S1740925X0700049X>
- MacDonald, J. M., Beach, M. G., Porpiglia, E., Sheehan, A. E., Watts, R. J., & Freeman, M. R. (2006). The *Drosophila* cell corpse engulfment receptor Draper mediates glial clearance of severed axons. *Neuron*, 50, 869–881. <https://doi.org/10.1016/j.neuron.2006.04.028>
- Macdonald, J. M., Doherty, J., Hackett, R., & Freeman, M. R. (2013). The c-Jun kinase signaling cascade promotes glial engulfment activity through activation of Draper and phagocytic function. *Cell Death and Differentiation*, 20, 1140–1148. <https://doi.org/10.1038/cdd.2013.30>
- Maskos, K. (2005). Crystal structures of MMPs in complex with physiological and pharmacological inhibitors. *Biochimie*, 87, 249–263.
- Morgunova, E., Tuuttila, A., Bergmann, U., Isupov, M., Lindqvist, Y., Schneider, G., & Tryggvason, K. (1999). Structure of human pro-matrix metalloproteinase-2: Activation mechanism revealed. *Science*, 284, 1667–1670. <https://doi.org/10.1126/science.284.5420.1667>
- Murphy, G., & Nagase, H. (2008). Progress in matrix metalloproteinase research. *Molecular Aspects of Medicine*, 29(5), 290–308. <https://doi.org/10.1016/j.mam.2008.05.002>
- Nagase, H., Visse, R., & Murphy, G. (2006). Structure and function of matrix metalloproteinases and TIMPs. *Cardiovascular Research*, 69, 562–573.
- Nagase, H., & Woessner, J. F. (1999). Matrix metalloproteinases. *The Journal of Biological Chemistry*, 274(31), 21491–21494. <https://doi.org/10.1074/jbc.274.31.21491>
- Page-McCaw, A. (2008). Remodeling the model organism: Matrix metalloproteinase functions in invertebrates. *Seminars in Cell and Developmental Biology*, 19, 14–23.
- Page-McCaw, A., Ewald, A. J., & Werb, Z. (2007). Matrix metalloproteinases and the regulation of tissue remodeling. *Nature Reviews Molecular Cell Biology*, 8, 221–233. <https://doi.org/10.1038/nrm2125>
- Page-McCaw, A., Serano, J., Sante, J. M., & Rubin, G. M. (2003). *Drosophila* matrix metalloproteinases are required for tissue remodeling, but not embryonic development. *Developmental Cell*, 4, 95–106.
- Pastor-Pareja, J. C., Wu, M., & Xu, T. (2008). An innate immune response of blood cells to tumors and tissue damage in *Drosophila*. *Dis. Model Mech*, 1, 144–154.
- Patterson, M. L., Atkinson, S. J., Knauper, V., & Murphy, G. (2001). Specific collagenolysis by gelatinase A, MMP-2, is determined by the hemopexin domain and not the fibronectin-like domain. *FEBS Letters*, 503, 158–162. [https://doi.org/10.1016/S0014-5793\(01\)02723-6](https://doi.org/10.1016/S0014-5793(01)02723-6)
- Pham, L. N., & Schneider, D. S. (2008). Evidence for specificity and memory in the insect innate immune response. *Insect Immunology*, 97–127. <https://doi.org/10.1016/B978-012373976-6.50007-0>
- Purice, M. D., Ray, A., Munzel, E. J., Pope, B. J., Park, D. J., Speese, S. D., & Logan, M. A. (2017). A novel *Drosophila* injury model reveals severed axons are cleared through a Draper/MMP1 signalling cascade. *eLife*, 6, e23611. <https://doi.org/10.7554/eLife.23611>
- Quintero-Fabian, S., Arreola, R., Becerril-Villanueva, E., Torres-Romero, J. C., Arana-Argaez, V., Lara-Riegos, J., Ramirez-Camacho, M. A., & Alvarez-Sanchez, M. E. (2019). Role of matrix metalloproteinases in angiogenesis and cancer. *Frontiers in Oncology*, 9, 1370. <https://doi.org/10.3389/fonc.2019.01370>
- Ra, H. J., & Parks, W. C. (2007). Control of matrix metalloproteinase catalytic activity. *Matrix Biology*, 26, 587–596.
- Raza, Q. S., Vanderploeg, J. L., & Jacobs, R. (2017). Matrix metalloproteinases are required for membrane motility and lumenogenesis during *Drosophila* heart development. *PLoS One*, 12, e0171905. <https://doi.org/10.1371/journal.pone.0171905>
- Rotstein, B., & Paululat, A. (2016). On the morphology of *Drosophila* heart. *J Cardiovasc Dev Dis*, 3, 15. <https://doi.org/10.3390/jcdd3020015>
- Steven, L. J., & Page-McCaw, A. (2012). A secreted MMP is required for reepithelialization during wound healing. *Molecular Biology of the Cell*, 23, 1068–1079. <https://doi.org/10.1091/mbc.E11-09-0745>
- Thomas, S. M., & Brugge, J. S. (1997). Cellular functions regulated by Src family kinases. *Annual Review of Cell and Developmental Biology*, 13, 513–609.
- Uhlirova, M., & Bohmann, D. (2006). JNK- and Fos-regulated Mmp1 expression cooperates with Ras to induce invasive tumors in *Drosophila*. *EMBO Journal*, 25, 5294–5304. <https://doi.org/10.1038/sj.emboj.7601401>
- Verma, R. P., & Hansch, C. (2007). Matrix metalloproteinases (MMPs): Chemical- biological functions and (Q)SARs. *Bioorganic and Medicinal Chemistry*, 15, 2223–2268. <https://doi.org/10.1016/j.bmc.2007.01.011>

- Vidal, M., & Cagan, R. L. (2006). *Drosophila* models for cancer research. *Current Opinion in Genetics & Development*, 16, 10–16. <https://doi.org/10.1016/j.gde.2005.12.004>
- Vidal, M., Larson, D. E., & Cagan, R. L. (2006). Csk deficient boundary cells are eliminated from normal *Drosophila* epithelia by exclusion, migration and apoptosis. *Developmental Cell*, 10, 33–44. <https://doi.org/10.1016/j.devcel.2005.11.007>
- Vidal, M., Salavaggione, L., Ylagan, L., Wilkins, M., Watson, M., Weilbaecher, K., & Cagan, R. (2010). A role of epithelial microenvironment at tumor boundaries: Evidence from *Drosophila* and human squamous cell carcinomas. *The American Journal of Pathology*, 176, 3007–3014. <https://doi.org/10.2353/ajpath.2010.090253>
- Visse, R., & Nagase, H. (2003). Matrix metalloproteinases and tissue inhibitors of metalloproteinases: Structure, function, and biochemistry. *Circulation Research*, 92, 827–839. <https://doi.org/10.1161/01.RES.0000070112.80711.3D>
- Weston, C. R., & Davis, R. J. (2007). The JNK signal transduction pathway. *Current Opinion in Cell Biology*, 19, 142–149.
- Zhang, S., Dailey, G. M., Kwan, E., Glasheen, B. M., Sroga, G. E., & Page-McCaw, A. (2006). An MMP liberates the Ninjurin A ectodomain to signal a loss of cell adhesion. *Genes and Development*, 20, 1899–1910. <https://doi.org/10.1101/gad.1426906>

## SUPPORTING INFORMATION

Additional supporting information may be found in the online version of the article at the publisher's website.

**How to cite this article:** Bindhani, B., Maity, S., Chakrabarti, I., & Saha, S. K. (2021). Roles of matrix metalloproteinases in development, immunology, and ovulation in fruit Fly (*Drosophila*). *Archives of Insect Biochemistry and Physiology*, e21849. <https://doi.org/10.1002/arch.21849>





# Source details

[Feedback >](#) [Compare sources >](#)

## Archives of Insect Biochemistry and Physiology

Scopus coverage years: from 1983 to Present

Publisher: Wiley-Blackwell

ISSN: 0739-4462 E-ISSN: 1520-6327

Subject area: [Agricultural and Biological Sciences: Insect Science](#) [Biochemistry, Genetics and Molecular Biology: Physiology](#)

[Biochemistry, Genetics and Molecular Biology: Biochemistry](#)

Source type: Journal

[View all documents >](#)

[Set document alert](#)

[Save to source list](#)

CiteScore 2022

3.8



SJR 2022

0.529



SNIP 2022

0.692



CiteScore

[CiteScore rank & trend](#)

[Scopus content coverage](#)



# Self Nano-Emulsifying Curcumin (SNEC30) attenuates arsenic-induced cell death in mice

Zarqua Jamal<sup>a</sup>, Joydeep Das<sup>a</sup>, Payal Gupta<sup>b</sup>, Pubali Dhar<sup>c</sup>, Sreya Chattopadhyay<sup>b</sup>,  
Urmil Chatterji<sup>a,d,\*</sup>

<sup>a</sup> Cancer Research Laboratory, Department of Zoology, University of Calcutta, 35 Ballygunge Circular Road, Kolkata, 700 019, India

<sup>b</sup> Department of Physiology, University of Calcutta, 92 Acharya Prafulla Chandra Road, Kolkata, 700 009, India

<sup>c</sup> Laboratory of Food Science and Technology, Food and Nutrition Division, University of Calcutta, 20 B Judges Court Road, Alipore, Kolkata, 700027, India

<sup>d</sup> Centre for Research in Nanoscience and Nanotechnology, Technology Campus, University of Calcutta, JD-2 Sector III, Salt Lake City, Kolkata, 700 098, India

## ARTICLE INFO

Handling Editor: Dr. Aristidis Tsatsakis

### Keywords:

Arsenic  
Self Nano-Emulsifying Curcumin (SNEC30)  
ROS  
Autophagy  
Apoptosis  
Anti-oxidant

## ABSTRACT

Several precedents have confirmed numerous infirmities caused by arsenic poisoning, including immune suppression and cancer. Exposure to arsenic leads to alterations of the cellular machinery and eventually cell death, depending on the dose and duration of exposure. Oxidative stress induced by arsenic is the major mechanism by which it inflicts cellular toxicity, challenging the survival-support - autophagy and culminating in apoptosis in the thymus and spleen of mice. Curcumin, a potent dietary anti-oxidant with known anti-apoptotic and anti-inflammatory properties, was assessed for therapeutic benefits. However, the major caveat of this polyphenol is its low water solubility and limited bioavailability. Therefore, Self Nano-Emulsifying Curcumin (SNEC30) was used to treat mice exposed to arsenic. When administered, SNEC30 effectively ameliorated the adverse effects of arsenic in mice, by restoring structural alterations and reducing ROS-mediated cell death, thereby endorsing the importance of nutraceuticals in counteracting heavy metal-induced cellular toxicity.

## 1. Introduction

Toxicity due to heavy metals is a major problem and claims numerous lives worldwide, since they are stable and bio-accumulative within cells [1]. In recent years, increasing ecological and worldwide public health concern regarding environmental contamination by heavy metals has drawn a great deal of attention. Most importantly, deleterious upshots induced by heavy metals are insidious hazards leading to irreversible health effects and unfavorable outcomes [2]. Such contamination may occur as a result of industrial exposure, air effluence and water pollution. Several studies have shown that one such heavy metal, arsenic, induces apoptosis in many cell types from different organs, including skin, immune organs, reproductive organs, liver, and neuronal cells, and can disrupt the physiological homeostasis in exposed organisms [3–6]. Moreover, with the aid of ongoing research, it has become increasingly lucid that there are important dose-, time-, and tissue-specific differences in the effects of inorganic arsenic III compounds, as well as important gene-environment and co-exposure interactions, which determine how arsenic alters disease risk under a

particular exposure circumstance [7–11]. Toxicity of arsenic is also dependent on the valency of arsenic. Inorganic trivalent arsenic poses to be far more toxic than pentavalent organic arsenic. Toxicity incurred by this group of compounds is largely due to the inhibition of pyruvate dehydrogenase, culminating in a reduced activity of the citric acid cycle and production of cellular ATP. Trivalent arsenic has high affinity for sulfhydryl moieties and therefore leads to inhibition of other cellular enzymes through sulfhydryl group binding [12]. Arsenate, on the other hand, acts as an analog of phosphate that competes for phosphate transporters in glycolytic and cellular respiration pathways leading to the uncoupling of oxidative phosphorylation. Organic arsenic is mostly common in seafood as arsenobetaine and arsenocholine, which are non-toxic compounds [13]. Although, it has become a general notion that organic arsenic is harmless, recent findings have proved that some organic arsenic compounds are as toxic as inorganic arsenic [14].

Earlier studies in our lab have shown that arsenic leads to various toxicities to the reproductive and immune organs, primarily by ROS generation and accumulative oxidative stress [3,6]. Since arsenic-induced immune modulation and cell death can severely affect

\* Corresponding author at: Cancer Research Laboratory, Department of Zoology, University of Calcutta, 35 Ballygunge Circular Road, Kolkata, 700 019, India.  
E-mail address: [urmichatterji@gmail.com](mailto:urmichatterji@gmail.com) (U. Chatterji).

<https://doi.org/10.1016/j.toxrep.2021.07.010>

Received 19 January 2021; Received in revised form 17 March 2021; Accepted 15 July 2021

Available online 17 July 2021

2214-7500/© 2021 The Authors.

Published by Elsevier B.V. This is an open access article under the CC BY-NC-ND license

(<http://creativecommons.org/licenses/by-nc-nd/4.0/>).

normal physiological functioning, it was imperative to investigate possible therapeutic alternatives to counteract the stress.

Cellular damage by heavy metals is a persisting predicament for which no safe and effective therapy is available till date. Several prescribed drugs are banned regularly due to their severe side effects. Effective treatment approaches to tackle this problem are lacking; hence, novel strategies need to be adopted to defy the arsenic calamity. In recent years, herbal products have gained increasing interest to combat heavy metal poisoning because of their non-toxic and effective anti-oxidative properties [15]. Amongst such products curcumin, a hydrophobic polyphenol derived from the rhizome of the herb *Curcuma longa* [16], is widely known for its anti-inflammatory and antioxidant properties [17,18]. In addition, curcumin also exhibits anti-tumor, analgesic, immunostimulant, antiviral, antibacterial and antifungal properties. The chief components of this phytochemical include flavonoids and volatile compounds, such as tumerone, atlantone, and zingiberone [18]. Curcumin can treat diseases, like diabetes, asthma, allergies, neurodegenerative diseases, arthritis and atherosclerosis. In addition, curcumin can potentially modify crucial pathways involved in inflammation and carcinogenesis [18]. Reports have associated curcumin with the amelioration of copper-induced neurodegenerative diseases in *D. melanogaster* [16]. Prevalent studies have also pointed towards the fact that curcumin can prove to be more active in conjunction with other antioxidants like resveratrol and gallic acid and the trio have been found to ameliorate glyoxal-induced damage to the renal cells [19].

Curcumin has been developed as a leading compound for formulating new chemotherapeutic agents for treatment of several ailments owing to its pharmacological safety [20,21]. Curcumin is also believed to possess anti-carcinogenic and pro-oxidant properties that render it competent for the treatment of numerous diseases, including pancreatic malignancy, multiple myeloma, colon carcinoma, dementia, Alzheimer's disease and psoriatic skin [22–24]. Curcumin counteracted the adverse effects of sodium arsenite ( $\text{Na AsO}_2$ ) by inducing activities of antioxidant enzymes [25] and was effective in preventing DNA damage, cell injury and apoptosis [26]. However, studies over the past three decades have revealed that bioavailability of curcumin is severely curtailed by its low water solubility, poor absorption, restricted distribution and high excretion [27].

Numerous nano-formulations including liposomes, polymeric nanoparticles, micelles, nanogels, niosomes, cyclodextrins, dendrimers, silver nanoparticles, and solid lipids have been developed over time to resolve these limitations [28,29]. Curcumin-phospholipid complexes have also been designed to overcome the limitations of absorption [30]. In this study, Self Nano-Emulsifying Curcumin 30 mg (SNEC30), a patented formulation was used to ameliorate the deleterious effects of arsenic on the primary and secondary immune organs in mice. The formulation is prepared by dissolving curcumin in a lipid system which is converted into an emulsion in the stomach. This enables complete dissolution and rapid absorption of curcumin into the bloodstream, enabling immediate action against painful and inflammatory conditions ensuring relatively high bioavailability and stability. Since the effects of SNEC30 on arsenic-induced cell death have not been investigated till date, the present study attempts to substantiate an effective strategy for combating arsenic-induced toxicity in the thymus and spleen of mice.

## 2. Materials and methods

Chemicals and kits: Natrium-*meta*-arsenite ( $\text{NaAsO}_2$ ) was obtained from Merck, Darmstadt, Germany; SNEC30 was obtained from Arbro Pharmaceuticals Pvt. Ltd. (US patent no: US8835509); Annexin-FITC Apoptosis Detection kit was purchased from Bio Legend, USA; Acridine Orange and DCFDA from Abcam, U.K. cleaved PARP, Akt, pAkt1 ( $\text{T}^{450}$ ), mTOR antibodies were procured from Abcam. Beclin1, LC3, Bax, Bcl2, p53 and p-mTOR antibodies were procured from Santa Cruz Biotechnologies, USA. Secondary antibodies (anti-mouse and anti-rabbit

were obtained from Santa Cruz Biotechnologies. GSH, CAT, SOD, DTNB and pyrogallol were all obtained from Sigma-Aldrich, USA.

### 2.1. Animals

Male Swiss albino mice, aged 10 weeks weighing 25 g, were procured from licensed breeding houses and maintained under controlled conditions ( $25 \pm 2$  °C room temperature,  $50 \pm 15$  % RH and normal photoperiod of 12 h dark and 12 h light) throughout the experiment. The animals were given sterile food pellets and water *ad libitum* and allowed to acclimatize to the laboratory environment for 7 days prior to commencement of the experiments. All animal experiments were conducted as per approval and guidelines of the Institutional Animal Ethical Committee, Government of India (Registration Number 885/ac/05/CPCSEA). Principles of Laboratory Animal Care (NIH Publication No 85-23, revised in 1985) as well as specific Indian Laws of Animal Protection (ILAP) were followed throughout the experimental schedule. All care was taken to minimize the number of animals used and their suffering.

### 2.2. Selection of optimum arsenic and curcumin dose

Sodium arsenite ( $\text{Na AsO}_2$ ) was administered in drinking water for 7 days followed by SNEC30 treatment for 14 days. Mice were divided randomly into six groups, each containing six animals ( $n = 6$ ). The groups were as follows: Group I (control group, received arsenic-free water), Group II (received 5 ppm arsenic in drinking water), Group III (received 300 ppm arsenic in drinking water), Group IV (received drinking water with SNEC30 alone), Group V (received 5 ppm of arsenic + SNEC30) and Group VI (received 300 ppm of arsenic + SNEC30). The doses of  $\text{NaAsO}_2$  selected were based on previously published studies [31,32] and the optimal concentration found in ground water (5 ppm) of South and Southeast Asian Belt including India, Bangladesh, Nepal, Vietnam and China [33]. An acute lethal dose, *i.e.*, 300 ppm, was selected keeping in mind the accidental ingestion of insecticides or pesticides and exposures that usually occur to miners, smelters, among others [33]. SNEC30 emulsion was administered with drinking water at a dose of 0.5 mg/kg of body weight, as recommended by the manufacturer.

### 2.3. Tissue collection

After treatment with arsenic and SNEC30, mice were sacrificed by means of rapid cervical dislocation. Thymus and spleen of the mice were promptly removed, weighed in an electrical monopan balance (Lutron GM-300 P) and processed for all subsequent experiments.

### 2.4. Analytical characterization of SNEC30

The SNEC30 nanoemulsion used in this study was analytically characterized for its contents using HPLC (Agilent 1260 Infinity II series), Agilent Technologies Pvt. Ltd., India, equipped with computation software (Open lab CDS, Chemstation Edition), G7122A degasser, G7111A quaternary pump, G1528C manual injector, G7165A MWD detector and a proshell 120EC-C18, 4  $\mu\text{m}$  ( $4.5 \times 150$  mm) column.

### 2.5. Emulsion structure visualization

Cryogenic scanning electron microscopy (Cryo-SEM; Zeiss EVO-18-Special edition, Germany) was used to study the microstructure of the nanoemulsion. 50  $\mu\text{L}$  of the samples were initially frozen to  $-180$  °C in liquid nitrogen and then fractured and etched at  $-110$  °C inside a preparation chamber. The samples were then coated with a gold-palladium alloy at a temperature of  $-170$  °C in a sputter coater (Quorum Q150TES) and then visualized with the help of a scanning electron microscope (Zeiss EVO-18, Germany).

## 2.6. Histology and morphometric analysis

Spleen and thymus slices from control and treated animals were fixed in Bouin's fluid, dehydrated in graded alcohol (50–100 %) and embedded in paraffin. Thin sections (5  $\mu\text{m}$ ) were stained with routine hematoxylin-eosin stain for photo-microscopic assessment [9] under a light microscope (Dewinter Optical Inc., India). The stained sections were subjected to morphometric analysis using the Dewinter Caliper Pro software (Vers. 4.1).

## 2.7. Scanning electron microscopy

Spleen and thymus were dissected and fixed overnight in 2.5 % glutaraldehyde with 0.2 M phosphate buffer at 4 °C. Fixed tissues were washed and subsequently dehydrated through ascending grades of ethanol, placed in chilled acetone, and air dried, overnight [3]. After critical point drying, the tissues were coated with gold-palladium in a sputter coater (Quorum Q150TES) and finally viewed by SEM (Zeiss EVO-18-Special edition, Germany); [3].

## 2.8. Single cell suspension

Thymus and spleen obtained from the sacrificed mice were washed in PBS and gently tapped with sterile blunt ended forceps. The single cells were sieved with the help of nylon mesh (pore size 40  $\mu\text{m}$ ) and washed three times with PBS. Cells were then counted and  $1 \times 10^6/\text{mL}$  cell suspensions were used for the experiments [34].

## 2.9. Estimation of intracellular ROS generation

ROS generation in the thymus and spleen of arsenic, arsenic + SNEC30 and SNEC30 only exposed mice was measured using the oxidation sensitive fluorescence probe, 2',7'-dichlorodihydrofluorescein diacetate (DCFDA, Abcam). In presence of ROS, DCFDA is oxidized to form a fluorescent compound 2',7'-dichlorofluorescein (DCF). 20  $\mu\text{M}$  DCFDA were added to the cell suspension prepared from the thymus and spleen of the experimental groups and incubated for 30 min at 37 °C in the dark [3]. DCF fluorescence was detected by a FACS scan flow cytometer (BD FACS VERSE, USA) at 530 nm and was analyzed by the BD FACSuite™ software.

## 2.10. Estimation of ROS scavenging enzymes

### 2.10.1. Preparation of post-mitochondrial supernatant (PMS)

Thymus and spleen, procured from the experimental animals were homogenized in 0.1 M PBS with KCl (1.17 % w/v) and centrifuged at 800 G for 5 min at 4 °C to separate the nuclear debris. The supernatant obtained was re-centrifuged at 10,500 G for 20 min to obtain the post mitochondrial fraction [34].

Reduced glutathione (GSH) content of thymocytes and splenocytes was determined from protein-free filtrate of thymic post-mitochondrial supernatant (PMS) based on the reduction of 5,5'-dithio-bis-(2-nitrobenzoic acid) (DTNB) at 412 nm, by the method of [35]. GSH content was measured from a standard curve, and expressed in  $\mu\text{M}/\text{mg}$  protein.

Catalase (CAT) activity in thymocytes and splenocytes was evaluated spectrophotometrically from thymic and splenic PMS, based on the method described by Claiborne [36]. Decomposition of  $\text{H}_2\text{O}_2$  to  $\text{H}_2\text{O}$  and  $\text{O}_2$  by CAT present in the protein-free filtrate at 240 nm was expressed as  $\mu\text{M}$  of  $\text{H}_2\text{O}_2$  U/mg of protein.

Superoxide dismutase (SOD) activity was assayed from the cell lysates of thymocytes and splenocytes following the method described by Marklund and Marklund [37], based on the auto-oxidation rate of pyrogallol at 420 nm and inhibition of this auto-oxidation by SOD where 50 % inhibition corresponded to one unit of enzyme activity. Activity was expressed as units/mg of protein.

## 2.11. Detection of acidic vesicles

Acridine orange (1 mg/mL) was added to untreated as well as treated cells for 15 min at 37 °C. Next, cells were washed twice with PBS. Images of cells were obtained using Olympus laser-scanning confocal microscope (FV-10 ASW 3.0 viewer image browser) at 450 nm and 593 nm for the detection of acidic vesicular organelles [3].

## 2.12. Analysis of apoptotic cells by flow cytometry

Cells ( $1 \times 10^6$ ) from thymus and spleen of control, arsenic and curcumin-exposed mice ( $n = 6$ ) were collected and stained with Annexin V-FITC and propidium iodide (PI). Cells were eventually analyzed on a flow cytometer (BD ACCURI, BD Biosciences, USA) and analyzed by BD ACCURI C6 software (Vers. 1.0.264.21). The experiment was performed in triplicate for statistical significance [3].

## 2.13. Immunoblotting

Cells were washed and lysed in ice-cold RIPA cell lysis buffer (150 mM NaCl, 50 mM Tris, 0.1 % Triton X-100 and 0.1 % sodium dodecyl sulphate (SDS) containing protease inhibitors [4-(2-aminoethyl) benzenesulphonyl fluoride], EDTA, leupeptin, aprotinin and bestatin, SIGMA). Protein concentration was determined using the Bradford assay. Proteins were resolved by SDS-polyacrylamide gel electrophoresis and transferred onto nitrocellulose membranes. The membranes were subsequently probed with primary antibodies against p53, Bax, Bcl-2, LC3, Beclin-1, cleaved-caspase 3, cleaved-PARP, Akt, p-Akt, mTOR and p-mTOR overnight at 4 °C. Antibody to  $\beta$ -tubulin was used as loading control. After incubation with horseradish peroxidase-conjugated secondary antibodies, antibody binding was assessed by using enhanced chemiluminescence. Bands were quantified using Image J software (Vers. 1.46r) [3].

## 2.14. Statistical analysis

Results of the experiments, performed in triplicates ( $n = 6$ ), were expressed as mean  $\pm$  standard error, using a statistical software package (Graphpad Prism, Vers. 6.0). Each arsenic treated group was compared to the control and the differences between the group mean values were evaluated by Student's *t*-test as all data sets were normally distributed; *p*-values less than 0.05 were considered statistically significant.

## 3. Results

### 3.1. Characterization of curcuminoid nanoemulsion

In order to determine the purity of the nanoemulsion and ensure that its contents would enter the cells of the thymus and spleen, HPLC was used to identify and quantify the three curcuminoids, viz., curcumin, demethoxycurcumin and bismethoxycurcumin in SNEC30. Fig. 1A provides the sample information and Fig. 1A (table) shows the retention time obtained from the experiment which positively identifies all three curcuminoids compared to the standard run. Based on the regression lines obtained from the standard curve, the percentage area under the peak reflecting the concentration of each component was recorded. The data shows that the SNEC30 nanoemulsion contains 80.26 % curcumin, 17.86 % demethoxycurcumin and 1.88 % bis-demethoxycurcumin (Fig. 1A, table). The cryo-SEM micrographs revealed multiple frozen droplets of the nanoemulsion, with particle diameter ranging from 25 nm to 250 nm. It was also noted that the particles formed aggregates upon being frozen (Fig. 1B).

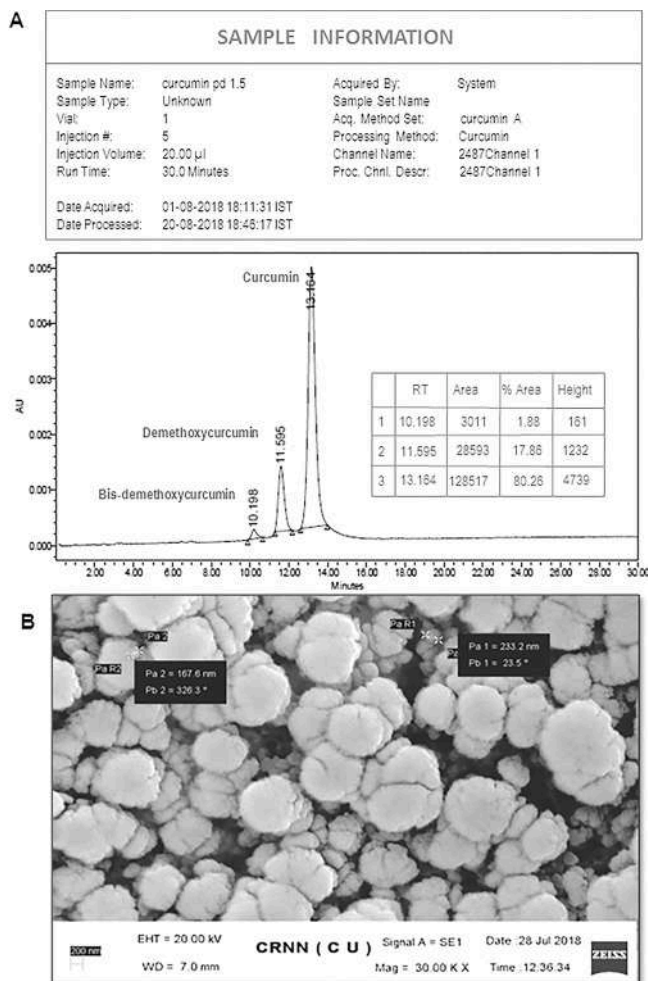


**Fig. 1. Characterization of SNEC30.** (A) HPLC chromatogram of curcumin nanoemulsion by employing Agilent 1260, Infinity II series HPLC. A gradient system of 1 % formic acid in acetonitrile, 60/40 v/v was used ( $\lambda_{\max}$  424 nm). The peak time of curcumin, demethoxycurcumin and bisdemethoxycurcumin was 13.164, 11.595 and 10.198 min. (B) SEM micrograph of SNEC30 nano-emulsion, showing particle size to be in the range of 25–250 nm. Images are at 30,000 $\times$ ; bar, 200 nm.

### 3.2. SNEC30 restores arsenic-induced histopathological alterations in the thymus and spleen

Histological analyses of the thymic sections of arsenic treated mice compared to that of untreated mice (Supplementary Fig. 1; Fig. 2A), depicted significant alterations in morphology of 5 and 300 ppm treatment groups (Fig. 2B and C). Areas of lymphocyte depletion (marked by solid arrows, Fig. 2B) were evident. Loss of cortico-medullary demarcation and dilated sinusoids (indicated by asterisks) were also observed (Fig. 2B and C). Accumulation of apoptotic bodies (pointed by broken arrows) increased by 6- and 8.3-fold ( $p < 0.001$ ), (Fig. 2B and C). Capsular disintegration and loss of trabecular structures were evident (Fig. 2B and C). Thymus histology of 300 ppm group revealed inflammation marked by eosinophil stained area, indicated by solid arrow (Fig. 2C). Administration of SNEC30 after arsenic exposure ameliorated the aforesaid degenerative effects of arsenic on the thymus (Fig. 2D). There was a marked reduction in the scores of apoptotic bodies (3.7- and 3.36-fold, respectively;  $p < 0.001$ ) in the 5 ppm+SNEC30 and 300 ppm+SNEC30 groups compared to the 5 and 300 ppm arsenic-only treated groups. The sinusoids formed due to arsenic exposure were seen to regenerate and inflammation caused was healed (Fig. 2E and F). Reformation of trabeculae and capsule was also observed.

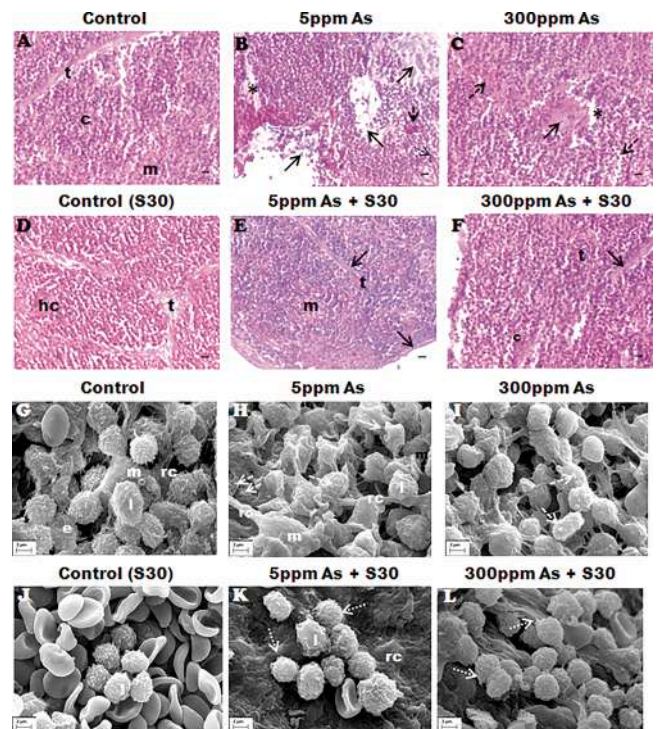


**Fig. 2. Effect of SNEC30 treatment on the tissue architecture of arsenic-exposed mice thymus.** Mice ( $n = 6$ ) exposed to arsenic for 7 days were treated with SNEC30+As for 14 days. Arsenic-treated sections (B and C), showed a significant decrease in cellularity as compared to the untreated one (A). Broken arrows indicate pyknotic nuclei; solid arrows indicate loss of cells; asterisks indicate dilated sinusoids. (D) Section from mice treated with SNEC30, depicting normal histology. Arrows mark partial recovery in terms of organization and tissue architecture in sections treated simultaneously with SNEC30 along with arsenic for 14 days (E and F); c, cortex; m, medulla; t, trabeculae, hc, Hassall's corpuscle; magnification 40 $\times$ ; scale bar 10  $\mu$ m. (G–L) represent the ultra structural images of thymus by scanning electron microscopy at a magnification of 10,000 $\times$ ; scale bar 2  $\mu$ m. (G) Micrograph of control thymus depicting normal surface morphology. Loss of microprocesses from lymphocytes are marked by arrows, broken arrows indicate cell-membrane blebs (H and I). (J) Micrograph of SNEC30 treated thymus, depicting normal features. Dotted arrows indicate restoration of the surface morphology of the tissue upon treatment with SNEC30 (K and L); l, lymphocytes; rc, reticular cells; e, epithelial cells; m, macrophages.

Scanning electron microscopic studies revealed a decrease in the size of thymocytes of 5 ppm (1.3 folds;  $p < 0.05$ ) and 300 ppm (1.7 folds;  $p < 0.01$ ) compared to the control (Fig. 2G), loss of interlobular septae, an increase in surface irregularities and loss of homogeneity and compactness in the structural organization of the tissues in the arsenic-treated groups (Fig. 2H and I) were found. Additionally, distinct protrusions simulating membrane blebbing (indicated by broken arrows), a definitive indication of apoptosis, was observed (Fig. 2H and I). Loss in cellular receptors was common in both 5 and 300 ppm of arsenic treated groups (Fig. 2H and I). Thymocytes of animals treated with SNEC30 alone resembled those of the untreated mice (Fig. 2J). Normal spherical structures of the cells were restored and compactness was revived in 5 ppm + SNEC30 group and 300 ppm + SNEC30 group compared to 5 and 300 ppm arsenic-treated groups. Membrane blebbing was reduced and surface receptors (marked by dotted arrows) were seen to reform (Fig. 2K and L).

The spleen of the arsenic-treated animals was also severely affected (Supplementary Fig. 2). Compared to the control (Fig. 3A), histological and morphometric results demonstrated an increase in the red pulp area of 5 ppm (1.3-fold;  $p < 0.05$ ), as well as, 300 ppm groups (3.6-fold;  $p < 0.001$ ). The tissues appeared to be congested with hemolyzed blood cells

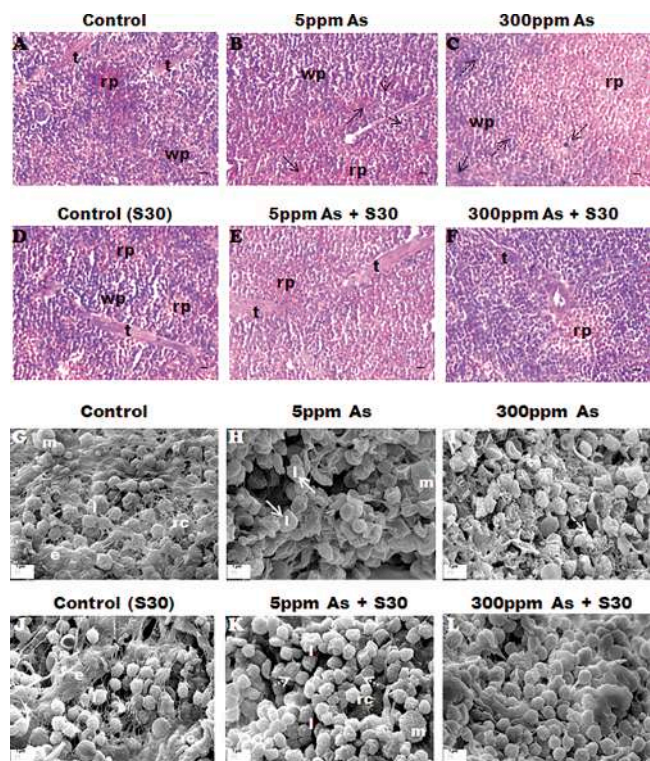


**Fig. 3.** Ameliorative effects of SNEC30 on arsenic-induced spleen injury. Histopathological evaluation of arsenic-exposed mice ( $n = 6$ ) spleen was performed by means of standard H&E staining. (A) Control mice spleen section, showing normal tissue architecture. (B and C) Arsenic intoxicated mice spleen sections, illustrating expansion in red pulp area, tingible bodies marked by arrows and pyknotic nuclei marked by broken arrows. (D) Section of spleen from mice treated with SNEC30 for 14 days, depicting intact histological structure. (E and F) Sections of spleen treated with arsenic followed by SNEC30 nanoemulsion + As, depicting marked reduction in the red pulp area and the restoration of tissue histology back to normalcy; wp, white pulp; rp, red pulp; t, trabaculae, c, capsule; magnification  $40\times$ ; scale bar  $10\ \mu\text{m}$ . (G–L) SEM micrographs of spleen at a magnification of  $5000\times$ . (G) Micrograph of control spleen with normal structural integrity. (H) Solid arrows indicate splenocytes with increased diameters in 5 ppm arsenic treated group and broken arrows mark blebbing of cellular membrane, indicative of apoptotic cells in 300 ppm group (I). (J) Micrograph of SNEC30 treated spleen, depicting normal features. (K and L) SNEC30+As treated groups showing restoration of cellular size, shape and reduction in apoptosing cells. l, lymphocytes; m, macrophages; rc, reticular cells; e, epithelial cells; scale bar  $1\ \mu\text{m}$  (For interpretation of the references to colour in this figure legend, the reader is referred to the web version of this article).

in arsenic exposed groups. There was a decrease in the number of trabeculae. Many lymphocytes were observed with pyknotic nuclei (broken arrows; Fig. 3B and C). Upon treatment with curcumin nanoemulsion, the red pulp area reduced significantly in the 5 ppm + SNEC30 (1.3-fold;  $p < 0.05$ ) and 300 ppm+SNEC30 (1.6-fold;  $p < 0.01$ ) treated groups and the spleen was found to be reconstituted (Fig. 3E and F). Marked reduction in cells with pyknotic nuclei was observed, and was comparable to SNEC30 treated mice (Fig. 3D). Scanning electron microscopic studies revealed that compared to the control (Fig. 3G), an increase in the size of splenocytes of 5 ppm arsenic-treated group (1.8-fold;  $p < 0.001$ ). Loss of interlobular septae, an increase in surface irregularities and loss of homogeneity and compactness in the structural organization of the tissues (Fig. 3H) was also observed. At the 300 ppm concentration, cell shrinkage and absolute disintegration of the integrity of the tissue was noted (Fig. 3I). Distinct protrusions simulating membrane blebbing (broken arrows) was also observed (Fig. 3I). Spleen of animals treated with SNEC30 alone resembled those of the control

(Fig. 3J). Splenocytes of 5 ppm arsenic + SNEC30 group was seen to regain its normal size (dotted arrows) which was found to decrease by 1.6 fold ( $p < 0.01$ ), compared to those of the 5 ppm arsenic treated group. Splenocytes of the 300 ppm arsenic+SNEC30 group depicted reduced membrane blebbing and the tissue was seen to regain compactness and integrity (Fig. 3K and L).

### 3.3. SNEC30 reinstates arsenic-induced redox imbalance in immune cells

It is well established that arsenic induces reactive oxygen species (ROS) generation, which is chiefly responsible for the disruptive effects on the immune organs. Subsequently, the level of DCF fluorescence was monitored using 2',7'-dichlorodihydrofluorescein diacetate (DCFDA) for directly measuring the redox state of a cell. Generation of arsenic-induced intracellular ROS was clearly evident in the thymus of 5 ppm (1.5-fold;  $p < 0.01$ ) and 300 ppm (2.1-fold;  $p < 0.01$ ) groups (Fig. 4A and B) and in the spleen of 5 ppm (1.8 fold;  $p < 0.01$ ) and 300 ppm (2.25 fold;  $p < 0.001$ ) groups (Fig. 4F and G). After treatment with SNEC30, ROS generation was reduced significantly in the thymus by a 2-fold ( $p <$

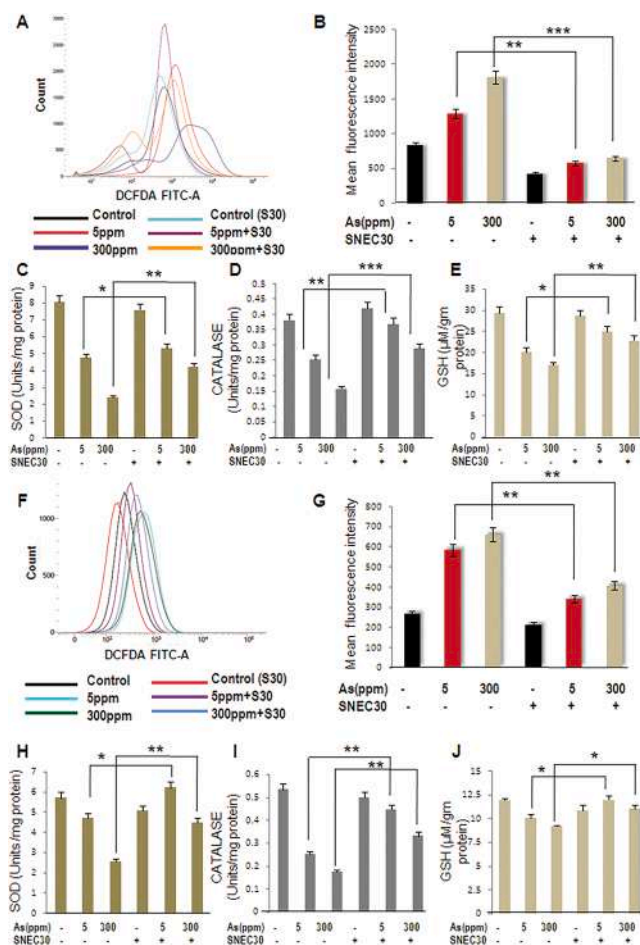


**Fig. 4.** Alterations in the levels of ROS in response to arsenic and SNEC30 treatment. Representative histogram profiles of DCF fluorescence of thymus (A and B) and spleen (F and G). Figures illustrate a dose-dependent increase in ROS generation upon exposure to arsenic for 7 days. Treatment with SNEC30+As for 14 days following arsenic treatment counteracted the oxidative effects of arsenic and downregulated arsenic-induced ROS generation. Error bars represent S.D. from the mean of three independent experiments. (C–E and H–J) Depicts results of enzyme assays carried out for measuring the activities of ROS scavenging enzymes SOD, CAT and the level of reduced glutathione GSH in thymus and spleen of mice treated with only arsenic for 7 days and SNEC30+As for 14 days. Error bars represent S.D. from the mean of three independent experiments. \* $p < 0.05$ , \*\* $p < 0.01$ , \*\*\* $p < 0.001$ .

0.01) and a 2.8-fold ( $p < 0.001$ ) in the 5 ppm+SNEC30 and 300 ppm+SNEC30 exposed groups, respectively, as compared with the arsenic-treated animals (Fig. 4A and B) and by a 1.4-fold ( $p < 0.05$ ) in the 5 ppm+SNEC30 and a 2.4-fold ( $p < 0.01$ ) in the 300 ppm+SNEC30 treated groups of spleen (Fig. 4F and G), compared to the arsenic only-treated mice.

Since dose-dependent increase in ROS was observed, we subsequently investigated the activity of ROS scavenging enzymes, which are the key players of the endogenous defense system that combat the damage instituted by arsenic exposure. Our results indicated that arsenic led to considerable dose-dependent reduction in the activity of SOD, CAT and GSH of both the thymus and spleen (Fig. 4C–E and H–J). After treatment with SNEC30, significant restoration of the activity of SOD, CAT and GSH were noted (Table 1). The results collectively suggested that SNEC30 could attenuate NaAsO<sub>2</sub>-induced oxidative stress.

### 3.4. Effect of SNEC30 on arsenic-induced altered expression of autophagic markers of thymus and spleen

Confocal imaging was carried out with cells of the respective tissues stained with acridine orange and representative micrographs of control, arsenic and arsenic + SNEC30-treated cells from thymus and spleen are shown in Fig. 5A and B. Both 5 ppm and 300 ppm arsenic treatments enhanced formation of autophagosomes in thymocytes and splenocytes ( $p < 0.05$  and  $p < 0.001$ , respectively). Upon treatment with SNEC30, reduction in accumulation of acidic vesicles was observed in both the thymus (Fig. 5A) and spleen (Fig. 5B) of 5 ppm + SNEC30-treated mice, and was significant in the 300 ppm + SNEC30-treated mice ( $p < 0.01$ ). To further establish the active involvement of autophagy in arsenic-mediated stress management, expression of the components of PI3K pathway regulating autophagy was investigated. Significant reduction in the expressions of PI3K, phospho-Akt and phospho-mTOR ( $p < 0.001$ ) were observed in the thymus (Fig. 5C) and spleen (Fig. 5D). Concomitantly, enhanced expression of Beclin-1 and LC3-II ( $p < 0.001$ ) further confirmed ensuing autophagy in the respective tissues following arsenic treatment. Treatment with SNEC30 revealed that arsenic-induced autophagy could be attenuated (Fig. 5C and D) and it was validated both by acridine orange staining (Fig. 5A and B) and western blot which showed a marked increase in the expressions of PI3K, phospho-Akt and phospho-mTOR ( $p < 0.01$ ) together with reduced expression of Beclin 1

**Table 1**  
**SOD, CAT and GSH levels of arsenic treated and arsenic as well as SNEC30 treated mice.** One experimental set of mice was exposed to 5 ppm and 300 ppm sodium meta-arsenite for 7 days and another set was treated with arsenic for 7 days followed by 0.5 mg/kg BW. of SNEC30+arsenic (5 and 300 ppm) for 14 days. Arsenic exposure led to a significant decrease in SOD and CAT activities and caused a reduction in the levels of reduced GSH. Treatment with SNEC30 led to an improvement in the activities of the ROS scavenging enzymes SOD and CAT and an increase in GSH levels. The data shown is representative of experiments carried out in triplicates, \* $p < 0.05$ , \*\* $p < 0.01$  and \*\*\* $p < 0.001$  as compared with the control, for the first set; \* $p < 0.05$ , \*\* $p < 0.01$  and \*\*\* $p < 0.001$  as compared with respective arsenic only treated groups, for the second set. (For interpretation of the references to colour in this Table legend, the reader is referred to the web version of this article).

Organ/AO Factor	5 ppm		300 ppm		5 ppm + SNEC 30		300 ppm + SNEC 30	
	Fold change	P value	Fold change	P value	Fold change	P value	Fold change	P value
Thymus SOD	2.2↓	0.01	3.36↓	0.001	1.47↑	0.01	1.8↑	0.01
Thymus CAT	1.5↓	0.01	2.4↓	0.001	1.5↑	0.01	2.4↑	0.001
Thymus GSH	1.45↓	0.01	1.72↓	0.01	1.25↑	0.05	1.43↑	0.01
Spleen SOD	1.2↓	0.05	2.28↓	0.001	1.3↑	0.05	1.8↑	0.01
Spleen CAT	2.12↓	0.01	2.8↓	0.001	1.76↑	0.01	1.88↑	0.01
Spleen GSH	1.2↓	0.01	1.33↓	0.01	1.2↑	0.05	1.22↑	0.05

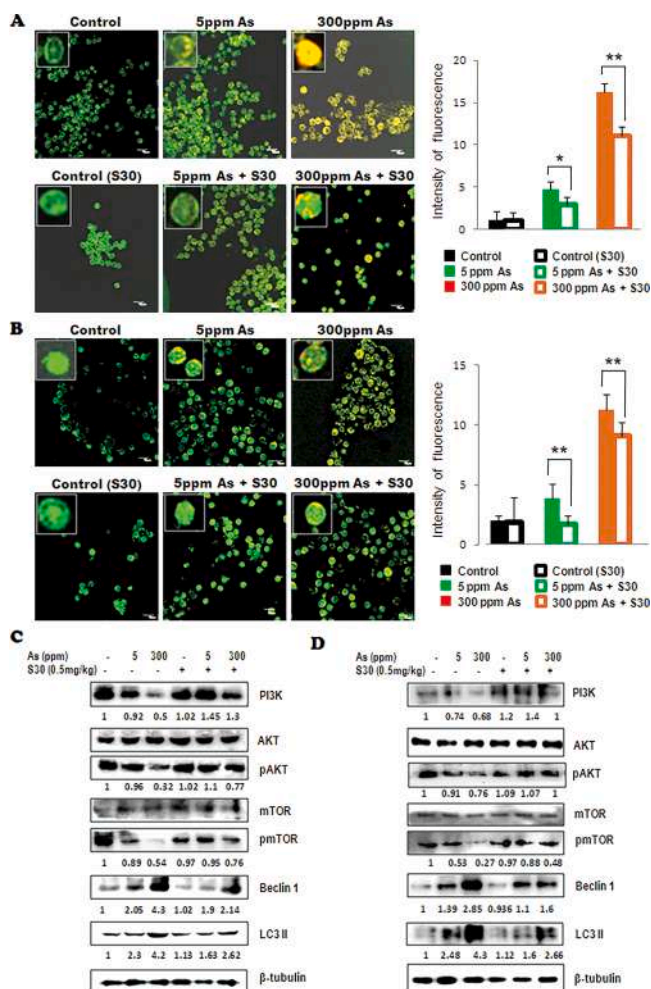


**Fig. 5. Monitoring alterations in autophagy in thymus and spleen of Swiss-albino mice using SNEC30 after arsenic exposure.** (A and B) Cellular autophagy in thymus (A) and spleen (B) measured by AO staining. The presence of acridine orange stained acidic vesicles in the thymus and spleen cells, visualized by confocal microscopy (scale bar 10 μm) confirmed autophagy upon arsenic exposure. With the administration of SNEC30, there was a decrease in the fluorescence intensity of the cells of thymus and spleen indicating towards a reduction in the fluorescence intensity of the cells of thymus and spleen indicating towards a reduction in the acidic vesicular accumulation. The intensity of fluorescence in thymocytes and splenocytes of arsenic groups versus SNEC30+As groups was quantified (right panels), error bars represent S.D. from the mean of three independent experiments. \* $p < 0.05$ , \*\* $p < 0.01$ . (C and D) Western blots showing expression of autophagic protein markers in thymus (C) and spleen (D). β-tubulin was used as loading control and respective fold changes are represented as ratio of net band pixel density of arsenic treated groups to the control. The data shown is a representative of the experiments carried out in triplicates.

and LC3-II in the thymus (Fig. 5C) and spleen (Fig. 5D), compared to the arsenic only treated groups.

### 3.5. Effect of SNEC30 on arsenic-induced apoptotic death of immune cells

As evaluated by Annexin V/PI assay, there were significantly more apoptotic cells in the thymus (Fig. 6A) and spleen (Fig. 6C) of the arsenic-exposed mice, as compared to the untreated mice ( $p < 0.01$ ). Concomitantly, changes in apoptotic markers were observed in the thymus and spleen of 5 ppm and 300 ppm arsenic-treated groups over controls. A dose-dependent decrease in the expression of Bcl-2 ( $p < 0.001$ ) and an increase in the expression of Bax ( $p < 0.05$ ), cleaved Caspase 3 ( $p < 0.01$ ) and cleaved PARP ( $p < 0.001$ ) was observed (Fig. 6B and D). Interestingly, significantly increased expression of p53

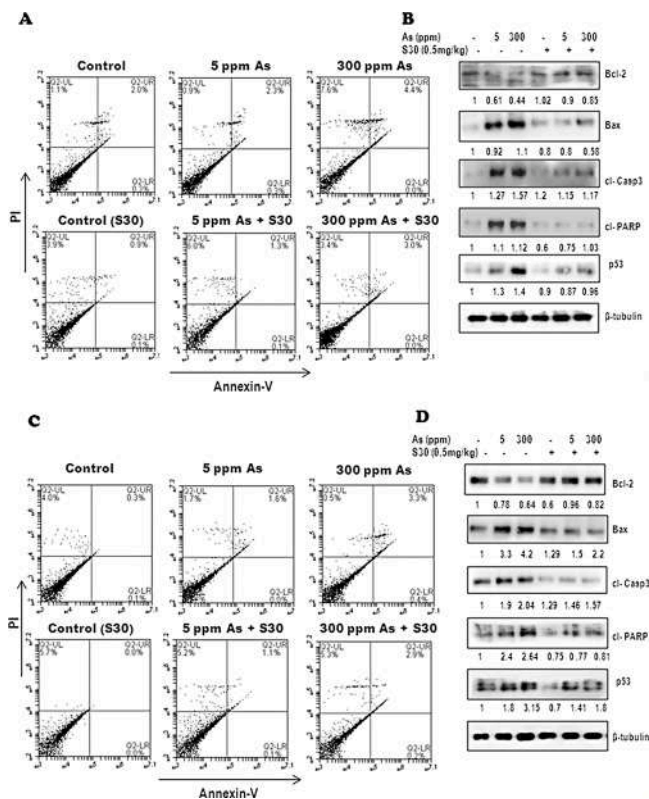


**Fig. 6.** SNEC30 attenuates arsenic-induced cell death in mouse thymus and spleen. (A and C) Quantified panels of Annexin V-FITC and PI double staining graphs obtained from the thymus (A) and spleen (C) of mice treated with sodium arsenite for 7 days followed by SNEC30+As treatment for 14 days. (B and D) Immunoblots of apoptotic protein markers from thymus (B) and spleen (F) of arsenic and SNEC30+As treated mice.  $\beta$ -tubulin was used as loading control and respective fold changes are represented as ratio of net band pixel density of arsenic and SNEC30+As treated groups to the control. Data are representative of three independent experiments carried out in triplicates.

( $p < 0.001$ ), indicated that apoptosis in response to arsenic was p53-dependent. Treatment with SNEC30 reduced the number of apoptotic cells in

the thymus by a 2-fold ( $p < 0.001$ ) and spleen by a 1.5-fold ( $p < 0.05$ ) compared with mice treated with arsenic alone (Fig. 6A and C). In addition, the expressions of both pro- and anti-apoptotic markers were also observed to undergo restoration towards normal levels after treatment with SNEC30 (Fig. 6B and D).

#### 4. Discussion

The involvement of the immune organs and association of the immune system in the regulation of arsenic-mediated toxicity has not been delineated till date. Given the fact that generation of ROS is the most distinct mechanism of arsenic toxicity, it was speculated that compounds having anti-oxidant property might be effective in combating arsenic toxicity. Numerous studies have confirmed that curcumin exerts extensive pharmacological actions in various diseases, including immune-suppression in mice, mostly by virtue of its antioxidant properties [38–40]. Curcumin may also be effective both in the prevention of diabetes mellitus and in attenuating the associated complications, particularly cardiovascular complications [41]. Recently, it has been demonstrated that curcumin has a high affinity with protease and can be considered as an effective Covid-19 anti-protease drug [42]. Both epidemiological and experimental studies have established a favorable correlation between amelioration of heavy metal toxicity and application of curcumin [43,44]. However, a major caveat in applying

curcumin is its relatively low absorption and water solubility, which considerably limits its potency. In order to enhance rapid absorption, SNEC30 has been formulated with self nano-emulsifying drug delivery system (SNEDDS) to enhance the bioavailability of curcumin, without any adverse side effects. Therefore, SNEC30 was implemented to attenuate the damage induced by arsenic on the primary and secondary immune organs in mice.

The noxious effects of ROS might be exerted at the DNA level, also known as DNA oxidation, leading to mutations and possibly cancer [6, 45], at the protein level causing enzyme inhibition, denaturation and protein degradation, and at the lipid level leading to lipid peroxidation. Keeping in line with previous studies, our results indicated a sharp rise in cellular ROS in the thymus and spleen upon arsenic treatment. Activities of antioxidant enzymes, such as CAT and SOD, which are known to be the first line of defense and protect biological molecules from oxidative stress [46], have been shown to reduce significantly in response to arsenic treatment. In addition, GSH levels were also depleted after arsenic treatment, indicating thiol attenuation. These special markers have been proven to be authentic in the diagnosis of arsenic-related organ toxicity. Administration of SNEC30 for 14 days significantly restored the activities of these enzymes in the thymus and spleen of mice, suggesting that SNEC30 could successfully attenuate oxidative stress in  $\text{NaAsO}_2$ -treated mice without causing tissue damage.

Recent studies have shown that a variety of cell homeostasis mechanisms work together to reduce ROS-induced damage to cells and attempt to promote cell survival under conditions of stress. Autophagy is one of the major mechanisms maintaining cellular homeostasis [47]. ROS and autophagy play important roles in stress response in cells through a number of complicated signaling pathways [48,49]. However, if cells are severely damaged, autophagy backs out as a cell survival mechanism and drives the cells towards apoptosis either by active degradation of cellular organelles or by accelerated rate of passive non-selective degradation of cellular components, challenging cell survivability [3]. Concomitant with these reports, we have shown an increased autophagic activity in the arsenic-exposed thymus and spleen of mice, leading to accelerated p53-mediated intrinsic apoptosis. As a respite, treatment with SNEC30 was found to effectively counteract the toxic effects of sodium arsenite-induced cellular toxicity and restore structural and functional homeostasis in the experimental model. Furthermore, SNEC30 prevented the occurrence of apoptosis in the immune organs and assured overall improvement in the physiology of the mice.

#### 5. Conclusion

Exposure to arsenic leads to a severe imbalance of general physiological conditions of an organism, including suppression of the immune system, and may culminate in life-threatening diseases. The anti-oxidant properties of SNEC30, which prevent further deterioration and reverse the damages to the immune organs, assures beneficial outcome for organisms who are inadvertently exposed to environmental and acute doses of arsenic. Amelioration by SNEC30 includes reformation of tissue architecture, decline in arsenic-induced oxidative stress by virtue of its antioxidant potential, and reduction of cell death in the thymus and spleen of Swiss albino mice. Therefore, it may be reiterated that dietary intervention and SNEC30 supplementation will help in curbing the adverse effects of arsenic in organisms. Nevertheless, a more detailed molecular evaluation of the therapeutic efficacies of this formulation will endorse efficient clinical outcome, since SNEC30 has no side effects and promotes improvement of overall health. In addition, the delivery of this nanoemulsion, either *via* oral or systemic routes, need to be delineated and justified for better efficacy of the formulation in patients. Additionally, whether SNEC30 should be used alone or in combination with other drugs which could enhance its effectiveness is a question worthy of investigation in future.



## CRediT authorship contribution statement

**Zarqua Jamal:** Data curation, Formal analysis, Investigation, Validation, Writing - original draft, Writing - review & editing. **Joydeep Das:** Data curation, Investigation. **Payal Gupta:** Data curation. **Pubali Dhar:** Formal analysis, Resources. **Sreya Chattopadhyay:** Formal analysis, Resources. **Urmi Chatterji:** Conceptualization, Funding acquisition, Project administration, Resources, Validation, Writing - review & editing.

## Declaration of Competing Interest

The authors declare that they have no known competing financial interests or personal relationships that could have appeared to influence the work reported in this paper.

## Acknowledgements

We acknowledge the University Grants Commission (UGC), Government of India, for grant to U.C. and fellowship support to Z.J. We would also like to acknowledge the Central Instrument Facility of CRNN (University of Calcutta) for providing flow cytometry and SEM facilities. We are also thankful to DST-FIST, UGC-SAP and DST-PURSE for infrastructure support.

## Appendix A. Supplementary data

Supplementary material related to this article can be found, in the online version, at doi:<https://doi.org/10.1016/j.toxrep.2021.07.010>.

## References

- P.B. Tchounwou, C.G. Yedjou, A.K. Patlolla, D.J. Sutton, Heavy metal toxicity and the environment, *J. Exp. Zool. Suppl.* 101 (2014) 133–164, [https://doi.org/10.1007/978-3-7643-8340-4\\_6](https://doi.org/10.1007/978-3-7643-8340-4_6).
- Q. Zhou, Y. Gu, X. Yue, G. Mao, Y. Wang, H. Su, et al., Combined toxicity and underlying mechanisms of a mixture of eight heavy metals, *Mol. Med. Rep.* 15 (2017) 859–866, <https://doi.org/10.3892/mmr.2016.6089>.
- Z. Jamal, J. Das, S. Ghosh, A. Gupta, S. Chattopadhyay, U. Chatterji, Arsenic-induced immunomodulatory effects disorder the survival-death interface by stabilizing the Hsp90/Beclin1 interaction, *Chemosphere* 238 (2019) 124647, <https://doi.org/10.1016/j.chemosphere.2019.124647>.
- H. Zhao, Y. Wang, M. Guo, D. Fei, M. Mu, H. Yu, et al., Hepatoprotective effects of zinc (II) via cytochrome P-450/reactive oxygen species and canonical apoptosis pathways after arsenite waterborne exposure in common carp, *Chemosphere* 236 (2019), 124869, <https://doi.org/10.1016/j.chemosphere.2019.124869>.
- Q. Tang, L. Bai, Z. Zou, P. Meng, Y. Xia, S. Cheng, et al., Ferroptosis is newly characterized form of neuronal cell death in response to arsenite exposure, *Neurotoxicology* 67 (2018) 27–36, <https://doi.org/10.1016/j.neuro.2018.04.012>.
- A. Chatterjee, U. Chatterji, All Trans retinoic acid ameliorates arsenic induced oxidative stress and apoptosis in the rat uterus by modulating MAPK signaling proteins, *J. Cell. Biochem.* 118 (2017) 3796–3809, <https://doi.org/10.1002/jcb.26029>.
- C.J. Chen, C.W. Chen, M.M. Wu, T.L. Kuo, Cancer potential in liver, lung, bladder and kidney due to ingested inorganic arsenic in drinking water, *Br. J. Cancer* 66 (1992) 888–892, <https://doi.org/10.1038/bjc.1992.380>.
- C.H. Tseng, C.K. Chong, C.P. Tseng, Y.M. Hsueh, H.Y. Chiou, C.C. Tseng, et al., Long-term arsenic exposure and ischemic heart disease in arseniasis-hyperendemic villages in Taiwan, *Toxicol. Lett.* 137 (2003) 15–21, [https://doi.org/10.1016/s0378-4274\(02\)00377-6](https://doi.org/10.1016/s0378-4274(02)00377-6).
- A. Chatterjee, U. Chatterji, Arsenic abrogates the estrogen-signaling pathway in the rat uterus, *Reprod. Biol. Endocrinol.* 8 (2010) 80, <https://doi.org/10.1186/1477-7827-8-80>.
- A. Chatterjee, U. Chatterji, All-trans retinoic acid protects against arsenic-induced uterine toxicity in female Sprague-Dawley rats, *Toxicol. Appl. Pharmacol.* 257 (2011) 250–263, <https://doi.org/10.1016/j.taap.2011.09.011>.
- M. Argos, L. Tong, S. Roy, M. Sabarinathan, A. Ahmed, M.T. Islam, et al., Screening for gene-environment (G×E) interaction using omics data from exposed individuals: an application to gene-arsenic interaction, *Mamm. Genome* 29 (2018) 101–111, <https://doi.org/10.1007/s00335-018-9737-8>.
- K. Jomova, Z. Jenisova, M. Feszterova, S. Baros, J. Liska, D. Hudecova, et al., Arsenic: toxicity, oxidative stress and human disease, *J. Appl. Toxicol.* 31 (2011) 95–107, <https://doi.org/10.1002/jat.1649>.
- K.A. Francesconi, Arsenic species in seafood: origin and human health implications, *Pure Appl. Chem.* 82 (2010) 373–381, <https://doi.org/10.1351/PAC-CON-09-07-01>.
- M. Molin, S.M. Ulven, H.M. Meltzer, J. Alexander, Arsenic in the human food chain, biotransformation and toxicology—Review focusing on seafood arsenic, *J. Trace Elem. Med. Biol.* 31 (2015) 249–259, <https://doi.org/10.1016/j.jtemb.2015.01.010>.
- S. Gao, X. Duan, X. Wang, D. Dong, D. Liu, X. Li, et al., Curcumin attenuates arsenic induced hepatic injuries and oxidative stress in experimental mice through activation of Nrf2 pathway, promotion of arsenic methylation and urinary excretion, *Food Chem. Toxicol.* 59 (2013) 739–747, <https://doi.org/10.1016/j.fct.2013.07.032>.
- A.O. Abolaji, K.D. Fasae, C.E. Iwezor, M. Aschner, E.O. Farombi, Curcumin attenuates copper-induced oxidative stress and neurotoxicity in *Drosophila melanogaster*, *Toxicol. Rep.* 7 (2020) 261–268, <https://doi.org/10.1016/j.toxrep.2020.01.015>.
- M. Suzuki, T. Betsuyaku, Y. Ito, K. Nagai, N. Odajima, C. Moriyama, et al., Curcumin attenuates elastase- and cigarette smoke-induced pulmonary emphysema in mice, *Am. J. Physiol. Lung Cell Mol. Physiol.* 296 (2009) L614–23, <https://doi.org/10.1152/ajplung.90443.2008>.
- B. Salehi, P. Lopez-Jornet, E.P. López, D. Calina, M. Sharifi-Rad, K. Ramírez-Alarcón, et al., Plant-derived bioactives in oral mucosal lesions: a key emphasis to curcumin, lycopene, chamomile, *Aloe vera*, green tea and coffee properties, *Biomolecules* 9 (2019) 106, <https://doi.org/10.3390/biom9030106>.
- M. Hashemzaei, K. Tabrizian, Z. Alizadeh, S. Pasandideh, R. Rezaee, C. Mamoulakis, Resveratrol, curcumin and gallic acid attenuate glyoxal-induced damage to rat renal cells, *Toxicol. Rep.* 7 (2020) 1571–1577, <https://doi.org/10.1016/j.toxrep.2020.11.008>.
- S. Shishodia, G. Sethi, B.B. Aggarwal, Curcumin: getting back to the roots, *Ann. N. Y. Acad. Sci.* 1056 (2005) 206–217, <https://doi.org/10.1196/annals.1352.010>.
- B.B. Aggarwal, S.C. Gupta, B. Sung, Curcumin: an orally bioavailable blocker of TNF and other pro-inflammatory biomarkers, *Br. J. Pharmacol.* 169 (2013) 1672–1692, <https://doi.org/10.1111/bph.12131>.
- K. Hede, Chinese folk treatment reveals power of arsenic to treat cancer, new studies under way, *J. Natl. Cancer Inst.* 99 (2007) 667–668, <https://doi.org/10.1093/jnci/djk191>.
- H. Hatcher, R. Planalp, J. Cho, F.M. Torti, S.V. Torti, Curcumin: from ancient medicine to current clinical trials, *Cell. Mol. Life Sci.* 65 (2008) 1631–1652, <https://doi.org/10.1007/s00018-008-7452-4>.
- V. Krup, L. Hedge Prakash, A. Harini, Pharmacological activities of turmeric (*Curcuma longa* Linn): a Review, *J. Homeop. Ayurv. Med.* 2 (2013) 133, <https://doi.org/10.4172/2167-1206.1000133>.
- F.M. El-Demerdash, M.I. Yousef, F.M. Radwan, Ameliorating effect of curcumin on sodium arsenite-induced oxidative damage and lipid peroxidation in different rat organs, *Food Chem. Toxicol.* 47 (2009) 249–254, <https://doi.org/10.1016/j.fct.2008.11.013>.
- W.H. Chan, H.J. Wu, Protective effects of curcumin on methylglyoxal induced oxidative DNA damage and cell injury in human mononuclear cells, *Acta Pharmacol. Sin.* 27 (2006) 1192–1198, <https://doi.org/10.1111/j.1745-7254.2006.00374.x>.
- S. Prasad, A.K. Tyagi, B.B. Aggarwal, Recent developments in delivery, bioavailability, absorption and metabolism of curcumin: the golden pigment from golden spice, *Cancer Res. Treat.* 46 (2014) 2–18, <https://doi.org/10.4143/crt.2014.46.1.2>.
- B. Salehi, D. Calina, A.O. Docea, N. Koirala, S. Aryal, D. Lombardo, L. Pasqua, et al., Curcumin's nanomedicine formulations for therapeutic application in neurological diseases, *J. Clin. Med.* 9 (2020) 430, <https://doi.org/10.3390/jcm9020430>.
- N. Ghalandaralaki, A.M. Alizadeh, Nanotechnology-applied curcumin for different diseases therapy, *Biomed Res. Int.* 2014 (2014), <https://doi.org/10.1155/2014/394264>, 394264.
- K. Maiti, K. Mukherjee, A. Ganta, B.P. Saha, P.K. Mukherjee, et al., Curcumin-phospholipid complex: Preparation, therapeutic evaluation and pharmacokinetic study in rats, *Int. J. Pharm.* 330 (2007) 155–163, <https://doi.org/10.1016/j.ijpharm.2006.09.025>.
- M. Chakraborty, A. Mukherjee, K.M. Ahmed, A review of groundwater arsenic in the Bengal Basin, Bangladesh and India: from source to sink, *Curr. Pollut. Rep.* 1 (2015) 220–247, <https://doi.org/10.1007/s40726-015-0022-0>.
- A. Basu, P. Sen, A. Jha, Environmental arsenic toxicity in West Bengal, India: a brief policy review, *Indian J. Public Health* 59 (2015) 295–298, <https://doi.org/10.4103/0019-557x.169659>.
- E. Shaji, M. Santosh, K.V. Sarath, P. Prakash, V. Deepchand, B.V. Divya, Arsenic contamination of groundwater: a global synopsis with focus on the Indian Peninsula, *Geosci. Front.* (2020), <https://doi.org/10.1016/j.gsf.2020.08.015>.
- S. Choudhury, P. Gupta, S. Ghosh, S. Mukherjee, P. Chakraborty, U. Chatterji, et al., Arsenic-induced dose-dependent modulation of the NF-κB/IL-6 axis in thymocytes triggers differential immune responses, *Toxicology* 357–358 (2016) 85–96, <https://doi.org/10.1016/j.tox.2016.06.005>.
- D.J. Jollow, J.R. Mitchell, N. Zampaglione, J.R. Gillette, Bromobenzene-induced liver necrosis. Protective role of glutathione and evidence for 3, 4-bromobenzene oxide as the hepatotoxic metabolite, *Pharmacology* 11 (1974) 151–169, <https://doi.org/10.1159/000136485>.
- A. Claiborne, *Catalase Activity*, vol. 1, CRC Press, Boca Raton FL, 1985, pp. 283–284.
- S. Marklund, G. Marklund, Involvement of superoxide anion radical in the autoxidation of pyrogallol and a convenient assay for superoxide dismutase, *Eur. J. Biochem.* 47 (1974) 469–474, <https://doi.org/10.1111/j.1432-1033.1974.tb03714.x>.

- [38] S.C.J. Chueh, M.K. Lai, I.S. Liu, F.C. Teng, J. Chen, Curcumin enhances the immunosuppressive activity of cyclosporine in rat cardiac allografts and in mixed lymphocyte reactions, *Transplant. Proc.* 35 (2003) 1603–1605, [https://doi.org/10.1016/s0041-1345\(03\)00377-4](https://doi.org/10.1016/s0041-1345(03)00377-4).
- [39] S. Sharma, K. Chopra, S.K. Kulkarni, J.N. Agrewala, Resveratrol and curcumin suppress immune response through CD28/CTLA-4 and CD80 co-stimulatory pathway, *Clin. Exp. Immunol.* 147 (2007) 155–163, <https://doi.org/10.1111/j.1365-2249.2006.03257.x>.
- [40] A.C. Bharti, A. Panigrahi, P.K. Sharma, N. Gupta, R. Kumar, S. Shukla, et al., Clinical relevance of curcumin-induced immunosuppression in living-related donor renal transplant: an in vitro analysis, *Exp. Clin. Transplant.* 8 (2010) 161–171.
- [41] D. Margină, O.T. Oлару, M. Ilie, D. Grădinaru, C. Guțu, S. Voicu, A. Dinischiotu, D. A. Spandidos, A.M. Tsatsakis, Assessment of the potential health benefits of certain total extracts from *Vitis vinifera*, *Aesculus hypocastanum* and *Curcuma longa*, *Exp. Ther. Med.* 10 (2015) 1681–1688, <https://doi.org/10.3892/etm.2015.2724>.
- [42] N. Mohammadi, N. Shaghaghi, Inhibitory effect of eight secondary metabolites from conventional medicinal plants on COVID-19 virus protease by molecular docking analysis, *ChemRxiv* (2020), <https://doi.org/10.26434/chemrxiv.11987475.v1>. Preprint.
- [43] S. Daniel, J.L. Limson, A. Dairam, G.M. Watkins, S. Daya, Through metal binding, curcumin protects against lead- and cadmium-induced lipid peroxidation in rat brain homogenates and against lead-induced tissue damage in rat brain, *J. Inorg. Biochem.* 98 (2004) 266–275, <https://doi.org/10.1016/j.jinorgbio.2003.10.014>.
- [44] W.R. García-Niño, J. Pedraza-Chaverrí, Protective effect of curcumin against heavy metals-induced liver damage, *Food Chem. Toxicol.* 69 (2014) 182–201, <https://doi.org/10.1016/j.fct.2014.04.016>.
- [45] L. Benbrahim-Tallaa, R.A. Waterland, M. Styblo, W.E. Achanzar, M.M. Webber, M. P. Waalkes, Molecular events associated with arsenic-induced malignant transformation of human prostatic epithelial cells: aberrant genomic DNA methylation and K-ras oncogene activation, *Toxicol. Appl. Pharmacol.* 206 (2005) 288–298, <https://doi.org/10.1016/j.taap.2004.11.017>.
- [46] M.K. Singh, S.S. Yadav, V. Gupta, S. Khattri, Immunomodulatory role of *Emblica officinalis* in arsenic induced oxidative damage and apoptosis in thymocytes of mice, *BMC Complement. Altern. Med.* 13 (2013) 193, <https://doi.org/10.1186/1472-6882-13-193>.
- [47] Y. Xu, S.O. Kim, Y. Li, J. Han, Autophagy contributes to caspase-independent macrophage cell death, *J. Biol. Chem.* 281 (2006) 19179–19187, <https://doi.org/10.1074/jbc.M513377200>.
- [48] B.R. Underwood, S. Imarisio, A. Fleming, C. Rose, G. Krishna, P. Heard, et al., Antioxidants can inhibit basal autophagy and enhance neurodegeneration in models of polyglutamine disease, *Hum. Mol. Genet.* 19 (2010) 3413–3429, <https://doi.org/10.1093/hmg/ddq253>.
- [49] G. Filomeni, D.D. Zio, F. Cecconi, Oxidative stress and autophagy: the clash between damage and metabolic needs, *Cell Death Differ.* 22 (2014) 377–388, <https://doi.org/10.1038/cdd.2014.150>.



## Source details

[Feedback >](#) [Compare sources >](#)

### Toxicology Reports

Open Access [i](#)

Scopus coverage years: from 2014 to Present

Publisher: Elsevier

ISSN: 2214-7500

Subject area: [Environmental Science: Health, Toxicology and Mutagenesis](#) [Pharmacology, Toxicology and Pharmaceuticals: Toxicology](#)

Source type: Journal

[View all documents >](#)[Set document alert](#)[Save to source list](#)

CiteScore 2022

7.2 [i](#)

SJR 2022

0.730 [i](#)

SNIP 2022

1.351 [i](#)

[CiteScore](#)[CiteScore rank & trend](#)[Scopus content coverage](#)

# The Imperceptible Contagion: Arsenic as a Neuro-Immune-Endocrine Disruptor

Aniruddha Chatterjee<sup>1</sup> · Zarqua Jamal<sup>2</sup> · Joydeep Das<sup>3</sup> · Ananya Banerjee<sup>4</sup> ·  
Urmi Chatterji<sup>4</sup>

Received: 6 July 2021 / Revised: 7 September 2021 / Accepted: 12 September 2021  
© Zoological Society, Kolkata, India 2021

**Abstract** Chronic exposure to inorganic arsenic (iAS) in drinking water is a serious health concern all over the world. Despondently for the Indian sub-continent, the scenario is still not very promising. Arsenic disrupts multiple systems in the body and acts as a neuro-immune-endocrine disruptor as well as a potent carcinogen. The molecular mechanism of iAS action has been defined over the last decade. Several alternatives have been proposed, including oxidative stress, genotoxicity, cytotoxicity, altered cell proliferation, epigenetic changes, and changes to the metagenome, as well as, alterations of signal transduction pathways. iAS is also known to assault the gut-brain axis, gonadal axes, all the major endocrinological organs namely thyroid, adrenal, pancreas, as well as immunological organs like thymus and spleen. iAS is known to exert its deleterious effects at environmentally relevant as well as at higher doses and exhibit atypical dose-dependent responses in different organs. In this article, we aim to summarize the existing information on the different neuro-endocrinological axes and immunological organs targeted by iAS, its teratogenic and carcinogenic potential and the diverse array of mechanisms by which

arsenic exerts its action. This review attempts to integrate the epidemiological data with in vivo and in vitro studies to offer plausible explanations. We also provide a cohesive approach to garner a broader perspective on outlining the therapeutic and restorative strategies against iAS using antioxidants, as well as nano-formulated compounds, since oxidative stress has been unequivocally accepted to be a major cause of arsenic-induced toxicity.

**Keywords** Arsenic · Endocrine disruptor · Oxidative stress · Antioxidants · Signaling pathways · Gut-brain axis

## Introduction

### The Problem

Arsenicosis prompts several different irreversible tribulations in human organs and is known to be a potent cancer-causing agent as well (Chatterjee and Chatterji, 2010, 2011; Bahrami et al., 2020). It is reported to be associated with skin lesions, gastric, cardiovascular, reproductive, psychological and neurological disorders (Tseng et al. 2003; Tseng 2005). The impacts of chronic arsenic exposure are an after-effect of an imbalance between pro- and antioxidant homeostasis, leading to oxidative stress (Gao et al., 2013). Arsenic is well known for generation of free radical and inducing apoptosis in different cell types. There are several reports demonstrating diverse mechanism of arsenic mediated apoptosis in different cell types (Roy et al., 2016; Chatterjee and Chatterji, 2017; Jamal et al., 2019). To combat the curses of this noxious metalloid, the neuro-immune-endocrine systems and the responses elicited against it should be powerful enough for the well being of the host. However, if the

✉ Urmi Chatterji  
urmichatterji@gmail.com

<sup>1</sup> Department of Zoology, Scottish Church College, Kolkata, India

<sup>2</sup> Department of Zoology, Banwarilal Bhalotia College, Asansol, India

<sup>3</sup> Department of Zoology, Dinabandhu Andrews College, Kolkata, India

<sup>4</sup> Cancer Research Lab, Department of Zoology, University of Calcutta, 35 Ballygunge Circular Road, Kolkata 700019, India

respective organs itself are compromised, then what becomes of the exposed individuals is a major cause of concern.

Arsenic is a perceived profoundly harmful metalloid, responsible for various human infections and influencing huge masses of population in various parts of the world. In India, 21 states have arsenic concentrations higher than the permissible limit of 0.01 mg per litre (mg/L), set by the World Health Organization. Over 9.6 million people in West Bengal, 1.6 million in Assam, 1.2 million in Bihar, 0.5 million in Uttar Pradesh and 0.013 million in Jharkhand are at immediate risk from groundwater arsenic contamination, according to the latest data published by the National Rural Drinking Water Programme (NRDWP) of the Ministry of Jal Shakti (MoJS) (Negi, 2021). The primary source of the contamination found in rivers is caused by the untreated sewage effluents. Apart from ground water arsenic, humans may also be exposed to arsenic through food, water, air; or by ingestion of arsenic in pesticides. Accidental exposure to acute arsenic may also occur in miners and smelters.

### **Arsenic as a Unique Endocrine-Disrupting Chemical (EDC) with Properties of an Environmental Estrogen**

Inorganic arsenic (iAS) has been reported to be a potent endocrine disruptor (Meakin et al., 2019). A unique *in vitro* study has suggested that arsenic may act as an environmental estrogen (Stoica et al., 2000). An environmental estrogen, according to the definition of Miller and Sharpe (1998), refers to 'a chemical which originates outside the human body but has the potential to alter endogenous steroid hormone levels or may itself mimic the action of a steroid hormone'. There are reports which state that arsenic can directly interfere with the enzymes involved in hormone biosynthesis (Chattopadhyay et al., 2001), thus altering the endogenous hormone levels, and hence support the fact that arsenic may have potential estrogenic properties. In addition, studies have suggested that arsenic can interfere with ER functioning (Davey et al., 2007). Environmentally relevant doses of arsenic have been reported to have a highly selective effect on *in vivo* gene expression (Hamilton et al., 1998). It has been observed that arsenic can act as a potent endocrine disruptor, and can alter the hormone-activated gene transcription, mediated by all the five steroid hormone receptors, namely glucocorticoid receptor (GR), progesterone receptor (PR), mineralocorticoid receptor (MR), androgen receptor (AR) and estrogen receptor (ER) (Stoica et al., 2000). These receptors show a similar and complex dose-dependent response to arsenic administration. They enhance hormone dependent gene

transcription at very low doses and suppress the same at higher doses (Bodwell et al., 2006). Steroid hormones and their receptors have been shown to play crucial roles in many disease processes, including those associated with chronic arsenic exposure such as cancer, diabetes, cardiovascular diseases, and reproductive and developmental problems (Bodwell et al., 2006). The estrogen signaling system is a key factor in induction or promotion of the carcinogenic process after exposure to estrogen (Dickson and Stancel, 2000). The mechanism of action of estrogens with carcinogenic properties, such as 16 $\alpha$ -hydroxyesterone and 2- and 4-hydroxy catechol estrogens, has been discussed by Yager and Liehr (1996). The estrogen receptor, a ligand inducible transcription factor, is a primary element of estrogen signaling pathway that helps to regulate estrogen-related cell proliferation (Dickson and Stancel, 2000). Studies over the last two decades have enumerated that stimulation of ER results in activation of a variety of genes important in carcinogenesis, as well as apoptosis (Dickson and Stancel, 2000; Divekar et al., 2020), which still merits further investigation.

### **Arsenic can Mimic Steroid Hormones and Disrupt Steroid Hormone Signaling Pathways**

Several possible modes of arsenic action have been proposed. One possibility is that arsenic can modify levels of hormones. It has previously been reported that arsenic can act as a transcriptional activator of the membrane transporter, P-glycoprotein (Maitra and Hamilton, 2005), and changes in the levels of P-glycoprotein can alter intracellular steroid concentrations (Freedman et al., 1988; Davies et al., 2005). A second possible mechanism is that arsenic can act as a hormone-mimetic agonist, or as a competitive or non-competitive antagonist of hormone receptor interaction. Arsenic has been found to mimic the effects of estrogen, activates the receptor in a manner similar to estradiol and leads to increase in ER-regulated gene expression (Stoica et al., 2000). Interestingly, ER is the most divergent of the steroid receptors, and closely related to the common ancestral form from which they have evolved, whereas the four other steroid receptors are closely related to each other and may reflect a much more recent evolutionary duplication and specialization within higher vertebrates (Thornton, 2001). ER shares only 15%, 52%, and 30% identities in the regulatory domains, DNA binding domain (DBD), and hormone ligand-binding domains (LBD), respectively, with other steroid receptors. In contrast, GR, MR, PR and AR share 90–94% identities within the DBD and 55–57% identities within the LBD (Davey et al., 2007). ER has been reported to have divergent co-regulatory interactions and undergo unique SRE

binding and gene activation. Nevertheless, it has been suggested that enhancement of gene activation by arsenic may involve activation steps prior to DNA binding, and the suppressive effects may involve events downstream of activation and binding (Davey et al., 2007). The actual target of arsenic action seems to be part of the shared machinery used to regulate gene expression rather than alter the receptor itself (Davey et al., 2007). Studies have suggested that arsenic can interfere with ER functioning although the exact mechanism remains to be ascertained. Kitchin and Wallace (2008) reported that trivalent arsenicals may bind to several protein targets *in vivo*. One such target is human estrogen receptor alpha where three arsenite binding sites are present (two C<sub>4</sub> zinc finger regions and the hormone binding region). Hence, receptor binding may be stated to be a potent mechanism of arsenic action in humans, although such binding is species specific and not yet established in other mammalian models.

### Effect of Arsenic on Female Reproductive Physiology, Infertility and Associated Disorders

The gonadotropin hormones along with estradiol are required for the maintenance of female uterine physiology after puberty (Jana et al., 2006). The bonafide action of estradiol in the uterus is to promote angiogenesis and cellular proliferation to prepare it for implantation. In responsive tissues, the ER stimulates the expression of specific estrogen-regulated genes and the sensitivity of a given tissue to estrogens varies with the levels of estrogen receptor (Korach et al., 1997). Among the downstream components of estrogen signaling, vascular endothelial growth factor is a potent stimulator of angiogenesis and also a prognostic factor for many tumors, including those of endocrine-responsive tissues such as the breast and uterus. It actually helps the uterus to prepare itself for the incoming blastocyst through neo-vasculogenesis and other functions like increasing microvascular permeability (Rockwell et al., 2002). Numerous studies suggest that estrogens directly regulate VEGF expression at the transcriptional level rendering them an important downstream estrogen responsive gene (Hyder et al., 2000).

Estrogen increases the cellular proliferation rate by recruiting non-cycling cells into the cell cycle, shortening the overall cell cycle time by reducing the length of the G<sub>1</sub> phase and promoting cell entry to the S phase (Clarke et al. 2001). Activation of growth factor receptors regulates G<sub>1</sub> phase cyclins and associated cyclin-dependent kinases. Thus, estrogen may also play a direct role in regulation of cyclin D1 expression. It appears that arsenate may be associated with estrogen-related genetic events in the uterus that may lead to hyperplasia. The effect of arsenic

on cellular proliferation can be further confirmed by studying the nuclear proliferation marker Ki-67. Being expressed in all the cycle phases, Ki-67 is a particularly suitable marker for proliferating cells (Schluter et al., 1993), and is often preferred in cell kinetic studies to other proliferation markers, whose expression is limited to well-defined phases or even sub-phases of the cycle (Gong et al., 1994).

Studies from our laboratory have shown that that arsenic exposure diminishes the circulating levels of both gonadotropins and estradiol. Arsenic treatment significantly downregulated the expression of ER $\alpha$  and its downstream element VEGF in the uterus, indicating that arsenic suppresses the bonafide action of estradiol on the uterus by decreasing the expression of specific receptors, at both the mRNA transcript and protein levels, in the rat uterus that eventually disrupts the estrogen signaling pathway and the G<sub>1</sub> cell cycle proteins, Cyclin D1 and CDK4, responsible for cell proliferation as well as enhanced expression of Ki-67 (Chatterjee and Chatterji, 2010, 2011).

An interesting point to note is that arsenic exposure did not affect the total body weight during the exposure period of 28 days, but decreased the uterine wet weight by almost 30% and constant diestrus was observed in arsenic-treated rats. It may be attributed to the fact that estradiol regulates uterine weight, and thus, low levels of estradiol lead to the specific reduction of uterine wet weight in the exposed animals. Arsenic also leads to tissue degeneration in the uterus. The degenerative changes may also be attributed to adverse effects caused by decreased serum estradiol levels, since uterine growth is primarily dependent on estradiol. The insufficient concentration of estradiol failed to maintain the normal uterine architecture and led to degeneration of the luminal epithelial cells and endometrial glands (Chatterjee and Chatterji, 2010; 2011).

Several studies have suggested that women who live in arsenic-contaminated areas have higher than normal rates of spontaneous abortion and stillbirths (Milton et al., 2005; Sen and Chaudhuri, 2008; Sohel et al., 2010; Table 1).

It is evident from several studies that arsenic exposure reduces the circulating levels of gonadotropins as well as that of estradiol (E<sub>2</sub>). This is further supported by the fact that ovarian steroidogenesis involves enzymes regulated by the gonadotropins FSH and LH, both of which have been reported to be inhibited following arsenic exposure (Sarkar et al., 1991; Hinshelwood et al., 1994). Consequently, low serum levels of FSH and LH in arsenic-treated rats led to reduction in estradiol production and consequently its secretion into the circulation. Some reports have postulated that the decrease in gonadotropin levels may be due to an increase in plasma glucocorticoids in arsenic-treated rats, which may suppress the sensitivity of gonadotroph cells to GnRH and therefore may prevent gonadotropin secretion

**Table 1** Adverse pregnancy outcomes per 1,000 live births among the respondents from Bangladesh

Pregnancy outcome	Exposed (number of individuals)	Non-exposed (number of individuals)	p-Value
Spontaneous abortions	68.8	23.7	0.008
Still births	53.1	23.7	0.046
Preterm births	68.8	27.1	0.018

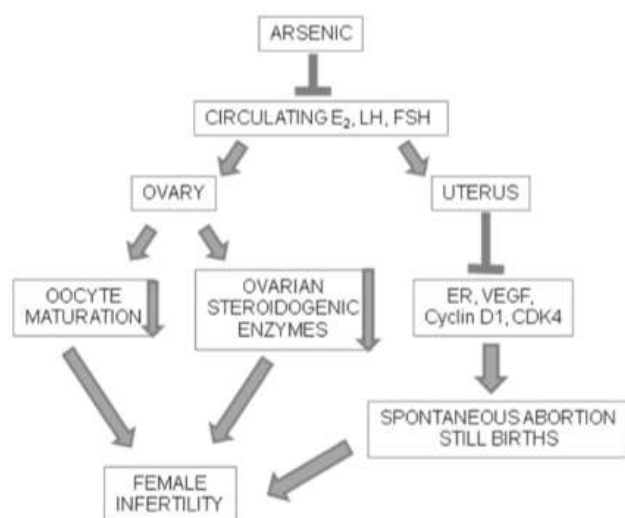
(Ghosh et al., 1999). An increase in ACTH levels in response to arsenic is also known to suppress gonadotropin secretion (Jana et al., 2006). The maturation of the oocyte in ovary is directly controlled by gonadotropins from anterior pituitary namely FSH and LH. The reduction in circulating LH and FSH hampers oocyte maturation in the ovary as well as other steroidogenic enzymes from ovary (Sarkar et al., 1991; Jana et al., 2006). Studies have revealed that arsenic treatment significantly downregulated the expression of ER $\alpha$  and consequently its downstream element VEGF in the uterus (Chatterjee and Chatterji, 2010; 2011). Estradiol-regulated VEGF is chiefly responsible for modulating *in vivo* angiogenesis in the uterus, and its down regulation by arsenic may be a primary cause for spontaneous abortions, still-births and other reproductive failures leading to female infertility (Fig. 1).

### Effect of Arsenic on Male Reproductive Physiology, Infertility and Associated Disorders

Studies have characterized arsenic-induced male infertility by abnormal structural features, decreased counts, and decreased mobility of sperm in humans as well as animal models. A significant decrease in the plasma FSH, LH and

testosterone levels as well as the testicular D5-3 $\beta$ -HSD and 17 $\beta$ -HSD activities support these findings in arsenite treated rats and mice (Pant et al., 2001; Centeno et al., 2002; Sarkar et al., 2003). LH and FSH have been known to be required for the initiation and maintenance of spermatogenesis in pre-pubertal and pubertal rats (Chowdhury, 1979) and for the sperm count in pubertal rats (Russell et al., 1987). The reduction of FSH and LH and a consequent reduction in testosterone production may, therefore, be held responsible for the arsenite-induced changes in spermatogenesis. The reduction in the number of Type A spermatogonia in arsenite-treated rats is possibly due to the increased rate of degeneration in absence of normal FSH levels (Sarkar et al., 2003). Higher doses of sodium arsenite has been reported to increase adrenocortical activity and elevated serum corticosterone level (Biswas et al., 1994), which in turn may reduce the serum gonadotropin and testosterone levels (Phillips et al., 1989). Glucocorticoids also directly suppress testosterone production and secretion by decreasing the testicular LH receptors (Bambino et al., 1981), resulting in the reduction of spermatogenesis and sperm count.

Epidemiological studies have reported that arsenic mediated metabolic disorders; such as that of  $\beta$  oxidation in the mitochondria are the major contributory factors to adverse male fertility outcomes (Chi et al., 2019). An epidemiological study on a Chinese cohort has confirmed that arsenic exposure with food leads to reduced semen quality (Xu et al., 2012). Animal studies corroborate these findings by reporting arsenic accumulation in epididymis, testis, prostate and seminal vesicle upon chronic exposure (Chen et al., 2020). Arsenic induced disruption of male reproductive axis involves unique abrogation of androgen receptor activity unlike any other steroid hormone receptor. Arsenic has been reported to inhibit the transcriptional activity of androgen receptor (AR) in the sertoli cells. *In vivo* studies have revealed that arsenic inhibits AR recruitment to an AR target gene enhancer sequence (Rosenblatt and Burstein, 2009). However, it does not affect (i) hormone binding or receptor binding to androgen response element (ARE), (ii) nuclear translocation of the AR, or (iii) change AR protein levels.

**Fig. 1** Proposed model of arsenic action on female infertility

As reported in the female system, VEGF is one of the important growth factors related to the male reproductive system, as well. VEGF can promote angiogenesis and also plays an important role in resistance to apoptosis. The receptors of VEGF include VEGFR-1, VEGFR-2, and VEGFR-3; after VEGF combined with VEGFR2, it can promote cell division and anti-apoptotic activity (Chen and Shen, 2016). Chronic arsenic exposure has been reported to disrupt the activity of VEGF signaling and promote apoptosis of spermatozoa, which is a prime factor behind male infertility (Yan-Ping et al., 2017).

Recent proteomic studies have reported that arsenic exposure at environmentally and physiologically relevant doses, decrease testosterone level and reduces sperm quality in rats by up regulating 36 proteins and 8 metabolites and down regulating 34 proteins and 5 metabolites out of which 16 proteins and 2 metabolites are unambiguously related to spermatogenesis, sperm function and fertilization, fertility, internal genitalia development, and mating behavior. The major ones have been shown in Fig. 2. Involvement of ERK/AKT/NF- $\kappa$ B signaling pathways have been implicated in the same (Huang et al., 2016). Metabolomic studies have further been able to map arsenic induced male infertility markers. N1-acetyl-N2-formyl-5-methoxykynuramine (AFMK), estrone and carnitine have been reported to be the most significant markers of male infertility related to oxidative stress, disrupted fatty acid metabolism and steroid hormone production (Wu et al., 2021) (Fig. 2).

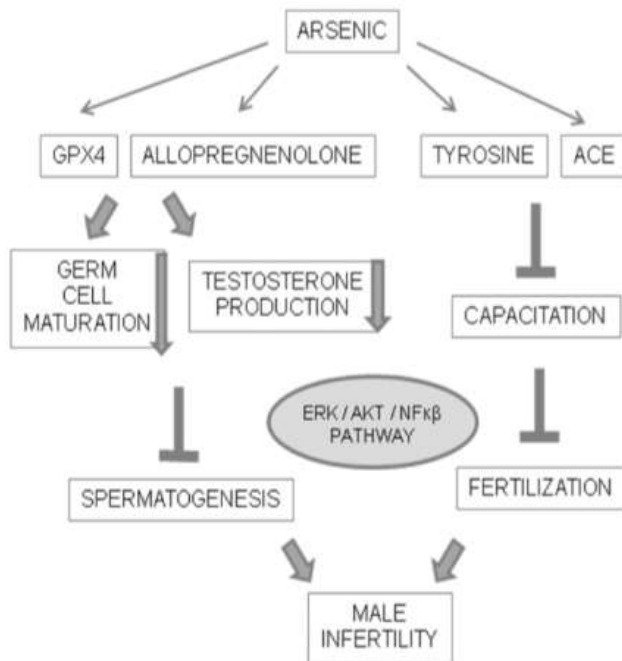


**Fig. 2** Proposed model of arsenic action on male infertility

## Effect of Arsenic on Thyroid Physiology

The relationship between arsenic toxicity and disruption of thyroid function variables has been assessed. According to Jain (2015), levels of thyroid-stimulating hormones (TSH), free thyroxine (FT4), free triiodothyronine (FT3) and thyroglobulin (TGN) were compared between traffic cops in urban areas and pedestrians of rural areas who were exposed to arsenic. A positive relation between arsenic levels and TSH/TGN and a negative connection between arsenic levels and FT3/FT4 were displayed (Jain, 2015). The metalloid has accounted for disruption of thyroid hormone receptors (Davey et al., 2008) and also acts as a possible source of environmental goitrogen (Chang et al., 1991). Additionally, arsenic significantly affected a thyroid hormone receptor-dependent developmental process in experimental model animal systems (Davey et al., 2008). Reports have also indicated that arsenic from seafood expanded plasma TSH. The elevation in TSH was associated with plasma arsenic in a dose-dependent manner (Molin et al., 2017). In addition, functional aspect of the thyroid hormones could have an impact upon arsenic accumulation and toxicity in liver and kidney of rat since both liver and kidney are thyroid-responsive organs (Allen and Rana, 2003).

If exposed to arsenic during pregnancy, the thyroid hormone parameters of the neonate could be directly affected without being interceded by maternal effect of exposure. Maternal serum arsenic levels in the first, second trimester and average arsenic exposure level during pregnancy and cord serum arsenic level may be hazardous factors influencing neonatal thyroid hormones. These findings affirm that neonates are more sensitive to the thyrotoxicity of arsenic exposure (Liang et al., 2020). Fetal thyroid sections from maternally arsenic trioxide (ATO) treated group showed a totally disorganized and disrupted histology of thyroid gland. The concentrations of serum T3 and T4 were significantly lowered while the concentration of serum TSH was considerably heightened in both dams and fetuses. These disorders indicate a materno-fetal hypothyroid state (Ahmed et al., 2019). In this scenario too, the most probable cause of the damage might be generation of ROS, since it is reported to be the most important stimulating component of arsenic toxicity (Marrocco et al. 2017).

## Maternal Exposure to Arsenic: Developmental and Teratogenic Disorders in Newborns

Arsenic has been reported to cause several developmental problems in humans as well as animals (Bodwell et al., 2006). A number of studies (Ferm and Carpenter, 1968;



Hood and Bishop, 1972; Burk and Beaudoin, 1977; Lyster, 1977; Nagymajtenyi et al., 1985) recorded significant reduction in fetal weight and in the number of live fetuses, exencephaly, encephaloceles, skeletal defects and urogenital system abnormalities as well as high male-to-female birth ratio in rodent fetuses at intravenous doses ranging from 15–30 mg kg<sup>-1</sup> day<sup>-1</sup> and inhalation dose of 28.5 mg m<sup>-3</sup> for 4 h day<sup>-1</sup> to an aerosol of arsenic trioxide during critical period of gestation. However, Holson et al. (1999; 2000a; 2000b) suggested that the animal studies were inappropriate and there is absence of robust data to suggest developmental toxicity of arsenic in rodents. As for human studies, significantly higher frequency of spontaneous abortions (11% vs 7.6%) and reduced birth weights were recorded for a population living near a copper smelter when compared with control populations (Nordstrom et al., 1978a). However, DeSesso (2001) reviewed that iAS does not pose any danger to developing offspring when maternal exposure occurs by relevant routes at environmentally relevant concentrations. Contrastingly, Vahter (2008) in his review reported arsenic to be a potent carcinogen which may easily pass through the placenta and may induce a number of effects in the fetus, some of which result in fetal loss or growth retardation. Some of the changes induced in fetal or infant life may lead to detectable adverse health effects later in childhood as well as in adult life. In addition, their children exhibit low birth weight, since ingested iAS can cross the placenta in humans, exposing the fetus to the chemical (Llanos and Ronco, 2009; Rudge et al., 2009; Ahmed et al., 2011). Oral animal studies have also reported that iAS at high doses is fetotoxic and causes birth defects (Waalkes et al., 2003, 2004, 2007; Markowski et al., 2011). Potential modes of action include epigenetic effects, mainly DNA hypomethylation, interaction with steroid hormones (e.g. estrogens, immune suppression, neurotoxicity and inhibition of numerous enzymes) at fairly low exposure levels. Later, Kozul-Horvath et al. (2012) reported that exposure to arsenic at levels at par with the current U.S. drinking water standard, during critical periods of development induces a number of adverse health effects for both the dam and offspring, which may contribute to the increased disease risks observed in human populations. Several epidemiological studies have suggested iAS to be a potent teratogen for neural tube defects (Amitai and koren, 2018) and maternal arsenic levels in the 3rd trimester seemed to have significant impacts on birth outcomes in female infants (Liu et al., 2018). Recent epidemiological studies have reported that in utero arsenic exposure is associated with various types of genetic damage such as DNA strand break and micronuclei formation in newborns, potentially contributing to the development of diseases, including cancer, later in life (Navasumrit et al., 2019).

Studies involving system biology have made some really interesting findings and reported that endocrine disruption to be an important contributing factor in arsenic induced birth defects. The glucocorticoid receptor pathway has been predicted to be a key mediator of arsenic induced birth defects in bioinformatic models. Structural malformations induced by iAS were prevented when signaling of the glucocorticoid receptor pathway was inhibited, in chick embryo. Further, glucocorticoid receptor inhibition demonstrated partial to complete protection from iAS-induced neuro-developmental toxicity in vitro (Ahir et al., 2013).

### Arsenic and the Gut-brain Axis: The Routes and Results

Exposure to arsenic-contaminated water and food or its inhalation due to occupational hazards steer the emergence of serious complications to affect almost all cellular processes and organ systems of human physiology. Amongst all, the brain and gut is not an exception. Interestingly, it is yet to be discerned whether the effects of arsenic on the brain is direct or whether the gut indirectly influences the neurotransmitters and eventually, human behavior.

### Arsenic: A Neurotoxin

Arsenic is considered as major threat to human population due to its carcinogenic and non-carcinogenic deleterious manifestations (Zhou et al., 2018, Parvez et al., 2013). The central nervous system (CNS) is not spared from this poisoning (Tolins et al., 2014). Arsenic penetrates the blood brain barrier to be deposited in several regions of the brain (Prakash et al., 2016). A chronic treatment (more than one month) with high dose i.e. in ppm level (Tyler and Allan, 2014) is mostly required for significant arsenic deposition in rodent brain (Luo et al., 2009, Jiang et al., 2014). Treatment with different doses of arsenic ranging from 0.05 ppm to 50 ppm for 4 months revealed a significant arsenic deposition in brain in 50 ppm exposed group of mice only, but striatal dopamine content decreased significantly in lower exposed female groups also (Bardullas et al., 2009). Arsenic treatment (100 ug L<sup>-1</sup> for 15 days) in adult mice causes cognitive impairment as reflected by a bunch of behavioral studies (Cronican et al., 2013). All these facts may indicate that brain anomalies and behavioral changes may occur regardless of arsenic deposition in brain. Some other mechanisms may act as key players here.

Endothelial cells, astrocyte end-feet and pericytes (PCs) are the three major cellular components of the

blood–brain barrier (BBB). Tight junctions (TJs) form a diffusion barrier between cerebral endothelial cells, allowing passive diffusion of water, some gases, and hydrophobic molecules while permitting elective transport of glucose and some amino acids for neural function. TJs dysfunction may set the stage for a variety of neurological complications and neuro-inflammatory disorders (Ballabh et al., 2004). Increasing arsenic exposure over time might effectively modify TJ proteins (occludin, claudin, ZO-1, ZO- 2), causing the blood–brain barrier to become more permeable. Arsenic can effectively reduce TJs and mTOR protein expression while simultaneously increasing Beclin 1, LC3, and Atg12 levels (Yoon et al., 2006; Altman et al., 2008). Thus arsenic can easily cross the BBB and induce autophagy.

Several epidemiological and clinical studies report arsenic mediated learning and memory impairment, cognitive deficit and mood disorders (Tyler and Allan, 2014). Arsenic exposure (20 mg/kg BW) decreases the level of neurotransmitters like serotonin, epinephrine, homovanillic acid, that affects neurochemical and behavioral functions. Apart from that, arsenic induced apoptosis in hippocampus, neuro-inflammation and impaired neurodevelopment demonstrate a highly neurotoxic nature of arsenic (Sun et al., 2017, Bellinger et al., 2013). It also triggers microglial activation (Singh et al., 2018) which is considered as a well-known marker in both depression and anxiety like behavior (Wang et al., 2018).

Neurotransmitters, which are responsible for communicating between cells in the brain, are affected by arsenic-induced neurotoxicity. Arsenic inversely modulates nor-epinephrine level and helps in inducing dopamine and serotonin level (Mejia et al., 1997). The arsenic effect can change the levels of  $\gamma$ -aminobutyric acid (GABA), glutamate, and other biogenic amines. In addition to that, arsenic may reduce the number of synaptic vesicles in the synapse (Nagaraja et al., 1994). iAS intake by rats reduces the activity of acetyl cholinesterase (AChE), which aids in the metabolism of another neurotransmitter, acetylcholine. In arsenic-treated rats, there was a decrease in muscarinic cholinergic receptor binding in the frontal cortex (26%–43%) and hippocampus (21%–34%) associated with low acetyl cholinesterase activity as compared to control rats. Partial learning and memory, as well as muscle strength are reported to be impaired as a result of arsenic induction, which was linked to cholinergic changes (Chandravanshi et al., 2014). Neuronal cell death has been established as a determinant of cholinergic cell damage in this context. In addition to that, arsenic decreases the expression of brain-derived neurotrophic factor (BDNF) which plays a crucial role in memory and cognition (Sun et al., 2015). Thus, bleaching of blood–brain barrier, perturbation in

neurotransmitter levels, microglial activation are the sequel of arsenic exposure which further lead to more deadly effects.

### Mechanism of Action: ROS Generation and Apoptosis

It is well established that arsenic toxicity is largely mediated through its capability to generate reactive oxygen species (ROS) (Bernstam and Nraigu, 2000; Ramanathan et al., 2003, Jomova et al., 2011), as shown mostly in *in vitro* studies. It is a well-known fact that arsenic exposure leads to inhibition of the antioxidant defense mechanism of the body (Zarazua et al., 2006). ROS generated in response to arsenic exposure lead to accumulation of intracellular hydrogen peroxide by activation of superoxide-producing enzymes such as NADPH oxidase and cause lipid per-oxidation (Chen et al., 1998; Bernstam and Nraigu, 2000). The enzymatic antioxidants like superoxide dismutase, catalase and glutathione peroxidase also get reduced as a result of subsequent free radical generation (Flora 1999; Shila et al., 2005; Flora 2011), and the free radical species thus generated lead to DNA damage and act as a tumor promoter or apoptotic inducer (Waalkes et al., 2003). Arsenic-induced oxidative stress has been studied for different cancers and disorders in humans, but the precise mechanism of arsenic-induced endocrine disruption is yet to be elucidated.

ROS are physiologically required for various biochemical pathways necessary for reproduction (Agarwal et al., 2005). It is known that ROS are present in the female reproductive tract comprising of ovaries and fallopian tube (Behrman et al., 2001) as well as the embryos (Guerin et al., 2001), where they play a physiological role in oocyte maturation, ovarian steroidogenesis, corpus luteal function and luteolysis (Agarwal et al., 2005). *In vivo* levels of ROS are tightly controlled by enzymatic antioxidants that scavenge and neutralize free radicals to maintain an optimal, physiologic oxygen tension in the reproductive system. ROS are like double edged swords and any disruption of this balance mechanism may lead to oxidative stress. Oxidative stress influences the entire reproductive span of women's life and even thereafter, i.e. after menopause as well as in man. It has been suggested that the age-related decline in fertility is modulated by oxidative stress (de Bruin et al., 2002). Oxidative stress in the female reproduction has also been linked with patho-physiology of free radical-induced birth defects (Loeken, 2004) and other situations such as abortions (Lagod et al., 2001), and initiation of preterm labor (Wall et al., 2002; Pressman et al., 2003).

The pathological effects of ROS are exerted by various mechanisms including lipid damage, inhibition of protein synthesis, and depletion of ATP (Ray et al., 2004). A burst of placental oxidative stress during establishment of maternal circulation may cause early pregnancy loss (Jau-niaux et al., 2000; 2003). Oxidative stress may also have a role in patients with recurrent abortions albeit with no known etiology (Agarwal et al., 2005). Increase in oxidative stress leading to disruption of androgenic profile, DNA damage and disorders in the spermatogenic pathway have been suggested to be the leading cause of male infertility due to arsenic exposure (Renu et al., 2018). It has been suggested that iAS mediated male reproductive toxicity is mediated by the pituitary–testicular axis (Jana et al., 2006, Huang et al., 2016).

In a normal cell, apoptosis generally occurs to maintain cellular homeostasis, but can also be initiated under stress conditions like infection, drug treatment, as well as arsenic exposure (Huang et al., 1999). Depending on the dose of exposure, arsenic may either induce apoptosis or carcinogenesis, depending on specific cellular signaling pathways that may be activated. Cells with arsenic load can be eliminated through apoptosis if the damage is severe enough. Among all apoptosis-related genes, p53 is particularly important (Jiang et al., 2001). p53 is well known for suppression of cellular proliferation through two distinct mechanisms. In normal cells p53 induces G<sub>1</sub> arrest in response to DNA-damaging agents, presumably allowing the cells to perform critical repair functions before progressing through the cell cycle (Linke et al., 1997). On the other hand, in abnormally proliferating cells, induction of p53 leads to apoptosis (Midgley et al., 1995). Furthermore, wild-type p53 protein levels increase during apoptosis induced by DNA-damaging agents (Zhan et al., 1996). p53 may be activated by UV rays, hypoxia, gamma-rays etc. Several cysteine residues in the central domain of the protein are critical for p53 binding to the specific DNA sequence. Since the reduction or oxidation of disulphide bonds often occurs at a posttranslational level, p53 is considered as one of the oxidative stress response transcription factors (Valko et al., 2006). ROS have been correlated with p53-mediated apoptosis. Upon overexpression of p53, levels of ROS rise, and inhibition of ROS by antioxidants inhibits apoptosis. The p53 family commonly upregulate at least two proteins that participate in ROS-mediated apoptosis: ferrodoxin reductase (FDXR) and REDD1/HIF-1. In addition to the generation of ROS, p53 induces the expression of p85, which may function as a signalling molecule during ROS-mediated p53-dependent apoptosis (Valko et al., 2006). Among the apoptosis effector entities, members of the caspase family play key roles in the execution of apoptosis (Cohen, 1997). Among the family of caspases, caspase-3 is the major effector of

apoptosis (Jiang et al., 2001). Caspase-3 is activated in a variety of cell types during apoptosis (Soignet et al., 1998). Arsenic is known to induce apoptosis by causing DNA damage, by inducing proteases which cleaves PARP and other vital proteins, or through up regulation of p53 and active caspase-3 (Jiang et al., 2001). It is well established that p53-induced cell death involves procaspase-3 cleavage and eventually activation of caspase-3. Caspase-3 may be activated in apoptotic cells by both extrinsic (death ligand) and intrinsic (mitochondrial) pathways. Studies from our laboratory have shown concomitant increase in p53 and active caspase-3 upon arsenic treatment in the rat uterine cells (Chatterjee and Chatterji, 2017).

It has been hypothesized that the chief cause of arsenic toxicity is the imbalance of pro-oxidant and antioxidant system of body, characterized by increased production of free radicals during metabolism, and subsequent development of oxidative stress (Yamanaka et al., 1991). Generation of high concentrations of ROS due to arsenic exposure is known to suppress the functions of the antioxidant defense system of body (Ahmad et al., 2000, Liu et al., 2001; Zarazua et al., 2006, Chatterjee and Chatterji, 2017) and lead to accumulation of intracellular hydrogen peroxide by activation of superoxide-producing enzymes, such as NADPH oxidase (Chen et al., 1998; Bernstam and Nraigu, 2000). ROS signaling is critical for the responses of cytokines, growth factors, and regulation of transcription factors that promote apoptosis (Shi et al., 2004). The enzymatic antioxidants like superoxide dismutase (SOD), catalase (CAT), glutathione peroxidase (GPx) and glutathione-S-transferase (GST) also get reduced as a result of subsequent free radical generation (Flora, 1999; Shila et al., 2005, Chatterjee and Chatterji, 2017). Free radical scavenging enzymes are the first line of defense against oxidative injury. Status of these antioxidant enzymes provides an appropriate way to assess the pro-oxidant and antioxidant status in tissues (Sharma et al., 2009). For example, reduced glutathione (GSH) is very important for maintaining the cellular redox status induced by arsenic. Depletion of GSH is considered to be a marker of oxidative stress (Spear and Aust, 1995). There are three ways in which arsenic can down regulate cellular GSH levels—(a) GSH is proposed as the electron donor for the conversion of pentavalent to trivalent arsenicals and plays a critical role in both the enzymatic and non-enzymatic reduction of pentavalent to trivalent arsenicals and in the complexation of arsenicals to form arsenothiols during the methylation process; (b) arsenite has high affinity to GSH as GSH and other monothiols along with dithiols are required for methylation of arsenicals—a primary step in their metabolism; and (c) free radicals induced by arsenic can oxidize GSH. GSH and the GSH-related enzymes, glutathione peroxidase (GPX), glutathione reductase (GR)

and glutathione S-transferase (GST), are important antioxidants that play crucial roles in the detoxification of arsenic. These enzymes exhibit different substrate specificities and collaborate to provide the main enzymatic defense system against oxidative stress in mammalian cells. Cellular GPX (cGPX) prevents the formation of ROS by catalyzing the decomposition of hydrogen peroxide with the concomitant oxidation of GSH to GSSG (Zakharyan and Aposhian, 1999; Yeh et al., 2002; Flora, 2011). Inhibition of antioxidants are known to cause oxidative damage of cellular macromolecules, including DNA (Poli et al., 2004), leading to apoptosis, through oxidation sensitive signaling pathways (Kamat et al., 2005). The fundamental executors of the ROS mediated apoptotic pathways are Bcl-2 family proteins and caspases. Bcl-2 family members regulate apoptosis by modulating the release of cytochrome c from the mitochondria (Green and Reed, 1998). In the cytosol, Apaf-1, pro-caspase 9 and released cytochrome c from the mitochondria interact to form the apoptosome that drives activation of caspase-3. In absence of an effective repair machinery, the cell proceeds towards apoptosis (Das et al., 2010). It has been reported that arsenic significantly decreased the live cell population and increased cellular apoptosis in rats exposed for 28 days (Chatterjee and Chatterji, 2017).

It is known that inhibition of the PI3K/Akt pathway elicits anti-apoptotic response and promotes cellular proliferation (Goussetis and Platanias, 2010). It is also well established that, arsenic-mediated cellular apoptosis is coordinated by MAPKs, such as ERK1/ERK2 and JNK (Eguchi et al., 2011). Activation of each signaling pathway is type and stimulus specific. For example, endogenous ROS production induces ERK but not p38, whereas exogenous ROS treatment induces p38 and not ERK (Graham-Evans et al., 2004; Valko et al., 2006). It has also been reported that high levels of arsenite stimulated the JNK signaling pathway and induced apoptosis (Qu et al., 2002). Concomitant with these reports, up regulation of p-JNK and p-ERK1/2 has been shown upon arsenic treatment for 28 days. ERK activation is often concomitant with p21 induction under physiological conditions. This statement is also in agreement with our findings where up regulation in the level of p21 has been observed upon arsenic treatment, indicating increase in number of apoptotic cells (Chatterjee and Chatterji, 2017). Hence, it may be commented that arsenic induced apoptosis follows the extrinsic pathway via up regulation of ERK-JNK pathway and downregulation of PI3K/AKT pathway (Fig. 3).

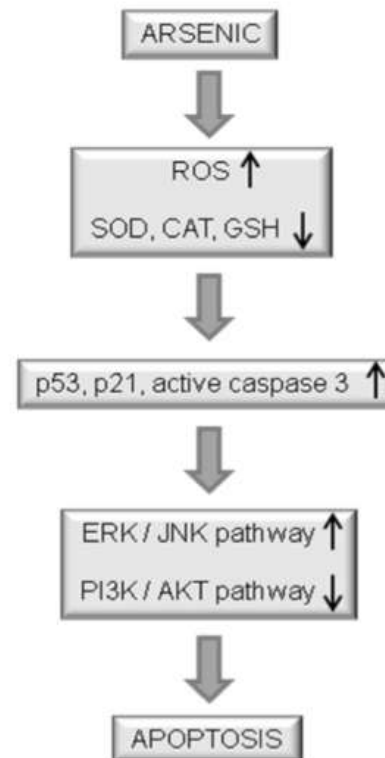


**Fig. 3** Proposed pathway of arsenic action on apoptosis

### Epigenetic Features of Arsenic-Induced Carcinogenesis: DNA Hypermethylation and Hypomethylation

Differential DNA methylation patterns have been observed in individuals with high urinary arsenic concentrations, suggesting that these alterations may be important for non-genotoxic arsenic induced carcinogenesis. Arsenic exposure has been shown to induce global DNA hypomethylation, as well as specific gene promoter methylation changes through the alteration of CpG methylation status (Sage et al., 2017).

### Global Hypomethylation

S-adenosylmethionine methyltransferase (SAM) is a cofactor that acts as a methyl-group donor for many biomolecules. The production of methylated arsenic species leads to the depletion of SAM and a decrease in the availability of methyl groups. Global hypomethylation can lead to chromatin remodeling, allowing for the transcription of previously inaccessible oncogenes and cancer-associated genes. It has been reported that exposure to 5  $\mu$ M iAs over 29 weeks may transform cells malignantly. This is performed by hypomethylation near the transcriptional start site of these genes. Evidence of global

hypomethylation as a result of iAs exposure has been shown in multiple cancer types, including prostate, breast and liver cancers. Furthermore, widespread DNA hypomethylation in hepatocytes is implicated in the increased expression of pro-growth genes, particularly the estrogen receptor. iAs exposure was observed to be a putative cause of significant DNA hypomethylation in adult peripheral blood mononuclear cells, suggesting possible involvement in lymphatic cancers. Hence, global DNA hypomethylation seems to be quite significant in arsenic-induced carcinogenesis (Bailey et al., 2013).

### Promoter Hypermethylation

In a genome-wide study, it was discovered that 2919 genes showed differential DNA methylation profiles when exposed to concentrations of iAs around current WHO guideline levels (at or above 10 µg/L), most of which were identified as CpG islands near the transcription start site. Exposure to higher arsenic concentrations between 250 and 500 µg/L showed a similar relationship between iAs exposure and promoter hypermethylation. Arsenic levels above 500 µg/L were associated with increased methyl acceptance capacity of promoter DNA. Thus a probable threshold exists at which global hypomethylation may become more prevalent in arsenic-induced carcinogenesis. These observations suggest that arsenic may be able to induce tumorigenesis and cancer progression through the epigenetic silencing of tumor suppressors as well as the epigenetic activation of oncogenes or associated genes. One of the most notable examples of this is the significant hypermethylation of the TP53 promoter, the level of which was elevated in arsenic-induced skin cancers. Evidence of promoter hypermethylation has been shown in a number of cancer types, including prostate, skin, a bladder, although the exact role of this in carcinogenesis has yet to be fully elucidated (Pelch et al., 2015).

Both hypomethylation and hypermethylation have been related with cell differentiation and malignant transformation. At the point when these progressions happen simultaneously, as they seem to do following ongoing arsenic exposure, methylation changes in the specific genetic sites might be more pertinent to carcinogenesis than the universal pattern in DNA methylation. The localized nature of these changes unequivocally suggests that these occurrences are targeted and specific in nature. It has been contended that arsenic alters the epigenetic status of chromatin and the alteration is accompanied with a decrease in the methylation state of DNA. Arsenic-induced DNA hypomethylation is a function of dose and exposure duration and may lead to oncogenic activation (Reichard and Puga, 2010). Acute arsenic exposure or arsenic

exposure at non-transforming levels does not bring about global hypomethylation of DNA. Transcription of DNA methyl transferase was elevated but the activity of this enzyme was reduced with arsenic transformation. Taken together, these outcomes show arsenic may act as a cancer-causing agent by prompting DNA hypomethylation, which thus causes erroneous gene expression, and they establish a legitimate hypothesis of component in arsenic carcinogenesis (Zhao et al., 1997). Concurrently, a few research studies have indicated hypermethylation of tumor suppressor genes like p53, whose expression was found to be increased seven-folds upon arsenic exposure (Reichard and Puga, 2010).

### Arsenic as an Immune Disruptor

Studies in our laboratory were performed using male Swiss albino mice as the experimental model. The primary immune organ (thymus) and the secondary immune organ (spleen) were selected for evaluating the impact of exposure to acute arsenic concentrations in drinking water. A series of data both structural and molecular, pointed towards the debilitating effects on the respective organs. The outcomes showed ensuing damage to the general structure of the cells and organelle design of the particular tissues as revealed by the micrographs of histology, scanning and transmission electron microscopy (Jamal et al., 2019). An expansion in the generation of ROS led to an intense imbalance in the measure of ROS produced and action of the ROS scavenging enzymes. The subsequent oxidative pressure set off inflammatory responses as shown by cytokine investigation from serum of arsenic-treated mice. Immunophenotyping from thymocytes and splenocytes showed a reduction in the CD4-CD8 T Cell proportion, pointing towards an immuno-suppressed condition. Activation of the Hsp90-mediated autophagy, through the stabilization of Beclin1 protein, a crucial factor for the initiation of autophagosomes was observed as an initial survival pathway. Inception of autophagy and apoptosis was apparent at lower doses and was found to expand in a dose-wise manner, as affirmed by the data collected through electron microscopy western blot, confocal imaging and flow cytometry (Jamal et al., 2019). Taken together, according to our findings, arsenic-induced oxidative pressure and immunotoxicity might be involved to invigorate lopsidedness between free radical generation and the anti-oxidant system, culminating in inflammation and eventually autophagy-initiated apoptosis in the immune organs (Jamal et al., 2019; Jamal et al., 2021).

## Plausible Therapeutic Interventions

### All-trans Retinoic Acid Ameliorates Arsenic-induced Endocrine Disruption

Arsenic exposure has been identified with serious medical conditions since quite a long while. Arsenic, a metalloid found universally across the globe, is perhaps one of the most unsafe EDCs (endocrine disruptors) which lead to a wide range of health hazards including skin sores, malignant growth, cardiovascular and immunological problems (Choudhury et al., 2016; Sabir et al., 2019; Jamal et al., 2019). There is no limit to the damages that endocrine disruptors like arsenic can do to our bodies: elevating production of certain hormones and diminishing others; emulating hormones; transforming one hormone into another; meddling with hormone signaling; inducing cells to apoptose prematurely; and accumulating in endocrine organs (<https://www.epa.gov/consumer-guides/dirty-dozen-endocrine-disruptors>). Arsenic additionally follows up on various endocrine organs and can alter the hormones engaged in glucose metabolism (Kulshrestha et al., 2014). Sodium arsenite disrupts the estrogen signaling pathway (Chatterjee and Chatterji, 2010) and diminishes circulating estradiol and gonadotropin levels in a dose and time-dependent way generally by producing ROS and hence, oxidative stress (Chatterjee and Chatterji, 2011, 2017). Arsenic, as a strong endocrine disruptor, can change steroid hormone receptor-mediated gene regulation at very low, environmentally relevant concentrations in cell cultures and also in animal models (Davey et al., 2008). There are adequate confirmations supporting the way that arsenic in drinking water is related with enlistment of stress mostly through deregulation of the working of endocrine organs, at last prompting hormone discharge in a disrupted manner. The role of arsenic in the endocrine disturbance is another arising space of interest that requires real understanding and examination, particularly its mechanistics. The ubiquitous presence of arsenic along with the serious wellbeing impacts legitimizes further exploration, schooling and mindfulness in regards to preventive activity to decrease human exposure to this endocrine disruptor. The impact of evidences is sufficient enough to recommend the essential requirement for additional investigations.

Mechanistically, elevated levels of ROS generated by arsenic is the chief driving force that accentuate perturbation of cellular redox balance and eventually cell death (Zarazua et al., 2006; Ling et al., 2017). Since, characteristic phyto-products procured from dietary sources contain a wide assortment of anti-oxidants, as of late, various investigations have been completed to survey the defensive capability of dietary antioxidants against arsenic-induced

oxidative stress and apoptosis (Singh et al., 2013) and their preventive impacts on arsenic-induced oxidative genotoxicity and apoptosis (Muthumani et al., 2015), indicating that increasing intracellular antioxidant levels may have preventive or restorative consequences for arsenic-instigated toxicity. *All-trans* retinoic acid (ATRA), a functioning metabolite of vitamin A, is known for its anti-oxidant properties (Palace et al., 1999) and studies have shown that ATRA is a promising remedial specialist against arsenic-induced endocrine disturbances in animal models, and overcomes arsenic-induced deterioration of the endocrine homeostasis.

Studies from our laboratory have shown that 4 ppm arsenic-exposed female Sprague Dawley rats which were concomitantly treated with 0.5 mg Kg<sup>-1</sup> ATRA (E-Merck, USA) for 28 days moderately recovered from arsenic-induced disruptions. However, continuous ATRA administration for a period of 56 days was significantly more effective in restoring the expression levels of LH, FSH and estradiol, along with estrogen receptor, VEGF, Ki-67, G1 cell cycle regulatory proteins and the histological architecture of the uterus (Chatterjee and Chatterji, 2011). Being a lipophilic molecule, ATRA can easily diffuse through the cellular membrane (Le Doze et al., 2000) and reduce oxidative stress and apoptosis (Ahlemeyer et al., 2001). Consequently, we have observed that administration of ATRA increased the levels of serum estradiol and gonadotropins, which indicates significant protection of the levels of rate-limiting enzymes for the pituitary gonadotropins and ovarian hormones. This finding is further supported by the reports that retinoic acid may promote biosynthesis of estradiol production in JEG-3 cells and CTB cells isolated and from normal placenta, increase aromatase activity (Zhu et al., 2002), and also stimulate 17 $\beta$ -HSD production in JEG-3 cells (Piao et al., 1995). Stimulation for short period with ATRA increases the aromatase activity and mRNA expression of p450arom in JEG3 cells. In addition, retinoic acids promote the biosynthesis of estradiol by up regulating the transcription of CYP19A1 and 17HSD1 genes and stabilizing p450arom transcripts (Zhu et al., 2002). Interestingly, ATRA showed pronounced recovery, as compared to those animals which were fed with arsenic-free water for a period of almost two months (Chatterjee and Chatterji, 2011). It may be attributed to the fact that when agents leading to oxidative stress are removed, the stress reduces over time (Huang et al., 2009). Some proteins recover fast, the others very slowly (Chevallet et al., 2003). Since arsenic has been seen to persist in the body even when exposure to arsenic was withdrawn and arsenic-free water was administered, it may be stated that slow revival of detoxifying agents, such as catalase, superoxide dismutase and glutathione, may lead incomplete recovery and hence, administration of ATRA

for 28 days after arsenic withdrawal was beneficial for the animals (Chatterjee and Chatterji, 2017) (Fig. 4). Furthermore, in rats retention time of arsenic in blood is much longer compared to humans primarily because of retention in hemoglobin of red blood cells. Arsenic can significantly accumulate in rat RBCs because of the binding of the reactive arsenic metabolite, dimethylarsinous acid (DMAIII), to a highly reactive cysteine residue in rat Hb (Vahter, 1999; Lu et al., 2004). ATRA treatment also ameliorated the damage caused by oxidative stress by down regulating the ROS generation in response to arsenic treatment, increasing the cellular enzymatic and non-enzymatic antioxidant levels namely catalase, Superoxide-dismutase and Glutathione in the rat uterine cells. It thereby protects the uterine cells from apoptosis by down regulating p53 and active caspase-3 (Chatterjee and Chatterji, 2017) (Fig. 4).

The activity of ATRA is mediated primarily by members of the retinoic acid receptor (RAR) subfamily, namely RAR $\alpha$ , RAR $\beta$  and RAR $\gamma$ . They all belong to the nuclear

receptor superfamily of transcription factors. RARs form heterodimers with members of the retinoid X receptor (RXR) subfamily and act as ligand-induced transcription factors through binding specific RA response elements (RAREs) located in target genes promoters. RARs also have non-genomic effects and activate kinase signaling pathways, which influences the transcription of the RA target genes. Hence, it may be hypothesized that ATRA may express its corrective action against arsenic induced endocrine disruption via genomic as well as non-genomic pathways (di Masi et al., 2015).

In a similar fashion, it may be hypothesized that ATRA helps to restore the imbalances caused by arsenic in the major endocrine glands of the body namely thyroid, adrenal and pancreas and their biological activity such as-

- glucose metabolism ((Kulshrestha et al., 2014) by counteracting the disruption in the pancreatic acinar cells and plasma level of the chief glucose metabolizing hormone insulin.

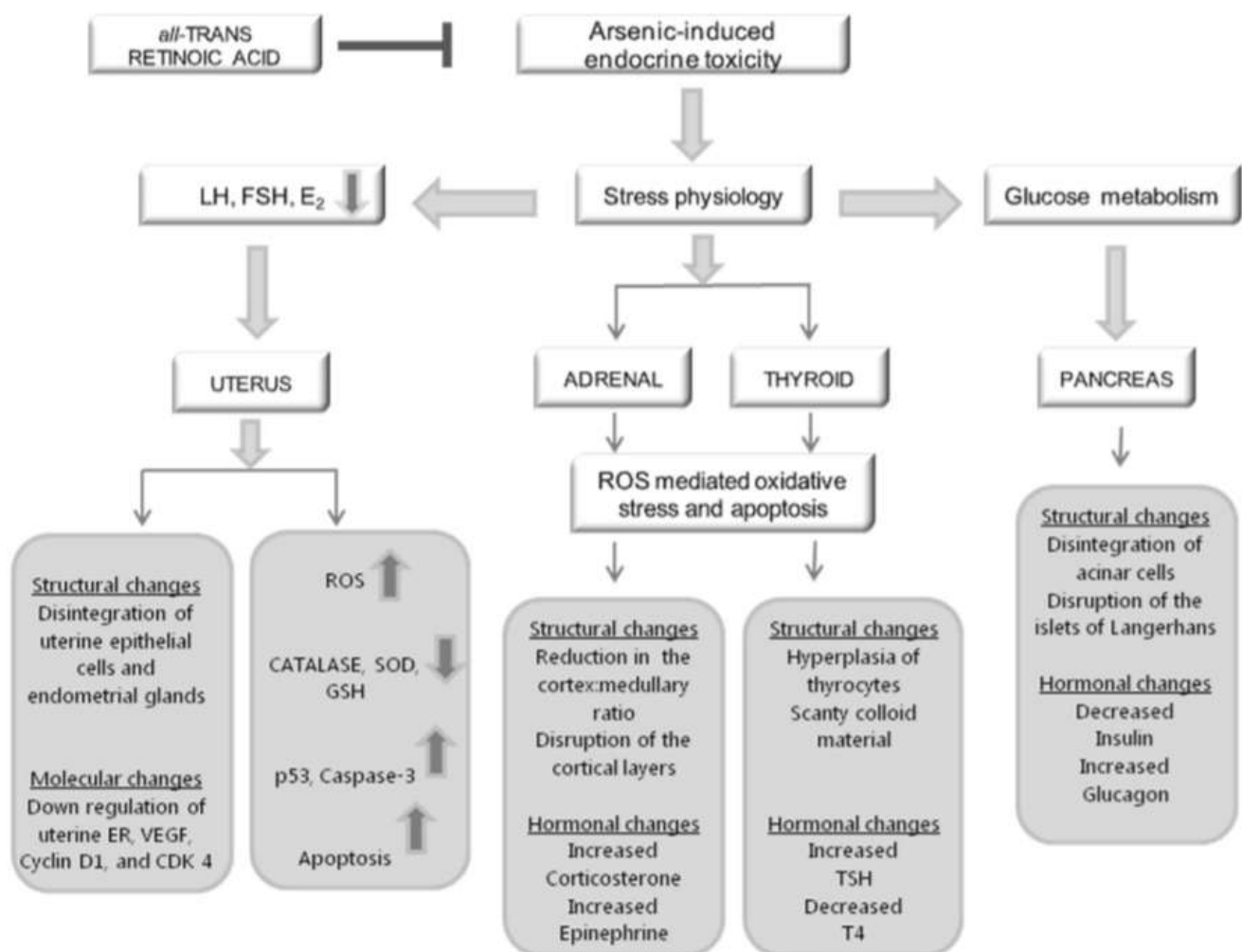


**Fig. 4** Reversal of arsenic-induced deleterious effects by *all-trans* retinoic acid

- counteracting ROS mediated stress and disruption of thyroid and adrenal cellular structure as well as their hormonal secretions namely T4 (Ciarrocca et al., 2012), corticosterone (Chattopadhyay and Ghosh, 2010) and epinephrine (Sabir et al., 2019)

We propose a tentative model of ATRA mediated curative action on thyroid, adrenal and pancreas in line with recuperative action of ATRA as shown in rat uterus (Fig. 4).

### • Curcumin Nanoemulsion as an Effective Remedy

Till date there is no safe and compelling treatment accessible for heavy metal inebriation. Many medications are being prohibited frequently because of their extreme results. Existing treatment approaches are not efficacious enough to handle this issue. Appropriate techniques in this manner should be embraced to oppose arsenic cataclysm. Lately, phytochemicals have acquired expanding interest to battle the substantial heavy metal poisoning on account of their non-toxic and potent anti-oxidative property (Gao et al., 2013). Curcumin, a characteristic dietary polyphenolic compound, extracted from the rhizome of *Curcuma longa*, has attracted incredible consideration because of its strong antioxidant properties and therapeutic potential against many human ailments (Ohtsu et al., 2002; Aggarwal et al., 2009). However, its bioactivity is curtailed due to inadequate solubility and permeability. To overcome this drawback, self-nano-emulsifying-curcumin (SNEC30), with relatively high bioavailability and stability, was formulated. In a mice model SNEC30 was found to be beneficial in the rehabilitation of the histo-architecture of the thymus and spleen (Jamal et al., 2021). Administration of SNEC30 to the mice led to restoration of the activities of ROS scavenging enzymes, which affirmed the active participation of this drug in attenuating arsenic-induced oxidative stress by its antioxidant properties. Autophagy, which was heightened in the thymus and spleen of arsenic exposed mice, was seen be restored to basal levels after SNEC30 treatment. SNEC30 administration was also observed to be significantly efficacious in preventing the occurrence of intrinsic apoptosis in the mice thymus and spleen (Fig. 5) (Jamal et al., 2021).

Therefore, it very well might be presumed that dietary intercession and SNEC30 supplementation will potentially help in smothering the impacts of arsenic in the populace exposed to arsenic in drinking water and have an advantageous sanative worth among the generally burdened populaces. In any case, a more definite molecular mechanics of restorative properties of SNEC30 is needed along with clinical preliminaries for the identification of

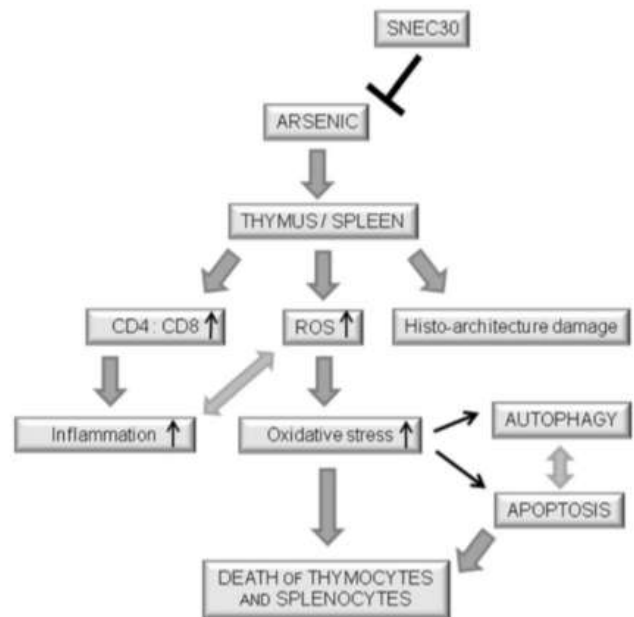


**Fig. 5** Effects of arsenic induced immune-modulation and reversal by curcumin nanoemulsion

the capability of this drug in the avoidance as well as treatment of arsenic-actuated infections. Also, regardless of whether SNEC30 ought to be utilized alone or in blend with extra medications which could improve its adequacy is an inquiry deserving of examination later on.

### Basic Mechanisms Behind Arsenic-Mediated Toxicity

#### Arsenic-Induced Diabetes and Obesity

Arsenic is known to evoke inflammatory response both in vivo and in vitro conditions and this trigger sometime lead to the onset of arsenic-induced diabetes and obesity. Arsenic exposure stimulates inflammatory cells which activates nuclear transcription factor (NF- $\kappa$ B) and aids its nuclear migration. It accelerates an elevation and reduction in the levels of pro-inflammatory (IL-6, TNF- $\alpha$ ) and anti-inflammatory (IL-10) cytokines respectively (Farkhondeh et al., 2019). In addition to this, arsenic exposure induces an imbalance in ROS-antioxidant equilibrium. Increased ROS generation causes damage to proteins, lipids, nucleic acids, membranes and organelles, which can lead to activation of cell death processes such as apoptosis (Jamal et al., 2019).



## Arsenic-Induced Mitochondrial Dysfunction

In arsenic-induced genotoxicity, mitochondria are the primary focus. Arsenic's mutagenic response is manifested in mitochondrial damage. By producing ROS and DNA fragmentation, mitochondrial membrane potential decreases in tandem with arsenic toxicity. The induction of apoptosis by  $As_2O_3$  is linked to the overproduction of ROS. The accumulation of hydrogen peroxide ( $H_2O_2$ ) lowers the mitochondrial membrane potential, causing cytochrome C to be released and the caspase cascade to be activated (Miller et al., 2002). Mitochondrial apoptotic markers including bax, bak, bid, and bim, are altered (Medda et al., 2020). Many superoxide anions are produced as a result of mitochondrial damage, which react with nitric oxide to produce highly reactive peroxynitrites. Arsenic affects mitochondrial oxidations in the absence of inorganic phosphate and by activating the mitochondrial ATPase, according to in vitro studies (Medda et al., 2020). This Arsenic-induced mitochondrial dysfunction is reported to cause neurotoxicity (Prakash et al., 2016). Thus inflammation, ROS generation and apoptosis induced by arsenic produce cytotoxic effects (Fig. 6) Moreover, arsenic can

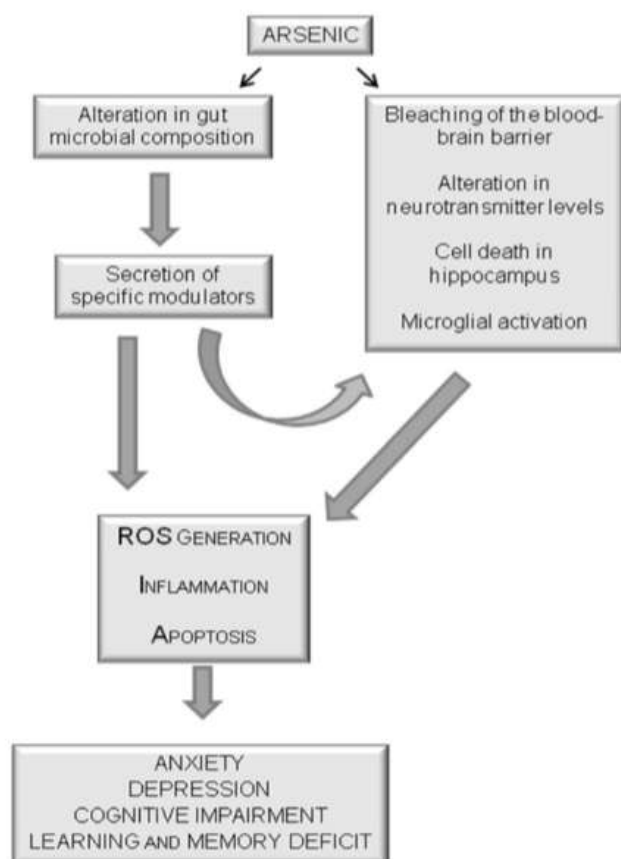


**Fig. 6** Effect of arsenic on gut brain axis

induce DNA damage and epigenetic modifications which can promote carcinogenesis (Bustaffa et al., 2014).

## Arsenic-Induced Alteration in Gut Microbial Flora

Since arsenic enters the body through oral exposure, intestinal epithelium is the first barrier that it faces to be absorbed (Calatayud et al., 2012). Mammalian gastrointestinal tract is housed by trillions of microorganisms known as gut microbiota (Thursby and Juge, 2017). A normal bacterial population is always maintained in intestine that imparts some benefit to the host by regulating metabolism, structural integrity of gut mucosal barrier and provides protection against pathogen (Jandhyala et al., 2015). Apart from that, they have very promising role in shaping the brain architecture and behaviour by immune, endocrine and hormonal regulations, known as gut-brain axis (Carabotti et al., 2015). Preclinical observations implicates perturbation in gut microbial population in pathophysiology of many brain complications like autism, Alzheimer's disease, Parkinson's disease, anxiety and depression (Zhu et al., 2020). In pathogenic conditions, dysbiosis i.e. alteration in gut microbial composition is reported to increase intestinal permeability (Jacob and Jacob, 2019). Pathogenic bacteria-derived molecules get an access through leaky intestine and can induce several downstream detrimental effects as found in patients with diseases like irritable bowel syndrome (IBS), alcoholic liver disease, type 1 and type 2 diabetes and depression (Fukui, 2016). Increase in intestinal permeability is a common phenomenon in case of brain diseases (Benakis et al., 2020). Several epidemiological studies show the presence of intestinal lesions and histopathological changes in gastrointestinal tract decades before the onset of neurodegenerative diseases (Ambrosini et al., 2019).

The standard profile of microbial population can be reshaped by several factors including altered food habit, stress and environmental pollutants like arsenic (Jin et al., 2017). Arsenic mediated disruption in gut microbial composition and parallel onset of inflammatory status is already shown (Fig. 6) (Gokulan et al., 2018). Study regarding associated metagenomics revealed increase in lipopolysaccharide (LPS) biosynthesis related gene expression in response to arsenic treatment (Chi et al., 2017). Arsenic mediated richness of gram-negative bacteria is found on human skin (Jyoti et al., 2011). Similarly, the gut may contribute to inflammation by increasing LPS levels (Choiniere and Wang, 2016), which shows detrimental effects like neuronal loss and microglial activation (Fig. 6) (Zhao et al., 2019).

Arsenic absorption primarily takes place through inhalation or oral route and is rarely absorbed through the

skin. During oral consumption, 90% of the total arsenic gets deposited in gastrointestinal tract which is greater than that of other heavy metals. Absorbed arsenic binds to red blood cells, and deposits in the liver, kidneys, muscle, bone, hair, skin, and nails, but is expelled mainly through the urine. Arsenic metabolism is a very complex process where pentavalent iAS gets converted into mono-methylated and di-methylated species which eases the path of its excretion. On the other hand it is reported that arsenic-methylating bacteria in the gut can produce significant amount of mono, di and tri-methylated trivalent arsenic species from iAS and they are more toxic (with lower LD<sub>50</sub>) than pentavalent compounds (Mochizuki. 2019).

## Conclusions

Presence of arsenic in ground water and its detrimental effects have gradually been recognized as a serious threat across the globe, mainly in Indian subcontinent. Various experiments have been conducted to identify its toxic effects on every system of mammalian physiology. With time, the mode of action of arsenic has been almost elucidated. Generation of ROS, onset of apoptosis, DNA damage and epigenetic modifications are the weapons that arsenic uses to destroy the homeostasis of a physiological system. Keeping the mechanisms in mind, therapeutic approaches are designed side by side to combat this toxicity in every system. Arsenic exerts most of these effects after significant amount of deposition. In the context of neurotoxicity, arsenic deposition in brain is a consequence of chronic exposure with high dose. But as arsenic is showing deleterious effects in lower doses also, scientists have become curious to know that whether it can show toxic effects irrespective of its deposition. Alteration in gut microbial composition can be a tool here. The mechanism of action that it can follow to exert harmful effects without deposition, will pave a path towards the new arena of arsenic research with a sketch of advanced restorative measures.

**Acknowledgements** The authors gratefully acknowledge the contribution of all who have contributed to the review. The authors thank the University Grants Commission (31-227/2005 (SR) dated 31.3.2006; 41-128/2012(SR) dated 31.3.2012), and the Department of Zoology, University of Calcutta, DST-FIST and DST-PURSE for financial and infrastructure support, respectively.

**Author contribution** All authors have contributed equally to drafting of the manuscript.

## Declarations

**Conflict of interest** The authors declare no financial, academic, commercial, political or personal conflict of interest.

## References

- Agarwal, A., S. Gupta, and R.K. Sharma. 2005. Role of oxidative stress in female reproduction. *Reproductive Biology and Endocrinology* 3: 28–38.
- Aggarwal, B., and B. Sung. 2009. *Pharmacological Basis for the Role of Curcumin in Chronic Diseases: An Age-Old Spice with Modern Target*. 30 (2): 85–94.
- Ahir, B.K., A.P. Sanders, J.E. Rager, and R.C. Fry. 2013. Systems biology and birth defects prevention: Blockade of the glucocorticoid receptor prevents arsenic-induced birth defects. *Environmental Health Perspectives* 121 (3): 332–338.
- Ahlemeyer, B., E. Bauerbach, M. Plath, M. Steuber, C. Heers, and F. Tegtmeier. 2001. Retinoic acid reduces apoptosis and oxidative stress by preservation of SOD protein level. *Free Radical Biology & Medicine* 30: 1067–1077.
- Ahmad, S., K.T. Kitchin, and W.R. Cullen. 2000. Arsenic species that cause release of iron from ferritin and generation of activated oxygen. *Archives of Biochemistry and Biophysics* 382: 195–202.
- Ahmed, R.G., and A.W. El-Gareib. 2019. Gestational arsenic trioxide exposure acts as a developing neuroendocrine-disruptor by Downregulating Nrf2/PPAR $\gamma$  and upregulating caspase-3/NF- $\kappa$ B/Cox2/BAX/iNOS/ROS. *Dose Response* 17 (2): 1559325819858266.
- Ahmed, S., S. Mahabbat-e Khoda, R.S. Rekha, R.M. Gardner, S.S. Ameer, S. Moore, E.C. Ekstrom, M. Vahter, and R. Raqib. 2011. Arsenic-associated oxidative stress, inflammation and immune disruption in human placenta and cord blood. *Environmental Health Perspectives* 119: 258–264.
- Allen, T., and S.V. Rana. 2003. Oxidative stress by inorganic arsenic: Modulation by thyroid hormones in rat. *Comparative Biochemistry and Physiology Part c: Toxicology & Pharmacology* 135: 157–162.
- Altman, J.K., P. Yoon, E. Katsoulidis, B. Kroczyńska, A. Sassano, A.J. Redig, H. Glaser, A. Jordan, M.S. Tallman, N. Hay, and L.C. Plataniak. 2008. Regulatory effects of mammalian target of rapamycin-mediated signals in the generation of arsenic trioxide responses. *Journal of Biological Chemistry* 283 (4): 1992–2001.
- Ambrosini, Y.M., D. Borchering, A. Kanthasamy, H.J. Kim, A.A. Willette, A. Jergens, K. Allenspach, and J.P. Mochel. 2019. The gut-brain axis in neurodegenerative diseases and relevance of the canine model: A Review. *Front Aging Neurosci.* 11: 130.
- Amitai, Y., and G. Koren. 2018. High risk for neural tube defects; the role of arsenic in drinking water and rice in Asia. *Medical Hypotheses* 119: 88–90.
- Bahrami, A., T. Sathyapalan, S.A. Moallem, and A. Sahebkar. 2020. Counteracting arsenic toxicity: Curcumin to the rescue? *J Hazard Mater.* 400:123160
- Bailey, K.A., M.C. Wu, W.O. Ward, L. Smeester, J.E. Rager, G. Garcia-Vargas, L.M. Del Razo, Z. Drobna, M. Styblo, and R.C. Fry. 2013. Arsenic and the epigenome: Interindividual differences in arsenic metabolism related to distinct patterns of DNA methylation. *Journal of Biochemical and Molecular Toxicology* 27: 106–115.
- Ballabh, P., A. Braun, and M. Nedergaard. 2004. The blood-brain barrier: An overview: Structure, regulation, and clinical implications. *Neurobiology of Diseases* 16 (1): 1–13.
- Bambino, T.H., and A.J. Hsueh. 1981. Direct inhibitory effect of glucocorticoids upon testicular luteinizing hormone receptor and steroidogenesis *in vivo* and *in vitro*. *Endocrinology* 108 (6): 2142–2148.
- Bardullas, U., J.H. Limon-Pacheco, M. Giordano, L. Carrizales, M.S. Mendoza-Trejo, and V.M. Rodriguez. 2009. Chronic low-level arsenic exposure causes gender-specific alterations in locomotor

- activity, dopaminergic systems, and thioredoxin expression in mice. *Toxicol. Appl Pharm.* 239: 169–177.
- Behrman, H.R., P.H. Kodaman, S.L. Preston, and S. Gao. 2001. Oxidative stress and the ovary. *Journal of the Society for Gynecologic Investigation* 8: S40–42.
- Bellinger, D.C. 2013. Inorganic arsenic exposure and children's neurodevelopment: A review of the evidence. *Toxics* 1 (1): 2–7.
- Benakis, C., C. Martin-Gallausiaux, J.P. Trezzi, P. Melton, A. Liesz, and P. Wilmes. 2020. The microbiome-gut-brain axis in acute and chronic brain diseases. *Current Opinion in Neurobiology* 61: 1–9.
- Bernstam, L., and J. Nraigu. 2000. Molecular aspects of arsenic stress. *Journal of Toxicology and Environmental Health. Part b, Critical Reviews* 3: 293–322.
- Biswas, N.M., G. Roy Chowdhury, and M. Sarkar. 1994. Effect of sodium arsenite on adrenocortical activities in male rats: Dose-duration dependent responses. *Medical Science Research* 23: 153–154.
- Bodwell, J.E., J.A. Gosse, A.P. Nomikos, and J.W. Hamilton. 2006. Arsenic disruption of steroid receptor gene activation: Complex dose-response effects are shared by several steroid receptors. *Chem Res Toxicol.* 19: 1619–1629.
- Burk, D., and A.R. Beaudoin. 1977. Arsenate-induced renal agenesis in rats. *Teratol* 16: 247–260.
- Bustaffa, E., A. Stoccoro, F. Bianchi, and L. Migliore. 2014. Genotoxic and epigenetic mechanisms in arsenic carcinogenicity. *Archives of Toxicology* 88: 1043–1067.
- Calatayud, M., J.A. Barrios, D. Vélez, and V. Devesa. 2012. In vitro study of transporters involved in intestinal absorption of inorganic arsenic. *Chemical Research in Toxicology* 25: 446–453.
- Carabotti, M., A. Scirocco, M.A. Maselli, and C. Severi. 2015. The gut-brain axis: Interactions between enteric microbiota, central and enteric nervous systems. *Annals of Gastroenterology* 28 (2): 203–209.
- Centeno, J.A., F.G. Mullick, L. Martinez, N.P. Page, H. Gibb, D. Longfellow, C. Thompson, and E.R. Ladich. 2002. Pathology related to chronic arsenic exposure. *Environmental Health Perspectives* 110 (Suppl 5): 883–886.
- Chandravanshi, L.P., and D.K. Patel. 2017. Subchronic early life arsenic exposure at low doses impaired the biogenic amine neurotransmitter and nitric oxide levels in different brain regions of rats. *Journal of Environmental & Analytical Toxicology* 7: 477.
- Chandravanshi, L.P., R.S. Yadava, R.K. Shukla, A. Singha, S. Sultana, A.B. Pant, D. Parmar, and V.K. Khanna. 2014. Reversibility of changes in brain cholinergic receptors and acetylcholinesterase activity in rats following early life arsenic exposure. *International Journal of Development Neuroscience* 38 (1): 91–104.
- Chang, T.C., M.C. Hong, and C.J. Chen. 1991. Higher prevalence of goiter in endemic area of blackfoot disease of Taiwan. *Journal of the Formosan Medical Association* 90: 941–946.
- Chatterjee, A., and U. Chatterji. 2010. Arsenic abrogates the estrogen-signaling pathway in the rat uterus. *Reproductive Biology and Endocrinology* 8: 80–91.
- Chatterjee, A., and U. Chatterji. 2011. All-trans retinoic acid protects against arsenic-induced uterine toxicity in female Sprague-Dawley rats. *Toxicology and Applied Pharmacology* 257 (2): 250–263.
- Chatterjee, A., and U. Chatterji. 2017. All-Trans Retinoic acid ameliorates arsenic-induced oxidative stress and apoptosis in the rat uterus by modulating MAPK Signaling proteins. *Journal of Cellular Biochemistry* 118 (11): 3796–3809.
- Chattopadhyay, S., and D. Ghosh. 2010. The involvement of hypophyseal-gonadal and hypophyseal-adrenal axes in arsenic-mediated ovarian and uterine toxicity: Modulation by hCG. *Journal of Biochemical and Molecular Toxicology* 24 (1): 29–41.
- Chattopadhyay, S., S. Ghosh, J. Debnath, and D. Ghosh. 2001. Protection of sodium arsenite-induced ovarian toxicity by coadministration of L-Ascorbate (Vitamin C) in mature Wistar strain rat. *Archives of Environmental Contamination and Toxicology* 41: 83–89.
- Chen, J.L., and J.H. Shen. 2016. The research progress of VEGF and its receptors in. *World latest Medicine Information* 16: 44.
- Chen, Y.C., S.Y. Lin-Shiau, and J.K. Lin. 1998. Involvement of reactive oxygen species and caspase-3 activation in arsenite-induced apoptosis. *Journal of Cellular Physiology* 177: 324–333.
- Chen, H., G. Liu, N. Qiao, Z. Kang, L. Hu, J. Liao, F. Yang, C. Pang, B. Liu, Q. Zeng, Y. Li, and Y. Li. 2020. Toxic effects of arsenic trioxide on spermatogonia are associated with oxidative stress, mitochondrial dysfunction, autophagy and metabolomic alterations. *Ecotoxicology Environmental Safety* 190: 110063.
- Chevallet, M., E. Wagner, S. Luche, A. van Dorsselaer, E. Leize-Wagner, and T. Rabilloud. 2003. Regeneration of peroxiredoxins during recovery after oxidative stress: Only some overoxidized peroxiredoxins can be reduced during recovery after oxidative stress. *Journal of Biological Chemistry* 278: 37146–37153.
- Chi, L., X. Bian, B. Gao, P. Tu, H. Ru, and K. Lu. 2017. The effects of an environmentally relevant level of arsenic on the gut microbiome and its functional Metagenome. *Toxicological Sciences* 160 (2): 193–204.
- Chi, L., P. Tu, C.W. Liu, Y. Lai, J. Xue, H. Ru, and K. Lu. 2019. Chronic arsenic exposure induces oxidative stress and perturbs serum lysolipids and fecal unsaturated fatty acid metabolism. *Chemical Research in Toxicology* 32 (6): 1204–1211.
- Choiniere, J., and L. Wang. 2016. Exposure to inorganic arsenic can lead to gut microbe perturbation and hepatocellular carcinoma. *Acta Pharm Sin b.* 6 (5): 426–429.
- Choudhury, S., P. Gupta, S. Ghosh, S. Mukherjee, P. Chakraborty, U. Chatterji, and S. Chattopadhyay. 2016. Arsenic-induced dose-dependent modulation of the NF- $\kappa$ B/IL-6 axis in thymocytes triggers differential immune responses. *Toxicology* 357–358: 85–96.
- Chowdhury, A.K. 1979. Dependence of testicular germ cells on hormones: A quantitative study in hypophysectomized testosterone-treated rats. *Journal of Endocrinology* 82 (3): 331–340.
- Ciarrocca, M., F. Tomei, T. Caciari, C. Cetica, J.C. Andrè, M. Fiaschetti, M.P. Schifano, B. Scala, L. Scimitto, G. Tomei, and A. Sancini. 2012. Exposure to arsenic in urban and rural areas and effects on thyroid hormones. *Inhalation Toxicology* 24 (9): 589–598.
- Clarke, R., F. Leonessa, J.N. Welch, and T.C. Skaar. 2001. Cellular and molecular pharmacology of antiestrogen action and resistance. *Pharmacological Reviews* 53: 25–71.
- Cohen, G.M. 1997. Caspases: The executioners of apoptosis. *The Biochemical Journal* 326: 1–16.
- Cronican, A.A., N.F. Fitz, A. Carter, M. Saleem, S. Shiva, A. Barchowsky, R. Koldamova, J. Schug, and I. Lefterov. 2013. Genome-wide alteration of histone H3K9 acetylation pattern in mouse offspring paternally exposed to arsenic. *PLoS One* 8 (2): e3478.
- Das, J., J. Ghosh, P. Manna, and P.C. Sil. 2010. Protective role of taurine against arsenic-induced mitochondria-dependent hepatic apoptosis via the inhibition of PKC $\delta$ -JNK pathway. *PLoS One.* 5: e12602.
- Davey, J.C., J.E. Bodwell, J.A. Gosse, and J.W. Hamilton. 2007. Arsenic as an endocrine disruptor: Effects of arsenic on estrogen receptor-mediated gene expression in vivo and in cell culture. *Toxicological Sciences* 98: 75–86.

- Davey, J.C., A.P. Nomikos, M. Wungjiranirun, J.R. Sherman, L. Ingram, C. Batki, J.P. Lariviere, and J.W. Hamilton. 2008. Arsenic as an endocrine disruptor: Arsenic disrupts retinoic acid receptor- and thyroid hormone receptor-mediated gene regulation and thyroid hormone-mediated amphibian tail metamorphosis. *Environmental Health Perspectives* 116: 165–172.
- Davies, T.H., Y.M. Ning, and E.R. Sanchez. 2005. Differential control of glucocorticoid receptor hormone-binding function by tetratricopeptide repeats (TPR) proteins and the immunosuppressive ligand FK506. *Biochem.* 44: 2030–2038.
- de Bruin, J.P., M. Dorland, E.R. Spek, G. Posthuma, M. van Haaften, C.W. Looman, and E.R. teVelde. 2002. Ultrastructure of the resting ovarian follicle pool in healthy young women. *Biology of Reproduction* 66: 1151–1160.
- DeSesso, M. 2001. Teratogen update: Inorganic arsenic. *Teratology* 63: 170–173.
- Dheer, R., J. Patterson, M. Dudash, E.N. Stachler, K.J. Bibb, D.B. Stolz, and J.F. Stolz. 2015. Arsenic induces structural and compositional colonic microbiome change and promotes host nitrogen and amino acid metabolism. *Toxicology and Applied Pharmacology* 289 (3): 397–408.
- di Masi, A., L. Leboffe, E. De Marinis, F. Pagano, L. Cicconi, C. Rochette-Egly, F. Lo-Coco, P. Ascenzi, and C. Nervi. 2015. Retinoic acid receptors: From molecular mechanisms to cancer therapy. *Molecular Aspects of Medicine* 41: 1–115.
- Dickson, R.B., and G.M. Stancel. 2000. Estrogen receptor-mediated processes in normal and cancer Cells. *J Natl Cancer Inst Monogr.* 27: 135–145.
- Dirty dozen endocrine disruptors. <https://www.ewg.org/consumer-guides/dirty-dozen-endocrine-disruptors>.
- Divekar, S.D., H.H. Li, D.A. Parodi, T.B. Ghafouri, R. Chen, K. Cyrus, A.E. Foxworth, A.J. Fornace, C. Byrne, and M.B. Martin. 2020. Arsenite and cadmium promote the development of mammary tumors. *Carcinogenesis* 41 (7): 1005–1014.
- Eguchi, R., Y. Fujimori, H. Takeda, C. Tabata, T. Ohta, K. Kuribayashi, K. Fukuoka, and T. Nakano. 2011. Arsenic trioxide induces apoptosis through JNK and ERK in human mesothelioma cells. *Journal of Cellular Physiology* 226: 762–768.
- Farkhondeh, T., S. Samarghandian, and M. Azimi-Nezhad. 2019. The role of arsenic in obesity and diabetes. *Journal of Cellular Physiology* 234 (8): 12516–12529.
- Ferm, V.H., and S.J. Carpenter. 1968. Malformations induced by sodium arsenate. *Journal of Reproduction Fertility* 17: 199–201.
- Flora, S.J.S. 1999. Arsenic-induced oxidative stress and its reversibility following combined administration of N-acetylcysteine and meso 2, 3-dimercaptosuccinic acid in rats. *Clinical and Experimental Pharmacology and Physiology* 26: 865–869.
- Flora, S.J.S. 2011. Arsenic-induced oxidative stress and its reversibility. *Free Radical Biology & Medicine* 51: 257–281.
- Freedman, L.P., B.F. Luisi, Z.R. Korszun, R. Basavappa, P.B. Sigler, and K.R. Yamamoto. 1988. The function and structure of the metal coordination sites within the glucocorticoid receptor DNA binding domain. *Nature* 334: 543–546.
- Fukui, H. 2016. Increased intestinal permeability and decreased barrier function: Does it really influence the risk of inflammation? *Inflamm Intest Diseases* 1 (3): 135–145.
- Gao, S., X. Duan, X. Wang, D. Dong, D. Liu, X. Li, G. Sun, and B. Li. 2013. Curcumin attenuates arsenic induced hepatic injuries and oxidative stress in experimental mice through activation of Nrf2 pathway, promotion of arsenic methylation and urinary excretion. *Food and Chemical Toxicology* 59: 739–747.
- Ghosh, D., S. Chattopadhyay, and J. Debnath. 1999. Effect of sodium arsenite on adrenocortical activity in immature female rats: Evidence of dose dependent response. *Journal of Environmental Sciences* 11: 419–422.
- Gokulan, K., M.G. Arnold, J. Jensen, M. Vanlandingham, N.C. Twaddle, D.R. Doerge, C.E. Cerniglia, and S. Khare. 2018. Exposure to arsenite in CD 1 mice during juvenile and adult stages effects on intestinal microbiota and gut associated immune status. *mBio.* 9 (4): 01418–18.
- Gong, J., X. Li, F. Traganos, and Z. Darzynkiewicz. 1994. Expression of G<sub>1</sub> and G<sub>2</sub> cyclins measured in individual cells by multiparameter flow cytometry: a new tool in the analysis of the cell cycle. *Cell Prolif.* 27: 357–371.
- Goussetis, D.J., and L.C. Platanius. 2010. Arsenic trioxide and the phosphoinositide 3-Kinase/Akt pathway in chronic lymphocytic leukemia. *Clinical Cancer Research* 16: 4311–4312.
- Graham-Evans, B., H.H.P. Cohly, H. Yu, and P.B. Tchounwou. 2004. Arsenic-induced genotoxic and cytotoxic effects in human keratinocytes, melanocytes and dendritic cells. *International Journal of Environmental Research and Public Health* 1: 83–89.
- Green, D.R., and J.C. Reed. 1998. Mitochondria and apoptosis. *Science* 281: 1309–1312.
- Guerin, P., S. El Moutassim, and Y. Menezo. 2001. Oxidative stress and protection against reactive oxygen species in the pre-implantation embryo and its surroundings. *Human Reproduction Update* 7: 175–189.
- Hamilton, J.W., R.C. Kaltreider, O.V. Bajenova, M.A. Ihnat, J. McCaffrey, B.W. Turpie, E.E. Rowell, J. Oh, M.J. Nemeth, C.A. Pesce, and J.P. Lariviere. 1998. Molecular basis for effects of carcinogenic heavy metals on inducible gene expression. *Environmental Health Perspectives* 106: 1005–1015.
- Hinshelwood, M.M., M. Demter-Arloto, G.D. Means, and E.R. Simpson. 1994. Expression of genes encoding steroidogenic enzymes in the ovary. In *Molecular biology of the female reproductive system*, 129–145. London: Academic Press.
- Holson, J.F., D.G. Stump, C.E. Ulrich, and C.H. Farr. 1999. Absence of prenatal developmental toxicity from inhaled arsenic trioxide in rats. *Toxicological Sciences* 51: 87–97.
- Holson, J.F., J.M. DeSesso, C.F. Jacobson, and C.H. Farr. 2000a. Appropriate use of animal models in the assessment of risk during prenatal development: An illustration using inorganic arsenic. *Teratology* 62: 51–71.
- Holson, J.F., D.G. Stump, K.J. Clevidence, J.F. Knapp, and C.H. Farr. 2000b. Evaluation of the prenatal developmental toxicity of orally administered arsenic trioxide in rats. *Food and Chemical Toxicology* 38: 459–466.
- Hood, R.D., and S.L. Bishop. 1972. Teratogenic effects of sodium arsenate in mice. *Archives of Environmental Health* 24: 62–65.
- Huang, C., W.Y. Ma, J. Li, and Z. Dong. 1999. Arsenic induces apoptosis through a c-jun N<sub>H2</sub>-terminal kinase-dependent, p53-independent pathway. *Cancer Research* 59: 3053–3058.
- Huang, M.C., C.H. Chen, Peng FC., Tang, and SH, Chen CC. . 2009. Alterations in oxidative stress status during early alcohol withdrawal in alcoholic patients. *Journal of the Formosan Medical Association* 108: 560–569.
- Huang, Q., L. Luo, A. Alamdar, J. Zhang, L. Liu, M. Tian, S.A. Eqani, and H. Shen. 2016. Integrated proteomics and metabolomics analysis of rat testis: Mechanism of arsenic-induced male reproductive toxicity. *Science and Reports* 6: 32518.
- Hyder, S.M., Z. Nawaz, C. Chiappetta, and G.M. Stancel. 2000. Identification of functional estrogen response elements in the gene coding for the potent angiogenic factor vascular endothelial growth factor. *Cancer Research* 60: 3183–3190.
- Iacob, S., and D.G. Iacob. 2019. Infectious threats, the intestinal barrier, and its trojan horse: Dysbiosis. *Frontiers in Microbiology* 10: 1676.
- Jain, R.B. 2015. Association between arsenic exposure and thyroid function: data from NHANES 2007–2010.
- Jamal, Z., J. Das, P. Gupta, P. Dhar, S. Chattopadhyay, and U. Chatterji. 2021. Self Nano-Emulsifying Curcumin (SNEC30)

- attenuates arsenic-induced cell death in mice. *Toxicology Reports* 8: 1428–1436.
- Jamal, Z., J. Das, S. Ghosh, A. Gupta, S. Chattopadhyay, and U. Chatterji. 2019. Arsenic-induced immunomodulatory effects disorient the survival-death interface by stabilizing the Hsp90/Beclin1 interaction. *Chemosphere*. 238: 124647.
- Jana, K., S. Jana, and P.K. Samanta. 2006. Effects of chronic exposure to sodium arsenite on hypothalamo-pituitary-testicular activities in adult rats: Possible an estrogenic mode of action. *Rep Biology Endocrinology* 4: 1–13.
- Jana, S., S. Chattopadhyay, A. Dey, H. Perveen, and D. Dolai. 2018. Involvement of metallothionein, homocysteine and B-vitamins in the attenuation of arsenic-induced uterine disorders in response to the oral application of hydro-ethanolic extract of *Moringa oleifera* seed: A preliminary study. *Drug and Chemical Toxicology* 13: 1–12.
- Jandhyala, S.M., R. Talukdar, C. Subramanyam, H. Vuyyuru, M. Sasikala, and D.N. Reddy. 2015. Role of normal gut microbiota. *World Journal of Gastroenterology* 21 (29): 8787–8803.
- Jauniaux, E., A.L. Watson, J. Hempstock, Y.P. Bao, J.N. Skepper, and G.J. Burton. 2000. Onset of maternal arterial blood flow and placental oxidative stress. A possible factor in human early pregnancy failure. *American Journal of Pathology* 157: 2111–2122.
- Jauniaux, E., J. Hempstock, N. Greenwold, and G.J. Burton. 2003. Trophoblastic oxidative stress in relation to temporal and regional differences in maternal placental blood flow in normal and abnormal early pregnancies. *American Journal of Pathology* 162: 115–125.
- Jiang, X.H., B.C.Y. Wong, S.T. Yuen, S.H. Jiang, C.H. Cho, K.C. Lai, M.C. Lin, H.F. Kung, and S.K. Lam. 2001. Arsenic trioxide induces apoptosis in human gastric cancer cells through up-regulation of p53 and activation of caspase-3. *International Journal of Cancer* 91: 173–179.
- Jiang, S., J. Su, S. Yao, Y. Zhang, F. Cao, F. Wang, H. Wang, J. Li, and S. Xi. 2014. Fluoride and arsenic exposure impair learning and memory and decreases mGluR5 expression in the hippocampus and cortex in rats. *PLoS One* 9: e96041.
- Jin, Y., S. Wu, Z. Zeng, and Z. Fu. 2017. Effects of environmental pollutants on gut microbiota. *Environmental Pollution* 222: 1–9.
- Jomova, K., Z. Jenisova, M. Feszterova, S. Baros, J. Liska, D. Hudecova, C.J. Rhodes, and M. Valko. 2011. Arsenic: Toxicity, oxidative stress and human disease. *Journal of Applied Toxicology* 31: 95–100.
- Jyoti, A., T.S. Bonny, and M.A. Hossain. 2011. Arsenic poisoning alters the composition of skin microflora of human. *Research Journal of Microbiology* 6 (6): 524–533.
- Kamat, C.D., D.E. Green, S. Curilla, L. Warnke, J.W. Hamilton, S. Sturup, C. Clark, and M.A. Ihnat. 2005. Role of HIF signaling on tumorigenesis in response to chronic low-dose arsenic administration. *Toxicological Sciences* 86: 248–257.
- Kitchin, K.T., and K. Wallace. 2008. The role of protein binding of trivalent arsenicals in arsenic carcinogenesis and toxicity. *Journal of Inorganic Biochemistry* 102: 532–539.
- Korach, K.S., V.L. Davis, S.W. Curtis, and W.P. Bocchinfuso. 1997. *Xenoestrogens and estrogen receptor action in Endocrine Toxicol*, 2nd ed. Washington, DC: Taylor & Francis. pp. 181–211.
- Kozul-Horvath, C.D., F. Zandbergen, B.P. Jackson, R.I. Enelow, and J.W. Hamilton. 2012. Effects of low-dose drinking water arsenic on mouse fetal and postnatal growth and development. *PLoS One*. 7 (5): e38249.
- Kulshrestha, A., U. Jarouliya, G.B.K.S. Prasad, S.J.S. Flora, and P.S. Bisen. 2014. Arsenic-induced abnormalities in glucose metabolism: Biochemical basis and potential therapeutic and nutritional interventions. *World Journal of Translation Medicine* 3: 96–111.
- Lagod, L., T. Paszkowski, R. Sikorski, and R. Rola. 2001. The antioxidant-prooxidant balance in pregnancy complicated by spontaneous abortion. *Ginekologia Polska* 72: 1073–1078.
- Le Doze, F., D. Debruyne, F. Albessard, L. Barre, and G.L. Defer. 2000. Pharmacokinetics of all-trans retinoic acid, 13-cis retinoic acid, and fenretinide in plasma and brain of Rat. *Drug Metabolism and Disposition* 28: 205–208.
- Liang, C., Y. Han, L. Ma, X. Wu, K. Huang, S. Yan, Z. Li, X. Xia, W. Pan, J. Sheng, Q. Wang, S. Tong, Y. Cao, and F. Tao. 2020. Low levels of arsenic exposure during pregnancy and maternal and neonatal thyroid hormone parameters: The determinants for these associations. *Environ Int*. 145: 106114.
- Ling, S., Q. Shan, P. Liu, T. Feng, X. Zhang, P. Xiang, K. Chen, H. Xie, P. Song, L. Zhou, J. Liu, S. Zheng, and X. Xu. 2017. Metformin ameliorates arsenic trioxide hepato toxicity via inhibiting mitochondrial complex I. *Cell Death Dis*. 8: e3159.
- Linke, S.P., K.C. Clarkin, and G.M. Wahl. 1997. p53 mediates permanent arrest over multiple cell cycles in response to gamma-irradiation. *Cancer Research* 57: 1171–1179.
- Liu, J., H.M. Shen, and C.N. Ong. 2001. Role of intracellular thiol depletion, mitochondrial dysfunction and reactive oxygen species in *Salvia miltiorrhiza*-induced apoptosis in human hepatoma HepG2 cells. *Life Sciences* 69: 1833–1850.
- Liu, H., S. Lu, B. Zhang, W. Xia, W. Liu, Y. Peng, H. Zhang, K. Wu, S. Xu, and Y. Li. 2018. Maternal arsenic exposure and birth outcomes: A birth cohort study in Wuhan China. *Environ Pollut*. 236: 817–823.
- Llanos, M.N., and A.M. Ronco. 2009. Fetal growth restriction is related to placental levels of cadmium, lead and arsenic but not with antioxidant activities. *Reproductive Toxicology* 27: 88–92.
- Loeken, M.R. 2004. Free radicals and birth defects. *The Journal of Maternal-Fetal & Neonatal Medicine* 15: 6–14.
- Lu, M., H. Wang, X.F. Li, X. Lu, W.R. Cullen, L.L. Arnold, S.M. Cohen, and X.C. Le. 2004. Evidence of hemoglobin binding to arsenic as a basis for the accumulation of arsenic in rat blood. *Chemical Research in Toxicology* 17: 1733–1742.
- Lu, K., R.P. Abo, K.A. Schlieper, M.E. Graffam, S. Levine, J.S. Wishnok, J.A. Swenberg, S.R. Tannenbaum, and J.G. Fox. 2014. Arsenic exposure perturbs the gut microbiome and its metabolic profile in mice: An integrated metagenomics and metabolomics analysis. *Environmental Health Perspectives* 112: 284–291.
- Luo, J.H., Z.Q. Qiu, L. Zhang, and W.Q. Shu. 2009. Arsenite exposure altered the expression of NMDA receptor and postsynaptic signalling proteins in rat hippocampus. *Toxicology Letters* 211: 39–44.
- Lyster, W.R. 1977. Arsenic and sex ratio in man. *Med J Austral*. 2: 442.
- Maitra, R., and J.W. Hamilton. 2005. Arsenite regulates cystic fibrosis transmembrane conductance regulator and P-glycoprotein: Evidence of pathway independence. *Cellular Physiology and Biochemistry* 16: 109–118.
- Markowski, V.P., D. Currie, E.A. Reeve, D. Thompson, and J.P. Wise Sr. 2011. Tissue-specific and dose-related accumulation of arsenic in mouse offspring following maternal consumption of arsenic-contaminated water. *Basic & Clinical Pharmacology & Toxicology* 108: 326–332.
- Marrocco, I., F. Altieri, and I. Peluso. 2017. Measurement and clinical significance of biomarkers of oxidative stress in humans. *Oxidative Medicine and Cellular Longevity* 2017: 1–32.
- Meakin, C.J., E.M. Martin, J.T. Szilagyi, L.A. Nylander-French, and R.C. Fry. 2019. Inorganic arsenic as an endocrine disruptor: modulation of the glucocorticoid receptor pathway in placental cells via CpG Methylation. *Chemical Research in Toxicology* 32 (3): 493–499.

- Medda, N., R. Patra, T.K. Ghosh, and S. Maiti. 2020. Neurotoxic mechanism of arsenic: synergistic effect of mitochondrial instability, oxidative stress, and hormonal-neurotransmitter impairment. *Biological Trace Element Research* 198 (1): 8–15.
- Mejía, J.J., F. Díaz-Barriga, J. Calderón, C. Ríos, and M.E. Jiménez-Capdeville. 1997. Effects of lead-arsenic combined exposure on central monoaminergic systems. *Neurotoxicology and Teratology* 19 (6): 489–497.
- Midgley, C.A., B. Owens, C.V. Briscoe, D.B. Thomas, D.P. Lane, and P.A. Hall. 1995. Coupling between gamma irradiation, p53 induction and the apoptotic response depends upon cell type in vivo. *Journal of Cell Science* 108: 1843–1848.
- Miller, W.R., and R.M. Sharpe. 1998. Environmental oestrogens and human reproductive cancers. *Endocrine-Related Cancer*. 5: 69–96.
- Miller, W.H., H.M. Schipper, J.S. Lee, J. Singer, and S. Waxman. 2002. Mechanisms of action of arsenic trioxide. *Cancer Research* 62 (14): 3893–3903.
- Milton, A.H., W. Smith, B. Rahman, Z. Hasan, U. Kulsum, K. Dear, M. Rakibuddin, and A. Ali. 2005. Chronic arsenic exposure and adverse pregnancy outcomes in Bangladesh. *Epidemiol* 16 (1): 82–86.
- Mochizuki, H. 2019. Arsenic neurotoxicity in humans. *International Journal of Molecular Sciences* 20 (14): 3418.
- Molin, M., S.M. Ulven, L. Dahl, A.K. Lundebye, M. Holck, J. Alexander, H.M. Meltzer, and T.A. Ydersbond. 2017. Arsenic in seafood is associated with increased thyroid-stimulating hormone (TSH) in healthy volunteers - A randomized controlled trial. *Journal of Trace Elements in Medicine and Biology* 44: 1–7.
- Muthumani, M., and S. Miltonprabu. 2015. Ameliorative efficacy of tetrahydro-curcumin against arsenic induced oxidative damage, dyslipidemia and hepatic mitochondrial toxicity in rats. *Chemico-Biological Interactions* 235: 95–105.
- Nagaraja, T.N., and T. Desiraju. 1994. Effects on operant learning and brain acetylcholine esterase activity in rats following chronic inorganic arsenic intake. *Human and Experimental Toxicology* 13 (5): 353–356.
- Nagymajtenyi, L., A. Selyes, and G. Berencsi. 1985. Chromosomal aberrations and fetotoxic effects of atmospheric arsenic exposure in mice. *Journal of Applied Toxicology* 5: 61–63.
- Navasumrit, P., K. Chaisatra, J. Promvijit, V. Parnlob, S. Waraprasit, C. Chompoobut, T.T. Binh, D.N. Hai, N.D. Bao, N.K. Hai, K.W. Kim, L.D. Samson, J.H. Graziano, C. Mahidol, and M. Ruchirawat. 2019. Exposure to arsenic in utero is associated with various types of DNA damage and micronuclei in newborns: A birth cohort study. *Environmental Health* 18 (1): 51.
- Negi, R.S. Time to combat water contamination in India. ET Health World. The Economic Times. 2021.
- Nordstrom, S., L. Beckman, and I. Nordenson. 1978a. Occupational and environmental risks in and around a smelter in northern Sweden I. Variations in Birth Weight. *Hereditas* 88: 43–46.
- Nordstrom, S., L. Beckman, and I. Nordenson. 1978b. Occupational and environmental risks in and around a smelter in northern Sweden III. Frequencies of Spontaneous Abortions. *Hereditas*. 88: 51–54.
- Nordstrom, S., L. Beckman, and I. Nordenson. 1979a. Occupational and environmental risks in and around a smelter in northern Sweden. V. Spontaneous abortion among female employees and decreased birth weight in their offspring. *Hereditas* 90: 291–296.
- Nordstrom, S., L. Beckman, and I. Nordenson. 1979b. Occupational and environmental risks in and around a smelter in northern Sweden VI. Congenital Malformations. *Hereditas* 90: 297–302.
- Nriagu, J.O., P. Bhattacharya, A.B. Mukherjee, J. Bundschuh, R. Zevenhoven, and R.H. Loeppert. 2007. Arsenic in soil and ground water: An overview. *Trace Metals and Other Contaminants in Environment*. 9: 3–60.
- Ohtsu, H., Z. Xiao, J. Ishida, M. Nagai, H.K. Wang, H. Itokawa, C.Y. Su, C. Shih, T. Chiang, E. Chang, Y. Lee, M.Y. Tsai, C. Chang, and K.H. Lee. 2002. Curcumin analogues as novel androgen receptor antagonists with potential as anti-prostate cancer agents. *J Med Chem*. 45 (23): 5037–5042.
- Palace, V.P., N. Khaper, Q. Qin, and P.K. Singal. 1999. Antioxidant potentials of vitamin A and carotenoids and their relevance to heart disease. *Free Radical Biology & Medicine* 26: 746–761.
- Pant, N., R. Kumar, R.C. Murthy, and S.P. Srivastava. 2001. Male reproductive effect of arsenic in mice. *BioMetals* 14: 113–117.
- Parvez, F., Y. Chen, M. Yunus, C. Olopade, S. Segers, V. Slovovich, M. Argos, R. Hasan, A. Ahmed, T. Islam, M.M. Akter, J.H. Graziano, and H. Ahsan. 2013. Arsenic exposure and impaired lung function: Finding from a large population-based cohort study. *American Journal of Respiratory and Critical Care Medicine* 188 (7): 813–819.
- Pelch, K.E., E.J. Tokar, B.A. Merrick, and M.P. Waalkes. 2015. Differential DNA methylation profile of key genes in malignant prostate epithelial cells transformed by iAs or cadmium. *Toxicology and Applied Pharmacology* 286: 159–167.
- Phillips, D.M., V. Lakshmi, and C. Monder. 1989. Corticosteroid 11 beta-dehydrogenase in rat testis. *Endocrinol*. 125 (1): 209–216.
- Piao, Y.S., H. Peltoketo, J. Oikarinen, and R. Vihko. 1995. Coordination of transcription of the human 17 $\beta$ -hydroxysteroid dehydrogenase type I gene (EDH17B2) by a cell-specific enhancer and a silencer: Identification of a retinoic acid response element. *Molecular Endocrinology* 9: 1633–1644.
- Poli, G., G. Leonarduzzi, F. Biasi, and E. Chiarotto. 2004. Oxidative stress and cell signaling. *Current Medicinal Chemistry* 11: 1163–1182.
- Prakash, C., M. Soni, and V. Kumar. 2016. Mitochondrial oxidative stress and dysfunction in arsenic neurotoxicity: A review. *Journal of Applied Toxicology* 36 (2): 179–188.
- Pressman, E.K., J.L. Cavanaugh, M. Mingione, E.P. Norkus, and J.R. Woods. 2003. Effects of maternal antioxidant supplementation on maternal and fetal antioxidant levels: A randomized, double-blind study. *American Journal of Obstetrics and Gynecology* 189: 1720–1725.
- Qu, W., C.D. Bortner, T. Sakurai, M.J. Hobson, and M.P. Waalkes. 2002. Acquisition of apoptotic resistance in arsenic-induced malignant transformation: Role of the JNK signal transduction pathway. *Carcinogenesis* 23: 151–159.
- Ramanathan, K., S. Shila, S. Kumaran, and C. Pannerselvam. 2003. Ascorbic acid and alpha-tocopherol as potent modulators on arsenic induced toxicity in mitochondria. *Journal of Nutritional Biochemistry* 3: 293–322.
- Ray, S.D., T.S. Lam, J.A. Rotollo, S. Phadke, C. Patel, A. Dontabhaktuni, S. Mohammad, H. Lee, S. Strika, A. Dobrogowska, C. Bruculeri, A. Chou, S. Patel, R. Patel, T. Manolas, and S. Stohs. 2004. Oxidative stress is the masteroperator of drug and chemically-induced programmed and unprogrammed cell death: Implications of natural antioxidants in vivo. *BioFactors* 21: 223–232.
- Reichard, J.F., and A. Puga. 2010. Effects of arsenic exposure on DNA methylation and epigenetic gene regulation. *Epigenomics* 2 (1): 87–104.
- Renu, K., H. Madhyastha, R. Madhyastha, M. Maruyama, S. Vinayagam, and A. ValsalaGopalakrishnan. 2018. Review on molecular and biochemical insights of arsenic-mediated male reproductive toxicity. *Life Sciences* 212: 37–58.
- Rockwell, L.C., S. Pillai, C.E. Olson, and R.D. Koos. 2002. Inhibition of vascular endothelial growth factor/vascular permeability factor action blocks estrogen-induced uterine edema and implantation in rodents. *Biology of Reproduction* 67: 1804–1810.

- Rosenblatt, A.E., and K.L. Burstein. 2009. Inhibition of androgen receptor transcriptional activity as a novel mechanism of action of arsenic. *Molecular Endocrinology* 23 (3): 412–421.
- Roy, S., B. Narzary, A. Ray, et al. 2016. Arsenic-induced instrumental genes of apoptotic signal amplification in death-survival interplay. *Cell Death & Disease* 2: 16078.
- Rudge, C.V., H.B. Röllin, C.M. Nogueira, Y. Thomassen, M.C. Rudge, and J.Q. Odland. 2009. The placenta as a barrier for toxic and essential elements in paired maternal and cord blood samples of South African delivering women. *Journal of Environmental Monitoring* 11: 1322–1330.
- Russell, L.D., L.E. Alger, and L.G. Nequin. 1987. Hormonal control of pubertal spermatogenesis. *Endocrinology* 120 (4): 1615–1632.
- Sabir S, Akash MSH, Fiayyaz F, Saleem U, Mehmood MH, Rehman K. 2019. Role of cadmium and arsenic as endocrine disruptors in the metabolism of carbohydrates: Inserting the association into perspectives. *Biomed Pharmacother*. 114: 108802.
- Sage, A.P., B.C. Minatel, K.W. Ng, G.L. Stewart, T.J.B. Dummer, W.L. Lam, and V.D. Martinez. 2017. Oncogenomic disruptions in Arsenic-induced carcinogenesis. *Oncotarget* 8: 25736–25755.
- Sarkar, M., G.R. Chaudhuri, A. Chattopadhyay, and N.M. Biswas. 2003. Effect of sodium arsenite on spermatogenesis, plasma gonadotrophins and testosterone in rats. *Asian Journal of Andrology* 5: 27–31.
- Sarkar, M., N.M. Biswas, and D. Ghosh. 1991. Effect of sodium arsenite on testicular  $\Delta 5-3\beta$ ,  $17\beta$ -HSD activities in albino rats: dose and duration dependent responses. *Medical Science Respiration* 19: 789–790.
- Schluter, C., M. Duchrow, C. Wohlenberg, M.H.G. Becker, G. Key, Flad Hans-D, and J. Gerder. 1993. The cell proliferation-associated antigen of antibody Ki-67: A very large, ubiquitous nuclear protein with numerous repeated elements, representing a new kind of cell cycle-maintaining proteins. *Journal of Cell Biology* 123: 515–522.
- Sen, J., and A.B. Chaudhuri. 2008. Arsenic exposure through drinking water and its effect on pregnancy outcome in Bengali women. *Arhiv Za Higijenu Rada i Toksikologiju* 59 (4): 271–275.
- Sharma, A., M.K. Sharma, and M. Kumar. 2009. Modulatory role of *Embllica officinalis* fruit extract against arsenic induced oxidative stress in Swiss albino mice. *Chemico-Biol Interact*. 180: 20–30.
- Shi, H., X. Shi, and K.J. Liu. 2004. Oxidative mechanism of arsenic toxicity and carcinogenesis. *Molecular and Cellular Biochemistry* 255: 67–78.
- Shila, S., V. Kokilavani, M. Subathra, and C. Panneerselvam. 2005. Brain regional responses in antioxidant system to  $\alpha$ -lipoic acid in arsenic intoxicated rat. *Toxicol*. 210: 25–36.
- Singh, M.K., S.S. Yadav, V. Gupta, and S. Khattri. 2013. Immunomodulatory role of *Embllica officinalis* in arsenic induced oxidative damage and apoptosis in thymocytes of mice. *BMC Complementary and Alternative Medicine* 13: 193.
- Singh, M.K., S. Dwivedi, S.S. Yadav, P. Sharma, and S. Khattri. 2014. Arsenic-induced hepatic toxicity and its attenuation by fruit extract of *Embllica Officinalis* (amla) in mice. *Indian Journal of Clinical Biochemistry* 29: 29–37.
- Singh, M.K., S.S. Yadav, R.S. Yadav, A. Chauhan, D. Katiyar, and S. Khattri. 2015. Protective effect of *Embllica-officinalis* in arsenic induced biochemical alteration and inflammation in mice. *Springer plus* 4: 438.
- Singh, V., S. Kushwaha, R. Gera, J.A. Ansari, J. Mishra, J. Dewangan, S. Patnaik, and D. Ghosh. 2018. Sneaky entry of  $IFN\gamma$  through arsenic-induced leaky blood–brain barrier reduces CD200 expression by microglial pro-inflammatory cytokine. *Molecular Neurobiology* 56 (2): 1488–1499.
- Sohel, N., M. Vahter, M. Ali, M. Rahman, A. Rahman, P.K. Streatfield, P.S. Kanaroglou, and L.A. Persson. 2010. Spatial patterns of fetal loss and infant death in an arsenic-affected area in Bangladesh. *International Journal of Health Geographics* 9: 53–63.
- Soignet, S.L., P. Maslak, Z.G. Wang, S. Jhanwar, E. Calleja, L.J. Dardashti, D. Corso, A. DeBlasio, J. Gabrilove, D.A. Scheinberg, P.P. Pandolfi, and R.P. Warrell Jr. 1998. Complete remission after treatment of acute promyelocytic leukemia with arsenic trioxide. *New England Journal of Medicine* 339: 1341–1348.
- Spear, N., and S.D. Aust. 1995. Effects of glutathione on Fenton reagent-dependent radical production and DNA oxidation. *Archives of Biochemistry and Biophysics* 24 (1): 111–116.
- Stoica, A., E. Pentecost, and M.B. Martin. 2000. Effects of arsenite on estrogen receptor- $\alpha$  expression and activity in MCF-7 breast cancer cells. *Endocrinol*. 114: 3595–3602.
- Sun, H., Y. Yang, H. Shao, W. Sun, M. Gu, H. Wang, L. Jiang, L. Qu, D. Sun, and Y. Gao. 2017. Sodium-arsenite induced learning and memory impairment is associated with endoplasmic reticulum stress-mediated apoptosis in rat hippocampus. *Frontiers in Molecular Neuroscience* 10: 286.
- Sun, B.F., Q.Q. Wang, Z.J. Yu, Y. Yu, C.L. Xiao, C.S. Kang, G. Ge, Y. Lingu, J.D. Zhu, Y.M. Li, S.P. Luo, D. Yang, L. Li, W.Y. Zhang, and G. Tian. 2015. Exercise prevents memory impairment induced by arsenic exposure in mice: Implication of hippocampal BDNF and CREB. *PLoS One* 10 (9): e0137810.
- Thornton, J.W. 2001. Evolution of vertebrate steroid receptors from an ancestral estrogen receptor by ligand exploitation and serial genome expansions. *Proceedings of the National Academy of Sciences of the United States of America* 98: 5671–5676.
- Thursby, E., and N. Juge. 2017. Introduction to the human gut microbiota. *The Biochemical Journal* 474 (11): 1823–1836.
- Tolins, M., M. Ruchirawat, and P. Landrigan. 2014. The developmental neurotoxicity of arsenic: Cognitive and behavioural consequences of early life exposure. *Annals of Global Health* 80 (4): 303–314.
- Tseng, C.H. 2005. Blackfoot disease and arsenic: A never-ending story. *Journal of Environmental Science and Health. Part C* 23: 55–74.
- Tseng, C.H., C.K. Chong, C.P. Tseng, Y.M. Hsueh, H.Y. Chiou, C.C. Tseng, and C.J. Chen. 2003. Long-term arsenic exposure and ischemic heart disease in arseniasis-hyperendemic villages in Taiwan. *Toxicology Letters* 137: 15–21.
- Tyler, C.R., and A.M. Allan. 2014. The effect of arsenic exposure on neurological and cognitive dysfunction in human and rodent studies: A review. *Curr Envir Health Rpt*. 1: 132–147.
- Vahter, M. 1999. Methylation of inorganic arsenic in different mammalian species and population groups. *Science Progress* 82: 69–88.
- Vahter, M. 2008. Health effects of early life exposure to arsenic. *Basic & Clinical Pharmacology & Toxicology* 102 (2): 204–211.
- Valko, M., C.J. Rhodes, J. Moncol, M. Izakovic, and M. Mazur. 2006. Free radicals, metals and antioxidants in oxidative stress-induced cancer. *Chemico-Biological Interactions* 160: 1–40.
- Waalkes, M.P., J.M. Ward, J. Liu, and B.A. Diwan. 2003. Transplacental carcinogenicity of inorganic arsenic in the drinking water: Induction of hepatic, ovarian, pulmonary, and adrenal tumors in mice. *Toxicology and Applied Pharmacology* 186: 7–17.
- Waalkes, M.P., J. Liu, and B.A. Diwan. 2007. Transplacental arsenic carcinogenesis in mice. *Toxicology and Applied Pharmacology* 222: 271–280.
- Waalkes, M.P., J. Liu, H. Chen, Y. Xie, W.E. Achanzar, Y.S. Zhou, M.L. Cheng, and B.A. Diwan. 2004. Estrogen signaling in livers of male mice with hepatocellular carcinoma induced by exposure to arsenic in utero. *Journal of National Cancer Institution* 96: 466–474.

- Wall, P.D., E.K. Pressman, and J.R. Woods Jr. 2002. Preterm premature rupture of the membranes and antioxidants: The free radical connection. *Journal of Perinatal Medicine* 30: 447–457.
- Wang, Y.L., Q.Q. Han, W.Q. Gong, D.H. Pan, L.Z. Wang, W. Hu, M. Yang, B. Li, J. Yu, and Q. Liu. 2018. Microglial activation mediates chronic mild stress-induced depressive- and anxiety-like behavior in adult rats. *Journal of Neuroinflammation* 15: 21.
- Wu, Y., R. Ding, X. Zhang, J. Zhang, Q. Huang, L. Liu, and H. Shen. 2021. Meek-in-metabolite analysis: A novel strategy to identify connections between arsenic exposure and male infertility. *Environ Int.* 147: 106360.
- Xu, W., H. Bao, F. Liu, L. Liu, Y.G. Zhu, J. She, S. Dong, M. Cai, L. Li, C. Li, and H. Shen. 2012. Environmental exposure to arsenic may reduce human semen quality: Associations derived from a Chinese cross-sectional study. *Environmental Health* 9 (11): 46.
- Yager, J.D., and J.G. Liehr. 1996. Molecular mechanisms of estrogen carcinogenesis. *Annual Review of Pharmacology and Toxicology* 36: 203–232.
- Yamanaka, K., A. Hasegawa, R. Sawamura, and S. Okada. 1991. Cellular response to oxidative damage in lung induced by the administration of dimethylarsinic acid, a major metabolite of inorganic arsenics, in mice. *Toxicology and Applied Pharmacology* 108: 205–213.
- Yan-Ping, D., G. Xiao-Kin, M. Xiao Ping, and Quan Y. Ying. 2017. Effects of chronic exposure to sodium arsenite on expressions of VEGF and VEGFR2 proteins in the epididymis of rat. *BioMed Research International*. 2017: 2597256.
- Yeh, J.Y., L.C. Cheng, B.R. Ou, P.D. Whanger, and L.W. Chang. 2002. Differential influences of various arsenic compounds on glutathione redox status and antioxidative enzymes in porcine endothelial cells. *Cellular and Molecular Life Sciences* 59: 1972–1982.
- Yoon, P., N. Giafis, J. Smith, H. Mears, E. Katsoulidis, A. Sassano, J. Altman, A.J. Redig, M.S. Tallman, and L.C. Platanias. 2006. Activation of mammalian target of rapamycin and the p70 S6 kinase by arsenic trioxide in BCR-ABL-expressing cells. *Molecular Cancer Therapeutics* 5 (11): 2815–2823.
- Zakharyan, R.A., and H.V. Aposhian. 1999. Enzymatic reduction of arsenic compounds in mammalian systems: The rate-limiting enzyme of rabbit liver arsenic biotransformation is MMA(V) reductase. *Chemical Research in Toxicology* 12: 1278–1283.
- Zarazua, S., F. Perez-Severiano, J.M. Delgado, L.M. Martinez, D. Ortiz-Perez, and M.E. Jimenez-Capdeville. 2006. Decreased nitric oxide production in the rat brain after chronic arsenic exposure. *Neurochemical Research* 31: 1069–1077.
- Zhan, Q., I. Alamo, and K. Yu. 1996. The apoptosis-associated gamma-ray response of BCL-X<sub>L</sub> depends on normal p53 function. *Oncogene* 13: 2287–2293.
- Zhao, C.Q., M.R. Young, B.A. Diwan, T.P. Coogan, and M.P. Waalkes. 1997. Association of arsenic-induced malignant transformation with DNA hypomethylation and aberrant gene expression. *Proceedings of the National Academy of Sciences of the United States of America* 94 (20): 10907–10912.
- Zhao, J., W. Bi, S. Xiao, X. Lan, X. Cheng, J. Zhang, D. Lu, W. Wei, Y. Wang, H. Li, Y. Fu, and L. Zhu. 2019. Neuroinflammation induced by lipopolysaccharide causes cognitive impairment in mice. *Science and Reports* 9: 5790.
- Zhou, Q., and S. Xi. 2018. A review on arsenic carcinogenesis: Epidemiology, metabolism, genotoxicity and epigenetic changes. *Regulatory Toxicology and Pharmacology* 99: 78–88.
- Zhu, S.J., Y. Li, H. Li, Y.L. Wang, Z.J. Xiao, and P. Vihko. 2002. Retinoic acids promote the action of aromatase and 17 $\beta$ -hydroxysteroid dehydrogenase type 1 on the biosynthesis of 17 $\beta$ -estradiol in placental cells. *Journal of Endocrinology* 172: 31–43.
- Zhu, S., Y. Jiang, K. Xu, M. Cui, W. Ye, G. Zhao, L. Jin, and X. Chen. 2020. The progress of gut microbiome research related to brain disorders. *J Neuroinflammation*. 17: 25.

**Publisher's Note** Springer Nature remains neutral with regard to jurisdictional claims in published maps and institutional affiliations.





## Source details

[Feedback >](#) [Compare sources >](#)

### Proceedings of the Zoological Society

Scopus coverage years: from 2009 to Present

Publisher: Springer Nature

ISSN: 0373-5893 E-ISSN: 0974-6919

Subject area: [Agricultural and Biological Sciences: Insect Science](#) [Agricultural and Biological Sciences: Animal Science and Zoology](#)

[Agricultural and Biological Sciences: Ecology, Evolution, Behavior and Systematics](#) [Agricultural and Biological Sciences: Aquatic Science](#) [View all](#) ∨

Source type: Journal

[View all documents >](#)

[Set document alert](#)

[Save to source list](#)

CiteScore 2022

1.4



SJR 2022

0.217



SNIP 2022

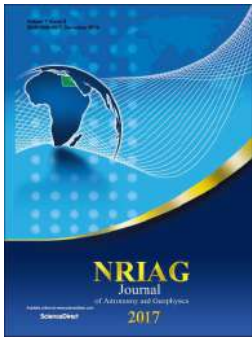
0.470



[CiteScore](#)

[CiteScore rank & trend](#)

[Scopus content coverage](#)



## A SOC based avalanche model to study the magnetosphere-ionosphere energy transfer and AE index fluctuations

Adrija Banerjee, Amaresh Bej, T. N. Chatterjee & Abhijit Majumdar

To cite this article: Adrija Banerjee, Amaresh Bej, T. N. Chatterjee & Abhijit Majumdar (2021): A SOC based avalanche model to study the magnetosphere-ionosphere energy transfer and AE index fluctuations, NRIAG Journal of Astronomy and Geophysics, DOI: [10.1080/20909977.2021.2005335](https://doi.org/10.1080/20909977.2021.2005335)

To link to this article: <https://doi.org/10.1080/20909977.2021.2005335>



© 2021 The Author(s). Published by Informa UK Limited, trading as Taylor & Francis Group.



Published online: 24 Nov 2021.



Submit your article to this journal [↗](#)



View related articles [↗](#)



View Crossmark data [↗](#)



# A SOC based avalanche model to study the magnetosphere-ionosphere energy transfer and AE index fluctuations

Adrija Banerjee<sup>a</sup>, Amaresh Bej<sup>a</sup>, T. N. Chatterjee<sup>b</sup> and Abhijit Majumdar<sup>a</sup>

<sup>a</sup>Department of Physics, Indian Institute of Engineering Science and Technology, Howrah, India; <sup>b</sup>Department of Electronics, Dinabandhu Andrews College, Kolkata, India

## ABSTRACT

Magnetosphere-ionosphere energy transfer and AE fluctuations are studied using a cellular automata model of terrestrial magnetosphere based on the concept of self-organised criticality (SOC). The model is a SOC-driven dissipative dynamical system with both spatial and temporal degrees of freedom. The input parameter to this model is derived from the real-time values of solar wind ion density and flow speed data. Both the direction and intensity of the real-time values of the  $B_z$  component of the interplanetary magnetic field (IMF) are the factors controlling the energy injection into the system. The model produces an output series which can be regarded as a mathematical representation of the AE index. The spectral response of the simulated output follows a  $1/f^{\beta}$  power law, demonstrates a breakpoint at  $f_0 = 0.050$  mHz (5.5 hours) having slopes  $\beta_A = 2.2-2.4$  for  $f > f_0$  and  $\beta_B = 0.9-1.0$  for  $f < f_0$ , the typical characteristics of the natural AE index. The entire 23<sup>rd</sup> solar cycle had been studied using the model. The parameter  $K_A$  plays a significant role in the entire process.  $K_A$  represents the remaining percentage of the released energy from the previous magnetosphere-ionosphere energy transfer, stored in the ionosphere.

## ARTICLE HISTORY

Received 12 May 2021  
Revised 31 October 2021  
Accepted 8 November 2021

## KEYWORDS

Plasmas; solar wind;  
magnetic reconnection;  
geomagnetic index

## 1. Introduction

Magnetosphere-ionosphere interaction and the subsequent energy transfer is a significant phenomenon in magnetospheric dynamics. During a strong solar wind-magnetosphere coupling, a large amount of solar wind energy enters the geospace. A part of the energy is stored in the magnetotail and another part drives the convection of plasma particles in the magnetosphere. As the solar wind injection continues, the stored energy in the magnetotail reaches an unstable state, triggering magnetic reconnection. A huge amount of energy is released in the ionosphere causing magnetic fluctuations in the auroral zone. The auroral electrojet (AE) index is a global and instantaneous measurement of the auroral zone magnetic activities. The geomagnetic fluctuation in the horizontal component of the Earth's magnetic field  $H$  in the auroral region is measured in 10–13 observatories situated around the auroral zone. For each station, the average value of  $H$  of the five international quietest days of the month is considered as the base value of the measurement. For normalisation of data, the base value is subtracted from each data of the station. Then, all the normalised data from all the stations are plotted and superimposed on each other. The maximum and minimum deviations of  $H$  are termed as Auroral Upper (AU) and Auroral Lower (AL) index, respectively, which form the upper boundary and lower

boundary of the envelope. If there are no disturbances from the distant axially symmetric fields or zonal currents, the AU and AL indices are the direct measurement of the maximum eastward and westward electrojet currents at any time. AE index is defined as the maximum total amplitude of the eastward and westward electrojet currents, that is,  $AE = AU - AL$ . As the AE index is the difference value of AU and AL indices, it is independent of the ionospheric zonal current or distant axially symmetric fields (Davis and Sugiura 1966). AE index is extensively used in aeronomy, solar-terrestrial physics, geomagnetism, and auroral studies.

The physical meaning of the AE index, the nature of the eastward and westward electrojets, the limitations of AU and AL indices have been discussed (Rostoker 1972, 2002; Baumjohann 1982; Kamide and Kokubun 1996; Kamide and Rostoker 2004) along with a detailed study of spatial and temporal distributions of magnetic effects of the electrojets (Allen and Kroehl 1975), statistical analysis (Nakamura et al. 2015) and its relation with the polar cap index (Vennerström et al. 1991; Vassiliadis et al. 1996). It has been also established that the AE index is subject to universal time variation (Davis and Sugiura 1966; Ahn et al. 2000a), seasonal variation (Ahn et al., 2000b; Cliver et al. 2000; Lyatsky et al. 2001; Russell and McPherron 1973; Temerin and Li 2002, 2006),

annual variation (Lyatsky et al. 2001; Pulkkinen et al. 2011), and solar cycle variation (Ahn et al., 2000b). Different dynamical and numerical models have been presented to predict and study auroral electrojets. The analogue model proposed by (Goertz et al. 1993) and reviewed by (McPherron and Rostoker 1993), the Faraday loop model (Klimas et al. 1992, 1994), using linear prediction filter (LPF) technique (Bargatze et al. 1985) which is further modified as local-linear prediction technique by (Vassiliadis et al. 1995), by artificial intelligence (Hernandez et al. 1993; Gleisner and Lundstedt 1997, 2001; Gavrishchaka and Ganguli 2001; Weigel 2003; Chen and Sharma 2006), by stochastic approach (Pulkkinen et al. 2006) and also using solar wind parameters (Li et al. 2007; Luo et al. 2013).

Previously, we studied the characteristic structure of the Dst index, the global measurement of geomagnetic activities in Earth, and realised the series as a positively correlated fractional Brownian motion, displaying long-range correlation (Banerjee et al. 2011). But, we also understood the complexity of the non-linear dynamics of the geomagnetic fluctuations and the difficulties in predicting them. To gain an insight into the magnetospheric dynamics, we focused our study to develop a cellular automata model of terrestrial magnetosphere based on the concept of self-organised criticality and sandpile dynamics. According to the concept, a dissipative, dynamical system with both spatial and temporal degrees of freedom naturally evolved to a self-organised critical state without much specification of the initial conditions. The dynamical behaviour of a pile of sand is the most prominent example of this type of system. Let us start with a grain of sand and continue to add more grains to it, gradually forming a pile. The increment of the slope enhances the characteristic size of the largest avalanches. As a result, the equilibrium state of the sandpile is seriously disturbed. Eventually, when the slope becomes very large, the pile reaches a critical state. Now, adding a single grain of sand further to the pile collapses it. An avalanche of sand is released from the pile, the base area increases, and the system again returns to a state of equilibrium (Bak et al. 1987, 1988).

The concept of self-organised criticality (SOC) and sandpile model can be the basis of an analytical study of magneto-ionospheric dynamics. The solar wind, a stream of energised plasma particles is emitted from the outer atmosphere of the Sun and approaches the Earth. The interplanetary magnetic field (IMF) is trapped in the solar wind. Near the terrestrial space, the solar wind flow speed varies from a minimum of 260 km/sec to a maximum of 750 km/sec while the ion density varies in a much wider range, from  $0.1 \text{ cm}^{-3}$  to  $100 \text{ cm}^{-3}$  (Russell 2001). The density fluctuation is the primary controller of the variations in the dynamic pressure, which further controls the solar wind-

magnetosphere reconnection. When the solar wind interacts with the terrestrial magnetosphere, this supersonic flow creates a standing shock wave or bow shock in the day-side of the magnetosphere and converts it into a subsonic flow. Majority of the energised solar wind plasma particles is heated and then get deflected around the Earth at the bow shock. The day-side magnetosphere is compressed down while the night-side magnetosphere is stretched up to about 100 Earth radii comprising the magnetotail (Nishida 2000; Borovsky and Valdivia 2018). The trapped interplanetary magnetic field (IMF) plays a crucial role in controlling the intensity and duration of solar wind-magnetosphere coupling. For a northward IMF  $B_z$ , the cusp shifts away from the equatorial region and further narrows down with the increasing intensity of  $B_z$ , decreasing the amount of energy injection into the magnetosphere. But, for a southward IMF  $B_z$ , the cusp shifts towards the equatorial region and widens out gradually as the intensity of  $B_z$  increases, triggering an injection of a large amount of solar wind energy into the magnetosphere (Lu et al. 2013). The magnetotail becomes a reservoir of this energy. As the solar wind injection continues, the magnetotail grows further by accumulating more and more energy. Eventually, the magnetotail growth reaches a critical point, becomes unstable and magnetic reconnection occurs in the tail. A part of the stored energy is released through flow kinetic energy and plasma heating, producing substorm (Borovsky and Valdivia 2018). Substorm originates deep in the magnetosphere, near the geostationary orbit (Antonova and Ganushkina 2000). It is a short but intense earthward convection of magnetic flux in the magnetotail which injects energised particles in the dipolar region, also substantially increasing the auroral electrojets (McPherron et al. 1973). The Joule energy extracted from the magnetosphere is dissipated in the ionosphere through auroral electrojets, the field-aligned currents flowing between the nightside magnetosphere and nightside ionosphere (Strangeway 2013). The subsequent magnetic fluctuations in the auroral region are measured by the AE index.

SOC has long been proposed as a possible explanation of magnetospheric dynamics. Sandpile model was selected as the first example displaying the concept of self-organised criticality, introduced by Bak et al. in their 1987 and 1988 papers. Since then, the application of this theory has produced numerous significant analyses of magnetospheric activities by some eminent researchers. Consolini observed SOC-triggered behaviour in the power spectral density and burst size distribution of the AE index (Consolini 1997). Using the sign-singularity analysis, magnetic field fluctuations in the near-tail regions were investigated based on the concept of self-organised criticality and 2nd-order phase transition (Consolini and Lui 1999).

Chapman et al. presented a sandpile cellular automaton model to study magnetospheric dynamics (Chapman et al. 1998) and Klimas presented a first-order physical model of plasma sheet (Klimas et al. 2000). Further studies on modelling continued based on the SOC approach with interesting conclusions (Takalo et al. 1999; Uritsky and Semenov 2000). Other notable works discussed in detail the distinctive features of SOC-driven instabilities and their effects in the context of nonlinear dynamics of magnetosphere (Chang 1992, 1999; Uritsky 1996; Uritsky and Pudovkin 1998a; Sitnov et al. 2000). (Dobias and Wanliss 2009) suggested that both the storm and sub-storm characteristics are consistent with the behaviour of the critical system and follow the fractal point process (FPP).

(Uritsky and Pudovkin 1998b) developed a two-dimensional sandpile model of the magnetosphere current sheet to study the AE fluctuations. The model was a rectangular matrix of  $x$  and  $y$  dimensions. Each element of the matrix was characterised by an amount of energy. Also, a critical threshold of energy was assigned to all of the elements to determine the stability of the element after each energy injection. They investigated the avalanche formations, energy redistribution, and plasma sheet instabilities of the SOC-driven system in reaction to external disturbances. It was suggested that the spatially localised magnetotail instabilities can be regarded as SOC avalanches and the superposition of these avalanches of different sizes finally produces the characteristic low-frequency  $1/f$ -like fluctuations of the AE index (Uritsky and Pudovkin 1998b). Uritsky et al. continued the study of the above two-dimensional sandpile model in their 2001 paper to explain geomagnetic substorms as a self-organised critical dynamic of the perturbed magnetosphere. In their study, the total accumulated energy in the system, as well as the energy dissipated from the system, were revealed to be the two major factors controlling the overall dynamics of the system. Moreover, the spectral characteristics of the model output showed striking similarities with the natural AE fluctuations (Uritsky et al. 2001).

Based on the model (Uritsky et al. 2001), we developed a sandpile-like cellular automata model of Earth's magnetosphere in our previous paper (Banerjee et al. 2015). The model is a SOC-driven dissipative dynamical system with both spatial and temporal degrees of freedom. It is a two-dimensional array of finite dimensions and is characterised by energy  $E$ . The input energy to this model is derived from the real-time value of solar ion density and flow speed data. Both the direction and intensity of the real-time value of the  $B_Z$  component of the interplanetary magnetic field (IMF) are the factors controlling the amount of solar wind energy injected into the system at any time. The total accumulated energy of the

system is estimated to produce a simulated output representing the Dst index. The spectral characteristics of the simulated output closely follow the natural Dst index, establishing the acceptability of the model (Banerjee et al. 2015). We continued our study with the model investigating the solar wind-magnetosphere interaction, the injection of plasma particles, and the aspects of internal magnetospheric dynamics as a subsequent effect (Banerjee et al. 2019).

In the present paper, we extend our sandpile-like cellular automata model to study the dynamical behaviour of the auroral zone magnetic activities by focusing on the transferred energy from the system. The model, a representation of the Earth's magnetosphere, is a lattice of  $n \times n$  elements, having spatial and temporal degrees of freedom. Each element is characterised by an energy  $E$ , which is analogous to the slope of the sandpile. The input to the model is solar wind energy, derived from the real-time value of solar ion density and flow speed data. The input energy is injected into the system through a set of elements, representing the cusp. Both the direction and intensity of IMF  $B_Z$  are the factors controlling the width of the cusp, hence the amount of energy injection into the system. The injected energy is altering the potential energy of the elements of the lattice. Each element has a critical value of energy, known as the excitation threshold. As the energy injection continues, the energy gradually piles up in the elements, similar to the storing of energy in the magnetotail. If the energy of any element reaches the point of criticality by exceeding the excitation threshold, spatially localised instabilities are formed, representing the instability formation in the magnetotail. The pile collapses by releasing avalanches of energy in various sizes and shapes. The released energy is distributed among the adjacent elements and the process continues, gradually spreading throughout the lattice. The excess energy reaching the upper or lower margins is transmitted outside the lattice, representing the magnetosphere-ionosphere energy transfer. The amount of transferred energy at any time  $t$  is estimated. By some numerical calculations, an output time series is produced from this estimated energy. The simulated output can be regarded as a mathematical representation of the AE index. It is observed that the simulated series exhibits  $1/f^\beta$ -like power spectrum. The power-law exponents  $\beta_A$  and  $\beta_B$  of the power spectral density of the simulated output are evaluated for both the high- and low-frequency regions respectively for all the years of the entire 23<sup>rd</sup> solar cycle. Finally, by comparing the values of  $\beta_A$  and  $\beta_B$  with that of the real-time AE index, it is observed that the simulated output closely follows the natural AE fluctuations depending on the exact value of the parameter  $K_A$ .  $K_A$  represents the remaining percentage of the

transferred energy of the previous magnetosphere-ionosphere energy transfer, stored in the ionosphere. In our previous work (Banerjee et al. 2019), the real-time solar wind and IMF  $B_Z$  data of the 23<sup>rd</sup> solar cycle were used as the input to the model to investigate the solar wind-magnetosphere energy transfer. As we are continuing our study on the model, in the present work, we used the same input dataset to analyse the magnetosphere-ionosphere energy transfer.

## 2. Method and data

The cellular automata-based sandpile model used here is an extension of the model presented in our previous papers (Banerjee et al. 2015, 2019) which is in turn based on the model presented by (Uritsky et al. 2001). The model, representation of the Earth's magnetosphere, is a finite matrix of  $n \times n$  elements having spatial and temporal degrees of freedom. Each element is characterised by an energy  $E$ , which is analogous to the slope of the sandpile.  $E$  has an arbitrary unit. The threshold value of energy for each element is indicated as  $E_{TH}$ , the excitation threshold (Uritsky et al. 2001). The input to the model is solar wind energy.

The input energy  $dE$  is estimated using the real-time ion density and flow speed data obeying the equation (Banerjee et al. 2015, 2019)

$$dE = \text{norm} \left( \frac{1}{2} \times \text{ion density} \times \text{flow speed}^2 \right) \quad (1)$$

As the solar wind flows towards the Earth, it interacts with the magnetosphere. Depending on the intensity and direction of IMF  $B_Z$ , a part of the solar wind energy is injected into the magnetosphere through the cusp while the major part of the solar wind energy is deflected at the bow shock and flows across the Earth. A small fraction of this deflected energy penetrates into the magnetosphere. In this model, the factor  $K$  represents this small fractional value. Thus, all the elements of the lattice are credited with the energy  $K \times dE$  at every initial stage. This alters the potential energy of each element as (Banerjee et al. 2015, 2019)

$$E_{t+1}(i, j) = E_t(i, j) + K \times dE, \text{ for all } i \text{ and } j \quad (2)$$

As the two-dimensional lattice is analogical to the terrestrial magnetosphere, the cusp width  $W_C$  in the model is a set of selected elements including and surrounding the centre one, the element at  $i = n/2$ ,  $j = n/2$ . The number of elements in the set, that is, the size of the cusp width  $W_C$  is controlled by both the direction and intensity of IMF  $B_Z$ , following the equations (Banerjee et al. 2015):

$$W_C = [(2 \times w) + 1]^2 \quad (3)$$

where

$$w = (K_d \times B_Z) \text{ for southward } B_Z \quad (4)$$

and

$$w = [K_d \times (B_{Z_{\max}} - B_Z)] \text{ for northward } B_Z \quad (5)$$

Here  $B_{Z_{\max}}$  is the maximum value of northward  $B_Z$  and  $K_d$  is the associated proportionality factor.  $K_d$  is a function of the direction of the IMF  $B_Z$ . As the energy injection increases for southward  $B_Z$  and decreases for northward  $B_Z$ , the numerical value of  $K_d$  is higher for the southward direction than that of the northward direction.

During a solar wind-magnetosphere coupling, the solar wind energy  $dE$  is injected into the system through the cusp width  $W_C$  following the relation (Uritsky et al. 2001; Banerjee et al. 2015, 2019),

$$E_{t+1}(i, j) = [E_t(i, j) + dE] \text{ for } i = \left(\frac{n}{2} \pm w\right) \text{ and } j = \left(\frac{n}{2} \pm w\right) \quad (6)$$

The threshold value of energy for each element is indicated as  $E_{TH}$ , the excitation threshold. After the energy injection, if  $E(i, j) < E_{TH}$ , the element is stable. If  $E(i, j) > E_{TH}$ , the element is unstable and releases four units of energy to return to a stable state. The released energy is distributed among its four adjacent neighbours according to the following equations (Uritsky et al. 2001; Banerjee et al. 2015, 2019),

$$E_{t+1}(i, j) = E_t(i, j) - 4 \quad (7)$$

A small value of energy  $E_d$  is dissipated during the distribution process. The energy of the adjacent elements alters as (Uritsky et al. 2001; Banerjee et al. 2015, 2019)

$$E_{t+1}(i \pm 1, j \pm 1) = E_t(i \pm 1, j \pm 1) + \left(1 - \frac{E_d}{4}\right) \quad (8)$$

Figure 1 illustrates the energy transfer process in a two-dimensional lattice. The unstable elements [ $E(i, j) > E_{TH}$ ] are marked with black shade, the stable elements [ $E(i, j) < E_{TH}$ ] with grey shade, and the elements with zero or negligible energy with white shade. Initially, all the elements of the lattice have zero energy. The input energy is injected into the system through the cusp  $W_C$  altering its energy above  $E_{TH}$ , as shown in Figure 1(a). Thus, the centre element is in black shade. The cusp  $W_C$  here consists of only one element, the element at the centre of the lattice ( $i = n/2$ ,  $j = n/2$ ). In the next Figure 1(b), the unstable element distributes four units of its energy to its four adjacent neighbours. Two of the neighbouring elements, marked in black shade became unstable, receiving the excess energy. In the final Figure 1(c), the two unstable elements further distribute their energy to return to stability. This way, the injected energy is distributed and redistributed throughout the lattice.

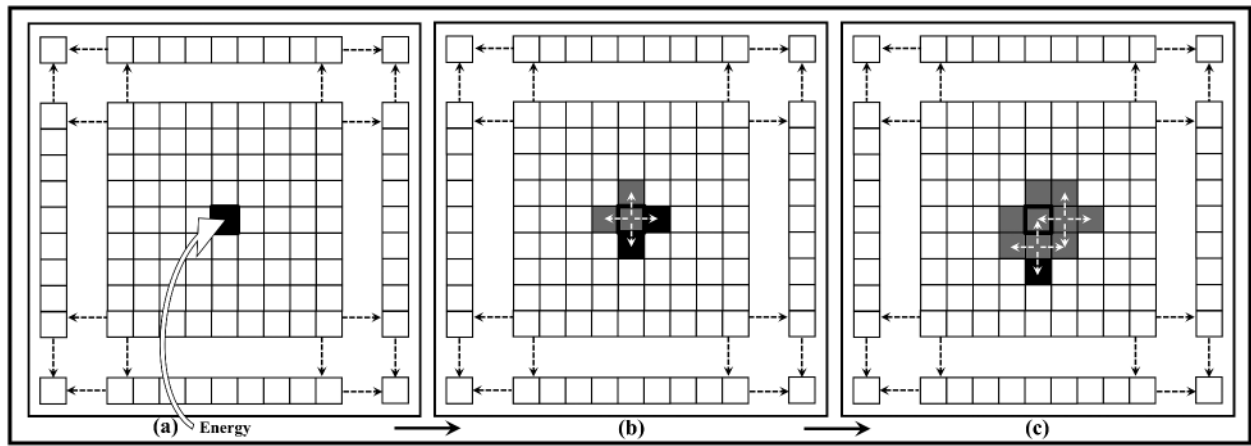


**Figure 1.** The energy distribution in a two-dimensional lattice. The unstable elements  $[E(i, j) > E_{TH}]$  are marked with black shade, the stable elements  $[E(i, j) < E_{TH}]$  with grey shade, and the elements with zero or negligible energy with white shade. Initially, all the elements of the lattice have zero energy. (a) The input energy is injected into the system through the cusp  $W_C$  altering its energy above  $E_{TH}$ . The cusp  $W_C$  here consists of only one element, the element at the centre of the lattice ( $i = n/2, j = n/2$ ). (b) The unstable element distributes four units of its energy to its four adjacent neighbours. Two of the neighbouring elements became unstable. (c) The two unstable elements further distribute their energy to return to stability. This way, the injected energy is distributed and redistributed throughout the lattice.

With analogy to the Earth, the system is spherical, meaning the elements belonging to the columns  $j = n$  and  $j = 1$  are adjacent neighbours. If the energy of any element belonging to the column  $j = n$  has crossed the threshold, one unit of its surplus energy is distributed to its neighbour element in column  $j = 1$  and vice versa. The dissipation of energy through the marginal grids is only applicable for the upper and lower marginal rows, not for the marginal left or marginal right columns. Open boundary condition has been considered for the marginal rows of the lattice. After a consecutive distribution and redistribution, when the released energy finally reaches the marginal upper [ $i = 1, j = (1 \text{ to } n)$ ] and lower [ $i = n, j = (1 \text{ to } n)$ ] grids, it transmits outside the system.

Figure 2 displays the state of the elements of the lattice after a consecutive energy injection, distribution, and redistribution. All the elements have a considerable amount of energy while some of them become unstable. In Figure 2(a), in the marginal rows, two of the elements are unstable in both the upper and lower grids. In the next Figure 2(b), the unstable elements in the marginal rows dissipate their excess energy and a part of this energy is released outside the lattice, representing the magnetosphere-ionosphere energy transfer.

After the consecutive distribution and redistribution, the total internal accumulated energy of the lattice at any time  $t$  can be calculated as (Uritsky et al. 2001; Banerjee et al. 2015, 2019)

$$E_{\text{Total}} = \sum E(i, j) \text{ for all } i \text{ and } j \quad (9)$$

The number of unstable states, that is, elements having energy  $E > E_{TH}$  at any time  $t$  is estimated by the relation (Uritsky et al. 2001)

$$S_{UN} = \sum S_{ij} \text{ for all } i \text{ and } j \quad (10)$$

where  $S_{ij} = 1$  if  $E > E_{TH}$  and  $S_{ij} = 0$  if  $E < E_{TH}$

The upper and the lower grids can be considered as the northern and southern polar cusps of the Earth while the energy transfer process is similar to magnetosphere-ionosphere energy coupling. In the actual measurement of the AE index, all the magnetometer stations are located in the northern hemisphere for recording the associated data. Following this instance, we too considered and based our calculations on the total excess energy dissipating only through the upper grid [ $i = 1, j = (1 \text{ to } n)$ ] of the lattice. We denote  $T_R$  as the time delay between the initial energy injection to the model and the beginning of the energy transfer through the upper marginal grid.  $T_R$  estimates the total time for the energy to reach the boundary after successive distribution and redistribution processes for each input injection. The total amount of released energy outside the lattice at any time  $t$  can be estimated as (Banerjee et al. 2019)

$$E_R = \sum E(i, j) \text{ for } i = 1, j = (1 \text{ to } n) \quad (11)$$

The released energy generates two currents,  $I_W$  and  $I_E$ , the numerical equivalents of the auroral westward and eastward currents in the ionosphere, respectively. The auroral electrojet is estimated as the difference value of these two currents. For the calculation of electrojets, we considered the dissipated energy from any element belonging to the odd columns, that is,  $j = 1, 3, 5, \dots, (n-1)$  are contributing to the westward electrojet while the energy from any element belonging to the even columns, that is,  $j = 2, 4, 6, \dots, n$  are contributing to the eastward electrojet. Thus, mathematically

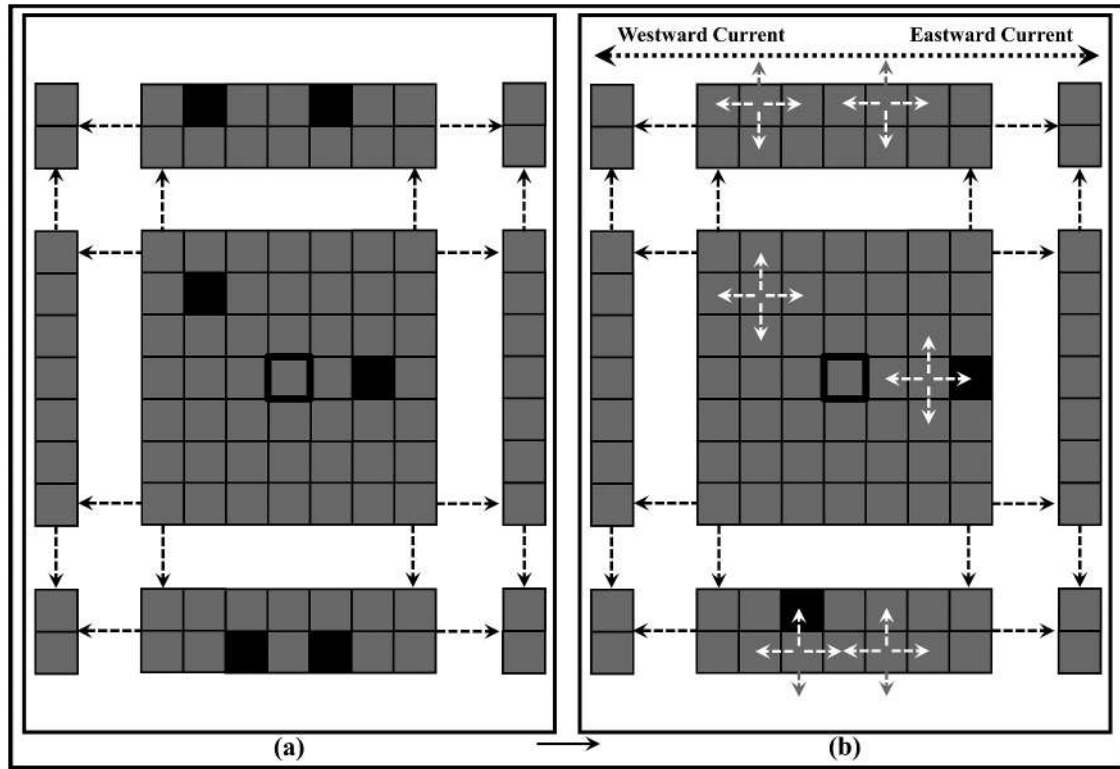


**Figure 2.** The state of the elements of the lattice after a consecutive energy injection, distribution, and redistribution. The unstable elements  $[E(i, j) > E_{TH}]$  are marked with black shade, the stable elements  $[E(i, j) < E_{TH}]$  with grey shade and the elements. All the elements have a considerable amount of energy while some of them become unstable. (a) In the marginal rows, two of the elements are unstable in both the upper and lower grids. (b) The unstable elements in the marginal rows dissipate their excess energy and a part of this energy is released outside the lattice, representing the magnetosphere-ionosphere energy transfer.

$$E_w(t) = \sum E(i, j) \text{ for } i = 1, j = 1, 3, 5, \dots, (n-1) \quad (12)$$

and

$$E_e(t) = \sum E(i, j) \text{ for } i = 1, j = 2, 4, 6, \dots, n \quad (13)$$

As the distribution process continues, more and more excess energy piles up outside the boundary regions of the lattice. The series  $E_w(t)$  and  $E_e(t)$  are the estimations of the total accumulated energy released in the ionosphere responsible for the westward and eastward electrojet currents, respectively. The released energy takes time to completely dissipate through the current system in the ionosphere and a part of this energy remains stored in the ionosphere. During the next magnetosphere-ionosphere energy transfer, this stored energy from the previous transfer acts as a base value and adds up with the newly released value of energy. Here, we introduce a parameter, namely  $K_A$  which determines the remaining part of the released energy of the previous transfer, stored in the ionosphere.  $K_A$  has a fractional value.

The remaining energy in the westward region is

$$E_{rw}(t) = K_A \times E_w(t-1) \quad (14)$$

whereas the remaining energy in the eastward region is

$$E_{re}(t) = K_A \times E_e(t-1) \quad (15)$$

Mathematically, the total westward energy at any time  $t$  is

$$E_{tw} = \sum [E_w(t) + E_{rw}(t)] \text{ for all } t \quad (16)$$

and the total eastward energy at any time  $t$  is

$$E_{te} = \sum [E_e(t) + E_{re}(t)] \text{ for all } t \quad (17)$$

These two energy components,  $E_{tw}(t)$  and  $E_{te}(t)$  then drive two currents in the opposite direction throughout the auroral region, namely the westward electrojet current and the eastward electrojet current, respectively.

The maximum westward electrojet current can be considered as

$$I_W = \sqrt{E_{tw}} \quad (18)$$

and the maximum eastward electrojet current as

$$I_E = \sqrt{E_{te}} \quad (19)$$

The differential value of these two components is

$$E_N = \text{abs}(I_E - I_W) \quad (20)$$

For further refinement,  $E_N$  is processed by a filter and labelled as  $E_A$ . Finally, the output time-series  $E_A$  can be regarded as a numerical representation of the natural auroral electrojet index, AE.



For our analysis, we used the hourly averaged AE index, solar wind ion density, flow speed, and  $B_Z$  component of the interplanetary magnetic field (IMF) data from the year 1997 to the year 2007 of the 23<sup>rd</sup> solar cycle. The dimension of the lattice is  $50 \times 50$ . Similar to our original study of the model (Banerjee et al. 2015), the numerical value of the various variables of the model are taken as  $K = 0.0025$ , local dissipation term  $E_d = 0.05$ ,  $K_d = 0.5$  for southward direction, and  $K_d = 0.005$  for northward direction. The input to the model is estimated using equation 1.

### 2.1. Data source

Here we used the hourly averaged AE index, solar wind ion density, flow speed, and  $B_Z$  component of the interplanetary magnetic field (IMF) data from the year 1997 to the year 2007 of the 23<sup>rd</sup> solar cycle as extracted from NASA/GSFC's OMNI data set through OMNIWeb. The OMNI data were obtained from the GSFC/SPDF OMNIWeb interface at <http://omniweb.gsfc.nasa.gov> (King & Papitashvili 2005).

### 3. Result and discussions

The threshold excitation  $E_{TH}$  is crucial for the central characteristics of a SOC system as it allows the existence of multiple metastable states across which the avalanches are carried out throughout the system. The potential energy  $E$  of any element in the lattice is analogical to the slope of an actual sandpile. An unstable element having energy  $E(i, j) > E_{TH}$  releases four units of energy to return to stability. Thus, a minimum value of  $E_{TH} = 5$  is required to keep the potential energy of the element at a positive non-zero value and to avoid the total internal energy of the system reaching zero or negative energy states at any time. To analyse the dynamical behaviour of the

system, the model is subjected to three different  $E_{TH}$  values,  $E_{TH} = 5$ ,  $E_{TH} = 7$ , and  $E_{TH} = 9$ . After the energy injection and distribution, the total accumulated internal energy of the lattice,  $E_{Total}$ , the total number of unstable states,  $S_{UN}$ , and the total amount of released energy,  $E_R$  at any time  $t$  can be calculated according to Equations 9, 10, and 11 respectively. Figure 3 illustrates the time vs.  $E_{Total}$  plot for the three values of  $E_{TH}$  for the year 2002. As the threshold value increases, the rate of energy distribution and dissipation decreases while the total internal energy of the system continues to increase gradually. It takes much more time for the system to achieve a meta-stable state, delaying the SOC dynamics and avalanches throughout the lattice to form properly. As the rate of distribution reduces, the elements in the marginal grids start to store and release energy to the outside of the lattice far more lately, thus delaying the energy transfer process representing the magnetosphere-ionosphere energy coupling in the model. We denote  $T_R$  as the time delay between the initial energy injection to the model and the beginning of energy transfer through the upper marginal grid. It is observed from the analysis, that the value of  $T_R$  is  $T_R = 1434$  hours for  $E_{TH} = 5$ ,  $T_R = 1934$  hours for  $E_{TH} = 7$  and  $T_R = 2520$  hours for  $E_{TH} = 9$ . Thus, for further analysis of the system, we considered  $E_{TH} = 5$  as the value for the excitation threshold. Figure 5(b), the plot for the simulated time-series  $E_A$ , shows the estimation of  $E_A$  initiating from the value of  $T_R = 1434$  hours for  $E_{TH} = 5$  as from this value of  $T_R$  the marginal grid starts to release energy outside the system.

Figure 4 demonstrates the plots for  $dE$ ,  $E_{Total}$ ,  $S_{UN}$ , and  $E_R$  for the September–October period of the year 2002. As seen from the figure,  $dE$  has large values for the marked timeline. The injected energy piles up in the lattice increasing the number of unstable states  $S_{UN}$ , the total energy of the lattice,  $E_{Total}$ , reaches a critical point and then gradually returns to

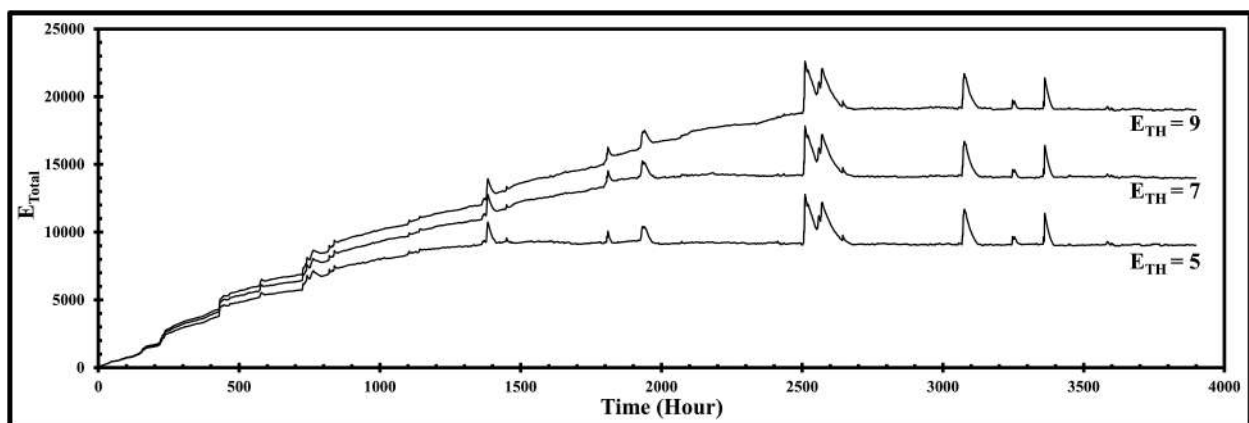


**Figure 3.** Time vs.  $E_{Total}$  plot for the three values of  $E_{TH}$  for the year 2002. As the threshold value increases, the rate of energy distribution and dissipation decreases while the total internal energy of the system continues to increase gradually. It takes much more time for the system to achieve a meta-stable state.

a metastable state by releasing a burst of avalanches. The avalanches take a time to reach the upper marginal grid through successive distribution and redistribution processes, thus  $E_R$  shows high-energy values dissipating from the upper grid after a while.

After the injection of the energy followed by subsequent distribution and redistribution, the model output  $E_A$  is generated estimating the released energy outside the lattice as discussed in the method section. The output series  $E_A$  is the numerical representation of the natural AE index. The power spectral density (PSD) of the simulated output  $E_A$  is calculated and plotted in a log–log graph. The plot demonstrates the characteristic  $1/f^\beta$  behaviour of the natural AE fluctuations along with the spectral break at  $f_0$ . A detailed study of the plot revealed the value of breakpoint  $f_0$  as  $f_0 = 0.050$  mHz (5.5 hours), as shown in Figure 7(b). A power law is fitted separately in both the high ( $f > f_0$ ) and low frequency ( $f < f_0$ ) regions of the plot to determine the power-law coefficients (slope of the spectral response)  $\beta_A$  and  $\beta_B$ , respectively. Now keeping the other parameter constant, if the value of  $K_A$  is varied in the range of 0.10 to 1.00, the  $\beta$  values also vary within ranges. As, for a particular value of  $K_A$ , the

$\beta$  values of the simulated series closely match with that of the natural AE index, they are noted down along with the value of  $K_A$ , as shown in Table 1. The  $\beta$  values of the real-time AE index are also displayed in Table 1 for a comparative study.

Figure 5(a,b) are the time series of the natural AE index and the simulated  $E_A$  series of the year 2002, respectively. For comparative purposes, a magnified portion of the natural AE index and that of the simulated  $E_A$  series of the year 2002 are displayed in Figure 6(a, b), respectively. The real-time AE index is estimated as the difference value of AU and AL indices where the AU and AL indices are the direct measurements of the maximum eastward and westward electrojet currents. (Ahn et al., 2000b) studied the variation pattern of the yearly mean AL index and AU index for 20 years and suggested their absolute values are proportional to each other. The maximum is observed for the AU index in summer while for the AL index, it is in equinoctial months. Both the indices exhibit higher values in the descending phase of the solar cycle (Ahn et al., 2000b). In the current model, the simulated AE index is estimated following the same relation as the difference value between the maximum eastward and

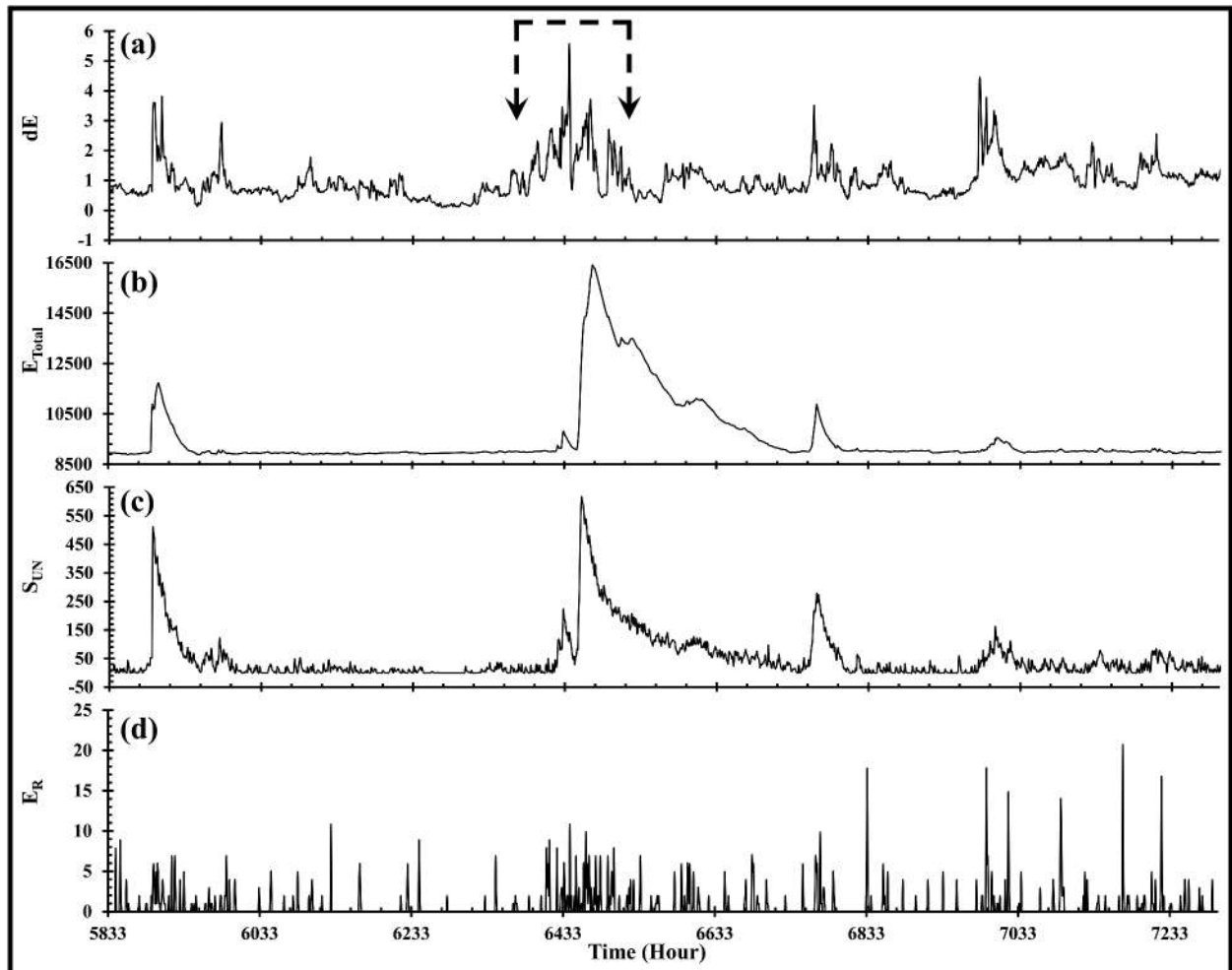


**Figure 4.** Plots for the September–October period of the year 2002 (a) Input energy,  $dE$  (b) the total accumulated internal energy of the lattice,  $E_{Total}$  (c) the total number of unstable states,  $S_{UN}$ , and (d) the total amount of released energy,  $E_R$ .

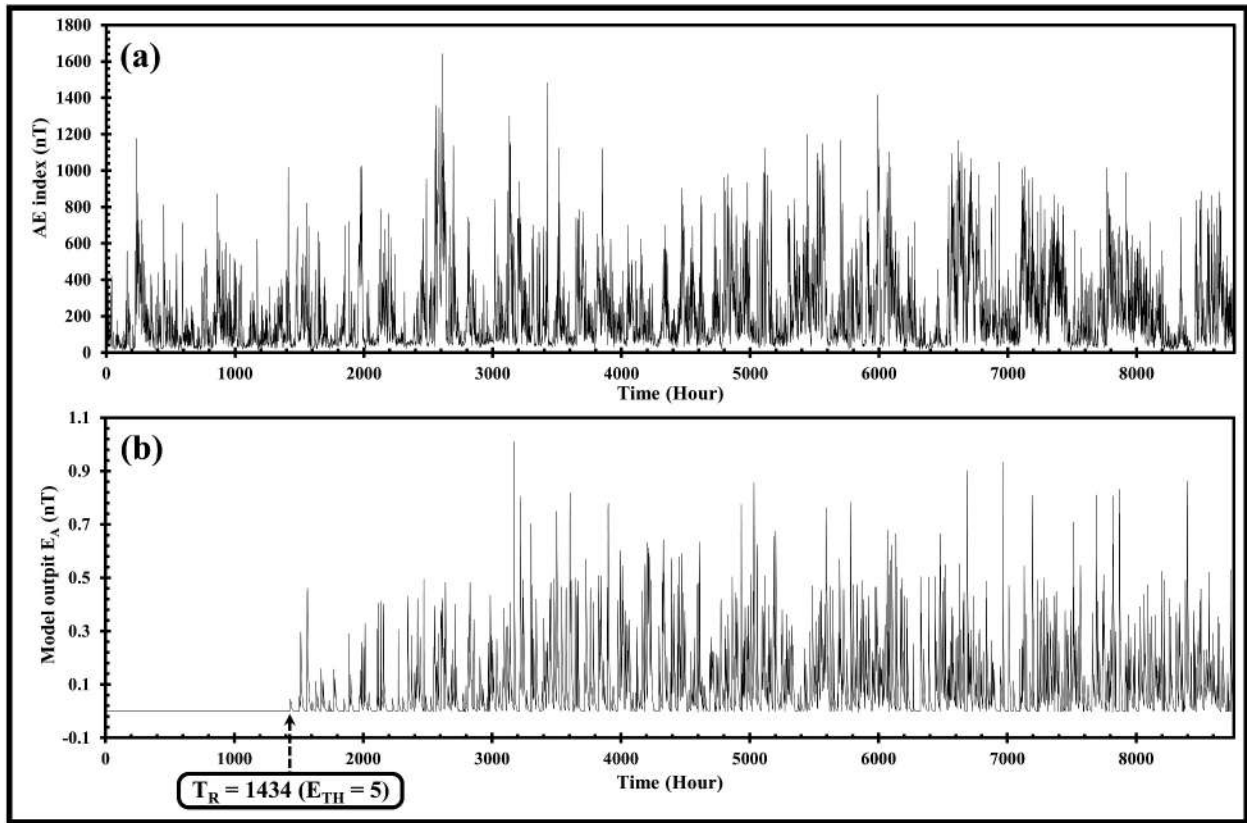


**Figure 5.** (a) The time-series of the natural AE index of the year 2002 (b) The simulated model output time-series,  $E_A$  of the year 2002.  $T_R = 1434$  hours for  $E_{TH} = 5$  is the time delay between the initial energy injection to the model and the starting of energy transfer through the upper marginal grid.

**Table 1.** The power-law coefficients (slope of the spectral response) of the power spectral density associated with the real-time AE index and the simulated model output  $E_A$  for all the years of the 23<sup>rd</sup> solar cycle. The spectral break is at  $f_0 = 0.050$  mHz (5.5 hours).  $\beta_A$  denotes the value of the slope for  $f > f_0$  and  $\beta_B$  denotes the value of the slope for  $f < f_0$ . The parameter  $K_A$  is associated with the series  $E_A$  and shows different values for different years.

Year	Real-Time AE Index Series		$K_A$	Model Output $E_A$ Series	
	$\beta_A$	$\beta_B$		$\beta_A$	$\beta_B$
1997	$2.366 \pm 0.103$	$1.009 \pm 0.046$	0.82	$2.389 \pm 0.126$	$0.945 \pm 0.068$
1998	$2.464 \pm 0.111$	$1.066 \pm 0.046$	0.70	$2.229 \pm 0.105$	$0.961 \pm 0.062$
1999	$2.383 \pm 0.104$	$0.933 \pm 0.043$	0.70	$2.359 \pm 0.125$	$0.950 \pm 0.063$
2000	$2.130 \pm 0.101$	$1.007 \pm 0.046$	0.74	$2.325 \pm 0.102$	$0.963 \pm 0.057$
2001	$2.276 \pm 0.102$	$1.035 \pm 0.043$	0.70	$2.282 \pm 0.115$	$1.023 \pm 0.065$
2002	$2.170 \pm 0.109$	$0.985 \pm 0.045$	0.73	$2.372 \pm 0.120$	$0.955 \pm 0.065$
2003	$2.060 \pm 0.100$	$0.914 \pm 0.043$	0.68	$2.248 \pm 0.128$	$0.964 \pm 0.067$
2004	$2.285 \pm 0.109$	$0.979 \pm 0.044$	0.74	$2.210 \pm 0.128$	$0.985 \pm 0.065$
2005	$2.218 \pm 0.108$	$0.990 \pm 0.043$	0.72	$2.222 \pm 0.125$	$0.962 \pm 0.065$
2006	$2.499 \pm 0.107$	$1.006 \pm 0.044$	0.77	$2.226 \pm 0.123$	$0.962 \pm 0.069$
2007	$2.183 \pm 0.103$	$0.902 \pm 0.043$	0.78	$2.352 \pm 0.112$	$0.953 \pm 0.067$

westward electrojets. In Figure 5, the May–June summer months of the year 2002 is the period for about the time, Time = 2800 hours – 4200 hours. As can be seen from Figure 5(a), the values of the real-time AE index are in the higher ranges for these months. The simulated series in Figure 5(b) also demonstrates the same. Again, in Figure 5, the period of about the time, Time = 5800 hours – 6600 hours marks the equinoctial month of September. Here, also the values of the simulated series of Figure 5(b) show higher values, similarly to the real-time AE index, as shown in Figure 5(a).

Figure 7(a, b) illustrate the log–log plot of the PSD of the real-time AE index and the simulated  $E_A$  series of the year 2002, respectively. It is observed from the plots that the simulated  $E_A$  series exhibits the characteristic  $1/f^\beta$  behaviour of the natural AE fluctuations along with the spectral break at  $f_0$ . As can be seen from Figure 7(b), for the value of  $K_A = 0.73$ , the simulated series has values  $\beta_A = -2.372 \pm 0.120$  and  $\beta_B = -0.955 \pm 0.065$  which nearly matches the values  $\beta_A = -2.170 \pm 0.109$  and  $\beta_B = -0.985 \pm 0.045$  of the natural AE fluctuations. The spectral point and the

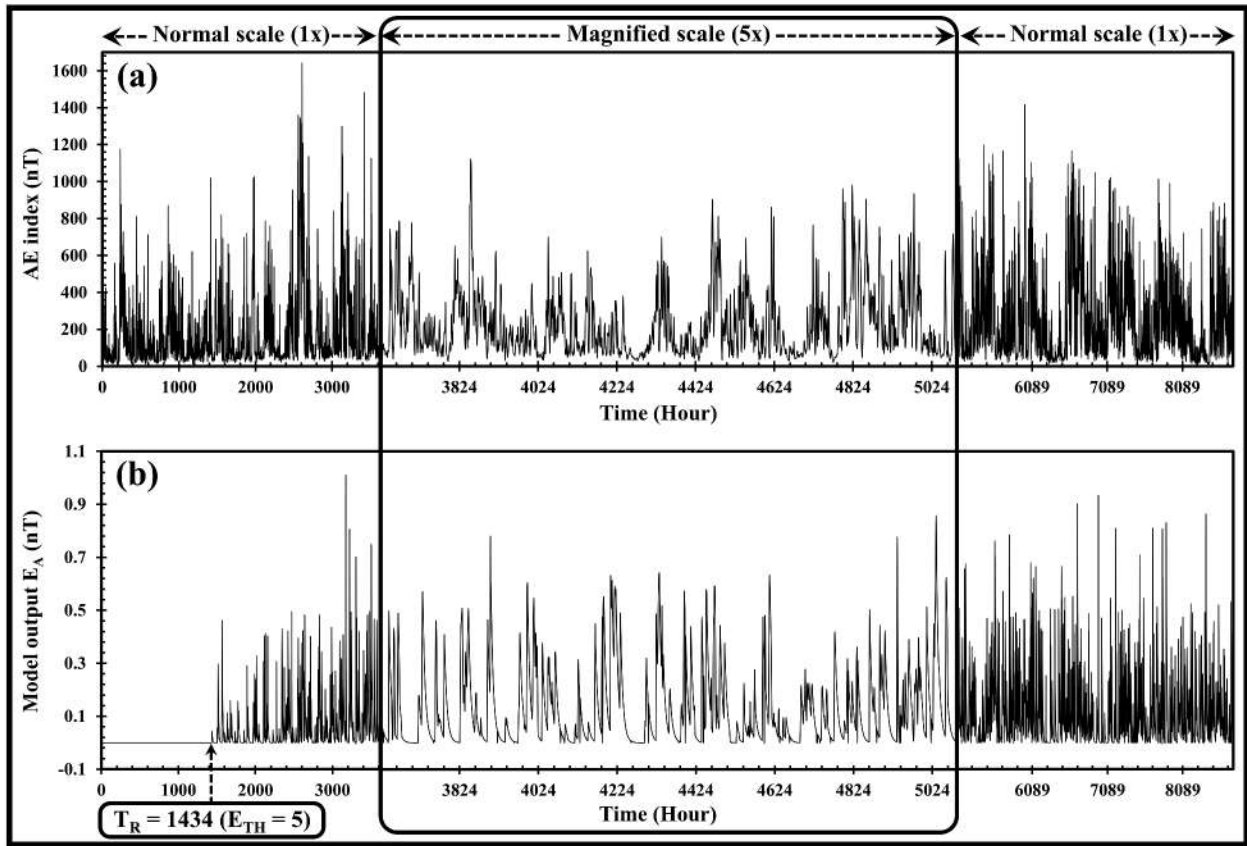


Figure 6. (a) The magnified version of the time-series of the natural AE index of the year 2002 (b) The magnified version of the simulated model output time-series,  $E_A$  of the year 2002.

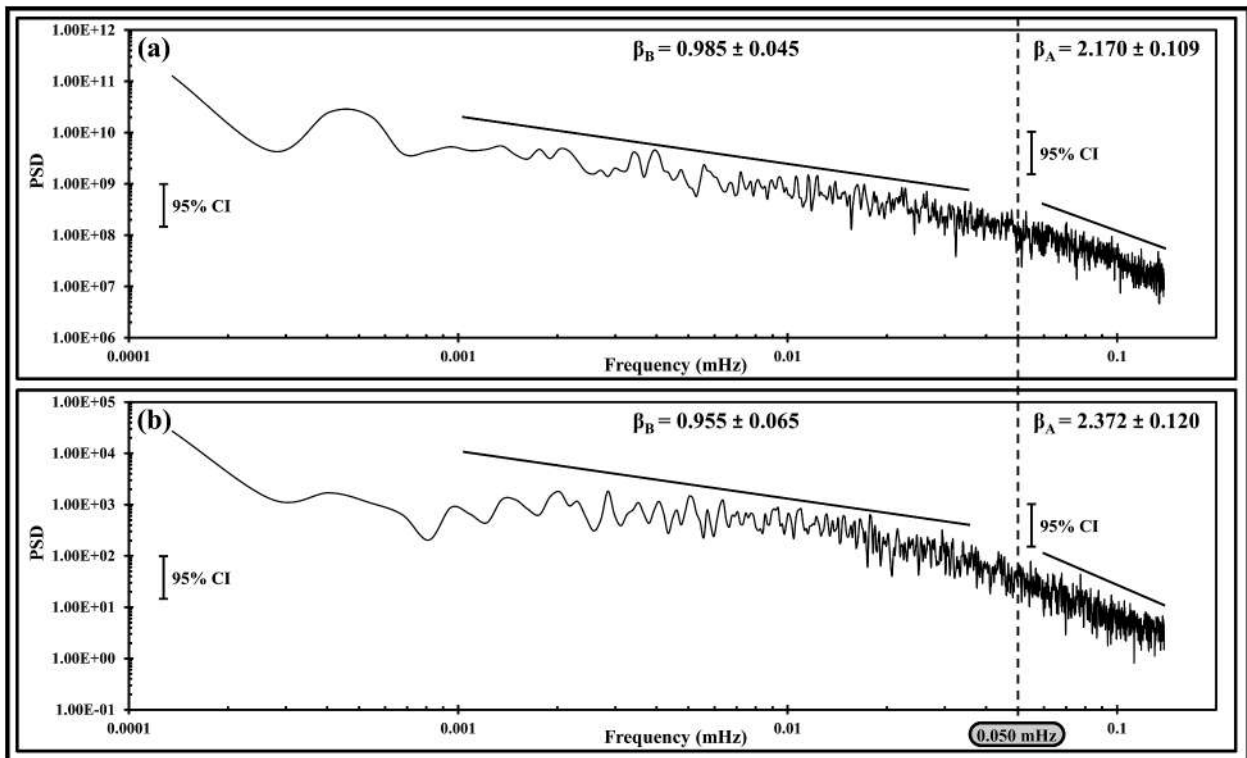


Figure 7. (a) The log-log plot of the power spectral density (PSD) of the real-time AE index of the year 2002. The  $\beta$  values of the series are estimated as  $\beta_A = -2.170 \pm 0.109$  and  $\beta_B = -0.985 \pm 0.045$  with a spectral break at  $f_0 = 0.050$  mHz (5.5 hours). (b) The log-log plot of the power spectral density (PSD) simulated model output  $E_A$  of the year 2002. For the value of  $K_A = 0.73$ , the  $\beta$  values of the series are estimated as  $\beta_A = -2.372 \pm 0.120$  and  $\beta_B = -0.955 \pm 0.065$  with a spectral break at  $f_0 = 0.050$  mHz (5.5 hours).

slopes of the two frequency regions of the  $1/f^\beta$  power spectrum of the natural AE index had long been a study of keen interest. (Tsurutani et al. 1990) estimated the values of the slopes as  $\beta_A = 2.2$  and  $\beta_B = 0.98$  with a breakpoint at  $f_0 = 0.050$  mHz (5.5 hours) for the hourly average AE data of the period of years 1971–1974. (Uritsky and Pudovkin 1998b) found out the values as  $\beta_A = 2.10$  and  $\beta_B = 0.95$  with a breakpoint at  $f_0 = 0.055$  mHz (5 hours) for the hourly average AE data of the period of years 1973–1974. (Woodard et al. 2005) compared all the prominent studies (Tsurutani et al. 1990; Consolini et al. 1996; Uritsky and Pudovkin 1998b; Price and Newman 2001; Watkins 2002) investigating the slopes of the two spectral regions and breakpoint of natural AE fluctuations and concluded the values of slopes as  $\beta_A = 2.4 \pm 0.26$  and  $\beta_B = 1.0 \pm 0.10$ . It is observed from Table 1 that for a particular value of the parameter  $K_A$ , the  $\beta$  values of the simulated series  $E_A$  are estimated as  $\beta_A = 2.2\text{--}2.4$  and  $\beta_B = 0.9\text{--}1.0$  with a spectral break at  $f_0 = 0.050$  mHz (5.5 hours), the typical values associated with natural AE index as reported by all these previous works.

The parameter  $K_A$  plays a significant role in estimating the simulated  $E_A$  series from the total released energy. As observed from Table 1, for a particular year and a particular value of  $K_A$ , the  $\beta$  values of the simulated output series  $E_A$  are in the specified ranges of the same associated with the natural AE index. For the entire 23<sup>rd</sup> solar cycle, the value of  $K_A$  is in the range of  $K_A = 0.68\text{--}0.82$ . It is observed from the result, that the transferred solar wind energy does not dissipate completely through the westward and eastward auroral electrojet currents in an instant, rather a significant part of it remains present in the ionosphere even in the time of the next magnetosphere-ionosphere energy transfer. The parameter  $K_A$  has a fractional value. As can be seen in equations (14) and (15),  $K_A$  is denoting the remaining fraction of the total accumulated released energy of the previous state, reserved in the ionosphere. The excess energy transferred from the magnetosphere to the ionosphere is then being added up with this base value and forms the westward and eastward currents that are the two key factors for measuring the AE index.

The magnetosphere-ionosphere energy transfer and the stored part of this energy in the ionosphere are primarily controlled by the solar wind injection into the magnetosphere. Again, the amount of injected solar wind energy in the magnetosphere varies with the intensity, and duration of solar wind-magnetosphere coupling. Also, the solar cycle has a significant effect on energy injection. During solar storms, there is a large deposit of energy into the magnetosphere which changes the normal quiet time dynamics of the magneto-ionosphere system. Figure 4 illustrates such a case of a large amount of solar wind

injection into the magnetosphere. As shown in Figure 4(a), the marked period in the figure is distinguished by the continuous injection of a large amount of energy  $dE$  into the magnetosphere for hours. Consequently, the total accumulated energy of the lattice,  $E_{\text{Total}}$ , gradually starts to pile up in the system, altering its state of equilibrium. The value of the number of unstable states,  $S_{\text{UN}}$ , also increases indicating the instability formation in the lattice. Figure 4(b, c) show the plots for  $E_{\text{Total}}$  and  $S_{\text{UN}}$ , respectively. As the large values of energy injection continue,  $E_{\text{Total}}$  finally reaches a critical point and the pile collapses. The excess energy is released as a burst of avalanches inside the lattice restoring the stability of the system. After the successive distribution and redistribution process, the excess energy of the lattice is finally transferred outside its boundary region representing the magnetosphere-ionosphere energy transfer. As seen from Figure 4(d), the amount of released energy  $E_R$  increases after a while as a consequence of the continuous injection of large values of  $dE$  in the magnetosphere. The released energy in the ionosphere is dissipated through the auroral electrojets, the field-aligned currents flowing between the nightside magnetosphere and nightside ionosphere. But it takes time to completely dissipate through the current system in the ionosphere and a part of this energy remains stored in the ionosphere. The factor  $K_A$  estimates the amount of this stored energy.

As observed from the result, for the entire 23<sup>rd</sup> solar cycle, the value of  $K_A$  is slightly varying,  $K_A = 0.68\text{--}0.82$ . In the model, the parameter  $K_A$  does not estimate the actual value of the stored energy, rather it indicates the percentage value of the transferred energy that remains stored in the ionosphere. As shown in Table 1, the value of  $K_A$  for the year 2002 is  $K_A = 0.73$ . This value indicates, at any current state  $t$ , 73% of the transferred energy of the previous state ( $t-1$ ), remains stored in the ionosphere. Thus, the transmitted energy does not dissipate instantly after each magnetosphere-ionosphere energy transfer, rather a substantial percentage (73%) of this energy remains reserved in the ionosphere during the next magnetosphere-ionosphere energy transfer. If the solar wind energy injection into the magnetosphere increases at any time  $t$ , the amount of total released energy in the ionosphere also increases for this  $t$ . Since  $K_A$  indicates the remaining percentage value of this released energy, the actual amount of the reserved energy in the ionosphere also increases as an effect of the large solar wind injection. Similarly, if the input injection is small, the amount of released energy decreases, decreasing the actual amount of reserved energy in the ionosphere. Thus, the actual amount of the reserved energy in the ionosphere varies with the variation in the intensity of injected solar wind in the magnetosphere and the parameter  $K_A$  represents its

percentage relationship with the total transferred energy. For the 23<sup>rd</sup> cycle, the value of  $K_A$  ranges between  $K_A = 0.68$ – $0.82$ , indicating that for each year, a substantial percentage of the transferred energy remains stored in the ionosphere.

#### 4. Conclusions

AE index is a global and instantaneous measurement of the magnetic fluctuations in the Earth's polar region in response to an external perturbation. In this paper, we developed a numerical cellular automata model of Earth's magnetosphere based on the concept of self-organised criticality and sandpile dynamics to study the complex dynamics of the magnetosphere-ionosphere energy transfer process and AE fluctuations. Our model is a dissipative, dynamical  $n \times n$  two-dimensional system of finite potential energy and open boundary conditions having the real-time values of solar ion density, flow speed, and IMF  $B_z$  as the input parameters. It is analogical to the Earth's magnetosphere while the upper and lower margins of the lattice can be considered as the north and south polar cusps of the Earth. The solar wind is a stream of energised plasma particles emitted from the outer atmosphere of the Sun. As the direction of IMF  $B_z$  is southward, a strong coupling occurs between the solar wind and terrestrial magnetosphere injecting a significant amount of solar wind energy into the geospace. Gradually, the energy piles up and reaches a self-organised critical condition after which adding up a small amount of energy into the pile can form a spatially localised magnetospheric instability. To maintain the equilibrium, the system redistributes itself and the excess energy is released as an outburst of avalanches of various sizes in the neighbouring regions. As long as there is local instability, the distribution process continues and successively spread over throughout the system, finally transmitting a large amount of energy into the ionosphere through the polar cusps. The transferred solar wind energy causes magnetic fluctuations in the auroral region and the AE index is the global measurement of the intensity of the fluctuations. In our proposed cellular automata model, the marginal grids of the lattice are equivalent to the polar cusps. The excess energy transferred through the upper grid of the lattice is measured and by some mathematical process a simulated time series has been derived which can be considered as a numerical representation of the real-time AE index.

The spectral response of the simulated output series  $E_A$  follows a  $1/f^\beta$  power law, demonstrates a breakpoint at  $f_0 = 0.050$  mHz (5.5 hours) having slopes  $\beta_A = 2.2$ – $2.4$  for  $f > f_0$  and  $\beta_B = 0.9$ – $1.0$  for

$f < f_0$ , the typical characteristics of natural AE index. It is observed that the parameter  $K_A$  plays a significant role in the entire process of forming a proper  $E_A$  time series estimated from the released energy.  $K_A$  represents the percentage of the released energy from the previous magnetosphere-ionosphere energy transfer, which remains stored in the ionosphere. Its value varies in a small range of  $K_A = 0.68$ – $0.82$  for the eleven years of the 23<sup>rd</sup> solar cycle, indicating a substantial percentage of the transferred energy remains reserved in the ionosphere for each year.

The excitation threshold  $E_{TH}$  is crucial in forming the SOC dynamics of the model. As an unstable element release four units of energy, for a small value of  $E_{TH}$ , the total internal energy of the system can achieve zero or negative potential for some of the values of  $t$ . In contrast, a large value of  $E_{TH}$  causes the piling up of solar wind energy in the system, reducing the rate of energy distribution as well as dissipation. The total internal energy of the system continues to increase gradually and the system takes a much larger time to achieve a metastable state and to form the SOC dynamics properly. Thus, a moderate value of  $E_{TH} = 5$  is optimum for the proposed model.

Overall, it can be concluded that our proposed model is a simple first-order avalanche model of the Earth's magnetosphere where the real-time solar parameters are the inputs. The model generates a simulated output series  $E_A$  which shows statistical similarity to the real-time AE index. Also, the parameter  $K_A$  varies over a small range of  $K_A = 0.68$ – $0.82$  which suggests a high percentage of the transferred solar wind energy remains reserved in the ionosphere. In our previous work (Banerjee et al. 2015) we presented a SOC-based cellular automata model and focused on the nature of solar wind-magnetosphere energy transfer and its subsequent effect in the magnetosphere. In continuation of this project, the current work is a further refinement of that model to study the magnetosphere-ionosphere energy transfer process. Future work can be focused to develop a composite cellular automata model of the magnetosphere to study all the intricate characteristics of the solar wind-magnetosphere-ionosphere dynamics.

#### Acknowledgements

We acknowledge the use of NASA/GSFC's Space Physics Data Facility's OMNIWeb (or CDAWeb or ftp) service, and OMNI data. We express our sincere gratitude to the National Research Institute of Astronomy and Geophysics, Egypt for their generous support regarding the arrangement of funding. We are also thankful to Parthasarathi Chakrabarti, Director, IEST, Shibpur, Howrah, India and Somnath Mukherjee, Principal of Dinabandhu Andrews

College, Kolkata, India for their encouragement and support for the present work. Finally, we would like to sincerely thank the anonymous reviewers for their most valuable comments and suggestions to improve the quality of this paper.

## Disclosure statement

No potential conflict of interest was reported by the author(s).

## References

- Ahn B-H, Kroehl HW, Kamide Y, Kihn EA. 2000a. Universal time variations of the auroral electrojet indices. *Journal of Geophysical Research: Space Physics*. 105(A1):267–275. doi:10.1029/1999ja900364.
- Ahn B-H, Kroehl HW, Kamide Y, Kihn EA. 2000b. Seasonal and solar cycle variations of the auroral electrojet indices. *J Atmos Sol-Terr Phys*. 62(14):1301–1310. doi:10.1016/s1364-6826(00)00073-0.
- Allen JH, Kroehl HW. 1975. Spatial and temporal distributions of magnetic effects of auroral electrojets as derived from AE indices. *J Geophys Res*. 80(25):3667–3677. doi:10.1029/ja080i025p03667.
- Antonova EE, Ganushkina NY. 2000. Inner magnetosphere currents and their role in the magnetosphere dynamics. *Physics and Chemistry of the Earth, Part C: Solar, Terrestrial & Planetary Science*. 25(1–2):23–26. doi:10.1016/s1464-1917(99)00028-8.
- Bak P, Tang C, Wiesenfeld K. 1987. Self-organized criticality: an explanation of the 1/f noise. *Phys Rev Lett*. 59(4):381–384. doi:10.1103/physrevlett.59.381.
- Bak P, Tang C, Wiesenfeld K. 1988. Self-organized criticality. *Phys Rev A*. 38(1):364–374. doi:10.1103/physreva.38.364.
- Banerjee A, Bej A, Chatterjee TN. 2011. On the existence of a long range correlation in the geomagnetic disturbance storm time (Dst) index. *Astrophys Space Sci*. 337(1):23–32. doi:10.1007/s10509-011-0836-1.
- Banerjee A, Bej A, Chatterjee TN. 2015. A cellular automata-based model of Earth's magnetosphere in relation with Dst index. *Space Weather*. 13(5):259–270. doi:10.1002/2014sw001138.
- Banerjee A, Bej A, Chatterjee TN, Majumdar A. 2019. An SOC approach to study the solar wind-magnetosphere energy coupling. *Earth and Space Science*. 6(4):565–576. doi:10.1029/2018ea000468.
- Bargatze LF, Baker DN, McPherron RL, Hones EW Jr. 1985. Magnetospheric impulse response for many levels of geomagnetic activity. *J Geophys Res*. 90(A7):6387. doi:10.1029/ja090ia07p06387.
- Baumjohann W. 1982. Ionospheric and field-aligned current systems in the auroral zone: a concise review. *Adv Space Res*. 2(10):55–62. doi:10.1016/0273-1177(82)90363-5.
- Borovsky JE, Valdivia JA. 2018. The earth's magnetosphere: a systems science overview and assessment. *Surveys in Geophysics*. 39(5):817–859. doi:10.1007/s10712-018-9487-x.
- Chang T. 1992. Low-dimensional behavior and symmetry breaking of stochastic systems near criticality—can these effects be observed in space and in the laboratory? *IEEE Trans Plasma Sci*. 20(6):691–694. doi:10.1109/27.199515.
- Chang T. 1999. Self-organized criticality, multi-fractal spectra, sporadic localized reconnections and intermittent turbulence in the magnetotail. *Phys Plasmas*. 6(11):4137–4145. doi:10.1063/1.873678.
- Chapman SC, Watkins NW, Dendy RO, Helander P, Rowlands G. 1998. A simple avalanche model as an analogue for magnetospheric activity. *Geophys Res Lett*. 25(13):2397–2400. doi:10.1029/98gl51700.
- Chen J, Sharma AS. 2006. Modeling and prediction of the magnetospheric dynamics during intense geomagnetic storms. *J Geophys Res*. 111(A4). doi:10.1029/2005ja011359.
- Cliver EW, Kamide Y, Ling AG. 2000. Mountains versus valleys: semiannual variation of geomagnetic activity. *Journal of Geophysical Research: Space Physics*. 105(A2):2413–2424. doi:10.1029/1999ja900439.
- Consolini G (1997). Sandpile cellular automata and magnetospheric dynamics. In Aiello S, et al (Eds.), *Conference Proceedings “Cosmic Physics in the Year 2000”* (Vol. 58, pp. 123–126). SIF, Bologna, Italy.
- Consolini G, Lui ATY. 1999. Sign-singularity analysis of current disruption. *Geophys Res Lett*. 26(12):1673–1676. doi:10.1029/1999gl900355.
- Consolini G, Marcucci MF, Candidi M. 1996. Multifractal structure of auroral electrojet index data. *Phys Rev Lett*. 76(21):4082–4085. doi:10.1103/physrevlett.76.4082.
- Davis TN, Sugiura M. 1966. Auroral electrojet activity index AE and its universal time variations. *J Geophys Res*. 71(3):785–801. doi:10.1029/jz071i003p00785.
- Dobias P, Wanliss JA. 2009. Intermittency of storms and substorms: is it related to the critical behaviour? *Ann Geophys*. 27(5):2011–2018. doi:10.5194/angeo-27-2011-2009.
- Gavrishchaka VV, Ganguli SB. 2001. Optimization of the neural-network geomagnetic model for forecasting large-amplitude substorm events. *Journal of Geophysical Research: Space Physics*. 106(A4):6247–6257. doi:10.1029/2000ja900137.
- Gleisner H, Lundstedt H. 1997. Response of the auroral electrojets to the solar wind modeled with neural networks. *Journal of Geophysical Research: Space Physics*. 102(A7):14269–14278. doi:10.1029/96ja03068.
- Gleisner H, Lundstedt H. 2001. Auroral electrojet predictions with dynamic neural networks. *Journal of Geophysical Research: Space Physics*. 106(A11):24541–24549. doi:10.1029/2001ja900046.
- Goertz CK, Shan L-H, Smith RA. 1993. Prediction of geomagnetic activity. *Journal of Geophysical Research: Space Physics*. 98(A5):7673–7684. doi:10.1029/92ja01193.
- Hernandez JV, Tajima T, Horton W. 1993. Neural net forecasting for geomagnetic activity. *Geophys Res Lett*. 20(23):2707–2710. doi:10.1029/93gl02848.
- Kamide Y, Kokubun S. 1996. Two-component auroral electrojet: importance for substorm studies. *Journal of Geophysical Research: Space Physics*. 101(A6):13027–13046. doi:10.1029/96ja00142.
- Kamide Y, Rostoker G. 2004. What is the physical meaning of the AE index? *Eos, Transactions American Geophysical Union*. 85(19):188. doi:10.1029/2004eo190010.
- King JH, Papitashvili NE. 2005. Solar wind spatial scales in and comparisons of hourly wind and ACE plasma and magnetic field data. *J Geophys Res*. 110(A2). doi:10.1029/2004ja010649.
- Klimas AJ, Baker DN, Roberts DA, Fairfield DH, Büchner J. 1992. A nonlinear dynamical analogue model of geomagnetic activity. *J Geophys Res*. 97(A8):12253. doi:10.1029/92ja00794.

- Klimas AJ, Baker DN, Vassiliadis D, Roberts DA. 1994. Substorm recurrence during steady and variable solar wind driving: evidence for a normal mode in the unloading dynamics of the magnetosphere. *J Geophys Res.* 99 (A8):14855. doi:10.1029/94ja01240.
- Klimas AJ, Valdivia JA, Vassiliadis D, Baker DN, Hesse M, Takalo J. 2000. Self-organized criticality in the substorm phenomenon and its relation to localized reconnection in the magnetospheric plasma sheet. *Journal of Geophysical Research: Space Physics.* 105(A8):18765–18780. doi:10.1029/1999ja000319.
- Li X, Oh KS, Temerin M. 2007. Prediction of the AL index using solar wind parameters. *Journal of Geophysical Research: Space Physics.* 112(A6):n/a–n/a. doi:10.1029/2006ja011918.
- Lu JY, Liu Z-Q, Kabin K, Jing H, Zhao MX, Wang Y. 2013. The IMF dependence of the magnetopause from global MHD simulations. *Journal of Geophysical Research: Space Physics.* 118(6):3113–3125. doi:10.1002/jgra.50324.
- Luo B, Li X, Temerin M, Liu S. 2013. Prediction of the AU, AL, and AE indices using solar wind parameters. *Journal of Geophysical Research: Space Physics.* 118 (12):7683–7694. doi:10.1002/2013ja019188.
- Lyatsky W, Newell PT, Hamza A. 2001. Solar illumination as cause of the equinoctial preference for geomagnetic activity. *Geophys Res Lett.* 28(12):2353–2356. doi:10.1029/2000gl012803.
- McPherron RL, Rostoker G. 1993. Comment on “Prediction of geomagnetic activity” by C. K. Goertz, Lin-Hua Shan, and R. A. Smith. *Journal of Geophysical Research: Space Physics.* 98(A5):7685–7686. doi:10.1029/92ja01194.
- McPherron RL, Russell CT, Aubry MP. 1973. Satellite studies of magnetospheric substorms on August 15, 1968: 9. Phenomenological model for substorms. *J Geophys Res.* 78(16):3131–3149. doi:10.1029/ja078i016p03131.
- Nakamura M, Yoneda A, Oda M, Tsubouchi K. 2015. Statistical analysis of extreme auroral electrojet indices. *Earth, Planets and Space.* 67(1). doi:10.1186/s40623-015-0321-0.
- Nishida A. 2000. The Earth's dynamic magnetotail. *Space Sci Rev.* 91(3/4):507–577. doi:10.1023/A:1005223124330
- Price CP, Newman DE. 2001. Using the R/S statistic to analyze AE data. *J Atmos Sol-Terr Phys.* 63 (13):1387–1397. doi:10.1016/s1364-6826(00)00240-6.
- Pulkkinen A, Klimas A, Vassiliadis D, Uritsky V. 2006. Role of stochastic fluctuations in the magnetosphere-ionosphere system: a stochastic model for the AE index variations. *J Geophys Res.* 111(A10). doi:10.1029/2006ja011661.
- Pulkkinen TI, Tanskanen EI, Viljanen A, Partamies N, Kauristie K. 2011. Auroral electrojets during deep solar minimum at the end of solar cycle 23. *Journal of Geophysical Research: Space Physics.* 116(A4):n/a–n/a. doi:10.1029/2010ja016098.
- Rostoker G. 1972. Geomagnetic indices. *Reviews of Geophysics.* 10(4):935. doi:10.1029/rg010i004p00935.
- Rostoker G (2002), Why we have not yet solved the substorm problem, in Sixth International Conference on Substorms, edited by Winglee RM, pp. 1–8. University of Washington, Seattle.
- Russell CT. 2001. Solar wind and interplanetary magnetic field: a tutorial. In: *Space Weather* (eds P. Song, H. J. Singer and G. L. Siscoe). p. 73–89. doi:10.1029/gm125p0073.
- Russell CT, McPherron RL. 1973. Semiannual variation of geomagnetic activity. *J Geophys Res.* 78(1):92–108. doi:10.1029/ja078i001p00092.
- Sitnov MI, Sharma AS, Papadopoulos K, Vassiliadis D, Valdivia JA, Klimas AJ, Baker DN. 2000. Phase transition-like behavior of the magnetosphere during substorms. *Journal of Geophysical Research: Space Physics.* 105(A6):12955–12974. doi:10.1029/1999ja000279.
- Strangeway RJ. 2013. The relationship between magnetospheric processes and auroral field-aligned current morphology. In: *Geophysical monograph series.* American Geophysical Union; p. 355–364. doi:10.1029/2012gm001211
- Takalo J, Timonen J, Klimas A, Valdivia J, Vassiliadis D. 1999. Nonlinear energy dissipation in a cellular automaton magnetotail field model. *Geophys Res Lett.* 26 (13):1813–1816. doi:10.1029/1999gl900429.
- Temerin M, Li X. 2002. A new model for the prediction of Dst on the basis of the solar wind. *Journal of Geophysical Research: Space Physics.* 107(A12):31–8. doi:10.1029/2001ja007532.
- Temerin, M., & Li, X. 2006. DST model for 1995–2002. *Journal of Geophysical Research.* 111(A4). doi:10.1029/2005ja011257
- Tsurutani BT, Sugiura M, Iyemori T, Goldstein BE, Gonzalez WD, Akasofu SI, Smith EJ. 1990. The nonlinear response of AE to the IMF BSdriver: a spectral break at 5 hours. *Geophys Res Lett.* 17(3):279–282. doi:10.1029/gl017i003p00279.
- Uritsky VM (1996). 1/f-like spectra of geomagnetic fluctuations: expression of self-organized criticality? In *Book of abstracts of the International Conference on Problems of Geocosmos, St. Petersburg (Russia).* June 17–23, (p. 110).
- Uritsky VM, Pudovkin MI. 1998a. Fractal dynamics of AE-index of geomagnetic activity as a marker of the self-organized criticality in the magnetosphere (in Russian). *Geomagnetizm iAeronomia.* 38(3):17–28.
- Uritsky VM, Pudovkin MI. 1998b. Low frequency 1/f-like fluctuations of the AE-index as a possible manifestation of self-organized criticality in the magnetosphere. *Ann Geophys.* 16(12):1580–1588. doi:10.1007/s00585-998-1580-x.
- Uritsky VM, Pudovkin MI, Steen A. 2001. Geomagnetic substorms as perturbed self-organized critical dynamics of the magnetosphere. *Journal of Atmospheric and Solar-Terrestrial Physics.* 63(13):1415–1424. doi:10.1016/S1364-6826(00)00243-1.
- Uritsky VM, Semenov VS. 2000. A sandpile model for global statistics of reconnection events in the magnetotail. In: Biernat HK, Farrugia CJ, Vogl DF, editors. *The solar wind - magnetosphere system* (Vol. 3). Wien: Osterreichische Akademie der Wissenschaften; p. 299–308.
- Vassiliadis D, Angelopoulos V, Baker DN, Klimas AJ. 1996. The relation between the northern polar cap and auroral electrojet geomagnetic indices in the wintertime. *Geophys Res Lett.* 23(20):2781–2784. doi:10.1029/96gl02575.
- Vassiliadis D, Klimas AJ, Baker DN, Roberts DA. 1995. A description of the solar wind-magnetosphere coupling based on nonlinear filters. *Journal of Geophysical Research: Space Physics.* 100(A3):3495–3512. doi:10.1029/94ja02725.



- Vennerstrøm S, Friis-Christensen E, Troshichev OA, Andersen VG. 1991. Comparison between the polar cap index, PC, and the auroral electrojet indices AE, AL, and AU. *J Geophys Res.* 96(A1):101. doi:[10.1029/90ja01975](https://doi.org/10.1029/90ja01975).
- Watkins NW. 2002. Scaling in the space climatology of the auroral indices: is SOC the only possible description? *Nonlinear Process Geophys.* 9(5/6):389–397. doi:[10.5194/npg-9-389-2002](https://doi.org/10.5194/npg-9-389-2002).
- Weigel RS. 2003. Solar wind coupling to and predictability of ground magnetic fields and their time derivatives. *J Geophys Res.* 108(A7). doi:[10.1029/2002ja009627](https://doi.org/10.1029/2002ja009627).
- Woodard R, Newman DE, Sánchez R, Carreras BA. 2005. On the identification of soc dynamics in the sun-earth system. In *Multiscale coupling of sun-earth processes*. Edited by Lui ATY, Kamide Y, Consolini G. p. 55–68. Elsevier Science BV; doi:[10.1016/b978-044451881-1/50005-8](https://doi.org/10.1016/b978-044451881-1/50005-8).

● Cited documents ● Uncited documents



1

0

2018

### NRIAG Journal of Astronomy and Geophysics

Not yet assigned quartile

SJR 2022

0

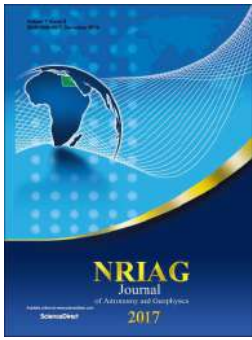


powered by scimagojr.com

← Show this widget in your own website

Just copy the code below and paste within your html code:

```
<a href="https://www.scimagojr.com" data-bbox="796 697 983 757">
```



## A SOC based avalanche model to study the magnetosphere-ionosphere energy transfer and AE index fluctuations

Adrija Banerjee, Amaresh Bej, T. N. Chatterjee & Abhijit Majumdar

To cite this article: Adrija Banerjee, Amaresh Bej, T. N. Chatterjee & Abhijit Majumdar (2021): A SOC based avalanche model to study the magnetosphere-ionosphere energy transfer and AE index fluctuations, NRIAG Journal of Astronomy and Geophysics, DOI: [10.1080/20909977.2021.2005335](https://doi.org/10.1080/20909977.2021.2005335)

To link to this article: <https://doi.org/10.1080/20909977.2021.2005335>



© 2021 The Author(s). Published by Informa UK Limited, trading as Taylor & Francis Group.



Published online: 24 Nov 2021.



Submit your article to this journal [↗](#)



View related articles [↗](#)



View Crossmark data [↗](#)



# A SOC based avalanche model to study the magnetosphere-ionosphere energy transfer and AE index fluctuations

Adrija Banerjee<sup>a</sup>, Amaresh Bej<sup>a</sup>, T. N. Chatterjee<sup>b</sup> and Abhijit Majumdar<sup>a</sup>

<sup>a</sup>Department of Physics, Indian Institute of Engineering Science and Technology, Howrah, India; <sup>b</sup>Department of Electronics, Dinabandhu Andrews College, Kolkata, India

## ABSTRACT

Magnetosphere-ionosphere energy transfer and AE fluctuations are studied using a cellular automata model of terrestrial magnetosphere based on the concept of self-organised criticality (SOC). The model is a SOC-driven dissipative dynamical system with both spatial and temporal degrees of freedom. The input parameter to this model is derived from the real-time values of solar wind ion density and flow speed data. Both the direction and intensity of the real-time values of the  $B_z$  component of the interplanetary magnetic field (IMF) are the factors controlling the energy injection into the system. The model produces an output series which can be regarded as a mathematical representation of the AE index. The spectral response of the simulated output follows a  $1/f^{\beta}$  power law, demonstrates a breakpoint at  $f_0 = 0.050$  mHz (5.5 hours) having slopes  $\beta_A = 2.2-2.4$  for  $f > f_0$  and  $\beta_B = 0.9-1.0$  for  $f < f_0$ , the typical characteristics of the natural AE index. The entire 23<sup>rd</sup> solar cycle had been studied using the model. The parameter  $K_A$  plays a significant role in the entire process.  $K_A$  represents the remaining percentage of the released energy from the previous magnetosphere-ionosphere energy transfer, stored in the ionosphere.

## ARTICLE HISTORY

Received 12 May 2021  
Revised 31 October 2021  
Accepted 8 November 2021

## KEYWORDS

Plasmas; solar wind;  
magnetic reconnection;  
geomagnetic index

## 1. Introduction

Magnetosphere-ionosphere interaction and the subsequent energy transfer is a significant phenomenon in magnetospheric dynamics. During a strong solar wind-magnetosphere coupling, a large amount of solar wind energy enters the geospace. A part of the energy is stored in the magnetotail and another part drives the convection of plasma particles in the magnetosphere. As the solar wind injection continues, the stored energy in the magnetotail reaches an unstable state, triggering magnetic reconnection. A huge amount of energy is released in the ionosphere causing magnetic fluctuations in the auroral zone. The auroral electrojet (AE) index is a global and instantaneous measurement of the auroral zone magnetic activities. The geomagnetic fluctuation in the horizontal component of the Earth's magnetic field  $H$  in the auroral region is measured in 10–13 observatories situated around the auroral zone. For each station, the average value of  $H$  of the five international quietest days of the month is considered as the base value of the measurement. For normalisation of data, the base value is subtracted from each data of the station. Then, all the normalised data from all the stations are plotted and superimposed on each other. The maximum and minimum deviations of  $H$  are termed as Auroral Upper (AU) and Auroral Lower (AL) index, respectively, which form the upper boundary and lower

boundary of the envelope. If there are no disturbances from the distant axially symmetric fields or zonal currents, the AU and AL indices are the direct measurement of the maximum eastward and westward electrojet currents at any time. AE index is defined as the maximum total amplitude of the eastward and westward electrojet currents, that is,  $AE = AU - AL$ . As the AE index is the difference value of AU and AL indices, it is independent of the ionospheric zonal current or distant axially symmetric fields (Davis and Sugiura 1966). AE index is extensively used in aeronomy, solar-terrestrial physics, geomagnetism, and auroral studies.

The physical meaning of the AE index, the nature of the eastward and westward electrojets, the limitations of AU and AL indices have been discussed (Rostoker 1972, 2002; Baumjohann 1982; Kamide and Kokubun 1996; Kamide and Rostoker 2004) along with a detailed study of spatial and temporal distributions of magnetic effects of the electrojets (Allen and Kroehl 1975), statistical analysis (Nakamura et al. 2015) and its relation with the polar cap index (Vennerström et al. 1991; Vassiliadis et al. 1996). It has been also established that the AE index is subject to universal time variation (Davis and Sugiura 1966; Ahn et al. 2000a), seasonal variation (Ahn et al., 2000b; Cliver et al. 2000; Lyatsky et al. 2001; Russell and McPherron 1973; Temerin and Li 2002, 2006),

annual variation (Lyatsky et al. 2001; Pulkkinen et al. 2011), and solar cycle variation (Ahn et al., 2000b). Different dynamical and numerical models have been presented to predict and study auroral electrojets. The analogue model proposed by (Goertz et al. 1993) and reviewed by (McPherron and Rostoker 1993), the Faraday loop model (Klimas et al. 1992, 1994), using linear prediction filter (LPF) technique (Bargatze et al. 1985) which is further modified as local-linear prediction technique by (Vassiliadis et al. 1995), by artificial intelligence (Hernandez et al. 1993; Gleisner and Lundstedt 1997, 2001; Gavrishchaka and Ganguli 2001; Weigel 2003; Chen and Sharma 2006), by stochastic approach (Pulkkinen et al. 2006) and also using solar wind parameters (Li et al. 2007; Luo et al. 2013).

Previously, we studied the characteristic structure of the Dst index, the global measurement of geomagnetic activities in Earth, and realised the series as a positively correlated fractional Brownian motion, displaying long-range correlation (Banerjee et al. 2011). But, we also understood the complexity of the non-linear dynamics of the geomagnetic fluctuations and the difficulties in predicting them. To gain an insight into the magnetospheric dynamics, we focused our study to develop a cellular automata model of terrestrial magnetosphere based on the concept of self-organised criticality and sandpile dynamics. According to the concept, a dissipative, dynamical system with both spatial and temporal degrees of freedom naturally evolved to a self-organised critical state without much specification of the initial conditions. The dynamical behaviour of a pile of sand is the most prominent example of this type of system. Let us start with a grain of sand and continue to add more grains to it, gradually forming a pile. The increment of the slope enhances the characteristic size of the largest avalanches. As a result, the equilibrium state of the sandpile is seriously disturbed. Eventually, when the slope becomes very large, the pile reaches a critical state. Now, adding a single grain of sand further to the pile collapses it. An avalanche of sand is released from the pile, the base area increases, and the system again returns to a state of equilibrium (Bak et al. 1987, 1988).

The concept of self-organised criticality (SOC) and sandpile model can be the basis of an analytical study of magneto-ionospheric dynamics. The solar wind, a stream of energised plasma particles is emitted from the outer atmosphere of the Sun and approaches the Earth. The interplanetary magnetic field (IMF) is trapped in the solar wind. Near the terrestrial space, the solar wind flow speed varies from a minimum of 260 km/sec to a maximum of 750 km/sec while the ion density varies in a much wider range, from  $0.1 \text{ cm}^{-3}$  to  $100 \text{ cm}^{-3}$  (Russell 2001). The density fluctuation is the primary controller of the variations in the dynamic pressure, which further controls the solar wind-

magnetosphere reconnection. When the solar wind interacts with the terrestrial magnetosphere, this supersonic flow creates a standing shock wave or bow shock in the day-side of the magnetosphere and converts it into a subsonic flow. Majority of the energised solar wind plasma particles is heated and then get deflected around the Earth at the bow shock. The day-side magnetosphere is compressed down while the night-side magnetosphere is stretched up to about 100 Earth radii comprising the magnetotail (Nishida 2000; Borovsky and Valdivia 2018). The trapped interplanetary magnetic field (IMF) plays a crucial role in controlling the intensity and duration of solar wind-magnetosphere coupling. For a northward IMF  $B_z$ , the cusp shifts away from the equatorial region and further narrows down with the increasing intensity of  $B_z$ , decreasing the amount of energy injection into the magnetosphere. But, for a southward IMF  $B_z$ , the cusp shifts towards the equatorial region and widens out gradually as the intensity of  $B_z$  increases, triggering an injection of a large amount of solar wind energy into the magnetosphere (Lu et al. 2013). The magnetotail becomes a reservoir of this energy. As the solar wind injection continues, the magnetotail grows further by accumulating more and more energy. Eventually, the magnetotail growth reaches a critical point, becomes unstable and magnetic reconnection occurs in the tail. A part of the stored energy is released through flow kinetic energy and plasma heating, producing substorm (Borovsky and Valdivia 2018). Substorm originates deep in the magnetosphere, near the geostationary orbit (Antonova and Ganushkina 2000). It is a short but intense earthward convection of magnetic flux in the magnetotail which injects energised particles in the dipolar region, also substantially increasing the auroral electrojets (McPherron et al. 1973). The Joule energy extracted from the magnetosphere is dissipated in the ionosphere through auroral electrojets, the field-aligned currents flowing between the nightside magnetosphere and nightside ionosphere (Strangeway 2013). The subsequent magnetic fluctuations in the auroral region are measured by the AE index.

SOC has long been proposed as a possible explanation of magnetospheric dynamics. Sandpile model was selected as the first example displaying the concept of self-organised criticality, introduced by Bak et al. in their 1987 and 1988 papers. Since then, the application of this theory has produced numerous significant analyses of magnetospheric activities by some eminent researchers. Consolini observed SOC-triggered behaviour in the power spectral density and burst size distribution of the AE index (Consolini 1997). Using the sign-singularity analysis, magnetic field fluctuations in the near-tail regions were investigated based on the concept of self-organised criticality and 2nd-order phase transition (Consolini and Lui 1999).

Chapman et al. presented a sandpile cellular automaton model to study magnetospheric dynamics (Chapman et al. 1998) and Klimas presented a first-order physical model of plasma sheet (Klimas et al. 2000). Further studies on modelling continued based on the SOC approach with interesting conclusions (Takalo et al. 1999; Uritsky and Semenov 2000). Other notable works discussed in detail the distinctive features of SOC-driven instabilities and their effects in the context of nonlinear dynamics of magnetosphere (Chang 1992, 1999; Uritsky 1996; Uritsky and Pudovkin 1998a; Sitnov et al. 2000). (Dobias and Wanliss 2009) suggested that both the storm and sub-storm characteristics are consistent with the behaviour of the critical system and follow the fractal point process (FPP).

(Uritsky and Pudovkin 1998b) developed a two-dimensional sandpile model of the magnetosphere current sheet to study the AE fluctuations. The model was a rectangular matrix of  $x$  and  $y$  dimensions. Each element of the matrix was characterised by an amount of energy. Also, a critical threshold of energy was assigned to all of the elements to determine the stability of the element after each energy injection. They investigated the avalanche formations, energy redistribution, and plasma sheet instabilities of the SOC-driven system in reaction to external disturbances. It was suggested that the spatially localised magnetotail instabilities can be regarded as SOC avalanches and the superposition of these avalanches of different sizes finally produces the characteristic low-frequency  $1/f$ -like fluctuations of the AE index (Uritsky and Pudovkin 1998b). Uritsky et al. continued the study of the above two-dimensional sandpile model in their 2001 paper to explain geomagnetic substorms as a self-organised critical dynamic of the perturbed magnetosphere. In their study, the total accumulated energy in the system, as well as the energy dissipated from the system, were revealed to be the two major factors controlling the overall dynamics of the system. Moreover, the spectral characteristics of the model output showed striking similarities with the natural AE fluctuations (Uritsky et al. 2001).

Based on the model (Uritsky et al. 2001), we developed a sandpile-like cellular automata model of Earth's magnetosphere in our previous paper (Banerjee et al. 2015). The model is a SOC-driven dissipative dynamical system with both spatial and temporal degrees of freedom. It is a two-dimensional array of finite dimensions and is characterised by energy  $E$ . The input energy to this model is derived from the real-time value of solar ion density and flow speed data. Both the direction and intensity of the real-time value of the  $B_Z$  component of the interplanetary magnetic field (IMF) are the factors controlling the amount of solar wind energy injected into the system at any time. The total accumulated energy of the

system is estimated to produce a simulated output representing the Dst index. The spectral characteristics of the simulated output closely follow the natural Dst index, establishing the acceptability of the model (Banerjee et al. 2015). We continued our study with the model investigating the solar wind-magnetosphere interaction, the injection of plasma particles, and the aspects of internal magnetospheric dynamics as a subsequent effect (Banerjee et al. 2019).

In the present paper, we extend our sandpile-like cellular automata model to study the dynamical behaviour of the auroral zone magnetic activities by focusing on the transferred energy from the system. The model, a representation of the Earth's magnetosphere, is a lattice of  $n \times n$  elements, having spatial and temporal degrees of freedom. Each element is characterised by an energy  $E$ , which is analogous to the slope of the sandpile. The input to the model is solar wind energy, derived from the real-time value of solar ion density and flow speed data. The input energy is injected into the system through a set of elements, representing the cusp. Both the direction and intensity of IMF  $B_Z$  are the factors controlling the width of the cusp, hence the amount of energy injection into the system. The injected energy is altering the potential energy of the elements of the lattice. Each element has a critical value of energy, known as the excitation threshold. As the energy injection continues, the energy gradually piles up in the elements, similar to the storing of energy in the magnetotail. If the energy of any element reaches the point of criticality by exceeding the excitation threshold, spatially localised instabilities are formed, representing the instability formation in the magnetotail. The pile collapses by releasing avalanches of energy in various sizes and shapes. The released energy is distributed among the adjacent elements and the process continues, gradually spreading throughout the lattice. The excess energy reaching the upper or lower margins is transmitted outside the lattice, representing the magnetosphere-ionosphere energy transfer. The amount of transferred energy at any time  $t$  is estimated. By some numerical calculations, an output time series is produced from this estimated energy. The simulated output can be regarded as a mathematical representation of the AE index. It is observed that the simulated series exhibits  $1/f^\beta$ -like power spectrum. The power-law exponents  $\beta_A$  and  $\beta_B$  of the power spectral density of the simulated output are evaluated for both the high- and low-frequency regions respectively for all the years of the entire 23<sup>rd</sup> solar cycle. Finally, by comparing the values of  $\beta_A$  and  $\beta_B$  with that of the real-time AE index, it is observed that the simulated output closely follows the natural AE fluctuations depending on the exact value of the parameter  $K_A$ .  $K_A$  represents the remaining percentage of the

transferred energy of the previous magnetosphere-ionosphere energy transfer, stored in the ionosphere. In our previous work (Banerjee et al. 2019), the real-time solar wind and IMF  $B_Z$  data of the 23<sup>rd</sup> solar cycle were used as the input to the model to investigate the solar wind-magnetosphere energy transfer. As we are continuing our study on the model, in the present work, we used the same input dataset to analyse the magnetosphere-ionosphere energy transfer.

## 2. Method and data

The cellular automata-based sandpile model used here is an extension of the model presented in our previous papers (Banerjee et al. 2015, 2019) which is in turn based on the model presented by (Uritsky et al. 2001). The model, representation of the Earth's magnetosphere, is a finite matrix of  $n \times n$  elements having spatial and temporal degrees of freedom. Each element is characterised by an energy  $E$ , which is analogous to the slope of the sandpile.  $E$  has an arbitrary unit. The threshold value of energy for each element is indicated as  $E_{TH}$ , the excitation threshold (Uritsky et al. 2001). The input to the model is solar wind energy.

The input energy  $dE$  is estimated using the real-time ion density and flow speed data obeying the equation (Banerjee et al. 2015, 2019)

$$dE = \text{norm} \left( \frac{1}{2} \times \text{ion density} \times \text{flow speed}^2 \right) \quad (1)$$

As the solar wind flows towards the Earth, it interacts with the magnetosphere. Depending on the intensity and direction of IMF  $B_Z$ , a part of the solar wind energy is injected into the magnetosphere through the cusp while the major part of the solar wind energy is deflected at the bow shock and flows across the Earth. A small fraction of this deflected energy penetrates into the magnetosphere. In this model, the factor  $K$  represents this small fractional value. Thus, all the elements of the lattice are credited with the energy  $K \times dE$  at every initial stage. This alters the potential energy of each element as (Banerjee et al. 2015, 2019)

$$E_{t+1}(i, j) = E_t(i, j) + K \times dE, \text{ for all } i \text{ and } j \quad (2)$$

As the two-dimensional lattice is analogical to the terrestrial magnetosphere, the cusp width  $W_C$  in the model is a set of selected elements including and surrounding the centre one, the element at  $i = n/2$ ,  $j = n/2$ . The number of elements in the set, that is, the size of the cusp width  $W_C$  is controlled by both the direction and intensity of IMF  $B_Z$ , following the equations (Banerjee et al. 2015):

$$W_C = [(2 \times w) + 1]^2 \quad (3)$$

where

$$w = (K_d \times B_Z) \text{ for southward } B_Z \quad (4)$$

and

$$w = [K_d \times (B_{Z_{\max}} - B_Z)] \text{ for northward } B_Z \quad (5)$$

Here  $B_{Z_{\max}}$  is the maximum value of northward  $B_Z$  and  $K_d$  is the associated proportionality factor.  $K_d$  is a function of the direction of the IMF  $B_Z$ . As the energy injection increases for southward  $B_Z$  and decreases for northward  $B_Z$ , the numerical value of  $K_d$  is higher for the southward direction than that of the northward direction.

During a solar wind-magnetosphere coupling, the solar wind energy  $dE$  is injected into the system through the cusp width  $W_C$  following the relation (Uritsky et al. 2001; Banerjee et al. 2015, 2019),

$$E_{t+1}(i, j) = [E_t(i, j) + dE] \text{ for } i = \left(\frac{n}{2} \pm w\right) \text{ and } j = \left(\frac{n}{2} \pm w\right) \quad (6)$$

The threshold value of energy for each element is indicated as  $E_{TH}$ , the excitation threshold. After the energy injection, if  $E(i, j) < E_{TH}$ , the element is stable. If  $E(i, j) > E_{TH}$ , the element is unstable and releases four units of energy to return to a stable state. The released energy is distributed among its four adjacent neighbours according to the following equations (Uritsky et al. 2001; Banerjee et al. 2015, 2019),

$$E_{t+1}(i, j) = E_t(i, j) - 4 \quad (7)$$

A small value of energy  $E_d$  is dissipated during the distribution process. The energy of the adjacent elements alters as (Uritsky et al. 2001; Banerjee et al. 2015, 2019)

$$E_{t+1}(i \pm 1, j \pm 1) = E_t(i \pm 1, j \pm 1) + \left(1 - \frac{E_d}{4}\right) \quad (8)$$

Figure 1 illustrates the energy transfer process in a two-dimensional lattice. The unstable elements [ $E(i, j) > E_{TH}$ ] are marked with black shade, the stable elements [ $E(i, j) < E_{TH}$ ] with grey shade, and the elements with zero or negligible energy with white shade. Initially, all the elements of the lattice have zero energy. The input energy is injected into the system through the cusp  $W_C$  altering its energy above  $E_{TH}$ , as shown in Figure 1(a). Thus, the centre element is in black shade. The cusp  $W_C$  here consists of only one element, the element at the centre of the lattice ( $i = n/2$ ,  $j = n/2$ ). In the next Figure 1(b), the unstable element distributes four units of its energy to its four adjacent neighbours. Two of the neighbouring elements, marked in black shade became unstable, receiving the excess energy. In the final Figure 1(c), the two unstable elements further distribute their energy to return to stability. This way, the injected energy is distributed and redistributed throughout the lattice.

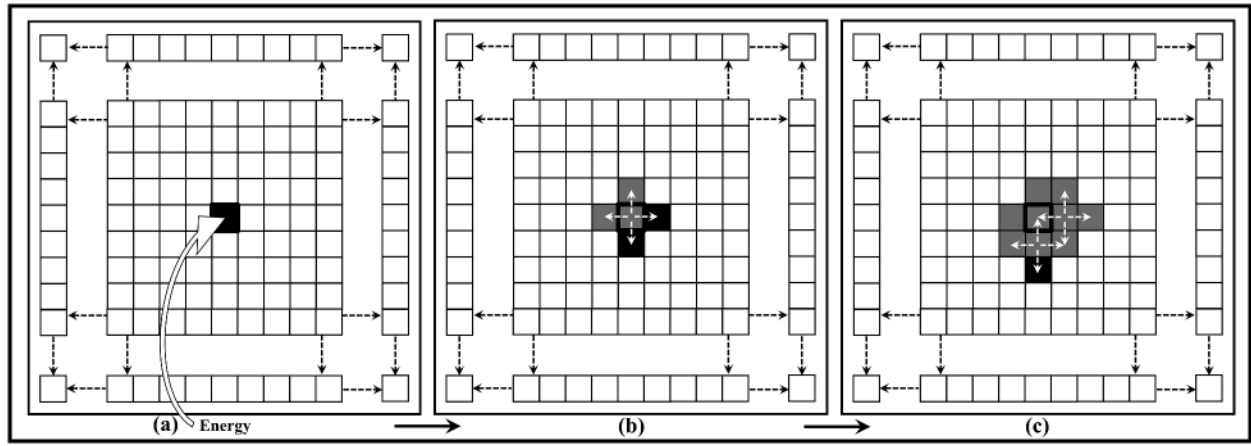


**Figure 1.** The energy distribution in a two-dimensional lattice. The unstable elements  $[E(i, j) > E_{TH}]$  are marked with black shade, the stable elements  $[E(i, j) < E_{TH}]$  with grey shade, and the elements with zero or negligible energy with white shade. Initially, all the elements of the lattice have zero energy. (a) The input energy is injected into the system through the cusp  $W_C$  altering its energy above  $E_{TH}$ . The cusp  $W_C$  here consists of only one element, the element at the centre of the lattice ( $i = n/2, j = n/2$ ). (b) The unstable element distributes four units of its energy to its four adjacent neighbours. Two of the neighbouring elements became unstable. (c) The two unstable elements further distribute their energy to return to stability. This way, the injected energy is distributed and redistributed throughout the lattice.

With analogy to the Earth, the system is spherical, meaning the elements belonging to the columns  $j = n$  and  $j = 1$  are adjacent neighbours. If the energy of any element belonging to the column  $j = n$  has crossed the threshold, one unit of its surplus energy is distributed to its neighbour element in column  $j = 1$  and vice versa. The dissipation of energy through the marginal grids is only applicable for the upper and lower marginal rows, not for the marginal left or marginal right columns. Open boundary condition has been considered for the marginal rows of the lattice. After a consecutive distribution and redistribution, when the released energy finally reaches the marginal upper [ $i = 1, j = (1 \text{ to } n)$ ] and lower [ $i = n, j = (1 \text{ to } n)$ ] grids, it transmits outside the system.

Figure 2 displays the state of the elements of the lattice after a consecutive energy injection, distribution, and redistribution. All the elements have a considerable amount of energy while some of them become unstable. In Figure 2(a), in the marginal rows, two of the elements are unstable in both the upper and lower grids. In the next Figure 2(b), the unstable elements in the marginal rows dissipate their excess energy and a part of this energy is released outside the lattice, representing the magnetosphere-ionosphere energy transfer.

After the consecutive distribution and redistribution, the total internal accumulated energy of the lattice at any time  $t$  can be calculated as (Uritsky et al. 2001; Banerjee et al. 2015, 2019)

$$E_{\text{Total}} = \sum E(i, j) \text{ for all } i \text{ and } j \quad (9)$$

The number of unstable states, that is, elements having energy  $E > E_{TH}$  at any time  $t$  is estimated by the relation (Uritsky et al. 2001)

$$S_{UN} = \sum S_{ij} \text{ for all } i \text{ and } j \quad (10)$$

where  $S_{ij} = 1$  if  $E > E_{TH}$  and  $S_{ij} = 0$  if  $E < E_{TH}$

The upper and the lower grids can be considered as the northern and southern polar cusps of the Earth while the energy transfer process is similar to magnetosphere-ionosphere energy coupling. In the actual measurement of the AE index, all the magnetometer stations are located in the northern hemisphere for recording the associated data. Following this instance, we too considered and based our calculations on the total excess energy dissipating only through the upper grid [ $i = 1, j = (1 \text{ to } n)$ ] of the lattice. We denote  $T_R$  as the time delay between the initial energy injection to the model and the beginning of the energy transfer through the upper marginal grid.  $T_R$  estimates the total time for the energy to reach the boundary after successive distribution and redistribution processes for each input injection. The total amount of released energy outside the lattice at any time  $t$  can be estimated as (Banerjee et al. 2019)

$$E_R = \sum E(i, j) \text{ for } i = 1, j = (1 \text{ to } n) \quad (11)$$

The released energy generates two currents,  $I_W$  and  $I_E$ , the numerical equivalents of the auroral westward and eastward currents in the ionosphere, respectively. The auroral electrojet is estimated as the difference value of these two currents. For the calculation of electrojets, we considered the dissipated energy from any element belonging to the odd columns, that is,  $j = 1, 3, 5, \dots, (n-1)$  are contributing to the westward electrojet while the energy from any element belonging to the even columns, that is,  $j = 2, 4, 6, \dots, n$  are contributing to the eastward electrojet. Thus, mathematically



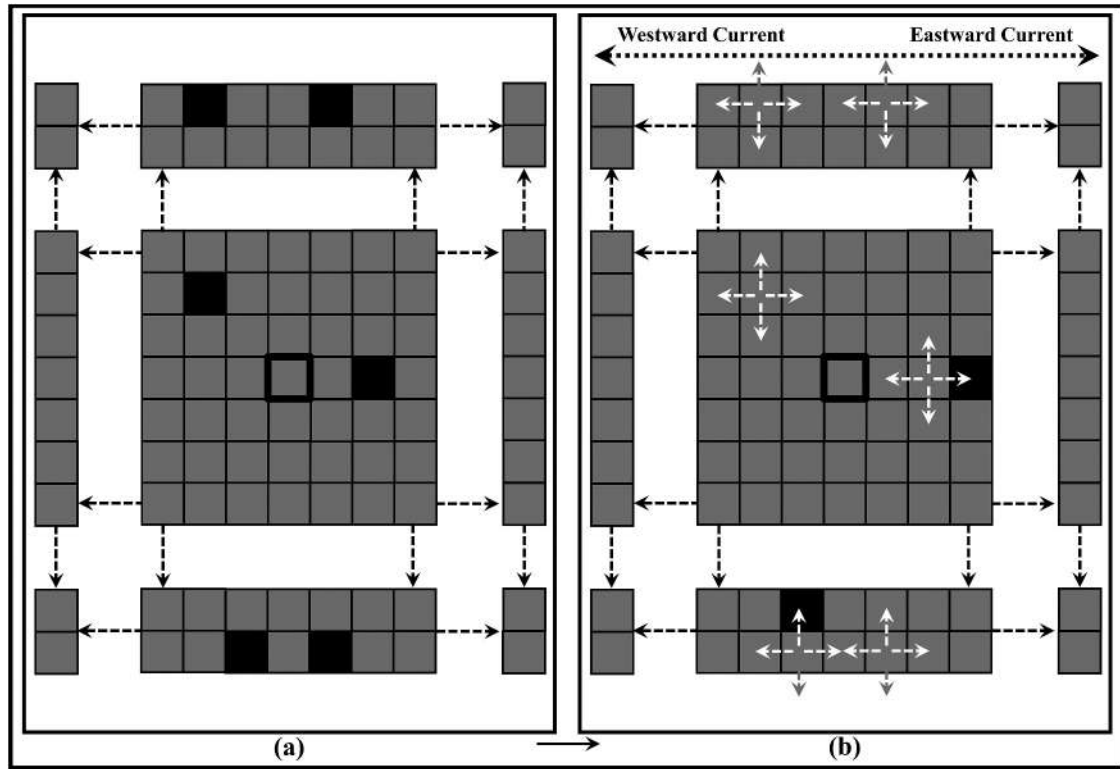


**Figure 2.** The state of the elements of the lattice after a consecutive energy injection, distribution, and redistribution. The unstable elements  $[E(i, j) > E_{TH}]$  are marked with black shade, the stable elements  $[E(i, j) < E_{TH}]$  with grey shade and the elements. All the elements have a considerable amount of energy while some of them become unstable. (a) In the marginal rows, two of the elements are unstable in both the upper and lower grids. (b) The unstable elements in the marginal rows dissipate their excess energy and a part of this energy is released outside the lattice, representing the magnetosphere-ionosphere energy transfer.

$$E_w(t) = \sum E(i, j) \text{ for } i = 1, j = 1, 3, 5, \dots, (n-1) \quad (12)$$

and

$$E_e(t) = \sum E(i, j) \text{ for } i = 1, j = 2, 4, 6, \dots, n \quad (13)$$

As the distribution process continues, more and more excess energy piles up outside the boundary regions of the lattice. The series  $E_w(t)$  and  $E_e(t)$  are the estimations of the total accumulated energy released in the ionosphere responsible for the westward and eastward electrojet currents, respectively. The released energy takes time to completely dissipate through the current system in the ionosphere and a part of this energy remains stored in the ionosphere. During the next magnetosphere-ionosphere energy transfer, this stored energy from the previous transfer acts as a base value and adds up with the newly released value of energy. Here, we introduce a parameter, namely  $K_A$  which determines the remaining part of the released energy of the previous transfer, stored in the ionosphere.  $K_A$  has a fractional value.

The remaining energy in the westward region is

$$E_{rw}(t) = K_A \times E_w(t-1) \quad (14)$$

whereas the remaining energy in the eastward region is

$$E_{re}(t) = K_A \times E_e(t-1) \quad (15)$$

Mathematically, the total westward energy at any time  $t$  is

$$E_{tw} = \sum [E_w(t) + E_{rw}(t)] \text{ for all } t \quad (16)$$

and the total eastward energy at any time  $t$  is

$$E_{te} = \sum [E_e(t) + E_{re}(t)] \text{ for all } t \quad (17)$$

These two energy components,  $E_{tw}(t)$  and  $E_{te}(t)$  then drive two currents in the opposite direction throughout the auroral region, namely the westward electrojet current and the eastward electrojet current, respectively.

The maximum westward electrojet current can be considered as

$$I_W = \sqrt{E_{tw}} \quad (18)$$

and the maximum eastward electrojet current as

$$I_E = \sqrt{E_{te}} \quad (19)$$

The differential value of these two components is

$$E_N = \text{abs}(I_E - I_W) \quad (20)$$

For further refinement,  $E_N$  is processed by a filter and labelled as  $E_A$ . Finally, the output time-series  $E_A$  can be regarded as a numerical representation of the natural auroral electrojet index, AE.

For our analysis, we used the hourly averaged AE index, solar wind ion density, flow speed, and  $B_Z$  component of the interplanetary magnetic field (IMF) data from the year 1997 to the year 2007 of the 23<sup>rd</sup> solar cycle. The dimension of the lattice is  $50 \times 50$ . Similar to our original study of the model (Banerjee et al. 2015), the numerical value of the various variables of the model are taken as  $K = 0.0025$ , local dissipation term  $E_d = 0.05$ ,  $K_d = 0.5$  for southward direction, and  $K_d = 0.005$  for northward direction. The input to the model is estimated using equation 1.

### 2.1. Data source

Here we used the hourly averaged AE index, solar wind ion density, flow speed, and  $B_Z$  component of the interplanetary magnetic field (IMF) data from the year 1997 to the year 2007 of the 23<sup>rd</sup> solar cycle as extracted from NASA/GSFC's OMNI data set through OMNIWeb. The OMNI data were obtained from the GSFC/SPDF OMNIWeb interface at <http://omniweb.gsfc.nasa.gov> (King & Papitashvili 2005).

### 3. Result and discussions

The threshold excitation  $E_{TH}$  is crucial for the central characteristics of a SOC system as it allows the existence of multiple metastable states across which the avalanches are carried out throughout the system. The potential energy  $E$  of any element in the lattice is analogical to the slope of an actual sandpile. An unstable element having energy  $E(i, j) > E_{TH}$  releases four units of energy to return to stability. Thus, a minimum value of  $E_{TH} = 5$  is required to keep the potential energy of the element at a positive non-zero value and to avoid the total internal energy of the system reaching zero or negative energy states at any time. To analyse the dynamical behaviour of the

system, the model is subjected to three different  $E_{TH}$  values,  $E_{TH} = 5$ ,  $E_{TH} = 7$ , and  $E_{TH} = 9$ . After the energy injection and distribution, the total accumulated internal energy of the lattice,  $E_{Total}$ , the total number of unstable states,  $S_{UN}$ , and the total amount of released energy,  $E_R$  at any time  $t$  can be calculated according to Equations 9, 10, and 11 respectively. Figure 3 illustrates the time vs.  $E_{Total}$  plot for the three values of  $E_{TH}$  for the year 2002. As the threshold value increases, the rate of energy distribution and dissipation decreases while the total internal energy of the system continues to increase gradually. It takes much more time for the system to achieve a meta-stable state, delaying the SOC dynamics and avalanches throughout the lattice to form properly. As the rate of distribution reduces, the elements in the marginal grids start to store and release energy to the outside of the lattice far more lately, thus delaying the energy transfer process representing the magnetosphere-ionosphere energy coupling in the model. We denote  $T_R$  as the time delay between the initial energy injection to the model and the beginning of energy transfer through the upper marginal grid. It is observed from the analysis, that the value of  $T_R$  is  $T_R = 1434$  hours for  $E_{TH} = 5$ ,  $T_R = 1934$  hours for  $E_{TH} = 7$  and  $T_R = 2520$  hours for  $E_{TH} = 9$ . Thus, for further analysis of the system, we considered  $E_{TH} = 5$  as the value for the excitation threshold. Figure 5(b), the plot for the simulated time-series  $E_A$ , shows the estimation of  $E_A$  initiating from the value of  $T_R = 1434$  hours for  $E_{TH} = 5$  as from this value of  $T_R$  the marginal grid starts to release energy outside the system.

Figure 4 demonstrates the plots for  $dE$ ,  $E_{Total}$ ,  $S_{UN}$ , and  $E_R$  for the September–October period of the year 2002. As seen from the figure,  $dE$  has large values for the marked timeline. The injected energy piles up in the lattice increasing the number of unstable states  $S_{UN}$ , the total energy of the lattice,  $E_{Total}$ , reaches a critical point and then gradually returns to

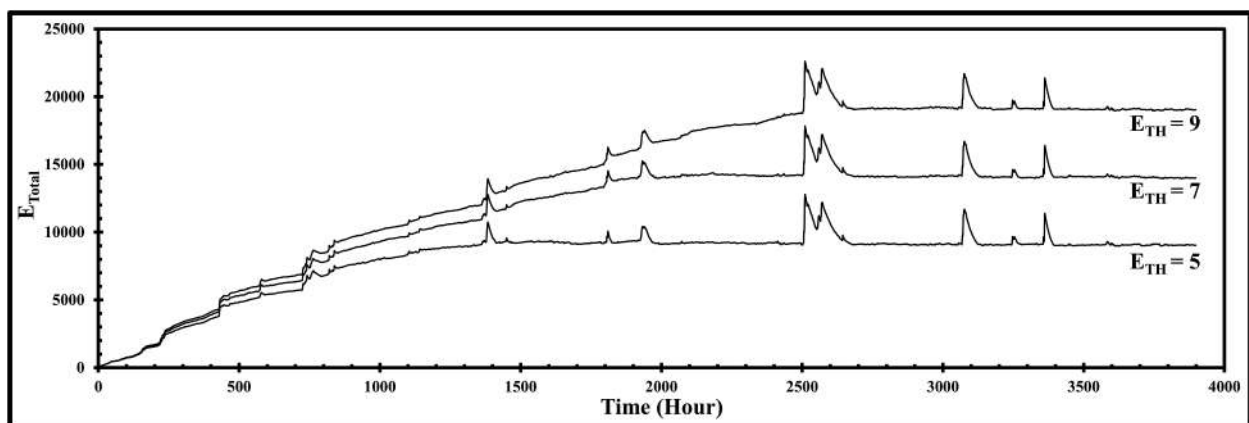


**Figure 3.** Time vs.  $E_{Total}$  plot for the three values of  $E_{TH}$  for the year 2002. As the threshold value increases, the rate of energy distribution and dissipation decreases while the total internal energy of the system continues to increase gradually. It takes much more time for the system to achieve a meta-stable state.

a metastable state by releasing a burst of avalanches. The avalanches take a time to reach the upper marginal grid through successive distribution and redistribution processes, thus  $E_R$  shows high-energy values dissipating from the upper grid after a while.

After the injection of the energy followed by subsequent distribution and redistribution, the model output  $E_A$  is generated estimating the released energy outside the lattice as discussed in the method section. The output series  $E_A$  is the numerical representation of the natural AE index. The power spectral density (PSD) of the simulated output  $E_A$  is calculated and plotted in a log–log graph. The plot demonstrates the characteristic  $1/f^\beta$  behaviour of the natural AE fluctuations along with the spectral break at  $f_0$ . A detailed study of the plot revealed the value of breakpoint  $f_0$  as  $f_0 = 0.050$  mHz (5.5 hours), as shown in Figure 7(b). A power law is fitted separately in both the high ( $f > f_0$ ) and low frequency ( $f < f_0$ ) regions of the plot to determine the power-law coefficients (slope of the spectral response)  $\beta_A$  and  $\beta_B$ , respectively. Now keeping the other parameter constant, if the value of  $K_A$  is varied in the range of 0.10 to 1.00, the  $\beta$  values also vary within ranges. As, for a particular value of  $K_A$ , the

$\beta$  values of the simulated series closely match with that of the natural AE index, they are noted down along with the value of  $K_A$ , as shown in Table 1. The  $\beta$  values of the real-time AE index are also displayed in Table 1 for a comparative study.

Figure 5(a,b) are the time series of the natural AE index and the simulated  $E_A$  series of the year 2002, respectively. For comparative purposes, a magnified portion of the natural AE index and that of the simulated  $E_A$  series of the year 2002 are displayed in Figure 6(a, b), respectively. The real-time AE index is estimated as the difference value of AU and AL indices where the AU and AL indices are the direct measurements of the maximum eastward and westward electrojet currents. (Ahn et al., 2000b) studied the variation pattern of the yearly mean AL index and AU index for 20 years and suggested their absolute values are proportional to each other. The maximum is observed for the AU index in summer while for the AL index, it is in equinoctial months. Both the indices exhibit higher values in the descending phase of the solar cycle (Ahn et al., 2000b). In the current model, the simulated AE index is estimated following the same relation as the difference value between the maximum eastward and

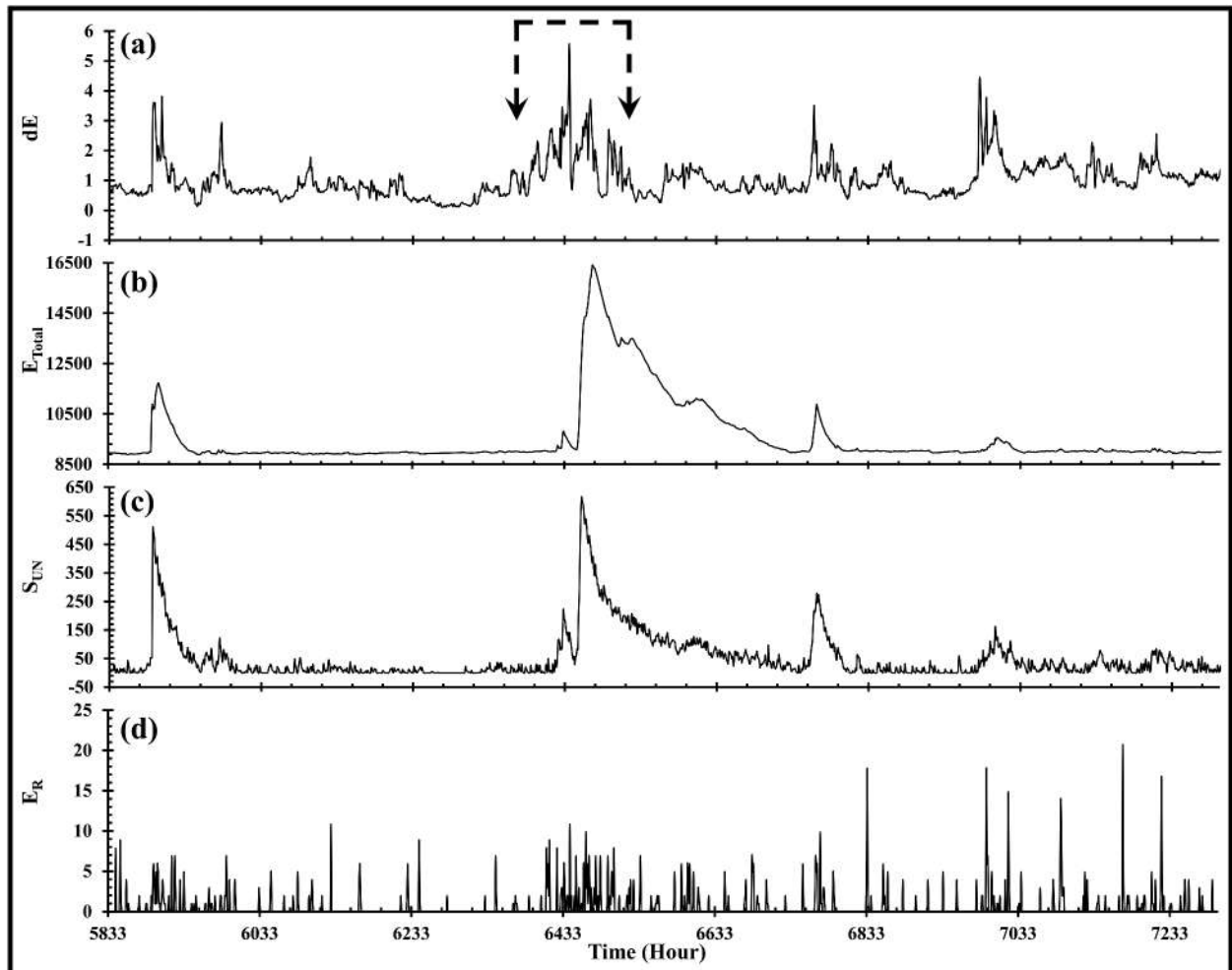


**Figure 4.** Plots for the September–October period of the year 2002 (a) Input energy,  $dE$  (b) the total accumulated internal energy of the lattice,  $E_{Total}$  (c) the total number of unstable states,  $S_{UN}$ , and (d) the total amount of released energy,  $E_R$ .

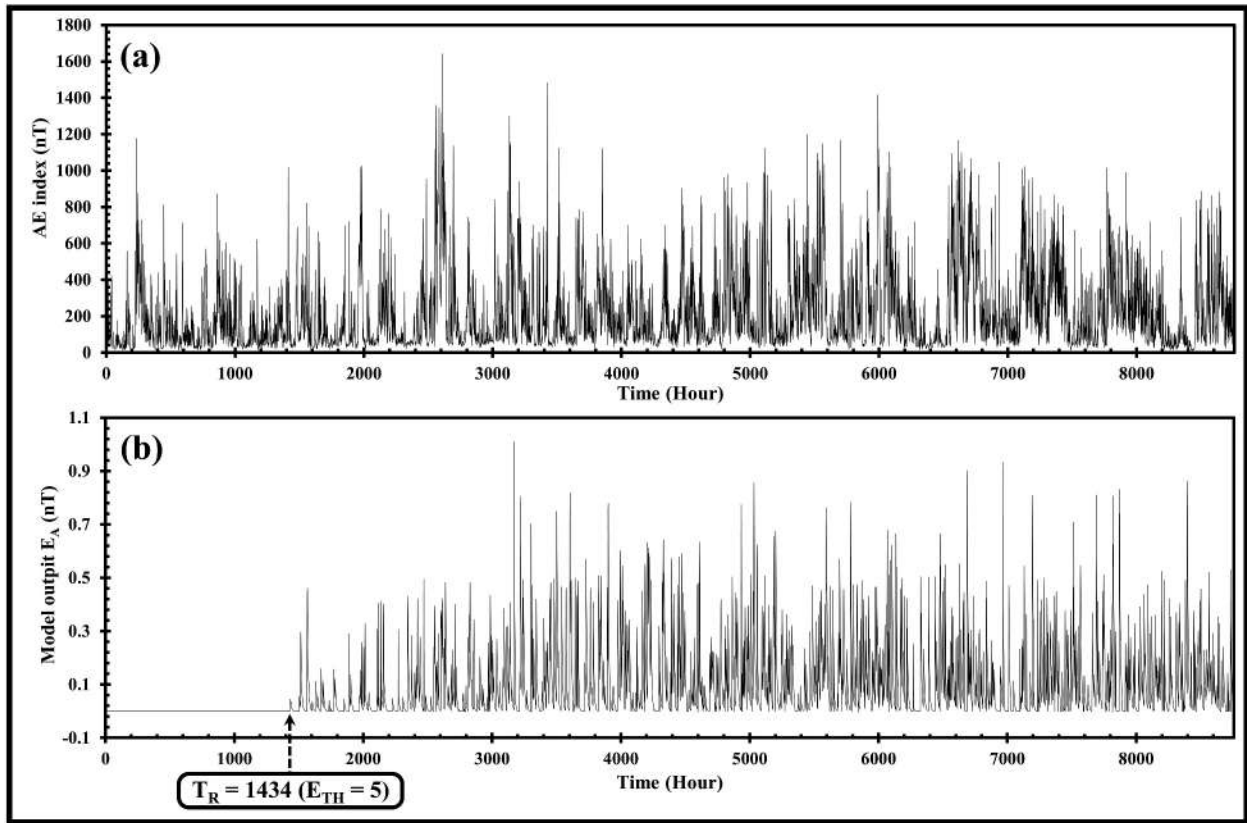


**Figure 5.** (a) The time-series of the natural AE index of the year 2002 (b) The simulated model output time-series,  $E_A$  of the year 2002.  $T_R = 1434$  hours for  $E_{TH} = 5$  is the time delay between the initial energy injection to the model and the starting of energy transfer through the upper marginal grid.

**Table 1.** The power-law coefficients (slope of the spectral response) of the power spectral density associated with the real-time AE index and the simulated model output  $E_A$  for all the years of the 23<sup>rd</sup> solar cycle. The spectral break is at  $f_0 = 0.050$  mHz (5.5 hours).  $\beta_A$  denotes the value of the slope for  $f > f_0$  and  $\beta_B$  denotes the value of the slope for  $f < f_0$ . The parameter  $K_A$  is associated with the series  $E_A$  and shows different values for different years.

Year	Real-Time AE Index Series		$K_A$	Model Output $E_A$ Series	
	$\beta_A$	$\beta_B$		$\beta_A$	$\beta_B$
1997	$2.366 \pm 0.103$	$1.009 \pm 0.046$	0.82	$2.389 \pm 0.126$	$0.945 \pm 0.068$
1998	$2.464 \pm 0.111$	$1.066 \pm 0.046$	0.70	$2.229 \pm 0.105$	$0.961 \pm 0.062$
1999	$2.383 \pm 0.104$	$0.933 \pm 0.043$	0.70	$2.359 \pm 0.125$	$0.950 \pm 0.063$
2000	$2.130 \pm 0.101$	$1.007 \pm 0.046$	0.74	$2.325 \pm 0.102$	$0.963 \pm 0.057$
2001	$2.276 \pm 0.102$	$1.035 \pm 0.043$	0.70	$2.282 \pm 0.115$	$1.023 \pm 0.065$
2002	$2.170 \pm 0.109$	$0.985 \pm 0.045$	0.73	$2.372 \pm 0.120$	$0.955 \pm 0.065$
2003	$2.060 \pm 0.100$	$0.914 \pm 0.043$	0.68	$2.248 \pm 0.128$	$0.964 \pm 0.067$
2004	$2.285 \pm 0.109$	$0.979 \pm 0.044$	0.74	$2.210 \pm 0.128$	$0.985 \pm 0.065$
2005	$2.218 \pm 0.108$	$0.990 \pm 0.043$	0.72	$2.222 \pm 0.125$	$0.962 \pm 0.065$
2006	$2.499 \pm 0.107$	$1.006 \pm 0.044$	0.77	$2.226 \pm 0.123$	$0.962 \pm 0.069$
2007	$2.183 \pm 0.103$	$0.902 \pm 0.043$	0.78	$2.352 \pm 0.112$	$0.953 \pm 0.067$

westward electrojets. In Figure 5, the May–June summer months of the year 2002 is the period for about the time, Time = 2800 hours – 4200 hours. As can be seen from Figure 5(a), the values of the real-time AE index are in the higher ranges for these months. The simulated series in Figure 5(b) also demonstrates the same. Again, in Figure 5, the period of about the time, Time = 5800 hours – 6600 hours marks the equinoctial month of September. Here, also the values of the simulated series of Figure 5(b) show higher values, similarly to the real-time AE index, as shown in Figure 5(a).

Figure 7(a, b) illustrate the log–log plot of the PSD of the real-time AE index and the simulated  $E_A$  series of the year 2002, respectively. It is observed from the plots that the simulated  $E_A$  series exhibits the characteristic  $1/f^\beta$  behaviour of the natural AE fluctuations along with the spectral break at  $f_0$ . As can be seen from Figure 7(b), for the value of  $K_A = 0.73$ , the simulated series has values  $\beta_A = -2.372 \pm 0.120$  and  $\beta_B = -0.955 \pm 0.065$  which nearly matches the values  $\beta_A = -2.170 \pm 0.109$  and  $\beta_B = -0.985 \pm 0.045$  of the natural AE fluctuations. The spectral point and the

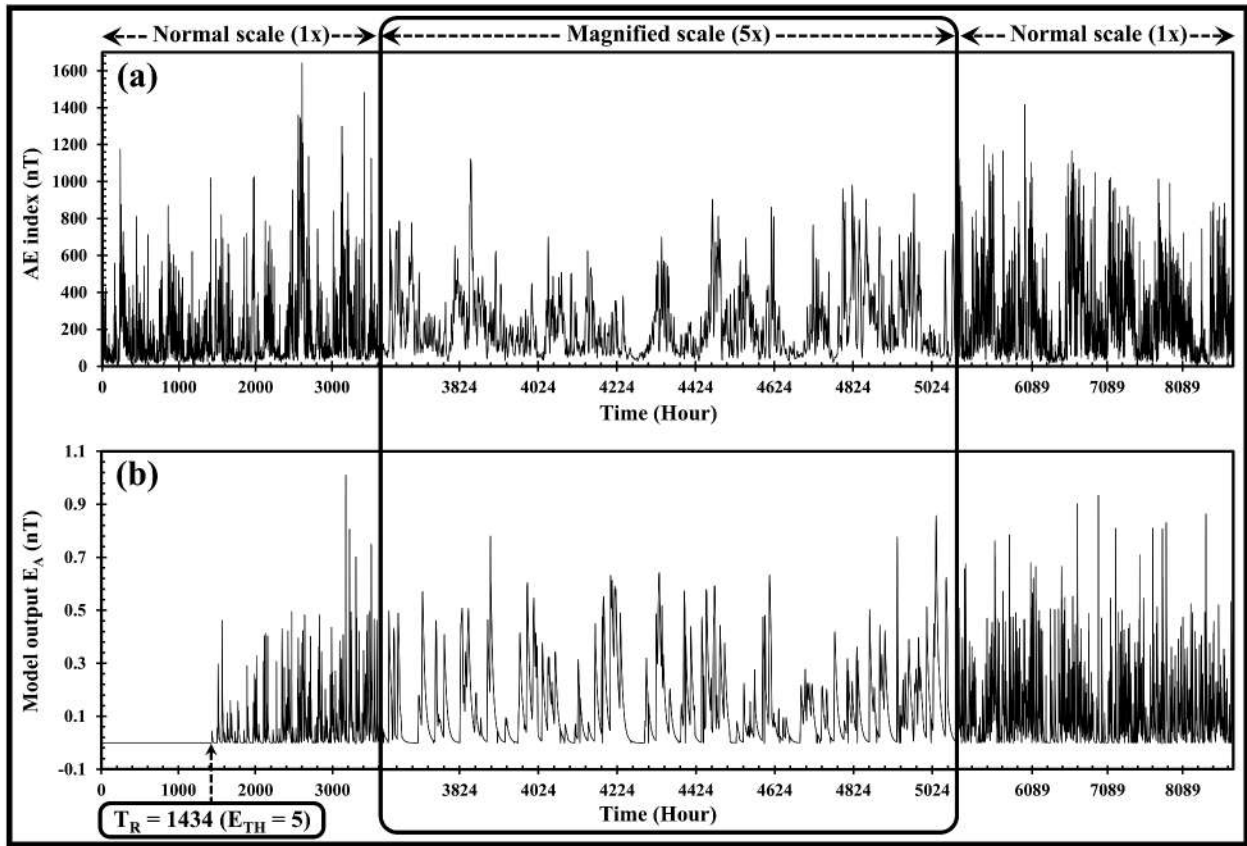


Figure 6. (a) The magnified version of the time-series of the natural AE index of the year 2002 (b) The magnified version of the simulated model output time-series,  $E_A$  of the year 2002.

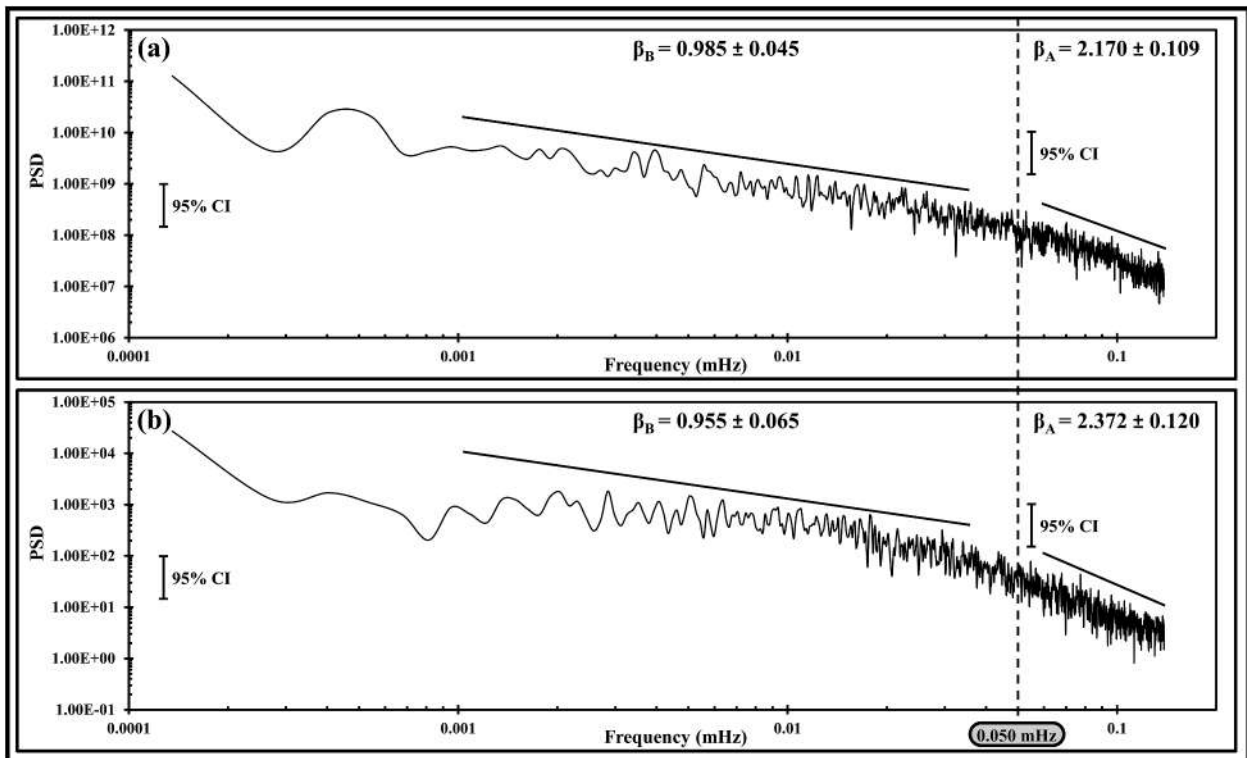


Figure 7. (a) The log-log plot of the power spectral density (PSD) of the real-time AE index of the year 2002. The  $\beta$  values of the series are estimated as  $\beta_A = -2.170 \pm 0.109$  and  $\beta_B = -0.985 \pm 0.045$  with a spectral break at  $f_0 = 0.050$  mHz (5.5 hours). (b) The log-log plot of the power spectral density (PSD) simulated model output  $E_A$  of the year 2002. For the value of  $K_A = 0.73$ , the  $\beta$  values of the series are estimated as  $\beta_A = -2.372 \pm 0.120$  and  $\beta_B = -0.955 \pm 0.065$  with a spectral break at  $f_0 = 0.050$  mHz (5.5 hours).

slopes of the two frequency regions of the  $1/f^\beta$  power spectrum of the natural AE index had long been a study of keen interest. (Tsurutani et al. 1990) estimated the values of the slopes as  $\beta_A = 2.2$  and  $\beta_B = 0.98$  with a breakpoint at  $f_0 = 0.050$  mHz (5.5 hours) for the hourly average AE data of the period of years 1971–1974. (Uritsky and Pudovkin 1998b) found out the values as  $\beta_A = 2.10$  and  $\beta_B = 0.95$  with a breakpoint at  $f_0 = 0.055$  mHz (5 hours) for the hourly average AE data of the period of years 1973–1974. (Woodard et al. 2005) compared all the prominent studies (Tsurutani et al. 1990; Consolini et al. 1996; Uritsky and Pudovkin 1998b; Price and Newman 2001; Watkins 2002) investigating the slopes of the two spectral regions and breakpoint of natural AE fluctuations and concluded the values of slopes as  $\beta_A = 2.4 \pm 0.26$  and  $\beta_B = 1.0 \pm 0.10$ . It is observed from Table 1 that for a particular value of the parameter  $K_A$ , the  $\beta$  values of the simulated series  $E_A$  are estimated as  $\beta_A = 2.2$ – $2.4$  and  $\beta_B = 0.9$ – $1.0$  with a spectral break at  $f_0 = 0.050$  mHz (5.5 hours), the typical values associated with natural AE index as reported by all these previous works.

The parameter  $K_A$  plays a significant role in estimating the simulated  $E_A$  series from the total released energy. As observed from Table 1, for a particular year and a particular value of  $K_A$ , the  $\beta$  values of the simulated output series  $E_A$  are in the specified ranges of the same associated with the natural AE index. For the entire 23<sup>rd</sup> solar cycle, the value of  $K_A$  is in the range of  $K_A = 0.68$ – $0.82$ . It is observed from the result, that the transferred solar wind energy does not dissipate completely through the westward and eastward auroral electrojet currents in an instant, rather a significant part of it remains present in the ionosphere even in the time of the next magnetosphere-ionosphere energy transfer. The parameter  $K_A$  has a fractional value. As can be seen in equations (14) and (15),  $K_A$  is denoting the remaining fraction of the total accumulated released energy of the previous state, reserved in the ionosphere. The excess energy transferred from the magnetosphere to the ionosphere is then being added up with this base value and forms the westward and eastward currents that are the two key factors for measuring the AE index.

The magnetosphere-ionosphere energy transfer and the stored part of this energy in the ionosphere are primarily controlled by the solar wind injection into the magnetosphere. Again, the amount of injected solar wind energy in the magnetosphere varies with the intensity, and duration of solar wind-magnetosphere coupling. Also, the solar cycle has a significant effect on energy injection. During solar storms, there is a large deposit of energy into the magnetosphere which changes the normal quiet time dynamics of the magneto-ionosphere system. Figure 4 illustrates such a case of a large amount of solar wind

injection into the magnetosphere. As shown in Figure 4(a), the marked period in the figure is distinguished by the continuous injection of a large amount of energy  $dE$  into the magnetosphere for hours. Consequently, the total accumulated energy of the lattice,  $E_{Total}$ , gradually starts to pile up in the system, altering its state of equilibrium. The value of the number of unstable states,  $S_{UN}$ , also increases indicating the instability formation in the lattice. Figure 4(b, c) show the plots for  $E_{Total}$  and  $S_{UN}$ , respectively. As the large values of energy injection continue,  $E_{Total}$  finally reaches a critical point and the pile collapses. The excess energy is released as a burst of avalanches inside the lattice restoring the stability of the system. After the successive distribution and redistribution process, the excess energy of the lattice is finally transferred outside its boundary region representing the magnetosphere-ionosphere energy transfer. As seen from Figure 4(d), the amount of released energy  $E_R$  increases after a while as a consequence of the continuous injection of large values of  $dE$  in the magnetosphere. The released energy in the ionosphere is dissipated through the auroral electrojets, the field-aligned currents flowing between the nightside magnetosphere and nightside ionosphere. But it takes time to completely dissipate through the current system in the ionosphere and a part of this energy remains stored in the ionosphere. The factor  $K_A$  estimates the amount of this stored energy.

As observed from the result, for the entire 23<sup>rd</sup> solar cycle, the value of  $K_A$  is slightly varying,  $K_A = 0.68$ – $0.82$ . In the model, the parameter  $K_A$  does not estimate the actual value of the stored energy, rather it indicates the percentage value of the transferred energy that remains stored in the ionosphere. As shown in Table 1, the value of  $K_A$  for the year 2002 is  $K_A = 0.73$ . This value indicates, at any current state  $t$ , 73% of the transferred energy of the previous state ( $t-1$ ), remains stored in the ionosphere. Thus, the transmitted energy does not dissipate instantly after each magnetosphere-ionosphere energy transfer, rather a substantial percentage (73%) of this energy remains reserved in the ionosphere during the next magnetosphere-ionosphere energy transfer. If the solar wind energy injection into the magnetosphere increases at any time  $t$ , the amount of total released energy in the ionosphere also increases for this  $t$ . Since  $K_A$  indicates the remaining percentage value of this released energy, the actual amount of the reserved energy in the ionosphere also increases as an effect of the large solar wind injection. Similarly, if the input injection is small, the amount of released energy decreases, decreasing the actual amount of reserved energy in the ionosphere. Thus, the actual amount of the reserved energy in the ionosphere varies with the variation in the intensity of injected solar wind in the magnetosphere and the parameter  $K_A$  represents its

percentage relationship with the total transferred energy. For the 23<sup>rd</sup> cycle, the value of  $K_A$  ranges between  $K_A = 0.68$ – $0.82$ , indicating that for each year, a substantial percentage of the transferred energy remains stored in the ionosphere.

#### 4. Conclusions

AE index is a global and instantaneous measurement of the magnetic fluctuations in the Earth's polar region in response to an external perturbation. In this paper, we developed a numerical cellular automata model of Earth's magnetosphere based on the concept of self-organised criticality and sandpile dynamics to study the complex dynamics of the magnetosphere-ionosphere energy transfer process and AE fluctuations. Our model is a dissipative, dynamical  $n \times n$  two-dimensional system of finite potential energy and open boundary conditions having the real-time values of solar ion density, flow speed, and IMF  $B_z$  as the input parameters. It is analogical to the Earth's magnetosphere while the upper and lower margins of the lattice can be considered as the north and south polar cusps of the Earth. The solar wind is a stream of energised plasma particles emitted from the outer atmosphere of the Sun. As the direction of IMF  $B_z$  is southward, a strong coupling occurs between the solar wind and terrestrial magnetosphere injecting a significant amount of solar wind energy into the geospace. Gradually, the energy piles up and reaches a self-organised critical condition after which adding up a small amount of energy into the pile can form a spatially localised magnetospheric instability. To maintain the equilibrium, the system redistributes itself and the excess energy is released as an outburst of avalanches of various sizes in the neighbouring regions. As long as there is local instability, the distribution process continues and successively spread over throughout the system, finally transmitting a large amount of energy into the ionosphere through the polar cusps. The transferred solar wind energy causes magnetic fluctuations in the auroral region and the AE index is the global measurement of the intensity of the fluctuations. In our proposed cellular automata model, the marginal grids of the lattice are equivalent to the polar cusps. The excess energy transferred through the upper grid of the lattice is measured and by some mathematical process a simulated time series has been derived which can be considered as a numerical representation of the real-time AE index.

The spectral response of the simulated output series  $E_A$  follows a  $1/f^\beta$  power law, demonstrates a breakpoint at  $f_0 = 0.050$  mHz (5.5 hours) having slopes  $\beta_A = 2.2$ – $2.4$  for  $f > f_0$  and  $\beta_B = 0.9$ – $1.0$  for

$f < f_0$ , the typical characteristics of natural AE index. It is observed that the parameter  $K_A$  plays a significant role in the entire process of forming a proper  $E_A$  time series estimated from the released energy.  $K_A$  represents the percentage of the released energy from the previous magnetosphere-ionosphere energy transfer, which remains stored in the ionosphere. Its value varies in a small range of  $K_A = 0.68$ – $0.82$  for the eleven years of the 23<sup>rd</sup> solar cycle, indicating a substantial percentage of the transferred energy remains reserved in the ionosphere for each year.

The excitation threshold  $E_{TH}$  is crucial in forming the SOC dynamics of the model. As an unstable element release four units of energy, for a small value of  $E_{TH}$ , the total internal energy of the system can achieve zero or negative potential for some of the values of  $t$ . In contrast, a large value of  $E_{TH}$  causes the piling up of solar wind energy in the system, reducing the rate of energy distribution as well as dissipation. The total internal energy of the system continues to increase gradually and the system takes a much larger time to achieve a metastable state and to form the SOC dynamics properly. Thus, a moderate value of  $E_{TH} = 5$  is optimum for the proposed model.

Overall, it can be concluded that our proposed model is a simple first-order avalanche model of the Earth's magnetosphere where the real-time solar parameters are the inputs. The model generates a simulated output series  $E_A$  which shows statistical similarity to the real-time AE index. Also, the parameter  $K_A$  varies over a small range of  $K_A = 0.68$ – $0.82$  which suggests a high percentage of the transferred solar wind energy remains reserved in the ionosphere. In our previous work (Banerjee et al. 2015) we presented a SOC-based cellular automata model and focused on the nature of solar wind-magnetosphere energy transfer and its subsequent effect in the magnetosphere. In continuation of this project, the current work is a further refinement of that model to study the magnetosphere-ionosphere energy transfer process. Future work can be focused to develop a composite cellular automata model of the magnetosphere to study all the intricate characteristics of the solar wind-magnetosphere-ionosphere dynamics.

#### Acknowledgements

We acknowledge the use of NASA/GSFC's Space Physics Data Facility's OMNIWeb (or CDAWeb or ftp) service, and OMNI data. We express our sincere gratitude to the National Research Institute of Astronomy and Geophysics, Egypt for their generous support regarding the arrangement of funding. We are also thankful to Parthasarathi Chakrabarti, Director, IEST, Shibpur, Howrah, India and Somnath Mukherjee, Principal of Dinabandhu Andrews

College, Kolkata, India for their encouragement and support for the present work. Finally, we would like to sincerely thank the anonymous reviewers for their most valuable comments and suggestions to improve the quality of this paper.

## Disclosure statement

No potential conflict of interest was reported by the author(s).

## References

- Ahn B-H, Kroehl HW, Kamide Y, Kihn EA. 2000a. Universal time variations of the auroral electrojet indices. *Journal of Geophysical Research: Space Physics*. 105(A1):267–275. doi:10.1029/1999ja900364.
- Ahn B-H, Kroehl HW, Kamide Y, Kihn EA. 2000b. Seasonal and solar cycle variations of the auroral electrojet indices. *J Atmos Sol-Terr Phys*. 62(14):1301–1310. doi:10.1016/s1364-6826(00)00073-0.
- Allen JH, Kroehl HW. 1975. Spatial and temporal distributions of magnetic effects of auroral electrojets as derived from AE indices. *J Geophys Res*. 80(25):3667–3677. doi:10.1029/ja080i025p03667.
- Antonova EE, Ganushkina NY. 2000. Inner magnetosphere currents and their role in the magnetosphere dynamics. *Physics and Chemistry of the Earth, Part C: Solar, Terrestrial & Planetary Science*. 25(1–2):23–26. doi:10.1016/s1464-1917(99)00028-8.
- Bak P, Tang C, Wiesenfeld K. 1987. Self-organized criticality: an explanation of the 1/f noise. *Phys Rev Lett*. 59(4):381–384. doi:10.1103/physrevlett.59.381.
- Bak P, Tang C, Wiesenfeld K. 1988. Self-organized criticality. *Phys Rev A*. 38(1):364–374. doi:10.1103/physreva.38.364.
- Banerjee A, Bej A, Chatterjee TN. 2011. On the existence of a long range correlation in the geomagnetic disturbance storm time (Dst) index. *Astrophys Space Sci*. 337(1):23–32. doi:10.1007/s10509-011-0836-1.
- Banerjee A, Bej A, Chatterjee TN. 2015. A cellular automata-based model of Earth's magnetosphere in relation with Dst index. *Space Weather*. 13(5):259–270. doi:10.1002/2014sw001138.
- Banerjee A, Bej A, Chatterjee TN, Majumdar A. 2019. An SOC approach to study the solar wind-magnetosphere energy coupling. *Earth and Space Science*. 6(4):565–576. doi:10.1029/2018ea000468.
- Bargatze LF, Baker DN, McPherron RL, Hones EW Jr. 1985. Magnetospheric impulse response for many levels of geomagnetic activity. *J Geophys Res*. 90(A7):6387. doi:10.1029/ja090ia07p06387.
- Baumjohann W. 1982. Ionospheric and field-aligned current systems in the auroral zone: a concise review. *Adv Space Res*. 2(10):55–62. doi:10.1016/0273-1177(82)90363-5.
- Borovsky JE, Valdivia JA. 2018. The earth's magnetosphere: a systems science overview and assessment. *Surveys in Geophysics*. 39(5):817–859. doi:10.1007/s10712-018-9487-x.
- Chang T. 1992. Low-dimensional behavior and symmetry breaking of stochastic systems near criticality—can these effects be observed in space and in the laboratory? *IEEE Trans Plasma Sci*. 20(6):691–694. doi:10.1109/27.199515.
- Chang T. 1999. Self-organized criticality, multi-fractal spectra, sporadic localized reconnections and intermittent turbulence in the magnetotail. *Phys Plasmas*. 6(11):4137–4145. doi:10.1063/1.873678.
- Chapman SC, Watkins NW, Dendy RO, Helander P, Rowlands G. 1998. A simple avalanche model as an analogue for magnetospheric activity. *Geophys Res Lett*. 25(13):2397–2400. doi:10.1029/98gl51700.
- Chen J, Sharma AS. 2006. Modeling and prediction of the magnetospheric dynamics during intense geomagnetic storms. *J Geophys Res*. 111(A4). doi:10.1029/2005ja011359.
- Cliver EW, Kamide Y, Ling AG. 2000. Mountains versus valleys: semiannual variation of geomagnetic activity. *Journal of Geophysical Research: Space Physics*. 105(A2):2413–2424. doi:10.1029/1999ja900439.
- Consolini G (1997). Sandpile cellular automata and magnetospheric dynamics. In Aiello S, et al (Eds.), *Conference Proceedings “Cosmic Physics in the Year 2000”* (Vol. 58, pp. 123–126). SIF, Bologna, Italy.
- Consolini G, Lui ATY. 1999. Sign-singularity analysis of current disruption. *Geophys Res Lett*. 26(12):1673–1676. doi:10.1029/1999gl900355.
- Consolini G, Marcucci MF, Candidi M. 1996. Multifractal structure of auroral electrojet index data. *Phys Rev Lett*. 76(21):4082–4085. doi:10.1103/physrevlett.76.4082.
- Davis TN, Sugiura M. 1966. Auroral electrojet activity index AE and its universal time variations. *J Geophys Res*. 71(3):785–801. doi:10.1029/jz071i003p00785.
- Dobias P, Wanliss JA. 2009. Intermittency of storms and substorms: is it related to the critical behaviour? *Ann Geophys*. 27(5):2011–2018. doi:10.5194/angeo-27-2011-2009.
- Gavrishchaka VV, Ganguli SB. 2001. Optimization of the neural-network geomagnetic model for forecasting large-amplitude substorm events. *Journal of Geophysical Research: Space Physics*. 106(A4):6247–6257. doi:10.1029/2000ja900137.
- Gleisner H, Lundstedt H. 1997. Response of the auroral electrojets to the solar wind modeled with neural networks. *Journal of Geophysical Research: Space Physics*. 102(A7):14269–14278. doi:10.1029/96ja03068.
- Gleisner H, Lundstedt H. 2001. Auroral electrojet predictions with dynamic neural networks. *Journal of Geophysical Research: Space Physics*. 106(A11):24541–24549. doi:10.1029/2001ja900046.
- Goertz CK, Shan L-H, Smith RA. 1993. Prediction of geomagnetic activity. *Journal of Geophysical Research: Space Physics*. 98(A5):7673–7684. doi:10.1029/92ja01193.
- Hernandez JV, Tajima T, Horton W. 1993. Neural net forecasting for geomagnetic activity. *Geophys Res Lett*. 20(23):2707–2710. doi:10.1029/93gl02848.
- Kamide Y, Kokubun S. 1996. Two-component auroral electrojet: importance for substorm studies. *Journal of Geophysical Research: Space Physics*. 101(A6):13027–13046. doi:10.1029/96ja00142.
- Kamide Y, Rostoker G. 2004. What is the physical meaning of the AE index? *Eos, Transactions American Geophysical Union*. 85(19):188. doi:10.1029/2004eo190010.
- King JH, Papitashvili NE. 2005. Solar wind spatial scales in and comparisons of hourly wind and ACE plasma and magnetic field data. *J Geophys Res*. 110(A2). doi:10.1029/2004ja010649.
- Klimas AJ, Baker DN, Roberts DA, Fairfield DH, Büchner J. 1992. A nonlinear dynamical analogue model of geomagnetic activity. *J Geophys Res*. 97(A8):12253. doi:10.1029/92ja00794.



- Klimas AJ, Baker DN, Vassiliadis D, Roberts DA. 1994. Substorm recurrence during steady and variable solar wind driving: evidence for a normal mode in the unloading dynamics of the magnetosphere. *J Geophys Res.* 99 (A8):14855. doi:10.1029/94ja01240.
- Klimas AJ, Valdivia JA, Vassiliadis D, Baker DN, Hesse M, Takalo J. 2000. Self-organized criticality in the substorm phenomenon and its relation to localized reconnection in the magnetospheric plasma sheet. *Journal of Geophysical Research: Space Physics.* 105(A8):18765–18780. doi:10.1029/1999ja000319.
- Li X, Oh KS, Temerin M. 2007. Prediction of the AL index using solar wind parameters. *Journal of Geophysical Research: Space Physics.* 112(A6):n/a–n/a. doi:10.1029/2006ja011918.
- Lu JY, Liu Z-Q, Kabin K, Jing H, Zhao MX, Wang Y. 2013. The IMF dependence of the magnetopause from global MHD simulations. *Journal of Geophysical Research: Space Physics.* 118(6):3113–3125. doi:10.1002/jgra.50324.
- Luo B, Li X, Temerin M, Liu S. 2013. Prediction of the AU, AL, and AE indices using solar wind parameters. *Journal of Geophysical Research: Space Physics.* 118 (12):7683–7694. doi:10.1002/2013ja019188.
- Lyatsky W, Newell PT, Hamza A. 2001. Solar illumination as cause of the equinoctial preference for geomagnetic activity. *Geophys Res Lett.* 28(12):2353–2356. doi:10.1029/2000gl012803.
- McPherron RL, Rostoker G. 1993. Comment on “Prediction of geomagnetic activity” by C. K. Goertz, Lin-Hua Shan, and R. A. Smith. *Journal of Geophysical Research: Space Physics.* 98(A5):7685–7686. doi:10.1029/92ja01194.
- McPherron RL, Russell CT, Aubry MP. 1973. Satellite studies of magnetospheric substorms on August 15, 1968: 9. Phenomenological model for substorms. *J Geophys Res.* 78(16):3131–3149. doi:10.1029/ja078i016p03131.
- Nakamura M, Yoneda A, Oda M, Tsubouchi K. 2015. Statistical analysis of extreme auroral electrojet indices. *Earth, Planets and Space.* 67(1). doi:10.1186/s40623-015-0321-0.
- Nishida A. 2000. The Earth's dynamic magnetotail. *Space Sci Rev.* 91(3/4):507–577. doi:10.1023/A:1005223124330
- Price CP, Newman DE. 2001. Using the R/S statistic to analyze AE data. *J Atmos Sol-Terr Phys.* 63 (13):1387–1397. doi:10.1016/s1364-6826(00)00240-6.
- Pulkkinen A, Klimas A, Vassiliadis D, Uritsky V. 2006. Role of stochastic fluctuations in the magnetosphere-ionosphere system: a stochastic model for the AE index variations. *J Geophys Res.* 111(A10). doi:10.1029/2006ja011661.
- Pulkkinen TI, Tanskanen EI, Viljanen A, Partamies N, Kauristie K. 2011. Auroral electrojets during deep solar minimum at the end of solar cycle 23. *Journal of Geophysical Research: Space Physics.* 116(A4):n/a–n/a. doi:10.1029/2010ja016098.
- Rostoker G. 1972. Geomagnetic indices. *Reviews of Geophysics.* 10(4):935. doi:10.1029/rg010i004p00935.
- Rostoker G (2002), Why we have not yet solved the substorm problem, in Sixth International Conference on Substorms, edited by Winglee RM, pp. 1–8. University of Washington, Seattle.
- Russell CT. 2001. Solar wind and interplanetary magnetic field: a tutorial. In: *Space Weather* (eds P. Song, H. J. Singer and G. L. Siscoe). p. 73–89. doi:10.1029/gm125p0073.
- Russell CT, McPherron RL. 1973. Semiannual variation of geomagnetic activity. *J Geophys Res.* 78(1):92–108. doi:10.1029/ja078i001p00092.
- Sitnov MI, Sharma AS, Papadopoulos K, Vassiliadis D, Valdivia JA, Klimas AJ, Baker DN. 2000. Phase transition-like behavior of the magnetosphere during substorms. *Journal of Geophysical Research: Space Physics.* 105(A6):12955–12974. doi:10.1029/1999ja000279.
- Strangeway RJ. 2013. The relationship between magnetospheric processes and auroral field-aligned current morphology. In: *Geophysical monograph series.* American Geophysical Union; p. 355–364. doi:10.1029/2012gm001211
- Takalo J, Timonen J, Klimas A, Valdivia J, Vassiliadis D. 1999. Nonlinear energy dissipation in a cellular automaton magnetotail field model. *Geophys Res Lett.* 26 (13):1813–1816. doi:10.1029/1999gl900429.
- Temerin M, Li X. 2002. A new model for the prediction of Dst on the basis of the solar wind. *Journal of Geophysical Research: Space Physics.* 107(A12):31–8. doi:10.1029/2001ja007532.
- Temerin, M., & Li, X. 2006. DST model for 1995–2002. *Journal of Geophysical Research.* 111(A4). doi:10.1029/2005ja011257
- Tsurutani BT, Sugiura M, Iyemori T, Goldstein BE, Gonzalez WD, Akasofu SI, Smith EJ. 1990. The nonlinear response of AE to the IMF BSdriver: a spectral break at 5 hours. *Geophys Res Lett.* 17(3):279–282. doi:10.1029/gl017i003p00279.
- Uritsky VM (1996). 1/f-like spectra of geomagnetic fluctuations: expression of self-organized criticality? In *Book of abstracts of the International Conference on Problems of Geocosmos, St. Petersburg (Russia).* June 17–23, (p. 110).
- Uritsky VM, Pudovkin MI. 1998a. Fractal dynamics of AE-index of geomagnetic activity as a marker of the self-organized criticality in the magnetosphere (in Russian). *Geomagnetizm i Aeronomia.* 38(3):17–28.
- Uritsky VM, Pudovkin MI. 1998b. Low frequency 1/f-like fluctuations of the AE-index as a possible manifestation of self-organized criticality in the magnetosphere. *Ann Geophys.* 16(12):1580–1588. doi:10.1007/s00585-998-1580-x.
- Uritsky VM, Pudovkin MI, Steen A. 2001. Geomagnetic substorms as perturbed self-organized critical dynamics of the magnetosphere. *Journal of Atmospheric and Solar-Terrestrial Physics.* 63(13):1415–1424. doi:10.1016/S1364-6826(00)00243-1.
- Uritsky VM, Semenov VS. 2000. A sandpile model for global statistics of reconnection events in the magnetotail. In: Biernat HK, Farrugia CJ, Vogl DF, editors. *The solar wind - magnetosphere system* (Vol. 3). Wien: Osterreichische Akademie der Wissenschaften; p. 299–308.
- Vassiliadis D, Angelopoulos V, Baker DN, Klimas AJ. 1996. The relation between the northern polar cap and auroral electrojet geomagnetic indices in the wintertime. *Geophys Res Lett.* 23(20):2781–2784. doi:10.1029/96gl02575.
- Vassiliadis D, Klimas AJ, Baker DN, Roberts DA. 1995. A description of the solar wind-magnetosphere coupling based on nonlinear filters. *Journal of Geophysical Research: Space Physics.* 100(A3):3495–3512. doi:10.1029/94ja02725.

- Vennerstrøm S, Friis-Christensen E, Troshichev OA, Andersen VG. 1991. Comparison between the polar cap index, PC, and the auroral electrojet indices AE, AL, and AU. *J Geophys Res.* 96(A1):101. doi:[10.1029/90ja01975](https://doi.org/10.1029/90ja01975).
- Watkins NW. 2002. Scaling in the space climatology of the auroral indices: is SOC the only possible description? *Nonlinear Process Geophys.* 9(5/6):389–397. doi:[10.5194/npg-9-389-2002](https://doi.org/10.5194/npg-9-389-2002).
- Weigel RS. 2003. Solar wind coupling to and predictability of ground magnetic fields and their time derivatives. *J Geophys Res.* 108(A7). doi:[10.1029/2002ja009627](https://doi.org/10.1029/2002ja009627).
- Woodard R, Newman DE, Sánchez R, Carreras BA. 2005. On the identification of soc dynamics in the sun-earth system. In *Multiscale coupling of sun-earth processes*. Edited by Lui ATY, Kamide Y, Consolini G. p. 55–68. Elsevier Science BV; doi:[10.1016/b978-044451881-1/50005-8](https://doi.org/10.1016/b978-044451881-1/50005-8).

2018

0

2018

● Cited documents ● Uncited documents



1

0

2018

### NRIAG Journal of Astronomy and Geophysics

Not yet assigned quartile

SJR 2022

0

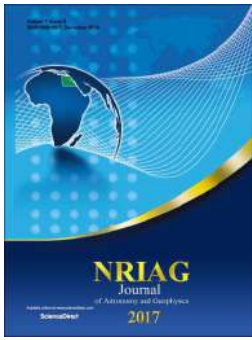


powered by scimagojr.com

← Show this widget in your own website

Just copy the code below and paste within your html code:

```
<a href="https://www.scimagojr.com" data-bbox="788 714 970 759">
```



## A SOC based avalanche model to study the magnetosphere-ionosphere energy transfer and AE index fluctuations

Adrija Banerjee, Amaresh Bej, T. N. Chatterjee & Abhijit Majumdar

To cite this article: Adrija Banerjee, Amaresh Bej, T. N. Chatterjee & Abhijit Majumdar (2021): A SOC based avalanche model to study the magnetosphere-ionosphere energy transfer and AE index fluctuations, NRIAG Journal of Astronomy and Geophysics, DOI: [10.1080/20909977.2021.2005335](https://doi.org/10.1080/20909977.2021.2005335)

To link to this article: <https://doi.org/10.1080/20909977.2021.2005335>



© 2021 The Author(s). Published by Informa UK Limited, trading as Taylor & Francis Group.



Published online: 24 Nov 2021.



Submit your article to this journal [↗](#)



View related articles [↗](#)



View Crossmark data [↗](#)



# A SOC based avalanche model to study the magnetosphere-ionosphere energy transfer and AE index fluctuations

Adrija Banerjee<sup>a</sup>, Amaresh Bej<sup>a</sup>, T. N. Chatterjee<sup>b</sup> and Abhijit Majumdar<sup>a</sup>

<sup>a</sup>Department of Physics, Indian Institute of Engineering Science and Technology, Howrah, India; <sup>b</sup>Department of Electronics, Dinabandhu Andrews College, Kolkata, India

## ABSTRACT

Magnetosphere-ionosphere energy transfer and AE fluctuations are studied using a cellular automata model of terrestrial magnetosphere based on the concept of self-organised criticality (SOC). The model is a SOC-driven dissipative dynamical system with both spatial and temporal degrees of freedom. The input parameter to this model is derived from the real-time values of solar wind ion density and flow speed data. Both the direction and intensity of the real-time values of the  $B_z$  component of the interplanetary magnetic field (IMF) are the factors controlling the energy injection into the system. The model produces an output series which can be regarded as a mathematical representation of the AE index. The spectral response of the simulated output follows a  $1/f^{\beta}$  power law, demonstrates a breakpoint at  $f_0 = 0.050$  mHz (5.5 hours) having slopes  $\beta_A = 2.2-2.4$  for  $f > f_0$  and  $\beta_B = 0.9-1.0$  for  $f < f_0$ , the typical characteristics of the natural AE index. The entire 23<sup>rd</sup> solar cycle had been studied using the model. The parameter  $K_A$  plays a significant role in the entire process.  $K_A$  represents the remaining percentage of the released energy from the previous magnetosphere-ionosphere energy transfer, stored in the ionosphere.

## ARTICLE HISTORY

Received 12 May 2021  
Revised 31 October 2021  
Accepted 8 November 2021

## KEYWORDS

Plasmas; solar wind;  
magnetic reconnection;  
geomagnetic index

## 1. Introduction

Magnetosphere-ionosphere interaction and the subsequent energy transfer is a significant phenomenon in magnetospheric dynamics. During a strong solar wind-magnetosphere coupling, a large amount of solar wind energy enters the geospace. A part of the energy is stored in the magnetotail and another part drives the convection of plasma particles in the magnetosphere. As the solar wind injection continues, the stored energy in the magnetotail reaches an unstable state, triggering magnetic reconnection. A huge amount of energy is released in the ionosphere causing magnetic fluctuations in the auroral zone. The auroral electrojet (AE) index is a global and instantaneous measurement of the auroral zone magnetic activities. The geomagnetic fluctuation in the horizontal component of the Earth's magnetic field  $H$  in the auroral region is measured in 10–13 observatories situated around the auroral zone. For each station, the average value of  $H$  of the five international quietest days of the month is considered as the base value of the measurement. For normalisation of data, the base value is subtracted from each data of the station. Then, all the normalised data from all the stations are plotted and superimposed on each other. The maximum and minimum deviations of  $H$  are termed as Auroral Upper (AU) and Auroral Lower (AL) index, respectively, which form the upper boundary and lower

boundary of the envelope. If there are no disturbances from the distant axially symmetric fields or zonal currents, the AU and AL indices are the direct measurement of the maximum eastward and westward electrojet currents at any time. AE index is defined as the maximum total amplitude of the eastward and westward electrojet currents, that is,  $AE = AU - AL$ . As the AE index is the difference value of AU and AL indices, it is independent of the ionospheric zonal current or distant axially symmetric fields (Davis and Sugiura 1966). AE index is extensively used in aeronomy, solar-terrestrial physics, geomagnetism, and auroral studies.

The physical meaning of the AE index, the nature of the eastward and westward electrojets, the limitations of AU and AL indices have been discussed (Rostoker 1972, 2002; Baumjohann 1982; Kamide and Kokubun 1996; Kamide and Rostoker 2004) along with a detailed study of spatial and temporal distributions of magnetic effects of the electrojets (Allen and Kroehl 1975), statistical analysis (Nakamura et al. 2015) and its relation with the polar cap index (Vennerström et al. 1991; Vassiliadis et al. 1996). It has been also established that the AE index is subject to universal time variation (Davis and Sugiura 1966; Ahn et al. 2000a), seasonal variation (Ahn et al., 2000b; Cliver et al. 2000; Lyatsky et al. 2001; Russell and McPherron 1973; Temerin and Li 2002, 2006),

annual variation (Lyatsky et al. 2001; Pulkkinen et al. 2011), and solar cycle variation (Ahn et al., 2000b). Different dynamical and numerical models have been presented to predict and study auroral electrojets. The analogue model proposed by (Goertz et al. 1993) and reviewed by (McPherron and Rostoker 1993), the Faraday loop model (Klimas et al. 1992, 1994), using linear prediction filter (LPF) technique (Bargatze et al. 1985) which is further modified as local-linear prediction technique by (Vassiliadis et al. 1995), by artificial intelligence (Hernandez et al. 1993; Gleisner and Lundstedt 1997, 2001; Gavrishchaka and Ganguli 2001; Weigel 2003; Chen and Sharma 2006), by stochastic approach (Pulkkinen et al. 2006) and also using solar wind parameters (Li et al. 2007; Luo et al. 2013).

Previously, we studied the characteristic structure of the Dst index, the global measurement of geomagnetic activities in Earth, and realised the series as a positively correlated fractional Brownian motion, displaying long-range correlation (Banerjee et al. 2011). But, we also understood the complexity of the non-linear dynamics of the geomagnetic fluctuations and the difficulties in predicting them. To gain an insight into the magnetospheric dynamics, we focused our study to develop a cellular automata model of terrestrial magnetosphere based on the concept of self-organised criticality and sandpile dynamics. According to the concept, a dissipative, dynamical system with both spatial and temporal degrees of freedom naturally evolved to a self-organised critical state without much specification of the initial conditions. The dynamical behaviour of a pile of sand is the most prominent example of this type of system. Let us start with a grain of sand and continue to add more grains to it, gradually forming a pile. The increment of the slope enhances the characteristic size of the largest avalanches. As a result, the equilibrium state of the sandpile is seriously disturbed. Eventually, when the slope becomes very large, the pile reaches a critical state. Now, adding a single grain of sand further to the pile collapses it. An avalanche of sand is released from the pile, the base area increases, and the system again returns to a state of equilibrium (Bak et al. 1987, 1988).

The concept of self-organised criticality (SOC) and sandpile model can be the basis of an analytical study of magneto-ionospheric dynamics. The solar wind, a stream of energised plasma particles is emitted from the outer atmosphere of the Sun and approaches the Earth. The interplanetary magnetic field (IMF) is trapped in the solar wind. Near the terrestrial space, the solar wind flow speed varies from a minimum of 260 km/sec to a maximum of 750 km/sec while the ion density varies in a much wider range, from  $0.1 \text{ cm}^{-3}$  to  $100 \text{ cm}^{-3}$  (Russell 2001). The density fluctuation is the primary controller of the variations in the dynamic pressure, which further controls the solar wind-

magnetosphere reconnection. When the solar wind interacts with the terrestrial magnetosphere, this supersonic flow creates a standing shock wave or bow shock in the day-side of the magnetosphere and converts it into a subsonic flow. Majority of the energised solar wind plasma particles is heated and then get deflected around the Earth at the bow shock. The day-side magnetosphere is compressed down while the night-side magnetosphere is stretched up to about 100 Earth radii comprising the magnetotail (Nishida 2000; Borovsky and Valdivia 2018). The trapped interplanetary magnetic field (IMF) plays a crucial role in controlling the intensity and duration of solar wind-magnetosphere coupling. For a northward IMF  $B_z$ , the cusp shifts away from the equatorial region and further narrows down with the increasing intensity of  $B_z$ , decreasing the amount of energy injection into the magnetosphere. But, for a southward IMF  $B_z$ , the cusp shifts towards the equatorial region and widens out gradually as the intensity of  $B_z$  increases, triggering an injection of a large amount of solar wind energy into the magnetosphere (Lu et al. 2013). The magnetotail becomes a reservoir of this energy. As the solar wind injection continues, the magnetotail grows further by accumulating more and more energy. Eventually, the magnetotail growth reaches a critical point, becomes unstable and magnetic reconnection occurs in the tail. A part of the stored energy is released through flow kinetic energy and plasma heating, producing substorm (Borovsky and Valdivia 2018). Substorm originates deep in the magnetosphere, near the geostationary orbit (Antonova and Ganushkina 2000). It is a short but intense earthward convection of magnetic flux in the magnetotail which injects energised particles in the dipolar region, also substantially increasing the auroral electrojets (McPherron et al. 1973). The Joule energy extracted from the magnetosphere is dissipated in the ionosphere through auroral electrojets, the field-aligned currents flowing between the nightside magnetosphere and nightside ionosphere (Strangeway 2013). The subsequent magnetic fluctuations in the auroral region are measured by the AE index.

SOC has long been proposed as a possible explanation of magnetospheric dynamics. Sandpile model was selected as the first example displaying the concept of self-organised criticality, introduced by Bak et al. in their 1987 and 1988 papers. Since then, the application of this theory has produced numerous significant analyses of magnetospheric activities by some eminent researchers. Consolini observed SOC-triggered behaviour in the power spectral density and burst size distribution of the AE index (Consolini 1997). Using the sign-singularity analysis, magnetic field fluctuations in the near-tail regions were investigated based on the concept of self-organised criticality and 2nd-order phase transition (Consolini and Lui 1999).

Chapman et al. presented a sandpile cellular automaton model to study magnetospheric dynamics (Chapman et al. 1998) and Klimas presented a first-order physical model of plasma sheet (Klimas et al. 2000). Further studies on modelling continued based on the SOC approach with interesting conclusions (Takalo et al. 1999; Uritsky and Semenov 2000). Other notable works discussed in detail the distinctive features of SOC-driven instabilities and their effects in the context of nonlinear dynamics of magnetosphere (Chang 1992, 1999; Uritsky 1996; Uritsky and Pudovkin 1998a; Sitnov et al. 2000). (Dobias and Wanliss 2009) suggested that both the storm and sub-storm characteristics are consistent with the behaviour of the critical system and follow the fractal point process (FPP).

(Uritsky and Pudovkin 1998b) developed a two-dimensional sandpile model of the magnetosphere current sheet to study the AE fluctuations. The model was a rectangular matrix of  $x$  and  $y$  dimensions. Each element of the matrix was characterised by an amount of energy. Also, a critical threshold of energy was assigned to all of the elements to determine the stability of the element after each energy injection. They investigated the avalanche formations, energy redistribution, and plasma sheet instabilities of the SOC-driven system in reaction to external disturbances. It was suggested that the spatially localised magnetotail instabilities can be regarded as SOC avalanches and the superposition of these avalanches of different sizes finally produces the characteristic low-frequency  $1/f$ -like fluctuations of the AE index (Uritsky and Pudovkin 1998b). Uritsky et al. continued the study of the above two-dimensional sandpile model in their 2001 paper to explain geomagnetic substorms as a self-organised critical dynamic of the perturbed magnetosphere. In their study, the total accumulated energy in the system, as well as the energy dissipated from the system, were revealed to be the two major factors controlling the overall dynamics of the system. Moreover, the spectral characteristics of the model output showed striking similarities with the natural AE fluctuations (Uritsky et al. 2001).

Based on the model (Uritsky et al. 2001), we developed a sandpile-like cellular automata model of Earth's magnetosphere in our previous paper (Banerjee et al. 2015). The model is a SOC-driven dissipative dynamical system with both spatial and temporal degrees of freedom. It is a two-dimensional array of finite dimensions and is characterised by energy  $E$ . The input energy to this model is derived from the real-time value of solar ion density and flow speed data. Both the direction and intensity of the real-time value of the  $B_Z$  component of the interplanetary magnetic field (IMF) are the factors controlling the amount of solar wind energy injected into the system at any time. The total accumulated energy of the

system is estimated to produce a simulated output representing the Dst index. The spectral characteristics of the simulated output closely follow the natural Dst index, establishing the acceptability of the model (Banerjee et al. 2015). We continued our study with the model investigating the solar wind-magnetosphere interaction, the injection of plasma particles, and the aspects of internal magnetospheric dynamics as a subsequent effect (Banerjee et al. 2019).

In the present paper, we extend our sandpile-like cellular automata model to study the dynamical behaviour of the auroral zone magnetic activities by focusing on the transferred energy from the system. The model, a representation of the Earth's magnetosphere, is a lattice of  $n \times n$  elements, having spatial and temporal degrees of freedom. Each element is characterised by an energy  $E$ , which is analogous to the slope of the sandpile. The input to the model is solar wind energy, derived from the real-time value of solar ion density and flow speed data. The input energy is injected into the system through a set of elements, representing the cusp. Both the direction and intensity of IMF  $B_Z$  are the factors controlling the width of the cusp, hence the amount of energy injection into the system. The injected energy is altering the potential energy of the elements of the lattice. Each element has a critical value of energy, known as the excitation threshold. As the energy injection continues, the energy gradually piles up in the elements, similar to the storing of energy in the magnetotail. If the energy of any element reaches the point of criticality by exceeding the excitation threshold, spatially localised instabilities are formed, representing the instability formation in the magnetotail. The pile collapses by releasing avalanches of energy in various sizes and shapes. The released energy is distributed among the adjacent elements and the process continues, gradually spreading throughout the lattice. The excess energy reaching the upper or lower margins is transmitted outside the lattice, representing the magnetosphere-ionosphere energy transfer. The amount of transferred energy at any time  $t$  is estimated. By some numerical calculations, an output time series is produced from this estimated energy. The simulated output can be regarded as a mathematical representation of the AE index. It is observed that the simulated series exhibits  $1/f^\beta$ -like power spectrum. The power-law exponents  $\beta_A$  and  $\beta_B$  of the power spectral density of the simulated output are evaluated for both the high- and low-frequency regions respectively for all the years of the entire 23<sup>rd</sup> solar cycle. Finally, by comparing the values of  $\beta_A$  and  $\beta_B$  with that of the real-time AE index, it is observed that the simulated output closely follows the natural AE fluctuations depending on the exact value of the parameter  $K_A$ .  $K_A$  represents the remaining percentage of the

transferred energy of the previous magnetosphere-ionosphere energy transfer, stored in the ionosphere. In our previous work (Banerjee et al. 2019), the real-time solar wind and IMF  $B_Z$  data of the 23<sup>rd</sup> solar cycle were used as the input to the model to investigate the solar wind-magnetosphere energy transfer. As we are continuing our study on the model, in the present work, we used the same input dataset to analyse the magnetosphere-ionosphere energy transfer.

## 2. Method and data

The cellular automata-based sandpile model used here is an extension of the model presented in our previous papers (Banerjee et al. 2015, 2019) which is in turn based on the model presented by (Uritsky et al. 2001). The model, representation of the Earth's magnetosphere, is a finite matrix of  $n \times n$  elements having spatial and temporal degrees of freedom. Each element is characterised by an energy  $E$ , which is analogous to the slope of the sandpile.  $E$  has an arbitrary unit. The threshold value of energy for each element is indicated as  $E_{TH}$ , the excitation threshold (Uritsky et al. 2001). The input to the model is solar wind energy.

The input energy  $dE$  is estimated using the real-time ion density and flow speed data obeying the equation (Banerjee et al. 2015, 2019)

$$dE = \text{norm} \left( \frac{1}{2} \times \text{ion density} \times \text{flow speed}^2 \right) \quad (1)$$

As the solar wind flows towards the Earth, it interacts with the magnetosphere. Depending on the intensity and direction of IMF  $B_Z$ , a part of the solar wind energy is injected into the magnetosphere through the cusp while the major part of the solar wind energy is deflected at the bow shock and flows across the Earth. A small fraction of this deflected energy penetrates into the magnetosphere. In this model, the factor  $K$  represents this small fractional value. Thus, all the elements of the lattice are credited with the energy  $K \times dE$  at every initial stage. This alters the potential energy of each element as (Banerjee et al. 2015, 2019)

$$E_{t+1}(i, j) = E_t(i, j) + K \times dE, \text{ for all } i \text{ and } j \quad (2)$$

As the two-dimensional lattice is analogical to the terrestrial magnetosphere, the cusp width  $W_C$  in the model is a set of selected elements including and surrounding the centre one, the element at  $i = n/2$ ,  $j = n/2$ . The number of elements in the set, that is, the size of the cusp width  $W_C$  is controlled by both the direction and intensity of IMF  $B_Z$ , following the equations (Banerjee et al. 2015):

$$W_C = [(2 \times w) + 1]^2 \quad (3)$$

where

$$w = (K_d \times B_Z) \text{ for southward } B_Z \quad (4)$$

and

$$w = [K_d \times (B_{Z_{\max}} - B_Z)] \text{ for northward } B_Z \quad (5)$$

Here  $B_{Z_{\max}}$  is the maximum value of northward  $B_Z$  and  $K_d$  is the associated proportionality factor.  $K_d$  is a function of the direction of the IMF  $B_Z$ . As the energy injection increases for southward  $B_Z$  and decreases for northward  $B_Z$ , the numerical value of  $K_d$  is higher for the southward direction than that of the northward direction.

During a solar wind-magnetosphere coupling, the solar wind energy  $dE$  is injected into the system through the cusp width  $W_C$  following the relation (Uritsky et al. 2001; Banerjee et al. 2015, 2019),

$$E_{t+1}(i, j) = [E_t(i, j) + dE] \text{ for } i = \left(\frac{n}{2} \pm w\right) \text{ and } j = \left(\frac{n}{2} \pm w\right) \quad (6)$$

The threshold value of energy for each element is indicated as  $E_{TH}$ , the excitation threshold. After the energy injection, if  $E(i, j) < E_{TH}$ , the element is stable. If  $E(i, j) > E_{TH}$ , the element is unstable and releases four units of energy to return to a stable state. The released energy is distributed among its four adjacent neighbours according to the following equations (Uritsky et al. 2001; Banerjee et al. 2015, 2019),

$$E_{t+1}(i, j) = E_t(i, j) - 4 \quad (7)$$

A small value of energy  $E_d$  is dissipated during the distribution process. The energy of the adjacent elements alters as (Uritsky et al. 2001; Banerjee et al. 2015, 2019)

$$E_{t+1}(i \pm 1, j \pm 1) = E_t(i \pm 1, j \pm 1) + \left(1 - \frac{E_d}{4}\right) \quad (8)$$

Figure 1 illustrates the energy transfer process in a two-dimensional lattice. The unstable elements [ $E(i, j) > E_{TH}$ ] are marked with black shade, the stable elements [ $E(i, j) < E_{TH}$ ] with grey shade, and the elements with zero or negligible energy with white shade. Initially, all the elements of the lattice have zero energy. The input energy is injected into the system through the cusp  $W_C$  altering its energy above  $E_{TH}$ , as shown in Figure 1(a). Thus, the centre element is in black shade. The cusp  $W_C$  here consists of only one element, the element at the centre of the lattice ( $i = n/2$ ,  $j = n/2$ ). In the next Figure 1(b), the unstable element distributes four units of its energy to its four adjacent neighbours. Two of the neighbouring elements, marked in black shade became unstable, receiving the excess energy. In the final Figure 1(c), the two unstable elements further distribute their energy to return to stability. This way, the injected energy is distributed and redistributed throughout the lattice.



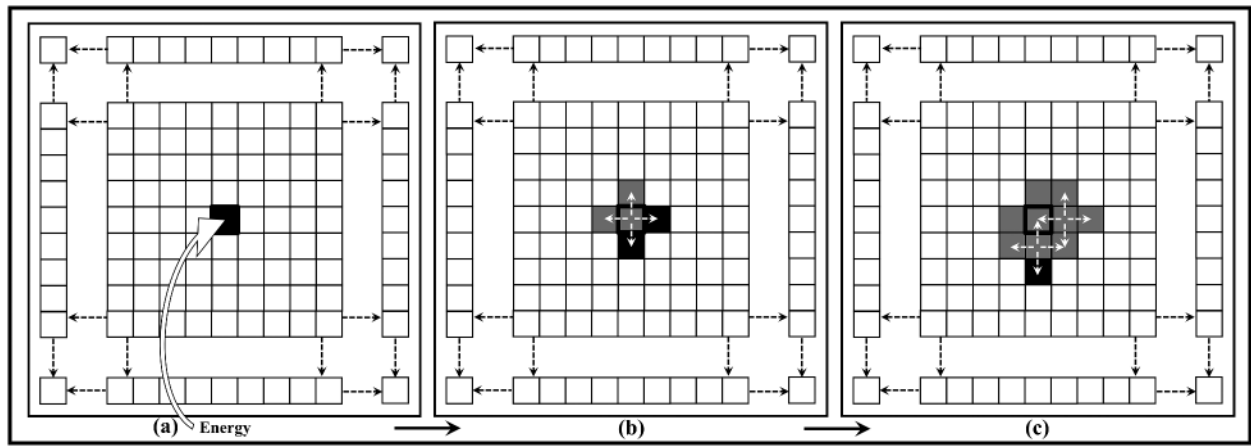


**Figure 1.** The energy distribution in a two-dimensional lattice. The unstable elements  $[E(i, j) > E_{TH}]$  are marked with black shade, the stable elements  $[E(i, j) < E_{TH}]$  with grey shade, and the elements with zero or negligible energy with white shade. Initially, all the elements of the lattice have zero energy. (a) The input energy is injected into the system through the cusp  $W_C$  altering its energy above  $E_{TH}$ . The cusp  $W_C$  here consists of only one element, the element at the centre of the lattice ( $i = n/2, j = n/2$ ). (b) The unstable element distributes four units of its energy to its four adjacent neighbours. Two of the neighbouring elements became unstable. (c) The two unstable elements further distribute their energy to return to stability. This way, the injected energy is distributed and redistributed throughout the lattice.

With analogy to the Earth, the system is spherical, meaning the elements belonging to the columns  $j = n$  and  $j = 1$  are adjacent neighbours. If the energy of any element belonging to the column  $j = n$  has crossed the threshold, one unit of its surplus energy is distributed to its neighbour element in column  $j = 1$  and vice versa. The dissipation of energy through the marginal grids is only applicable for the upper and lower marginal rows, not for the marginal left or marginal right columns. Open boundary condition has been considered for the marginal rows of the lattice. After a consecutive distribution and redistribution, when the released energy finally reaches the marginal upper [ $i = 1, j = (1 \text{ to } n)$ ] and lower [ $i = n, j = (1 \text{ to } n)$ ] grids, it transmits outside the system.

Figure 2 displays the state of the elements of the lattice after a consecutive energy injection, distribution, and redistribution. All the elements have a considerable amount of energy while some of them become unstable. In Figure 2(a), in the marginal rows, two of the elements are unstable in both the upper and lower grids. In the next Figure 2(b), the unstable elements in the marginal rows dissipate their excess energy and a part of this energy is released outside the lattice, representing the magnetosphere-ionosphere energy transfer.

After the consecutive distribution and redistribution, the total internal accumulated energy of the lattice at any time  $t$  can be calculated as (Uritsky et al. 2001; Banerjee et al. 2015, 2019)

$$E_{\text{Total}} = \sum E(i, j) \text{ for all } i \text{ and } j \quad (9)$$

The number of unstable states, that is, elements having energy  $E > E_{TH}$  at any time  $t$  is estimated by the relation (Uritsky et al. 2001)

$$S_{UN} = \sum S_{ij} \text{ for all } i \text{ and } j \quad (10)$$

where  $S_{ij} = 1$  if  $E > E_{TH}$  and  $S_{ij} = 0$  if  $E < E_{TH}$

The upper and the lower grids can be considered as the northern and southern polar cusps of the Earth while the energy transfer process is similar to magnetosphere-ionosphere energy coupling. In the actual measurement of the AE index, all the magnetometer stations are located in the northern hemisphere for recording the associated data. Following this instance, we too considered and based our calculations on the total excess energy dissipating only through the upper grid [ $i = 1, j = (1 \text{ to } n)$ ] of the lattice. We denote  $T_R$  as the time delay between the initial energy injection to the model and the beginning of the energy transfer through the upper marginal grid.  $T_R$  estimates the total time for the energy to reach the boundary after successive distribution and redistribution processes for each input injection. The total amount of released energy outside the lattice at any time  $t$  can be estimated as (Banerjee et al. 2019)

$$E_R = \sum E(i, j) \text{ for } i = 1, j = (1 \text{ to } n) \quad (11)$$

The released energy generates two currents,  $I_W$  and  $I_E$ , the numerical equivalents of the auroral westward and eastward currents in the ionosphere, respectively. The auroral electrojet is estimated as the difference value of these two currents. For the calculation of electrojets, we considered the dissipated energy from any element belonging to the odd columns, that is,  $j = 1, 3, 5, \dots, (n-1)$  are contributing to the westward electrojet while the energy from any element belonging to the even columns, that is,  $j = 2, 4, 6, \dots, n$  are contributing to the eastward electrojet. Thus, mathematically

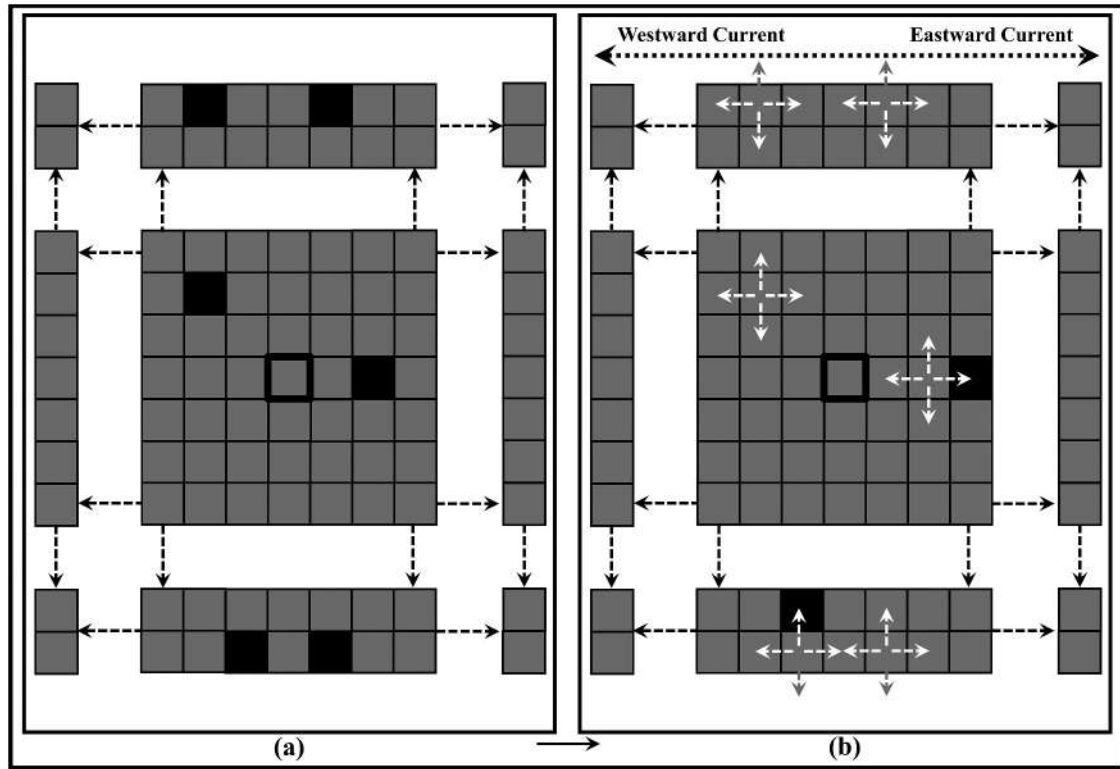


**Figure 2.** The state of the elements of the lattice after a consecutive energy injection, distribution, and redistribution. The unstable elements  $[E(i, j) > E_{TH}]$  are marked with black shade, the stable elements  $[E(i, j) < E_{TH}]$  with grey shade and the elements. All the elements have a considerable amount of energy while some of them become unstable. (a) In the marginal rows, two of the elements are unstable in both the upper and lower grids. (b) The unstable elements in the marginal rows dissipate their excess energy and a part of this energy is released outside the lattice, representing the magnetosphere-ionosphere energy transfer.

$$E_w(t) = \sum E(i, j) \text{ for } i = 1, j = 1, 3, 5, \dots, (n-1) \quad (12)$$

and

$$E_e(t) = \sum E(i, j) \text{ for } i = 1, j = 2, 4, 6, \dots, n \quad (13)$$

As the distribution process continues, more and more excess energy piles up outside the boundary regions of the lattice. The series  $E_w(t)$  and  $E_e(t)$  are the estimations of the total accumulated energy released in the ionosphere responsible for the westward and eastward electrojet currents, respectively. The released energy takes time to completely dissipate through the current system in the ionosphere and a part of this energy remains stored in the ionosphere. During the next magnetosphere-ionosphere energy transfer, this stored energy from the previous transfer acts as a base value and adds up with the newly released value of energy. Here, we introduce a parameter, namely  $K_A$  which determines the remaining part of the released energy of the previous transfer, stored in the ionosphere.  $K_A$  has a fractional value.

The remaining energy in the westward region is

$$E_{rw}(t) = K_A \times E_w(t-1) \quad (14)$$

whereas the remaining energy in the eastward region is

$$E_{re}(t) = K_A \times E_e(t-1) \quad (15)$$

Mathematically, the total westward energy at any time  $t$  is

$$E_{tw} = \sum [E_w(t) + E_{rw}(t)] \text{ for all } t \quad (16)$$

and the total eastward energy at any time  $t$  is

$$E_{te} = \sum [E_e(t) + E_{re}(t)] \text{ for all } t \quad (17)$$

These two energy components,  $E_{tw}(t)$  and  $E_{te}(t)$  then drive two currents in the opposite direction throughout the auroral region, namely the westward electrojet current and the eastward electrojet current, respectively.

The maximum westward electrojet current can be considered as

$$I_W = \sqrt{E_{tw}} \quad (18)$$

and the maximum eastward electrojet current as

$$I_E = \sqrt{E_{te}} \quad (19)$$

The differential value of these two components is

$$E_N = \text{abs}(I_E - I_W) \quad (20)$$

For further refinement,  $E_N$  is processed by a filter and labelled as  $E_A$ . Finally, the output time-series  $E_A$  can be regarded as a numerical representation of the natural auroral electrojet index, AE.

For our analysis, we used the hourly averaged AE index, solar wind ion density, flow speed, and  $B_Z$  component of the interplanetary magnetic field (IMF) data from the year 1997 to the year 2007 of the 23<sup>rd</sup> solar cycle. The dimension of the lattice is  $50 \times 50$ . Similar to our original study of the model (Banerjee et al. 2015), the numerical value of the various variables of the model are taken as  $K = 0.0025$ , local dissipation term  $E_d = 0.05$ ,  $K_d = 0.5$  for southward direction, and  $K_d = 0.005$  for northward direction. The input to the model is estimated using equation 1.

### 2.1. Data source

Here we used the hourly averaged AE index, solar wind ion density, flow speed, and  $B_Z$  component of the interplanetary magnetic field (IMF) data from the year 1997 to the year 2007 of the 23<sup>rd</sup> solar cycle as extracted from NASA/GSFC's OMNI data set through OMNIWeb. The OMNI data were obtained from the GSFC/SPDF OMNIWeb interface at <http://omniweb.gsfc.nasa.gov> (King & Papitashvili 2005).

### 3. Result and discussions

The threshold excitation  $E_{TH}$  is crucial for the central characteristics of a SOC system as it allows the existence of multiple metastable states across which the avalanches are carried out throughout the system. The potential energy  $E$  of any element in the lattice is analogical to the slope of an actual sandpile. An unstable element having energy  $E(i, j) > E_{TH}$  releases four units of energy to return to stability. Thus, a minimum value of  $E_{TH} = 5$  is required to keep the potential energy of the element at a positive non-zero value and to avoid the total internal energy of the system reaching zero or negative energy states at any time. To analyse the dynamical behaviour of the

system, the model is subjected to three different  $E_{TH}$  values,  $E_{TH} = 5$ ,  $E_{TH} = 7$ , and  $E_{TH} = 9$ . After the energy injection and distribution, the total accumulated internal energy of the lattice,  $E_{Total}$ , the total number of unstable states,  $S_{UN}$ , and the total amount of released energy,  $E_R$  at any time  $t$  can be calculated according to Equations 9, 10, and 11 respectively. Figure 3 illustrates the time vs.  $E_{Total}$  plot for the three values of  $E_{TH}$  for the year 2002. As the threshold value increases, the rate of energy distribution and dissipation decreases while the total internal energy of the system continues to increase gradually. It takes much more time for the system to achieve a meta-stable state, delaying the SOC dynamics and avalanches throughout the lattice to form properly. As the rate of distribution reduces, the elements in the marginal grids start to store and release energy to the outside of the lattice far more lately, thus delaying the energy transfer process representing the magnetosphere-ionosphere energy coupling in the model. We denote  $T_R$  as the time delay between the initial energy injection to the model and the beginning of energy transfer through the upper marginal grid. It is observed from the analysis, that the value of  $T_R$  is  $T_R = 1434$  hours for  $E_{TH} = 5$ ,  $T_R = 1934$  hours for  $E_{TH} = 7$  and  $T_R = 2520$  hours for  $E_{TH} = 9$ . Thus, for further analysis of the system, we considered  $E_{TH} = 5$  as the value for the excitation threshold. Figure 5(b), the plot for the simulated time-series  $E_A$ , shows the estimation of  $E_A$  initiating from the value of  $T_R = 1434$  hours for  $E_{TH} = 5$  as from this value of  $T_R$  the marginal grid starts to release energy outside the system.

Figure 4 demonstrates the plots for  $dE$ ,  $E_{Total}$ ,  $S_{UN}$ , and  $E_R$  for the September–October period of the year 2002. As seen from the figure,  $dE$  has large values for the marked timeline. The injected energy piles up in the lattice increasing the number of unstable states  $S_{UN}$ , the total energy of the lattice,  $E_{Total}$ , reaches a critical point and then gradually returns to

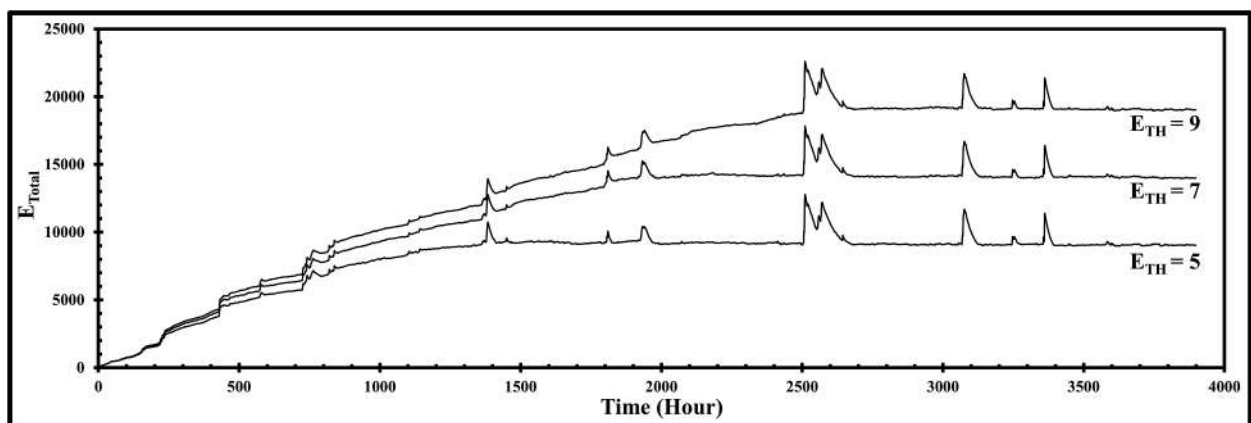


**Figure 3.** Time vs.  $E_{Total}$  plot for the three values of  $E_{TH}$  for the year 2002. As the threshold value increases, the rate of energy distribution and dissipation decreases while the total internal energy of the system continues to increase gradually. It takes much more time for the system to achieve a meta-stable state.

a metastable state by releasing a burst of avalanches. The avalanches take a time to reach the upper marginal grid through successive distribution and redistribution processes, thus  $E_R$  shows high-energy values dissipating from the upper grid after a while.

After the injection of the energy followed by subsequent distribution and redistribution, the model output  $E_A$  is generated estimating the released energy outside the lattice as discussed in the method section. The output series  $E_A$  is the numerical representation of the natural AE index. The power spectral density (PSD) of the simulated output  $E_A$  is calculated and plotted in a log–log graph. The plot demonstrates the characteristic  $1/f^\beta$  behaviour of the natural AE fluctuations along with the spectral break at  $f_0$ . A detailed study of the plot revealed the value of breakpoint  $f_0$  as  $f_0 = 0.050$  mHz (5.5 hours), as shown in Figure 7(b). A power law is fitted separately in both the high ( $f > f_0$ ) and low frequency ( $f < f_0$ ) regions of the plot to determine the power-law coefficients (slope of the spectral response)  $\beta_A$  and  $\beta_B$ , respectively. Now keeping the other parameter constant, if the value of  $K_A$  is varied in the range of 0.10 to 1.00, the  $\beta$  values also vary within ranges. As, for a particular value of  $K_A$ , the

$\beta$  values of the simulated series closely match with that of the natural AE index, they are noted down along with the value of  $K_A$ , as shown in Table 1. The  $\beta$  values of the real-time AE index are also displayed in Table 1 for a comparative study.

Figure 5(a,b) are the time series of the natural AE index and the simulated  $E_A$  series of the year 2002, respectively. For comparative purposes, a magnified portion of the natural AE index and that of the simulated  $E_A$  series of the year 2002 are displayed in Figure 6(a, b), respectively. The real-time AE index is estimated as the difference value of AU and AL indices where the AU and AL indices are the direct measurements of the maximum eastward and westward electrojet currents. (Ahn et al., 2000b) studied the variation pattern of the yearly mean AL index and AU index for 20 years and suggested their absolute values are proportional to each other. The maximum is observed for the AU index in summer while for the AL index, it is in equinoctial months. Both the indices exhibit higher values in the descending phase of the solar cycle (Ahn et al., 2000b). In the current model, the simulated AE index is estimated following the same relation as the difference value between the maximum eastward and

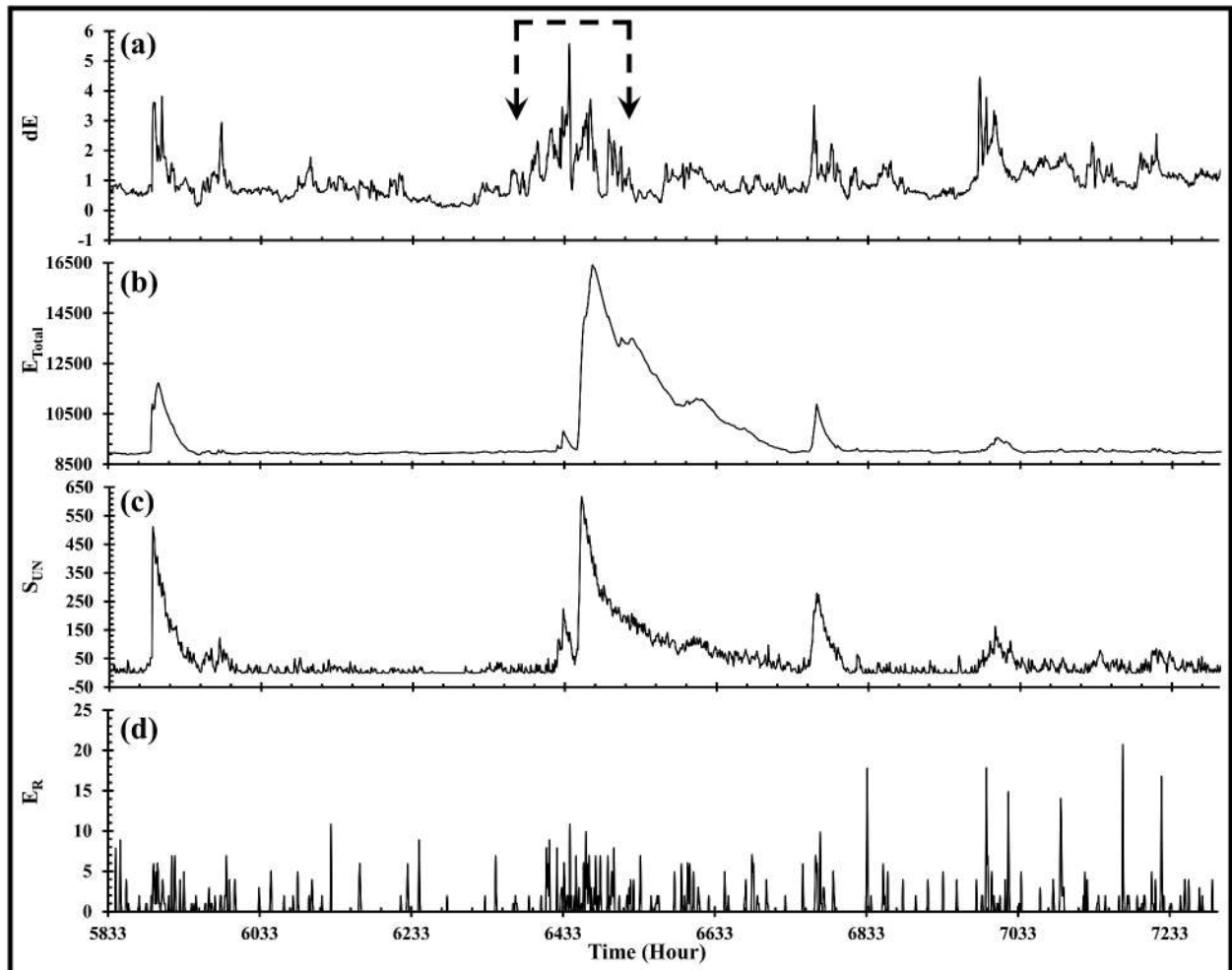


**Figure 4.** Plots for the September–October period of the year 2002 (a) Input energy,  $dE$  (b) the total accumulated internal energy of the lattice,  $E_{Total}$  (c) the total number of unstable states,  $S_{UN}$ , and (d) the total amount of released energy,  $E_R$ .

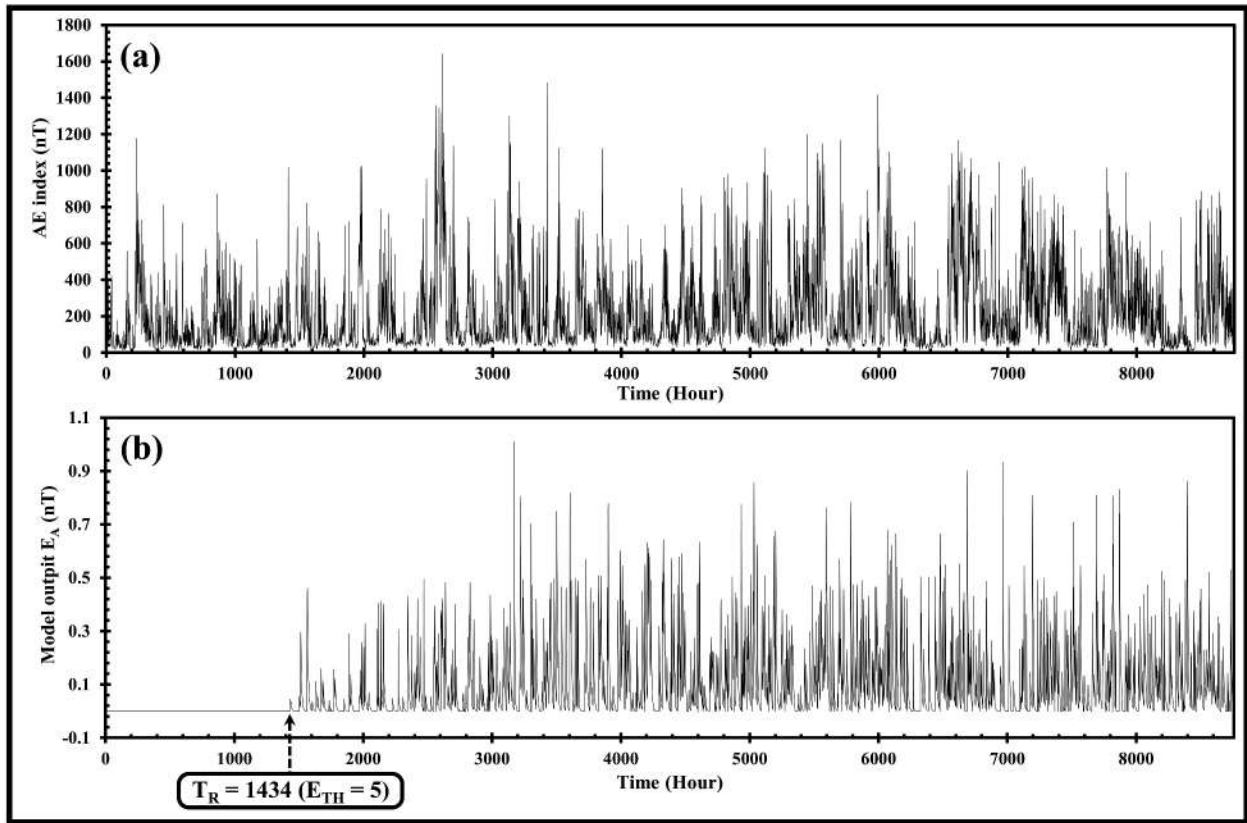


**Figure 5.** (a) The time-series of the natural AE index of the year 2002 (b) The simulated model output time-series,  $E_A$  of the year 2002.  $T_R = 1434$  hours for  $E_{TH} = 5$  is the time delay between the initial energy injection to the model and the starting of energy transfer through the upper marginal grid.

**Table 1.** The power-law coefficients (slope of the spectral response) of the power spectral density associated with the real-time AE index and the simulated model output  $E_A$  for all the years of the 23<sup>rd</sup> solar cycle. The spectral break is at  $f_0 = 0.050$  mHz (5.5 hours).  $\beta_A$  denotes the value of the slope for  $f > f_0$  and  $\beta_B$  denotes the value of the slope for  $f < f_0$ . The parameter  $K_A$  is associated with the series  $E_A$  and shows different values for different years.

Year	Real-Time AE Index Series		$K_A$	Model Output $E_A$ Series	
	$\beta_A$	$\beta_B$		$\beta_A$	$\beta_B$
1997	$2.366 \pm 0.103$	$1.009 \pm 0.046$	0.82	$2.389 \pm 0.126$	$0.945 \pm 0.068$
1998	$2.464 \pm 0.111$	$1.066 \pm 0.046$	0.70	$2.229 \pm 0.105$	$0.961 \pm 0.062$
1999	$2.383 \pm 0.104$	$0.933 \pm 0.043$	0.70	$2.359 \pm 0.125$	$0.950 \pm 0.063$
2000	$2.130 \pm 0.101$	$1.007 \pm 0.046$	0.74	$2.325 \pm 0.102$	$0.963 \pm 0.057$
2001	$2.276 \pm 0.102$	$1.035 \pm 0.043$	0.70	$2.282 \pm 0.115$	$1.023 \pm 0.065$
2002	$2.170 \pm 0.109$	$0.985 \pm 0.045$	0.73	$2.372 \pm 0.120$	$0.955 \pm 0.065$
2003	$2.060 \pm 0.100$	$0.914 \pm 0.043$	0.68	$2.248 \pm 0.128$	$0.964 \pm 0.067$
2004	$2.285 \pm 0.109$	$0.979 \pm 0.044$	0.74	$2.210 \pm 0.128$	$0.985 \pm 0.065$
2005	$2.218 \pm 0.108$	$0.990 \pm 0.043$	0.72	$2.222 \pm 0.125$	$0.962 \pm 0.065$
2006	$2.499 \pm 0.107$	$1.006 \pm 0.044$	0.77	$2.226 \pm 0.123$	$0.962 \pm 0.069$
2007	$2.183 \pm 0.103$	$0.902 \pm 0.043$	0.78	$2.352 \pm 0.112$	$0.953 \pm 0.067$

westward electrojets. In Figure 5, the May–June summer months of the year 2002 is the period for about the time, Time = 2800 hours – 4200 hours. As can be seen from Figure 5(a), the values of the real-time AE index are in the higher ranges for these months. The simulated series in Figure 5(b) also demonstrates the same. Again, in Figure 5, the period of about the time, Time = 5800 hours – 6600 hours marks the equinoctial month of September. Here, also the values of the simulated series of Figure 5(b) show higher values, similarly to the real-time AE index, as shown in Figure 5(a).

Figure 7(a, b) illustrate the log–log plot of the PSD of the real-time AE index and the simulated  $E_A$  series of the year 2002, respectively. It is observed from the plots that the simulated  $E_A$  series exhibits the characteristic  $1/f^\beta$  behaviour of the natural AE fluctuations along with the spectral break at  $f_0$ . As can be seen from Figure 7(b), for the value of  $K_A = 0.73$ , the simulated series has values  $\beta_A = -2.372 \pm 0.120$  and  $\beta_B = -0.955 \pm 0.065$  which nearly matches the values  $\beta_A = -2.170 \pm 0.109$  and  $\beta_B = -0.985 \pm 0.045$  of the natural AE fluctuations. The spectral point and the

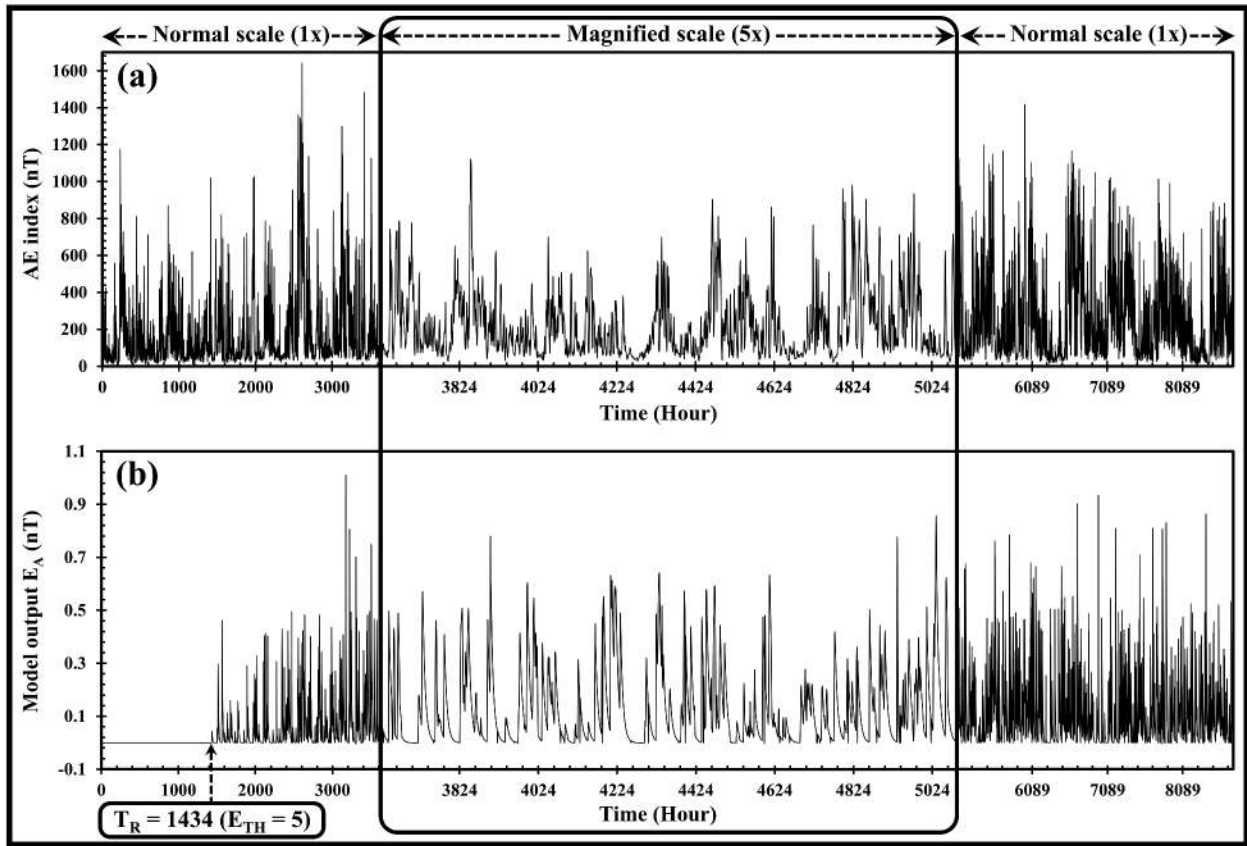


Figure 6. (a) The magnified version of the time-series of the natural AE index of the year 2002 (b) The magnified version of the simulated model output time-series,  $E_A$  of the year 2002.

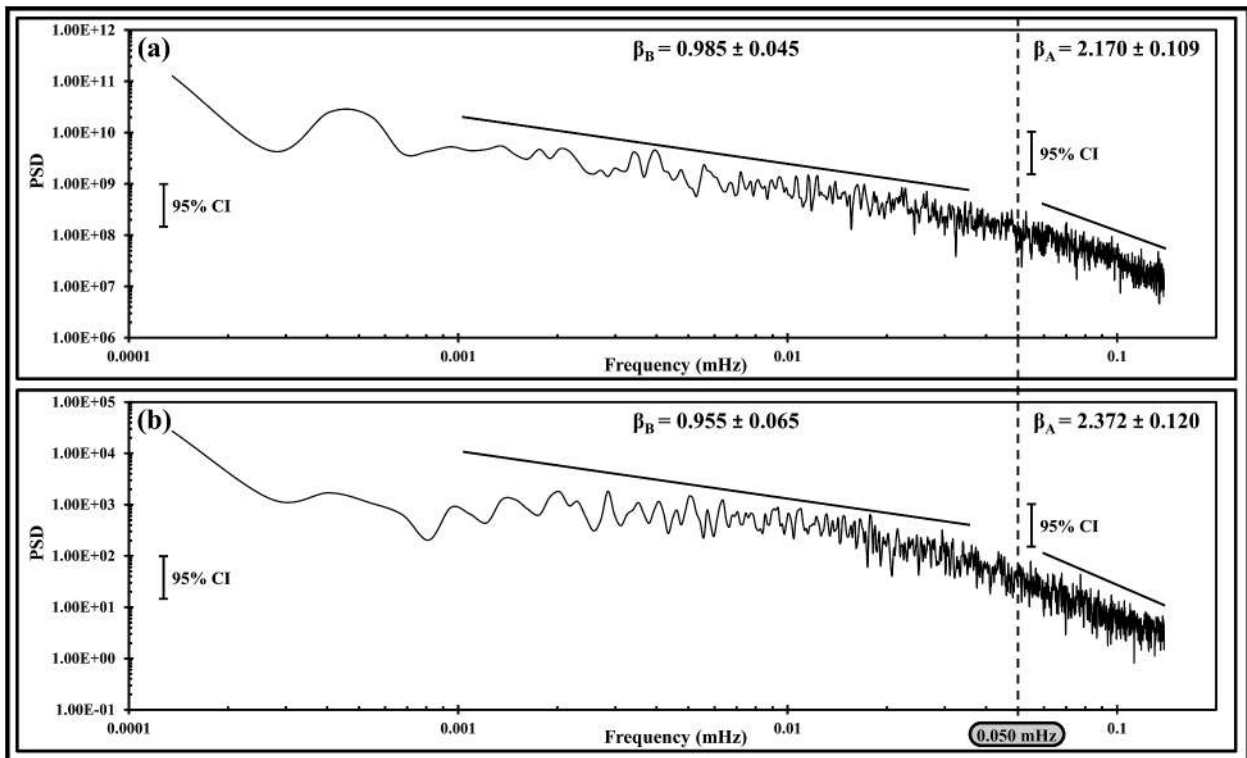


Figure 7. (a) The log-log plot of the power spectral density (PSD) of the real-time AE index of the year 2002. The  $\beta$  values of the series are estimated as  $\beta_A = -2.170 \pm 0.109$  and  $\beta_B = -0.985 \pm 0.045$  with a spectral break at  $f_0 = 0.050$  mHz (5.5 hours). (b) The log-log plot of the power spectral density (PSD) simulated model output  $E_A$  of the year 2002. For the value of  $K_A = 0.73$ , the  $\beta$  values of the series are estimated as  $\beta_A = -2.372 \pm 0.120$  and  $\beta_B = -0.955 \pm 0.065$  with a spectral break at  $f_0 = 0.050$  mHz (5.5 hours).

slopes of the two frequency regions of the  $1/f^\beta$  power spectrum of the natural AE index had long been a study of keen interest. (Tsurutani et al. 1990) estimated the values of the slopes as  $\beta_A = 2.2$  and  $\beta_B = 0.98$  with a breakpoint at  $f_0 = 0.050$  mHz (5.5 hours) for the hourly average AE data of the period of years 1971–1974. (Uritsky and Pudovkin 1998b) found out the values as  $\beta_A = 2.10$  and  $\beta_B = 0.95$  with a breakpoint at  $f_0 = 0.055$  mHz (5 hours) for the hourly average AE data of the period of years 1973–1974. (Woodard et al. 2005) compared all the prominent studies (Tsurutani et al. 1990; Consolini et al. 1996; Uritsky and Pudovkin 1998b; Price and Newman 2001; Watkins 2002) investigating the slopes of the two spectral regions and breakpoint of natural AE fluctuations and concluded the values of slopes as  $\beta_A = 2.4 \pm 0.26$  and  $\beta_B = 1.0 \pm 0.10$ . It is observed from Table 1 that for a particular value of the parameter  $K_A$ , the  $\beta$  values of the simulated series  $E_A$  are estimated as  $\beta_A = 2.2$ – $2.4$  and  $\beta_B = 0.9$ – $1.0$  with a spectral break at  $f_0 = 0.050$  mHz (5.5 hours), the typical values associated with natural AE index as reported by all these previous works.

The parameter  $K_A$  plays a significant role in estimating the simulated  $E_A$  series from the total released energy. As observed from Table 1, for a particular year and a particular value of  $K_A$ , the  $\beta$  values of the simulated output series  $E_A$  are in the specified ranges of the same associated with the natural AE index. For the entire 23<sup>rd</sup> solar cycle, the value of  $K_A$  is in the range of  $K_A = 0.68$ – $0.82$ . It is observed from the result, that the transferred solar wind energy does not dissipate completely through the westward and eastward auroral electrojet currents in an instant, rather a significant part of it remains present in the ionosphere even in the time of the next magnetosphere-ionosphere energy transfer. The parameter  $K_A$  has a fractional value. As can be seen in equations (14) and (15),  $K_A$  is denoting the remaining fraction of the total accumulated released energy of the previous state, reserved in the ionosphere. The excess energy transferred from the magnetosphere to the ionosphere is then being added up with this base value and forms the westward and eastward currents that are the two key factors for measuring the AE index.

The magnetosphere-ionosphere energy transfer and the stored part of this energy in the ionosphere are primarily controlled by the solar wind injection into the magnetosphere. Again, the amount of injected solar wind energy in the magnetosphere varies with the intensity, and duration of solar wind-magnetosphere coupling. Also, the solar cycle has a significant effect on energy injection. During solar storms, there is a large deposit of energy into the magnetosphere which changes the normal quiet time dynamics of the magneto-ionosphere system. Figure 4 illustrates such a case of a large amount of solar wind

injection into the magnetosphere. As shown in Figure 4(a), the marked period in the figure is distinguished by the continuous injection of a large amount of energy  $dE$  into the magnetosphere for hours. Consequently, the total accumulated energy of the lattice,  $E_{Total}$ , gradually starts to pile up in the system, altering its state of equilibrium. The value of the number of unstable states,  $S_{UN}$ , also increases indicating the instability formation in the lattice. Figure 4(b, c) show the plots for  $E_{Total}$  and  $S_{UN}$ , respectively. As the large values of energy injection continue,  $E_{Total}$  finally reaches a critical point and the pile collapses. The excess energy is released as a burst of avalanches inside the lattice restoring the stability of the system. After the successive distribution and redistribution process, the excess energy of the lattice is finally transferred outside its boundary region representing the magnetosphere-ionosphere energy transfer. As seen from Figure 4(d), the amount of released energy  $E_R$  increases after a while as a consequence of the continuous injection of large values of  $dE$  in the magnetosphere. The released energy in the ionosphere is dissipated through the auroral electrojets, the field-aligned currents flowing between the nightside magnetosphere and nightside ionosphere. But it takes time to completely dissipate through the current system in the ionosphere and a part of this energy remains stored in the ionosphere. The factor  $K_A$  estimates the amount of this stored energy.

As observed from the result, for the entire 23<sup>rd</sup> solar cycle, the value of  $K_A$  is slightly varying,  $K_A = 0.68$ – $0.82$ . In the model, the parameter  $K_A$  does not estimate the actual value of the stored energy, rather it indicates the percentage value of the transferred energy that remains stored in the ionosphere. As shown in Table 1, the value of  $K_A$  for the year 2002 is  $K_A = 0.73$ . This value indicates, at any current state  $t$ , 73% of the transferred energy of the previous state ( $t-1$ ), remains stored in the ionosphere. Thus, the transmitted energy does not dissipate instantly after each magnetosphere-ionosphere energy transfer, rather a substantial percentage (73%) of this energy remains reserved in the ionosphere during the next magnetosphere-ionosphere energy transfer. If the solar wind energy injection into the magnetosphere increases at any time  $t$ , the amount of total released energy in the ionosphere also increases for this  $t$ . Since  $K_A$  indicates the remaining percentage value of this released energy, the actual amount of the reserved energy in the ionosphere also increases as an effect of the large solar wind injection. Similarly, if the input injection is small, the amount of released energy decreases, decreasing the actual amount of reserved energy in the ionosphere. Thus, the actual amount of the reserved energy in the ionosphere varies with the variation in the intensity of injected solar wind in the magnetosphere and the parameter  $K_A$  represents its

percentage relationship with the total transferred energy. For the 23<sup>rd</sup> cycle, the value of  $K_A$  ranges between  $K_A = 0.68$ – $0.82$ , indicating that for each year, a substantial percentage of the transferred energy remains stored in the ionosphere.

#### 4. Conclusions

AE index is a global and instantaneous measurement of the magnetic fluctuations in the Earth's polar region in response to an external perturbation. In this paper, we developed a numerical cellular automata model of Earth's magnetosphere based on the concept of self-organised criticality and sandpile dynamics to study the complex dynamics of the magnetosphere-ionosphere energy transfer process and AE fluctuations. Our model is a dissipative, dynamical  $n \times n$  two-dimensional system of finite potential energy and open boundary conditions having the real-time values of solar ion density, flow speed, and IMF  $B_z$  as the input parameters. It is analogical to the Earth's magnetosphere while the upper and lower margins of the lattice can be considered as the north and south polar cusps of the Earth. The solar wind is a stream of energised plasma particles emitted from the outer atmosphere of the Sun. As the direction of IMF  $B_z$  is southward, a strong coupling occurs between the solar wind and terrestrial magnetosphere injecting a significant amount of solar wind energy into the geospace. Gradually, the energy piles up and reaches a self-organised critical condition after which adding up a small amount of energy into the pile can form a spatially localised magnetospheric instability. To maintain the equilibrium, the system redistributes itself and the excess energy is released as an outburst of avalanches of various sizes in the neighbouring regions. As long as there is local instability, the distribution process continues and successively spread over throughout the system, finally transmitting a large amount of energy into the ionosphere through the polar cusps. The transferred solar wind energy causes magnetic fluctuations in the auroral region and the AE index is the global measurement of the intensity of the fluctuations. In our proposed cellular automata model, the marginal grids of the lattice are equivalent to the polar cusps. The excess energy transferred through the upper grid of the lattice is measured and by some mathematical process a simulated time series has been derived which can be considered as a numerical representation of the real-time AE index.

The spectral response of the simulated output series  $E_A$  follows a  $1/f^\beta$  power law, demonstrates a breakpoint at  $f_0 = 0.050$  mHz (5.5 hours) having slopes  $\beta_A = 2.2$ – $2.4$  for  $f > f_0$  and  $\beta_B = 0.9$ – $1.0$  for

$f < f_0$ , the typical characteristics of natural AE index. It is observed that the parameter  $K_A$  plays a significant role in the entire process of forming a proper  $E_A$  time series estimated from the released energy.  $K_A$  represents the percentage of the released energy from the previous magnetosphere-ionosphere energy transfer, which remains stored in the ionosphere. Its value varies in a small range of  $K_A = 0.68$ – $0.82$  for the eleven years of the 23<sup>rd</sup> solar cycle, indicating a substantial percentage of the transferred energy remains reserved in the ionosphere for each year.

The excitation threshold  $E_{TH}$  is crucial in forming the SOC dynamics of the model. As an unstable element release four units of energy, for a small value of  $E_{TH}$ , the total internal energy of the system can achieve zero or negative potential for some of the values of  $t$ . In contrast, a large value of  $E_{TH}$  causes the piling up of solar wind energy in the system, reducing the rate of energy distribution as well as dissipation. The total internal energy of the system continues to increase gradually and the system takes a much larger time to achieve a metastable state and to form the SOC dynamics properly. Thus, a moderate value of  $E_{TH} = 5$  is optimum for the proposed model.

Overall, it can be concluded that our proposed model is a simple first-order avalanche model of the Earth's magnetosphere where the real-time solar parameters are the inputs. The model generates a simulated output series  $E_A$  which shows statistical similarity to the real-time AE index. Also, the parameter  $K_A$  varies over a small range of  $K_A = 0.68$ – $0.82$  which suggests a high percentage of the transferred solar wind energy remains reserved in the ionosphere. In our previous work (Banerjee et al. 2015) we presented a SOC-based cellular automata model and focused on the nature of solar wind-magnetosphere energy transfer and its subsequent effect in the magnetosphere. In continuation of this project, the current work is a further refinement of that model to study the magnetosphere-ionosphere energy transfer process. Future work can be focused to develop a composite cellular automata model of the magnetosphere to study all the intricate characteristics of the solar wind-magnetosphere-ionosphere dynamics.

#### Acknowledgements

We acknowledge the use of NASA/GSFC's Space Physics Data Facility's OMNIWeb (or CDAWeb or ftp) service, and OMNI data. We express our sincere gratitude to the National Research Institute of Astronomy and Geophysics, Egypt for their generous support regarding the arrangement of funding. We are also thankful to Parthasarathi Chakrabarti, Director, IEST, Shibpur, Howrah, India and Somnath Mukherjee, Principal of Dinabandhu Andrews



College, Kolkata, India for their encouragement and support for the present work. Finally, we would like to sincerely thank the anonymous reviewers for their most valuable comments and suggestions to improve the quality of this paper.

## Disclosure statement

No potential conflict of interest was reported by the author(s).

## References

- Ahn B-H, Kroehl HW, Kamide Y, Kihn EA. 2000a. Universal time variations of the auroral electrojet indices. *Journal of Geophysical Research: Space Physics*. 105(A1):267–275. doi:10.1029/1999ja900364.
- Ahn B-H, Kroehl HW, Kamide Y, Kihn EA. 2000b. Seasonal and solar cycle variations of the auroral electrojet indices. *J Atmos Sol-Terr Phys*. 62(14):1301–1310. doi:10.1016/s1364-6826(00)00073-0.
- Allen JH, Kroehl HW. 1975. Spatial and temporal distributions of magnetic effects of auroral electrojets as derived from AE indices. *J Geophys Res*. 80(25):3667–3677. doi:10.1029/ja080i025p03667.
- Antonova EE, Ganushkina NY. 2000. Inner magnetosphere currents and their role in the magnetosphere dynamics. *Physics and Chemistry of the Earth, Part C: Solar, Terrestrial & Planetary Science*. 25(1–2):23–26. doi:10.1016/s1464-1917(99)00028-8.
- Bak P, Tang C, Wiesenfeld K. 1987. Self-organized criticality: an explanation of the 1/f noise. *Phys Rev Lett*. 59(4):381–384. doi:10.1103/physrevlett.59.381.
- Bak P, Tang C, Wiesenfeld K. 1988. Self-organized criticality. *Phys Rev A*. 38(1):364–374. doi:10.1103/physreva.38.364.
- Banerjee A, Bej A, Chatterjee TN. 2011. On the existence of a long range correlation in the geomagnetic disturbance storm time (Dst) index. *Astrophys Space Sci*. 337(1):23–32. doi:10.1007/s10509-011-0836-1.
- Banerjee A, Bej A, Chatterjee TN. 2015. A cellular automata-based model of Earth's magnetosphere in relation with Dst index. *Space Weather*. 13(5):259–270. doi:10.1002/2014sw001138.
- Banerjee A, Bej A, Chatterjee TN, Majumdar A. 2019. An SOC approach to study the solar wind-magnetosphere energy coupling. *Earth and Space Science*. 6(4):565–576. doi:10.1029/2018ea000468.
- Bargatze LF, Baker DN, McPherron RL, Hones EW Jr. 1985. Magnetospheric impulse response for many levels of geomagnetic activity. *J Geophys Res*. 90(A7):6387. doi:10.1029/ja090ia07p06387.
- Baumjohann W. 1982. Ionospheric and field-aligned current systems in the auroral zone: a concise review. *Adv Space Res*. 2(10):55–62. doi:10.1016/0273-1177(82)90363-5.
- Borovsky JE, Valdivia JA. 2018. The earth's magnetosphere: a systems science overview and assessment. *Surveys in Geophysics*. 39(5):817–859. doi:10.1007/s10712-018-9487-x.
- Chang T. 1992. Low-dimensional behavior and symmetry breaking of stochastic systems near criticality—can these effects be observed in space and in the laboratory? *IEEE Trans Plasma Sci*. 20(6):691–694. doi:10.1109/27.199515.
- Chang T. 1999. Self-organized criticality, multi-fractal spectra, sporadic localized reconnections and intermittent turbulence in the magnetotail. *Phys Plasmas*. 6(11):4137–4145. doi:10.1063/1.873678.
- Chapman SC, Watkins NW, Dendy RO, Helander P, Rowlands G. 1998. A simple avalanche model as an analogue for magnetospheric activity. *Geophys Res Lett*. 25(13):2397–2400. doi:10.1029/98gl51700.
- Chen J, Sharma AS. 2006. Modeling and prediction of the magnetospheric dynamics during intense geospace storms. *J Geophys Res*. 111(A4). doi:10.1029/2005ja011359.
- Cliver EW, Kamide Y, Ling AG. 2000. Mountains versus valleys: semiannual variation of geomagnetic activity. *Journal of Geophysical Research: Space Physics*. 105(A2):2413–2424. doi:10.1029/1999ja900439.
- Consolini G (1997). Sandpile cellular automata and magnetospheric dynamics. In Aiello S, et al (Eds.), *Conference Proceedings “Cosmic Physics in the Year 2000”* (Vol. 58, pp. 123–126). SIF, Bologna, Italy.
- Consolini G, Lui ATY. 1999. Sign-singularity analysis of current disruption. *Geophys Res Lett*. 26(12):1673–1676. doi:10.1029/1999gl900355.
- Consolini G, Marcucci MF, Candidi M. 1996. Multifractal structure of auroral electrojet index data. *Phys Rev Lett*. 76(21):4082–4085. doi:10.1103/physrevlett.76.4082.
- Davis TN, Sugiura M. 1966. Auroral electrojet activity index AE and its universal time variations. *J Geophys Res*. 71(3):785–801. doi:10.1029/jz071i003p00785.
- Dobias P, Wanliss JA. 2009. Intermittency of storms and substorms: is it related to the critical behaviour? *Ann Geophys*. 27(5):2011–2018. doi:10.5194/angeo-27-2011-2009.
- Gavrishchaka VV, Ganguli SB. 2001. Optimization of the neural-network geomagnetic model for forecasting large-amplitude substorm events. *Journal of Geophysical Research: Space Physics*. 106(A4):6247–6257. doi:10.1029/2000ja900137.
- Gleisner H, Lundstedt H. 1997. Response of the auroral electrojets to the solar wind modeled with neural networks. *Journal of Geophysical Research: Space Physics*. 102(A7):14269–14278. doi:10.1029/96ja03068.
- Gleisner H, Lundstedt H. 2001. Auroral electrojet predictions with dynamic neural networks. *Journal of Geophysical Research: Space Physics*. 106(A11):24541–24549. doi:10.1029/2001ja900046.
- Goertz CK, Shan L-H, Smith RA. 1993. Prediction of geomagnetic activity. *Journal of Geophysical Research: Space Physics*. 98(A5):7673–7684. doi:10.1029/92ja01193.
- Hernandez JV, Tajima T, Horton W. 1993. Neural net forecasting for geomagnetic activity. *Geophys Res Lett*. 20(23):2707–2710. doi:10.1029/93gl02848.
- Kamide Y, Kokubun S. 1996. Two-component auroral electrojet: importance for substorm studies. *Journal of Geophysical Research: Space Physics*. 101(A6):13027–13046. doi:10.1029/96ja00142.
- Kamide Y, Rostoker G. 2004. What is the physical meaning of the AE index? *Eos, Transactions American Geophysical Union*. 85(19):188. doi:10.1029/2004eo190010.
- King JH, Papitashvili NE. 2005. Solar wind spatial scales in and comparisons of hourly wind and ACE plasma and magnetic field data. *J Geophys Res*. 110(A2). doi:10.1029/2004ja010649.
- Klimas AJ, Baker DN, Roberts DA, Fairfield DH, Büchner J. 1992. A nonlinear dynamical analogue model of geomagnetic activity. *J Geophys Res*. 97(A8):12253. doi:10.1029/92ja00794.

- Klimas AJ, Baker DN, Vassiliadis D, Roberts DA. 1994. Substorm recurrence during steady and variable solar wind driving: evidence for a normal mode in the unloading dynamics of the magnetosphere. *J Geophys Res.* 99 (A8):14855. doi:10.1029/94ja01240.
- Klimas AJ, Valdivia JA, Vassiliadis D, Baker DN, Hesse M, Takalo J. 2000. Self-organized criticality in the substorm phenomenon and its relation to localized reconnection in the magnetospheric plasma sheet. *Journal of Geophysical Research: Space Physics.* 105(A8):18765–18780. doi:10.1029/1999ja000319.
- Li X, Oh KS, Temerin M. 2007. Prediction of the AL index using solar wind parameters. *Journal of Geophysical Research: Space Physics.* 112(A6):n/a–n/a. doi:10.1029/2006ja011918.
- Lu JY, Liu Z-Q, Kabin K, Jing H, Zhao MX, Wang Y. 2013. The IMF dependence of the magnetopause from global MHD simulations. *Journal of Geophysical Research: Space Physics.* 118(6):3113–3125. doi:10.1002/jgra.50324.
- Luo B, Li X, Temerin M, Liu S. 2013. Prediction of the AU, AL, and AE indices using solar wind parameters. *Journal of Geophysical Research: Space Physics.* 118 (12):7683–7694. doi:10.1002/2013ja019188.
- Lyatsky W, Newell PT, Hamza A. 2001. Solar illumination as cause of the equinoctial preference for geomagnetic activity. *Geophys Res Lett.* 28(12):2353–2356. doi:10.1029/2000gl012803.
- McPherron RL, Rostoker G. 1993. Comment on “Prediction of geomagnetic activity” by C. K. Goertz, Lin-Hua Shan, and R. A. Smith. *Journal of Geophysical Research: Space Physics.* 98(A5):7685–7686. doi:10.1029/92ja01194.
- McPherron RL, Russell CT, Aubry MP. 1973. Satellite studies of magnetospheric substorms on August 15, 1968: 9. Phenomenological model for substorms. *J Geophys Res.* 78(16):3131–3149. doi:10.1029/ja078i016p03131.
- Nakamura M, Yoneda A, Oda M, Tsubouchi K. 2015. Statistical analysis of extreme auroral electrojet indices. *Earth, Planets and Space.* 67(1). doi:10.1186/s40623-015-0321-0.
- Nishida A. 2000. The Earth's dynamic magnetotail. *Space Sci Rev.* 91(3/4):507–577. doi:10.1023/A:1005223124330
- Price CP, Newman DE. 2001. Using the R/S statistic to analyze AE data. *J Atmos Sol-Terr Phys.* 63 (13):1387–1397. doi:10.1016/s1364-6826(00)00240-6.
- Pulkkinen A, Klimas A, Vassiliadis D, Uritsky V. 2006. Role of stochastic fluctuations in the magnetosphere-ionosphere system: a stochastic model for the AE index variations. *J Geophys Res.* 111(A10). doi:10.1029/2006ja011661.
- Pulkkinen TI, Tanskanen EI, Viljanen A, Partamies N, Kauristie K. 2011. Auroral electrojets during deep solar minimum at the end of solar cycle 23. *Journal of Geophysical Research: Space Physics.* 116(A4):n/a–n/a. doi:10.1029/2010ja016098.
- Rostoker G. 1972. Geomagnetic indices. *Reviews of Geophysics.* 10(4):935. doi:10.1029/rg010i004p00935.
- Rostoker G (2002), Why we have not yet solved the substorm problem, in Sixth International Conference on Substorms, edited by Winglee RM, pp. 1–8. University of Washington, Seattle.
- Russell CT. 2001. Solar wind and interplanetary magnetic field: a tutorial. In: *Space Weather* (eds P. Song, H. J. Singer and G. L. Siscoe). p. 73–89. doi:10.1029/gm125p0073.
- Russell CT, McPherron RL. 1973. Semiannual variation of geomagnetic activity. *J Geophys Res.* 78(1):92–108. doi:10.1029/ja078i001p00092.
- Sitnov MI, Sharma AS, Papadopoulos K, Vassiliadis D, Valdivia JA, Klimas AJ, Baker DN. 2000. Phase transition-like behavior of the magnetosphere during substorms. *Journal of Geophysical Research: Space Physics.* 105(A6):12955–12974. doi:10.1029/1999ja000279.
- Strangeway RJ. 2013. The relationship between magnetospheric processes and auroral field-aligned current morphology. In: *Geophysical monograph series.* American Geophysical Union; p. 355–364. doi:10.1029/2012gm001211
- Takalo J, Timonen J, Klimas A, Valdivia J, Vassiliadis D. 1999. Nonlinear energy dissipation in a cellular automaton magnetotail field model. *Geophys Res Lett.* 26 (13):1813–1816. doi:10.1029/1999gl900429.
- Temerin M, Li X. 2002. A new model for the prediction of Dst on the basis of the solar wind. *Journal of Geophysical Research: Space Physics.* 107(A12):31–8. doi:10.1029/2001ja007532.
- Temerin, M., & Li, X. 2006. DST model for 1995–2002. *Journal of Geophysical Research.* 111(A4). doi:10.1029/2005ja011257
- Tsurutani BT, Sugiura M, Iyemori T, Goldstein BE, Gonzalez WD, Akasofu SI, Smith EJ. 1990. The nonlinear response of AE to the IMF BSdriver: a spectral break at 5 hours. *Geophys Res Lett.* 17(3):279–282. doi:10.1029/gl017i003p00279.
- Uritsky VM (1996). 1/f-like spectra of geomagnetic fluctuations: expression of self-organized criticality? In *Book of abstracts of the International Conference on Problems of Geocosmos, St. Petersburg (Russia).* June 17–23, (p. 110).
- Uritsky VM, Pudovkin MI. 1998a. Fractal dynamics of AE-index of geomagnetic activity as a marker of the self-organized criticality in the magnetosphere (in Russian). *Geomagnetizm iAeronomia.* 38(3):17–28.
- Uritsky VM, Pudovkin MI. 1998b. Low frequency 1/f-like fluctuations of the AE-index as a possible manifestation of self-organized criticality in the magnetosphere. *Ann Geophys.* 16(12):1580–1588. doi:10.1007/s00585-998-1580-x.
- Uritsky VM, Pudovkin MI, Steen A. 2001. Geomagnetic substorms as perturbed self-organized critical dynamics of the magnetosphere. *Journal of Atmospheric and Solar-Terrestrial Physics.* 63(13):1415–1424. doi:10.1016/S1364-6826(00)00243-1.
- Uritsky VM, Semenov VS. 2000. A sandpile model for global statistics of reconnection events in the magnetotail. In: Biernat HK, Farrugia CJ, Vogl DF, editors. *The solar wind - magnetosphere system* (Vol. 3). Wien: Osterreichische Akademie der Wissenschaften; p. 299–308.
- Vassiliadis D, Angelopoulos V, Baker DN, Klimas AJ. 1996. The relation between the northern polar cap and auroral electrojet geomagnetic indices in the wintertime. *Geophys Res Lett.* 23(20):2781–2784. doi:10.1029/96gl02575.
- Vassiliadis D, Klimas AJ, Baker DN, Roberts DA. 1995. A description of the solar wind-magnetosphere coupling based on nonlinear filters. *Journal of Geophysical Research: Space Physics.* 100(A3):3495–3512. doi:10.1029/94ja02725.

- Vennerstrøm S, Friis-Christensen E, Troshichev OA, Andersen VG. 1991. Comparison between the polar cap index, PC, and the auroral electrojet indices AE, AL, and AU. *J Geophys Res.* 96(A1):101. doi:[10.1029/90ja01975](https://doi.org/10.1029/90ja01975).
- Watkins NW. 2002. Scaling in the space climatology of the auroral indices: is SOC the only possible description? *Nonlinear Process Geophys.* 9(5/6):389–397. doi:[10.5194/npg-9-389-2002](https://doi.org/10.5194/npg-9-389-2002).
- Weigel RS. 2003. Solar wind coupling to and predictability of ground magnetic fields and their time derivatives. *J Geophys Res.* 108(A7). doi:[10.1029/2002ja009627](https://doi.org/10.1029/2002ja009627).
- Woodard R, Newman DE, Sánchez R, Carreras BA. 2005. On the identification of soc dynamics in the sun-earth system. In *Multiscale coupling of sun-earth processes*. Edited by Lui ATY, Kamide Y, Consolini G. p. 55–68. Elsevier Science BV; doi:[10.1016/b978-044451881-1/50005-8](https://doi.org/10.1016/b978-044451881-1/50005-8).

2018

0

2018

● Cited documents ● Uncited documents



1

0

2018

### NRIAG Journal of Astronomy and Geophysics

Not yet assigned quartile

SJR 2022

0



powered by scimagojr.com

← Show this widget in your own website

Just copy the code below and paste within your html code:

```
<a href="https://www.scimagojr.com" data-bbox="788 714 970 759">
```



# One-hour ahead prediction of the Dst index based on the optimum state space reconstruction and pattern recognition

Amaresh Bej<sup>1</sup>, Adrija Banerjee<sup>1,a</sup> , T. N. Chatterjee<sup>2</sup>, Abhijit Majumdar<sup>1</sup>

<sup>1</sup> Department of Physics, Indian Institute of Engineering Science and Technology, Shibpur, P.O.-Botanic Garden, Howrah, West Bengal 711103, India

<sup>2</sup> Department of Electronics, Dinabandhu Andrews College, 54, Raja S.C. Mullick Road, Garia, Kolkata, West Bengal 700084, India

Received: 5 July 2021 / Accepted: 5 April 2022

© The Author(s), under exclusive licence to Società Italiana di Fisica and Springer-Verlag GmbH Germany, part of Springer Nature 2022

**Abstract** The Disturbance storm time (Dst) index is the global estimation of the intensity of the terrestrial geomagnetic activities as well as the primary indicator of the geomagnetic storm. As the adverse effect of a powerful geomagnetic event has become a serious threat to modern human society, extracting meaningful information concealed in the complex structures of this time series can form the ground of a successful prediction algorithm. In this paper, we introduce a new probabilistic model based on the concept of adaptive delta modulation and optimum state space to analyze, identify and characterize the patterns enfolded in the layers of the 1-h Dst index and then predict Dst data using these patterns. The study reveals some significant insights. The exact dimension  $M$  of the optimum state space for the Dst index is found to be at  $M = 10$ . Also, the series is a combination of multiple distinguished repeating and non-repeating patterns, denoting a high degree of predictability of the  $M$ th data of the series from its previous  $(M-1)$  binary data. Eventually, the simulated output of the probabilistic model exhibits a high value of correlation coefficient with the real-time Dst index. Interestingly, the technique only requires the Dst index data as an input of the probabilistic model and is found to be very effective for the entire 24th solar cycle.

## 1 Introduction

The disturbance storm time (Dst) index is an indication of the geomagnetic activities in the terrestrial magnetosphere and is frequently used in characterizing the intensity of geomagnetic storms. It is computed based on the average value of the horizontal component of the Earth's magnetic field recorded at four different observatories, namely Hermanus (34.40°S, 19.22°E in geographic latitude and longitude), Kakioka (36.23°N, 140.18°E), Honolulu (21.32°N, 158.02°W), and San Juan (18.01°N, 66.15°W) [1]. These stations are evenly spaced in longitude and near enough to the magnetic equator to nullify the influence of the auroral effect as much as possible, again also placed at a significant distance away from the magnetic equator to minimize the influence of the equatorial electrojet current flowing in the ionosphere [2, 3].

Severe geomagnetic activity poses a potential threat to modern human society as a powerful storm can wreak havoc by collapsing all the electrical systems in the affected area, including power grids, computer and communication networks, satellite and navigation systems, military intelligence, and so on. The phenomenon is a sequence of striking the Earth by an intense geomagnetic storm followed by the entering of a stream of charged plasma particles into the geospace through the solar wind-magnetosphere reconnection that results in an induction of an electric field in the magnetosphere. As a consequence, voltage differences are generated between the ground points of the electrical networks that drive a current, namely geomagnetically induced current (GIC), flowing through the electrical hardware. The value of this GIC can be as high as 100 Ampere which is substantially beyond the specified range of tolerance of the electrical circuits causing fatal damages to the entire system [4]. Needless to say, our modern human society is almost entirely dependent on technology based on electrical power more than ever, thus a GIC-triggered catastrophic collapse of the electrical infrastructure in a large region includes enormous monetary losses, wastages of manpower, and prolonged unavoidable hazards. As an example, an intense geomagnetic storm on March 13, 1989, caused the entire Hydro Quebec system to get shut down resulting in more than 6 million customers surviving without electricity for nine hours [4, 5]. In 2003, the Wide Area Augmentation System (WAAS) operated by the Federal Aviation Administration (FAA) was affected by the Halloween solar storm and collapsed for approximately 30 h causing serious damages to many satellite systems including the Japanese ADEOS-2 satellite. In the past years, the Nordic countries along with the USA and Canada had faced unbearable consequences of geomagnetic storms, like the complete disruption of electric power-grids, hours of blackouts, damages of navigation as well as communication systems, disruption of satellite hardware and computer networks. In a report by the Oak Ridge National Laboratory, a geomagnetic storm, slightly stronger than March 1989 one, can result in an enormous blackout in the whole north-eastern area of the USA including a huge \$36 billion

<sup>a</sup> e-mail: [adrija\\_bnrj@yahoo.co.in](mailto:adrija_bnrj@yahoo.co.in) (corresponding author)

monetary loss in gross domestic product. [4, 6–9]. The perils of these intense geomagnetic storms, that occurred in the European countries in the last decades, also had been discussed and analyzed in several reports and original studies [10–12].

As there is no successful mechanism to estimate the exact future data from the present resources, a proper probabilistic model for forecasting the occurrence and intensity of geomagnetic storms is the need of the hour to save society from huge monetary losses and related hazards. McPherron et al. [13] proposed a probabilistic forecasting method, found to be most applicable for low to moderate storms during the declining phase of the solar cycle. Chandorkar et al. [14] presented an innovative forecasting method based on an autoregressive Gaussian process approach. The inputs to the model are previous values of the Dst index, solar wind speed and IMF  $B_z$ . The model generates a One Step Ahead prediction of the Dst index, requiring a small set of data for the training and validation. Xu et al. [15] studied the prediction of the Dst index using the Bagging ensemble-learning algorithm, which is a combination of an artificial neural network, support vector regression, and a long short-term memory network. They presented a model which takes several solar wind parameters like interplanetary total magnetic field, total electric field, IMF  $B_z$ , solar wind speed, plasma temperature and proton pressure as inputs and forecasts Dst index values 1–6 h in advance. Boynton et al. [16] developed a mathematical model based on NARMAX algorithm to study the dynamics of the Dst index. A solar wind-magnetosphere coupling function is used as the input to the model. The model shows a high forecasting ability of the occurrence, duration and intensity of the geomagnetic storm. A probabilistic algorithm combining Long Short-Term Memory recurrent neural network with Gaussian Process model was developed by Gruet et al. [17]. The model predicts the Dst index 6-h ahead with a correlation coefficient higher than 0.873 and root mean square error lower than 9.86. Wei et al. [18] constructed an effective forecasting algorithm for the Dst index using the multiresolution B spline wavelet decompositions which takes  $VB_s$  and the solar wind parameter as inputs. Zhu et al. [19] developed a multi-input–single-output discrete-time model based on the NARMAX algorithm which forecasts the dynamics of the Dst index better than the single-input NARMAX models. Also, a comparative study of the Dst forecast models for the intense geomagnetic storm was presented by Ji et al. [20]. In this work, six Dst forecast models are compared during intense geomagnetic storms. The models are Burton et al. [21], Boynton et al. [16], Fenrich and Luhmann [22], O'Brien and McPherron [23], Temerin and Li [24, 25] Wang et al. [26]. The input data to the model are solar wind parameters. The study concluded that the Temerin and Li model is the best one for predicting geomagnetic storms having values  $-100 \text{ nT} \leq \text{Dst} \leq -200 \text{ nT}$ . It is also better than the other models in terms of various parameters and interplanetary structures.

All these models are highly effective as prediction tools for the Dst index but are controlled by several factors and most importantly, take more than one input parameter for proper forecasting. In the current study, we propose a new and alternative method to predict the Dst index based on the concept of pattern recognition. The proposed probabilistic model has several features which distinguish it from the previous studies. A detailed database of different patterns is formed from the real-time data of an entire solar cycle to be used in the processing unit of the model. Also, the model needs only the previous values of the real-time Dst index to predict the future value and no other data of geomagnetic indices or solar wind parameters are required for this method. Both the mean absolute error and root-mean-square error are significantly small. Moreover, the primary algorithm of the model ensures minimum loss of information in analyzing the time series.

For several past years, pattern recognition became a widely used technique to study and analyze the existing regularities in an otherwise complex time series. A significant number of research works have been devoted to study the geomagnetic disturbances based on this method [27–31].

To find some specific patterns repeating themselves in a complex time series like the Dst index can lead us to a method of prediction of future data of the series from a previous set of data as well as some significant revelations of its underlying structure. In our previous works, we inspected the dynamical nature of the Dst index and in general geomagnetic storms [32–34]. We analyzed the Dst index using an innovative graphical method, namely visibility algorithm and observed the series can be categorized as a fractional Brownian motion having long-range correlation [32]. In the next study, we developed a cellular automata model of the terrestrial magnetosphere based on the concept of self-organized criticality and sandpile dynamics. Real-time solar wind parameters and IMF  $B_z$  data are the input to the model. The spectral response of the simulated output shows statistical similarity with that of the natural Dst index. The integral dynamics of geomagnetic disturbances is observed as a self-organized critical behavior of a perturbed system resulting in avalanche formations [33]. We refined the model further by introducing a new solar wind-magnetosphere coupling function to the model. The analysis reveals that the solar activities had a direct influence over the solar wind-magnetosphere coupling. Also, a substantial time delay is observed between the initial injection of solar wind into the magnetosphere and its consequent effect on the Earth's magnetic field [34]. All these studies make us realize that the Dst index has a complex and intricate structure, resulting from various underlying physical mechanisms, thus unpredictable in conventional methods. Identifying and characterizing the repetitive patterns hidden in the structure of the Dst index may lead us to a successful prediction algorithm. In the current paper, we continue our study of geomagnetic disturbances and propose a probabilistic model of the Dst index based on delta modulation, optimum state space (OSS) reconstruction, and pattern recognition.

Delta modulation is a simple one-bit special case of digital pulse code modulation technique. Adaptive delta modulation is a refined version of the linear delta modulation where the step size is not fixed. Numerous studies have been presented in the past years to delta modulate an analog or continuous data series to minimize the quantization error as well as to maximize the accuracy of the modulation [35–42]. Patterns, extracted from an analog signal, do not show scale-free or scale-invariant behaviors. To construct a scale-free pattern, the analog signal needs to be converted into a binary string. Delta modulation is such a technique, generally used

for analog to digital conversion. As our current study is mainly based on identifying the patterns of the Dst index, delta modulation is used to convert the time series into its binary form to extract scale-free patterns hidden in its layers.

The time series prediction can be considered as a pattern recognition problem by forecasting the future data from the previous patterns. For this, the optimum dimension of the phase space must be evaluated [43, 44]. Conventionally, there are three distinct methods available for optimum state space reconstruction, discussed as follows:

- (1) Singular value analysis: In this method, the covariance matrix associated with the time series is estimated and the related eigenvalues are calculated. The presence of high-dimensional noise in the time series constructs the floor of the eigenvalue spectrum. The value of the optimum state space can be determined from that spectrum. The calculations used in this method are simple though have some difficulties during the analysis of the outcome. It fails to differentiate between two dynamical systems having nearly similar Fourier spectrums. Also, the method has a strong dependence on the notion of the noise floor, thus inapplicable for colored noise [44].
- (2) False neighborhood: A false neighbor is a point having a minimum distance from the input point, where the input space dimension is smaller than the optimum space dimension. By increasing the distance between them by a scale factor, eventually, the number of false neighbors leads to zero and the optimum dimension can be reached. This method is also simple but has disadvantages too. Firstly, it is difficult to determine the exact value of the scale factor or criteria to identify a false neighbor. Secondly, for oversampled data, the points close in time but distant in space can wrongly be considered as true neighbors. Thirdly, if the embedding dimension becomes less than optimum, the distance between the neighbors remains unchanged for the points outside the attractor. Finally, the method requires a large number of data [44].
- (3) Saturation of attractor properties: In a dynamical system, an attractor is a set of states toward which a system tends to evolve. This analysis is based on the concept of unfolding the attractor by a large dimension. As the optimum dimension has been reached, the attractor properties dependent on the distance of the points in the phase space become independent of the embedding dimension. The method needs a large set of data to properly estimate the optimum dimension, which is its only disadvantage [44].

Previously, Chatterjee [44] established a probabilistic model based on the artificial neural network (ANN) to predict the 10.7 cm radio flux in advance. In that paper, Chatterjee coined a modified technique to reconstruct the optimum state space by a variation of this method based on entropy and information. In the modified method, an algorithm is developed to determine the optimum dimension of state space by estimating the metric entropy of the time series. The most advantageous point of this analysis is that it ensures minimum loss of information to reconstruct the optimum state space. As the value of the optimum dimension of the state space is determined, the prediction time can be calculated by using this value in a mathematical relation. Then the value of the prediction time is used in the ANN probabilistic model to generate output data by feeding the model a set of previous data. It was observed that the model predicts 10.7 cm radio flux quite accurately in 1 day in advance and the methodology is suitable to predict any time-series influenced by solar parameters. Since the Dst index is such a geomagnetic time-series, we consider this technique of optimum space reconstruction to be fruitful enough for our present work. In our study, we follow the algorithm of optimum state space reconstruction presented by Chatterjee [44], then instead of developing an ANN model as Chatterjee [44], we establish a novel technique of predicting the Dst index based on pattern recognition.

## 2 Method

The proposed prediction algorithm in the current work follows the steps: (1) Conversion of the Dst index time-series to an  $n$ -bit binary string using an adaptive delta modulation technique, (2) Formation of a set of pattern by taking  $m$  consecutive bits from the binary string where the value of  $m$  ranges from 1 to  $n-1$ , (3) Recording of the number of occurrence of each pattern in the binary string by applying the sliding window protocol, (4) Determination of the optimum value of the state space ' $M$ ' from the recorded data by calculating the correlation sum, (5) To find out all the  $M$ -bit patterns from the binary string including their number of occurrences, (6) Calculation of the probability of the least significant binary bit  $D_0$  being '1' or '0' in a  $M$ -bit pattern after a specific combination of the rest of the bits  $D_{M-1} \dots D_2 D_1$ , (7) Formation of a general database for all the  $M$ -bit patterns of the 11-year solar cycle, consisting of  $2^{M-1}$  number of patterns including the probability of occurrence of the least significant bit that calculated in the previous step, (8) Establishing a probabilistic prediction model by using this general database and a demodulation algorithm, where the model takes  $(M-1)$  consecutive real-time data in the input to generate the future value of the  $M$ th data, (9) Comparison of the probabilistic model output with the real-time Dst index after a suitable number of iterations. The acceptability of the model is verified by calculating the correlation coefficient between the model output and the real-time Dst index series.

### 2.1 Converting the Dst index time series into a binary string using the delta modulation technique

Delta modulation technique can be regarded as a 1-bit differential pulse code modulation (DPCM) scheme. A reference signal is initiated, the input signal is sampled, and then by comparing the reference signal with the input signal, the increase or decrease in relative amplitude is determined. If the input signal has a higher amplitude than the reference signal, the value of the output is set

to '1' and the reference signal is increased by a predefined step size  $\Delta$ . If the input signal has a lower amplitude than the reference signal, the value of the output is '0' and the reference signal is decreased by  $\Delta$ . In both cases, the  $\Delta$  is a multivalued predefined variable and not the exact difference between the input and the reference signal. In this way, the difference value of the amplitudes is quantized in only two levels, corresponding to the positive or negative differences, whereas a no-change condition causes the modulated signal to remain at the same state of the previous sample. The output signal is a 1-bit binary data series that contains only the change in information.

Delta modulation with limited adaptivity technique is a modified version of the classic delta modulation. Application of this technique on a Dst index time series converts the series to a 1-bit binary string. Let  $X_i(t)$  is the input Dst index series having  $n$  number of data, where  $t = 1, 2, 3, \dots, n$ . At first, a second series,  $X_r(t)$  known as the reference signal is computed from  $X_i(t)$ . The first three values of  $X_r(t)$  are the same as  $X_i(t)$ , i.e.,

$$X_r(t) = X_i(t) \text{ for } t = 1 \text{ to } 3 \quad (1)$$

For  $t > 3$ , to compute  $X_r(t)$  in general, the term  $X_r(t-1)$  is compared with the term  $X_i(t)$  to check if there is an increment or decrement in the values. Here, If  $X_i(t) > X_r(t-1)$ , there is an increment and a factor  $\Delta_I$  is added to the term  $X_r(t-1)$  to determine the value of  $X_r(t)$ . If  $X_i(t) < X_r(t-1)$ , there is a decrement and a factor  $\Delta_D$  is subtracted from the term  $X_r(t-1)$  to determine the value of  $X_r(t)$ . The factor  $\Delta$  is called the step size of the reference signal as it continues to track the change in values between two consecutive steps. Mathematically, for  $t = 4$  to  $n$ ,

$$X_r(t) = X_r(t-1) + \Delta_I \text{ when } X_i(t) > X_r(t-1) \quad (2)$$

and

$$X_r(t) = X_r(t-1) - \Delta_D \text{ when } X_i(t) < X_r(t-1) \quad (3)$$

where

$$\Delta_I = K_I \times \sigma_D \times 2^d \text{ for } 0 \leq d \leq 2 \quad (4)$$

and

$$\Delta_D = K_D \times \sigma_D \times 2^d \text{ for } 0 \leq d \leq 2 \quad (5)$$

here  $K_I$  and  $K_D$  are two constants and  $\sigma_D$  is the standard deviation of the absolute differential values of the input series  $X_i(t)$  and is calculated as:

$$\sigma_D = \sqrt{\frac{1}{(n-1)} \sum_{t=1}^{(n-1)} [|X_i(t) - X_i(t+1)| - \bar{X}_D]^2} \quad (6)$$

where

$$\bar{X}_D = \frac{1}{(n-1)} \sum_{t=1}^{(n-1)} |X_i(t) - X_i(t+1)| \quad (7)$$

In Eqs. 4 and 5, the value of  $d$  is limited to only three values, 0, 1, and 2, explaining the name of the technique as 'delta modulation with limited adaptivity.' If the increment (decrement) between the two terms,  $X_i(t)$  and  $X_r(t-1)$  continues for three consecutive steps, the value of  $d$  becomes 0, 1, and 2 for the first, second, and third step, respectively. But, if the fourth consecutive step also shows an increment (decrement), the value of  $d$  is still 2 and remains so for any further consecutive increments (decrements). Whenever there is a decrement (increment) in the next step, the value of  $d$  is reset to 0.

As the reference signal  $X_r(t)$  has been formed, the output series  $Y_{dm}(t)$  is computed using the equations.:

$$Y_{dm}(t) = 1 \text{ for } X_r(t+1) \geq X_r(t) \quad (8)$$

and

$$Y_{dm}(t) = 0 \text{ for } X_r(t+1) < X_r(t) \quad (9)$$

Thus,  $Y_{dm}(t)$  becomes the delta-modulated 1-bit binary string output having  $(n-1)$  number of terms.



## 2.2 Finding the number of occurrences of a pattern by sliding window technique

In this step, an  $m$ -bit data string or pattern is formed from the series  $Y_{dm}(t)$  by taking  $m$  number of consecutive bits, starting from the 1<sup>st</sup> bit of the series. As there are at least two points are required to construct a two-dimensional pattern and also the length of the series  $Y_{dm}(t)$  is  $(n-1)$ , the value of  $m$  is in the range of 2 to  $(n-2)$ . Then by the sliding window technique, for  $m = 2$  to  $(n-2)$ , the number of occurrences of all possible  $2^m$  patterns in the series  $Y_{dm}(t)$  is determined. For example, for  $m = 2$  the series  $Y_{dm}(t)$  is scanned with the patterns 00, 01, 10, and 11. The method is repeated for all considerable values from  $m = 2$  onward and is stored carefully. A database is formed for different values of  $m$  and each of them contains a  $2^m$  number of patterns including their respective number of occurrences in the series  $Y_{dm}(t)$ .

## 2.3 Determination of the optimum state space

A state space is a multi-dimensional space of all possible configurations of a system. It is a useful abstraction for reasoning about the behavior of a given system and applies to all types of systems like single input single output systems, multiple inputs and multiple outputs systems, linear and nonlinear systems, time-varying, and time-invariant systems. The state in the state-space analysis refers to the smallest set of variables whose knowledge at the initial time together with the knowledge of input for the successive future time gives the complete knowledge of the behavior of the system at any time  $t$ . The state variables in the state space analysis are the smallest set of variables that help us to determine the state of a dynamical system.

When the state space is continuous it is often a smooth manifold. In this case, it is called the phase space. A phase space can also be infinite-dimensional. A dynamical system consists of abstract phase space or state space, whose coordinates describe the state at any instant, and a dynamical rule that specifies the immediate future of all state variables, given only the present values of those same state variables. Mathematically, a dynamical system is described by an initial value problem. The implication is that there is a notion of time and that a state at one time evolves to a state or possibly a collection of states at a later time. Thus, states can be ordered by time, and time can be thought of as a single quantity.

A dynamical system is deterministic if there is a unique consequence to every state or it is stochastic where there is a probability distribution of possible consequents. It can be discrete or continuous time. The Discrete-time system has its states evaluated only after certain discrete intervals. It is a combination of a state space, a set of time, and a set of evolution rules. A dynamical system can be considered as a model describing the temporal evolution of a process. The evolution rule provides a prediction of the next state or states that follow from the current state space value. The rule is deterministic if each state has a unique consequence, and is stochastic if there is more than one possible consequent for a given state. A stochastic evolution with discrete time but continuous phase space is an iterated function system. In this case, there is a collection of functions  $f_\alpha$  indexed by parameters  $\alpha$ . The evolution is random with the next state  $s_{t+1} = f_\alpha(s_t)$  where  $\alpha$  is selected from a probability distribution.

Now, to understand the dynamics of a stochastic discrete time series, the development of the evaluation rules are required. To develop such a set of rules, the entire series is divided into many  $m$ -dimensional hyperspaces and each of them is assigned a state variable that carries some pieces of information. Then the rules are created based on the dimension along with the information extracted from those state variables. As the hyperspace can be considered of any dimension, the developed rules will be different for their increment in dimension resulting in a rapid variance in the evaluation process. Each hyperspace holds a piece of information that may be meaningful or meaningless depending upon the value of their dimension. Needless to say, the meaningless information can only lead us to unnecessary complexity to develop the evaluation rules that can ruin the dynamics of the system. To overcome this problem, a set of meaningful rules having finite dimensions and appropriate information are required to analyze such a stochastic evaluation process. That is called the reconstruction of the optimum state space.

In the 2001 paper, Chatterjee [44] discussed the reconstruction of the optimum state space in detail and opted for the method namely ‘saturation of attractor properties.’ In a dynamical system, an attractor is a set toward which a variable evolves over time i.e., points close to the attractor remain nearby despite slight disturbance. The attractor is a region in  $n$ -dimensional space. It can be a point, a finite set of points, a curve, a manifold, or even a complicated set with a fractal structure. The method, ‘saturation of attractor properties,’ unfolds the attractor by a large dimension. In this method, when the optimum dimension has been reached, the attractor properties dependent on the distance of the points in the phase space become independent of the embedding dimension. The only limitation of this method is the requirement of a large set of data to properly estimate the optimum dimension. Since we are using a dataset that is large enough and the method ensures minimum loss of information to reconstruct the optimum state space, it is considered the most suitable one for our analysis. The method is described as follows:

Consider a dynamic system that is represented by a time series of  $X_T, X_{2T}, \dots, X_{NT}$  where  $N$  is the number of the observational values and  $T$  is the time interval. The state of the system is located in an  $m$ -dimensional hyperspace by a point having the coordinates  $X_T, X_{2T}, \dots, X_{mT}$ . The state at  $t = t + 1$  is denoted by  $X_{2T}, X_{3T}, \dots, X_{(m+1)T}$ , and so on, whereas the position vectors of each point are  $X_1, X_2, \dots, X_N$ . The trajectory of the system is the connecting line of all these points in order and the attractor is the region where the trajectory repeatedly returns. Now, by choosing a large enough dimension, the attractor can be unfolded properly. If the necessary  $m$ th dimension has been attained, all the properties of the attractor which are dependent on the distance of points in the phase space become independent of the value of the embedding dimension and no more information will be available beyond that dimension [45]. In this case, the data are a 1-bit binary string, and also no further sampling is required as the series is discrete with

some specific resolution. Now, considering the initial state is known with precision  $r$ , we are calculating the correlation sum that consists of centring the hypersphere on a point in phase space, letting the radius of the hypersphere grow until all points are enclosed [46]. The correlation sum  $C(r, m, N)$  is a function of the Hamming distance  $r$ , dimension  $m$ , and a total number of data  $N$  and is expressed as:

$$C(r, m, N) = \frac{1}{2^{m-1}} \sum_{j=1}^N G_j(r) \tag{10}$$

To calculate  $C(r, m, N)$ , the value for all the points lying within the range of  $r$  from a point is taken into account. The Hamming distance  $r$  is a metric for comparing two binary data strings of equal length or more specifically, it is the distance between two binary strings. In our case, we have taken a binary set of consecutive patterns having dimension  $m$  and Hamming distance  $r = 1$  i.e., the minimum Hamming distance is considered for the analysis. Also, the bit sequence of the two patterns in the set is exactly similar from  $D_m$  to  $D_1$  except for the only difference in the least significant bit  $D_0$  (LSB) to retain the  $r = 1$ . If the number of occurrences of the pattern having  $D_0 = 0$  is  $O_0$  and  $D_0 = 1$  is  $O_1$ , the expectation,  $G_j(r)$ , of  $D_0$  to be appeared as ‘1’ over ‘0’ is:

$$G_j(r) = \left[ \frac{O_1}{O_0 + O_1} - 0.5 \right]^2 \tag{11}$$

In this way, the expectations  $G_j(r)$  are calculated for all sets of patterns in the database obtained from the sliding window technique.

Thus, the optimum state space can be estimated from each yearly time series by calculating  $C(r, m, N)$  for different values of dimension  $m$ . A graph of the generalized correlation sum  $C(r, m, N)$  is plotted against the increasing value of  $m$ . At a particular point of  $m = M$ , where the slope of the plot becomes opposite in direction, the optimum state space is achieved beyond which no further information is available. Though the concept is generally associated with thermodynamics, in information theory it is defined as the amount of information required to locate the system in a specified state [47].

### 2.4 Finding M-bit patterns

As the optimum dimension  $M$  is estimated, the next part of the work is to find all the distinguished  $M$ -bit patterns from the binary string  $Y_{dm}(t)$ . A maximum of  $2^M$  patterns can be found. The patterns and their number of occurrences in the string  $Y_{dm}(t)$  are recorded to form a complete general database considering the entire 23rd Solar cycle.

### 2.5 Probability calculation

Let us denote an  $M$ -bit pattern as  $D_{M-1} \dots D_1 D_0$ . A study of the database can determine the probability of the LSB  $D_0$  to be ‘1’ or ‘0’ after a specific combination of the rest of the bits  $D_{M-1} \dots D_2 D_1$ . For example, consider an optimum dimension  $M = 4$ , where a specific set of a pattern has unit Hamming distance at LSB. Say, the set contains two consecutive binary patterns that are 0000 and 0001 having the number of occurrences 40 and 60, respectively. Thus, for the combination  $D_3 D_2 D_1 = 000$ , the probability of occurrence  $P(D_0 = 0)$  is 0.4 and  $P(D_0 = 1)$  is 0.6. Mathematically, the probability

$$P(D_0 = 0) = \frac{O_0}{O_0 + O_1} \tag{12}$$

and

$$P(D_0 = 1) = \frac{O_1}{O_0 + O_1} \tag{13}$$

where the number of occurrences of the pattern having  $D_0 = 0$  is  $O_0$  and  $D_0 = 1$  is  $O_1$ .

In this fashion, the entire general database of  $M$ -bit patterns associated with the binary string  $Y_{dm}(t)$  is analyzed and the probability of occurrence  $P(D_0 = 0)$  and  $P(D_0 = 1)$  for all the combinations of  $D_{M-1} \dots D_2 D_1$  are determined and stored. Now, the application of this general database can estimate the  $M$ th value of any real-time series from its previous  $(M-1)$  data.

### 2.6 Prediction model

The model is based on the general database. The input to the model is a real-time Dst index series,  $X_i(t)$ . The model requires  $(M-1)$  consecutive data of the input series to predict the  $M$ th data. As the model receives the first  $(M-1)$  number of input data, i.e., the values of  $X_i(t)$  for  $t = 1$  to  $(M-1)$ , it converts the  $(M-1)$  input data series into a binary string  $D_{M-1} \dots D_2 D_1$ , using the delta modulation method discussed in 2.1. The probability of occurrence  $P(D_0 = 0)$  or  $P(D_0 = 1)$  for this particular combination  $D_{M-1} \dots D_2 D_1$  is found from the database of patterns. The value of  $D_0$  is determined according to the value of  $P$ .  $D_0$  is either ‘1’ or ‘0’. The final output  $Y_{Dst}(t)$  is determined by demodulating the value of  $D_0$  in its analog form using the following eqs. In the case of  $D_0 = 0$ ,

$$Y_{Dst}(t) = X_i(t - 1) - K_D \times \sigma_D \times 2^d \begin{cases} d = 0 \text{ when } D_{M-2} = \phi \text{ and } D_{M-1} = 1 \\ d = 1 \text{ when } D_{M-2} = 1 \text{ and } D_{M-1} = 0 \\ d = 2 \text{ when } D_{M-2} = 0 \text{ and } D_{M-1} = 0 \end{cases} \tag{14}$$

and in the case of  $D_0 = 1$

$$Y_{Dst}(t) = X_i(t - 1) + K_I \times \sigma_D \times 2^d \begin{cases} d = 0 \text{ when } D_{M-2} = \phi \text{ and } D_{M-1} = 0 \\ d = 1 \text{ when } D_{M-2} = 1 \text{ and } D_{M-1} = 1 \\ d = 2 \text{ when } D_{M-2} = 0 \text{ and } D_{M-1} = 1 \end{cases} \tag{15}$$

where  $\phi =$  don't care condition *i.e.*, either 0 or 1, the values of  $K_I$  and  $K_D$  are prefixed, and the standard deviation of the absolute differential values of the input series is  $\sigma_D$  which is considered as unity for estimating the data of the 24th solar cycle. The first output data of the model are generated at  $t = M$  using the values of the input  $X_i(t)$  for  $t = 1$  to  $(M-1)$ . In the next step, again  $(M-1)$  consecutive input data, *i.e.*, values of  $X_i(t)$ , for  $t = 2$  to  $M$ , are required to produce the output at  $t = M + 1$ . In this way, the model generates every  $M^{\text{th}}$  data from the previous  $(M-1)$  data and continues to do so for all the next  $t$  values, generating a simulated output series, namely  $Y_{Dst}(t)$ . To verify the effectiveness of the model, the model output  $Y_{Dst}(t)$  is compared with the real-time Dst index series  $X_i(t)$  and the associated correlation coefficient  $C_c$ , the mean absolute error  $E_{ma}$  and the root-mean-square error  $E_{rms}$  are determined. The following eqs. are used to calculate the said three quantities:

$$C_c = \frac{\text{Cov}[X_i(t), Y_{Dst}(t)]}{\sqrt{\text{Var}[X_i(t)], \text{Var}[Y_{Dst}(t)]}} \tag{16}$$

$$E_{ma} = \frac{1}{n} \sum_{t=1}^n |X_i(t) - Y_{Dst}(t)| \tag{17}$$

$$E_{rms} = \sqrt{\frac{\sum_{t=1}^n [X_i(t) - Y_{Dst}(t)]^2}{n}} \tag{18}$$

### 3 Data source

Here we used the hourly averaged Dst data from the year 1997 to the year 2018 as extracted from NASA/GSFC's OMNI data set through OMNIWeb. The OMNI data were obtained from the GSFC/SPDF OMNIWeb interface at <http://omniweb.gsfc.nasa.gov> [48].

### 4 Results and discussion

Every solar cycle has its rising, maximum, declining, and minimum phases. Also, the geomagnetic storm can be classified into several categories, namely weak, moderate, strong, severe, and great storm. The Dst index belongs to the different categories are usually analyzed and studied separately. But, in our case, the model has been analyzed using the real-time Dst index data of each year of the 23rd solar cycle, *i.e.*, from the year 1997 to 2007, that includes all the phases of the solar cycle and are not segregated between the different storm period. Initially, the input Dst index series  $X_i(t)$  is converted to a 1-bit binary string  $Y_{dm}(t)$  using the delta modulation technique discussed in the method sect. While analyzing the nature of the Dst index, it is found that the rising and the falling properties of the index series are different. The rising of the series is much slower compared to the falling. So,  $K_I$  and  $K_D$  are two different constants assigned corresponding to the increment and decrement phenomenon and estimated experimentally to their best suitable values. Now, the 1-bit binary string  $Y_{dm}(t)$  is demodulated as  $Y_{ddm}(t)$  to test the accuracy of modulation. For every year of the entire 23rd solar cycle, the correlation coefficients are calculated between the original series  $X_i(t)$  and the demodulated series  $Y_{ddm}(t)$  and considered as the accuracy of modulation. The value of  $K_I$  and  $K_D$  are calculated as  $K_I = 0.54$  and  $K_D = 1.30$  to achieve the highest accuracy of modulation *i.e.*, 92% ~ 97% in our case.

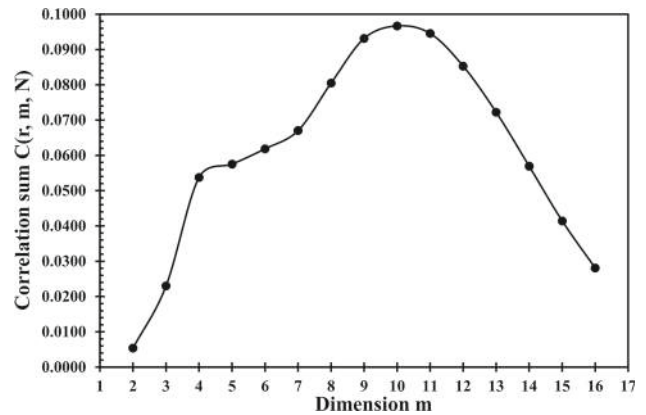
Once the binary string  $Y_{dm}(t)$  is obtained, all the possible patterns are determined using the sliding window technique. Now, the smallest binary pattern can be constructed using at least two successive data points. Thus, the correlation sum  $C(r, m, N)$  is calculated starting from  $m = 2$ . By increasing the dimension  $m$  gradually, the  $C(r, m, N)$  gained the highest value. Upon further increment, the corresponding value started decreasing and at  $m = 16$ , the value of the  $C(r, m, N)$  became sufficiently small to expect any increment thereafter. The decrement of the correlation sum indicates the inadequacy of any new information. The process is executed for all eleven years of the 23<sup>rd</sup> Solar cycle to get a general database of patterns for  $m = 2$  to 16. Table 1 shows the values of the embedded dimension vs correlation sum for the 1-h Dst index, respectively, for the range of the years 1997–2007.

The correlation sum  $C(r, m, N)$  is calculated considering the probability of occurrences of each pattern *i.e.*, their actual contribution in the data series. The nature of patterns present in each year is different along with their number of occurrences. A significant number of common patterns are observed throughout the entire cycle, whereas a small number of distinguished patterns occur only once. As a result, the degree of predictability varies for each year, hence the difference in yearly maximum correlation sum. Figure 1 is the graphical representation of the plots for embedded dimension  $m$  versus mean value of the correlation sum of 11 years associated with the 1-h Dst index series. As seen in Fig. 1, for the Dst index, the optimum state space is achieved for dimension  $M = 10$ . It signifies that the hourly Dst index series has the highest substantial correlated information up to 10 h and no more new information

**Table 1** The year-wise correlation sum  $C(r, m, N)$  is plotted for increasing value of dimension  $m$  for 1-h Dst index for the entire 23rd solar cycle

Dimension	Year											
	1997	1998	1999	2000	2001	2002	2003	2004	2005	2006	2007	
2	0.0158	0.0038	0.0040	0.0046	0.0058	0.0041	0.0043	0.0045	0.0047	0.0037	0.0037	
3	0.0355	0.0188	0.0213	0.0245	0.0253	0.0192	0.0231	0.0234	0.0257	0.0192	0.0173	
4	0.0443	0.0486	0.0539	0.0584	0.0613	0.0461	0.0601	0.0579	0.0645	0.0493	0.0468	
5	0.0496	0.0506	0.0587	0.0633	0.0681	0.0478	0.0611	0.0625	0.0676	0.0531	0.0502	
6	0.0539	0.0545	0.0610	0.0699	0.0681	0.0503	0.0706	0.0706	0.0686	0.0585	0.0544	
7	0.0614	0.0591	0.0659	0.0703	0.0744	0.0545	0.0800	0.0786	0.0737	0.0619	0.0576	
8	0.0713	0.0635	0.0821	0.0918	0.0927	0.0629	0.0879	0.0916	0.0870	0.0815	0.0731	
9	0.0938	0.0838	0.0891	0.0956	0.1001	0.0850	0.0955	0.0957	0.1081	0.0906	0.0870	
10	0.1003	0.0979	0.0871	0.0950	0.1002	0.0905	0.0989	0.0996	0.1025	0.0952	0.0961	
11	0.0965	0.0940	0.0898	0.0987	0.0950	0.0940	0.0960	0.0919	0.0957	0.0942	0.0941	
12	0.0861	0.0892	0.0837	0.0875	0.0827	0.0873	0.0833	0.0805	0.0852	0.0845	0.0882	
13	0.0740	0.0767	0.0723	0.0713	0.0673	0.0773	0.0695	0.0674	0.0691	0.0727	0.0767	
14	0.0608	0.0611	0.0571	0.0549	0.0521	0.0619	0.0534	0.0526	0.0519	0.0592	0.0611	
15	0.0450	0.0449	0.0418	0.0392	0.0371	0.0454	0.0384	0.0383	0.0368	0.0438	0.0448	
16	0.0304	0.0307	0.0285	0.0261	0.0246	0.0312	0.0261	0.0263	0.0243	0.0298	0.0308	

**Fig. 1** The 11 years mean values of the correlation sums  $C(r, m, N)$  are plotted against dimension  $m$  for the 1-h Dst index series considering the 23rd solar cycle



can be retrieved from the series beyond that limit. Thus, resting on the current data point i.e., 9th data point and using the last 8 data points corresponding to the last 8 h, the 10th data point or one-hour advanced data can be estimated using those patterns.

Concerning that estimation, all the 10-bit distinguished patterns for the series  $Y_{dm}(t)$  are identified and stored. The highest possible combinations of binary string for Dst index are 1024 (as  $2^M = 1024$ , where  $M = 10$ ). For the series, all the possible combinations of binary strings are added sequentially for 11 years to consider every single occurred pattern. Figure 2 illustrates the binomial degree distribution of the number of occurrences of the patterns for  $M = 10$  for the hourly Dst index series, which indicates the presence and absence of the entire set of patterns for the 23rd solar cycle.

The demodulated waveforms of some scale-free and periodically occurred patterns are shown in Fig. 3 where the relative amplitudes are plotted in the y-axis. The pattern corresponding to Fig. 3a is the most common and occurred more than 1500 times. Figure 3b, c, and d are chosen randomly from the range of occurrence between 1500 and 1000, 1000 and 500, and 500 and 100, respectively. Studying the database, the probability  $P(D_0 = 0)$  and  $P(D_0 = 1)$  for all these patterns are also estimated and included in the database.

As the general database had been formed, the next step is to study the prediction model of the Dst index discussed in Sect. 2.6 based on this database. The prediction model is analyzed for all the years of the 24th solar cycle, i.e., for the years 2008–2018 using the general database derived from the data of the previous 23rd solar cycle.

The value of  $M = 10$ , which means nine previous consecutive bits are required to generate the 10th data. Thus, the input to the prediction model is any set of nine consecutive values of the real-time Dst index  $X_i(t)$  to generate the predicted output  $Y_{Dst}(t)$  for the next  $t$ . As there is a probability factor in estimating the output  $Y_{Dst}(t)$ , the model is simulated for numerous iterations,  $I_r = 1$  to 250. After each iteration,  $Y_{Dst}(t)$  is compared with the real-time series  $X_i(t)$  and the associated correlation coefficient is estimated. Table 2 shows the value of the correlation coefficients  $C_c$ , mean absolute error  $E_{ma}$ , and root-mean-square error  $E_{rms}$  between the original Dst index  $X_i(t)$  and the predicted model output  $Y_{Dst}(t)$  after 250 iterations for the entire 24th solar cycle. Figure 4 demonstrates

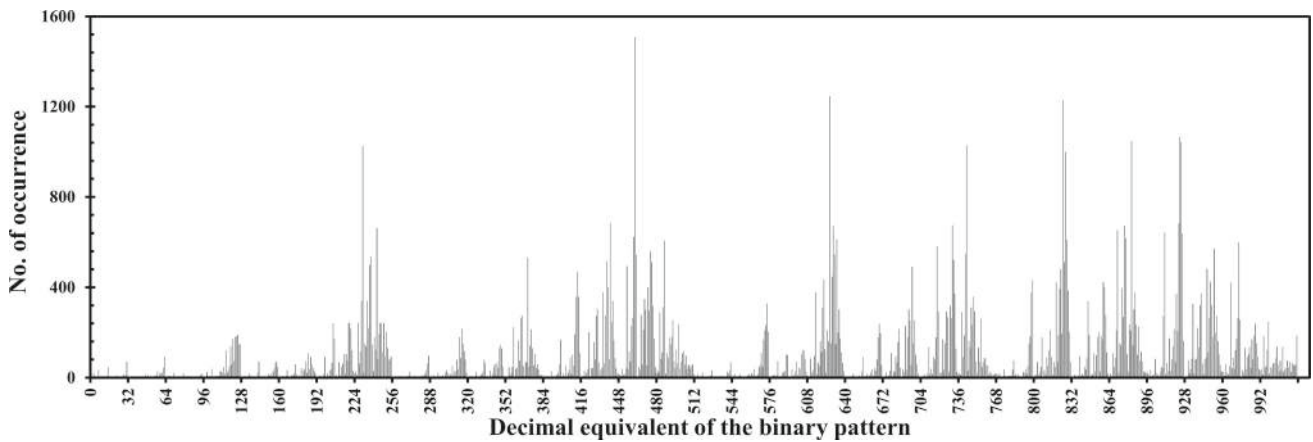
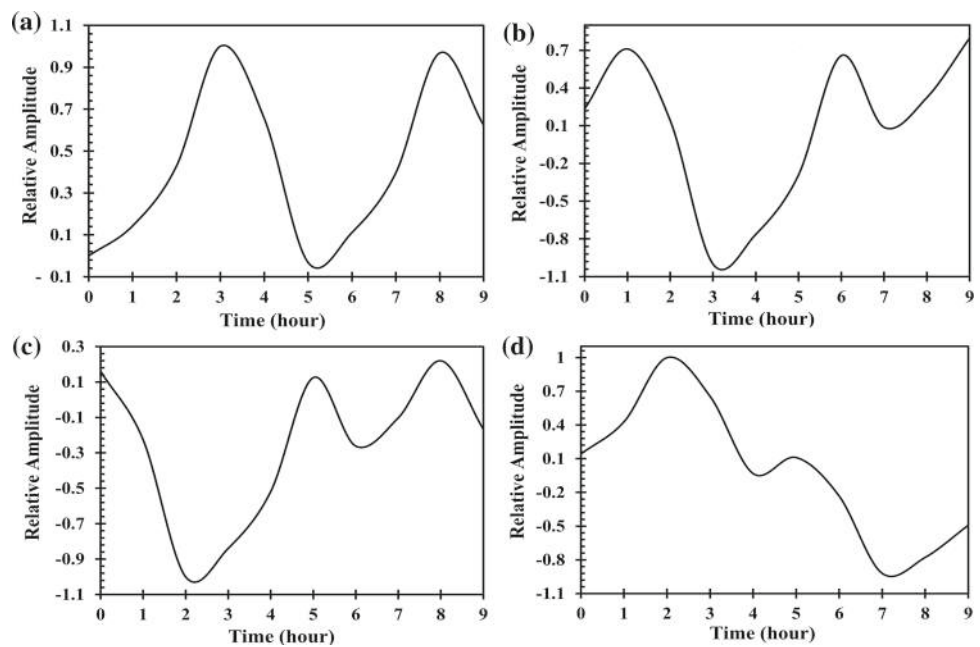


**Fig. 2** The Binomial degree distribution of the number of occurrences of the patterns is plotted for dimension  $M = 10$  for 1-h Dst index series for the entire 23rd solar cycle. The decimal equivalents of the binary patterns or words are plotted sequentially on the x-axis

**Fig. 3** The demodulated waveform of four periodically occurred patterns are shown where the corresponding binary sequences are **a** 0111001110, **b** 1100111011, **c** 1001110110, and **d** 1110010011. The number of their occurrences are 1509, 1000, 671, and 174



the correlation coefficients between  $X_i(t)$  and  $Y_{Dst}(t)$  for an increasing value of the number of iterations  $I_r = 1$  to 250, for the year 2016. The plot shows that the model becomes stabilized at  $I_r = 250$  quite well.

It is observed from Table 2, that the correlation coefficients between the original Dst index  $X_i(t)$  and the model output  $Y_{Dst}(t)$  are greater than 90% for each of the years of the 24th solar cycle, establishing the acceptability of the probabilistic model. Also, the associated values of mean absolute error and root-mean-square error are sufficiently small. The result indicates that the model can predict the Dst index data one hour in advance taking only the previous nine consecutive real-time Dst values as input. For a comparative study, the original Dst index  $X_i(t)$  and the model output  $Y_{Dst}(t)$  for the year 2016 are shown in Fig. 5a and b, respectively. Also, for detailed observation, the two series consisting of 5 days of data ranging between 3 May and 7 May of the same year is plotted in Fig. 5c for the same year.

The entire analysis reveals some prominent features about the probabilistic model and the overall method. A yearly continuous dataset of the real-time Dst index for each of the eleven years of the 23rd solar cycle is considered here to construct the pattern database. No segregation is made in the Dst dataset based on the phase of the solar cycle or the intensity of the geomagnetic storm. Thus, the model is applicable for the Dst index at any period, be it a quiet time or an intense storm. Then the delta modulation converts the analog Dst index series into a 1-bit binary string. Patterns, extracted from an analog signal, do not show scale-free or scale-invariant behaviors. But as the signal is transformed into a binary string in this method, the identified patterns are scale-free. The scale-invariance properties of the identified patterns are much useful to find any similar pattern of variable amplitude, which aids to construct the database consisting of all the patterns hidden in the structure of the Dst index series. Also, the optimum state space is reconstructed to identify the length of the optimum information in the hyperspace of the Dst index series. As observed

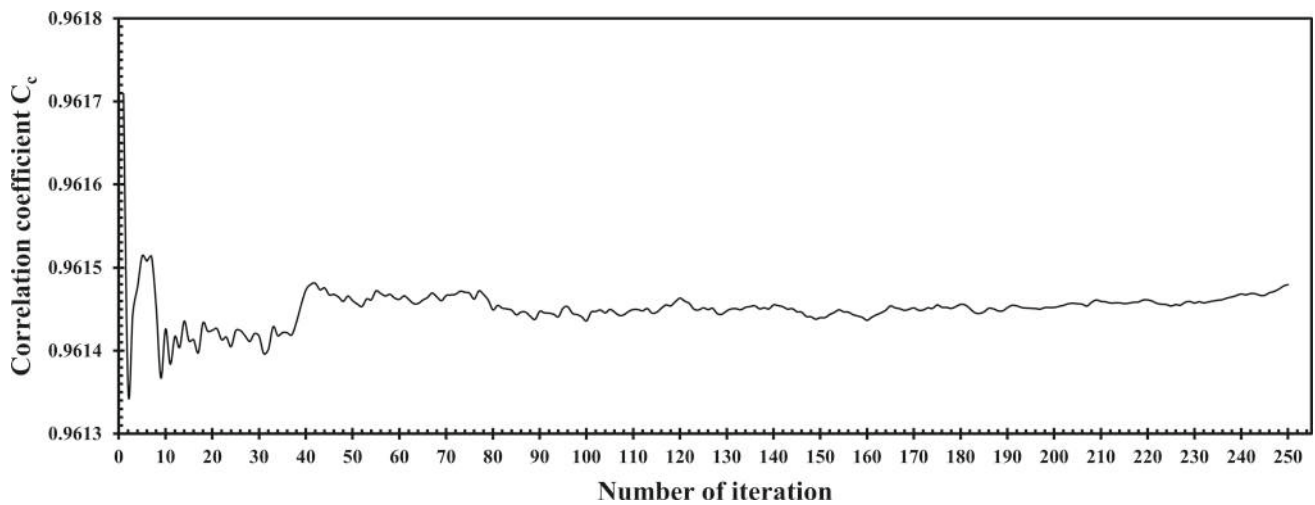


**Fig. 4** The value of the correlation coefficients between the original Dst index  $X_i(t)$  and the predicted model output  $Y_{Dst}(t)$  is plotted against the number of iterations performed for the year 2016

**Table 2** shows the value of the correlation coefficients  $C_c$ , mean absolute error  $E_{ma}$ , and root-mean-square error  $E_{rms}$  between the original Dst index  $X_i(t)$  and the predicted model output  $Y_{Dst}(t)$  after 250 iterations of the 24th solar cycle

Year	Correlation coefficient $C_c$	Mean absolute error $E_{ma}$	Root-mean-square error $E_{rms}$
2008	0.9488	2.6275	3.5234
2009	0.9285	2.4877	3.3017
2010	0.9542	2.7175	3.6655
2011	0.9595	2.9842	4.3502
2012	0.9757	3.1861	4.5221
2013	0.9683	2.9979	4.2113
2014	0.9636	3.1088	4.2498
2015	0.9725	3.5395	5.1543
2016	0.9615	3.1705	4.3541
2017	0.9611	3.1973	4.4571
2018	0.9570	2.8031	3.7861

from the result, no extra information can be retrieved from the series beyond the dimension  $M = 10$ , it is the optimum value of the state space. The saturation of attractor properties, used here to reconstruct the optimum state space, ensures minimum loss of information while estimating the optimum value. It is one of the key features of this method. Moreover, the model has a minimum dependency on external factors. A future Dst index value can be estimated only by using a finite set of previous Dst values and the pattern database as the input to the model. No other solar wind parameters or interplanetary magnetic field data are required. In the current analysis, the pattern database is constructed using the hourly real-time Dst index of the 23rd solar cycle. Using this database and nine previous values of Dst data, the model can predict the tenth Dst value in one hour advance for the entire 24th solar cycle, with a correlation coefficient up to 97.57%. Further, the maximum mean absolute error and root-mean-square error are found to be sufficiently small, 3.5395 and 5.1543, respectively.

### 5 Conclusion

The Dst index is a measurement of the geomagnetic activities on Earth and is widely used to indicate the intensity and occurrence of geomagnetic storms. Identifying significant patterns enfolded in the hidden layers and extracting substantial information from the inherent structures can be extremely rewarding in developing a successful forecasting algorithm. Moreover, an insight into the complex physical structure of this natural time series explains a lot of its characteristic features and dynamical behaviors. In this paper, we introduce a new method to predict the Dst index based on the concept of pattern recognition and optimum state space reconstruction. The analysis is a composite one; first to identify and characterize the significant patterns hidden in the structures of the 1-h Dst index series and then, development of a probabilistic model based on these patterns to forecast Dst data long before its actual occurrence. The algorithm includes adaptive delta modulation to convert the series into a binary string, the reconstruction of the optimum state space, construction of a database containing the probability of occurrence of the pattern, and finally, the development of a probabilistic predictive model to estimate the future data in one hour advance. The model has two inputs, the first one is the

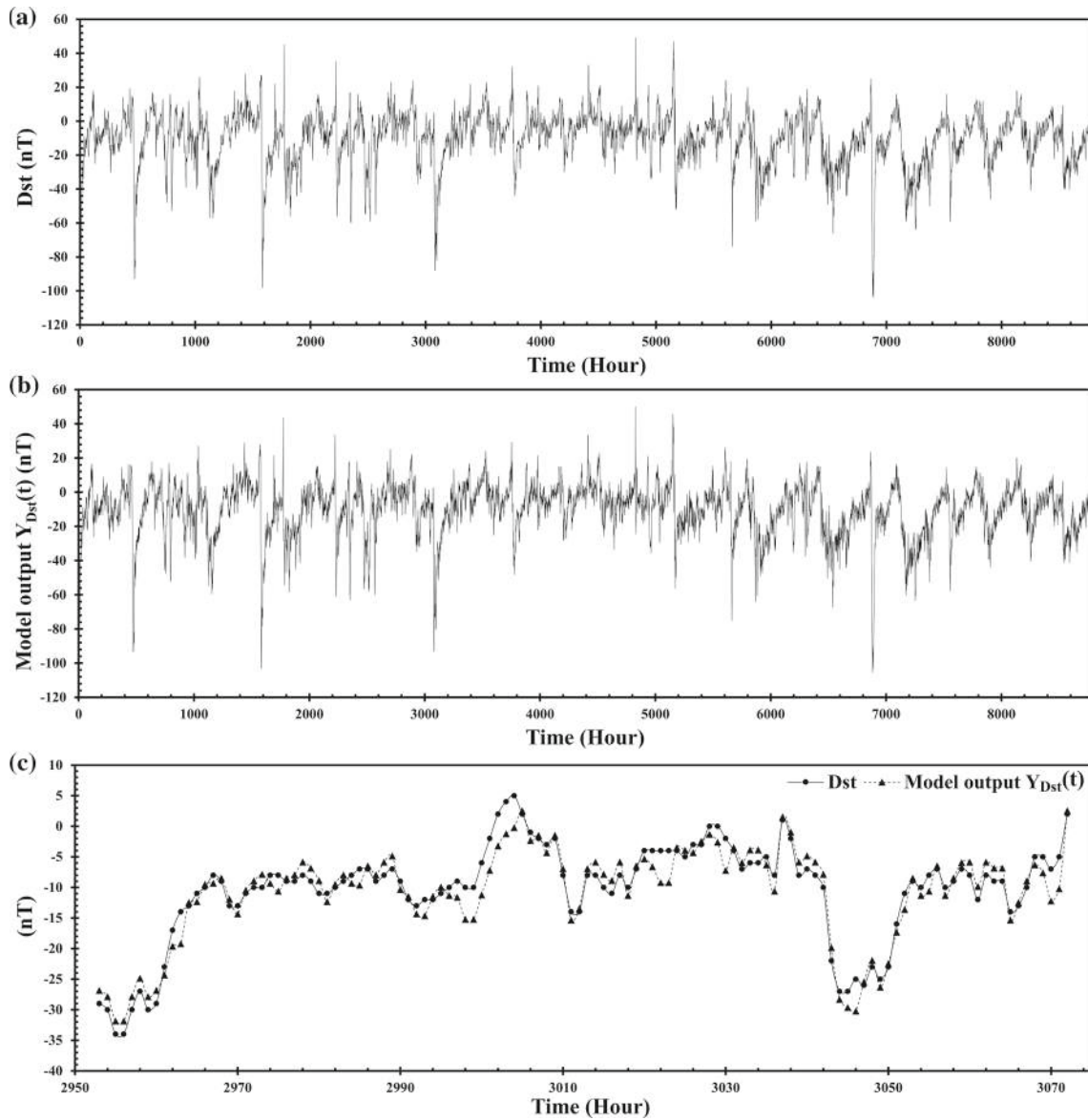


**Fig. 5** **a** The original 1-h Dst index  $X_i(t)$  for the year 2016, **b** the model output  $Y_{Dst}(t)$  for the same year, and **(c)** a comparative of the two series consisting of 5 days of data ranging between 3 May 2016 and 7 May 2016

database of the pattern created using the data of the entire 23rd solar cycle, and the second one is any set of nine consecutive data of the real-time Dst index of the 24th solar cycle to predict the 10th value. The predicted output is compared with each yearly data of the 24th solar cycle based on three parameters namely correlation coefficient, mean absolute error, and root-mean-square error for the statistical validation of the model. It has been observed that the values of the correlation coefficients between the real-time and predicted series are more than 90% for each of the years whereas the associated values of mean absolute error and root-mean-square error are significantly small. These results established the predictive performance of the model quite in a good way, using the database formed from the data of the 23<sup>rd</sup> solar cycle to predict the data of the next 24<sup>th</sup> solar cycle. Also, the model needs only the previous values of the real-time Dst index to predict the future value in one hour advance and no other data of geomagnetic indices or solar wind parameters are required for this method. One hour is sufficient to activate any controlling system to temporarily shut down the electrical hardware or power grids to save them from the perils of the coming storm. Moreover, the model takes a moderate number of iterations to be stabilized making a much lower computational time. Again, the study also revealed that the underlying physical structure of the Dst index is a complex composition of numerous distinguished patterns, occurring through the series in various frequencies. Some common patterns repeat through the entire solar cycle numerous times, whereas some are not. A small number of distinguished patterns occurs only once. As a result, the degree of predictability, as well as the maximum correlation sum, varies

in a small range for each year. Finally, for the Dst index, the optimum state space is achieved for the dimension  $M = 10$ , denoting no more new information can be retrieved from the time series beyond this particular dimension.

Geomagnetic disturbances on Earth are a complex phenomenon, and a powerful storm is need to be predicted a sufficient time before saving society from its adverse effects. Dst index, the global measurement of the geomagnetic storm, also represents the internal dynamical nature of this natural event, an overlapping of various physical processes or patterns forming an intricate structure. The current study was focused to identify and analyze the characteristics of these patterns enfolded in the dynamical structure of the Dst index to develop a successful prediction algorithm for this time series and in general, geomagnetic storm. The structure and traits of these patterns are very much intriguing and demand detailed study in the future to gain a much deeper knowledge of geomagnetic disturbances. The database of patterns can be continually updated with time incorporating all the available data to get various types of patterns and much more accuracy in predicting the future value.

**Supplementary Information** The online version contains supplementary material available at <https://doi.org/10.1140/epjp/s13360-022-02687-7>.

**Acknowledgements** We acknowledge the use of NASA/GSFC's Space Physics Data Facility's OMNIWeb (or CDAWeb or ftp) service, OMNI data and SIDC, RWC Belgium, World Data Centre. Data sets corresponding to Table 1 and Figure 3 are also available from the corresponding author on specific requests. We are thankful to Parthasarathi Chakrabarti, Director, IEST, Shibpur, Howrah, India, for the institutional support. We are also thankful to Somnath Mukherjee, Principal of Dinabandhu Andrews College, Kolkata, India for the cordial support and constant encouragement. Finally, we are also very much thankful to the anonymous reviewer for the significant insight into our manuscript by which, we are getting further encouraged to unfold the information hidden inside the geomagnetic data series.

**Authors' contributions** The authors have an equal contribution to the development of the manuscript.

**Funding** Self-funded as we are independent researchers.

## Declarations

**Conflict of interest** Nil.

**Ethics approval** Not applicable.

**Consent to participate** Not applicable.

**Consent for publication** Not applicable.

**Code availability** No.

**Data availability** Data are available on request made to the corresponding author.

## References

1. M. Sugiura, T. Kamei, Equatorial DST index 1957–1986, in IAGA Bull. 40, edited by A. Bertheliet, and M. Menvielle, Int. Serv. of Geomagn. Indices Publ. Off., Saint Maur, France (1991)
2. M. Sugiura, Hourly values of equatorial Dst for IGY. Annals of the International Geophysical Year, vol. 35, pp. 945–948 (Pergamon Press, Oxford, U. K.) (1964)
3. J.A. Wanliss, K.M. Showalter, High-resolution global storm index: Dst versus SYM-H. J. Geophys. Res. **111**, A02202 (2006). <https://doi.org/10.1029/2005JA011034>
4. J.G. Kappenman, L.J. Zanetti, W.A. Radasky, Geomagnetic storms can threaten electric power grid. Am. Geophys. Union Earth Space **9**(7), 9–11 (1997)
5. Hydro-Québec, Understanding electricity. Retrieved 2010-10-2 (1989)
6. CENTRA Technology Inc., Geomagnetic Storms Report Prepared for the Office of Risk Management and Analysis United States Department of Homeland Security (2011)
7. NOAA technical memorandum OAR SEC-88, Halloween space weather storms of 2003. Space Environment Center, Boulder, Colorado, June 2004 (2003)
8. L.J. Lanzerotti, Space Weather Effects on Technologies, in *Space Weather*. ed. by P. Song, H.J. Singer, G.L. Siscoe (AGU, Washington, 2013)
9. National Research Council, Severe Space Weather Events, Understanding Societal and Economic Impacts. A Workshop Report, Washington, DC, The National Academies Press (2008)
10. A. Pulkkinen, E. Bernabeu, J. Eichner, C. Beggan, A.W.P. Thomson, Generation of 100-year geomagnetically induced current scenarios. Space Weather **10**, S04003 (2012). <https://doi.org/10.1029/2011SW000750>
11. A.W.P. Thomson, E.B. Dawson, S.J. Reay, Quantifying extreme behavior in geomagnetic activity. Space Weather **9**, S10001 (2011). <https://doi.org/10.1029/2011SW000696>
12. A. Viljanen, R. Pirjola, E. Prácsér, S. Ahmadzai, V. Singh, Geomagnetically induced currents in Europe: characteristics based on a local power grid model. Space Weather **11**, 575–584 (2013). <https://doi.org/10.1002/swe.20098>



13. R.L. McPherron, G. Siscoe, N.U. Crooker, N. Arge, Probabilistic Forecasting of the Dst Index, in *The Inner Magnetosphere: Physics and Modeling*, ed. by T.I. Pulkkinen, N.A. Tsyganenko, R.H.W. Friedel (AGU, Washington, 2005)
14. M. Chandorkar, E. Camporeale, S. Wing, Probabilistic forecasting of the disturbance storm time index: an autoregressive Gaussian process approach. *Space Weather* **15**, 1004–1019 (2017). <https://doi.org/10.1002/2017SW001627>
15. S.B. Xu, S.Y. Huang, Z.G. Yuan, X.H. Deng, K. Jiang, Prediction of the Dst index with bagging ensemble-learning algorithm. *Astrophys. J. Suppl. Ser.* **248**(1), 14 (2020). <https://doi.org/10.3847/1538-4365/ab880e>
16. R.J. Boynton, M.A. Balikhin, S.A. Billings, A.S. Sharma, O.A. Amariutei, Data derived NARMAX Dst model. *Ann. Geophys.* **29**, 965–971 (2011). <https://doi.org/10.5194/angeo-29-965-2011>
17. M.A. Gruet, M. Chandorkar, A. Sicard, E. Camporeale, Multiple-hour-ahead forecast of the Dst index using a combination of long short-term memory neural network and Gaussian process. *Space Weather* **16**, 1882–1896 (2018). <https://doi.org/10.1029/2018SW001898>
18. H.L. Wei, S.A. Billings, M. Balikhin, Prediction of the Dst index using multiresolution wavelet models. *J. Geophys. Res.* **109**, A07212 (2004). <https://doi.org/10.1029/2003JA010332>
19. D. Zhu, S.A. Billings, M.A. Balikhin, S. Wing, H. Alleyne, Multi-input data derived Dst model. *J. Geophys. Res.* **112**, A06205 (2007). <https://doi.org/10.1029/2006JA012079>
20. E.Y. Ji, Y.J. Moon, N. Gopalswamy, D.H. Lee, Comparison of Dst forecast models for intense geomagnetic storms. *J. Geophys. Res.* **117**, A03209 (2012). <https://doi.org/10.1029/2011JA016872>
21. R.K. Burton, R.L. McPherron, C.T. Russell, An empirical relationship between interplanetary conditions and Dst. *J. Geophys. Res.* **80**, 4204–4214 (1975)
22. F.R. Fenrich, J.G. Luhmann, Geomagnetic response to magnetic clouds of different polarity. *Geophys. Res. Lett.* **25**, 2999–3002 (1998)
23. T.P. O'Brien, R.L. McPherron, An empirical phase space analysis of ring current dynamics: solar wind control of injection and decay. *J. Geophys. Res.* **105**, 7707–7720 (2000)
24. M. Temerin, X. Li, A new model for the prediction of Dst on the basis of the solar wind. *J. Geophys. Res.* **107**(A12), 1472 (2002). <https://doi.org/10.1029/2001JA007532>
25. M. Temerin, X. Li, Dst model for 1995–2002. *J. Geophys. Res.* **111**, A04221 (2006). <https://doi.org/10.1029/2005JA011257>
26. C.B. Wang, J.K. Chao, C.H. Lin, Influence of the solar wind dynamic pressure on the decay and injection of the ring current. *J. Geophys. Res.* **108**(A9), 1341 (2003). <https://doi.org/10.1029/2003JA009851>
27. J. Chen, P.J. Cargill, P.J. Palmadesso, Predicting solar wind structures and their geoeffectiveness. *J. Geophys. Res.* **102**(A7), 14701–14720 (1997). <https://doi.org/10.1029/97JA00936>
28. I. V. Kovalevskij, Yu. I. Morozov, Geomagnetic storm as an object of pattern recognition. ITEF-74, USSR (1986)
29. J.V. Kovalevsky, Yu.I. Morozov, *Pattern Recognition Methods in Analysis of Complex Physical Phenomena* (IZMIRAN, Russia, Moscow, 1990)
30. J. V. Kovalevsky, E. I. Kovalevskaya, Application of pattern recognition methods in analysis of complex physical phenomena in geospace: geomagnetospheric storms. Correlated phenomena at the sun, in the heliosphere and in geospace. In: proceedings 31st ESLAB symposium, ESTEC, Noordwijk, ESA SP-415, pp. 431–436 (1997)
31. X.P. Zeng, Y.F. Lin, C. Lu, Z.X. Feng, Q.H. Guo, Application of pattern recognition method to the prediction of geomagnetic storms. *Chin. J. Sp. Sci.* **4**, 42–50 (1984)
32. A. Banerjee, A. Bej, T.N. Chatterjee, On the existence of a long range correlation in the geomagnetic disturbance storm time (Dst) index. *Astrophys. Space Sci.* **337**, 23–32 (2012). <https://doi.org/10.1007/s10509-011-0836-1>
33. A. Banerjee, A. Bej, T.N. Chatterjee, A cellular automata-based model of Earth's magnetosphere in relation with Dst index. *Space Weather* **13**, 259–270 (2015). <https://doi.org/10.1002/2014SW001138>
34. A. Banerjee, A. Bej, T.N. Chatterjee, A. Majumdar, An SOC approach to study the solar wind-magnetosphere energy coupling. *Earth Space Sci.* **6**, 565–576 (2019). <https://doi.org/10.1029/2018EA000468>
35. J.E. Abate, Linear and adaptive delta modulation. *Proc. IEEE* **55**(3), 298–308 (1967). <https://doi.org/10.1109/PROC.1967.5486>
36. C. C. Cutler, Differential quantization of communication signals. *Nokia Bell Labs, U.S. Patent* **2**, 605, 361 (1952)
37. F. DeJager, Delta modulation, a method of PCM transmission using a 1-unit code'. *Phillips Res. Rept. No.* **7**, 442–466 (1952)
38. D.J. Goodman, A digital approach to adaptive delta modulation. *Bell Syst. Tech. J.* **50**, 1421–1426 (1971). <https://doi.org/10.1002/j.1538-7305.1971.tb02560.x>
39. R. Gregorian, J.G. Gord, A continuously variable slope adaptive delta modulation codec system. *IEEE J. Solid-State Circuits* **18**(6), 692–700 (1983). <https://doi.org/10.1109/JSSC.1983.1052019>
40. C. Halijak, J. Tripp, A deterministic study of delta modulation. *IEEE Trans. Automat. Contr.* **8**(4), 339–347 (1963). <https://doi.org/10.1109/tac.1963.1105592>
41. M.H. Weik, *Computer Science and Communications Dictionary* (Springer, Boston, 2000), pp. 382–382
42. C.M. Zierhofer, Adaptive sigma-delta modulation with one-bit quantization. *IEEE Trans. Circuits Syst. II* **47**(5), 408–415 (2000). <https://doi.org/10.1109/82.842109>
43. H.D.I. Abarbanel, R. Brown, J.J. Sidorowich, L.S. Tsimring, The analysis of observed chaotic data in physical systems. *Rev. Mod. Phys.* **65**(4), 1331–1392 (1993). <https://doi.org/10.1103/RevModPhys.65.1331>
44. T.N. Chatterjee, On the application of information theory to the optimum state-space reconstruction of the short-term solar radio flux (10.7cm), and its prediction via a neural network. *Mon. Not. R. Astron. Soc.* **323**, 101–108 (2001). <https://doi.org/10.1046/j.1365-8711.2001.04110.x>
45. C.E. Shannon, A mathematical theory of communication. *Bell Syst. Tech. J.* **27**, 623–656 (1948). <https://doi.org/10.1002/j.1538-7305.1948.tb00917.x>
46. K. Pawelzik, H.G. Schuster, Generalized dimensions and entropies from a measured time series. *Phys. Rev. A* **35**(1), 481–484 (1987). <https://doi.org/10.1103/physreva.35.481>
47. S. Eubank, J.D. Farmer, An Introduction to Chaos and Prediction, in *Lectures in the Science of Complexity*, ed. by E. Jen. SFI studies in the science of complexity. (Addison-Wesley, MA, 1990), p. 75
48. J.H. King, N.E. Papitashvili, Solar wind spatial scales in and comparisons of hourly wind and ACE plasma and magnetic field data. *J. Geophys. Res.* **110**, A02209 (2005). <https://doi.org/10.1029/2004JA010649>



# Source details

[Feedback >](#) [Compare sources >](#)

## European Physical Journal Plus

Scopus coverage years: from 2011 to Present

Publisher: Springer Nature

ISSN: 2190-5444

Subject area: [Chemical Engineering: Fluid Flow and Transfer Processes](#) [Physics and Astronomy: General Physics and Astronomy](#)

Source type: Journal

[View all documents >](#)

[Set document alert](#)

[Save to source list](#)

CiteScore 2022

4.9



SJR 2022

0.548



SNIP 2022

0.979





# One-hour ahead prediction of the Dst index based on the optimum state space reconstruction and pattern recognition

Amaresh Bej<sup>1</sup>, Adrija Banerjee<sup>1,a</sup> , T. N. Chatterjee<sup>2</sup>, Abhijit Majumdar<sup>1</sup>

<sup>1</sup> Department of Physics, Indian Institute of Engineering Science and Technology, Shibpur, P.O.-Botanic Garden, Howrah, West Bengal 711103, India

<sup>2</sup> Department of Electronics, Dinabandhu Andrews College, 54, Raja S.C. Mullick Road, Garia, Kolkata, West Bengal 700084, India

Received: 5 July 2021 / Accepted: 5 April 2022

© The Author(s), under exclusive licence to Società Italiana di Fisica and Springer-Verlag GmbH Germany, part of Springer Nature 2022

**Abstract** The Disturbance storm time (Dst) index is the global estimation of the intensity of the terrestrial geomagnetic activities as well as the primary indicator of the geomagnetic storm. As the adverse effect of a powerful geomagnetic event has become a serious threat to modern human society, extracting meaningful information concealed in the complex structures of this time series can form the ground of a successful prediction algorithm. In this paper, we introduce a new probabilistic model based on the concept of adaptive delta modulation and optimum state space to analyze, identify and characterize the patterns enfolded in the layers of the 1-h Dst index and then predict Dst data using these patterns. The study reveals some significant insights. The exact dimension  $M$  of the optimum state space for the Dst index is found to be at  $M = 10$ . Also, the series is a combination of multiple distinguished repeating and non-repeating patterns, denoting a high degree of predictability of the  $M$ th data of the series from its previous  $(M-1)$  binary data. Eventually, the simulated output of the probabilistic model exhibits a high value of correlation coefficient with the real-time Dst index. Interestingly, the technique only requires the Dst index data as an input of the probabilistic model and is found to be very effective for the entire 24th solar cycle.

## 1 Introduction

The disturbance storm time (Dst) index is an indication of the geomagnetic activities in the terrestrial magnetosphere and is frequently used in characterizing the intensity of geomagnetic storms. It is computed based on the average value of the horizontal component of the Earth's magnetic field recorded at four different observatories, namely Hermanus (34.40°S, 19.22°E in geographic latitude and longitude), Kakioka (36.23°N, 140.18°E), Honolulu (21.32°N, 158.02°W), and San Juan (18.01°N, 66.15°W) [1]. These stations are evenly spaced in longitude and near enough to the magnetic equator to nullify the influence of the auroral effect as much as possible, again also placed at a significant distance away from the magnetic equator to minimize the influence of the equatorial electrojet current flowing in the ionosphere [2, 3].

Severe geomagnetic activity poses a potential threat to modern human society as a powerful storm can wreak havoc by collapsing all the electrical systems in the affected area, including power grids, computer and communication networks, satellite and navigation systems, military intelligence, and so on. The phenomenon is a sequence of striking the Earth by an intense geomagnetic storm followed by the entering of a stream of charged plasma particles into the geospace through the solar wind-magnetosphere reconnection that results in an induction of an electric field in the magnetosphere. As a consequence, voltage differences are generated between the ground points of the electrical networks that drive a current, namely geomagnetically induced current (GIC), flowing through the electrical hardware. The value of this GIC can be as high as 100 Ampere which is substantially beyond the specified range of tolerance of the electrical circuits causing fatal damages to the entire system [4]. Needless to say, our modern human society is almost entirely dependent on technology based on electrical power more than ever, thus a GIC-triggered catastrophic collapse of the electrical infrastructure in a large region includes enormous monetary losses, wastages of manpower, and prolonged unavoidable hazards. As an example, an intense geomagnetic storm on March 13, 1989, caused the entire Hydro Quebec system to get shut down resulting in more than 6 million customers surviving without electricity for nine hours [4, 5]. In 2003, the Wide Area Augmentation System (WAAS) operated by the Federal Aviation Administration (FAA) was affected by the Halloween solar storm and collapsed for approximately 30 h causing serious damages to many satellite systems including the Japanese ADEOS-2 satellite. In the past years, the Nordic countries along with the USA and Canada had faced unbearable consequences of geomagnetic storms, like the complete disruption of electric power-grids, hours of blackouts, damages of navigation as well as communication systems, disruption of satellite hardware and computer networks. In a report by the Oak Ridge National Laboratory, a geomagnetic storm, slightly stronger than March 1989 one, can result in an enormous blackout in the whole north-eastern area of the USA including a huge \$36 billion

<sup>a</sup> e-mail: [adrija\\_bnrj@yahoo.co.in](mailto:adrija_bnrj@yahoo.co.in) (corresponding author)

monetary loss in gross domestic product. [4, 6–9]. The perils of these intense geomagnetic storms, that occurred in the European countries in the last decades, also had been discussed and analyzed in several reports and original studies [10–12].

As there is no successful mechanism to estimate the exact future data from the present resources, a proper probabilistic model for forecasting the occurrence and intensity of geomagnetic storms is the need of the hour to save society from huge monetary losses and related hazards. McPherron et al. [13] proposed a probabilistic forecasting method, found to be most applicable for low to moderate storms during the declining phase of the solar cycle. Chandorkar et al. [14] presented an innovative forecasting method based on an autoregressive Gaussian process approach. The inputs to the model are previous values of the Dst index, solar wind speed and IMF  $B_z$ . The model generates a One Step Ahead prediction of the Dst index, requiring a small set of data for the training and validation. Xu et al. [15] studied the prediction of the Dst index using the Bagging ensemble-learning algorithm, which is a combination of an artificial neural network, support vector regression, and a long short-term memory network. They presented a model which takes several solar wind parameters like interplanetary total magnetic field, total electric field, IMF  $B_z$ , solar wind speed, plasma temperature and proton pressure as inputs and forecasts Dst index values 1–6 h in advance. Boynton et al. [16] developed a mathematical model based on NARMAX algorithm to study the dynamics of the Dst index. A solar wind-magnetosphere coupling function is used as the input to the model. The model shows a high forecasting ability of the occurrence, duration and intensity of the geomagnetic storm. A probabilistic algorithm combining Long Short-Term Memory recurrent neural network with Gaussian Process model was developed by Gruet et al. [17]. The model predicts the Dst index 6-h ahead with a correlation coefficient higher than 0.873 and root mean square error lower than 9.86. Wei et al. [18] constructed an effective forecasting algorithm for the Dst index using the multiresolution B spline wavelet decompositions which takes  $VB_s$  and the solar wind parameter as inputs. Zhu et al. [19] developed a multi-input–single-output discrete-time model based on the NARMAX algorithm which forecasts the dynamics of the Dst index better than the single-input NARMAX models. Also, a comparative study of the Dst forecast models for the intense geomagnetic storm was presented by Ji et al. [20]. In this work, six Dst forecast models are compared during intense geomagnetic storms. The models are Burton et al. [21], Boynton et al. [16], Fenrich and Luhmann [22], O'Brien and McPherron [23], Temerin and Li [24, 25] Wang et al. [26]. The input data to the model are solar wind parameters. The study concluded that the Temerin and Li model is the best one for predicting geomagnetic storms having values  $-100 \text{ nT} \leq \text{Dst} \leq -200 \text{ nT}$ . It is also better than the other models in terms of various parameters and interplanetary structures.

All these models are highly effective as prediction tools for the Dst index but are controlled by several factors and most importantly, take more than one input parameter for proper forecasting. In the current study, we propose a new and alternative method to predict the Dst index based on the concept of pattern recognition. The proposed probabilistic model has several features which distinguish it from the previous studies. A detailed database of different patterns is formed from the real-time data of an entire solar cycle to be used in the processing unit of the model. Also, the model needs only the previous values of the real-time Dst index to predict the future value and no other data of geomagnetic indices or solar wind parameters are required for this method. Both the mean absolute error and root-mean-square error are significantly small. Moreover, the primary algorithm of the model ensures minimum loss of information in analyzing the time series.

For several past years, pattern recognition became a widely used technique to study and analyze the existing regularities in an otherwise complex time series. A significant number of research works have been devoted to study the geomagnetic disturbances based on this method [27–31].

To find some specific patterns repeating themselves in a complex time series like the Dst index can lead us to a method of prediction of future data of the series from a previous set of data as well as some significant revelations of its underlying structure. In our previous works, we inspected the dynamical nature of the Dst index and in general geomagnetic storms [32–34]. We analyzed the Dst index using an innovative graphical method, namely visibility algorithm and observed the series can be categorized as a fractional Brownian motion having long-range correlation [32]. In the next study, we developed a cellular automata model of the terrestrial magnetosphere based on the concept of self-organized criticality and sandpile dynamics. Real-time solar wind parameters and IMF  $B_z$  data are the input to the model. The spectral response of the simulated output shows statistical similarity with that of the natural Dst index. The integral dynamics of geomagnetic disturbances is observed as a self-organized critical behavior of a perturbed system resulting in avalanche formations [33]. We refined the model further by introducing a new solar wind-magnetosphere coupling function to the model. The analysis reveals that the solar activities had a direct influence over the solar wind-magnetosphere coupling. Also, a substantial time delay is observed between the initial injection of solar wind into the magnetosphere and its consequent effect on the Earth's magnetic field [34]. All these studies make us realize that the Dst index has a complex and intricate structure, resulting from various underlying physical mechanisms, thus unpredictable in conventional methods. Identifying and characterizing the repetitive patterns hidden in the structure of the Dst index may lead us to a successful prediction algorithm. In the current paper, we continue our study of geomagnetic disturbances and propose a probabilistic model of the Dst index based on delta modulation, optimum state space (OSS) reconstruction, and pattern recognition.

Delta modulation is a simple one-bit special case of digital pulse code modulation technique. Adaptive delta modulation is a refined version of the linear delta modulation where the step size is not fixed. Numerous studies have been presented in the past years to delta modulate an analog or continuous data series to minimize the quantization error as well as to maximize the accuracy of the modulation [35–42]. Patterns, extracted from an analog signal, do not show scale-free or scale-invariant behaviors. To construct a scale-free pattern, the analog signal needs to be converted into a binary string. Delta modulation is such a technique, generally used

for analog to digital conversion. As our current study is mainly based on identifying the patterns of the Dst index, delta modulation is used to convert the time series into its binary form to extract scale-free patterns hidden in its layers.

The time series prediction can be considered as a pattern recognition problem by forecasting the future data from the previous patterns. For this, the optimum dimension of the phase space must be evaluated [43, 44]. Conventionally, there are three distinct methods available for optimum state space reconstruction, discussed as follows:

- (1) Singular value analysis: In this method, the covariance matrix associated with the time series is estimated and the related eigenvalues are calculated. The presence of high-dimensional noise in the time series constructs the floor of the eigenvalue spectrum. The value of the optimum state space can be determined from that spectrum. The calculations used in this method are simple though have some difficulties during the analysis of the outcome. It fails to differentiate between two dynamical systems having nearly similar Fourier spectrums. Also, the method has a strong dependence on the notion of the noise floor, thus inapplicable for colored noise [44].
- (2) False neighborhood: A false neighbor is a point having a minimum distance from the input point, where the input space dimension is smaller than the optimum space dimension. By increasing the distance between them by a scale factor, eventually, the number of false neighbors leads to zero and the optimum dimension can be reached. This method is also simple but has disadvantages too. Firstly, it is difficult to determine the exact value of the scale factor or criteria to identify a false neighbor. Secondly, for oversampled data, the points close in time but distant in space can wrongly be considered as true neighbors. Thirdly, if the embedding dimension becomes less than optimum, the distance between the neighbors remains unchanged for the points outside the attractor. Finally, the method requires a large number of data [44].
- (3) Saturation of attractor properties: In a dynamical system, an attractor is a set of states toward which a system tends to evolve. This analysis is based on the concept of unfolding the attractor by a large dimension. As the optimum dimension has been reached, the attractor properties dependent on the distance of the points in the phase space become independent of the embedding dimension. The method needs a large set of data to properly estimate the optimum dimension, which is its only disadvantage [44].

Previously, Chatterjee [44] established a probabilistic model based on the artificial neural network (ANN) to predict the 10.7 cm radio flux in advance. In that paper, Chatterjee coined a modified technique to reconstruct the optimum state space by a variation of this method based on entropy and information. In the modified method, an algorithm is developed to determine the optimum dimension of state space by estimating the metric entropy of the time series. The most advantageous point of this analysis is that it ensures minimum loss of information to reconstruct the optimum state space. As the value of the optimum dimension of the state space is determined, the prediction time can be calculated by using this value in a mathematical relation. Then the value of the prediction time is used in the ANN probabilistic model to generate output data by feeding the model a set of previous data. It was observed that the model predicts 10.7 cm radio flux quite accurately in 1 day in advance and the methodology is suitable to predict any time-series influenced by solar parameters. Since the Dst index is such a geomagnetic time-series, we consider this technique of optimum space reconstruction to be fruitful enough for our present work. In our study, we follow the algorithm of optimum state space reconstruction presented by Chatterjee [44], then instead of developing an ANN model as Chatterjee [44], we establish a novel technique of predicting the Dst index based on pattern recognition.

## 2 Method

The proposed prediction algorithm in the current work follows the steps: (1) Conversion of the Dst index time-series to an  $n$ -bit binary string using an adaptive delta modulation technique, (2) Formation of a set of pattern by taking  $m$  consecutive bits from the binary string where the value of  $m$  ranges from 1 to  $n-1$ , (3) Recording of the number of occurrence of each pattern in the binary string by applying the sliding window protocol, (4) Determination of the optimum value of the state space ' $M$ ' from the recorded data by calculating the correlation sum, (5) To find out all the  $M$ -bit patterns from the binary string including their number of occurrences, (6) Calculation of the probability of the least significant binary bit  $D_0$  being '1' or '0' in a  $M$ -bit pattern after a specific combination of the rest of the bits  $D_{M-1} \dots D_2 D_1$ , (7) Formation of a general database for all the  $M$ -bit patterns of the 11-year solar cycle, consisting of  $2^{M-1}$  number of patterns including the probability of occurrence of the least significant bit that calculated in the previous step, (8) Establishing a probabilistic prediction model by using this general database and a demodulation algorithm, where the model takes  $(M-1)$  consecutive real-time data in the input to generate the future value of the  $M$ th data, (9) Comparison of the probabilistic model output with the real-time Dst index after a suitable number of iterations. The acceptability of the model is verified by calculating the correlation coefficient between the model output and the real-time Dst index series.

### 2.1 Converting the Dst index time series into a binary string using the delta modulation technique

Delta modulation technique can be regarded as a 1-bit differential pulse code modulation (DPCM) scheme. A reference signal is initiated, the input signal is sampled, and then by comparing the reference signal with the input signal, the increase or decrease in relative amplitude is determined. If the input signal has a higher amplitude than the reference signal, the value of the output is set

to '1' and the reference signal is increased by a predefined step size  $\Delta$ . If the input signal has a lower amplitude than the reference signal, the value of the output is '0' and the reference signal is decreased by  $\Delta$ . In both cases, the  $\Delta$  is a multivalued predefined variable and not the exact difference between the input and the reference signal. In this way, the difference value of the amplitudes is quantized in only two levels, corresponding to the positive or negative differences, whereas a no-change condition causes the modulated signal to remain at the same state of the previous sample. The output signal is a 1-bit binary data series that contains only the change in information.

Delta modulation with limited adaptivity technique is a modified version of the classic delta modulation. Application of this technique on a Dst index time series converts the series to a 1-bit binary string. Let  $X_i(t)$  is the input Dst index series having  $n$  number of data, where  $t = 1, 2, 3, \dots, n$ . At first, a second series,  $X_r(t)$  known as the reference signal is computed from  $X_i(t)$ . The first three values of  $X_r(t)$  are the same as  $X_i(t)$ , i.e.,

$$X_r(t) = X_i(t) \text{ for } t = 1 \text{ to } 3 \quad (1)$$

For  $t > 3$ , to compute  $X_r(t)$  in general, the term  $X_r(t-1)$  is compared with the term  $X_i(t)$  to check if there is an increment or decrement in the values. Here, If  $X_i(t) > X_r(t-1)$ , there is an increment and a factor  $\Delta_I$  is added to the term  $X_r(t-1)$  to determine the value of  $X_r(t)$ . If  $X_i(t) < X_r(t-1)$ , there is a decrement and a factor  $\Delta_D$  is subtracted from the term  $X_r(t-1)$  to determine the value of  $X_r(t)$ . The factor  $\Delta$  is called the step size of the reference signal as it continues to track the change in values between two consecutive steps. Mathematically, for  $t = 4$  to  $n$ ,

$$X_r(t) = X_r(t-1) + \Delta_I \text{ when } X_i(t) > X_r(t-1) \quad (2)$$

and

$$X_r(t) = X_r(t-1) - \Delta_D \text{ when } X_i(t) < X_r(t-1) \quad (3)$$

where

$$\Delta_I = K_I \times \sigma_D \times 2^d \text{ for } 0 \leq d \leq 2 \quad (4)$$

and

$$\Delta_D = K_D \times \sigma_D \times 2^d \text{ for } 0 \leq d \leq 2 \quad (5)$$

here  $K_I$  and  $K_D$  are two constants and  $\sigma_D$  is the standard deviation of the absolute differential values of the input series  $X_i(t)$  and is calculated as:

$$\sigma_D = \sqrt{\frac{1}{(n-1)} \sum_{t=1}^{(n-1)} [|X_i(t) - X_i(t+1)| - \bar{X}_D]^2} \quad (6)$$

where

$$\bar{X}_D = \frac{1}{(n-1)} \sum_{t=1}^{(n-1)} |X_i(t) - X_i(t+1)| \quad (7)$$

In Eqs. 4 and 5, the value of  $d$  is limited to only three values, 0, 1, and 2, explaining the name of the technique as 'delta modulation with limited adaptivity.' If the increment (decrement) between the two terms,  $X_i(t)$  and  $X_r(t-1)$  continues for three consecutive steps, the value of  $d$  becomes 0, 1, and 2 for the first, second, and third step, respectively. But, if the fourth consecutive step also shows an increment (decrement), the value of  $d$  is still 2 and remains so for any further consecutive increments (decrements). Whenever there is a decrement (increment) in the next step, the value of  $d$  is reset to 0.

As the reference signal  $X_r(t)$  has been formed, the output series  $Y_{dm}(t)$  is computed using the equations.:

$$Y_{dm}(t) = 1 \text{ for } X_r(t+1) \geq X_r(t) \quad (8)$$

and

$$Y_{dm}(t) = 0 \text{ for } X_r(t+1) < X_r(t) \quad (9)$$

Thus,  $Y_{dm}(t)$  becomes the delta-modulated 1-bit binary string output having  $(n-1)$  number of terms.

## 2.2 Finding the number of occurrences of a pattern by sliding window technique

In this step, an  $m$ -bit data string or pattern is formed from the series  $Y_{dm}(t)$  by taking  $m$  number of consecutive bits, starting from the 1<sup>st</sup> bit of the series. As there are at least two points are required to construct a two-dimensional pattern and also the length of the series  $Y_{dm}(t)$  is  $(n-1)$ , the value of  $m$  is in the range of 2 to  $(n-2)$ . Then by the sliding window technique, for  $m = 2$  to  $(n-2)$ , the number of occurrences of all possible  $2^m$  patterns in the series  $Y_{dm}(t)$  is determined. For example, for  $m = 2$  the series  $Y_{dm}(t)$  is scanned with the patterns 00, 01, 10, and 11. The method is repeated for all considerable values from  $m = 2$  onward and is stored carefully. A database is formed for different values of  $m$  and each of them contains a  $2^m$  number of patterns including their respective number of occurrences in the series  $Y_{dm}(t)$ .

## 2.3 Determination of the optimum state space

A state space is a multi-dimensional space of all possible configurations of a system. It is a useful abstraction for reasoning about the behavior of a given system and applies to all types of systems like single input single output systems, multiple inputs and multiple outputs systems, linear and nonlinear systems, time-varying, and time-invariant systems. The state in the state-space analysis refers to the smallest set of variables whose knowledge at the initial time together with the knowledge of input for the successive future time gives the complete knowledge of the behavior of the system at any time  $t$ . The state variables in the state space analysis are the smallest set of variables that help us to determine the state of a dynamical system.

When the state space is continuous it is often a smooth manifold. In this case, it is called the phase space. A phase space can also be infinite-dimensional. A dynamical system consists of abstract phase space or state space, whose coordinates describe the state at any instant, and a dynamical rule that specifies the immediate future of all state variables, given only the present values of those same state variables. Mathematically, a dynamical system is described by an initial value problem. The implication is that there is a notion of time and that a state at one time evolves to a state or possibly a collection of states at a later time. Thus, states can be ordered by time, and time can be thought of as a single quantity.

A dynamical system is deterministic if there is a unique consequence to every state or it is stochastic where there is a probability distribution of possible consequents. It can be discrete or continuous time. The Discrete-time system has its states evaluated only after certain discrete intervals. It is a combination of a state space, a set of time, and a set of evolution rules. A dynamical system can be considered as a model describing the temporal evolution of a process. The evolution rule provides a prediction of the next state or states that follow from the current state space value. The rule is deterministic if each state has a unique consequence, and is stochastic if there is more than one possible consequent for a given state. A stochastic evolution with discrete time but continuous phase space is an iterated function system. In this case, there is a collection of functions  $f_\alpha$  indexed by parameters  $\alpha$ . The evolution is random with the next state  $s_{t+1} = f_\alpha(s_t)$  where  $\alpha$  is selected from a probability distribution.

Now, to understand the dynamics of a stochastic discrete time series, the development of the evaluation rules are required. To develop such a set of rules, the entire series is divided into many  $m$ -dimensional hyperspaces and each of them is assigned a state variable that carries some pieces of information. Then the rules are created based on the dimension along with the information extracted from those state variables. As the hyperspace can be considered of any dimension, the developed rules will be different for their increment in dimension resulting in a rapid variance in the evaluation process. Each hyperspace holds a piece of information that may be meaningful or meaningless depending upon the value of their dimension. Needless to say, the meaningless information can only lead us to unnecessary complexity to develop the evaluation rules that can ruin the dynamics of the system. To overcome this problem, a set of meaningful rules having finite dimensions and appropriate information are required to analyze such a stochastic evaluation process. That is called the reconstruction of the optimum state space.

In the 2001 paper, Chatterjee [44] discussed the reconstruction of the optimum state space in detail and opted for the method namely ‘saturation of attractor properties.’ In a dynamical system, an attractor is a set toward which a variable evolves over time i.e., points close to the attractor remain nearby despite slight disturbance. The attractor is a region in  $n$ -dimensional space. It can be a point, a finite set of points, a curve, a manifold, or even a complicated set with a fractal structure. The method, ‘saturation of attractor properties,’ unfolds the attractor by a large dimension. In this method, when the optimum dimension has been reached, the attractor properties dependent on the distance of the points in the phase space become independent of the embedding dimension. The only limitation of this method is the requirement of a large set of data to properly estimate the optimum dimension. Since we are using a dataset that is large enough and the method ensures minimum loss of information to reconstruct the optimum state space, it is considered the most suitable one for our analysis. The method is described as follows:

Consider a dynamic system that is represented by a time series of  $X_T, X_{2T}, \dots, X_{NT}$  where  $N$  is the number of the observational values and  $T$  is the time interval. The state of the system is located in an  $m$ -dimensional hyperspace by a point having the coordinates  $X_T, X_{2T}, \dots, X_{mT}$ . The state at  $t = t + 1$  is denoted by  $X_{2T}, X_{3T}, \dots, X_{(m+1)T}$ , and so on, whereas the position vectors of each point are  $X_1, X_2, \dots, X_N$ . The trajectory of the system is the connecting line of all these points in order and the attractor is the region where the trajectory repeatedly returns. Now, by choosing a large enough dimension, the attractor can be unfolded properly. If the necessary  $m$ th dimension has been attained, all the properties of the attractor which are dependent on the distance of points in the phase space become independent of the value of the embedding dimension and no more information will be available beyond that dimension [45]. In this case, the data are a 1-bit binary string, and also no further sampling is required as the series is discrete with

some specific resolution. Now, considering the initial state is known with precision  $r$ , we are calculating the correlation sum that consists of centring the hypersphere on a point in phase space, letting the radius of the hypersphere grow until all points are enclosed [46]. The correlation sum  $C(r, m, N)$  is a function of the Hamming distance  $r$ , dimension  $m$ , and a total number of data  $N$  and is expressed as:

$$C(r, m, N) = \frac{1}{2^{m-1}} \sum_{j=1}^N G_j(r) \tag{10}$$

To calculate  $C(r, m, N)$ , the value for all the points lying within the range of  $r$  from a point is taken into account. The Hamming distance  $r$  is a metric for comparing two binary data strings of equal length or more specifically, it is the distance between two binary strings. In our case, we have taken a binary set of consecutive patterns having dimension  $m$  and Hamming distance  $r = 1$  i.e., the minimum Hamming distance is considered for the analysis. Also, the bit sequence of the two patterns in the set is exactly similar from  $D_m$  to  $D_1$  except for the only difference in the least significant bit  $D_0$  (LSB) to retain the  $r = 1$ . If the number of occurrences of the pattern having  $D_0 = 0$  is  $O_0$  and  $D_0 = 1$  is  $O_1$ , the expectation,  $G_j(r)$ , of  $D_0$  to be appeared as ‘1’ over ‘0’ is:

$$G_j(r) = \left[ \frac{O_1}{O_0 + O_1} - 0.5 \right]^2 \tag{11}$$

In this way, the expectations  $G_j(r)$  are calculated for all sets of patterns in the database obtained from the sliding window technique.

Thus, the optimum state space can be estimated from each yearly time series by calculating  $C(r, m, N)$  for different values of dimension  $m$ . A graph of the generalized correlation sum  $C(r, m, N)$  is plotted against the increasing value of  $m$ . At a particular point of  $m = M$ , where the slope of the plot becomes opposite in direction, the optimum state space is achieved beyond which no further information is available. Though the concept is generally associated with thermodynamics, in information theory it is defined as the amount of information required to locate the system in a specified state [47].

### 2.4 Finding M-bit patterns

As the optimum dimension  $M$  is estimated, the next part of the work is to find all the distinguished  $M$ -bit patterns from the binary string  $Y_{dm}(t)$ . A maximum of  $2^M$  patterns can be found. The patterns and their number of occurrences in the string  $Y_{dm}(t)$  are recorded to form a complete general database considering the entire 23rd Solar cycle.

### 2.5 Probability calculation

Let us denote an  $M$ -bit pattern as  $D_{M-1} \dots D_1 D_0$ . A study of the database can determine the probability of the LSB  $D_0$  to be ‘1’ or ‘0’ after a specific combination of the rest of the bits  $D_{M-1} \dots D_2 D_1$ . For example, consider an optimum dimension  $M = 4$ , where a specific set of a pattern has unit Hamming distance at LSB. Say, the set contains two consecutive binary patterns that are 0000 and 0001 having the number of occurrences 40 and 60, respectively. Thus, for the combination  $D_3 D_2 D_1 = 000$ , the probability of occurrence  $P(D_0 = 0)$  is 0.4 and  $P(D_0 = 1)$  is 0.6. Mathematically, the probability

$$P(D_0 = 0) = \frac{O_0}{O_0 + O_1} \tag{12}$$

and

$$P(D_0 = 1) = \frac{O_1}{O_0 + O_1} \tag{13}$$

where the number of occurrences of the pattern having  $D_0 = 0$  is  $O_0$  and  $D_0 = 1$  is  $O_1$ .

In this fashion, the entire general database of  $M$ -bit patterns associated with the binary string  $Y_{dm}(t)$  is analyzed and the probability of occurrence  $P(D_0 = 0)$  and  $P(D_0 = 1)$  for all the combinations of  $D_{M-1} \dots D_2 D_1$  are determined and stored. Now, the application of this general database can estimate the  $M$ th value of any real-time series from its previous  $(M-1)$  data.

### 2.6 Prediction model

The model is based on the general database. The input to the model is a real-time Dst index series,  $X_i(t)$ . The model requires  $(M-1)$  consecutive data of the input series to predict the  $M$ th data. As the model receives the first  $(M-1)$  number of input data, i.e., the values of  $X_i(t)$  for  $t = 1$  to  $(M-1)$ , it converts the  $(M-1)$  input data series into a binary string  $D_{M-1} \dots D_2 D_1$ , using the delta modulation method discussed in 2.1. The probability of occurrence  $P(D_0 = 0)$  or  $P(D_0 = 1)$  for this particular combination  $D_{M-1} \dots D_2 D_1$  is found from the database of patterns. The value of  $D_0$  is determined according to the value of  $P$ .  $D_0$  is either ‘1’ or ‘0’. The final output  $Y_{Dst}(t)$  is determined by demodulating the value of  $D_0$  in its analog form using the following eqs. In the case of  $D_0 = 0$ ,

$$Y_{Dst}(t) = X_i(t - 1) - K_D \times \sigma_D \times 2^d \begin{cases} d = 0 \text{ when } D_{M-2} = \phi \text{ and } D_{M-1} = 1 \\ d = 1 \text{ when } D_{M-2} = 1 \text{ and } D_{M-1} = 0 \\ d = 2 \text{ when } D_{M-2} = 0 \text{ and } D_{M-1} = 0 \end{cases} \tag{14}$$



and in the case of  $D_0 = 1$

$$Y_{Dst}(t) = X_i(t - 1) + K_I \times \sigma_D \times 2^d \begin{cases} d = 0 \text{ when } D_{M-2} = \phi \text{ and } D_{M-1} = 0 \\ d = 1 \text{ when } D_{M-2} = 1 \text{ and } D_{M-1} = 1 \\ d = 2 \text{ when } D_{M-2} = 0 \text{ and } D_{M-1} = 1 \end{cases} \tag{15}$$

where  $\phi =$  don't care condition *i.e.*, either 0 or 1, the values of  $K_I$  and  $K_D$  are prefixed, and the standard deviation of the absolute differential values of the input series is  $\sigma_D$  which is considered as unity for estimating the data of the 24th solar cycle. The first output data of the model are generated at  $t = M$  using the values of the input  $X_i(t)$  for  $t = 1$  to  $(M-1)$ . In the next step, again  $(M-1)$  consecutive input data, *i.e.*, values of  $X_i(t)$ , for  $t = 2$  to  $M$ , are required to produce the output at  $t = M + 1$ . In this way, the model generates every  $M^{\text{th}}$  data from the previous  $(M-1)$  data and continues to do so for all the next  $t$  values, generating a simulated output series, namely  $Y_{Dst}(t)$ . To verify the effectiveness of the model, the model output  $Y_{Dst}(t)$  is compared with the real-time Dst index series  $X_i(t)$  and the associated correlation coefficient  $C_c$ , the mean absolute error  $E_{ma}$  and the root-mean-square error  $E_{rms}$  are determined. The following eqs. are used to calculate the said three quantities:

$$C_c = \frac{\text{Cov}[X_i(t), Y_{Dst}(t)]}{\sqrt{\text{Var}[X_i(t)], \text{Var}[Y_{Dst}(t)]}} \tag{16}$$

$$E_{ma} = \frac{1}{n} \sum_{t=1}^n |X_i(t) - Y_{Dst}(t)| \tag{17}$$

$$E_{rms} = \sqrt{\frac{\sum_{t=1}^n [X_i(t) - Y_{Dst}(t)]^2}{n}} \tag{18}$$

### 3 Data source

Here we used the hourly averaged Dst data from the year 1997 to the year 2018 as extracted from NASA/GSFC's OMNI data set through OMNIWeb. The OMNI data were obtained from the GSFC/SPDF OMNIWeb interface at <http://omniweb.gsfc.nasa.gov> [48].

### 4 Results and discussion

Every solar cycle has its rising, maximum, declining, and minimum phases. Also, the geomagnetic storm can be classified into several categories, namely weak, moderate, strong, severe, and great storm. The Dst index belongs to the different categories are usually analyzed and studied separately. But, in our case, the model has been analyzed using the real-time Dst index data of each year of the 23rd solar cycle, *i.e.*, from the year 1997 to 2007, that includes all the phases of the solar cycle and are not segregated between the different storm period. Initially, the input Dst index series  $X_i(t)$  is converted to a 1-bit binary string  $Y_{dm}(t)$  using the delta modulation technique discussed in the method sect. While analyzing the nature of the Dst index, it is found that the rising and the falling properties of the index series are different. The rising of the series is much slower compared to the falling. So,  $K_I$  and  $K_D$  are two different constants assigned corresponding to the increment and decrement phenomenon and estimated experimentally to their best suitable values. Now, the 1-bit binary string  $Y_{dm}(t)$  is demodulated as  $Y_{ddm}(t)$  to test the accuracy of modulation. For every year of the entire 23rd solar cycle, the correlation coefficients are calculated between the original series  $X_i(t)$  and the demodulated series  $Y_{ddm}(t)$  and considered as the accuracy of modulation. The value of  $K_I$  and  $K_D$  are calculated as  $K_I = 0.54$  and  $K_D = 1.30$  to achieve the highest accuracy of modulation *i.e.*, 92% ~ 97% in our case.

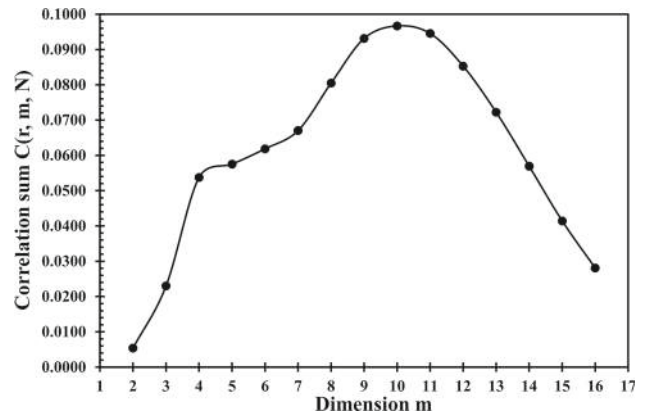
Once the binary string  $Y_{dm}(t)$  is obtained, all the possible patterns are determined using the sliding window technique. Now, the smallest binary pattern can be constructed using at least two successive data points. Thus, the correlation sum  $C(r, m, N)$  is calculated starting from  $m = 2$ . By increasing the dimension  $m$  gradually, the  $C(r, m, N)$  gained the highest value. Upon further increment, the corresponding value started decreasing and at  $m = 16$ , the value of the  $C(r, m, N)$  became sufficiently small to expect any increment thereafter. The decrement of the correlation sum indicates the inadequacy of any new information. The process is executed for all eleven years of the 23<sup>rd</sup> Solar cycle to get a general database of patterns for  $m = 2$  to 16. Table 1 shows the values of the embedded dimension vs correlation sum for the 1-h Dst index, respectively, for the range of the years 1997–2007.

The correlation sum  $C(r, m, N)$  is calculated considering the probability of occurrences of each pattern *i.e.*, their actual contribution in the data series. The nature of patterns present in each year is different along with their number of occurrences. A significant number of common patterns are observed throughout the entire cycle, whereas a small number of distinguished patterns occur only once. As a result, the degree of predictability varies for each year, hence the difference in yearly maximum correlation sum. Figure 1 is the graphical representation of the plots for embedded dimension  $m$  versus mean value of the correlation sum of 11 years associated with the 1-h Dst index series. As seen in Fig. 1, for the Dst index, the optimum state space is achieved for dimension  $M = 10$ . It signifies that the hourly Dst index series has the highest substantial correlated information up to 10 h and no more new information

**Table 1** The year-wise correlation sum  $C(r, m, N)$  is plotted for increasing value of dimension  $m$  for 1-h Dst index for the entire 23rd solar cycle

Dimension	Year											
	1997	1998	1999	2000	2001	2002	2003	2004	2005	2006	2007	
2	0.0158	0.0038	0.0040	0.0046	0.0058	0.0041	0.0043	0.0045	0.0047	0.0037	0.0037	
3	0.0355	0.0188	0.0213	0.0245	0.0253	0.0192	0.0231	0.0234	0.0257	0.0192	0.0173	
4	0.0443	0.0486	0.0539	0.0584	0.0613	0.0461	0.0601	0.0579	0.0645	0.0493	0.0468	
5	0.0496	0.0506	0.0587	0.0633	0.0681	0.0478	0.0611	0.0625	0.0676	0.0531	0.0502	
6	0.0539	0.0545	0.0610	0.0699	0.0681	0.0503	0.0706	0.0706	0.0686	0.0585	0.0544	
7	0.0614	0.0591	0.0659	0.0703	0.0744	0.0545	0.0800	0.0786	0.0737	0.0619	0.0576	
8	0.0713	0.0635	0.0821	0.0918	0.0927	0.0629	0.0879	0.0916	0.0870	0.0815	0.0731	
9	0.0938	0.0838	0.0891	0.0956	0.1001	0.0850	0.0955	0.0957	0.1081	0.0906	0.0870	
10	0.1003	0.0979	0.0871	0.0950	0.1002	0.0905	0.0989	0.0996	0.1025	0.0952	0.0961	
11	0.0965	0.0940	0.0898	0.0987	0.0950	0.0940	0.0960	0.0919	0.0957	0.0942	0.0941	
12	0.0861	0.0892	0.0837	0.0875	0.0827	0.0873	0.0833	0.0805	0.0852	0.0845	0.0882	
13	0.0740	0.0767	0.0723	0.0713	0.0673	0.0773	0.0695	0.0674	0.0691	0.0727	0.0767	
14	0.0608	0.0611	0.0571	0.0549	0.0521	0.0619	0.0534	0.0526	0.0519	0.0592	0.0611	
15	0.0450	0.0449	0.0418	0.0392	0.0371	0.0454	0.0384	0.0383	0.0368	0.0438	0.0448	
16	0.0304	0.0307	0.0285	0.0261	0.0246	0.0312	0.0261	0.0263	0.0243	0.0298	0.0308	

**Fig. 1** The 11 years mean values of the correlation sums  $C(r, m, N)$  are plotted against dimension  $m$  for the 1-h Dst index series considering the 23rd solar cycle



can be retrieved from the series beyond that limit. Thus, resting on the current data point i.e., 9th data point and using the last 8 data points corresponding to the last 8 h, the 10th data point or one-hour advanced data can be estimated using those patterns.

Concerning that estimation, all the 10-bit distinguished patterns for the series  $Y_{dm}(t)$  are identified and stored. The highest possible combinations of binary string for Dst index are 1024 (as  $2^M = 1024$ , where  $M = 10$ ). For the series, all the possible combinations of binary strings are added sequentially for 11 years to consider every single occurred pattern. Figure 2 illustrates the binomial degree distribution of the number of occurrences of the patterns for  $M = 10$  for the hourly Dst index series, which indicates the presence and absence of the entire set of patterns for the 23rd solar cycle.

The demodulated waveforms of some scale-free and periodically occurred patterns are shown in Fig. 3 where the relative amplitudes are plotted in the y-axis. The pattern corresponding to Fig. 3a is the most common and occurred more than 1500 times. Figure 3b, c, and d are chosen randomly from the range of occurrence between 1500 and 1000, 1000 and 500, and 500 and 100, respectively. Studying the database, the probability  $P(D_0 = 0)$  and  $P(D_0 = 1)$  for all these patterns are also estimated and included in the database.

As the general database had been formed, the next step is to study the prediction model of the Dst index discussed in Sect. 2.6 based on this database. The prediction model is analyzed for all the years of the 24th solar cycle, i.e., for the years 2008–2018 using the general database derived from the data of the previous 23rd solar cycle.

The value of  $M = 10$ , which means nine previous consecutive bits are required to generate the 10th data. Thus, the input to the prediction model is any set of nine consecutive values of the real-time Dst index  $X_i(t)$  to generate the predicted output  $Y_{Dst}(t)$  for the next  $t$ . As there is a probability factor in estimating the output  $Y_{Dst}(t)$ , the model is simulated for numerous iterations,  $I_r = 1$  to 250. After each iteration,  $Y_{Dst}(t)$  is compared with the real-time series  $X_i(t)$  and the associated correlation coefficient is estimated. Table 2 shows the value of the correlation coefficients  $C_c$ , mean absolute error  $E_{ma}$ , and root-mean-square error  $E_{rms}$  between the original Dst index  $X_i(t)$  and the predicted model output  $Y_{Dst}(t)$  after 250 iterations for the entire 24th solar cycle. Figure 4 demonstrates

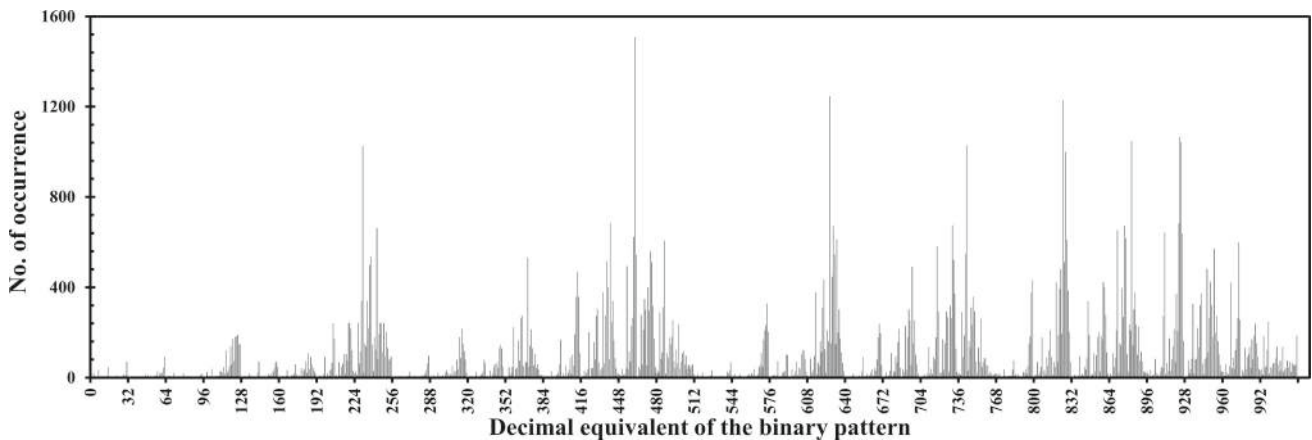
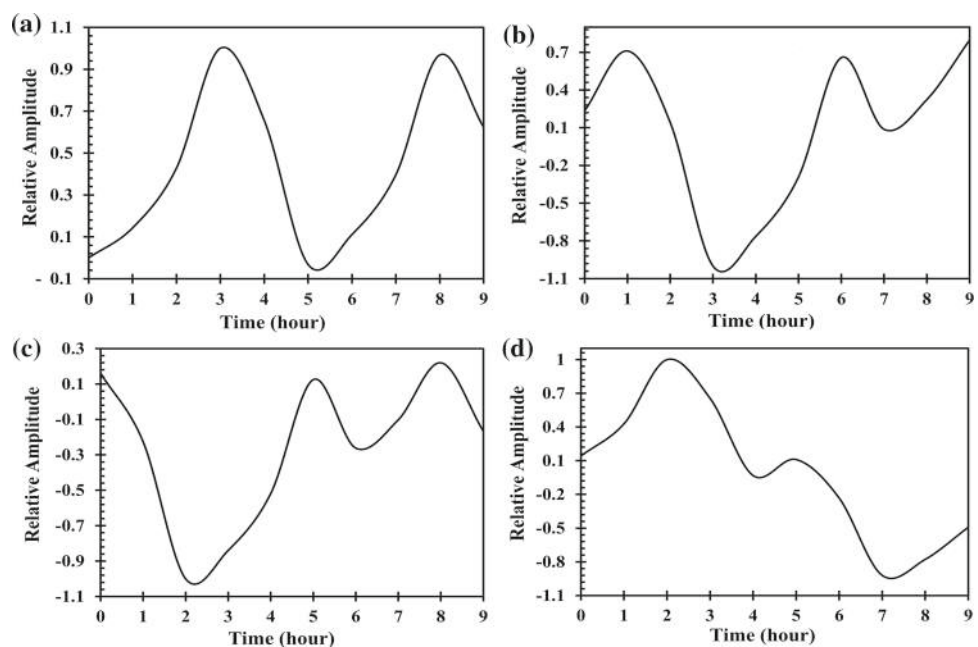


**Fig. 2** The Binomial degree distribution of the number of occurrences of the patterns is plotted for dimension  $M = 10$  for 1-h Dst index series for the entire 23rd solar cycle. The decimal equivalents of the binary patterns or words are plotted sequentially on the x-axis

**Fig. 3** The demodulated waveform of four periodically occurred patterns are shown where the corresponding binary sequences are **a** 0111001110, **b** 1100111011, **c** 1001110110, and **d** 1110010011. The number of their occurrences are 1509, 1000, 671, and 174



the correlation coefficients between  $X_i(t)$  and  $Y_{Dst}(t)$  for an increasing value of the number of iterations  $I_r = 1$  to 250, for the year 2016. The plot shows that the model becomes stabilized at  $I_r = 250$  quite well.

It is observed from Table 2, that the correlation coefficients between the original Dst index  $X_i(t)$  and the model output  $Y_{Dst}(t)$  are greater than 90% for each of the years of the 24th solar cycle, establishing the acceptability of the probabilistic model. Also, the associated values of mean absolute error and root-mean-square error are sufficiently small. The result indicates that the model can predict the Dst index data one hour in advance taking only the previous nine consecutive real-time Dst values as input. For a comparative study, the original Dst index  $X_i(t)$  and the model output  $Y_{Dst}(t)$  for the year 2016 are shown in Fig. 5a and b, respectively. Also, for detailed observation, the two series consisting of 5 days of data ranging between 3 May and 7 May of the same year is plotted in Fig. 5c for the same year.

The entire analysis reveals some prominent features about the probabilistic model and the overall method. A yearly continuous dataset of the real-time Dst index for each of the eleven years of the 23rd solar cycle is considered here to construct the pattern database. No segregation is made in the Dst dataset based on the phase of the solar cycle or the intensity of the geomagnetic storm. Thus, the model is applicable for the Dst index at any period, be it a quiet time or an intense storm. Then the delta modulation converts the analog Dst index series into a 1-bit binary string. Patterns, extracted from an analog signal, do not show scale-free or scale-invariant behaviors. But as the signal is transformed into a binary string in this method, the identified patterns are scale-free. The scale-invariance properties of the identified patterns are much useful to find any similar pattern of variable amplitude, which aids to construct the database consisting of all the patterns hidden in the structure of the Dst index series. Also, the optimum state space is reconstructed to identify the length of the optimum information in the hyperspace of the Dst index series. As observed

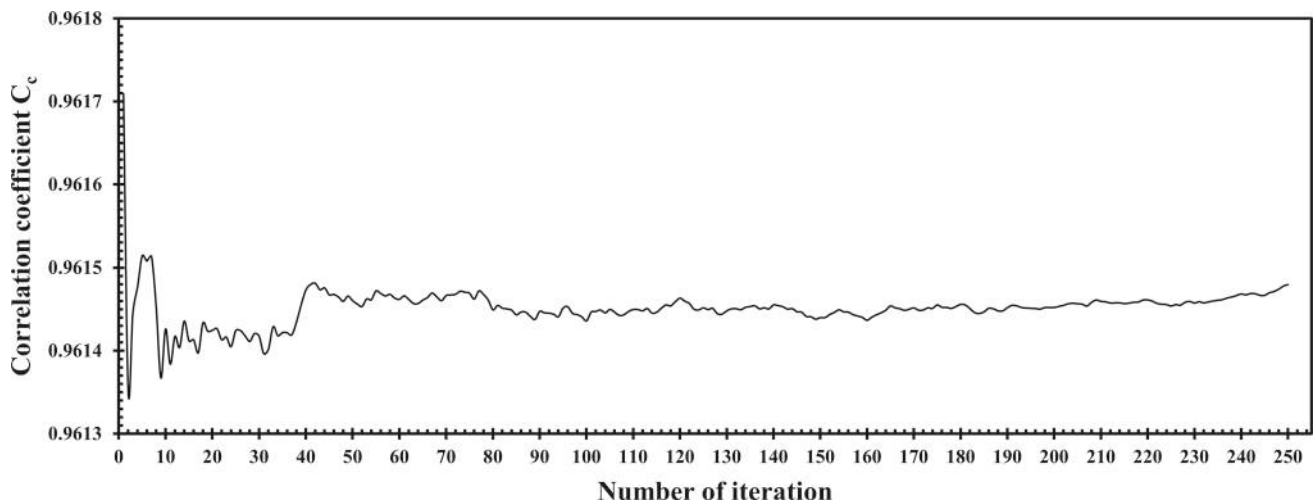


**Fig. 4** The value of the correlation coefficients between the original Dst index  $X_i(t)$  and the predicted model output  $Y_{Dst}(t)$  is plotted against the number of iterations performed for the year 2016

**Table 2** shows the value of the correlation coefficients  $C_c$ , mean absolute error  $E_{ma}$ , and root-mean-square error  $E_{rms}$  between the original Dst index  $X_i(t)$  and the predicted model output  $Y_{Dst}(t)$  after 250 iterations of the 24th solar cycle

Year	Correlation coefficient $C_c$	Mean absolute error $E_{ma}$	Root-mean-square error $E_{rms}$
2008	0.9488	2.6275	3.5234
2009	0.9285	2.4877	3.3017
2010	0.9542	2.7175	3.6655
2011	0.9595	2.9842	4.3502
2012	0.9757	3.1861	4.5221
2013	0.9683	2.9979	4.2113
2014	0.9636	3.1088	4.2498
2015	0.9725	3.5395	5.1543
2016	0.9615	3.1705	4.3541
2017	0.9611	3.1973	4.4571
2018	0.9570	2.8031	3.7861

from the result, no extra information can be retrieved from the series beyond the dimension  $M = 10$ , it is the optimum value of the state space. The saturation of attractor properties, used here to reconstruct the optimum state space, ensures minimum loss of information while estimating the optimum value. It is one of the key features of this method. Moreover, the model has a minimum dependency on external factors. A future Dst index value can be estimated only by using a finite set of previous Dst values and the pattern database as the input to the model. No other solar wind parameters or interplanetary magnetic field data are required. In the current analysis, the pattern database is constructed using the hourly real-time Dst index of the 23rd solar cycle. Using this database and nine previous values of Dst data, the model can predict the tenth Dst value in one hour advance for the entire 24th solar cycle, with a correlation coefficient up to 97.57%. Further, the maximum mean absolute error and root-mean-square error are found to be sufficiently small, 3.5395 and 5.1543, respectively.

## 5 Conclusion

The Dst index is a measurement of the geomagnetic activities on Earth and is widely used to indicate the intensity and occurrence of geomagnetic storms. Identifying significant patterns enfolded in the hidden layers and extracting substantial information from the inherent structures can be extremely rewarding in developing a successful forecasting algorithm. Moreover, an insight into the complex physical structure of this natural time series explains a lot of its characteristic features and dynamical behaviors. In this paper, we introduce a new method to predict the Dst index based on the concept of pattern recognition and optimum state space reconstruction. The analysis is a composite one; first to identify and characterize the significant patterns hidden in the structures of the 1-h Dst index series and then, development of a probabilistic model based on these patterns to forecast Dst data long before its actual occurrence. The algorithm includes adaptive delta modulation to convert the series into a binary string, the reconstruction of the optimum state space, construction of a database containing the probability of occurrence of the pattern, and finally, the development of a probabilistic predictive model to estimate the future data in one hour advance. The model has two inputs, the first one is the

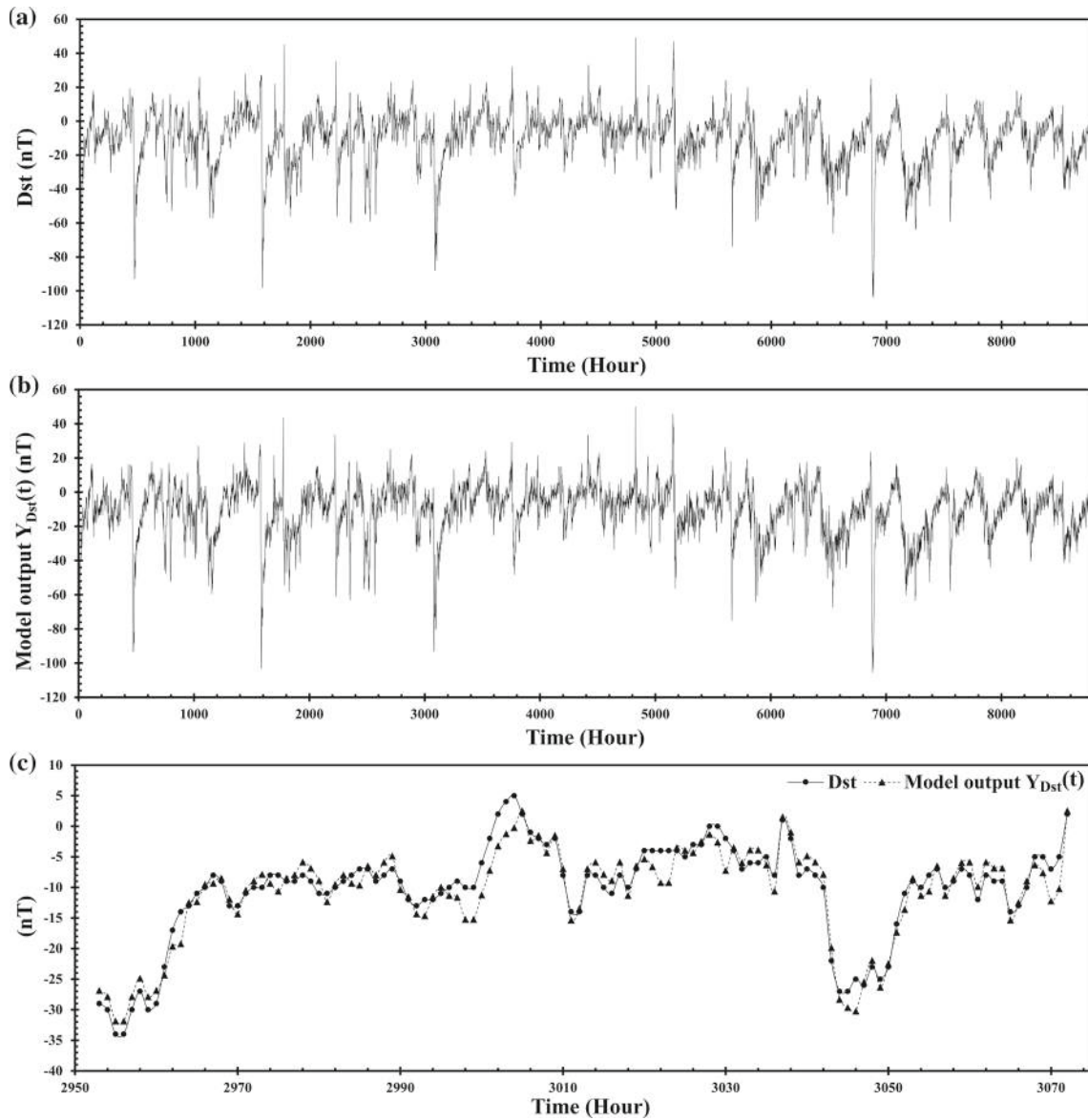


**Fig. 5** **a** The original 1-h Dst index  $X_i(t)$  for the year 2016, **b** the model output  $Y_{Dst}(t)$  for the same year, and **(c)** a comparative of the two series consisting of 5 days of data ranging between 3 May 2016 and 7 May 2016

database of the pattern created using the data of the entire 23rd solar cycle, and the second one is any set of nine consecutive data of the real-time Dst index of the 24th solar cycle to predict the 10th value. The predicted output is compared with each yearly data of the 24th solar cycle based on three parameters namely correlation coefficient, mean absolute error, and root-mean-square error for the statistical validation of the model. It has been observed that the values of the correlation coefficients between the real-time and predicted series are more than 90% for each of the years whereas the associated values of mean absolute error and root-mean-square error are significantly small. These results established the predictive performance of the model quite in a good way, using the database formed from the data of the 23<sup>rd</sup> solar cycle to predict the data of the next 24<sup>th</sup> solar cycle. Also, the model needs only the previous values of the real-time Dst index to predict the future value in one hour advance and no other data of geomagnetic indices or solar wind parameters are required for this method. One hour is sufficient to activate any controlling system to temporarily shut down the electrical hardware or power grids to save them from the perils of the coming storm. Moreover, the model takes a moderate number of iterations to be stabilized making a much lower computational time. Again, the study also revealed that the underlying physical structure of the Dst index is a complex composition of numerous distinguished patterns, occurring through the series in various frequencies. Some common patterns repeat through the entire solar cycle numerous times, whereas some are not. A small number of distinguished patterns occurs only once. As a result, the degree of predictability, as well as the maximum correlation sum, varies

in a small range for each year. Finally, for the Dst index, the optimum state space is achieved for the dimension  $M = 10$ , denoting no more new information can be retrieved from the time series beyond this particular dimension.

Geomagnetic disturbances on Earth are a complex phenomenon, and a powerful storm is need to be predicted a sufficient time before saving society from its adverse effects. Dst index, the global measurement of the geomagnetic storm, also represents the internal dynamical nature of this natural event, an overlapping of various physical processes or patterns forming an intricate structure. The current study was focused to identify and analyze the characteristics of these patterns enfolded in the dynamical structure of the Dst index to develop a successful prediction algorithm for this time series and in general, geomagnetic storm. The structure and traits of these patterns are very much intriguing and demand detailed study in the future to gain a much deeper knowledge of geomagnetic disturbances. The database of patterns can be continually updated with time incorporating all the available data to get various types of patterns and much more accuracy in predicting the future value.

**Supplementary Information** The online version contains supplementary material available at <https://doi.org/10.1140/epjp/s13360-022-02687-7>.

**Acknowledgements** We acknowledge the use of NASA/GSFC's Space Physics Data Facility's OMNIWeb (or CDAWeb or ftp) service, OMNI data and SIDC, RWC Belgium, World Data Centre. Data sets corresponding to Table 1 and Figure 3 are also available from the corresponding author on specific requests. We are thankful to Parthasarathi Chakrabarti, Director, IEST, Shibpur, Howrah, India, for the institutional support. We are also thankful to Somnath Mukherjee, Principal of Dinabandhu Andrews College, Kolkata, India for the cordial support and constant encouragement. Finally, we are also very much thankful to the anonymous reviewer for the significant insight into our manuscript by which, we are getting further encouraged to unfold the information hidden inside the geomagnetic data series.

**Authors' contributions** The authors have an equal contribution to the development of the manuscript.

**Funding** Self-funded as we are independent researchers.

## Declarations

**Conflict of interest** Nil.

**Ethics approval** Not applicable.

**Consent to participate** Not applicable.

**Consent for publication** Not applicable.

**Code availability** No.

**Data availability** Data are available on request made to the corresponding author.

## References

1. M. Sugiura, T. Kamei, Equatorial DST index 1957–1986, in IAGA Bull. 40, edited by A. Bertheliet, and M. Menvielle, Int. Serv. of Geomagn. Indices Publ. Off., Saint Maur, France (1991)
2. M. Sugiura, Hourly values of equatorial Dst for IGY. Annals of the International Geophysical Year, vol. 35, pp. 945–948 (Pergamon Press, Oxford, U. K.) (1964)
3. J.A. Wanliss, K.M. Showalter, High-resolution global storm index: Dst versus SYM-H. J. Geophys. Res. **111**, A02202 (2006). <https://doi.org/10.1029/2005JA011034>
4. J.G. Kappenman, L.J. Zanetti, W.A. Radasky, Geomagnetic storms can threaten electric power grid. Am. Geophys. Union Earth Space **9**(7), 9–11 (1997)
5. Hydro-Québec, Understanding electricity. Retrieved 2010-10-2 (1989)
6. CENTRA Technology Inc., Geomagnetic Storms Report Prepared for the Office of Risk Management and Analysis United States Department of Homeland Security (2011)
7. NOAA technical memorandum OAR SEC-88, Halloween space weather storms of 2003. Space Environment Center, Boulder, Colorado, June 2004 (2003)
8. L.J. Lanzerotti, Space Weather Effects on Technologies, in *Space Weather*. ed. by P. Song, H.J. Singer, G.L. Siscoe (AGU, Washington, 2013)
9. National Research Council, Severe Space Weather Events, Understanding Societal and Economic Impacts. A Workshop Report, Washington, DC, The National Academies Press (2008)
10. A. Pulkkinen, E. Bernabeu, J. Eichner, C. Beggan, A.W.P. Thomson, Generation of 100-year geomagnetically induced current scenarios. Space Weather **10**, S04003 (2012). <https://doi.org/10.1029/2011SW000750>
11. A.W.P. Thomson, E.B. Dawson, S.J. Reay, Quantifying extreme behavior in geomagnetic activity. Space Weather **9**, S10001 (2011). <https://doi.org/10.1029/2011SW000696>
12. A. Viljanen, R. Pirjola, E. Prácer, S. Ahmadzai, V. Singh, Geomagnetically induced currents in Europe: characteristics based on a local power grid model. Space Weather **11**, 575–584 (2013). <https://doi.org/10.1002/swe.20098>

13. R.L. McPherron, G. Siscoe, N.U. Crooker, N. Arge, Probabilistic Forecasting of the Dst Index, in *The Inner Magnetosphere: Physics and Modeling*. ed. by T.I. Pulkkinen, N.A. Tsyganenko, R.H.W. Friedel (AGU, Washington, 2005)
14. M. Chandorkar, E. Camporeale, S. Wing, Probabilistic forecasting of the disturbance storm time index: an autoregressive Gaussian process approach. *Space Weather* **15**, 1004–1019 (2017). <https://doi.org/10.1002/2017SW001627>
15. S.B. Xu, S.Y. Huang, Z.G. Yuan, X.H. Deng, K. Jiang, Prediction of the Dst index with bagging ensemble-learning algorithm. *Astrophys. J. Suppl. Ser.* **248**(1), 14 (2020). <https://doi.org/10.3847/1538-4365/ab880e>
16. R.J. Boynton, M.A. Balikhin, S.A. Billings, A.S. Sharma, O.A. Amariutei, Data derived NARMAX Dst model. *Ann. Geophys.* **29**, 965–971 (2011). <https://doi.org/10.5194/angeo-29-965-2011>
17. M.A. Gruet, M. Chandorkar, A. Sicard, E. Camporeale, Multiple-hour-ahead forecast of the Dst index using a combination of long short-term memory neural network and Gaussian process. *Space Weather* **16**, 1882–1896 (2018). <https://doi.org/10.1029/2018SW001898>
18. H.L. Wei, S.A. Billings, M. Balikhin, Prediction of the Dst index using multiresolution wavelet models. *J. Geophys. Res.* **109**, A07212 (2004). <https://doi.org/10.1029/2003JA010332>
19. D. Zhu, S.A. Billings, M.A. Balikhin, S. Wing, H. Alleyne, Multi-input data derived Dst model. *J. Geophys. Res.* **112**, A06205 (2007). <https://doi.org/10.1029/2006JA012079>
20. E.Y. Ji, Y.J. Moon, N. Gopalswamy, D.H. Lee, Comparison of Dst forecast models for intense geomagnetic storms. *J. Geophys. Res.* **117**, A03209 (2012). <https://doi.org/10.1029/2011JA016872>
21. R.K. Burton, R.L. McPherron, C.T. Russell, An empirical relationship between interplanetary conditions and Dst. *J. Geophys. Res.* **80**, 4204–4214 (1975)
22. F.R. Fenrich, J.G. Luhmann, Geomagnetic response to magnetic clouds of different polarity. *Geophys. Res. Lett.* **25**, 2999–3002 (1998)
23. T.P. O'Brien, R.L. McPherron, An empirical phase space analysis of ring current dynamics: solar wind control of injection and decay. *J. Geophys. Res.* **105**, 7707–7720 (2000)
24. M. Temerin, X. Li, A new model for the prediction of Dst on the basis of the solar wind. *J. Geophys. Res.* **107**(A12), 1472 (2002). <https://doi.org/10.1029/2001JA007532>
25. M. Temerin, X. Li, Dst model for 1995–2002. *J. Geophys. Res.* **111**, A04221 (2006). <https://doi.org/10.1029/2005JA011257>
26. C.B. Wang, J.K. Chao, C.H. Lin, Influence of the solar wind dynamic pressure on the decay and injection of the ring current. *J. Geophys. Res.* **108**(A9), 1341 (2003). <https://doi.org/10.1029/2003JA009851>
27. J. Chen, P.J. Cargill, P.J. Palmadesso, Predicting solar wind structures and their geoeffectiveness. *J. Geophys. Res.* **102**(A7), 14701–14720 (1997). <https://doi.org/10.1029/97JA00936>
28. I. V. Kovalevskij, Yu. I. Morozov, Geomagnetic storm as an object of pattern recognition. ITEF-74, USSR (1986)
29. J.V. Kovalevsky, Yu.I. Morozov, *Pattern Recognition Methods in Analysis of Complex Physical Phenomena* (IZMIRAN, Russia, Moscow, 1990)
30. J. V. Kovalevsky, E. I. Kovalevskaya, Application of pattern recognition methods in analysis of complex physical phenomena in geospace: geomagnetospheric storms. Correlated phenomena at the sun, in the heliosphere and in geospace. In: proceedings 31st ESLAB symposium, ESTEC, Noordwijk, ESA SP-415, pp. 431–436 (1997)
31. X.P. Zeng, Y.F. Lin, C. Lu, Z.X. Feng, Q.H. Guo, Application of pattern recognition method to the prediction of geomagnetic storms. *Chin. J. Sp. Sci.* **4**, 42–50 (1984)
32. A. Banerjee, A. Bej, T.N. Chatterjee, On the existence of a long range correlation in the geomagnetic disturbance storm time (Dst) index. *Astrophys. Space Sci.* **337**, 23–32 (2012). <https://doi.org/10.1007/s10509-011-0836-1>
33. A. Banerjee, A. Bej, T.N. Chatterjee, A cellular automata-based model of Earth's magnetosphere in relation with Dst index. *Space Weather* **13**, 259–270 (2015). <https://doi.org/10.1002/2014SW001138>
34. A. Banerjee, A. Bej, T.N. Chatterjee, A. Majumdar, An SOC approach to study the solar wind-magnetosphere energy coupling. *Earth Space Sci.* **6**, 565–576 (2019). <https://doi.org/10.1029/2018EA000468>
35. J.E. Abate, Linear and adaptive delta modulation. *Proc. IEEE* **55**(3), 298–308 (1967). <https://doi.org/10.1109/PROC.1967.5486>
36. C. C. Cutler, Differential quantization of communication signals. *Nokia Bell Labs, U.S. Patent* **2**, 605, 361 (1952)
37. F. DeJager, Delta modulation, a method of PCM transmission using a 1-unit code'. *Phillips Res. Rept. No.* **7**, 442–466 (1952)
38. D.J. Goodman, A digital approach to adaptive delta modulation. *Bell Syst. Tech. J.* **50**, 1421–1426 (1971). <https://doi.org/10.1002/j.1538-7305.1971.tb02560.x>
39. R. Gregorian, J.G. Gord, A continuously variable slope adaptive delta modulation codec system. *IEEE J. Solid-State Circuits* **18**(6), 692–700 (1983). <https://doi.org/10.1109/JSSC.1983.1052019>
40. C. Halijak, J. Tripp, A deterministic study of delta modulation. *IEEE Trans. Automat. Contr.* **8**(4), 339–347 (1963). <https://doi.org/10.1109/tac.1963.1105592>
41. M.H. Weik, *Computer Science and Communications Dictionary* (Springer, Boston, 2000), pp. 382–382
42. C.M. Zierhofer, Adaptive sigma-delta modulation with one-bit quantization. *IEEE Trans. Circuits Syst. II* **47**(5), 408–415 (2000). <https://doi.org/10.1109/82.842109>
43. H.D.I. Abarbanel, R. Brown, J.J. Sidorowich, L.S. Tsimring, The analysis of observed chaotic data in physical systems. *Rev. Mod. Phys.* **65**(4), 1331–1392 (1993). <https://doi.org/10.1103/RevModPhys.65.1331>
44. T.N. Chatterjee, On the application of information theory to the optimum state-space reconstruction of the short-term solar radio flux (10.7cm), and its prediction via a neural network. *Mon. Not. R. Astron. Soc.* **323**, 101–108 (2001). <https://doi.org/10.1046/j.1365-8711.2001.04110.x>
45. C.E. Shannon, A mathematical theory of communication. *Bell Syst. Tech. J.* **27**, 623–656 (1948). <https://doi.org/10.1002/j.1538-7305.1948.tb00917.x>
46. K. Pawelzik, H.G. Schuster, Generalized dimensions and entropies from a measured time series. *Phys. Rev. A* **35**(1), 481–484 (1987). <https://doi.org/10.1103/physreva.35.481>
47. S. Eubank, J.D. Farmer, An Introduction to Chaos and Prediction, in *Lectures in the Science of Complexity*. ed. by E. Jen. SFI studies in the science of complexity. (Addison-Wesley, MA, 1990), p. 75
48. J.H. King, N.E. Papitashvili, Solar wind spatial scales in and comparisons of hourly wind and ACE plasma and magnetic field data. *J. Geophys. Res.* **110**, A02209 (2005). <https://doi.org/10.1029/2004JA010649>



# Source details

[Feedback](#) > [Compare sources](#) >

## European Physical Journal Plus

Scopus coverage years: from 2011 to Present

Publisher: Springer Nature

ISSN: 2190-5444

Subject area: [Chemical Engineering: Fluid Flow and Transfer Processes](#) [Physics and Astronomy: General Physics and Astronomy](#)

Source type: Journal

[View all documents](#) >

[Set document alert](#)

[Save to source list](#)

CiteScore 2022

4.9



SJR 2022

0.548



SNIP 2022

0.979







# One-hour ahead prediction of the Dst index based on the optimum state space reconstruction and pattern recognition

Amaresh Bej<sup>1</sup>, Adrija Banerjee<sup>1,a</sup> , T. N. Chatterjee<sup>2</sup>, Abhijit Majumdar<sup>1</sup>

<sup>1</sup> Department of Physics, Indian Institute of Engineering Science and Technology, Shibpur, P.O.-Botanic Garden, Howrah, West Bengal 711103, India

<sup>2</sup> Department of Electronics, Dinabandhu Andrews College, 54, Raja S.C. Mullick Road, Garia, Kolkata, West Bengal 700084, India

Received: 5 July 2021 / Accepted: 5 April 2022

© The Author(s), under exclusive licence to Società Italiana di Fisica and Springer-Verlag GmbH Germany, part of Springer Nature 2022

**Abstract** The Disturbance storm time (Dst) index is the global estimation of the intensity of the terrestrial geomagnetic activities as well as the primary indicator of the geomagnetic storm. As the adverse effect of a powerful geomagnetic event has become a serious threat to modern human society, extracting meaningful information concealed in the complex structures of this time series can form the ground of a successful prediction algorithm. In this paper, we introduce a new probabilistic model based on the concept of adaptive delta modulation and optimum state space to analyze, identify and characterize the patterns enfolded in the layers of the 1-h Dst index and then predict Dst data using these patterns. The study reveals some significant insights. The exact dimension  $M$  of the optimum state space for the Dst index is found to be at  $M = 10$ . Also, the series is a combination of multiple distinguished repeating and non-repeating patterns, denoting a high degree of predictability of the  $M$ th data of the series from its previous  $(M-1)$  binary data. Eventually, the simulated output of the probabilistic model exhibits a high value of correlation coefficient with the real-time Dst index. Interestingly, the technique only requires the Dst index data as an input of the probabilistic model and is found to be very effective for the entire 24th solar cycle.

## 1 Introduction

The disturbance storm time (Dst) index is an indication of the geomagnetic activities in the terrestrial magnetosphere and is frequently used in characterizing the intensity of geomagnetic storms. It is computed based on the average value of the horizontal component of the Earth's magnetic field recorded at four different observatories, namely Hermanus (34.40°S, 19.22°E in geographic latitude and longitude), Kakioka (36.23°N, 140.18°E), Honolulu (21.32°N, 158.02°W), and San Juan (18.01°N, 66.15°W) [1]. These stations are evenly spaced in longitude and near enough to the magnetic equator to nullify the influence of the auroral effect as much as possible, again also placed at a significant distance away from the magnetic equator to minimize the influence of the equatorial electrojet current flowing in the ionosphere [2, 3].

Severe geomagnetic activity poses a potential threat to modern human society as a powerful storm can wreak havoc by collapsing all the electrical systems in the affected area, including power grids, computer and communication networks, satellite and navigation systems, military intelligence, and so on. The phenomenon is a sequence of striking the Earth by an intense geomagnetic storm followed by the entering of a stream of charged plasma particles into the geospace through the solar wind-magnetosphere reconnection that results in an induction of an electric field in the magnetosphere. As a consequence, voltage differences are generated between the ground points of the electrical networks that drive a current, namely geomagnetically induced current (GIC), flowing through the electrical hardware. The value of this GIC can be as high as 100 Ampere which is substantially beyond the specified range of tolerance of the electrical circuits causing fatal damages to the entire system [4]. Needless to say, our modern human society is almost entirely dependent on technology based on electrical power more than ever, thus a GIC-triggered catastrophic collapse of the electrical infrastructure in a large region includes enormous monetary losses, wastages of manpower, and prolonged unavoidable hazards. As an example, an intense geomagnetic storm on March 13, 1989, caused the entire Hydro Quebec system to get shut down resulting in more than 6 million customers surviving without electricity for nine hours [4, 5]. In 2003, the Wide Area Augmentation System (WAAS) operated by the Federal Aviation Administration (FAA) was affected by the Halloween solar storm and collapsed for approximately 30 h causing serious damages to many satellite systems including the Japanese ADEOS-2 satellite. In the past years, the Nordic countries along with the USA and Canada had faced unbearable consequences of geomagnetic storms, like the complete disruption of electric power-grids, hours of blackouts, damages of navigation as well as communication systems, disruption of satellite hardware and computer networks. In a report by the Oak Ridge National Laboratory, a geomagnetic storm, slightly stronger than March 1989 one, can result in an enormous blackout in the whole north-eastern area of the USA including a huge \$36 billion

<sup>a</sup> e-mail: [adrija\\_bnrj@yahoo.co.in](mailto:adrija_bnrj@yahoo.co.in) (corresponding author)

monetary loss in gross domestic product. [4, 6–9]. The perils of these intense geomagnetic storms, that occurred in the European countries in the last decades, also had been discussed and analyzed in several reports and original studies [10–12].

As there is no successful mechanism to estimate the exact future data from the present resources, a proper probabilistic model for forecasting the occurrence and intensity of geomagnetic storms is the need of the hour to save society from huge monetary losses and related hazards. McPherron et al. [13] proposed a probabilistic forecasting method, found to be most applicable for low to moderate storms during the declining phase of the solar cycle. Chandorkar et al. [14] presented an innovative forecasting method based on an autoregressive Gaussian process approach. The inputs to the model are previous values of the Dst index, solar wind speed and IMF  $B_z$ . The model generates a One Step Ahead prediction of the Dst index, requiring a small set of data for the training and validation. Xu et al. [15] studied the prediction of the Dst index using the Bagging ensemble-learning algorithm, which is a combination of an artificial neural network, support vector regression, and a long short-term memory network. They presented a model which takes several solar wind parameters like interplanetary total magnetic field, total electric field, IMF  $B_z$ , solar wind speed, plasma temperature and proton pressure as inputs and forecasts Dst index values 1–6 h in advance. Boynton et al. [16] developed a mathematical model based on NARMAX algorithm to study the dynamics of the Dst index. A solar wind-magnetosphere coupling function is used as the input to the model. The model shows a high forecasting ability of the occurrence, duration and intensity of the geomagnetic storm. A probabilistic algorithm combining Long Short-Term Memory recurrent neural network with Gaussian Process model was developed by Gruet et al. [17]. The model predicts the Dst index 6-h ahead with a correlation coefficient higher than 0.873 and root mean square error lower than 9.86. Wei et al. [18] constructed an effective forecasting algorithm for the Dst index using the multiresolution B spline wavelet decompositions which takes  $VB_s$  and the solar wind parameter as inputs. Zhu et al. [19] developed a multi-input–single-output discrete-time model based on the NARMAX algorithm which forecasts the dynamics of the Dst index better than the single-input NARMAX models. Also, a comparative study of the Dst forecast models for the intense geomagnetic storm was presented by Ji et al. [20]. In this work, six Dst forecast models are compared during intense geomagnetic storms. The models are Burton et al. [21], Boynton et al. [16], Fenrich and Luhmann [22], O'Brien and McPherron [23], Temerin and Li [24, 25] Wang et al. [26]. The input data to the model are solar wind parameters. The study concluded that the Temerin and Li model is the best one for predicting geomagnetic storms having values  $-100 \text{ nT} \leq \text{Dst} \leq -200 \text{ nT}$ . It is also better than the other models in terms of various parameters and interplanetary structures.

All these models are highly effective as prediction tools for the Dst index but are controlled by several factors and most importantly, take more than one input parameter for proper forecasting. In the current study, we propose a new and alternative method to predict the Dst index based on the concept of pattern recognition. The proposed probabilistic model has several features which distinguish it from the previous studies. A detailed database of different patterns is formed from the real-time data of an entire solar cycle to be used in the processing unit of the model. Also, the model needs only the previous values of the real-time Dst index to predict the future value and no other data of geomagnetic indices or solar wind parameters are required for this method. Both the mean absolute error and root-mean-square error are significantly small. Moreover, the primary algorithm of the model ensures minimum loss of information in analyzing the time series.

For several past years, pattern recognition became a widely used technique to study and analyze the existing regularities in an otherwise complex time series. A significant number of research works have been devoted to study the geomagnetic disturbances based on this method [27–31].

To find some specific patterns repeating themselves in a complex time series like the Dst index can lead us to a method of prediction of future data of the series from a previous set of data as well as some significant revelations of its underlying structure. In our previous works, we inspected the dynamical nature of the Dst index and in general geomagnetic storms [32–34]. We analyzed the Dst index using an innovative graphical method, namely visibility algorithm and observed the series can be categorized as a fractional Brownian motion having long-range correlation [32]. In the next study, we developed a cellular automata model of the terrestrial magnetosphere based on the concept of self-organized criticality and sandpile dynamics. Real-time solar wind parameters and IMF  $B_z$  data are the input to the model. The spectral response of the simulated output shows statistical similarity with that of the natural Dst index. The integral dynamics of geomagnetic disturbances is observed as a self-organized critical behavior of a perturbed system resulting in avalanche formations [33]. We refined the model further by introducing a new solar wind-magnetosphere coupling function to the model. The analysis reveals that the solar activities had a direct influence over the solar wind-magnetosphere coupling. Also, a substantial time delay is observed between the initial injection of solar wind into the magnetosphere and its consequent effect on the Earth's magnetic field [34]. All these studies make us realize that the Dst index has a complex and intricate structure, resulting from various underlying physical mechanisms, thus unpredictable in conventional methods. Identifying and characterizing the repetitive patterns hidden in the structure of the Dst index may lead us to a successful prediction algorithm. In the current paper, we continue our study of geomagnetic disturbances and propose a probabilistic model of the Dst index based on delta modulation, optimum state space (OSS) reconstruction, and pattern recognition.

Delta modulation is a simple one-bit special case of digital pulse code modulation technique. Adaptive delta modulation is a refined version of the linear delta modulation where the step size is not fixed. Numerous studies have been presented in the past years to delta modulate an analog or continuous data series to minimize the quantization error as well as to maximize the accuracy of the modulation [35–42]. Patterns, extracted from an analog signal, do not show scale-free or scale-invariant behaviors. To construct a scale-free pattern, the analog signal needs to be converted into a binary string. Delta modulation is such a technique, generally used

for analog to digital conversion. As our current study is mainly based on identifying the patterns of the Dst index, delta modulation is used to convert the time series into its binary form to extract scale-free patterns hidden in its layers.

The time series prediction can be considered as a pattern recognition problem by forecasting the future data from the previous patterns. For this, the optimum dimension of the phase space must be evaluated [43, 44]. Conventionally, there are three distinct methods available for optimum state space reconstruction, discussed as follows:

- (1) Singular value analysis: In this method, the covariance matrix associated with the time series is estimated and the related eigenvalues are calculated. The presence of high-dimensional noise in the time series constructs the floor of the eigenvalue spectrum. The value of the optimum state space can be determined from that spectrum. The calculations used in this method are simple though have some difficulties during the analysis of the outcome. It fails to differentiate between two dynamical systems having nearly similar Fourier spectrums. Also, the method has a strong dependence on the notion of the noise floor, thus inapplicable for colored noise [44].
- (2) False neighborhood: A false neighbor is a point having a minimum distance from the input point, where the input space dimension is smaller than the optimum space dimension. By increasing the distance between them by a scale factor, eventually, the number of false neighbors leads to zero and the optimum dimension can be reached. This method is also simple but has disadvantages too. Firstly, it is difficult to determine the exact value of the scale factor or criteria to identify a false neighbor. Secondly, for oversampled data, the points close in time but distant in space can wrongly be considered as true neighbors. Thirdly, if the embedding dimension becomes less than optimum, the distance between the neighbors remains unchanged for the points outside the attractor. Finally, the method requires a large number of data [44].
- (3) Saturation of attractor properties: In a dynamical system, an attractor is a set of states toward which a system tends to evolve. This analysis is based on the concept of unfolding the attractor by a large dimension. As the optimum dimension has been reached, the attractor properties dependent on the distance of the points in the phase space become independent of the embedding dimension. The method needs a large set of data to properly estimate the optimum dimension, which is its only disadvantage [44].

Previously, Chatterjee [44] established a probabilistic model based on the artificial neural network (ANN) to predict the 10.7 cm radio flux in advance. In that paper, Chatterjee coined a modified technique to reconstruct the optimum state space by a variation of this method based on entropy and information. In the modified method, an algorithm is developed to determine the optimum dimension of state space by estimating the metric entropy of the time series. The most advantageous point of this analysis is that it ensures minimum loss of information to reconstruct the optimum state space. As the value of the optimum dimension of the state space is determined, the prediction time can be calculated by using this value in a mathematical relation. Then the value of the prediction time is used in the ANN probabilistic model to generate output data by feeding the model a set of previous data. It was observed that the model predicts 10.7 cm radio flux quite accurately in 1 day in advance and the methodology is suitable to predict any time-series influenced by solar parameters. Since the Dst index is such a geomagnetic time-series, we consider this technique of optimum space reconstruction to be fruitful enough for our present work. In our study, we follow the algorithm of optimum state space reconstruction presented by Chatterjee [44], then instead of developing an ANN model as Chatterjee [44], we establish a novel technique of predicting the Dst index based on pattern recognition.

## 2 Method

The proposed prediction algorithm in the current work follows the steps: (1) Conversion of the Dst index time-series to an  $n$ -bit binary string using an adaptive delta modulation technique, (2) Formation of a set of pattern by taking  $m$  consecutive bits from the binary string where the value of  $m$  ranges from 1 to  $n-1$ , (3) Recording of the number of occurrence of each pattern in the binary string by applying the sliding window protocol, (4) Determination of the optimum value of the state space ' $M$ ' from the recorded data by calculating the correlation sum, (5) To find out all the  $M$ -bit patterns from the binary string including their number of occurrences, (6) Calculation of the probability of the least significant binary bit  $D_0$  being '1' or '0' in a  $M$ -bit pattern after a specific combination of the rest of the bits  $D_{M-1} \dots D_2 D_1$ , (7) Formation of a general database for all the  $M$ -bit patterns of the 11-year solar cycle, consisting of  $2^{M-1}$  number of patterns including the probability of occurrence of the least significant bit that calculated in the previous step, (8) Establishing a probabilistic prediction model by using this general database and a demodulation algorithm, where the model takes  $(M-1)$  consecutive real-time data in the input to generate the future value of the  $M$ th data, (9) Comparison of the probabilistic model output with the real-time Dst index after a suitable number of iterations. The acceptability of the model is verified by calculating the correlation coefficient between the model output and the real-time Dst index series.

### 2.1 Converting the Dst index time series into a binary string using the delta modulation technique

Delta modulation technique can be regarded as a 1-bit differential pulse code modulation (DPCM) scheme. A reference signal is initiated, the input signal is sampled, and then by comparing the reference signal with the input signal, the increase or decrease in relative amplitude is determined. If the input signal has a higher amplitude than the reference signal, the value of the output is set

to '1' and the reference signal is increased by a predefined step size  $\Delta$ . If the input signal has a lower amplitude than the reference signal, the value of the output is '0' and the reference signal is decreased by  $\Delta$ . In both cases, the  $\Delta$  is a multivalued predefined variable and not the exact difference between the input and the reference signal. In this way, the difference value of the amplitudes is quantized in only two levels, corresponding to the positive or negative differences, whereas a no-change condition causes the modulated signal to remain at the same state of the previous sample. The output signal is a 1-bit binary data series that contains only the change in information.

Delta modulation with limited adaptivity technique is a modified version of the classic delta modulation. Application of this technique on a Dst index time series converts the series to a 1-bit binary string. Let  $X_i(t)$  is the input Dst index series having  $n$  number of data, where  $t = 1, 2, 3, \dots, n$ . At first, a second series,  $X_r(t)$  known as the reference signal is computed from  $X_i(t)$ . The first three values of  $X_r(t)$  are the same as  $X_i(t)$ , i.e.,

$$X_r(t) = X_i(t) \text{ for } t = 1 \text{ to } 3 \quad (1)$$

For  $t > 3$ , to compute  $X_r(t)$  in general, the term  $X_r(t-1)$  is compared with the term  $X_i(t)$  to check if there is an increment or decrement in the values. Here, If  $X_i(t) > X_r(t-1)$ , there is an increment and a factor  $\Delta_I$  is added to the term  $X_r(t-1)$  to determine the value of  $X_r(t)$ . If  $X_i(t) < X_r(t-1)$ , there is a decrement and a factor  $\Delta_D$  is subtracted from the term  $X_r(t-1)$  to determine the value of  $X_r(t)$ . The factor  $\Delta$  is called the step size of the reference signal as it continues to track the change in values between two consecutive steps. Mathematically, for  $t = 4$  to  $n$ ,

$$X_r(t) = X_r(t-1) + \Delta_I \text{ when } X_i(t) > X_r(t-1) \quad (2)$$

and

$$X_r(t) = X_r(t-1) - \Delta_D \text{ when } X_i(t) < X_r(t-1) \quad (3)$$

where

$$\Delta_I = K_I \times \sigma_D \times 2^d \text{ for } 0 \leq d \leq 2 \quad (4)$$

and

$$\Delta_D = K_D \times \sigma_D \times 2^d \text{ for } 0 \leq d \leq 2 \quad (5)$$

here  $K_I$  and  $K_D$  are two constants and  $\sigma_D$  is the standard deviation of the absolute differential values of the input series  $X_i(t)$  and is calculated as:

$$\sigma_D = \sqrt{\frac{1}{(n-1)} \sum_{t=1}^{(n-1)} [|X_i(t) - X_i(t+1)| - \bar{X}_D]^2} \quad (6)$$

where

$$\bar{X}_D = \frac{1}{(n-1)} \sum_{t=1}^{(n-1)} |X_i(t) - X_i(t+1)| \quad (7)$$

In Eqs. 4 and 5, the value of  $d$  is limited to only three values, 0, 1, and 2, explaining the name of the technique as 'delta modulation with limited adaptivity.' If the increment (decrement) between the two terms,  $X_i(t)$  and  $X_r(t-1)$  continues for three consecutive steps, the value of  $d$  becomes 0, 1, and 2 for the first, second, and third step, respectively. But, if the fourth consecutive step also shows an increment (decrement), the value of  $d$  is still 2 and remains so for any further consecutive increments (decrements). Whenever there is a decrement (increment) in the next step, the value of  $d$  is reset to 0.

As the reference signal  $X_r(t)$  has been formed, the output series  $Y_{dm}(t)$  is computed using the equations.:

$$Y_{dm}(t) = 1 \text{ for } X_r(t+1) \geq X_r(t) \quad (8)$$

and

$$Y_{dm}(t) = 0 \text{ for } X_r(t+1) < X_r(t) \quad (9)$$

Thus,  $Y_{dm}(t)$  becomes the delta-modulated 1-bit binary string output having  $(n-1)$  number of terms.

## 2.2 Finding the number of occurrences of a pattern by sliding window technique

In this step, an  $m$ -bit data string or pattern is formed from the series  $Y_{dm}(t)$  by taking  $m$  number of consecutive bits, starting from the 1<sup>st</sup> bit of the series. As there are at least two points are required to construct a two-dimensional pattern and also the length of the series  $Y_{dm}(t)$  is  $(n-1)$ , the value of  $m$  is in the range of 2 to  $(n-2)$ . Then by the sliding window technique, for  $m = 2$  to  $(n-2)$ , the number of occurrences of all possible  $2^m$  patterns in the series  $Y_{dm}(t)$  is determined. For example, for  $m = 2$  the series  $Y_{dm}(t)$  is scanned with the patterns 00, 01, 10, and 11. The method is repeated for all considerable values from  $m = 2$  onward and is stored carefully. A database is formed for different values of  $m$  and each of them contains a  $2^m$  number of patterns including their respective number of occurrences in the series  $Y_{dm}(t)$ .

## 2.3 Determination of the optimum state space

A state space is a multi-dimensional space of all possible configurations of a system. It is a useful abstraction for reasoning about the behavior of a given system and applies to all types of systems like single input single output systems, multiple inputs and multiple outputs systems, linear and nonlinear systems, time-varying, and time-invariant systems. The state in the state-space analysis refers to the smallest set of variables whose knowledge at the initial time together with the knowledge of input for the successive future time gives the complete knowledge of the behavior of the system at any time  $t$ . The state variables in the state space analysis are the smallest set of variables that help us to determine the state of a dynamical system.

When the state space is continuous it is often a smooth manifold. In this case, it is called the phase space. A phase space can also be infinite-dimensional. A dynamical system consists of abstract phase space or state space, whose coordinates describe the state at any instant, and a dynamical rule that specifies the immediate future of all state variables, given only the present values of those same state variables. Mathematically, a dynamical system is described by an initial value problem. The implication is that there is a notion of time and that a state at one time evolves to a state or possibly a collection of states at a later time. Thus, states can be ordered by time, and time can be thought of as a single quantity.

A dynamical system is deterministic if there is a unique consequence to every state or it is stochastic where there is a probability distribution of possible consequents. It can be discrete or continuous time. The Discrete-time system has its states evaluated only after certain discrete intervals. It is a combination of a state space, a set of time, and a set of evolution rules. A dynamical system can be considered as a model describing the temporal evolution of a process. The evolution rule provides a prediction of the next state or states that follow from the current state space value. The rule is deterministic if each state has a unique consequence, and is stochastic if there is more than one possible consequent for a given state. A stochastic evolution with discrete time but continuous phase space is an iterated function system. In this case, there is a collection of functions  $f_\alpha$  indexed by parameters  $\alpha$ . The evolution is random with the next state  $s_{t+1} = f_\alpha(s_t)$  where  $\alpha$  is selected from a probability distribution.

Now, to understand the dynamics of a stochastic discrete time series, the development of the evaluation rules are required. To develop such a set of rules, the entire series is divided into many  $m$ -dimensional hyperspaces and each of them is assigned a state variable that carries some pieces of information. Then the rules are created based on the dimension along with the information extracted from those state variables. As the hyperspace can be considered of any dimension, the developed rules will be different for their increment in dimension resulting in a rapid variance in the evaluation process. Each hyperspace holds a piece of information that may be meaningful or meaningless depending upon the value of their dimension. Needless to say, the meaningless information can only lead us to unnecessary complexity to develop the evaluation rules that can ruin the dynamics of the system. To overcome this problem, a set of meaningful rules having finite dimensions and appropriate information are required to analyze such a stochastic evaluation process. That is called the reconstruction of the optimum state space.

In the 2001 paper, Chatterjee [44] discussed the reconstruction of the optimum state space in detail and opted for the method namely ‘saturation of attractor properties.’ In a dynamical system, an attractor is a set toward which a variable evolves over time i.e., points close to the attractor remain nearby despite slight disturbance. The attractor is a region in  $n$ -dimensional space. It can be a point, a finite set of points, a curve, a manifold, or even a complicated set with a fractal structure. The method, ‘saturation of attractor properties,’ unfolds the attractor by a large dimension. In this method, when the optimum dimension has been reached, the attractor properties dependent on the distance of the points in the phase space become independent of the embedding dimension. The only limitation of this method is the requirement of a large set of data to properly estimate the optimum dimension. Since we are using a dataset that is large enough and the method ensures minimum loss of information to reconstruct the optimum state space, it is considered the most suitable one for our analysis. The method is described as follows:

Consider a dynamic system that is represented by a time series of  $X_T, X_{2T}, \dots, X_{NT}$  where  $N$  is the number of the observational values and  $T$  is the time interval. The state of the system is located in an  $m$ -dimensional hyperspace by a point having the coordinates  $X_T, X_{2T}, \dots, X_{mT}$ . The state at  $t = t + 1$  is denoted by  $X_{2T}, X_{3T}, \dots, X_{(m+1)T}$ , and so on, whereas the position vectors of each point are  $X_1, X_2, \dots, X_N$ . The trajectory of the system is the connecting line of all these points in order and the attractor is the region where the trajectory repeatedly returns. Now, by choosing a large enough dimension, the attractor can be unfolded properly. If the necessary  $m$ th dimension has been attained, all the properties of the attractor which are dependent on the distance of points in the phase space become independent of the value of the embedding dimension and no more information will be available beyond that dimension [45]. In this case, the data are a 1-bit binary string, and also no further sampling is required as the series is discrete with

some specific resolution. Now, considering the initial state is known with precision  $r$ , we are calculating the correlation sum that consists of centring the hypersphere on a point in phase space, letting the radius of the hypersphere grow until all points are enclosed [46]. The correlation sum  $C(r, m, N)$  is a function of the Hamming distance  $r$ , dimension  $m$ , and a total number of data  $N$  and is expressed as:

$$C(r, m, N) = \frac{1}{2^{m-1}} \sum_{j=1}^N G_j(r) \tag{10}$$

To calculate  $C(r, m, N)$ , the value for all the points lying within the range of  $r$  from a point is taken into account. The Hamming distance  $r$  is a metric for comparing two binary data strings of equal length or more specifically, it is the distance between two binary strings. In our case, we have taken a binary set of consecutive patterns having dimension  $m$  and Hamming distance  $r = 1$  i.e., the minimum Hamming distance is considered for the analysis. Also, the bit sequence of the two patterns in the set is exactly similar from  $D_m$  to  $D_1$  except for the only difference in the least significant bit  $D_0$  (LSB) to retain the  $r = 1$ . If the number of occurrences of the pattern having  $D_0 = 0$  is  $O_0$  and  $D_0 = 1$  is  $O_1$ , the expectation,  $G_j(r)$ , of  $D_0$  to be appeared as ‘1’ over ‘0’ is:

$$G_j(r) = \left[ \frac{O_1}{O_0 + O_1} - 0.5 \right]^2 \tag{11}$$

In this way, the expectations  $G_j(r)$  are calculated for all sets of patterns in the database obtained from the sliding window technique.

Thus, the optimum state space can be estimated from each yearly time series by calculating  $C(r, m, N)$  for different values of dimension  $m$ . A graph of the generalized correlation sum  $C(r, m, N)$  is plotted against the increasing value of  $m$ . At a particular point of  $m = M$ , where the slope of the plot becomes opposite in direction, the optimum state space is achieved beyond which no further information is available. Though the concept is generally associated with thermodynamics, in information theory it is defined as the amount of information required to locate the system in a specified state [47].

### 2.4 Finding M-bit patterns

As the optimum dimension  $M$  is estimated, the next part of the work is to find all the distinguished  $M$ -bit patterns from the binary string  $Y_{dm}(t)$ . A maximum of  $2^M$  patterns can be found. The patterns and their number of occurrences in the string  $Y_{dm}(t)$  are recorded to form a complete general database considering the entire 23rd Solar cycle.

### 2.5 Probability calculation

Let us denote an  $M$ -bit pattern as  $D_{M-1} \dots D_1 D_0$ . A study of the database can determine the probability of the LSB  $D_0$  to be ‘1’ or ‘0’ after a specific combination of the rest of the bits  $D_{M-1} \dots D_2 D_1$ . For example, consider an optimum dimension  $M = 4$ , where a specific set of a pattern has unit Hamming distance at LSB. Say, the set contains two consecutive binary patterns that are 0000 and 0001 having the number of occurrences 40 and 60, respectively. Thus, for the combination  $D_3 D_2 D_1 = 000$ , the probability of occurrence  $P(D_0 = 0)$  is 0.4 and  $P(D_0 = 1)$  is 0.6. Mathematically, the probability

$$P(D_0 = 0) = \frac{O_0}{O_0 + O_1} \tag{12}$$

and

$$P(D_0 = 1) = \frac{O_1}{O_0 + O_1} \tag{13}$$

where the number of occurrences of the pattern having  $D_0 = 0$  is  $O_0$  and  $D_0 = 1$  is  $O_1$ .

In this fashion, the entire general database of  $M$ -bit patterns associated with the binary string  $Y_{dm}(t)$  is analyzed and the probability of occurrence  $P(D_0 = 0)$  and  $P(D_0 = 1)$  for all the combinations of  $D_{M-1} \dots D_2 D_1$  are determined and stored. Now, the application of this general database can estimate the  $M$ th value of any real-time series from its previous  $(M-1)$  data.

### 2.6 Prediction model

The model is based on the general database. The input to the model is a real-time Dst index series,  $X_i(t)$ . The model requires  $(M-1)$  consecutive data of the input series to predict the  $M$ th data. As the model receives the first  $(M-1)$  number of input data, i.e., the values of  $X_i(t)$  for  $t = 1$  to  $(M-1)$ , it converts the  $(M-1)$  input data series into a binary string  $D_{M-1} \dots D_2 D_1$ , using the delta modulation method discussed in 2.1. The probability of occurrence  $P(D_0 = 0)$  or  $P(D_0 = 1)$  for this particular combination  $D_{M-1} \dots D_2 D_1$  is found from the database of patterns. The value of  $D_0$  is determined according to the value of  $P$ .  $D_0$  is either ‘1’ or ‘0’. The final output  $Y_{Dst}(t)$  is determined by demodulating the value of  $D_0$  in its analog form using the following eqs. In the case of  $D_0 = 0$ ,

$$Y_{Dst}(t) = X_i(t - 1) - K_D \times \sigma_D \times 2^d \begin{cases} d = 0 \text{ when } D_{M-2} = \phi \text{ and } D_{M-1} = 1 \\ d = 1 \text{ when } D_{M-2} = 1 \text{ and } D_{M-1} = 0 \\ d = 2 \text{ when } D_{M-2} = 0 \text{ and } D_{M-1} = 0 \end{cases} \tag{14}$$

and in the case of  $D_0 = 1$

$$Y_{Dst}(t) = X_i(t - 1) + K_I \times \sigma_D \times 2^d \begin{cases} d = 0 \text{ when } D_{M-2} = \phi \text{ and } D_{M-1} = 0 \\ d = 1 \text{ when } D_{M-2} = 1 \text{ and } D_{M-1} = 1 \\ d = 2 \text{ when } D_{M-2} = 0 \text{ and } D_{M-1} = 1 \end{cases} \tag{15}$$

where  $\phi =$  don't care condition *i.e.*, either 0 or 1, the values of  $K_I$  and  $K_D$  are prefixed, and the standard deviation of the absolute differential values of the input series is  $\sigma_D$  which is considered as unity for estimating the data of the 24th solar cycle. The first output data of the model are generated at  $t = M$  using the values of the input  $X_i(t)$  for  $t = 1$  to  $(M-1)$ . In the next step, again  $(M-1)$  consecutive input data, *i.e.*, values of  $X_i(t)$ , for  $t = 2$  to  $M$ , are required to produce the output at  $t = M + 1$ . In this way, the model generates every  $M^{\text{th}}$  data from the previous  $(M-1)$  data and continues to do so for all the next  $t$  values, generating a simulated output series, namely  $Y_{Dst}(t)$ . To verify the effectiveness of the model, the model output  $Y_{Dst}(t)$  is compared with the real-time Dst index series  $X_i(t)$  and the associated correlation coefficient  $C_c$ , the mean absolute error  $E_{ma}$  and the root-mean-square error  $E_{rms}$  are determined. The following eqs. are used to calculate the said three quantities:

$$C_c = \frac{\text{Cov}[X_i(t), Y_{Dst}(t)]}{\sqrt{\text{Var}[X_i(t)], \text{Var}[Y_{Dst}(t)]}} \tag{16}$$

$$E_{ma} = \frac{1}{n} \sum_{t=1}^n |X_i(t) - Y_{Dst}(t)| \tag{17}$$

$$E_{rms} = \sqrt{\frac{\sum_{t=1}^n [X_i(t) - Y_{Dst}(t)]^2}{n}} \tag{18}$$

### 3 Data source

Here we used the hourly averaged Dst data from the year 1997 to the year 2018 as extracted from NASA/GSFC's OMNI data set through OMNIWeb. The OMNI data were obtained from the GSFC/SPDF OMNIWeb interface at <http://omniweb.gsfc.nasa.gov> [48].

### 4 Results and discussion

Every solar cycle has its rising, maximum, declining, and minimum phases. Also, the geomagnetic storm can be classified into several categories, namely weak, moderate, strong, severe, and great storm. The Dst index belongs to the different categories are usually analyzed and studied separately. But, in our case, the model has been analyzed using the real-time Dst index data of each year of the 23rd solar cycle, *i.e.*, from the year 1997 to 2007, that includes all the phases of the solar cycle and are not segregated between the different storm period. Initially, the input Dst index series  $X_i(t)$  is converted to a 1-bit binary string  $Y_{dm}(t)$  using the delta modulation technique discussed in the method sect. While analyzing the nature of the Dst index, it is found that the rising and the falling properties of the index series are different. The rising of the series is much slower compared to the falling. So,  $K_I$  and  $K_D$  are two different constants assigned corresponding to the increment and decrement phenomenon and estimated experimentally to their best suitable values. Now, the 1-bit binary string  $Y_{dm}(t)$  is demodulated as  $Y_{ddm}(t)$  to test the accuracy of modulation. For every year of the entire 23rd solar cycle, the correlation coefficients are calculated between the original series  $X_i(t)$  and the demodulated series  $Y_{ddm}(t)$  and considered as the accuracy of modulation. The value of  $K_I$  and  $K_D$  are calculated as  $K_I = 0.54$  and  $K_D = 1.30$  to achieve the highest accuracy of modulation *i.e.*, 92% ~ 97% in our case.

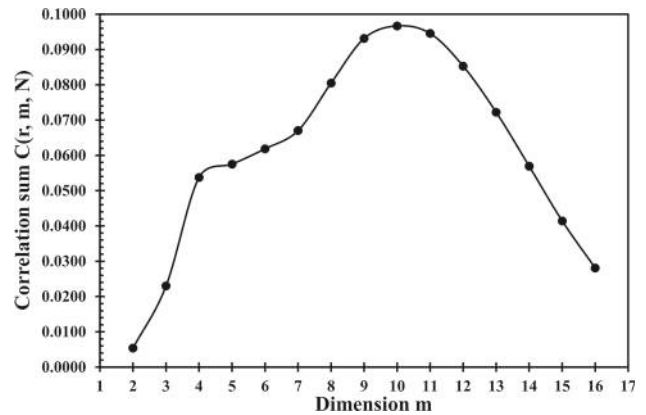
Once the binary string  $Y_{dm}(t)$  is obtained, all the possible patterns are determined using the sliding window technique. Now, the smallest binary pattern can be constructed using at least two successive data points. Thus, the correlation sum  $C(r, m, N)$  is calculated starting from  $m = 2$ . By increasing the dimension  $m$  gradually, the  $C(r, m, N)$  gained the highest value. Upon further increment, the corresponding value started decreasing and at  $m = 16$ , the value of the  $C(r, m, N)$  became sufficiently small to expect any increment thereafter. The decrement of the correlation sum indicates the inadequacy of any new information. The process is executed for all eleven years of the 23<sup>rd</sup> Solar cycle to get a general database of patterns for  $m = 2$  to 16. Table 1 shows the values of the embedded dimension vs correlation sum for the 1-h Dst index, respectively, for the range of the years 1997–2007.

The correlation sum  $C(r, m, N)$  is calculated considering the probability of occurrences of each pattern *i.e.*, their actual contribution in the data series. The nature of patterns present in each year is different along with their number of occurrences. A significant number of common patterns are observed throughout the entire cycle, whereas a small number of distinguished patterns occur only once. As a result, the degree of predictability varies for each year, hence the difference in yearly maximum correlation sum. Figure 1 is the graphical representation of the plots for embedded dimension  $m$  versus mean value of the correlation sum of 11 years associated with the 1-h Dst index series. As seen in Fig. 1, for the Dst index, the optimum state space is achieved for dimension  $M = 10$ . It signifies that the hourly Dst index series has the highest substantial correlated information up to 10 h and no more new information

**Table 1** The year-wise correlation sum  $C(r, m, N)$  is plotted for increasing value of dimension  $m$  for 1-h Dst index for the entire 23rd solar cycle

Dimension	Year										
	1997	1998	1999	2000	2001	2002	2003	2004	2005	2006	2007
2	0.0158	0.0038	0.0040	0.0046	0.0058	0.0041	0.0043	0.0045	0.0047	0.0037	0.0037
3	0.0355	0.0188	0.0213	0.0245	0.0253	0.0192	0.0231	0.0234	0.0257	0.0192	0.0173
4	0.0443	0.0486	0.0539	0.0584	0.0613	0.0461	0.0601	0.0579	0.0645	0.0493	0.0468
5	0.0496	0.0506	0.0587	0.0633	0.0681	0.0478	0.0611	0.0625	0.0676	0.0531	0.0502
6	0.0539	0.0545	0.0610	0.0699	0.0681	0.0503	0.0706	0.0706	0.0686	0.0585	0.0544
7	0.0614	0.0591	0.0659	0.0703	0.0744	0.0545	0.0800	0.0786	0.0737	0.0619	0.0576
8	0.0713	0.0635	0.0821	0.0918	0.0927	0.0629	0.0879	0.0916	0.0870	0.0815	0.0731
9	0.0938	0.0838	0.0891	0.0956	0.1001	0.0850	0.0955	0.0957	0.1081	0.0906	0.0870
10	0.1003	0.0979	0.0871	0.0950	0.1002	0.0905	0.0989	0.0996	0.1025	0.0952	0.0961
11	0.0965	0.0940	0.0898	0.0987	0.0950	0.0940	0.0960	0.0919	0.0957	0.0942	0.0941
12	0.0861	0.0892	0.0837	0.0875	0.0827	0.0873	0.0833	0.0805	0.0852	0.0845	0.0882
13	0.0740	0.0767	0.0723	0.0713	0.0673	0.0773	0.0695	0.0674	0.0691	0.0727	0.0767
14	0.0608	0.0611	0.0571	0.0549	0.0521	0.0619	0.0534	0.0526	0.0519	0.0592	0.0611
15	0.0450	0.0449	0.0418	0.0392	0.0371	0.0454	0.0384	0.0383	0.0368	0.0438	0.0448
16	0.0304	0.0307	0.0285	0.0261	0.0246	0.0312	0.0261	0.0263	0.0243	0.0298	0.0308

**Fig. 1** The 11 years mean values of the correlation sums  $C(r, m, N)$  are plotted against dimension  $m$  for the 1-h Dst index series considering the 23rd solar cycle



can be retrieved from the series beyond that limit. Thus, resting on the current data point i.e., 9th data point and using the last 8 data points corresponding to the last 8 h, the 10th data point or one-hour advanced data can be estimated using those patterns.

Concerning that estimation, all the 10-bit distinguished patterns for the series  $Y_{dm}(t)$  are identified and stored. The highest possible combinations of binary string for Dst index are 1024 (as  $2^M = 1024$ , where  $M = 10$ ). For the series, all the possible combinations of binary strings are added sequentially for 11 years to consider every single occurred pattern. Figure 2 illustrates the binomial degree distribution of the number of occurrences of the patterns for  $M = 10$  for the hourly Dst index series, which indicates the presence and absence of the entire set of patterns for the 23rd solar cycle.

The demodulated waveforms of some scale-free and periodically occurred patterns are shown in Fig. 3 where the relative amplitudes are plotted in the y-axis. The pattern corresponding to Fig. 3a is the most common and occurred more than 1500 times. Figure 3b, c, and d are chosen randomly from the range of occurrence between 1500 and 1000, 1000 and 500, and 500 and 100, respectively. Studying the database, the probability  $P(D_0 = 0)$  and  $P(D_0 = 1)$  for all these patterns are also estimated and included in the database.

As the general database had been formed, the next step is to study the prediction model of the Dst index discussed in Sect. 2.6 based on this database. The prediction model is analyzed for all the years of the 24th solar cycle, i.e., for the years 2008–2018 using the general database derived from the data of the previous 23rd solar cycle.

The value of  $M = 10$ , which means nine previous consecutive bits are required to generate the 10th data. Thus, the input to the prediction model is any set of nine consecutive values of the real-time Dst index  $X_i(t)$  to generate the predicted output  $Y_{Dst}(t)$  for the next  $t$ . As there is a probability factor in estimating the output  $Y_{Dst}(t)$ , the model is simulated for numerous iterations,  $I_r = 1$  to 250. After each iteration,  $Y_{Dst}(t)$  is compared with the real-time series  $X_i(t)$  and the associated correlation coefficient is estimated. Table 2 shows the value of the correlation coefficients  $C_c$ , mean absolute error  $E_{ma}$ , and root-mean-square error  $E_{rms}$  between the original Dst index  $X_i(t)$  and the predicted model output  $Y_{Dst}(t)$  after 250 iterations for the entire 24th solar cycle. Figure 4 demonstrates



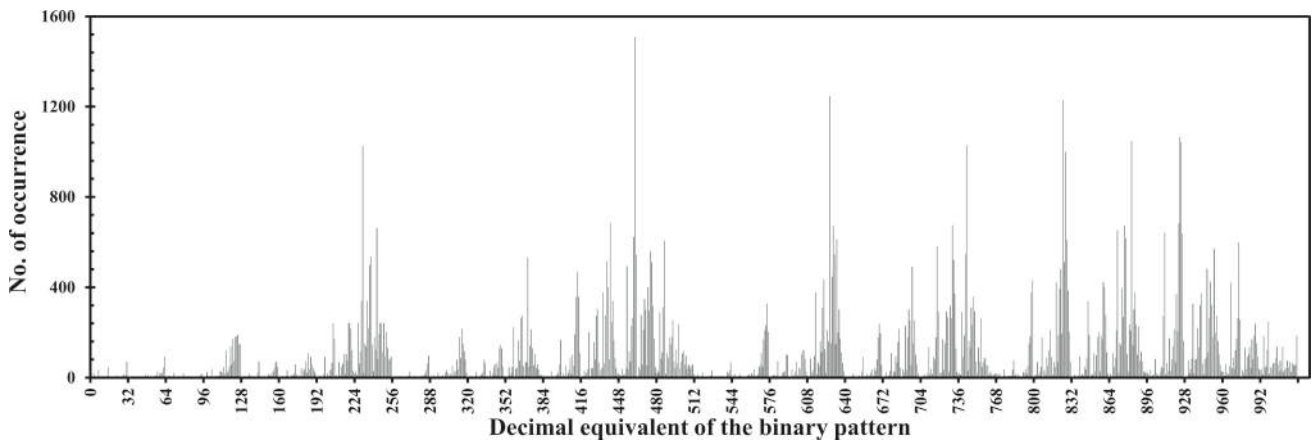
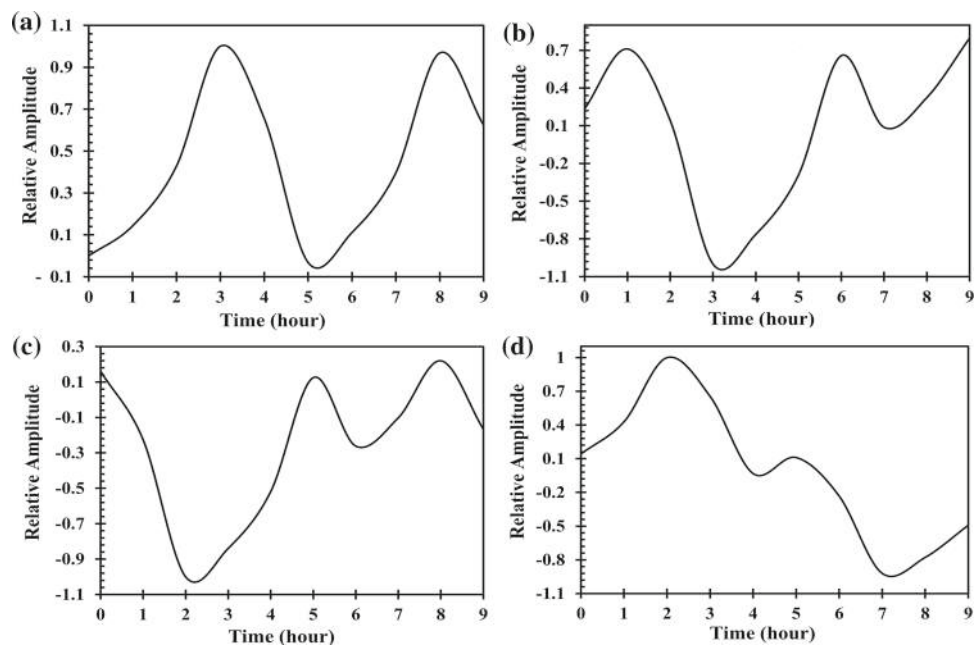


**Fig. 2** The Binomial degree distribution of the number of occurrences of the patterns is plotted for dimension  $M = 10$  for 1-h Dst index series for the entire 23rd solar cycle. The decimal equivalents of the binary patterns or words are plotted sequentially on the x-axis

**Fig. 3** The demodulated waveform of four periodically occurred patterns are shown where the corresponding binary sequences are **a** 0111001110, **b** 1100111011, **c** 1001110110, and **d** 1110010011. The number of their occurrences are 1509, 1000, 671, and 174



the correlation coefficients between  $X_i(t)$  and  $Y_{Dst}(t)$  for an increasing value of the number of iterations  $I_r = 1$  to 250, for the year 2016. The plot shows that the model becomes stabilized at  $I_r = 250$  quite well.

It is observed from Table 2, that the correlation coefficients between the original Dst index  $X_i(t)$  and the model output  $Y_{Dst}(t)$  are greater than 90% for each of the years of the 24th solar cycle, establishing the acceptability of the probabilistic model. Also, the associated values of mean absolute error and root-mean-square error are sufficiently small. The result indicates that the model can predict the Dst index data one hour in advance taking only the previous nine consecutive real-time Dst values as input. For a comparative study, the original Dst index  $X_i(t)$  and the model output  $Y_{Dst}(t)$  for the year 2016 are shown in Fig. 5a and b, respectively. Also, for detailed observation, the two series consisting of 5 days of data ranging between 3 May and 7 May of the same year is plotted in Fig. 5c for the same year.

The entire analysis reveals some prominent features about the probabilistic model and the overall method. A yearly continuous dataset of the real-time Dst index for each of the eleven years of the 23rd solar cycle is considered here to construct the pattern database. No segregation is made in the Dst dataset based on the phase of the solar cycle or the intensity of the geomagnetic storm. Thus, the model is applicable for the Dst index at any period, be it a quiet time or an intense storm. Then the delta modulation converts the analog Dst index series into a 1-bit binary string. Patterns, extracted from an analog signal, do not show scale-free or scale-invariant behaviors. But as the signal is transformed into a binary string in this method, the identified patterns are scale-free. The scale-invariance properties of the identified patterns are much useful to find any similar pattern of variable amplitude, which aids to construct the database consisting of all the patterns hidden in the structure of the Dst index series. Also, the optimum state space is reconstructed to identify the length of the optimum information in the hyperspace of the Dst index series. As observed

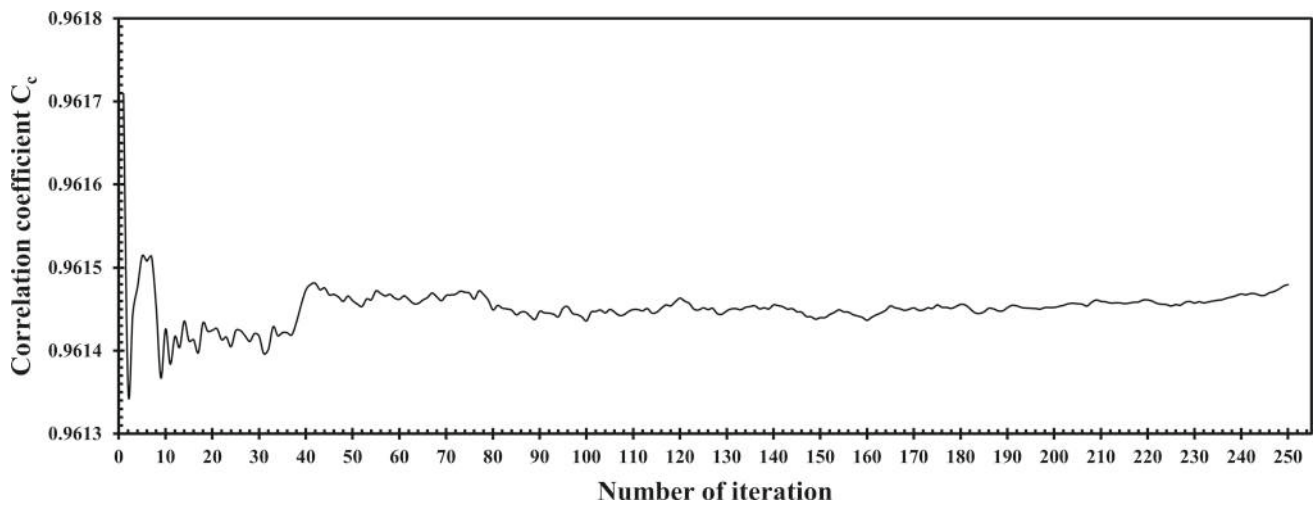


**Fig. 4** The value of the correlation coefficients between the original Dst index  $X_i(t)$  and the predicted model output  $Y_{Dst}(t)$  is plotted against the number of iterations performed for the year 2016

**Table 2** shows the value of the correlation coefficients  $C_c$ , mean absolute error  $E_{ma}$ , and root-mean-square error  $E_{rms}$  between the original Dst index  $X_i(t)$  and the predicted model output  $Y_{Dst}(t)$  after 250 iterations of the 24th solar cycle

Year	Correlation coefficient $C_c$	Mean absolute error $E_{ma}$	Root-mean-square error $E_{rms}$
2008	0.9488	2.6275	3.5234
2009	0.9285	2.4877	3.3017
2010	0.9542	2.7175	3.6655
2011	0.9595	2.9842	4.3502
2012	0.9757	3.1861	4.5221
2013	0.9683	2.9979	4.2113
2014	0.9636	3.1088	4.2498
2015	0.9725	3.5395	5.1543
2016	0.9615	3.1705	4.3541
2017	0.9611	3.1973	4.4571
2018	0.9570	2.8031	3.7861

from the result, no extra information can be retrieved from the series beyond the dimension  $M = 10$ , it is the optimum value of the state space. The saturation of attractor properties, used here to reconstruct the optimum state space, ensures minimum loss of information while estimating the optimum value. It is one of the key features of this method. Moreover, the model has a minimum dependency on external factors. A future Dst index value can be estimated only by using a finite set of previous Dst values and the pattern database as the input to the model. No other solar wind parameters or interplanetary magnetic field data are required. In the current analysis, the pattern database is constructed using the hourly real-time Dst index of the 23rd solar cycle. Using this database and nine previous values of Dst data, the model can predict the tenth Dst value in one hour advance for the entire 24th solar cycle, with a correlation coefficient up to 97.57%. Further, the maximum mean absolute error and root-mean-square error are found to be sufficiently small, 3.5395 and 5.1543, respectively.

### 5 Conclusion

The Dst index is a measurement of the geomagnetic activities on Earth and is widely used to indicate the intensity and occurrence of geomagnetic storms. Identifying significant patterns enfolded in the hidden layers and extracting substantial information from the inherent structures can be extremely rewarding in developing a successful forecasting algorithm. Moreover, an insight into the complex physical structure of this natural time series explains a lot of its characteristic features and dynamical behaviors. In this paper, we introduce a new method to predict the Dst index based on the concept of pattern recognition and optimum state space reconstruction. The analysis is a composite one; first to identify and characterize the significant patterns hidden in the structures of the 1-h Dst index series and then, development of a probabilistic model based on these patterns to forecast Dst data long before its actual occurrence. The algorithm includes adaptive delta modulation to convert the series into a binary string, the reconstruction of the optimum state space, construction of a database containing the probability of occurrence of the pattern, and finally, the development of a probabilistic predictive model to estimate the future data in one hour advance. The model has two inputs, the first one is the

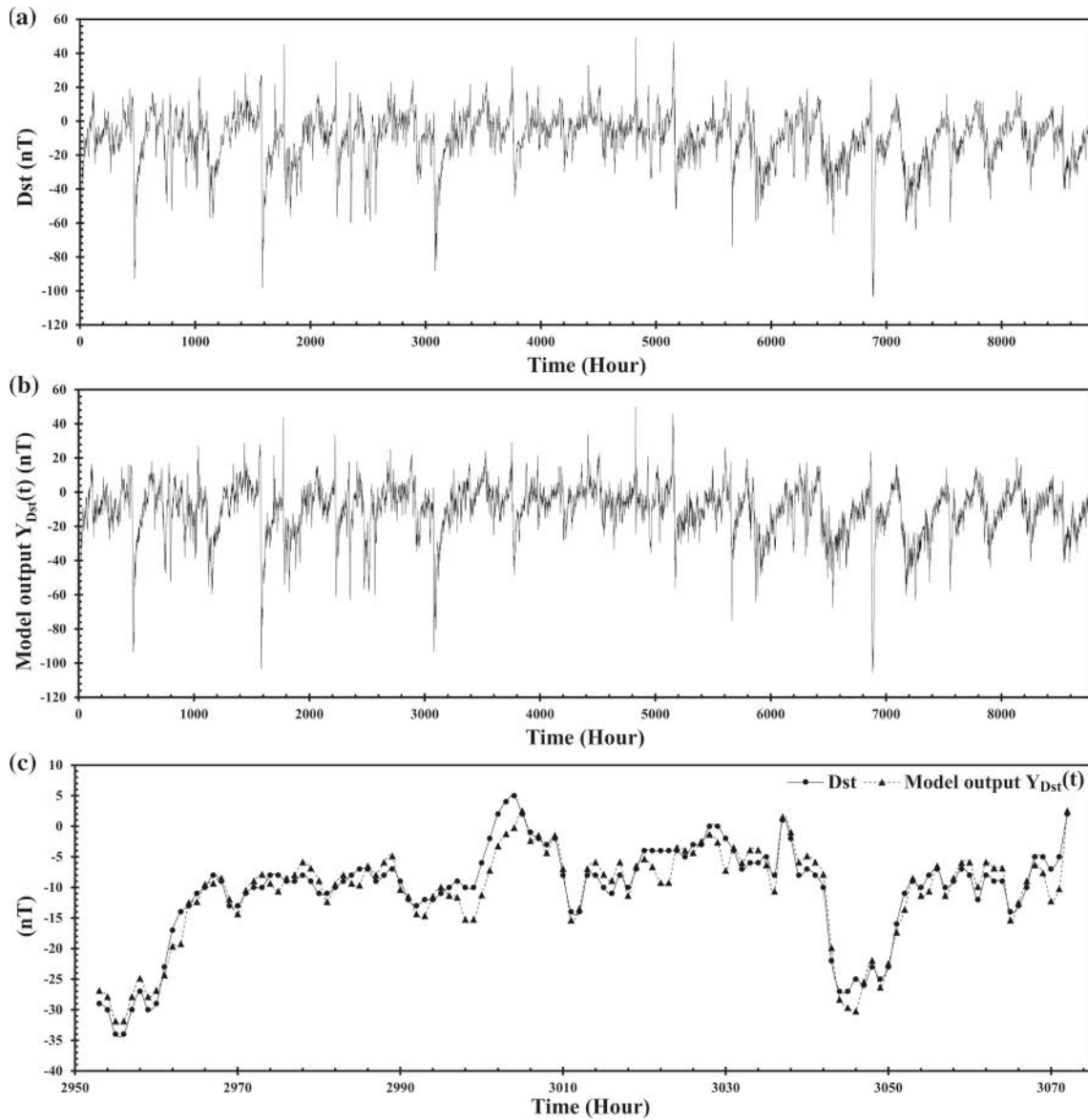


**Fig. 5** **a** The original 1-h Dst index  $X_i(t)$  for the year 2016, **b** the model output  $Y_{Dst}(t)$  for the same year, and **(c)** a comparative of the two series consisting of 5 days of data ranging between 3 May 2016 and 7 May 2016

database of the pattern created using the data of the entire 23rd solar cycle, and the second one is any set of nine consecutive data of the real-time Dst index of the 24th solar cycle to predict the 10th value. The predicted output is compared with each yearly data of the 24th solar cycle based on three parameters namely correlation coefficient, mean absolute error, and root-mean-square error for the statistical validation of the model. It has been observed that the values of the correlation coefficients between the real-time and predicted series are more than 90% for each of the years whereas the associated values of mean absolute error and root-mean-square error are significantly small. These results established the predictive performance of the model quite in a good way, using the database formed from the data of the 23<sup>rd</sup> solar cycle to predict the data of the next 24<sup>th</sup> solar cycle. Also, the model needs only the previous values of the real-time Dst index to predict the future value in one hour advance and no other data of geomagnetic indices or solar wind parameters are required for this method. One hour is sufficient to activate any controlling system to temporarily shut down the electrical hardware or power grids to save them from the perils of the coming storm. Moreover, the model takes a moderate number of iterations to be stabilized making a much lower computational time. Again, the study also revealed that the underlying physical structure of the Dst index is a complex composition of numerous distinguished patterns, occurring through the series in various frequencies. Some common patterns repeat through the entire solar cycle numerous times, whereas some are not. A small number of distinguished patterns occurs only once. As a result, the degree of predictability, as well as the maximum correlation sum, varies

in a small range for each year. Finally, for the Dst index, the optimum state space is achieved for the dimension  $M = 10$ , denoting no more new information can be retrieved from the time series beyond this particular dimension.

Geomagnetic disturbances on Earth are a complex phenomenon, and a powerful storm is need to be predicted a sufficient time before saving society from its adverse effects. Dst index, the global measurement of the geomagnetic storm, also represents the internal dynamical nature of this natural event, an overlapping of various physical processes or patterns forming an intricate structure. The current study was focused to identify and analyze the characteristics of these patterns enfolded in the dynamical structure of the Dst index to develop a successful prediction algorithm for this time series and in general, geomagnetic storm. The structure and traits of these patterns are very much intriguing and demand detailed study in the future to gain a much deeper knowledge of geomagnetic disturbances. The database of patterns can be continually updated with time incorporating all the available data to get various types of patterns and much more accuracy in predicting the future value.

**Supplementary Information** The online version contains supplementary material available at <https://doi.org/10.1140/epjp/s13360-022-02687-7>.

**Acknowledgements** We acknowledge the use of NASA/GSFC's Space Physics Data Facility's OMNIWeb (or CDAWeb or ftp) service, OMNI data and SIDC, RWC Belgium, World Data Centre. Data sets corresponding to Table 1 and Figure 3 are also available from the corresponding author on specific requests. We are thankful to Parthasarathi Chakrabarti, Director, IEST, Shibpur, Howrah, India, for the institutional support. We are also thankful to Somnath Mukherjee, Principal of Dinabandhu Andrews College, Kolkata, India for the cordial support and constant encouragement. Finally, we are also very much thankful to the anonymous reviewer for the significant insight into our manuscript by which, we are getting further encouraged to unfold the information hidden inside the geomagnetic data series.

**Authors' contributions** The authors have an equal contribution to the development of the manuscript.

**Funding** Self-funded as we are independent researchers.

## Declarations

**Conflict of interest** Nil.

**Ethics approval** Not applicable.

**Consent to participate** Not applicable.

**Consent for publication** Not applicable.

**Code availability** No.

**Data availability** Data are available on request made to the corresponding author.

## References

1. M. Sugiura, T. Kamei, Equatorial DST index 1957–1986, in IAGA Bull. 40, edited by A. Bertheliet, and M. Menvielle, Int. Serv. of Geomagn. Indices Publ. Off., Saint Maur, France (1991)
2. M. Sugiura, Hourly values of equatorial Dst for IGY. Annals of the International Geophysical Year, vol. 35, pp. 945–948 (Pergamon Press, Oxford, U. K.) (1964)
3. J.A. Wanliss, K.M. Showalter, High-resolution global storm index: Dst versus SYM-H. J. Geophys. Res. **111**, A02202 (2006). <https://doi.org/10.1029/2005JA011034>
4. J.G. Kappenman, L.J. Zanetti, W.A. Radasky, Geomagnetic storms can threaten electric power grid. Am. Geophys. Union Earth Space **9**(7), 9–11 (1997)
5. Hydro-Québec, Understanding electricity. Retrieved 2010-10-2 (1989)
6. CENTRA Technology Inc., Geomagnetic Storms Report Prepared for the Office of Risk Management and Analysis United States Department of Homeland Security (2011)
7. NOAA technical memorandum OAR SEC-88, Halloween space weather storms of 2003. Space Environment Center, Boulder, Colorado, June 2004 (2003)
8. L.J. Lanzerotti, Space Weather Effects on Technologies, in *Space Weather*. ed. by P. Song, H.J. Singer, G.L. Siscoe (AGU, Washington, 2013)
9. National Research Council, Severe Space Weather Events, Understanding Societal and Economic Impacts. A Workshop Report, Washington, DC, The National Academies Press (2008)
10. A. Pulkkinen, E. Bernabeu, J. Eichner, C. Beggan, A.W.P. Thomson, Generation of 100-year geomagnetically induced current scenarios. Space Weather **10**, S04003 (2012). <https://doi.org/10.1029/2011SW000750>
11. A.W.P. Thomson, E.B. Dawson, S.J. Reay, Quantifying extreme behavior in geomagnetic activity. Space Weather **9**, S10001 (2011). <https://doi.org/10.1029/2011SW000696>
12. A. Viljanen, R. Pirjola, E. Prácsér, S. Ahmadzai, V. Singh, Geomagnetically induced currents in Europe: characteristics based on a local power grid model. Space Weather **11**, 575–584 (2013). <https://doi.org/10.1002/swe.20098>

13. R.L. McPherron, G. Siscoe, N.U. Crooker, N. Arge, Probabilistic Forecasting of the Dst Index, in *The Inner Magnetosphere: Physics and Modeling*, ed. by T.I. Pulkkinen, N.A. Tsyganenko, R.H.W. Friedel (AGU, Washington, 2005)
14. M. Chandorkar, E. Camporeale, S. Wing, Probabilistic forecasting of the disturbance storm time index: an autoregressive Gaussian process approach. *Space Weather* **15**, 1004–1019 (2017). <https://doi.org/10.1002/2017SW001627>
15. S.B. Xu, S.Y. Huang, Z.G. Yuan, X.H. Deng, K. Jiang, Prediction of the Dst index with bagging ensemble-learning algorithm. *Astrophys. J. Suppl. Ser.* **248**(1), 14 (2020). <https://doi.org/10.3847/1538-4365/ab880e>
16. R.J. Boynton, M.A. Balikhin, S.A. Billings, A.S. Sharma, O.A. Amariutei, Data derived NARMAX Dst model. *Ann. Geophys.* **29**, 965–971 (2011). <https://doi.org/10.5194/angeo-29-965-2011>
17. M.A. Gruet, M. Chandorkar, A. Sicard, E. Camporeale, Multiple-hour-ahead forecast of the Dst index using a combination of long short-term memory neural network and Gaussian process. *Space Weather* **16**, 1882–1896 (2018). <https://doi.org/10.1029/2018SW001898>
18. H.L. Wei, S.A. Billings, M. Balikhin, Prediction of the Dst index using multiresolution wavelet models. *J. Geophys. Res.* **109**, A07212 (2004). <https://doi.org/10.1029/2003JA010332>
19. D. Zhu, S.A. Billings, M.A. Balikhin, S. Wing, H. Alleyne, Multi-input data derived Dst model. *J. Geophys. Res.* **112**, A06205 (2007). <https://doi.org/10.1029/2006JA012079>
20. E.Y. Ji, Y.J. Moon, N. Gopalswamy, D.H. Lee, Comparison of Dst forecast models for intense geomagnetic storms. *J. Geophys. Res.* **117**, A03209 (2012). <https://doi.org/10.1029/2011JA016872>
21. R.K. Burton, R.L. McPherron, C.T. Russell, An empirical relationship between interplanetary conditions and Dst. *J. Geophys. Res.* **80**, 4204–4214 (1975)
22. F.R. Fenrich, J.G. Luhmann, Geomagnetic response to magnetic clouds of different polarity. *Geophys. Res. Lett.* **25**, 2999–3002 (1998)
23. T.P. O'Brien, R.L. McPherron, An empirical phase space analysis of ring current dynamics: solar wind control of injection and decay. *J. Geophys. Res.* **105**, 7707–7720 (2000)
24. M. Temerin, X. Li, A new model for the prediction of Dst on the basis of the solar wind. *J. Geophys. Res.* **107**(A12), 1472 (2002). <https://doi.org/10.1029/2001JA007532>
25. M. Temerin, X. Li, Dst model for 1995–2002. *J. Geophys. Res.* **111**, A04221 (2006). <https://doi.org/10.1029/2005JA011257>
26. C.B. Wang, J.K. Chao, C.H. Lin, Influence of the solar wind dynamic pressure on the decay and injection of the ring current. *J. Geophys. Res.* **108**(A9), 1341 (2003). <https://doi.org/10.1029/2003JA009851>
27. J. Chen, P.J. Cargill, P.J. Palmadesso, Predicting solar wind structures and their geoeffectiveness. *J. Geophys. Res.* **102**(A7), 14701–14720 (1997). <https://doi.org/10.1029/97JA00936>
28. I. V. Kovalevskij, Yu. I. Morozov, Geomagnetic storm as an object of pattern recognition. ITEF-74, USSR (1986)
29. J.V. Kovalevsky, Yu.I. Morozov, *Pattern Recognition Methods in Analysis of Complex Physical Phenomena* (IZMIRAN, Russia, Moscow, 1990)
30. J. V. Kovalevsky, E. I. Kovalevskaya, Application of pattern recognition methods in analysis of complex physical phenomena in geospace: geomagnetospheric storms. Correlated phenomena at the sun, in the heliosphere and in geospace. In: proceedings 31st ESLAB symposium, ESTEC, Noordwijk, ESA SP-415, pp. 431–436 (1997)
31. X.P. Zeng, Y.F. Lin, C. Lu, Z.X. Feng, Q.H. Guo, Application of pattern recognition method to the prediction of geomagnetic storms. *Chin. J. Sp. Sci.* **4**, 42–50 (1984)
32. A. Banerjee, A. Bej, T.N. Chatterjee, On the existence of a long range correlation in the geomagnetic disturbance storm time (Dst) index. *Astrophys. Space Sci.* **337**, 23–32 (2012). <https://doi.org/10.1007/s10509-011-0836-1>
33. A. Banerjee, A. Bej, T.N. Chatterjee, A cellular automata-based model of Earth's magnetosphere in relation with Dst index. *Space Weather* **13**, 259–270 (2015). <https://doi.org/10.1002/2014SW001138>
34. A. Banerjee, A. Bej, T.N. Chatterjee, A. Majumdar, An SOC approach to study the solar wind-magnetosphere energy coupling. *Earth Space Sci.* **6**, 565–576 (2019). <https://doi.org/10.1029/2018EA000468>
35. J.E. Abate, Linear and adaptive delta modulation. *Proc. IEEE* **55**(3), 298–308 (1967). <https://doi.org/10.1109/PROC.1967.5486>
36. C. C. Cutler, Differential quantization of communication signals. *Nokia Bell Labs, U.S. Patent* **2**, 605, 361 (1952)
37. F. DeJager, Delta modulation, a method of PCM transmission using a 1-unit code'. *Phillips Res. Rept. No.* **7**, 442–466 (1952)
38. D.J. Goodman, A digital approach to adaptive delta modulation. *Bell Syst. Tech. J.* **50**, 1421–1426 (1971). <https://doi.org/10.1002/j.1538-7305.1971.tb02560.x>
39. R. Gregorian, J.G. Gord, A continuously variable slope adaptive delta modulation codec system. *IEEE J. Solid-State Circuits* **18**(6), 692–700 (1983). <https://doi.org/10.1109/JSSC.1983.1052019>
40. C. Halijak, J. Tripp, A deterministic study of delta modulation. *IEEE Trans. Automat. Contr.* **8**(4), 339–347 (1963). <https://doi.org/10.1109/tac.1963.1105592>
41. M.H. Weik, *Computer Science and Communications Dictionary* (Springer, Boston, 2000), pp. 382–382
42. C.M. Zierhofer, Adaptive sigma-delta modulation with one-bit quantization. *IEEE Trans. Circuits Syst. II* **47**(5), 408–415 (2000). <https://doi.org/10.1109/82.842109>
43. H.D.I. Abarbanel, R. Brown, J.J. Sidorowich, L.S. Tsimring, The analysis of observed chaotic data in physical systems. *Rev. Mod. Phys.* **65**(4), 1331–1392 (1993). <https://doi.org/10.1103/RevModPhys.65.1331>
44. T.N. Chatterjee, On the application of information theory to the optimum state-space reconstruction of the short-term solar radio flux (10.7cm), and its prediction via a neural network. *Mon. Not. R. Astron. Soc.* **323**, 101–108 (2001). <https://doi.org/10.1046/j.1365-8711.2001.04110.x>
45. C.E. Shannon, A mathematical theory of communication. *Bell Syst. Tech. J.* **27**, 623–656 (1948). <https://doi.org/10.1002/j.1538-7305.1948.tb00917.x>
46. K. Pawelzik, H.G. Schuster, Generalized dimensions and entropies from a measured time series. *Phys. Rev. A* **35**(1), 481–484 (1987). <https://doi.org/10.1103/physreva.35.481>
47. S. Eubank, J.D. Farmer, An Introduction to Chaos and Prediction, in *Lectures in the Science of Complexity*, ed. by E. Jen. SFI studies in the science of complexity. (Addison-Wesley, MA, 1990), p. 75
48. J.H. King, N.E. Papitashvili, Solar wind spatial scales in and comparisons of hourly wind and ACE plasma and magnetic field data. *J. Geophys. Res.* **110**, A02209 (2005). <https://doi.org/10.1029/2004JA010649>



# Source details

[Feedback >](#) [Compare sources >](#)

## European Physical Journal Plus

Scopus coverage years: from 2011 to Present

Publisher: Springer Nature

ISSN: 2190-5444

Subject area: [Chemical Engineering: Fluid Flow and Transfer Processes](#) [Physics and Astronomy: General Physics and Astronomy](#)

Source type: Journal

[View all documents >](#)

[Set document alert](#)

[Save to source list](#)

CiteScore 2022

4.9



SJR 2022

0.548



SNIP 2022

0.979





## Review

## Synthesis of nanosilica from agricultural wastes and its multifaceted applications: A review

Jit Sarkar<sup>a</sup>, Deepanjan Mridha<sup>b</sup>, Joy Sarkar<sup>c</sup>, Jonathan Tersur Orasugh<sup>d</sup>,  
Bhuvan Gangopadhyay<sup>d</sup>, Dipankar Chattopadhyay<sup>d</sup>, Tarit Roychowdhury<sup>b</sup>,  
Krishnendu Acharya<sup>a,\*</sup>

<sup>a</sup> *Molecular and Applied Mycology and Plant Pathology Laboratory, Department of Botany, University of Calcutta, Kolkata, West Bengal, Pin 700019, India*

<sup>b</sup> *School of Environmental Studies, Jadavpur University, Jadavpur, Kolkata, West Bengal, Pin 700032, India*

<sup>c</sup> *Department of Botany, Dinabandhu Andrews College, Garia, Kolkata, West Bengal, Pin 700084, India*

<sup>d</sup> *Department of Polymer Science and Technology, University of Calcutta, 92 A. P. C. Road, Kolkata, West Bengal, Pin 700 009, India*

## ARTICLE INFO

## Keywords:

Agricultural waste  
Application  
Bioremediation  
Silica nanoparticles  
Synthesis

## ABSTRACT

Agricultural wastes management is one of the biggest burdens in the 21st century. To reduce pollution from agricultural waste, different types of research have been conducted to convert agricultural wastes into value-added products. In recent decades, agricultural wastes are utilized as source material for nanoparticle synthesis. Nanoparticles with large surface area, small size, biocompatibility, and adjustable functionalization are now booming in different areas of science and technology. Among different types of nanoparticles, the silica nanoparticles (SiNPs) were favored to synthesize from agro-wastes as the major agricultural crop residues are silica enriched, especially the cereal crops. Moreover, the bound silica in the agricultural wastes is conventionally extracted by thermal, chemical, and biological treatment. Owing to the structural flexibility, tuneable pore size, and less toxicity made the SiNPs are more attractive to use in various fields than other metallic nanoparticles. SiNPs are now extensively used in biomedical, agricultural, and environmental remediation purposes. This review paper is an assemblage of different approaches aimed to synthesize nanosilica from agro-wastes along with its potential application areas.

### 1. Introduction

Agricultural activities produce a substantial amount of agro-wastes. The use of agricultural crop residues in the production of value-added products like nanoparticles, pulp, biochar, organic fertilizer and biogas, etc might be a significant solution to the problem of agro-waste disposal (Bhuvaneshwari et al., 2019; Nagendran, 2011). The burning of agricultural waste or crop residue was also considered to pose a serious health risk (Nagendran, 2011). Apart from exposing most individuals in the immediate vicinity to high quantities of particulate matter, it is also a major cause of regional pollution (Bhuvaneshwari et al., 2019). However, the alarming increase in air pollution, particularly in 2015 and beyond, the substantial increase in air pollution level has been observed due to the burning of agricultural wastes in various parts of the world which has drawn the attention of different international agencies to level out the issue of management of agricultural waste. East Asian countries like China, India, Pakistan, and Bangladesh are the major

\* Corresponding author.

E-mail address: [krish\\_paper@yahoo.com](mailto:krish_paper@yahoo.com) (K. Acharya).

grower of cereal crops. China is one of the largest carbon emitters in the world followed by India (FAOSTAT, 2021. <http://www.fao.org/faostat/en/#data/GB>). According to earlier studies, in-situ agricultural crop residue combustion in Asian nations was claimed to represent more than 33% of total biomass combustion (Chen et al., 2019). India, the world's second-largest agro-based economy with year-round crop cultivation after China. The Indian Ministry of New and Renewable Energy (MNRE) states that India produces a total of 500 Million Tons (Mt) of crop residue each year. Part of this 500 Mt of agricultural residue has been used for fodder and other purposes, however, the rest of the residue (92 Mt) is still burnt in different agricultural fields across India. (NPMCR, 2014). Over the last few years, environmentalists from all over the world have turned their attention to the agricultural sector to develop a proper plan for reducing agro waste. There are so many avenues to utilize agro-waste for sustainable redevelopment and reuse. Nanotechnology is such an avenue that has immense potential to explore for mitigation of agro-waste. Nanotechnology is one such option with enormous potential for reducing the agro-waste problem. Nanotechnology has provided a solution for the long-term conversion of agricultural waste into recyclable raw materials that can be processed and utilized in a range of applications, as well as a raw material for nanomaterial synthesis. In an attempt to protect the environment from the uprising agricultural waste, researchers investigated the possibility of evaluating agricultural waste and by-products in the manufacture of many materials such as composite materials like (Bahrami et al., 2018; Bhuvaneshwari et al., 2019), adsorbents (Liu et al., 2013; Mullick et al., 2018; Tang et al., 2018), fillers (Maslowski et al., 2018; Pongdong et al., 2018), additional cement materials (Ataie and Riding, 2016; Binici et al., 2008) and even silica-based materials (Chen et al., 2010; Kamath and Proctor, 1998; Ma et al., 2016; Soltani et al., 2017).

Silica is one of the abundant elements present on earth and is mainly found in sand, quartz, flint, and a variety of other minerals. The Spatial atom of Si shows tetrahedral coordination with four oxygen atoms around the central Si atom. The illustration of the both amorphous and crystalline structure of silicon dioxide was shown in Fig. 1a and b, respectively. The four  $\text{SiO}_4$  tetrahedra oxygen atoms are shared by each of the more thermodynamically stable crystalline forms of silica, yielding a net chemical formula like  $\text{SiO}_2$ . The central tetrahedron is shared with all four of the  $\alpha$ -quartz unit cells in the corner shown in Fig. 1b. Two of its corner oxygen atoms are shared with the two tetrahedral-centered faces and only one of its oxygen atoms shares with the other  $\text{SiO}_4$ -tetrahedrons on the four-edge tetrahedral. Maximum vertices of twenty-four for this section of the seven  $\text{SiO}_4$  tetrahedra are considered as part of silica unit cells.  $\text{SiO}_2$  exists in two forms i.e., amorphous and crystalline. All crystalline shapes include a  $\text{SiO}_4$  tetrahedral structure, which, excluding stishovite and fibrous silica, is connected in different arrangements. The framework silicates are also known as silica of  $\text{SiO}_2$ . The silicon-oxygen bonding system differs depending on its crystal shapes. In the case of  $\alpha$ -quartz, the length of the bond is 161 p.m., where, as in  $\alpha$ -tridymite, it is between 154 and 171 p.m., respectively. Based on their composition the Si-O-Si bond angle ranges from low values of  $140^\circ$  ( $\alpha$ -tridymite) to  $180^\circ$  ( $\beta$ -tridymite) (Wiberg et al., 2001). The Si-O-Si bond angle in  $\alpha$ -quartz is  $144^\circ$  and the length of bond between Si and O is 1.60 Å. The arrangement relies on the properties of silica. The molar weight and silica densities were  $60.08 \text{ g mol}^{-1}$  and  $2648 \text{ g cm}^{-3}$ , respectively. Solubility in water depends heavily on its crystalline form. Silica nanoparticles have a broad spectrum of applications. It is used as drivers, semiconductor and medical appliances, sensors, coatings, rubber, plastics, cosmetics, and catalysts, etc. In the area of photon properties and transmissions (like fibers), energy recovery, and electronics, there has been increasing demand for nanosilica due to its adjustable properties and small module (Nguyen et al., 2019). Usually, amorphous silica produces from quartz sand that requires high temperature and pressure (Faizul et al., 2013). Sol-gel is another method that has been used for silica production but this procedure is not feasible due to the high cost of raw material. The production of nanosilica from agro-waste products not only gives rise to new synthetic methods because of the abundance of silica present in various agro-waste materials but also opens avenues to minimize agro-waste pollution. Keeping all this in the background, the goal of this study is to highlight the various agro-wastes that can be used as raw materials for SiNP synthesis; assess available techniques to produce SiNPs from various agro-waste, and address the application of SiNPs in different fields.

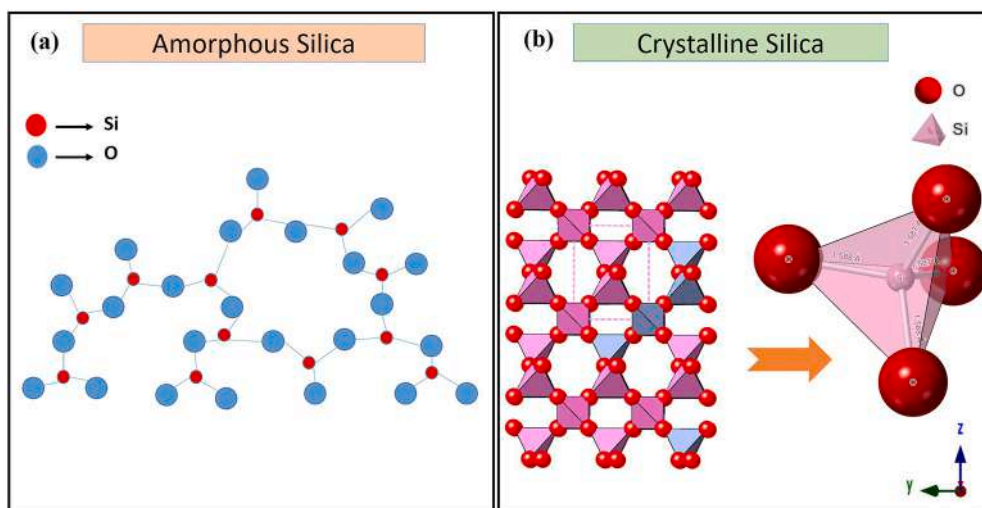


Fig. 1. Graphical illustration of amorphous silica (a) and crystalline silica (b).



## 2. Global burden of crop residue burning

The agricultural sector plays a significant part in the world's overall economic development. A large number of agricultural activities for securing food demands, resulting in an overall increase in environmental pollution and waste. A limited quantity of crop residue has been traditionally used as animal bedding, cattle fodder, and rests are either burned down or left to landfill areas. The burning of biomass is a popular phenomenon worldwide, which has a great impact on air, soil, and water pollution. Crop residue burning in the field not only produces a huge amount of greenhouse gases (CHGs) but also destroys soil fertility and biodiversity (Pushpa and Lohani, 2018). The burning of crop residues in different countries is varied and depends on the pattern of crop residue usage in every country. According to the Food and Agricultural Organization of the United Nations (FAOSTAT) in Asian countries, almost 50% of the crop residues are burnt on agricultural fields (<http://www.fao.org/faostat/en/#data/GB>). China, India, Russian Federation, Brazil, and the USA are the five major countries that massively burnt crop residue in the agricultural fields (Fig. 2). So, instead of burning the crop residue, the produced crop residues can be utilized in the various sector to minimize agro-wastes-related issues.

## 3. Types of crop residue utilized for SiNP synthesis

After harvesting, the residual component, also known as crop residues, contains both plant residues left over from harvest as well as processed residues that are still useful after all manufacturing processes have been completed. Stalks and stubbles (straws), leaves, and seed pods are common examples of field residues and some examples of processed wastes are bagasse and sugar cane molasses. These agricultural wastes can be utilized as a precursor of silica (Fig. 3). The major benefit of utilizing agricultural waste is that it is readily available at the end of each harvesting season. As a result, agricultural waste-based nanoparticle synthesis methods are always more cost-effective than other approaches. The chemical composition of these agro-based crop wastes was provided in Table 1. Silica is found in agricultural plant ash residues, along with metal and alkali oxides such as  $\text{Fe}_2\text{O}_3$ ,  $\text{Al}_2\text{O}_3$ ,  $\text{ZnO}$ ,  $\text{MnO}$ ,  $\text{CuO}$ ,  $\text{TiO}_2$ ,  $\text{Sr}_2\text{O}_3$ ,  $\text{K}_2\text{O}$ ,  $\text{MgO}$ ,  $\text{CaO}$ ,  $\text{Na}_2\text{O}$ , and others. Crop residues have a  $\text{SiO}_2$  concentration that ranges from 9 to 93%. Some intermediate Si-accumulating dicots, such as rapeseed, mustard, and groundnut have lower  $\text{SiO}_2$  concentrations of up to 50% by weight. Due to their active silica absorption, crop residues from monocotyledonous plants, such as sorghum, rice, wheat, and corn, have significant amounts of silica, reaching up to 90 wt % (Setiawan and Chiang, 2021). Due to the high silica content of cereal crops and the availability of cereal crop residues, researchers all over the globe have been attempting to synthesis biogenic silica from cereal crop waste (Arumugam and Ponnusami, 2013; Bhagiyalakshmi et al., 2010; Binod et al., 2010; Drummond and Drummond, 1996; Okoronkwo et al., 2013; Purномо et al., 2011; Rangaraj and Venkatachalam, 2017).

### 3.1. Rice husk and straw

Rice husk is a major residue that came after the de-husking of rice. The rice husk is a common rice milling leftover that is mostly composed of cellulose (28.7–35.6%), hemicellulose (12.0–29.3%), lignin (15.4–20.0%), and silica (8.7–12.1%) (Isikgor and Becer,

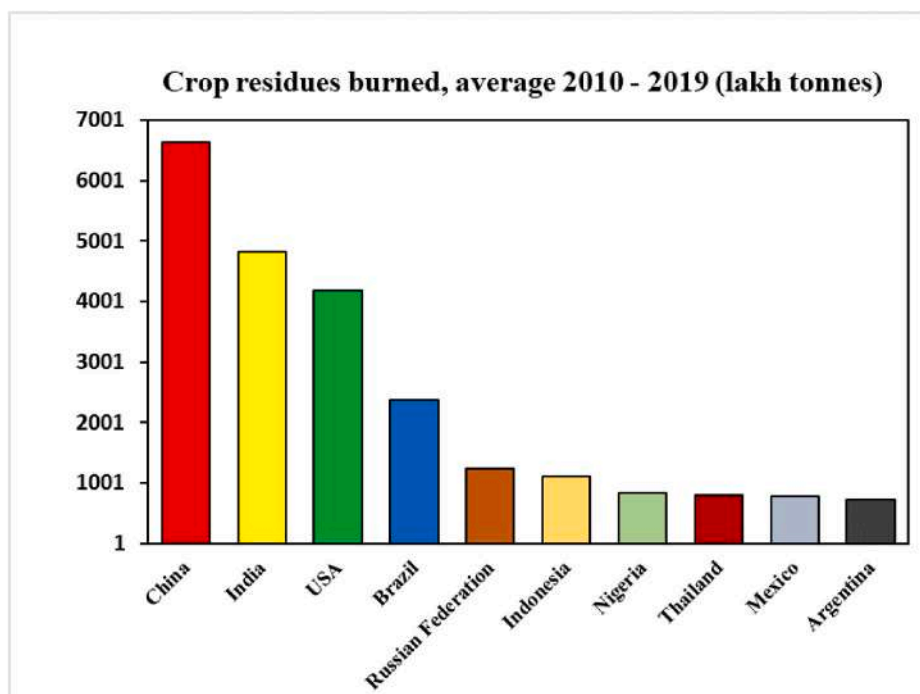


Fig. 2. Graphical representation of world's top 10 emitters country,  $\text{CO}_2$  equivalent (Derived or calculated from FAOSTAT data).



Fig. 3. Generalised illustration of Chemical, Thermal, and Biological treatments performed for synthesis of SiNPs from various agro-wastes.

**Table 1**  
Chemical composition of agricultural waste ash utilized in silica nanoparticle synthesis.

Composition	SiO <sub>2</sub> (%)	CaO (%)	Fe <sub>2</sub> O <sub>3</sub> (%)	MgO (%)	K <sub>2</sub> O (%)	Others (%)	Ref.
Rice husk	80–97	0.5–2	0.1–0.5	3.05–2	0.2–3	1.5–4.5	(Faizul et al., 2013; Patel et al., 2017b; Sapawe et al., 2018)
Wheat straw	50–55	8–10	0.5–2	2–2.5	8–12	4–6	Patel et al. (2017b)
Bamboo leaf	60–80	7.5	1–1.5	1.8–2	6.5–6	7.6–8	(Madani Hosseini et al., 2011; Olutoge and Oladunmoye, 2017)
Sugarcane bagasse	50–97	1–2	3–4	0.5–1	4.2–4	5.1–15	(Rahman et al., 2015; Rovani et al., 2018)
Corn cobs	8.5	10.7	1.16	10.2	0.79	5–15	El-Sayed and Khairy (2017)
Palm kernel shell	42.6	4.3	5.6	2.20	0.50	1–1.7	Osuji and Lukuman (2018)
Coconut Shell	38	5	15.5	1.9	0.83	30–35	Utsev and Taku (2012)
Ground nut shell	41.42	11.2	12.6	3.51	11.89	16–18	Alaneme et al. (2014)
Olive-stone	32–46	19.6–20.8	4.8–5.9	0.53–3.71	4.6–31.2	12–16	(Aburawi and Al-Madani, 2018; Bonet-Martínez et al., 2020)

2015; Liu et al., 2017). Rice plants obtain silica by polymerizing water-soluble silicic acid (H<sub>4</sub>SiO<sub>4</sub>) absorbed from the soil into insoluble polysilicic acids, which are then precipitated as amorphous silica and deposited in plant cell walls (Bhattacharya and Mandal, 2018). The silica present in rice husk is the most amorphous hydrated form of SiO<sub>2</sub>. Other than raw rice husk, processed rice husk biomass like ash was also utilized for the production of SiNPs (Mor et al., 2017). Rice husk ash (RHA) is produced after the combustion of rice husks and is widely available, particularly in rice-growing nations (Steven et al., 2021). Surprisingly, RHA has a silica concentration of about 80–95 wt %, attracting it to be used for industrial purposes. Nanoparticles with a purity of about 99.9% can be obtained from RHA. Rice husk contains various other impurities other than silica like K<sub>2</sub>O, Na<sub>2</sub>O, and Fe<sub>2</sub>O<sub>3</sub> in little amount, which may be percolated by acid treatment (Kasinathan et al., 2010; Thuadaj and Nuntiya, 2008). Like rice husk, rice straw also consists of lignocellulose (32–47%), cellulose (19–45%), lignin (5–24%), and silica (10–15%) (Dutta et al., 2014). Rice straw is also a good source of silica and approximately 10 million tons of silica can be produced from unused rice straw (Dutta et al., 2014).

### 3.2. Wheat straw and husk

Wheat is another cereal crop that is largely cultivated and as a result that a huge amount of agro-waste has been produced every year from wheat straw and husk (600–900 Mt) (Yemiş and Mazza, 2012). Wheat straw has risen to prominence as a source of silica in

the recent decade, attracting attention for its ability to generate porous silica at cheap cost and high efficiency, giving wheat straw a high added value. The polymerized  $\text{Si}(\text{OH})_4$  known as phytoliths, which is the most commonly found species in plants, is usually the major type of silica source (Ma et al., 2016). Studies found wheat straw and husk can serve as a precursor of silica production as wheat straw and husk ash contains 50–55% and 80–90% of silica in amorphous form, respectively (Bakar et al., 2016; Naqvi et al., 2011; Patel et al., 2017).

### 3.3. Bamboo leaves

Bamboo stems are being traditionally used for construction and pulp production. Bamboo leaves which are produced after the processing of the bamboo plant are a potential agro-waste that has a substantial amount of silica in it. The silica concentration in different parts of bamboo plants ranged from 0.03% in roots to 9.95 percent in leaves (Ding et al., 2008). Like rice husk ash, bamboo leaf ash also has a significant amount of silica (>70%) in it with a large surface area (Sethy et al., 2019). Relevant studies have revealed that bamboo leaf ash has a high silica content (75.90–82.86%) (Mohapatra et al., 2011).

Apart from bamboo leaves, bamboo sticks have also contained silica in them. A study was performed in 2016 to examine the physical and chemical characteristics of betung bamboo, and the findings had shown that bamboo sticks had a silica content of 3.51% on a dry weight basis (Fatriasari and Hermiatil, 2016). In a similar manner, both bamboo sticks ash and bamboo leaves ash were investigated for their silica content, and it was reported that 45.73% and 79.93% of silica were recovered from bamboo sticks ash and bamboo leaves ash, respectively (Dirna et al., 2020). However, certain factors like leaf maturity, the origin of bamboo, and soil can influence the silica content in bamboo leaves. Despite all of the biotic and abiotic constants, investigations have shown that it is feasible to extract more than 50% amorphous silica from bamboo leaves with an average size of 25 nm (purity: 99%) and a large surface area of  $428 \text{ m}^2\text{g}^{-1}$  (Rangaraj and Venkatachalam, 2017).

### 3.4. Sugarcane bagasse

Sugarcane bagasse might be viewed as one of the agriculture-based residues secured from the processing of sugarcane businesses (Hariharan and Sivakumar, 2013). Sugarcane bagasse is a solid waste that produces after the extraction of juice from sugarcane. Sugarcane bagasse is mainly made up of cellulose, hemicellulose, and lignin. Attempts have also been made to recover sodium silicate from sugarcane bagasse ash as a precursor to silica particle production.

(Boonmee and Jarukumjorn, 2019). Bagasse from sugarcane has a high silicon concentration and is widely available in agricultural countries. The concentration and availability of different forms of silicon in the soil has an impact on the amount of silica deposited in sugarcane bagasse (Norsuraya et al., 2016). Sugarcane bagasse ashes are also known as green building materials since they contain a lot of silica and have pozzolanic (cement-like) characteristics (Rajamani et al., 2021). Several studies that utilized sugarcane bagasse ash for silica production have reported high silica content (50–97%) (Norsuraya et al., 2016; Rahman et al., 2015; Vaibhav et al., 2015). Rovani et al. (2018) utilized sugarcane waste ash to produce highly pure SiNPs (>99%  $\text{SiO}_2$ ).

### 3.5. Corncob

Corncob is produced after harvesting the grains from corn. Like rice, wheat, bamboo, and sugarcane; maize is also accumulating a good amount of silica in its body. Corn cob is composed of cellulose and lignin and contains significant elements like silicon (0.133 wt %), calcium (0.022 wt %), and aluminum (0.022 wt %) (Chanadee and Chaiyarat, 2016). Corncob ash is used as a raw material for the production of silicates, silica, and silica nanoparticles that includes more than 60% silica by mass and small quantities of metallic impurities (Velmurugan et al., 2015). Different studies have been reported that corn cob ash having a silica content of 27%–60% and the extracted silica mostly amorphous in nature (Adesanya and Raheem, 2009; Okoronkwo et al., 2013; Sapawe et al., 2018; Shim et al., 2015). It might be an economically feasible raw material for silicates, silica, and silica nanoparticles. Corncob ash is the most cost-effective source of silica because it is obtained as a fine powder after combustion and thus does not require further grinding.

### 3.6. Other sources

Besides the above-mentioned silica-rich agro-waste sources, sugarbeet (*Beta vulgaris*), and horsetail (*Equisetum* sp.), are known to have significant quantities of biogenic silica (San et al., 2014). Sugarbeet is a particularly appealing source of biogenic silica since its silica concentration is contained mostly in bagasse. Sugarbeet bagasse is a large-scale agro-industrial waste that is frequently utilized as a boiler fuel to generate steam during the sugar manufacturing process. Palm kernel shell (PKS) is obtained when the kernel is separated from the endocarp. They are agricultural leftovers that can be produced during the processing of crude palm oil. Recent work has effectively extracted 56.65% amorphous silica from palm kernel shell ash in order to mitigate palm oil processing residues (Imoisili et al., 2020). Aside from PKS, the coconut husk is also contained silica and has immense potential as an alternative silica source. According to earlier studies, the silica content of coconut shell ash accounts for 38% (Utsev and Taku, 2012). Conversely, recent work revealed that the percentage of silica in coconut husk ash ranged from 8% to 11% (Anuar et al., 2018). Lastly, the groundnut shell and olive stone wastes can also be a source of silica as the chemical composition of the groundnut shell ash and olive stone ash are indicates the presence of silica (>30 wt%) in them (Alaneme et al., 2018; Pinheiro et al., 2018).

## 4. Different processes utilized for SiNP synthesis from agro-waste

To produce SiNPs from agricultural wastes, the studies utilized thermal, chemical, and biological treatment (Fig. 4). The description of different methodologies involved in the production of SiNPs was discussed in the following section.

#### 4.1. Thermal treatment

Thermal degradation can be performed by pyrolysis with the help of muffle furnace, fixed bed furnace, cyclone furnace, fluidized reactor, inclined step-grate oven, tubular reactor or rotary kiln. Silica can be obtained from agricultural wastes by thermal treatment using a muffle/electric furnace at various temperatures for different periods. Patil et al. (2014) burned down the rice husk ash (RHA) in a muffle furnace at 700 °C for 6 h. The amount of SiO<sub>2</sub> in the RHA after burning out was 94.95%. In another experiment, pyrolyzed rice husk (PRH) was produced from RH was in a fluidized bed reactor at a temperature of 475 °C. The PRH was again heated at 800 °C and processed through the alkaline digestion method to obtain sodium silicate. The produced sodium silicate was further treated with 1 M H<sub>3</sub>PO<sub>4</sub> to adjust the pH between 3.2 and 5.7. The sodium silicate solution was also mixed with polyethylene glycol (PEG) to produce porous silica-PEG composite (Li et al., 2011). The results showed that the decreasing pH had a great impact on the surface area and pore diameter of obtained silica. At pH 3.2, the silica had the highest surface area (1018 m<sup>2</sup>/g) and pore volume (2.30 nm). Vaibhav et al. (2015) used rice husk, sugarcane bagasse, groundnut shell, and bamboo leaves as substrates to produce silica. All the collected agro-wastes were initially sintered at 900 °C for 7 h. The produced ashes were treated with alkali extraction following acid treatment to get SiNPs. The SEM analysis of SiNPs showed particle sizes of 20–40 nm. The produced SiNPs was 98% and the yield of SiNPs was highest from rice husk (78%) as compared to sugarcane bagasse and bamboo leaves. Umeda and Kondoh (2010) used rice straw and husk to produce amorphous silica. However, this study utilized combustion energy (1073–1273 K) to produce silica which is not environmentally suitable. Gu et al. (2013) utilized the pyrolysis technique instead of the combustion method to produce SiNPs from RH. The study pyrolyzed the RH at varied temperatures (500–650 °C) to optimize the optimal temperature to produce SiNPs. The study observed that 610 °C was an optimal temperature for pyrolysis of RH and the SiNPs produced at this temperature were nearly spherical with a particle size of 8–10 nm. The impact of N<sub>2</sub> and CO<sub>2</sub> pyrolysis gases on improving the purity and textural characteristics of produced SiNPs were thoroughly investigated in subsequent research (Gu et al., 2015). The study found that the purity of the SiNPs was more under a CO<sub>2</sub> atmosphere (97.5%) as compared N<sub>2</sub> atmosphere. However, the surface area of SiNPs was more under the N<sub>2</sub> atmosphere (352.6 m<sup>2</sup>/g) as compared to the CO<sub>2</sub> atmosphere. The particle size of the synthesized SiNPs was <20 nm. Thermal treatment paves the path for chemical synthesis; all the studies primarily treated the agro wastes thermally before extract or isolate SiNPs chemically from agro-waste ash.

#### 4.2. Chemical treatment

Alkaline digestion followed by acid neutralization was primarily used for the chemical extraction of SiNPs from both agricultural wastes and agricultural waste ash (Fig. 5). Kalapathy et al. (2000) successfully extracted highly pure silica (91%) from rice husk using an alkaline digestion method with 1N NaOH. Alkaline digestion with NaOH produced Sodium silicate which was further treated with HCl for 18 h to produce silica. However, the produced silica still had some sodium (4%) impurities in it. An earlier study found that the surface area of obtained silica was severely affected by acid treatment. Liou and Yang (2011) employed different acids like HCl, H<sub>2</sub>SO<sub>4</sub>,

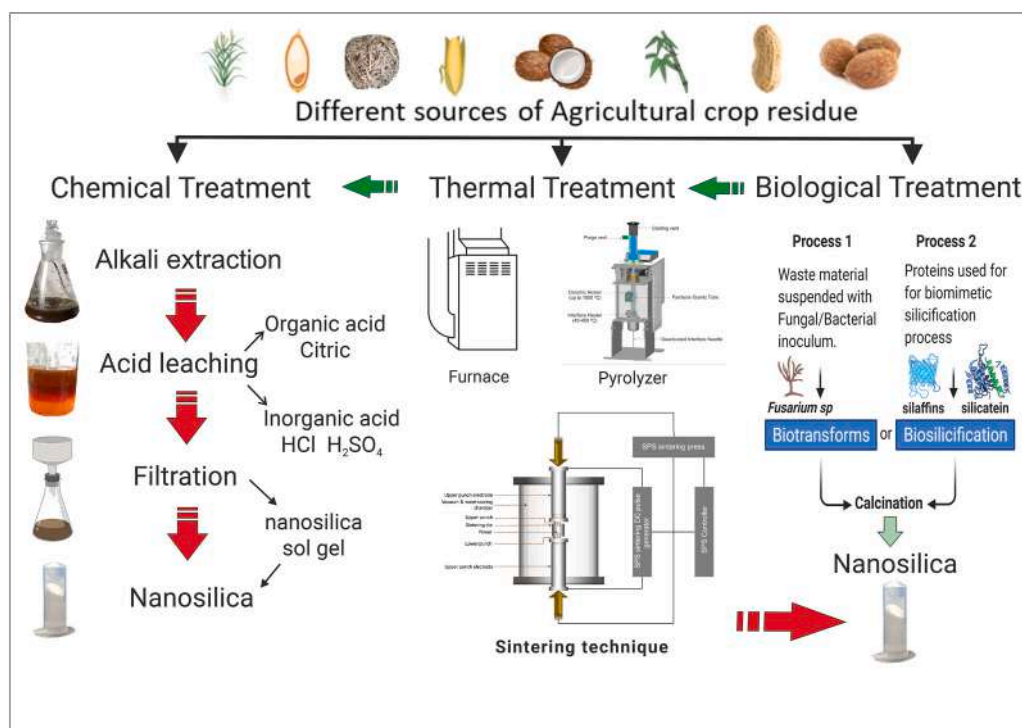
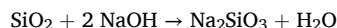


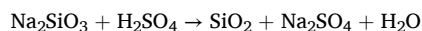
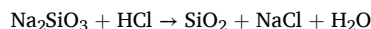
Fig. 4. Multifaced application of SiNPs in different fields.

$C_2H_2O_4$ , and  $C_6H_8O_7$  to check their effect on the surface area of silica. The result showed minimum and maximum surface area obtained in silica extracted with  $C_6H_8O_7$  and HCl, respectively. Selvakumar et al. (2014) pre-treated the RHA with different acids (6 N HCl, 6 N  $HNO_3$ , 6 N  $H_2SO_4$ ) before alkaline digestion followed by acid neutralization to improve the quality of the silica product.

The reaction mechanism of RHA mixed with NaOH solution was:



Silica was precipitated by acid neutralization from sodium-silicate.



Cui et al. (2015) synthesized mesoporous  $SiO_2$  microspheres from wheat husk ash using an alkaline extraction procedure with NaOH followed by acid precipitation with HCl. The prepared  $SiO_2$  microspheres were amorphous with approximate diameters and specific surface area of 227 nm and  $8.23 \text{ m}^2/\text{g}$ , respectively.

Witoon et al. (2008) used RHA and chitosan as a template for the synthesis of bimodal porous silica (BPS). The BPS was synthesized through the sol-gel method with a variation of pH 2–6. The results showed that pH and chitosan template had a greater impact on the surface area and pore volume of the synthesized BPS. The chitosan template not only increased the surface area (in the range of  $366\text{--}627 \text{ m}^2/\text{g}$ ) but also pore volume ( $0.65\text{--}1.70 \text{ cm}^3/\text{g}$ ) and thermal stability of the BPS compared to BPS synthesized without chitosan. Compared to (Witoon et al., 2008), other studies synthesized spherical, porous SiNPs from rice husk without templates using the sol-gel method (Adam et al., 2011; Zulkifli et al., 2013). Adam et al. (2011) reported that the synthesized SiNPs had a surface area, pore-volume, and pore size of  $245 \text{ m}^2/\text{g}$  and  $0.78 \text{ cc/g}$  and  $5.6\text{--}9.6 \text{ nm}$ , respectively. The TEM study showed the particle of the synthesized SiNPs range between 15 and 91 nm. Zulkifli et al. (2013) prepared sodium silicate ( $Na_2SiO_3$ ) from rice husk which was used as a precursor for the synthesis of mesoporous SiNPs. In this experiment, the precursor ( $Na_2SiO_3$ ) was mixed with phosphoric acid to precipitate the  $SiO_2$ . The obtained silica was further calcined at  $550 \text{ }^\circ\text{C}$  for 30 min. The surface area, range of particle size, and pore volume of the spherical SiNPs were  $\sim 364 \text{ m}^2/\text{g}$ ,  $75\text{--}252 \text{ nm}$ , and  $\sim 8 \text{ nm}$ , respectively.

Velmurugan et al. (2015) developed a simple method to synthesized amorphous silica from corn cob ash using the sol-gel method and alkaline treatment followed by acid precipitation. The TEM study demonstrates that the obtained amorphous silica had an average size of 50 nm. The FTIR spectra confirmed the presence of siloxane and silanol groups. In addition to the sol-gel technique, another study was conducted to investigate the impact of pH on alkaline extraction of silica from corncob ash afterward acid precipitation (Shim et al., 2015). This study extensively noted the role of pH (pH: 7–10) in the formation of stable SiNPs. The results demonstrated that at pH 7, 99.5% pure silica can be produced. The produced SiNPs at pH 7 had a high surface area, high reactivity, and an average particle size of 60 nm. Durairaj et al. (2019) also used the sol-gel technique to extract silica from bamboo leaf ash and observed that the synthesized silica had a large specific surface area ( $60.40 \text{ m}^2/\text{g}$ ). Palm kernel shell ash (PKSA) had been used for the synthesis of SiNPs via the sol-gel technique (Imoisili et al., 2020). The yield of silica from this experiment was 54.35%. The surface area and the particle



Fig. 5. Preparation of SiNPs from rice and wheat husk.

size of the synthesized SiNPs were 438 m<sup>2</sup>/g and 50–98 nm, respectively. In contrast to the usage of strong acids for example HCl and H<sub>2</sub>SO<sub>4</sub>, the use of organic acid may be a more environmentally acceptable way to reduce environmental risks (Pa et al., 2016). Due to lower toxicity, organic acid like citric acid has been used sometimes for the leaching process over strong acid. Palm ash, for example, was treated with varying concentrations of citric acid to extract silica (Pa et al., 2016). The obtained silica in this experiment was amorphous and more than 90% pure. The downside of these discussed thermal and chemical treatments was that all these procedures need high energy or heat and hazardous acid and basic substances to synthesize SiNPs from agricultural wastes. To tone down the environmental impact, researchers are now trying to utilize the biological route to produce environmentally safe SiNPs.

#### 4.3. Biological treatments

The purpose for biological synthesis over chemical and thermal synthesis lies in its low toxicity, fast and easy isolation, eco-friendly nature, and safety (Shah et al., 2015). Thus, a large number of researchers have drawn attention to the bioinspired synthesis of nanosilica as a unique way to manufacture different nanomaterials. Among bio conversion technologies, the bio-digestion process has received a lot of attention for extracting value-added products from waste. For instance, Californian red worms have been used to bio-digest rice husk and then extract nano silica (Estevez et al., 2009a). In their research, the worms are fed rice husks for five months and the excreted humus was then neutralized with CaCO<sub>3</sub> and calcined at various temperatures (500, 600, 700 °C), and then digested with a mixture of HCl and HNO<sub>3</sub> (1:3). Silica particles were obtained at a range of 55–250 nm depending on the calcination temperature. From these studies it is known that to obtain a single nanoparticle, calcination temperature must be lower than 600 °C. Different fungal genus like *Aspergillus*, *Fusarium*, and *Penicillium* also offer to promise extracellular bio-production capability for various metal nanoparticles, whereas *Verticillium* sp. might be collected for intracellular nanoparticle synthesis (Karande et al., 2021). For example, Piela et al. (2020) used *Fusarium culmorum* to bioconvert corn cob husk into SiNPs of specified size (40–70 nm) and shape (spherical) (Fig. 6). Rohatgi et al. (1987) produced SiNPs from rice husk by microbial fermentation utilizing the white-rot fungus. Zielonka et al. (2018) used *Aspergillus parasiticus* to synthesized SiNPs with sizes ranging from 3 to 400 nm from rice husk by fungus-driven biotransformation. In another study, Bansal et al. (2005) synthesized nanocrystalline silica from rice straw using fungus *Fusarium oxysporum*, which rapidly biotransforms naturally occurring amorphous biosilica into crystalline form. In their study, they used 10 g of rice straw and suspended with an aqueous suspension of *Fusarium oxysporum* and incubated on a shaker (250 rpm) for 24 h at 27 °C temperature. Filtration was done through time-dependent intervals. The filtrate was mixed with phenol-chloroform (1:1) solution and centrifuged at 6000 rpm for 10 min to obtained nanosilica suspension and finally gone through calcination at 400 °C for 2 h followed by lyophilization. They were able to synthesized quasi-spherical nanocrystalline silica ranging 2–6 nm.

Above mentioned biological processes are employed for the reduction of chemicals used as pre-treating agents for different agro waste. Apart from that recent investigation divulges proteins such as silaffins, silicatein, and polyamines from marine diatom and sponges are the essential biomolecule for the biomimetic silicification process. In the biosilicification process, Silaffins and long-chain polyamines (LCPAs) synergistically act as a major key factor for the conversion of silicon ions to amorphous nanosilica (Luckarift et al., 2004). Although the fundamental conception of biomimetic synthesis of nanosilica looks very straightforward, the underlying mechanism is not well understood. The effectiveness of the different treatments (thermal, chemical, and biological) used for the production of nano silica from agro-waste is compared in Table 2.

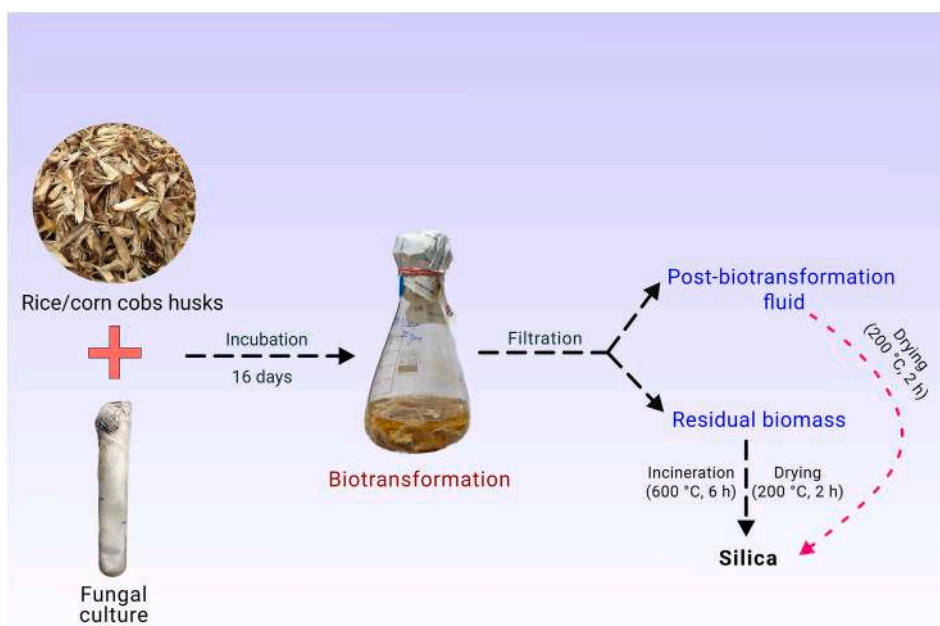


Fig. 6. Biotransformation of silica nanoparticles from agricultural wasteeusing fungi.

## 5. Multifaced applications of SiNPs

The structural flexibility and advanced features of SiNPs opened avenues of the different pathways of applications. Currently, SiNPs are used in different fields of science and technology such as drug delivery, biomedical imaging, biosensor, tissue engineering, agriculture, industry, and environmental remediation (Fig. 7).

### 5.1. Drug delivery

The main aim of drug delivery is to transport the therapeutic agent to the specific site without any change or loss in its structure and

**Table 2**

Comparative study based on different treatments involved for extraction of SiNPs and their practicality.

Process	Effective outlooks	Research gaps and modification	References
Thermal treatment (Intering/ Roasting/Calcination)	Pyrolysis of pre-processed rice husk is more worthwhile owing to reduced cost and simple synthetic pathway.	Owing to the degradation of hemicellulose and lignin at 200–260 °C and 280–360 °C respectively, they cannot be collected simultaneously with nanosilica.	Gu et al. (2013)
	The metals present in RHA are washed out from the volatiles when they are subjected to thermal decomposition.	Considerable agglomeration is observed when RHA calcinated at 700°C.	Sankar et al. (2018)
	If RHA is subjected to be burnt at controlled condition the amorphous silica thus produced will be reactive in nature. In order to synthesize more stable silica, it should be subjected to roasting in air.	Though there is a considerable increase in pore size, there is much decrease in pore volume when the calcination is carried out from 500 to 100°C	Rafiee et al. (2012)
	In TGA analysis of synthesized silica it is evident that, there is a mass loss upto 200°C due to vapourisation of water molecules. The range from 200 to 600 °C indicates the of residual sodium salts. The peak at 600 °C and 800 °C tallies with the sintering temperature used in the calcination process.	Calcination above 500 °C also leads to the decrease in surface area.	Liou and Yang (2011)
Chemical treatment (Alkaline extraction and acid coagulation/Acid hydrolysis/Leaching with acid)	NaOH arrangement was included rice husk debris and this blend was refluxed in a secured Erlenmeyer jar for 1 h with steady mixing. The arrangement was sifted through ashless channel paper and the buildup (carbon) was evacuated. The filtrate shaped was sodium silicate arrangement, which was cooled to room temperature; Silica in gel structure was delivered after titration with corrosive (HCl or H <sub>2</sub> SO <sub>4</sub> ) with steady mixing until pH 7. The arrangement was matured for 18 h at room temperature to shape gel (silica).	Costly, longer response time requires, various steps with the utilization of different kinds of synthetics.	Kalpathy et al. (2000)
	NaOH reacts with SiO <sub>2</sub> to form Na <sub>2</sub> SiO <sub>3</sub> . The acidification step is vital as with consequent acidification, silicon hydroxide species condenses to form siloxane bond (Si-O-Si).	Owing to the corrosive nature of conventional acids like hydrochloric acid, nitric acid and sulphuric acid- there rises a problem for disposal of used acid remnants.	Zulkifli et al. (2013)
	The acid leaching at pH 1 was found to be most effective in eliminating Ca, Mn and Fe from the RHA.	Carrying out the leaching process with conventional acids is also expensive when nanosilica is subjected to be produced at an industrial scale.	Kalpathy et al. (2000)
	Acid treatment is also needed as the precipitation of silica does take place at a pH < 10.	Another concern regarding acid coagulation is the mobility of the acid remnants. Thus, if they are disposed in soil it will lead to the removal of vital nutrients and micronutrients. This will specifically result in boron deficiency in plants, as water soluble boron functionalities are removed.	Affandi et al. (2009)
Biological treatment	Prior to the presence of more cations at higher pH, triggers a probability of contamination on the nanosilica surface. The TEM micrograph exhibits more aggregation at pH 7 compared to pH 10.	Leached acid remnants from landfills if get contaminated with water results in- lowering of pH. Washed metal, organic and inorganic functionalities constitute the contamination. There is a risk of percolation of these contaminants through the subsoil, which may result in the contamination of groundwater.	Shim et al. (2015)
	Different bacterial and fungal strains were being utilized for degradation of organic matter present. This process is environment friendly and don't involve any hazardous chemical. After, microbial digestion the residual matter was filtered and burned to isolate silica.	The process time taking and still involved combustion or high heat treatment to extract silica.	(Bansal et al., 2005; Rohatgi et al., 1987)

function. The controlled release of the cargo molecules from their nanocarrier is also a prerequisite for developing a systematic carrier for drug delivery. For achieving this objective, [Aughenbaugh et al. \(2001\)](#) developed SiO<sub>2</sub> xerogels as a carrier for the controlled release of cargo molecules. Mesoporous silica nanoparticles (MSNs) have been extensively studied as a suitable carrier for drug delivery over other traditional drug nanocarriers, especially in the delivery of hydrophobic drugs ([Deodhar et al., 2017](#); [Lu et al., 2007](#)). Because of the poor solubility and low absorption, the efficacy of hydrophobic drugs was restricted during oral administration ([Jong and Borm, 2008](#)). The large surface area and pore volume of SiNPs facilitate the entrapment of the drug. Porous silica particles grafted with thermoresponsive polymers with thermally triggered on/off gating mechanisms, in particular, have demonstrated improved performance as a hybrid drug delivery system capable of controlling the release of different drugs in a variety of mediums that resemble complex biological environments ([Jadhav and Scalarone, 2018](#)). These MSNs have high chemical stability, biocompatibility and functional group modification of these SiNPs are accountable for controlled release of drug ([Yao et al., 2017](#)). [Zhang et al. \(2010\)](#) loaded hydrophobic drug Telmisartan (TEL) in MSNs for improvement of oral absorption. Their finding showed that MSNs can significantly improve dissolution and permeability of TEL. [Gangwar et al. \(2013\)](#) was also successfully developed curcumin conjugated with SiNPs and administrated it against HeLa cell lines and fibroblast cells to check cytotoxicity. In another study, [Lu et al. \(2007\)](#) constructed a fluorescence mesoporous silica nanoparticle (FMSN) for the administration of Camptothecin (CPT), a poorly soluble anticancer drug. The encapsulation of CPT into FMSNs not only enhances the solubility of the drug but also induces anti-cancerous activity. [Porrang et al. \(2021\)](#) utilized rice and wheat husk-derived silica to synthesize MSNs in both discrete and continuous modes and then used the produced MSNs as a carrier for anticancer drugs (Doxorubicin). When compared to MSNs synthesized in continuous mode at pH 5.4, the results revealed that MSNs synthesized in discrete mode at pH 5.4 had a higher accumulative released drug and a high-efficiency anticancer effect on the MCF-7 cell line.

## 5.2. Biomedical imaging

The probe designed for biomedical imaging should combine low toxicity with high sensitivity, resolution, and stability. Quantum dots (QDs) are widely used in biomedical fields and quintessential nanoprobe are used in the detection of single molecules and live-cell imaging. However, the presence of toxic metals (Cd and Pb) in QDs and their insolubility in water is a subject of concern. On the other hand, hydrophilic nature, less toxicity, and large pore volume of MSNs can serve as an alternative option for various medical imaging applications ([Du et al., 2016](#); [Xie et al., 2013](#)). In order to monitor the intracellular pH values, [Tsou et al. \(2014\)](#) had designed

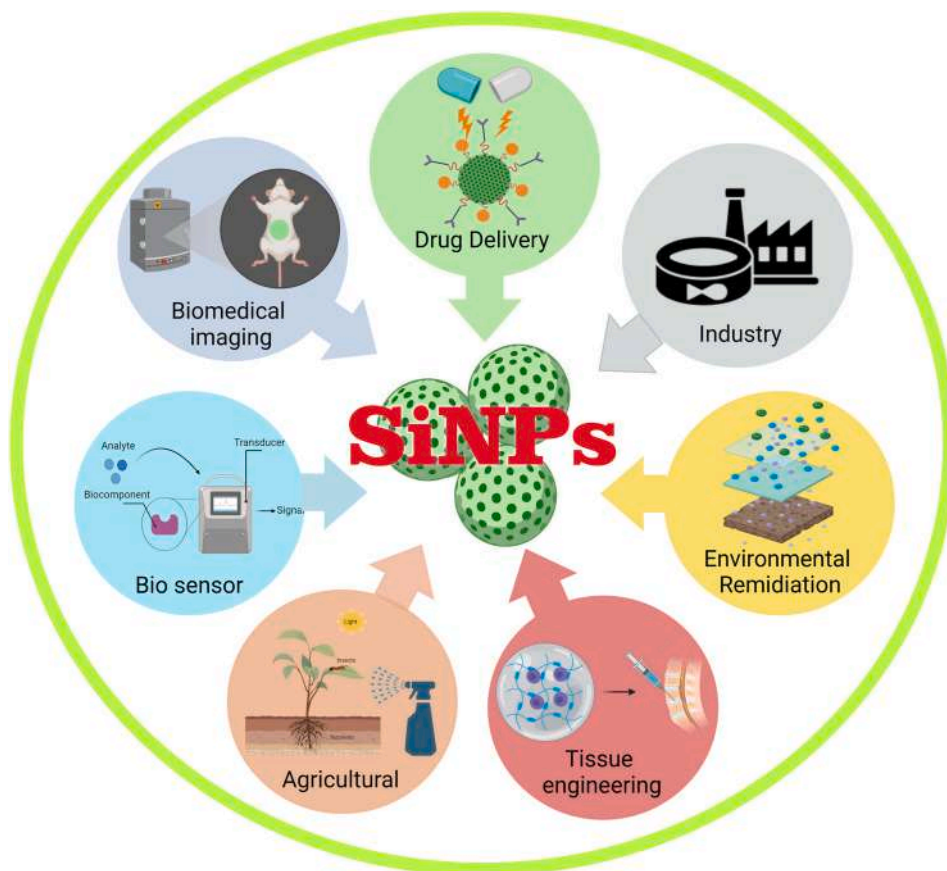


Fig. 7. Multifaced application of SiNPs in different fields.



hollow mesoporous silica nanoparticles (HMSNs) and loaded these modified MSNs with two pH-sensitive dyes (fluorescein isothiocyanate and rhodamine B isothiocyanate). A multifunctional platform reported for controlled drug delivery, magnetic hyperthermia, and photothermal therapy using MMSN/QGD nanosystem loaded with Doxorubicin (DOX) exhibit significant synergistic effect as compared to chemotherapy, magnetic hyperthermia, or photothermal therapy alone and can efficiently kill cancer cells (breast cancer 4T1) with higher efficacy (Yao et al., 2017).

### 5.3. Biosensor

Owing to structural flexibility, a large surface area/pore volume of engineered nanostructures are emerged as a lucrative biosensing agent to detect various analytes in both *in vivo* and *in vitro* conditions. Metal nanoparticles (gold, silver, and platinum) and metal-organic nanoparticles have been extensively used and studied as nano biosensors (Wu et al., 2011). The large pore volume and optical transparency of silica nanoparticles are excellent options for biosensing applications. Khabbaz et al. (2015) has successfully designed a fluorescent aptasensor, immobilized on the surface SiNPs for detection of kanamycin. Recently, 3-mercaptopropyl trimethoxysilane-functionalized silica nanoparticles were developed by Rahimi-Mohseni et al. (2018), as a nano biosensor for voltammetric determination of the wide range of L-tyrosine (0.05–600  $\mu\text{M}$ ) in the blood plasma sample. Wang et al. (2014) developed a laccase biosensor relying on phytic acid-functionalized silica nanoparticles ( $\text{SiO}_2\text{-PA}$  NPs) for monitoring dopamine (DA) levels in blood serum samples. The result showed that the biosensor had good sensitivity and reproducibility against DA.

### 5.4. Tissue engineering

The field of regenerative medication is extremely encouraging for treating sicknesses and supplanting lost or harmed tissue (Langer and Vacanti, 1993). Mesoporous silica nanoparticles (MSNs) have an incredible breadth and are being sought after in the field of tissue building. MSNs comprise a flexible medication conveyance framework and can likewise be utilized as platforms for immature microorganisms to develop or even offer signs to undeveloped cells to manage undifferentiated organism arrangement. MSNs can be a vital piece of future biomaterial innovation (Rosenholm et al., 2016; Xu et al., 2014). Polymeric scaffolds serve as a three-dimensional layout for cell attachment, proliferation, differentiation, and tissue formation. Based on this idea, Mehra et al. (2015) fabricated SiNPs-incorporated PLGA/gelatin electrospun nanofibrous scaffolds for stem cell culture and tissue engineering applications. In another study, MSNs combined with bone-forming peptide (BFP) derived from bone morphogenetic protein-7 (BMP-7) had been used for osteogenic differentiation of human mesenchymal stem cells (hMSCs) (Luo et al., 2015). The result of this study confirmed that BFP released from the SiNPs at a concentration of 500  $\mu\text{g}/\text{mL}$  can stimulate the osteogenic differentiation of hMSCs.

### 5.5. Agriculture

The agricultural sector suffers unrestorable loss in plant yield due to the occurrence of different biotic and abiotic stress. Exposure to heavy metals or metalloids can have a significant impact on plant growth and yield (Mridha et al., 2021). However, a recent study showed that the application of SiNP significantly reduced the inhibitory effects of Cd and As on rice seedling development. SiNP supplementation also hindered Cd and As translocation from roots to shoots, as well as Cd- and As-induced reactive oxygen species generation in rice seedlings (Chen et al., 2021). Continuous application of chemical fertilizers and pesticides to increase productivity and control pests, respectively cause degradation of soil and environment. Various recent investigation have revealed that SiNPs can increase plant growth and production significantly (Siddiqui et al., 2014; Siddiqui and Al-Whaibi, 2014; Strout et al., 2013). SiNPs are not only observed to carry organic and inorganic (NPK) fertilizers at their specific site of delivery but also controlled their release into soil and water (Janmohammadi et al., 2016). Wanyika et al. (2012) investigated SiNPs for potent pesticide application. The role of SiNPs in pest control has been studied in two ways: (a) SiNPs were directly sprayed in the field to insects or their larvae, and (b) commercial pesticides loaded into the MSNs to control the release and efficacy of pesticide against pests. Rouhani et al. (2013) has shown that SiNPs was lethal to the cowpea seed beetle (*Callosobruchus maculatus*). The SiNPs synthesized from diatom silica fistule served as a carrier of different herbicides (chloroacetanilide, anilide, and benzimidazole) into the field in its active form (Lodriche et al., 2013). The application of nano-zeolite (crystalline aluminosilicates) into soil helped to improve soil quality and increase the water retention capacity of the soil (Sekhon, 2014). Thus, it was helpful to overcome drought in the arid region (Ghanbari and Ariafer, 2013).

### 5.6. Industrial

SiNPs-based molecular surface imprinting (MIP) was used for selective determination of rhodamine B (RhB) in complex food matrices. The silica-based MIPs are tested for specific recognition of RhB from standard mixture solution containing structural analogs of RhB. These silica-based MIPs were also successfully determined the content of RhB in red wine and beverages (Long et al., 2016). The low concentration of SiNPs (1–8% by weight) in combination with two-part epoxy formulation was reported to increase the toughness, glass transition temperature, and single-lap shear strength of the adhesive (Kinloch et al., 2005). The modified alumina/silica nanocomposites were synthesized with the hydrothermal method and were used as an additive in lubricating oil. The result showed that the anti-friction and anti-wear performance of these alumina/silica nanocomposites were much better than the pure alumina and silica nanoparticles (Jiao et al., 2011). In a recent study, magnetic gold mesoporous silica nanoparticles (mAu@PSNs) were developed to offer a suitable matrix for cellulase immobilization. The mAu@PSNs nano-systems raised the thermal stability and reusability of cellulase (Poorakbar et al., 2018).

### 5.7. Environmental remediation

The structural flexibility of SiNPs attracts researchers to carry out different remediation works using SiNPs or silica

nanocomposites. The hydroxyl group on the surface of silica are known as Silanols which may preferentially complex specific chemicals or metal ions. However, changing the pH value improves the interactions of different compounds with silanols (Jadhav et al., 2019). Silanols may also be pH sensitive. As a result, bare silica nanoparticles are also evaluated for dye removal. Rovani et al. (2018) successfully removed acid orange 8 colors from water using bare silica particles prepared from sugarcane bagasse. Durairaj et al. (2019) used bamboo leaf-derived SiNPs to remove Cadmium (Cd) and Congo red (CR) from aqueous solutions. The optimum removal of Cd and CR from an aqueous solution was obtained at pH 7 and 100 mg adsorbent doses. Nasreen et al. (2018) found that MSNs are good adsorbents of heavy metals, phenols, and PAHs. The absorption of heavy metals and other pollutants by MSNs are in the following order: Cr > Pb > As > Hg > phenols > PAHs. Metal ion adsorption by mesoporous silicas is offered one of the most common and simple methods, since the adsorbent (MSNs) can be easily recovered and reused (Jadhav et al., 2020). Because of this characteristic, there is a lot of interest in researching mesoporous silica for heavy metal ion removal (Karbassian, 2018). A comparative study was conducted to study the efficacy of graphite oxide, silica nanoparticles, and silica/graphite oxide nanocomposite for removal of heavy metals (nickel, zinc, lead, cadmium, chromium) from the aqueous solution. The study recommended graphite oxide/silica nanocomposites were the most effective adsorbent of heavy metals as compared to graphite oxide and silica nanoparticles alone (Sheet et al., 2014). Silica nanoparticles are being used for various removal purposes. The highly hydrophobic polydimethylsiloxane (PDMS) coated silica nanoparticles were developed and used for the separation of oil from oil/water mixture. The result of this study found the gelled mixture of hydrophobized silica and oil was stable for 7 days after separation (Cho et al., 2014). Low-cost porous silica nanoparticles were designed for the removal of methylene blue from water and the synthesized porous SiNPs can be used 5 times for effective removal of methylene blue (Yu et al., 2018). Mesoporous silica was immobilized in a cellulose acetate matrix for the effective removal of boron. The synthesized hybrid nanomaterials were reported to remove boron up to 93% from acidic form (phenylboronic acid) (Albertini et al., 2018). Yang et al. (2013) reported SiNPs were able to capture positively charged atmospheric lead (Pb) due to their large surface area and negative charge. Different researchers used a composite of silica nanoparticles as an adsorbent of toxic/hazardous substances from wastewater. Silica composite of superparamagnetic zirconia (SPMZ)  $ZrO_2/SiO_2/Fe_3O_4$  nanoparticles selectively adsorbed fluoride from a multi-component system and at pH 4 this nanosystem has an absorption capacity of 14.7 mg F/g (Chang et al., 2011). Sodium dodecylbenzene sulfonate (SDBS) was used to decontaminate radioactive waste especially Cs ions. A modified Silica NP with an amine group has been designed to decontaminate SDBS in the process of waste treatment (Kim et al., 2019).

## 6. Future perspectives

Despite recent advances in the field of agro wastes-based SiNP synthesis, there is still a need for further study. The burning of agrowastes to remove organic components releases greenhouse gases and a considerable amount of particulate matter. To make high-purity silica, strong acids are required, which are extremely harmful to the environment and human life. Furthermore, the entire synthesis method is complicated. To eliminate metal alkali and prevent hazardous residues, milder acids such as citric acid (Umeda and Kondoh, 2010) and acetic acid (Carmona et al., 2013) can be used in the chelation process. Two approaches that can be used for decomposing organic substances and generating nano-sized particles from agricultural wastes are laser ablation (San et al., 2014) and bio-digestion (Estevez et al., 2009b; Torres et al., 2017). Agricultural wastes biomass (rice husk, rice straw, wheat husk, wheat straw, bamboo leaves, etc.) contains lignocellulose, silica, and other compounds. Among the lignocellulosic components, cellulose makes up a large percentage of plant biomass, and cellulose is a homogenous polymer made up of glucose monomers. At the time of silica extraction from agricultural wastes, organic compounds and metal alkali impurities are eliminated as undesirable materials and discarded without further processing. As a result, using an integrated technology-based approach to properly recover important components from agricultural wastes is desirable. Numerous studies have been conducted to synthesize silica as well as other important compounds. Cellulose nanofibers (CNFs) and cellulose nanocrystals (CNCs) can be made from cellulose (Shahi et al., 2021). Therefore, the study aimed at fractional synthesis of SiNPs, CNFs, and CNCs is required for the proper utilization of agrowastes. For the synthesis of lignin and  $SiO_2$  in nano shape, Kauldhar et al. (2021) treated sugarcane bagasse with ethanol to remove salt-based impurities, followed by acid catalytic hydrolysis and treatment with a peroxide alkaline mixture. A distinct feature of this approach was the simultaneous separation of pure silica nanocubes (35 nm) and spherical-shaped lignin (20 nm) in a single stage. Zhang et al. (2015) simultaneously produced D-xylose, lignin, ethanol, and amorphous superfine silica from rice husk. In another study, activated carbon and silica were synthesized from rice husk (An et al., 2010; Liu et al., 2012).

## 7. Conclusion

An overview of the synthesis of agricultural waste biomass-assisted SiNPs, as well as their potential applications in many sectors, were discussed in this article. Due to the availability of silica and worldwide productivity, crop wastes can be a cost-effective silica precursor. Till now cereal crop residues are being emerged as a potential substrate for nanosilica synthesis. Looking forward to the silica synthesis procedure, it was evident that biological treatment was way more eco-friendly and environmentally sustainable; yet, the process of biological treatment is a much slower process than thermal and chemical treatment. Silica nanoparticles with adjustable textural properties produced from agricultural wastes are gaining popularity in medical, agricultural, industrial, and environmental remediation applications.

## Declaration of competing interest

On behalf of all listed authors, the corresponding author declares that there is not any sort of financial and non-financial conflict of interest in the subject materials mentioned in this manuscript.

## Acknowledgments

We thank Ms. Shrayana Basu (Department of Botany, University of Calcutta) and Mr. Pallab Chakraborty (Department of Botany, Acharya Prafulla Chandra College) for helping to make a graphical illustration for this article.

## References

- Aburawi, M.M., Al-Madani, H.M., 2018. The effect of using ash residues of olive fruits on the properties of cement mortar. In: <https://doi.org/10.21467/PROCEEDINGS.4.1>, 351,360.
- Adam, F., Chew, T.-S., Andas, J., 2011. A simple template-free sol-gel synthesis of spherical nanosilica from agricultural biomass. *J. Sol. Gel Sci. Technol.* 59 (3 59), 580–583. <https://doi.org/10.1007/S10971-011-2531-7>, 2011.
- Adesanya, D.A., Raheem, A.A., 2009. A study of the workability and compressive strength characteristics of corn cob ash blended cement concrete. *Construct. Build. Mater.* 23, 311–317. <https://doi.org/10.1016/J.CONBUILDMAT.2007.12.004>.
- Affandi, S., Setyawan, H., Winardi, S., Purwanto, A., Balgis, R., 2009. A facile method for production of high-purity silica xerogels from bagasse ash. *Adv. Powder Technol.* 20, 468–472. <https://doi.org/10.1016/j.apt.2009.03.008>.
- Alaneme, K.K., Bodunrin, M.O., Awe, A.A., 2018. Microstructure, mechanical and fracture properties of groundnut shell ash and silicon carbide dispersion strengthened aluminium matrix composites. *Journal of King Saud University - Engineering Sciences* 30, 96–103. <https://doi.org/10.1016/J.JKSUES.2016.01.001>.
- Alaneme, K.K., Fatile, B.O., Borode, J.O., 2014. Mechanical and corrosion behaviour of Zn-27Al based composites reinforced with groundnut shell ash and silicon carbide. *Tribology in Industry* 36, 195–203.
- Albertini, F., Ribeiro, T., Alves, S., Baleizão, C., Farinha, J.P.S., 2018. Boron-chelating membranes based in hybrid mesoporous silica nanoparticles for water purification. *Mater. Des.* 141, 407–413. <https://doi.org/10.1016/J.MATDES.2018.01.001>.
- An, D., Guo, Y., Zhu, Y., Wang, Z., 2010. A green route to preparation of silica powders with rice husk ash and waste gas. *Chem. Eng. J.* 162, 509–514. <https://doi.org/10.1016/J.CEJ.2010.05.052>.
- Anuar, M.F., Fen, Y.W., Zaid, M.H.M., Matori, K.A., Khaidir, R.E.M., 2018. Synthesis and structural properties of coconut husk as potential silica source. *Results in Physics* 11, 1–4. <https://doi.org/10.1016/J.RINP.2018.08.018>.
- Arumugam, A., Ponnusami, V., 2013. Modified SBA-15 synthesized using sugarcane leaf ash for nickel adsorption. *Indian J. Chem. Technol.* 20, 101–105.
- Ataie, F.F., Riding, K.A., 2016. Influence of agricultural residue ash on early cement hydration and chemical admixtures adsorption. *Construct. Build. Mater.* 106, 274–281. <https://doi.org/10.1016/j.conbuildmat.2015.12.091>.
- Aughenbaugh, W., Radin, S., Ducheyne, P., 2001. Silica sol-gel for the controlled release of antibiotics. II. The effect of synthesis parameters on the in vitro release kinetics of vancomycin. *J. Biomed. Mater. Res.* 57, 321–326. <https://doi.org/10.1002/1097-4636>.
- Bahrami, A., Soltani, N., Pech-Canul, M.L., Soltani, S., González, L.A., Gutiérrez, C.A., Tapp, J., Möller, A., Gurlo, A., 2018. Bilayer graded Al/B<sub>4</sub>C/rice husk ash composite: wettability behavior, thermo-mechanical, and electrical properties. *J. Compos. Mater.* 52, 3745–3758. <https://doi.org/10.1177/0021998318769993>.
- Bakar, R.A., Yahya, R., Gan, S.N., 2016. Production of high purity amorphous silica from rice husk. *Procedia Chemistry* 19, 189–195. <https://doi.org/10.1016/j.proche.2016.03.092>.
- Bansal, V., Rautaray, D., Bharde, A., Ahire, K., Sanyal, A., Ahmad, A., Sastry, M., 2005. Fungus-mediated biosynthesis of silica and titania particles. *J. Mater. Chem.* 15, 2583–2589. <https://doi.org/10.1039/b503008k>.
- Bhagiyalakshmi, M., Yun, L.J., Anuradha, R., Jang, H.T., 2010. Utilization of rice husk ash as silica source for the synthesis of mesoporous silicas and their application to CO<sub>2</sub> adsorption through TREN/TEPA grafting. *J. Hazard Mater.* 175, 928–938. <https://doi.org/10.1016/j.jhazmat.2009.10.097>.
- Bhattacharya, M., Mandal, M.K., 2018. Synthesis of rice straw extracted nano-silica-composite membrane for CO<sub>2</sub> separation. *J. Clean. Prod.* 186, 241–252. <https://doi.org/10.1016/J.JCLEPRO.2018.03.099>.
- Bhuvaneshwari, S., Hettiarachchi, H., Meegoda, J.N., 2019a. Crop residue burning in India: policy challenges and potential solutions. *Int. J. Environ. Res. Publ. Health* 16. <https://doi.org/10.3390/ijerph16050832>.
- Bhuvaneshwari, S., Hettiarachchi, H., Meegoda, J.N., 2019b. Crop residue burning in India: policy challenges and potential solutions. *Int. J. Environ. Res. Publ. Health* 16. <https://doi.org/10.3390/ijerph16050832>.
- Binici, H., Yucegok, F., Aksogan, O., Kaplan, H., 2008. Effect of corncob, wheat straw, and plane leaf ashes as mineral admixtures on concrete durability. *J. Mater. Civ. Eng.* 20, 478–483. [https://doi.org/10.1061/\(ASCE\)0899-1561\(2008\)20:7\(478\)](https://doi.org/10.1061/(ASCE)0899-1561(2008)20:7(478)).
- Binod, P., Sindhu, R., Singhanian, R.R., Vikram, S., Devi, L., Nagalakshmi, S., Kurien, N., Sukumaran, R.K., Pandey, A., 2010. Bioethanol production from rice straw: an overview. *Bioresour. Technol.* 101, 4767–4774. <https://doi.org/10.1016/j.biortech.2009.10.079>.
- Bonet-Martínez, E., García-Cobo, P., Pérez-Villarejo, L., Castro, E., Eliche-Quesada, D., 2020. Effect of olive-pine bottom ash on properties of geopolymers based on metakaolin. *Materials* 2020 13. <https://doi.org/10.3390/MA13040901>, 901 13, 901.
- Boonmee, A., Jarukunjom, K., 2019. Preparation and characterization of silica nanoparticles from sugarcane bagasse ash for using as a filler in natural rubber composites. *Polymer Bulletin* 2019 77 (7 77), 3457–3472. <https://doi.org/10.1007/S00289-019-02925-6>.
- Carmona, V.B., Oliveira, R.M., Silva, W.T.L., Mattoso, L.H.C., Marconini, J.M., 2013. Nanosilica from rice husk: extraction and characterization. *Ind. Crop. Prod.* 43, 291–296. <https://doi.org/10.1016/J.INDCROP.2012.06.050>.
- Chanadee, T., Chaiyarat, S., 2016. Preparation and Characterization of Low Cost Silica Powder from Sweet Corn Cobs (*Zea mays Saccharata* L).
- Chang, C.F., Chang, C.Y., Hsu, T.L., 2011. Removal of fluoride from aqueous solution with the superparamagnetic zirconia material. *Desalination* 279, 375–382. <https://doi.org/10.1016/J.DESAL.2011.06.039>.
- Chen, H., Wang, F., Zhang, C., Shi, Y., Jin, G., Yuan, S., 2010. Preparation of nano-silica materials: the concept from wheat straw. *J. Non-Cryst. Solids* 356, 2781–2785. <https://doi.org/10.1016/j.jnoncrysol.2010.09.051>.
- Chen, Huiqiong, Liang, X., Gong, X., Reinfelder, J.R., Chen, Huamei, Sun, C., Liu, X., Zhang, S., Li, F., Liu, C., Zhao, J., Yi, J., 2021. Comparative physiological and transcriptomic analyses illuminate common mechanisms by which silicon alleviates cadmium and arsenic toxicity in rice seedlings. *Journal of Environmental Sciences* 109, 88–101. <https://doi.org/10.1016/J.JES.2021.02.030>.
- Chen, J., Gong, Y., Wang, S., Guan, B., Balkovic, J., Kraxner, F., 2019. To burn or retain crop residues on croplands? An integrated analysis of crop residue management in China. *Sci. Total Environ.* 662, 141–150. <https://doi.org/10.1016/J.SCITOTENV.2019.01.150>.
- Cho, Y.K., Park, E.J., Kim, Y.D., 2014. Removal of oil by gelation using hydrophobic silica nanoparticles. *J. Ind. Eng. Chem.* 20, 1231–1235. <https://doi.org/10.1016/J.JIEC.2013.08.005>.
- Cui, J., Sun, H., Luo, Z., Sun, J., Wen, Z., 2015. Preparation of low surface area SiO<sub>2</sub> microsphere from wheat husk ash with a facile precipitation process. *Mater. Lett.* 156, 42–45. <https://doi.org/10.1016/J.MATLET.2015.04.134>.
- Deodhar, G.V., Adams, M.L., Trewn, B.G., 2017. Controlled release and intracellular protein delivery from mesoporous silica nanoparticles. *Biotechnol. J.* 12 <https://doi.org/10.1002/BIOT.201600408>.
- Ding, T.P., Zhou, J.X., Wan, D.F., Chen, Z.Y., Wang, C.Y., Zhang, F., 2008. Silicon isotope fractionation in bamboo and its significance to the biogeochemical cycle of silicon. *Geochim. Cosmochim. Acta* 72, 1381–1395. <https://doi.org/10.1016/J.GCA.2008.01.008>.
- Dirna, F.C., Rahayu, I., Maddu, A., Darmawan, W., Nandika, D., Prihatini, E., 2020. Nanosilica synthesis from betung bamboo sticks and leaves by ultrasonication. *Nanotechnol. Sci. Appl.* 13, 131–136. <https://doi.org/10.2147/NSA.S282357>.
- Drummond, A.R.F., Drummond, I.W., 1996. Pyrolysis of sugar cane bagasse in a wire-mesh reactor. *Ind. Eng. Chem. Res.* 35, 1263–1268. <https://doi.org/10.1021/ie950391a>.
- Du, X., Li, X., Xiong, L., Zhang, X., Kleitz, F., Qiao, S.Z., 2016. Mesoporous silica nanoparticles with organo-bridged silsesquioxane framework as innovative platforms for bioimaging and therapeutic agent delivery. *Biomaterials* 91, 90–127. <https://doi.org/10.1016/J.BIOMATERIALS.2016.03.019>.

- Durairaj, K., Senthilkumar, P., Velmurugan, P., Dhamodaran, K., Kadirvelu, K., Kumaran, S., 2019. Sol-gel mediated synthesis of silica nanoparticle from *Bambusa vulgaris* leaves and its environmental applications: kinetics and isotherms studies. *Journal of Sol-Gel Science and Technology* 2019 90 (3 90), 653–664. <https://doi.org/10.1007/S10971-019-04922-7>.
- Dutta, S.K., Halder, G., Mandal, M.K., 2014. Modeling and optimization of bi-directional delignification of rice straw for production of bio-fuel feedstock using central composite design approach. *Energy* 71, 579–587. <https://doi.org/10.1016/J.ENERGY.2014.04.108>.
- El-Sayed, S.A., Khairy, M., 2017. Preparation and characterization of fuel pellets from corn cob and wheat dust with binder. *Iranian (Iranica) Journal of Energy & Environment* 8, 71–87. <https://doi.org/10.5829/IDOSI.IJEE.2017.08.01.13>.
- Estevez, M., Vargas, S., Castaño, V.M., Rodriguez, R., 2009a. Silica nano-particles produced by worms through a bio-digestion process of rice husk. *J. Non-Cryst. Solids* 355, 844–850. <https://doi.org/10.1016/J.JNONCRYOL.2009.04.011>.
- Estevez, M., Vargas, S., Castaño, V.M., Rodriguez, R., 2009b. Silica nano-particles produced by worms through a bio-digestion process of rice husk. *J. Non-Cryst. Solids* 355, 844–850. <https://doi.org/10.1016/j.jnoncrysol.2009.04.011>.
- Faizul, C.P., Abdullah, C., Fazlul, B., 2013. Review of extraction of silica from agricultural wastes using acid leaching treatment. In: *Advanced Materials Engineering and Technology, Advanced Materials Research*. Trans Tech Publications Ltd, pp. 997–1000. <https://doi.org/10.4028/www.scientific.net/AMR.626.997>.
- FAOSTAT, 2021. <http://www.fao.org/faostat/en/#data/GB>. Accessed on: 23.05.2021.
- Patriasari, W., Hermiatil, E., 2016. Lignocellulosic biomass for bioproduct: its potency and technology development. *Journal of Lignocellulose Technology* 1, 11–40.
- Gangwar, R.K., Tomar, G.B., Dhumale, V.A., Zinjarde, S., Sharma, R.B., Datar, S., 2013. Curcumin conjugated silica nanoparticles for improving bioavailability and its anticancer applications. *J. Agric. Food Chem.* 61, 9632–9637. <https://doi.org/10.1021/JF402894X>.
- Ghanbari, M., Ariafar, S., 2013. The Effects of Water Deficit and Zeolite Application on Growth Traits and Oil Yield of Medicinal Peppermint (*Mentha Piperita* L.). Undefined.
- Gu, S., Zhou, J., Luo, Z., Wang, Q., Ni, M., 2013. A detailed study of the effects of pyrolysis temperature and feedstock particle size on the preparation of nanosilica from rice husk. *Ind. Crop. Prod.* 50, 540–549. <https://doi.org/10.1016/j.indcrop.2013.08.004>.
- Gu, S., Zhou, J., Yu, C., Luo, Z., Wang, Q., Shi, Z., 2015. A novel two-staged thermal synthesis method of generating nanosilica from rice husk via pre-pyrolysis combined with calcination. *Ind. Crop. Prod.* 65, 1–6. <https://doi.org/10.1016/J.INDCROP.2014.11.045>.
- Hariharan, V., Sivakumar, G., 2013. Studies on synthesized nanosilica obtained from bagasse ash. *International Journal of ChemTech Research* 5, 1263–1266.
- Imoisili, P.E., Ukoba, K.O., Jen, T.C., 2020a. Green technology extraction and characterisation of silica nanoparticles from palm kernel shell ash via sol-gel. *Journal of Materials Research and Technology* 9, 307–313. <https://doi.org/10.1016/J.JMRT.2019.10.059>.
- Imoisili, P.E., Ukoba, K.O., Jen, T.C., 2020b. Synthesis and characterization of amorphous mesoporous silica from palm kernel shell ash. *Bol. Soc. Espanola Ceram. Vidr.* 59, 159–164. <https://doi.org/10.1016/J.BSECV.2019.09.006>.
- Isikgor, F.H., Becer, C.R., 2015. Lignocellulosic biomass: a sustainable platform for the production of bio-based chemicals and polymers. *Polym. Chem.* 6, 4497–4559. <https://doi.org/10.1039/C5PY00263J>.
- Jadhav, S.A., Garud, H.B., Patil, A.H., Patil, G.D., Patil, C.R., Dongale, T.D., Patil, P.S., 2019. Recent advancements in silica nanoparticles based technologies for removal of dyes from water. *Colloid and Interface Science Communications* 30, 100181. <https://doi.org/10.1016/J.COLCOM.2019.100181>.
- Jadhav, S.A., Patil, V.S., Shinde, P.S., Thoravath, S.S., Patil, P.S., 2020. A short review on recent progress in mesoporous silicas for the removal of metal ions from water. *Chemical Papers* 2020 74 (12 74), 4143–4157. <https://doi.org/10.1007/S11696-020-01255-6>.
- Jadhav, S.A., Scalapone, D., Jadhav, S.A., Scalapone, D., 2018. Thermoresponsive polymer grafted porous silicas as smart nanocarriers. *Aust. J. Chem.* 71, 477–481. <https://doi.org/10.1071/CH18229>.
- Janmohammadi, M., Amanzadeh, T., Sabaghnia, N., Ion, V., 2016. Effect of nano-silicon foliar application on safflower growth under organic and inorganic fertilizer regimes. *Bot. Lith.* 22, 53–64. <https://doi.org/10.1515/BOTLIT-2016-0005>.
- Jiao, D., Zheng, S., Wang, Y., Guan, R., Cao, B., 2011. The tribology properties of alumina/silica composite nanoparticles as lubricant additives. *Appl. Surf. Sci.* 257, 5720–5725. <https://doi.org/10.1016/J.APSUSC.2011.01.084>.
- Jong, W.H. De, Borm, P.J., 2008. Drug delivery and nanoparticles: applications and hazards. *Int. J. Nanomed.* 3, 133. <https://doi.org/10.2147/IJN.S596>.
- Kalapathy, U., Proctor, A., Shultz, J., 2000. A simple method for production of pure silica from rice hull ash. *Bioresour. Technol.* 73, 257–262. [https://doi.org/10.1016/S0960-8524\(99\)00127-3](https://doi.org/10.1016/S0960-8524(99)00127-3).
- Kamath, S.R., Proctor, A., 1998. Silica gel from rice hull ash: preparation and characterization. *Cereal Chem.* 75, 484–487. <https://doi.org/10.1094/CCHEM.1998.75.4.484>.
- Karande, S.D., Jadhav, S.A., Garud, H.B., Kalantre, V.A., Burungale, S.H., Patil, P.S., 2021. Green and sustainable synthesis of silica nanoparticles. *Nanotechnology for Environmental Engineering* 2021 6 (2 6), 1–14. <https://doi.org/10.1007/S41204-021-00124-1>.
- Karbassian, F., 2018. Porous silicon. In: *Ghrub, T.H. (Ed.), Porosity - Process, Technologies and Applications, first ed.* InTech.
- Kasinathan, A., Rama, R., Sivakumar, G., 2010. Extraction, synthesis and characterization of nanosilica from rice husk ash. *Int. J. Nanotechnol. Appl.* 4, 61–66.
- Kauldhar, B.S., Sooch, B.S., Rai, S.K., Kumar, V., Yadav, S.K., 2021. Recovery of nanosized silica and lignin from sugarcane bagasse waste and their engineering in fabrication of composite membrane for water purification. *Environ. Sci. Pollut. Control Ser.* 28, 7491–7502. <https://doi.org/10.1007/S11356-020-11105-3/FIGURES/1>.
- Khabbaz, L.S., Hassanzadeh-Khayyat, M., Zaree, P., Ramezani, M., Abnous, K., Taghdisi, S.M., 2015. Detection of kanamycin by using an aptamer-based biosensor using silica nanoparticles. *Analytical Methods* 7, 8611–8616. <https://doi.org/10.1039/C5AY01807B>.
- Kim, D., Kim, J., Lee, K.W., Lee, T.S., 2019. Removal of sodium dodecylbenzenesulfonate using surface-functionalized mesoporous silica nanoparticles. *Microporous Mesoporous Mater.* 275, 270–277. <https://doi.org/10.1016/J.MICROMESO.2018.09.007>.
- Kinloch, A.J., Mohammed, R.D., Taylor, A.C., Sprenger, C., Egan, D., 2005. The effect of silica nano particles and rubber particles on the toughness of multiphase thermosetting epoxy polymers. *J. Mater. Sci.* 40, 5083–5086. <https://doi.org/10.1007/s10853-005-1716-2>.
- Langer, R., Vacanti, J.P., 1993. Tissue engineering. *Science* 260, 920–926. <https://doi.org/10.1126/science.8493529>.
- Li, D., Chen, D., Zhu, X., 2011. Reduction in time required for synthesis of high specific surface area silica from pyrolyzed rice husk by precipitation at low pH. *Bioresour. Technol.* 102, 7001–7003. <https://doi.org/10.1016/j.biortech.2011.04.020>.
- Liou, T.H., Yang, C.C., 2011. Synthesis and surface characteristics of nanosilica produced from alkali-extracted rice husk ash. *Mater. Sci. Eng. B: Solid-State Materials for Advanced Technology* 176, 521–529. <https://doi.org/10.1016/j.mseb.2011.01.007>.
- Liu, J., Su, Y., Li, Q., Yue, Q., Gao, B., 2013. Preparation of wheat straw based superabsorbent resins and their applications as adsorbents for ammonium and phosphate removal. *Bioresour. Technol.* 143, 32–39. <https://doi.org/10.1016/j.biortech.2013.05.100>.
- Liu, P., Tang, H., Lu, M., Gao, C., Wang, F., Ding, Y., Zhang, S., Yang, M., 2017. Preparation of nanosilica-immobilized antioxidant and the antioxidative behavior in low density polyethylene. *Polym. Degrad. Stabil.* 135, 1–7. <https://doi.org/10.1016/j.polydegradstab.2016.10.013>.
- Liu, Y., Guo, Y., Gao, W., Wang, Zhuo, Ma, Y., Wang, Zichen, 2012. Simultaneous preparation of silica and activated carbon from rice husk ash. *J. Clean. Prod.* 32, 204–209. <https://doi.org/10.1016/J.JCLEPRO.2012.03.021>.
- Lodriche, S.S., Soltani, S., Mirzazadeh, R., 2013. SILICON NANOCARRIER FOR DELIVERY OF DRUG, PESTICIDES AND HERBICIDES, AND FOR WASTE WATER TREATMENT. *US* 2013/02254.12 A1.
- Long, Z., Xu, W., Lu, Y., Qiu, H., 2016. Nanosilica-based molecularly imprinted polymer nanoshell for specific recognition and determination of rhodamine B in red wine and beverages. *J. Chromatogr. B* 1029 (1030), 230–238. <https://doi.org/10.1016/J.JCHROMB.2016.06.030>.
- Lu, J., Liang, M., Zink, J.I., Tamanoi, F., 2007. Mesoporous silica nanoparticles as a delivery system for hydrophobic anticancer drugs. *Small* 3, 1341–1346. <https://doi.org/10.1002/SMLL.200700005>.
- Luckarift, H.R., Spain, J.C., Naik, R.R., Stone, M.O., 2004. Enzyme immobilization in a biomimetic silica support. *Nat. Biotechnol.* 22, 211–213. <https://doi.org/10.1038/NBT931>.
- Luo, Z., Deng, Y., Zhang, R., Wang, M., Bai, Y., Zhao, Q., Lyu, Y., Wei, J., Wei, S., 2015. Peptide-laden mesoporous silica nanoparticles with promoted bioactivity and osteo-differentiation ability for bone tissue engineering. *Colloids Surf. B Biointerfaces* 131, 73–82. <https://doi.org/10.1016/J.COLSURFB.2015.04.043>.

- Ma, Y., Chen, H., Shi, Y., Yuan, S., 2016. Low cost synthesis of mesoporous molecular sieve MCM-41 from wheat straw ash using CTAB as surfactant. *Mater. Res. Bull.* 77, 258–264. <https://doi.org/10.1016/j.materresbull.2016.01.052>.
- Madani Hosseini, M., Shao, Y., Whalen, J.K., 2011. Biocement production from silicon-rich plant residues: perspectives and future potential in Canada. *Biosyst. Eng.* 110, 351–362. <https://doi.org/10.1016/j.BIOSYSTEMSENG.2011.09.010>.
- Maslowski, M., Miedzianowska, J., Strzelec, K., 2018. Influence of wheat, rye, and triticale straw on the properties of natural rubber composites. *Adv. Polym. Technol.* 37, 2866–2878. <https://doi.org/10.1002/adv.21958>.
- Mehrasa, M., Asadollahi, M.A., Ghaedi, K., Salehi, H., Arpanaei, A., 2015. Electrospun aligned PLGA and PLGA/gelatin nanofibers embedded with silica nanoparticles for tissue engineering. *Int. J. Biol. Macromol.* 79, 687–695. <https://doi.org/10.1016/j.IJBIOMAC.2015.05.050>.
- Mohapatra, S., Sakthivel, R., Roy, G.S., Varma, S., Singh, S.K., Mishra, D.K., 2011. Synthesis of  $\beta$ -SiC powder from bamboo leaf in a DC extended thermal plasma reactor. <https://doi.org/10.1080/10426914.2011.557127>. <https://doi.org/10.1080/10426914.2011.557127>, 1362,1368.
- Mor, S., Manchanda, C.K., Kansal, S.K., Ravindra, K., 2017. Nanosilica extraction from processed agricultural residue using green technology. *J. Clean. Prod.* 143, 1284–1290. <https://doi.org/10.1016/j.jclepro.2016.11.142>.
- Mridha, D., Paul, I., De, A., Ray, I., Das, A., Joardar, M., Chowdhury, N.R., Bhadoria, P.B.S., Roychowdhury, T., 2021. Rice seed (IR64) priming with potassium humate for improvement of seed germination, seedling growth and antioxidant defense system under arsenic stress. *Ecotoxicol. Environ. Saf.* 219, 112313. <https://doi.org/10.1016/j.ECOENV.2021.112313>.
- Mullick, A., Moullick, S., Bhattacharjee, S., 2018. Removal of hexavalent chromium from aqueous solutions by low-cost rice husk-based activated carbon: kinetic and thermodynamic studies. *Indian Chem. Eng.* 60, 58–71. <https://doi.org/10.1080/00194506.2017.1288173>.
- Nagendran, R., 2011a. Agricultural Waste and Pollution. Elsevier Inc, Waste. <https://doi.org/10.1016/B978-0-12-381475-3.10024-5>.
- Nagendran, R., 2011b. Agricultural Waste and Pollution. In: Waste. Elsevier Inc., pp. 341–355. <https://doi.org/10.1016/B978-0-12-381475-3.10024-5>.
- Naqvi, J., Shah, F.H., Mansha, M., 2011. Extraction of amorphous silica from wheat husk by using KMnO<sub>4</sub>. *JOURNAL OF FACULTY OF ENGINEERING & TECHNOLOGY* 18, 39–46.
- Nasreen, S., Rafique, U., Ehrman, S., Ashraf, M.A., 2018. Synthesis and characterization of mesoporous silica nanoparticles for environmental remediation of metals, PAHs and phenols. *Ekoloji* 27, 1625–1637.
- Nguyen, V.H., Vu, C.M., Choi, H.J., Kien, B.X., 2019. Nanosilica extracted from hexafluorosilicic acid of waste fertilizer as reinforcement material for natural rubber: preparation and mechanical characteristics. *Materials* 12. <https://doi.org/10.3390/ma12172707>.
- Norsuraya, S., Fazlena, H., Norhasyimi, R., 2016a. Sugarcane bagasse as a renewable source of silica to synthesize santa barbara amorphous-15 (SBA-15). *Procedia Engineering* 148, 839–846. <https://doi.org/10.1016/J.PROENG.2016.06.627>.
- Norsuraya, S., Fazlena, H., Norhasyimi, R., 2016b. Sugarcane bagasse as a renewable source of silica to synthesize santa barbara amorphous-15 (SBA-15). *Procedia Engineering* 148, 839–846. <https://doi.org/10.1016/j.proeng.2016.06.627>.
- NPMCR, 2014. National Policy for Management of Crop Residues (NPMCR). Department of Agriculture and Cooperation, Department of Agriculture and Cooperation, Ministry of Agriculture, Government of India.
- Okoronkwo, E.A., Imoisili, P., Olusunle, S., 2013. Extraction and characterization of amorphous silica from corn cob ash by sol-gel method. *Chemistry and Materials Research* 3, 68–72.
- Olutoge, F.A., Oladunmoye, O.M., 2017. Bamboo leaf ash as supplementary cementitious material. *American Journal of Engineering Research* 6, 1–8.
- Osuji, S., Lukuman, B.I., 2018. Investigation of the properties of self-compacting concrete with palm kernel shell ash as mineral additive. *Journal of Civil Engineering and Construction Technology* 9, 11–18. <https://doi.org/10.5897/JCECT2017.0473>.
- Pa, F.C., Chik, A., Bari, M.F., 2016. Palm ash as an alternative source for silica production. In: MATEC Web of Conferences. <https://doi.org/10.1051/mateconf/20167801062>.
- Patel, K.G., Shettigar, R.R., Misra, N.M., 2017a. Recent advance in silica production technologies from agricultural waste stream—review. *Journal of Advanced Agricultural Technologies* 4, 274–279. <https://doi.org/10.18178/joaat.4.3.274-279>.
- Patel, K.G., Shettigar, R.R., Misra, N.M., 2017b. Recent advance in silica production technologies from agricultural waste stream—review. *Journal of Advanced Agricultural Technologies* 4, 274–279. <https://doi.org/10.18178/JOAAT.4.3.274-279>.
- Patil, R., Dongre, R., Meshram, J., 2014. Preparation of Silica Powder from Rice Husk.
- Piela, A., Żymaničzyk-Duda, E., Brzezińska-Rodak, M., Duda, M., Grzesiak, J., Saeid, A., Mironiuk, M., Klimek-Ochab, M., 2020. Biogenic synthesis of silica nanoparticles from corn cobs husks. Dependence of the productivity on the method of raw material processing. *Bioorganic Chemistry* 99, 103773. <https://doi.org/10.1016/J.BIOORG.2020.103773>.
- Pinheiro, S., Font, A., Soriano, L., Tashima, M.M., Monzó, J., Borrachero, M.V., Payá, J., Borrachero, Maria Victoria, Payá, Jordi, 2018. Olive-stone biomass ash (OBA): an alternative alkaline source for the blast furnace slag activation. *Construction and Building Materials* 178, 327–338. <https://doi.org/10.1016/j.conbuildmat.2018.05.157>.
- Pongdong, W., Kummerlöwe, C., Vennemann, N., Thitithammawong, A., Nakason, C., 2018. A comparative investigation of rice husk ash and siliceous earth as reinforcing fillers in dynamically cured blends of epoxidized natural rubber (ENR) and thermoplastic polyurethane (TPU). *Journal of Polymers and the Environment* 26, 1145–1159. <https://doi.org/10.1007/s10924-017-1022-5>.
- Poorakbar, E., Shafiee, A., Saboury, A.A., Rad, B.L., Khoshnevisan, K., Ma' mani, L., Derakhshankhah, H., Ganjali, M.R., Hosseini, M., 2018. Synthesis of magnetic gold mesoporous silica nanoparticles core shell for cellulase enzyme immobilization: improvement of enzymatic activity and thermal stability. *Process Biochemistry* 71, 92–100. <https://doi.org/10.1016/J.PROCBIO.2018.05.012>.
- Porrang, S., Rahemi, N., Davaran, S., Mahdavi, M., Hassanzadeh, B., 2021. Preparation and in-vitro evaluation of mesoporous biogenic silica nanoparticles obtained from rice and wheat husk as a biocompatible carrier for anti-cancer drug delivery. *European journal of pharmaceutical sciences : official journal of the European Federation for Pharmaceutical Sciences* 163. <https://doi.org/10.1016/J.EJPS.2021.105866>.
- Purnomo, C.W., Salim, C., Hinode, H., 2011. Preparation and characterization of activated carbon from bagasse fly ash. *Journal of Analytical and Applied Pyrolysis* 91, 257–262. <https://doi.org/10.1016/j.jaap.2011.02.017>.
- Pushpa, S.S., Lohani, 2018. Silica nanoparticles : its green synthesis and importance in agriculture. *Journal of Pharmacognosy and Phytochemistry* 7, 3383–3393.
- Rafiee, E., Shahebrahimi, S., Feyzi, M., Shaterzadeh, M., 2012. Optimization of synthesis and characterization of nanosilica produced from rice husk (a common waste material). *International Nano Letters* 2, 1–8. <https://doi.org/10.1186/2228-5326-2-29>.
- Rahimi-Mohseni, M., Raoof, J.B., Ojani, R., Aghajanzadeh, T.A., Bagheri Hashkavayi, A., 2018. Development of a new paper based nano-biosensor using the co-catalytic effect of tyrosinase from banana peel tissue (Musa Cavendish) and functionalized silica nanoparticles for voltammetric determination of l-tyrosine. *International Journal of Biological Macromolecules* 113, 648–654. <https://doi.org/10.1016/J.IJBIOMAC.2018.02.060>.
- Rahman, N.A., Widhiana, I., Juliastuti, S.R., Setyawan, H., 2015. Synthesis of mesoporous silica with controlled pore structure from bagasse ash as a silica source. *Colloids and Surfaces A: Physicochemical and Engineering Aspects Complete* 1–7. <https://doi.org/10.1016/J.COLSURFA.2015.03.018>.
- Rajamani, S., Santhosh, R., Raghunath, R., Jadhav, S.A., 2021. Value-added chemicals from sugarcane bagasse using ionic liquids. *Chemical Papers* 2021 75 (11 75), 5605–5622. <https://doi.org/10.1007/S11696-021-01732-6>.
- Rangaraj, S., Venkatachalam, R., 2017. A lucrative chemical processing of bamboo leaf biomass to synthesize biocompatible amorphous silica nanoparticles of biomedical importance. *Applied Nanoscience* 2017 7 (5 7), 145–153. <https://doi.org/10.1007/S13204-017-0557-Z>.
- Rohatgi, K., Prasad, S.V., Rohatgi, P.K., 1987a. Release of silica-rich particles from rice husk by microbial fermentation. *Journal of Materials Science Letters* 1987 6 (7 6), 829–831. <https://doi.org/10.1007/BF01729027>.
- Rohatgi, K., Prasad, S.V., Rohatgi, P.K., 1987b. Release of silica-rich particles from rice husk by microbial fermentation. *Journal of Materials Science Letters* 6, 829–831. <https://doi.org/10.1007/BF01729027>.
- Rosenholm, J.M., Gulín-Sarfraz, T., Mamaeva, V., Niemi, R., Özliseli, E., Desai, D., Antfolk, D., Von Haartman, E., Lindberg, D., Prabhakar, N., Närejoja, T., Sahlgren, C., 2016. Prolonged dye release from mesoporous silica-based imaging probes facilitates long-term optical tracking of cell populations in vivo. *Small* 12, 1578–1592. <https://doi.org/10.1002/sml.201503392>.

- Rouhani, M., Samih, M., Kalantari, S., 2013. Insecticidal effect of silica and silver nanoparticles on the cowpea seed beetle, *Callosobruchus maculatus* F.(Col.: bruchidae). *J Entomol Res* 4, 297–305.
- Rovani, S., Santos, J.J., Corio, P., Fungaro, D.A., 2018a. Highly pure silica nanoparticles with high adsorption capacity obtained from sugarcane waste ash. *ACS Omega* 3, 2618–2627. <https://doi.org/10.1021/acsomega.8b00092>.
- Rovani, S., Santos, J.J., Corio, P., Fungaro, D.A., 2018b. Highly pure silica nanoparticles with high adsorption capacity obtained from sugarcane waste ash. *ACS Omega* 3, 2618–2627. <https://doi.org/10.1021/ACSOMEGA.8B00092>.
- San, N.O., Kurşungöz, C., Tümtaş, Y., Yaşa, Ö., Ortaç, B., Tekinay, T., 2014. Novel one-step synthesis of silica nanoparticles from sugarbeet bagasse by laser ablation and their effects on the growth of freshwater algae culture. *Particuology* 17, 29–35. <https://doi.org/10.1016/J.PARTIC.2013.11.003>.
- Sankar, S., Kaur, N., Lee, S., Kim, D.Y., 2018. Rapid sonochemical synthesis of spherical silica nanoparticles derived from brown rice husk. *Ceramics International* 44, 8720–8724. <https://doi.org/10.1016/j.ceramint.2018.02.090>.
- Sapawe, N., Surayah Osman, N., Zulkhairi Zakaria, M., Amirul Shahab Syed Mohamad Fikry, S., Amir Mat Aris, M., 2018. Synthesis of green silica from agricultural waste by sol-gel method. *Materials Today: Proceedings* 5, 21861–21866. <https://doi.org/10.1016/J.MATPR.2018.07.043>.
- Sekhon, B.S., 2014. Nanotechnology in agri-food production: an overview. *Nanotechnology, Science and Applications* 7, 31. <https://doi.org/10.2147/NSA.S39406>.
- Selvakumar, K.V., Umesh, A., Ezhilkumar, P., Gayatri, S., Vinith, P., Vignesh, V., 2014. Extraction of silica from burnt paddy husk. *International Journal of ChemTech Research* 6, 4455–4459.
- Sethy, N.K., Arif, Z., Mishra, P.K., Kumar, P., 2019. Synthesis of SiO<sub>2</sub> nanoparticle from bamboo leaf and its incorporation in PDMS membrane to enhance its separation properties. *Journal of Polymer Engineering* 39, 679–687. <https://doi.org/10.1515/POLYENG-2019-0120>.
- Setiawan, W.K., Chiang, K.Y., 2021. Crop residues as potential sustainable precursors for developing silica materials: a review. *Waste and Biomass Valorization* 12, 2207–2236. <https://doi.org/10.1007/S12649-020-01126-X>.
- Shah, M., Fawcett, D., Sharma, S., Tripathy, S.K., Poinern, G.E.J., 2015. Green synthesis of metallic nanoparticles via biological entities. *Materials* 8 (11), 7278–7308. <https://doi.org/10.3390/ma8115377>.
- Shahi, N., Wang, P., Adhikari, S., Min, B., Rangari, V.K., 2021. Biopolymers fractionation and synthesis of nanocellulose/silica nanoparticles from agricultural byproducts. *ACS Sustainable Chemistry & Engineering* 9, 6284–6295. <https://doi.org/10.1021/ACSUSCHEMENG.0C09342>.
- Sheet, I., Kabbani, A., Holail, H., 2014. Removal of heavy metals using nanostructured graphite oxide, silica nanoparticles and silica/graphite oxide composite. *Energy Procedia* 50, 130–138. <https://doi.org/10.1016/J.EGYPRO.2014.06.016>.
- Shim, J., Velmurugan, P., Oh, B.T., 2015. Extraction and physical characterization of amorphous silica made from corn cob ash at variable pH conditions via sol gel processing. *Journal of Industrial and Engineering Chemistry* 30, 249–253. <https://doi.org/10.1016/j.jiec.2015.05.029>.
- Siddiqui, M.H., Al-Wahaibi, M.H., 2014. Role of nano-SiO<sub>2</sub> in germination of tomato (*Lycopersicon esculentum* seeds Mill.). *Saudi Journal of Biological Sciences* 21, 13–17. <https://doi.org/10.1016/J.SJBS.2013.04.005>.
- Siddiqui, M.H., Al-Wahaibi, M.H., Faisal, M., Sahli, A.A. al., 2014. Nano-silicon dioxide mitigates the adverse effects of salt stress on *Cucurbita pepo* L. *Environmental Toxicology and Chemistry* 33, 2429–2437. <https://doi.org/10.1002/ETC.2697>.
- Soltani, N., Simon, U., Bahrami, A., Wang, X., Selve, S., Epping, J.D., Pech-Cantul, M.I., Bekheet, M.F., Gurlo, A., 2017. Macroporous polymer-derived SiO<sub>2</sub>/SiOC monoliths freeze-cast from polysiloxane and amorphous silica derived from rice husk. *Journal of the European Ceramic Society* 37, 4809–4820. <https://doi.org/10.1016/j.jeurceramsoc.2017.06.023>.
- Steven, S., Restiawaty, E., Pasyimi, P., Bindar, Y., 2021. An appropriate acid leaching sequence in rice husk ash extraction to enhance the produced green silica quality for sustainable industrial silica gel purpose. *Journal of the Taiwan Institute of Chemical Engineers* 122, 51–57. <https://doi.org/10.1016/J.JTICE.2021.04.053>.
- Strout, G., Russell, S.D., Pulsifer, D.P., Erten, S., Lakhtakia, A., Lee, D.W., 2013. Silica nanoparticles aid in structural leaf coloration in the Malaysian tropical rainforest understorey herb *Mapania caudata*. *Annals of Botany* 112, 1141–1148. <https://doi.org/10.1093/AOB/MCT172>.
- Tang, M., Zhang, R., Pu, Y., 2018. Wheat straw modified with palmitic acid as an efficient oil spill adsorbent. *Fibers and Polymers* 19, 949–955. <https://doi.org/10.1007/s12221-018-7733-y>.
- Thuadajj, N., Nuntiya, A., 2008. Preparation of nanosilica powder from rice husk ash by precipitation method. *Chiang Mai Journal of Science* 35, 206–211.
- Torres, M.G., Muñoz, S.V., Martínez, A.R., Hernández, V.S., Saucedo, A.V., Cervantes, E.R., Talavera, R.R., Rivera, M., Castro, M., del, P.C., 2017. Morphology-controlled Silicon Oxide Particles Produced by Red Wiggler Worms. *Powder Technology C*, pp. 205–212. <https://doi.org/10.1016/J.POWTEC.2017.01.011>.
- Tsou, C.J., Hung, Y., Mou, C.Y., 2014. Hollow mesoporous silica nanoparticles with tunable shell thickness and pore size distribution for application as broad-ranging pH nanosensor. *Microporous and Mesoporous Materials* 190, 181–188. <https://doi.org/10.1016/J.MICROMESO.2014.02.011>.
- Umeda, J., Kondoh, K., 2010. High-purification of amorphous silica originated from rice husks by combination of polysaccharide hydrolysis and metallic impurities removal. *Industrial Crops and Products* 32, 539–544. <https://doi.org/10.1016/j.indcrop.2010.07.002>.
- Utsev, J.T., Taku, J.K., 2012. Coconut shell ash as partial replacement of ordinary portland cement in concrete production. *International Journal of Scientific & Technology Research* 1, 86–89.
- Vaibhav, V., Vijayalakshmi, U., Roopan, S.M., 2015. Agricultural waste as a source for the production of silica nanoparticles. *Spectrochimica Acta - Part A: Molecular and Biomolecular Spectroscopy* 139, 515–520. <https://doi.org/10.1016/j.saa.2014.12.083>.
- Velmurugan, P., Shim, J., Lee, K.J., Cho, M., Lim, S.S., Seo, S.K., Cho, K.M., Bang, K.S., Oh, B.T., 2015. Extraction, characterization, and catalytic potential of amorphous silica from corn cobs by sol-gel method. *Journal of Industrial and Engineering Chemistry* 29, 298–303. <https://doi.org/10.1016/J.JIEC.2015.04.009>.
- Wang, K., Liu, P., Ye, Y., Li, J., Zhao, W., Huang, X., 2014. Fabrication of a novel laccase biosensor based on silica nanoparticles modified with phytic acid for sensitive detection of dopamine. *Sensors and Actuators B: Chemical* 197, 292–299. <https://doi.org/10.1016/J.SNB.2014.03.002>.
- Wanyika, H., Gatebe, E., Kioni, P., Tang, Z., Gao, Y., 2012. Mesoporous silica nanoparticles carrier for urea: potential applications in agrochemical delivery systems. *Journal of Nanoscience and Nanotechnology* 12, 2221–2228. <https://doi.org/10.1166/JNN.2012.5801>.
- Wiberg, N., Holleman, A.F., Wiberg, E., 2001. *Holleman-Wiberg's Inorganic Chemistry, first ed.* Academic Press.
- Witoon, T., Chareonpanich, M., Limtrakul, J., 2008. Synthesis of bimodal porous silica from rice husk ash via sol-gel process using chitosan as template. *Materials Letters* 62, 1476–1479. <https://doi.org/10.1016/j.matlet.2007.09.004>.
- Wu, B., Kuang, Y., Zhang, X., Chen, J., 2011. Noble metal nanoparticles/carbon nanotubes nanohybrids: synthesis and applications. *Nano Today* 6, 75–90. <https://doi.org/10.1016/J.NANTOD.2010.12.008>.
- Xie, M., Shi, H., Ma, K., Shen, H., Li, B., Shen, S., Wang, X., Jin, Y., 2013. Hybrid nanoparticles for drug delivery and bioimaging: mesoporous silica nanoparticles functionalized with carboxyl groups and a near-infrared fluorescent dye. *Journal of Colloid and Interface Science* 395, 306–314. <https://doi.org/10.1016/J.JCIS.2013.01.001>.
- Xu, J.J., Zhao, W.W., Song, S., Fan, C., Chen, H.Y., 2014. Functional Nanoprobes for Ultrasensitive Detection of Biomolecules: an Update. *Chemical Society Reviews*. <https://doi.org/10.1039/c3cs60277j>.
- Yang, X., Shen, Z., Zhang, B., Yang, J., Hong, W.X., Zhuang, Z., Liu, J., 2013. Silica nanoparticles capture atmospheric lead: implications in the treatment of environmental heavy metal pollution. *Chemosphere* 90, 653–656. <https://doi.org/10.1016/J.CHEMOSPHERE.2012.09.033>.
- Yao, X., Niu, X., Ma, K., Huang, P., Grothe, J., Kaskel, S., Zhu, Y., 2017. Graphene quantum dots-capped magnetic mesoporous silica nanoparticles as a multifunctional platform for controlled drug delivery, magnetic hyperthermia, and photothermal therapy. *Small* 13, 1602225. <https://doi.org/10.1002/SMLL.201602225>.
- Yemiş, O., Mazza, G., 2012. Optimization of furfural and 5-hydroxymethylfurfural production from wheat straw by a microwave-assisted process. *Bioresource Technology* 109, 215–223. <https://doi.org/10.1016/J.BIORTECH.2012.01.031>.
- Yu, Z.-H., Zhai, S.-R., Guo, H., Lv, T.-M., Song, Y., Zhang, F., Ma, H.-C., 2018. Removal of methylene blue over low-cost mesoporous silica nanoparticles prepared with naturally occurring diatomite. *Journal of Sol-Gel Science and Technology* 2018 88 (3 88), 541–550. <https://doi.org/10.1007/S10971-018-4859-8>.
- Zhang, H., Ding, X., Chen, X., Ma, Y., Wang, Z., Zhao, X., 2015. A new method of utilizing rice husk: consecutively preparing d-xylose, organosolv lignin, ethanol and amorphous superfine silica. *Journal of Hazardous Materials* 291, 65–73. <https://doi.org/10.1016/J.JHAZMAT.2015.03.003>.

- Zhang, Y., Zhi, Z., Jiang, T., Zhang, J., Wang, Z., Wang, S., 2010. Spherical mesoporous silica nanoparticles for loading and release of the poorly water-soluble drug telmisartan. *Journal of controlled release : official journal of the Controlled Release Society* 145, 257–263. <https://doi.org/10.1016/J.JCONREL.2010.04.029>.
- Zielonka, A., Żymańczyk-Duda, E., Brzezińska-Rodak, M., Duda, M., Grzesiak, J., Klimek-Ochab, M., 2018. Nanosilica synthesis mediated by *Aspergillus parasiticus* strain. *Fungal Biology* 122, 333–344. <https://doi.org/10.1016/J.FUNBIO.2018.02.004>.
- Zulkifli, N., Ab Rahman, I., Mohamad, D., Husein, A., 2013. A green sol-gel route for the synthesis of structurally controlled silica particles from rice husk for dental composite filler. *Ceramics International* 39, 4559–4567. <https://doi.org/10.1016/j.ceramint.2012.11.052>.



# Source details

Feedback > Compare sources >

## Biocatalysis and Agricultural Biotechnology

Scopus coverage years: from 2012 to Present

Publisher: Elsevier

ISSN: 1878-8181

Subject area: [Agricultural and Biological Sciences: Agronomy and Crop Science](#) [Agricultural and Biological Sciences: Food Science](#)

[Immunology and Microbiology: Applied Microbiology and Biotechnology](#) [Biochemistry, Genetics and Molecular Biology: Biotechnology](#) [View all](#) v

Source type: Journal

[View all documents](#) >

[Set document alert](#)

[Save to source list](#)

CiteScore 2022

8.4



SJR 2022

0.655



SNIP 2022

1.126







## Green synthesis of iron oxide nanoparticles and their ameliorative effect on arsenic stress relief in *Oryza sativa* seedlings

Arindam Chatterjee<sup>a,1</sup>, Deepanjan Mridha<sup>b,1</sup>, Jishnu Banerjee<sup>c</sup>,  
Sumedha Chanda<sup>d</sup>, Kasturi Ray<sup>d</sup>, Krishnendu Acharya<sup>e,f</sup>, Madhusudan Das<sup>a</sup>,  
Tarit Roychowdhury<sup>b</sup>, Joy Sarkar<sup>c,\*</sup>

<sup>a</sup> Department of Zoology, University of Calcutta, Kolkata, 700019, India

<sup>b</sup> School of Environmental Studies, Jadavpur University, Kolkata, 700032, India

<sup>c</sup> Department of Botany, Dinabandhu Andrews College, Garia, Kolkata, West Bengal, 700084, India

<sup>d</sup> Department of Botany, Lady Brabourne College, Shurawady Avenue, Kolkata, West Bengal, 700 017, India

<sup>e</sup> Molecular and Applied Mycology and Plant Pathology Laboratory, Centre of Advanced Study, Department of Botany, University of Calcutta, Kolkata, West Bengal, 700019, India

<sup>f</sup> Center for Research in Nanoscience & Nanotechnology, Technology Campus, University of Calcutta, Kolkata, West Bengal, 700098, India

### ARTICLE INFO

#### Keywords:

*Adiantum lunulatum*

Arsenic

Iron oxide nanoparticles

Oxidative stress

Rice seedlings and seed germination

### ABSTRACT

Nanotechnology has immense potential in the field of agriculture. This study utilized an eco-friendly method to synthesize iron oxide nanoparticles (FeO-NPs) using leaf extract of *Adiantum lunulatum*. The synthesized FeO-NPs were characterized by UV-visible spectroscopy, FTIR, zeta potential, XRD, EDX and TEM analysis. The nanoparticles were quasi-spherical, with a mean particle size of  $5 \pm 1$  nm (range: 3–10 nm). The 100 mg/L dose of FeO-NPs was further applied in the rice growth medium to check the effect of FeO-NPs on the growth of rice seedlings against arsenic (As) stress. FeO-NPs significantly improved seed germination by 9.8% and 15.4%, respectively, of seeds germinated under 50  $\mu$ m AsIII and 50  $\mu$ m AsV stress when compared to seed germinated in only 50  $\mu$ m AsIII and 50  $\mu$ m AsV. The phytotoxic effect of AsIII on seed germination, seedling growth, chlorophyll content was more severe than AsV. However, IONP fertigation helps the rice plants to overcome the detrimental effect caused by As exposure. FeO-NPs increased the growth and vigour of the seedlings under As stress. The uptake and translocation of As by seedlings were decreased with IONP fertigation under As stress. The reduced accumulation of As in seedlings treated with FeO-NPs caused a significant ( $p \leq 0.05$ ) reduction in oxidative stress and antioxidants activities. All these findings indicated that the synthesis of FeO-NPs using *Adiantum lunulatum* leaf extract not only produces safe and non-toxic FeO-NPs but these FeO-NPs can be also efficiently improve the rice seedling growth under As stressed condition.

### Abbreviations

FeO-NPs Iron oxide nanoparticles

As Arsenic

\* Corresponding author.

E-mail address: [jsarkar80@gmail.com](mailto:jsarkar80@gmail.com) (J. Sarkar).

<sup>1</sup> These authors have contributed equally to this work.

<https://doi.org/10.1016/j.bcab.2021.102207>

Received 9 September 2021; Received in revised form 2 November 2021; Accepted 3 November 2021

Available online 7 November 2021

1878-8181/© 2021 Elsevier Ltd. All rights reserved.

NMeNP	Non-metallic nanoparticle
MeNP	Metallic nanoparticle
TEM	Transmission electron microscope
SEM	Scanning electron microscope
EDX	Energy Dispersive X-ray Spectroscopy
FTIR	Fourier transform infrared spectroscopy
DAS	Days after seeding
VG I	Vigour Index I
RWC	Relative water content
TW	Turgid weight
DW	Dry weight
TBARS	Thiobarbituric acid reactive substances
PVP	Polyvinylpyrrolidone
NBT	Nitroblue tetrazolium
AAS	Atomic Absorption spectrometry
SRMs	Standard reference materials
TF	Translocation factor
SD	Standard deviation
EL	Electrolyte leakage
SOD	Superoxide dismutase
APX	Ascorbate peroxidase
CAT	Catalase

## 1. Introduction

Nanoparticles are the particulate scatterings or strong particles with the nano-range between 10 and 1000 nm. Nanoparticles are of broadly two types non-metallic nanoparticle (NMeNP) and metallic nanoparticle (MeNP). NMeNP includes various bio-polymers, carbon-related compounds etc (Dasgupta et al., 2017). Metallic nanoparticles (MeNPs) are in increasing demand due to their innate metallic properties. They are widely used in the field of sensing (El-Ansary and Faddah, 2010), catalytic (Astruc, 2020), agriculture (Y. Ghidan and M. Al Antary, 2020) medicine, etc. (Murthy, 2007). Iron nanoparticles (FeO-NPs) are being widely used due to their size and magnetic properties. It was first widely employed for the clean-up of polluted soil and groundwater. FeO-NPs are also applied as (i) absorbent of toxic chemicals and/or (ii) photocatalysts for conversion/degradation of toxic pollutants to non-toxic forms (Xu et al., 2012). FeO-NPs have been successfully employed for wastewater treatment and removal of toxic elements like arsenic (Jang et al., 2008; Xu et al., 2012; Zou et al., 2016) and also as exceptional nano fertilizers (Rui et al., 2016). Among the different phases of iron nanoparticles,  $\alpha$ -Fe<sub>2</sub>O<sub>3</sub> nanoparticles are a widely studied material, which has a wide array of applications.

Synthesis of FeO-NPs is mainly carried out by chemical route using different reducing chemicals (Gupta et al., 2010). The chemicals, used during chemical synthesis and by-products generated after these chemical reactions, are hazardous in nature (Das et al., 2017). Therefore, biologically synthesized nanoparticles are preferred over chemically synthesized nanoparticles due to their less toxicity and environment-friendly nature. Plant contains a variety of terpenoids, polysaccharides, phenols, and flavonoids which act as reducing agents and facilitate the formation of stable MeNPs (Sarkar et al., 2020). FeO-NPs were synthesized using tea, gardenia, and *Aloe vera* leaf extracts in several investigations (Ahmmad et al., 2013; Karade et al., 2019; Mukherjee et al., 2016).

Lower groups of plants like algae (Saif et al., 2016), bryophytes (Acharya and Sarkar, 2014; Saif et al., 2016), fungi (Acharya et al., 2010; Sarkar et al., 2011a, 2011b, 2011c, 2012a, 2012b, 2013, 2014, 2017; Sarkar and Acharya, 2017) are preferred cryptograms for producing metal nanoparticles. However, the potential of several pteridophytes (fern and fern allies) for the synthesis of nanoparticles has received less attention. Until recently, only a few species have been utilized, including *Pteris tripartite* (Baskaran et al., 2016), *Adiantum capillus-veneris* (Chatterjee et al., 2019), *Adiantum philippense* (Chatterjee et al., 2019), *Asplenium scolopendrium* (Chatterjee et al., 2019), *Actinopteris radiata* (Chatterjee et al., 2019), *Azolla microphylla* (Chatterjee et al., 2019), and others (Sarkar et al., 2020). However, *Adiantum lunulatum* Burm. f. is well-known for its antibacterial, antioxidant, and other therapeutic characteristics (Mengane, 2016). The plant extract may have anti-hyperglycemic properties, as well as some therapeutic properties against influenza and TB. A recent study also confirmed that the synthesis of copper oxide NPs using *Adiantum lunulatum* plant extract has an ameliorative effect on defense and antioxidant enzymes activities of *Lens culinaris* (Sarkar et al., 2020).

Arsenic (As) contamination of soil and water is a major problem in various parts of the world (Chowdhury et al., 2020b,a). Arsenic exposure to humans can also cause potential carcinogenic and non-carcinogenic effects (Joardar et al., 2021a,b(Joardar et al., 2021b)). In Southeast Asia, Ganga-Meghna-Brahmaputra flood plain is considered as worst As affected area (Das et al., 2021a,b; De et al., 2021). Rice is a major crop and main source of food for people living in this part of the world. However, a substantial amount of rice is still cultivated in As contaminated soil and water (Chowdhury et al., 2020b; Mridha et al., 2021). The presence of inorganic As species (AsIII and AsV) in soil and water causes a phytotoxic effect when enters the plant (Mridha et al., 2021; Ray et al., 2021; Sarkar et al., 2020, 2021). Several kinds of research had been attempted to remove or immobilise As from water and soil using different chemically synthesized nanoparticles. However, the non-toxicity of green synthesized FeO-NPs make them a lucrative option to remediate As from

soil and water. Previously, green synthesized  $\alpha$ -Fe<sub>2</sub>O<sub>3</sub> NPs were used for the removal of As from wastewater (Mukherjee et al., 2016). Likewise, green synthesized iron oxide nanoparticles using *Excoecaria cochinchinensis* leaves were utilized to stabilize soil As fraction (Su et al., 2020). Different doses of chemically synthesized FeO-NPs were also utilized to remediate As stress in plants (Bidi et al., 2021; Shabnam et al., 2019a). However, limited research has been carried out with green synthesized FeO-NPs to alleviate As toxicity from the plant (Khan et al., 2021). Therefore, the main goal of this study was designed to synthesize FeO-NPs through a green route by using *Adiantum lunulatum* plant leaves extract as a reducing agent and investigate the efficiency of synthesized FeO-NPs in the alleviation of arsenic stress from rice plants during the seedling stage.

## 2. Materials and methods

### 2.1. Synthesis and characterization of FeO-NPs

#### 2.1.1. Plant material and chemicals

Freshly plucked *Adiantum lunulatum* Burm. f. was collected from a local area in Garia, Kolkata, West Bengal (22.4629°N 88.3968°E). Iron (III) chloride hexahydrate (FeCl<sub>3</sub>·6H<sub>2</sub>O) and sodium hydroxide (NaOH) pellets were purchased from Merck, Germany. The chemicals were further used without any purification. During plant extraction and nanoparticle synthesis, deionized water was used.

#### 2.2. Preparation of plant extract and synthesis of FeO-NPs

20 to 35 plant samples were collected initially and weighted in a digital balance. From there 10 gm of plant samples were selected (usually 5 to 10 plants depending on the size of the plant) and was washed out with tap water to remove any particulate contamination and thereafter with deionized water, respectively. The superficial water was soaked from the plant surface with a paper towel. Further, the pinnae of the plant were taken and a paste was made out of it in the mortar and pestle and 100 ml of deionized water was added to it (Sarkar et al., 2020). Finally, the extract was attained with the help of a Whatman's filter paper no.1 in a conical flask thrice to get the plant extract.

The green synthesis of iron oxide (Fe<sub>2</sub>O<sub>3</sub>) nanoparticles using plant extract was performed by a bottom-up process approach and reduction technique by a single pot system revamping the procedure by Sarkar et al. (2020). At first, the measured amount (100 ml of 3 mM) of FeCl<sub>3</sub>·6H<sub>2</sub>O was added to a beaker. Then the plant extract was added slowly into the solution. Finally, the FeCl<sub>3</sub> solution reacted with 100 ml of filtered plant extract. The entire reaction was done at pH 11 by adding 1 M NaOH. The mixture was stirred continuously for a minimum of 1 h and the formation of a dark brown colour solution confirmed the synthesis of FeO-NPs. The synthesized FeO-NPs were separated by centrifugation at 12,000×g for 15 min and the pellet containing FeO-NPs were washed (3 times) with deionized water followed by drying at 80 °C for 3 h and stored for further use.

#### 2.3. Characterization of FeO-NPs

The UV–visible spectra of the synthesized FeO-NPs had been recorded using a Hitachi 330 spectrophotometer. The morphological, topographical, size and purity of the nanoparticles were analysed by a transmission electron microscope (TEM) [Tecnai G2 spirit Biotwin (FP 5018/40), operating at around 80 kV accelerating voltage] and a scanning electron microscope (SEM) (Hitachi S 3400 N) outfitted with an Energy Dispersive X-ray Spectroscopy (EDX), respectively. The zeta potential (Charge distribution) of the nanoparticles was studied using a Beckman Coulter DelsaTM Nano Particle Analyzer (USA) by illuminating the solution with a He–Ne laser (658 nm) in a sample cell. The crystallinity of the FeO-NPs was analysed by XRD. The diffractogram was documented by PANalytical, XPERTPRO diffractometer using CuK $\alpha$  (Cu K $\alpha$  radiation,  $\lambda$  1.54443) as X-ray source running at 45 kV and 30 mA. To identify the functional groups, present in synthesized FeO-NPs, Fourier transform infrared spectroscopy (FTIR, Shimadzu 8400 S) was employed to record and analyse the spectral data range between 4000 and 400 cm<sup>-1</sup>.

#### 2.4. Plant material, seed preparation and experimental design

Rice (*Oryza sativa* L. c.v. Ranjit) seeds were collected from the Madhusudankati village (22°54'14.51" N, 88°46'25.36" E), Gaighata block, West Bengal, India which is one of the worst As affected area of India. The rice seeds were surfaced sterilized with H<sub>2</sub>O<sub>2</sub> (30%) solution for 10 min and then washed with distilled water three times. The seeds were then kept for germination in their respective treatment. Total five treatments were designed for this experiment and all the treatments were set up in triplicate. In each treatment 20 rice seeds were placed for germination. The experiment has 50  $\mu$ M of both AsIII (NaAsO<sub>2</sub>, MW: 129.91 g mol<sup>-1</sup>) and AsV (Na<sub>3</sub>AsO<sub>4</sub>, MW: 207.88 g mol<sup>-1</sup>) along with 100 mg/L of FeO-NPs. The details of the five experimental sets were: control (Hogland medium); 50  $\mu$ M AsIII; 50  $\mu$ M AsV; 50  $\mu$ M AsIII + FeO-NPs and 50  $\mu$ M AsV + FeO-NPs. The treatments were produced by adding As and FeO-NPs, respectively in the Hogland solution. Before application, the FeO-NPs were sonicated using a probe sonicator for 5 min to achieve homogenised distribution in the nutrient solution. The pH of the nutrient medium was maintained between 5.7 and 6.0 using 0.1 M KOH and HCl, and the nutrient medium was changed after every 3 days. The entire experiment was conducted for 14 days after seeding (DAS).

#### 2.5. Seed germination and seedling vigour

The seeds in their respective treatment were grown hydroponically under a controlled environment. For rice seed germination, all treatments were kept in dark at 27  $\pm$  1 °C with a humidity of 60–70%. The germination of seeds was counted at 3 DAS and a seed was considered as germinated only when the radicle length was found  $\geq$  2 mm (Mridha et al., 2021). After 3 DAS, the germinated seeds were kept under controlled photoperiod (14/10 h light/dark cycle) till 14 DAS (Zhang et al., 2021). The seedling vigour at 14 DAS was

measured according to [Mridha et al. \(2021\)](#).

$$\text{Vigour Index I (VG I)} = \text{Standard Germination \%} \times \{\text{Average Seedling Length (Root + Shoot)}\}$$

## 2.6. Determination of relative water content (RWC)

For the determination of RWC in seedlings, the fresh leaf was weighed and placed in a Petri dish containing distilled water. The Petri dish was then kept in dark at room temperature inside a BOD incubator for 24 h. Afterwards, the turgid weight (TW) of the leaf was taken. The leaf sample was again kept in the oven for drying at 80 °C and after 24 h, the dry weight (DW) was measured. The RWC of rice seedlings were calculated according to [Barrs and Weatherley \(1962\)](#).

$$\text{RWC} = \frac{\text{FW} - \text{DW}}{\text{TW} - \text{DW}} \times 100$$

## 2.7. Estimation of chlorophyll content

The chlorophyll (a and b) content of the rice seedlings was measured based on the Arnon method ([Arnon, 1949](#)). The seedling leaf was homogenised with 80% acetone and centrifuged at 10,000×g for 10 min. The absorbance of the leaf extract was measured spectrophotometrically at 663 nm (chlorophyll a) and 645 nm (chlorophyll b).

## 2.8. Estimation of electrolyte leakage

The fresh leaf tissues (500 mg) were segmented into pieces and vacuumed for 20 min in 20 ml deionized water. Conductivities (C1) were measured after the leaves were maintained in the dark for additional 2 h at room temperature. The conductivities (C2) were tested again after the leaf samples were put in boiling water for 15 min. The percentage of electrolyte leakages were estimated according to the following formula ([Cao et al., 2007](#)).

$$\text{EL} = \frac{c_1}{c_2} \times 100$$

## 2.9. Determination of H<sub>2</sub>O<sub>2</sub>, lipid peroxidation and proline content

The amount of H<sub>2</sub>O<sub>2</sub>, TBARS (thiobarbituric acid reactive substances) and proline content in root and shoot leaf of rice seedlings were measured according to the proposed methods of [Velikova et al. \(2000\)](#) ([Velikova et al., 2000](#)), [Heath and Packer \(1968\)](#) ([Heath and Packer, 1968](#)) and [Bates et al. \(1973\)](#) ([Bates, L. S., Waldren, R & Teare, 1973](#)), respectively. The detailed methodology of H<sub>2</sub>O<sub>2</sub>, TBARS and proline estimation were followed according to [Mridha et al. \(2021\)](#).

## 2.10. Antioxidant enzymes activities

The antioxidant enzyme assays were performed by extracting 0.2 g of root and shoot tissues of rice seedlings in 2 ml of chilled 0.1 M potassium phosphate buffer (pH 7.0) containing 1 mM EDTA and 1% (w/v) Polyvinylpyrrolidone (PVP). The protein content of antioxidant enzyme extracts was measured according to [Lowry et al. \(1951\)](#) ([Lowry et al. \(1951\)](#)). Superoxide dismutase (SOD; EC 1.15.1.1), activities were estimated by measuring its ability to inhibit photochemical reduction of nitroblue tetrazolium (NBT), as prescribed by the scientific manuscript of [Beauchamp and Fridovich \(1971\)](#) ([Beauchamp and Fridovich \(1971\)](#)). For the ascorbate peroxidase (APX; EC 1.11.1.11) assay, the H<sub>2</sub>O<sub>2</sub> dependent ascorbic acid ( $\epsilon = 2.8 \text{ mM}^{-1} \text{ cm}^{-1}$ ) oxidation was taken into account by measuring the decrease in absorbance for 1 min at 290 nm [Nakano and Asada \(1981\)](#). The catalase (CAT; EC 1.11.1.6) activity was determined after 0.1 ml of enzyme extract was mixed with 1.5 ml of 50 mM phosphate buffer followed by 15 mM H<sub>2</sub>O<sub>2</sub>. After an incubation period of 1 min, the continuously decreasing absorbances of the mixtures were measured every 1 min interval at 240 nm [Aebi \(1984\)](#).

## 2.11. Arsenic and iron content in rice seedling

For estimation of As and Fe content in rice seedling, 0.02–0.1 g of dried root and shoot tissues were digested overnight with 2 ml of HNO<sub>3</sub> and 1 ml H<sub>2</sub>O<sub>2</sub>. The digested samples were then placed on a hotplate for evaporation. Afterwards, the evaporated samples were subjected to volume makeup and filtered through Whatman filter paper (0.45 µm). The analysis of As and Fe content of root and shoot tissues were performed through Atomic Absorption spectrometry (AAS) ([Chowdhury et al., 2020b](#); [Mridha et al., 2021](#)).

## 2.12. Quality control and quality assurance

The standard reference materials (SRMs) of rice flour 1568a and tomato leaf 1573a and spiked samples were analysed during the estimation of As and Fe to maintain the quality control and assurance of the analysis. The digestion of SRM 1568a (rice flour) and 1573a (tomato leaf) samples, followed by As analysis, yield  $96.3 \pm 0.4\%$  and  $94.2 \pm 0.8\%$  recovery, against their certified value of  $0.29 \pm 0.03$  and  $0.1126 \pm 0.0014$  mg/kg, respectively. The recovery of Fe from the SRM 1568a (rice flour) and 1573a (tomato leaf) were  $93.7 \pm 1.2\%$  and  $95.3 \pm 0.9\%$ , against their respective certified values of  $7.4 \pm 0.9$  mg/kg and  $368 \pm 7$  mg/kg.

## 2.13. Translocation of As and Fe

The translocation of As and Fe from root to shoot of rice seedling was calculated according to the following equation ([Chowdhury et al., 2020b](#))



**Fig. 1.** Three conical flasks containing (a) only *Adiantum lunulatum* Extract (ALE), (b) the reaction mixture of ALE and  $\text{FeCl}_3$  solution, (c) only  $\text{FeCl}_3$  solution, respectively.

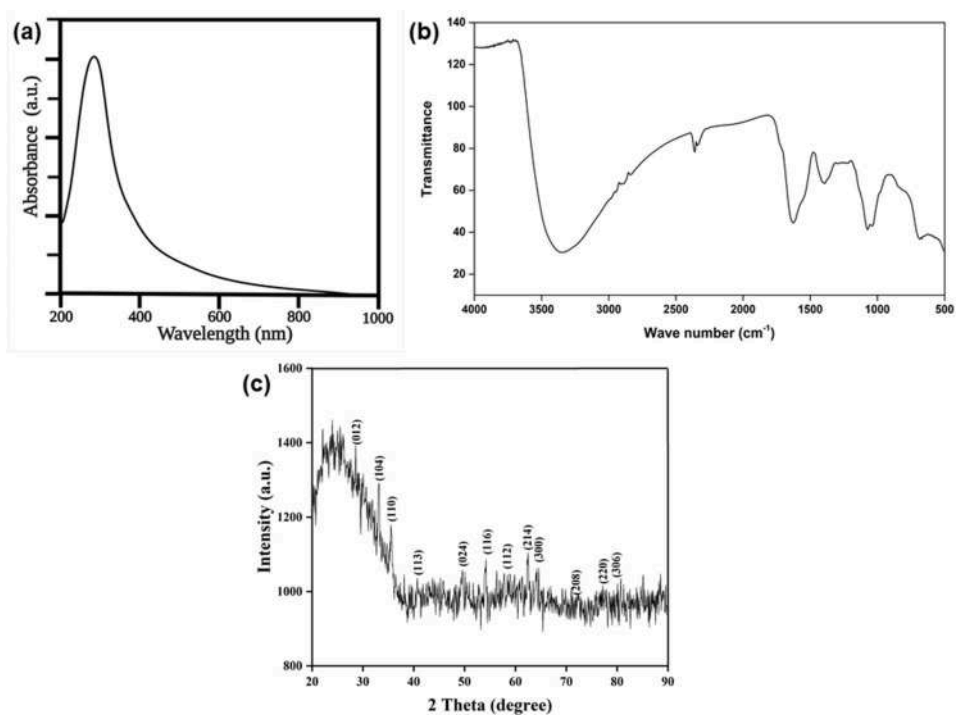


**Fig. 2.** The UV–visible absorption spectrum (a) (Created with BioRender.com), FTIR spectra (b) and XRD pattern (c) of green synthesized FeO-NPs. (For interpretation of the references to colour in this figure legend, the reader is referred to the web version of this article.)

$$\text{Translocation factor (TF)} = \frac{\text{Concentration of As or Fe in shoot (mg/kg)}}{\text{Concentration As or Fe in root (mg/kg)}}$$

The value of  $\text{TF} > 1$  indicates that the plant can translocate metal or metalloid effectively from root to shoot (Chowdhury et al., 2020b).

#### 2.14. Statistical analysis

All experimental results were collected in triplicate and the data was demonstrated as average value  $\pm$  standard deviation (SD). The one-way ANOVA test followed Tukey-HSD ( $p \leq 0.05$ ) test was carried out to present the difference between treatments in Origin (2019b) (Origin Lab Corporation).

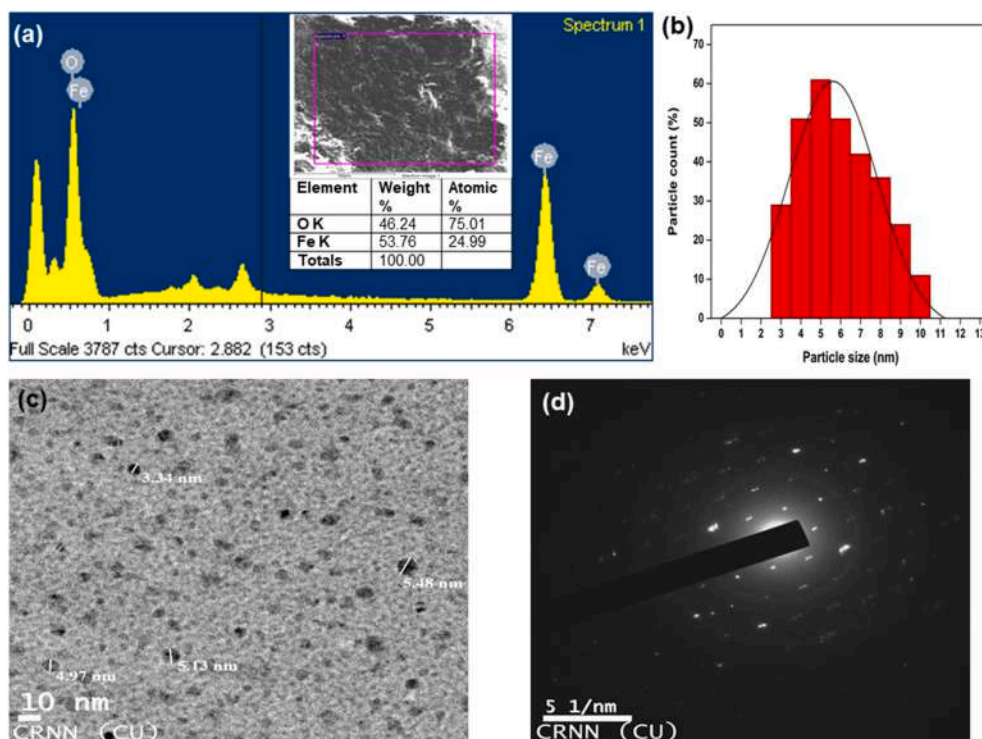


Fig. 3. EDX spectrum (a), Particle size (b), TEM (c) and SAED pattern (d) of green synthesized FeO-NPs. (For interpretation of the references to colour in this figure legend, the reader is referred to the Web version of this article.)

### 3. Results and discussion

#### 3.1. Physiological characteristics of the plant

The plant is rhizomatous and grows sub-erect to erect. Rachis and the body appear glossy and glabrous. The lamina is lanceolate and pinnate. The plant's entire loftiness extends from 9 to 18 inches and is non-articulate. The stem turns from brownish to dark colour when it matures. Pinnae are coarsely rubbery, dark green or pale in colour, glabrous on both sides, and come in groups of up to 10 pairs, alternating, stalked, fan-shaped (Hillis, 1987; Pallavi, 2011; Verdcourt, 2002). The pinnate venation pattern is dichotomous (Pallavi, 2011). Unlike sporangia, which are confined in sporocarps, sporophylls are not assembled in strobili. Sori are not dorsal and feature a false indusium, with sporangia forming in distinct groups (Kramer and Green, 1990).

The stem has 3–4 layers of sclerenchymatous ground tissue, trailed by parenchymatous cells in a transverse cross section. Xylems are both exarch and diarch and seem to be V-shaped with two inward-facing arms (Kramer and Green, 1990; Pallavi, 2011; Resmi et al., 2016; van den Boom, 2016). The exine of the spore appears rugulate in SEM images, which is a distinguishing characteristic of the species (Tryon and Lugardon, 1991). As a result of the aforementioned recommendations, the specimen is identified as *Adiantum lunulatum* Burm.f. (= *A. philippense* Linn.) (Family Pteridaceae) (Chatterjee et al., 2019; Sarkar et al., 2020).

#### 3.2. Characterization of green synthesized FeO-NPs

##### 3.2.1. UV-visible spectroscopic analysis of FeO-NPs

The stimulation of the surface plasmon resonance of FeO-NPs gave the reaction solution its distinctive brown-red colour, which served as a useful spectroscopic hallmark of their production (Fig. 1). In the identical experimental circumstances, neither the positive control group (FeCl<sub>3</sub> Solution) nor the negative control group (ALE) showed any significant colour change. Using a UV-Visible spectrophotometer, the reduction of ferric oxide was analysed spectroscopically. This revealed a 270 nm absorbance peak (Fig. 2a), which was unique to FeO-NPs (Saif et al., 2016).

##### 3.2.2. Zeta potential of FeO-NPs

The zeta potential of FeO-NPs revealed a negative surface charge with a value of  $-0.23$  mv, as illustrated in Supplementary Fig. 1. When all of the particles in a suspension have a negative or positive zeta potential, they reject each other and have little propensity to join together. When maintained for more than a month, the slightly negative charge on the nanoparticles was presumably responsible for the excellent stability of the FeO-NPs, which did not form any aggregates (Sarkar et al., 2020).

##### 3.2.3. FTIR analysis of FeO-NPs

The FTIR spectra of the green synthesized FeO-NPs highlighted the functional groups present in FeO-NP (Fig. 2b). The peak that

**Table 1**  
Effects of FeO-NPs and As stress on seed germination, root growth, shoot growth, seedling fresh weight and seedling vigour.

Treatments	Germination (%)	Root length (cm)	Shoot length (cm)	Fresh wt. (mg)	Vigour index
Control	93.33 ± 5.77a	9.22 ± 0.43a	18.76 ± 0.3a	148.27 ± 7.76a	2611.37 ± 148.63a
AsIII	61.66 ± 2.88 d	2.13 ± 0.35e	7.46 ± 0.31e	90.33 ± 4.8c	591.31 ± 104.2e
AsV	65±5dc	4.38 ± 0.2 d	10.33 ± 0.35 d	96.34 ± 5.69c	956.15 ± 137.4 d
AsIII + IONPs	68.33 ± 2.88c	5.58 ± 0.65c	14.2 ± 0.45c	109.45 ± 6.64bc	1351.56 ± 157.69c
AsV + IONPs	76.88 ± 5.77	6.74 ± 0.3 b	15.6 ± 0.3 b	117.62 ± 5.3 b	1717.49 ± 149.8 b

The same letters within the same column indicate values are not significantly different at  $P \leq 0.05$  using Tukey's HSD multiple comparison test.

appeared near  $660\text{ cm}^{-1}$  could be assigned to the stretching vibration of the Fe–O–Fe bond in  $\alpha$ -FeO-NPs (Rahman et al., 2011). The peaks found in between  $3400$  and  $3300\text{ cm}^{-1}$ ,  $1630\text{ cm}^{-1}$ ,  $1400\text{ cm}^{-1}$  and  $1057\text{ cm}^{-1}$  were assigned to stretching vibration of O–H bond, stretching vibration C=O bond, bending vibration of C–H and stretching vibration of C–N bond, respectively (Karade et al., 2019; Mukherjee et al., 2016). The occurrence of these bonds can be attributed to the presence of the phenolic hydroxyl group, phenolic acids, terpenoids-phenols, and aliphatic amines. These functional groups are also responsible for the reduction of  $\text{Fe}^{3+}$  ions and behave as the capping agent of the nanoparticles (Karade et al., 2019).

### 3.2.4. XRD study of IONPs

The XRD measurement is frequently found to be a valuable analytical tool for determining the crystalline nature of freshly generated compounds and their phases. The XRD pattern of the FeO-NPs, shown in Fig. 2c, clearly identified the fcc structure of  $\alpha$ - $\text{Fe}_2\text{O}_3$  nanoparticles (JCPDS file, No. 89–2810) (51). XRD peaks noticed at 2 values of  $28^\circ$ ,  $33^\circ$ ,  $35^\circ$ ,  $41^\circ$ ,  $49^\circ$ ,  $54^\circ$ ,  $57^\circ$ ,  $62^\circ$ , and  $64^\circ$  for the generated nanoparticles corresponded to the (012), (110), (113), (202), (024), (116), (018), (214), and (300) planes of the  $\alpha$ - $\text{Fe}_2\text{O}_3$  nanoparticles, respectively (Soflaee et al., 2015; Zangeneh Kamali et al., 2014). During this measurement, a sequence of diffraction peaks was detected that were consistent with the theory. The prominent peaks of the XRD pattern suggest that the green synthesized FeO-NPs were well-crystallized  $\alpha$ - $\text{Fe}_2\text{O}_3$  (Han et al., 2013).

### 3.2.5. EDX observation of FeO-NPs

The EDX spectrum from one of the densely populated ferric oxide nanoparticles regions, obtained in the spot-profile mode, is shown in Fig. 3a. EDX spectra showed two distinct signals of iron (Fe) and oxygen (O) in synthesized FeO-NPs (Mukherjee et al., 2016). Peak related to any other element did not appear in the EDX spectrum, which confirmed that the synthesized FeO-NPs were made of Fe and O.

### 3.2.6. Transmission electron microscopy of FeO-NPs

A transmission electron microscope (TEM) study was carried out to analyse the size and morphology of the synthesized FeO-NPs. The average size of these FeO-NPs was  $5 \pm 1\text{ nm}$  (Range: 3–10 nm) (Fig. 3b) (Mukherjee et al., 2016). In nature, particles were found to be quasi-spherical and mono-disperse (Fig. 3c). Further analysis of FeO-NPs using SAED patterns indicated that the shells of large-size nanoparticles, as well as a fraction of small nanoparticles, are made up of highly crystalline iron oxide (Fig. 3d). A similar type of findings has been observed earlier (Simeonidis et al., 2008). The majority of the FeO-NPs in the TEM picture was not in physical touch but were separated by a suitably undeviating inter-particle distance.

## 3.3. Effect of FeO-NPs and As stress on seed germination and seedling growth

One of the most important parameters to evaluate in this study is seed germination. The control group had the highest germination percentage (93.33%) of all of the treatments (Table 1). The germination of rice seedlings was affected by both AsIII and AsV stress (Table 1). Previous studies by Choudhury et al., (2011) and Shri et al., (2009) also indicate the same consequences of As toxicity. (Rahman et al., (2012) reported that the moisture content and nutrient absorption in seeds were considerably decreased with an increase in arsenic (As) concentration. However, the application of FeO-NPs significantly ( $p \leq 0.05$ ) improved the germination by 9.8% and 15.4% as compared to seeds germinated in AsIII and AsV, respectively. Khan et al. (2021) reported that the application of 5 ppm FeO-NPs increased the rice seed germination by 65% under As stressed condition. Earlier study observed that FeO-NPs diffuses through the seed-coat of mung bean (*Vigna radiata*) seeds and increases the water uptake, activity of amylase and starch metabolism of seeds, which in turn led to increase the germination of mung bean plants (Raju et al., 2016). The root and shoot growth of rice seedlings were significantly ( $p \leq 0.05$ ) affected under AsIII and AsV stress (Supplementary Fig. 2). The root growth was hindered under As stress due to the initial exposure of the root to the As stressed environment (Mridha et al., 2021). The As toxicity also restrict the shoot growth by inhibiting the cell division, hydrolytic enzyme activity and translocation of nutrients from root to shoot (Karimi et al., 2013). The biomass yield was also minimal due to the lowered root and shoot growth. AsIII had a greater phytotoxic effect on seedling growth than AsV, which is consistent with previous research (Mridha et al., 2021). Arsenic (III) inhibits the metabolic process by interacting with thiol groups. However, FeO-NPs significantly ( $p \leq 0.05$ ) improved the biomass and the seedling vigour (Bidi et al., 2021). FeO-NPs improved seed germination, root and shoot length, fresh weight, and vigour index, reducing As absorption and protecting seedlings from abiotic stress (Khan et al., 2021). Moreover, FeO-NPs promotes plant growth by improving hormonal (gibberellin and cytokinin) regulation, photosynthetic activity and redox process of the plants under heavy metal stress (Mahakham et al., 2017; Rizwan et al., 2019).

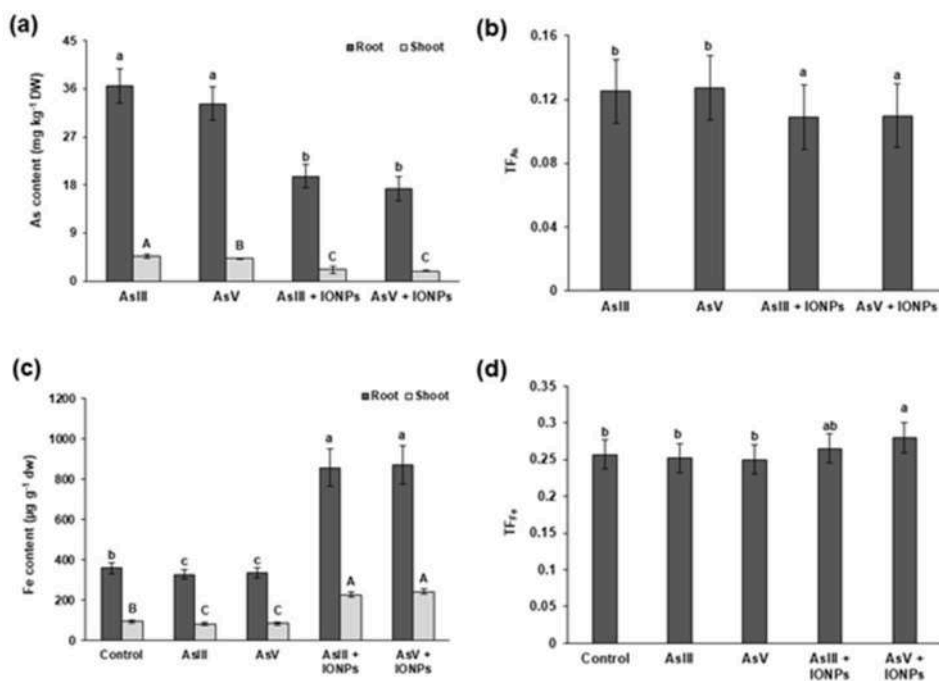


Fig. 4. Arsenic content (a), arsenic translocation factor (b), iron content (c) and iron translocation factor (d) of 14 DAS rice seedlings. Vertical bars represent mean with standard deviation and the same letters in the vertical bars are not significantly different (Tukey's HSD multiple comparisons at  $p \leq 0.05$ ).

### 3.4. Effect of FeO-NPs on As and Fe uptake and translocation

Higher As content was recorded in root and shoot tissue of rice seedling grown in only AsIII and AsV, respectively, as compared to those grown in different As species along with FeO-NPs (Fig. 3a). The As species enters into the plant system via different transporters and aquaporin channels present in plant root. Plant roots inadvertently take up AsV through phosphate transporters, whereas AsIII enters through silicic acid *trans*-porters and some aquaporin channels (Wang et al., 2018). FeO-NPs application in growth medium significantly ( $p \leq 0.05$ ) reduced the As accumulation in the root by 46.36% and 48.17% under AsIII and AsV stress, respectively. A similar reduction in heavy metals uptake by rice plants under FeO-NPs fertigation was also confirmed in other studies (Sebastian et al., 2018; Shabnam et al., 2019b). The FeO-NPs adsorbed the As ions on its surface, hence the bioavailability of As to plants was reduced (Chowdhury et al., 2020b). The competitive uptake of As and Fe at the root surface could be a possible reason for the reduced uptake of As in rice seedlings (Bidi et al., 2021). Supplementation of FeO-NPs also reduced the translocation of As from root to shoot by 13.6% and 14.2% as compared to seedlings grown in only AsIII and AsV (Fig. 3b). Application of FeO-NPs increased the Fe accumulation and its subsequent translocation from root to shoot in As stressed rice seedlings (Fig. 3c and d). The accumulation of Fe in root and shoot of rice seedlings treated with FeO-NPs were significantly ( $p \leq 0.05$ ) increased by 61.5% and 65.4%, respectively. Fe is classified as a micronutrient and required for plant metabolism. Fe also plays a crucial role in both redox reactions and photosynthetic pigment synthesis. The deficiency of Fe in plants caused leaf necrosis, stunted growth; Fe deficiency also disrupts the electron transport chain (Raes et al., 2014). An earlier study found As toxicity hampered the rice plant growth by minimizing the Fe accumulation and translocation (Ghorbani et al., 2021) and these observations were also matched with our findings where uptake and translocation of Fe were comparatively less in seedlings treated only with As (AsIII and AsV) as compared to control. As a result, fertigation with FeO-NPs counteracts the phytotoxic effect of As by restoring Fe homeostasis.

### 3.5. Effect of FeO-NPs and As on oxidative stress, lipid peroxidation, electrolyte leakage and proline

The As phytotoxicity in plants triggers the accumulation of reactive oxygen species (ROS) in plants which further causes oxidative stress in plants. A significant ( $p \leq 0.05$ ) increase in  $H_2O_2$  content was observed in root and shoot of rice seedling under only As (AsIII and AsV) stressed conditions as compared to the seedlings treated with FeO-NPs (Fig. 4a). The FeO-NPs treatment reduced the shoot  $H_2O_2$  content by 35.84% and 47.66% as compared to AsIII and AsV treatment, respectively. The increment in  $H_2O_2$  content can cause oxidative damage to lipids and proteins and eventually rupture the cell wall and makes the cell leaky (Gunes et al., 2008).

TBARS is a measure of lipid peroxidation and also is an indirect measurement of ROS generated in the plants. Arsenic accumulation in root and shoot increased accumulation of  $H_2O_2$  which in turn damages biomacromolecules such as membrane lipids and induces membrane lipid peroxidation (Bidi et al., 2021; Mridha et al., 2021). The amount of TBARS in seedling root was increased by 25.9% and 32.9% under AsIII and AsV treatment, respectively, as compared to AsIII + FeO-NPs and AsV + FeO-NPs treated seedlings (Fig. 4b). Mousavi et al. (2020) also observed a similar level of lipid peroxidation due to oxidative stress caused by As toxicity (Mousavi et al., 2020). The hike in lipid peroxidation caused an increase in electrolyte leakage in seedlings treated only with As (AsIII and AsV).



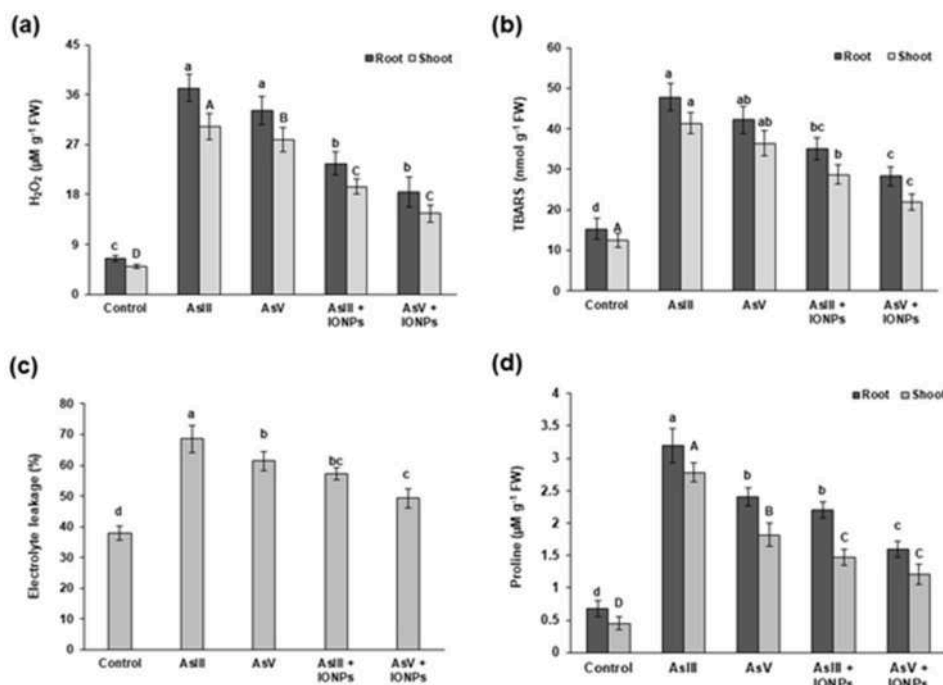


Fig. 5. Hydrogen peroxide (H<sub>2</sub>O<sub>2</sub>) (a), TBARS (b), electrolyte leakage (c) and proline (d) content in 14 DAS rice seedlings. Vertical bars represent mean with standard deviation and the same letters in the vertical bars are not significantly different (Tukey's HSD multiple comparisons at  $p \leq 0.05$ ).

However, the application of FeO-NPs reduced the electrolyte leakage (EL) in rice seedlings by 16.6% and 19.7% as compared to the seedlings treated with only AsIII and AsV, respectively (Fig. 4c). The IONP mediated reduction in oxidative stress markers and EL was also reported in an earlier study (Adrees et al., 2020).

Plants, when exposed to As stress, tend to accumulate free proline, which is an osmolyte that is responsible for maintaining optimum osmotic potential (Moullick et al., 2016). However, excess levels of proline can hamper substrate-level phosphorylation and inhibit certain metabolic reactions (Alia and Saradhi, 1991). To mitigate oxidative damage caused by As exposure in plants, higher levels of proline was observed in root and shoot of seedlings treated only with AsIII and AsV, respectively (Fig. 4d). The application of FeO-NPs in growth medium significantly ( $p \leq 0.05$ ) reduced the shoot proline content by 47.12% and 33.51% as compared to only AsIII and AsV treatment, respectively. Bidi et al. (2021) also observed a similar reduction in proline level when rice seedlings were fertigated with FeO-NPs under As stressed conditions (Bidi et al., 2021). Moreover, FeO-NPs succeeded in the reduction of H<sub>2</sub>O<sub>2</sub>, TBARS, EL and proline level in rice seedlings by lowering the As uptake and translocation.

### 3.6. Effect of FeO-NPs and As stress on chlorophyll and RWC

Photosynthetic pigments are an integral part of the plant's machinery and are used as a stress indicator. This study confirmed that the chlorophyll content of seedlings was found to decrease due to As toxicity (Fig. 5a). Chlorophyll (a and b) content of rice seedlings was found minimal under AsIII and AsV treatment by 61.41%, 45.14%, 54.06% and 50.13%, 29.1%, 40.6% as compared to control, AsIII + FeO-NPs and AsV + FeO-NPs, respectively. The generation of ROS under As stressed conditions triggered lipid peroxidation that may cause damage to the chloroplast (de Andrade et al., 2015). As stress in plants can also induce chlorophyllase activity or reduce the synthesis of precursor molecule ( $\delta$ -aminolevulinic acid) and enzyme activities that involved in the biosynthesis of chlorophyll (Sakarvadia et al., 2018). However, the application of FeO-NPs was found to elevate the chlorophyll content in rice seedlings which were grown under AsIII and AsV stress. Iron is a micronutrient that is necessary for chloroplast production, photosynthesis, respiration, and DNA synthesis (Mushtaq et al., 2020). FeO-NPs were earlier proven to increase the chlorophyll content in As stressed rice plants and Cd stressed wheat plants (Rizwan et al., 2019; Shabnam et al., 2019b). The study also suggests that FeO-NPs up-regulate photosynthetic genes which in turn led to the increase in chlorophyll content of the plants (Tombuloglu et al., 2019). The current study found that As stress harms RWC content (Fig. 5b), which conforms with the results of other studies (Hasanuzzaman et al., 2013). However, the RWC content in seedlings treated with FeO-NPs has been increased by 16% and 10.6% as compared to the seedlings treated only with AsIII and AsV, respectively. Since FeO-NPs enhanced the root development, the water-use efficiency of the plants also increased, which in turn led to the increase in RWC of the plants under As stress. A similar study using FeO-NPs found that the drought tolerance ability of soyabean plants was improved (Linh et al., 2020).

### 3.7. Effect of FeO-NPs and As on antioxidant enzyme activities

To scavenge away the ROS mediated phytotoxicity, plants depend on certain enzymes such as SOD, APX and CAT. In the present

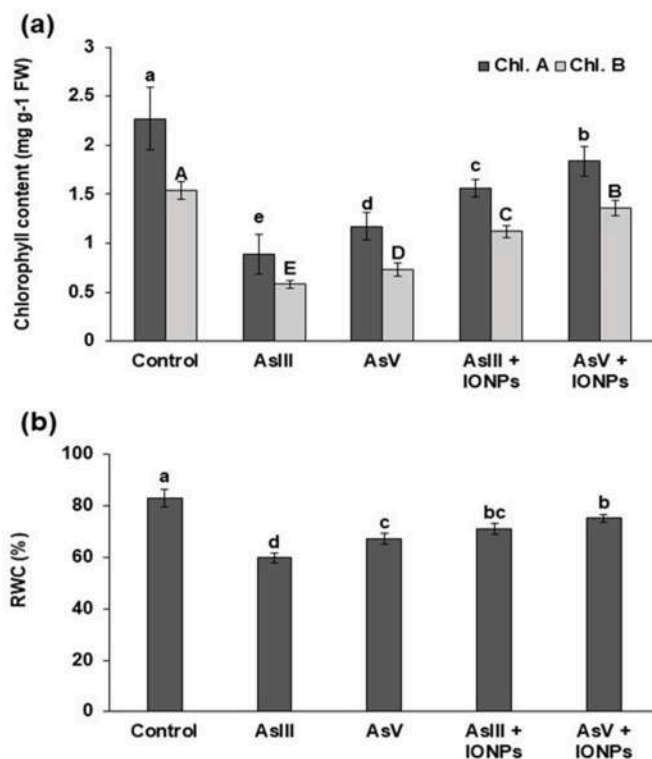


Fig. 6. Chlorophyll *a*, *b* content (a) and RWC (b) in 14 DAS rice seedlings. Vertical bars represent mean with standard deviation and the same letters in the vertical bars are not significantly different (Tukey's HSD multiple comparisons at  $p \leq 0.05$ ).

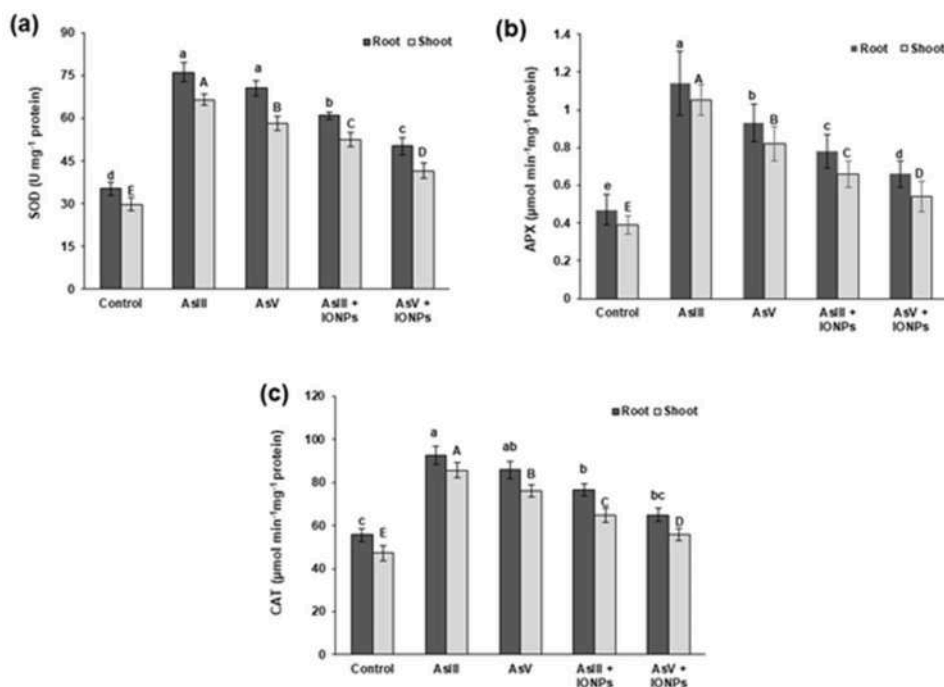


Fig. 7. Superoxide dismutase [SOD] (a), Ascorbate peroxidase [APX] (b) and Catalase [CAT] (c) activities in root and shoot of 14 DAS rice seedlings. Vertical bars represent mean with standard deviation and the same letters in the vertical bars are not significantly different (Tukey's HSD multiple comparisons at  $p \leq 0.05$ ).

study, As stress has significantly ( $p \leq 0.05$ ) enhanced the activity of SOD, APX and CAT. SOD initially converts the intracellular superoxide ( $O_2^{\bullet-}$ ) radical into  $H_2O_2$ . The AsIII and AsV stress increased the activity of SOD in the shoot of rice seedling by 55.1%, 21.12%, 37.6% and 48.8%, 10.1%, 28.8% as compared to control, AsIII + FeO-NPs and AsV + FeO-NPs, respectively (Fig. 6a). Mridha et al. (2021) observed increased SOD activity in rice seedlings when exposed to AsIII and AsV stress. The produced  $H_2O_2$  was further converted to water and molecular oxygen by CAT and APX (Ighodaro and Akinloye, 2019). The higher accumulation of  $H_2O_2$  in root and shoot tissues of rice seedlings caused a significant ( $p \leq 0.05$ ) increase in APX and CAT activity (Fig. 6b and c). CAT diminished different types of reactive oxygen during stress conditions and inhibit cell wall destruction (Jiang and Zhang, 2001). However, the lesser accumulation of ROS caused a subsequent reduction in the activity of SOD, APX and CAT in root and shoot of rice seedlings treated with FeO-NPs (Fig. 7). Different investigations have confirmed that using FeO-NPs lowered antioxidant enzyme activity under abiotic stress settings, which is consistent with our findings (Khan et al., 2020; Mohasseli et al., 2020).

#### 4. Conclusion

The present study confirmed that *Adiantum lunulatum* leaf extract can be used for the green synthesis of environmentally safe FeO-NPs in a non-toxic way. The green synthesized FeO-NPs were quasi-spherical with a mean size of  $5 \pm 1$  nm. This study also demonstrated that the application of FeO-NPs alleviates the As induced toxicity from the rice plant during the seedling stage. The ameliorative effect of FeO-NPs was prominent against As induced oxidative stress. FeO-NPs reduced the bioavailability of As to rice seedlings which in turn minimize oxidative stress and improve the seedling growth. Thus, findings from this study furnish the prospect for the utilization of green synthesized FeO-NPs to alleviate the As toxicity in plants. However, further field-scale study needs to be done to check the efficiency of FeO-NPs in this aspect. Study on optimization of FeO-NPs dosage need to be done to obtain the best possible efficacy against As toxicity. Despite its prominent ameliorative effects against As toxicity in plants, iron nanoparticles can be detrimental to microbes and soil animals, necessitating further investigation.

#### Declaration of competing interest

The authors declare that they have no known competing financial interests or personal relationships that could have appeared to influence the work reported in this paper.

#### Acknowledgements

Arindam Chatterjee and Deepanjan Mridha, both authors contributed equally to this article.

#### Appendix A. Supplementary data

Supplementary data to this article can be found online at <https://doi.org/10.1016/j.bcab.2021.102207>.

#### Authors' contributions

Joy Sarkar: Conceptualization; Arindam Chatterjee, Deepanjan Mridha, Jishnu Banerjee, Sumedha Chanda, Kasturi Ray: Methodology; Joy Sarkar, Arindam Chatterjee, Deepanjan Mridha: Formal analysis and investigation; Arindam Chatterjee, Deepanjan Mridha, Jishnu Banerjee: Writing – original draft preparation; Joy Sarkar, Krishnendu Acharya, Madhusudan Das, Tarit Roychowdhury: Writing – review and editing; Funding acquisition: N/A; Krishnendu Acharya, Madhusudan Das, Tarit Roychowdhury: Resources; Joy Sarkar, Krishnendu Acharya, Madhusudan Das, Tarit Roychowdhury: Supervision.

#### Availability of data and material

Not applicable.

#### Code availability

Not applicable.

#### Ethics approval

Not applicable.

#### Funding

We don't have any funding support from any organizational or institutional level.

#### Permission to reproduce material from other sources

Not applicable.

## Consent to participate

All the authors mutually agree to participate in this work.

## Consent for publication

All the authors mutually agree to submit the manuscript for publication.

## References

- Acharya, K., Sarkar, J., 2014. Bryo-synthesis of gold nanoparticles. *Int. J. Pharmaceut. Sci. Rev. Res.* 29, 82–86.
- Acharya, K., Sarkar, J., Deo, S.S., Goyal, P.K.B./S.K.B./A., 2010. Mycosynthesis of nanoparticles. In: *Advances in Biotechnology*. Bentham Science Publishers Ltd, pp. 204–215. <https://doi.org/10.1111/j.1600-0404.1995.tb01711.x>.
- Adrees, M., Khan, Z.S., Ali, S., Hafeez, M., Khalid, S., ur Rehman, M.Z., Hussain, A., Hussain, K., Shahid Chatha, S.A., Rizwan, M., 2020. Simultaneous mitigation of cadmium and drought stress in wheat by soil application of iron nanoparticles. *Chemosphere* 238, 124681. <https://doi.org/10.1016/J.CHEMOSPHERE.2019.124681>.
- Aebi, H., 1984. [13] catalase in vitro. *Methods Enzymol.* 105, 121–126. [https://doi.org/10.1016/S0076-6879\(84\)05016-3](https://doi.org/10.1016/S0076-6879(84)05016-3).
- Ahmmad, B., Leonard, K., Shariful Islam, M., Kurawaki, J., Muruganandham, M., Ohkubo, T., Kuroda, Y., 2013. Green synthesis of mesoporous hematite ( $\alpha$ -Fe<sub>2</sub>O<sub>3</sub>) nanoparticles and their photocatalytic activity. *Adv. Powder Technol.* 24, 160–167. <https://doi.org/10.1016/j.apt.2012.04.005>.
- Alia, Saradhi, P.P., 1991. Proline accumulation under heavy metal stress. *J. Plant Physiol.* 138, 554–558. [https://doi.org/10.1016/S0176-1617\(11\)80240-3](https://doi.org/10.1016/S0176-1617(11)80240-3).
- Arnon, D.I., 1949. Copper enzymes in isolated chloroplasts. polyphenoloxidase in *Beta vulgaris*. *Plant Physiol.* 24, 1–15. <https://doi.org/10.1104/pp.24.1.1>.
- Astruc, D., 2020. Introduction: nanoparticles in catalysis. *Chem. Rev.* <https://doi.org/10.1021/acs.chemrev.8b00696>.
- Barrs, H., Weatherley, P., 1962. A Re-examination of the relative turgidity technique for estimating water deficits in leaves. *Aust. J. Biol. Sci.* 15, 413–428. <https://doi.org/10.1071/bi9620413>.
- Baskaran, X., Vigila, A.V.G., Parmelazhagan, T., Muralidhara-Rao, D., Zhang, S., 2016. Biosynthesis, characterization, and evaluation of bioactivities of leaf extract-mediated biocompatible silver nanoparticles from an early tracheophyte, *Pteris tripartita* Sw. *Int. J. Nanomed.* 11, 5789–5805. <https://doi.org/10.2147/IJN.S108208>.
- Bates, L.S., Waldren, R., Teare, I.D., 1973. Rapid determination of free proline for water stress studies. *Plant Soil.* <https://doi.org/10.1007/BF00018060>.
- Beauchamp, C., Fridovich, I., 1971. Superoxide dismutase: improved assays and an assay applicable to acrylamide gels. *Anal. Biochem.* 44, 276–287. [https://doi.org/10.1016/0003-2697\(71\)90370-8](https://doi.org/10.1016/0003-2697(71)90370-8).
- Bidi, H., Fallah, H., Niknejad, Y., Barari Tari, D., 2021. Iron oxide nanoparticles alleviate arsenic phytotoxicity in rice by improving iron uptake, oxidative stress tolerance and diminishing arsenic accumulation. *Plant Physiol. Biochem.* 163, 348–357. <https://doi.org/10.1016/j.plaphy.2021.04.020>.
- Cao, W.H., Liu, J., He, X.J., Mu, R.L., Zhou, H.L., Chen, S.Y., Zhang, J.S., 2007. Modulation of ethylene responses affects plant salt-stress responses. *Plant Physiol.* 143, 707–719. <https://doi.org/10.1104/pp.106.094292>.
- Chatterjee, A., Khatua, S., Acharya, K., Sarkar, J., 2019. A green approach for the synthesis of antimicrobial bio-surfactant silver nanoparticles by using a fern. *Digest Journal of Nanomaterials and Biostructures* 14, 479–490.
- Choudhury, B., Chowdhury, S., Biswas, A.K., 2011. Regulation of growth and metabolism in rice (*Oryza sativa* L.) by arsenic and its possible reversal by phosphate. *J. Plant Interact.* 6 (1), 15–24. <https://doi.org/10.1080/17429140903487552>.
- Chowdhury, N.R., Das, A., Joardar, M., De, A., Mridha, D., Das, R., Rahman, M.M., Roychowdhury, T., 2020a. Flow of arsenic between rice grain and water: Its interaction, accumulation and distribution in different fractions of cooked rice. *Sci. Total Environ.* 731 <https://doi.org/10.1016/j.scitotenv.2020.13893>, 138937.
- Chowdhury, N.R., Das, A., Mukherjee, M., Swain, S., Joardar, M., De, A., Mridha, D., Roychowdhury, T., 2020b. Monsoonal paddy cultivation with phase-wise arsenic distribution in exposed and control sites of West Bengal, alongside its assimilation in rice grain. *J. Hazard Mater.* 400 <https://doi.org/10.1016/j.jhazmat.2020.123206>.
- Das, A., Joardar, M., Chowdhury, N.R., De, A., Mridha, D., Roychowdhury, T., 2021a. Arsenic toxicity in livestock growing in arsenic endemic and control sites of West Bengal: risk for human and environment. *Environ. Geochem. Health* 43 (8), 3005–3025. <https://doi.org/10.1007/s10653-021-00808-2>.
- Das, A., Joardar, M., De, A., Mridha, D., Chowdhury, N.R., Khan, M.T.B.K., Chakrabarty, P., Roychowdhury, T., 2021b. Pollution index and health risk assessment of arsenic through different groundwater sources and its load on soil-paddy-rice system in a part of Murshidabad district of West Bengal, India. *Groundw. Sustain. Dev.* 15 (3), 100652. <https://doi.org/10.1016/j.gsd.2021.100652>.
- Das, R.K., Pachapur, V.L., Lonappan, L., Naghdi, M., Pulicharla, R., Maiti, S., Cleodan, M., Dalila, L.M.A., Sarma, S.J., Brar, S.K., 2017. Biological synthesis of metallic nanoparticles: plants, animals and microbial aspects. *Nanotechnology for Environmental Engineering.* <https://doi.org/10.1007/s41204-017-0029-4>.
- Dasgupta, A., Sarkar, J., Ghosh, M., Bhattacharya, A., Mukherjee, A., Chattopadhyay, D., Acharya, K., 2017. Green conversion of graphene oxide to graphene nanosheets and its biosafety study. *PLoS One* 12, e0171607. <https://doi.org/10.1371/journal.pone.0171607>.
- de Andrade, S.A.L., Domingues, A.P., Mazzafera, P., 2015. Photosynthesis is induced in rice plants that associate with arbuscular mycorrhizal fungi and are grown under arsenate and arsenite stress. *Chemosphere* 134, 141–149. <https://doi.org/10.1016/J.CHEMOSPHERE.2015.04.023>.
- De, A., Mridha, D., Bandopadhyay, B., Roychowdhury, T., Panja, A.S., 2021. Arsenic and its effect on nutritional properties of oyster mushrooms with reference to health risk assessment. *Biol. Trace Elem. Res.* 199 (3), 1170–1178. <https://doi.org/10.1007/s12011-020-02224-6>.
- El-Ansary, A., Faddah, L.M., 2010. Nanoparticles as biochemical sensors. *Nanotechnology, Science and Applications.* <https://doi.org/10.2147/NSA.S8199>.
- Ghidan, Y., M, A., Al Antary, T., 2020. Applications of nanotechnology in agriculture. In: *Applications of Nanobiotechnology*. IntechOpen. <https://doi.org/10.5772/intechopen.88390>.
- Ghorbani, A., Tafteh, M., Roudbari, N., Pishkar, L., Zhang, W., Wu, C., 2021. Piriformospora indica augments arsenic tolerance in rice (*Oryza sativa*) by immobilizing arsenic in roots and improving iron translocation to shoots. *Ecotoxicol. Environ. Saf.* 209, 111793. <https://doi.org/10.1016/J.ECOENV.2020.111793>.
- Gunes, A., Pilbeam, D.J., Inal, A., 2008. Effect of arsenic–phosphorus interaction on arsenic-induced oxidative stress in chickpea plants, 2008 *Plant Soil* 314 (1 314), 211–220. <https://doi.org/10.1007/S11104-008-9719-9>.
- Gupta, R.K., Ghosh, K., Dong, L., Kahol, P.K., 2010. Green synthesis of hematite ( $\alpha$ -Fe<sub>2</sub>O<sub>3</sub>) submicron particles. *Mater. Lett.* 64, 2132–2134. <https://doi.org/10.1016/j.matlet.2010.07.014>.
- Han, C., Han, J., Li, Q., Xie, J., 2013. Wet chemical controllable synthesis of hematite ellipsoids with structurally enhanced visible light property. *Sci. World J.* 1–5. <https://doi.org/10.1155/2013/410594>, 2013.
- Hasanuzzaman, M., Nahar, K., Alam, M.M., Roychowdhury, R., Fujita, M., 2013. Physiological, biochemical, and molecular mechanisms of heat stress tolerance in plants, 2013 *Int. J. Mol. Sci.* 14, 9643–9684. <https://doi.org/10.3390/IJMS14059643>, 14, 9643–9684.
- Heath, R.L., Packer, L., 1968. Photoperoxidation in isolated chloroplasts. I. Kinetics and stoichiometry of fatty acid peroxidation. *Arch. Biochem. Biophys.* 125, 189–198. [https://doi.org/10.1016/0003-9861\(68\)90654-1](https://doi.org/10.1016/0003-9861(68)90654-1).
- Hillis, D.M., 1987. Molecular versus morphological approaches to systematics. *Annu. Rev. Ecol. Systemat.* 18, 23–42. <https://doi.org/10.1146/ANNUREV.ES.18.110187.000323>.
- Ighodaro, O.M., Akinloye, O.A., 2019. First line defence antioxidants-superoxide dismutase (SOD), catalase (CAT) and glutathione peroxidase (GPX): their fundamental role in the entire antioxidant defence grid. *Alexandria Journal of Medicine* 54, 287–293. <https://doi.org/10.4314/bafm.v54i4>.

- Jang, M., Chen, W., Cannon, F.S., 2008. Preloading hydrous ferric oxide into granular activated carbon for arsenic removal. *Environ. Sci. Technol.* 42, 3369–3374. <https://doi.org/10.1021/es7025399>.
- Jiang, M., Zhang, J., 2001. Effect of abscisic acid on active oxygen species, antioxidative defence system and oxidative damage in leaves of maize seedlings. *Plant Cell Physiol.* 42, 1265–1273. <https://doi.org/10.1093/PCP/PCE162>.
- Joardar, M., Das, A., Chowdhury, N.R., Mridha, D., De, A., Majumdar, K.K., Roychowdhury, T., 2021a. Health effect and risk assessment of the populations exposed to different arsenic levels in drinking water and foodstuffs from four villages in arsenic endemic Gaighata block, West Bengal, India. *Environ. Geochem. Health.* <https://doi.org/10.1007/s10653-021-00823-3>.
- Joardar, M., Das, A., Mridha, D., De, A., Chowdhury, N.R., Roychowdhury, T.R., 2021b. Evaluation of acute and chronic arsenic exposure on school children from exposed and apparently control areas of West Bengal, India. *Expos. Health* 13, 33–50. <https://doi.org/10.1007/s12403-020-00360-x>.
- Karade, V.C., Parit, S.B., Dawkar, V.v., Devan, R.S., Choudhary, R.J., Kedge, V.v., Pawar, N.v., Kim, J.H., Chougale, A.D., 2019. A green approach for the synthesis of  $\alpha$ -Fe<sub>2</sub>O<sub>3</sub> nanoparticles from *Gardenia resinifera* plant and its in vitro hyperthermia application. *Heliyon* 5, e02044. <https://doi.org/10.1016/j.heliyon.2019.e02044>.
- Karimi, N., Shayesteh, L.S., Ghasempour, H., 2013. Effect of Arsenic on germination of *Isatis cappadocica* Desv., A newly discovered Arsenic hyperaccumulator. *Acta Biol. Cracov. Bot.* 55, 61–67. <https://doi.org/10.2478/abscb-2013-0019>.
- Khan, S., Akhtar, N., Rehman, S.U., Shujah, S., Rha, E.S., Jamil, M., 2020. Biosynthesized iron oxide nanoparticles (Fe<sub>3</sub>O<sub>4</sub> NPs) mitigate arsenic toxicity in rice seedlings. *Toxics* 9. <https://doi.org/10.3390/TOXICS9010002>. Page 2 of 9, 2, 2021.
- Kramer, K.U., Green, P.S., 1990. Introduction to Pteridophytes and Gymnosperms, Pteridophytes and Gymnosperms. Springer, Berlin, Heidelberg. [https://doi.org/10.1007/978-3-662-02604-5\\_1](https://doi.org/10.1007/978-3-662-02604-5_1).
- Lin, T.M., Mai, N.C., Hoe, P.T., Lien, L.Q., Ban, N.K., Hien, L.T.T., Chau, N.H., Van, N.T., 2020. Metal-based nanoparticles enhance drought tolerance in soybean. *J. Nanomater.* <https://doi.org/10.1155/2020/4056563>, 2020.
- Lowry, O.H., Rosebrough, N.J., Farr, A.L., Randall, R.J., 1951. Protein measurement with the folin phenol reagent. *J. Biol. Chem.* [https://doi.org/10.1016/S0021-9258\(19\)52451-6](https://doi.org/10.1016/S0021-9258(19)52451-6).
- Mahakham, W., Sarmah, A.K., Maensiri, S., Theerakulpit, P., 2017. Nanopriming technology for enhancing germination and starch metabolism of aged rice seeds using phyto-synthesized silver nanoparticles, 2017 Sci. Rep. 7 (1 7), 1–21. <https://doi.org/10.1038/s41598-017-08669-5>.
- Mengane, S.K., 2016. Phytochemical analysis of *Adiantum lunulatum*. *International Journal of Current Microbiology and Applied Sciences* 5, 351–356. <https://doi.org/10.20546/ijcmas.2016.511.040>.
- Mohasseli, V., Farbood, F., Moradi, A., 2020. Antioxidant defense and metabolic responses of lemon balm (*Melissa officinalis* L.) to Fe-nano-particles under reduced irrigation regimes. *Ind. Crop. Prod.* 149, 112338. <https://doi.org/10.1016/J.INDCROP.2020.112338>.
- Moullick, D., Ghosh, D., Chandra Santra, S., 2016. Evaluation of effectiveness of seed priming with selenium in rice during germination under arsenic stress. *Plant Physiol. Biochem.* 109, 571–578. <https://doi.org/10.1016/J.PLAPHY.2016.11.004>.
- Mousavi, S.R., Yosoof, N., Hormoz, F., Davood Barari, T., 2020. Methyl jasmonate alleviates arsenic toxicity in rice. *Plant Cell Rep.* 39, 1041–1060.
- Mridha, D., Paul, I., De, A., Ray, I., Das, A., Joardar, M., Chowdhury, N.R., Bhadoria, P.B.S., Roychowdhury, T., 2021. Rice seed (IR64) priming with potassium humate for improvement of seed germination, seedling growth and antioxidant defense system under arsenic stress. *Ecotoxicol. Environ. Saf.* 219, 112313. <https://doi.org/10.1016/j.ecoenv.2021.112313>.
- Mukherjee, D., Ghosh, S., Majumdar, S., Annapurma, K., 2016. Green Synthesis of A-Fe 2 O 3 Nanoparticles for arsenic(V) Remediation with a Novel Aspect for Sludge Management. <https://doi.org/10.1016/j.jece.2015.12.010>.
- Murthy, S.K., 2007. Nanoparticles in modern medicine: state of the art and future challenges. *Int. J. Nanomed.* 2, 129–141.
- Mushtaq, T., Shah, A.A., Akram, W., Yasin, N.A., 2020. Synergistic ameliorative effect of iron oxide nanoparticles and *Bacillus subtilis* S4 against arsenic toxicity in *Cucurbita moschata*: polyamines, antioxidants, and physicochemical studies. *Int. J. Phytoremediation* 22 (13), 1408–1419. <https://doi.org/10.1080/15226514.2020.1781052>.
- Nakano, Y., Asada, K., 1981. Hydrogen peroxide is scavenged by ascorbate-specific peroxidase in spinach chloroplasts. *Plant Cell Physiol.* 22, 867–880. <https://doi.org/10.1093/oxfordjournals.pcp.a076232>.
- Pallavi, G., 2011. An ethno-pharmaco-botanical review of hamsapadi –*Adiantum lunulatum* Burm. F. (A. Philippense Linn.). *International Journal of Pharmaceutical & Biological Archive* 2.
- Raes, K., Knockaert, D., Struijs, K., van Camp, J., 2014. Role of processing on bioaccessibility of minerals: influence of localization of minerals and anti-nutritional factors in the plant. *Trends Food Sci. Technol.* 37, 32–41. <https://doi.org/10.1016/J.TIFS.2014.02.002>.
- Rahman, M.M., Khan, S.B., Jamal, A., Faisal, M., Aisiri, A.M., 2011. Iron oxide nanoparticles. *Nanomaterials*. <https://doi.org/10.5772/27698>.
- Rahman, M.M., Rahman, M.A., Maki, T., Hasegawa, H., 2012. Phytotoxicity of arsenate and salinity on early seedling growth of rice (*Oryza sativa* L.): A threat to sustainable rice cultivation in South and South-East Asia. *Bull. Environ. Contam. Toxicol.* 88, 695–702. <https://doi.org/10.1007/s00128-012-0580-4>.
- Raju, D., Mehta, U., Beedu, S., 2016. Biogenic green synthesis of monodispersed gum kondagogu (*Cochlospermum gossypium*) iron nanocomposite material and its application in germination and growth of mung bean (*Vigna radiata*) as a plant model. *IET Nanobiotechnol.* 10, 141–146. <https://doi.org/10.1049/IET-NBT.2015.0112>.
- Ray, I., Mridha, D., Roychowdhury, T., 2021. Waste derived amendments and their efficacy in mitigation of Arsenic contamination in soil and soil-plant systems: A review. *Environ. Technol. Innov.* 24, 101976. <https://doi.org/10.1016/j.eti.2021.101976>.
- Resmi, S., Thomas, V.P., Sreenivas, V.K., 2016. Anatomical studies of selected species of *Adiantum* L. In Kerala. *South Indian Journal of Biological Sciences* 2, 115. <https://doi.org/10.22205/SIJBS/2016/V2/I1/100356>.
- Rizwan, M., Ali, S., Ali, B., Adrees, M., Arshad, M., Hussain, A., Zia ur Rehman, M., Waris, A.A., 2019. Zinc and iron oxide nanoparticles improved the plant growth and reduced the oxidative stress and cadmium concentration in wheat. *Chemosphere* 214, 269–277. <https://doi.org/10.1016/J.CHEMOSPHERE.2018.09.120>.
- Rui, M., Ma, C., Hao, Y., Guo, J., Rui, Y., Tang, X., Zhao, Q., Fan, X., Zhang, Z., Hou, T., Zhu, S., 2016. Iron oxide nanoparticles as a potential iron fertilizer for peanut (*Arachis hypogaea*). *Front. Plant Sci.* 7 <https://doi.org/10.3389/fpls.2016.00815>.
- Saif, S., Tahir, A., Chen, Y., 2016. Green synthesis of iron nanoparticles and their environmental applications and implications. *Nanomaterials*. <https://doi.org/10.3390/nano6110209>.
- Sakarvadia, H., Ru, K., Hi, S., Kunjadia, B.B., 2018. Effect of zinc and iron application on leaf chlorophyll, carotenoid, grain yield and quality of wheat in calcareous soil of Saurashtra region. *International Journal of Chemical Studies* 6, 2092–2095.
- Sarkar, J., Acharya, K., 2017. *Alternaria alternata* culture filtrate mediated bio-reduction of chloroplatinate to platinum nanoparticles. *Synth. React. Inorg. Metal-Organ. Nano-Metal Chem.* 47, 365–369. <https://doi.org/10.1080/15533174.2016.1186062>.
- Sarkar, J., Chattopadhyay, D., Patra, S., Deo, S.S., Sinha, S., Ghosh, M., Mukherjee, A., Acharya, K., 2011a. *Alternaria alternata* mediated synthesis of protein capped silver nanoparticles and their genotoxic activity. *Digest Journal of Nanomaterials and Biostructures* 6, 563–573.
- Sarkar, J., Dey, P., Saha, S., Acharya, K., 2011b. Mycosynthesis of selenium nanoparticles. *Micro & Nano Lett.* 6, 599–602. <https://doi.org/10.1049/mnl.2011.0227>.
- Sarkar, J., Saha, S., Chattopadhyay, D., Patra, S., Acharya, K., 2011c. Mycosynthesis of silver nanoparticles and investigation of their antimicrobial activity. *J. Nanosci. Nanoeng. Appl.* 1, 17–26.
- Sarkar, J., Mridha, D., Sarkar, J., Orasugh, J.T., Gangopadhyay, B., Chattopadhyay, D., Roychowdhury, T., Acharya, K., 2021. Synthesis of Nanosilica from Agricultural Wastes and its Multifaceted Applications: A Review. *Biocatal. Agric. Biotechnol.* 37, 102175. <https://doi.org/10.1016/j.bcab.2021.102175>.
- Sarkar, J., Ray, S., Chattopadhyay, D., Laskar, A., Acharya, K., 2012a. Mycosynthesis of gold nanoparticles using a phytopathogen *Alternaria alternata*. *Bioproc. Biosyst. Eng.* 35, 637–643. <https://doi.org/10.1007/s00449-011-0646-4>.
- Sarkar, J., Saha, S., Dey, P., Acharya, K., 2012b. Production of selenium nanorods by phytopathogen, *Alternaria alternata*. *Adv. Sci. Lett.* 10, 111–114. <https://doi.org/10.1166/asl.2012.2137>.
- Sarkar, J., Kalyan Roy, S., Laskar, A., Chattopadhyay, D., Acharya, K., 2013. Bio-reduction of chloroaurate ions to gold nanoparticles by culture filtrate of *Pleurotus sapidus* Quél. *Mater. Lett.* 92, 313–316. <https://doi.org/10.1016/j.matlet.2012.10.130>.

- Sarkar, J., Ghosh, M., Mukherjee, A., Chattopadhyay, D., Acharya, K., 2014. Biosynthesis and safety evaluation of ZnO nanoparticles. *Bioproc. Biosyst. Eng.* 37, 165–171. <https://doi.org/10.1007/s00449-013-0982-7>.
- Sarkar, J., Mollick, MdM.R., Chattopadhyay, D., Acharya, K., 2017. An eco-friendly route of  $\gamma$ -Fe<sub>2</sub>O<sub>3</sub> nanoparticles formation and investigation of the mechanical properties of the HPMC- $\gamma$ -Fe<sub>2</sub>O<sub>3</sub> nanocomposites. *Bioproc. Biosyst. Eng.* 40, 351–359. <https://doi.org/10.1007/s00449-016-1702-x>.
- Sarkar, J., Chakraborty, N., Chatterjee, A., Bhattacharjee, A., Dasgupta, D., Acharya, K., 2020. Green synthesized copper oxide nanoparticles ameliorate defence and antioxidant enzymes in *Lens culinaris*. *Nanomaterials* 10. <https://doi.org/10.3390/nano10020312>.
- Sebastian, A., Nangia, A., Prasad, M.N.V., 2018. A green synthetic route to phenolics fabricated magnetite nanoparticles from coconut husk extract: implications to treat metal contaminated water and heavy metal stress in *Oryza sativa* L. *J. Clean. Prod.* 174, 355–366. <https://doi.org/10.1016/J.JCLEPRO.2017.10.343>.
- Shabnam, N., Kim, M., Kim, H., 2019a. Iron (III) oxide nanoparticles alleviate arsenic induced stunting in *Vigna radiata*. *Ecotoxicol. Environ. Saf.* 183 <https://doi.org/10.1016/j.ecoenv.2019.109496>.
- Shabnam, N., Kim, M., Kim, H., 2019b. Iron (III) oxide nanoparticles alleviate arsenic induced stunting in *Vigna radiata*. *Ecotoxicol. Environ. Saf.* 183, 109496. <https://doi.org/10.1016/J.ECOENV.2019.109496>.
- Shri, M., Kumar, S., Chakraborty, D., Trivedi, P.K., Mallick, S., Misra, P., Shukla, D., Mishra, S., Srivastava, S., Tripathi, R.D., Tuli, R., 2009. Effect of arsenic on growth, oxidative stress, and antioxidant system in rice seedlings. *Ecotoxicol. Environ. Saf.* 72 (4), 1102–1110. <https://doi.org/10.1016/j.ecoenv.2008.09.022>.
- Simeonidis, K., Mourdikoudis, S., Tsiaoussis, I., Angelakeris, M., Dendrinou-Samara, C., Kalogirou, O., 2008. Structural and magnetic features of heterogeneously nucleated Fe-oxide nanoparticles. *J. Magn. Magn Mater.* 320, 1631–1638. <https://doi.org/10.1016/j.jmmm.2008.01.028>.
- Soflaee, F., Farahmandjou, M., Firoozabadi, T.P., 2015. Polymer-mediated synthesis of iron oxide (Fe<sub>2</sub>O<sub>3</sub>) nanorod. *Chin. J. Phys.* 53, 1–9. <https://doi.org/10.6122/CJP.20150413>.
- Su, B., Lin, J., Owens, G., Chen, Z., 2020. Impact of green synthesized iron oxide nanoparticles on the distribution and transformation of As species in contaminated soil. *Environ. Pollut.* 258 <https://doi.org/10.1016/j.envpol.2019.113668>.
- Tombuloglu, H., Slimani, Y., Tombuloglu, G., Almessiere, M., Baykal, A., 2019. Uptake and translocation of magnetite (Fe<sub>3</sub>O<sub>4</sub>) nanoparticles and its impact on photosynthetic genes in barley (*Hordeum vulgare* L.). *Chemosphere* 226, 110–122. <https://doi.org/10.1016/J.CHEMOSPHERE.2019.03.075>.
- Tryon, A.F., Lugardon, B., 1991. Spores of the Pteridophyta, Spores of the Pteridophyta. Springer, New York. <https://doi.org/10.1007/978-1-4613-8991-0>.
- van den Boom, P.P.G., 2016. Lichens and lichenicolous fungi of the Azores (Portugal), collected on São Miguel and Terceira with the descriptions of seven new species. *Acta Bot. Hung.* 58, 199–222. <https://doi.org/10.1556/034.58.2016.1-2.11>.
- Velikova, V., Yordanov, I., Edreva, A., 2000. Oxidative stress and some antioxidant systems in acid rain-treated bean plants protective role of exogenous polyamines. *Plant Sci.* 151, 59–66. [https://doi.org/10.1016/S0168-9452\(99\)00197-1](https://doi.org/10.1016/S0168-9452(99)00197-1).
- Verdcourt, B., 2002. Flora of tropical east africa - adiantaceae. In: *Flora of Tropical East Africa*.
- Wang, C., Bermejo, E.S., Chen, Y., Banks, J.A., Salt, D.E., Zhao, F.J., 2018. Dissecting the components controlling root-to-shoot arsenic translocation in *Arabidopsis thaliana*. *New Phytol.* 217 (1), 206–218. <https://doi.org/10.1111/nph.14761>.
- Xu, P., Zeng, G.M., Huang, D.L., Feng, C.L., Hu, S., Zhao, M.H., Lai, C., Wei, Z., Huang, C., Xie, G.X., Liu, Z.F., 2012. Use of iron oxide nanomaterials in wastewater treatment: a review. *Sci. Total Environ.* <https://doi.org/10.1016/j.scitotenv.2012.02.023>.
- Zangeneh Kamali, K., Alagarsamy, P., Huang, N.M., Ong, B.H., Lim, H.N., 2014. Hematite nanoparticles-modified electrode based electrochemical sensing platform for dopamine. *Sci. World J.* 1–13. <https://doi.org/10.1155/2014/396135>, 2014.
- Zhang, S., Zhang, Y., Kangning, L., Yan, M., Zhang, J., Yu, M., Tang, S., Wang, L., Qu, H., Luo, L., Xuan, W., Xu, G., 2021. Nitrogen mediates flowering time and nitrogen use efficiency via floral regulators in rice. *Curr. Biol.* 31 (4), 671–683. <https://doi.org/10.1016/j.cub.2020.10.095>.
- Zou, Y., Wang, Xiangxue, Khan, A., Wang, P., Liu, Y., Alsaedi, A., Hayat, T., Wang, Xiangke, 2016. Environmental remediation and application of nanoscale zero-valent iron and its composites for the removal of heavy metal ions: a review. *Environ. Sci. Technol.* 50, 7290–7304. <https://doi.org/10.1021/acs.est.6b01897>.



## Source details

[Feedback >](#) [Compare sources >](#)

### Biocatalysis and Agricultural Biotechnology

Scopus coverage years: from 2012 to Present

Publisher: Elsevier

ISSN: 1878-8181

Subject area:

[Agricultural and Biological Sciences: Agronomy and Crop Science](#)[Agricultural and Biological Sciences: Food Science](#)[Immunology and Microbiology: Applied Microbiology and Biotechnology](#)[Biochemistry, Genetics and Molecular Biology: Biotechnology](#)[View all](#)

Source type: Journal

[View all documents >](#)[Set document alert](#)[Save to source list](#)

CiteScore 2022

8.4

SJR 2022

0.655

SNIP 2022

1.126

## Review

# COVID-19: morphology and mechanism of the SARS-CoV-2, global outbreak, medication, vaccines and future of the virus

Prithu Bhattacharyya<sup>1,†</sup>, Sunandana Das<sup>1,†</sup>, Sahasrabdi Aich<sup>2,†</sup>, Joy Sarkar<sup>1,\*</sup> 

<sup>1</sup>Department of Botany, Dinabandhu Andrews College, Garia, Kolkata, 700084 West Bengal, India, <sup>2</sup>Department of Botany, Vivekananda College, Thakurpukur, Kolkata, 700063 West Bengal, India

## TABLE OF CONTENTS

1. Abstract
2. Introduction
3. Global outbreak
4. Symptoms
5. Mechanisms
6. Preventive measures
7. Possible medications
8. Vaccines designed against SARS-CoV-2
9. Conclusions
10. Author contributions
11. Ethics approval and consent to participate
12. Acknowledgment
13. Funding
14. Conflict of interest
15. Availability of data and material
16. Code availability
17. References

## 1. Abstract

Severe Acute Respiratory Syndrome Coronavirus-2 (SARS-CoV-2) is a lethal virus that was detected back on 31st December 2019 in Wuhan, Hubei province in China, and since then this virus has been spreading across the globe causing a global outbreak and has left the world fighting against the virus. The disease caused by the SARS-CoV-2 was named COVID-19 and this was declared a pandemic disease by the World Health Organization on 11th March 2020. Several nations are trying to develop a vaccine that can save millions of lives. This review outlines the morphological features of the virus describing the outer and inner structures of the virus along with the entry mechanism of the virus into the host body and the infection process. Detailed reports of global outbreak along with preventive measures have also been included, with special emphasis on China, the United States of America, India, Italy, and South Korea. Broad-spectrum antiviral drugs being used at vari-

ous health care centres around the world, namely Remdesivir, Camostat & Nafamostat, Famotidine, Chloroquine & Hydroxychloroquine, Lopinavir/ritonavir, Ivermectin, and Tocilizumab & Sarilumab have also been included. World Health Organization guidelines on preventive measures and use of soaps, alcohol-based hand-rubs and wearing face masks have also been described. The vaccines that are in one of the phases of human trials, namely Oxford University's vaccine, the United States-based Moderna's vaccine, India's Covaxin and the Russian vaccine, have also been incorporated in the review article.

## 2. Introduction

The Coronavirus disease 19 (COVID-19), considered a highly transmittable disease was first reported during mid-January, 2020 in Wuhan, Hubei province in China. The SARS-CoV-2 is phylogenetically related to the previously known SARS-CoV virus. During the outbreak of the



novel Coronavirus (SARS-CoV-2), the world has seen what a virus can do to mankind. Coronavirus is placed in the family Coronaviridae in the Nidovirales order. COVID-19 is caused by an RNA virus (ssRNA) 50–200 nm in diameter consisting of four structural proteins, namely spike protein, envelope protein, membrane protein, and nucleocapsid protein [1]. The virus has crown-like spikes on its outer surface, i.e., corona thus the virus came to be known as coronavirus due to the resemblance [2]. SARS-CoV-2 also has the common structure of coronaviruses with spike protein on its outer surface (Fig. 1). It consists of different polyproteins, nucleoproteins, and membrane proteins, for example—RNA polymerase, 3-chymotrypsin-like protease, papain-like protease, helicase, glycoprotein, and accessory proteins [2]. In a host, membrane-derived lipid bilayer that envelops the helical nucleocapsid which contains the RNA virus, the coronavirus surface viral protein spike, membrane and envelope are inserted [3]. The genome of coronavirus is between 26 and 32 kb in size and consists of 6–11 open reading frames and 9680 amino acid polyproteins are encoded. About 67% of the genome is present in the first ORF which encodes 16 non-structural proteins, while the rest of ORFs encode for structural and accessory proteins. There is an insufficiency of the hemagglutinin-esterase gene in the genome of SARS-CoV-2. Two untranslated flanking regions are found at the 5' end of 265 and 3' end of 358 nucleotides. There are no notable dissimilarities between open reading frames and non-structural proteins for sequence variation among SARS-CoV and SARS-CoV-2. Two viral cysteine proteases namely papain-like protease, chymotrypsin-like, 3-chymotrypsin-like or main protease, helicase, and others are found in the non-structural proteins, perhaps took part in the transcription and replication of SARS-CoV-2. The spike glycoprotein structure of SARS-CoV-2 is similar to the spike protein of SARS-CoV with a root-mean-square deviation of 3.8 Å [3].

There have been various natural and artificial drugs that have been used in the treatment of COVID-19. Various potential antimalarial drugs namely, hydroxychloroquine and azithromycin, antifilarial drug ivermectin and certain antiviral drugs have been put to test against the COVID-19. There was a probability that certain probability that the use of hydroxychloroquine, ivermectin, azithromycin, remdesivir, and a few more drugs as single agents or in combinations with immunomodulators would work against COVID-19 [4].

Mesenchymal stem cells and their derived exosomes are considered to have potential effects as immunomodulatory agents for COVID-19 patients. It has been earlier observed that stem cell research and treatment exhibited encouraging results for various diseases such as diabetes, cancer and neurodegeneration. Lately, mesenchymal stem cells (MSCs) have been applied as possible therapeutic agents for treating SARS-CoV-2. They release certain cytokines to inhibit viral infections, which are usually

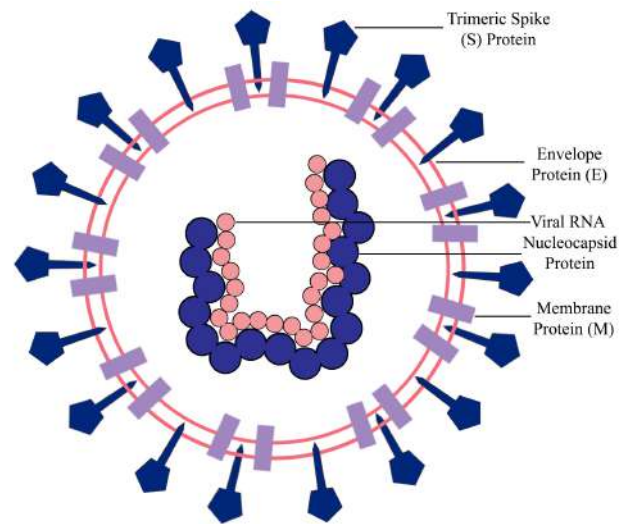


**Fig. 1. Morphological structure of Severe Acute Respiratory Syndrome Coronavirus 2 (SARS-CoV-2).**

present naturally; however, the mesenchymal stem cells exist in their niche before being quarantined from the source tissue. Thus, mesenchymal stem cells and their exosomes (MSCs-Exo) are anticipated to survive even after transplantation into the body of a COVID-19 patient. Since the treatment with the help of mesenchymal stem cells is still uncertain, various trials and researches are being performed to measure its effectiveness [1].

Ilimaquinone (marine sponge metabolite) exhibited inhibitory prospects against SARS-CoV-2. It was assessed in comparison with hydroxychloroquine, azithromycin, favipiravir, ivermectin and remdesivir at the active binding pockets of 9 different vital SARS-CoV-2 target proteins, following an *in silico* molecular interaction centred approach [5, 6].

Medications that have been used against COVID-19, along with precautionary measures, and also a detailed list of COVID-19 vaccines have been listed further in this review.

### 3. Global outbreak

#### 3.1 Americas

In the United States, the first COVID-19 was reported and confirmed on 20th January 2020 [7]. The United States and South Korea encountered their first COVID-19 cases around similar timeframes [8]. A 35-year-old man with a 4-day record of mild fever and cough was put on record by an urgent care clinic in Snohomish County, Washington on 19th January 2020. After investigation, it was discovered that he was on a family visit to Wuhan, China, and he returned to Washington State on 15th January 2020. The patient was concerned about his symptoms when he saw a health alert from the United States Centers for Disease Con-

trol and Prevention about the outbreak of the COVID-19 in China, so he decided to get himself checked at a health care centre. He was a healthy non-smoker with only a history of hypertriglyceridemia. Various tests were performed on him, and the initial results were normal for all the tests, but later on, he was diagnosed with COVID-19 [7].

The United States was slow to start large-scale coronavirus testing. As of 27th February 2020, less than 4000 tests were being performed in the United States [9–11]. On 5th March 2020, the Vice President of the United States, also the leader of the coronavirus response team, acknowledged that the United States was not performing enough tests to meet the future demand. Lesser than 10,000 tests had been performed in the United States as of 11th March 2020 [12, 13]. The United States was testing approximately 125 people per million of their population by mid of March 2020. That was substantially lower than various other nations [14]. By the end of March 2020, the United States had tested over a million suspected people who showed symptoms [15]. Inaccuracies were encountered because of shortage of testing, the rate of growth in cases and the total number of confirmed cases was reasonably inaccurate [16]. The general recommendation was to test 500,000 people per day before the termination of social distancing, while the United States was testing around 150,000 people per day [17]. The United States approximately started testing 240,000 to 260,000 people per day as of the first week of May 2020, which was still not sufficient to suppress the outbreak of COVID-19 [18–20].

In mid-March 2020, the United States government issued orders for people to stay at home, avoid public gatherings, and made it obligatory for entertainment cum recreation venues shut down for the time being. Dine-in restaurants and other non-essential businesses were also ordered to remain closed so that the spread of the virus could be suppressed. Several pharmacies, financial institutions, grocery stores, mass media and critical infrastructure were usually allowed to keep functioning. Police checkpoints were also set up at state borders [21]. About nine-tenths of the United States population was under restriction as of 2nd April 2020 [22]. 42,034,347 total cases in the United States were reported on 22nd September 2021, with approximately 671,728 deaths [23].

### 3.2 Europe

On January 31st, 2020, Italy reported its first COVID-19 cases, two Chinese tourists were tested positive in Rome [24]. The Chinese couple arrived in Italy on 23rd January 2020 via Milan Malpensa Airport. Then they reached Rome via Verona and Parma on 28th January 2020. On 29th January 2020, they developed some symptoms and were assisted to the Lazzaro Spallanzani National Institute for Infectious Diseases, and after performing tests, they were reported COVID-19 positive [25]. A week later, an Italian citizen was deported back to Italy from Wuhan,

China. He was then hospitalized and later tested positive for COVID-19. On 21st February 2020, 16 COVID-19 positive cases were reported in Lombardy, Italy [26]. 22nd February 2020, saw Italy's first COVID-19 death and an addition of 60 more cases [27]. By the first week of March 2020, the outbreak was seen all over Italy [28].

On 31st January 2020, the Italian government professed a state of emergency and also deferred all flights that were destined to and from China. The two main clusters of COVID-19 positive cases were identified to be a part of the eleven municipalities in northern Italy, most of the cases traced back to these two primary clusters [29]. Lockdown was imposed on these areas, and violating the lockdown would result in a penalty of €206 and possibly imprisonment for 3 months [30]. The Italian army along with the law enforcement departments was instructed to manage the lockdown [31]. Quarantine was imposed in Lombardy and 14 other northern and central provinces in Piedmont, Emilia-Romagna, Veneto, and Marche, were put under lockdown on 8th March 2020. The next day, quarantine was imposed all over Italy, putting over 60 million people under quarantine [32, 33]. The Italian government prohibited people from going out on the streets and shut down all non-essential businesses and organizations [34]. Italy tested over 3,923,000 people as of 26th July 2020. The genuine number of infected people in Italy was projected to be much greater than the official count as Italy did not implement an adequate amount of tests. Internationally lost COVID-19 cases [35, 36]. During mid-March, 2020, an increase in the number of deaths along with a slowdown in the number of new cases per day was seen [37]. The president of the Italian National Institute of Health on 31st March 2020, declared that the outbreak had reached its peak in Italy [38].

The effects of the lockdown were evident, Italy reported a decline in the number of new cases and deaths per day. An increased discharge rate was also observed and in turn, the intensive care units were starting to be less occupied [39]. Educational institutions were shut down in ten municipalities in Lombardy, one in Emilia Romagna, and one in Veneto. Various public events were also cancelled during this lockdown period [40]. All religious services were cancelled [41]. Regional trains were also shut down in the severely affected areas, with trains skipping Codogno, Casalpusterlengo and Maleo stations [42, 43]. Basilica Di San Marco in Venice, along with La Scala, Duomo di Milano and Piccolo Teatro in Milan were closed until further notice [44–46]. 4,641,890 total cases in Italy were reported on 22nd September 2021, with approximately 130,421 deaths [23].

### 3.3 South East Asia

#### 3.3.1 China

A group of 59 people were reported on 31st December 2019 to be infected with pneumonia who were allied to the Hunan Seafood Wholesale Market in Wuhan, Hubei Province in China [7]. The 59 alleged patients with symptoms such as fever and dry cough were relocated to a hospital shortly. On the very same day, the native health authority issued an epidemiological alert, and on the following day, the market ceased activity. After the alert was issued, the establishment of a group of experts was initiated, which included physicians, virologists, epidemiologists and government officials [47].

The cause of commencement of these infections is unknown, the diagnosis of the people infected with pneumonia was being done based on clinical features, which included chest imaging, and blacklisting of the regular bacterial and viral pathogens which caused pneumonia. In Jinyintan Hospital, Wuhan, China, the infected patients were isolated using airborne precautions for aerosol-generating procedures, and N95 masks were also being provided to them. The National Health Commission of China and the Ethics Commission of Jinyintan Hospital permitted this study [47]. Chinese health authorities validated that a novel coronavirus, 2019-nCoV is allied to the group of pneumonia patients who had been suspected on 31st December 2019 [7]. An outbreak of a novel coronavirus was encountered by China, where approximately 1800 patients died and over 70,000 patients were infected within the first 50 days of the epidemic. This novel virus belonged to the  $\beta$  group of coronaviruses. The Chinese researchers named this novel virus the Wuhan coronavirus or the 2019 novel coronavirus. Later, the virus was termed SARS-CoV-2 and the disease as COVID-19 by the International Committee on Taxonomy of Viruses [2]. The 2019-nCoV was named severe acute respiratory syndrome coronavirus 2 (SARS-CoV-2) since the first one (SARS-CoV-1) which is also known as the Chinese bat coronavirus, originated and caused an epidemic of severe human respiratory disease, 17 years ago in China [48].

In China, it was assumed in the beginning that patients infected with Wuhan coronavirus were originally suffering from pneumonia, who may have visited the seafood market and probably consumed infected animals or birds. Further studies reported that few of the patients who were declared COVID-19 positive did not even have a travel history to the seafood market. This study confirmed human to human transmission of the virus, which was further reported in approximately more than 100 countries worldwide [2]. To curb the epidemic, the Chinese authorities quarantined 17 cities and over 50 million people were a part of this procedure [49].

During the initial phase of the COVID-19 pandemic, blood count, coagulation profile and serum bio-

chemical test were being performed. Respiratory specimens were collected which included nasal and pharyngeal swabs, bronchoalveolar lavage fluid and a few others, which were tested for various typical viruses including influenza, respiratory syncytial virus, adenovirus, SARS-CoV and MERS-CoV using instantaneous reverse transcription-polymerase chain reaction evaluations approved by the Chinese National Medical Products Administration. Frequent fungal and bacterial check-ups were also executed. Oseltamivir and other antibiotics were administered to the COVID-19 patients orally or intravenously. For acute community developed pneumonia patients, methyl prednisolone corticosteroid therapy was provided, and oxygen support to those suffering from severe hypoxemia. Thorough check-ups were performed for the COVID-19 positive patients to confirm the viral clearance before being discharged from the hospital [47]. 124,232 total cases in China were reported on 22nd September 2021, with approximately 5689 deaths [23].

#### 3.3.2 India

On 30th January 2020, India reported its first COVID-19 case [50]. The Epidemic Disease Act of 1897 was invoked, educational institutions and various commercial foundations had been shut down from mid-March, 2020. As most of the positive cases were linked to people visiting from other countries, the Indian Government decided to suspend all tourist visas. Lockdown was imposed in over 75 districts across the country where COVID-19 cases had been confirmed. On 22nd March 2020, the Janta Curfew was declared by the Indian Prime Minister. The people of India were requested to stay at home for a few weeks and also work from home in possible cases [51]. The first positive case in India was reported to be a student in Kerala who was a student of The Wuhan University and had returned to India after the pandemic alert was declared. As of 7th February 2020, 3 positive cases were reported in Kerala, all of whom had a travel record to Wuhan, China. 33 positive cases were reported by the first week of March, 2020, 16 of the 33 cases were Italian tourists. 114 COVID-19 cases were confirmed as of 16th March 2020. The numbers rose to 17,264 by 19th April 2020 [52].

On 18th January 2020, the Indian Government issued orders, instructing 3 major airports in India, namely, Delhi, Kolkata and Mumbai to perform screening of travellers from China. All international sea ports also performed screening. Screening of all flights from Singapore, Hong Kong, Thailand, Japan, South Korea, Vietnam, Nepal, Indonesia, Malaysia and China were made compulsory from 23rd February 2020. Soon the list was discontinued, all international and domestic flights were made subject to compulsory screening. It was made essential that every passenger filled up a self-declaration form which was then transferred to health and immigration officials, it was also necessary that the passenger was quarantined for at

least a week [53]. As of 30th March 2020, 1,524,266 passenger screenings were performed at airports. Quarantine centres were set up, along with a few hospitals and stadiums being turned into quarantine facilities too. Containment zones were set up where a group of positive cases were reported, which was followed by a buffer zone [52].

A total number of 830,201 tests had been performed in India as of 30th April 2020. Guidelines were issued by the Indian Council of Medical Research on the usage of Truenat™ beta CoV (Molbio Diagnostics Private Limited, Kolkata, India) while screening [54]. As of April 26, 2020, the production capacity of indigenous N-95 masks and personal protective equipment kits was approximately 100,000 per day. 2033 COVID-19 facilities with over 190,000 isolation beds, approximately 24,000 ICU beds and more than 12,000 ventilators were made available as of 23rd April 2020. Two high-risk groups, first the people over 65 years of age, and the second being children under 10 years of age, were advised to avoid public gatherings and stay at home. A 21-day nationwide lockdown was imposed on 24th March 2020. People were banned from stepping out of their homes. A 19-day extension was declared on 14th April 2020 [52]. 33,531,498 total cases in India were reported on 22nd September 2021, with approximately 445,768 deaths [23].

### 3.3.3 South Korea

South Korea has shown well-organized methods for restraining the COVID-19 disease. On 20th January 2020, South Korea reported their very first COVID-19 case [55]. The early outbreak at about 30 cases showed that most of the cases were foreign or from family members. The 31st case caused a lot of trouble for declining the tests and continuing to attend Shincheonji Sunday services which is a religious movement in the Daegu district of South Korea, which is also known as a cult to many and it undergoes missionary activities in Wuhan where the pandemic had its beginning. About 3 weeks later sporadic cluster outbreaks were spreading reportedly in large crowded places like churches or long-term-care facilities [56]. South Korea reported its highest number of cases from 20th February 2020, to 9th March 2020, mainly in Daegu all of which originated from Shincheonji [55]. 876 cases were reported from 30th March 2020 to 13th April 2020, where 81.5% of the cases were from people living outside of South Korea and about 27.5% of people were related to long-term-care hospitals [56]. After resolving the cases linked to the religious group South Korea successfully sustained the number of new cases from the middle of April 2020, from 100 cases to less than 50 cases every day. After the 2015 MERS outbreak, South Korea was already prepared to cope with COVID-19 because of their experience in overcoming the difficulties. To combat the difficult times, several health-care personnel went to Daegu where the initial outbreak occurred. The citizens or ordinary people also started helping

by working at mask production factories to prevent shortage of masks [56]. The government also provided masks satisfactorily to the citizens who showed their IDs [55]. In Daegu, due to the swift spread of COVID-19, the number of critically ill patients increased and the health care system could not treat everyone; as a result, some patients died fighting the disease. Intensive care units with airborne infection isolation rooms are extremely necessary for the treatment of critically ill patients and to overcome these, temporary airborne infection isolation rooms were set up with negative air machines in intensive care units, which was also done in the past to fight the breakout of MERS [57]. South Korea's death toll increased with the rapid increase of the disease which led to social distancing for the prevention of the disease. Due to globalization, one country can influence others, so Korea's anti-COVID-19 initiatives could be helpful to other countries pursuing successful steps to tackle this disease. Compared to the United States and Europe, South Korea reported a lower number of cases each day because the government worked efficiently to knock down the rise of the pandemic [55].

Since COVID-19 has spread rapidly, diagnostic testing was an important strategy in South Korea, systematic COVID-19 monitoring, effective tracking of infected people, and proper care of infected people were the most important features of the government's policies [55]. In Seoul, the Korean government quickly approved private-sector testing and developed several makeshift testing kiosks or walk through examination institutions to avoid interaction between medical staff and patients so patients were also diagnosed inside their cars. Screening clinics in public health centres were set up for testing people reckoned to show symptoms like fever or cough to keep the hospitals and healthcare institutions safe and free from the virus. Such measures varied operating models to adapt to the growing demand for diagnostic tests in a more beneficial way. An infected person after being detected receives a real-time text message on their phone via the local government near the patient's area and disinfecting is done at the screening facilities they went to. Tracking of the affected patient can be done in the same way by knowing about the movement locations using credit cards, mobile phone GPS and security camera recordings and the government also make the general public aware of the affected person by providing necessary information. Daily the emergency alert system warns the public via their mobile phones and makes them aware of the newly reported cases [56].

To keep COVID-19 contained within a group of people contact tracing is necessary. A well-developed system has been developed through which epidemiological investigations were done in health care institutions and the isolation of the probable patients was approved thus stopping the further spread. The people who came in close contact with the patient were put in self-quarantine for 2 weeks and were connected to one-on-one government employees

via a mobile phone-based 'self-quarantine protection app', which the Korean government launched as a tool to monitor symptoms of the disease. When the self-quarantine rules were violated, this software warned the public health staff and helped them tracking the symptoms of the person two times each day. The health staff conducted this tracing system primarily and monitoring took a few days. Several central agencies worked together to establish a swift tracking program at the beginning of April 2020, and through this system, the agencies shared real-time information. These brand new apps also focused on geo-locating and identifying affected people. Across the city, wide-ranged data analysis tools were used to check the real-time environment, transportation and well-being. The said system is Infectious Disease Control and Prevention Act based which allows personal information to be used for proper epidemiological investigations during the outbreak of any contagious diseases. However, a robust security framework assured the Korean people of no false use of the information by being anonymous [55].

In South Korea, the government treated COVID-19 patients based on the seriousness of the illness and made room for them correspondingly to hospital or other health care centres. Confirmed COVID-19 patients were first detected by health specialists at public health care centres and then they were categorized according to the severity of symptoms, which included asymptomatic, mild, moderate, severe and extremely severe. Every group based on the severity of illness was treated differently and were admitted to separate hospitals. Patients with moderate, severe and extremely severe symptoms were treated at National infectious disease hospitals and various other government-designated institutions, whereas patients with mild symptoms were examined at their retrospective homes and health care centres. Healthcare specialists examined them twice a day to make sure that they are ready to be transferred to other healthcare centres if symptoms worsen or are ready to be discharged if their symptoms diminish [56]. The central and the local governments of South Korea appointed numerous hospitals as infectious disease hospitals. AI was another technology used by them for better detection efficiency and patient categorization. Chest X-Ray AI is an example of such technology, used to identify unusual detections on chest X-rays, categorizing intensive care patients and find lung abnormalities within a few seconds. Treatment of COVID-19 patients in South Korea concentrated on identifying and prioritizing patients with high risk, especially those over 60 years of age or those with any other comorbidities and transferring them immediately to hospitals, however patients with low-risk were instructed to stay at home quarantine. Few of the possibly efficacious drugs ritonavir/lopinavir, ribavirin, hydroxychloroquine and interferon were advised for severe patients. At a certain point due to the high demand for masks, there was a shortage of mask supply. The South Korean government also executed

a rule for the 5-day rotational distribution of masks from 9th March 2020 to treat every citizen equally [55].

One of the major factors that helped South Korea to rapidly lower the outbreak of COVID-19 was wearing face masks in public and only a few cases were reported in May and June 2020. Citizens were instructed to avoid gatherings and congested places and to follow quarantine formalities which included washing hands, wearing face masks and maintaining social distancing [55, 58]. It was reported from a current survey that about 63.2% of Koreans wear a mask whenever they go outside. Whereas, another international study reported that in the case of the COVID-19 pandemic the rate of wearing face masks was even higher, approximately 94% and that was the highest rate amongst 28 countries. Another reason was in 2015, an outbreak of Middle East respiratory syndrome coronavirus (MERS-CoV) infection caused 38 deaths with 186 total cases. Another instance was witnessed by South Korea in 2015; an outbreak of Middle East respiratory syndrome coronavirus (MERS-CoV) infection caused 38 deaths with 186 total cases. This led to the gradual acceptance of the use of face masks in public, and thus during the COVID-19 pandemic, the people were well aware of the situation and accepted the use of face masks very quickly [58]. Amongst the Organization for Economic Cooperation and Development Countries, South Korea is known to have the highest particulate matter level. Medical specialists of South Korea also warned about the health problems which can originate due to this problem, ranging from infant health abnormalities to increased adult deaths, thus wearing face masks was highly recommended. Over the recent years, due to the high alerts imposed by the South Korean government from April 2014, the people also became well aware of this increasing particulate matter level and thus practised wearing masks whenever outside. Korean pop singers made wearing face masks fashionable which also influenced the common people. Thus, it can be concluded that in South Korea, wearing face masks and following self-quarantine principles played a major role in lowering the spread of SARS-CoV-2 [58, 59].

It was around 27th January 2020, members of the Korea Centers for Disease Control and Prevention instructed the infectious disease specialists from the Korean Society for Laboratory Medicine and 20 other pharmaceutical companies to quickly start the production of detection test kits [55]. On January 31st, 2020, the latest one-step real-time polymerase chain reaction test kit, giving results within just 6 hours was ratified and made available in 18 Research Institute of Public Health and Environment locations. Around mid-March, 2020, a hospital in South Korea invented a walk-in diagnosis booth that implemented the principle of a negative pressure glove box. As of 10th April 2020, a total of 580 healthcare centres and public health centres were able to perform detection tests. And around 23 March 2020, the number of daily tests was about 100,000

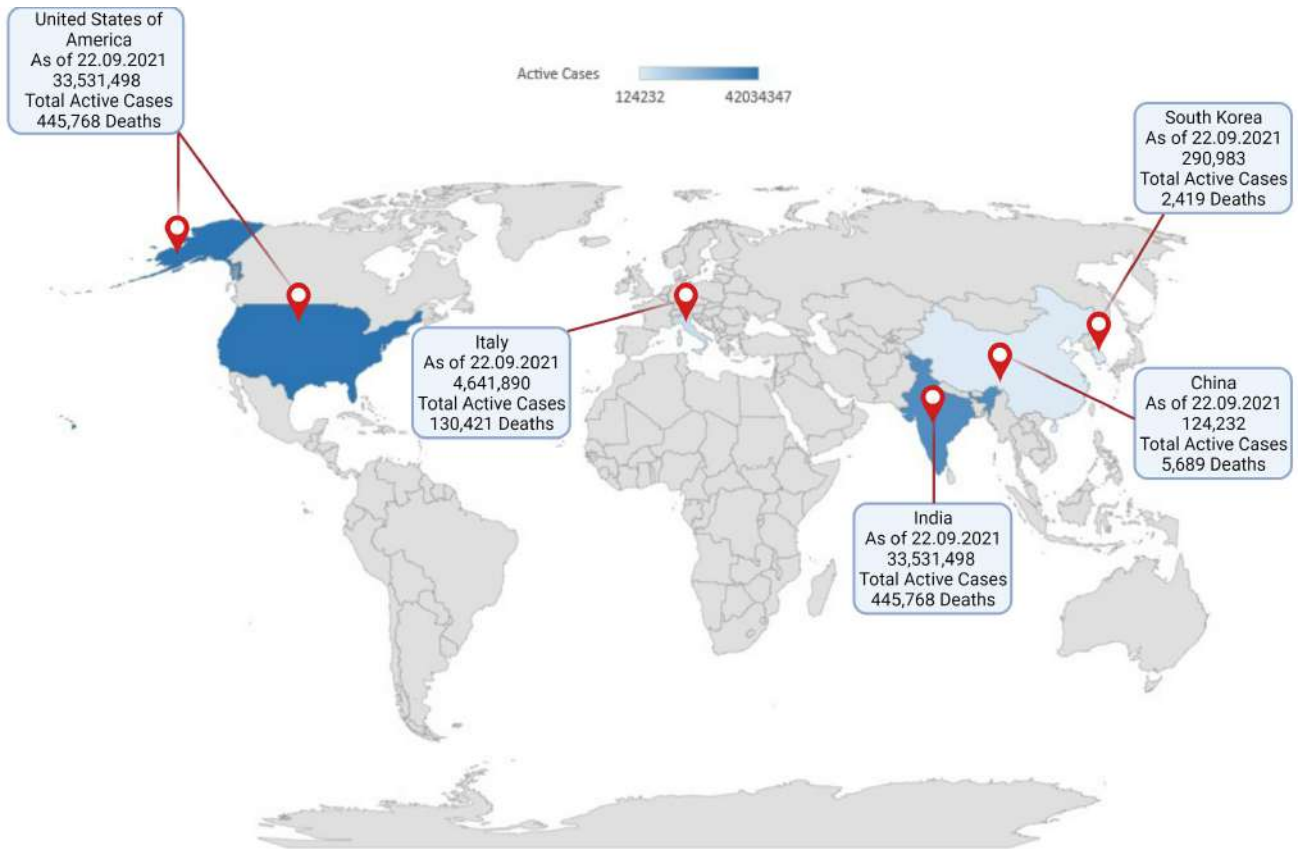


Fig. 2. World map depicting the total number of cases and deaths in China, United States of America, India, Italy, and South Korea, as of 22nd September 2021 (Created with BioRender.com).

and a total of 518,743 tests were performed till 23rd April 2020 [56]. 290,983 total cases in South Korea were reported on 22nd September 2021, with approximately 2419 deaths (Fig. 2) [23].

#### 4. Symptoms

Coronaviruses including SARS-CoV, SARS-CoV-2, HCoV-NL63 have been proven to be present in tears through RT-PCR techniques. Conjunctivitis is also being considered as another symptom of COVID-19, especially after taking into account the increasing number of case reports of COVID-19 patients infected with conjunctivitis. Various researchers are considering another probability of a different viral mechanism by which the coronavirus can enter the host body through epithelial cells of the eyes [60].

Various oral diseases like mouth ulcers, necrotising gingivitis, blisters, salivary gland alterations, gustatory dysfunction were mainly reported in the clinical reports which examined the oral health of COVID-19 patients. Moreover, the lesions were proven associated with loss of taste and smell. SAR-CoV-2 showed tropism for endothelial cells and COVID-19 facilitated endotheliitis was proven capable of stimulating inflammation of oral tissues and thereby enabling the further spread of the virus. Tis-

sue homeostasis and delayed disease recovery are also some of the critical symptoms caused due to higher level of pro-inflammatory mediators in patients infected with COVID-19 [61].

#### 5. Mechanisms

The most significant factor for the initiation of COVID-19 host-pathogen interaction is the host body where the evolution of the viral cell takes place. Human RNA virus SARS-CoV-2 caused the viral disease COVID-19. The virus undergoes several genetic manipulations to get to its mutated characters for the initiation of the infection and the struggle for existence inside the host body [62].

The virus has glycoprotein spikes on its outer surface which result in the attachment and entry of the virus into the host cells [63]. The process of entry of the virus is reliant on cellular proteases which helps to split the spike proteins for example—Human Airway Trypsin, cathepsins and transmembrane protease serine 2. The most important receptor of SARS-CoV-2 is angiotensin-converting enzyme 2. The critical lysine 31 residue present on the angiotensin-converting enzyme 2 human receptor identifies the 394 glutamine residue of the SARS-CoV-2 in the receptor-binding domain region. The life cycle of SARS-CoV-2 begins when

the Spike protein binds to the cellular receptor angiotensin-converting enzyme 2 [2, 64, 65].

Employing the endosomal pathway, the viral envelope fusion with the cell membrane is assisted by the conformation change in the S protein after receptor binding. The RNA is then released in the host cell by SARS-CoV-2. Viral replicase polyproteins pp1a and 1ab are translated from the Genome RNA which is then broken down by viral proteinases into small products. Discontinuous transcription of the polymerase generates a series of sub-genomic mRNAs which are translated into appropriate viral proteins. The virion's viral proteins and genome RNA is accumulated eventually in the Golgi body and endoplasmic reticulum. Then through vesicles, it is transported and let out of the cell. An effectual environment for external stability and survival of SARS-CoV-2 functions as an intermediate from one host to another [2].

Its host body is feasible and more conveyable than any other coronavirus. Temperature changes and relative humidity increases the rate of exposure of the host to some pathogen and also penetration and persistence of the pathogen within the host body [62]. SARS-CoV-2 through numerous clinical outputs is received by the environment, mainly in the form of droplets or aerosol that is predominantly the respiratory secretions from an infected individual that can be either a susceptible host or a carrier. It can survive in this form in various inanimate objects that can carry these pathogens. These droplets or aerosol can protect the virus on its own after it is accepted in the external environment and helps in sustaining it for a long time; in aerosol media the virus can stay in a stable form for three hours and on steel surface, the stability of the virus is about 2–3 days [66]. It acts as a maintaining media of the virus outside the host body. This is one of the reasons for the firmness of SARS-CoV-2 in the external environment [62]. The following flowchart describes the mechanism of infection of the SARS-CoV-2 (Fig. 3).

Rapid replication of SAR-CoV-2 takes place after the initiation of infection and acute inflammatory outcomes were also observed due to cytokine storms. This consequent inflammatory outcome causes severe damage in capillary endothelial cells, alveolar epithelia, which in turn results in interstitial and alveolar edema and also disrupts pulmonary activities. These losses lead to acute hypoxic respiratory failure and result in acute respiratory distress syndrome (ARDS) [4].

## 6. Preventive measures

Currently, the world is facing a threatening health crisis with the emergence and spread of coronavirus disease (COVID-19). This disease is usually transmitted by contact with an infected droplet or by inhalation, and its incubation period ranges from 2 to 14 days. The symptoms of this disease include fever, dry cough, tiredness, sore throat along

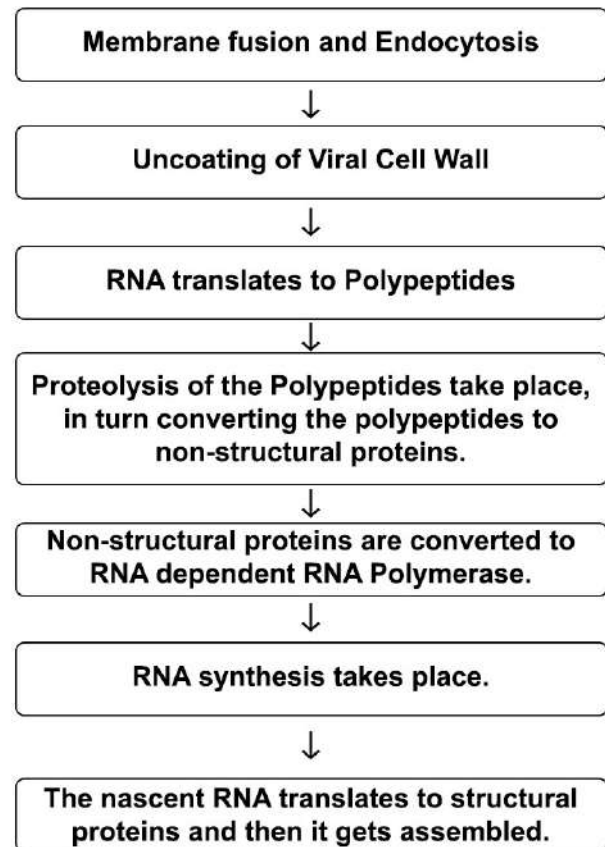


Fig. 3. Mechanism of infection of SARS-CoV-2 in humans.

with few others. The majority of infected people are experiencing mild to moderate respiratory sickness and are recovering without any such special treatment. Elderly people and those with any other existing disease like diabetes, cardiovascular disease, chronic respiratory disease, and cancer are more prone to severe illness [67, 68]. Due to the lack of a therapeutic vaccine or any other antiviral treatment, the only possible way to prevent the spread of COVID-19 is to obey the following preventive measures [69]. These include isolation, social distancing, quarantine, maintaining personal hygiene.

### 6.1 Isolation

Isolation is when an infected person is separated from an uninfected person and which can be done in a hospital or at home for mild infections. The period for isolation should be at least 13 days since the initiation of COVID-19 symptoms. To make the isolation process work the detection of infected people should be done early, i.e., before the commencement of shedding of the virus [70].

### 6.2 Quarantine

Quarantine is needed for asymptomatic or healthy people, who may or may not have been exposed to an infected person but was not showing any such symptoms. Such a person should stay in quarantine for 14 days to make

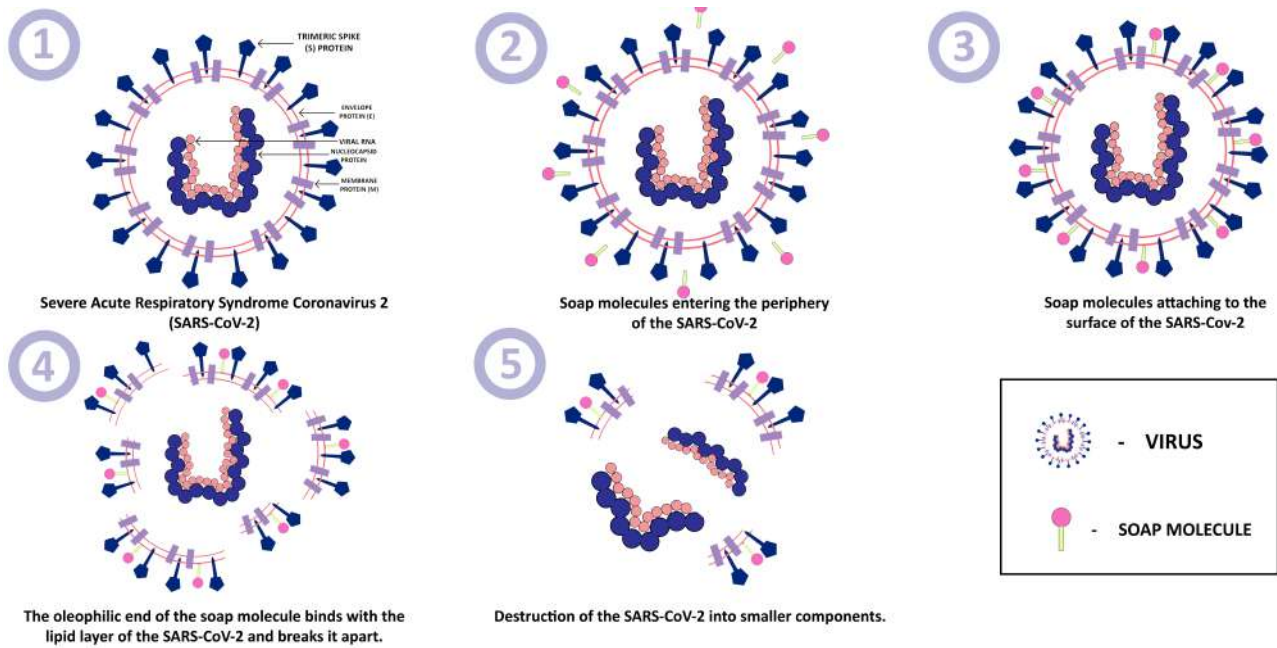


Fig. 4. The action of soap on Severe Acute Respiratory Syndrome Coronavirus-2.

sure whether that person is infected or not. Ideally, quarantine involves movement limitations, along with medical assistance and observation during the period of the quarantine. Quarantine usually can be done in the home or selected hotels and can be done at an individual level or community level. If symptoms were developed in people in the quarantine they were further investigated at the chosen health care centre. The main objective of quarantine is to stop the spread of this disease by efficiently reducing the  $R_0$  or the reproduction number of the disease to less than one [70].

### 6.3 Containment measures

When it is no longer possible to individually select infected persons and those who were in contact with them, a next method should be applied which is to implement containment measures throughout the whole community. This is meant for a whole community, region or a city instructed to lower interactions within them and to encourage people to maintain social distancing, avoid gathering, increasing awareness to slow down community transmission. Communitywide containment measures are a lot more complex process than isolation and quarantine since a larger number of people is concerned [70].

### 6.4 Personal hygiene

Maintaining personal hygiene is a very basic yet important step in preventing the spread of the COVID-19. Some vital guidelines given by WHO are as follows:

(1) Maintaining a distance of about 1metre from others whenever one goes out [71].

(2) Going to crowded places should be avoided since their people are more likely to come in contact with

each other and that way risk of virus spreading is more [71].

(3) While going outside one should always wear a mask and avoid touching the face, nose or eyes since contaminated hands can also spread this virus [71].

(4) If one is having a mild cough, cold, headache, sore throat they should stay at home and undergo self-isolation [71].

(5) Staying physically active and eating healthy foods is another imperative way to boost the body's natural immunity [71].

(6) One of the World Health Organization's important recommendations towards every individual is to wash hands frequently with any kind of soap available for at least 20seconds. World Health Organization also stated that alcohol-based hand rubs having at least 60% alcohol content can be used as a replacement for soap [48, 71].

### 6.5 The effect of soap and alcohol-based hand rubs on coronavirus

Most of the viruses including coronavirus have their genetic material enclosed by a layer of fat which is known as a lipid envelope. Soap molecules have two ends one is hydrophilic and the other one is oleophilic. The oleophilic end tends to attract the lipid layer of the virus and thus the fat layer gets pulled when soap interacts with the virus. The oleophilic end also interacts with the bond which binds the RNA and the lipid envelope and thus destroys the virus into smaller components which later gets removed by water (Fig. 4). But this whole mechanism takes about 20 seconds. Just like soap alcohol-based hand rubs also destroy the lipid envelope and thereby inactivates the virus. The alcohol-based hand rubs also denature the spike pro-



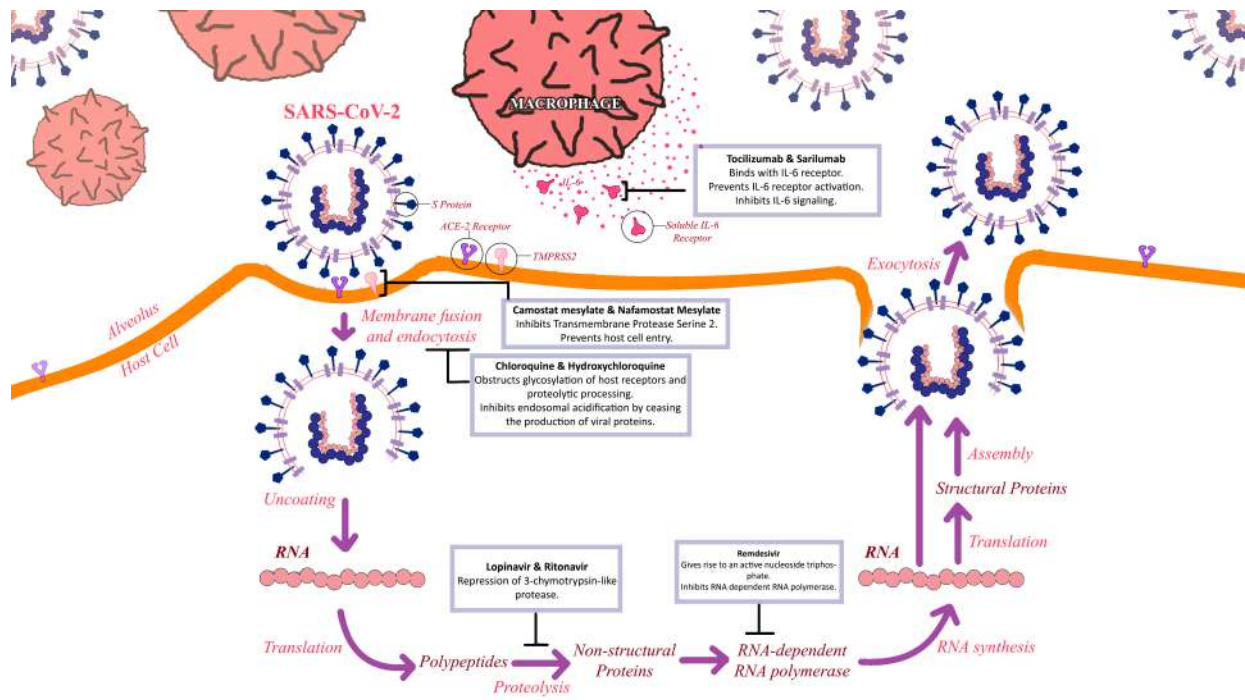


**Fig. 5. The mechanism of Severe Acute Respiratory Syndrome Coronavirus-2 entry into the host body and the actions of the discussed medications.** ACE2, Angiotensin-Converting Enzyme 2; S protein, Spike Protein; and TMPRSS2, Transmembrane protease, serine 2.

teins present at the outer surface of the virus, which helps the virus to enter the host body. The hand rubs should contain 60% alcohol content for this mechanism to be effective [72].

## 7. Possible medications

Since the inception of the breakout, various medications that affected COVID-19 have been offered. Numerous antiviral compounds were made a part of the latest guidelines from the National Health Commission, including interferon, chloroquine phosphate, ribavirin, arbidol, lopinavir/ritonavir. Angiotensin receptor blockers, such as losartan have also been recommended for the treatment of COVID-19. The COVID-19 treatment guidelines are varied between countries. The guidelines presented by World Health Organization are very general, suggesting administration of symptoms, and handling pediatric patients, pregnant women and patients with underlying comorbidities with great awareness. As of now, no approved treatment for COVID-19 has been proposed [73].

### 7.1 Medicinal plants

Medicinal plants along with their bioactive molecules have certain antiviral properties which are being considered to have potential inhibiting capabilities against SARS-CoV-2 infection (Table 1, Ref. [5]). These plants are recognized to have established antiviral properties which can inhibit viral replication and can cure certain viral infections. Some of these plants were exclusively chosen based

**Table 1. A list of the medicinal plants acting against specific target proteins and receptors are tabulated below [5].**

Specific target proteins and receptors	Name of the plants
Angiotensin-converting enzyme-2 (ACE-2)	1. <i>Rheum palmatum</i> L.
	2. <i>Citrus aurantium</i> L.
	3. <i>Rubia tinctorum</i> L.
	4. <i>Allium sativum</i> L.
3 Chymotrypsin-like protease (3CLpro)	1. <i>Torreya nucifera</i> L.
	2. <i>Houttuynia cordata</i> Thunb
	3. <i>Artemisia annua</i> L.
	4. <i>Angelica keiskei</i> (Miq.) Koidz.
RNA-dependent RNA polymerase (RdRp)	1. <i>Salvia miltiorrhiza</i> Bunge.
	2. <i>Houttuynia cordata</i> Thunb.

on the mode of action and potency, along with specific ethnobotanical evidence against coronaviruses. These plants have proven effects against specific target proteins and receptors like ACE-2 (Angiotensin-converting enzyme-2) receptor, 3CLpro (3 Chymotrypsin-like proteases), and RdRp (RNA-dependent RNA polymerase) which are mostly used by coronaviruses, and in turn, inhibits the replication of RNA [5].

The advice is to furnish supportive administration according to each patient's requirements, like antipyretics for fever, oxygen therapy for respiratory distress. World Health Organization's recommendations suggest that severe cases should be treated with observational antimicrobial therapy, with mechanical ventilation

used depending on the patient's condition. The treatment protocols across countries are pretty alike and include hydroxychloroquine, chloroquine phosphate, remdesivir, lopinavir/ritonavir (Fig. 5) [73]. The drugs which are being tested for possible treatment against COVID-19 covers two perspectives: those drugs which aim for the replication cycle of the virus and those which aim to manage the symptoms of this disease [74]. Some of the capable repurposed drugs to fight against this virus are listed below.

## 7.2 Chloroquine and hydroxychloroquine

Chloroquine and hydroxychloroquine are some known polymerase inhibitors previously used as medications for malaria. In the case of COVID-19, the virus is thought to obstruct glycosylation of host receptors, proteolytic processing and inhibits endosomal acidification by ceasing the production of viral proteins. Chloroquine in initial in vitro studies was successful in blocking COVID-19 infection at a less-micromolar concentration [74].

A succession of more than 100 COVID-19 cases was reported to be successfully treated in China by the use of chloroquine/hydroxychloroquine, which resulted in developed radiologic results, reduced disease advancement, and superior viral clearance. These reports could not be validated because of the lack of published data. A different arbitrary investigation of 30 COVID-19 patients in China was reported, it was found that they furnished no benefit over standard treatment. Another study in France presented the reports of 36 patients, of which 20 were treated with hydroxychloroquine, and the other 16 were given standard treatment. This report included improved virologic clearance with hydroxychloroquine compared to the patients receiving standard treatment. The patients in the French study who were treated with hydroxychloroquine further showed critical illness or intolerance of the medications. In addition to these limitations, concerns of additive cardiotoxicity with combination therapy were not supportive to the adoption of this medication without additional studies [75].

At a renowned medical centre in New York City, the involvement of hydroxychloroquine concerning patient's deaths was recorded. The patients who were treated with hydroxychloroquine were critically ill compared to the patients who were not treated with hydroxychloroquine. The study concluded that there was no significant involvement of hydroxychloroquine in a patient's death [76].

An international clinical trial known as The Solidarity Trial was supervised by The World Health Organization and its associates to help determine an effective treatment for COVID-19. Lopinavir/ritonavir, Remdesivir and Lopinavir/ritonavir with Interferon  $\beta$ -1a were the proposed treatment choices for the trial. By investigating numerous pieces of evidence from laboratory, clinical and animal studies, these treatment options were initially preferred. As of 17th June 2020, the hydroxychloroquine arm which was initially integrated into the study, was terminated; this was

due to the negative results that hydroxychloroquine portrayed as it did not reduce the mortality of the hospitalized COVID-19 patients as compared to standard care [75].

Records from The Solidarity Trial, The French discovery trial along with The UK's Recovery Trial were reported recently and showed that the use of hydroxychloroquine does not reduce the mortality of the hospitalized COVID-19 patients as compared to standard care [77].

## 7.3 Lopinavir/ritonavir

United States Food and Drug Administration [FDA] permitted oral drug—lopinavir/ritonavir was previously used for treating HIV and also exhibited action against other novel coronaviruses in an in vitro study employing repression of 3-chymotrypsin-like protease. The clinical studies that were associated with SARS concluded in reduced mortality and intubation rates, but their retrospective, experimental character prevents decisive outcomes. The initial peak viral replication phase which is about 7–10 days is very crucial for the administration of the drug since delayed treatment commencement with lopinavir/ritonavir would have no positive clinical outcomes [74].

Lopinavir/ritonavir is generally used in a medicating schedule for COVID-19 treatment as 400 mg/100 mg twice daily for a maximum of 14 days. Gastrointestinal distress such as hepatotoxicity, nausea and diarrhoea are a few of the side effects that lopinavir/ritonavir have on COVID-19 patients. In a recent randomized clinical trial, roughly 50% of the patients who were treated with lopinavir/ritonavir underwent adverse effects and 14% of the patients terminated its use due to gastrointestinal problems [75].

According to the solidarity trial published by the World Health Organization on 15th October 2020, lopinavir/ritonavir had little or no consequence on overall mortality, the commencement of ventilation and the total period of hospital stay in hospitalized patients [78].

## 7.4 Nafamostat and camostat

The camostat mesylate (NI-03) is a serine protease inhibitor that is effective against transmembrane protease serine 2 which inhibits SARS-CoV-2 infection in human lung cells. It was also previously used in Japan for the treatment of pancreatitis. As a medicament of COVID-19, the suitability of camostat mesylate is under evaluation in a clinical trial. Though, it is not known if sufficient compound concentrations in the lung can be attained to inhibit the viral spread [74, 75].

Due to the lack of this data, other serine protease inhibitors for obstruction of SARS-CoV-2 access being tested are very significant. Gabexate mesylate and nafamostat mesylate were tested along with camostat mesylate for suppression of SARS-CoV-2 infection in lung cells. All these drugs are permitted for human use in Japan.

The transmembrane protease serine 2-dependent host cell entry of MERS-CoV is suppressed by nafamostat mesylate. According to the results, gabexate mesylate suppressed spike protein directed host cell entry of SARS-CoV-2 minutely, whereas camostat mesylate suppressed the host entry efficiently. United States Food and Drug Administration (FDA) accepted drug, nafamostat mesylate inhibited SARS-CoV-2 spike protein operated host cell entry with much higher efficiency than camostat mesylate, with an effective concentration of 50% in the low-nanomolar range [79]. Nafamostat mesylate worked better than camostat mesylate in blocking SARS-CoV-2 infection in human lungs with greater efficiency [79].

### 7.5 Famotidine

Famotidine, the H<sub>2</sub> receptor competitor heartburn drug is being analyzed as a possible treatment for COVID-19. It was reported in Wuhan, China that patients were consuming heartburn medication after being infected by COVID-19; this reduced the likelihood of the patients' death [80]. A papain-like protease which is encoded by the genome of SARS-CoV-2 is very essential in the entry of SARS-CoV into the host body, which is restricted by famotidine [74].

### 7.6 Ivermectin

A broad-spectrum anti-parasitic drug, ivermectin is also effective against few invertebrates, is a lipophilic macrolide. In the case of COVID-19, it binds and weakens the cell-transport proteins which allow them entry into the nucleus. Observations obtained from a randomized clinical trial showed that the administration of ivermectin resulted in a reduced death rate, 7% compared to 21% in the case of patients kept under normal treatment. As for intubated patients, the death rate reduced from 21% to 7% [74, 81, 82]. In an in vitro study, it was reported that ivermectin treatment promisingly killed approximately all viral particles in 48 hours. This study was the first to approve the antiviral effect of ivermectin against COVID-19, and it concluded that it inhibited the importin  $\alpha/\beta$  receptor which is in charge of the transportation of viral proteins into the nucleus of the host cell. The authors anticipated human trials to be performed so that the possible advantages of ivermectin in the treatment of COVID-19 can be confirmed [83].

### 7.7 Tocilizumab and sarilumab

Approximately 200 patients with COVID-19 in a retrospective study, experienced major types of ailments and had greater inflammatory cytokine Interleukin-6 levels. It was assumed that cytokine-release syndrome is involved in worsening the reactions caused by the virus and resulted in acute respiratory distress syndrome even when the viral load seemed to reduce [84]. Clinical trials are being performed to test a variety of drugs that can block various cytokines. Tocilizumab and sarilumab are two of the drugs being tested out, both of which are monoclonal-

antibody competitors of Interleukin-6 receptors that are usually used as a treatment of rheumatoid arthritis and cytokine release syndrome by chimeric antigen receptor T-cell therapy. Tocilizumab, a United States Food and Drug Administration (FDA) approved medicine showed encouraging results in a randomized controlled study. A phase 2 analysis of sarilumab used in a group of patients in critical condition portrayed positive results, but a negative result was seen in a group of severely ill patients (patients requiring oxygen supplementation but not intubation). A higher dosage of sarilumab was being administered in the severe group during the third phase of the trial, while there was no change in the dosage in the case of critically ill patients [74]. A report comprising of COVID-19 positive patients showed that tocilizumab was used as a regimen of 400 mg, where 91% of patients portrayed enhanced respiratory function, faster decrease in body temperature and successful discharge, most of the patients receiving only one dose [75]. Administration of intravenous and subcutaneous tocilizumab was capable of lowering the risk of intubation or death in patients suffering from acute COVID-19 pneumonia [85].

### 7.8 Remdesivir

Remdesivir (GS-5734), a monophosphate prodrug of parent adenosine analogue which when metabolized gives rise to an active nucleoside triphosphate. In the case of COVID-19, remdesivir inhibits RNA dependent RNA polymerase. Remdesivir is a broad-spectrum antiviral drug that has confirmed effects against RNA viruses, including Coronaviridae, Flaviviridae and Filoviridae. Remdesivir was formerly developed to treat Ebola virus infection and was also effective to prevent lung bleeding, lower viral lung titers in case of murine lung infections caused by MERS-CoV [75, 86].

In Japan, the use of remdesivir in patients undergoing treatment against COVID-19 has been approved. The United States Food and Drug Administration (FDA) also permitted the use of remdesivir as an Emergency Authorization for the treatment of severely ill COVID-19 patients [87]. Successful use of remdesivir against COVID-19 has been reported in several case reports [75].

In a study, the hospitalized patients who had been infected by SARS-CoV-2 were randomized into 3 groups of patients, two of the groups were put under 5 days and 10 days of remdesivir treatment, and the third group was put under standard treatment. The study was based on results from an 11 day-long examination of the patients, which ranged from an increase in oxygen level to hospital discharge and ventilatory support to death. Another objective of this study was to determine the antagonistic effects of remdesivir administered patients compared to standard care.

On the 11th day, the results showed that patients of the 5-days treatment group gained improvement in clini-

cal status as compared to the group receiving standard care. Also, a non-statistical increase in the degradation of a patient's health in the standard care group was observed compared to the groups receiving remdesivir treatment. Remdesivir use should be prohibited for those who are hypersensitive to any of the ingredients of remdesivir. If any clinical side effects are observed, the administration of the drug should be immediately ceased and significant treatment should be initiated. When patients with moderate COVID-19 infection were treated with remdesivir, a 5-days course showed higher rates of improvement compared to those treated with standard care, ultimately annexing more evidence in favour of the use of remdesivir [87].

## 8. Vaccines designed against SARS-CoV-2

During the global outbreak of the novel Coronavirus, the scientific world is facing a major crisis due to the lack of any therapeutic vaccine. As of July 2020, over 160 vaccines for the novel Coronavirus are under development all around the globe. 25 candidate vaccines have progressed to one of the three phases of trials on humans, according to the World Health Organization. Among the 25 candidate vaccines, two Indian vaccines, namely the vaccines from Zydus and Bharat Biotech make it to the list. As of 28th July 2020, pre-clinical trials were in progress in 139 other vaccine candidates. The United States-based Moderna Therapeutics had a lead in the production of the vaccine as it had completed its phase I and II trials and already entered the phase III trials with over 30,000 volunteers being tested with the vaccine [88].

### 8.1 United States-based Moderna vaccine and Pfizer vaccine

Two 30,000-subject trials of COVID-19 vaccines were made operational by Moderna Incorporated and Pfizer Incorporated. Both the vaccines were based on the latest technology that allowed for faster development and manufacturing than normal vaccine production. The United States government made a \$1 billion investment in Moderna, which never actually brought a vaccine to the market. Pfizer also had an agreement in which the company agreed to sell the vaccines to 50 million United States citizens for approximately \$2 billion. During the announcement for Moderna's giant phase III trial, the director of the United States National Institutes of Health reportedly said that the goal of having an effective vaccine by the end of 2020 was a pretty tough one, but it was the right goal for the Americans. Pfizer vowed to produce over 1.3 billion doses of the vaccine by the end of 2021 [89].

The potential side effects of the Moderna vaccine after injecting the jab in the arm, include pain, redness, and swelling. On the other hand, tiredness, headache, muscle pain, chills, fever and nausea can be the few side effects that can be felt throughout the body. According to the results

from clinical trials, the efficacy rate of the Moderna vaccine was noted to be 94.1% after two doses of the vaccine, in patients with no prior COVID-19 infection history [90].

The possible side effects of the Pfizer vaccine after injecting the jab in the arm, include pain, redness, and swelling. Also, tiredness, headache, muscle pain, chills, fever and nausea can be the few side effects that can be felt throughout the body. According to the results from clinical trials, the efficacy rate of the Pfizer vaccine was noted to be 95%, in patients with no prior COVID-19 infection history [91].

### 8.2 Oxford University's COVID-19 vaccine (AstraZeneca)

A perfect vaccine against SARS-CoV-2 would be the one that protects the elderly people, immunosuppressed patients and people with comorbidities, would grant defence for at least 6 months; and would prevent further transmission of this virus. In the case of immunosuppressed patients, viral vectored vaccines lacking replication were used, taking into account the safety of those patients. ChAdOx1 was also able to produce immune responses in elderly people and this vaccine can be produced at a large scale, making it an encouraging contender to develop the vaccine against COVID-19. In the case of primates other than humans, this vaccine was able to develop an immune response to protect the lower respiratory tract against infection, after high dosage application of this vaccine. It can be concluded that ChAdOx1 nCoV-19 was secure, enduring and was able to produce an immune response, while paracetamol was used to reduce the expected side effects. Only a single dose triggered both humoral and cellular responses against SARS-CoV-2, with a booster immunization enhancing neutralizing antibody titers [92].

The initial findings of the first-in-human medical trial upheld clinical advancements into progressing to the phase 2 and phase 3 tests. Elderly people with comorbidities, those who are involved in healthcare works and people with more chances of vulnerability towards SARS-CoV-2 are being recruited and tested for the effectiveness, welfare and immunogenicity of ChAdOx1 nCoV-19 as single dosage or two dosage administration courses for more tests in the United Kingdom and abroad [92].

The possible side effects of the AstraZeneca vaccine after injecting the jab in the arm, include pain, redness, swelling, tenderness, itch, warmth, and swollen armpit glands. Also, fatigue, headache, muscle pain, diarrhoea, arthralgia, myalgia, fever, nausea, chills and shiver can be the few side effects that can be felt throughout the body. According to the results from AstraZeneca's primary analysis of phase 3 trial data, the efficacy rate of the vaccine was noted to be 76% after two doses of the vaccine [93–95].

**Table 2. A list of available approved vaccines in the market active against COVID-19 [90, 91, 93–95, 98, 100–106].**

Name	Vaccine type	Primary developers	Country of origin	Efficacy rate	Side effects
Comirnaty (BNT162b2)	mRNA-based vaccine	Pfizer, BioNTech, Fosun Pharma	Multinational	95%	In the arm: Pain, redness, swelling. Rest of the body: Tiredness, headache, muscle pain, chills, fever, nausea.
Moderna COVID-19 Vaccine (mRNA-1273) (AZD1222)	mRNA-based vaccine	Moderna, BARDA, NIAID	United States	94.10%	In the arm: Pain, redness, swelling. Rest of the body: Tiredness, headache, muscle pain, chills, fever, nausea.
COVID-19 Vaccine Janssen (JNJ-78436735; Ad26.COV2.S)	Non-replicating viral vector	Janssen Vaccines (Johnson & Johnson)	The Netherlands, United States	66.30%	In the arm: Pain, redness, swelling. Rest of the body: Tiredness, headache, muscle pain, chills, fever, nausea.
COVID-19 Vaccine AstraZeneca also known as Covishield	Adenovirus vaccine	BARDA, OWS	United Kingdom	76%	In the arm: Pain, redness, swelling, tenderness, itch, warmth, and swollen armpit glands. Rest of the body: Fatigue, headache, muscle pain, diarrhoea, arthralgia, myalgia, fever, nausea, chills and shiver.
CoronaVac	Inactivated vaccine (formalin with alum adjuvant)	Sinovac	China	50.38% to 91.25%	In the arm: Pain. Rest of the body: Elevated blood pressure, headache, dizziness, and rash.
BBIBP-CorV	Inactivated vaccine	Beijing Institute of Biological Products, China National Pharmaceutical Group (Sinopharm)	China	86%	In the arm: Swelling, scleroma, rash, and itching. Rest of the body: Headache, fever, fatigue, muscle ache, joint pain, cough, difficulty breathing, nausea, diarrhoea, and itchy skin.
Sputnik V	Recombinant adenovirus vaccine (rAd26 and rAd5)	Gamaleya Research Institute, Acellena	Russia	91.60%	In the arm: Pain. Rest of the body: Weakness, and fatigue, with mild flu-like symptoms.
Covaxin	Inactivated vaccine	Bharat Biotech, ICMR	India	81%	In the arm: Pain, redness, swelling, itch. Rest of the body: Malaise, headache, fever, nausea, vomiting and rashes.

### 8.3 Russia based Sputnik V

The first country to finish clinical trials of the COVID-19 vaccine on humans was Russia, as per media reports the outcomes demonstrated the vaccine's effectiveness. In a report, Elena Smolyarchuk stated that the research was completed and it proved that the vaccine was safe for humans, and the volunteers would be discharged on 15th and 20th July 2020. Two potential COVID-19 vaccines were approved for clinical trials by Russia. Gamaleya National Research Center for Epidemiology and Microbiology was in charge of the development of the Sputnik V vaccine. A liquid vaccine for intramuscular administration was carried at Burdenko Military Hospital. While another vaccine named EpiVacCorona, which is a peptide vaccine was tested under the Vektor State Research Center of Virology and Biotechnology. Immunity boost against the coronavirus was seen in the case of the volunteers on whom the vaccine was tested. According to the Russian defence ministry, the data analysis by the Gamaleya National Research Center for Epidemiology and Microbiology showed that volunteers of the first and second groups formed an immune response after they got injected with the vaccine [96, 97].

The possible side effects of the Sputnik V vaccine after injecting the jab in the arm, include pain, weakness, and fatigue, with mild flu-like symptoms. According to the reports of COVID-19 patients from 21 days after the first dose of the vaccine, the efficacy rate of the Sputnik V vaccine was noted to be 91.6% [98].

### 8.4 India based Covaxin

Bharat Biotech is an Indian biotech company that has obtained consent from the Drug Controller General of India (DCGI) to propel its COVID-19 vaccine prospect Covaxin on humans in a controlled human trial. This is the very first time an Indian domestic vaccine was approved to be tested. Approval by DCGI would allow the company to initiate Phase I and Phase II studies. In association with the Indian Council of Medical Research's National Institute of Virology, Covaxin is created. Bharat Biotech's facility in Genome Valley, Hyderabad was responsible for the development of the immobilized vaccine [99].

The possible side effects of the Covaxin vaccine after injecting the jab in the arm, include pain, redness, swelling, and itch. Also, malaise, headache, fever, nausea, vomiting and rashes can be the few side effects that can be felt throughout the body. An extreme allergic reaction may very hardly occur after getting a dose of Covaxin. According to the results from phase 3 trial data, the efficacy rate of the Covaxin vaccine was noted to be 81% after two doses of the vaccine [100].

A list of available vaccines along with their type, nature, name of developers, country of origin, efficacy rate and all the possible side effects has been well documented in the Table 2 (Ref. [90, 91, 93–95, 98, 100–106]).

## 9. Conclusions

The worldwide spread of this pandemic has shaken the world in a way that recovery seems far-fetched. But the hopes and the future possibilities are helping everyone to keep going. As of 27th July 2020, the total number of cases worldwide was noted to be 16,114,449 along with 646,641 deaths. The most number of cases being accounted in Americas (8,610,134), Europe is second (3,234,043), and South-East Asia with the third most confirmed cases (1,786,145). During such tough times, with no possible cure for the virus, implementing preventive measures would possibly be the best strategy to fight against COVID-19. To decrease the spread of the virus, widespread testing measures should be executed, with an increase in the testing rate. Newly developed and improved tracking systems along with testing kits would help the world flatten the curve. Global vaccine trials are being performed in different countries, which is the only hope for a few countries where the virus has vastly spread. The distress this pandemic has caused will take some time to fade away even after overcoming this in the future. The daily lifestyle will differ in the post-COVID-19 situations. In the future, scientists would be more prepared for the upcoming viruses and other microbial organisms that could cause such devastating losses to human life. Many aspects of COVID-19 that the scientists have observed or discovered will help them to overcome other viruses or microbial organisms that are close to SARS-CoV-2. Even with the arrival of any vaccine against COVID-19, the end of this disease will still be uncertain so people should be aware. They should maintain proper hygiene and should follow basic preventive measures such as wearing masks and maintaining social distancing. The social and economic losses several countries have suffered from this pandemic will impact the future of the people. But people should remain optimistic and learn from this adversity and be more prepared in the upcoming years.

## 10. Author contributions

Conceptualization—PB, SD, SA; Methodology—PB, SD, SA; Formal analysis and investigation—PB, SD, SA; Writing—original draft preparation—PB, SD, SA; Writing—review and editing—JS; Supervision—JS.

## 11. Ethics approval and consent to participate

Not applicable.

## 12. Acknowledgment

Not applicable.

### 13. Funding

This research received no external funding.

### 14. Conflict of interest

The authors declare no conflict of interest.

### 15. Availability of data and material

Not applicable.

### 16. Code availability

Not applicable.

### 17. References

- [1] Alzahrani FA, Saadeldin IM, Ahmad A, Kumar D, Azhar EI, Siddiqui AJ, *et al.* The Potential Use of Mesenchymal Stem Cells and their Derived Exosomes as Immunomodulatory Agents for COVID-19 Patients. *Stem Cells International*. 2020; 2020: 1–11.
- [2] Shereen MA, Khan S, Kazmi A, Bashir N, Siddique R. COVID-19 infection: Origin, transmission, and characteristics of human coronaviruses. *Journal of Advanced Research*. 2020; 24: 91–98.
- [3] Kumar R, Nagpal S, Kaushik S, Mendiratta S. COVID-19 diagnostic approaches: different roads to the same destination. *VirusDisease*. 2020; 31: 97–105.
- [4] Siddiqui AJ, Jahan S, Ashraf SA, Alreshidi M, Ashraf MS, Patel M, *et al.* Current status and strategic possibilities on potential use of combinational drug therapy against COVID-19 caused by SARS-CoV-2. *Journal of Biomolecular Structure and Dynamics*. 2020: 1–14.
- [5] Siddiqui AJ, Danciu C, Ashraf SA, Moin A, Singh R, Alreshidi M, *et al.* Plants-derived biomolecules as potent antiviral phyto-medicines: New insights on ethnobotanical evidences against coronaviruses. *Plants*. 2020; 9: 1244.
- [6] Surti M, Patel M, Adnan M, Moin A, Ashraf SA, Siddiqui AJ, *et al.* Ilimaquinone (marine sponge metabolite) as a novel inhibitor of SARS-CoV-2 key target proteins in comparison with suggested COVID-19 drugs: designing, docking and molecular dynamics simulation study. *RSC Advances*. 2020; 10: 37707–37720.
- [7] Holshue ML, DeBolt C, Lindquist S, Lofy KH, Wiesman J, Bruce H, *et al.* First Case of 2019 Novel Coronavirus in the United States. *New England Journal of Medicine*. 2020; 382: 929–936.
- [8] Meyer R. There's One Big Reason the U.S. Economy Can't Reopen. Available at: <https://www.theatlantic.com/science/archive/2020/05/theres-only-one-way-out-of-this-mess/611431/> (Accessed: 12 October 2020).
- [9] Wang J, Huth L, Umlauf T. How the CDC's Restrictive Testing Guidelines Hid the Coronavirus Epidemic: U.S. health officials' slow response to the global spread led to a lag in testing. *The Wall Street Journal*. 2020.
- [10] Wamsley L. Trump Administration Announces Measures To Speed Coronavirus Testing. NPR. 2020. Available at: <https://www.npr.org/sections/health-shots/2020/03/13/815363944/trump-administration-announces-measures-to-speed-coronavirus-testing> (Accessed: 12 October 2020).
- [11] Woods A. FDA authorizes coronavirus test that could drastically speed up screening. *Fox News*. 2020. Available at: <https://www.foxnews.com/health/fda-authorizes-coronavirus-test-could-speed-screening> (Accessed: 12 October 2020).
- [12] Mak T, Pfeiffer S, Jingnan H, Benincasa R, Smith G, Shapiro J, *et al.* A Month After Emergency Declaration, Trump's Promises Largely Unfulfilled. NPR. 2020. Available at: <https://www.npr.org/2020/04/13/832797592/a-month-after-emergency-declaration-trumps-promises-largely-unfulfilled> (Accessed: 12 October 2020).
- [13] Blake A. A timeline of Trump playing down the coronavirus threat. Available at: <https://www.washingtonpost.com/politics/2020/03/12/trump-coronavirus-timeline/> (Accessed: 12 October 2020).
- [14] Stolberg SG, Stockman F, LaFraniere S. Testing Remains Scarce as Governors Weigh Reopening States. *The New York Times*. 2020. Available at: <https://www.nytimes.com/2020/04/25/us/politics/virus-testing-shortages-states-trump.html> (Accessed: 12 October 2020).
- [15] Sprunt B, Montanaro D. FACT CHECK: Trump Claims U.S. Testing For Coronavirus Most Per Capita—It's Not. NPR. 2020. Available at: <https://www.npr.org/sections/coronavirus-live-updates/2020/04/02/826368789/fact-check-trump-claims-u-s-testing-for-coronavirus-most-per-capita-its-not> (Accessed: 12 October 2020).
- [16] TT of Israel. Defence minister claims Israel's biological institute developed virus antibody. *The Times of Israel*. 2020. Available at: <https://www.timesofisrael.com/defense-minister-claims-israels-biological-institute-developed-virus-vaccine/> (Accessed: 12 October 2020).
- [17] Branswell H. CDC launches studies to get more precise count of undetected Covid-19 cases. *STAT*. 2020. Available at: <https://www.statnews.com/2020/04/04/cdc-launches-studies-to-get-more-precise-count-of-undetected-covid-19-cases/> (Accessed: 12 October 2020).
- [18] Resnick B. Social distancing can't last forever. Here's what should come next. *RealClear*. 2020. Available at: [https://www.realclearpolicy.com/2020/03/31/social\\_distancing\\_cant\\_last\\_forever\\_heres\\_what\\_comes\\_next\\_487888.html](https://www.realclearpolicy.com/2020/03/31/social_distancing_cant_last_forever_heres_what_comes_next_487888.html) (Accessed: 12 October 2020).
- [19] Burton TM, Restuccia A, Hopkins JS. U.S. Moves to Expand Array of Drug Therapies Deployed Against Coronavirus. *The Wall Street Journal*. 2020.
- [20] Peñaloza M. Feds Warn Merchants Against Coronavirus Treatment Claims. NPR. 2020. Available at: <https://www.wnno.org/2020-04-01/feds-warn-merchants-against-coronavirus-treatment-claims> (Accessed: 12 October 2020).
- [21] The New York Times. Michigan Militia Puts Armed Protest in the Spotlight. 2020. Available at: <https://apnews.com/article/gun-politics-virus-outbreak-ap-top-news-az-state-wire-mi-state-wire-c04cc1df0c958053489bd24bb7fce93f> (Accessed: 12 October 2020).
- [22] Gearan A, Wagner J. Trump expresses support for angry anti-shutdown protesters as more states lift coronavirus lockdowns. *The Washington Post*. 2020. Available at: [https://www.washingtonpost.com/politics/trump-expresses-support-for-angry-anti-shutdown-protesters-as-more-states-lift-coronavirus-lockdowns/2020/05/01/25570dbe-8b9f-11ea-8ac1-bfb250876b7a\\_story.html](https://www.washingtonpost.com/politics/trump-expresses-support-for-angry-anti-shutdown-protesters-as-more-states-lift-coronavirus-lockdowns/2020/05/01/25570dbe-8b9f-11ea-8ac1-bfb250876b7a_story.html) (Accessed: 12 October 2020).
- [23] World Health Organization. WHO Coronavirus (COVID-19) Dashboard. 2021. Available at: <https://covid19.who.int/> (Accessed: 12 October 2020).
- [24] Severgnini C. Coronavirus, first two cases in Italy "Two Chinese people are on vacation in Rome" They arrived in Milan on 23 January. Available at: [https://www.corriere.it/cronache/20\\_gennaio\\_30/coronavirus-italia-corona-9d6dc436-4343-11ea-bdc8-faf1f56f19b7.shtml](https://www.corriere.it/cronache/20_gennaio_30/coronavirus-italia-corona-9d6dc436-4343-11ea-bdc8-faf1f56f19b7.shtml) (Accessed: 12 October 2020).
- [25] Frignani R. Coronavirus, first two cases in Italy: two Chinese tourists, husband and wife. In Italy for 7 days (landed in Milan). Available at: [https://www.corriere.it/cronache/20\\_gennaio\\_](https://www.corriere.it/cronache/20_gennaio_)

- 31/virus-primi-due-casi-italia-due-cinesi-marito-moglie-itali-a-dieci-giorni-e365df1c-43b3-11ea-bdc8-faf1f56f19b7.shtml (Accessed: 12 October 2020).
- [26] Anzolin E, Amante A. First Italian dies of coronavirus as outbreak flares in north. Ynetnews. 2020. Available at: <https://www.reuters.com/article/us-china-health-italy-idUSKBN20F0UI> (Accessed: 12 October 2020).
- [27] Ravizza S. Coronavirus: first cases in Milan. What do we know about the new infections in Lombardy, Veneto and Piedmont. Available at: [https://www.corriere.it/cronache/20-febbraio\\_22/coronavirus-italia-nuovi-contagi-lombardia-veneto-245e72d4-5540-11ea-8418-2150c9ca483e.shtml](https://www.corriere.it/cronache/20-febbraio_22/coronavirus-italia-nuovi-contagi-lombardia-veneto-245e72d4-5540-11ea-8418-2150c9ca483e.shtml) (Accessed: 12 October 2020).
- [28] Avvenire. Coronavirus. Hit all regions. Civil Protection: here are the updated numbers. Available at: <https://www.avvenire.it/attualita/pagine/coronavirus-aggiornamento-5-marzo-2020> (Accessed: 12 October 2020).
- [29] Ananasso A, de Stabile E, Gagliardi G, Matteucci P. Coronavirus in Italy: all the news from February. Available at: [https://www.repubblica.it/cronaca/2020/02/22/news/coronavirus\\_in\\_italia\\_aggiornamento\\_ora\\_per\\_ora-249241616/](https://www.repubblica.it/cronaca/2020/02/22/news/coronavirus_in_italia_aggiornamento_ora_per_ora-249241616/) (Accessed: 12 October 2020).
- [30] Bartoloni M. Coronavirus, how quarantine works and what threatens those who violate it (arrest). Available at: [https://www.ilsole24ore.com/art/coronavirus-chi-viola-quarantena-rischia-l-arresto-fino-tre-mesi-ACrnlLB?refresh\\_ce=1](https://www.ilsole24ore.com/art/coronavirus-chi-viola-quarantena-rischia-l-arresto-fino-tre-mesi-ACrnlLB?refresh_ce=1) (Accessed: 12 October 2020).
- [31] BBC. Coronavirus: Venice Carnival closes as Italy imposes lockdown. 2020. Available at: <https://www.bbc.com/news/world-europe-51602007> (Accessed: 12 October 2020).
- [32] BBC. Coronavirus: Northern Italy quarantines 16 million people. 2020. Available at: <https://www.bbc.com/news/world-mid-east-51787238> (Accessed: 12 October 2020).
- [33] BBC. Coronavirus: Italy extends emergency measures nationwide. 2020. Available at: <https://www.bbc.com/news/world-europe-51810673> (Accessed: 12 October 2020).
- [34] Safi M, Giuffrida A, Farrer M. Coronavirus: Italy bans any movement inside country as toll rises 5,500. 2020. Available at: <https://www.theguardian.com/world/2020/mar/22/italian-pm-warns-of-worst-crisis-since-ww2-as-coronavirus-deaths-leap-by-almost-800> (Accessed: 12 October 2020).
- [35] Lau H, Khosrawipour V, Kocbach P, Mikolajczyk A, Ichii H, Schubert J, *et al.* Internationally lost COVID-19 cases. *Journal of Microbiology, Immunology and Infection.* 2020; 53: 454–458.
- [36] Reuters. The total number of Italian coronavirus cases could be ‘10 times higher’ than known tally, according to one official. Available at: <https://www.cnbc.com/2020/03/24/italian-coronavirus-cases-seen-10-times-higher-than-official-tally.html> (Accessed: 12 October 2020).
- [37] The Local. Italy’s coronavirus deaths rise slightly, but new cases continue to slow. 2020. Available at: <https://www.thelocal.it/20200330/latest-coronavirus-deaths-italy> (Accessed: 12 October 2020).
- [38] Agenzia Italia. “Italy has peaked,” says the Higher Institute of Health. 2020. Available at: <https://www.agi.it/cronaca/news/2020-03-31/coronavirus-istituto-superiore-sanit-picco-8038210/> (Accessed: 12 October 2020).
- [39] The Local. Pressure on Italy’s intensive care wards eases as new coronavirus cases slow again. 2020. Available at: <https://www.thelocal.it/20200406/latest-coronavirus-numbers-italy> (Accessed: 12 October 2020).
- [40] della Sera C. Schools closed for Coronavirus in Lombardy, Veneto and Emilia Romagna: the list of municipalities. Available at: [https://www.corriere.it/cronache/20-febbraio\\_21/scuole-chiuse-il-coronavirus-lombardia-lodi-piacenza-codogno-a190ccee-54bd-11ea-9196-da7d305401b7.shtml](https://www.corriere.it/cronache/20-febbraio_21/scuole-chiuse-il-coronavirus-lombardia-lodi-piacenza-codogno-a190ccee-54bd-11ea-9196-da7d305401b7.shtml) (Accessed: 12 October 2020).
- [41] Matteucci P. Coronaviruses, school and university closures, demonstrations and public places: measures region by region. 2020. Available at: [https://www.repubblica.it/cronaca/2020/02/23/news/coronavirus\\_scuole\\_chiuse\\_e\\_niente\\_carnevale\\_tutti\\_i\\_provvedimenti-249355737/](https://www.repubblica.it/cronaca/2020/02/23/news/coronavirus_scuole_chiuse_e_niente_carnevale_tutti_i_provvedimenti-249355737/) (Accessed: 12 October 2020).
- [42] Lorello M. Coronavirus, for a suspended teaching week in Lombardy universities. Milan municipality and large companies: at-risk workers stay at home. 2020. Available at: [https://milano.repubblica.it/cronaca/2020/02/22/news/coronavirus\\_il\\_comune\\_di\\_milano\\_sospende\\_dal\\_lavoro\\_i\\_dipendenti\\_che\\_abitano\\_delle\\_zone\\_coinvolte-249252812/](https://milano.repubblica.it/cronaca/2020/02/22/news/coronavirus_il_comune_di_milano_sospende_dal_lavoro_i_dipendenti_che_abitano_delle_zone_coinvolte-249252812/) (Accessed: 12 October 2020).
- [43] della Sera C. Coronavirus, trains stopped for hours in Lecce and Milan. Convoys do not stop in the municipalities at risk of the Lodigiano. Available at: [https://www.corriere.it/cronache/20-febbraio\\_22/coronavirus-treni-fermi-ore-lecce-milano-nessuno-stop-comuni-rischio-lodigiano-431e997c-553d-11ea-8418-2150c9ca483e.shtml](https://www.corriere.it/cronache/20-febbraio_22/coronavirus-treni-fermi-ore-lecce-milano-nessuno-stop-comuni-rischio-lodigiano-431e997c-553d-11ea-8418-2150c9ca483e.shtml) (Accessed: 12 October 2020).
- [44] Repubblica L. The closed staircase for the coronavirus: in more than two centuries it had happened only six times. 2020. Available at: [https://milano.repubblica.it/cronaca/2020/02/23/news/coronavirus\\_scala\\_milano\\_chiusure\\_nella\\_storia-249380233/](https://milano.repubblica.it/cronaca/2020/02/23/news/coronavirus_scala_milano_chiusure_nella_storia-249380233/) (Accessed: 12 October 2020).
- [45] Giannattasio M. Coronavirus, closed schools, gyms and clubs: guide to curfew in the North. Available at: [https://milano.corriere.it/notizie/cronaca/20-febbraio\\_23/coronavirus-chiuse-scuole-palestre-locali-guida-coprifuoco-nord-00193c74-568a-11ea-b447-d9646dbdb12a.shtml](https://milano.corriere.it/notizie/cronaca/20-febbraio_23/coronavirus-chiuse-scuole-palestre-locali-guida-coprifuoco-nord-00193c74-568a-11ea-b447-d9646dbdb12a.shtml) (Accessed: 12 October 2020).
- [46] Avvenire. Coronavirus. Churches open but Masses suspended. Archbishop Delpini’s Prayer. 2020. Available at: <https://www.avvenire.it/chiesa/pagine/milano-l-arcivescovo-delpini-un-pensiero-di-benedizione> (Accessed: day month year).
- [47] Huang C, Wang Y, Li X, Ren L, Zhao J, Hu Y, *et al.* Clinical features of patients infected with 2019 novel coronavirus in Wuhan, China. *Lancet.* 2020; 395: 497–506.
- [48] Leitner T, Kumar S. Where did SARS-CoV-2 Come from? *Molecular Biology and Evolution.* 2020; 37: 2463–2464.
- [49] Mahase E. China coronavirus: mild but infectious cases may make it hard to control outbreak, report warns. *British Medical Journal.* 2020; 368: m325.
- [50] Vara V. Coronavirus in India: how the COVID-19 could impact the fast-growing economy. 2020. Available at: <https://www.pharmaceutical-technology.com/features/coronavirus-affected-countries-india-measures-impact-pharma-economy/> (Accessed: 12 October 2020).
- [51] Kachroo V. Novel Coronavirus (COVID-19) in India: Current Scenario. *International Journal of Research and Review.* 2020; 7: 435–447.
- [52] Negandhi H, Zodpey S, Dua A, Vasudevan A, Raja M. Our fight against the rapidly evolving COVID-19 pandemic: a review of India’s actions and proposed way forward. *Indian Journal of Community Medicine.* 2020; 45: 117–124.
- [53] Delhi P. India’s response to COVID outbreak. 2020. Available at: <https://pib.gov.in/PressReleasePage.aspx?PRID=1608727> (Accessed: 12 October 2020).
- [54] Sharma A. Truenat Beta Test for COVID-19 detection in India. Invest India. 2020. Available at: <https://www.investindia.gov.in/team-india-blogs/truenat-beta-test-covid-19-detection-india> (Accessed: 12 October 2020).
- [55] Kim PS. South Korea’s fast response to coronavirus disease: implications on public policy and public management theory. *Public Management Review.* 2020; 1–12. (in press)
- [56] Kang J, Jang YY, Kim J, Han S, Lee KR, Kim M, *et al.* South Korea’s responses to stop the COVID-19 pandemic. *American Journal of Infection Control.* 2020; 48: 1080–1086.
- [57] Lee SY, Choi SH, Park JE, Hwang S, Kwon KT. Crucial role of temporary airborne infection isolation rooms in an intensive



- care unit: containing the COVID-19 outbreak in South Korea. *Critical Care*. 2020; 24: 238.
- [58] Lim S, Yoon HI, Song K, Kim ES, Kim HB. Face masks and containment of COVID-19: experience from South Korea. *Journal of Hospital Infection*. 2020; 106: 206–207.
- [59] Chung DJ. What South Korea Teaches The World About Fighting COVID. 2020. Available at: <https://www.forbes.com/sites/hbsworkingknowledge/2020/06/16/what-south-korea-teaches-the-world-about-fighting-covid/?sh=6fae3a5c3e36> (Accessed: 12 October 2020).
- [60] Panoutsopoulos AA. Conjunctivitis as a Sentinel of SARS-CoV-2 Infection: a need of Revision for Mild Symptoms. *SN Comprehensive Clinical Medicine*. 2020; 2: 859–864.
- [61] Brandini DA, Takamiya AS, Thakkar P, Schaller S, Rahat R, Naqvi AR. Covid-19 and oral diseases: Crosstalk, synergy or association? *Reviews in Medical Virology*. 2021. (in press)
- [62] Das P, Choudhuri T. Decoding the global outbreak of COVID-19: the nature is behind the scene. *VirusDisease*. 2020; 31: 106–112.
- [63] Walls AC, Park Y, Tortorici MA, Wall A, McGuire AT, Veesler D. Structure, Function, and Antigenicity of the SARS-CoV-2 Spike Glycoprotein. *Cell*. 2020; 181: 281–292.e6.
- [64] Bertram S, Glowacka I, Müller MA, Lavender H, Gnirss K, Nehlmeier I, *et al.* Cleavage and activation of the severe acute respiratory syndrome coronavirus spike protein by human airway trypsin-like protease. *Journal of Virology*. 2011; 85: 13363–13372.
- [65] Glowacka I, Bertram S, Müller MA, Allen P, Soilleux E, Pfeifferle S, *et al.* Evidence that TMPRSS2 activates the severe acute respiratory syndrome coronavirus spike protein for membrane fusion and reduces viral control by the humoral immune response. *Journal of Virology*. 2011; 85: 4122–4134.
- [66] van Doremalen N, Bushmaker T, Morris DH, Holbrook MG, Gamble A, Williamson BN, *et al.* Aerosol and Surface Stability of SARS-CoV-2 as Compared with SARS-CoV-1. *New England Journal of Medicine*. 2020; 382: 1564–1567.
- [67] World Health Organization. Coronavirus. Available at: [https://www.who.int/health-topics/coronavirus#tab=tab\\_1](https://www.who.int/health-topics/coronavirus#tab=tab_1) (Accessed: 12 October 2020).
- [68] Singhal T. A Review of Coronavirus Disease-2019 (COVID-19) the Indian Journal of Pediatrics. 2020; 87: 281–286.
- [69] Beiu C, Mihai M, Popa L, Cima L, Popescu MN. Frequent Hand Washing for COVID-19 Prevention can Cause Hand Dermatitis: Management Tips. *Cureus*. 2020; 12: e7506.
- [70] Wilder-Smith A, Chiew CJ, Lee VJ. Can we contain the COVID-19 outbreak with the same measures as for SARS? *Lancet Infectious Diseases*. 2020; 20: e102–e107.
- [71] World Health Organization. Coronavirus disease (COVID-19) advice for the public. Available at: <https://www.who.int/emergencies/diseases/novel-coronavirus-2019/advice-for-public> (Accessed: 12 October 2020).
- [72] Resnick B. How soap absolutely annihilates the coronavirus. Available at: <https://www.vox.com/science-and-health/2020/3/11/21173187/coronavirus-covid-19-hand-washing-sanitizer-compared-soap-is-dope> (Accessed: 12 October 2020).
- [73] Tobaiqy M, Qashqary M, Al-Dahery S, Mujallad A, Hershman AA, Kamal MA, *et al.* Therapeutic management of patients with COVID-19: a systematic review. *Infection Prevention in Practice*. 2020; 2: 100061.
- [74] Shaffer L. 15 drugs being tested to treat COVID-19 and how they would work. *Nature Medicine*. 2020. (in press)
- [75] Sanders JM, Monogue ML, Jodlowski TZ, Cutrell JB. Pharmacologic Treatments for Coronavirus Disease 2019 (COVID-19). *Journal of the American Medical Association*. 2020; 323: 1824–1836.
- [76] Geleris J, Sun Y, Platt J, Zucker J, Baldwin M, Hripcsak G, *et al.* Observational Study of Hydroxychloroquine in Hospitalized Patients with Covid-19. *New England Journal of Medicine*. 2020; 382: 2411–2418.
- [77] World Health Organization. Q&A : Hydroxychloroquine and COVID-19. Available at: <https://www.who.int/news-room/q-a-detail/coronavirus-disease-covid-19-hydroxychloroquine> (Accessed: 12 October 2020).
- [78] WHO Solidarity Trial Consortium, Pan H, Peto R, Henaou-Restrepo AM, Preziosi MP, Sathiyamoorthy V, *et al.* Repurposed Antiviral Drugs for Covid-19 — Interim WHO Solidarity Trial Results. *New England Journal of Medicine*. 2021; 384: 497–511.
- [79] Hoffmann M, Schroeder S, Kleine-Weber H, Müller MA, Drosten C, Pöhlmann S. Nafamostat Mesylate Blocks Activation of SARS-CoV-2: New Treatment Option for COVID-19. *Antimicrobial Agents and Chemotherapy*. 2020; 64: 1–3.
- [80] Freedberg DE, Conigliaro J, Wang TC, Tracey KJ, Callahan MV, Abrams JA, *et al.* Famotidine Use is Associated with Improved Clinical Outcomes in Hospitalized COVID-19 Patients: a Propensity Score Matched Retrospective Cohort Study. *Gastroenterology*. 2020; 159: 1129–1131.e3.
- [81] Rajter JC, Sherman MS, Fatteh N, Vogel F, Sacks J, Rajter J. Use of Ivermectin is Associated with Lower Mortality in Hospitalized Patients with Coronavirus Disease 2019. *Chest*. 2021; 159: 85–92.
- [82] Vallejos J, Zoni R, Bangher M, Villamandos S, Bobadilla A, Plano F, *et al.* Ivermectin to prevent hospitalizations in patients with COVID-19 (IVERCOR-COVID19): a structured summary of a study protocol for a randomized controlled trial. *Trials*. 2020; 21: 965.
- [83] Heidary F, Gharebaghi R. Ivermectin: a systematic review from antiviral effects to COVID-19 complementary regimen. *Journal of Antibiotics*. 2020; 73: 593–602.
- [84] Zhou F, Yu T, Du R, Fan G, Liu Y, Liu Z, *et al.* Clinical course and risk factors for mortality of adult inpatients with COVID-19 in Wuhan, China: a retrospective cohort study. *Lancet*. 2020; 395: 1054–1062.
- [85] Guaraldi G, Meschiari M, Cozzi-Lepri A, Milic J, Tonelli R, Menozzi M, *et al.* Tocilizumab in patients with severe COVID-19: a retrospective cohort study. *Lancet Rheumatology*. 2020; 2: e474–e484.
- [86] Grein J, Ohmagari N, Shin D, Diaz G, Asperges E, Castagna A, *et al.* Compassionate Use of Remdesivir for Patients with Severe Covid-19. *New England Journal of Medicine*. 2020; 382: 2327–2336.
- [87] Spinner CD, Gottlieb RL, Criner GJ, Arribas López JR, Cattelan AM, Soriano Viladomiu A, *et al.* Effect of Remdesivir vs Standard Care on Clinical Status at 11 Days in Patients with Moderate COVID-19: A Randomized Clinical Trial. *Journal of the American Medical Association*. 2020; 324: 1048–1057.
- [88] TI Express. Covid-19 vaccine tracker, July 28: India is at the centre of vaccine, and Moderna's phase III trials. Available at: <https://indianexpress.com/article/explained/covid-coronavirus-vaccine-update-6526457/> (Accessed: 12 October 2020).
- [89] O'Donnell C. Moderna, Pfizer start decisive Covid-19 vaccine trials, eye year-end launches. *Reuters*. 2020. Available at: <https://timesofindia.indiatimes.com/home/science/moderna-pfizer-start-decisive-covid-19-vaccine-trials-eye-year-end-launches/articleshow/77210988.cms> (Accessed: 12 October 2020).
- [90] CDC. Moderna COVID-19 Vaccine Overview and Safety. 2021. Available at: <https://www.cdc.gov/coronavirus/2019-ncov/vaccines/different-vaccines/Moderna.html> (Accessed: 12 October 2020).
- [91] CDC. Pfizer-BioNTech COVID-19 Vaccine Overview and Safety. 2021. Available at: <https://www.cdc.gov/coronavirus/2019-ncov/vaccines/different-vaccines/Pfizer-BioNTech.html> (Accessed: 12 October 2020).
- [92] Folegatti PM, Ewer KJ, Aley PK, Angus B, Becker S, Bellij-Rammerstorfer S, *et al.* Safety and immunogenicity of the ChAdOx1 nCoV-19 vaccine against SARS-CoV-2: a preliminary report of a phase 1/2, single-blind, randomised controlled trial. *Lancet*. 2020; 396: 467–478.

- [93] Minseo Jeong. Oxford-AstraZeneca vaccine: What to know about side effects. 2021. Available at: <https://www.medicalnewstoday.com/articles/oxford-astrazeneca-vaccine-what-to-know-about-side-effects> (Accessed: 12 October 2020).
- [94] C Bonquin. Five most common side effects of AstraZeneca, Sinovac vaccines. 2021. Available at: <https://www.cnnphilippines.com/news/2021/4/20/Five-most-common-side-effects-AstraZeneca-Sinovac-vaccines.html> (Accessed: 12 October 2020).
- [95] Menni C, Klaser K, May A, Polidori L, Capdevila J, Louca P, *et al.* Vaccine side-effects and SARS-CoV-2 infection after vaccination in users of the COVID Symptom Study app in the UK: a prospective observational study. *The Lancet Infectious Diseases*. 2021; 21: 939–949.
- [96] IANS. Russia 1st nation to finish human trials for Covid-19 vaccine. 2020. Available at: <https://health.economictimes.india.com/news/industry/russia-1st-nation-to-finish-human-trials-for-covid-19-vaccine/76938659> (Accessed: 12 October 2020).
- [97] Beall M, Bolt B, Felton C, Germann L, Goode AL, Kyril S, *et al.* EpiVacCorona Vaccine. 2021. Available at: <https://www.precisionvaccinations.com/vaccines/epivaccorona-vaccine> (Accessed: 12 October 2020).
- [98] Jones I, Roy P. Sputnik V COVID-19 vaccine candidate appears safe and effective. *Lancet*. 2021; 397: 642–643.
- [99] CTA. India's first Covid-19 vaccine by Bharat Biotech to enter trials. 2020. Available at: <https://www.clinicaltrialsarena.com/news/india-bharat-biotech-vaccine-trials/> (Accessed: 12 October 2020).
- [100] BHARATB iotech. COVAXIN SARS-CoV-2 VACCINE BY BHARAT BIOTECH. Available at: <https://www.bharatbiotech.com/images/covaxin/covaxin-fact-sheet.pdf> (Accessed: 12 October 2020).
- [101] Craven J. COVID-19 vaccine tracker. *Regulatory Focus*. 2021. Available at: <https://www.raps.org/news-and-articles/news-articles/2020/3/covid-19-vaccine-tracker> (Accessed: 12 October 2020).
- [102] Terry M. UPDATED Comparing COVID-19 Vaccines: Timelines, Types and Prices. 2021. Available at: <https://www.biospace.com/article/comparing-covid-19-vaccines-pfizer-biotech-moderna-astrazeneca-oxford-j-and-j-russia-s-sputnik-v/> (Accessed: 12 October 2020).
- [103] Hilotin J. UAE: Ministry of Health announces 86 per cent vaccine efficacy. 2020. Available at: <https://gulfnews.com/uae/health/uae-ministry-of-health-announces-86-per-cent-vaccine-efficacy-1.1607490555571> (Accessed: 12 October 2020).
- [104] CDC. Johnson & Johnson's Janssen COVID-19 Vaccine Overview and Safety. 2021. Available at: <https://www.cdc.gov/coronavirus/2019-ncov/vaccines/different-vaccines/janssen.html> (Accessed: 12 October 2020).
- [105] Corum J, Zimmer C. How the Sinovac Vaccine Works. 2021. Available at: <https://www.nytimes.com/interactive/2020/health/sinovac-covid-19-vaccine.html> (Accessed: 12 October 2020).
- [106] Everington K. Full list of adverse reactions from China's Sinopharm vaccine revealed. 2021. Available at: <https://www.taiwannews.com.tw/en/news/4098913> (Accessed: 12 October 2020).

**Keywords:** COVID-19; Global outbreak; Morphology; Oxford's vaccine; Remdesivir; SARS-CoV-2

**Send correspondence to:** Joy Sarkar, Department of Botany, Dinabandhu Andrews College, Garia, Kolkata, 700084 West Bengal, India, E-mail: [jsarkar80@gmail.com](mailto:jsarkar80@gmail.com)

† These authors contributed equally.



# Source details

[Feedback >](#) [Compare sources >](#)

## Frontiers in Bioscience - Elite

Formerly included in: [Frontiers in Bioscience - Landmark](#)

[Open Access](#) [i](#)

Scopus coverage years: from 2009 to Present

Publisher: IMR Press Limited

ISSN: 1945-0494 E-ISSN: 1945-0508

Subject area: [Immunology and Microbiology: General Immunology and Microbiology](#)

[Biochemistry, Genetics and Molecular Biology: General Biochemistry, Genetics and Molecular Biology](#)

Source type: Journal

[View all documents >](#)[Set document alert](#)[Save to source list](#)

CiteScore 2022

3.2



SJR 2022

0.414



SNIP 2022

0.705



Contents lists available at [ScienceDirect](https://www.sciencedirect.com)

# Clinical Epidemiology and Global Health

journal homepage: [www.elsevier.com/locate/cegh](http://www.elsevier.com/locate/cegh)

Review article

## A comprehensive review of various categories of face masks resistant to Covid-19

Sonali Das<sup>a,1</sup>, Sagarika Sarkar<sup>b,1</sup>, Anusree Das<sup>a,1</sup>, Shreyosree Das<sup>a,1</sup>, Pallab Chakraborty<sup>c,1</sup>, Joy Sarkar<sup>a,\*</sup>

<sup>a</sup> Department of Botany, Dinabandhu Andrews College, 54, Raja S.C. Mallick Road, Garia, Kolkata, West Bengal, 700084, India

<sup>b</sup> Department of Botany, Sarojini Naidu College for Women, 30, Jessore Rd, K.B.Sarani, Golpark, Kolkata, West Bengal, 700028, India

<sup>c</sup> Department of Botany, Acharya Prafulla Chandra College, New Barrakpur, Kolkata, West Bengal, 700131, India



### ARTICLE INFO

**Keywords:**  
COVID-19  
WHO  
Mask  
Pandemic

### ABSTRACT

The science about the usage of face masks by the common public to avert COVID-19 transmission is proceeding swiftly. A primary route of transmission of COVID-19 is probably through small respiratory droplets, and it is transmissible from asymptomatic and pre-symptomatic individuals. According to the World Health Organization, wearing a mask in public can help reduce the transmission of the COVID-19 virus. Different categories and types of masks and their usage are reviewed in this work. In a nutshell, this review work elucidates the aspects of utilizing the various face masks along with all possibilities to fight against the ongoing pandemic of COVID-19.

### 1. Introduction

World Health Organization (WHO), announced on January 30, 2020, a Public Health Emergency of International Concern (PHEIC) in response to the emergence of a novel coronavirus in Wuhan, China. Later, on March 11, 2020, WHO announced COVID-19 to be a pandemic, it is the 2nd pandemic of the 21st century after the pandemic of 2009 caused by influenza A H1N1.<sup>1,2</sup>

In the declaration by WHO on February 11, 2020, the Coronavirus disease (COVID-19) is caused by the virus named severe acute respiratory syndrome coronavirus 2 (SARS-CoV-2), which is genetically related to the coronavirus responsible for the SARS outbreak of 2003.<sup>3</sup>

As of August 29, 2020, more than 24.7 million cases have been reported across 188 countries and territories, causing more than 837,000 deaths with a recovering of 16.2 million people. In this case, proactive infection monitoring criteria have been executed in hospital set-ups.<sup>4,5</sup>

To control the further outbreak of pandemic disease COVID-19 among people, WHO provided some guidelines and instructions to the general public to follow such as the continuous practice of hand hygiene, maintaining social distancing, wearing a mask in public, avoiding social gatherings and practising self-isolation and home quarantine. In addition, with the guidelines of WHO, the authorities also implemented some rules such as quarantine and testing of all travellers, closing and

regulating the city and country borders, along with massive testing for case detection by RT-PCR (reverse-transcription polymerase chain reaction) technique. Later, stay at home order, lockdowns, home isolation, cancellation of mass gatherings and prohibiting traveling were acquired to several degrees and at various time points in several countries to alleviate the threat of community transmission. It is unclear when the outbreak will end, and there are no known vaccines or antiviral therapies that are 100% effective against the coronavirus.<sup>3,5</sup> Though there has been working on immunization and numerous vaccines have been created so far, none of them can guarantee 100 % efficacy against SARS-CoV-2.<sup>6-8</sup>

To handle the ongoing COVID -19 pandemic situation, the US Centers for Disease Control and Prevention (CDC) had recommended the public to put on face masks. Many Asian countries, which have had greater experience with new coronavirus infections, use public masks significantly more frequently. Face Masks have been recommended as a primary potent tool to control the COVID-19 outbreak in China.<sup>9</sup> However, the World Health Organization (WHO) advises that face masks should only be worn by individuals caring for patients with suspected COVID-19 or those who are actively sneezing or coughing.<sup>10</sup>

Many governments around the world have introduced policies that recommend the wearing of masks to slow down the expanse of COVID-19. Mandatory use and enforcement vary globally. While several

\* Corresponding author.

E-mail address: [jsarkar80@gmail.com](mailto:jsarkar80@gmail.com) (J. Sarkar).

<sup>1</sup> These authors have contributed equally to this work.

<https://doi.org/10.1016/j.cegh.2021.100835>

Received 30 March 2021; Received in revised form 28 June 2021; Accepted 21 July 2021

Available online 2 August 2021

2213-3984/© 2021 The Author(s). Published by Elsevier B.V. on behalf of INDIACLEN. This is an open access article under the CC BY-NC-ND license

(<http://creativecommons.org/licenses/by-nc-nd/4.0/>).

countries have passed legislation requiring the use of masks, others, like China, India, Japan, South Korea, and Taiwan, have issued more precise guidelines.<sup>11</sup>

With the exponential spread and emergence of COVID 19, the usage and utility of masks and respirators for the common people have been advised by the government.<sup>10</sup> The US CDC has recommended that the usage of Medical masks, surgical masks, cloth masks, fabric masks, and extended use of respirators can be deliberated with proper caution. Medical masks i.e., N95 respirators and surgical masks are prioritized for healthcare professionals which appears to protect against the virus.<sup>12</sup> Countries, like Italy and Mexico, provided single-use masks for the common public upon mandating their use.<sup>11</sup> If medical masks, surgical masks or respirators are not available then the general public can use homemade cloth masks that provide lesser protection but still afford the efficacy.<sup>13</sup> Japan offered cotton masks without imposing mandatory use, whereas the Czech Republic and the United Kingdom urged citizens to use reusable masks.<sup>11</sup> There is not yet enough data to determine which combination of mask policies are most effective in slowing the expanse of infection. However, it is advised to wear reusable face coverings or masks for the general public as an alternative to the single use face mask or surgical face masks used in healthcare sector. The usage of reusable cloth mask are effective in combating virus transmission to a certain extent when combined with non-clinical interventions such as maintaining social distance and hand hygiene.<sup>11</sup> In one of the surveys, it is reported that 28,000 people aged between 16 and 74 years in 15 countries wore face masks because of the coronavirus outbreak. About more than 70 % of people in India, China, Italy, Japan and Vietnam wore reusable face masks to protect themselves from coronavirus outbreaks. In the USA and other countries, the percentage is 50 % and above.<sup>9,11</sup> The sensations during the previous five months show that mask usage was usually high (>75 %) in certain locations, such as Asia and South and Central America, whereas it was always low (25 %) in Northern Europe. In some nations, an improvement over time has been observed, which might help in evaluating the surging cases of covid-19 or mask-related requirements and guidance.<sup>11</sup>

These and associated data can support inform public health communications campaigns and endeavors considering mask-wearing to help slow the expanse of COVID-19 and could be borrowed to help

evaluate how policies associate to practice around the world.

In this paper, we seek to elucidate the different aspects of masks. Specifically, we explore the different varieties of masks, their material composition and effectiveness in protecting the wearer from an airborne virus along with the guidelines of usage of masks and caring method of masks in detail.

We tend to provide more information to the general public about the types of masks and what mask they should choose in case of no medical or surgical mask is available.

### 1.1. Transmission characteristics of Covid-19

Every day, new information concerning the COVID-19's transmission emerges. It is mainly a respiratory disease and the spread of infection with this virus can range from people with mild, non-respiratory symptoms to extreme acute respiratory ailment, along with organ dysfunction, sepsis and death, while some infected people have no symptoms at all. According to recent reports, the coronavirus is transmitted among people via contact routes and respiratory droplets. Transmission can also happen through fomites in the infected person's immediate environment. Therefore, transmission can occur by direct contact with an infected person, or indirectly by contact with surfaces or objects used on or by the infected person<sup>5,14</sup> (Fig. 1).

The threshold for the droplet size is ranging from 5  $\mu\text{m}$  to 10  $\mu\text{m}$ . Droplet transmission happens when a healthy individual comes in close contact within 1 m with an infected person and is exposed to infectious respiratory droplets, through coughing, sneezing or close personal contact by mouth or nose.<sup>15</sup>

Airborne transmission of the COVID-19 virus may be possible in particular conditions where procedures to generate aerosols are performed. The research community has been discussing, whether the coronavirus, might furthermore circulate by aerosols in the deficiency of aerosol-generating procedures (AGPs). This is a province of strong research. As, air testing in clinical atmospheres where AGPs were not conducted, found RNA virus in some observations but not in others.<sup>16</sup> Nevertheless, the existence of viral RNA is never similar to replication and infection competent (viable) virus that could be transmissible and able to adequate inoculum to commence invasive infection. Few

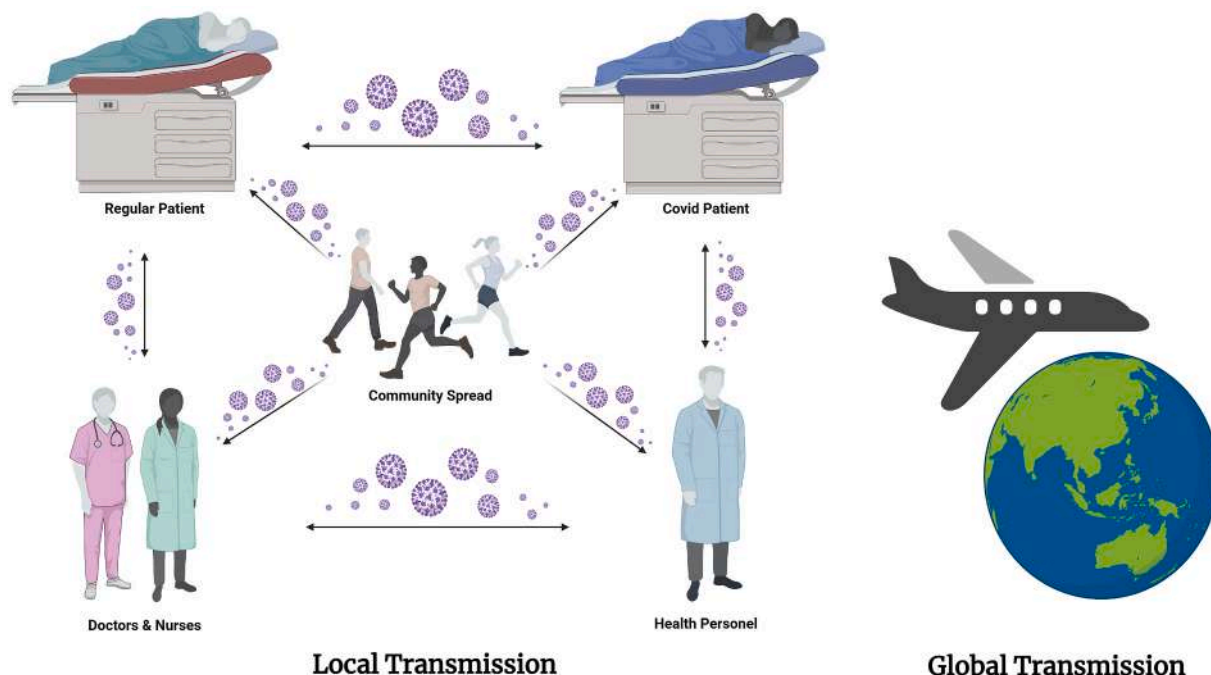


Fig. 1. Diagram shows the different modes of COVID-19 disease transmission (Created with BioRender.com).

experimental studies performed by aerobiology laboratories have found the viable virus and viral RNA, but these were experimentally induced AGP where aerosols were produced artificially using high-powered jet nebulizers and do not imitate normal human cough conditions.<sup>17</sup>

To address several of the acknowledged research gaps connected with AGPs and COVID-19 virus airborne propagation, high-quality research involving randomised trials in a variety of situations is required.

Recent information recommends that maximum expanse of COVID-19 is happening from symptomatic people to others in near contact, when not wearing proper PPE. Amongst the infected persons with symptoms, viral RNA can be found in their specimens', weeks afterwards the commencement of sickness. However, for moderately infected individuals, the viable virus was not discovered after 8 days after the onset of symptoms, albeit this can change for very ill patients.<sup>18</sup> In pre-symptomatic transmission, the infected person with no symptoms can transmit the virus to others. SARS-CoV-2 has an incubation period of 5- to 6-days, but it can last up to 14 days.<sup>19,20</sup> Besides that, some data indicate that many people may test positive for coronavirus, using polymerase chain reaction (PCR) testing, 1–4 days before any symptoms develop.<sup>21</sup>

As per reports, some individuals infected with the SARS-CoV-2 virus does not ever develop any symptoms, though they can shed the virus that may, therefore, be transmitted to other people. According to a recent systematic analysis, 6 %–42 % of infected people are asymptomatic, and most of the studies in their evaluation have limitations due to inadequate symptom reporting. Comprehensive researches on the transmission from asymptomatic people are tough to perform, but the accessible proof from contact tracing documented by the Member States implies that asymptotically infected patients are much less likely to transmit the virus than those who develop symptoms.<sup>22</sup>

### 1.2. Recommendations for wearing a face mask

There have been reports on the usage of surgical face masks on patients with pulmonary tuberculosis, which significantly reduced transmission and offer an adjunct measure for reducing TB transmission from infectious patients to healthy persons.<sup>23,24</sup> The surgical mask has further been revealed to disengage other human coronaviruses during coughing. In addition, a meta-analysis of randomised trials found that surgical masks and N95 respirators were equally effective in preventing influenza-like illness and laboratory-confirmed influenza among healthcare workers.<sup>25</sup>

The use of a mask to control a respiratory illness is a well-established method. A relevant investigation discovered that a cloth mask obstructed 96 % of viral quantity on normal when used eight inches away to wheeze from a COVID-19-infected patient.<sup>26</sup> It has been shown that every 10-fold increase in viral amount results in an additional 26 % increase in patient fatalities from acute infections caused by highly deadly viruses.<sup>27</sup>

The research focused on aerosol disclosure has found that all kinds of masks are at least somewhat beneficial at defending the wearer. Van der Sande et al. in 2008 reported that any mask can decrease aerosol exposure and are reasonably reliable over time. Researchers found that any type of mask use is likely to decrease viral exposure and infection hazard on a community grade, despite its improper fit.<sup>28</sup>

However, the examination of particle filtration is likely to misjudge the efficiency of masks, as the number of particles that are secreted as an aerosol is relatively small.<sup>29</sup> Both homemade and medical masks are considerably useful in minimizing the number of microorganisms and can reduce the spread of infection, though the surgical mask was much better and be more useful in obstructing transmission in comparison to homemade masks.<sup>28</sup> The scarcity of surgical masks and N95 respirators is a major issue. According to the current CDC advice, a healthy person should wear a cloth face mask in public.<sup>30</sup>

The importance of utilizing masks for health care persons has been

detected in Chinese hospitals where, in each hospital, medical professionals wearing masks (particularly in quarantine areas) had no COVID-19 infections, instead of being around COVID-19 patients while other medical professionals had 10 or more infections in hospitals because of not wearing the mask.<sup>31</sup>

### 1.3. Categories of face masks recommended by WHO

During this COVID-19 epidemic, the usage of masks is suggested by Governments and WHO to control the further expanse of SARS-CoV-2. The usage of masks has followed various guidance from several community health organizations and governments. The WHO and other public health organizations approve that masks can inhibit the expanse of respiratory viral diseases, especially in COVID-19 case.<sup>32</sup>

WHO recommends various kinds of masks for use in pandemic COVID-19 (Fig. 2). These types are mentioned as below:

#### 1.4. Categories of face masks include

1. Cloth face masks
2. Medical or surgical masks
3. Respirators:
  - (i) Filtering facepiece respirator
    - NIOSH respirator filter masks
  - (ii) Full-length face shield
  - (iii) Self-contained breathing apparatus (SCBA)

### 2. Cloth face masks

A cloth face mask is inexpensive and made of everyday cotton fabric that is worn over the mouth and nose. Many health authorities are instructed to use these cloth masks for protection if medical masks are unavailable in stocks.<sup>33</sup>

It is solely made of several varieties of cloth material. Studies demonstrate that the efficiency of these cloth masks, when compared to the N95 mask, is less effective against the SARS-CoV-2 but they can still provide the basic protection. It does provide the user protection against the air contaminants like pollens and dust particles. Therefore, it was limited approved in case of a pandemic.

Before the coronavirus outbreak, several Asian countries, including Vietnam and China, investigated the use of cloth masks in the community and healthcare.<sup>34,35</sup> Cotton cloth masks were reported to be used by Health Care Workers (HCWs) in China during the outbreak of severe acute respiratory syndrome (SARS) in 2002.<sup>36</sup>

#### 2.1. Types of cloth masks

Based on laboratory data and WHO's instruction, cloth masks are of three types: (a) Cloth mask 1, (b) Cloth mask 2, (c) Cloth mask 3.

Cloth mask 1 contains a latex exhalation valve, which worked better than the other two cloth masks that did not have an exhalation valve. The capability of filtration efficiencies of cloth masks 2 and 3 varied among the several PSL (polystyrene latex) sizes. Cloth masks 2 and 3 are more susceptible to penetration than cloth mask 1. Cloth mask 1, is an outstanding filtering mask with a conical or tetrahedral shape, that fits well with the general population. It also has 3 layers with a hydrophilic inner layer, filter in the middle layer and a hydrophobic outer layer whereas cloth masks 2 and 3 have simple rectangle long nooses and they do not possess three layers. Cloth mask 2 has two layers i.e. filter and hydrophobic outer layer while cloth mask 3 has only one thin layer (Fig. 3). This technique does not fit on the mannequin, allowing the leakage of a considerable percentage of components to infiltrate via the mask. When comparing filtering effectiveness and fit, cloth mask 1 outperformed the other two masks. However, the cloth mask 2 performed better when compared to cloth mask 3.<sup>37</sup>

The most protective cloth face masks require at least three layers



**Fig. 2.** Diagram shows the pictorial view of different types of masks: a. Surgical Mask b. Cloth Mask c. Cloth Mask with Head Loop d. Fold Model Type K95 Mask without Respirator with Head Loop e. Fold Model Type N95 Mask with Respirator and Head Loop f. Cup Model Type N95 Mask with Respirator and Head Loop g. Full-Length Face Shield.

with a hydrophilic inner layer (e.g. cotton) to consume moisture from the wearer's breathing and hydrophobic outer layers (e.g. polyester).<sup>37</sup>

Another study demonstrated that homemade masks made of tea cloth delivered safety during short- and long-term activities.<sup>28</sup> Ma et al. demonstrated that while N95 respirators obstructed 99.98 % of avian influenza virus, cloth homemade masks and surgical masks were comparative 95.15 % and 97.14 %, respectively. These homemade masks were created from polyester and kitchen towels and were used in the experiment.<sup>34,38</sup>

### 3. Medical or surgical mask

During this moment of global health emergency caused by the COVID-19, WHO recommends medical or surgical masks for nurses, doctors, patients, and all hospital personnel, as well as all healthcare units, to protect themselves from COVID-19 exposure. A fluid-resistant (Type-IIR) medical face cover is utilized to keep safe against droplets.

If worn by the sufferer, it will underestimate the disbandment of enormous respiratory droplets that will defend workers against both droplets and influenced by the transmission of viruses. If worn by healthcare workers it will protect against droplet communication, when within 1–2 m of the victim. Danger removal by at least 80 % is reckoned.<sup>39</sup> Surgical masks contain three layers: an internal tender absorbent sheet, a central polypropylene obstacle, and an exterior hydrophobic surface. This face mask delivers protection from droplets in a clinical setting. The design of the surgical masks relies on the mode; usually, the masks are three-ply (three layers) and 4 ply (four layers). This three-ply fabric is composed of a meltblown polymer, most generally polypropylene, placed between the non-woven fabric. It has 3 layers, the external layer repels water droplets, the middle layer serves as a filter and the interior layer absorbs moisture (Fig. 4a & 4b). Numerous analyses are carried out to disclose the removal of viral detection, which in turn was found to be 25-fold for coarse aerosols, 2.5 fold for neat particles. Surgical face masks deliver the fundamental option in a pandemic. It had the



**Fig. 3.** Diagram shows the different types of cloth masks and their layering pattern: **a.** Cloth Mask 1 **b.** Different layering pattern of Cloth Mask 1 **c.** Cloth Mask 2 **d.** Different layering pattern of Cloth Mask 2 **e.** Cloth Mask 3 **f.** Different layering pattern of Cloth Mask 3.

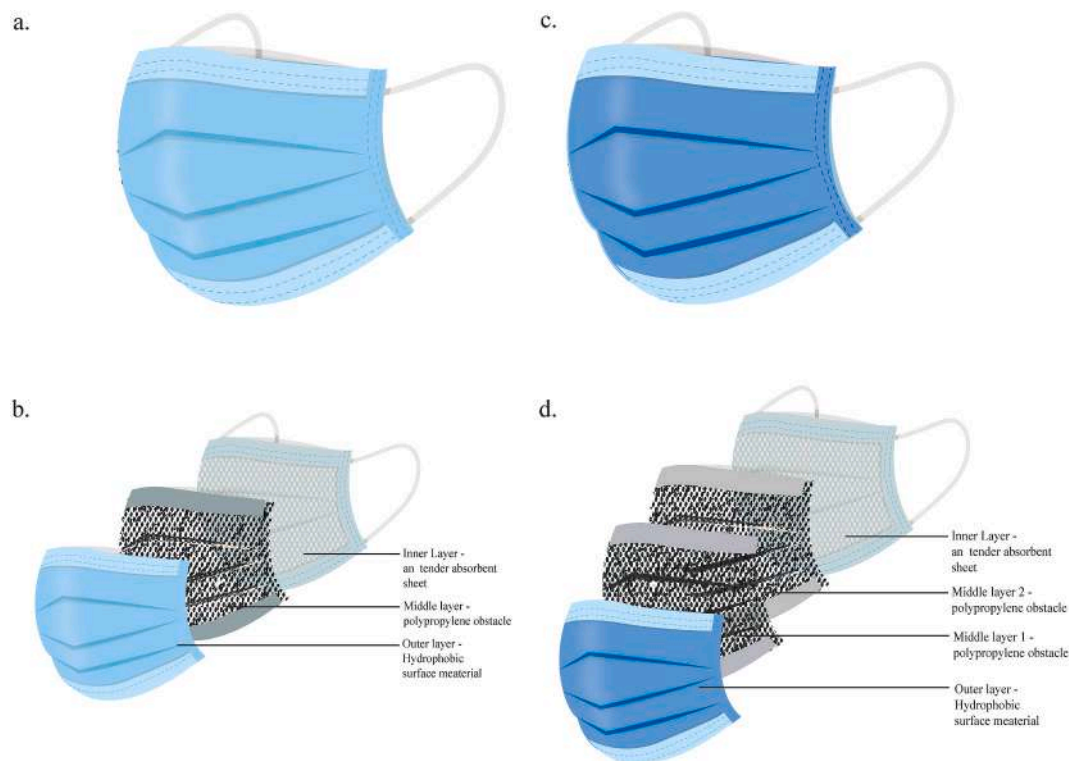


**Fig. 4.** Diagram shows the different types of surgical masks and their layering pattern: **a.** 3-ply surgical mask **b.** Different layering pattern of 3-ply surgical mask **c.** 4-ply surgical mask **d.** Different layering pattern of 4-ply surgical mask.

drawback of not constraining the release of minor droplets.<sup>40</sup>

The 4 ply surgical mask is like a 3 ply face mask along with an added additional layer with an activated carbon filter or one more filtering layer (Fig. 4c & 4d). The first layer is composed of polypropylene spun bond non-woven, second is with an active carbon filter fiber or another filtering layer. The 3rd layer is with melt-blown nonwoven fabric and the final layer is with polypropylene spun bond non-woven. They also have flexible nose strips to give extreme protection and satisfaction to the user. It also protects against odors as well as organic vapors.<sup>40</sup>

#### 4. Respirators

FFP 1/2/3 or NIOSH respirators and other respirators are seal-tested respirators and they are capable to protect health care workers especially those who directly come in contact with the patients. This apparatus causes a blockage around the nose and mouth and has twisted fibres with filters. WHO instructed about respirators, described below:

##### (i) Filtering Face-piece Respirators:

The term filtering facepiece (FFP) is utilized in source to high-performance screening masks. Filtration is executed by a variety of



complex polypropylene microfibers and electrostatic rates. It is borrowed to filter out vapors, dust particles and infectious agents. It is primarily borrowed in the workplace having more pollutants. It has the benefit of cleansing air and cutting down the hazard of contamination of the wearer. Such mechanical filter respirators protect against the inhalation of particulates such as dust particles, droplets, and aerosols.<sup>40</sup>

**Types of FFP Mask:** There are three categories of protection. For FFP1, FFP2 and FFP3 these are 4-, 10- and 20-folds, respectively. FFP1 Filters at least 80 % of airborne particles and FFP2 Filters at least 94 % of airborne particles.<sup>40</sup>

The third category of FFP3 provides the longest aspect of precaution and is the only one recommended for UK healthcare locations, particularly in AGPs, such as intubation and non-invasive ventilation. They must comply with industry standards, including stringent industry tests with biological aerosols and a maximum leakage of 2 %. FFP3 respirators provide 99% protection against COVID-19 in screening elements ranging in size from 100 to 5000 nm, including airborne tiny droplets.<sup>41,42</sup>

NIOSH recognized different types of respirators are most popularly known as FFP respirators. As per the shape, it may be (i) cup model type or (ii) fold model type or (iii) linear model type.<sup>43</sup> (Fig. 5).

- **NIOSH respirators filter masks:**

The NIOSH respirators screening masks are respiratory guarding equipment manufactured to conform a remarkably close facial clothing and very productive filtration of airborne components.

#### 4.1. Types of NIOSH respirator filter masks

Based on filtering particles and efficiency of resistance to oil, NIOSH respirator filter are of three types: N, P, R.

Depend on particle filtering efficiency *N*-type respirators are of three categories- N95, N99, and N100. N95 respirators are generally used in healthcare vicinities and are a subset of N95 Filtering Facepiece Respirators (FFRs), often cited as N95s.<sup>37</sup> The N95 designation means that under experimental circumstances which are approved by the United States CDC and National Institute for Occupational Safety and Health, the respirator hurdles at least 95 % of strong and watery aerosol trial components. The most incredibly used is N95 which is called electrets filters, which has a filtration of 95 % of aerosols N90/N95 face mask is one of nine NIOSH certified particle respirators. Obtaining an N95 mask as an example, “N” means not resistant to oil. “95” means that the particle concentration in the mask is 95 % poorer than that outside the mask when disclosure to a specified number of special test particles. 95 % is not the normal filter rate, but the slightest value. N95 is not a certain product name. As long as the product meets the N95 criterion and upholds NIOSH review, it can be called “N95 mask”. The degree of safety is N95, which means that under the test circumstances stipulated in NIOSH standard, the filtering efficacy of the filter substance of the mask for non-oily particles (such as acid mist, dust, paint mist,

microorganism, etc.) attains 95 %. Nevertheless, various companies manufacture several N95 and its effectiveness relies on the size of penetrating particles. It has 4 layers-inner, filter, support and layer mask filter layer from outside to inside with a ventilator fan to permit reinforce breathing. N95 are of two categories- The standard N95 and surgical N95, which is more worthwhile.<sup>40</sup> (Fig. 6).

Some other variants to the N95 mask are also available like N90, valved N90, valved N95, KN90 and KN95. In the case of the N90 mask, the number 90 signifies the effectiveness of the mask to filter out 2.5 p. m. dust particles. While KN90 respirators with valves are more favorable for industries of non-ferrous metal processing, food processing, metallurgy, construction works and all additional oil and non-oil particles pollutants such as dust particles, smoke fog. KN90 can apprehend more than 90 % of particles. Although it is not as beneficial as KN90 in the case of particle conservation. KN90 is a promising choice to travel in a mist for a short time.<sup>11,40</sup>

There are a variety of respirators on the market that match the same design criteria as N95s, and they are approved as KN95s in China. These respirators are fundamentally the same. The KN95 filters out at least 95% of particles down to 0.3  $\mu\text{m}$  (Fig. 7). To be more useful, these respirators also must develop a seal around the nose and face when worn. Genuine N95s will have NIOSH written in block letters on the respirator, including testing and certification numbers, as well as the identification, N95. This can help recognize the fake masks on the markets.<sup>40</sup>

The usage of valves in face masks such as the valved N90 and N95 are stated as not prohibiting the virus from escaping out of the mask. The valve is almost a ‘one-way valve’ that only insures the person wearing it and does not purify the aerosols coming out. So, an asymptomatic person with coronavirus can scatter the infection to people when the valve discharges the unfiltered exhaled air in the sudden environment. Therefore, in a sealed area, people around the carrier have an increased threat of conceivable disclosure to the Covid-19. Asymptomatic transmission disseminates the infection to another person. On the other hand, a mask without a valve will not permit the virus to circulate.<sup>40</sup>

The R and P masks have friction to oils but the high-performance 100 refers to the lowest percentage of factors screened under trial conditions. Both R-type (Resistant to oil) and P-type (Strongly Resistant to oil/Oil Proof) of respirators differentiate into three types, viz., R95, R99, R100, and P95, P99, P100 respectively. Their filtering power is at least 99 % and 99.7 % respectively.<sup>42</sup> The P100 respirator has a filtration of 99.7 %. Studies were performed to find and distinguish the efficiency of N95 and P100 before and post-exercise. The permeability values were more or less the same with both before exercise. But, the outline after exercise demonstrated change, having the benefit of using P100 masks.<sup>40</sup>

- (ii) Full-length face shield:

It is made out of elastic headbands and a clear polycarbonate shield that runs across the face (Fig. 8). It prohibits the wearer from splashes of coughing and other liquid droplets. It had the advantage of being light and cost-effective. It is primarily used in a clinical area.<sup>40</sup>

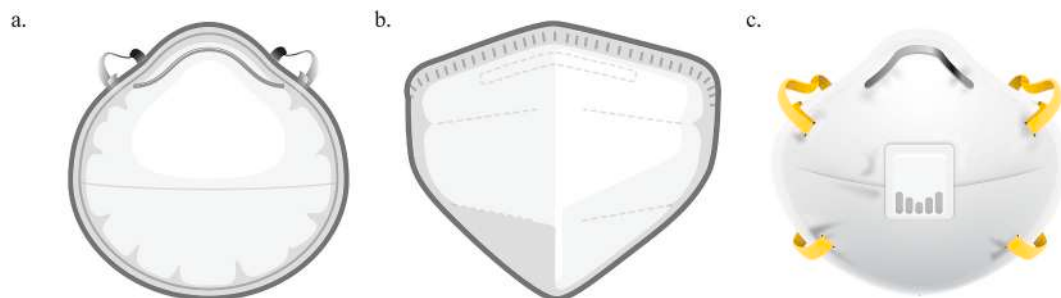


**Fig. 5.** Diagram shows the different shaped Filtering Face-Piece Respirators a. Cup Model Type b. Fold Model Type c. Liner Model Type (Created with Bio-Render.com).

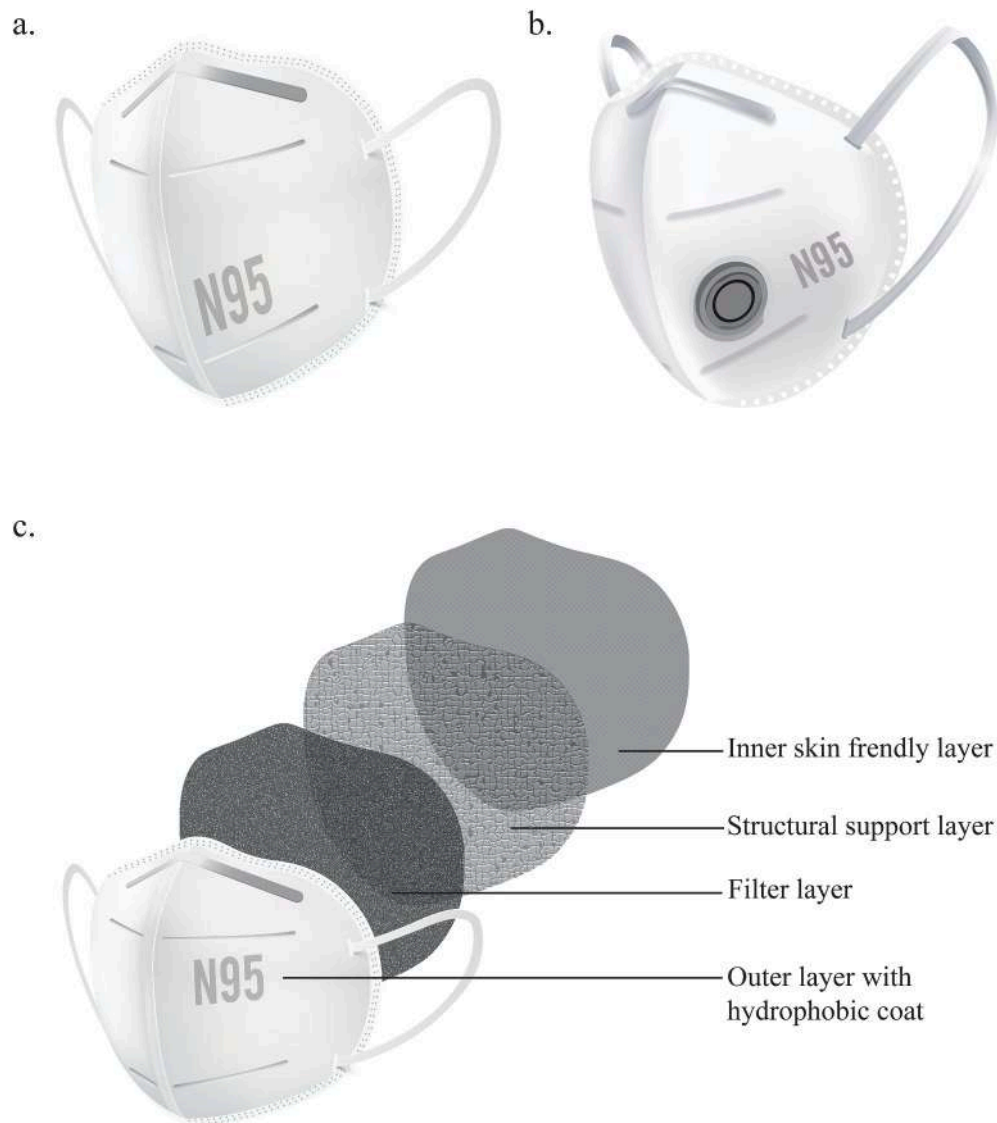


**Fig. 6.** Diagram shows the N95 mask and its layering pattern: **a.** N95 mask without respirator **b.** N95 mask with respirator **c.** Different layering pattern of N95 mask without respirator.

Full-length face shields come through different structures, but all deliver a plastic boundary for the face to protect against droplets and virus particles. The faceguard coverings will ensure that it reaches the chin and that there is no gap between the forehead and the face-shield guard. The laboratory study showed that the face guard was capable of inhibiting 96 % viral particles when worn by health care personnel within 18 inches of cough.<sup>44</sup> Yet social distancing, wearing masks must be important for avoiding viral respiratory diseases.<sup>22,45</sup>

#### (iii) Self-contained breathing apparatus (SCBA)

It comprises a facepiece that is connected to an allowance of liquid air or liquid oxygen. A hose and a regulator are used to keep the SCBA in place (Fig. 9). It primarily gives protect against airborne pollutants, making it easy for those working in a smoky environment. It is employed as personal firefighting cautionary. It has the disadvantage of being hefty, which limits the user's mobility in the workplace.<sup>40</sup>

Table 1 shows the many types of masks, their materials, characteristics, and purposes, as well as their percentage of effectiveness in protecting against the Coronavirus.

#### 4.2. Mechanistic significance of wearing a mask

Over the last several months, the use of facemasks has been identified as one of the most important and cost-effective mitigating strategies for delaying COVID-19 transmission. In addition to government and public health officials' advice and mandates for mask use, a growing number of scientific studies have demonstrated the effectiveness of masks and universal masking.

Face Masks and different PPE items serve as a physical obstacle to respiratory droplets. An in vitro model with basis and receiver figures was developed to test the impact of the mask on filtering away radio-labelled aerosol. Masking at the source mannequin was invariably more beneficial at reducing radio-labelled aerosols entering the receiver mannequin, whereas the only practical setup where the receiver mannequin could be equally adequately conserved was if the receiver mannequin wore an N95 mask enclosed with Vaseline.<sup>47</sup> Hence, masks can work as a physical obstacle and seem to be more significant when worn by an infected person.

The use of a mask by the infected person helps in reducing virus transmission. The surgical mask was examined for its potentiality to hinder the discharge of numerous viruses by investigating the quantity



Fig. 7. Diagram shows the K95 mask.

of virus existing in the exhaled breath of the infected person. The researchers were able to obtain the particles distinguished by size ( $>$  or  $<$  5  $\mu\text{m}$ ). With the mask on, a critical decline in coronaviruses in both smaller and bigger particles was investigated. The mask reduced the number of influenza viruses identified in bigger particles, but not in smaller particles. After wearing a mask, no coronavirus was found in any of the 11 patients, although influenza was found in the respiratory particles of one of them.<sup>48</sup> This means that surgical face masks can reduce coronavirus and influenza transmission from an infected person. Participants were encouraged to cough for influenza trial, and no influenza could be detected by reverse transcriptase-polymerase chain reaction (RT-PCR) for 9 infected patients using both N95 and surgical masks.<sup>49</sup> When the exhaled influenza virus was divided into amounts based on size, surgical masks were found to be highly effective at eliminating influenza from the large coarse portion ( $\geq 5 \mu\text{m}$ ).<sup>50</sup> Individuals who come into contact with an infected person can benefit from wearing face masks. During the SARS outbreak in Hong Kong, hospital faculties were asked about the preventative measures they took and this data was linked to whether or not they were infected. Wearing face masks was determined to be the most effective preventative measure in reducing the risk of infection, and those who wore surgical masks or N95 masks were not among the 11 infected employees. Nonetheless, two groups of people who wore paper masks became sick, implying that the types of masks were also important.<sup>51</sup> A study distinguished the effectiveness of surgical and N95 masks against viral respiratory infections in healthcare employees. When healthcare workers used

surgical masks or N95 masks, there was no significant difference in influenza infection outcomes, implying that both types of medical masks can protect equally.<sup>52</sup> A meta-analysis was conducted on clinical surveys to investigate the protective impact of masks. Wearing a face mask protect persons against influenza-like illness, illustrating a risk ratio of 0.34, with a 95 % confidence duration between 0.14 and 0.82. According to the study, there was a minimal difference in protection between N95 masks and surgical masks, with a hazard ratio of 0.84 and a 95 % confidence duration of 0.36–1.99, indicating no significant difference in risk.<sup>53</sup> A study conducted by Eikenberry et al. suggested that the widespread use of masks by the general public can significantly reduce population transmission rates and death tolls.<sup>54</sup> Hence, the study finds that the widespread use of face masks has the potential to significantly minimise community transmission and the threat of a COVID-19 pandemic. These data can be used to support and inform public health communications campaigns and undertakings involving the use of masks to help limit the spread of COVID-19, as well as to examine how policies and practices interact around the world.

#### 4.3. Caring methods of non-medical masks

Masks should be worn by only one person and should not be shared. When masks become wet or dirty, they should be changed immediately; a patchy mask should not be worn for an extended amount of time. While removing the mask avoid touching the front side of the mask and do not touch any other part of the face after removing. Abandon the mask or keep it in a sealable pouch until it is cleaned and washed again. Afterwards, instantly practice hand hygiene. Non-medical masks should be washed frequently and handled carefully.

Do not use the mask, if the fabrics look notably worn out. The highest permissible washing temperature for clothing textiles used to make masks should be checked. Clean it in with soap or detergent in warm, hot water (60 °C). Non-woven polypropylene (PP) spun-bond perhaps washed at high temperatures, up to 125 °C.<sup>55</sup> Naturalistic fibres may fend with high-temperature ironing and washes. Cleanup the mask exquisitely but avoid too much abrasion, extending or rubbing. The summation of cotton and non-woven PP spun bond can undergo high temperatures, masks formed of these compounds perhaps fumigated or steamed.

When warm water is not obtainable, wash the mask with detergent or soap at room temperature water, pursued by either (i) steaming mask for 1 min or, (ii) drench face cover in 0.1 % chlorine for 1 min. Rinse the mask properly with room temperature water to avoid any toxic chlorine accessorial.

Though the cloth masks may be created in huge quantities in a short amount of time, they can be reused after being decontaminated using a variety of methods, the most effective of which is washing in hot water with soap. Other methods or products, to get contaminant free cloth masks, are the use of bleach, isopropyl alcohol, or hydrogen peroxide;

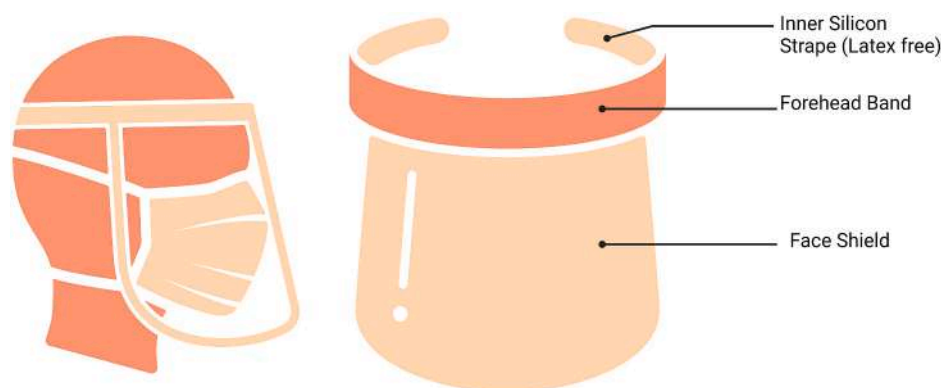


Fig. 8. Diagram shows the full-length face shield and its layering pattern (Created with BioRender.com).

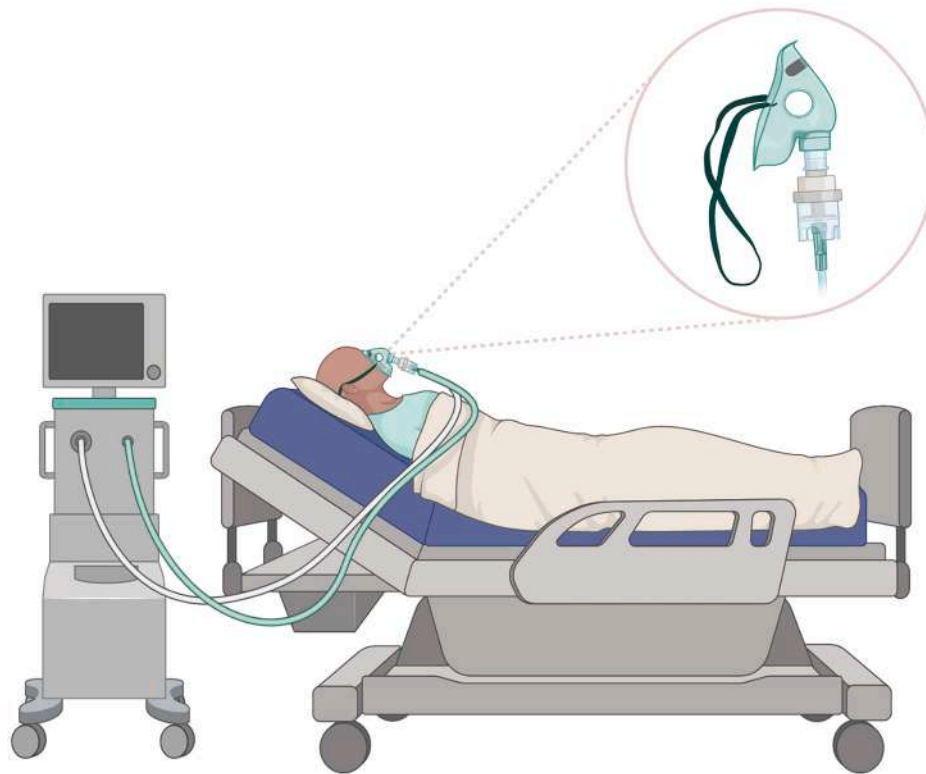


Fig. 9. Diagram shows the Self-Contained Breathing Apparatus (Created with BioRender.com).

Table 1

A detailed summary of the different types of masks and their effectiveness in protecting against the SARS-CoV-2 virus.

Type of mask	Materials used	Description	Efficiency in percentage	Purpose	Respiratory filter	Reusable	Reference
Cloth Face Mask	Common textiles, usually cotton	The most protective cloth face masks require at least three layers with a hydrophilic inner layer (e.g. cotton) to consume moisture from the wearer's breathing and hydrophobic outer layers (e.g. polyester).	Zero % efficient at 0.3 $\mu\text{m}$	Dust, pollen, virus and bacteria	No	Reusable	40,46
Surgical Face Mask	Non-woven fabric	This mask has been certified by the Food and drug administration. This category of mask protects the mouth, nose, eye, cheeks and forehead. It is mostly referred to the Medical professional dealing with operations drive through COVID-19 patients.	60%–80 % filtration of particles as small as 0.3 $\mu\text{m}$	Virus, bacteria, pollen and dust particles	No	Disposable	40,46
N95 Face Mask	Fine mesh of synthetic polymer fibres, specifically a non-woven polypropylene fabric.	This mask is mostly recommended by health care workers and first medical responders dealing with COVID-19 patients.	95 % efficient of particles sized 0.1–0.3 $\mu\text{m}$	Virus, bacteria, pollens, liquid like sprays against non-oil particles	Yes	Reusable	12,40,46
FFPR (P100) Face Mask	Fine mesh of synthetic polymer fibres, specifically a non-woven polypropylene fabric.	Unlike the surgical mask, this type of mask is mostly used to stop the spread of airborne diseases and also is dispensable.	99.97 % efficient of particles sized 0.1–0.3 $\mu\text{m}$	Virus, bacteria, dust particles.	Yes	Reusable	12,40,46
KN95 Face Mask	Non-woven fabric, often made from polypropylene.	They are composed of four layers: outer, filter, cotton and inner layers.	80%–95 % efficient of particles down to 0.3 $\mu\text{m}$	Virus, bacteria, pollens, liquid-like sprays against non-oil particles	Yes	Reusable	40
Face shield	Flimsier	This mask is made of flimsier, which cover the entire face from the forehead to chin and is secure with a headband cushioned.	Effective with perhaps surgical or N95 masks worn.	Liquid like most sprays.	No	Reusable	40,46
SCBA	A back-plate that holds the cylinder and reduces the air from high pressure (200–300 bar) to medium pressure (5–11 bar) and, in turn, supplies a face mask.	Mostly worn by firefighters to ease fresh breath when in contact with hazardous environments.	99 % of knotted than 0.3 $\mu\text{m}$ .	Emergency conditions, viruses, bacteria, smoke particles, and non-oil particles.	Yes	Reusable	40,46

autoclaving or microwaving; and the application of ultraviolet radiation or dry heat.<sup>56</sup> Unlike disposable medical masks and respirators, the material of cloth masks is unlikely to degrade from standard decontamination procedures. Hospitals, on the other hand, will be burdened with the additional task of washing and decontaminating worn masks. If healthcare personnel do decontamination on their own, they may not wash masks frequently enough, putting themselves at risk of infection.<sup>12</sup>

If you wear a none medical mask, do not touch it unnecessarily. Masks of any type are not comfortable and can cause users to touch their faces often to adjust the mask. This can be complicated, as that is specifically how the virus would enter your body.

Cloth masks should be washed after each use, or sooner if they appear soiled. Follow any particular instructions provided by the manufacturer. Use the warmest washer and dryer settings that are safe for the fabric. If you don't have access to a dryer or washer, you can wash a face mask in bleach and air dry it. To prepare the solution, add 4 tablespoons of bleach in 1 L of normal water, then saturate the mask in that solution for 4–5 min. After saturation, wash the mask thoroughly with normal water and let it air dry completely in presence of sunlight.<sup>57</sup>

In a nutshell, one must follow the following protocols to maintain the hygiene of the masks:

A. Store wet or dirty masks in a plastic bag: If your mask is filthy or wet from saliva, sweat, make-up, or different liquids or entities, keep it in an impenetrable plastic bag until you can clean it. To avoid mould growth, wash contaminated or wet masks as soon as possible. Damp masks are less useful than dry masks since they are difficult to breathe through.<sup>58,59</sup>

B. Masks that aren't damp or soiled should be stored in a clean paper bag: You can save your mask for later use by temporarily storing it. After touching a used mask, properly dispose of it and wash your hands. To keep it clean between uses, store it in a dry, breathable bag (such as a paper or mesh fabric bag). Keep the same side of your mask facing out while reusing it. If you need to remove your mask to drink or eat outside of the house, place it in a safe place, such as your pouch, handbag, or paper bag. After removing your mask, make sure to rinse or sanitize your hands. Replace the mask with the same side facing out after eating. After re-applying your mask, make sure to rinse or sterilise both hands once again.<sup>58,59</sup>

C. Wash your mask: Wash your cotton mask whenever it gets soiled, or at least once a day. If you're using a disposable face mask, throw it away after one use.<sup>58</sup>

- (i) Using a washing machine: Include your mask in your regular laundry. Use ordinary laundry detergent and the appropriate settings for the fabric, as directed on label.<sup>58</sup>
- (ii) By hand: Rinse your mask with soap or laundry detergent and water. To get rid of any soap or detergent, wash it fully with clean water.<sup>58</sup>

D. Dry your mask: Use a warm or hot drier to completely dry your mask. Allow your mask to dry completely in direct sunlight. If you can't dangle it in the sunshine, hang it or spread it out flat to dry.<sup>58</sup>

WHO is cooperating with research and development partners and the scientific community involved in fabric design and textile engineering to simplify a fine knowledge of the efficiency and utility of non-medical masks. WHO impulse countries that have emanated recommendations on the usage of both non-medical and medical masks by having people in community settings to propulsion research on this significant issue. Such research is urgent to look at if SARS-CoV-2 particles may be eradicated by non-medical masks of impoverished integrity worn through an individual with syndromes of COVID-19 if that individual is sneezing, speaking, or coughing. Research is also required on non-medical mask use by children and several medically difficult individuals and settings as above mentioned.

#### 4.4. Categories of individuals who should wear medical masks against the expanse of COVID-19

Coronavirus disease (COVID-19) is an infectious disease caused by the SARS-CoV-2 virus, which was recently found. The mask is used in many ways depending on the type of person.<sup>60</sup> These divisions are described properly below:

#### 4.5. Hospital

##### 4.5.1. Monitoring area

During interacting with victims, all medical crews such as nurses and the paramedical team would use disposable triple-layer surgical masks.

##### 4.5.2. Isolation department

In the isolation cabins, all victims should be maintained that they must wear a disposable triple-layer surgical mask. Nursing and medical staff included in clinical caring in isolation faculties would need a triple-layer surgical mask, including extra Personal Protective Equipment (PPE). Nevertheless, if the staff is related to any aerosol-generating protocols like intubation, suction and nebulization then they must use the N95 respirator. Likewise, if the medical crew requisite to obtain clinical specimens from victims, then they must use N95 respirators.<sup>60</sup>

##### 4.5.3. Critical care faculty

While nursing and medical staff are implicated in crucial care in the Intensive Care Unit (ICU) then they must utilize N95 Respirators.

##### 4.5.4. In laboratory room

In laboratories, all staff are working and examining clinical samples related to pathogens like Influenza then they should use N95 Respirators.

##### 4.5.5. Mortuary

Personnel involved in dealing with dead bodies of verified patients of seasonal influenza should utilize a triple-layer surgical mask, along with other infection measure procedures.

##### 4.5.6. Ambulance staff

The motorist of the ambulance appointed for shifting patients with Influenza should utilize a triple-layer medical mask. The paramedics in the patient bedroom should borrow a triple-layer surgical mask and though the performance of any aerosol-generating procedures are contemplated (suction, oxygen administration by nasal catheter, intubation, nebulization, etc.) Likewise, in these situations, an N95 respirator should be worn at all times.<sup>60</sup>

#### 4.6. Health employees in community setting

##### 4.6.1. Doctors

Doctors treating Influenza-Like Illness (ILI) in general practice, as well as other health care workers working with them, should utilize a triple-layer surgical mask at the screening centre.<sup>60</sup>

##### 4.6.2. Healthcare workers

Health workers involved in community surveillance contact tracing and health monitoring of cases at home or under home quarantine should use a triple-layer surgical mask.<sup>22</sup>

##### 4.6.3. Security personnel

When operating in an infected/potentially infected location, such as an influenza ward in a screening centre or a hospital, security staff should wear a triple-layer surgical mask.<sup>22</sup>

The specifics of individuals who should use a medical mask or other respirators during certain activities are listed in [Table 2](#).

#### 4.7. Guidelines for using the mask for the general public

Many countries recommend fabric masks or homemade masks for the common public to prevent the spread of pandemic disease.

##### 4.7.1. Public settings

Masks should be worn in public locations, such as grocery shops, public meetings, at work, closed locations, along with schools, colleges, temples, mosques, churches, etc. In the above criteria, people should use a non-medical mask such as a cloth mask.<sup>60</sup>

##### 4.7.2. During transport

Non-medical masks should be worn on public transit and in specific work scenarios that bring the person in close contact or potentially close contact with others, such as cashiers, social workers, and servers, and medical masks should be used only when necessary.<sup>60</sup>

##### 4.7.3. Senior citizens

When people's age is above  $\geq 60$ , then they should use medical masks. However, N95 respirator masks can also be used for protection.<sup>60</sup>

##### 4.7.4. Other people

People with underlying comorbidities, such as cardiovascular illness or chronic lung disease, diabetes mellitus, cancer, cerebrovascular disease, immunosuppression must use a medical mask.<sup>22,60</sup>

##### 4.7.5. Symptomatic public

Persons with any syndromes suggestive of COVID-19 and close family contacts of such suspect/confirmed cases undergoing home care should also use a triple-layered medical mask.<sup>22,60</sup>

To prevent the coronavirus outbreak, the mask should be worn by<sup>62,63</sup>:

1. People who are 2 years of age and senior citizens.
2. Whenever you are in social background.
3. Each time when you are travelling on a bus, plane, train, or different kinds of public vehicle. Wear masks also in-vehicle hubs such as stations and airports.
4. At the time, when you are around folks who do not occupy with you, constituting inside your house or inside somebody else's residence.
5. Inside your house if somebody you stay with is sick with signs of COVID-19 or has tested positive for COVID-19.

Although, CDC acknowledges there are certain instances when wearing a face mask may not be conceivable always. In these instances, evaluate alternatives and adaptations.

The subsequent types of people can be exempted from the requirement to wear a face mask<sup>62,63</sup>:

1. A kid under the age of 2 years;
2. A person with a disability who cannot, or cannot safely, use a face mask for reasons related to their condition.<sup>62,63</sup>
3. Certain groups of people who may find it difficult to wear a mask: Relevant and consistent use of masks may be struggling for some children and communities of any age with specific disabilities, along with the people who have high sensitiveness to substances on their faces, trouble realizing why wearing a face mask is defensive (such as people with an intellectual disability), and those who have issues regulating their behavior in social situations.<sup>62,63</sup>
4. Those caring for youngsters and those with specific disabilities who may need assistance with wearing masks. In that scenario, they should seek advice from their healthcare providers concerning the person they're caring for who is wearing a mask. If they are unable to wear a mask, speak with their healthcare providers about other ways to reduce transmission risk and ensure proper mask fit and size. They should discard their mask before napping, sleeping, when they may

**Table 2**

Categories of individuals who should wear medical or other respiratory masks.

Setting	Categories on individuals	Types of masks	Activity	Reference
Screening	Health Care Workers (HCWs).	Medical mask.	Preliminary contact not comprising direct contact.	46,61
	Patients with signs suggestive of COVID-19.	Medical mask.	Any	34,46,61
Patient room	Patients without symptoms suggestive of COVID-19.	If the prevalence of COVID-19 is high, utilize a medical mask. But when the condition is in control, cloth face coverings/masks may be used.	Any	46,61
	Health Care Workers (HCWs)	Medical mask	1. Providing direct care (no aerosol-generating procedures) 2. Direct care (aerosol-generating methods are repeatedly in place) When they are entering the patient's room for cleaning or in general when they cleaning contaminated stuff.	46,61
Administrative rooms	Cleaners	FFP2/N95 respirators or medical mask if available	Administrative duties that do not comprise contact with COVID-19 patients.	46,61
	All staff, along with HCWs.	If they are not in direct contact with patients suffering from COVID-19 they can Maintain physical distance (if that is not possible) then they should wear an N95 or cloth face masks.	Administrative duties that do not comprise contact with COVID-19 patients.	46,61
Laboratory	Lab technician	N95/FFP2 respirators	Manipulation of respiratory specimens of supposed COVID-19 patients.	34,46,61
Waiting compartment	Patients with signs suggestive of COVID-19	Medical mask	Any	46,61
	Patients without signs	Mask is not required if physical	Any	46,61

(continued on next page)

Table 2 (continued)

Setting	Categories on individuals	Types of masks	Activity	Reference
Consultation room	Health Care Workers (HCWs) Patients Cleaners	distance is maintained.		
		Medical Mask	Physical inspection	46,61
		Medical Mask Medical Mask	Any After and between consultations with patients with respiratory signs	46,61 46,61
Locations of transit where patients are not permitted	All staff, along with Health Care Workers	Maintain physical expanse (if not possible, cloth face masks can be utilized).	Any kind of activity that does not include physical contact with COVID-19 patients	46,61
Home	Patients with signs suggestive of COVID-19 Caregivers	Medical mask	Any	46,61
		Medical mask	Entering patients' rooms or providing direct care	46,61
		Medical mask	Entering patients' room or providing direct care	46,61
Community Settings	Anyone	Maintain physical distance (N95, FFP respirators and cloth face masks can be used).	Outdoors	46,61
		Maintain physical distance. No mask required	Indoors	46,61

fall asleep (such as in a stroller or car seat), and in conditions when continuous maintenance is not feasible.<sup>62</sup>

But consider prioritizing wearing a mask at least in public locations and when around people who don't live in your home, especially when indoors. Masks may not be essential when you and the person you are looking after is away from each other, or with other people who live in the same home. Though some neighborhoods may have mask requirements while out in public and these requirements should always be obeyed.<sup>62</sup>

People who are deaf or having difficulty in hearing, and those who will interact with people who have difficulty in the hearing should consider wearing a cloth mask with a clear panel. If you are unable to get a clear mask, consider utilizing written communication, closed featuring, or reducing background noise to make communication reasonable while wearing a mask that blocks lips.

People with specific underlying medical conditions like having any respiratory problem or asthma can also wear a mask, but they should first take advice from their doctor.<sup>62</sup>

If a person works in an area where masks could increase the risk of heat-related disease or cause safety issues (such as straps getting stuck in

machinery), they should consult with a healthcare expert and occupational safety to determine whether the mask is appropriate or not.<sup>62</sup>

#### 4.8. Guidelines about utilizing masks in pandemic COVID-19

Masks may be used for safety for healthy persons (when worn to defend themselves when in contact with an infected person) or for source supervision, according to the WHO's revised guidelines (worn through an infected person to obstruct onward transmission).<sup>64</sup>

The current protocols over face masks usage have deviated from the present guidelines provided by WHO. It was argued that there was insufficient evidence to suggest that healthy persons should wear face masks and that surgical face masks should only be worn by those who were sick or caring for patients.<sup>64</sup>

#### 4.9. Guidance on the use of masks in health care settings

In the context of situations with acquainted or suspected society transmission or severe explosions of COVID-19, WHO provides the following guidance<sup>64,65</sup>:

- Health employees, along with community health employees and caretakers, who are employed in clinical sectors should constantly wear a medical mask at the time of their periodic activities throughout the whole shift; apart from when drinking and eating or altering their mask to look after a patient who compels droplet precautions for other purposes.<sup>64,65</sup>
- According to the WHO statement, it is incredibly significant to obtain the constant usage of masks in probable massive transmission hazard areas along with triage, household physician, GP practices, emergency areas, outpatient divisions, cancer, transplant departments, long-period health crisis, COVID-19 determined departments and residential facilities.<sup>64</sup>
- Throughout the whole shift, at the time of utilizing medical masks, health employees should be assured that the medical mask is altered when damp, stained, or ruined; the medical mask is never contacted to adjust it or replaced from the face for any intention; the medical mask (as well as different personal protective equipment) is omitted and altered after taking care for any patient on droplet precautions for other pathogens.<sup>65</sup>
- Faculty members who do not work in the medical field are not required to wear a mask throughout their daily activities.
- Masks should never be shared among health professionals and should be suitably eliminated whenever discarded and never reused.
- A particulate respirator is as defensive as a US National Institute for Occupational Safety and Health-approved N99, N95, US FDA surgical N95, European Union standard FFP2 or FFP3, or equivalent, should be worn in environments for COVID-19 victims where AGPs are conducted. In these environments, the constant usage of masks by health professionals throughout their whole shift is highly recommended.<sup>64,65</sup>
- To be completely beneficial, the consecutive wearing of a face mask among health employees, throughout their exhaustive shift, should be executed along with maintaining constant hand hygiene and corporal distancing between health staff in disseminated and congested areas where mask usage can be unfeasible such as restaurants, clothing spaces, etc.

The probable risks and hazards should be gingerly taken into report when acquiring this strategy of targeted continuous usage of medical mask, which includes:

- Self-contamination owing to the manipulation of the face mask by filthy hands.<sup>30,31</sup>
- Probable self-contamination can appear where medical masks are not altered when damp, contaminated or destroyed.

- Conceivable advancement of facial skin injuries, stinging dermatitis, or deepening acne, when utilized for several hours.
- Masks perhaps uneasy to wear.
- Erroneous understanding of protection, heading to potentially minor allegiance to well-acknowledged preventative criteria certain as hand hygiene and corporal distancing.
- The hazard of droplet transmission and splashing to the eyes, whether mask-wearing is not integrated with eye safety.
- Inconvenience for or complication wearing masks by particular susceptible communities certain as those including mental health illnesses, the deaf, developmental disabilities, rough of hearing society, and children.
- A complication of wearing them in warm and moist atmospheres.<sup>66</sup>

#### 4.10. Guidance on the use of masks for the general public

WHO approves that individuals with any symptoms suggestive of COVID-19 should follow these guidelines<sup>64,65</sup>:

- Wearing a medical mask, self-sequester, and look for the medical recommendation as early as they begin to feel sick with possible symptoms of COVID-19, even if symptoms are mild. Symptoms include cough, fever, tiredness, loss of enthusiasm, muscle irritation, and shortness of breath. Other non-particular signs include bruise throat, diarrhoea, nasal congestion, headache, vomiting, nausea, losing of taste and odour foregoing the beginning of respiratory signs have further been reported.<sup>67,68</sup>
- Senior people and immunosuppressed sufferers may have anomalous symptoms such as exhaustion, lowered alertness, lessened mobility, diarrhoea, delirium, loss of hunger, and lack of fever.<sup>69-71</sup> It is significant to report these initial symptoms for few people infected with COVID-19 may be very mild and indefinite.
- One must follow instructions on how to wear, take off, and dispose of face masks and maintain hand hygiene.<sup>22</sup>
- All additional conditions, particularly in respiratory hygiene, thorough hand washing, and maintaining a social distance of at least 1 m from other people, are required.<sup>72</sup>

In the circumstances of the COVID-19 pandemic, it is instructed that all individuals, nonetheless of whether they are utilizing face masks or not, should:

- Avoid mass gatherings.
- The physical distance of at least 1 m from another person should be followed, especially from the person with respiratory symptoms like gasping, coughing or sneezing.
- Practice hand hygiene repeatedly uses an alcohol-based hand sanitizer or soap and water.
- Use respiratory hygiene by covering the nose and mouth with a bent elbow or tissue paper when gasping or sneezing, after usage, discard the tissue instantly, and sanitize your hands with a sanitizer or soap and water.
- One should refrain from constant touching of eyes, nose and mouth.

#### 4.11. Guidance on the use of medical masks for the care of COVID-19 patients at home

WHO delivers advice on how to look after patients with suspected COVID-19 at the household when looking after in a medical facility or other residential setting is not possible. Home care may be considered when isolation in non-traditional settings is unavailable or unsafe. Specific guidance for the use of medical mask at-home care is:<sup>73</sup>

- Always wear a mask and at least once a day changes the mask and use the fresh and dry mask.

- Individuals who cannot tolerate a medical mask must maintain respiratory hygiene and practice hand hygiene frequently.
- Always wear a mask when present in the same room as the infected person.

#### 4.12. Probable advantages of using masks<sup>22,73</sup>

The potential benefits of the usage of masks by a healthy person:

- It helps in reducing the risk of exposure to infection from infected individuals before they develop any symptoms.
- Minimized probable stigmatization of people wearing masks to prohibit infecting others or of people looking after the COVID-19 patients in non-clinical environments.
- Make people realize that they can play a part in contributing to stopping the spread of the virus.
- Making people be responsible citizens by practising hand hygiene, not touching nose and mouth.
- It also provides social and economic privileges. Amidst the worldwide deficiency of PPE and surgical masks, urging the public to generate their cloth masks can emphasize personal business and public integration. Additionally, the output of non-medical masks may extend an origin of earnings for those who elect to develop masks among their societies.
- Fabric masks can further be a kind of cultural representation, motivating the public to an acknowledgement of safety regulations in general. The protected reuse of fabric masks will furthermore lessen waste, prices, and contribute to sustainability.

#### 4.13. Mask Management<sup>73</sup>

For several types of masks, relevant usage and dumping are necessary to assure that they are beneficial and to ignore any upgrade in transmission.

WHO (World Health Organization) recommends the subsequent guidance on the appropriate usage of masks, derived from best procedures in health care settings<sup>22,73</sup>:

- Before wearing the mask, always ensure hand hygiene.
- Avoid contacting the mask while wearing it.
- Wear the mask cautiously assuring it coats the nose or mouth, adjust to the nose, and wrap it securely to reduce any gaps between the face and the mask.
- Discard the mask using a reasonable technique.
- While removing the mask, do not touch the front part of the mask and remove it from the back.
- After disposal or a used mask is inadvertently touched, immediately clean hands with an alcohol-based sanitizer, or soap and water.
- Don't reuse again single-used masks.
- Replace the mask as early as it becomes damp with a new clean, dry mask.
- Abandon the single-use masks after each use and dispose of them carefully.

## 5. Conclusion

Covid-19 has created a huge impact on economic, educational, psychological, and people's livelihood worldwide. Regulating SARS-CoV-2 transmission at the source by a face mask is a well-established strategy. Medical mask and N95 mask shortages have become major problems all over the world. Homemade cloth or fabric masks, however, were highly recommended by researchers as a way to reduce COVID-19 transmission. As per reports, there are no proven vaccines or specific treatments available which show cent percent efficacy to prevent this pandemic yet. Though the work has been going on vaccination by International research organizations and they developed several vaccines



to date but nothing provides the hundred percent effectiveness against COVID-19. Until then, it is recommended that every individual should wear face masks in community places and maintain other protective measures. Everyone as a responsible citizen must follow the guidelines and instructions recommended by WHO and the Government to combat the pandemic situation.

The general public can use cloth masks especially cloth mask 1 as an alternative to medical and surgical masks in case they are not available. Till now, the three-layered cloth mask 1 provides the best filtering technique. Besides this people can also use the KN95 mask as an alternative to the N95 mask because it also provides similar effectiveness as N95 masks.

It is recommended for people to wear a mask whenever possible to prevent themselves from the coronavirus outbreak.

#### Author contributions

Conceptualization, J.S.; resources, S.D., A.D. and S.D.; writing—draft preparation, S.D., A.D., S.D., and S.S.; writing—review and editing, J.S. and S.S.; image preparation, P.C. and J.S.; visualization, J.S.; supervision, J.S.; All authors have read and agreed to the published version of the manuscript.

#### Declaration of competing interest

A conflict of interest occurs when an individual's objectivity is potentially compromised by a desire for financial gain, prominence, professional advancement or a successful outcome. *CEGH* Editors strive to ensure that what is published in the Journal is as balanced, objective and evidence-based as possible. Since it can be difficult to distinguish between an actual conflict of interest and a perceived conflict of interest, the Journal requires authors to disclose all and any potential conflicts of interest.

#### Acknowledgements

This study received no financial support from the government, commercial, or non-profit funding bodies.

#### References

- WHO. WHO Director-General's Opening Remarks at the Media Briefing on COVID-19 - 11 March 2020.
- Chan JFW, Kok KH, Zhu Z, et al. Genomic characterization of the 2019 novel human-pathogenic coronavirus isolated from a patient with atypical pneumonia after visiting Wuhan. *Emerg Microb Infect.* 2020;9(1):221–236. <https://doi.org/10.1080/22221751.2020.1719902>.
- Cheng VCC, Wong SC, Chuang VWM, et al. The role of community-wide wearing of face mask for control of coronavirus disease 2019 (COVID-19) epidemic due to SARS-CoV-2. *J Infect.* 2020;81(1):107–114. <https://doi.org/10.1016/j.jinf.2020.04.024>.
- Cheng VCC, Wong SC, To KKW, Ho PL, Yuen KY. Preparedness and proactive infection control measures against the emerging novel coronavirus in China. *J Hosp Infect.* 2020;104(3):254–255. <https://doi.org/10.1016/j.jhin.2020.01.010>.
- Cheng VCC, Wong SC, Chen JHK, et al. Escalating infection control response to the rapidly evolving epidemiology of the coronavirus disease 2019 (COVID-19) due to SARS-CoV-2 in Hong Kong. *Infect Control Hosp Epidemiol.* 2020;41(5):493–498. <https://doi.org/10.1017/ice.2020.58>.
- Olliaro P, Torrelee E, Vaillant M. COVID-19 vaccine efficacy and effectiveness—the elephant (not) in the room. *The Lancet Microbe.* 2021. [https://doi.org/10.1016/s2666-5247\(21\)00069-0](https://doi.org/10.1016/s2666-5247(21)00069-0), 0(0).
- Bar-Zeev N, Inglesby T. COVID-19 vaccines: early success and remaining challenges. *Lancet.* 2020;396(10255):868–869. [https://doi.org/10.1016/S0140-6736\(20\)31867-5](https://doi.org/10.1016/S0140-6736(20)31867-5).
- Kaur SP, Gupta V. COVID-19 Vaccine: a comprehensive status report. *Virus Res.* 2020; 288:198114. <https://doi.org/10.1016/j.virusres.2020.198114>.
- Howard J, Huang A, Li Z, et al. Face Masks against COVID-19: An Evidence Review. Published online April 2020. doi:10.20944/preprints202004.0203.v1.
- Abd-Elseyed A, Karri J. Utility of standard face mask options for health care workers during the COVID-19 pandemic. *Anesth Analg.* Published online 2020:4-6. doi:10.1213/ANE.0000000000004841.
- Lisa Allison A, Ambrose-Dempster E, Domenech Aparisi T, Bawn M, Casas M. Article title: the impact and effectiveness of the general public wearing masks to reduce the spread of pandemics in the UK: a multidisciplinary comparison of single-use masks

- versus reusable face masks. UCL Open Environ Prepr. Published online October 2020. doi:10.14324/111.444/000031.v2.
- MacIntyre CR, Chughtai AA, Rahman B, et al. The efficacy of medical masks and respirators against respiratory infection in healthcare workers. *Influenza Other Respir Viruses.* 2017;11(6):511–517. <https://doi.org/10.1111/irv.12474>.
  - Davies A, Thompson KA, Giri K, Kafatos G, Walker J, Bennett A. Testing the efficacy of homemade masks: would they protect in an influenza pandemic? *Disaster Med Public Health Prep.* 2013;7(4):413–418. <https://doi.org/10.1017/dmp.2013.43>.
  - Ong SWX, Tan YK, Chia PY, et al. Air, surface environmental, and personal protective equipment contamination by severe acute respiratory syndrome coronavirus 2 (SARS-CoV-2) from a symptomatic patient. *JAMA, J Am Med Assoc.* 2020;323(16): 1610–1612. <https://doi.org/10.1001/jama.2020.3227>.
  - Liu J, Liao X, Qian S, et al. Community transmission of severe acute respiratory syndrome Coronavirus 2, Shenzhen, China, 2020. *Emerg Infect Dis.* 2020;26(6): 1320–1323. <https://doi.org/10.3201/eid2606.200239>.
  - Guo ZD, Wang ZY, Zhang SF, et al. Aerosol and surface distribution of severe acute respiratory syndrome coronavirus 2 in hospital wards, wuhan, China, 2020. *Emerg Infect Dis.* 2020;26(7):1586–1591. <https://doi.org/10.3201/eid2607.200885>.
  - Van Doremalen N, Bushmaker T, Morris DH, et al. Aerosol and surface stability of SARS-CoV-2 as compared with SARS-CoV-1. *N Engl J Med.* 2020;382(16):1564–1567. <https://doi.org/10.1056/NEJMc2004973>.
  - Wölfel R, Corman VM, Guggemos W, et al. Virological assessment of hospitalized patients with COVID-2019. *Nature.* 2020;581(7809):465–469. <https://doi.org/10.1038/s41586-020-2196-x>.
  - Yu P, Zhu J, Zhang Z, Han Y. A familial cluster of infection associated with the 2019 novel coronavirus indicating possible person-to-person transmission during the incubation period. *J Infect Dis.* 2020;221(11):1757–1761. <https://doi.org/10.1093/infdis/jiaa077>.
  - Lauer SA, Grantz KH, Bi Q, et al. The incubation period of coronavirus disease 2019 (CoVID-19) from publicly reported confirmed cases: estimation and application. *Ann Intern Med.* 2020;172(9):577–582. <https://doi.org/10.7326/M20-0504>.
  - Kimball A, Hatfield KM, Arons M, et al. Asymptomatic and presymptomatic SARS-CoV-2 infections in residents of a long-term care skilled nursing facility — king county, Washington, March 2020. *MMWR Morb Mortal Wkly Rep.* 2020;69(13): 377–381. <https://doi.org/10.15585/mmwr.mm6913e1>.
  - Advice on the Use of Masks in the Community, during Home Care and in Healthcare Settings in the Context of the Novel Coronavirus (COVID-19) Outbreak.
  - Migliori GB, Nardelli E, Yedilbayev A, et al. Reducing tuberculosis transmission: a consensus document from the world health organization regional office for europe. *Eur Respir J.* 2019;53(6). <https://doi.org/10.1183/13993003.00391-2019>.
  - Dharmadhikari AS, Mphahlele M, Stoltz A, et al. Surgical face masks worn by patients with multidrug-resistant tuberculosis: impact on infectivity of air on a hospital ward. *Am J Respir Crit Care Med.* 2012;185(10):1104–1109. <https://doi.org/10.1164/rccm.201107-11900C>.
  - Long Y, Hu T, Liu L, et al. Effectiveness of N95 respirators versus surgical masks against influenza: a systematic review and meta-analysis. *J Evid Base Med.* 2020;13(2):93–101. <https://doi.org/10.1111/jebm.12381>.
  - Bae S, Kim MC, Kim JY, et al. Retraction: effectiveness of surgical and cotton masks in blocking SARS-CoV-2: a controlled comparison in 4 patients (annals of internal medicine (2020)). *Ann Intern Med.* 2020;173(1):W22–W23. <https://doi.org/10.7326/M20-1342>.
  - Jiang S-C, Zhang Z-W, Fu Y-F, et al. *More Patient Deaths: A Correlation Analysis.* vol. 12. 2019.
  - van der Sande M, Teunis P, Sabel R. Professional and Home-Made Face Masks Reduce Exposure to Respiratory Infections Among the General Population. *Pai M, ed. PLoS One.* 2008;vol. 3(7), e2618. <https://doi.org/10.1371/journal.pone.0002618>.
  - Papineni RS, Rosenthal FS. The size distribution of droplets in the exhaled breath of healthy human subjects. *J Aerosol Med Depos Clear Eff Lung.* 1997;10(2):105–116. <https://doi.org/10.1089/jam.1997.10.105>.
  - How to Protect Yourself & Others | CDC.
  - Wang X, Pan Z, Cheng Z. Association between 2019-nCoV transmission and N95 respirator use. *J Hosp Infect.* 2020;105(1):104–105. <https://doi.org/10.1016/j.jhin.2020.02.021>.
  - Setti L, Passarini F, De Gennaro G, et al. Airborne transmission route of covid-19: why 2 meters/6 feet of inter-personal distance could not be enough. *Int J Environ Res Publ Health.* 2020;17(8):2932. <https://doi.org/10.3390/ijerph17082932>.
  - Theresa Tam Offers New Advice: Wear a Non-medical Face Mask when Shopping or Using Public Transit - the Globe and Mail.
  - Yang P, Seale H, Raina MacIntyre C, et al. Mask-wearing and respiratory infection in healthcare workers in Beijing, China. *Braz J Infect Dis.* 2011;15(2):102–108. [https://doi.org/10.1016/s1413-8670\(11\)70153-2](https://doi.org/10.1016/s1413-8670(11)70153-2).
  - Jain M, Kim ST, Xu C, Li H, Rose G. Efficacy and Use of Cloth Masks: A Scoping Review. doi:10.7759/cureus.10423.
  - Pang X, Zhu Z, Xu F, et al. Evaluation of control measures implemented in the severe acute respiratory syndrome outbreak in Beijing, 2003. *J Am Med Assoc.* 2003;290(24):3215–3221. <https://doi.org/10.1001/jama.290.24.3215>.
  - Shakya KM, Noyes A, Kallin R, Peltier RE. Evaluating the efficacy of cloth facemasks in reducing particulate matter exposure. *J Expo Sci Environ Epidemiol.* 2017;27(3): 352–357. <https://doi.org/10.1038/jes.2016.42>.
  - Ma QX, Shan H, Zhang HL, Li GM, Yang RM, Chen JM. Potential utilities of mask-wearing and instant hand hygiene for fighting SARS-CoV-2. *J Med Virol.* 2020;92(9): 1567–1571. <https://doi.org/10.1002/jmv.25805>.
  - Investigation and Initial Clinical Management of Possible Human Cases of Avian Influenza Viruses that Have Been Associated with Severe Human Disease.* 2020.
  - Tcharkhtchi A, Abbasnezhad N, Zarbini Seydani M, Zirak N, Farzaneh S, Shirinbayan M. An overview of filtration efficiency through the masks: mechanisms

- of the aerosols penetration. *Bioact Mater.* 2021;6(1):106–122. <https://doi.org/10.1016/j.bioactmat.2020.08.002>.
- 41 J G, M C, C M, B C Evaluating the Protection Afforded by Surgical Masks against Influenza Bioaerosols : Gross Protection of Surgical Masks Compared to Filtering Facepiece Respirators. Published online January 2008.
  - 42 Balazy A, Toivola M, Adhikari A, Sivasubramani SK, Reponen T, Grinshpun SA. Do N95 respirators provide 95% protection level against airborne viruses, and how adequate are surgical masks? *Am J Infect Contr.* 2006;34(2):51–57. <https://doi.org/10.1016/j.ajic.2005.08.018>.
  - 43 Marambio-Jones C, Hoek EMV. A review of the antibacterial effects of silver nanoparticles and potential implications for human health and the environment. *J Nanoparticle Res.* 2010;12(5):1531–1551. <https://doi.org/10.1007/s11051-010-9900-y>.
  - 44 Lindsley WG, Noti JD, Blachere FM, Szalajda JV, Beezhold DH. Efficacy of face shields against cough aerosol droplets from a cough simulator. *J Occup Environ Hyg.* 2014;11(8):509–518. <https://doi.org/10.1080/15459624.2013.877591>.
  - 45 Makison Booth C, Clayton M, Crook B, Gawn JM. Effectiveness of surgical masks against influenza bioaerosols. *J Hosp Infect.* 2013;84(1):22–26. <https://doi.org/10.1016/j.jhin.2013.02.007>.
  - 46 MacIntyre CR, Chughtai AA. Facemasks for the prevention of infection in healthcare and community settings. *BMJ.* 2015;350. <https://doi.org/10.1136/bmj.h694>.
  - 47 Patel RB, Skaria SD, Mansour MM, Smaldone GC. Respiratory source control using a surgical mask: an in vitro study. *J Occup Environ Hyg.* 2016;13(7):569–576. <https://doi.org/10.1080/15459624.2015.1043050>.
  - 48 Leung NHL, Chu DKW, Shiu EYC, et al. Respiratory virus shedding in exhaled breath and efficacy of face masks. *Nat Med.* 2020;26(5):676–680. <https://doi.org/10.1038/s41591-020-0843-2>.
  - 49 Johnson DF, Druce JD, Birch C, Grayson ML. A quantitative assessment of the efficacy of surgical and N95 masks to filter influenza virus in patients with acute influenza infection. *Clin Infect Dis.* 2009;49(2):275–277. <https://doi.org/10.1086/600041>.
  - 50 Milton DK, Fabian MP, Cowling BJ, Grantham ML, McDevitt JJ. Influenza virus aerosols in human exhaled breath: particle size, culturability, and effect of surgical masks. *PLoS Pathog.* 2013;9(3):1003205. <https://doi.org/10.1371/journal.ppat.1003205>.
  - 51 Seto WH, Tsang D, Yung RWH, et al. Effectiveness of precautions against droplets and contact in prevention of nosocomial transmission of severe acute respiratory syndrome (SARS). *Lancet.* 2003;361(9368):1519–1520. [https://doi.org/10.1016/S0140-6736\(03\)13168-6](https://doi.org/10.1016/S0140-6736(03)13168-6).
  - 52 Radonovich LJ, Simberkoff MS, Bessesen MT, et al. N95 respirators vs medical masks for preventing influenza among health care personnel: a randomized clinical trial. *JAMA, J Am Med Assoc.* 2019;322(9):824–833. <https://doi.org/10.1001/jama.2019.11645>.
  - 53 Offeddu V, Yung CF, Low MSF, Tam CC. Effectiveness of masks and respirators against respiratory infections in healthcare workers: a systematic review and meta-analysis. *Clin Infect Dis.* 2017;65(11):1934–1942. <https://doi.org/10.1093/cid/cix681>.
  - 54 Eikenberry SE, Mancuso M, Iboi E, et al. To mask or not to mask: modeling the potential for face mask use by the general public to curtail the COVID-19 pandemic. *Infect Dis Model.* 2020;5:293–308. <https://doi.org/10.1016/j.idm.2020.04.001>.
  - 55 Liao L, Xiao W, Zhao M, et al. Can N95 respirators Be reused after disinfection? How many times? *ACS Nano.* 2020;14(5):6348–6356. <https://doi.org/10.1021/acsnano.0c03597>.
  - 56 THE NATIONAL ACADEMIES PRESS Reusability of Facemasks during an Influenza Pandemic: Facing the Flu. 2006. <https://doi.org/10.17226/11637>. Published online 2006.
  - 57 A Guide to Using Nonmedical Masks - UTHealth News - UTHealth..
  - 58 How to Wash a Cloth Face Covering | CDC..
  - 59 Coronavirus Disease (COVID-19): Masks.
  - 60 Assadi M, Gholamrezanezhad A, Jokar N, et al. Key elements of preparedness for pandemic coronavirus disease 2019 (COVID-19) in nuclear medicine units. *Eur J Nucl Med Mol Imag.* 2020;47(8):1779–1786. <https://doi.org/10.1007/s00259-020-04780-4>.
  - 61 Cook TM. Personal protective equipment during the coronavirus disease (COVID) 2019 pandemic – a narrative review. *Anaesthesia.* 2020;75(7):920–927. <https://doi.org/10.1111/anae.15071>.
  - 62 COVID-19: Considerations for Wearing Masks | CDC.
  - 63 Your Guide to Masks | CDC.
  - 64 WHO | Infection Prevention and Control of Epidemic-And Pandemic Prone Acute Respiratory Infections in Health Care. WHO; 2015. Published online.
  - 65 Infection Prevention and Control during Health Care when Novel Coronavirus (nCoV) Infection Is Suspected.
  - 66 Ł. Matusiak, Szepietowska M, Krajewski PK, Białynicki-Birula R, Szepietowski JC. The use of face masks during the COVID-19 pandemic in Poland: a survey study of 2315 young adults. *Dermatol Ther;* 2020. <https://doi.org/10.1111/dth.13909>. Published online.
  - 67 Giacomelli A, Pezzati L, Conti F, et al. Self-reported olfactory and taste disorders in patients with severe acute respiratory coronavirus 2 infection: a cross-sectional study. *Clin Infect Dis.* 2020;71(15):889–890. <https://doi.org/10.1093/cid/ciaa330>.
  - 68 Tong JY, Wong A, Zhu D, Fastenberg JH, Tham T. The prevalence of olfactory and gustatory dysfunction in COVID-19 patients: a systematic review and meta-analysis. *Otolaryngol Head Neck Surg.* 2020;163(1):3–11. <https://doi.org/10.1177/0194599820926473>.
  - 69 Arons MM, Hatfield KM, Reddy SC, et al. Presymptomatic SARS-CoV-2 infections and transmission in a skilled nursing facility. *N Engl J Med.* 2020;382(22):2081–2090. <https://doi.org/10.1056/NEJMoa2008457>.
  - 70 Tay HS, Harwood R. Atypical presentation of COVID-19 in a frail older person. *Age Ageing.* 2020;49(4):523–524. <https://doi.org/10.1093/ageing/afaa068>.
  - 71 McMichael TM, Currie DW, Clark S, et al. Epidemiology of covid-19 in a long-term care facility in King County, Washington. *N Engl J Med.* 2020;382(21):2008–2011. <https://doi.org/10.1056/NEJMoa2005412>.
  - 72 Chu DK, Akl EA, Duda S, Solo K, Yaacoub S, Schünemann HJ. Physical distancing, face masks, and eye protection to prevent person-to-person transmission of SARS-CoV-2 and COVID-19: a systematic review and meta-analysis. [www.thelancet.com](http://www.thelancet.com); 2020, 395.
  - 73 World Health Organization. Home Care for Patients with Suspected Novel Coronavirus (COVID-19) Infection Presenting with Mild Symptoms, and Management of Their Contacts: Interim Guidance, 04 February 2020. *World Heal.* World Health Organization; 2020, 2020.



# Source details

[Feedback >](#) [Compare sources >](#)

## Clinical Epidemiology and Global Health

Open Access

Scopus coverage years: from 2013 to Present

Publisher: Elsevier

E-ISSN: 2213-3984

Subject area: [Medicine: Public Health, Environmental and Occupational Health](#) [Medicine: Infectious Diseases](#) [Medicine: Epidemiology](#)  
[Medicine: Microbiology \(medical\)](#)

Source type: Journal

[View all documents >](#)

[Set document alert](#)

[Save to source list](#)

CiteScore 2022

4.3

SJR 2022

0.615

SNIP 2022

0.995



## Green synthesis of copper/copper oxide nanoparticles and their applications: a review

Nilanjan Chakraborty, Jishnu Banerjee, Pallab Chakraborty, Anuron Banerjee, Sumedha Chanda, Kasturi Ray, Krishnendu Acharya & Joy Sarkar

To cite this article: Nilanjan Chakraborty, Jishnu Banerjee, Pallab Chakraborty, Anuron Banerjee, Sumedha Chanda, Kasturi Ray, Krishnendu Acharya & Joy Sarkar (2022) Green synthesis of copper/copper oxide nanoparticles and their applications: a review, Green Chemistry Letters and Reviews, 15:1, 185-213, DOI: [10.1080/17518253.2022.2025916](https://doi.org/10.1080/17518253.2022.2025916)

To link to this article: <https://doi.org/10.1080/17518253.2022.2025916>



© 2022 The Author(s). Published by Informa UK Limited, trading as Taylor & Francis Group



Published online: 27 Jan 2022.



Submit your article to this journal [↗](#)











View related articles [↗](#)



View Crossmark data [↗](#)

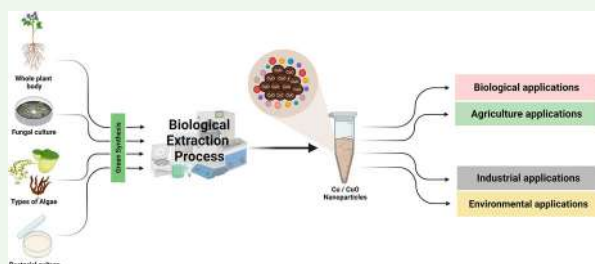
## Green synthesis of copper/copper oxide nanoparticles and their applications: a review

Nilanjan Chakraborty <sup>a</sup>, Jishnu Banerjee <sup>b</sup>, Pallab Chakraborty <sup>c</sup>, Anuron Banerjee <sup>a</sup>,  
Sumedha Chanda <sup>d</sup>, Kasturi Ray <sup>d</sup>, Krishnendu Acharya <sup>e,f</sup> and Joy Sarkar <sup>b</sup>

<sup>a</sup>Department of Botany, Scottish Church College, Kolkata, India; <sup>b</sup>Department of Botany, Dinabandhu Andrews College, Kolkata, India; <sup>c</sup>Department of Botany, Acharya Prafulla Chandra College, Kolkata, India; <sup>d</sup>Department of Botany, Lady Brabourne College, Kolkata, India; <sup>e</sup>Molecular and Applied Mycology and Plant Pathology Laboratory, Centre of Advanced Study, Department of Botany, University of Calcutta, Kolkata, India; <sup>f</sup>Center for Research in Nanoscience & Nanotechnology, University of Calcutta, Kolkata, India

### ABSTRACT

Copper and Copper oxide nanoparticles have garnered a lot of attention among the metal oxide nanoparticles, especially because of their many characteristics and applications in many disciplines, notably nanomedicine and biomedical sciences. We have covered all of the conceivable green production techniques of copper/copper oxide nanoparticles in this review. This manuscript also diagrammatically depicts the exact mechanism of all conceivable biosynthetic routes. We also look at the antibacterial, antifungal, antiviral, and anticancer properties of biosynthesized copper/copper oxide nanoparticles, as well as their effects on plant growth, nutrition, and defense mechanism.



Abbreviations: Cu/CuO NPs: Copper/Copper Oxide nanoparticles; DLS: Dynamic Light Scattering; EDS: Energy Dispersive X-ray Spectroscopy; EDX: Energy dispersive X-Ray; FFT: Fast Fourier transform; FTIR: Fourier transform infrared spectroscopy; HR-TEM: High-resolution transmission electron microscopy, HeLa: Henrietta Lacks; IR: infrared; LSV: Linear sweep voltammetry; NTA: Nanoparticle tracking analysis; PPE: Personal protective equipment; PSA: Particle size analyzer; SEM: Scanning electron microscope; SPR: Surface plasmon resonance; TEM: Transmission electron microscopy; VEGF: Vascular endothelial growth factor; XRD: X-ray diffraction.

### ARTICLE HISTORY

Received 21 September 2021  
Accepted 31 December 2021

### KEYWORDS



Anticancer activity;  
Antimicrobial activity;  
Copper/Copper oxide  
nanoparticles; Green  
synthesis; Plant defense

## 1. Introduction

In the sphere of research, nanotechnology is a relatively new approach. This technology is now widely used (1) in diversified fields. The smaller dimension of nanomaterials, ranges from 1–100 nanometers (nm) (1), alters their physicochemical properties like shape, size, and chemical composition. In the twenty-first century, a more in-depth investigation of metallic NPs was carried out by several researchers (2).

Bionanotechnology is a rapidly growing field of nanotechnology in which bio-organisms are extensively used

to synthesize nanomaterials and the synthesized nanomaterials are simultaneously used to improve the quality of life of the organisms (2). Biological synthesis uses the biological principle of oxidation and reduction by microbial enzymes or plant phytochemicals (3). In recent times physical and chemical methods are mainly used for the synthesis of inorganic NPs (2). Both physical and chemical methods have some disadvantages like low-productivity, non-eco-friendly, toxic, and capital intensive. For these reasons, biological synthesis is trying to replace the chemical methods of producing NPs (4–23).

**CONTACT** Joy Sarkar  [jsarkar80@gmail.com](mailto:jsarkar80@gmail.com)  Department of Botany, Dinabandhu Andrews College, Garia, Kolkata, West Bengal 700084, India

© 2022 The Author(s). Published by Informa UK Limited, trading as Taylor & Francis Group  
This is an Open Access article distributed under the terms of the Creative Commons Attribution License (<http://creativecommons.org/licenses/by/4.0/>), which permits unrestricted use, distribution, and reproduction in any medium, provided the original work is properly cited.

Numerous reports and studies have demonstrated that this green synthesis process has already manufactured a large number of metal/metal oxide nanoparticles such as silver (Ag), gold (Au), selenium (Se), platinum (Pt), zinc oxide (ZnO) and iron oxide ( $\text{Fe}_2\text{O}_3$ ), graphene oxide etc. (4–22). Additionally, those studies reported that several metal nanoparticles have a variety of biological and biochemical activities, but CuNPs have recently gained attention. Copper plays a variety of roles in humans, including serving as a cofactor for numerous enzymes involved in neuropeptide production, cell signaling pathway regulation, antioxidant defence, and immune cell function (24, 25). Copper is needed by plants for a variety of metabolic and physicochemical processes. It's one of the most crucial trace elements for plant growth (26). It is present in both humans and plants in a very small amount and helps to regulate different metabolic and biological activities as it acts as cofactors for different enzymes. It is responsible for the normal functioning of different essential proteins/enzymes such as amino oxidase, cytochrome c oxidase, and plastocyanin since it is a cofactor for multiple enzymes (27, 28). Copper oxide, on the other hand, has antimicrobial, antibacterial, antifungal, antimicrobial, antifungal, magnetic phase change, gas sensing, biocidal, superconductive, catalytic, and optical properties (29). CuO has a bandgap of 1.7 eV and is a p-type semiconductor. The application of biologically synthesized copper nanoparticles (CuNPs) was found to be a promising bioactive agent in this context.

CuONPs are made by different physicochemical methods like sol-gel technique (30), sonochemical (31), electrochemical method (32), microwave irradiations (33), solid-state reaction method (34), alkoxide based route (35) etc. Likewise, these nanoparticles are also generated by the algal, fungal, plant and other biosynthesis routes. In this review, we have focused on almost all the biosynthetic routes of CuNPs/CuONPs. The detailed mechanism of all the possible biosynthetic routes is diagrammatically represented in this manuscript. On the other hand, high catalytic and chemical reactivity, large surface area, and ability to interact with microbe's cells are some of the attributes of CuNPs/CuONPs which enables their application in different fields like agricultural, biomedical, textile, and environmental sectors (36). Our review also focuses on the potential applications of biosynthesized CuNPs/CuONPs.

## 2. Green synthesis of nanoparticles

Green synthesis can be defined as the derivation of materials from green or eco-friendly resources by the use of solvent, good reducing agent, and harmless

material for stabilization (37). Additionally, this synthesis route is straightforward, cost-effective, dependable, sustainable, and relatively repeatable, and results in more stable compounds. Thus, researchers have expressed an interest in developing a variety of nanomaterials via this biosynthesis route, including metal/metal oxide nanoparticles, hybrid materials, and bioinspired materials. As a result, green synthesis is widely regarded as a necessary tool for mitigating the negative consequences of conventional nanoparticle synthesis methods used in laboratories and industries (38). In that context, traditional nanoparticle producing techniques like chemical and physical synthesis are found to be costly, hazardous, and unfriendly to the environment (39). Not only that chemical synthesis of nano-production may sometime affect biological activities by some factors like size distribution, morphology, surface charge, surface chemistry, capping agents, etc. (40, 41). To avoid the harmful effect, researchers have discovered the precise green pathways, or naturally occurring sources and their products, that may be utilized to synthesize nanoparticles, to address these issues. To circumvent these negative consequences, researchers have identified the precise green pathways, or naturally occurring sources and their products, that can be employed to manufacture nanoparticles.

Nanoparticle synthesis can be divided into two categories (Figure 1): (i) Top down method and (ii) bottom up method. The physical route of nanoparticle synthesis is emphasized in the top down method, whereas the chemical and biological methods are emphasized in the bottom up method.

Physical synthesis route consists of pulsed laser ablation, arc discharge, spray pyrolysis, ball milling, vapor and gas phase, pulsed wire discharge, lithography etc. On the other hand, chemical synthesis route consists of chemical reduction, sonochemical, microemulsion, photochemical, electrochemical, pyrolysis, microwave, solvothermal, coprecipitation etc.

Additionally, green nanoparticle synthesis can be divided into the following categories (Figure 1):

- (a) Phyto routes like utilization of plants and plant extracts
- (b) Microbial routes like the utilization of microorganisms such as fungi, yeasts (eukaryotes), bacteria, and actinomycetes
- (c) Bio-template routes like the utilization of membranes, viruses, and diatoms as templates

Both extracellular and intracellular biological approaches have been employed to synthesize nanoparticles. Although the precise method for the creation of

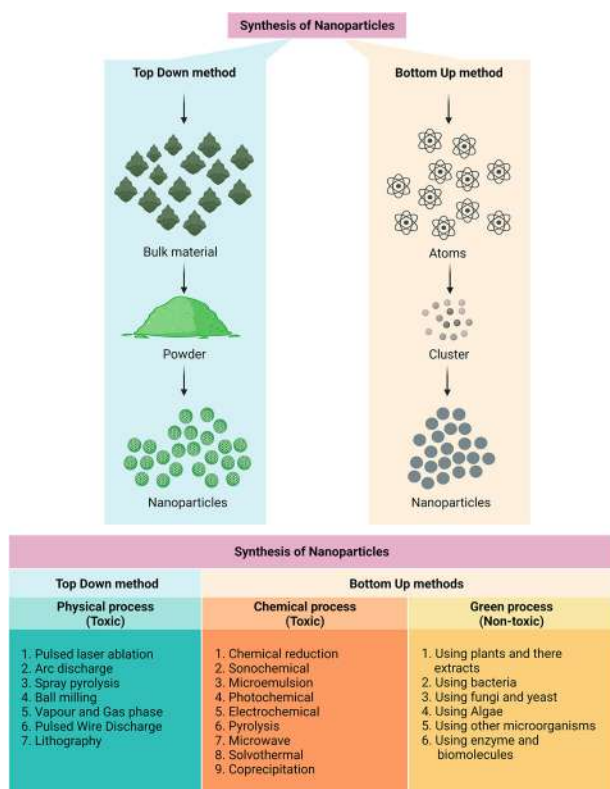


**Figure 1.** Various routes of nanoparticles synthesis (Created with BioRender.com).

nanoparticles utilizing biological agents has yet to be discovered, it is suggested that distinct biomolecules are involved for nanoparticle synthesis. Furthermore, the methods for intracellular and extracellular nanoparticle formation differ, and it appears that the cell wall of microorganisms plays a key role in intracellular nanoparticle synthesis whereas extracellular enzymes play a key role in extracellular nanoparticle synthesis. Extracellular nanoparticle synthesis has surpassed intracellular nanoparticle synthesis in popularity due to its faster production rate and simpler synthesis procedure (42).

### 2.1. Probable mechanism of biosynthesis of Cu/CuO-NPs

Cu ions come in a variety of oxidation values, including Cu(I), Cu(II), and a few Cu(III) ions. In terms of plant extract, fungal extract, algal extract, bacterial extract, precursor concentration, pH, and temperature, the synthesis technique reported for CuO, Cu<sub>2</sub>O, and Cu<sub>4</sub>O<sub>3</sub> is the same to date. These variables, however, have the greatest impact on the type of Cu particles generated during green synthesis (43). During the green synthesis, the biomolecules present in the sample extract reduce the Cu<sup>2+</sup> ion to Cu<sup>0</sup> state and simultaneously oxidize it to form CuO nanoparticles. Certain biomolecules found

in the sample extract serve as a capping agent and also aid in the stabilization of the produced nanoparticles (43).

### 2.2. Green synthesis of Cu/CuO-NPs by plant extracts

The environmentally accepted 'green chemistry' idea has been applied to the biosynthesis of nanoparticles for the creation of clean and environmentally friendly nanoparticles, which incorporates bacteria, fungi, plants, actinomycetes, and other organisms, and is referred to as 'green synthesis'. Biosynthesis of nanoparticles utilizing the organisms mentioned above exemplifies a green alternative for the creation of nanoparticles with novel characteristics. Unicellular and multicellular organisms are permitted to respond in these syntheses.

Plants are renowned as nature's chemical factories since they are low-cost and low maintenance. Because extremely minute quantities of these heavy metals are hazardous even at very low concentrations, plants have shown exceptional potential in heavy metal detoxification as well as accumulation, through which environmental contaminants may be overcome (44–50). Nanoparticle synthesis using plant extract has benefits over other biological synthesis methods, such as microorganisms, because the rate of metal nanoparticle synthesis with the help of plant extract is more persistent (51), significantly faster (52, 53), and extremely mono-dispersive (54) in respect to other biological methods (55). The main challenges for using microorganisms include the toxicity of certain bacteria, the isolation procedure of microorganisms, and the tedious incubation procedure which make them unsuitable for many researchers. Plant extracts are therefore a remarkable source of synthesis of metal and metal oxide nanoparticles (55–57). Additionally, the reaction kinetics of plant-assisted nanoparticle synthesis is much faster than other biosynthetic methods that are comparable to chemical nanoparticle production. Plant components such as fruit, leaf, stem, and root have been frequently employed for the green route of nanoparticle production due to the high-quality phytochemicals they generate.

Here, for the mentioned reason, Copper oxide nanoparticles have been widely synthesized using various plant extracts (58–60). In this plant-based manufacturing process, the metal salt is mixed with the plant extracts, and the reaction takes 1–3 h to complete at room temperature (Figure 2). Plant extracts include a variety of bioactive metabolites, including flavonoids, phenols, proteins, terpenoids, and tannins, which serve as

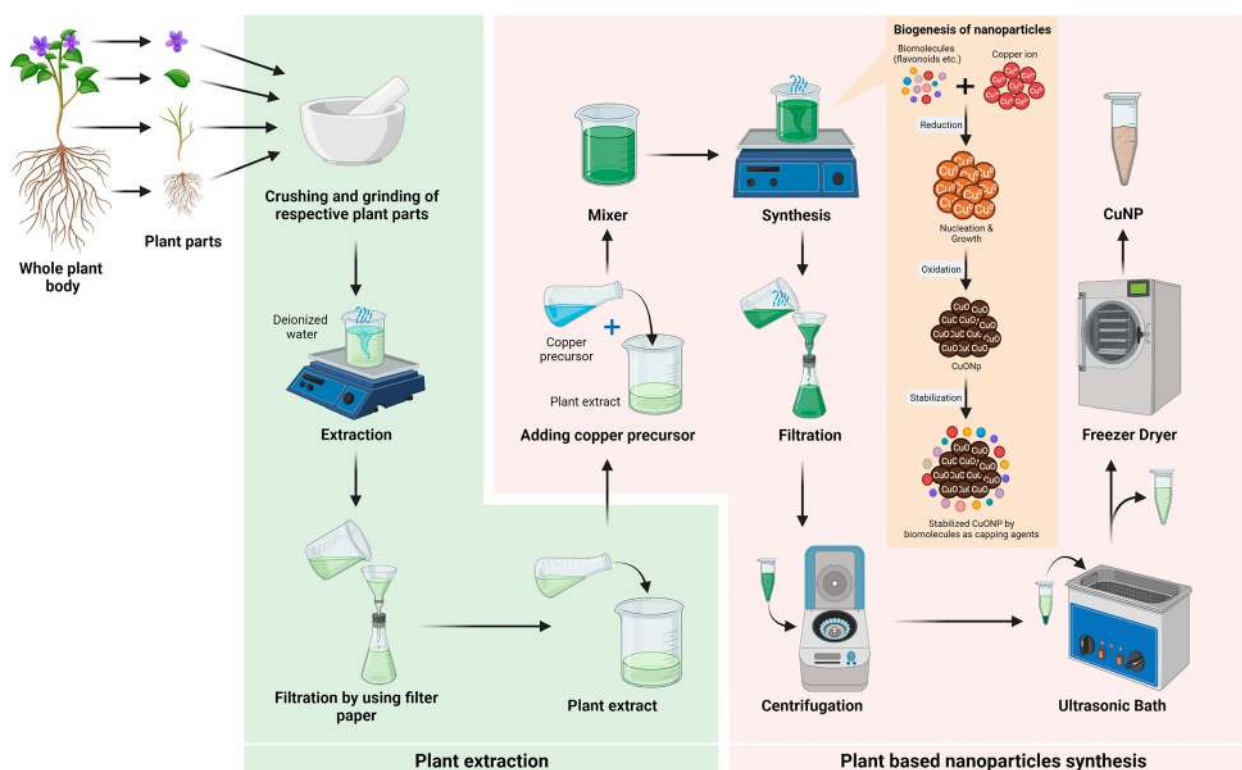


**Figure 2.** Graphical representation of biomediated synthesis of copper oxide nanoparticles using plant extract (Created with BioRender.com).

reducing and stabilizing agents, transforming metallic ions into nanoparticles (38, 44, 61). The plant extract produces electrons, which cause copper salts to get reduced. Copper oxide nanoparticles are formed when phytochemicals react with copper ions, resulting in reduction. Table 1 summarizes the major contributions of biomediated synthesis of copper oxide nanoparticles using various plants.

### 2.3. Green synthesis of Cu/CuO-NPs by using bacteria

Bacteria have been used to make a variety of nanoparticles in recent years, including copper oxide nanoparticles (127). Different materials with fascinating shapes and nanoscale dimensions have been produced using bacteria via an intracellular or extracellular route (Figure 3). Bacteria have a great potential for nanoparticles production. They offer benefits such as a short generation period, ease of culture, benign experimental conditions, excellent stability, extracellular nanoparticle synthesis, and ease of genetic modification (37). It is known that when microorganisms are maintained in a hazardous metal environment, they develop a method to live by converting poisonous metal ions into non-toxic forms such as metal sulfide/oxides. It has been

well established that when bacteria are introduced to an environment containing high levels of hazardous metals, they can survive by converting harmful metal ions to non-toxic metal oxides (128–131). Bacteria have been shown to generate a variety of essential thiol-containing chemicals in response to oxidative stress. These molecules function as a capping agent in the bacterially driven production of nanoparticles, preventing metal oxide nanoparticles from oxidizing (128, 132, 133). The mechanism behind the nanoscale change isn't fully understood to date. Nanoparticle production also requires moderate experimental parameters such as pH, temperature, simple downstream processing, and a short creation period (134). Some of the contributions of biomediated synthesis of copper oxide nanoparticles using different bacteria are shown in Table 2.

### 2.4. Green synthesis of Cu/CuO-NPs by using fungi

Various fungal species have been utilized to synthesize copper oxide and other metal nanoparticles in recent years (127). Fungi, as compared to other microbes, have a lot of potential for nanoparticle production. In comparison to bacteria, fungi tolerate agitation, flow pressure, and other conditions in the bioreactor or any



**Table 1.** Biosynthesis of Cu/CuO nanoparticles by different plants.

Sl. No.	Plants/ plant extract	Precursor	Part used	Size of NPs (in nm)	Shape / structure / morphology	Characterization techniques used	Reference
1.	<i>Carica papaya</i> L.	Copper Chloride (CuCl <sub>2</sub> )	Leaves	20 (in avg.)	Nearly spherical and Crystalline	UV-Vis, XRD, FTIR, SEM, and TEM	(62)
2.	<i>Citrus medica</i> L.	Copper (II) Sulfate Pentahydrate (CuSO <sub>4</sub> .5H <sub>2</sub> O)	Fruit	20 (in avg.)	Crystalline	UV-Vis, NTA and XRD	(63)
3.	<i>Euphorbia esula</i> L.	Copper Sulfate (CuSO <sub>4</sub> )	Leaves	20–110	Spherical	UV-Visible spectroscopy, XRD, FTIR	(64)
4.	<i>Pistacia</i> sp.	Cupric Chloride Dihydrate	Leaves	9 (in avg.)	Crystallized nanowires with 10 nm diameter	XRD, FTIR and SEM	(65)
5.	<i>Nerium oleander</i> L.	Copper Sulfate (CuSO <sub>4</sub> )	Leaves	21	Spherical	UV-Vis and FTIR	(66, 67)
6.	<i>Syzygium aromaticum</i> (L.) Merr. & L.M.Perry	Copper Sulfate (CuSO <sub>4</sub> )	Flower	14–50	Spherical and granular nature	UV-visible spectroscopy, XRD, TEM and SEM	(66, 68)
7.	<i>Ocimum sanctum</i> L.	Copper (II) Sulfate Pentahydrate (CuSO <sub>4</sub> .5H <sub>2</sub> O)	Leaves	77 (in avg.)	Spherical	XRD and FTIR	(66)
8.	<i>Ocimum tenuiflorum</i> L.	Copper (II) Sulfate Pentahydrate (CuSO <sub>4</sub> .5H <sub>2</sub> O)	Leaves	72	Hexagonal wurtzite crystal structure	UV-visible spectroscopy, XRD, FTIR, SEM and EDAX	(66)
9.	<i>Citrus limon</i> (L.) Osbeck	Copper Chloride (CuCl <sub>2</sub> )	Fruits	60–100	Nearly spherical	UV-Vis, FTIR, XRD, SEM and TEM	(69, 70)
10.	<i>Malva sylvestris</i> L.	Copper Chloride Dihydrate (CuCl <sub>2</sub> .2H <sub>2</sub> O)	Leaves	14 (in avg.)	Spherical	XRD, FTIR and SEM	(66)
11.	<i>Albizia lebeck</i> (L.) Benth.	Copper Sulfate (CuSO <sub>4</sub> )	Leaves	100 (in avg.)	Roughly spherical	UV-Vis, SEM, TEM, EDS and XRD	(66)
12.	<i>Datura metel</i> L.	Copper (II) Sulfate Pentahydrate (CuSO <sub>4</sub> .5H <sub>2</sub> O)	Leaves	15–20	Spherical	UV-Vis, PSA, TEM, EDX and FTIR	(71)
13.	<i>Magnolia kobus</i> DC.	Copper (II) Sulfate Pentahydrate (CuSO <sub>4</sub> .5H <sub>2</sub> O)	Leaves	37–110	Spherical	UV-Vis, ICP, EDS, XPS, and HR-TEM	(72)
14.	<i>Ginkgo biloba</i> L.	Cupric Chloride Dihydrate (CuCl <sub>2</sub> .2H <sub>2</sub> O)	Leaves	15–20	Spherical	UV-Vis, TEM, EDS, and FTIR	(73)
15.	<i>Artabotrys odoratissimus</i> R.Br.	Copper (II) Sulfate Pentahydrate (CuSO <sub>4</sub> .5H <sub>2</sub> O)	Leaves	135 (in avg.)	Spherical	PSA	(74)
16.	<i>Capparis zeylanica</i> L.	Copper Sulfate (CuSO <sub>4</sub> )	Leaves	50–100	Cubical structure	UV-Vis, FTIR, XRD, SEM, EDX and TEM	(75)
17.	<i>Aloe vera</i> (L.) Burm.f.	Copper (II) Acetate Dihydrate (Cu(CH <sub>3</sub> COOH) <sub>2</sub> .2H <sub>2</sub> O)	Flowers	40 (in avg.)	Spherical	UV-Vis, FE-SEM, and FTIR	(76)
18.	<i>Cinnamum</i> sp.	Copper Sulfate (CuSO <sub>4</sub> )	Leaves, flowers and roots	18.17-91.28	Spherical	UV-Vis and DLS	(77)
19.	<i>Inula helenium</i>	Copper Sulfate (CuSO <sub>4</sub> )	Leaves, flowers and roots	32.41	Spherical	UV-Vis and DLS	(77)
20.	<i>Matricaria chamomilla</i> L. (Vernacular name: Chamomile)	Copper Sulfate (CuSO <sub>4</sub> )	Leaves, flowers and roots	58.77	Spherical	UV-Vis and DLS	(77)
21.	<i>Urtica</i> sp.	Copper Sulfate (CuSO <sub>4</sub> )	Leaves, flowers and roots	6.5	Spherical	UV-Vis and DLS	(77)
22.	<i>Glycyrrhiza glabra</i> L.	Copper Sulfate (CuSO <sub>4</sub> )	Leaves, flowers and roots	28.21	Spherical	UV-Vis and DLS	(77)
23.	<i>Schizandra chinensis</i> (Turcz.) Baill.	Copper Sulfate (CuSO <sub>4</sub> )	Leaves, flowers and roots	32	Spherical	UV-Vis and DLS	(77)
24.	<i>Eucalyptus</i> sp.	Copper Sulfate (CuSO <sub>4</sub> )	Leaves	38.62 (in avg.)	Spherical	UV-Vis, FTIR, XRD and SEM	(78)
25.	<i>Zingiber officinale</i> Roscoe	Copper Sulfate (CuSO <sub>4</sub> )	Rhizome	25–40	Spherical	UV-Vis and XRD	(79)
26.	<i>Eupatorium glandulosum</i> Michx.	Cupric Nitrate	Leaves	55.91 (in avg.)	Spherical	UV-Vis, FTIR, PSA, TEM and AFM.	(66)
27.	<i>Psidium guajava</i> L.	Cupric Chloride Dihydrate (CuCl <sub>2</sub> .2H <sub>2</sub> O)	Leaves	13.13 ± 0.19	Spherical	UV-Vis	(66)
28.	<i>Glycine max</i> (L.) Merr.	Copper Sulfate (CuSO <sub>4</sub> )	Seeds	20 (in avg.)	Spherical	UV-Vis, TEM and DLS	(66)
29.	<i>Bacopa monnieri</i> (L.) Wettst.	Copper (II) Sulfate Pentahydrate (CuSO <sub>4</sub> .5H <sub>2</sub> O)	Leaves	20–50	Spherical	UV-Vis, FTIR and HR-TEM	(80)

(Continued)

Table 1. Continued.

Sl. No.	Plants/ plant extract	Precursor	Part used	Size of NPs (in nm)	Shape / structure / morphology	Characterization techniques used	Reference
30.	<i>Ocimum basilicum</i> L.	Copper (II) Sulfate Pentahydrate (CuSO <sub>4</sub> ·5H <sub>2</sub> O)	Leaves	40–60	Spherical	UV-Vis, FTIR and HR-TEM	(80)
31.	<i>Asparagus adscendens</i> Roxb.	Copper (II) Sulfate Pentahydrate (CuSO <sub>4</sub> ·5H <sub>2</sub> O)	Leaves	10–15	Spherical	UV-Vis, FTIR and HR-TEM	(80)
32.	<i>Withania somnifera</i> (L.) Dunal	Copper (II) Sulfate Pentahydrate (CuSO <sub>4</sub> ·5H <sub>2</sub> O)	Leaves	50–60	Spherical	UV-Vis, FTIR and HR-TEM	(80)
33.	<i>Phyllanthus emblica</i> L.	Copper Sulfate (CuSO <sub>4</sub> )	Fruits	15–30	Spherical	UV-Vis, FTIR, XRD, SEM, EDAX	
34.	<i>Sterculia urens</i> Roxb. (Vernacular name: Gum karaya)	Cupric Chloride Dihydrate	Gum	4.8 ± 1.6	Spherical	XRD, FTIR, TEM, SEM and XPS	(66)
35.	<i>Gymnema sylvestre</i> (Retz.) R.Br. ex Sm.	Copper Sulfate (CuSO <sub>4</sub> )	Leaves	65–302	Spherical	UV-Vis, FTIR and SEM	(81)
36.	<i>Ixora coccinea</i> L.	Copper Sulfate (CuSO <sub>4</sub> )	Leaves	80–110	Spherical	XRD, FTIR, SEM, TEM,	(82)
37.	<i>Moringa oleifera</i> Lam.	Copper Sulfate (CuSO <sub>4</sub> )	Leaves	6–61	Spherical	XRD, FTIR, SEM, TEM,	(83)
38.	<i>Tridax procumbens</i> (L.) L.	Copper Sulfate (CuSO <sub>4</sub> )	Leaves	16 (in avg.)	Spherical	UV-Vis, XRD, FTIR, SEM, TEM	(84)
39.	<i>Camellia sinensis</i> (L.) Kuntze	Copper Sulfate (CuSO <sub>4</sub> )	Leaves	50–100	Spherical	UV-Vis, FTIR, XRD, SEM,	(85)
40.	<i>Juglans regia</i> L.	Copper Sulfate (CuSO <sub>4</sub> )	Leaves	80 (in avg.)	Spherical	UV-Vis, FTIR, XRD, SEM,	(86)
41.	<i>Acalypha indica</i> L.	Copper Sulfate (CuSO <sub>4</sub> )	Leaves	26–30	Spherical	UV-Vis, FTIR, XRD, SEM, EDX, and TEM	(87)
42.	<i>Punica granatum</i> L.	Copper Acetate Monohydrate [Cu (CH <sub>3</sub> COO) <sub>2</sub> ·H <sub>2</sub> O]	Peel extract	40 (in avg.)	Spherical	UV-Vis, XRD, FTIR, SEM	(88)
43.	<i>Musa acuminata</i> Colla	Copper Nitrate Trihydrate Solution (Cu (NO <sub>3</sub> ) <sub>2</sub> ·3H <sub>2</sub> O)	Peel extract	60 (in avg.)	Spherical	XRD, EDX, FE-SEM, FTIR	(89)
44.	<i>Cordia sebestena</i> L.	Copper (II) Nitrate Trihydrate Solution (Cu(NO <sub>3</sub> ) <sub>2</sub> ·3H <sub>2</sub> O)	Flowers	20–40	Spherical	FESEM-EDX, XRD, FTIR, SEM, TEM	(90)
45.	<i>Hibiscus rosa-sinensis</i> L.	Copper Acetate Solution (Cu (CH <sub>3</sub> COO) <sub>2</sub> ·H <sub>2</sub> O)	Flowers	26.54	Spherical	UV-Vis, XRD, FTIR, and SEM	(91)
46.	<i>Caesalpinia pulcherrima</i> (L.) Sw.	Copper (II) Nitrate (Cu(NO <sub>3</sub> ) <sub>2</sub> ·XH <sub>2</sub> O)	Flowers	20 (in avg.)	Spherical	UV-Vis, FTIR, XRD, EDAX and SEM.	(92)
47.	<i>Rheum palmatum</i> L.	Copper Chloride (CuCl <sub>2</sub> )	Roots	30 (in avg.)	Spherical	UV-Vis, EDX, XRD, FTIR, SEM, TEM	(93)
48.	<i>Desmodium gangeticum</i> (L.) DC.	Copper Sulfate (CuSO <sub>4</sub> )	Roots	12 (in avg.)	Spherical	UV-Vis, TGA, XRD, FTIR, TEM, and SEM	(94)
49.	<i>Phaseolus vulgaris</i> L.	Copper Sulfate (CuSO <sub>4</sub> )	Whole plant	26.6 (in avg.)	Spherical	XRD, Raman, FTIR, TEM, XPS, DLS, SEM, SAED, and EDX	(95)
50.	<i>Coffea arabica</i> L.	Copper Sulfate (CuSO <sub>4</sub> )	Whole plant	262 (in avg.)	Crystalline	UV-Vis, FTIR, XRD, SEM	(96)
51.	<i>Quercus</i> sp.	Copper Sulfate (CuSO <sub>4</sub> )	Whole plant	20–30	Quasi-spherical	FE-SEM, XRD, FTIR	(97)
52.	<i>Ziziphus mauritiana</i> Lam.	Copper Sulfate (CuSO <sub>4</sub> )	Whole plant	20–45	Spherical	XRD, SEM, EDX, TEM	(81)
53.	<i>Ferulago angulata</i> (Schltdl.) Boiss.	Copper (II) Acetate Monohydrate (Cu (CH <sub>3</sub> COO) <sub>2</sub> ·H <sub>2</sub> O)	Whole plant	44 (in avg.)	Spherical	XRD, SEM, EDX, TEM	(98)
54.	<i>Gloriosa superba</i> L.	Copper Sulfate (CuSO <sub>4</sub> )	Whole plant	5–10	Spherical	XRD, SEM, EDX, TEM	(99)
55.	<i>Syzygium alternifolium</i> (Wight) Walp.	Copper Sulfate (CuSO <sub>4</sub> )	Bark	17.2 (in avg.)	Spherical	UV-Vis, XRD, FTIR, DLS, Zeta, TEM	(100)
56.	<i>Zea mays</i> L.	Copper Sulfate (CuSO <sub>4</sub> )	Dry husk	36–73	Spherical	XRD, HR-TEM, EDX, FTIR	(101)
57.	<i>Caesalpinia bonducella</i> (L.) Fleming	Copper Sulfate (CuSO <sub>4</sub> )	Seeds	13.07 (in avg.)	Spherical	UV-Vis, XRD, FTIR, and SEM	(102)
58.	<i>Vitis vinifera</i> L. (Vernacular name: Erzincan Cumin)	Copper Sulfate (CuSO <sub>4</sub> )	Fruits	25–50	Uniform spherical	UV-Vis, FTIR, XRD and SEM	(103)
59.	<i>Cedrus deodara</i> (Roxb. ex D.Don) G.Don	Copper Sulfate (CuSO <sub>4</sub> )	Aqueous extract	16	Spherical	FTIR, UV-Vis, XRD, TEM	(104)
60.	<i>Abutilon indicum</i> (L.) Sweet	Copper (II) Nitrate Trihydrate (Cu (NO <sub>3</sub> ) <sub>2</sub> ·3H <sub>2</sub> O)	Leaves	16.78	Spherical	XRD, EDX, UV-Vis, SEM	(105)
61.	<i>Aloe barbadensis</i> Mill.	Copper Sulfate (CuSO <sub>4</sub> )	Leaves	20 (in avg.)	Spherical	UV-Vis, SEM, TEM, XRD, FTIR	(106)
62.	<i>Ficus religiosa</i> L.	Copper Sulfate (CuSO <sub>4</sub> ·5H <sub>2</sub> O)	Leaves	577 (in avg.)	Spherical	FE-SEM, UV-Vis, XRD, FTIR, DLS	(107)
63.	<i>Phoenix dactylifera</i> L.	Copper Sulfate (CuSO <sub>4</sub> )	Leaves	20–28	Spherical	UV-Vis, FTIR, XRD, SEM, and EDAX	(108)
64.	<i>Centella asiatica</i> (L.) Urb.	Copper Chloride (CuCl <sub>2</sub> ·2H <sub>2</sub> O)	Leaves	5 (in avg.)	Spherical	UV-Vis, IR, EDX	(109)
65.	<i>Azadirachta indica</i> A.Juss.	Copper Chloride (CuCl <sub>2</sub> ·2H <sub>2</sub> O)	Leaves	38 (in avg.)	Spherical	UV-Vis, FTIR, XRD, SEM, EDX, DLS and TEM	(110)

(Continued)

Table 1. Continued.

Sl. No.	Plants/ plant extract	Precursor	Part used	Size of NPs (in nm)	Shape / structure / morphology	Characterization techniques used	Reference
66.	<i>Drypetes sepiaria</i> (Wight & Arn.) Pax & K.Hoffm.	Copper Nitrate (Cu(NO <sub>3</sub> ) <sub>2</sub> ·3H <sub>2</sub> O)	Leaves	298 (in avg.)	Spherical	UV-Vis, IR, XRD, and TEM, FTIR	(111)
67.	<i>Encostemma littorale</i> Blume	Copper Sulfate (CuSO <sub>4</sub> )	Leaves	30 (in avg.)	Spherical	UV-Vis, IR, XRD, and TEM, FTIR	(112)
68.	<i>Cordia myxa</i> L.	Copper Sulfate (CuSO <sub>4</sub> ·5H <sub>2</sub> O)	Leaves	20–106	Spherical	XRD, TEM, FTIR	(113)
69.	<i>Arachis hypogaea</i> L.	Copper (II) Aetate Monohydrate	Leaves	30–50	Spherical	UV-Vis, XRD, FTIR, and SEM	(114)
70.	<i>Leucaena leucocephala</i> (Lam.) de Wit	Copper Acetate Monohydrate (Cu (CH <sub>3</sub> COO) <sub>2</sub> ·H <sub>2</sub> O)	Leaves	10–15	Spherical	UV-Vis, XRD, FTIR, and SEM, BET	(115)
71.	<i>Piper betle</i> L.	Copper Sulfate (CuSO <sub>4</sub> )	Leaves	50–100	Spherical	XRD, SEM, EDX, TEM	(116)
72.	<i>Tabernaemontana divaricata</i> (L.) R.Br. ex Roem. & Schult.	Copper Sulfate (CuSO <sub>4</sub> )	Leaves	48 (in avg.)	Spherical	UV-Vis, FTIR, XRD, EDAX, TEM and SEM	(117)
73.	<i>Ailanthus altissima</i> (Mill.) Swingle	Copper Sulfate (CuSO <sub>4</sub> )	Leaves	20 (in avg.)	Spherical	UV-Vis, SEM, TEM, FTIR	(118)
74.	<i>Saraca indica</i> L.	Copper Chloride (Cu Cl <sub>2</sub> ·2H <sub>2</sub> O)	Leaves	40–70	Spherical	UV-Vis, XRD, EDX, FTIR, XPS, SEM, HR-TEM, TEM and SAED	(119)
75.	<i>Spinacia oleracea</i> L.	Copper Sulfate (CuSO <sub>4</sub> ·5H <sub>2</sub> O)	Leaves	1–12	Spherical	XRD, TEM	(120)
76.	<i>Eclipta prostrata</i> (L.) L.	Copper acetate	Leaves	23–57	Spherical	UV-Vis, FTIR, XRD, SEM, HR-TEM, EDS	(121)
77.	<i>Cassia auriculata</i> L.	Copper Sulfate (CuSO <sub>4</sub> )	Leaves	23 (in avg.)	Spherical	FTIR, UV-Vis, XRD, TEM, DLS	(122)
78.	<i>Solanum lycopersicum</i> L.	Copper Sulfate (CuSO <sub>4</sub> ·5H <sub>2</sub> O)	Leaves	20–40	Spherical	UV-Vis, FTIR, FE-SEM, HR-TEM, XRD, DLS	(123)
79.	<i>Populus ciliata</i> Wall. ex Royle	Copper Nitrate Hexahydrate (Cu (NO <sub>3</sub> ) <sub>3</sub> ·6H <sub>2</sub> O)	Leaves	50–60	Spherical	FTIR, UV-Vis, EDX, SEM, XRD, TEM	(124)
80.	<i>Bauhinia tomentosa</i> L.	Copper Sulfate (CuSO <sub>4</sub> )	Leaves	22–40	Spherical	UV-Vis, XRD, TEM, EDX, FTIR	(81)
81.	<i>Alternanthera sessilis</i> (L.) R.Br. ex DC.	Copper Sulfate (CuSO <sub>4</sub> )	Leaves	22.6-25.2	Spherical	SEM- EDAX, FTIR, XPS	(81)
82.	<i>Citrofortunella microcarpa</i> (Bunge) Wijnands	Copper Sulfate (CuSO <sub>4</sub> )	Leaves	54–68	Spherical	UV-Vis, FTIR, XRD, SEM and EDS	(125)
83.	<i>Olea europaea</i> L.	Copper Sulfate (CuSO <sub>4</sub> )	Leaves	20–50	Spherical	UV-Vis, FTIR, XRD, TEM, and SEM	(125)
84.	<i>Adiantum lunulatum</i> Burm. f.	Copper Sulfate (CuSO <sub>4</sub> )	Whole Plant	1–20	Quasi-spherical	UV-Vis, DLS, Zeta Potential, FTIR, XRD, TEM and EDX	(54)
85.	<i>Sida acuta</i> Burm.f.	Copper Sulfate (CuSO <sub>4</sub> )	Leaves	50	Crystalline	SEM, TEM, FTIR, Single beam spectroscopy, UV-vis	(126)

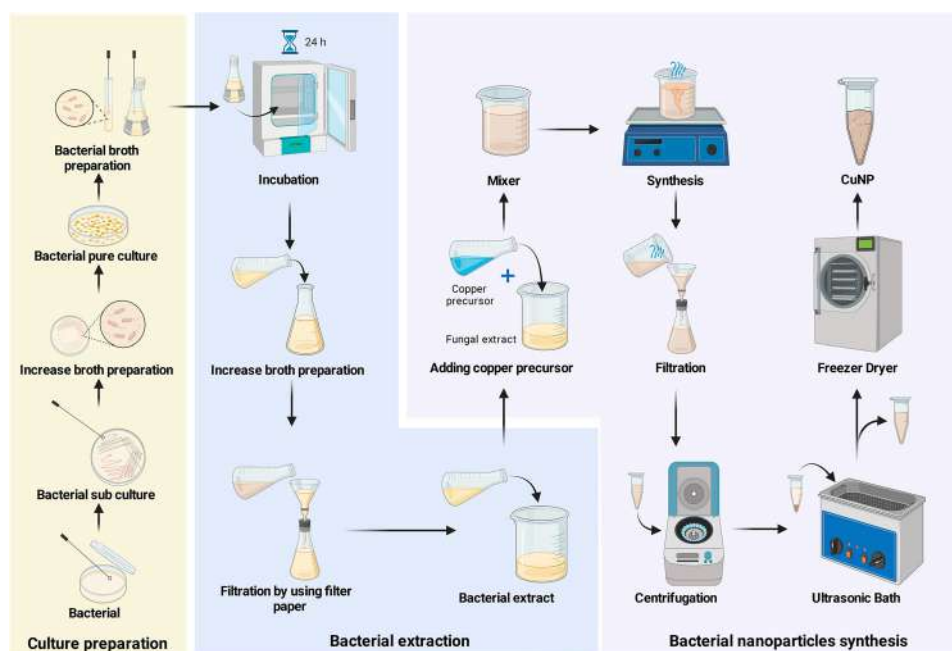


**Figure 3.** Graphical representation of biomediated synthesis of copper oxide nanoparticles using bacteria (Created with BioRender.com).

other growth chamber. For the biogenic production of nanoparticles, cell-free extracts of microorganisms, function as reducing, catalytic, or capping agents (127). *Trichoderma* species produce a wide range of bioactive metabolites, including pyrones, polyketides, terpenes, diketopiperazine, glycolipids, and a large number of reductive enzymes that aid in the production of not just CuO nanoparticles but also Ag and ZnO nanoparticles (152–154). Fungi use both internal and external routes to create various nanoparticles. The size of nanoparticles produced inside fungal species may be smaller than those produced by the extracellular pathway, with superior dispersity and dimensions. (155). Nanoparticle fabrication via the extracellular route provides several advantages. The nanoparticles created might be devoid of cell components. The extracellular route of fungus has mostly been used to synthesize nanoparticles because fungi secrete several types of metabolites that function as reducing and stabilizing agents for nanoparticle formation (154). Metal oxide nanoparticles, particularly copper oxide nanoparticles, have been synthesized using several fungus strains.

So, in this endeavor, several different species of fungus were studied, and it was discovered that fungi are excellent candidates since they release huge amounts of enzymes and are easier to work within the laboratory. *Penicillium aurantiogriseum*, *Penicillium citrinum*, and *Penicillium waksmanii* all produce CuNPs extracellularly (156). Majumder (157) described the production of CuNPs from *Fusarium oxysporum* at

room temperature, which was then screened for copper extraction from integrated circuits and produced in nano form. Dead biomass of *Hypocrea lixii* recovered from the metal mine was used to manufacture spherical CuNPs with an average size of 24.5 nm, and an infrared spectroscopy investigation was conducted, they discovered that amide groups in proteins were responsible for the CuNPs stability and capping agents (158). Some of the contributions of biomediated synthesis of copper oxide nanoparticles using different fungi are shown in Table 3 (Figure 4).

### 2.5. Green synthesis of Cu/CuO-NPs by using algae

Algal members have gained importance in the synthesis of CuONPs when these nanoparticles with sizes ranging from 5 to 45 and 6 to 7.8 nm have been effectively produced by utilizing a boiling aqueous extract from the brown algae *Bifurcaria bifurcata* (170) and *Cystoseira trinodis* (171) respectively. Ramaswamy et al. (172) also employed an aqueous extract from brown seaweed (*Sargassum polycystum*) to make CuONPs. An autoclaved aqueous extract from the green microalgae *Botryococcus braunii* generated CuONPs with sizes ranging from 2–10 nm (173). Alternatively, Bhattacharya et al. (174) used a slightly different technique, heating the extract at 50°C rather than boiling it, to get an aqueous extract from the microalgae, *Anabaena cylindrica* and

**Table 2.** Biosynthesis of Cu/CuO nanoparticles by bacteria.

Sl No.	Bacterial Culture	Gram Nature	Precursor	Mode of Synthesis	Size of NPs (in nm)	Shape / Structure / Morphology	Characterization techniques used	Reference
1.	<i>Escherichia coli</i> (Migula) Castellani and Chalmers	Gram-negative	Copper Sulfate (CuSO <sub>4</sub> )	Extracellular	100–150	Quasi-spherical	TEM, SEM, XRD, FTIR	(135–137)
2.	<i>Mycobacterium psychrotolerans</i> Trujillo and <i>Morganella morganii</i> RP42 Winslow	Gram-negative	Copper Sulfate (CuSO <sub>4</sub> )	Extracellular	15–20	Quasi-spherical cubic	SPR, FFT, UV-Vis, XPS, HR-TEM, LSV	(138)
3.	<i>Pseudomonas fluorescens</i> Migula	Gram-negative	Copper Sulfate (CuSO <sub>4</sub> )	Extracellular	20–80	Spherical and hexagonal	TEM, SEM, EDS, UV-Vis, SPR	(139)
4.	<i>Pseudomonas stutzeri</i> (Lehmann and Neumann) Sijderius	Gram-negative	Copper Sulfate (CuSO <sub>4</sub> )	Extracellular	8–15	FCC, spherical	TEM, SEM, EDS, UV-Vis, SPR	(140)
5.	<i>Pseudomonas stutzeri</i> (Lehmann and Neumann) Sijderius	Gram-negative	Copper Sulfate (CuSO <sub>4</sub> )	Extracellular	50–150	FCC, cubic	TEM, SEM, EDS, UV-Vis, SPR	(141)
6.	<i>Serratia</i> sp.	Gram-negative	Copper Sulfate (CuSO <sub>4</sub> )	Extracellular	10–30	Polydisperse	TEM, SEM, EDS, UV-Vis, SPR, EDX analysis	(142)
7.	<i>Streptomyces</i> sp.	Gram-negative	Copper Sulfate (CuSO <sub>4</sub> )	Extracellular	100–150	Spherical	TEM, SEM, EDS, UV-Vis, SPR, EDX analysis	(143)
8.	<i>Streptomyces cyaneus</i> (Krassilnikov) Waksman	Gram-positive	Copper (II) sulfate pentahydrate (CuSO <sub>4</sub> ·5H <sub>2</sub> O)	Extracellular	29.8	Spherical	UV-Vis, DLS, FTIR, TEM, XRD	(136, 144)
9.	<i>Shewanella loihica</i> PV-4	Gram-negative	Copper (II) chloride dihydrate (CuCl <sub>2</sub> ·2H <sub>2</sub> O)	Extracellular	6–20	FCC, cubic	TEM, EDX, XRD, XPS	(145)
10.	<i>Salmonella typhimurium</i>	Gram-negative	Copper (II) sulfate pentahydrate (CuSO <sub>4</sub> ·5H <sub>2</sub> O)	Extracellular	49	Spherical	UV-Vis, DLS, SEM	(146)
11.	<i>Bacillus cereus</i>	Gram-positive	Copper (II) sulfate pentahydrate (CuSO <sub>4</sub> ·5H <sub>2</sub> O)	Extracellular	11–33	Spherical	UV-Vis, DLS, Zeta, FTIR, EDX, SEM, TEM, AFM, XRD	(147)
12.	<i>Streptomyces</i> sp. MHM38	Gram-positive	Copper (II) sulfate pentahydrate (CuSO <sub>4</sub> ·5H <sub>2</sub> O)	Extracellular	1.72–13.49	Spherical	UV-Vis, EDX, TEM, XRD	(148)
13.	<i>Lactobacillus casei</i> subsp. <i>casei</i>	Gram-positive	Copper (II) sulfate pentahydrate (CuSO <sub>4</sub> ·5H <sub>2</sub> O)	Extracellular	30–75	Spherical	FTIR, XRD, FESEM, TEM	(149)
14.	<i>Morganella</i> sp.	Gram-negative	Copper (II) sulfate pentahydrate (CuSO <sub>4</sub> ·5H <sub>2</sub> O)	Extracellular	15–20	Spherical	UV-Vis, TEM, HR-TEM, XPS	(150)
15.	<i>Actinomycetes</i>	Gram-positive mycelial	Copper (II) sulfate pentahydrate (CuSO <sub>4</sub> ·5H <sub>2</sub> O)	Extracellular	61.7	Spherical	UV-Vis, DLS, Zeta, FTIR, EDX, SEM, TEM, XRD	(151)

effectively able to generate CuONPs from that extract with a particle size of 3.6 nm.

Thus, the numerous algal members responsible for the reduction and stabilization process using copper as a promotor, as well as their diverse organic components, have yet to be identified in detail (Figure 5). As a result, it's vital to focus research on the usage of biomolecules in green synthesis on CuONPs to expand their biological applications. These are listed in Table 4.

### 3. Characterization of CU/CUONPs

To establish the demand for the generation of nanoparticles one researcher should go through a series of characterization. After the synthesis of NPs, the crystal structure and chemical composition are the initial stage in the characterization process (177). The size and morphology of the Cu/CuONPs were investigated

using scanning electron microscopy, transmission electron microscopy, dynamic light scattering, particle analyzers, and field emission scanning electron microscopy, while UV-visible spectroscopy, X-ray diffraction, Fourier transform infrared spectroscopy, surface plasmon resonance, and energy-dispersive X-ray spectroscopy were used to analyze the elemental chemical compositions of Cu/CuONPs (Figure 6) (178).

### 4. Applications of copper nanoparticles (CUNPs)

CuNPs have diverse scientific applications. They are very effective against different pathogenic microbes. A high concentration of CuNPs generates reactive oxygen species in bacterial cells which eventually cause cell lysis. Moreover, CuNPs have exhibited anticancer and antifungal activities. Due to their antimicrobial activity,

**Table 3.** Biosynthesis of Cu/CuO nanoparticles by fungi.

Sl. No.	Fungal Culture	Precursor	Mode of Synthesis	Size of NPs (in nm)	Shape / Structure / Morphology	Characterization techniques used	Reference
1.	<i>Fusarium oxysporum</i> Schldtl.	Metallic copper	Extracellular	93–115	–	TEM, SEM, UV- Vis	(157)
2.	<i>Hypocrea lixii</i> Pat.	Metallic copper	Extracellular	24.5 (in avg.)	Spherical	TEM, SEM, UV-Vis	(158)
3.	(a) <i>Penicillium aurantiogriseum</i> Dierckx (b) <i>Penicillium citrinum</i> Thom (c) <i>Penicillium waksmanii</i> K.W. Zaleski	Copper Sulfate (CuSO <sub>4</sub> )	Extracellular	89–250 85–295 79–179	Spherical	TEM, SEM, DLS, UV-Vis, FTIR, AFM	(156, 159)
4.	<i>Stereum hirsutum</i> (Willd.) Pers.	Copper salts (CuSO <sub>4</sub> , CuCl <sub>2</sub> )	Extracellular	4–5	monodispersed, spherical	TEM, FTIR, XRD, and Zeta Potential	(160)
5.	<i>Rhodotorula mucilaginosa</i> (A. Jörg.) F.C. Harrison	CuCl <sub>2</sub>	Extracellular	10.5 (in avg.)	Spherical		(158)
6.	<i>Aspergillus niger</i> Tiegh.	Copper Sulfate (CuSO <sub>4</sub> )	Extracellular	5–100	Spherical	TEM, SEM, DLS, UV-Vis, FTIR	(161)
7.	<i>Trichoderma harzianum</i> Rifai	Copper (II) Sulfate pentahydrate (CuSO <sub>4</sub> ·5H <sub>2</sub> O)	Extracellular	5–18	Dense agglomerate and spherical	TEM, SEM, DLS, UV-Vis, XRD	(154)
8.	<i>Aspergillus flavus</i> Link	Copper (II) Sulfate pentahydrate (CuSO <sub>4</sub> ·5H <sub>2</sub> O)	Extracellular	20 (in avg.)	Spherical	TEM, UV-Vis, XRD, FTIR, NTA	(162)
9.	<i>Trichoderma asperellum</i> Samuels, Lieckf. & Nirenberg	Copper nitrate (Cu(NO <sub>3</sub> ) <sub>2</sub> ·3H <sub>2</sub> O)	Extracellular	110 (in avg.)	Spherical	FETEM, HR SEM	(163)
10.	<i>Aspergillus fumigatus</i> Fresen.	Copper nitrate (Cu(NO <sub>3</sub> ) <sub>2</sub> ·3H <sub>2</sub> O)	Extracellular	8 (in avg.)	Spherical	UV-Vis, HRTEM, Zeta, FTIR, XRD, EDX	(164)
11.	<i>Neurospora crassa</i> Shear & B.O. Dodge	Copper(II) chloride (CuCl <sub>2</sub> )	Extracellular	10–20	Spherical	TEM, SEM, FTIR, EDX, XRD	(165)
12.	<i>Pestalotiopsis</i> sp.	Copper(II) chloride (CuCl <sub>2</sub> )	Extracellular	10–20	Spherical	TEM, SEM, FTIR, EDX, XRD	(165)
13.	<i>Myrothecium gramineum</i> Lib.	Copper(II) chloride (CuCl <sub>2</sub> )	Extracellular	10–20	Spherical	TEM, SEM, FTIR, EDX, XRD	(165)
14.	<i>Alternaria alternata</i> (Fr.) Keissl.	Copper (II) Sulfate pentahydrate (CuSO <sub>4</sub> ·5H <sub>2</sub> O)	Extracellular	60–80	Spherical	TEM, EDX, XRF, SDD	(166)
15.	<i>Botrytis cinerea</i> Pers.	Copper (II) Sulfate pentahydrate (CuSO <sub>4</sub> ·5H <sub>2</sub> O)	Extracellular	60–80	Spherical	TEM, EDX, XRF, SDD	(166)
16.	<i>Aspergillus oryzae</i> (Ahlb.) Cohn	Copper (II) Sulfate pentahydrate (CuSO <sub>4</sub> ·5H <sub>2</sub> O)	Extracellular	55	Spherical	UV-Vis., TEM, DLS, XRD, EDX, SEM and FT-IR	(81)
17.	<i>Aspergillus terreus</i> (Ahlb.) Cohn	Copper (II) Sulfate pentahydrate (CuSO <sub>4</sub> ·5H <sub>2</sub> O)	Extracellular	15.75	Spherical	UV-Vis, FT-IR, XRD, TEM and SEM	(167)
i.	<i>Penicillium chrysogenum</i> Thom	Copper (II) Sulfate pentahydrate (CuSO <sub>4</sub> ·5H <sub>2</sub> O)	Extracellular	9.70	Spherical	UV-Vis., XRD, FTIR, DLS, EDX TEM, SEM	(168)
ii.	<i>Pleurotus ostreatus</i> (Kalchbr.) Pilát	Copper nitrate (Cu(NO <sub>3</sub> ) <sub>2</sub> ·3H <sub>2</sub> O)	Extracellular	10–190	Spherical	UV-Vis, TEM, DLS, XRD, XRD and FT-IR	(169)

it is also used for food preservation and agricultural field to draw protection against different pathogenic fungi and bacteria (179). Copper-based nano fertilizer and nano-insecticides promote growth and nutrients in crop plants. Copper-based bioremediation plays a pivotal role in waste-water treatment and removal of heavy metals from soil. Copper is a good conductor of electricity hence it is used as a super-conductor and has a significant contribution to the modern electronic field (180). In Figure 7, we have summarized the different applications of CuNPs and also elaborate its major application in the following context.

#### 4.1. Antimicrobial activity

In the past few decades, metal and metal oxides nanoparticles are being used to treat different bacterial and viral diseases. Nanoparticles based antibiotics and other drugs gained a special attraction since it is less toxic, eco-friendly and exhibited potential disease curing activity. Several reports demonstrated that Cu and CuONPs have tremendous antimicrobial activities against different pathogenic microbes. High concentrations of CuNPs are toxic to the different bacterial pathogens of both humans and plants (181). CuNP has

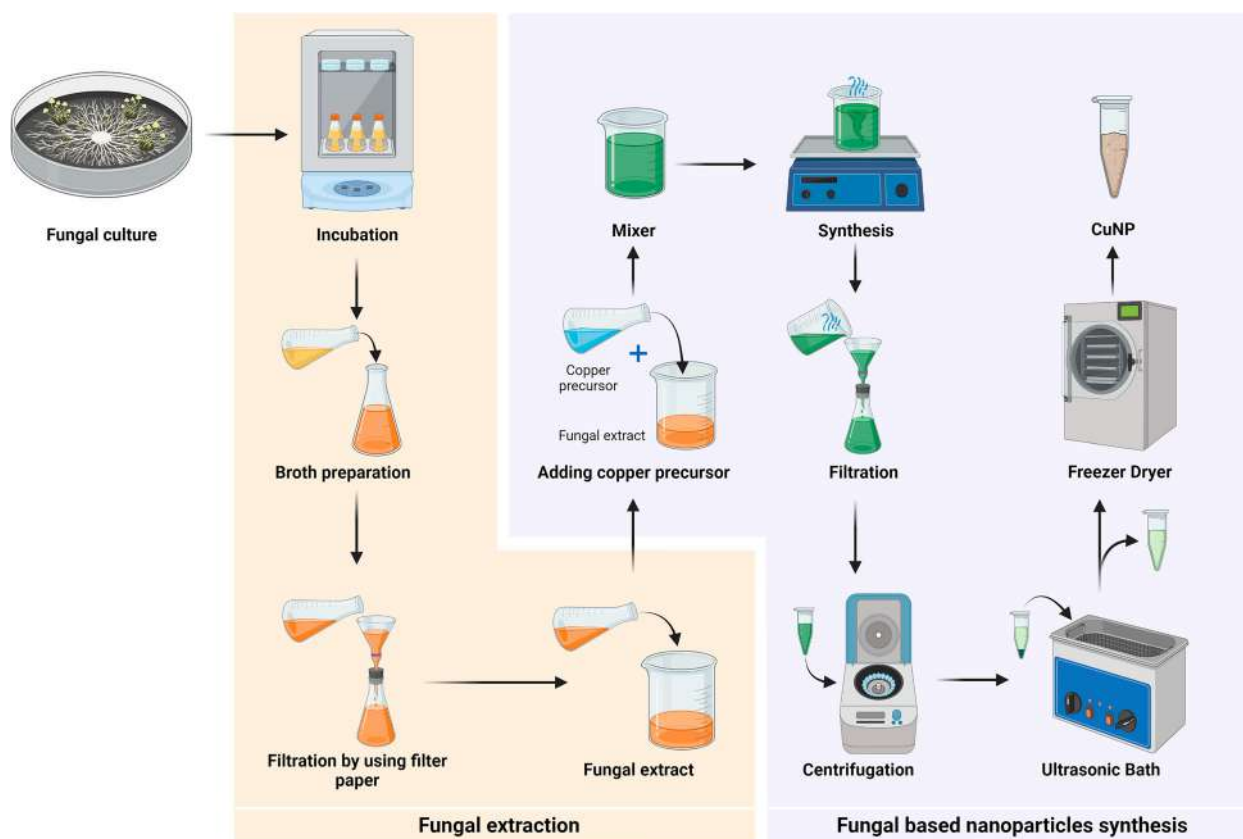


**Figure 4.** Graphical representation of biomediated synthesis of copper oxide nanoparticles using different fungi (Created with BioRender.com).

some unique features like small size, high surface area, biocompatibility, high biological and chemical reactivity which helps to kill bacterial cells efficiently. Bio fabricated CuNPs possess antimicrobial activity against both gram-positive and gram-negative pathogenic bacterial strains (182). Green synthesized Cu and CuONPs exhibited potential antibacterial activity against *Pseudomonas aeruginosa*, *Clostridium difficile*, *Staphylococcus aureus* and *Escherichia coli* (36, 81). The fabrication of CuNPs using *Gloriosa superba* leaf extract showed inhibition against gram-positive bacteria *Staphylococcus aureus* and gram-negative bacteria *Klebsiella aerogenes* (179). Green synthesized CuONP using *Sida acuta* leaf extracts can be used commercially in the textile industry as a potential antimicrobial agent. It was found that *S. acuta* coated CuONPs can inhibit both Gram positive and Gram negative bacteria when it was applied in the cotton fabrics (126). Besides antibacterial activity, the antiviral activity of green synthesized CuNP has also been confirmed. Green synthesized CuNPs using clove fruit extract can inhibit the Newcastle disease virus (183). In the following table, we have listed the application of CuNPs as an anti-microbial agent against different microbes (Table 5).

When bacterial cells come in contact with CuNPs, it develops toxicity inside the bacterial cell which leads to several malfunctions and ultimately kills the cells. Due to the small particle size of the CuNPs it can easily take entry inside the bacterial cell through the cell membrane. The carboxylic and amines group present in the bacterial cell membrane helps to attract the Cu ions efficiently. The toxicity of CuNPs greatly varies with the size and shape of the particles. (192). CuNPs accumulates reactive oxygen species which can disrupt the cell membrane and provide direct cellular toxicity (185). Copper has a great redox potential which can act as an electron donor or acceptor by producing Cu ions. These ions are very toxic for bacterial cells and accumulate superoxides and hydroxyl radicals leading to oxidative stress. These ROS generation can interfere with the cellular process of bacteria like DNA replication, cell division and metabolism (36). CuNP mediated toxicity in bacterial cells promotes degradation of mitochondria, ribosomes and different proteins channels present in the bacterial cell membrane. The exact mechanism of antimicrobial activity is still under study. A probable antimicrobial mechanism of CuNPs is presented in the following diagram (Figure 8).

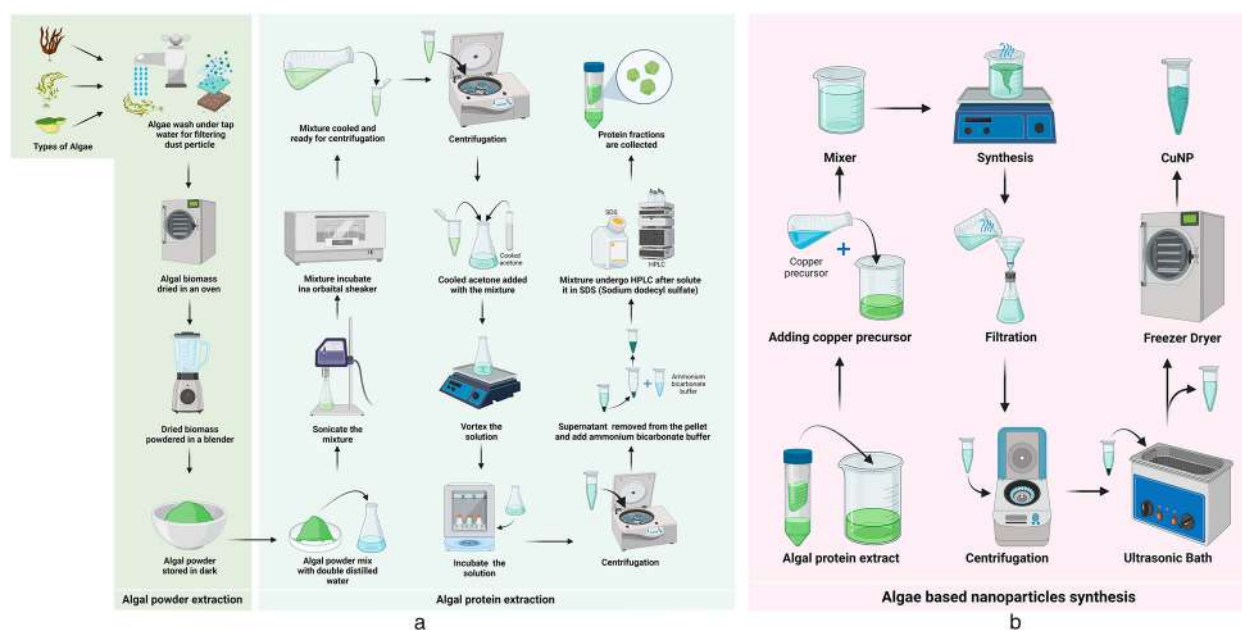


**Figure 5.** (a) Graphical representation of the preparation of the algal protein extract for the synthesis of copper oxide nanoparticles using different algae (Created with BioRender.com) (b) Graphical representation of biomediated synthesis of copper oxide nanoparticles using different algae protein extract (Created with BioRender.com).

#### 4.2. Antifungal activity and crop protection

In the current medical sector, the fungal disease has become a severe health threat and many patients die every year especially those with a poor immune system. Though there are several antifungal drugs available in the market, but the development of drug resistance is a severe threat. Several studies revealed that CuNPs can be used as an antifungal agent since they can inhibit several pathogenic fungi in both humans and plants (193). However, more studies are needed to ensure the exact antifungal mechanisms of CuNPs and their future use as an antifungal agent. Green synthesized CuNPs can control several pathogenic fungal strains like *Fusarium oxysporum* Schldl., *Alternaria solani* (Ellis & G. Martin) L.R. Jones, *Aspergillus niger* Tiegh., and *Penicillium citrinum* Thom (194). CuNPs

synthesized by using Chitosan exhibited antifungal activity against tomato plant pathogen *A. solani* and *F. oxysporum* (195). Chemically synthesized CuNPs are highly effective against *Candida albicans* (C.P. Robin) Berkhout and *Aspergillus flavus* Link (196). In another report CuNPs exhibited antifungal activity against some destructive crop pathogens like *Alternaria alternata* (Fr.) Keissl., *Curvularia lunata* (Wakker) Boedijn and *Phoma destructiva* Plowr. (197). Green synthesized CuNPs using *Syzygium alternifolium* (Wight) Walp. are known to have antifungal activity against some plant pathogens. CuNPs can be used in the formulation of nanofungicides. In a field study, it was found that Cu based fungicides are more effective than other agrochemicals against tomato pathogen *Phytophthora infestans* (Mont.) de Bary (198). Since CuNP has potential antimicrobial and antifungal properties it could be

**Table 4.** Biosynthesis of Cu/CuO nanoparticles by algae.

Sl No.	Algal extract	Precursor	Size of NPs (in nm)	Shape/ Structure / Morphology	Characterization techniques used	Reference
i.	<i>Bifurcaria bifurcata</i> R. Ross	Copper Sulphate solution (CuSO <sub>4</sub> .5H <sub>2</sub> O)	5–45	Crystallite	UV-Vis, TEM, FTIR, XRD	(170)
ii.	<i>Cystoseira trinodis</i> (Forsskål) C. Agardh	Copper Sulfate (CuSO <sub>4</sub> )	6–7.8	Crystallite	TEM, SEM, XRD, FTIR, EDX, Raman, UV-Vis	(171)
iii.	<i>Botryococcus braunii</i> Kützting	Copper Acetate Cu (CH <sub>3</sub> COO) <sub>2</sub>	10–70	Cubical and Spherical	UV-Vis, FTIR, SEM, X-Ray Diffraction.	(173)
iv.	<i>Anabaena cylindrica</i> Lemmermann	Copper Sulphate solution (CuSO <sub>4</sub> .5H <sub>2</sub> O)	3.6 (in avg.)	Crystallite	XRD, XPS, EDX	(174)
v.	<i>Macrocyctis pyrifera</i> (L.) C.Ag.	Copper Sulfate (CuSO <sub>4</sub> )	2–50	Spherical	DLS, Zeta Potential, FTIR, TEM, EDS	(175)
vi.	<i>Sargassum polycystum</i> C. Agardh	Aqueous copper	–	Spherical	TEM, SEM, XRD, FTIR, EDX, UV-Vis	(176)



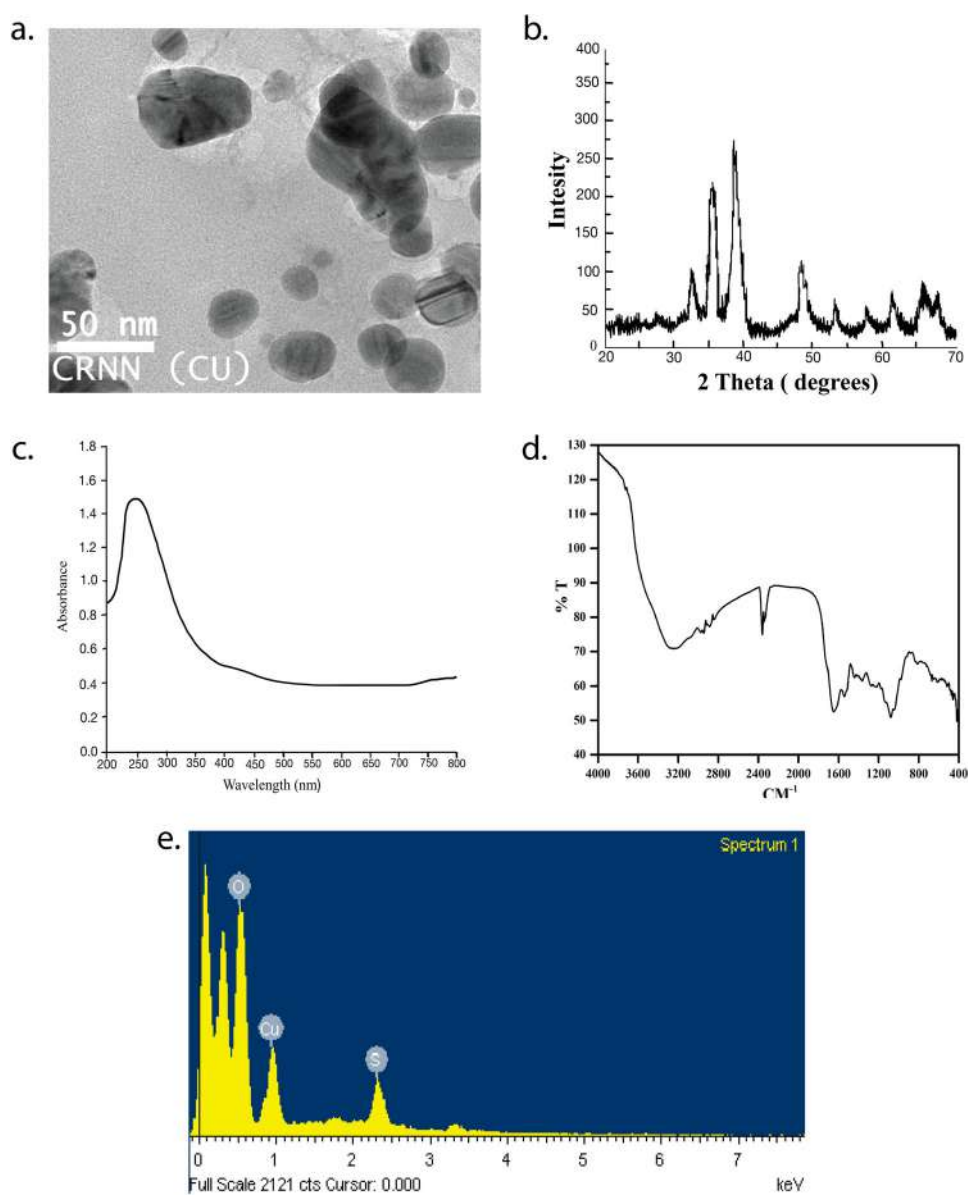


**Figure 6.** Characterization of synthesized copper oxide nanoparticles (CuONPs) (a) TEM images of CuONPs (b) XRD analysis of CuONPs (c) UV-Visible Spectroscopic analysis of CuONPs (d) FTIR analysis of CuONPs (e) EDX analysis of CuONPs.

used in food preservation and food packaging as well. High concentrations of copper provide direct toxicity to several food spoilage microbes and fungi (81). Some antifungal applications of CuNPs are listed below (Table 6).

### 4.3. Anticancer activity

Currently, cancer is the most dangerous and common disease which increases the mortality rate worldwide. Till now no promising drugs are available in the market to treat cancer. The most commonly used radiotherapy and chemotherapy have tremendous side effects and are also expensive processes. Several

studies are still under process to discover an alternative nontoxic biological drug. In this regard, it was found that the emergence of nanotechnology helps to treat different types of cancer efficiently. Biologically synthesized Cu and CuO nanoparticles exhibited promising results when it tested against some human cancer cell lines (Table 7) (201–207).

Green synthesized CuNPs using dry black beans can inhibit the growth of human cervical carcinoma and also showed cytotoxicity against HeLa cell line by producing ROS (204). The mechanism of CuNP mediated anticancer activity includes oxidative stresses, accumulation of ROS, chromosomal aberration, genetic material fragmentation, production of caspases, enhancement of

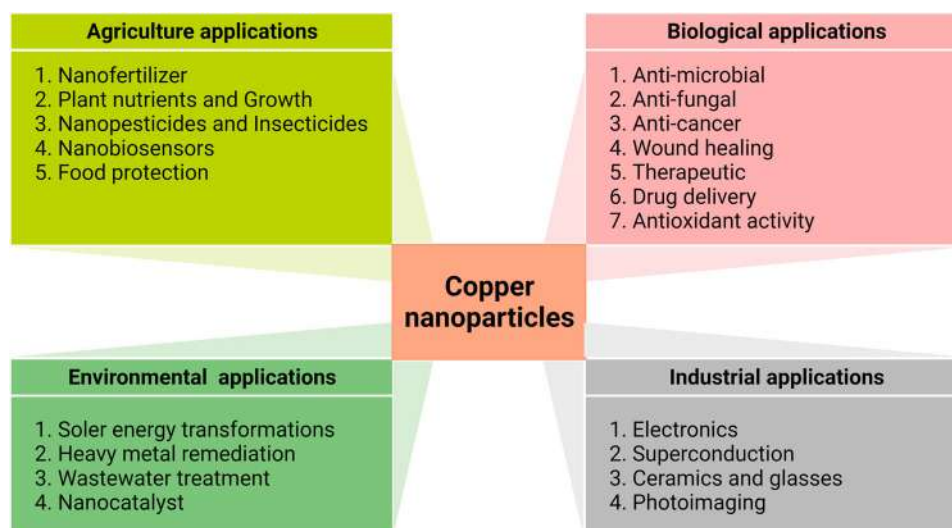


**Figure 7.** Applications of copper nanoparticles (Created with BioRender.com).

intrinsic and extrinsic apoptotic pathways (Figure 9) (192).

In a study, it was found that green synthesized CuONPs can inhibit the growth of A549 adenocarcinomic human alveolar epithelial cells. A high concentration of CuONPs promotes cellular toxicity and DNA damage in the A549 lung cells (208). In addition to this, it was also found that biologically synthesized chitosan/copper oxide nanocomposite using a bioflavonoid rutin, also exhibited antiproliferative efficiency when it was tested against A549 human lung cancer cell line (209). CuNP mediated anticancer activity has been observed in CaCO-2 human colon cancer cells, Mcf-7 breast cancer cells, HepG-2 hepatic cancer cells and HeLa cells (210). In a study, it was found that when HeLa cells are treated with copper oxide nanoparticles it showed oxidative stress mediated mitochondrial degradation. The

normal control cells depicted by a normal mitochondrial structure whereas the treated cancer cells are characterized by a condensed clumped structure of mitochondria which leads to apoptosis of the cancer cells (83). When the similar study was done with HepG-2 hepatic cancer cell line it exhibited enhanced apoptosis by upregulating the tumor suppressor gene and down regulating the antiapoptotic gene bcl-2 (211).

To explain this finding, it is important to note that various factors, including size distribution, shape, and surface chemistry of biogenic nanoparticles, can influence their cytotoxicity. Different cytotoxicity responses may result from changes in various parameters. Furthermore, biomolecules are responsible for bioreduction of metal ions to their nano-forms in the biosynthetic method. These biomolecules are attached to the surface of biosynthesized nanoparticles and act

**Table 5.** Applications of green synthesized CuNPs as antimicrobial agent.

Sl. No.	Biological source	Chemical used	Antimicrobial Application	Reference
1.	<i>Eucalyptus globulus</i> Labill.	CuSO <sub>4</sub>	It accumulates ROS inside the bacterial cells which lead to cell destruction.	(137)
2.	<i>Zea mays</i> L.	Cu	It is effective against some pathogenic bacteria like <i>Bacillus lichiniformis</i> and <i>Pseudomonas aeruginosa</i> .	(184)
3.	<i>Citrus medica</i> L.	(CH <sub>3</sub> COO) <sub>2</sub> CuSO <sub>4</sub>	It can inhibit several crop pathogens and also inhibit the growth of <i>Propionibacterium acnes</i> and <i>Klebsiella pneumoniae</i> .	(63)
4.	<i>Camellia sinensis</i> (L.) Kuntze	Cu(NO <sub>3</sub> ) <sub>2</sub>	It can inhibit the growth of <i>Vibrio cholerae</i> and <i>Klebsiella pneumoniae</i> .	(185)
5.	<i>Bacillus cereus</i> Frankland and Frankland	CuSO <sub>4</sub>	It can control the growth of pathogenic bacteria like <i>P. aeruginosa</i> , <i>Staphylococcus aureus</i> , <i>E. coli</i> and <i>Bacillus subtilis</i> .	(186)
6.	<i>Nerium oleander</i> L.	CuSO <sub>4</sub>	Antibacterial activity against <i>Salmonella typhi</i> , <i>E. coli</i> , <i>Bacillus subtilis</i> and <i>Staphylococcus aureus</i> .	(187)
7.	<i>Sida acuta</i> Burm.f.	CuSO <sub>4</sub>	Exhibited tremendous antimicrobial activity against some human pathogens and also effective against bacterial contamination in the textile industries.	(126, 188)
8.	<i>Punica granatum</i> L.	CuSO <sub>4</sub>	Exhibited antimicrobial activity against <i>Micrococcus luteus</i> , <i>Salmonella enteric</i> and <i>Enterobacter aerogenes</i> .	(189)
9.	<i>Pseudomonas fluorescens</i> Migula	CuSO <sub>4</sub>	Inhibit the growth of <i>Bacillus</i> and <i>E. coli</i> .	(134)
10.	Chitosan derived from fungal cell wall	CuSO <sub>4</sub>	Effective against <i>Salmonella paratyphi</i> .	(190)
11.	<i>Ocimum sanctum</i> L.	CuSO <sub>4</sub>	Antimicrobial activity against human pathogenic microbes.	(191)

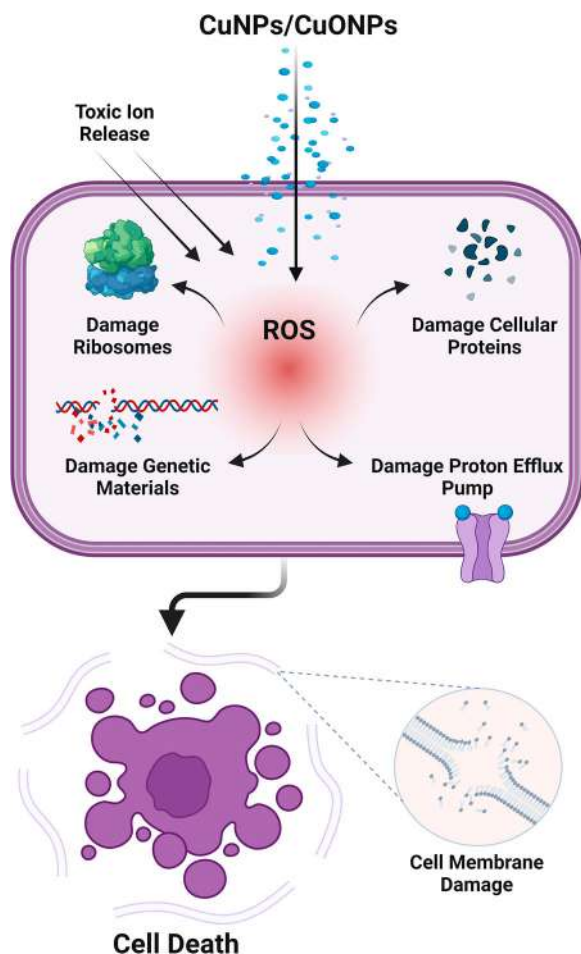


**Figure 8.** Probable antimicrobial mechanism of Cu/CuONPs (Created with BioRender.com).

as a stabilizer, preventing the nanoparticles from aggregating. These biomolecules adhering to the surface of the nanoparticles, have the potential to alter the surface chemistry of various nanoparticles and interfere with their ability to respond to their biological environment. As a result, the biological sources used to make nanoparticles may have an impact on their cytotoxicity response (212–215).

#### 4.4. Plant growth, nutrients and defense booster

Plants need to uptake different minerals and nutrients elements for their proper growth and development. Plants nutrients are divided into two classes macronutrients and micronutrients. Macronutrients are generally required in high concentrations and micronutrients are required comparatively in low concentrations. Both these macro and micronutrients are essential for maintaining structural integrity and normal growth in plants. Deficiency of which causes disease and death of different plant parts (81, 216). In plants, copper is required in very low concentrations as it is a micronutrient. A high concentration of Cu promotes toxicity and hampered growth in plants. Plant chloroplast contains a maximum number of Cu as it helps in chloroplast and other pigments synthesis. Cu deficiency leads to several abnormal conditions like young leaf distortion, necrosis, stem bending, affects vegetative growth and reduces grain quality in crop plants (217). CuNP mediated plant growth responses depend upon several factors like concentration, size, plant species and structure of the particles. In a study, it was found that CuNPs can stimulate root and shoot growth in *Phaseolus radiates* and *Triticum aestivum*. The growth response typically varies with varying concentrations of CuNPs. When wheat plants were treated with 20, 25, 30 and 35 ppm concentrations of CuNPs it showed better growth and yields. Concentrations above 1000 ppm reduced growth in wheat followed by a decrease in yields (218). When CuNPs were applied on *Allium cepa* with 20 µg/ml concentrations it enhanced growth and mitotic index. The mitotic index decreased with increasing concentrations of CuNPs (219). Applications of CuONPs increased shoot and root growth in *Zea mays* (220). Application of CuONPs on transgenic cotton plants enhanced expression of exogenous genes which code for Bt toxins in leaves (221). On the contrary high concentration of CuNPs has a negative

**Table 6.** Antifungal activity of different green synthesized CuNPs.

Sl. No.	Biological source	Chemical used	Antifungal Application	Reference
1.	<i>Cissus quadrangularis</i> L.	Cu (CH <sub>3</sub> COO) <sub>2</sub>	Inhibit the growth of pathogenic fungi <i>Aspergillus flavus</i> Link and <i>A. niger</i> Tiegh.	(81)
2.	<i>Brassica juncea</i> (L.) Czern.	CuSO <sub>4</sub>	Inhibit the growth of <i>Alternaria alternata</i> , <i>Phoma destructiva</i> and <i>Curvularia lunata</i> (Wakker) Boedijn.	(81)
3.	<i>Citrus medica</i> L.	CuSO <sub>4</sub>	Effective against pathogenic fungi <i>Fusarium graminearum</i> Schwabe, <i>F. oxysporum</i> Schltdl. and <i>F. culmorum</i> (Wm.G. Sm.) Sacc.	(63)
4.	<i>Oxalis corniculata</i> L.	CuSO <sub>4</sub>	Inhibit the growth of <i>A. alternata</i> , <i>Pythium ultimum</i> Trow and <i>A. niger</i> Tiegh.	(199)
5.	<i>Syzygium alternifolium</i> (Wight) Walp.	Cu(NO <sub>3</sub> ) <sub>2</sub>	Effective against <i>Trichoderma harzianum</i> Rifai	(183)
6.	<i>Penicillium chrysogenum</i> Thom	CuSO <sub>4</sub>	Antifungal activity against <i>A. solani</i> (Ellis & G. Martin) L.R. Jones, <i>A. niger</i> Tiegh. and <i>F. oxysporum</i> Schltdl.	(194)
7.	<i>Syzygium aromaticum</i> (L.) Merr. & L.M.Perry	CuSO <sub>4</sub>	Exhibited antifungal activity against pathogenic fungi <i>A. niger</i> Tiegh. and <i>A. flavus</i> Link.	(200)

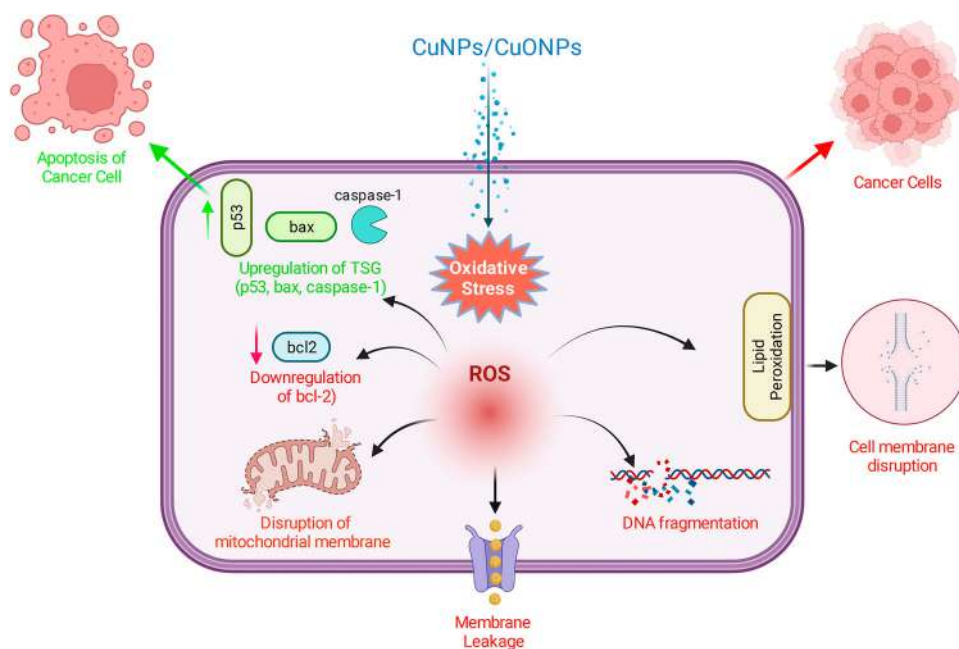
**Table 7.** Different anticancer properties of CuNPs.

Sl. No.	Biological source	Tested cell lines	Anticancer activity	Reference
1.	<i>Camellia sinensis</i> (L.) Kuntze	MCF-7	Promotes significant cytotoxicity against breast cancer cells.	(174)
2.	<i>Bacillus cereus</i> Frankland and Frankland	A549 CaCO-2 HCT 116	Inhibit the growth of the tested cancer cell line.	(153)
3.	<i>Ficus religiosa</i> L.	A459	Inhibit lung cancer cells by inducing ROS mediated apoptosis.	(175)
4.	<i>Phaseolus vulgaris</i> L.	HeLa	Inhibit the growth of human cervical cancer cells which includes ROS mediated apoptosis and mitochondrial malfunctions.	(171)
5.	<i>Syzygium alternifolium</i> (Wight) Walp.	MCF-7	Inhibit the growth of breast cancer cells by promoting direct cytotoxicity.	(150)
6.	<i>Cordia myxa</i> L.	AMJ-13 MCF-7	Inhibit breast cancer cell growth.	(176)
7.	<i>Calotropis procera</i> (Aiton) Dryand.	BHK 21 HeLa A549	Promotes apoptotic destruction of the tested cancer cell lines.	(177)
8.	<i>Lactobacillus casei</i>	AGS HT-29	Inhibit the growth of human gastric cancer cells and colorectal cancer cells by promoting cytotoxicity and apoptosis.	(178)

impact on plant growth. CuNPs with different concentrations ranging from 200 to 1000 mg/l exhibited a negative impact on the growth of *Raphanus sativus*, *Triticum aestivum*, *Lolium perenne* and *Phaseolus radiates* (222). Application of CuONPs at a higher concentration in *Arabidopsis thaliana* seedlings inhibited root and shoot growth and also decreased chlorophyll contents (223). Recently, we have shown that treatment of CuONPs significantly boost up the defense enzymes, total phenol and other defense parameters along with plant vigor in *Lens culinaris* through nitric oxide signaling pathway (224). Possible mechanism has been illustrated in Figure 10.

#### 4.5. Wound healing

Several studies over the last few years have ensured that CuNPs can be used as wound healing agents providing protection against infections. Wounds and cuts on the body surface are the most common pathway through which different infectious microorganisms take entry into the body. To prevent infection, it is very necessary to remove microbes from the wound site. As discussed earlier, CuNPs has potential antimicrobial and antifungal activity so it may be used in wound healing purposes (225). At the site of the wound Cu stimulates the formation of new blood vessels which leads to angiogenesis. Besides this CuNPs also stimulates the expression

**Figure 9.** Probable anti-cancer mechanism of Cu/CuONPs (Created with BioRender.com).

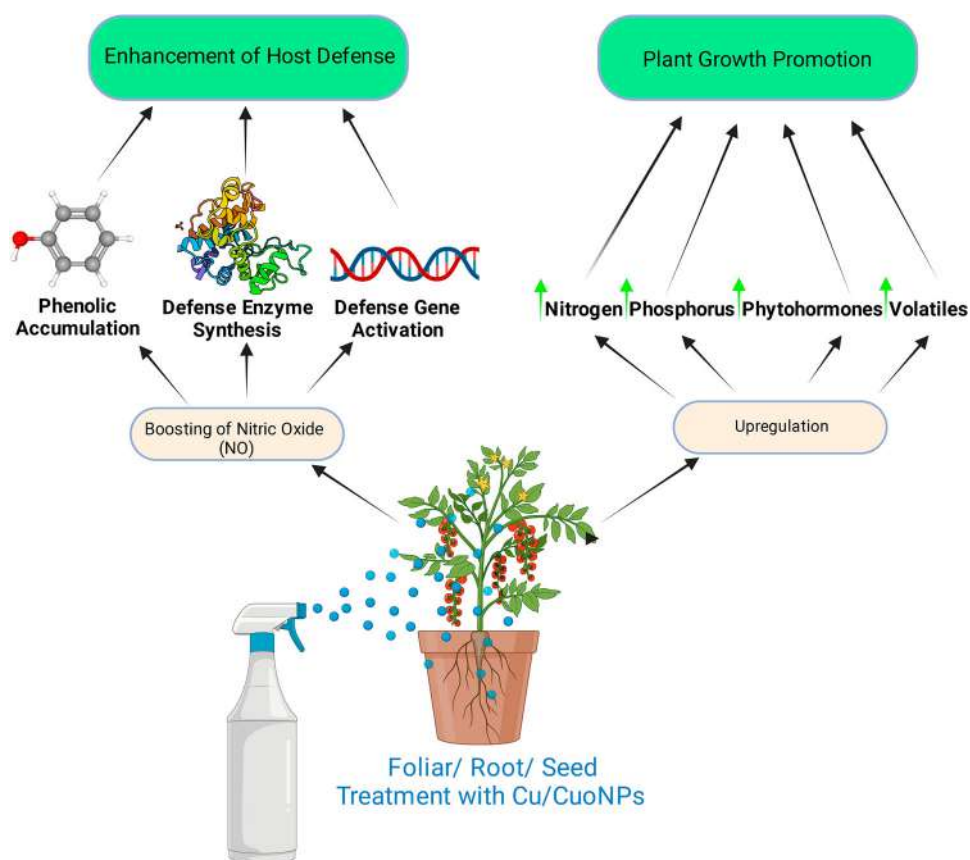


**Figure 10.** Schematic representation of defense induction and plant growth promotion by Cu/CuONPs (Created with BioRender.com).

of vascular endothelial growth factor (VEGF) that facilitates the transport of different nutrients and collagen formation necessary for repairing the wound (Figure 11). Application of Cu can halt severe phosphorus burn by the process of tissue remodeling. At the site of the wound Cu helps in maintaining the stability of fibrinogen and accumulates lysyl oxidase enzyme (210). Green synthesized CuNPs using *Falcaria vulgaris* leaf extracts exhibited potential cutaneous wound healing activity (226). In a study, a 500 mm cut was made on an anaesthetized animal. Three set up was made by applying biologically synthesized CuNP gel, nonbiologically synthesized CuNP and control. After some days it was found that biologically synthesized CuNPs were able to reduce 92% of the wound. Moreover, it promotes cell proliferation, cell migration and inhibits cyclooxygenase-2 enzyme at the wound site (186, 227).

#### 4.6. Other applications

CuNPs are now used in the textile industry for making antimicrobial personal protective equipment (PPE). In the fabric's polymer, nano-coppers are incorporated for making antimicrobial fabrics. CuNPs incorporated cotton fibers exhibited antimicrobial activities against

several pathogenic microbes (210). CuNPs can be used to treat polluted water in different industrial areas. Several reports have described that CuNPs are used in the disposal of industrial waste and effluent. Besides bioremediation activity, CuNPs has a potential biocatalytic activity that can reduce and degrade xanthenes dyes, congo red, rhodamin-B, and methylene blue (70). Due to fluorescence quenching properties, CuNPs could be used as biosensing and biolabelling agent (228). Since CuNPs has a very small size it can interact with different biomolecules efficiently and can be used as drug delivering system (179). Green synthesized CuNPs exhibited larvicidal activities against *Aedes aegypti* providing protection against dengue, zika and chikungunya (229).

#### 5. Future perspectives

In this era of nanotechnology, remarkable advancements are going on day by day in the field of nanoparticle synthesis and their sophisticated applications in the vast arena of science and technology. Besides others CuONPs/CuNPs have tremendous widespread applications, especially in biological systems. However, some nanosystems needs further sophistication and

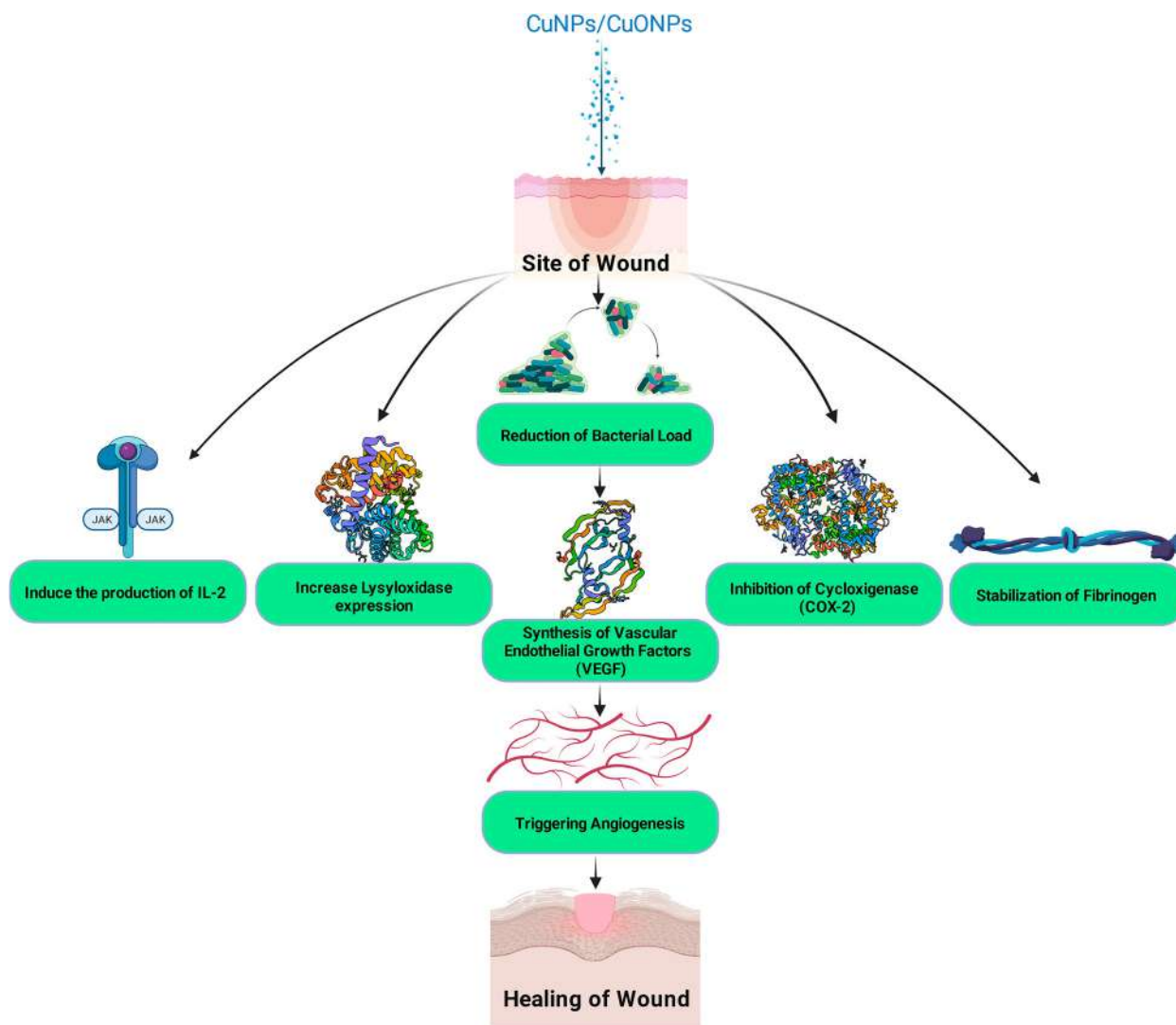


**Figure 11.** Probable wound healing mechanism of Cu/CuONPs (Created with BioRender.com).

they are still at the stage of infancy. More widespread research is still required to set the parameters. New cost-effective tools must be developed. Searching for new application of CuONPs/CuNPs has to be taken into consideration. Application of CuONPs/CuNPs in the research field of nano-sensors in film packaging of food, detection of microorganisms and toxic substances to check food quality etc. will give future directions. However, challenges and safety aspects can be taken as a serious concern. The findings of this review expand the prospects for the green synthesis of CuONPs/CuNPs and their use in a variety of biological and biotechnological domains.

## 6. Conclusion

In this present situation of global pollution and environmental consciousness it is utmost important to reduce

the use of hazardous compounds in various technical fields of application-based research. In this context, it is evident to utilize CuONPs/CuNPs as a hazard free compound, at various important sectors of research like drug delivery system, in solving various health issues, plant defence booster, textile industry, etc. However, synthesis part is very important as harmful substances are used in both physical and chemical methods of CuONPs/CuNPs production. The biological technique, on the other hand, is eco-friendly, cost-effective, dependable, stable, uses little energy, and is a straightforward procedure. In this study, a comprehensive idea has been given on the pros and cons of bio-based synthesis and their characterization including their every possible application. However, to advance the biomedical applications of CuONPs, additional research should be conducted on ways to reduce the toxicity of CuONPs while preserving and enhancing their biological efficiency.

## Acknowledgements

We do not have any funding support from any organizational or institutional level. The authors acknowledge the immense help received from the scholars whose articles are cited and included in references of this manuscript. The authors are also grateful to authors/editors/publishers of all those articles, journals and books from where the literature for this article has been reviewed and discussed.

## Author contribution

J.S., N.C.: conceptualization; J.S., N.C., J.B., P.C.: methodology; J.S., N.C., J.B., A.B.: formal analysis and investigation; J.S., N.C., J.B., A.B., S.C., K.R.: writing—original draft preparation; P.C., J.S., J.B., N.C.: Image preparation; J.S., N.C.: Writing – review and editing; K.A. J.S., N.C.: supervision.

## Disclosure statement

No potential conflict of interest was reported by the author(s).

## Funding

We do not have any funding support from any organizational or institutional level.

## ORCID

Nilanjan Chakraborty  <http://orcid.org/0000-0001-7351-3200>  
 Jishnu Banerjee  <http://orcid.org/0000-0002-5377-0848>  
 Pallab Chakraborty  <http://orcid.org/0000-0002-0484-1304>  
 Anuron Banerjee  <http://orcid.org/0000-0001-8521-9084>  
 Sumedha Chanda  <http://orcid.org/0000-0002-6208-505X>  
 Kasturi Ray  <http://orcid.org/0000-0002-5217-899X>  
 Krishnendu Acharya  <http://orcid.org/0000-0003-1193-1823>  
 Joy Sarkar  <http://orcid.org/0000-0002-6404-7428>

## References

- [1] Cristiano José de Andrade, B.; Maria de Andrade, L.; Anita Mendes, M.; Augusto Oller do Nascimento, C. An Overview on the Production of Microbial Copper Nanoparticles by Bacteria, Fungi and Algae, Type: Double Blind Peer Reviewed International Research Journal Publisher: Global Journals Inc. 17 (2017). <http://creativecommons> (accessed June 30, 2021).
- [2] Moses, V. Biological Synthesis of Copper Nanoparticles and its impact-a Review, Researchgate.Net. 3 (2016) 28–38. [www.ijpsi.org28%7C](http://www.ijpsi.org28%7C) (accessed June 30, 2021).
- [3] Barabadi, H. Nanobiotechnology: A Promising Scope of Gold Biotechnology. *Cell. Mol. Biol. (Noisy-Le-Grand)*. **2017**, *63*, 3–4. doi:10.14715/CMB/2017.63.12.2.
- [4] Acharya, K.; Sarkar, J.; Deo, S.S. Mycosynthesis of nanoparticles. In *Advances in Biotechnology*. 2009; pp. 204–215.

- [5] Sarkar, J.; Acharya, K. Alternaria Alternata Culture Filtrate Mediated Bioreduction of Chloroplatinate to Platinum Nanoparticles. *Synth. React. Inorg., Met.-Org., Nano-Met. Chem.* **2017**, *47*, 365–369. doi:10.1080/15533174.2016.1186062.
- [6] Acharya, K.; Sarkar, J. Bryo-synthesis of Gold Nanoparticles. *Int. J. Pharm. Sci. Rev. Res.* **2014**, *29*, 82–86.
- [7] Maity, D.; Bain, M.K.; Bhowmick, B.; Sarkar, J.; Saha, S.; Acharya, K.; Chakraborty, D.; Chattopadhyay, M. In Situ Synthesis, Characterization, and Antimicrobial Activity of Silver Nanoparticles Using Water Soluble Polymer. *J. Appl. Polym. Sci.* **2011**, *122*, 2189–2196.
- [8] Sarkar, J.; Dey, P.; Saha, S.; Acharya, K. Mycosynthesis of Selenium Nanoparticles. *Micro Nano Lett.* **2011**, *6*, 599–602. doi:10.1049/mnl.2011.0227.
- [9] Sarkar, J.; Saha, S.; Dey, P.; Acharya, K. Production of Selenium Nanorods by Phytopathogen, Alternaria Alternata. *Adv. Sci. Lett.* **2012**, *10*, 111–114. doi:10.1166/asl.2012.2137.
- [10] Sarkar, J.; Mollick, M.M.R.; Chattopadhyay, D.; Acharya, K. An Eco-friendly Route of  $\gamma$ -Fe<sub>2</sub>O<sub>3</sub> Nanoparticles Formation and Investigation of the Mechanical Properties of the HPMC- $\gamma$ -Fe<sub>2</sub>O<sub>3</sub> Nanocomposites. *Bioprocess Biosyst. Eng.* **2017**, *40*, 351–359. doi:10.1007/s00449-016-1702-x.
- [11] Sarkar, J.; Ray, S.; Chattopadhyay, D.; Laskar, A.; Acharya, K. Mycogenesis of Gold Nanoparticles Using a Phytopathogen Alternaria Alternata. *Bioprocess Biosyst. Eng.* **2012**, *35*, 637–643. doi:10.1007/s00449-011-0646-4.
- [12] Sarkar, J.; Ghosh, M.; Mukherjee, A.; Chattopadhyay, D.; Acharya, K. Biosynthesis and Safety Evaluation of ZnO Nanoparticles. *Bioprocess Biosyst. Eng.* **2014**, *37*, 165–171. doi:10.1007/s00449-013-0982-7.
- [13] Sarkar, J.; Saha, S.; Chattopadhyay, D.; Patra, S.; Acharya, K. Mycosynthesis of Silver Nanoparticles and Investigation of Their Antimicrobial Activity. *J. Nanosci. Nanoeng. Appl.* **2011**, *1*, 17–26.
- [14] Maity, G.N.; Sarkar, J.; Khatua, S.; Mondal, S.; Acharya, K. Green Synthesis of Silver Nanoparticles Using Mangrove Fruit Polysaccharide for Bacterial Growth Inhibition. *Asian J. Pharm. Clin. Res.* **2019**, *12*, 179–183.
- [15] Sarkar, J.; Kalyan Roy, S.; Laskar, A.; Chattopadhyay, D.; Acharya, K. Bioreduction of Chloroaurate Ions to Gold Nanoparticles by Culture Filtrate of Pleurotus Sapidus Quél. *Mater. Lett.* **2013**, *92*, 313–316. doi:10.1016/j.matlet.2012.10.130.
- [16] Chandra, S.; Chakraborty, N.; Dasgupta, A.; Sarkar, J.; Panda, K.; Acharya, K. Chitosan Nanoparticles: A Positive Modulator of Innate Immune Responses in Plants. *Sci. Rep.* **2015**, *5*, 15195. doi:10.1038/srep15195.
- [17] Dasgupta, A.; Sarkar, J.; Ghosh, M.; Bhattacharya, A.; Mukherjee, A.; Chattopadhyay, D.; Acharya, K. Green Conversion of Graphene Oxide to Graphene Nanosheets and its Biosafety Study. *Plos One* **2017**, *12*, e0171607. doi:10.1371/journal.pone.0171607.
- [18] Mollick, R.M.M.; Bhowmick, B.; Mondal, D.; Maity, D.; Rana, D.; Kumar Dash, S.; Chattopadhyay, S.; Roy, S.; Sarkar, J.; Acharya, K.; Chakraborty, M.; Chattopadhyay, D. Anticancer (in Vitro) and Antimicrobial Effect of Gold Nanoparticles Synthesized Using Abelmoschus

- Esculentus (L.) Pulp Extract via a Green Route. *RSC Adv.* **2014**, *4*, 37838. doi:10.1039/C4RA07285E.
- [19] Sarkar, J.; Chattopadhyay, D.; Patra, S.; Deo, S.S.; Sinha, S.; Ghosh, M.; Mukherjee, A.; Acharya, K. Alternaria Alternata Mediated Synthesis of Protein Capped Silver Nanoparticles and Their Genotoxic Activity. *Dig. J. Nanomater. Biostruct.* **2011**, *6*, 563–573.
- [20] Maity, D.; Mollick, M.M.R.; Mondal, D.; Bhowmick, B.; Bain, M.K.; Bankura, K.; Sarkar, J.; Acharya, K.; Chattopadhyay, D. Synthesis of Methylcellulose-Silver Nanocomposite and Investigation of Mechanical and Antimicrobial Properties. *Carbohydr. Polym.* **2012**, *90*, 1818–1825. doi:10.1016/j.carbpol.2012.07.082.
- [21] Mollick, M.M.R.; Bhowmick, B.; Maity, D.; Mondal, D.; Roy, I.; Sarkar, J.; Rana, D.; Acharya, K.; Chattopadhyay, S.; Chattopadhyay, D. Green Synthesis of Silver Nanoparticles-based Nanofluids and Investigation of Their Antimicrobial Activities. *Microfluid. Nanofluid.* **2014**, *16*, 541–551. doi:10.1007/s10404-013-1252-3.
- [22] Mollick, M.M.R.; Bhowmick, B.; Maity, D.; Mondal, D.; Bain, M.K.; Bankura, K.; Sarkar, J.; Rana, D.; Acharya, K.; Chattopadhyay, D. Green Synthesis of Silver Nanoparticles Using Paederia Foetida L. Leaf Extract and Assessment of Their Antimicrobial Activities. *Int. J. Green Nanotechnol.* **2012**, *4*, 230–239. doi:10.1080/19430892.2012.706103.
- [23] Jadhav, K.; Deore, S.; Dhamecha, D.; Hr, R.; Jagwani, S.; Jalalpure, S.; Bohara, R. Phytosynthesis of Silver Nanoparticles: Characterization, Biocompatibility Studies, and Anticancer Activity. *ACS. Biomater. Sci. Eng.* **2018**, *4*, 892–899. doi:10.1021/ACSBOMATERIALS.7B00707.
- [24] Georgopoulos, P.G.; Roy, A.; Yonone-Lioy, M.J.; Opiekun, R.E.; Lioy, P.J. Environmental Copper: Its Dynamics and Human Exposure Issues. *J. Toxicol. Environ. Health, Part B* **2001**, *4*, 341–394. doi:10.1080/109374001753146207.
- [25] Ghaderian, S.M.; Ravandi, A.A.G. Accumulation of Copper and Other Heavy Metals by Plants Growing on Sarcheshmeh Copper Mining Area, Iran. *J. Geochem. Explor.* **2012**, 25–32. doi:10.1016/J.GEXPLO.2012.06.022.
- [26] Kerkar, N.; Roberts, E.A. Clinical and Translational Perspectives on Wilson Disease (n.d.).
- [27] Sifri, C.D.; Burke, G.H.; Enfield, K.B. Reduced Health Care-Associated Infections in an Acute Care Community Hospital Using a Combination of Self-Disinfecting Copper-Impregnated Composite Hard Surfaces and Linens. *Am. J. Infect. Control* **2016**, *44*, 1565–1571. doi:10.1016/J.AJIC.2016.07.007.
- [28] Castillo-Duran, C.; Uauy, R. Copper Deficiency Impairs Growth of Infants Recovering from Malnutrition. *Am. J. Clin. Nutr.* **1988**, *47*, 710–714. doi:10.1093/AJCN/47.4.710.
- [29] Singh, A.v.; Patil, R.; Anand, A.; Milani, P.; Gade, W.N. Biological Synthesis of Copper Oxide Nano Particles Using Escherichia Coli. *Curr. Nanosci.* **2010**, *6*, 365–369. doi:10.2174/157341310791659062.
- [30] Yedurkar, S.; Maurya, C.; Mahanwar, P. A Biological Approach for the Synthesis of Copper Oxide Nanoparticles by Ixora coccinea Leaf Extract: *Jmaterenvirosci.Com.* **8** (2017) 1173–1178. <http://www.jmaterenvirosci.com/> (accessed June 30, 2021).
- [31] Vijay Kumar, R.; Elgamiel, R.; Diamant, Y.; Gedanken, A.; Norwig, J. Sonochemical Preparation and Characterization of Nanocrystalline Copper Oxide Embedded in Poly(Vinyl Alcohol) and its Effect on Crystal Growth of Copper Oxide. *Langmuir* **2001**, *17*, 1406–1410. doi:10.1021/la001331s.
- [32] Yin, A.J.; Li, J.; Jian, W.; Bennett, A.J.; Xu, J.M. Fabrication of Highly Ordered Metallic Nanowire Arrays by Electrodeposition. *Appl. Phys. Lett.* **2001**, *79*, 1039–1041. doi:10.1063/1.1389765.
- [33] Wang, H.; Xu, J.Z.; Zhu, J.J.; Chen, H.Y. Preparation of CuO Nanoparticles by Microwave Irradiation. *J. Cryst. Growth* **2002**, *244*, 88–94. doi:10.1016/S0022-0248(02)01571-3.
- [34] Xu, J.F.; Ji, W.; Shen, Z.X.; Tang, S.H.; Ye, X.R.; Jia, D.Z.; Xin, X.Q. Preparation and Characterization of CuO Nanocrystals. *J. Solid State Chem.* **1999**, *147*, 516–519. doi:10.1006/jssc.1999.8409.
- [35] Carnes, C.L.; Stipp, J.; Klabunde, K.J.; Bonevich, J. Synthesis, Characterization, and Adsorption Studies of Nanocrystalline Copper Oxide and Nickel Oxide. *Langmuir* **2002**, *18*, 1352–1359. doi:10.1021/la010701p.
- [36] Armacho-Flores, B.A.; Martínez-Álvarez, O.; Arenas-Camacho, M.C.; García-Conteras, R.; Argueta-Figueroa, L.; de La Fuente-Hernández, J.; Acosta-Torres, L.S. Copper: Synthesis Techniques in Nanoscale and Powerful Application as an Antimicrobial Agent. *J. Nanomater.* **2015**, 2015. doi:10.1155/2015/415238.
- [37] Jadoun, S.; Arif, R.; Jangid, N.K.; Meena, R.K. Green Synthesis of Nanoparticles Using Plant Extracts: A Review. *Environ. Chem. Lett.* **2021**, *19*, 355–374. doi:10.1007/s10311-020-01074-x.
- [38] Yedurkar, S.; Maurya, C.; Mahanwar, P. A Biological Approach for the Synthesis of Copper Oxide Nanoparticles by Ixora Coccinea Leaf Extract (2017).
- [39] Green Synthesis – an overview | ScienceDirect Topics (n.d.). <https://www.sciencedirect.com/topics/engineering/green-synthesis> (accessed July 3, 2021).
- [40] Barabadi, H.; Vahidi, H.; Mahjoub, M.A.; Kosar, Z.; Damavandi Kamali, K.; Ponmurugan, K.; Hosseini, O.; Rashedi, M.; Saravanan, M. Emerging Antineoplastic Gold Nanomaterials for Cervical Cancer Therapeutics: A Systematic Review. *J. Cluster Sci.* **2019**, *31* (6), 1173–1184. doi:10.1007/S10876-019-01733-2.
- [41] Saravanan, M.; Barabadi, H.; Vahidi, H.; Webster, T.J.; Medina-Cruz, D.; Mostafavi, E.; Vernet-Crua, A.; Cholula-Diaz, J.L.; Periakaruppan, P. Emerging theranostic silver and gold nanobiomaterials for breast cancer: Present status and future prospects. In *Handbook on Nanobiomaterials for Therapeutics and Diagnostic Applications* (2021) 439–456. doi:10.1016/B978-0-12-821013-0.00004-0.
- [42] Honary, S.; Gharaei-Fathabad, E.; Barabadi, H.; Naghibi, F. Fungus-mediated Synthesis of Gold Nanoparticles: A Novel Biological Approach to Nanoparticle Synthesis. *J. Nanosci. Nanotechnol.* **2013**, *13*, 1427–1430. doi:10.1166/JNN.2013.5989.
- [43] Letchumanan, D.; Sok, S.P.M.; Ibrahim, S.; Nagoor, N.H.; Arshad, N.M. Plant-Based Biosynthesis of Copper/Copper Oxide Nanoparticles: An Update on Their Applications in Biomedicine, Mechanisms, and Toxicity. *Biomolecules* **2021**, *11*. doi:10.3390/BIOM11040564.



- [44] Sutradhar, P.; Saha, M.; Maiti, D. Microwave Synthesis of Copper Oxide Nanoparticles Using tea Leaf and Coffee Powder Extracts and its Antibacterial Activity. *J. Nanostruct. Chem.* **2014**, *4*. doi:10.1007/s40097-014-0086-1.
- [45] Aminuzzaman, M.; Kei, L.M.; Liang, W.H. Green Synthesis of Copper Oxide (CuO) Nanoparticles Using Banana Peel Extract and Their Photocatalytic Activities. In *AIP Conference Proceedings*, American Institute of Physics Inc., 2017; p. 020016. doi:10.1063/1.4979387.
- [46] Aziz, W.J.; Jassim, H.A. A new Paradigm Shift to Prepare Copper Nanoparticles Using Biological Synthesis and Evaluation of Antimicrobial Activity. *Plant Arch.* **2018**, *18* (2), 2020–2024.
- [47] Selvan, S.M.; Anand, K.V.; Govindaraju, K.; Tamilselvan, S.; Kumar, V.G.; Subramanian, K.S.; Kannan, M.; Raja, K. Green Synthesis of Copper Oxide Nanoparticles and Mosquito Larvicidal Activity Against Dengue, Zika and Chikungunya Causing Vector *Aedes Aegypti*. *IET Nanobiotechnol.* **2018**, *12*, 1042–1046. doi:10.1049/iet-nbt.2018.5083.
- [48] Singh, J.; Kumar, V.; Kim, K.H.; Rawat, M. Biogenic Synthesis of Copper Oxide Nanoparticles Using Plant Extract and its Prodigious Potential for Photocatalytic Degradation of Dyes. *Environ. Res.* **2019**, *177*. doi:10.1016/j.envres.2019.108569.
- [49] Vishveshvar, K.; Krishnan, M.v.A.; Haribabu, K.; Vishnuprasad, S. Green Synthesis of Copper Oxide Nanoparticles Using *Ixiro Coccinea* Plant Leaves and its Characterization. *Bionanoscience.* **2018**, *8*, 554–558. doi:10.1007/s12668-018-0508-5.
- [50] Awwad, A.M. Antibacterial Activity of synthesized Copper Oxide Nanoparticles using *Malva sylvestris* Leaf Extract, Undefined. 2014.
- [51] Saif, S.; Tahir, A.; Chen, Y. Green Synthesis of Iron Nanoparticles and Their Environmental Applications and Implications. *Nanomaterials* **2016**, *6*, 209. doi:10.3390/nano6110209.
- [52] Makarov, V.v.; Love, A.J.; Sinitsyna, O.v.; Makarova, S.S.; Yaminsky, I.v.; Taliansky, M.E.; Kalinina, N.O. 'Green' Nanotechnologies: Synthesis of Metal Nanoparticles Using Plants. *Acta Naturae.* **2014**, *6*, 35–44.
- [53] Ahmed, S.; Ahmad, M.; Swami, B.L.; Ikram, S. A Review on Plants Extract Mediated Synthesis of Silver Nanoparticles for Antimicrobial Applications: A Green Expertise. *J. Adv. Res.* **2016**, *7*, 17–28. doi:10.1016/j.jare.2015.02.007.
- [54] Sarkar, J.; Chakraborty, N.; Chatterjee, A.; Bhattacharjee, A.; Dasgupta, D.; Acharya, K. Green Synthesized Copper Oxide Nanoparticles Ameliorate Defence and Antioxidant Enzymes in *Lens Culinaris*. *Nanomaterials* **2020**, *10*. doi:10.3390/nano10020312.
- [55] Ppn, V.K.; Shameem, U.; Kollu, P.; Pammi, S.V.N. Green Synthesis of Copper Oxide Nanoparticles Using *Aloe vera* Leaf Extract and Its Antibacterial Activity Against Fish Bacterial Pathogens Thermoelectric materials and perovskite solar cells View project Investigating magnetic properties of doped cerium oxide nanoparticles View project, (n.d.). doi:10.1007/s12668-015-0171-z.
- [56] Yugandhar, P.; Vasavi, T.; Devi, P.U.M.; Savithramma, N. Bioinspired Green Synthesis of Copper Oxide Nanoparticles from *Syzygium Alternifolium* (Wt.) Walp: Characterization and Evaluation of its Synergistic Antimicrobial and Anticancer Activity. *Appl. Nanosci.* **2017**, *7*, 417–427. doi:10.1007/s13204-017-0584-9.
- [57] Bordbar, M.; Sharifi-Zarchi, Z.; Khodadadi, B. Green Synthesis of Copper Oxide Nanoparticles/Clinoptilolite Using *Rheum Palmatum* L. Root Extract: High Catalytic Activity for Reduction of 4-Nitro Phenol, Rhodamine B, and Methylene Blue. *J. Sol-Gel Sci. Technol.* **2017**, *81*, 724–733. doi:10.1007/s10971-016-4239-1.
- [58] Ghidan, A.Y.; Al-Antary, T.M.; Awwad, A.M. Green Synthesis of Copper Oxide Nanoparticles Using *Punica Granatum* Peels Extract: Effect on Green Peach Aphid, Environmental Nanotechnology. *Monit. Manag.* **2016**, *6*, 95–98. doi:10.1016/j.enmm.2016.08.002.
- [59] Gunalan, S.; Sivaraj, R.; Venkatesh, R. Aloe Barbadensis Miller Mediated Green Synthesis of Mono-Disperse Copper Oxide Nanoparticles: Optical Properties. *Spectrochim. Acta A Mol. Biomol. Spectrosc.* **2012**, *97*, 1140–1144. doi:10.1016/j.saa.2012.07.096.
- [60] Siddiqui, H.; Qureshi, M.S.; Haque, F.Z. Biosynthesis of Flower-Shaped CuO Nanostructures and Their Photocatalytic and Antibacterial Activities. *Nano-Micro Lett.* **2020**, *12*, 1–11. doi:10.1007/s40820-019-0357-y.
- [61] Asemani, M.; Anarjan, N. Green Synthesis of Copper Oxide Nanoparticles Using *Juglans Regia* Leaf Extract and Assessment of Their Physico-Chemical and Biological Properties. *Green Process. Synth.* **2019**, *8*, 557–567. doi:10.1515/gps-2019-0025.
- [62] Phang, Y.K.; Aminuzzaman, M.; Akhtaruzzaman, M.; Muhammad, G.; Ogawa, S.; Watanabe, A.; Tey, L.H. Green Synthesis and Characterization of CuO Nanoparticles Derived from *Papaya* Peel Extract for the Photocatalytic Degradation of Palm oil Mill Effluent (POME). *Sustainability* **2021**, *13*, 1–15. doi:10.3390/su13020796.
- [63] Shende, S.; Ingle, A.P.; Gade, A.; Rai, M. Green Synthesis of Copper Nanoparticles by *Citrus Medica* Linn. (*Idilimbu*) Juice and Its Antimicrobial Activity. *World J. Microbiol. Biotechnol.* **2015**, *31*, 865–873. doi:10.1007/s11274-015-1840-3.
- [64] Nasrollahzadeh, M.; Sajadi, S.M.; Khalaj, M. Green Synthesis of Copper Nanoparticles Using Aqueous Extract of the Leaves of *Euphorbia Esula* L and Their Catalytic Activity for Ligand-Free Ullmann-Coupling Reaction and Reduction of 4-Nitrophenol. *RSC Adv.* **2014**, *4*, 47313–47318. doi:10.1039/c4ra08863 h.
- [65] Sastry, A.B.S.; Karthik Aamanchi, R.B.; Prasad, C.S.R.L.; Murty, B.S. Large-scale Green Synthesis of Cu Nanoparticles. *Environ. Chem. Lett.* **2013**, *11*, 183–187. doi:10.1007/s10311-012-0395-x.
- [66] Rafique, M.; Shaikh, A.J.; Rasheed, R.; Tahir, M.B.; Bakhat, H.F.; Rafique, M.S.; Rabbani, F. A Review on Synthesis, Characterization and Applications of Copper Nanoparticles Using Green Method. *Nano* **2017**, *12*. doi:10.1142/S1793292017500436.
- [67] Gopinath, M.; Subbaiya, R.; Selvam, M.M.; Suresh, D. Synthesis of Copper Nanoparticles from *Nerium Oleander* Leaf Aqueous Extract and its Antibacterial Activity. *Int. J. Curr. Microbiol. App. Sci.* **2014**, *3*, 814–818. <http://www.ijcmas.com> (accessed July 13, 2021).

- [68] Green synthesis of CuO NAPs using *Syzygium aromaticum* (Clove) | Download Scientific Diagram (n.d.). [https://www.researchgate.net/figure/Green-synthesis-of-CuO-NAPs-using-Syzygium-aromaticum-Clove\\_fig11\\_321183963](https://www.researchgate.net/figure/Green-synthesis-of-CuO-NAPs-using-Syzygium-aromaticum-Clove_fig11_321183963) (accessed July 13, 2021).
- [69] Kale, R.; Kane, P.; Jagtap, P.; Sheikh, J. Citrus Limon Leaves Mediated Synthesis Method for Copper Nanoparticles and its Structural Study. *Eur. J. Sci. (EJS)*. **2019**. doi:10.29198/EJS1903.
- [70] Rafique, M.; Shaikh, A.J.; Rasheed, R.; Tahir, M.B.; Bakhat, H.F.; Rafique, M.S.; Rabbani, F. A Review on Synthesis, Characterization and Applications of Copper Nanoparticles Using Green Method. *Nano*. **2017**, 12. doi:10.1142/S1793292017500436.
- [71] Parikh, P.; Zala, D.; Makwana, B.A. Biosynthesis of Copper Nanoparticles and Their Antimicrobial Activity. *Open Access Library PrePrints* **2014**, 1, 1–15. doi:10.4236/OALIB.PREPRINTS.1200067.
- [72] Lee, H.J.; Song, J.Y.; Kim, B.S. Biological Synthesis of Copper Nanoparticles Using *Magnolia Kobus* Leaf Extract and Their Antibacterial Activity. *J. Chem. Technol. Biotechnol.* **2013**, 88, 1971–1977. doi:10.1002/JCTB.4052.
- [73] Nasrollahzadeh, M.; Mohammad Sajadi, S. Green Synthesis of Copper Nanoparticles Using *Ginkgo Biloba* L. Leaf Extract and Their Catalytic Activity for the Huisgen [3+2] Cycloaddition of Azides and Alkynes at Room Temperature. *J. Colloid Interface Sci.* **2015**, 457, 141–147. doi:10.1016/J.JCIS.2015.07.004.
- [74] Kathad, U.; Gajera, H. Synthesis of Copper Nanoparticles by two Different Methods and Size Comparison. *Int. J. Pharma. Bio. Sci.* **2014**, 5, 533–540. [https://www.academia.edu/22434358/\\_SYNTHESIS\\_OF\\_COPPER\\_NANOPARTICLES\\_BY\\_TWO\\_DIFFERENT\\_METHODS\\_AND\\_SIZE\\_COMPARISON\\_](https://www.academia.edu/22434358/_SYNTHESIS_OF_COPPER_NANOPARTICLES_BY_TWO_DIFFERENT_METHODS_AND_SIZE_COMPARISON_) (accessed November 19, 2021).
- [75] Saranyaadevi, K.; Subha, V.; Ravindran, R.S.E.; Renganathan, S. Synthesis and Characterization of Copper Nanoparticle Using *Capparis Zeylanical* leaf Extract. *Int. J. ChemTech Res.* **2014**, 6, 4533–4541.
- [76] Karimi, J.; Mohsenzadeh, S. Rapid, Green, and Eco-Friendly Biosynthesis of Copper Nanoparticles Using Flower Extract of *Aloe Vera*. *Synth. React. Inorg., Met.-Org., Nano-Met. Chem.* **2015**, 45, 895–898. doi:10.1080/15533174.2013.862644.
- [77] Gandhi, N.; Sirisha, D.; Asthana, S. Microwave Mediated Green Synthesis Of Copper Nanoparticles Using Aqueous Extract Of *Piper Nigrum* Seeds And Particles Characterisation. *IAETSD J. Adv. Res. Appl. Sci.* **2018**, 5, 859–870. <http://iaetsdjaras.org/> (accessed November 20, 2021).
- [78] Salgado, P.; Mártire, D.O.; Vidal, G. Eucalyptus Extracts-Mediated Synthesis of Metallic and Metal Oxide Nanoparticles: Current Status and Perspectives. *Mater. Res. Express* **2019**, 6, 082006. doi:10.1088/2053-1591/AB254C.
- [79] Subhankari, I.; Nayak, P.L. Antimicrobial Activity of Copper Nanoparticles Synthesised by *Ginger* (*Zingiber Officinale*) Extract. *World J. Nano Sci. Technol.* **2013**, 2, 10–13. doi:10.5829/idosi.wjnst.2013.2.1.21133.
- [80] Thakur, S.; Sharma, S.; Thakur, S.; Rai, R. Green Synthesis of Copper Nano-Particles Using *Asparagus Adscendens* Roxb. Root and Leaf Extract and Their Antimicrobial Activities. *Int. J. Curr. Microbiol. Appl. Sci.* **2018**, 7, 683–694. doi:10.20546/IJCMAS.2018.704.077.
- [81] Waris, A.; Din, M.; Ali, A.; Ali, M.; Afridi, S.; Baset, A.; Ullah Khan, A. A Comprehensive Review of Green Synthesis of Copper Oxide Nanoparticles and Their Diverse Biomedical Applications. *Inorg. Chem. Commun.* **2021**, 123, 108369. doi:10.1016/J.INOCHE.2020.108369.
- [82] Vishveshvar, K.; Krishnan, M.v.A.; Haribabu, K.; Vishnuprasad, S. Green Synthesis of Copper Oxide Nanoparticles Using *Ixiro Coccinea* Plant Leaves and its Characterization. *Bionanoscience*. **2018**, 8 (2), 554–558. doi:10.1007/S12668-018-0508-5.
- [83] Nagajyothi, P.C.; Muthuraman, P.; Sreekanth, T.V.M.; Kim, D.H.; Shim, J. Green Synthesis: In-Vitro Anticancer Activity of Copper Oxide Nanoparticles Against Human Cervical Carcinoma Cells. *Arab. J. Chem.* **2017**, 10, 215–225. doi:10.1016/J.ARABJC.2016.01.011.
- [84] Selvan, S.M.; Anand, K.V.; Govindaraju, K.; Tamilselvan, S.; Kumar, V.G.; Subramanian, K.S.; Kannan, M.; Raja, K. Green Synthesis of Copper Oxide Nanoparticles and Mosquito Larvicidal Activity Against Dengue, Zika and Chikungunya Causing Vector *Aedes Aegypti*. *IET Nanobiotechnol.* **2018**, 12, 1042–1046. doi:10.1049/IET-NBT.2018.5083.
- [85] Sutradhar, P.; Saha, M.; Maiti, D. Microwave Synthesis of Copper Oxide Nanoparticles Using tea Leaf and Coffee Powder Extracts and its Antibacterial Activity. *J. Nanostructure Chem.* **2014**, 4 (1), 1–6. doi:10.1007/S40097-014-0086-1.
- [86] Asemani, M.; Anarjan, N. Green Synthesis of Copper Oxide Nanoparticles Using *Juglans Regia* Leaf Extract and Assessment of Their Physico-Chemical and Biological Properties. *Green Process. Synth.* **2019**, 8, 557–567. doi:10.1515/GPS-2019-0025/MACHINEREADABLECITATION/RIS.
- [87] Sivaraj, R.; Rahman, P.K.S.M.; Rajiv, P.; Narendhran, S.; Venckatesh, R. Biosynthesis and Characterization of *Acalypha Indica* Mediated Copper Oxide Nanoparticles and Evaluation of its Antimicrobial and Anticancer Activity. *Spectrochim. Acta. A Mol. Biomol. Spectrosc.* **2014**, 129, 255–258. doi:10.1016/J.SAA.2014.03.027.
- [88] Ghidan, A.Y.; Al-Antary, T.M.; Awwad, A.M. Green Synthesis of Copper Oxide Nanoparticles Using *Punica Granatum* Peels Extract: Effect on Green Peach Aphid. *Environ. Nanotechnol. Monit. Manag.* **2016**, 6, 95–98. doi:10.1016/j.enmm.2016.08.002.
- [89] Aminuzzaman, M.; Kei, L.M.; Liang, W.H. Green Synthesis of Copper Oxide (CuO) Nanoparticles Using Banana Peel Extract and their Photocatalytic Activities. In *AIP Conference Proceedings*, American Institute of Physics Inc., 2017. doi:10.1063/1.4979387.
- [90] Prakash, S.; Elavarasan, N.; Venkatesan, A.; Subashini, K.; Sowndharya, M.; Sujatha, V. Green Synthesis of Copper Oxide Nanoparticles and its Effective Applications in Biginelli Reaction, BTB Photodegradation and Antibacterial Activity. *Adv. Powder Technol.* **2018**, 29, 3315–3326. doi:10.1016/j.apt.2018.09.009.
- [91] Rajendran, A.; Siva, E.; Dhanraj, C.; Senthilkumar, S. A Green and Facile Approach for the Synthesis Copper Oxide Nanoparticles Using *Hibiscus Rosa-Sinensis* Flower Extracts and It's Antibacterial Activities (2018). doi:10.4172/2155-9821.1000324.

- [92] Kurkure, R.V.; Jaybhaye, S.; Sangle, A. International Journal on Recent and Innovation Trends in Computing and Communication Synthesis of Copper / Copper Oxide Nanoparticles in Eco-Friendly and Non-Toxic Manner from Floral Extract of *Caesalpinia pulcherrima* (n.d.). <http://www.ijritcc.org> (accessed June 24, 2021).
- [93] Bordbar, M.; Sharifi-Zarchi, Z.; Khodadadi, B. Green Synthesis of Copper Oxide Nanoparticles/Clinoptilolite Using Rheum Palmatum L. Root Extract: High Catalytic Activity for Reduction of 4-Nitro Phenol, Rhodamine B, and Methylene Blue. *J. Sol-Gel Sci. Technol.* **2017**, *81*, 724–733. doi:10.1007/s10971-016-4239-1.
- [94] (PDF) Synthesis of Copper oxide nanoparticles using *Desmodium gangeticum* aqueous root extract (n.d.). [https://www.researchgate.net/publication/285199536\\_Synthesis\\_of\\_Copper\\_oxide\\_nanoparticles\\_using\\_Desmodium\\_gangeticum\\_aqueous\\_root\\_extract](https://www.researchgate.net/publication/285199536_Synthesis_of_Copper_oxide_nanoparticles_using_Desmodium_gangeticum_aqueous_root_extract) (accessed June 25, 2021).
- [95] Mustafa, H.S.; Oraibi, A.G.; Ibrahim, K.M.; Ibrahim, N.K. Influence of Silver and Copper Nanoparticles on Physiological Characteristics of *Phaseolus Vulgaris* L. in Vitro and in Vivo. *Int. J. Curr. Microbiol. Appl. Sci.* **2017**, *6*, 834–843. doi:10.20546/ijcmas.2017.601.098.
- [96] Wang, G.; Zhao, K.; Gao, C.; Wang, J.; Mei, Y.; Zheng, X.; Zhu, P. Green Synthesis of Copper Nanoparticles Using Green Coffee Bean and Their Applications for Efficient Reduction of Organic Dyes. *J. Environ. Chem. Eng.* **2021**, *9*, 105331. doi:10.1016/j.jece.2021.105331.
- [97] Khatamifar, M.; Fatemi, S.J. Green Synthesis of Pure Copper Oxide Nanoparticles Using *Quercus Infectoria* Galls Extract, Thermal Behavior and Their Antimicrobial Effects. *Part. Sci. Technol.* **2021**. doi:10.1080/02726351.2021.1901810.
- [98] Shayegan Mehr, E.; Sorbiun, M.; Ramazani, A.; Taghavi Fardood, S. Plant-mediated Synthesis of Zinc Oxide and Copper Oxide Nanoparticles by Using *Ferulago Angulata* (Schlecht) Boiss Extract and Comparison of Their Photocatalytic Degradation of Rhodamine B (RhB) Under Visible Light Irradiation. *J. Mater. Sci.: Mater. Electron.* **2018**, *29*, 1333–1340. doi:10.1007/s10854-017-8039-3.
- [99] Naika, H.R.; Lingaraju, K.; Manjunath, K.; Kumar, D.; Nagaraju, G.; Suresh, D.; Nagabhushana, H. Green Synthesis of CuO Nanoparticles Using *Gloriosa Superba* L. Extract and Their Antibacterial Activity. *J. Taibah Univ. Sci.* **2015**, *9*, 7–12. doi:10.1016/J.JTUSCI.2014.04.006.
- [100] Yugandhar, P.; Vasavi, T.; Devi, P.U.M.; Savithramma, N. Bioinspired Green Synthesis of Copper Oxide Nanoparticles from *Syzygium Alternifolium* (Wt.) Walp: Characterization and Evaluation of its Synergistic Antimicrobial and Anticancer Activity. *Appl. Nanosci.* **2017**, *7*, 417–427. doi:10.1007/S13204-017-0584-9/FIGURES/10.
- [101] Nwanya, A.C.; Razanamahandry, L.C.; Bashir, A.K.H.; Ikpo, C.O.; Nwanya, S.C.; Botha, S.; Ntwampe, S.K.O.; Ezema, F.I.; Iwuoha, E.I.; Maaza, M. Industrial Textile Effluent Treatment and Antibacterial Effectiveness of *Zea Mays* L. Dry Husk Mediated bio-Synthesized Copper Oxide Nanoparticles. *J. Hazard. Mater.* **2019**, *375*, 281–289. doi:10.1016/J.JHAZMAT.2019.05.004.
- [102] Sukumar, S.; Rudrasenan, A.; Nambiar, D.P. Green-Synthesized Rice-Shaped Copper Oxide Nanoparticles Using *Caesalpinia Bonducella* Seed Extract and Their Applications. *ACS Omega* **2020**, *5*, 1040–1051. doi:10.1021/ACSOMEGA.9B02857.
- [103] Demirci Gultekin, D.; Nadaroglu, H.; Gungor, A.A.; Kishali, N.H. Biosynthesis and Characterization of Copper Oxide Nanoparticles Using Cimin Grape (*Vitis Vinifera* cv.) Extract. *Int. J. Sec. Metabolite.* **2017**, *4*, 77–84. doi:10.21448/ijsm.362672.
- [104] Ramzan, M.; Obodo, R.M.; Mukhtar, S.; Ilyas, S.Z.; Aziz, F.; Thovhogi, N. Green Synthesis of Copper Oxide Nanoparticles Using *Cedrus Deodara* Aqueous Extract for Antibacterial Activity. *Mater. Today Proc.* **2021**, *36*, 576–581. doi:10.1016/j.matpr.2020.05.472.
- [105] Ijaz, F.; Shahid, S.; Khan, S.A.; Ahmad, W.; Zaman, S. Green Synthesis of Copper Oxide Nanoparticles Using *Abutilon Indicum* Leaf Extract: Antimicrobial, Antioxidant and Photocatalytic dye Degradation Activities. *Trop. J. Pharm. Res.* **2017**, *16*, 743–753. doi:10.4314/tjpr.v16i4.2.
- [106] Gunalan, S.; Sivaraj, R.; Venckatesh, R. Aloe *Barbadensis* Miller Mediated Green Synthesis of Mono-Disperse Copper Oxide Nanoparticles: Optical Properties. *Spectrochim. Acta A Mol. Biomol. Spectrosc.* **2012**, *97*, 1140–1144. doi:10.1016/j.saa.2012.07.096.
- [107] Sankar, R.; Maheswari, R.; Karthik, S.; Shivashangari, K.S.; Ravikumar, V. Anticancer Activity of *Ficus Religiosa* Engineered Copper Oxide Nanoparticles. *Mater. Sci. Eng., C* **2014**, *44*, 234–239. doi:10.1016/j.msec.2014.08.030.
- [108] Berra, D.; Eddine, L.S.; Boubaker, B.; Ridha, O.M.; Berra, D.; Laouini, S.E.; Benhaoua, B.; Ouahrani, M.R.; Berrani, D.; Rahal, A. GREEN SYNTHESIS OF COPPER OXIDE NANOPARTICLES BY PHEONIX DACTYLIFERA L LEAVES EXTRACT Preparation methods keratin View project investigation of Nickel oxide thin films properties View project GREEN SYNTHESIS OF COPPER OXIDE NANOPARTICLES BY PHEONIX DACTYLIFERA L LEAVES EXTRACT, 2018. <https://www.researchgate.net/publication/329881371> (accessed June 28, 2021).
- [109] Nasrollahzadeh, M.; Sajjadi, M.; Mohammad Sajadi, S. Biosynthesis of Copper Nanoparticles Supported on Manganese Dioxide Nanoparticles Using *Centella Asiatica* L. Leaf Extract for the Efficient Catalytic Reduction of Organic Dyes and Nitroarenes. *Cuihua Xuebao/Chin. J. Catal.* **2018**, *39*, 109–117. doi:10.1016/S1872-2067(17)62915-2.
- [110] Nagar, N.; Devra, V. Green Synthesis and Characterization of Copper Nanoparticles Using *Azadirachta Indica* Leaves. *Mater. Chem. Phys.* **2018**, *213*, 44–51. doi:10.1016/j.matchemphys.2018.04.007.
- [111] Narasaiah, P.; Mandal, B.K.; Sarada, N.C. Biosynthesis of Copper Oxide nanoparticles from *Drypetes sepia* Leaf extract and their catalytic activity to dye degradation. In *IOP Conference Series: Materials Science and Engineering*, Institute of Physics Publishing, 2017: p. 022012. doi:10.1088/1757-899X/263/2/022012.
- [112] Chand Mali, S.; Raj, S.; Trivedi, R. Biosynthesis of Copper Oxide Nanoparticles Using *Enicostemma Axillare* (Lam.) Leaf Extract. *Biochem. Biophys. Rep.* **2019**, *20*, 100699. doi:10.1016/j.bbrep.2019.100699.

- [113] Ali Thamer, N.; Tareq Barakat, N. Cytotoxic Activity of Green Synthesis Copper Oxide Nanoparticles Using Cordia Myxa L. Aqueous Extract on Some Breast Cancer Cell Lines. In *Journal of Physics: Conference Series*, Institute of Physics Publishing, 2019: p. 062104. doi:10.1088/1742-6596/1294/6/062104.
- [114] Ramesh, C.; HariPrasad, M.; Ragnathan, V. Effect of Arachis Hypogaea L. Leaf Extract on Barfoeds Solution; Green Synthesis of Cu<sub>2</sub>O Nanoparticles and its Antibacterial Effect. *Curr. Nanosci.* **2011**, *7*, 995–999. doi:10.2174/157341311798220781.
- [115] Aher, Y.B.; Jain, G.H.; Patil, G.E.; Savale, A.R.; Ghotekar, S.K.; Pore, D.M.; Pansambal, S.S.; Deshmukh, K.K. Biosynthesis of Copper Oxide Nanoparticles Using Leaves Extract of Leucaena leucocephala L. and Their Promising Upshot Against the Selected Human Pathogens, Islamic Azad University- Tonekabon Branch, 2017. [http://www.ijmcm.ir/article\\_531739.html](http://www.ijmcm.ir/article_531739.html) (accessed June 29, 2021).
- [116] Praburaman, L.; Jang, J.S.; Muthusamy, G.; Arumugam, S.; Manoharan, K.; Cho, K.M.; Min, C.; Kamala-Kannan, S.; Byung-Taek, O. Piper Betle-Mediated Synthesis, Characterization, Antibacterial and Rat Splenocyte Cytotoxic Effects of Copper Oxide Nanoparticles, Artificial Cells. *Nanomed. Biotechnol.* **2016**, *44*, 1400–1405. doi:10.3109/21691401.2015.1029630.
- [117] Sivaraj, R.; Rahman, P.K.S.M.; Rajiv, P.; Salam, H.A.; Venckatesh, R. Biogenic Copper Oxide Nanoparticles Synthesis Using Tabernaemontana Divaricate Leaf Extract and its Antibacterial Activity Against Urinary Tract Pathogen. *Spectrochim. Acta A Mol. Biomol. Spectrosc.* **2014**, *133*, 178–181. doi:10.1016/j.saa.2014.05.048.
- [118] Biosynthesis of Copper Oxide Nanoparticles Using Ailanthus Altissima Leaf Extract and Antibacterial Activity by Akl Awwad, Mohammad Amer:: SSRN, (n.d.). [https://papers.ssrn.com/sol3/papers.cfm?abstract\\_id=3554169](https://papers.ssrn.com/sol3/papers.cfm?abstract_id=3554169) (accessed June 29, 2021).
- [119] Prasad, K.S.; Patra, A.; Shruthi, G.; Chandan, S. Aqueous Extract of Saraca Indica Leaves in the Synthesis of Copper Oxide Nanoparticles: Finding a way Towards Going Green. *J. Nanotechnol.* **2017**, *2017*. doi:10.1155/2017/7502610.
- [120] Ahmed, Y.; Hussain, J.; Asif, S. Green Synthesis of Copper Oxide and Cobalt Oxide Nanoparticles Using Spinacia Oleracea Leaf Extract (n.d.). doi:10.31224/OSF.IO/75FA6.
- [121] Chung, I.; Rahuman, A.A.; Marimuthu, S.; Kirthi, A.V.; Anbarasan, K.; Padmini, P.; Rajakumar, G. Green Synthesis of Copper Nanoparticles Using Eclipta Prostrata Leaves Extract and Their Antioxidant and Cytotoxic Activities. *Exp. Ther. Med.* **2017**, *14*, 18–24. doi:10.3892/etm.2017.4466.
- [122] Shi, L.B.; Tang, P.F.; Zhang, W.; Zhao, Y.P.; Zhang, L.C.; Zhang, H. Green Synthesis of CuO Nanoparticles Using Cassia Auriculata Leaf Extract and in Vitro Evaluation of Their Biocompatibility with Rheumatoid Arthritis Macrophages (RAW 264.7). *Trop. J. Pharm. Res.* **2017**, *16*, 185–192. doi:10.4314/tjpr.v16i1.25.
- [123] Vaidehi, D.; Bhuvaneshwari, V.; Bharathi, D.; Sheetal, B.P. Antibacterial and Photocatalytic Activity of Copper Oxide Nanoparticles Synthesized Using Solanum Lycopersicum Leaf Extract. *Mater. Res. Express* **2018**, *5*, 085403. doi:10.1088/2053-1591/aad426.
- [124] Hafeez, M.; Arshad, R.; Khan, J.; Akram, B.; Ahmad, M.N.; Hameed, M.U.; Haq, S. Populus Ciliata Mediated Synthesis of Copper Oxide Nanoparticles for Potential Biological Applications. *Mater. Res. Express* **2019**, *6*, 055043. doi:10.1088/2053-1591/ab0601.
- [125] Waris, A.; Din, M.; Ali, A.; Ali, M.; Afridi, S.; Baset, A.; Ullah Khan, A. A Comprehensive Review of Green Synthesis of Copper Oxide Nanoparticles and Their Diverse Biomedical Applications. *Inorg. Chem. Commun.* **2021**, *123*, 108369. doi:10.1016/j.inoche.2020.108369.
- [126] Sathiyavimal, S.; Vasantharaj, S.; Bharathi, D.; Saravanan, M.; Manikandan, E.; Kumar, S.S.; Pugazhendhi, A. Biogenesis of Copper Oxide Nanoparticles (CuONPs) Using Sida Acuta and Their Incorporation Over Cotton Fabrics to Prevent the Pathogenicity of Gram Negative and Gram Positive Bacteria. *J. Photochem. Photobiol., B* **2018**, *188*, 126–134. doi:10.1016/J.JPHOTOBIO.2018.09.014.
- [127] Narayanan, K.B.; Sakthivel, N. Biological Synthesis of Metal Nanoparticles by Microbes. *Adv. Colloid Interface Sci.* **2010**, *156*, 1–13. doi:10.1016/j.cis.2010.02.001.
- [128] Hasan, S.S.; Singh, S.; Parikh, R.Y.; Dharne, M.; Hasan, S.S.; Dharne, M.S.; Patole, M.S.; Prasad, B.L.v.; Shouche, Y.S. Bacterial Synthesis of Copper/Copper Oxide Nanoparticles Lipid Nanoparticles View Project Filaria Repository Project View Project Bacterial Synthesis of Copper/Copper Oxide Nanoparticles. *J. Nanosci. Nanotechnol.* **2008**, *8*, 1–6. doi:10.1166/jnn.2008.095.
- [129] Patil, R.; Anand, A.; Milani, P.; Singh, A.v.; Patil, R.; Gade, W.N. Biological Synthesis of Copper Oxide Nano Particles Using Escherichia coli, 2010. <https://www.researchgate.net/publication/274192333> (accessed July 5, 2021).
- [130] Sheini, F.J.; Ghasemi, N.; Jamali-Sheini, F.; Zekavati, R. CuO and Ag/CuO Nanoparticles: Biosynthesis and Antibacterial Properties Metal-Chalcogenide and Metal-Oxide nanostructures as different applications such as solar-cells, photodiode, photocatalyst, and cytotoxicity View project Optical Properties of Semiconducting Nanostructures for Photocatalytic Applications: Fundamental Understanding and Material Design View project CuO and Ag/CuO nanoparticles: Biosynthesis and antibacterial properties, Elsevier. (2017). doi:10.1016/j.matlet.2017.02.111.
- [131] Zarasvand, K.A.; Rai, V.R. Inhibition of a sulfate reducing bacterium, Desulfovibrio marinisediminis GSR3, by biosynthesized copper oxide nanoparticles, Springer (n.d.). doi:10.1007/s13205-016-0403-0.
- [132] Araújo, I.M.S.; Silva, R.R.; Pacheco, G.; Lustri, W.R.; Tercjak, A.; Gutierrez, J.; Júnior, J.R.S.; Azevedo, F.H.C.; Figueiredo, G.S.; Vega, M.L.; Ribeiro, S.J.L.; Barud, H.S. Hydrothermal Synthesis of Bacterial Cellulose-copper Oxide Nanocomposites and Evaluation of their Antimicrobial Activity A R T I C L E I N F O, Elsevier. (2017). doi:10.1016/j.carbpol.2017.09.081.
- [133] Kouhkan, M.; Ahangar, P.; Babaganjeh, L.A.; Allahyari-Devin, M. Biosynthesis of Copper Oxide Nanoparticles Using Lactobacillus Casei Subsp. Casei and its Anticancer and Antibacterial Activities. *Curr. Nanosci.*

- 2019**, 16, 101–111. doi:10.2174/1573413715666190318155801.
- [134] Shantkriti, S.; Rani, P. Biological Synthesis of Copper Nanoparticles Using *Pseudomonas Fluorescens*, 2014. <http://www.ijcmas.com> (accessed June 27, 2021).
- [135] Singh, A.V.; Patil, R.; Anand, A.; Milani, P.; Gade, W.N. Biological Synthesis of Copper Oxide Nano Particles Using *Escherichia Coli*. *Curr. Nanosci.* **2010**, 6, 365–369. doi:10.2174/157341310791659062.
- [136] El-Batal, A.I.; El-Sayyad, G.S.; El-Ghamery, A.; Gobara, M. Response Surface Methodology Optimization of Melanin Production by *Streptomyces Cyaneus* and Synthesis of Copper Oxide Nanoparticles Using Gamma Radiation. *J. Cluster Sci.* **2017**, 28, 1083–1112. doi:10.1007/s10876-016-1101-0.
- [137] Andra, S.; Balu, S.K.; Jeevanandham, J.; Muthalagu, M.; Vidyavathy, M.; Chan, Y.S.; Danquah, M.K. Phytosynthesized Metal Oxide Nanoparticles for Pharmaceutical Applications. *Naunyn-Schmiedeberg's Arch. Pharmacol.* **2019**, 392, 755–771. doi:10.1007/s00210-019-01666-7.
- [138] Ramanathan, R.; Field, M.R.; O'Mullane, A.P.; Smoker, P.M.; Bhargava, S.K.; Bansal, V. Aqueous Phase Synthesis of Copper Nanoparticles: A Link Between Heavy Metal Resistance and Nanoparticle Synthesis Ability in Bacterial Systems. *Nanoscale.* **2013**, 5, 2300–2306. doi:10.1039/c2nr32887a.
- [139] Srinivasan, S.; Rani, P. Biological Synthesis of Copper Nanoparticles Using *Pseudomonas Fluorescens*. *Int. J. Curr. Microbiol. Appl. Sci.* **2014**, 3, 374–383. <https://www.researchgate.net/publication/265783874> (accessed November 13, 2021).
- [140] Varshney, R.; Bhadauria, S.; Gaur, M.S.; Pasricha, R. Characterization of Copper Nanoparticles Synthesized by a Novel Microbiological Method. *JOM* **2010**, 62, 102–104. doi:10.1007/s11837-010-0171-y.
- [141] Varshney, R.; Bhadauria, S.; Gaur, M.S.; Pasricha, R. Copper Nanoparticles Synthesis from Electroplating Industry Effluent. *Nano. Biomed. Eng.* **2011**, 3, 115–119. doi:10.5101/nbe.v3i2.p115-119.
- [142] Hasan, S.S.; Singh, S.; Parikh, R.Y.; Dharm, M.S.; Patole, M.S.; Prasad, B.L.V.; Shouche, Y.S. Bacterial Synthesis of Copper/Copper Oxide Nanoparticles. *J. Nanosci. Nanotechnol.* **2008**, 8, 3191–3196. doi:10.1166/jnn.2008.095.
- [143] (PDF) Synthesis of Metal Oxide Nano Particles by *Streptomyces Sp* for Development of Antimicrobial Textiles (n.d.). [https://www.researchgate.net/publication/265209398\\_Synthesis\\_of\\_Metal\\_Oxide\\_Nano\\_Particles\\_by\\_Streptomyces\\_Sp\\_for\\_Development\\_of\\_Antimicrobial\\_Textiles](https://www.researchgate.net/publication/265209398_Synthesis_of_Metal_Oxide_Nano_Particles_by_Streptomyces_Sp_for_Development_of_Antimicrobial_Textiles) (accessed June 20, 2021).
- [144] A Comprehensive Review of Green Synthesis of Copper Oxide Nanoparticles and their Diverse Biomedical Applications | Elsevier Enhanced Reader (n.d.). <https://reader.elsevier.com/reader/sd/pii/S138770032030959X?token=1D6584391BF0B8660D5DFB0C1D3873C0025EB530756D2846ADE753F80D6C8BC922EB8036EF7B1FE72D20E626BF3F9890&originRegion=eu-west-1&originCreation=20210620074733> (accessed June 20, 2021).
- [145] Lv, Q.; Zhang, B.; Xing, X.; Zhao, Y.; Cai, R.; Wang, W.; Gu, Q. Biosynthesis of Copper Nanoparticles Using *Shewanella Loihica* PV-4 with Antibacterial Activity: Novel Approach and Mechanisms Investigation. *J. Hazard. Mater.* **2018**, 347, 141–149. doi:10.1016/J.JHAZMAT.2017.12.070.
- [146] Ghorbani, H.R.; Mehr, F.P.; Poor, A.K. Extracellular Synthesis of Copper Nanoparticles Using Culture Supernatants of *Salmonella Typhimurium*. *Orient. J. Chem.* **2015**, 3, 527–529. doi:10.13005/ojc/310165.
- [147] Tiwari, M.; Jain, P.; Chandrashekar Hariharapura, R.; Narayanan, K.; Bhat K, U.; Udupa, N.; Rao, J.V. Biosynthesis of Copper Nanoparticles Using Copper-Resistant *Bacillus Cereus*, a Soil Isolate. *Process Biochem.* **2016**, 51, 1348–1356. doi:10.1016/J.PROCBIO.2016.08.008.
- [148] Bukhari, S.I.; Hamed, M.M.; Al-Agamy, M.H.; Gazwi, H.S.S.; Radwan, H.H.; Youssif, A.M. Biosynthesis of Copper Oxide Nanoparticles Using *Streptomyces* MHM38 and Its Biological Applications. *J. Nanomater.* **2021**, 2021. doi:10.1155/2021/6693302.
- [149] Kouhkan, M.; Ahangar, P.; Babaganjeh, L.A.; Allahyari-Devin, M. Biosynthesis of Copper Oxide Nanoparticles Using *Lactobacillus Casei* Subsp. *Casei* and its Anticancer and Antibacterial Activities. *Curr. Nanosci.* **2019**, 16, 101–111. doi:10.2174/1573413715666190318155801.
- [150] Ramanathan, R.; Bhargava, S.; Bansal, V. Biological Synthesis of Copper/Copper Oxide Nanoparticles (2016) 17. <https://www.researchgate.net/publication/260302403> (accessed November 13, 2021).
- [151] Nabila, M.I.; Kannabiran, K. Biosynthesis, Characterization and Antibacterial Activity of Copper Oxide Nanoparticles (CuO NPs) from Actinomycetes. *Biocatal. Agric. Biotechnol.* **2018**, 15, 56–62. doi:10.1016/J.BCAB.2018.05.011.
- [152] Gupta, S.; Bector, S. Biosynthesis of Extracellular and Intracellular Gold Nanoparticles by *Aspergillus Fumigatus* and *A. Flavus*, *Antonie van Leeuwenhoek. Int. J. Gen. Mol. Microbiol.* **2013**, 103, 1113–1123. doi:10.1007/s10482-013-9892-6.
- [153] Fayaz, A.M.; Balaji, K.; Girilal, M.; Yadav, R.; Kalaichelvan, P.T.; Venketesan, R. Biogenic Synthesis of Silver Nanoparticles and Their Synergistic Effect with Antibiotics: A Study Against Gram-Positive and Gram-Negative Bacteria. *Nanomedicine* **2010**, 6, 103–109. doi:10.1016/j.nano.2009.04.006.
- [154] Consolo, V.F.; Torres-Nicolini, A.; Alvarez, V.A. Mycosynthetized Ag, CuO and ZnO Nanoparticles from a Promising *Trichoderma Harzianum* Strain and Their Antifungal Potential Against Important Phytopathogens. *Sci. Rep.* **2020**, 10, 1–9. doi:10.1038/s41598-020-77294-6.
- [155] Bioreduction of AuCl<sub>4</sub><sup>-</sup> Ions by the Fungus: *Verticillium* sp. and Surface Trapping of the Gold Nanoparticles Formed – Mukherjee – 2001 – *Angewandte Chemie International Edition* – Wiley Online Library (n.d.). <https://onlinelibrary.wiley.com/doi/abs/10.1002/1521-3773%2820011001%2940%3A19%3C3585%3A%3AAID-ANIE3585%3E3.O.CO%3B2-K> (accessed July 4, 2021).
- [156] Kasana, R.C.; Panwar, N.R.; Kaul, R.K.; Kumar, P. Biosynthesis and Effects of Copper Nanoparticles on Plants. *Environ. Chem. Lett.* **2017**, 15, 233–240. doi:10.1007/s10311-017-0615-5.
- [157] (PDF) Bioremediation: Copper Nanoparticles from Electronic-waste (n.d.). [https://www.researchgate.net/publication/284697750\\_Bioremediation\\_Copper\\_Nano\\_particles\\_from\\_Electronic-waste](https://www.researchgate.net/publication/284697750_Bioremediation_Copper_Nano_particles_from_Electronic-waste) (accessed June 20, 2021).

- [158] (PDF) An Overview on the Production of Microbial Copper Nanoparticles by Bacteria, Fungi and Algae, (n.d.). [https://www.researchgate.net/publication/317552695\\_An\\_Overview\\_on\\_the\\_Production\\_of\\_Microbial\\_Copper\\_Nanoparticles\\_by\\_Bacteria\\_Fungi\\_and\\_Algae](https://www.researchgate.net/publication/317552695_An_Overview_on_the_Production_of_Microbial_Copper_Nanoparticles_by_Bacteria_Fungi_and_Algae) (accessed June 20, 2021).
- [159] Honary, S.; Barabadi, H.; Gharaei-Fathabad, E.; Naghibi, F. Green Synthesis of Copper Oxide Nanoparticles Using *Penicillium Aurantiogriseum*, *Penicillium Citrinum* and *Penicillium Waksmanii*. *Dig. J. Nanomater. Biostruct.* **n.d.**, 7, 999–1005.
- [160] Cuevas, R.; Durán, N.; Diez, M.C.; Tortella, G.R.; Rubilar, O. Extracellular Biosynthesis of Copper and Copper Oxide Nanoparticles by *Stereum Hirsutum*, a Native White-rot Fungus from Chilean Forests. *J. Nanomater.* **2015**, 2015. doi:10.1155/2015/789089.
- [161] Noor, S.; Shah, Z.; Javed, A.; Ali, A.; Hussain, S.B.; Zafar, S.; Ali, H.; Muhammad, S.A. A Fungal Based Synthesis Method for Copper Nanoparticles with the Determination of Anticancer, Antidiabetic and Antibacterial Activities. *J. Microbiol. Methods* **2020**, 174, 105966. doi:10.1016/j.mimet.2020.105966.
- [162] Saitawadekar, A.; Kakde, U.B. Green Synthesis of Copper Nanoparticles Using *Aspergillus Flavus*. *J. Crit. Rev.* **2020**, 7, 1083–1090.
- [163] Saravanakumar, K.; Shanmugam, S.; Varukattu, N.B.; MubarakAli, D.; Kathiresan, K.; Wang, M.H. Biosynthesis and Characterization of Copper Oxide Nanoparticles from Indigenous Fungi and its Effect of Photothermolysis on Human Lung Carcinoma. *J. Photochem. Photobiol., B* **2019**, 190, 103–109. doi:10.1016/J.JPHOTOBIO.2018.11.017.
- [164] Ghareib, M.; Abdallah, W.; Abu Tahon, M.; Tallima, A. Biosynthesis of Copper Oxide Nanoparticles Using the Preformed Biomass of *Aspergillus Fumigatus* and Their Antibacterial and Photocatalytic Activities. *Dig. J. Nanomater. Biostruct.* **2019**, 14, 291–303.
- [165] Li, Q.; Gadd, G.M. Biosynthesis of Copper Carbonate Nanoparticles by Ureolytic Fungi. *Appl. Microbiol. Biotechnol.* **2017**, 101, 7397–7407. doi:10.1007/s00253-017-8451-x.
- [166] Kovačec, E.; Regvar, M.; van Elteren, J.T.; Arčon, I.; Papp, T.; Makovec, D.; Vogel-Mikuš, K. Biotransformation of Copper Oxide Nanoparticles by the Pathogenic Fungus *Botrytis Cinerea*. *Chemosphere* **2017**, 180, 178–185. doi:10.1016/J.CHEMOSPHERE.2017.04.022.
- [167] Mousa, A.M.; Abdel Aziz, O.A.; Al-Hagar, O.E.A.; Gizawy, M.A.; Allan, K.F.; Attallah, M.F. Biosynthetic new Composite Material Containing CuO Nanoparticles Produced by *Aspergillus Terreus* for 47 Sc Separation of Cancer Theranostics Application from Irradiated Ca Target, Applied Radiation and Isotopes: Including Data, Instrumentation and Methods for Use in Agriculture. *Ind. Med.* **2020**, 166. doi:10.1016/J.APRADISO.2020.109389.
- [168] El-Batal, A.I.; El-Sayyad, G.S.; Mosallam, F.M.; Fathy, R.M. *Penicillium Chrysogenum*-Mediated Mycogenic Synthesis of Copper Oxide Nanoparticles Using Gamma Rays for In Vitro Antimicrobial Activity Against Some Plant Pathogens. *J. Cluster Sci.* **2019**, 31 (1), 79–90. doi:10.1007/S10876-019-01619-3.
- [169] Saravanakumar, K.; Shanmugam, S.; Varukattu, N.B.; MubarakAli, D.; Kathiresan, K.; Wang, M.H. Biosynthesis and Characterization of Copper Oxide Nanoparticles from Indigenous Fungi and its Effect of Photothermolysis on Human Lung Carcinoma. *J. Photochem. Photobiol., B* **2019**, 190, 103–109. doi:10.1016/J.JPHOTOBIO.2018.11.017.
- [170] Abboud, Y.; Saffaj, T.; Chagraoui, A.; el Bouari, A.; Brouzi, K.; Tanane, O.; Ihssane, B. Biosynthesis, Characterization and Antimicrobial Activity of Copper Oxide Nanoparticles (CONPs) Produced Using Brown Alga Extract (*Bifurcaria Bifurcata*). *Appl. Nanosci.* **2014**, 4, 571–576. doi:10.1007/s13204-013-0233-x.
- [171] Gu, H.; Chen, X.; Chen, F.; Zhou, X.; Parsaee, Z. Ultrasound-assisted Biosynthesis of CuO-NPs Using Brown Alga *Cystoseira Trinodis*: Characterization, Photocatalytic AOP, DPPH Scavenging and Antibacterial Investigations. *Ultrason. Sonochem.* **2018**, 41, 109–119. doi:10.1016/j.ultsonch.2017.09.006.
- [172] Ramaswamy, S.V.P.; Narendhran, S.; Sivaraj, R. Potentiating Effect of Ecofriendly Synthesis of Copper Oxide Nanoparticles Using Brown Alga: Antimicrobial and Anticancer Activities – Google Search (n.d.). <https://www.google.com/search?q=Ramaswamy%2C+S.V.P.%3B+Narendhran%2C+S.%3B+Sivaraj%2C+R.+Potentiating+effect+of+ecofriendly+synthesis+of+copper+oxide+nanoparticles+using+brown+alga%3A+Antimicrobial+and+anticancer+activities&oeq=Ramaswamy%2C+S.V.P.%3B+Narendhran%2C+S.%3B+Sivaraj%2C+R.+Potentiating+effect+of+ecofriendly+synthesis+of+copper+oxide+nanoparticles+using+brown+alga%3A+Antimicrobial+and+anticancer+activities&aq=chrome..69157.352j0j9&sourceid=chrome&ie=UTF-8> (accessed June 27, 2021).
- [173] Arya, A.; Gupta, K.; Chundawat, T.S.; Vaya, D. Biogenic Synthesis of Copper and Silver Nanoparticles Using Green Alga *Botryococcus Braunii* and Its Antimicrobial Activity. *Bioinorg. Chem. Appl.* **2018**, 2018. doi:10.1155/2018/7879403.
- [174] Bhattacharya, P.; Swarnakar, S.; Ghosh, S.; Majumdar, S.; Banerjee, S. Disinfection of Drinking Water via Algae Mediated Green Synthesized Copper Oxide Nanoparticles and its Toxicity Evaluation. *J. Environ. Chem. Eng.* **2019**, 7. doi:10.1016/j.jece.2018.102867.
- [175] Araya-Castro, K.; Chao, T.C.; Durán-Vinet, B.; Cisternas, C.; Ciudad, G.; Rubilar, O. Green Synthesis of Copper Oxide Nanoparticles Using Protein Fractions from an Aqueous Extract of Brown Algae *Macrocystis Pyrifera*. *Processes* **2021**, 9, 1–10. doi:10.3390/pr9010078.
- [176] Ramaswamy, S.V.P.; Narendhran, S.; Sivaraj, R. Potentiating Effect of Ecofriendly Synthesis of Copper Oxide Nanoparticles Using Brown Alga: Antimicrobial and Anticancer Activities. *Bull. Mater. Sci.* **2016**, 39, 361–364. doi:10.1007/s12034-016-1173-3.
- [177] Mourdikoudis, S.; Pallares, R.M.; Thanh, N.T.K. Characterization Techniques for Nanoparticles: Comparison and Complementarity upon Studying Nanoparticle Properties. *Nanoscale.* **2018**, 10, 12871–12934. doi:10.1039/c8nr02278j.
- [178] Ananda Murthy, H.C.; Abebe, B.; Prakash, C.H.; Shantaveerayya, K. A Review on Green Synthesis and Applications of Cu and CuO Nanoparticles. *Mater. Sci. Res. India* **2018**, 15, 279–295. doi:10.13005/msri/150311.
- [179] Naika, H.R.; Lingaraju, K.; Manjunath, K.; Kumar, D.; Nagaraju, G.; Suresh, D.; Nagabhushana, H. Green

- Synthesis of CuO Nanoparticles Using Gloriosa Superba L. Extract and Their Antibacterial Activity. *J. Taibah Univ. Sci.* **2015**, *9*, 7–12. doi:10.1016/j.jtusci.2014.04.006.
- [180] EBSCOhost | 133549318 | Green synthesis of nanoparticles and their applications (n.d.). <https://web.a.ebscohost.com/abstract?direct=true&profile=ehost&scope=site&authtype=crawler&jrnl=09757619&AN=133549318&h=9XfgmsAohl9yOoo16aD7OwWx6gOfsP1kA3Vdd7CSwxkq%2fhWBq1E%2fbp4fDxi7yyt%2bW0vYq1eK3s3USB6rhscCcQ%3d%3d&crI=c&resultNs=AdminWebAuth&resultLocaI=ErrCrIAuth&crIhashurl=login.aspx%3fdirect%3dtrue%26profile%3dehost%26scope%3dsite%26authtype%3dcrawler%26jrnl%3d09757619%26AN%3d133549318> (accessed June 27, 2021).
- [181] Applerot, G.; Lellouche, J.; Lipovsky, A.; Nitzan, Y.; Lubart, R.; Gedanken, A.; Banin, E. Understanding the Antibacterial Mechanism of CuO Nanoparticles: Revealing the Route of Induced Oxidative Stress. *Small* **2012**, *8*, 3326–3337. doi:10.1002/sml.201200772.
- [182] Awwad, A.M.; Albiss, B.A.; Salem, N.M. Antibacterial Activity of synthesized Copper Oxide Nanoparticles using Malva sylvestris Leaf Extract, 2015. <http://www.isholar.in/index.php/SMU/article/view/85554> (accessed June 27, 2021).
- [183] Yugandhar, P.; Vasavi, T.; Uma Maheswari Devi, P.; Savithamma, N. Bioinspired Green Synthesis of Copper Oxide Nanoparticles from Syzygium Alternifolium (Wt.) Walp: Characterization and Evaluation of its Synergistic Antimicrobial and Anticancer Activity. *Appl. Nanosci.* **2017**, *7*, 417–427. doi:10.1007/s13204-017-0584-9.
- [184] Nwanya, A.C.; Razanamahandry, L.C.; Bashir, A.K.H.; Ikpo, C.O.; Nwanya, S.C.; Botha, S.; Ntwampe, S.K.O.; Ezema, F.I.; Iwuoha, E.I.; Maaza, M. Industrial Textile Effluent Treatment and Antibacterial Effectiveness of Zea Mays L. Dry Husk Mediated Bio-synthesized Copper Oxide Nanoparticles. *J. Hazard. Mater.* **2019**, *375*, 281–289. doi:10.1016/j.jhazmat.2019.05.004.
- [185] Sutradhar, P.; Saha, M.; Maiti, D. Microwave Synthesis of Copper Oxide Nanoparticles Using Tea Leaf and Coffee Powder Extracts and its Antibacterial Activity, Springer (n.d.). doi:10.1007/s40097-014-0086-1.
- [186] Tiwari, M.; Jain, P.; Hariharapura, R.C.; Narayanan, K.; Bhat K, U.; Udupa, N.; Rao, J.V. Biosynthesis of Copper Nanoparticles Using Copper-resistant Bacillus cereus, a Soil Isolate, Elsevier (n.d.), 2016. <https://www.sciencedirect.com/science/article/pii/S1359511316303233> (accessed June 27, 2021).
- [187] (1) (PDF) Green synthesis of copper nanoparticles by Citrus limon fruits extract, characterization and antibacterial activity | Chemistry International – Academia.edu, (n.d.). [https://www.academia.edu/49311623/Green\\_synthesis\\_of\\_copper\\_nanoparticles\\_by\\_Citrus\\_limon\\_fruits\\_extract\\_characterization\\_and\\_antibacterial\\_activity](https://www.academia.edu/49311623/Green_synthesis_of_copper_nanoparticles_by_Citrus_limon_fruits_extract_characterization_and_antibacterial_activity) (accessed June 27, 2021).
- [188] Selvan, S.M.; Anand, K.V.; Govindaraju, K.; Tamilselvan, S.; Kumar, V.G.; Subramanian, K.S.; Kannan, M.; Raja, K. Green Synthesis of Copper Oxide Nanoparticles and Mosquito Larvicidal Activity Against Dengue, Zika and Chikungunya Causing Vector Aedes Aegypti. *IET Nanobiotechnol.* **2018**, *12*, 1042–1046. doi:10.1049/iet-nbt.2018.5083.
- [189] Kaur, P.; Thakur, R.; Chaudhury, A. Biogenesis of Copper Nanoparticles Using Peel Extract of Punica Granatum and Their Antimicrobial Activity Against Opportunistic Pathogens. *Taylor & Francis* **2016**, *9*, 33–38. doi:10.1080/17518253.2016.1141238.
- [190] Muthukrishnan, S.; Murugan, I.; Selvaraj, M. Chitosan Nanoparticles Loaded with Thiamine Stimulate Growth and Enhances Protection Against Wilt Disease in Chickpea. *Carbohydr. Polym.* **2019**, *212*, 169–177. doi:10.1016/j.carbpol.2019.02.037.
- [191] Patel, B.H.; Channiwal, M.Z.; Chaudhari, S.B.; Mandot, A.A. Biosynthesis of Copper Nanoparticles; Its Characterization and Efficacy Against Human Pathogenic Bacterium, Elsevier (n.d.). 2016. <https://www.sciencedirect.com/science/article/pii/S2213343716301233> (accessed June 27, 2021).
- [192] Akintelu, S.A.; Folorunso, A.S.; Folorunso, F.A.; Oyebamiji, A.K. Green Synthesis of Copper Oxide Nanoparticles for Biomedical Application and Environmental Remediation, Elsevier (2020). <https://www.sciencedirect.com/science/article/pii/S2405844020313529> (accessed June 27, 2021).
- [193] Rajesh, K.M.; Ajitha, B.; Reddy, Y.A.K.; Suneetha, Y.; Reddy, P.S. Assisted Green Synthesis of Copper Nanoparticles Using Syzygium aromaticum Bud Extract: Physical, Optical and Antimicrobial Properties, Elsevier (n.d.), 2018. <https://www.sciencedirect.com/science/article/pii/S0030402617312871> (accessed June 28, 2021).
- [194] El-Batal, A.I.; El-Sayyad, G.S.; Mosallam, F.M.; Fathy, R.M. Penicillium Chrysogenum-Mediated Mycogenic Synthesis of Copper Oxide Nanoparticles Using Gamma Rays for In Vitro Antimicrobial Activity Against Some Plant Pathogens. *J. Cluster Sci.* **2020**, *31*, 79–90. doi:10.1007/s10876-019-01619-3.
- [195] Saharan, V.; Sharma, G.; Yadav, M.; Choudhary, M.K.; Sharma, S.S.; Pal, A.; Raliya, R.; Biswas, P. Synthesis and in vitro Antifungal Efficacy of Cu–chitosan Nanoparticles against Pathogenic Fungi of Tomato, Elsevier (n.d.), 2015. <https://www.sciencedirect.com/science/article/pii/S0141813015000380> (accessed June 27, 2021).
- [196] Ramyadevi, J.; Jeyasubramanian, K.; Marikani, A.; Rajakumar, G.; Rahuman, A.A.; Santhoshkumar, T.; Kirthi, A.V.; Jayaseelan, C.; Marimuthu, S. Copper Nanoparticles Synthesized by Polyol Process Used to Control Hematophagous Parasites. *Parasitol. Res.* **2011**, *109*, 1403–1415. doi:10.1007/s00436-011-2387-3.
- [197] Kanhed, P.; Birla, S.; Gaikwad, S.; Gade, A.; Seabra, A.B.; Rubilar, O.; Duran, N.; Rai, M. In Vitro Antifungal Efficacy of Copper Nanoparticles Against Selected Crop Pathogenic Fungi. *Mater. Lett.* **2014**, *115*, 13–17. doi:10.1016/j.matlet.2013.10.011.
- [198] Kasana, R.C.; Panwar, N.R.; Kaul, R.K.; Kumar, P. Biosynthesis and Effects of Copper Nanoparticles on Plants. *Environ. Chem. Lett.* **2017**, *15*, 233–240. doi:10.1007/s10311-017-0615-5.
- [199] Hassan, S.E.D.; Fouda, A.; Radwan, A.A.; Salem, S.S.; Barghoth, M.G.; Awad, M.A.; Abdo, A.M.; El-Gamal, M.S. Endophytic Actinomycetes Streptomyces spp Mediated Biosynthesis of Copper Oxide Nanoparticles as a Promising Tool for Biotechnological Applications. *J. Biol. Inorg. Chem.* **2019**. doi:10.1007/s00775-019-01654-5.

- [200] Rajesh, K.M.; Ajitha, B.; Reddy, Y.A.K.; Suneetha, Y.; Reddy, P.S. Assisted Green Synthesis of Copper Nanoparticles Using *Syzygium aromaticum* Bud Extract: Physical, Optical and Antimicrobial Properties, Elsevier (n.d.), 2018. <https://www.sciencedirect.com/science/article/pii/S0030402617312871> (accessed June 27, 2021).
- [201] Waris, A.; Din, M.; Ali, A.; Ali, M.; Afridi, S.; Baset, A.; Ullah Khan, A. A Comprehensive Review of Green Synthesis of Copper Oxide Nanoparticles and Their Diverse Biomedical Applications. *Inorg. Chem. Commun.* **2021**, *123*, 108369. doi:10.1016/j.inoche.2020.108369.
- [202] Emima Jeronsia, J.; Allwin Joseph, L.; Annie Vinosha, P.; Jerline Mary, A.; Jerome Das, S. Camellia Sinensis Leaf Extract Mediated Synthesis of Copper Oxide Nanostructures for Potential Biomedical Applications. In *Materials Today: Proceedings*; Elsevier Ltd, 2019; pp. 214–222.
- [203] Shankar, S.; Teng, X.; Rhim, J.W. Properties and Characterization of Agar/CuNP Bionanocomposite Films Prepared with Different Copper Salts and Reducing Agents. *Carbohydr. Polym.* **2014**, *114*, 484–492. doi:10.1016/j.carbpol.2014.08.036.
- [204] Nagajyothi, P.C.; Muthuraman, P.; Sreekanth, T.V.M.; Kim, D.H.; Shim, J. Green Synthesis: In-Vitro Anticancer Activity of Copper Oxide Nanoparticles Against Human Cervical Carcinoma Cells. *Arab. J. Chem.* **2017**, *10*, 215–225. doi:10.1016/j.arabj.2016.01.011.
- [205] Thamer, N.A.; Barakat, N.T. Cytotoxic Activity of Green Synthesis Copper Oxide Nanoparticles Using *cordia myxa* L. aqueous Extract on Some Breast Cancer Cell Lines, *lopscience.lop.Org* (n.d.), 2019. doi:10.1088/1742-6596/1294/6/062104.
- [206] Harne, S.; Sharma, A.; Dhaygude, M.; Joglekar, S.; Kodam, K.; Hudlikar, M. Novel Route for Rapid Biosynthesis of Copper Nanoparticles Using Aqueous Extract of *Calotropis Procera* L. Latex and Their Cytotoxicity on Tumor Cells. *Colloids Surf., B* **2012**, *95*, 284–288. doi:10.1016/j.colsurfb.2012.03.005.
- [207] Kouhkan, M.; Ahangar, P.; Babaganjeh, L.A.; Allahyari-Devin, M. Biosynthesis of Copper Oxide Nanoparticles Using *Lactobacillus Casei* Subsp. *Casei* and its Anticancer and Antibacterial Activities. *Curr. Nanosci.* **2019**, *16*, 101–111. doi:10.2174/1573413715666190318155801.
- [208] Pramanik, A.; Datta, A.K.; Das, D.; Kumbhakar, D.v.; Ghosh, B.; Mandal, A.; Gupta, S.; Saha, A.; Sengupta, S. Assessment of Nanotoxicity (Cadmium Sulphide and Copper Oxide) Using Cytogenetical Parameters in *Coriandrum Sativum* L. (Apiaceae). *Cytol. Genet.* **2018**, *52*, 299–308. doi:10.3103/S0095452718040084.
- [209] Bharathi, D.; Ranjithkumar, R.; Chandarshekar, B.; Bhuvaneshwari, V. Bio-inspired Synthesis of Chitosan/Copper Oxide Nanocomposite Using Rutin and Their Anti-Proliferative Activity in Human Lung Cancer Cells. *Int. J. Biol. Macromol.* **2019**, *141*, 476–483. doi:10.1016/J.IJBIOMAC.2019.08.235.
- [210] Harishchandra, B.D.; Pappuswamy, M.; Pu, A.; Shama, G.; Pragatheesh, A.; Anand, V.; Periyaswamy, T.; Sundaram, R. Copper Nanoparticles: A Review on Synthesis, Characterization and Applications. *Asian Pac. J. Cancer Biol.* **2020**, *5*, 201–210. doi:10.31557/apjcb.2020.5.4.201-210.
- [211] Siddiqui, M.A.; Alhadlaq, H.A.; Ahmad, J.; Al-Khedhairi, A.A.; Musarrat, J.; Ahamed, M. Copper Oxide Nanoparticles Induced Mitochondria Mediated Apoptosis in Human Hepatocarcinoma Cells. *PLoS One* **2013**, *8*. doi:10.1371/JOURNAL.PONE.0069534.
- [212] Barabadi, H.; Vahidi, H.; Damavandi Kamali, K.; Rashedi, M.; Saravanan, M. Antineoplastic Biogenic Silver Nanomaterials to Combat Cervical Cancer: A Novel Approach in Cancer Therapeutics. *J. Cluster Sci.* **2019**, *31* (4), 659–672. doi:10.1007/S10876-019-01697-3.
- [213] Khatua, A.; Prasad, A.; Priyadarshini, E.; Patel, A.K.; Naik, A.; Saravanan, M.; Barabadi, H.; Ghosh, I.; Paul, B.; Paulraj, R.; Meena, R. Emerging Antineoplastic Plant-Based Gold Nanoparticle Synthesis: A Mechanistic Exploration of Their Anticancer Activity Toward Cervical Cancer Cells. *J. Cluster Sci.* **2019**, *31* (6), 1329–1340. doi:10.1007/S10876-019-01742-1.
- [214] Barabadi, H.; Vahidi, H.; Mahjoub, M.A.; Kosar, Z.; Damavandi Kamali, K.; Ponmurugan, K.; Hosseini, O.; Rashedi, M.; Saravanan, M. Emerging Antineoplastic Gold Nanomaterials for Cervical Cancer Therapeutics: A Systematic Review. *J. Cluster Sci.* **2019**, *31* (6), 1173–1184. doi:10.1007/S10876-019-01733-2.
- [215] Barabadi, H.; Vahidi, H.; Damavandi Kamali, K.; Hosseini, O.; Mahjoub, M.A.; Rashedi, M.; Jazayeri Shoushtari, F.; Saravanan, M. Emerging Theranostic Gold Nanomaterials to Combat Lung Cancer: A Systematic Review. *J. Cluster Sci.* **2019**, *31* (2), 323–330. doi:10.1007/S10876-019-01650-4.
- [216] Banerjee, A.; Sarkar, A.; Acharya, K.; Chakraborty, N. Nanotechnology: An Emerging Hope in Crop Improvement. *Lett. Appl. NanoBioScience.* **2021**, *10*, 2784–2803. doi:10.33263/LIANBS104.27842803.
- [217] Siddiqi, K.S.; Husen, A. Current Status of Plant Metabolite-Based Fabrication of Copper/Copper Oxide Nanoparticles and Their Applications: A Review. *Biomater. Res.* **2020**, *24*, 1–15. doi:10.1186/s40824-020-00188-1.
- [218] Yasmeen, F.; Raja, N.I.; Razzaq, A.; Komatsu, S. Proteomic and Physiological Analyses of Wheat Seeds Exposed to Copper and Iron Nanoparticles. *Biochim. Biophys. Acta Proteins Proteom.* **2017**, *1865*, 28–42. doi:10.1016/j.bbapap.2016.10.001.
- [219] Nagaonkar, D.; Shende, S.; Rai, M. Biosynthesis of Copper Nanoparticles and its Effect on Actively Dividing Cells of Mitosis in *Allium Cepa*. *Biotechnol. Prog.* **2015**, *31*, 557–565. doi:10.1002/btpr.2040.
- [220] Maithreyee, M.N.; Gowda, R. Influence of Nanoparticles in Enhancing Seed Quality of Aged Seeds, 2015. <https://www.researchgate.net/publication/329683316> (accessed June 28, 2021).
- [221] Kasana, R.C.; Panwar, N.R.; Kaul, R.K.; Kumar, P. Biosynthesis and Effects of Copper Nanoparticles on Plants. *Environ. Chem. Lett.* **2017**, *15*, 233–240. doi:10.1007/s10311-017-0615-5.
- [222] Atha, D.H.; Wang, H.; Petersen, E.J.; Cleveland, D.; Holbrook, R.D.; Jaruga, P.; Dizdaroglu, M.; King, B.; Nelson, B.C. Copper Oxide Nanoparticle Mediated DNA Damage in Terrestrial Plant Models. *Environ. Sci. Technol.* **2012**, *46*, 1819–1827. doi:10.1021/es202660k.
- [223] Nair, P.M.G.; Chung, I.M. Impact of Copper Oxide Nanoparticles Exposure on Arabidopsis Thaliana



- Growth, Root System Development, Root Lignification, and Molecular Level Changes. *Environ. Sci. Pollut. Res.* **2014**, *21*, 12709–12722. doi:10.1007/s11356-014-3210-3.
- [224] Sarkar, J.; Chakraborty, N.; Chatterjee, A.; Bhattacharjee, A.; Dasgupta, D.; Acharya, K. Green Synthesized Copper Oxide Nanoparticles Ameliorate Defence and Antioxidant Enzymes in Lens Culinaris. *Nanomaterials* **2020**, *10*, 312. doi:10.3390/nano10020312.
- [225] Powar, N.S.; Patel, V.J.; Pagare, P.K.; Pandav, R.S. Chemical Methodologies Cu Nanoparticle: Synthesis, Characterization and Application Graphical Abstract. *Chem. Methodol.* **2019**, *3*, 457–480. doi:10.22034/chemm.2019.154075.1112.
- [226] Zangeneh, M.M.; Ghaneialvar, H.; Akbaribazm, M.; Ghanimatdan, M.; Abbasi, N.; Goorani, S.; Pirabbasi, E.; Zangeneh, A. Novel Synthesis of Falcaria vulgaris Leaf Extract Conjugated Copper Nanoparticles with Potent Cytotoxicity, Antioxidant, Antifungal, Antibacterial, and Cutaneous, Elsevier (n.d.), 2019. <https://www.sciencedirect.com/science/article/pii/S1011134419305317> (accessed June 27, 2021).
- [227] Diaz-Droguett, D.E.; Espinoza, R.; Fuenzalida, V.M. Copper Nanoparticles Grown Under Hydrogen: Study of the Surface Oxide. *Appl. Surf. Sci.* **2011**, *257*, 4597–4602. doi:10.1016/j.apsusc.2010.12.082.
- [228] Mandal, S.; De, S. Catalytic and Fluorescence Studies with Copper Nanoparticles Synthesized in Polysorbates of Varying Hydrophobicity. *Colloids Surf., A* **2015**, *467*, 233–250. doi:10.1016/j.colsurfa.2014.11.026.
- [229] Selves, J.; Long-Mira, E.; Mathieu, M.C.; Rochaix, P.; Ilié, M. Immunohistochemistry for Diagnosis of Metastatic Carcinomas of Unknown Primary Site. *Cancers. (Basel)* **2018**, *10*, 108. doi:10.3390/cancers10040108.



# Source details

[Feedback >](#) [Compare sources >](#)

## Green Chemistry Letters and Reviews

Open Access [i](#)

Scopus coverage years: from 2007 to Present

Publisher: Taylor & Francis

ISSN: 1751-8253 E-ISSN: 1751-7192

Subject area: [Chemistry: General Chemistry](#) [Environmental Science: Environmental Chemistry](#)

Source type: Journal

[View all documents >](#)

[Set document alert](#)

[Save to source list](#)

CiteScore 2022

6.0



SJR 2022

0.913



SNIP 2022

2.205





# Tuberculosis and COVID-19: A combined global threat to human civilization

Kanika Patra<sup>a,1</sup>, Sovona Batabyal<sup>a,1</sup>, Kashmira Mandal<sup>a,1</sup>, Dhriti Ghose<sup>a,\*</sup>, Joy Sarkar<sup>b,\*\*</sup>

<sup>a</sup> Department of Botany, Raja Narendra Lal Khan Women's College, Gope Palace, West Midnapore, West Bengal, 721102, India

<sup>b</sup> Department of Botany, Dinabandhu Andrews College, Garia, Kolkata, West Bengal, 700084, India

## ARTICLE INFO

### Keywords:

COVID-19  
Challenges  
Infection control and impact  
Pandemic  
Tuberculosis

## ABSTRACT

A new era has begun with the discovery of SARS-CoV-2 in a seafood market in Wuhan, China. The SARS-CoV-2 outbreak has wreaked havoc on health systems and generated worldwide attention. The world's attention was diverted from the treatment of the leading chronic infectious illness, *Mycobacterium tuberculosis*. The similarities in the performance of the two infectious species had obvious repercussions. Administrative efforts to combat SARS-CoV-2 have weakened the tuberculosis control chain. As a result, progress against tuberculosis has slowed. Thus, the goal of this review is to examine the impact of SARS-CoV-2 on a chronic public health issue: tuberculosis.

## 1. Introduction

The coronavirus has spread worldwide since the end of December 2019. The 2019 pandemic Coronavirus disease is expected to be our generation's largest worldwide health disaster.<sup>1</sup> While Wuhan had the first incidence of Coronavirus induced disease in China (SARS-CoV-2), it also moved to and expanded around the Republic of Thailand, Japan, USA, Philippines, Vietnam, including our country, India and spread all over the world. All other ancient epidemics that cause persistent lung illness and immunosuppression should not be eclipsed by this horrible epidemic. Tuberculosis, for example, was a long-ago disease before COVID-19 became a global epidemic.<sup>2</sup> It is a very old disease that has plagued humanity since the beginning of time. Tuberculosis symptoms have been discovered even in Egyptian skeletons.<sup>3,4</sup> Ancient India and China are the origins of the first literary accounts of TB. The pathogen *Mycobacterium tuberculosis* is the cause of this disease and the contagious nature of it makes people more vulnerable to it. MTB first appeared as a human pathogen in Africa some 70,000 years ago, then spread across the continent as a result of human migration and became a global Pandemic.<sup>5</sup>

Tuberculosis has a long-term course and necessitates long-term therapy. The World Health Organization advises multi-drug therapy because of the increased proclivity of the tuberculosis mycobacterium to become drug-resistant. Every year, over 2 lakh folks in India are affected by TB and on average around 20,000 people are infected every month in each state.<sup>3</sup> In 2018, approximately 10 million folks were globally contaminated with TB. Many TB patients who have a major risk of COVID-19 are not being diagnosed and treated promptly. SARS-CoV-2 is produced by the  $\beta$ -coronavirus genus from the Coronaviridae family's -Coronavirus genus. Over a hundred million infections and more than 2 million deaths, which are still rising, have been caused by this fatal virus. Various studies done by Indian Council for Medical Research have found that the third wave might have hit India by February 2022 with the new variant Omicron. But experts suggested that it will be less severe than the second wave.<sup>6</sup> However, a deeper look at COVID-19 data shows that India has already experienced the third wave. In 2020, the prompt nationwide lockdown may have helped to slow the virus from spreading and the country was exempted from the worst effects.

COVID-19 disease doubles the growth of tuberculosis in people. Several studies have shown that the cases of TB in COVID-19 patients are

**Abbreviations:** SARS-CoV-2, Severe acute respiratory syndrome coronavirus-2; MTB, *Mycobacterium tuberculosis*; MDT, Multi-drug therapy; ICMR, Indian Council for Medical Research; TB, Tuberculosis; WHO, World Health Organization; COVID-19, Coronavirus Disease-19; AFB, Acid-Fast Bacilli; CRP, C-Reactive Protein; RT-PCR, Reverse Transcription Polymerase Chain Reaction; HRCT, High-resolution Computed Tomography; BCG, Bacillus Calmette-Guérin; COPD, Chronic Obstructive Pulmonary Disease; ELISA, Enzyme Linked Immunosorbent Assay; BMI, Body mass index; LTBI, Latent Tuberculosis Infection.

\* Corresponding author. Department of Botany, Raja Narendra Lal Khan Women's College, Gope Palace, West Midnapore, West Bengal, 721102, India.

\*\* Corresponding author. Department of Botany, Dinabandhu Andrews College, 54 Raja S.C. Mallick Road, Garia, Kolkata, West Bengal, 700084, India.

E-mail addresses: [ghosedhriti25@gmail.com](mailto:ghosedhriti25@gmail.com) (D. Ghose), [jsarkar80@gmail.com](mailto:jsarkar80@gmail.com) (J. Sarkar).

<sup>1</sup> These authors have contributed equally to this work.

<https://doi.org/10.1016/j.cegh.2022.101031>

Received 6 January 2022; Received in revised form 13 March 2022; Accepted 21 March 2022

Available online 27 March 2022

2213-3984/© 2022 The Author(s). Published by Elsevier B.V. on behalf of INDIACLEN. This is an open access article under the CC BY-NC-ND license (<http://creativecommons.org/licenses/by-nc-nd/4.0/>).

0.37–4.47%. Specialists and scientists have predicted that Tuberculosis intensifies the action of COVID-19. Both TB and COVID-19 harm the lungs, which is a terrible concern in the COVID-19 pandemic. There is worldwide proof that patients with chronic respiratory diseases like TB have a risk of serious sickness and death from COVID-19. When COVID-19 or TB patients breathe out, they can discharge pathogens into the air.<sup>7</sup> Also, the poor immune system because of COVID-19 infection can make a person more susceptible to an active infectious disease like TB. There are some similarities between the symptoms of coronavirus disease and TB, For example, cough, difficulty breathing, fever, etc. According to Faramarz Valafar Lab, the TB bacterium remains dormant until immunity is impaired in COVID-19 disease and causes chronic lung disease and low immune system.<sup>8</sup> It's not unusual for people with severe lung disease like tuberculosis or those who have TB-related lung damage to perform poorly if they get another acute respiratory infection like COVID-19. However, both COVID-19 and TB have similar risk factors for poor outcomes, particularly diabetes, and older age. The burst of COVID-19 diseases drew worldwide attention; practically all healthcare services were diverted to handle this situation.

## 2. Global scenario and Indian aspects

The COVID-19 disease has had a devastating impact all over the world, where people have been struggling with TB for a long time. Numerous individuals have perished as a result of the financial crisis that has gripped many countries.<sup>9</sup>

COVID-19 has ceased 12 years of global progress against tuberculosis and influenced it severely, making the situation worse than initially thought.<sup>10</sup> However, the global impact of COVID-19 is worse than the TB epidemic. The COVID-19 was devastating in the first four-month of 2020 (January–April 2020). TB-related hospital discharges decreased during the countrywide lockdown mode in the first four months of 2020. It includes newly diagnosed instances of active TB cases. The total active TB visits to the surrounding areas and new latent TB infections were diagnosed.<sup>10</sup>

According to WHO preliminary statistics collated from 84 countries, an estimated 1.4 million fewer persons received tuberculosis treatment in 2020 (when the novel coronavirus was reported) than in 2019, a 21% decline from 2019. As per the modelling research predicted in the report, there could potentially be somewhere between 200,000 and 400,000 extra TB deaths worldwide by 2020.<sup>11</sup>

In 2020, India saw a 26% decrease in tuberculosis notifications compared to 2019. In March 2021, the country saw a major wave of recurring COVID-19 infections.<sup>9</sup> According to government statistics, India currently has approximately 27 lakh Tb cases, with over 2 lakh deaths annually. According to a health ministry review, COVID-19

reduced TB detection by 25% in India by 2020.<sup>12</sup> In 2019, 24.04 lakh instances of tuberculosis were registered in India, according to the study.<sup>13</sup> In 2020, the year of COVID-19, which was distinguished by a lockdown and measures to prevent the pandemic, the registered instances dropped by 25% to 18.02 lakh.

The COVID-19 pandemic has reversed the achievements in worldwide tuberculosis management and control achieved in the 12 years. Since 1997, the World Health Organization has published a Global Tuberculosis Report, which provides an up-to-date assessment of the global TB situation. It now includes information on how the COVID-19 may disrupt TB health care, treatment, and prevention activities.<sup>14</sup> However, even before the COVID-19 pandemic, worldwide TB control efforts were on the track, but the numerical disparity between the projected number of persons with TB globally and the numbers reported to health officials remained large (Fig. 1).

## 3. TB types

Infectious tuberculosis affects the lungs, but it can also affect other body parts. Extrapulmonary TB refers to TB that occurs outside of the lung as opposed to pulmonary TB, which affects the lungs. There are two stages to the disease, when a person has latent TB, they have bacteria in their body but no symptoms of the disease, and when they have active TB, they have signs and symptoms of an active TB infection.<sup>15</sup> In patients with COVID-19, pulmonary (73%) and extrapulmonary TB (17%) have both been reported. There have been reports of extrapulmonary TB in the lymph nodes, bone, larynx, and CNS in COVID-19 patients as well as in the digestive tract, genitourinary, pleural, and spinal regions.<sup>16</sup>

## 4. How are COVID-19 and tuberculosis alike and different?

Nowadays the problems of TB patients are increasing as a result of covid-19. The similarities and differences between covid-19 and TB are discussed here. Tuberculosis and COVID-19 share comparable clinical symptoms and manifestations, including fever, shortness of breath, etc [Table 1].<sup>17</sup> There are delicate distinctions between TB and COVID-19, although COVID-19 infection develops faster than Tuberculosis [Table 2].<sup>17,18</sup>

## 5. The challenges for managing tuberculosis during the COVID-19 pandemic

### 5.1. Methods of detection of COVID-19 and tuberculosis

The current COVID-19 outbreak has wreaked havoc on tuberculosis sufferers.<sup>17</sup> Due to the epidemic, identifying TB in the presence of

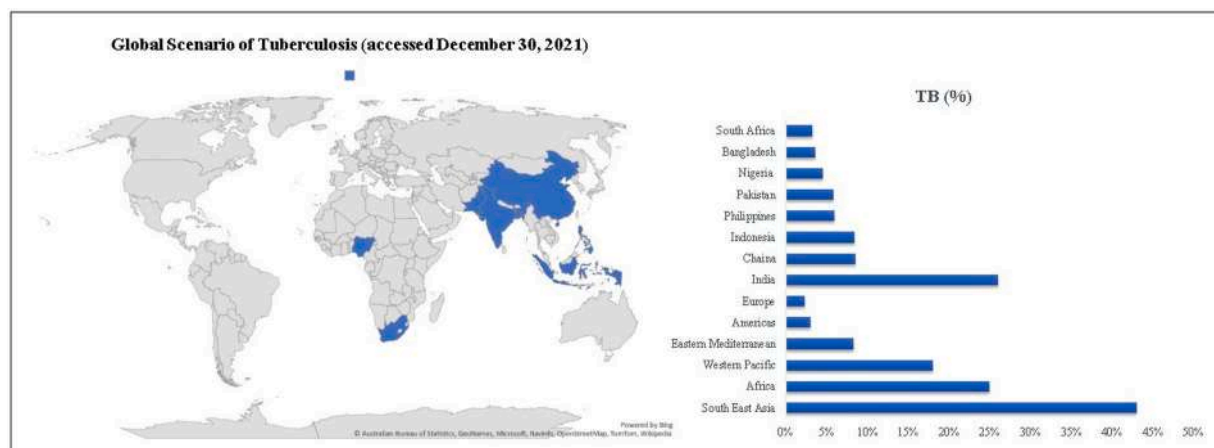


Fig. 1. Graphical representation of trends notification of people diagnosed with tuberculosis in the era of COVID-19.

**Table 1**  
**Similarities between COVID-19 and tuberculosis.**<sup>17</sup>

Characters	Tuberculosis	COVID-19
<b>Affected Organs</b>	Lung, but can affect any region of the body	Lung
<b>Symptoms</b>	Cough (Sometimes blood-tingling), fever, night sweats, weight loss	Cough, fever, breathing difficulty, chest pain, smell, and taste go away. Headache, tiredness is also seen. In some cases, vomiting and diarrhea occur.
<b>Immediate diagnosis</b>	Required	Required
<b>Disease type</b>	Airborne infectious disease	Airborne infectious disease
<b>Death rate</b>	High	High
<b>Public Consciousness</b>	When people avoid social distancing and are in close contact.	When people avoid social distancing and are in close contact.
<b>Affected Age Group</b>	This disease is affecting people of all ages.	In old age, this is an active disease. Though it affects people of all ages.

**Table 2**  
**Dissimilarities between COVID-19 and tuberculosis.**<sup>17,18</sup>

Characters	Tuberculosis	COVID-19
<b>Pathogen</b>	<i>Mycobacterium tuberculosis</i>	Severe Acute Respiratory Syndrome Coronavirus –2 Virus
<b>Nature of Pathogen</b>	Bacteria	
<b>Affected Host</b>	Only Human	Animals (Including-Bats and Human)
<b>Incubation Period</b>	Longer	Shorter (in between 7 and 14 days)
<b>Diagnostic Test</b>	Mantoux Test, AFB Smear and Culture Test, Chest X-Ray, TB Skin Test, Blood Test, etc.	Rapid Diagnostic Test, RT-PCR Test, Sometimes CRP Test, HRCT
<b>Treatment</b>	BCG Vaccine and Rifampin Antibiotic	Evidence Specific Drugs like Remdesivir, Lopinavir/ritonavir, Nafamostat, Camostat, Famotidine, Ivermectin, Tocilizumab, Sarilumab, and Vaccines like Sputnik-V, AZD1222, Ad5-nCoV, BNT162b1, mRNA-1273, NVX-CoV2373, BBV152, Corona Vac etc.
<b>Chances of Recovery</b>	Possible and can be completely cured	Complete cure may or may not happen

COVID-19 is difficult. Several potential constraints include the absence of technology in a given area to test for both COVID and TB, the health system's insufficiency to do both, a lack of appropriate health equipment, and transport barriers that could cause both illnesses to be misdiagnosed.<sup>19</sup> Because TB and COVID-19 have identical signs and symptoms (cough and fever), stigma may cause one of the diseases to be missed.<sup>20</sup> Diagnostic testing is, therefore, a vital step in the prevention and monitoring of diseases such as COVID-19 and tuberculosis. Parallel or combined testing is extremely important for persons who are at increased risk for developing one or both disorders including older populations and people with comorbidities like diabetes mellitus and

**Table 3**  
**Various methods of detection of COVID-19 and tuberculosis.**<sup>18,22–24</sup>

Name of the Techniques	COVID-19	Tuberculosis
<b>NAAT</b>	RT-PCR	Xpert MTB/RIF Ultra assay
<b>Smear Microscopy</b>	Not Applicable	ZN Stain/AR stain
<b>Antigen-based Test</b>	This test is also known as COVID-19 lateral flow tests or LFTs. These are rapid antigen tests used to detect SARS-COV-2 infection.	Not Applicable
<b>Serological Blood Test</b>	ELISA based test	Sero-diagnostic Test (Anda-TB IgG)
<b>Other Tests</b>	RT-LAMP Test, CRISPR based Test	Skin Test, Chest X-Ray Test, Sputum Test

chronic obstructive pulmonary disease<sup>21</sup> [Table 3].<sup>18,22–24</sup>

## 5.2. TB control actions

TB control tactics are being challenged as a result of resource divergence and an unavoidable shift in the objectives of the health system, resulting in poorer TB care quality and outcomes. The threat posed by COVID-19 could increase not just diagnostic ambiguity, but also stigmatisation of tuberculosis patients, particularly in low- and middle-income countries.<sup>25</sup> To minimize such effects, digital health technology, programs through improved communication, counselling, therapy might be used to assist patients. Also, respiratory physicians, vascular technicians of all levels can provide instructions for patients with pulmonary complications due to this COVID-19.<sup>26</sup>

## 5.3. BCG and COVID-19

The BCG vaccine is used to protect children from tuberculosis.<sup>27</sup> But after the COVID-19 pandemic, immunization services were suspended, which could lead to vaccine-preventable disease occurrence having a big cost on health systems.<sup>17</sup> In addition to protecting children against miliary TB and tuberculous meningitis, WHO highly advocates worldwide vaccination of BCG to ensure consistent vaccine availability worldwide.<sup>28</sup> Unexpectedly, new evidence suggests that BCG also boosts the immune system's antiviral response despite its projected selectivity for *Mycobacterium tuberculosis*. It has been claimed that COVID-19 mortality rates have decreased as a result of national BCG immunization efforts.<sup>28</sup> Even though it is yet unknown whether BCG prevents COVID-19 in adults. The long-term safety of this technique is yet to be proved.<sup>28</sup>

## 5.4. Risk factor

COVID-19 and TB share an imbalance of immune responses based on the individual immunological mechanism. It suggests co-infection may increase the risk of disease progression in both diseases.<sup>29</sup> Chronic lung disease, diabetes mellitus, smoking, and liver failure are only a few of the medical factors that increase the risk of severe sickness and the requirement for critical care units or mechanical ventilation associated with COVID-19. When tuberculosis is present in the body, smoking raises the chances of inadequate therapy resulting in delayed sputum cultivation and treatment. There is growing evidence of an increased probability of COVID-19 in people with diabetes that may lead to hospitalization, organ failure, and premature mortality.<sup>30</sup> In TB patients and COVID-19 patients, the combination of malnutrition and low BMI is a major risk factor for early mortality.<sup>31</sup>

## 5.5. Clinical features

Fever, productive cough and constitutional symptoms are present in pulmonary TB patients. In sub-sets of COVID-19 patients with TB

symptoms, they remain identical to patients without TB at the time of the occurrence. In contrast to solitary COVID-19 individuals, the majority of the coinfecting patients described are symptomatic. This could be due to the selection bias in the recruitment of solely symptomatic patients. The most prevalent symptoms include fever, dry cough, and dyspnoea. Other signs of chest tightness, chest pain, and diarrhea have been recorded. Hypoxia needing oxygen supplementation was also found among symptomatic patients. COVID-19 can appear in tuberculosis patients before or after the disease's emergence, which has a significant negative impact on patients' clinical image.<sup>16</sup>

### 5.6. Imaging

The features of pulmonary activity have been detected using HRCT and chest X-rays. In more than 40% of patients, HRCT has been the primary imaging mode. In tuberculosis patients who develop COVID-19, the development of multiple bilateral ground-glass opacity and air bronchogram consolidation have been recorded.<sup>32</sup>

### 5.7. Some major challenges that affected India

The population is the main obstacle in India's fight against the epidemic situation. In town slums, where population density can be high, social distancing becomes impossible leading to a potentially disastrous circumstance. Unfortunately, the attitude and actions of a few individuals have been a serious stumbling block in India's fight against COVID-19; there have been claims of civilians misrepresenting their travel history in order to avoid quarantine and people attending otherwise prohibited large gatherings.<sup>32</sup> The COVID-19 breakout has also hampered the control of tuberculosis and its related services severely. There is evidence that coronavirus infection exacerbates tuberculosis by causing lung tissue damage. Public transport is one of the severely affected services due to the COVID-19 epidemic. As a result, the TB patients suffered from a lack of transportation which in turn resulted in the rise of the death rate of the country. The lockdown to reduce the spread of COVID-19 has left many people jobless and led to a major financial crisis in India.<sup>33</sup> Economic decline has had a significant impact on people from lower socio-economic backgrounds throughout this pandemic. The purpose of knowing the major challenges in advance is to be able to fight against such a pandemic situation in the future.<sup>34</sup>

### 5.8. Coinfection

It is possible to develop active or non-progressive tuberculosis when infected with *Mycobacterium tuberculosis*. Latent Tuberculosis Infection can reactivate into symptomatic TB when the host's immune system is weakened. As a result, people with active tuberculosis or long-term tuberculosis are more susceptible to SARS-CoV-2 infection. It was found after detailed inspection that the immune system got worsened for the Mtb patients who had both SARS-CoV-2 and Mtb symptoms making their condition even worse. Additional to this, SARS-COV-2 infection of LTBI sufferers may result in future reinfection.<sup>35</sup>

## 6. Molecular interaction between COVID-19 and tuberculosis

The molecular connections between tuberculosis and COVID-19 in the context of co-infection are still a mystery. There has been very little research in this area, and the findings are summarised here.

Dormant *Mycobacterium tuberculosis* was reactivated by altruistic defense mechanism of the stem cell in mice coronavirus model system. This result shows increase in tuberculosis in synergism with COVID-19.<sup>36</sup> There is an assumption made from study done in a cohort of 49 patients that SARS-CoV-2 infection helps in active Tuberculosis development, although not confirmed due to lack of follow up studies.<sup>37</sup>

The development of SARS-CoV-2 coinfection, on the other hand, appears to be linked to tuberculosis.<sup>38</sup> SARS-CoV-2 specific immunity

was impaired by Tuberculosis, according to immunological research.<sup>39</sup> Many factors should be considered while acquiring Tuberculosis, SARS-CoV-2, or both at the same time, such as overcrowding, poor cleanliness, the existence of autoimmune illnesses, and so on.<sup>40,41</sup> At the molecular level, Fig. 2 depicts the possible mechanism and synergistic effects of SARS-CoV-2 and MTB.

## 7. Future strategies

The COVID-19 epidemic has underlined the importance of ensuring continued treatment and concern for TB-affected patients. Communication between patients and medical providers became difficult due to circumstances such as worldwide lockdown, TB service disruption, and social isolation. Patients may benefit from the use of digital technologies and virtual care. The proper classification of TB and COVID-19 patients should be included in future clinical studies. All features, such as clinical appearance, laboratory assessment, and test results, should be described in detail for future scientists.<sup>16</sup> A uniform treatment regimen and a consistent treatment protocol for both infections should be included in future research studies. Multiple drug interactions, as well as detrimental drug occurrences, must be recorded. Following the physician's advice based on susceptibility pattern, the multidrug antitubercular treatment can be safely used. In symptomatic patients, COVID-19 regimens should be utilized according to available medical reports, instructions, and guidelines. Now, strict control measures are needed for all patients admitted to the hospital (especially for those who are at higher risk, including the aged and patients with co-morbidities like tuberculosis). International scientific collaboration and government assistance are essential to the cumulative influence of infections among non-hospitalized TB patients in various aspects. These aspects include social insulation, patient training, availability of rapid testing, and patient support.<sup>16,42</sup>

## 8. Conclusion

The COVID-19 epidemic has had a negative influence on and disrupted the lives of people in a number of countries. Since both viral respiratory infections and tuberculosis impair the host's immune response, it's reasonable to assume that their lethal combination will have far more severe repercussions than they would have had separately. A stronger management strategy is required as a result of the risk that delaying TB treatment will exacerbate the patient's condition. As a result, diseases like COVID-19 and tuberculosis should be diagnosed and treated as soon as possible. In the case of Tuberculosis, patients should be identified and treated as soon as possible. Patients with tuberculosis and COVID-19 could be better monitored and treated if they were able to consult with one another through teleconference. Numerous effects, such as economic instability, healthcare worker sickness and resignation, and overwhelmed health facilities, have been highlighted as a result of the COVID-19 pandemic in the context of pre-existing endemic diseases, such as tuberculosis. All of these factors have the potential to impair the delivery of health care services, either directly or indirectly. To avoid this trouble, we need to do more research on this disease and find proper medicine that we can be aware of and deal with such epidemic situations in the future. Here our review sheds light on a long-standing infectious disease Tuberculosis and its correlation, molecular interaction, and its effects in different countries in midst of the COVID-19 pandemic.

## Authors' contributions

Conceptualization: [Dhriti Ghose], [Joy Sarkar]; Formal analysis and investigation: [Kanika Patra], [Sovona Batabyal], [Kashmira Mandal]; Writing – original draft preparation: [Sovona Batabyal], [Kanika Patra], [Kashmira Mandal]; Image Preparation: [Kanika Patra], [Sovona Batabyal]; Writing – review and editing: [Dhriti Ghose], [Joy Sarkar];

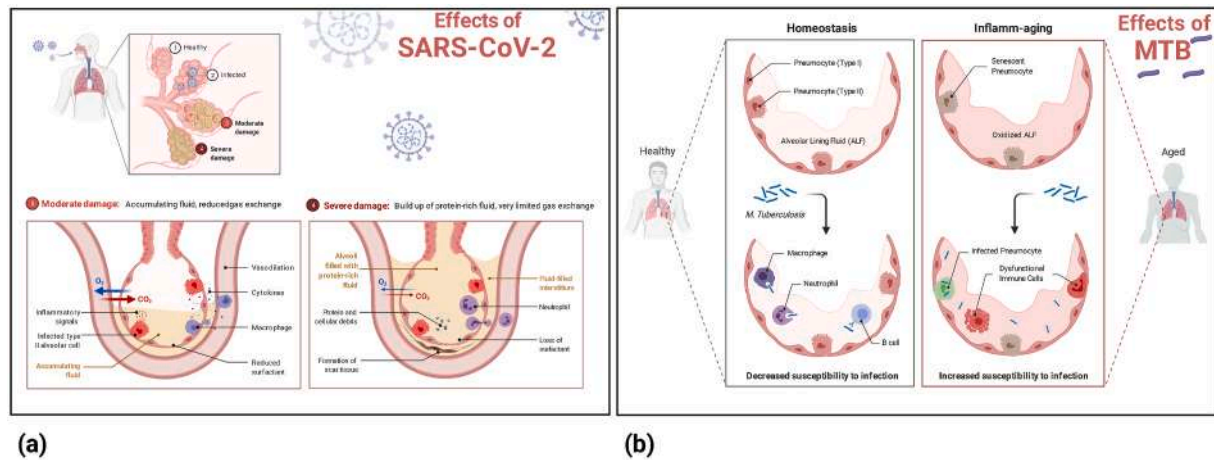


Fig. 2. Graphical representation of the possible mechanism and synergistic effects of SARS-CoV-2 (a) and MTB (b).

Funding acquisition: [N/A]; Resources: [N/A]; Supervision: [ Dhriti Ghose], [Joy Sarkar].

#### Availability of data and material

Not applicable.

#### Code availability

Not applicable.

#### Ethics approval

Not applicable.

#### Funding

We don't have any funding support from any organizational or institutional level.

#### Permission to reproduce material from other sources

Not applicable.

#### Consent to participate

All the authors mutually agree to participate in this work.

#### Consent for publication

All the authors mutually agree to submit the manuscript for publication.

#### Declaration of competing interest

On behalf of all listed authors, the corresponding authors declare that there is not any sort of financial and non-financial conflict of interest in the subject materials mentioned in this manuscript.

#### Acknowledgements

The authors acknowledge the immense help received from the scholars whose articles are cited and included in references of this manuscript. The authors are also grateful to authors/editors/publishers of all those articles, journals, and books from where the literature for this article has been reviewed and discussed.

#### References

- Zhu H, Wei L, Niu P. The novel coronavirus outbreak in Wuhan, China. *Global Health Res Pol.* 2020;5(1):1–3. <https://doi.org/10.1186/S41256-020-00135-6/METRICS>.
- Gagneux S. Host-pathogen coevolution in human tuberculosis. *Phil Trans Biol Sci.* 2012;367(1590):850–859. <https://doi.org/10.1098/RSTB.2011.0316>.
- History of tuberculosis | News-medical. <https://www.news-medical.net/amp/health/History-of-Tuberculosis.aspx>. Accessed December 30, 2021.
- Daniel TM. The history of tuberculosis. *Respir Med.* 2006;100(11):1862–1870. <https://doi.org/10.1016/J.RMED.2006.08.006>.
- Mycobacterium tuberculosis: our African follower for over 70,000 years – ScienceDaily. <https://www.sciencedaily.com/releases/2013/09/130901154024.htm>. Accessed December 30, 2021.
- When will Covid third wave hit India and will it be milder than previous two? IIT scientist weighs in. <https://www.livemint.com/news/india/when-will-covid-third-wave-hit-india-iit-scientist-weighs-in-11638804509673.html>. Accessed December 30, 2021.
- COVID-19 and TB. Frequently asked questions | the union. <https://theunion.org/our-work/covid-19/covid-19-and-tb-frequently-asked-questions>. Accessed December 30, 2021.
- COVID-19 could activate latent tuberculosis | NewsCenter | SDSU. [https://newscenter.sdsu.edu/sdsu\\_newscenter/news\\_story.aspx?sid=78173](https://newscenter.sdsu.edu/sdsu_newscenter/news_story.aspx?sid=78173). Accessed December 30, 2021.
- Tuberculosis deaths rise for the first time in more than a decade due to the COVID-19 pandemic. <https://www.who.int/news/item/14-10-2021-tuberculosis-deaths-rise-for-the-first-time-in-more-than-a-decade-due-to-the-covid-19-pandemic>. Accessed December 30, 2021.
- Fight against tuberculosis set back 12 years by Covid pandemic, report finds | Global development | the Guardian. <https://amp.theguardian.com/global-development/2021/mar/19/fight-against-tuberculosis-set-back-12-years-by-covid-pandemic-report-finds>. Accessed December 30, 2021.
- Impact of the COVID-19 pandemic on TB detection and mortality in 2020. <https://www.who.int/publications/m/item/impact-of-the-covid-19-pandemic-on-tb-detection-and-mortality-in-2020>. Accessed December 30, 2021.
- Covid brought down TB detection by 25% in India in 2020, analysis by health ministry finds. <https://theprint.in/health/world-tb-day-covid-brought-down-tb-detection-by-25-in-india-govt-analysis-finds/627607/>. Accessed December 30, 2021.
- India notifies 24.04 lakh Tuberculosis cases, 79,144 deaths in 2019, says report | Latest News India - Hindustan Times. December 30, 2021 <https://www.hindustantimes.com/india-news/india-notifies-24-04-lakh-tuberculosis-cases-79-144-deaths-in-2019-says-report/story-O3XBHO2AtaZLRmrgFdbjtm.html>.
- Global tuberculosis report 2020. <http://apps.who.int/bookorders>; 2020. Accessed December 30, 2021.
- Types of Tuberculosis (TB). <https://www.nationaljewish.org/conditions/tuberculosis/tb/types>. Accessed December 30, 2021.
- Mishra AK, George AA, Sahu KK, Lal A, Abraham G. Review of clinical profile, risk factors, and outcome in patients with Tuberculosis and COVID -19. *Acta Biomed : Atenet Parmensis.* 2021;92(1), 2021025. <https://doi.org/10.23750/ABM.V92I1.10738>.
- Jain VK, Iyengar KP, Samy DA, Vaishya R. Tuberculosis in the era of COVID-19 in India. *Diabetes, Metab Syndrome: Clin Res Rev.* 2020;14(5):1439–1443. <https://doi.org/10.1016/J.DSX.2020.07.034>.
- Visca D, Ong CWM, Tiberi S, et al. Tuberculosis and COVID-19 interaction: a review of biological, clinical and public health effects. *Pulmonology.* 2021;27(2):151–165. <https://doi.org/10.1016/J.PULMOE.2020.12.012>.
- What's holding up simultaneous testing of tuberculosis and COVID-19? | Devex. <https://www.devex.com/news/whats-holding-up-simultaneous-testing-of-tuberculosis-and-covid-19-99470>. Accessed December 31, 2021.

- 20 Shrinivasan R, Rane S, Pai M. India's syndemic of tuberculosis and COVID-19. *BMJ Global Health*. 2020;5(11), e003979. <https://doi.org/10.1136/BMJGH-2020-003979>.
- 21 Stop TB Partnership. <https://www.stoptb.org/>. Accessed December 30, 2021.
- 22 Serology testing for COVID-19 at CDC | CDC. <https://www.cdc.gov/coronavirus/2019-ncov/lab/serology-testing.html>. Accessed December 30, 2021.
- 23 Blood tests for TB | serological tests for TB. <https://tbfacts.org/serological-test-tb/>. Accessed December 30, 2021.
- 24 Types of COVID-19 test | News-medical. <https://www.news-medical.net/amp/health/Types-of-COVID-19-Test.aspx>. Accessed December 30, 2021.
- 25 Togun T, Kampmann B, Stoker NG, Lipman M. Anticipating the impact of the COVID-19 pandemic on TB patients and TB control programmes. *Ann Clin Microbiol Antimicrob*. 2020;19(1):1–6. <https://doi.org/10.1186/S12941-020-00363-1/METRICS>.
- 26 WHO | world health organization. <https://www.who.int/>. Accessed December 30, 2021.
- 27 de Bree CLCJ, Marijnissen RJ, Kel JM, et al. Bacillus Calmette-Guérin-Induced trained immunity is not protective for experimental influenza A/Anhui/1/2013 (H7N9) infection in mice. *Front Immunol*. 2018;9(APR). <https://doi.org/10.3389/FIMMU.2018.00869>.
- 28 Concern over a COVID-19-related BCG shortage | the union. <https://theunion.org/news/concern-over-a-covid-19-related-bcg-shortage>. Accessed December 30, 2021.
- 29 BCG vaccine shows effectiveness against Covid-19 in trial in India. <https://www.clinicaltrialsarena.com/news/bcg-vaccine-covid-trial/>; 2021. Accessed December 30, 2020.
- 30 Harries AD, Kumar AMV, Satyanarayana S, et al. TB and COVID-19: measuring key risk factors that affect treatment outcomes. *Int J Tubercul Lung Dis : Off J Int Union Tuberc Lung Dis*. 2021;25(4):329–331. <https://doi.org/10.5588/IJTL.D.21.0061>.
- 31 WHO | world health organization. <https://www.who.int/>. Accessed December 30, 2021.
- 32 Pal R, Yadav U. COVID-19 pandemic in India: present scenario and a steep climb ahead. *J Prim Care Community Health*. 2020;11. <https://doi.org/10.1177/2150132720939402>.
- 33 Gopalan HS, Misra A. COVID-19 pandemic and challenges for socio-economic issues, healthcare and National Health Programs in India. *Diabetes, Metab Syndrome*. 2020; 14(5):757. <https://doi.org/10.1016/J.DSX.2020.05.041>.
- 34 Klinton JS, Oga-Omenka C, Heitkamp P. TB and COVID – public and private health sectors adapt to a new reality. *J Clin Tuberc Other Mycobact Dis*. 2020;21, 100199. <https://doi.org/10.1016/J.JCTUBE.2020.100199>.
- 35 Gopaldaswamy R, Subbian S. Corticosteroids for COVID-19 therapy: potential implications on tuberculosis. *Int J Mol Sci*. 2021;22(7). <https://doi.org/10.3390/IJMS22073773>.
- 36 Crisan-Dabija R, Grigorescu C, Pavel CA, et al. Tuberculosis and COVID-19: lessons from the past viral outbreaks and possible future outcomes. *Can Respir J J Can Thorac Soc*. 2020. <https://doi.org/10.1155/2020/1401053>, 2020.
- 37 Tadolini M, Codecasa LR, García-García JM, et al. Active tuberculosis, sequelae and COVID-19 co-infection: first cohort of 49 cases. *Eur Respir J*. 2020;56(1). <https://doi.org/10.1183/13993003.01398-2020>.
- 38 Yasri S, Wiwanitkit V. Tuberculosis and novel Wuhan coronavirus infection: pathological interrelationship. *Indian J Tubercul*. 2020;67(2):264. <https://doi.org/10.1016/J.IJT.2020.02.004>.
- 39 Petrone L, Petruccioli E, Vanini V, et al. Coinfection of tuberculosis and COVID-19 limits the ability to in vitro respond to SARS-CoV-2. *Int J Infect Dis : IJID : Off Publ Int Soc Infect Dis*. 2021;113:S82–S87. <https://doi.org/10.1016/J.IJID.2021.02.090>. Suppl 1.
- 40 Guan W jie, Ni Zyi, Hu Y, et al. Clinical characteristics of coronavirus disease 2019 in China. *N Engl J Med*. 2020;382(18):1708–1720. [https://doi.org/10.1056/NEJMOA2002032/SUPPL\\_FILE/NEJMOA2002032\\_DISCLOSURES.PDF](https://doi.org/10.1056/NEJMOA2002032/SUPPL_FILE/NEJMOA2002032_DISCLOSURES.PDF).
- 41 *The End TB Strategy: Global Strategy and Targets for Tuberculosis Prevention, Care and Control after 2015*. 2014.
- 42 Research to ensure continuity of TB care amid COVID-19. <https://tdr.who.int/newsroom/news/item/24-03-2021-research-to-ensure-continuity-of-tb-care-amid-covid-19>. Accessed December 30, 2021.





# Source details

[Feedback >](#) [Compare sources >](#)

## Clinical Epidemiology and Global Health

Open Access

Scopus coverage years: from 2013 to Present

Publisher: Elsevier

E-ISSN: 2213-3984

Subject area:

Medicine: Public Health, Environmental and Occupational Health

Medicine: Infectious Diseases

Medicine: Epidemiology

Medicine: Microbiology (medical)

Source type: Journal

[View all documents >](#)

[Set document alert](#)

[Save to source list](#)

CiteScore 2022

4.3

SJR 2022

0.615

SNIP 2022

0.995



## Mucormycosis: A new threat to Coronavirus disease 2019 with special emphasis on India

Deganta Ghosh<sup>a,1</sup>, Sagardeep Dey<sup>a,1</sup>, Himanko Chakraborty<sup>a,1</sup>, Sneha Mukherjee<sup>a,1</sup>, Ankita Halder<sup>a,1</sup>, Akash Sarkar<sup>a,1</sup>, Pallab Chakraborty<sup>b,1</sup>, Rajdeep Ghosh<sup>c,1</sup>, Joy Sarkar<sup>a,\*</sup>

<sup>a</sup> Department of Botany, Dinabandhu Andrews College, Garia, Kolkata, West Bengal, India, 700084

<sup>b</sup> Department of Botany, Acharya Prafulla Chandra College, New Barrakpur, Kolkata, West Bengal, India, 700131

<sup>c</sup> GSL Medical College and General Hospital, Rajahmundry, Andhra Pradesh, India, 533296

### ARTICLE INFO

#### Keywords:

Corticosteroid  
COVID-19  
Diabetics  
Mucormycosis  
*Rhizopus*

### ABSTRACT

The main reason for the growth of mucormycosis in people with Coronavirus disease-2019 (COVID-19) is mainly produced by *Rhizopus* spp. The infective mechanisms and issues recognized in *Rhizopus* spp. are the cell wall, germination proteins, and enzymes assisted to iron sequestration, CoH protein, and positive regulation of the GRP78 cell receptor. Mucormycosis is mainly caused by the *Rhizopus* spp. such as *R. oryzae*, *R. microsporus*, *R. arrhizus*, *R. homothallicus*, etc. that are gifted to numerous host defense mechanisms and attribute to the endothelium via specific receptors, GRP78 simplifying their endocytosis and angio-invasion. Factors such as hyperglycemia, elevated iron concentrations, and ketoacidosis have been shown to contribute to the pathogenesis in the tentative situation. The analytical data of 'black fungus disease' or 'mucormycosis', specify India reported for about 42.3% of published cases, followed by the USA about 16.9%, Iraq, Bangladesh, Iran, Paraguay, and 1 case each from Brazil, Mexico, Italy, UK, China, France, Uruguay, Turkey, and Austria. The COVID-19 infection is maybe a predisposing factor for mucormycosis and is related to a high mortality rate. Early recognition and restriction of hyperglycemia, liposomal amphotericin B, and surgical debridement are the bases in the successful managing of mucormycosis.

### 1. Introduction

Mucormycosis is an uncommon angio obtrusive disease principally perceived in immunocompromised patients which happens because of the growth of mucorales.<sup>1</sup> The term 'Mucormycosis' was instituted by an American pathologist R. D. Baker and it can likewise be called Zygomycosis. Mucormycotina falls under the normal saprobes which are found in bad organic matter or soil. Infections are designated by instantaneous progression.<sup>2</sup> The Mucorales are not demanding creatures, they develop at temperature ranges between 25 °C and 55 °C.<sup>1</sup> Being ubiquitous organisms, Mucorales are dominant in commencing and accelerating the decay of organic materials. Since openness to spores of these growths is unavoidable, the uncommonness of the diseases is harmful and is a validation of an extremely basic inclination.<sup>3</sup>

The initially announced instance of mucormycosis traces back to 1885 when the German pathologist Paltauf depicted the primary case as Mucosis Mucorina.<sup>4</sup> The pace of mucormycosis expanded mostly in

immunocompromised individuals subsequently in the 1980s–1990s.<sup>2</sup>

Different types of mucormycosis that can be associated with COVID-19 infection are, rhino-cerebral mucormycosis, pulmonary mucormycosis, gastrointestinal mucormycosis, cutaneous mucormycosis, and miscellaneous. For the region of the head and neck, mucormycosis can be assorted into isolated nasal, rhino-orbital, or rhino-orbital-cerebral mucormycosis. In the case of sino-orbital mucormycosis, the mold mainly enters via the respiratory tract and is containing the nose and sinuses, into the orbital and intracranial structures with the possibility of further progression.<sup>5,6</sup> Pulmonary mucormycosis is a lethal aggressive fungal infection. It typically infects immunocompromised patients. Transbronchial biopsies and Bronchial alveolar lavage (BAL) are usually explained as non-septated hyphae in the case of pulmonary mucormycosis.<sup>7</sup> Mucormycosis in the gastrointestinal (GI) tract occurs due to the ingestion of the spores of the fungus. It is rarely reported in the COVID-19 patient.<sup>8</sup> Patients with persistent skin maceration or skin barrier disruptions (catheter insertion, trauma, injections, burn) are

\* Corresponding author.

E-mail address: [jsarkar80@gmail.com](mailto:jsarkar80@gmail.com) (J. Sarkar).

<sup>1</sup> These authors have contributed equally to this work.

<https://doi.org/10.1016/j.cegh.2022.101013>

Received 7 September 2021; Received in revised form 10 December 2021; Accepted 10 March 2022

Available online 19 March 2022

2213-3984/© 2022 The Authors. Published by Elsevier B.V. on behalf of INDIACLEN. This is an open access article under the CC BY-NC-ND license (<http://creativecommons.org/licenses/by-nc-nd/4.0/>).

suitable for increasing the risk of cutaneous mucormycosis.<sup>9</sup> The fungus can invade into adjacent fat, fascia, muscle, and even bone, while hematogenous spread with secondary vascular invasion is fewer common.<sup>10,11</sup> However, hematogenous dissemination with cutaneous mucormycosis has high fatality rates.<sup>12</sup>

From the perspective of disease to the immunocompromised people, mucormycosis likewise create a high danger for the patient determined to have serious COVID-19 pneumonia. This happens because of the hospitalized status, previous comorbidities, and treatment regimens

comprising of steroids and generally anti-toxins.<sup>13,14</sup> The predominance of mucormycosis in India is approximately 0.14 cases per 1000 populace, about multiple times the pervasiveness in different countries.<sup>15</sup> COVID-19 contamination has been related to parasitic diseases.<sup>16</sup> Globally, the most well-known danger factor related to mucormycosis is diabetes mellitus. In the prevalence of the COVID-19 pandemic, it is believed that this drop in resistance could be set off to these instances of mucormycosis.<sup>17</sup>

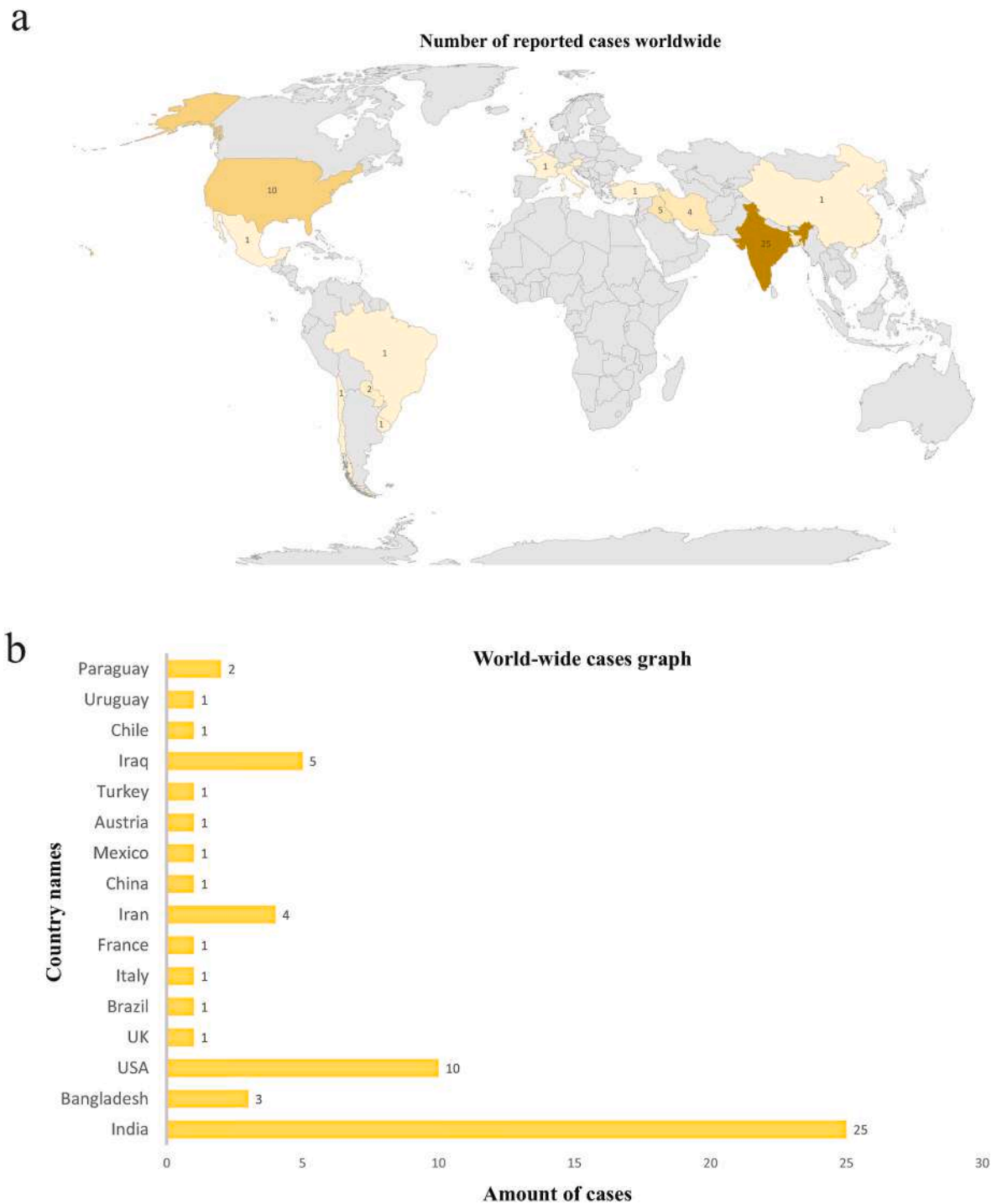


**Fig. 1.** A global presentation of the number of published case reports of Coronavirus disease 2019 (COVID-19) associated mucormycosis (till May 2021). (a) The color gradient segment of the map indicates the number of absolute cases reported worldwide, where the dark-colored portion represents the higher number of cases, while the light-colored portion represents a smaller number. (b) A schematic presentation showing the variation of the number of reported cases in different countries.<sup>20-23</sup>

## 2. Mucormycosis as COVID-19's deadly companion

The aggravation of COVID-19 in 2020 has effectively crushed the entire world in its first wave, where an enormous number of cases have been noticed including deaths and deterioration. The destruction proceeds in 2021 in the period of second-wave, more in the most exceedingly terrible structure.<sup>18</sup> The flood of COVID-19 in its subsequent wave has additionally left a path of infection and deaths, where the 'black fungus disease' or 'mucormycosis' went with. Mucormycosis is a rare but severe complication of COVID-19, which may lead to a threat to life.<sup>19,20</sup>

Up to May of 2021, we have dissected around 59 instances of mucormycosis throughout the world, related to the second wave of

COVID-19 (Fig. 1). The analytical data of "black fungus disease" specify India with a report of about 42.3% published cases (25/59), followed by the United States of America (10/59), Iraq (5/59), Bangladesh (4/59), Iran (4/59), Paraguay (2/59), and 1 case each from Brazil, Mexico, Italy, UK, China, France, Uruguay, Turkey, and Austria (Table 1). Most patients who torment this obstruction of mucormycosis had some significant comorbidity, by and large, diabetes mellitus, and diabetes ketoacidosis yet contaminations in immunocompetent patients have moreover been conceived.<sup>21,24</sup>

As indicated by several reports till September of 2021, India has been accounted for by 45,435 instances of mucormycosis and is crumbling step by step. The black fungus cases are on the skyscraper in Gujarat alongside Maharashtra with around 7109 and 10,139 cases respectively

**Table 1**

A brief number of cases of Coronavirus disease 2019 (COVID-19) associated mucormycosis reported worldwide.

Reported Area	Total No. of case	Age/Sex	Underlying Disease		Disease Type	Verified COVID-19	Medicine used for COVID-19	Fungal culture	Clinical Outcomes	Reference
			DM/DKA/T1DM/T2DM	Cancer						
India	25	23–78 M-22 F-3	DM-24 (32-78) No- 67 M	No All	Rhino-orbital: 23, 60 Rhino-orbital-cerebral: 40, 38, 51, 45, 56, 78, 67, 56, 37 Rhino-sinusitis: 43, 64, 49, 59 M, 59F Pulmonary: 55, 32, 43, 72 Sino-orbital: 38 Paranasal: 32	Confirmed	Steroid-51, 37, 43, 56, 78, 49, 60, 55, 38, 64, 60, 59F, 72 Tocilizumab-51, 37, 60 Remdisivir-32 M, 51, 37, 43, 56, 49, 55, 62 38, 67, 72, 38, 45 Not applied: 32F, 40, 23	Positive ( <i>Rhizopus</i> spp.)	Expired-10 Recovered-13 Unchanged-2	<a href="#">5,25,26</a>
Bangladesh	3	Not reported	Not reported	Not reported	Not reported	Not reported	Not reported	Not reported	Not reported	<a href="#">Link 1</a>
USA	10	33–79 M-8 F-2	DM-36, 48, 79, 68 DKA-36, 48, 33, 41 T1DM-60, 41 T2DM-44 No-49, 56	No- 9 (44F Yes)	Rhino-orbital: 33, 60 Rhino-orbital cerebral: 36, 48 Pulmonary: 44, 49, 79, 56 Rhino-cerebral: 41 Cutaneous: 68	Confirmed	Steroid- 36, 44, 48, 49, 60, 41, 79, 56, 68 Tocilizumab-33, 56 Remdesivir-36, 44, 48, 49, 60, 79	Positive all (79 M & 44F <i>Aspergillus</i> sp.)	Expired-6 Recovered-3 Unchanged-1	<a href="#">12,14,20,27–32</a>
UK	1	22 M-1	No	No	Pulmonary	Confirmed	Not applied	Positive	Expired	<a href="#">33</a>
Brazil	1	86 M-1	No	No	Gastrointestinal	Confirmed	Not applied	Positive ( <i>Rhizopus</i> spp.)	Expired	<a href="#">8</a>
Italy	1	66 M-1	No	No	Pulmonary	Confirmed	Not applied	Positive ( <i>Rhizopus</i> spp.)	Expired	<a href="#">34</a>
France	1	55 M-1	No	Yes	Pulmonary	Confirmed	Not applied	Positive ( <i>Aspergillus</i> spp.)	Expired	<a href="#">35</a>
Iran	4	40–61 M-2 F-2	DM-44, 54 DKA-No T1DM-No No-40, 61	No-All	Rhino-orbital: 61, 54 Rhino-orbital cerebral: 40 Rhino-sinusitis: 44 Rhino-cerebral	Confirmed	Steroid- 40, 44, 54,61 Tocilizumab-No Remdesivir-40, 54 Not applied	Positive ( <i>Rhizopus</i> spp.)	Expired-2 Recovered-2 Unchanged-No Expired	<a href="#">24,36,37</a>
China	1	32 F-1	No	No	Rhino-orbital	Confirmed	Not applied	Positive	Expired	<a href="#">23</a>
Mexico	1	24 F-1	DM-No DKA-24 T1DM-No	No	Rhino-orbital	Confirmed	Not applied	Positive ( <i>Rhizopus</i> spp.)	Expired	<a href="#">38</a>
Austria	1	53 M-1	No	Yes	Pulmonary	Confirmed	Not applied	Positive ( <i>Rhizopus</i> spp.)	Expired	<a href="#">39</a>
Turkey	1	56 F-1	DM-56 DKA-56 T1DM-No	No	Rhino-orbital sinusitis	Confirmed	Steroid- 56 Tocilizumab-No Remdesivir-No Not reported	Positive ( <i>Rhizopus</i> spp.)	Expired	<a href="#">40</a>
Uruguay	1	Not reported	Not reported	Not reported	Not reported	Not reported	Not reported	Not reported	Recovered	<a href="#">Link 2</a>
Paraguay	2	Not reported	Not reported	Not reported	Not reported	Not reported	Not reported	Not reported	Not reported	<a href="#">Link 3</a>
Iraq	5	Not reported	Not reported	Not reported	Not reported	Not reported	Not reported	Not reported	Not reported	<a href="#">Link 4</a>
Chile	1	Not reported	Not reported	Not reported	Not reported	Not reported	Not reported	Not reported	Not reported	<a href="#">Link 5</a>

M: Male, F: Female, DM: Diabetes mellitus, DKA: Diabetic ketoacidosis, T1DM: Type 1 diabetes mellitus, T2DM: Type 2 diabetes mellitus, COVID-19: Coronavirus disease 2019.

and around 1336 deaths in Maharashtra, and about 708 deaths in Gujarat, brought about by this dark organism (Link 6). Telangana and Madhya Pradesh have been seen with 2638 and 2370 sequentially, where Madhya Pradesh has seen the expiration of 167 individuals. Besides, 1947 cases and 351 deaths in Delhi have been accounted for, close by Haryana with 1764 cases and 268 deaths. Uttar Pradesh, Karnataka, and Rajasthan are confronting the deficiency of liposomal amphotericin B, guaranteeing with around 2477, 3906, and 3621 cases distributively, brought about by the verse growth of mucormycosis (Link 7; Link 9). The ongoing report uncovers the passageway of the dark parasite in West Bengal and Punjab with 179 and 158 cases approximately, where 11 deaths of individuals have been reported from West Bengal. Assam and Himachal Pradesh count with the least number of cases and may rise in the upcoming days (Fig. 2). The abrupt acceleration of dark organisms close by COVID-19 leads to the issues for the deficiency of liposomal amphotericin B in numerous states including Goa, Odisha, Kerala, and more. The 'black fungus disease' or 'mucormycosis' have been announced as an 'epidemic' by Rajasthan, Gujarat, and Odisha (Link 6; Link 7; Link 8; Link 9). However, various cases are expanding day by day which may lead towards another disturbance alongside COVID-19.<sup>21,22</sup>

A sudden escalation of mucormycosis is being reported in cases with COVID-19.<sup>22</sup> Many cases reveal the affliction of mucormycosis even while undergoing treatment for COVID-19 (Table 2).

In general, from the referenced cases on mucormycosis related COVID-19 in India, the most effective type of mucormycosis, that is, the sort which holds the more detrimental rate is Rhino-orbital cerebral mucormycosis with about 36%, alongside Rhino-sinusitis mucormycosis with 24%. The Rhino-orbital mucormycosis and Pulmonary mucormycosis holds about 20% and 16% respectively, while the Paranasal type holds the least number of cases with 4% of viability<sup>46-48</sup> (Fig. 3). Trigger off mucormycosis may prompt a deadly rise and could be fatal.

### 3. *Rhizopus*, the key player for COVID-19 associated mucormycosis

Mucormycosis is driving logically throughout the world, especially in India. The ruling fungal genera Mucorales, especially the *Rhizopus* species is the most well-known growths found in the patients of mucormycosis in both diabetic and non-diabetic COVID-19 patients. *Rhizopus* species appears differently concerning some others from the Mucorales family.<sup>21</sup> Since it is aseptate and making sporangioophores, it is remarkably quick in making and spreading sorts of molds with blackish and a bit of the caramel or brownish sporangia<sup>49</sup> (Fig. 4). Different aspiratory mucormycosis was perceived by going to the parasites with septate hyphae and sporangioophores through direct microscopy or despite fluorescent brighteners from clinical models like sputum, Bronchoalveolar Lavage Fluid (BALF), and so on also, by using the Lactophenol cotton blue (LCB) association in microscopy, the septate hyphal arrangement and the strain of hyphae were analyzed to see the microorganism.<sup>50,51</sup> To confirm the assurance, non-pigmented hyphae showing tissue assault should show up in tissue sections stained with hematoxylin and eosin (HE) staining, Periodic Acid Schiff (PAS), or Grocott-methenamine-silver (GMS).<sup>14,50</sup> The most notable species that cause mucormycosis after COVID-19 in India comprises *Rhizopus oryzae*, *Rhizopus microsporus*, *Rhizopus arrhizus*, *Rhizopus homothallicus*, and some different equally species. These developments now and again impact the immunocompetent, yet rather immunocompromised patients.<sup>21</sup>

In patients with seriously controlled diabetes mellitus, the persistently expanded blood glucose levels will provoke the debilitated neutrophil measure.<sup>52</sup> The parasites increase section through internal breath into the paranasal sinuses and may finally spread to be the sphenoid sinus and immense sinus. However most instances of mucormycosis are sporadic, and a sudden outburst of mucormycosis is ought to be lethal.<sup>53</sup>

### 3.1. Clinical expressions of the disease

Alongside COVID-19, the major cause for the increasing rate of mucormycosis triggered by *Rhizopus* spp. has been integrated with the upliftment of prevalence of diabetes mellitus (DM) and diabetic ketoacidosis (DKA). Infectious diseases hold up to 12% of all deaths in people with diabetes mellitus.<sup>54-56</sup> DM is a classical fear element for mucormycosis, associated with high ailment and mortality rate in COVID-19, while DKA also stands as an ideal risk factor.<sup>57,58</sup> In recent studies, euglycemic DKA is also being reported in COVID-19 patients.<sup>59</sup> The pervasiveness of type 1 DM and DKA in COVID-19 were much higher compared to the type 2 DM and DKA in the general population.<sup>58</sup> In addition, the utilization of immunosuppressive treatment like glucocorticoids and tocilizumab results in systemic immune adaptations by the infection that paved the way for mucormycosis contamination in patients during COVID-19.<sup>56</sup>

Mucormycosis would also be fatal for the patients who are seriously immunocompromised, likewise in cancer patients or AIDS patients.<sup>21</sup> The infection of mucormycosis targets the region of the nose, sinuses, orbit, central nervous system (CNS), lung (pulmonary), gastrointestinal tract (GIT), skin, jawbones, joints, heart, kidney, mediastinum (invasive type), and abdominal portion.<sup>1,60</sup> It is signaled by the appearance of hyphal invasion of sinus tissue in between a period of fewer than four weeks.<sup>61,62</sup> Fever, headache, coughing, shortness of breath, bloody vomit and, altered mental state are all the primary symptoms of the disease. Moreover, congestion with the nasal release (blackish/bloody), confined pain on the cheekbone, partial facial pain with swelling, blackish discoloration above the bridge of nose or palate, loosening of teeth, diminished or double vision, skin lesion is the severe symptoms for the distinctive types of mucormycosis.<sup>9,21</sup>

In the first instance, the expression of rhino-cerebral mucormycosis is compatible with either sinusitis or periorbital cellulitis and includes eye or facial pain with numbness, followed by the onset of conjunctival suffusion, blurry vision, and soft tissue swelling.<sup>63-67</sup> Fever is inconsistent and might be absent in up to half of cases; white blood cell counts are typically uplifted, as far as the patient has functioning bone marrow.<sup>64,67</sup> Histological features include mycotic invasion of blood vessels, vasculitis with thrombosis, tissue localized necrosis, hemorrhage, and intense neutrophilic infiltrate.<sup>68</sup>

The clinical indications of pulmonary mucormycosis include cough with chest pain and dyspnea.<sup>69</sup> This facilitates the result of inhalation or lymphatic spread. Patients with DKA can also thrive the disease, even though contamination in the patients is less conventional and less volatile than the infectious track that is typically seen in the patients with neutropenia.<sup>69,70</sup> Otherwise, it also arises in the leukemic patients undergoing chemotherapy.<sup>9</sup>

Patients who are at an intense danger of creating cutaneous mucormycosis are those with interruption of the typical defensive cutaneous hindrance. Typically, the factors of mucormycosis are incapable of nauseating intact skin. In immunocompromised and diabetic patients, the cutaneous lesions may also rise due to catheter insertion and insulin injection sites.<sup>71,72</sup> Infected surgical dressings have also been incriminated as a source of cutaneous mucormycosis.<sup>73,74</sup> Mucormycosis in the gastrointestinal tract is rare. It mainly hinders malnourished patients (especially infants or children) and is thought to arise from the ingestion of fungi.<sup>75-80</sup> The most frequently involved sites include the stomach, ileum, and colon. The symptoms are varied and based on the site affected. Fever and hematochezia may also arise, along with lenient abdominal pain and distention related to nausea and vomiting are the best fitted well-known manifestations.<sup>81-83</sup>

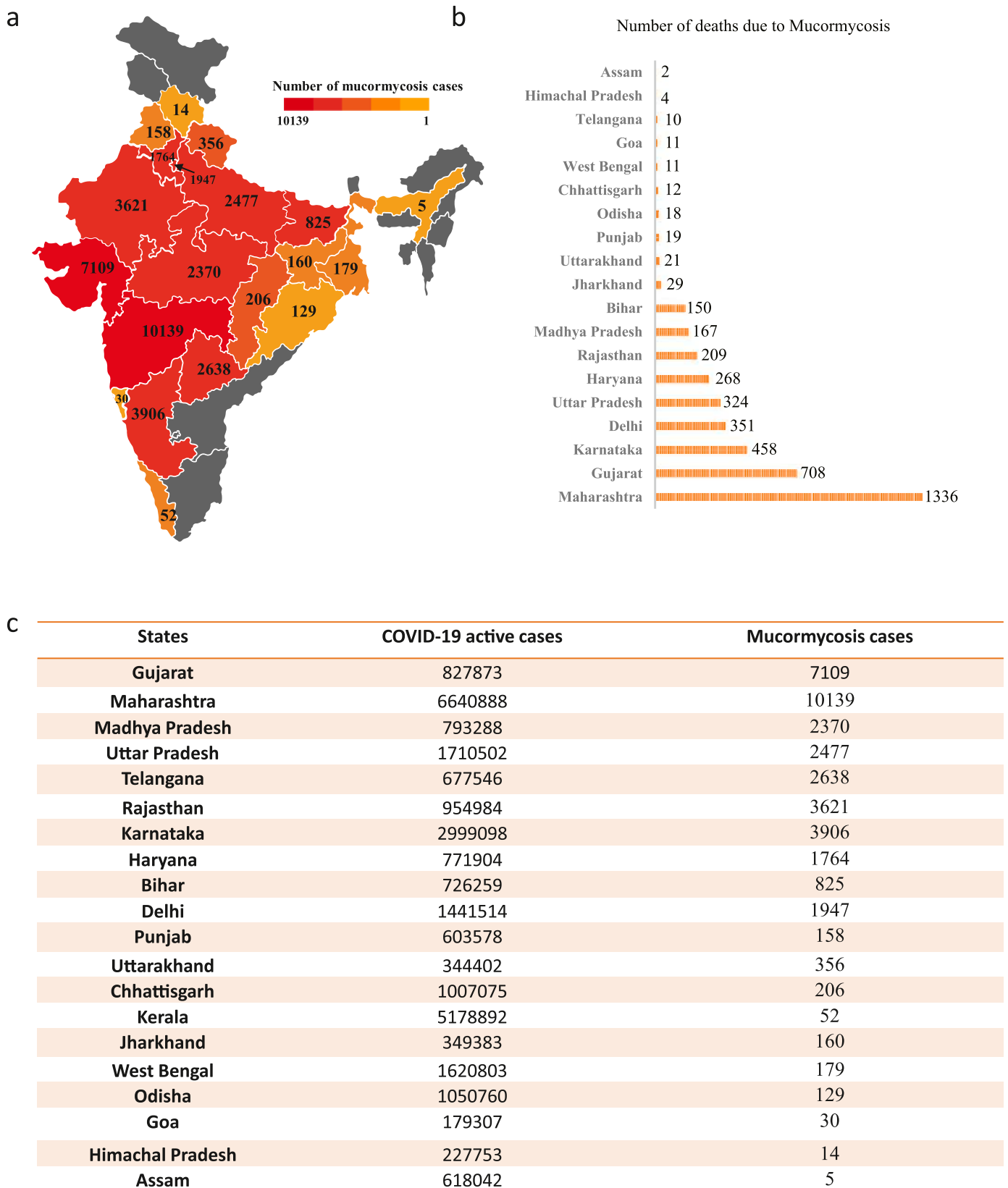


Fig. 2. An illustrative presentation on the number of cases of Coronavirus disease 2019 (COVID-19) associated mucormycosis reported in the different States of India (till September of 2021). (a) The colors provided in the different geographical area represents the variation in the number of cases. (b) A schematic presentation on the number of deaths in different States of India due to mucormycosis. (c) Up-to-date state-wise statistical indication of COVID-19 cases along with mucormycosis cases of India<sup>21,22</sup> (Link 6; Link 7; Link 8).

**Table 2**

A precise of cases reported in India on Coronavirus disease 2019 (COVID-19) associated mucormycosis.

Case No.	Age/Sex	Reported Area	Occurrence of fungal colonies during microscopy	Causative Agent	Disease Type	Underlying Disease	Infected internal body parts	Symptoms	Clinical outcomes	Reference
Case-1	32/F	Mangalore	Positive	<i>Rhizopus</i> spp.	Paranasal Mucormycosis	Diabetes mellitus, left eye complete ptosis, facial problem	Sinus and orbit	Orbital apex syndrome Rapidly lost eye vision	Recovered but no improvement in vision	41
Case-2	60/M	Mumbai	Positive	<i>Rhizopus</i> spp.	Rhino-orbital Mucormycosis	Diabetes mellitus, Lung disease	Sinus and orbit	orbital swelling, headache, nosebleed	Expired	42
Case-3	38/M	Mumbai	Positive	<i>Rhizopus oryzae</i>	Sino-orbital Mucormycosis	Diabetes mellitus	Sinus and orbit	Swelling and pain in the left eye	Recovered	5
Case-4	72/M	Hyderabad	Positive	<i>Rhizopus. oryzae</i>	Pulmonary Mucormycosis	Diabetes mellitus, hypertension	Lungs	Streaky hemoptysis	The patient is not improving	43
Case-5	40/F	Mangalore	Positive	<i>Rhizopus</i> spp.	Rhino orbital cerebral Mucormycosis	Diabetes mellitus	Sinus, orbit, and CNS	Swelling of the left eye and facial pain, rhinitis	Recovered	15
Case-6	38/M	Bangalore	Positive	<i>Rhizopus oryzae</i>	Rhino orbital cerebral Mucormycosis	Diabetes mellitus	Orbit, sinus	Right eye pain and chemosis	Expired	26
Case-7	51/F	Mumbai	Positive	<i>Rhizopus oryzae</i>	Rhino orbital cerebral Mucormycosis	Diabetes, Hypothyroidism	Eye, sinus, and CNS	Left side facial pain, nose block, periorbital pain, and headache	Recovered	26
Case-8	45/M	Puducherry	Positive	<i>Rhizopus oryzae</i>	Rhino orbital cerebral Mucormycosis	Diabetes mellitus, Hypertension, CKD	Eye damage, sinus, and CNS	Impairment of right eye vision	Recovered	26
Case-9	56/M	Bangalore	Positive	<i>Rhizopus oryzae</i>	Rhino orbital cerebral Mucormycosis	CKD, diabetes, hypertension, hyperthyroidism	Eye conjunctiva, brain	Right eye swelling	Expired	26
Case-10	78/M	Bangalore	Positive	<i>Rhizopus oryzae</i>	Rhino orbital cerebral Mucormycosis	Diabetes and hypertension	Sinus, orbit, and CNS	Holocranial headache	Expired	26
Case-11	43/M	Bangalore	Positive	<i>Rhizopus oryzae</i>	Rhino-sinusitis Mucormycosi	Diabetes mellitus, CLD	Sinus, nasal passages, oral cavity, and brain	Dryness and crusting in the nasal cavity	Recovered	26
Case-12	60/M	Delhi	Positive	<i>Rhizopus arrhizus</i>	Rhino-sinusitis Mucormycosis	Diabetes mellitus, deranged kidney function	Sinus and brain	Periorbital swelling, chemosis, restricted eye movement	Expired	44
Case-13	64/M	Delhi	Positive	<i>Rhizopus microsporus</i>	Rhino-sinusitis Mucormycosis	Diabetes mellitus, renal function failure	Sinus, nasal passages, oral cavity, and brain	Proptosis of the eye with Periorbital discoloration, blackening of the middle turbinate.	Expired	44
Case-14	67/M	Not Reported	Positive	<i>Rhizopus oryzae</i>	Rhino orbital cerebral Mucormycosis	Hypertension	Cornia, conjunctiva, eyelids, optic nerve damage	High fever, dizziness, blurred vision	Recovered	45
Case-15	49/M	Not Reported	Positive	<i>Rhizopus homothallicus</i>	Rhino-sinusitis Mucormycosis	Diabetes mellitus, problem in breathing	Sinus, brain, and nasal passages	High fever, facial swelling	Recovered	45
Case-16	23/M	Not Reported	Positive	<i>Rhizopus oryzae</i>	Rhino-orbital Mucormycosis	Diabetes mellitus, hypertension	Sinus and orbit	High fever, headache, periorbital pain, facial pain	Expired	45
Case-17	59/F	Delhi	Positive	<i>Rhizopus arrhizus</i>	Rhino-sinusitis Mucormycosis	Diabetes	Sinus and brain	High fever, facial swelling, blackening of turbinate	Recovered	45
Case-18	62/M		Positive						Expired	45

(continued on next page)

Table 2 (continued)

Case No.	Age/Sex	Reported Area	Occurrence of fungal colonies during microscopy	Causative Agent	Disease Type	Underlying Disease	Infected internal body parts	Symptoms	Clinical outcomes	Reference
		Not Reported		<i>Rhizopus oryzae</i>	Rhino orbital Mucormycosis	Diabetes mellitus, High pressure	Sinus and orbit	Periorbital pain, blurred vision, and headache		
Case-19	43/M	Not Reported	Positive	<i>Rhizopus oryzae</i>	Pulmonary mucormycosis	Diabetes mellitus, problems in renal area	Lung	Facial swelling, infection in the lung, high fever	Recovered	45
Case 20	32/M	Hyderabad	Positive	<i>Rhizopus arrhizus</i>	Pulmonary Mucormycosis	Diabetes mellitus	Lung	High fever, nasal tract infection, headache, infection in lung	Recovered	45
Case-21	60/M	Mumbai	Positive	<i>Rhizopus oryzae</i>	Rhino orbital Mucormycosis	Diabetes mellitus	Sinus and orbit	Periorbital pain, blurred vision	Expired	22
Case-22	55/M	Chandigarh	Positive	<i>Rhizopus spp.</i>	Pulmonary Mucormycosis	Diabetes mellitus, End-stage kidney disease	Lung	Facial swelling, infection in the lung, high fever	Recovered	22
Case-23	59/M	Delhi	Positive	<i>Rhizopus spp.</i>	Rhino sinusitis Mucormycosis	Diabetes mellitus, High pressure, Coronary artery disease	Sinus and brain	High fever and facial swelling, blackening of turbinate	Expired	25
Case-24	56/M	Bangalore	Positive	<i>Rhizopus oryzae</i>	Rhino orbital cerebral Mucormycosis	Diabetes mellitus	Cornia, conjunctiva, eyelids, optic nerve damage	Right eye pain and gradual loss of vision	Loss of follow up	26
Case-25	37/M	Not Reported	Positive	<i>Rhizopus oryzae</i>	Rhino orbital cerebral Mucormycosis	Diabetes mellitus	Cornia, conjunctiva, eyelids, optic nerve damage	Pain and bleeding from gums	Recovered	26

M: Male, F: Female, CKD: Chronic kidney disease, CLD: Chronic liver disease, CNS: Central nervous system.

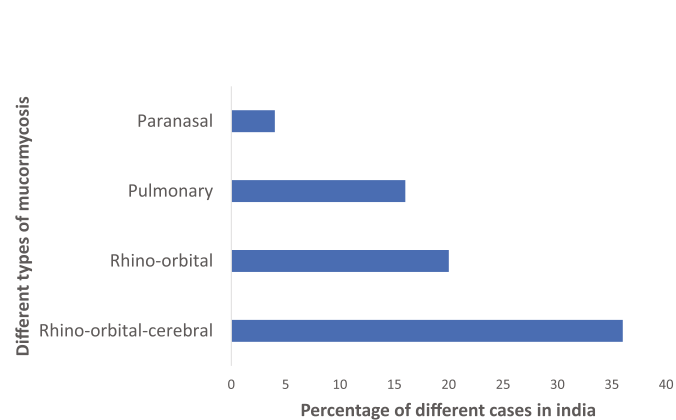


Fig. 3. An evanescent theory on the types of mucormycosis presenting their efficacious side on the Coronavirus disease 2019 (COVID-19) associated mucormycosis patients. The diagram represents rhino-orbital cerebral (36%) mucormycosis is the highest reported type in India followed by the rhino orbital (20%), pulmonary (16%), and paranasal (4%).<sup>21,22</sup>

#### 4. Molecular mechanism: the panoramic story of COVID-19 associated mucormycosis

##### 4.1. Exposition: Preface of the story

The attendance of Diabetes mellitus (DM), whether with or without Diabetic ketoacidosis (DKA), enhances the chance of acquiring mucormycosis, and DM is frequently linked to enhanced COVID-19 intensity. Meanwhile, corticosteroid use is regularly linked with uncontrolled hyperglycemia and the commencement of DKA. Acidosis causes a low pH, which is ideal for mucus spores to grow. Furthermore, use of steroid decreases the phagocytic nature of WBC (both first and second-line defensive mechanisms), impairs bronchoalveolar macrophage ingestion, migration, and phagolysosome fusion, and makes a diabetic patient more prone to mucormycosis.<sup>22</sup>

##### 4.2. Crisis period of the story

According to a well-known and established hypothesis about the pathogenesis of DM, elevated levels of glucose in the muscle, and adipose tissue induce cellular hypoxia, endoplasmic reticulum (ER) stress, enhanced discharge of reactive oxygen species (ROS), free fatty acids (FFA), and cytokine production. Interleukin-1 (IL-1 $\beta$ ) and tumor necrosis factor (TNF) are released by hypertrophic cells in adipose tissue, along with different chemokines. TNF- $\alpha$  recruits M1 macrophages, and



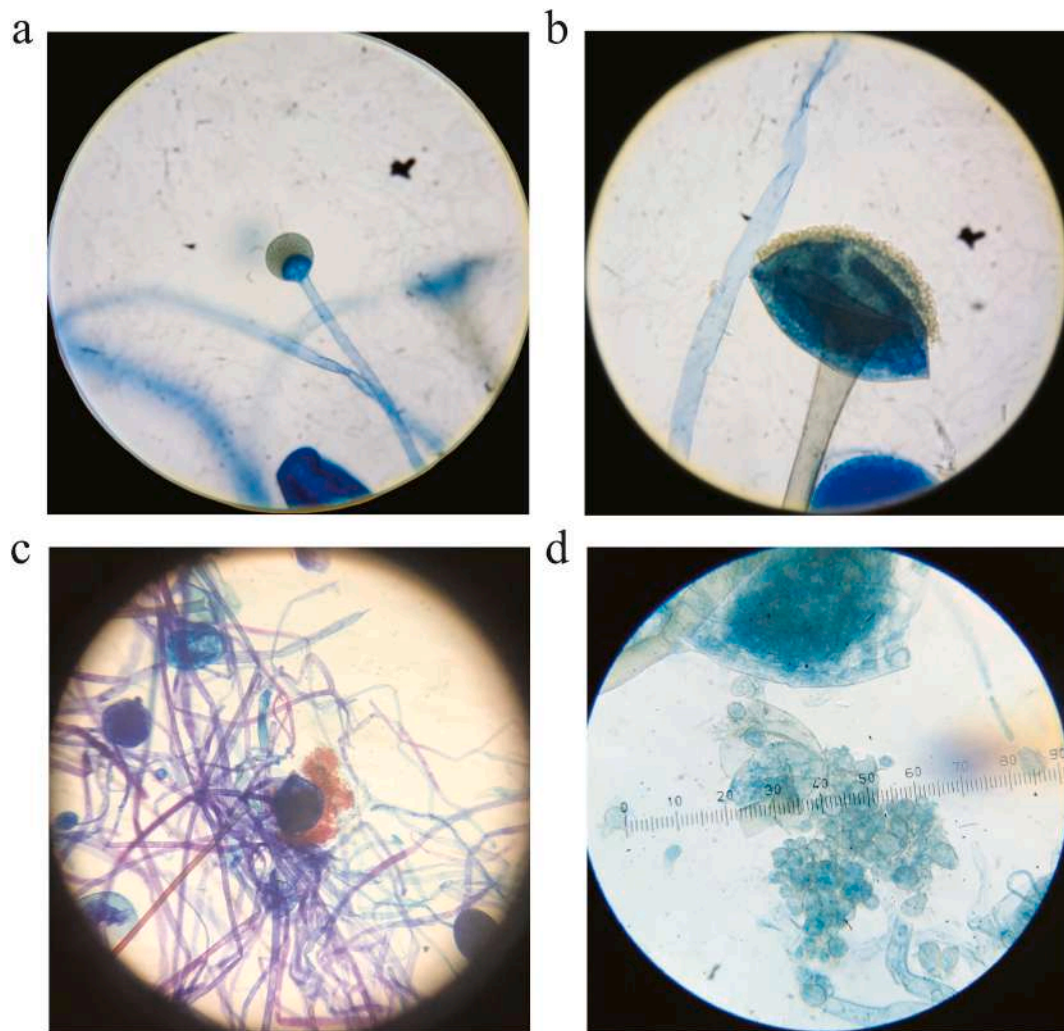


**Fig. 4.** Microscopic view of *Rhizopus* spp. under Lactophenol cotton blue (LCB) mount. (a–b) Compound microscopic view of *Rhizopus* sp. showing columella and brownish sporangia under ca.  $\times 100$  and ca.  $\times 450$  magnification, respectively. (c) Compound microscopic view of *Rhizopus* sp. showing the hyphal region under ca.  $\times 100$  magnification. (d) Compound microscopic view of *Rhizopus* sp. showing sporangiospores under ca.  $\times 450$  magnification.

its activation produces more pro-inflammatory cytokines (most notably IL-1 $\beta$ ) that cause chronic inflammation and the employment of additional M1 macrophages. FFA is also detected by TLR in the tissue cells, initiating JNK-AP-1 and IKK-NFKB signalling.<sup>84–86</sup> The utterance and discharge of pro-inflammatory cytokines are enhanced consequently, which promotes the native inflammatory state. In diabetes individuals, M1 macrophages infiltrate the tissue, producing a pro-inflammatory M1 macrophage response rather than a regulating M2 macrophage response. Because M2 macrophages seem to be better able to trigger and then destroy fungal cells, penetration of diabetic tissue with M1 macrophages could provide to *Rhizopus* spp. impedance to phagocytosis.<sup>87</sup>

Several cellular level injuries like endothelial damage, endothelialitis, lymphopenia, thrombosis, and a drop-down in the degree of CD4<sup>+</sup>, CD8<sup>+</sup>, and T-cells levels are frequently caused by COVID-19 which is ultimately putting the patient at risk of secondary or opportunistic fungal infection.<sup>22</sup>

Proteins like ferritin and transferrin show excessive glycosylation due to the effect of hyperglycemia which ultimately reduces their iron affinity.<sup>88</sup> Furthermore, the low pH environment in the blood vessels severely limits transferrin's ability to chelate iron in the presence of an acidotic state triggered by the generation of ketone bodies (e.g.,  $\beta$ -hydroxybutyrate [BHB]).<sup>89</sup> Thus, the availability of the free iron in the blood vessel is triggered and a combined effect of free iron, glucose, and BHB activates the hyphal expansion of the fungus.<sup>90,91</sup>

The fasting condition induced by a lack of insulin causes the catabolism of amino acids and triacylglycerols (TAGs), deposited in adipose tissue to become active as an energy source in diabetic patients. In serum, due to limited lipolysis, the concentrations of free fatty acids and glycerol, are much higher whereas the concentration of alanine is much higher due to muscle catabolism. Excess glucagon and insulin insufficiency stimulates gluconeogenesis, which uses those alanines and glycerol as substrates. Glucagon also advances the transformation of free fatty acids to ketones in the mitochondria. Insulin inhibits the transfer of the derivatives of free fatty acid to the matrix of mitochondria in normal conditions, but ketogenesis continues in the deficiency of insulin.<sup>85</sup> Numerous ketone bodies are produced by virtue of TAG metabolism, influencing serum pH and causing the malfunction of numerous serum enzymes. Few instances, such as hemoglobin and transferrin, remain protonated and unable to transport Fe<sup>+3</sup> at a pH of 6.88–7.3, resulting in a higher amount of Fe<sup>+3</sup> accessible in serum in diabetic patients. *Rhizopus* has a ketone reductase enzyme that enables the fungus to develop in this acidic condition apart from using the free Fe<sup>+3</sup> in these patients.<sup>92,93</sup> The acidosis produced by *Rhizopus* spp. affects other host enzymes, which hold a direct impression on chemotaxis and phagocytosis. Reduced iron levels have also been shown to promote the M1 pro-inflammatory LPS-induced response, suggesting that additional mechanism contributes to the dissemination of an adverse feedback to fungal allowance.<sup>94</sup>

#### 4.3. Rising period of the story

Free iron is another excellent resource for mucormycosis. According to several studies, iron plays a major function in *Rhizopus* and it is taken from the host via two methods, either siderophores (iron chelators) or high-affinity iron permeases.<sup>95–98</sup> Fungi battle with the host for the free iron in the siderophore system. Intrinsic and extrinsic siderophores are the two major types of fungi siderophores. Speaking of *Rhizopus*, both forms of siderophores are utilized. The major intrinsic siderophore, found in *Rhizopus*, is Rhizoferrin. It absorbs iron from outside the cell environment via a receptor-conciliated and energy-reliant method. Thirteen potential siderophore permeases are found after the genome-sequencing investigation of *R. oryzae* which could act as receptors for different siderophores. According to numerous protein crystallography experiments, rhizoferrin has a diaminobutane backbone connected to two citric acid residues with an R, R arrangement encircling a chiral centre.<sup>57,99</sup>

Another consideration for a better phagocytic response is reactive oxygen species (ROS). Owing to insulin resistance, hyperglycemia persists in people with diabetes, and in an attempt to lower glucose levels, glucose metabolism and secondary lipolysis are elevated via oxidative phosphorylation. Low pH in patients with diabetic ketoacidosis (DKA) makes more vulnerability to mucormycosis as a result of the summed-up oxidative climate which influences glutathione to remodel through the GSH/GSSG compound cycle. Advanced glycation end products (AGEs) and ROS produced by enhanced glucose metabolism cumulate in organs and tissues, causing typical micro and macrovascular changes in diabetic patients directing to an enlarged vulnerability to a *Rhizopus* infection.<sup>100,101</sup> Due to inadequacy of the cofactor NADPH, down-regulation of the major antioxidant system of glutathione (GSH/GSSG), which is the prime requirement for the reconstruction of reduced glutathione, ultimately reduces the ability of the patient to control the oxidative stress. The polyol route for glucose metabolism consumes NADPH quickly, resulting in a deficit of NADPH. Oxidative stress triggers inflammation through the NF- $\kappa$ B and TLR receptors, resulting in a long-term chronic inflammatory state.<sup>57,101</sup>

#### 4.4. The climax of the story: The interaction between GRP78 and CotH3

In transformed fibroblasts, the production rate of a particular protein was increased when the reduction of glucose was caused. Later on, that particular protein was discovered as glucose-regulated proteins (GRPs). GRP78 or glucose-regulated protein has a molecular weight of 78-kDa, was first identified as a heat shock protein that has a role in stress-related responses.<sup>102</sup> It is also known as immunoglobulin-binding protein (BiP) or HSP5a and is mostly found in the lumen of the endoplasmic reticulum (ER) and produced in mammalian cells. The HSP5a gene, which is found on chromosome 9q34, encodes GRP78. GRP78 is mostly found in the ER, although it has also been found in the cytoplasm, mitochondria, nucleus, plasma membrane, and secreted, even though it is primarily responsible for engaging endogenous cytoprotective mechanisms.<sup>103</sup> The nucleotide-binding domain (NBD) or ATPase and substrate-binding domain (SBD) or protein/peptide-binding domains are the two main functional domains of GRP78.<sup>104–106</sup> The function of this protein is controlled by the allosteric ATPase cycle in which the binding with ATP and hydrolyzation of ATP is performed by NBD whereas the SBD performs the job of bindings with polypeptides.<sup>104,105,107</sup> GRP78 has long been believed to be a molecular chaperone having a place with the HSP70 family that directs the unfolded protein reaction (UPR) to control ER stress and assumes a critical part in protein collapsing and quality control, just as misformed protein degradation.<sup>108,109</sup>

GRP78 expression has recently gained importance due to its translocation to the cell membrane's surface (csGRP78) during ER stress,<sup>110</sup> where it serves as a receptor and regulator in cell indicating by forming complexes with extracellular ligands and proteins attached to the cell

surface.<sup>111–113</sup> Recent Research reveals that hyperglycemia behaves like a stress trigger in ER which simultaneously initiates the overexpression of the GRP78 protein, based on the glucose concentration. MTJ-1 chaperone-mediated mechanism helps to translocate these GRP78 proteins from the ER to the cell surface.<sup>114</sup> Likewise, overexpression of csGRP78 has been found to play a crucial role as an entrance receptor for various pathogens, including the Ebola virus, Dengue virus, Coxsackievirus, and the new SARS-CoV2 virus, and other viruses and *Rhizopus* spp. as well.<sup>115–117</sup>

*Rhizopus* spp. interact with various receptors of epithelial cells of alveolar and nasal origin. When *Rhizopus* spp. infect nasal epithelial cells, csGRP78 is overexpressed, but not in alveolar epithelial cells. In addition, it was discovered that *Rhizopus* spp. interrelate with alveolar epithelial cells by binding to integrin-1 rather than csGRP78. Subcellular factors, like iron, glucose, and DKA trigger the excessive production of csGRP78 only in nasal epithelial cells and subsequently enhance the pathogenicity of *Rhizopus* spp.<sup>57</sup>

Following the discovery of GRP78 as a required receptor for the invasion of the species of Mucorales,<sup>115</sup> the hunt for a possible ligand led to the discovery of CotH in Mucorales.<sup>116</sup> As a result, in a wide spectrum of Mucorales species, the utterance of the CotH1, CotH2, and CotH3 genes has been identified. Nonetheless, research data has suggested that CotH3 is mostly produced in *R. oryzae* germinations and has a better ability to attach and so penetrate endothelium and nasal epithelial cells in the DKA environment.<sup>95,116,118,119</sup> On the other hand, CotH7 is the primary ligand that interrelates with integrin-1 of alveolar epithelial cells in the pulmonary mucormycosis, and it is not closely linked to CotH3 (50% amino acid identity).<sup>118</sup>

In Mucorales, csGRP78 binds particularly with spore coating homolog proteins (CotH), facilitating invasion and injury to endothelial cells.<sup>115,116,118,119</sup> By nature, CotH protein is a type of protein kinase and a member of a vast family of spore coating proteins. It has diversified functions. It is essential for protein assembly in the inner layer of the spore-coat. During sporulation, this protein is produced and shows its activity. ATP-dependent autophosphorylation and successive phosphorylation of serine residues of CotG and CotB proteins regulate its activity. The half-life of CotH is only four to 5 h. Its concentration drops quickly when the structural gene's transcription is turned off. Recent findings show its essential role in spore germination of many human pathogens like spore-producing fungi such as *Rhizopus oryzae* and the expression of many bacterial strains like *Bacillus anthracis*.<sup>116,120,121</sup>

The appearance and interaction of GRP78 and CotH leads to increased fungal interference and consequent endothelial injury in vitro.<sup>91,115</sup> As the iron chelation fused with pH reversal by sodium bicarbonate protects endothelial cells from *Rhizopus*-mediated invasion and injury,<sup>91</sup> it emerges that BHB-related acidosis has a straight effect on both GRP78 and CotH expression and an indirect effect by compromising transferrin's ability to chelate iron. Importantly, host cells with higher BHB, produced as a result of DKA, have lower blood pH, higher accessible serum iron, higher GRP78 expression in focussed organs (e.g., lungs and sinuses), and are more susceptible to mucormycosis.<sup>91,115</sup>

Thus, the extraordinary affectability of DKA patients to mucormycosis is clarified by the special communications of GRP78 and CotH proteins, just as their expanded articulation under hyperglycemia and ketoacidosis. Treatment with anti-GRP78 or anti-CotH antibodies protects DKA and neutropenic mice against mucormycosis, emphasizing the relevance of GRP78/CotH protein interactions in the progress of mucormycosis.<sup>115,116,122</sup> The discovery that reversing ketoacidosis in *Rhizopus*-infected animals by administering sodium bicarbonate (instead of insulin) enhances survival is also potentially clinically relevant.<sup>91</sup> Reversal of accelerated fungal expansion, reconstruction of immune function, and terminating of fungal invasion of host tissues are thought to be the causes of this protection. The activity of GRP78/CotH interactions in the neutropenic host, the other main patient category prone to mucormycosis, is currently unknown.<sup>122,123</sup>

#### 4.5. Falling action of the story

The processes that increase the interaction of invading fungus with endothelial/epithelial cells are beginning to gain a toehold, and they represent a key stage in the pathogenesis of diabetes-associated mucormycosis.<sup>115,116,118</sup> Thus, the DKA environment, high glucose, iron, and B-hydroxy butyrate (BHB) as the vital ketone body promote fungal development by promoting CotH3 expression.<sup>124</sup> The surface translocation of the GRP78 protein, which copes with endoplasmic reticulum stress occurred by hyperglycemia and an acid milieu, assists a tissue stage favorable to *Rhizopus* spp. establishment. Iron is released from sequestered protein transferrin by glycosylation mechanisms in the same tissular niche. As a result, high glucose concentrations, free iron availability,<sup>125</sup> and aerobic microenvironment boost CotH expression on the fungal cell surface facilitating GRP78/CotH3 contact for endothelial/epithelial invasion and fungal spread.<sup>124</sup> The fungus must interrelate with its basement membrane after infecting the apparent nasal epithelium because the spores and stem cells from germ tubes adhere to extracellular matrix constituents. The scrutiny of *Rhizopus* spp. sticking to plates coated with collagen IV and laminin supports this theory.<sup>126</sup>

#### 4.6. Resolution: The final consequences

Meanwhile, endothelial cells keep on creating GRP78 in all cubicles, and the hypha can connect with these proteins on the basal side where the existence of reticulin filaments is surpassed, permitting it to secure and outdo this region to later collaborate with GRP78 communicated on endothelial cells' luminal surface. When fungi become actualized in the lumen of blood vessels, they activate the extrinsic coagulation pathway, which causes cell injury and, as a result, the thrombus formed. This causes ischemia and prolonged hypoxia, resulting in tissue infarction and necrosis (Fig. 5). Finally, the microenvironment has changed and the disease has been established on the body.<sup>57</sup>

### 5. Proposed modes of investigation for COVID-19 associated mucormycosis

To date, there are no pathognomonic hematologic changes. Elevated white blood cell counts and acute-phase reactant levels indicate the abnormalities that are found reflect underlying predisposing conditions (e.g., diabetic ketoacidosis) and general indications of fungal infection. Blood cultures are virtually always negative. Plain orbit or sinus radiography is not a reliable investigation for this disease.<sup>95,127</sup>

Computed Tomography (CT) analysis indicates the extent of orbital and cranial involvement and progression of the disease. Magnetic resonance imaging (MRI) is also helpful by showing T2-weighted MR images, which demonstrate intracerebral extension while on the other hand, contrast-enhanced MRI scans give us a demonstration of the perineural spread of disease.<sup>128</sup>

Angiography or surgical exploration is necessary for areas of anatomic complexity. Biopsy with histopathologic examination remains the most sensitive and specific modality for definitive diagnosis. Microscopic investigation shows that aseptate hyphal elements of the species belong to the order Mucorales are wide (ranging from 6 to 30  $\mu\text{m}$ ), thick-walled, ribbon-like, and showing branch at right angles,<sup>42</sup> whereas the hyphae of *Aspergillus* and, *Fusarium* are comparatively thinner, highly septate and showing branch at acute angles (Fig. 6). The width of the fungus and its ribbon-like shape are the most distinctive characteristics for identifying mucormycosis.<sup>129,130</sup> Schiff or hematoxylin and eosin staining can be used to better visualize the Mucorales; they do not stain as well as methenamine silver.<sup>130</sup>

Histopathology is used to identify the Mucorales, but species identification is limited to culturing. Imaging techniques are used to investigate the condition's advancement and severity. For example, fungal sinusitis that is different from bacterial sinusitis is the most usual finding

on CT or MRI scans of the head and sinuses of a patient with rhino-orbital mucormycosis. MRI is more sensitive (by approximately 80%) than CT in the detection of orbital and CNS disease.<sup>131</sup> Nasal endoscopy is an excellent diagnostic method for determining the presence of mucormycosis, while the MRI findings are very useful and significant to show the spread of mucormycosis in different regions as a supportive example to make it clinically significant but these findings will be varying according to the case-by-case basis (Fig. 7).

The polymerase chain reaction (PCR) is used as a current diagnostic tool in the research of mucormycosis,<sup>132</sup> however, it has not yet been licensed by the U.S. Food and Drug Administration (FDA) for this purpose and it is a rare find.<sup>9</sup>

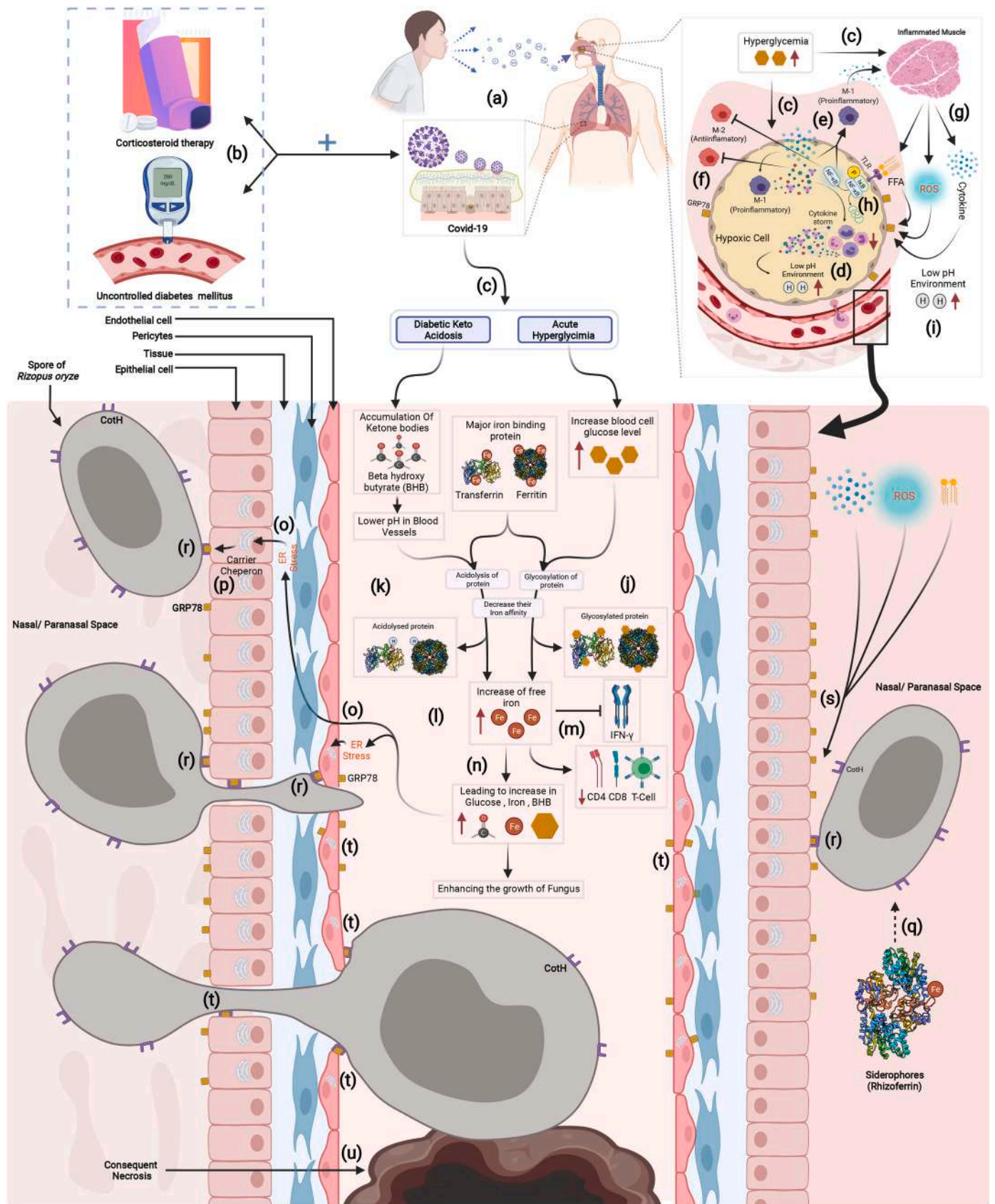
### 6. Current therapeutics for COVID-19 associated mucormycosis

As significant trouble, the prevalent COVID-19 spreads worldwide.<sup>25,133</sup> While various treatment options are estimated, at that time systemic glucocorticoids are shown to enhance the survival rate of COVID-19.<sup>25,134</sup> Glucocorticoids are not too expensive, available widely, and are shown to decrease fatality in COVID-19 patients with hypoxemia.<sup>9,25</sup> Unfortunately, the extensive use of glucocorticoids can develop secondary fungal infections like mucormycosis.<sup>25</sup> The medical diagnosis of mucormycosis requires treatment quickly, as the fungal invasion advances rapidly.<sup>50,135–137</sup> Simultaneously, the therapeutics of mucormycosis should be established as soon as possible, to reverse underlying risk factors.<sup>138</sup>

Surgical debridement (FESS or Functional Endoscopic Sinus Surgery is a minimally invasive technique used to restore sinus ventilation and normal function and/or orbital exenteration) not only decreases the burden of the disease but also permits better percolation of intravenous medical drugs. It reduces further disease spreading and permits to allow intraoperative diagnosis of necrotic tissue with applicable characteristics to provide the sample for microbiological and histopathological confirmation.<sup>139,140</sup> But prompt initiation of medication therapy and instant reversal of underlying risk factors are always the better alternatives to surgical debridement because it is crucial to maintain a high index of suspicion in patients who are at risk for mucormycosis at all times.<sup>138</sup>

Antifungals can also play an important role along with surgical debridement. The guidelines, accepted globally in 2019 for the management and diagnosis of mucormycosis by Mycoses Study Group Education and Research Consortium (MSGERC) and the European Confederation of Medical Mycology (ECMM) strongly prescribe surgical treatment if possible with the addition of systemic treatment of antifungals.<sup>141</sup> Liposomal Amphotericin B, Posaconazole and Amphotericin B lipid complex oral suspension can be treated as first-line antifungal agent monotherapy and Isavuconazole can be assisted like salvage therapy.<sup>141,142</sup> Irrigation of sinuses and orbit with (1 mg/ml) Amphotericin B improves the local drug concentration and is shown to enhance outcomes.<sup>143</sup> Intra-orbital and Retrobulbar injection in respect to Amphotericin B are also given in those patients who have no ability for surgical debridement (the dose of anesthesia along with retrobulbar injection is 1 ml of three 3.5 mg/ml).<sup>139,143,144</sup> The recent guideline of MSGERC and ECMM for mucormycosis management recommends liposomal amphotericin B (L-AMB), the dose is 5–10 mg/kg every day.<sup>141,145</sup> Adults and children are often administered to treat mucormycosis at start-up doses of 1 mg/kg daily for Amphotericin B deoxycholate (d-AMB) and 5 mg/kg daily for L-AMB and Amphotericin B lipid complex (ABLC).<sup>127</sup> The dose of 5 mg/kg is used to recommend when the implication of the nervous system is absent.<sup>25,141</sup> Amphotericin B has potential renal toxicity so that the dosage should be adjusted between 0.5 mg/kg/day and 1.5 mg/kg/day by the condition of the patient as well as disease. Hyperbaric oxygen (HBO) therapy should also be used in case of aggressive infection.<sup>9</sup>

For the hyperglycemic patient, the early treatment of liposomal amphotericin B and if necessary surgical treatment is needed.



(caption on next page)

**Fig. 5.** Diagram pictured the planned mechanisms for the immunopathogenesis of COVID-19 assisted mucormycosis in the immunocompromised diabetic individual<sup>22,57,124</sup> (Created with BioRender.com). (a) In COVID-19 severity, (b) uncontrolled diabetes mellitus and overdrive of Corticosteroid drugs increases the vulnerability to Mucorales infection due to diabetic ketoacidosis (DKA) and hyperglycemia. (c) An elevation in the glucose level of the adipose tissue induces endoplasmic reticulum (ER) stress, cellular hypoxia, enhanced discharge of free fatty acids (FFA), reactive oxygen species (ROS), and generate cytokine storm. (d) A diversified range of the cytokines like interleukin-1 (IL-1 $\beta$ ), tumor necrosis factor (TNF), and various types of chemokines are released to the cellular hypoxic environment. (e) These cytokines especially TNF- $\alpha$  recruits the proinflammatory M1 macrophages and (f) inhibits the activity of anti-inflammatory M2 macrophages. (g) The activated M1 macrophage again discharges more pro-inflammatory cytokines like IL-1 $\beta$ , FFA and generates ROS. (h) These FFA are also detected by TLR-4 in the tissue cells, initiating JNK-AP-I and IKK-NF $\kappa$ B (nuclear factor-kappa B) signalling. (i) Simultaneously, diabetic ketoacidosis (DKA) causes a low pH environment which ultimately enhances the cellular H<sup>+</sup> ion level. (j) Due to the activity of hyperglycemia, iron-scavenging proteins like ferritin and transferrin show increased glycosylation in the blood vessel, which lowers their iron affinity. (k) Furthermore, in the attendance of an acidotic condition promoted by the creation of ketone bodies (e.g.,  $\beta$ -hydroxybutyrate [BHB]), the low pH environment in the blood vessels substantially restricts transferrin's ability to chelate iron. (l) As a result, the accessibility of free iron in the blood vessel is stimulated whereas (m) the counts of IFN- $\gamma$ , CD4<sup>+</sup>, CD8<sup>+</sup>, and T-cell are sharply declined. (n) A combination of free iron, glucose, and BHB triggers epithelial fungal adhesion and tissular hyphal growth or opportunistic fungal infection. (o) This combination causes a stress response in ER, which drives to overexpression of the GRP78 protein. (p) The MTJ-1 chaperone aids in the translocation of GRP78 proteins from ER to the cell surface. (q) Fungi battle with the host for the presence of iron in the siderophore system. (r) High glucose concentrations, free iron availability, and an acid microenvironment boost CotH expression on the fungal cell surface, facilitating GRP78/CotH3 contact for epithelial/endothelial invasion and fungal spread. (s) The connection between GRP78 and CotH is additionally aided by ROS, FFA, and cytokines. (t) Meanwhile, endothelial cells pursue to generate GRP78 in all partitions, and the hypha connect with these proteins on the basal side and become internalized in the lumen of blood vessels. (u) They produce cell damage, thrombus formation, ischemia, prolonged hypoxia, tissue infarction, and finally necrosis by activating the external coagulation pathway.

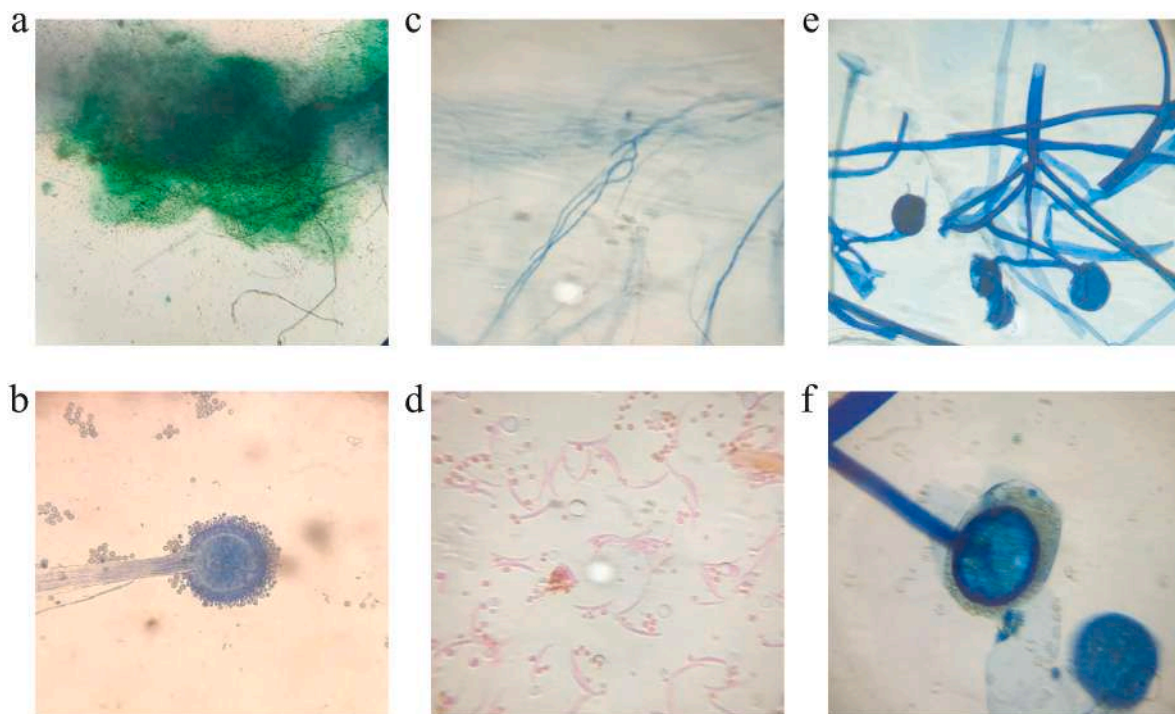


**Fig. 6.** Compound microscopic view of different types of fungal species. (a–b) Compound microscopic view of *Aspergillus* sp. showing perpendicular hyphal branching pattern under ca.  $\times 100$  and ca.  $\times 450$  magnification, respectively. (c–d) Compound microscopic view of *Fusarium* sp. showing conidia with conidiospores and dichotomous hyphal branching pattern under ca.  $\times 100$  and ca.  $\times 450$  magnification, respectively. (e–f) Compound microscopic view of *Rhizopus* sp. showing perpendicular hyphal branching pattern under ca.  $\times 100$  and ca.  $\times 450$  magnification, respectively.

Hyperglycemia is annoyed with COVID-19 effective therapy, namely glucocorticoids. Multi-organ dysfunction and co-existing Acute Respiratory Distress Syndrome (ARDS) prevent timely testing and diagnostic imaging.<sup>25,34</sup> The hospitals are overburdened by patients of COVID-19, and diagnostics after those surgeries can be curtailed significantly.<sup>34</sup> Hence, the mortality of COVID-19 associated mucormycosis may higher than non-COVID patients with mucormycosis because of the immunosuppressed condition of the patient, presence of acute hyperglycemia, and necessarily use of glucocorticoids to treat the severity of COVID-19.<sup>49,146,147</sup> Thus, in moderate COVID-19 cases (absence of hyperglycemia), the huge dose of glucocorticoid utilization must be avoided. Hence, the judicial considerable use of glucocorticoids in COVID-19 cases is necessary because this aggravates the hyperglycemia condition and advances the formation of diabetes ketoacidosis. Apart from this, in COVID-19 treatment, there is also an increment of D-Dimer as a product

of cross-linked fibrin (inappropriate blood clot or thrombus formation). To treat the inappropriate formation of thrombus, the immunomodulatory drug tocilizumab is using, which also unluckily, promotes the mucormycosis infection.<sup>68</sup> Therefore, the use of drugs like tocilizumab which are targeting the immune pathways is discouraged without any transparent benefit.<sup>25,148</sup> Moreover, the virus causes the dysregulation of the immune system and as a result, using consistent immunomodulatory medical drugs like tocilizumab can further raise this dreadful infection in the patients of COVID-19 disease.<sup>25,148,149</sup> So, it is necessary to use judiciously under intense monitoring of the patient to detect an early fungal infestation.<sup>138</sup>

## 7. Conclusion

The recurrence of mucormycosis, opportunistic microorganisms has

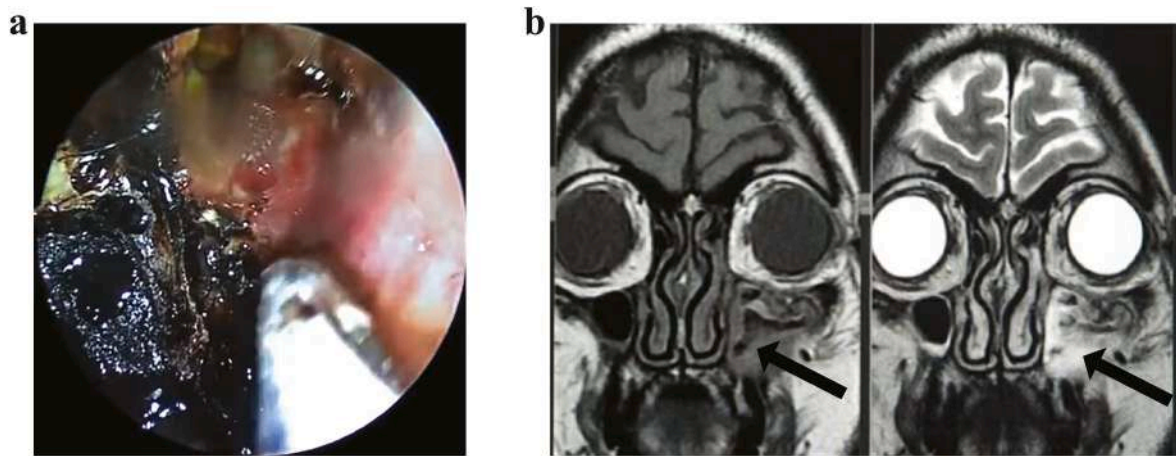


**Fig. 7.** Illustration of mucormycosis infection spreading to the nasal vestibules, maxillary sinus, and brain. (a) Nasal endoscopic view, showing the location of mucormycosis. (b) The magnetic resonance imaging (MRI) scan of the head and sinuses showing the location of pus accumulation and inflammation of the maxillary sinus due to mucormycosis (T1 weighted and T2 weighted MRI scans).

expanded altogether in the previous twenty years. This study gives an overview of comparative cases of different countries, along with the implications of the disease. The rise in mucormycosis emerges to be the result of certain factors including diabetes, uncontrolled use of glucocorticoids (which raises blood glucose, free iron that advances the probable fungal infection), and COVID-19 infection (cytokine storm, neutropenia, endothelial cell surface injury). The involvement between the fungal species of *Rhizopus* and the endothelial cells has also been featured. The mechanism concerning the pathogenesis of the disease has been comprehended and would initiate a vital role in future elevation. Recent tentative regimens for the treatment of mucormycosis comprises the usage of Amphotericin B and Isavuconazole. The administration of therapeutic substances should be closely managed to obtain a therapeutic impact at the moderate possible dose and for the shortest possible duration under keen observation. In the future, an improved establishment of the criteria regarding the diagnosis for COVID-19 associated mucormycosis is required including the radiological patterns of COVID-19 and the difficulty of isolating *Rhizopus* spp. Finally, rapid diagnosis and surgical debridement are considered to be the keystone for this life-threatening disease.

#### Authors' contributions

Conceptualization: [Joy Sarkar]; Methodology: [Joy Sarkar]; Formal analysis and investigation: [Joy Sarkar]; Writing – original draft preparation: [Deganta Ghosh], [Sagardeep Dey], [Himanko Chakraborty], [Ankita Halder], [Akash Sarkar], [Sneha Mukherjee], [Pallab Chakraborty], [Rajdeep Ghosh]; Writing – review and editing: [Joy Sarkar]; Funding acquisition: [N/A]; Resources: [N/A]; Supervision: [Joy Sarkar].

#### Declaration of competing interest

On behalf of all listed authors, the corresponding author declares that there is not any sort of financial and non-financial conflict of interest in the subject materials mentioned in this manuscript.

#### Acknowledgment

The authors like to acknowledge Mr. Debangan Chowdhury and Ms. Shreemoyee Palmal for providing us the microscopic images of *Aspergillus* sp. The authors like to thank Mr. Prithu Bhattacharyya for supplying us one of the microscopic images of *Rhizopus* sp. We also like to acknowledge [BioRender.com](https://www.biorender.com) for making the way suitable to get Fig. 5.

Deganta Ghosh, Sagardeep Dey, Himanko Chakraborty, Ankita Halder, Akash Sarkar, Sneha Mukherjee, Pallab Chakraborty, and Rajdeep Ghosh contributed equally to this article. We do not have any funding support from any organizational or institutional level.

#### References

- Sugar AM. Mucormycosis. *Clin Infect Dis*. 1992;14(1):126–129. [https://doi.org/10.1093/clinids/14.Supplement\\_1.S126](https://doi.org/10.1093/clinids/14.Supplement_1.S126).
- Nishanth G, Anitha N, Aravindha Babu N, Malathi L. Mucormycosis - a review. *Eur J Mol Clin Med*. 2020;7(3):1786–1791.
- Kwon-Chung KJ. Taxonomy of fungi causing mucormycosis and entomophthoromycosis (zygomycosis) and nomenclature of the disease: molecular mycologic perspectives. *Clin Infect Dis*. 2012;54(1):8–15. <https://doi.org/10.1093/cid/cir864>.
- Prakash H, Chakraborty A. Global epidemiology of mucormycosis. *J Fungi*. 2019;5(1). <https://doi.org/10.3390/jof5010026>.
- Maini A, Tomar G, Khanna D, Kini Y, Mehta H, Bhagyashree V. Sino-orbital mucormycosis in a COVID-19 patient: a case report. *Int J Surg Case Rep*. 2021;82(1). <https://doi.org/10.1016/j.ijscr.2021.105957>.
- Mohammadi R, Nazeri M, Amin Sayedayn SM, Ehteram H. A successful treatment of rhinocerebral mucormycosis due to *Rhizopus Oryzae*. *J Res Med Sci*. 2014;19(1):72.
- Fernandez JF, Maselli DJ, Simpson T, Restrepo MI. Pulmonary mucormycosis: what is the best strategy for therapy? *Respir Care*. 2013;58(5):60–63. <https://doi.org/10.4187/respcare.02106>.
- Do Monte ES, Dos Santos MEL, Ribeiro IB, et al. Rare and fatal gastrointestinal mucormycosis (Zygomycosis) in a COVID-19 patient: a case report. *Clin Endosc*. 2020;53(6):746–749. <https://doi.org/10.5946/CE.2020.180>.
- Spellberg B, Edwards J, Ibrahim A. Novel perspectives on mucormycosis: pathophysiology, presentation, and management. *Clin Microbiol Rev*. 2005;18(3):556–569. <https://doi.org/10.1128/CMR.18.3.556-569.2005>.
- Roden MM, Zaoutis TE, Buchanan WL, et al. Epidemiology and outcome of zygomycosis: a review of 929 reported cases. *Clin Infect Dis*. 2005;41(5):634–653. <https://doi.org/10.1086/432579>.
- Petrikos G, Skiada A, Lortholary O, Roilides E, Walsh TJ, Kontoyiannis DP. Epidemiology and clinical manifestations of mucormycosis. *Clin Infect Dis*. 2012;54(1):23–34. <https://doi.org/10.1093/cid/cir866>.
- Khatri A, Chang KM, Berlinut I, Wallach F. Mucormycosis after Coronavirus disease 2019 infection in a heart transplant recipient – case report and review of literature. *J Med Mycol*. 2021;31(2). <https://doi.org/10.1016/j.mycmed.2021.101125>.
- Bhatt K, Agolli A, Patel M H, et al. High mortality co-infections of COVID-19 patients: mucormycosis and other fungal infections. *Discoveries*. 2021;9(1). <https://doi.org/10.15190/d.2021.5>.
- Khan N, Gutierrez CG, Martinez DV, Proud KC. A case report of COVID-19 associated pulmonary mucormycosis. *Arch Clin Cases*. 2020;7(3):46–51. <https://doi.org/10.22551/2020.28.0703.10172>.
- Revannavar SM, Supriya P, Samaga L, Vineeth K. COVID-19 triggering mucormycosis in a susceptible patient: a new phenomenon in the developing world? *BMJ Case Rep*. 2021;14(4). <https://doi.org/10.1136/bcr-2021-241663>.
- Das S, Sarkar S, Das A, Das S, Chakraborty P, Sarkar J. A comprehensive review of various categories of face masks resistant to Covid-19. *Clin Epidemiol Global Health*. 2021;12:100835. <https://doi.org/10.1016/j.cegh.2021.100835>.
- Sharma S, Grover M, Bhargava S, Samdani S, Kataria T. Post coronavirus disease mucormycosis: a deadly addition to the pandemic spectrum. *J Laryngol Otol*. 2021; 135(5):442–447. <https://doi.org/10.1017/S0022215121000992>.

- 18 Segrelles-Calvo G, De Saraújo GR, Frases S. Systemic mycoses: a potential alert for complications in COVID-19 patients. *Future Microbiol.* 2020;15(14):1405–1413. <https://doi.org/10.2217/fmb-2020-0156>.
- 19 Satish D, Joy D, Ross AB. Mucormycosis coinfection associated with global COVID-19: a case series from India. *Int J Otorhinolaryngol Head Neck Surg.* 2021;7(5): 815–820. <https://doi.org/10.18203/issn.2454-5929.ijohns20211574>.
- 20 Alekseyev K, Didenko L, Chaudhry B. Rhinocerebral mucormycosis and COVID-19 pneumonia. *J Med Cases.* 2021;12(3):85–89. <https://doi.org/10.14740/jmc3637>.
- 21 Sahoo JP, Mishra AP, Pradhan P, Samal KC. Misfortune never comes alone - the new "black fungus" accompanying COVID-19 wave. *Biotica Res Today.* 2021;3(5): 318–320.
- 22 Singh AK, Singh R, Joshi SR, Mishra A. Mucormycosis in COVID-19: a systematic review of cases reported worldwide and in India. Diabetes, Metab Syndrome: Clin Res Rev. Published online 2021:1-7. doi:10.1016/j.dsx.2021.05.019.
- 23 Yeo CD, Kim JS, Kwon SH, et al. Rhinocerebral mucormycosis after functional endoscopic sinus surgery A case report. *Medicine.* 2018;97(51). <https://doi.org/10.1097/MD.0000000000003290>.
- 24 Ahmadikia K, Hashemi SJ, Khodavaisy S, et al. The double-edged sword of systemic corticosteroid therapy in viral pneumonia: a case report and comparative review of influenza-associated mucormycosis versus COVID-19 associated mucormycosis. *Mycoses.* 2021:1–11. <https://doi.org/10.1111/myc.13256>. Published online.
- 25 Garg D, Muthu V, Sehgal IS, et al. Coronavirus disease (Covid-19) associated mucormycosis (CAM): case report and systematic review of literature. *Mycopathologia.* 2021;186(2):289–298. <https://doi.org/10.1007/s11046-021-00528-2>.
- 26 Mishra N, Mutya VSS, Thomas A, et al. A case series of invasive mucormycosis in patients with COVID-19 infection. *Int J Otorhinolaryngol Head Neck Surg.* 2021;7(5): 867–870. <https://doi.org/10.18203/issn.2454-5929.ijohns20211583>.
- 27 Dallalazadeh LO, Ozzello DJ, Liu CY, Kikkawa DO, Korn BS. Secondary infection with rhino-orbital cerebral mucormycosis associated with COVID-19. *Orbit.* 2021: 1–4. <https://doi.org/10.1080/01676830.2021.1903044>. Published online.
- 28 Werthman-Ehrenreich A. Mucormycosis with orbital compartment syndrome in a patient with COVID-19. *AJEM (Am J Emerg Med).* 2021;(264):42. <https://doi.org/10.1016/j.ajem.2020.09.032>.
- 29 Placik DA, Taylor WL, Wnuk NM. Bronchopleural fistula development in the setting of novel therapies for acute respiratory distress syndrome in SARS-CoV-2 pneumonia. *Radiol Case Rep.* 2020;15(11):2378–2381. <https://doi.org/10.1016/j.radcr.2020.09.026>.
- 30 Mekonnen ZK, Ashraf DC, Jankowski T, et al. Acute invasive rhino-orbital mucormycosis in a patient with COVID-19-associated acute respiratory distress syndrome. *Ophthalmic Plast Reconstr Surg.* 2021;37(2):40–80. <https://doi.org/10.1097/IOP.0000000000001889>.
- 31 Johnson AK, Ghazarian Z, Cendrowski KD, Persichino JG. Pulmonary aspergillosis and mucormycosis in a patient with COVID-19. *Med Mycol Case Rep.* 2021;32: 64–67. <https://doi.org/10.1016/j.mmc.2021.03.006>.
- 32 Kanwar A, Jordan A, Olewiler S, Wehberg K, Cortes M, Jackson BR. A fatal case of rhizopus azygosporus pneumonia following covid-19. *J Fungi.* 2021;7(3):174. <https://doi.org/10.3390/jof7030174>.
- 33 Hanley B, Naresh KN, Roufosse C, et al. Histopathological findings and viral tropism in UK patients with severe fatal COVID-19: a post-mortem study. *The Lancet Microbe.* 2020;1(6):245–253. [https://doi.org/10.1016/S2666-5247\(20\)30115-4](https://doi.org/10.1016/S2666-5247(20)30115-4).
- 34 Pasero D, Sanna S, Liperi C, et al. A challenging complication following SARS-CoV-2 infection: a case of pulmonary mucormycosis. *Infection.* 2020:1–6. <https://doi.org/10.1007/s15010-020-01561-x>. Published online.
- 35 Bellanger AP, Navellou JC, Lepiller Q, et al. Mixed Mold Infection with Aspergillus fumigatus and Rhizopus Microsporus in a Severe Acute Respiratory Syndrome Coronavirus 2 (SARS-CoV-2) Patient. *Infectious Diseases Now.* Published online 2021. doi:10.1016/j.idnow.2021.01.010.
- 36 Karimi-Galougahi M, Arastou S, Haseli S. Fulminant mucormycosis complicating coronavirus disease 2019 (COVID-19). *Int Forum Allergy Rhinol.* 2021;11(6): 1029–1030. <https://doi.org/10.1002/alf.22785>.
- 37 Veisi A, Bagheri A, Eshaghi M, Rikhtehgar MH, Rezaei Kanavi M, Farjad R. Rhino-orbital mucormycosis during steroid therapy in COVID-19 patients: a case report. *Eur J Ophthalmol.* 2021:1–6. <https://doi.org/10.1177/11206721211009450>. Published online.
- 38 Waizel-Haiat S, Guerrero-Paz JA, Sanchez-Hurtado L, Calleja-Alarcon S, Romero-Gutierrez L. A case of fatal rhino-orbital mucormycosis associated with new onset diabetic ketoacidosis and COVID-19. *Cureus.* 2021;13(2). <https://doi.org/10.7759/cureus.13163>.
- 39 Zurl C, Hoenigl M, Schulz E, et al. Autopsy proven pulmonary mucormycosis due to Rhizopus microsporus in a critically ill COVID-19 patient with underlying hematological malignancy. *J Fungi.* 2021;7(2):88. <https://doi.org/10.3390/jof7020088>.
- 40 Sungurtekin H, Sargin F, Akbulut M, Karaduman S. Severe rhinocerebral mucormycosis case developed after COVID-19. *J Bacteriol Parasitol.* 2021;12(1): 1–3.
- 41 Saldanha M, Reddy R, Vincent MJ. Title of the article: paranasal mucormycosis in COVID-19 patient. *Indian J Otolaryngol Head Neck Surg.* Published online 2021:1-4. doi:10.1007/s12070-021-02574-0.
- 42 Mehta S, Pandey A. Rhino-orbital mucormycosis associated with COVID-19. *Cureus.* 2020;12(9). <https://doi.org/10.7759/cureus.10726>.
- 43 Kumar Chennamchetty V, Adimulapu S, Patel Kola B, De Padua M, Ambika C, Raghavendra Rao MD. Post-COVID pulmonary mucormycosis- A case report. *IP Indian J Immunol Respir Med.* 2021;6(1):62–66. <https://doi.org/10.18231/j.ijirm.2021.014>.
- 44 White PL, Dhillon R, Cordey A, et al. A National Strategy to Diagnose Coronavirus Disease 2019–Associated Invasive Fungal Disease in the Intensive Care Unit. *Clinical Infectious Diseases;* 2020. <https://doi.org/10.1093/cid/ciaa1298>. Published online.
- 45 Sarkar S, Gokhale T, Choudhury S, Deb A. COVID-19 and orbital mucormycosis. *Indian J Ophthalmol.* 2021;69(4):1002–1004. [https://doi.org/10.4103/ijo.IJO\\_3763\\_20](https://doi.org/10.4103/ijo.IJO_3763_20).
- 46 Chakrabarti A, Singh R. Mucormycosis in India: unique features. *Mycoses.* 2014;57(3):85–90. <https://doi.org/10.1111/myc.12243>.
- 47 Diwakar A, Dewan RK, Chowdhary A, Randhawa HS, Khanna G, Gaur SN. Zygomycosis - a case report and overview of the disease in India. *Mycoses.* 2007;50(4):247–254. <https://doi.org/10.1111/j.1439-0507.2007.01382.x>.
- 48 Meis JF, Chakrabarti A. Changing epidemiology of an emerging infection: Zygomycosis. *Clin Microbiol Infect.* 2009;15(5):10–14. <https://doi.org/10.1111/j.1469-0691.2009.02973.x>.
- 49 Patel A, Kaur H, Xess I, et al. A multicentre observational study on the epidemiology, risk factors, management and outcomes of mucormycosis in India. *Clin Microbiol Infect.* 2020;26(7):944. <https://doi.org/10.1016/j.cmi.2019.11.021>. e9-944.e15.
- 50 Skiada A, Lass-Floerl C, Klimko N, Ibrahim A, Roilides E, Petrlikos G. Challenges in the diagnosis and treatment of mucormycosis. *Med Mycol.* 2018;56(1):93–101. <https://doi.org/10.1093/mmy/myx101>.
- 51 Kr PK. Mucormycosis: a black fungus- post covid complications. *J Regen Biol Med.* 2021;3(4):1–8. [https://doi.org/10.37191/Mapsci-2582-385X-3\(4\)-078](https://doi.org/10.37191/Mapsci-2582-385X-3(4)-078).
- 52 Dadwal SS, Kontoyiannis DP. Recent advances in the molecular diagnosis of mucormycosis. *Expert Rev Mol Diagn.* 2018;18(10):845–854. <https://doi.org/10.1080/14737159.2018.1522250>.
- 53 Song G, Liang G, Liu W. Fungal Co-infections associated with global COVID-19 pandemic: a clinical and diagnostic perspective from China. *Mycopathologia.* 2020: 1–8. <https://doi.org/10.1007/s11046-020-00462-9>. Published online.
- 54 Zhou C, Byard RW. An analysis of the morbidity and mortality of diabetes mellitus in a forensic context. *J Forensic Sci.* 2018;63(4):1149–1154. <https://doi.org/10.1111/1556-4029.13674>.
- 55 Yang W, Dall TM, Beronjia K, et al. Economic costs of diabetes in the U.S. in 2017. *Diabetes Care.* 2018;41(5):917–928. <https://doi.org/10.2337/dci18-0007>.
- 56 John TM, Jacob CN, Kontoyiannis DP. When uncontrolled diabetes mellitus and severe covid-19 converge: the perfect storm for mucormycosis. *J Fungi.* 2021;7(4): 298. <https://doi.org/10.3390/jof7040298>.
- 57 Morales-Franco B, Nava-Villalba M, Medina-Guerrero EO, et al. Host-Pathogen molecular factors contribute to the pathogenesis of rhizopus spp. in diabetes mellitus. *Curr Trop Med Rep.* 2021:1–12. <https://doi.org/10.1007/s40475-020-00222-1>. Published online.
- 58 Goldman N, Fink D, Cai J, Lee YN, Davies Z. High prevalence of COVID-19-associated diabetic ketoacidosis in UK secondary care. *Diabetes Res Clin Pract.* 2020; 166(108291):1–7. <https://doi.org/10.1016/j.diabres.2020.108291>.
- 59 Oriot P, Hermans MP. Euglycemic diabetic ketoacidosis in a patient with type 1 diabetes and SARS-CoV-2 pneumonia: case report and review of the literature. *Acta Clin Belg.* *Int J Clin Lab Med.* 2020:1–5. <https://doi.org/10.1080/17843286.2020.1780390>. Published online.
- 60 Lantermier F, Dannaoui E, Morizot G, et al. A global analysis of mucormycosis in France: the RetroZygo study (2005–2007). *Clin Infect Dis.* 2012;54(1):S35–S43. <https://doi.org/10.1093/cid/cir880>.
- 61 Ferguson BJ. Definitions of fungal rhinosinusitis. *Otolaryngol Clin.* 2000;33(2): 227–235. [https://doi.org/10.1016/S0030-6665\(00\)80002-X](https://doi.org/10.1016/S0030-6665(00)80002-X).
- 62 Chakrabarti A, Denning DW, Ferguson BJ, et al. Fungal rhinosinusitis: a categorization and definitional schema addressing current controversies. *Laryngoscope.* 2009;119(9):1809–1818. <https://doi.org/10.1002/lary.20520>.
- 63 Dhiwakar M, Thakar A, Bahadur S. Improving outcomes in rhinocerebral mucormycosis - early diagnostic pointers and prognostic factors. *J Laryngol Otol.* 2003;117(11):861–865. <https://doi.org/10.1258/002221503322542854>.
- 64 Talmi YP, Goldschmied-Reouven A, Bakon M, et al. Rhino-orbital and rhino-orbito-cerebral mucormycosis. *Otolaryngol Head Neck Surg.* 2002;127(1):22–31. <https://doi.org/10.1067/mhn.2002.126587>.
- 65 Khor BS, Lee MH, Leu HS, Liu JW. Rhinocerebral mucormycosis in Taiwan. *J Microbiol Immunol Infect.* 2003;36(4):266–269.
- 66 Peterson KL, Wang M, Canalis RF, Abemayor E. Rhinocerebral mucormycosis: evolution of the disease and treatment options. *Laryngoscope.* 1997;107(7): 855–862. <https://doi.org/10.1097/00005537-199707000-00004>.
- 67 Thajeb P, Thajeb T, Dai D. Fatal strokes in patients with rhino-orbito-cerebral mucormycosis and associated vasculopathy. *Scand J Infect Dis.* 2004;36(9): 643–648. <https://doi.org/10.1080/00365540410020794>.
- 68 Atallah B, El Nekidy W, Mallah SI, et al. Thrombotic events following tocilizumab therapy in critically ill COVID-19 patients: a Façade for prognostic markers. *Thromb J.* 2020;18(22):1–6. <https://doi.org/10.1186/s12959-020-00236-9>.
- 69 Tedder M, Spratt JA, Anstadt MP, Hegde SS, Tedder SD, Lowe JE. Pulmonary mucormycosis: results of medical and surgical therapy. *Ann Thorac Surg.* 1994;57(4):1044–1050. [https://doi.org/10.1016/0003-4975\(94\)90243-7](https://doi.org/10.1016/0003-4975(94)90243-7).
- 70 Rothstein RD, Simon GL. Subacute pulmonary mucormycosis. *Med Mycol.* 1986;24(5):391–394. <https://doi.org/10.1080/02681218680000591>.
- 71 Kerr OA, Bong C, Wallis C, Tidman MJ. Primary cutaneous mucormycosis masquerading as pyoderma gangrenosum. *Br J Dermatol.* 2004;150(6):1212–1213. <https://doi.org/10.1111/j.1365-2133.2004.05826.x>.
- 72 Quinio D, Karam A, Leroy JP, et al. Zygomycosis caused by Cunninghamella bertholletiae in a kidney transplant recipient. *Med Mycol.* 2004;42(2):177–1780. <https://doi.org/10.1080/13693780310001644644>.

- 73 Gartenberg G, Bottone EJ, Keusch GT, Weitzman I. Hospital-acquired mucormycosis (rhizopus rhizopodiformis) of skin and subcutaneous tissue. *N Engl J Med*. 1978;299(20):1115–1118. <https://doi.org/10.1056/nejm197811162992007>.
- 74 Mead JH. Cutaneous Rhizopus infection. Occurrence as a postoperative complication associated with an elasticized adhesive dressing. *JAMA: J Am Med Assoc*. 1979;242(3):272–274. <https://doi.org/10.1001/jama.242.3.272>.
- 75 Amin SB, Ryan RM, Metlay LA, Watson WJ. Absidia corymbifera infections in neonates. *Clin Infect Dis*. 1998;26(4):990–992. <https://doi.org/10.1086/513940>.
- 76 Craig NM, Lueder FL, Pensler JM, et al. Disseminated rhizopus infection in a premature infant. *Pediatr Dermatol*. 1994;11(4):346–350. <https://doi.org/10.1111/j.1525-1470.1994.tb00103.x>.
- 77 Kecskes S, Reynolds G, Bennett G. Survival after gastrointestinal mucormycosis in a neonate. *J Paediatr Child Health*. 1997;33(4):356–359. <https://doi.org/10.1111/j.1440-1754.1997.tb01617.x>.
- 78 Kline MW. Mucormycosis in children: review of the literature and report of cases. *Pediatr Infect Dis*. 1985;4(6):672–676. <https://doi.org/10.1097/00006454-19851000-00015>.
- 79 Reimund E, Ramos A. Disseminated neonatal gastrointestinal mucormycosis: a case report and review of the literature. *Fetal Pediatr Pathol*. 1994;14(3):385–389. <https://doi.org/10.3109/15513819409024268>.
- 80 Sharma MC, Gill SS, Kashyap S, et al. Gastrointestinal mucormycosis—an uncommon isolated mucormycosis. *Indian J Gastroenterol: official journal of the Indian Society of Gastroenterology*. 1998;17(4):131–133.
- 81 Imhof A, Balajee SA, Fredricks DN, England JA, Marr KA. Breakthrough fungal infections in stem cell transplant recipients receiving voriconazole. *Clin Infect Dis*. 2004;39(5):743–746. <https://doi.org/10.1086/423274>.
- 82 Marty FM, Cosimi LA, Baden LR. Breakthrough zygomycosis after voriconazole treatment in recipients of hematopoietic stem-cell Transplants. *N Engl J Med*. 2004;350(9):950–952. <https://doi.org/10.1056/nejm200402263500923>.
- 83 Siwek GT, Dodgson KJ, De Magalhaes-Silverman M, et al. Invasive zygomycosis in hematopoietic stem cell transplant recipients receiving voriconazole prophylaxis. *Clin Infect Dis*. 2004;39(4):584–587. <https://doi.org/10.1086/422723>.
- 84 Kronsteiner B, Chaichana P, Sumonwiriya M, et al. Diabetes alters immune response patterns to acute melioidosis in humans. *Eur J Immunol*. 2019;49(7):1092–1106. <https://doi.org/10.1002/eji.201848037>.
- 85 Ayelign B, Negash M, Genetu M, Wondmagegn T, Shibabaw T. Immunological impacts of diabetes on the susceptibility of Mycobacterium tuberculosis. *J Immunol Res*. 2019;1–8. <https://doi.org/10.1155/2019/6196532>. Published online.
- 86 Liu C, Feng X, Li Q, Wang Y, Li Q, Hua M. Adiponectin, TNF- $\alpha$  and inflammatory cytokines and risk of type 2 diabetes: a systematic review and meta-analysis. *Cytokine*. 2016;86:100–109. <https://doi.org/10.1016/j.cyt.2016.06.028>.
- 87 Toniolo A, Cassani G, Puggioni A, et al. The diabetes pandemic and associated infections: suggestions for clinical microbiology. *Rev Med Microbiol*. 2019;30(1):1–17. <https://doi.org/10.1097/MRM.0000000000000155>.
- 88 Ribes JA, Vanover-Sams CL, Baker DJ. Zygomycetes in human disease. *Clin Microbiol Rev*. 2000;13(2):236–301. <https://doi.org/10.1128/cmr.13.2.236>.
- 89 Artis WM, Fountain JA, Delcher HK, Jones HE. A mechanism of susceptibility to mucormycosis in diabetic ketoacidosis: transferrin and iron availability. *Diabetes*. 1982;31(12):1109–1114. <https://doi.org/10.2337/diacare.31.12.1109>.
- 90 Fu Y, Lee H, Collins M, et al. Cloning and functional characterization of the Rhizopus oryzae high affinity iron permease (FTR1) gene. *FEMS (Fed Eur Microbiol Soc) Microbiol Lett*. 2004;235(1):169–176. <https://doi.org/10.1016/j.femsle.2004.04.031>.
- 91 Gebremariam T, Lin L, Liu M, et al. Bicarbonate correction of ketoacidosis alters host-pathogen interactions and alleviates mucormycosis. *J Clin Invest*. 2016;126(6):2280–2294. <https://doi.org/10.1172/JCI82744>.
- 92 Navarro-Mendoza MI, Pérez-Arques C, Murcia L, et al. Components of a new gene family of ferroxidases involved in virulence are functionally specialized in fungal dimorphism. *Sci Rep*. 2018;8:1–13. <https://doi.org/10.1038/s41598-018-26051-x>.
- 93 Andrianaki AM, Kyrmizi I, Thanopoulou K, et al. Iron restriction inside macrophages regulates pulmonary host defense against Rhizopus species. *Nat Commun*. 2018;9(1):3333. <https://doi.org/10.1038/s41467-018-05820-2>.
- 94 Agoro R, Taleb M, Quesniaux VFJ, Mura C. Cell iron status influences macrophage polarization. *PLoS One*. 2018;13(5). <https://doi.org/10.1371/journal.pone.0196921>.
- 95 Ibrahim AS, Spellberg B, Walsh TJ, Kontoyiannis DP. Pathogenesis of mucormycosis. *Clin Infect Dis*. 2012;54(1):S16–S22. <https://doi.org/10.1093/cid/cir865>.
- 96 Lax C, Pérez-arques C, Navarro-mendoza MI, et al. Genes, pathways, and mechanisms involved in the virulence of mucorales. *Genes*. 2020;11(3):317. <https://doi.org/10.3390/genes11030317>.
- 97 Petrikos G, Tsioutis C. Recent advances in the pathogenesis of mucormycoses. *Clin Therapeut*. 2018;40(6):894–902. <https://doi.org/10.1016/j.clinthera.2018.03.009>.
- 98 Farmakiotis D, Kontoyiannis DP. Mucormycoses. *Infect Dis Clin North Am*. 2016;30(1):143–163. <https://doi.org/10.1016/j.jidc.2015.10.011>.
- 99 Larcher G, Dias M, Razafimandimby B, Bomal D, Bouchara JP. Siderophore production by pathogenic mucorales and uptake of deferoxamine B. *Mycopathologia*. 2013;176(5–6):319–328. <https://doi.org/10.1007/s11046-013-9693-5>.
- 100 Magdaleno F, Blajszczak C, Charles-Ni-o C, et al. Aminoguanidine reduces diabetes-associated cardiac fibrosis. *Exp Ther Med*. 2019;18(4):3125–3138. <https://doi.org/10.3892/etm.2019.7921>.
- 101 De Melo LGP, Nunes SOV, Anderson G, et al. Shared metabolic and immune-inflammatory, oxidative and nitrosative stress pathways in the metabolic syndrome and mood disorders. *Prog Neuro Psychopharmacol Biol Psychiatr*. 2017;78:34–50. <https://doi.org/10.1016/j.pnpb.2017.04.027>.
- 102 Wang M, Wey S, Zhang Y, Ye R, Lee AS. Role of the unfolded protein response regulator GRP78/BiP in development, cancer, and neurological disorders. *Antioxidants Redox Signal*. 2009;11(9):2307–2316. <https://doi.org/10.1089/ars.2009.2485>.
- 103 Casas C. GRP78 at the centre of the stage in cancer and neuroprotection. *Front Neurosci*. 2017;11(177):1–15. <https://doi.org/10.3389/fnins.2017.00177>.
- 104 Ting J, Lee AS. Human gene encoding the 78,000-dalton glucose-regulated protein and its pseudogene: structure, conservation, and regulation. *DNA*. 1988;7(4):275–286. <https://doi.org/10.1089/dna.1988.7.275>.
- 105 Yang J, Nune M, Zong Y, Zhou L, Liu Q. Close and allosteric opening of the polypeptide-binding site in a human Hsp70 chaperone BiP. *Structure*. 2015;23(12):2191–2203. <https://doi.org/10.1016/j.str.2015.10.012>.
- 106 Hughes SJ, Antoshchenko T, Chen Y, Lu H, Pizarro JC, Park HW. Probing the ATP site of GRP78 with nucleotide triphosphate analogs. *PLoS One*. 2016;11(5), e0154862. <https://doi.org/10.1371/journal.pone.0154862>.
- 107 Hendershot LM, Valentine VA, Lee AS, Morris SW, Shapiro DN. Localization of the gene encoding human bip/grp78, the endoplasmic reticulum cognate of the hsp70 family, to chromosome 9q34. *Genomics*. 1994;20(2):281–284. <https://doi.org/10.1006/geno.1994.1166>.
- 108 Roller C, Maddalo D. The molecular chaperone GRP78/BiP in the development of chemoresistance: mechanism and possible treatment. *Front Pharmacol*. 2013;4(10):1–5. <https://doi.org/10.3389/fphar.2013.00010>.
- 109 Kwon JW, Jung I, Lee D. Glucose-regulated protein 78 in the aqueous humor in diabetic macular edema patients. *Medicine*. 2018;97(45), e12757. <https://doi.org/10.1097/MD.00000000000012757>.
- 110 Sun FC, Wei S, Li CW, Chang YS, Chao CC, Lai YK. Localization of GRP78 to mitochondria under the unfolded protein response. *Biochem J*. 2006;396(1):31–39. <https://doi.org/10.1042/BJ20051916>.
- 111 Ni M, Zhang Y, Lee AS. Beyond the endoplasmic reticulum: atypical GRP78 in cell viability, signalling and therapeutic targeting. *Biochem J*. 2011;434(2):181–188. <https://doi.org/10.1042/BJ20101569>.
- 112 Gonzalez-Gronow M, Selim MA, Papalás J, Pizzo SV. GRP78: a multifunctional receptor on the cell surface. *Antioxidants Redox Signal*. 2009;11(9):2299–2306. <https://doi.org/10.1089/ars.2009.2568>.
- 113 Crane ED, Al-Hashimi AA, Chen J, et al. Anti-GRP78 autoantibodies induce endothelial cell activation and accelerate the development of atherosclerotic lesions. *JCI insight*. 2018;3(24), e99363. <https://doi.org/10.1172/jci.insight.99363>.
- 114 Van Krieken R, Mehta N, Wang T, et al. Cell surface expression of 78-kDa glucose-regulated protein (GRP78) mediates diabetic nephropathy. *J Biol Chem*. 2019;294(19):7755–7768. <https://doi.org/10.1074/jbc.ra118.006939>.
- 115 Liu M, Spellberg B, Phan QT, et al. The endothelial cell receptor GRP78 is required for mucormycosis pathogenesis in diabetic mice. *J Clin Invest*. 2010;120(6):1914–1924. <https://doi.org/10.1172/JCI42164>.
- 116 Gebremariam T, Liu M, Luo G, et al. CotH3 mediates fungal invasion of host cells during mucormycosis. *J Clin Invest*. 2014;124(1):237–250. <https://doi.org/10.1172/JCI71349>.
- 117 Ha DP, Van Krieken R, Carlos AJ, Lee AS. The stress-inducible molecular chaperone GRP78 as potential therapeutic target for coronavirus infection. *J Infect*. 2020;81(3):452–482. <https://doi.org/10.1016/j.jinf.2020.06.017>.
- 118 Alqarhi A, Gebremariam T, Gu Y, et al. GRP78 and integrins play different roles in host cell invasion during mucormycosis. *mBio*. 2020;11(3). <https://doi.org/10.1128/mBio.01087-20>. e01087-20.
- 119 Shumilov E, Bacher U, Perske C, et al. In situ validation of the endothelial cell receptor GRP78 in a case of rhinocerebral mucormycosis. *Antimicrob Agents Chemother*. 2018;62(5). <https://doi.org/10.1128/AAC.00172-18>. e00172-18.
- 120 Istitico R, Sirec T, Giglio R, et al. Flexibility of the programme of spore coat formation in Bacillus subtilis: bypass of CotE requirement by over-production of CotH. *PLoS One*. 2013;8(9), e74949. <https://doi.org/10.1371/journal.pone.0074949>.
- 121 Nguyen KB, Sreelatha A, Durrant ES, et al. Phosphorylation of spore coat proteins by a family of atypical protein kinases. *Proc Natl Acad Sci USA*. 2016;113(25):E3482–E3491. <https://doi.org/10.1073/pnas.1605917113>.
- 122 Gebremariam T, Alkhazraji S, Soliman SSM, et al. Anti-CotH3 antibodies protect mice from mucormycosis by prevention of invasion and augmenting opsonophagocytosis. *Sci Adv*. 2019;5(6). <https://doi.org/10.1126/sciadv.aaw1327>.
- 123 Li J, Lee A. Stress induction of GRP78/BiP and its role in cancer. *Curr Mol Med*. 2006;6(1):45–54. <https://doi.org/10.2174/156652406775574523>.
- 124 Baldin C, Ibrahim AS. Molecular mechanisms of mucormycosis—the bitter and the sweet. *PLoS Pathog*. 2017;13(8):1–9. <https://doi.org/10.1371/journal.ppat.1006408>.
- 125 Boelaert JR, De Locht M, Van Cutsem J, et al. Mucormycosis during deferoxamine therapy is a siderophore-mediated infection: in vitro and in vivo animal studies. *J Clin Invest*. 1993;91(5):1979–1986. <https://doi.org/10.1172/JCI116419>.
- 126 Bouchara JP, Oumeziane NA, Lissitzky JC, Larcher G, Tronchin G, Chabasse D. Attachment of spores of the human pathogenic fungus Rhizopus oryzae to extracellular matrix components. *Eur J Cell Biol*. 1996;70(1):76–83.
- 127 Spellberg B, Walsh TJ, Kontoyiannis DP, Edwards JJ, Ibrahim AS. Recent advances in the management of mucormycosis: from bench to bedside. *Clin Infect Dis*. 2009;48(12):1743–1751. <https://doi.org/10.1086/599105>.
- 128 Therakathu J, Prabhu S, Irodi A, Sudhakar SV, Yadav VK, Rupa V. Imaging features of rhinocerebral mucormycosis: a study of 43 patients. *Egypt J Radiol Nucl Med*. 2018;49(2):447–452. <https://doi.org/10.1016/j.ejrnm.2018.01.001>.
- 129 Guarnier J, Brandt ME. Histopathologic diagnosis of fungal infections in the 21st century. *Clin Microbiol Rev*. 2011;24(2):247–280. <https://doi.org/10.1128/CMR.00053-10>.



- 130 Heaton SM, Weintrob AC, Downing K, et al. Histopathological techniques for the diagnosis of combat-related invasive fungal wound infections. *BMC Clin Pathol*. 2016;16(11). <https://doi.org/10.1186/s12907-016-0033-9>.
- 131 Herrera D, Dublin A, Ormsby E, Aminpour S, Howell L. Imaging findings of rhinocerebral mucormycosis. *Skull Base*. 2008;19(2):117–125. <https://doi.org/10.1055/s-2008-1093099>.
- 132 Baldin C, Soliman SSM, Jeon HH, et al. PCR-based approach targeting mucorales-specific gene family for diagnosis of mucormycosis. *J Clin Microbiol*. 2018;56(10), e00746. <https://doi.org/10.1128/JCM.00746-18>.
- 133 Singhal T. A review of coronavirus disease-2019 (COVID-19). *Indian J Pediatr*. 2020; 87(4):281–286. <https://doi.org/10.1007/s12098-020-03263-6>.
- 134 Veronese N, Demurtas J, Yang L, et al. Use of corticosteroids in Coronavirus disease 2019 pneumonia: a systematic review of the literature. *Front Med*. 2020;7(170). <https://doi.org/10.3389/fmed.2020.00170>.
- 135 Guinea J, Escibano P, Vena A, et al. Increasing incidence of mucormycosis in a large Spanish hospital from 2007 to 2015: epidemiology and microbiological characterization of the isolates. *PLoS One*. 2017;12(6):1–10. <https://doi.org/10.1371/journal.pone.0179136>.
- 136 Tissot F, Agrawal S, Pagano L, et al. ECIL-6 guidelines for the treatment of invasive candidiasis, aspergillosis and mucormycosis in leukemia and hematopoietic stem cell transplant patients. *Haematologica*. 2017;102(3):433–444. <https://doi.org/10.3324/haematol.2016.152900>.
- 137 Katragkou A, Walsh TJ, Roilides E. Why is mucormycosis more difficult to cure than more common mycoses? *Clin Microbiol Infect*. 2014;20(6):74–81. <https://doi.org/10.1111/1469-0691.12466>.
- 138 Spellberg B, Ibrahim AS. Recent advances in the treatment of mucormycosis. *Curr Infect Dis Rep*. 2010;12(6):423–429. <https://doi.org/10.1007/s11908-010-0129-9>.
- 139 Sen M, Lahane S, Lahane TP, Parekh R, Honavar SG. Mucor in a viral land: a Tale of two pathogens. *Indian J Ophthalmol*. 2021;69(2):244–252. [https://doi.org/10.4103/ijo.IJO\\_3774\\_20](https://doi.org/10.4103/ijo.IJO_3774_20).
- 140 Fox A, Janson B, Stiff H, et al. A multidisciplinary educational curriculum for the management of orbital compartment syndrome. *AJEM (Am J Emerg Med)*. 2020;38(6):1278–1280. <https://doi.org/10.1016/j.ajem.2019.12.002>.
- 141 Cornely OA, Alastruey-Izquierdo A, Arenz D, et al. Global guideline for the diagnosis and management of mucormycosis: an initiative of the European confederation of medical Mycology in cooperation with the mycoses study Group education and research Consortium. *Lancet Infect Dis*. 2019;19(12):405–421. [https://doi.org/10.1016/S1473-3099\(19\)30312-3](https://doi.org/10.1016/S1473-3099(19)30312-3).
- 142 Rawson TM, Moore LS, Zhu N, et al. Bacterial and fungal co-infection in individuals with coronavirus: a rapid review to support COVID-19 antimicrobial prescribing | Clinical Infectious Diseases | Oxford Academic. *Clin Infect Dis*. 2020;71(9): 2459–2468.
- 143 Lee AS, Lee PWY, Allworth A, Smith T, Sullivan TJ. Orbital mycoses in an adult subtropical population. *Eye*. 2020;34:1640–1647. <https://doi.org/10.1038/s41433-019-0733-3>.
- 144 Hirabayashi KE, Kalin-Hajdu E, Brodie FL, Kersten RC, Russell MS, Reza Vagefi M. Retrobulbar injection of amphotericin B for orbital mucormycosis. *Ophthalmic Plast Reconstr Surg*. 2017;33(4):e94–e97. <https://doi.org/10.1097/IOP.0000000000000806>.
- 145 Handzel O, Landau Z, Halperin D. Liposomal amphotericin B treatment for rhinocerebral mucormycosis: how much is enough? *Rhinology*. 2003;41(3): 184–186.
- 146 Muthu V, Agarwal R, Dhooria S, et al. Has the mortality from pulmonary mucormycosis changed over time? A systematic review and meta-analysis. *Clin Microbiol Infect*. 2021;27(4):538–549. <https://doi.org/10.1016/j.cmi.2020.12.035>.
- 147 Jeong W, Keighley C, Wolfe R, et al. Contemporary management and clinical outcomes of mucormycosis: a systematic review and meta-analysis of case reports. *Int J Antimicrob Agents*. 2019;53(5):589–597. <https://doi.org/10.1016/j.ijantimicag.2019.01.002>.
- 148 Kimmig LM, Wu D, Gold M, et al. IL-6 inhibition in critically ill COVID-19 patients is associated with increased secondary infections. *Front Med*. 2020;7(583897):1–7. <https://doi.org/10.3389/fmed.2020.583897>.
- 149 Kumar G, Adams A, Hererra M, et al. Predictors and outcomes of healthcare-associated infections in COVID-19 patients. *Int J Infect Dis*. 2021;104:287–292. <https://doi.org/10.1016/j.ijid.2020.11.135>.

### Related links

- Bangladesh reports 1st death by black fungus: <https://www.aa.com.tr/en/asia-pacific/bangladesh-reports-1st-death-by-black-fungus/2253604>.
- Uruguay reports "black fungus" in a patient recovered from COVID-19: <https://amp.dw.com/es/uruguay-reporta-hongo-negro-en-paciente-recuperado-de-covid-19/a-57695374>.
- Two cases of "black fungus" confirmed in Paraguay: <https://www.rdn.com.py/2021/05/27/confirman-dos-casos-de-hongo-negro-en-paraguay/>.
- Iraq detects five cases of the deadly "black fungus" among coronavirus patients: <https://globelivemedia.com/world/iraq-detects-five-cases-of-the-deadly-black-fungus-among-coronavirus-patients/>.
- First case of "black fungus" detected in Chile in a patient with Covid-19: it is the second reported in Latin America: <https://m.elmostrador.cl/dia/2021/05/28/detectan-primero-caso-de-hongo-negro-en-chile-en-paciente-con-covid-19-es-el-segundo-reportado-en-latinoamerica/>.
- 5,500 cases, 126 lives lost: Black fungus stalks states, Maharashtra worst-hit: [https://m.timesofindia.com/india/black-fungus-stalks-states-5500-cases-126-lives-lost/amp\\_articles/82813528.cms](https://m.timesofindia.com/india/black-fungus-stalks-states-5500-cases-126-lives-lost/amp_articles/82813528.cms).
- India faces black fungus epidemic as cases climb: <https://www.hindustantimes.com/india-news/india-faces-black-fungus-epidemic-as-cases-climb-101621550432802-amp.html>.
- Total Cases of Black Fungus In India Is 11717 State Gujarat And Maharashtra Has Maximum Number: <https://newsbust.in/total-cases-of-black-fungus-in-india-is-11717-state-gujarat-and-maharashtra-has-maximum-number/amp/>.
- Delhi faces acute shortage of Amphotericin B, drug used to treat black fungus, as cases rise in city: <https://www.indiatoday.in/amp/cities/delhi/story/delhi-shortage-amphotericin-drug-black-fungus-1805752-2021-05-22>.



# Source details

[Feedback >](#) [Compare sources >](#)

## Clinical Epidemiology and Global Health

Open Access [i](#)

Scopus coverage years: from 2013 to Present

Publisher: Elsevier

E-ISSN: 2213-3984

Subject area:

Medicine: Public Health, Environmental and Occupational Health

Medicine: Infectious Diseases

Medicine: Epidemiology

Medicine: Microbiology (medical)

Source type: Journal

[View all documents >](#)

[Set document alert](#)

[Save to source list](#)

CiteScore 2022

4.3



SJR 2022

0.615



SNIP 2022

0.995





## Drug-induced diabetes and hepatotoxicity in COVID-19 patients

**Keywords:**  
 COVID-19  
 Diabetes  
 Drug toxicity  
 Hepatotoxicity  
 Corticosteroid

Dear Editor,

COVID-19, a newly found diabetes-related health risk, has been linked to diabetic ketoacidosis and drug-related liver disorders. SARS-CoV-2 may cause pleiotropic changes in glucose metabolism, which could exacerbate the pathophysiology of pre-existing

diabetes or lead to new disease processes. In COVID-19 treatment, physicians often use glucocorticoid drugs such as methylprednisolone and dexamethasone to control the inflammatory changes during COVID-19 and prevent the severity. Corticosteroids stimulate endogenous glucose production, promote gluconeogenesis, and antagonize insulin's metabolic functions. They also increase the effects of other counterregulatory hormones, like glucagon and adrenaline, which stimulate endogenous glucose synthesis. It has also been demonstrated that the nuclear receptor peroxisome proliferator-activated receptor is required for the increase in endogenous glucose synthesis generated by corticosteroids. Corticosteroids inhibit peripheral glucose absorption in muscle and adipose tissue. Corticosteroids also reduce insulin synthesis and secretion from pancreatic  $\beta$ -cells, causing  $\beta$ -cell failure indirectly through lipotoxicity [1]. Normoglycemic individuals with

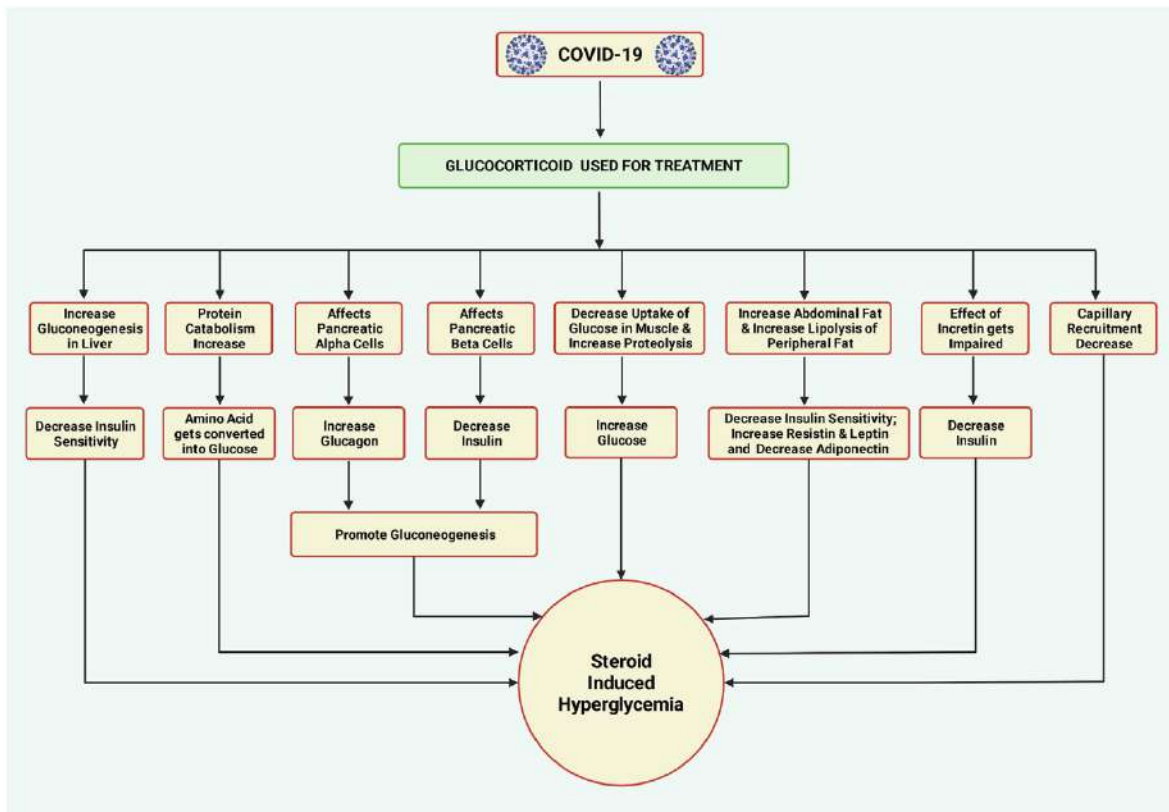


Fig. 1. Glucocorticoid-Induced Hyperglycemia [2]. (Created with BioRender.com).

decreased insulin sensitivity and insulin production at a low rate prior to steroid use who develop hyperglycemia as a result of the steroids they take (Fig. 1) [2]. Corticosteroids, which are produced from cholesterol metabolism, have the ability to disrupt numerous components of the body's glucose homeostasis. These compounds must be assessed since they alter liver metabolism and steatosis [3].

Various studies show drug-induced liver injury coupled with COVID-19 therapy. According to one study, more than half of the COVID-19 patients who had normal liver function indicators when they arrived had abnormal liver function markers one week later [4]. As per the randomized clinical trials lopivir-ritonavir treatment has been linked to increased AST, ALT, and bilirubin levels [5], whilst remdesivir has only been linked to elevated AST and ALT levels in both treated and control groups [6–8]. Additionally, the use of acetaminophen and hydroxychloroquine has been associated to abnormal liver markers [6,9]. Furthermore, the WHO safety report database clearly demonstrates that remdesivir use is associated with a statistically significant risk of liver damage [10]. The combination of angiotensin II receptor blockers and angiotensin-converting enzyme inhibitors causes increased liver enzymes [5]. Another study of 1040 COVID-19 patients recently revealed that 22.6% of the participants had elevated ALT/AST levels [11]. The tocilizumab medication group had a significantly higher ALT rise in the retrospective investigation of observational cohort analysis [12]. Favipiravir, an oral broad-spectrum, acting as an inhibitor of viral RNA-dependent RNA polymerase, causes cholestatic liver damage in those with ALD-related liver disease.

#### Declaration of competing interest

There are no financial and non-financial conflicts of interest.

#### References

- [1] Tamez-Pérez HE. Steroid hyperglycemia: prevalence, early detection and therapeutic recommendations: a narrative review. *World J Diabetes* 2015;6:1073. <https://doi.org/10.4239/wjd.v6.i8.1073>.
- [2] van Raalte DH, Ouwens DM, Diamant M. Novel insights into glucocorticoid-mediated diabetogenic effects: towards expansion of therapeutic options? *Eur J Clin Invest* 2009;39:81–93. <https://doi.org/10.1111/j.1365-2362.2008.02067.x>.
- [3] Alessi J, de Oliveira GB, Schaan BD, Telo GH. Dexamethasone in the era of COVID-19: friend or foe? An essay on the effects of dexamethasone and the potential risks of its inadvertent use in patients with diabetes. *Diabetol Metab Syndrome* 2020;12. <https://doi.org/10.1186/s13098-020-00583-7>.
- [4] Fan Z, Chen L, Li J, Cheng X, Yang J, Tian C, et al. Clinical features of COVID-19-related liver functional abnormality. *Clin Gastroenterol Hepatol* 2020;18:1561–6. <https://doi.org/10.1016/j.cgh.2020.04.002>.
- [5] Cai Q, Huang D, Yu H, Zhu Z, Xia ZSY, et al. COVID-19: abnormal liver function tests. *J Hepatol* 2020;73:566–74.
- [6] Hernandez Av, Roman YM, Pasupuleti V, Barboza JJ, Michael White C. Update alert 3: hydroxychloroquine or chloroquine for the treatment or prophylaxis of COVID-19. *Ann Intern Med* 2020;173:W156–7. <https://doi.org/10.7326/L20-1257>.
- [7] Goldman JD, Lye DCB, Hui DS, Marks KM, Bruno R, Montejano R, et al. Remdesivir for 5 or 10 Days in patients with severe covid-19. *N Engl J Med* 2020;383:1827–37. <https://doi.org/10.1056/nejmoa2015301>.
- [8] Beigel JH, Tomashek KM, Dodd LE, Mehta AK, Zingman BS, Kalil AC, et al. Remdesivir for the treatment of covid-19 - final report. *N Engl J Med* 2020;383:1813–26. <https://doi.org/10.1056/NEJMoa2007764>.
- [9] Acetaminophen, Livertox. LiverTox: clinical and research information on drug-induced liver injury 2020. Bethesda (MD): National Institute of Diabetes and Digestive and Kidney Disease; 2012.
- [10] Montastruc F, Thuriot S, Durrieu G. Hepatic disorders with the use of remdesivir for coronavirus 2019. *Clin Gastroenterol Hepatol* 2020;18:2835–6. <https://doi.org/10.1016/j.cgh.2020.07.050>.
- [11] Yip TCF, Lui GCY, Wong VWS, Chow VCY, Ho THY, Li TCM, et al. Liver injury is independently associated with adverse clinical outcomes in patients with COVID-19. *Gut* 2021;70:733–42. <https://doi.org/10.1136/gutjnl-2020-321726>.
- [12] Guaraldi g, Meschiari m, Cozzi- Lepri A, Milic J, Tonelli R, Menozzi M, et al. Tocilizumab in patients with severe COVID- 19: a retrospective cohort study. *Lancet Rheumatol* 2020;2:e474–84.

Rajdeep Ghosh, Ullash Basak  
GSL Medical College and General Hospital, NH 16, Lakshmi Puram,  
Rajahmundry, Andhra Pradesh, India

Debasish Ghosh  
Vishwanath Ayurved Mahavidyalaya and Hospital, 94, Grey Street,  
Kolkata, West Bengal, India

Joy Sarkar\*  
Department of Botany, Dinabandhu Andrews College, Garia, Kolkata,  
West Bengal, India

\* Corresponding author.  
E-mail address: [jsarkar80@gmail.com](mailto:jsarkar80@gmail.com) (J. Sarkar).

23 February 2022



## Source details

[Feedback >](#) [Compare sources >](#)

### Diabetes and Metabolic Syndrome: Clinical Research and Reviews

Scopus coverage years: from 2007 to Present

Publisher: Elsevier

ISSN: 1871-4021 E-ISSN: 1878-0334

Subject area: [Medicine: Internal Medicine](#) [Medicine: Endocrinology, Diabetes and Metabolism](#)

Source type: Journal

[View all documents >](#)[Set document alert](#)[Save to source list](#)

CiteScore 2022

15.4



SJR 2022

1.495



SNIP 2022

1.791





## Review article

# Clinical aspects and presumed etiology of multisystem inflammatory syndrome in children (MIS-C): A review

Anusrita Kundu<sup>a,1</sup>, Swagata Maji<sup>a,1</sup>, Suchismita Kumar<sup>a,1</sup>, Shreya Bhattacharya<sup>a,1</sup>, Pallab Chakraborty<sup>b,1</sup>, Joy Sarkar<sup>c,\*</sup>

<sup>a</sup> Department of Botany, Bethune College, Manicktala, Kolkata, West Bengal, 700006, India

<sup>b</sup> Department of Botany, Acharya Prafulla Chandra College, New Barrakpur, Kolkata, West Bengal, 700131, India

<sup>c</sup> Department of Botany, Dinabandhu Andrews College, Garia, Kolkata, West Bengal, 700084, India



## ARTICLE INFO

## Keywords:

MIS-C  
Pediatric patient  
SARS-CoV-2  
Kawasaki disease  
Multiorgan failure  
Macrophage and antibody-dependent enhancement (ADE)

## ABSTRACT

The COVID-19 outbreak sparked by SARS-CoV-2, begat significant rates of malady worldwide, where children with an abnormal post-COVID ailment called the Multisystem Inflammatory Syndrome (MIS-C), were reported by April 2020. Here we have reviewed the clinical characteristics of the pediatric patients and the prognosis currently being utilized. A vivid comparison of MIS-C with other clinical conditions has been done. We have addressed the probable etiology and fundamental machinery of the inflammatory reactions, which drive organ failure. The involvement of androgen receptors portrays the likelihood of asymptomatic illness in children below adolescence, contributing to the concept of antibody-dependent enhancement.

## 1. Introduction

The COVID-19 pandemic generated by Severe acute respiratory syndrome coronavirus 2 has swiftly expanded globally with about 18 million confirmed reports by August 2020, after a multitude of pneumonia occurrences resulting from unexplained causes was formerly detected in Wuhan (China) in December 2019. Children generally account for a tiny percentage of COVID-19 instances. However, there is confusion regarding the real disease risk of adolescents and children, due to asymptomatic illness, inadequate examination of diagnostically quiet or moderate cases, or doubts about the accuracy of existing testing protocols.<sup>1</sup> In children, COVID-19 hospitalization was uncommon, contributing to only 0.1% of all fatalities.<sup>2</sup> But between April 2020, and July 2020, there has been an upsurge in the incidence of a Kawasaki-like disease in youngsters by 30 times. Pediatricians in the United Kingdom

initially declared a group of children having fever, cardiovascular shock, and hyper inflammation in April 2020, with symptoms that were identical to those of Kawasaki Disease, cytokine storm, or toxic shock syndrome on the grounds of clinical studies recorded from United States, United Kingdom, Italy, Switzerland, and France.<sup>3</sup> The ailment was named “pediatric inflammatory multisystem syndrome temporally associated with SARS-CoV-2” by the Royal College of Pediatrics & Child Health. Next, the Centers for Disease Control and Prevention in the United States and the World Health Organization issued their separate case definitions for the ailment, renaming it as a multisystem inflammatory syndrome in children.<sup>4,5</sup> Scientists have named it profusely like “Kawashocky”, “Coronasacki”, “hyperinflammatory shock in children with COVID-19”, “pediatric COVID-19”, “Pediatric COVID-19 Associated Inflammatory Disorder” and many more because it’s a novel illness. Reports have been identified where, 15 children, 2–15 years old in the

**Abbreviations:** SARS-COV-2, Severe Acute Respiratory Syndrome Coronavirus 2; KD, Kawasaki Disease; PIMS-TS, Pediatric Inflammatory Multisystem Syndrome Temporally Associated; CDC, Centres for Disease Control and Prevention; PCAID, Pediatric COVID-19 Associated Inflammatory Disorder; MIS-C, Multisystem Inflammatory Syndrome in Children; RT-PCR, Real Time- Polymerase Chain Reaction; PPT, Prolonged Prothrombin Time; LVEF, Left Ventricular Ejection Fraction; ARDS, Acute Respiratory Distress Syndrome; CRP, C-reactive protein; BNP, Brain Natriuretic Peptide; TNP, Tumour Necrosis Factor; TSS, Toxic Shock Syndrome; SHLH/MAS, Secondary Hemophagocytic Lymphohistiocytosis/Macrophage Activation Syndrome; IVIG, Intravenous Immunoglobulin; PTT, The Prothrombin Time Test; ESR, Erythrocyte Sedimentation Rate; ACE2, Angiotensin-Converting Enzyme-2; TMPRSS2, Transmembrane Protease, Serine 2; TTSPs, Type II Transmembrane Serine Protease; AR, Allosomal Androgen Receptor; ADE, Antibody-Dependent Enhancement; NLRP3, NLR family Pyrin Domain Containing 3.

\* Corresponding author.

E-mail address: [jsarkar80@gmail.com](mailto:jsarkar80@gmail.com) (J. Sarkar).

<sup>1</sup> These authors have contributed equally to this work.

<https://doi.org/10.1016/j.cegh.2022.100966>

Received 10 November 2021; Received in revised form 8 January 2022; Accepted 12 January 2022

Available online 3 February 2022

2213-3984/© 2022 The Author(s). Published by Elsevier B.V. on behalf of INDIACLEN. This is an open access article under the CC BY-NC-ND license (<http://creativecommons.org/licenses/by-nc-nd/4.0/>).

United States with MIS-C were shifted to the intensive care unit, 102 youths with identical symptoms, were recorded in New York many of whom tested positive for SARS-CoV-2 infection.<sup>3,6,7</sup> 4196 MIS-C Patients and 37 MIS-C deaths, both meeting MIS-C case definitions were confirmed to the CDC by June 28, 2021.<sup>8</sup> Some organs and tissues, including the heart, lungs, blood vessels, kidneys, digestive system, nervous system, skin, and eyes, become severely inflamed in children who acquire MIS-C. The signs and symptoms vary depending on which body parts are affected.<sup>2,3,9-13</sup> It remains evident whether it is a post-sepsis or delayed infectious consequence or is chiefly connected with SARS-CoV-2 infection, although the recent epidemiologic accounts are extremely provocative of a relationship.<sup>13</sup>

## 2. Patient demographics

The demographic analysis deals with the assessment of the population, based on variables such as age, race, and sex. Several studies under the present body of knowledge and close monitoring of MIS-C patients have led to a subjective result of the appearance of this syndrome in children.

- Patients with MIS-C had a median age of 9 years. Between the ages of 5 and 13, half of the children with MIS-C were diagnosed. In other studies, the range of age is from 7 months to 20 years, with the highest proportion occurring in youths under the age of 21.<sup>4,8,9,13</sup>
- Early findings showed males may be highly represented, same as KD. MIS-C has yet to demonstrate a definite gender preference, but only a small male preponderance is found in six investigations. Sixty percent of reported patients were male, according to instances reported to the CDC on or before June 28, 2021.<sup>4,8,14-20</sup>
- Many studies have found that MIS-C has a significant impact on African American, African/Afro-Caribbean, and Hispanic youngsters. African/Afro-Caribbean children constituted the largest fraction of the cases in European research with relevant race/ethnicity data, ranging from 38% to 62% of MIS-C patients. The African American and Hispanic were around 18–40% and 24–45% respectively among the MIS-C affected children, in one of the U.S. reports. And, till June 2020, 62% of all cases confirmed to the CDC consisted of Hispanic children or Latino (1246 cases) or Black, Non-Hispanic (1175 cases).<sup>4,8,10,14,21-25</sup>
- Cases recorded at CDC till June 2020 show that 99% of MIS-C sufferers tested positive for SARS-CoV-2, the rest 1% of patients might have gotten into touch with a COVID-19 infected patient.<sup>8</sup> In a separate US analysis with 577 MIS-C patients, 52% had a positive SARS-CoV-2 Real Time-Polymerase Chain Reaction test result, 45% were solely SARS-CoV-2 antibody positive, 31% were positive for both, and an antibody test was not conducted in 19% of the cases.<sup>10</sup> Out of 29 patients in a finding, SARS-CoV-2 Polymerase Chain Reaction tests yielded positive results in 10 cases, while SARS-CoV-2 immunoglobulin G assays yielded positive results in 19 patients.<sup>26</sup> In these children, the initial COVID-19 infection is nearly often moderate or asymptomatic.<sup>27</sup>
- Feldstein et al. spotted that 73% of MIS-C affected patients were priorly healthy in case reports of 186 individuals.<sup>16</sup> A vast majority of studies found almost no comorbidities. Obesity and a history of asthma have been the most frequent comorbidities in individuals who did possess past medical issues across studies, with autoimmune illness, long-term lung ailment, diabetes, cancer, congenital heart disease, and neurological disorders as fundamental detections.<sup>4,14,15,18,21-23,28</sup>

### 2.1. Case definition of MIS-C

The WHO has published the case-definition MIS-C, where the following six criteria are to be fulfilled.

1. Age 0–19 years
2. Fever for  $\geq 3$  days
3. The clinical indication of the involvement of multiple organ systems (At least 2 of the mentioned manifestations)
  - i. Erythema, bilateral non-purulent conjunctivitis, or mucocutaneous or dermatological inflammation signs on mouth, hands, or feet.
  - ii. Hypotension or shock
  - iii. Cardiac disability, pericardial inflammation, coronary anomalies, or valvulitis (including echocardiographic findings or elevated troponin/brain natriuretic peptide)
  - iv. Presence of coagulopathy (prolonged prothrombin time; amplified D-dimer)
  - v. Acute gastrointestinal symptoms (diarrhoea, vomiting, or abdominal pain)
4. Inflammation markers that are elevated (namely, erythrocyte sedimentation rate, C-reactive protein, or procalcitonin).
5. Other microbiological causes of inflammation, like bacterial sepsis and staphylococcal/streptococcal toxic shock syndromes are not identified.
6. Reports testing positive for present or past SARS-CoV-2 pathogenesis by RT-PCR, antibody, or antigen test; or interaction with a person infected with COVID-19.<sup>1,4,11-13,27</sup>

CDC also has a separate case definition that focuses on evidence of clinical symptoms involving several organs.<sup>4,27,29</sup>

## 3. Clinical manifestation

Knowledge revolving around the clinical condition of MIS-C patients is unfolding day by day.<sup>11</sup> As a significant percentage of SARS-CoV-2 infections has escaped diagnosis, the overall population of children residing in the danger for MIS-C is unclear, owing to the possibility of asymptomatic or paucisymptomatic infections.<sup>4</sup> Based on a temporal link of SARS-CoV-2 invasion with MIS-C, the average time between primary infection and the incidence of MIS-C symptoms, in children with a recorded history of confirmed or suspected COVID-19 infection, is two to six weeks.<sup>4,29</sup> The establishment of a severe inflammatory state is one of the major symptoms of MIS-C including, spiking and persistent fever ( $>39^{\circ}\text{C}$ - $40^{\circ}\text{C}$ ) with severe asthenia for a few couples of days, myalgia, swollen hands or feet, and multisystem damage (Fig. 1).<sup>3,4,6,9,11,14,27-29</sup>

### 3.1. Cardiovascular symptoms and image finding

Patients initially felt chest pain, with an average delay of 6 days between the outset of clinical symptoms and the outset of heart failure symptoms. They experienced cardiogenic shock upon their entry to the pediatric intensive care unit and were provided with inotropic support.<sup>11,20,30</sup> All of the investigations found cardiac abnormalities using echocardiography or electrocardiography, highlighting the appearance of myocardial dysfunction.<sup>4</sup> Echocardiography revealed depressed systolic function, with left ventricular ejection fraction of  $<55\%$  (moderate dysfunction) and sometimes  $<30\%$  (severe dysfunction),<sup>19,21,30</sup> pericarditis (pericardial effusion) and myocarditis, atrioventricular valve regurgitation, cardiac dysrhythmia, coronary dilation, or aneurysms with a medial z score range of 2.0–2.8 indicating small aneurysm and rarely giant aneurysm were reported.<sup>3,4,10,12-14,21,27,29-31</sup> In adolescents with vasodilatory shock, cardiac magnetic resonance imaging (MRI) revealed signs of myocardial edema, necessitating fluid resuscitation.<sup>13,29</sup> Cardiac involvement is an extensive factor to differentiate MIS-C from COVID-19.<sup>10</sup>

### 3.2. Respiratory symptoms and image findings

Though COVID-19-like respiratory complaints are not often

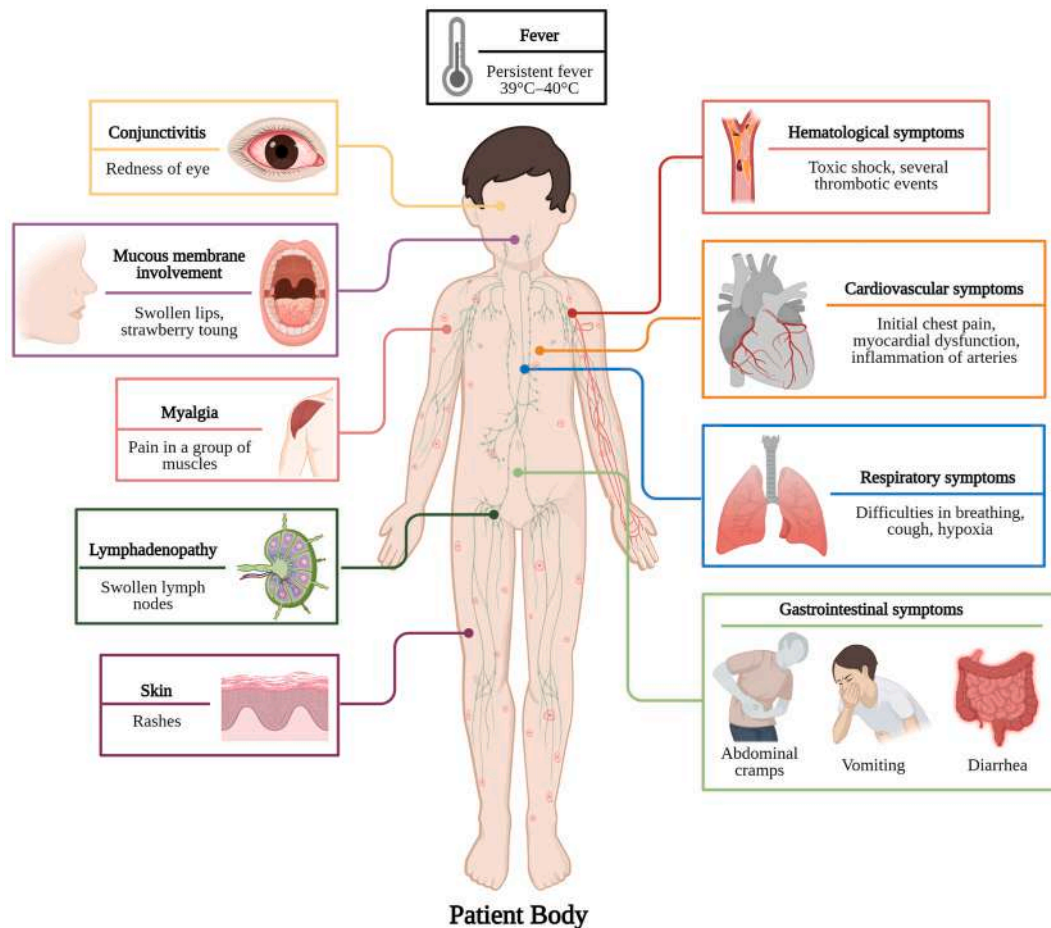


Fig. 1. Various types of MIS-C symptoms in pediatric patients. (Created with BioRender.com).

associated with MIS-C, difficulties in breathing like tachypnoea, cough, hypoxia, have been disclosed so far. Chest radiographs showed pulmonary edema, basilar opacities suggestive of atelectasis, either dependent or coercive as a consequence of pleural effusion, pulmonary infiltrates, pneumothorax, pulmonary hemorrhage, and bronchospasm, requiring the utility of bronchodilators continuously. Critical pulmonary infection, such as acute respiratory distress syndrome, was uncommon in children who needed supplemented oxygen or a ventilator for breathing support.<sup>4,6,10,11,21,27,29,31,32</sup>

### 3.3. Neurological symptoms and image findings

The youngsters have been observed with various neurologic issues. Headaches, hearing & visual problems, amnesia, meningitis, irritability, apathy, and lassitude are some of the symptoms. Encephalopathy, stroke or abrupt intracranial hemorrhage, uveitis, coma, seizures, demyelinating disease, aseptic meningoenzephalitis (strengthening pro-inflammatory Central nervous system feedback),<sup>31</sup> and brain death were among the profound neurologic findings seen in specific cases. Rare instances reported ischemic brain infarction, acute cerebral edema, and Guillain-Barre syndrome.<sup>4,10,11,20,27,29,31</sup>

### 3.4. Gastrointestinal symptoms and image finding

Gastrointestinal involvement was usually the most apparent attribute of MIS-C, reported in maximum patients often resembling abdominal infections.<sup>4,11,12</sup> Abdominal cramps, diarrhoea, and vomiting were among the prominent symptoms.<sup>4,11,12,14,27,29</sup> Abdominal ultrasonography and computed tomography of the abdomen and pelvis

disclosed grave results like appendicitis, gall bladder hydrops, ascites, mesenteric adenopathy, pleural effusions, enterocolitis, in certain cases terminal ileitis and colitis, all leading to hypovolemia. The pancreatic images reported pancreatomegaly, and those of the liver reported hepatomegaly, and biliary sludge, while increased renal echogenicity, lead to acute kidney failure.<sup>4,9,10,21,29,32</sup>

### 3.5. Mucocutaneous and dermatological symptoms

The mucocutaneous results were heterogeneous. Morbilliform, urticarial, scarlatiniform, and reticulated forms were among the morphologic features of exanthemas.<sup>26</sup> The area of the skin affected also differed where certain individuals were with restricted acrofacial inclusion while others harbored more extensive outbreaks.<sup>26</sup> Some studies have also revealed a strong age bias in the advent of symptoms.<sup>26</sup> The prevailing cutaneous records were conjunctivitis, hyperemia, periorbital swelling and erythema, and strawberry tongue. A few dermatological findings were whereas malar rashes, facial edema, palmar erythema, lip cracks, and lip hyperemia causing redness and swelling.<sup>4,10,11,21,26,29,32</sup> In a special case, a skin biopsy presented lymphocytic infiltrate as the root of skin lesion.<sup>26</sup>

### 3.6. Hematological findings

MIS-C patients were found with several thrombotic events where activation of coagulation lead to deep vein thrombosis, intracardiac thrombosis, cerebral venous sinus thrombosis, subarachnoid hemorrhage bringing about ischemic brain death.<sup>10,13,20,27,33</sup> A prothrombotic coagulopathy may be enhanced by MIS-C's hyperinflammatory



condition in conjunction with COVID-19 triggering pulmonary embolism.<sup>6,33</sup> Additional hematologic abnormalities comprise lymphopenia, neutrophilia, haematolysis, hypoxemia, ischemia, anemia, pancytopenia, and hemolytic uremic syndrome.<sup>10,11,33</sup>

### 3.7. Lymphatic findings

Swollen lymph node often called adenopathy has been noted as a common sign of inflammation in MIS-C-affected children encompassing distinct organs like mesenteric lymphadenitis and mediastinal and hilar lymphadenopathy which have been observed through thoracic imaging.<sup>6,11,32</sup>

### 3.8. Laboratory findings

The common feature found in every MIS-C patient is an extremely elevated level of inflammatory and cardiac indicators.<sup>4</sup> Inflammatory indicators like C-reactive protein, Serum interleukin-6, Ferritin, Procalcitonin are significantly raised.<sup>4,11,13,27,29,31,34–36</sup> The elevated values of CRP, Ferritin and Procalcitonin vary as 11.98–27.62 mg/dL, 370.7–1032.5 ng/ml and 8.41–31.96 ng/mL respectively.<sup>14</sup> The values of cardiac indicators like Troponin<sup>4</sup> and Brain natriuretic peptide<sup>4,11</sup> vary as 0.03–2.17 ng/mL, 229.5–1778.5 pg/mL respectively.<sup>14</sup> Another characteristic feature of MIS-C is raised levels of D-dimer,<sup>4,13,14,20,30–32,34–36</sup> Fibrinogen,<sup>4,13,14,29</sup> Factor VIII.<sup>13</sup> The value varies as 2.42–3.79 µg/mL for D-dimer<sup>14</sup> and 468.5–629 mg/mL for Fibrinogen.<sup>14</sup> The low percentage of Antithrombin III causes several types of thrombosis in patients.<sup>13</sup> Cytokines like Tumour necrosis factor, Interleukin-6, IL-1β are synthesized in excess amounts, which upregulate the inflammatory reaction.<sup>13,30</sup> MIS-C patients show abnormal Liver function test results having elevated Alanine transaminase and Aspartate transaminase.<sup>32,34,35</sup> The values of ALT and AST vary as 27.73–73.6 U/L and 36.25–56.75 U/L respectively.<sup>14</sup> MIS-C patients show a comparatively lower value of Lactate dehydrogenase enzyme than patients having severe COVID-19.<sup>14</sup> A higher Erythrocyte sedimentation rate value is also very common in MIS-C patients.<sup>11</sup> ESR value varies as 38–58 mm/hr<sup>14</sup> Low blood Sodium<sup>14</sup> and Albumin<sup>29,35,36,36</sup> and a high Creatinine<sup>34</sup> value are revealed by laboratory examination in MIS-C patients. According to a recent study, severe COVID-19 instances have a greater neutrophil to lymphocyte ratio.<sup>34</sup>

## 4. Comparing MIS-C with other associated diseases

Following the past COVID-19 infection, new publications have revealed that MIS-C possesses symptoms of an array of different disorders namely KD that had originated in Japan in 1967, Toxic Shock Syndrome that had originated in 1978, Secondary Hemophagocytic Lymphohistiocytosis/Macrophage Activation Syndrome, and Severe COVID-19 (Table 1).

## 5. A plausible course of patient management

There exist no definitive therapeutic guidelines for the treatment of MIS-C at this time, but few current administration and therapy options are available. Most of these treatment strategies have yielded a positive result.<sup>4</sup> Intravenous immunoglobulin and corticosteroids have been proven to be effective in various studies as a remedy for inflammation, leading to a quick recovery.<sup>4</sup> Use of IVIG similar to normal KD therapy and corticosteroids<sup>4,13,15,20,30,44</sup> has been encountered in MIS-C patients.<sup>9,11,13,21,26,32,45,46</sup> Patients with a low index of suspicion present with some but not all of the MIS-C symptoms should be examined for inflammatory screening, including a complete blood count and CRP, along with SARS-CoV-2 PCR and antibody testing.<sup>13</sup>

## 5.1. Hospital treatment

Empiric antibiotic coverage is prescribed in children, who have been assessed for having MIS-C and have been admitted to the hospital, with initial broad-spectrum antibiotics, since symptoms overlap with severe bacterial infections. Ceftriaxone is generally suggested if they are sick to a moderate extent. In cases of severe illness or shock, vancomycin, clindamycin, and cefepime, or vancomycin, meropenem, and gentamicin are recommended.<sup>13,45,47</sup> If redeliver (an antiviral drug with activity against SARS-CoV-2 approved for compassionate use in young children and restricted clinical trials) is available, it must be evaluated, especially for individuals who have been PCR positive and/or have a characteristic COVID-19 presentation.<sup>4,9,13,20,26,45</sup> For children, the current recommended dose is 5 mg/kg IV once (max dose 200 mg) on day 1, then 2.5 mg/kg IV daily for nine days (max dose 100 mg).<sup>13,45</sup> In case of all children exhibiting KD-like illness and evidence of significant inflammation (CRP >30 g/dL, ferritin >700 ng/mL), cardiac involvement, or multi-fold organ failure, 20–25 mg/kg/dose every 6 h (80–100 mg/kg/day) of aspirin is advised as a medication. However, individual health centers may use different amounts of aspirin. When a patient has been afebrile for 24 h or more, the aspirin dose typically reduces to 3–5 mg/kg as a single daily dose, which will be continued after discharge.<sup>9,11,13,30</sup> Anakinra is prescribed at a dose of 2–6 mg/kg/day IV/SQ, with the period of treatment determined with the help of a pediatric rheumatologist or immunologist.<sup>4,11–13,20,21,26,32,48–50</sup> A major percentage of patients got intravenous steroids, Infliximab, and IL-6 inhibitors (Tocilizumab or Siltuximab) as anti-inflammatory therapy.<sup>4,11–13,20,21,45,51,52</sup> Owing to the involvement of TNF-α in MIS-C, anti-TNF-α medication is useful for the control of auto-inflammatory disorders in which many cytokines are high, implying that anti-TNF-α therapy may stop a cytokine cascade on its own.<sup>51,53</sup>

## 5.2. ICU treatment

A significant percentage of MIS-C patients are referred to the ICU, frequently requiring respiratory and cardiac assistance. Several studies indicated that about 44–100% of the children were sent to the ICU.<sup>30</sup> A major proportion of children also required routine ventilation.<sup>18</sup> Mild to medium doses of vasoactive medicines, like vasopressors and inotropes, were regularly administered to MIS-C ICU patients due to shock-induced by myocardial dysfunction (e.g., acute myocarditis) and/or intense vasoplegia.<sup>22,30</sup>

## 5.3. Discharge norms

Studies have revealed several guidelines that are to be taken care of before patients are discharged off. Some of them include two days without fever, two days out of vasopressors and supplemented oxygen, two to four days of declining inflammatory markers like ferritin, D-dimer, CRP, lowers levels of troponin, standard Electrocardiogram (the German spelling- Elektrokardiogramm) with stable blood pressure.<sup>4,13,20,45,51</sup> Patients released from the emergency unit must receive particular discharge manuals including a follow-up clinic or telemedicine consultation within 72 h. A repetition of the laboratory tests must be conducted within one week. The interval between the initial echocardiography and the cardiology follow-up should be at least two weeks.<sup>13</sup>

## 6. Case study

COVID-19 instances (after COVID as well as current COVID) linked to MIS-C have been discovered all over the world. Some of the occurrences from various nations have been summarised in Table 2 and Table 3 simultaneously.

**Table 1**

Comparison between multisystem inflammatory syndrome in children (MIS-C), Kawasaki disease (KD), toxic shock syndrome (TSS), secondary hemophagocytic lymphohistiocytosis/macrophage activation syndrome (SHLH/MAS), and severe COVID-19.

Sl. No.	Characters	Multisystem inflammatory syndrome in children (MIS-C)	Other diseases associated with MIS-C				References	
			Kawasaki disease (KD)	Toxic Shock Syndrome (TSS)	Secondary Hemophagocytic lymphohistiocytosis/ Macrophage activation syndrome (SHLH/MAS)	Severe COVID-19 in children without MIS-C		Severe COVID-19 in adults
1.	Age of affected persons	Children of age range 8–10 are most commonly affected.	Usually in youngsters of less than five years of age.	Usually in children above the age of ten.	Mostly found in adults.	Adolescents are most commonly affected.	Death rates are increasing as people get older.	2,4,10,11,29,35,37
2.	Differences in gender	Males are mostly affected.	Males are mostly affected.	Females are mostly affected.	Occurs in males as well as females	There is no such differentiation. Both the genders are affected equally.	Males are mostly affected.	11,37
3.	Affected Ethnicity	Hispanic/Latino/African American	East Asian	No ethnic variation known	No difference	No difference	No difference	4,10,11,29,37
4.	Symptoms	A. Hypotension B. Rash	Generally absent	Almost always present	Generally absent	May be present or absent.	Almost always present	11,29
			Generally present	Generally present	Bleeding from the skin is noted in some cases.	May be present or absent.	May be present or absent.	2,4,38
	C. Fever D. Vomiting/ Diarrhoea/ or abdominal pain E. Respiratory distress F. Mucous Membrane Involvement	Present	Present	Present	Present	Present	Present	4,10,11,35,37–39
		Almost always present	Rare	Generally present	May be present or absent.	May be present or absent.	May be present or absent.	11,35,38,39
		Generally present	Rare	Almost always present	Generally present	Generally present	Generally present	11,37
		May be present or absent.	Generally present	May be present or absent.	Noted in some cases	Generally present	Generally present	11,38
5.	Underlying etiology	Assumed to be a post-infectious syndrome; the SARS-CoV-2 antibody test is frequently positive; in seronegative individuals, there is generally a history of exposure to a covid-19 positive individual.	No identifiable cause.	An infection caused by streptococcus or staphylococcus is a regular occurrence.	T-cells and macrophages possess hemophagocytic activity to expand and become highly activated.	There may be underlying comorbidity; SARS-CoV-2 RT-PCR is generally positive.	SARS-CoV-2 RT-PCR is frequently positive; Extreme sickness is frequently caused by pre-existing comorbidity.	4,29,37,404
6.	T Cells	Lymphopenia	Involvement of cytotoxic T cells	Lymphopenia	Activation and proliferation of CD8 <sup>+</sup> T cells and NK cells, including secretion of IFN $\gamma$	Usually, unaltered	Lymphopenia in severe disease	37,40
7.	Comorbidity as risk factors	Immune deficiency states may be present.	Rarely observed when it comes to original immunodeficiency and occasionally in case of acquired immunodeficiency.	Normally, nothing noteworthy	The cytokine storm plays a role in coronavirus infection. COVID-19-associated pneumonia. Some people have minimal or mild lung manifestations, with others having severe pulmonary dysfunction.	Comorbidity like malignancy, chronic lung disease and neurological disorder is linked to a more severe form of the disease.	Comorbidity like hypertension, diabetes mellitus, chronic heart disease is linked to a more severe form of the disease.	37,40,41

(continued on next page)

Table 1 (continued)

Sl. No.	Characters	Multisystem inflammatory syndrome in children (MIS-C)	Other diseases associated with MIS-C					References
			Kawasaki disease (KD)	Toxic Shock Syndrome (TSS)	Secondary Hemophagocytic lymphohistiocytosis/Macrophage activation syndrome (SHLH/MAS)	Severe COVID-19 in children without MIS-C	Severe COVID-19 in adults	
8.	Predominant manifestation	Gastrointestinal signs (abdominal discomfort, diarrhoea) are common, with more than 80% of patients experiencing them.	Symptoms of the gastrointestinal tract are rarely noticeable.	Rash, hypotension.	Unrelenting fevers, cytopenia, splenomegaly, hepatitis, coagulopathy, lymphadenitis, and hepatosplenomegaly multisystem organ failure, and death in its most severe form.	Cough, respiratory distress may be present, gastrointestinal symptoms are less common.	Cough, respiratory distress is common.	37,42,43
9.	Management	IVIG; steroids; IL-6 inhibitors IL-1 impede.	IVIG; steroid; IL-1 blockers	Antibiotics, IVIG	Involvement of particular cytokines in this phenomenon, especially TNF- $\alpha$ , IL-6, and IL-1 $\beta$	Antibiotics, antiviral medication, steroids, IVIG, IL-6 inhibitors	HCQS; steroids; IL-6 inhibitors, plasma in remission; antiviral therapies.	37,41

## 7. The most feasible mechanism of the build-out of MIS-C

Pediatric patients distressed with MIS-C exhibit large amounts of SARS-CoV-2 antibodies in their serum but test negative for the virus through RT-PCR, indicating that certified reports of COVID-19 are relatively few in children or they might have had a prior infection.<sup>1,3</sup> The feedback from antibodies in children was unique from those of the adults stating that the induction of adaptive immune reaction to SARS-CoV-2 virus in the former corresponds with the onset of inflammatory symptoms and is not influenced by viral attack.<sup>1</sup>

The dominant receptor for the ingress of the virus inside the human body is the Angiotensin-Converting Enzyme-2 receptor, which renders its activity along with Transmembrane protease, serine 2 cell surface protein, representing a type II Transmembrane Serine Protease, preferably in the alveolar pneumocytes.<sup>3,37,54–58</sup> Mainly TMPRSS2 sunders the S- protein of SARS-CoV-2 utilizing its protease activity, into two parts S1 and S2, which facilitate binding of the virus and its unification with the target cell respectively (Fig. 2A).<sup>3,37,59,60</sup> The gene encoding for TMPRSS2 protein has been spotted in chromosome 21 of humans, whose transcription is modulated by allosomal androgen receptor transcription factor.<sup>54,55,58,61,62</sup> Sex-steroid hormones such as testosterone reactive promoter sequence existing upstream of the gene, thereby deploy AR's activity through several signaling systems.<sup>54,55</sup> Though hints of estrogen affecting the task of TMPRSS2 have been obtained, nevertheless male sex hormones form the chief regulator of TMPRSS2 bringing about a lower rate of AR activity in females in contrast to males, featuring the varying levels of extremity and mortality due to COVID-19 disease in different genders.<sup>3,54,55,63,64</sup> Alongside lower amounts of androgens in prepubescent children conceals TMPRSS2 activity in their lung cells which contributes to the reduced prevalence and extremity of COVID-19 related inflammation in pediatric patients.<sup>3,41,54,55,65,66</sup> Thereupon, adrenarche is an essential milestone that describes the reason for the greater vulnerability of children 10–12 years or above, to MIS-C, signifying that those children have entered the adrenarche stage that enhances androgen output. This age-dependent revelation of ACE2 and TMPRSS2 eases viral entry in adolescents causing pronounced pathogenesis and MIS-C symptoms, while curbing viral access in pre-adolescents minimizing their symptoms.<sup>3,54,55,67,68</sup>

Moreover, the higher concentration of serum antibodies in pediatric patients portrays the possible operation of antibody-dependent enhancement mechanism<sup>3</sup> in provoking MIS-C, which is more certain

to arise as an outcome of acquired immune response and not due to enhanced multiplication of virus.<sup>1,3,69</sup> Certain viral disorders, like dengue and Zika virus infections, have well-documented ADE pathways.<sup>3,69</sup> Reports on MIS-C patients producing neutralizing<sup>70</sup> and non-neutralizing (binding) antibodies<sup>3</sup> as feedback to the spike protein of SARS-CoV-2 have been obtained. Neutralizing antibodies confers sterilizing immunity by negating the pathogenic effect of the virus while the non-neutralizing one attaches to the virus but doesn't possess the potential to nullify its virulence.<sup>3,41,70</sup> It is thought that when children are first exposed to the SARS-CoV-2 virus, their immune system produces both of these antibodies. Later on, the youngsters overridden with neutralizing antibodies are likely to suffer from asymptomatic sickness but, virus attack and critical multisystem inflammation are boosted in them with prevalent binding antibodies via ADE.<sup>3</sup> Non-neutralizing antibodies or inadequate quantities of neutralizing antibodies bound to the epitopes of SARS-CoV-2, in the patient's blood, promote its intake inside the host tissue which is described as ADE. This machinery is unassociated with the ACE2 pathway and involves uniting of the complex of virus epitope and virus-specific non-neutralizing antibody by dint of the F<sub>c</sub> domain of immunoglobulin to the immune cell's membrane harboring IgG Fc receptor (F<sub>c</sub>R).<sup>3,71</sup> This interaction activates macrophages, natural killer cells, lymphocytes, and monocytes causing cellular endocytosis.<sup>3,41</sup> (Fig. 2B). Endocytic Toll-like receptors such as TLR3, TLR7 detect the viral RNA and thus make the macrophages operational, inducing a surge of pro-inflammatory cytokines like TNF- $\alpha$ , IL-6, IL-18, IL-16, IL-1 $\beta$  occasionally by the NF- $\kappa$ B route.<sup>3,37,41,71–73</sup> This originates a cytokine storm mimicking the provocation of macrophages as seen in hemophagocytic lymphohistiocytosis.<sup>3,74</sup> CD68<sup>+</sup>, CD169<sup>+</sup> macrophages<sup>3</sup> aid in viral dispersion and induce pyroptosis via inflammation<sup>41,75</sup> (Fig. 2A). Pyroptosis indicates cell death linked to the NLR family pyrin domain containing 3 inflammasome activation systems. The cellular damage thus instigates the surrounding macrophages to generate chemokines and cytokines<sup>3</sup> furthermore indicators of inflammation can also help macrophages to engage T-cells in the infection area.<sup>41,72,76,77</sup> Elevated levels of IL-1 $\beta$  in blood serum evince the occurrence of pyroptosis.<sup>41</sup> A probable role of non-specific antibodies<sup>3</sup> has been put forward that justifies the genesis of MIS-C through ADE, in seropositive patients where non-specific antibodies unite with the virus aiding its intake by the immune cells. Gruber et al. (2020)<sup>78</sup> have also studied the role of auto-antibodies found against endothelial and gastrointestinal cells in MIS-C patients, which fails to distinguish

**Table 2**

Table showing the case studies of the individual patients having Post COVID-19 MIS-C.

Sl. No.	Region	Schedule of patient admission	Patient's description	Symptoms and image findings	Laboratory findings	Similarities with	Treatment	Reference
1.	Atlanta, Georgia	June 2020	A 25-year-old woman	Exhaustion, dyspnea, mild cough and low-grade fevers, vomiting, sore throat, diarrhoea, slight hypotension (blood pressure 98/56 mmHg) and usual blood oxygen level in indoor air, cervical lymphadenopathy; notable conjunctival injection; red and cracked lips; left lower abdominal tremble. Echocardiogram: Enlarged inferior vena cava, cardiac dysfunction. CT of abdomen/pelvis: Stranding of peri-pancreatic fat; pancreatitis, indefinite bilateral perinephric fat stranding.	Troponin-I was discovered at 0.06 ng/mL; high levels of creatinine (7.74 mg/dL), BNP (378 pg/ml), d-dimer (960 ng/ml), ferritin (798 ng/ml).	KD	To minimize the chances of thromboembolic and nephrotoxicity, IVIG (2 g/kg) was administered in uniform dosages on the second and third day of the hospital admission, along with aspirin (325 mg) for 7 days, and redeliver.	<sup>9</sup>
2.	New York	May 2020	An 11-year-old female	Initial: sore throat, uneasiness, low appetite, leg and abdominal pain, pruritus skin rash, fever (39.3 °C), tachycardia (126beats/minute), hypotension, slight dehydration, erythematous palm with a widespread reticular, non-blanching papular rash across the belly and bilateral upper extremities. Echocardiogram: Decreased systolic function of the left ventricle. Electrocardiogram: Showed sinus tachycardia and S1Q3T3 indicating strain on the right side of the heart.	Uplifted levels of troponin (0.112 ng/mL) and BNP (8718 pg/mL). White blood cell count increased to 14.18 causing lymphopenia. PTT yielded an increased value of 1.9 along with the raised levels of IL-6 (0.0–15.5 pg/mL), ferritin (13.00–150.00 ng/mL), D-dimer (0–243 ng/mL, procalcitonin (0.00–0.50 ng/mL), CRP (0.10–2.80 mg/L) and normal level of creatinine (0.53–0.79 mg/dL).	TSS, septic shock, cytokine storm, KD, SHLH	Furosemide along with antibiotics like clindamycin, ceftaroline, and piperacillin-tazobactam was administered. Enoxaparin was started as a comprehensive anticoagulant. Vitamin K was employed to improve elevated INR and PT. An IL-6 blocker, tocilizumab, was progressed along with convalescent plasma therapy and remdesivir.	<sup>45</sup>
3.	Not found	Not found	A 14-year-old boy	Fever, tachycardia and inflamed maculopapular rash on the face, abdominal sensitivity, as well as a perianal injury discharging pus. A 28-cm ileitis, a 2.3-cm perianal pustule, and a fistula were diagnosed on magnetic resonance enterography.	Initially, tests revealed a normal ESR rate (0–5 mg/L) and normal levels of CRP (0–15 mm/h). Increased serum amounts of IL-6 (73.4 pg/mL), IL-8 (21.8 pg/mL), IL-1 $\beta$ (0.4 pg/mL), TNF- $\alpha$ (97.8 pg/mL) were noticed in the cytokine profile up to eight days of hospitalization, which later on declined till the tenth day on treatment with infliximab.	KD	Azithromycin and hydroxychloroquine were used for SARS-CoV-2 infection, intravenous piperacillin/tazobactam was used to cure perianal abscess, and enoxaparin was utilized for the prevention of venous thromboembolism, along with intravenous fluid therapy.	<sup>51</sup>
4.	Kerala, India	April 2020	A 5-year-old boy	Fever of high intensity, abdominal cramps and watery stools, pyuria, bulbar conjunctivitis without pus and non-pitting edema of the feet and hands, tachycardia (130 beats per min), vasoplegia. Echocardiogram: Comprehensive left ventricular hypokinesia with medium systolic dysfunction (EF = 35%) and myocarditis was discovered. Chest X-ray: Disclosed cardiomegaly.	Inflammatory cytokines in blood serum-like CRP, ferritin, creatinine and liver enzymes were found to be upraised. The results of a complete blood count revealed neutrophilic leucocytosis.	KD	Pulmonary support using a high flow nasal cannula with a 2L/kg flow rate was attempted, as well as inotropic support was provided with adrenaline; Ceftriaxone, an injectable antibiotic, immunoglobulins, diuretic drugs, enalapril and methylprednisolone pulse (30 mg/kg/d for 3 d), were some of the remedies.	<sup>47</sup>

between self and non-self cells, ultimately attacking a patient's native tissues.<sup>1,78</sup> Thus, it can be inferred that localized inflammation and the build-up of pathogenic macrophage congregations in body tissues are

two especially common factors that cause MIS-C syndrome and more analysis is needed to illustrate the role of macrophages further.<sup>3</sup>

**Table 3**

Table showing the case studies of the cohorts having Post COVID-19 MIS-C.

Study	Region	Schedule of patient admission	Description of patients (number, age/ interquartile range [IQR])	Number of Patients detected positive	Symptoms and Image findings	Laboratory findings	Similarities with	Treatment	Reference
Trevor K. Young et al. (2020)	New York	April 1 to July 14, 2020	A cohort of a patient (total = 56) IQR = 0.7–17 years	PCR: 10/56 IgG Tests: 19/56 Mucocutaneous findings: 27/56	Fever for 1–2 days, mild cough. Major mucocutaneous findings (in 21) included strawberry tongue (in 8), lip crack (in 13), conjunctivitis (in 21), erythematous hands and feet (in 13), cheek (in 6) and orbit of the eye (in 7). Eruptions of several types, i.e., molliform (in 3), reticulate (in 3), scarlatiniform (in 5) and urticarial (in 5). Gastrointestinal and cardiac trouble.	D-dimer, BNP, and troponin levels were all enhanced.	KD	Injectable immunoglobulin, corticosteroids, Aspirin, Remdesivir, Anakinra.	<a href="#">26</a>
Blumfield et al. (2020)	New York	April 21– May 22, 2020	A cohort of patients (total = 16) IQR = 20 months to 20 years.	RT-PCR: 3/16 IgG Tests: 10/16 Both RT-PCR and IgG Tests: 1/16	Fever (in 16), erythema (in 10), emesis (in 12), diarrhoea (in 7), abdominal discomfort (in 11), conjunctivitis (in 8), headache (in 6), and hoarseness (in 5) were the first symptoms, followed by breathing issues and congestion (in 1), hypotension (in 10), and ischemia (in 7). Echocardiography: Systolic myocardial abnormality (in 10), ectatic coronary arteries (in 4), and pericardial effusion (in 2) were discovered on echocardiography. Chest radiography: Megalocardia (in 10), cardiogenic pulmonary edema (in 9), and a modest pleural discharge (in 7) were seen on chest radiographs, with only a few patients developing pneumonia (in 1) and acute respiratory distress syndrome (in 2). CT scan of abdomen and pelvis: Abdominal fluid build-up (in 6), hepatomegaly (in 6), mesenteric lymphadenitis (in 2), and thickening of the urinary (in 1) and gall bladder (in 3) walls were all seen on abdominal radiography.	Erythrocyte sedimentation rate (in 12), CRP (in 16), D-dimer (in 16), troponin (in six), and pro-BNP (in 15) values were all raised. High white blood cell count (in 13) leading to leucocytosis and hypoalbuminaemia (in 16) were encountered too.	Kawasaki Disease (KD)	Intravenous corticosteroids and Anakinra	<a href="#">32</a>
Belhadjer et al. (2020)	France and Switzerland	March 22 to April 30, 2020.	A cohort of a patient (total = 35) IQR = 2–16 years.	Nasopharyngeal swab PCR: 12/35 Fecal PCR: 2/35 Antibody Tests: 30/35	All of the children had a fever and weakness, and 80% of them had gastrointestinal issues (in 29) such as abdominalache, diarrhoea, and vomiting. Runny	Heightened IL- 6, D-dimer, troponin, CRP and BNP.	KD	Inotropic support, Immunoglobulin infusion, Intravenous corticosteroids, IL-1 inhibitor and therapeutic dose of heparin.	<a href="#">28</a>

(continued on next page)

Table 3 (continued)

Study	Region	Schedule of patient admission	Description of patients (number, age/interquartile range [IQR])	Number of Patients detected positive	Symptoms and Image findings	Laboratory findings	Similarities with	Treatment	Reference
Whittekhar E. et al. (2020)	England	March 23 to May 16, 2020.	A cohort of a patient (total = 58) IQR = 3 months-17 years.	PCR: 15/58 IgG Test: 40/58	nose (in 15), skin rashes (in 20), meningism (in 11), angina (in 6) mesenteric and cervical lymphadenopathy (in 21) were among the additional symptomatology. Echocardiography: It denoted impaired left ventricular systolic activity, with an EF of 30–50%, resulting in left ventricular hypokinesia (EF<45%) in 31 individuals.	All of the patients exhibited a significant inflammatory response in terms of elevated levels of CRP, troponin, ferritin, N-terminal pro-BNP and neutrophilia.	PIMS-TS and Kawasaki Disease (KD) shock syndrome.	Intravenous immunoglobulin (in 41), Corticosteroids (in 37), Anakinra (in 3) and Infliximab (in 8).	21
Kaushik et al. (2020)	New York	April 23 to May 23, 2020	A cohort of a patient (total = 33) IQR = 6–13 years.	RT-PCR: 11/33 Antibody Test: 27/33 Both test: 6/33	Major portion of the patients had fever (Avg. temperature of about 39.4C°) (in 31) and other symptoms like uneasiness of the stomach/vomiting (in 23), diarrhoea (in 16), dyspnoea (in 11), vertigo (in 3), low blood pressure (in 21), peritoneal pain (in 21), mucocutaneous involvement (in 7) like conjunctivitis (in 12) and dermatological symptoms like rashes (in 14), and also neurological involvement (in 4). Echocardiogram: Depressed LVEF with various range of EF was observed (in 21). Chest Radiograph: Megacardia (in 10) and in addition bilateral pulmonary opacities were noted (in 11).	Inflammatory indicators like CRP, procalcitonin, D-dimer, ferritin, ESR, and fibrinogen were found to be increased. There were also heightened markers of aberrant cardiac state like, troponin, N-proBNP, and BNP.	Toxic shock	Intravenous immunoglobulin (in 18), Corticosteroids (in 17), Tocilizumab (in 12), Remdesivir (in 7), Anakinra (in 4), Convalescent plasma therapy (in 1), Norepinephrine (in 10) and Dopamine (in 9).	3,4

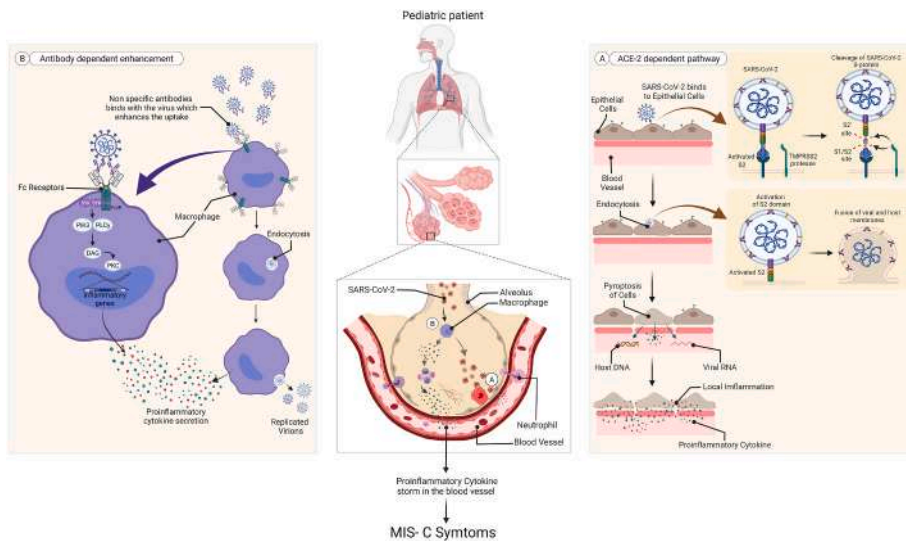


**Fig. 2.** The most likely mechanism for MIS-C expansion in pediatric patients.<sup>1,3</sup> **A.** ACE-2 dependent pathway **B.** Antibody-dependent enhancement. (Created with BioRender.com).

[ACE-2 = Angiotensin-converting enzyme 2. DAG = diacylglycerol. FcyR = Fc-gamma receptor. MIS-C = multisystem inflammatory syndrome in children. PIK3 = phosphoinositide 3 kinase. PKC = protein kinase C. PLC-γ = phospholipase C gamma. SARS-CoV-2 = severe acute respiratory syndrome coronavirus 2. SYK = tyrosine protein kinase SYK. TMPRSS2 = transmembrane serine protease 2.].

**8. Conclusion**

MIS-C is generally curable and rarely happens, but a certain lack of knowledge could make it severe in the long term aspect.<sup>4</sup> As it is a rare condition, most children who have it improve with medical treatment. However, some children swiftly deteriorate to the point where their lives are jeopardized. As the number of MIS-C cases related to COVID-19 is increasing incessantly, it can be clearly stated that COVID-19 is not only just a respiratory disease,<sup>6</sup> further elaborate research is needed to know more about the etiology of MIS-C associated with COVID-19, as it is still unknown how the risk factor for MIS-C varies among child community.<sup>4</sup> Children develop COVID-19, unlike adults, by ADE due to a lack of androgens,<sup>3,54</sup> which directly regulates the TMPRSS2 receptor.<sup>55,66</sup> Therefore, to prevent the transmission of COVID-19 in this age group, parents should be more careful of their children in surroundings with a high population density.<sup>4</sup> Precautions and safety measures such as social distancing, use of face masks, frequent washing of hands, use of alcohol-based disinfectants, should be followed in places like schools,<sup>4</sup> parks, crèche, etc. Parents, babysitters, teachers, and school officials should primarily be cognizant of the indications and signs of both COVID-19 and MIS-C so that proper treatment is provided before its late.

**Authors' contributions**

Conceptualization: [Joy Sarkar, Suchismita Kumar]; Formal analysis and investigation: [Anusrita Kundu, Joy Sarkar]; Writing – original draft preparation: [Anusrita Kundu], [Swagata Maji], [Suchismita Kumar], [Shreya Bhattacharya], [Pallab Chakraborty]; Image Preparation: [Pallab Chakraborty]; Writing – review and editing: [Joy Sarkar]; Funding acquisition: [N/A]; Resources: [N/A]; Supervision: [Joy Sarkar].

**Availability of data and material**

Not applicable.

**Code availability**

Not applicable.

**Ethics approval**

Not applicable.

**Funding**

We don't have any funding support from any organizational or institutional level.

**Permission to reproduce material from other sources**

Not applicable.

**Consent to participate**

All the authors mutually agree to participate in this work.

**Consent for publication**

All the authors mutually agree to submit the manuscript for publication.

**Declaration of competing interest**

On behalf of all listed authors, the corresponding author declares that there is not any sort of financial and non-financial conflict of interest in the subject materials mentioned in this manuscript.

**Acknowledgments**

We do not have any funding support from any organizational or institutional level. The authors acknowledge the immense help received from the scholars whose articles are cited and included in references of this manuscript. The authors are also grateful to authors/editors/publishers of all those articles, journals, and books from where the literature for this article has been reviewed and discussed.

**References**

- Jiang L, Tang K, Levin M, et al. COVID-19 and multisystem inflammatory syndrome in children and adolescents. *Lancet Infect Dis.* 2020;20(11):e276–e288. [https://doi.org/10.1016/S1473-3099\(20\)30651-4](https://doi.org/10.1016/S1473-3099(20)30651-4).
- Vella LA, Giles JR, Baxter AE, et al. Deep immune profiling of MIS-C demonstrates marked but transient immune activation compared to adult and pediatric COVID-19. *Science Immunology.* 2021;6(57):1–19. <https://doi.org/10.1126/SCIIMMUNOL.ABF7570>.
- Rothan HA, Byrareddy SN. The potential threat of multisystem inflammatory syndrome in children during the COVID-19 pandemic. *Pediatr Allergy Immunol.* 2021; 32(1):17–22. <https://doi.org/10.1111/pai.13361>.
- Rafferty MS, Burrows H, Joseph JP, Leveille J, Nihtianova S, Amirian ES. Multisystem inflammatory syndrome in children (MIS-C) and the coronavirus

- pandemic: current knowledge and implications for public health. *J Infect Public Health*. 2021;14(4):484–494. <https://doi.org/10.1016/j.jiph.2021.01.008>.
- 5 Riphagen S, Gomez X, Gonzalez-Martinez C, Wilkinson N, Theocharis P. Hyperinflammatory shock in children during COVID-19 pandemic. *Lancet*. 2020;395(10237):1607–1608. [https://doi.org/10.1016/S0140-6736\(20\)31094-1](https://doi.org/10.1016/S0140-6736(20)31094-1).
  - 6 Winant AJ, Blumfield E, Liszewski MC, Kurian J, Foust AM, Lee EY. Thoracic imaging findings of multisystem inflammatory syndrome in children associated with COVID-19: what radiologists need to know now. *Radiology: Cardiothorac Imag*. 2020;2(4). <https://doi.org/10.1148/ryct.2020200346>.
  - 7 Verdoni L, Mazza A, Gervasoni A, et al. An outbreak of severe Kawasaki-like disease at the Italian epicentre of the SARS-CoV-2 epidemic: an observational cohort study. *Lancet*. 2020;395(10239):1771–1778. [https://doi.org/10.1016/S0140-6736\(20\)31103-X](https://doi.org/10.1016/S0140-6736(20)31103-X).
  - 8 Health Department-Reported Cases of Multisystem Inflammatory Syndrome in Children (MIS-C) in the United States. 2021.
  - 9 Kofman AD, Sizemore EK, Detelich JF, Albrecht B, Piantadosi AL. A young adult with COVID-19 and multisystem inflammatory syndrome in children (MIS-C)-like illness: a case report. *BMC Infect Dis*. 2020;20(1):1–4. <https://doi.org/10.1186/s12879-020-05439-z>.
  - 10 Feldstein LR, Tenforde MW, Friedman KG, et al. Characteristics and outcomes of US children and adolescents with multisystem inflammatory syndrome in children (MIS-C) compared with severe acute COVID-19. *JAMA - J Am Med Assoc*. 2021;325(11):1074–1087. <https://doi.org/10.1001/jama.2021.2091>.
  - 11 Nakra N, Blumberg D, Herrera-Guerra A, Lakshminrusimha S. Multi-system inflammatory syndrome in children (MIS-C) following SARS-CoV-2 infection: review of clinical presentation, hypothetical pathogenesis, and proposed management. *Children*. 2020;7(7):69. <https://doi.org/10.3390/children7070069>.
  - 12 Radia T, Williams N, Agrawal P, et al. Multi-system inflammatory syndrome in children & adolescents (MIS-C): a systematic review of clinical features and presentation. *Paediatr Respir Rev*. 2021;38(xxxx):51–57. <https://doi.org/10.1016/j.prrv.2020.08.001>.
  - 13 Hennon TR, Penque MD, Abdul-Aziz R, et al. COVID-19 associated multisystem inflammatory syndrome in children (MIS-C) guidelines; a western New York approach. *Prog Pediatr Cardiol*. 2020;57, 101232. <https://doi.org/10.1016/j.pppedcard.2020.101232>.
  - 14 Reiff DD, Mannion ML, Samuy N, Scalici P, Cron RQ. Distinguishing active pediatric COVID-19 pneumonia from MIS-C. *Pediatr Rheumatol*. 2021;19(1):1–9. <https://doi.org/10.1186/s12969-021-00508-2>.
  - 15 Dufort EM, Koumans EH, Chow EJ, et al. Multisystem inflammatory syndrome in children in New York state. *N Engl J Med*. 2020;383(4):347–358. <https://doi.org/10.1056/nejmoa2021756>.
  - 16 Feldstein LR, Rose EB, Horwitz SM, et al. Multisystem inflammatory syndrome in U. S. Children and adolescents. *N Engl J Med*. 2020;383(4):334–346. <https://doi.org/10.1056/nejmoa2021680>.
  - 17 Lee PY, Day-Lewis M, Henderson LA, et al. Distinct clinical and immunological features of SARS-CoV-2-induced multisystem inflammatory syndrome in children. *J Clin Invest*. 2020;130(11):5942–5950. <https://doi.org/10.1172/JCI141113>.
  - 18 Moraleda Cinta, Serma-Pascual Miquel, Soriano-Arantes Antoni, et al. Multi-inflammatory syndrome in children related to SARS-CoV-2 in Spain. *Clin Infect Dis*. 2020;72(9). <https://doi.org/10.1093/cid/ciaa1042>. e397–e401.
  - 19 Ramcharan T, Nolan O, Lai CY, et al. Paediatric inflammatory multisystem syndrome: temporally associated with SARS-CoV-2 (PIMS-TS): cardiac features, management and short-term outcomes at a UK tertiary paediatric hospital. *Pediatr Cardiol*. 2020;41(7):1391–1401. <https://doi.org/10.1007/s00246-020-02391-2>.
  - 20 Kaushik S, Aydin SI, Derespina KR, et al. Multisystem inflammatory syndrome in children (MIS-C) associated with SARS-CoV-2 infection: a multi-institutional study from New York city. *J Pediatr*. 2020;224:24–29. <https://doi.org/10.1016/j.jpeds.2020.06.045>.
  - 21 Whittaker E, Bamford A, Kenny J, et al. Clinical characteristics of 58 children with a pediatric inflammatory multisystem syndrome temporally associated with SARS-CoV-2. *JAMA - J Am Med Assoc*. 2020;324(3):259–269. <https://doi.org/10.1001/jama.2020.10369>.
  - 22 Miller J, Cantor A, Zachariah P, Ahn D, Martinez M, Margolis KG. Gastrointestinal symptoms as a major presentation component of a novel multisystem inflammatory syndrome in children that is related to coronavirus disease 2019: a single center experience of 44 cases. *Gastroenterology*. 2020;159(4):1571–1574. <https://doi.org/10.1053/j.gastro.2020.05.079>. e2.
  - 23 Cheung EW, Zachariah P, Gorelik M, et al. Multisystem inflammatory syndrome related to COVID-19 in previously healthy children and adolescents in New York city. *JAMA - J Am Med Assoc*. 2020;324(3):294–296. <https://doi.org/10.1001/jama.2020.10374>.
  - 24 Poullety M, Borocco C, Ouldali N, et al. Paediatric multisystem inflammatory syndrome temporally associated with SARS-CoV-2 mimicking Kawasaki disease (Kawa-COVID-19): a multicentre cohort. *Ann Rheum Dis*. 2020;79(8):999–1006. <https://doi.org/10.1136/annrheumdis-2020-217960>.
  - 25 Toubiana J, Poirault C, Corsia A, et al. Kawasaki-like multisystem inflammatory syndrome in children during the covid-19 pandemic in Paris, France: prospective observational study. *BMJ (Clinical research ed)*. 2020;369, m2094. <https://doi.org/10.1136/bmj.m2094>.
  - 26 Young TK, Shaw KS, Shah JK, et al. Mucocutaneous manifestations of multisystem inflammatory syndrome in children during the COVID-19 pandemic. *JAMA Dermatology*. 2021;157(2):207–212. <https://doi.org/10.1001/jamadermatol.2020.4779>.
  - 27 Vogel TP, Top KA, Karatzios C, et al. Multisystem inflammatory syndrome in children and adults (MIS-C/A): case definition & guidelines for data collection, analysis, and presentation of immunization safety data. *Vaccine*. 2021;39(22):3037–3049. <https://doi.org/10.1016/j.vaccine.2021.01.054>.
  - 28 Belhadjer Z, Méot M, Bajolle F, et al. Acute heart failure in multisystem inflammatory syndrome in children in the context of global SARS-CoV-2 pandemic. *Circulation*. 2020;142(5):429–436. <https://doi.org/10.1161/CIRCULATIONAHA.120.048360>.
  - 29 F Son Mary Beth, MDKevin Friedman M. COVID-19: Multisystem Inflammatory Syndrome in Children (MIS-C) Clinical Features, Evaluation, and Diagnosis; 2021. Published <https://www.uptodate.com/contents/covid-19-multisystem-inflammatory-syndrome-in-children-mis-c-clinical-features-evaluation-and-diagnosis>.
  - 30 Belhadjer Z, Méot M, Bajolle F, et al. Acute heart failure in multisystem inflammatory syndrome in children in the context of global SARS-CoV-2 pandemic. *Circulation*. 2020;142(5):429–436. <https://doi.org/10.1161/CIRCULATIONAHA.120.048360>.
  - 31 De Paulis M, Oliveira DBL, Vieira RP, et al. Multisystem inflammatory syndrome associated with covid-19 with neurologic manifestations in a child: a brief report. *Pediatr Infect Dis J*. 2020;39(10):E321–E324. <https://doi.org/10.1097/INF.0000000000002834>.
  - 32 Flors L. Imaging findings in multisystem inflammatory syndrome in children (MIS-C) associated with coronavirus disease (COVID-19). *Am J Roentgenol*. 2021;216(2):518. <https://doi.org/10.2214/AJR.20.24423>.
  - 33 Whitworth H, Sartain SE, Kumar R, et al. Rate of thrombosis in children and adolescents hospitalized with COVID-19 or MIS-C. *Blood*. 2021;138(2):190–198. <https://doi.org/10.1182/blood.2020010218>.
  - 34 Ragab D, Salah Eldin H, Taemah M, Khattab R, Salem R. The COVID-19 cytokine storm; what we know so far. *Front Immunol*. 2020;11(June):1–4. <https://doi.org/10.3389/fimmu.2020.01446>.
  - 35 Sokolovsky S, Soni P, Hoffman T, Kahn P, Scheers-Masters J. COVID-19 associated Kawasaki-like multisystem inflammatory disease in an adult. *AJEM (Am J Emerg Med)*. 2021;39:253. <https://doi.org/10.1016/j.ajem.2020.06.053>. e1-253.e2.
  - 36 Sullivan C. Prolonged Pediatric Fever and Evaluating Patients for Kawasaki Disease, Toxic Shock Syndrome, and Multi-Inflammatory Syndrome of Children. *emDocs*; 2021. Published <https://www.emdocs.net/prolonged-pediatric-fever-and-evaluating-patients-for-kawasaki-disease-toxic-shock-syndrome-and-multi-inflammatory-syndrome-of-children/>.
  - 37 Kabeerdoss J, Pilianna RK, Karkhele R, Kumar TS, Danda D, Singh S. Severe COVID-19, multisystem inflammatory syndrome in children, and Kawasaki disease: immunological mechanisms, clinical manifestations and management. *Rheumatol Int*. 2021;41(1):19–32. <https://doi.org/10.1007/s00296-020-04749-4>.
  - 38 Li C feng, He X hu, Kuang W ying, Han T xin, Zhou Y fang. Macrophage activation syndrome in Chinese children with systemic onset juvenile idiopathic arthritis. *Zhonghua er ke za zhi = Chinese journal of pediatrics*. 2006;44(11):806–811.
  - 39 Ebina-Shibuya R, Namkoong H, Shibuya Y, Horita N. Multisystem inflammatory syndrome in children (MIS-C) with COVID-19: insights from simultaneous familial kawasaki disease cases. *Int J Infect Dis*. 2020;97:371–373. <https://doi.org/10.1016/j.ijid.2020.06.014>.
  - 40 Schuler G, Gross AA. Pathogenesis of macrophage activation syndrome and potential for cytokine-directed therapies. *Annu Rev Med*. 2015;66(October 2014):145–159. <https://doi.org/10.1146/annurev-med-061813-012806>.
  - 41 Otsuka R, Seino KI. Macrophage activation syndrome and COVID-19. *Inflamm Regen*. 2020;40(1). <https://doi.org/10.1186/s41232-020-00131-w>.
  - 42 Bose K, Saha S, Saha P, Mondal P. Macrophage activation syndrome: a potentially fatal complication of kawasaki disease. *Archives of Rheumatology*. 2015;30(2):178–180. <https://doi.org/10.5606/ArchRheumatol.2015.5186>.
  - 43 Weaver LK, Behrens EM. Hyperinflammation, rather than hemophagocytosis, is the common link between macrophage activation syndrome and hemophagocytic lymphohistiocytosis. *Curr Opin Rheumatol*. 2014;26(5):562–569. <https://doi.org/10.1097/BOR.0000000000000093>.
  - 44 De Graeff N, Groot N, Ozen S, et al. European consensus-based recommendations for the diagnosis and treatment of Kawasaki disease-the SHARE initiative. *Rheumatology*. 2019;58(4):672–682. <https://doi.org/10.1093/rheumatology/key344>.
  - 45 Greene AG, Saleh M, Roseman E, Sinert R. Toxic shock-like syndrome and COVID-19: multisystem inflammatory syndrome in children (MIS-C). *AJEM (Am J Emerg Med)*. 2020;38(11):2492. <https://doi.org/10.1016/j.ajem.2020.05.117>. e5-2492.e6.
  - 46 Giamarellos-Bourboulis EJ, Netea MG, Rovina N, et al. Complex immune dysregulation in COVID-19 patients with severe respiratory failure. *Cell Host Microbe*. 2020;27(6):992–1000. <https://doi.org/10.1016/j.chom.2020.04.009>. e3.
  - 47 Rauf A, Vijayan A, John ST, Krishnan R, Latheef A. Multisystem inflammatory syndrome with features of atypical kawasaki disease during COVID-19 pandemic. *Indian J Pediatr*. 2020;87(9):745–747. <https://doi.org/10.1007/s12098-020-03357-1>.
  - 48 Halyabar O, Chang MH, Schoettler ML, et al. Calm in the midst of cytokine storm: a collaborative approach to the diagnosis and treatment of hemophagocytic lymphohistiocytosis and macrophage activation syndrome. *Pediatr Rheumatol*. 2019;17(1):1–12. <https://doi.org/10.1186/s12969-019-0309-6>.
  - 49 McCrindle BW, Rowley AH, Newburger JW, et al. Diagnosis, Treatment, and Long-Term Management of Kawasaki Disease: A Scientific Statement for Health Professionals from the American Heart Association. vol. 135. 2017. <https://doi.org/10.1161/CIR.0000000000000484>.
  - 50 Rajasekaran S, Kruse K, Kovey K, et al. Therapeutic role of anakinra, an interleukin-1 receptor antagonist, in the management of secondary hemophagocytic lymphohistiocytosis/sepsis/multiple organ dysfunction/macrophage activating syndrome in critically ill children. *Pediatr Crit Care Med*. 2014;15(5):401–408. <https://doi.org/10.1097/PCC.0000000000000078>.
  - 51 Dolinger MT, Person H, Smith R, et al. Pediatric crohn disease and multisystem inflammatory syndrome in children (MIS-C) and COVID-19 treated with Infliximab. *J Pediatr Gastroenterol Nutr*. 2020;71(2):153–155. <https://doi.org/10.1097/MPG.0000000000002809>.



- 52 Michot JM, Albiges L, Chaput N, et al. Tocilizumab, an anti-IL-6 receptor antibody, to treat COVID-19-related respiratory failure: a case report. *Ann Oncol*. 2020;31(7):961–964. <https://doi.org/10.1016/j.annonc.2020.03.300>.
- 53 Feldmann M, Maini RN, Woody JN, et al. Trials of anti-tumour necrosis factor therapy for COVID-19 are urgently needed. *Lancet*. 2020;395(10234):1407–1409. [https://doi.org/10.1016/S0140-6736\(20\)30858-8](https://doi.org/10.1016/S0140-6736(20)30858-8).
- 54 Younis JS, Skorecki K, Abassi Z. The double edge sword of testosterone's role in the COVID-19 pandemic. *Front Endocrinol*. 2021;12(March):1–8. <https://doi.org/10.3389/fendo.2021.607179>.
- 55 Mihalopoulos M, Levine AC, Marayati NF, et al. The resilient child: sex-steroid hormones and COVID-19 incidence in pediatric patients. *J Endocr Soc*. 2020;4(9). <https://doi.org/10.1210/edso/bvaa106>.
- 56 Wan Y, Shang J, Graham R, Baric RS, Li F. Receptor recognition by the novel coronavirus from wuhan: an analysis based on decade-long structural studies of SARS coronavirus. *J Virol*. 2020;94(7). <https://doi.org/10.1128/jvi.00127-20>.
- 57 Zhou P, Lou Yang X, Wang XG, et al. A pneumonia outbreak associated with a new coronavirus of probable bat origin. *Nature*. 2020;579(7798):270–273. <https://doi.org/10.1038/s41586-020-2012-7>.
- 58 Lucas JM, Heinlein C, Kim T, et al. The androgen-regulated protease TMPRSS2 activates a proteolytic cascade involving components of the tumor microenvironment and promotes prostate cancer metastasis. *Cancer Discov*. 2014;4(11):1310–1325. <https://doi.org/10.1158/2159-8290.CD-13-1010>.
- 59 Glowacka I, Bertram S, Muller MA, et al. Evidence that TMPRSS2 activates the severe acute respiratory syndrome coronavirus spike protein for membrane fusion and reduces viral control by the humoral immune response. *J Virol*. 2011;85(9):4122–4134. <https://doi.org/10.1128/jvi.02232-10>.
- 60 Hoffmann M, Kleine-Weber H, Schroeder S, et al. SARS-CoV-2 cell entry depends on ACE2 and TMPRSS2 and is blocked by a clinically proven protease inhibitor. *Cell*. 2020;181(2):271–280. <https://doi.org/10.1016/j.cell.2020.02.052>. e8.
- 61 Rahman F, Christian HC. Non-classical actions of testosterone: an update. *Trends Endocrinol Metabol*. 2007;18(10):371–378. <https://doi.org/10.1016/j.tem.2007.09.004>.
- 62 Mikkonen L, Pihlajamaa P, Sahu B, Zhang FP, Jänne OA. Androgen receptor and androgen-dependent gene expression in lung. *Mol Cell Endocrinol*. 2010;317(1-2):14–24. <https://doi.org/10.1016/j.mce.2009.12.022>.
- 63 Yu J, Yu J, Mani RS, et al. An integrated network of androgen receptor, polycomb, and TMPRSS2-ERG gene fusions in prostate cancer progression. *Cancer Cell*. 2010;17(5):443–454. <https://doi.org/10.1016/j.ccr.2010.03.018>.
- 64 McCrohon JA, Death AK, Nakhla S, et al. Androgen receptor expression is greater in macrophages from male than from female donors. *Circulation*. 2000;101(3):224–226. <https://doi.org/10.1161/01.CIR.101.3.224>.
- 65 Kim JB, Lee JJ, Park JC, et al. Integrated analyses of single-cell atlases reveal age, gender, and smoking status associations with cell type-specific expression of mediators of SARS-CoV-2 viral entry and highlights inflammatory programs in putative target cells. *Angew Chem Int Ed*. 2018;6(11):951–952, 12(3):351–376.
- 66 Kashon ML, Hayes MJ, Shek PP, Sisk CL. Regulation of brain androgen receptor immunoreactivity by androgen in prepubertal male ferrets. *Biol Reprod*. 1995;52(5):1198–1205. <https://doi.org/10.1095/biolreprod52.5.1198>.
- 67 Denison MR. Severe acute respiratory syndrome coronavirus pathogenesis, disease and vaccines: an update. *Pediatr Infect Dis J*. 2004;23(11 SUPPL):207–214. <https://doi.org/10.1097/01.inf.0000144666.95284.05>.
- 68 Liu Y, Yan LM, Wan L, et al. Viral dynamics in mild and severe cases of COVID-19. *Lancet Infect Dis*. 2020;20(6):656–657. [https://doi.org/10.1016/S1473-3099\(20\)30232-2](https://doi.org/10.1016/S1473-3099(20)30232-2).
- 69 Rothan HA, Bidokhti MRM, Byrareddy SN. Current concerns and perspectives on Zika virus co-infection with arboviruses and HIV. *J Autoimmun*. 2018;89:11–20. <https://doi.org/10.1016/j.jaut.2018.01.002>.
- 70 Ho MS, Chen WJ, Chen HY, et al. Neutralizing antibody response and SARS severity. *Emerg Infect Dis*. 2005;11(11):1730–1737. <https://doi.org/10.3201/eid1111.040659>.
- 71 Wang SF, Tseng SP, Yen CH, et al. Antibody-dependent SARS coronavirus infection is mediated by antibodies against spike proteins. *Biochem Biophys Res Commun*. 2014;451(2):208–214. <https://doi.org/10.1016/j.bbrc.2014.07.090>.
- 72 Feng Z, Diao B, Wang R, et al. The novel severe acute respiratory syndrome coronavirus 2 (SARS-CoV-2) directly decimates human spleens and lymph nodes. *medRxiv*. 2020;2:1–18. <https://doi.org/10.1101/2020.03.27.20045427>.
- 73 Santoro MG, Rossi A, Amici C. NF- $\kappa$ B and virus infection: who controls whom. *EMBO J*. 2003;22(11):2552–2560. <https://doi.org/10.1093/emboj/cdg267>.
- 74 D'Antiga L. Coronaviruses and immunosuppressed patients: the facts during the third epidemic. *Liver Transplant*. 2020;26(6):832–834. <https://doi.org/10.1002/lt.25756>.
- 75 Rothan HA, Byrareddy SN. The epidemiology and pathogenesis of coronavirus disease (COVID-19) outbreak. *J Autoimmun*. 2020;109(February), 102433. <https://doi.org/10.1016/j.jaut.2020.102433>.
- 76 Yang M. *Cell Pyroptosis, a Potential Pathogenic Mechanism of 2019-nCoV Infection*. SSRN Electronic Journal; 2020. <https://doi.org/10.2139/ssrn.3527420>. Published online.
- 77 Malmgaard L, Melchjorsen J, Bowie AG, Mogensen SC, Paludan SR. Viral activation of macrophages through TLR-dependent and -independent pathways. *J Immunol*. 2004;173(11):6890–6898. <https://doi.org/10.4049/jimmunol.173.11.6890>.
- 78 Gruber CN, Patel RS, Trachtman R, et al. Mapping systemic inflammation and antibody responses in multisystem inflammatory syndrome in children (MIS-C). *Cell*. 2020;183(4):982–995. <https://doi.org/10.1016/j.cell.2020.09.034>. e14.



# Source details

[Feedback >](#) [Compare sources >](#)

## Clinical Epidemiology and Global Health

Open Access [i](#)

Scopus coverage years: from 2013 to Present

Publisher: Elsevier

E-ISSN: 2213-3984

Subject area: [Medicine: Public Health, Environmental and Occupational Health](#) [Medicine: Infectious Diseases](#) [Medicine: Epidemiology](#)

[Medicine: Microbiology \(medical\)](#)

Source type: Journal

[View all documents >](#)

[Set document alert](#)

[Save to source list](#)

CiteScore 2022

4.3



SJR 2022

0.615



SNIP 2022

0.995



See discussions, stats, and author profiles for this publication at: <https://www.researchgate.net/publication/357766100>

# Detection of UTI Pathogen-Killing Properties of *Coleus forskohlii* from Tissue Cultured In vitro and Ex vitro Plants

Article in *Proceedings of the National Academy of Sciences, India - Section B: Biological Sciences* · January 2022

DOI: 10.1007/s40011-021-01285-4

CITATIONS

10

READS

249

5 authors, including:



**Avijit Chakraborty**

Ramakrishna Mission Vivekananda Centenary College

14 PUBLICATIONS 82 CITATIONS

[SEE PROFILE](#)



**Sk. Moquammel Haque**

East Calcutta Girls' College, Lake Town, Kolkata 700089

39 PUBLICATIONS 466 CITATIONS

[SEE PROFILE](#)



**Diganta Dey**

Ashok Laboratory Clinical Testing Centre Pvt. Ltd., Kolkata

41 PUBLICATIONS 419 CITATIONS

[SEE PROFILE](#)



**Swapna Mukherjee**

28 PUBLICATIONS 394 CITATIONS

[SEE PROFILE](#)



# Detection of UTI Pathogen-Killing Properties of *Coleus forskohlii* from Tissue Cultured In vitro and Ex vitro Plants

Avijit Chakraborty<sup>1</sup> · Sk Moquammel Haque<sup>1,2</sup> · Diganta Dey<sup>3</sup> · Swapna Mukherjee<sup>4</sup> · Biswajit Ghosh<sup>1</sup>

Received: 15 December 2020 / Revised: 14 July 2021 / Accepted: 30 July 2021  
© The National Academy of Sciences, India 2022

**Abstract** Every year, 150 million people become affected, worldwide, by severe forms of multi-drug-resistant urinary tract infections (UTI). Several antibiotics are being tested to combat the diseases but newer types of resistance are emerging every year. This throws the challenge of searching of an alternative source of antibacterial compounds. The present study was conducted to evaluate the antimicrobial activities of in vitro and ex vitro grown plants of *Coleus forskohlii* against twenty MDR strains of UTI

bacteria. When methanolic leaf extracts were tested, seventeen among twenty UTI pathogens were found to be sensitive at only 0.75 mg/cup concentration, and three were resistant even at the 6.0 mg/cup concentration. Both the in vitro and ex vitro plants exhibited the highest efficacy against the pathogenic strain of *Klebsiella* (Isolate no-42285) with the ZI  $17.66 \pm 0.33$  and  $18.66 \pm 0.57$  mm, respectively. Naturally propagated in vivo plants showed significantly low activities compared to those of ex vitro grown plants. In vitro optimal multiplication of  $20.4 \pm 0.28$  shoots per explant was achieved in MS medium supplemented with 1.0 mg/l 6-benzylaminopurine and 0.1 mg/l  $\alpha$ -naphthalene acetic acid. A total of 38 and 35 compounds were detected from in vitro and ex vitro plant crude extract, respectively, through GC-MS including thiopene-2-carboxamide, 2-pyrazoline which are known to have potent antimicrobial activity. As both the ex vitro and in vitro plants were found to be highly efficient against most of the UTI pathogens tested, they may serve as a potential source of antimicrobial drug for an alternative therapy.

**Significance Statement** Present day, one of the major concerns is, the emergence bacterial diseases caused by the deadly strains, resistant to multiple drugs commonly used in health treatment. The finding of the present study describes that the plant extracts of *C. forskohlii* are promising in this respect with the potentiality of killing multi-drug resistant UTI pathogens of human, significantly. Another important part of this study is the establishment of fast growing plant tissue cultures from various tissues of the plant through micropropagation technique, in order to get a steady supply of the in vitro plants in high amount, throughout the year. Compounds present in the plant extracts were also identified through GC-MS analysis and found to contain compounds known as bioactive and antimicrobial in nature. So it can be said that these extracts can be used as an alternative source for the production of next generation drugs, without side effects.

✉ Biswajit Ghosh  
ghosh\_b2000@yahoo.co.in

Avijit Chakraborty  
avijit.microbio@gmail.com

Sk Moquammel Haque  
sm.haque@yahoo.in

Diganta Dey  
diganta\_dey2006@yahoo.com

Swapna Mukherjee  
swamuk15@gmail.com

<sup>1</sup> Plant Biotechnology Laboratory, Department of Botany, Ramakrishna Mission Vivekananda Centenary College, Rahara, Kolkata 700118, India

<sup>2</sup> Department of Botany, East Calcutta Girls' College, Lake Town, Kolkata 700089, India

<sup>3</sup> Department of Microbiology, Ashok Laboratory Clinical Testing Centre Private Limited, Kolkata 700068, India

<sup>4</sup> Department of Microbiology, Dinabandhu Andrews College, Garia, Kolkata 700084, India

**Keywords** Clinical isolates · *Coleus forskohlii* · GC–MS · Micropropagation · Multi-drug resistant · UTI bacteria

## Introduction

“One day no antibiotics may be left to treat common bacterial infections,” warns the World Health Organization. Antibiotics, that were once important weapons in fighting bacterial infections, now have lesser impact against infection. Abusive use of these drugs in human as well as in animal is leading to the accelerated emergence of multi-drug resistance strains [1]. As the efficacy of the antibiotics is now under threat, it has become urgent to develop alternatives for fighting pathogenic bacteria. A survey of World Health Organization (WHO) indicates that about 70 – 80% of the world population in the developing countries depends on herbal sources as their primary healthcare system [2]. Phytomedicinal research is as commendable as to be awarded the Nobel Prize in the year 2015, to the Chinese scientist Youyou Tu for discovering the antimalarial drug ‘artemisinin’ from *Artemisia annua* L. [3]. It is said that the future of phytomedicine as a discipline lies within high-quality products, able to compete with synthetic drug regarding safety and efficacy [4]. Medicinal plants are known to have curative properties due to the presence of secondary metabolites such as tannins, terpenoids, alkaloids, flavonoids, phenols, steroids, and glycosides [5]. The phytochemicals derived from plant have shown great promise in the treatment of various human diseases. Many plants of Lamiaceae family are used in traditional medicine because of their antimicrobial and antioxidant activities [6]. Unlike the crop plants, the agricultural land is not available for cultivation of medicinal plants; therefore, in vitro biomass production is an alternative choice to produce pharmaceutical compounds throughout the year without cultivation of land [7].

UTI has become the most common hospital-acquired infection. The most common cause of UTI are Gram negative bacteria. Members of this family include different pathogenic strains of *Escherichia*, *Klebsiella*, *Enterobacter* and *Proteus vulgaris* UTI strains are commonly found to be resistant to ampicillin, tetracycline, & trimethoprim-sulfamethoxazole. Some strains of *Pseudomonas* and *Proteus* were resistant to almost all the antibiotics except gentamycin [8]. Due to this wide range of drug resistance, urinary tract infection, formerly describe as ‘mild,’ has been a cause of concern. That is why the present study was taken up to explore the therapeutic potential of bioactive compounds of plant origin against the UTI pathogen.

*Coleus forskohlii* (Willd.) Briq., a plant of Indian origin, belongs to the family of Lamiaceae (previously Labiatae). This plant is very useful and has a high therapeutic value [9]. Forskolin, the major bioactive compound present in *C. forskohlii*, is a labdane diterpenoid and used to treat heart disorders, high blood pressure as well as respiratory disorders [10]. It has also been found to have potential antimicrobial activity against different standard strains of gram positive and gram negative bacteria including *S. aureus*, *Streptococcus mutans*, *Salmonella typhi*, and *Escherichia coli* [11].

Forskolin has been detected in dried roots of field grown plants and stem extracts (0.3 and 0.03%, respectively) by many researchers but not in leaf extracts even through liquid chromatography–mass spectroscopy (LC–MS) [12]. A comprehensive review on the in vitro culture of *C. forskohlii* revealed that very less or negligible amount of forskolin is present in the stem, leaf or callus culture induced from their explant [13].

We analyzed the leaf extract of in vitro and *ex vitro* plants of *C. forskohlii*, not only for the presence of forskolin but also for other major phytochemical constituents, by gas chromatography–mass spectroscopy (GC–MS).

Similarly, the aim of the present study was first, to demonstrate the antimicrobial property of the extracts against clinically isolated UTI pathogens and to compare between the naturally grown, in vitro and *ex vitro* grown plants. Secondly, profiling of chemical components present in the extracts by GC–MS. This is the first report of GC–MS of tissue culture raised plants of *C. forskohlii*. However, elucidation of mechanism of action of the extract or its individual components was beyond the scope of this study.

## Material and Methods

### Plant Source

#### *Naturally Propagated in vivo Plants*

*Coleus forskohlii* (Willd.) Briq. (family Lamiaceae) plants growing in the experimental garden of RKMVC college were used for this study. The soil of the garden was prepared by adding 100 kg cow manure and 50 kg vermin-compost per 100 square meter area. Young and healthy shoot tips (0.8 cm) from four-month-old plants were used as initial explant for in vitro culture establishment. Moderately mature leaves (opposite decussate leaves of third to sixth nodes from the tip) from ten-month-old plants were collected for Soxhlet extraction.

### *In vitro Plants*

Shoot multiplication and *in vitro* root induction of *C. forskohlii* plant were established following standard micro-propagation technique. Explants were collected from the naturally grown plants, growing in the experimental garden of RKMVC college.

**Micropropagation of *C. forskohlii*.** Shoot tips (1.0–1.2 cm) of field grown healthy plants of *C. forskohlii* (Willd.) Briq. (family Lamiaceae) were washed with 1.0% liquid detergent (Tween-20) for 2 min, then 2.0% fungicide (Bavistine®) for 10 min, finally disinfected with 0.1% mercuric chloride (HgCl<sub>2</sub>) for 6 min and rinsed thrice with sterile distilled water to remove trace of HgCl<sub>2</sub>. The shoot tips were implanted in MS medium [14] fortified with 1.0 mg/l 6-benzylaminopurine (BAP) and 0.1 mg/l  $\alpha$ -naphthalene acetic (NAA). Tubes were then kept at 25 °C under 16 h/8 h photoperiod in the tissue culture laboratory. Elongated shoots of about 2.0–2.5 cm (after 2–3 weeks) were implanted in MS medium supplemented with 1.0 mg/l indole-3-butyric acid (IBA) for root induction.

### *Ex vitro Plants*

About 3.5–4.0 cm long plantlets with well-developed root system were planted to small earthen pots containing ‘Soilrite’ and covered with transparent polybags to maintain 90–99% relative humidity as described by Haque and Ghosh [15]. After 3 weeks, the hardened plants were transferred to the experimental garden of RKMVC College, Rahara. The soil of the garden was prepared by adding 100 kg cow manure and 50 kg vermin-compost per 100 square meter area.

### Microbes Used

In the present study, both the UTI causing pathogenic strains of bacteria (isolated from the UTI patients) and the corresponding standard, laboratory strains of bacteria (used as control) were used.

### UTI Pathogens

UTI pathogens designating ISOLATE NO- 42,571, 42,423, 43,181, 43,529, 43,280, 43,509, 43,627, 42,369, 42,332, 42,313 (*Escherichia coli*), ISOLATE NO- 42,269, 43,164, 43,571, 42,436, 42,398 (*Klebsiella pneumoniae*), ISOLATE NO- 42,285, 42,006 (*Klebsiella sp.*) ISOLATE NO- 42,230 (*Pseudomonas aeruginosa*), ISOLATE NO- 43,546, 43,230 (*Staphylococcus saprophyticus*) were isolated from the urine samples of the patients. These strains were

maintained and cultured in Luria broth (HiMedia®, India) incubating at 37 °C and used for experiments.

**Isolation and Identification of UTI Pathogens** Urine samples from the diseased patients were collected (Ashok laboratory clinical testing center private limited, Kolkata 700,068, India, a BSL-3 laboratory and NABL accredited) and cultured for the isolation of bacteria following standard procedure. MacConkey agar and Nutrient agar plates (HiMedia®, India) were used to isolate UTI pathogens, loop full of urine samples was streaked on MacConkey agar and Nutrient agar plates (HiMedia®, India) and incubated for 24 h at 37 ± 2 °C. After incubation, isolated colonies were selected for further processing. Identification of the pathogenic bacteria was done in VITEK 2 COMPACT SYSTEM BIOMERIUEx machine. Vitek ID tubes containing 3.0 ml half-normal saline were incubated with 3–4 colonies of each sample and McFarland’s reading of ID tubes were taken with the instrument provided adjusting the MCF to s0.5 to s0.63. The suspensions from ID tubes were then transferred to AST tubes with the help of a pipette, and ID and AST cards were inserted into the tubes within 30 min of transfer. Data were collected after completion of the process. A routine presumptive identification was performed by Gram staining, oxidase activity, motility, catalase production, acid production in glucose, oxidation fermentation (OF) test (glucose lactose and sucrose fermentation), Indole test, Voges–Proskauer (VP) test and hydrogen sulfide production. A total of 120 samples of urine, collected from the UTI patients of different age and sex, were screened for the isolation of pathogens (online resource 1). The strains were then subjected to screening for antibiotic resistance.

**Detection of Antibiotic Resistance Among the Test Strains** Antibiotic sensitivity assay was performed to demonstrate the resistance against eight antibiotics namely amoxicillin, ciprofloxacin, gentamycin, norfloxacin, nitrofurantoin, clotrimazole, cefotaxime, tetracyclin by the standard disk diffusion method [16]. All the antibiotic disks, used in this study, were purchased from the HiMedia Pvt. Ltd. (Bombay, India), and their efficacies were checked using *E. coli* B strain (an antibiotic sensitive strain). We screened one hundred and twenty urine samples and identified twenty strains were resistant to all or most of the antibiotics (online resource 2).

### Standard Bacterial Strains

Standard strains of MTCC 3160 (*S. aureus*), MTCC 441 (*Bacillus subtilis*), MTCC 443 (*Escherichia coli*), MTCC 3542 (*P. aeruginosa*), MTCC 109 (*K. pneumoniae*) MTCC 3382 (*S. epidermidis*), MTCC 7621 (*Pseudomonas*

syringae), MTCC 1972 (*Streptococcus pyogenes*) were procured from Microbial Type Culture Collection (MTCC), Chandigarh, India. Bacterial strains of MTCC 3160, 441, 3542, 109, 3382 were maintained in nutrient broth MTCC 443 in tryptic soy broth, MTCC 1972 in rabbit blood broth, MTCC 7621 in yeast manitol medium (according to MTCC manual). All the bacterial strains were cultured overnight in nutrient broth for experimental purpose (HiMedia®, India.).

### Extraction of Plant Material

Moderately mature leaves of completely grown in vitro plants (8 weeks old with proper root, shoot and leaves) were collected for extraction. Leaves of (third to sixth nodes from the tip) ten months' old naturally propagated in vivo plants and tissue culture raised ex vitro plants were collected from experimental garden. Freshly collected 60 g leaves (FW) of in vitro plants, tissue culture raised field grown ex vitro plants, and naturally propagated field grown plants were subjected to dry at 40 °C for 7 days. After completely drying, the plant leaves were powdered, and 5.0 g of each sample was used for extraction. The extraction was carried out using Soxhlet apparatus at 80 °C for 15 h using methanol as a solvent. After extraction, solvent was evaporated and dried samples were kept at 4 °C for further use.

### Antibacterial Activity

#### Agar Well Diffusion Method

Antibacterial activities of the extracts were investigated using agar well diffusion method followed by Deans et al., with slight modification [17]. Wells of 6.0 mm diameter were punched into the Muller Hinton agar plates, and 60 µl of extracts were added to each hole. The dried plant extracts were re-suspended in dimethyl sulfoxide (DMSO) to make five concentrations, i.e., 0.75, 1.5, 3.0, 4.5 and 6.0 mg/cup were tested against all the microbial strains. The Petri dishes were incubated at 37 °C for 24 h. After incubation, the diameters of the zones of inhibition, formed around each hole, were measured and recorded. Testing was carried out for each bacterium and fungus, in triplicate. Negative control plates were prepared using 60 µl of DMSO, and positive control plates were prepared using each of chloramphenicol, ampicillin, amoxicillin, tetracycline at a concentration of 25 mg/ml.

#### Minimum Inhibitory Concentration

The 'Twofold broth dilution method' was used to determine the minimum inhibitory concentration (MIC) of the

plant extracts against all the pathogenic and standard microorganisms with minor modification following Ericsson and Sherris [18]. The dried plant extracts were re-suspended in DMSO to make 50 mg/ml concentration and then added to Luria broth by serial dilution method. Exact 100 µl inoculum of such broth was then added to every tube and incubated at 37 °C for 24 h. The MIC values for all the bacteria were noted for the lowest concentration of the plant extracts used.

#### Minimum Bactericidal Activity

Minimum bactericidal activity (MBC) was determined by plating the respective concentrations of the extracts, used to analyze the MIC values. Exact 100 µl of inoculum was applied to the plate, and data collected after 24 h of incubation.

### Gas Chromatography–Mass Spectroscopy

Methanol extracts of the leaves of in vitro, ex vitro and naturally grown *C. forskohlii* plants were analyzed by gas chromatography–mass spectroscopy (GC–MS) for the identification of different bioactive compounds present in the extracts. GC–MS was performed using column: TRWAXMS 30 × 0.25 mm × 0.25 µm df, equipment: Trace GC ultra, Thermo fisher scientific India pvt. Ltd. Gas flow: 1.0 ml/min split 20:1 detector: mass detector Polaris Q mass software data collection XCALIBUR. 1.0 µl of extract was injected in the injection port of GC column. Oven temperature program was: no hold up to 50 °C, for 2 min at the flow rate of 10 °C/min, 5 min hold up to 270 °C. Injector temperature 250 °C and total GC–MS running time 29 min. Helium Gas was used as carrier gas at a constant flow rate of 1 ml/min. MS program: library NIST (USA). Inlet line temperature was 250 °C, and source temperature was 230 °C. Mass scan was done at 50–650 m/z with solvent delay of 0–4 min and total mass spectrum running time was 51 min.

### Statistical Data Analyses

Each experiment, for determination of antimicrobial activity by agar well diffusion method, was repeated thrice with 5 concentrations per replicate. All data were subjected to one-way analysis of variance (ANOVA) using SPSS software for Windows (IBM® SPSS, version 19.0, Chicago, IL). After conducting an ANOVA, the means were further separated using Tukey's test at  $P \leq 0.05$ .

## Results and Discussion

### Micropropagation

Profuse shoot growth occurred within 4 weeks of implantation with the production of  $20.4 \pm 0.28$  shoots per explants. These multiplied shoots were elongated after one subculture in same medium composition (Fig. 1a). These shoots were well rooted in IBA (1.0 mg/l) containing root-inducing medium with  $14.2 \pm 0.18$  roots per shoot after 4 weeks (Fig. 1b). After 3 weeks, the hardened plants were transferred to the experimental garden of R.K.M.V.C. College, Rahara. Total  $83.2 \pm 3.4\%$  ex vitro plants were survived in the field conditions and grew healthily (Fig. 1c). Finally all ex vitro field grown plants were flowered after 10–11 months of field transfer (Fig. d, e). It is well known that the biomass production, using natural habitats of any plant, is time consuming and harvesting of wild population leads to the depletion of the resource, whereas biotechnological cultivation of plant through tissue culture is a cost effective, less time-consuming process which can easily be upgraded to industrial level [7]. Moreover, clonal propagation of any explant of a plant is essentially very useful for the production of the fruitful results. Morphological and health improvement of the plants were observed when plants were grown ex vitro compared to naturally grown plants. This fact led us to investigate the potency of tissue culture raised plants as a source of antimicrobial agents. Ex vitro grown plants seems fleshier and contains more hair with higher leaf content while naturally grown plants having lower leaf content and leaf hair also lesser than ex vitro grown plants. Morphologically ex vitro plants were more stable and healthy over naturally grown plants.

### Antimicrobial Activity of Extract

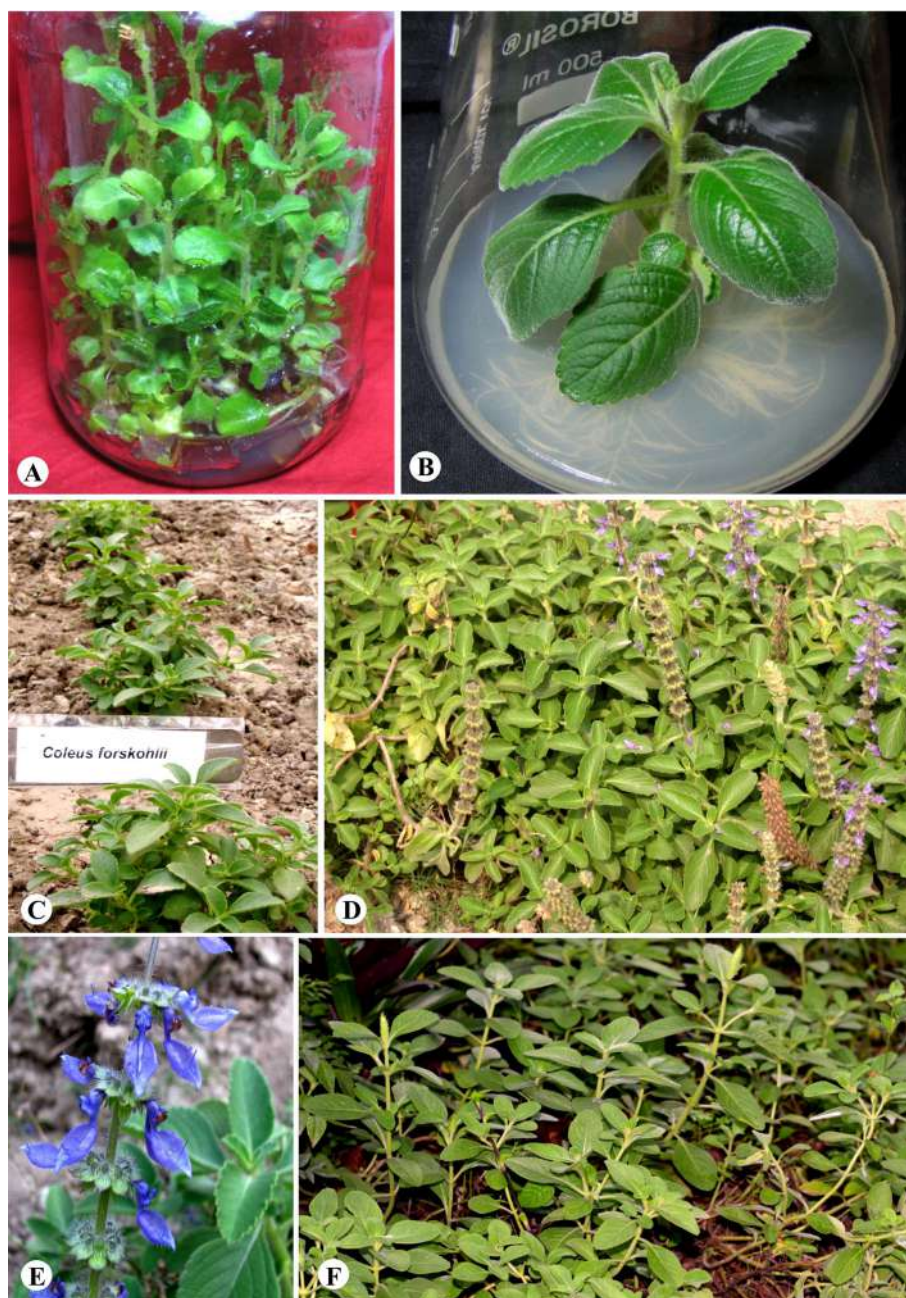
#### Agar Well Diffusion

All the pathogenic (excepting three) and standard bacteria (excepting one) were found to be sensitive to the methanol extracts of both in vitro and ex vitro plants (Table 1) while nine bacteria including pathogen and non-pathogen found resistant against naturally grown plant extract. Because of much lower activity in case of naturally grown plants, only maximum concentration (6.0 mg/cup) is used to represent the antimicrobial potency. The ex vitro plant extracts were more effective as antimicrobial agent compared to those of in vitro plants and naturally grown plants. Maximum diameter of zone of inhibition (DZI) of  $18.66 \pm 0.57$  mm was found with highest concentration of ex vitro plant extract (6.0 mg/cup) against pathogenic ISOLATE NO-

42,285 compared to its in vitro counterpart with a DZI of  $17.66 \pm 0.033$  mm and naturally grown part with a DZI of  $14 \pm 0.57$  mm. However, for ISOLATE NO- 42,423 and 42,313, all the concentrations of in vitro plant extracts were more effective than ex vitro extracts (DZI of  $16.00 \pm 0.81$  mm and  $12.33 \pm 0.47$  mm were obtained at a concentration of 6.0 mg/ml compared to  $12.66 \pm 0.47$  mm and  $9.66 \pm 0.94$  mm, respectively). Interestingly, in vitro extracts were found to be saturated at a concentration of 4.5 mg/cup as not much increase was found in DZI at higher concentrations. ISOLATE NO- 42,269 and 43,546 were found to be completely resistant to the plant extracts used and ISOLATE NO- 43,546 and 43,164 showed no or least inhibition. ISOLATE NO- 42313 showed an inhibition which is lesser than the average. Standard bacteria (excepting MTCC 109) showed inhibition with both types of plant extracts. Naturally grown plant extract were less effective against all the microbes tested than both in vitro and ex vitro plant extract. Here also, ex vitro extracts showed much higher inhibitory effects over in vitro extracts, as it was with clinical isolates. Undoubtedly, the outcome was very encouraging as, all the extracts of the plant leaves of naturally grown, in vitro and ex vitro, showed antibacterial activity against all the microbial strain tested in present study. According to effectivity, ex vitro plants were stronger, in vitro plants were moderately active and naturally grown were less effective against both pathogens and non-pathogens. Methanolic extracts of leaves have been used in our study, as the polarity index of methanol is 5.1, therefore all polar (and to some extent nonpolar) bioactive compounds are highly or at least fairly soluble. Previously, methanolic extracts of many plants of Lamiaceae family, including root and leaf extracts of *C. aromaticus* and *C. forskohlii*, has been shown to be antimicrobial in nature [19, 20]. Aqueous, ethanolic and methanolic extracts of nine species other than *Coleus* have also been reported to exhibit antimicrobial activity against UTI pathogens [21]. However, in this study, methanolic extracts showed better performance against UTI pathogens. It was also reported that if antimicrobial compound like commercial antibiotics were used with the plant extract it became more effective rather than using extract or antibiotics itself [22]. These initiatory studies motivated us to take up the plan of investigating UTI pathogens, which are resistant to multi-drugs. Among 20 such isolates, 18 were gram negative (ten *Escherichia coli*, seven *K. pneumoniae* and one *Pseudomonas aeruginosa*), and *E. coli* strains were found to be more effective than *K. pneumoniae*. According to the finding of Singh et al. 2017 [23], most of the strains including extended spectrum beta lactamase (ESBL) positive were found to be susceptible to the extract of the respective plant used in this study. Nevertheless, this study



**Fig. 1** Micropropagation of *Coleus forskohlii*. **a** in vitro multiplication, **b** in vitro grown complete plant with well-developed root system, **c** tissue culture raised ex vitro field grown plants of 3 months of age, **d** tissue culture raised ex vitro field grown plants (10 months age) in flowering stage, **e** Flowers of ex vitro plant, **f** naturally propagated in vivo field grown plants (10 months age) in flowering stage



is unique and a class by itself with adequate detail and no such work has been done before with *C. forskohlii*.

#### *MIC and MBC*

The results of MIC and MBC of the plant extracts (in vitro and ex vitro) are summarized in Table 2. In case of pathogenic bacteria ISOLATE NO- 4257, the MIC and MBC were found to be lowest with ex vitro, in vitro extract

(1.25 mg/ml and 1.75 mg/ml for in vitro and 0.75 mg/ml and 1.25 mg/ml for ex vitro plant extracts). Naturally grown plant extract shows less promising MIC and MBC than both in vitro and ex vitro plant extract. However, the plant extracts (in vitro and ex vitro) were not effective against MTCC 109 and pathogens designated as ISOLATE NO- 42,269, 42,436, and 43,280 wherein naturally grown plant extract ineffective against nine bacteria.

**Table 1** Antimicrobial activity of the tissue culture raised in vitro and ex vitro *Coleus forskohlii* plant (methanolic extract of leaf) against

Microorganisms		Zone of inhibition (mm)									
		Concentration (mg/cup) of in vitro plant extract					Concentration (mg/cup) of ex vitro plant extract				
Type	Isolate No	0.75	1.5	3.0	4.5	6.0	0.75	1.5	3.0	4.5	6.0
<b>(a) Pathogenic multidrug resistant urinary tract infecting bacterial strains</b>											
Pathogenic (multidrug resistant strains of urinary tract infecting bacteria)	42,571	10.00 ± 0.57 <sup>e</sup>	12.33 ± 0.66 <sup>d</sup>	13.33 ± 0.33 <sup>cd</sup>	14.00 ± 0.57 <sup>c</sup>	14.33 ± 0.33 <sup>c</sup>	14.66 ± 0.33 <sup>c</sup>	16.33 ± 0.66 <sup>b</sup>	18.00 ± 0.57 <sup>a</sup>	18.33 ± 0.33 <sup>a</sup>	18.33 ± 0.57 <sup>a</sup>
	42,423	11.33 ± 0.33 <sup>cd</sup>	13.33 ± 0.33 <sup>b</sup>	14.66 ± 0.66 <sup>a</sup>	15.66 ± 0.33 <sup>a</sup>	16.00 ± 0.33 <sup>a</sup>	8.33 ± 0.33 <sup>e</sup>	10.33 ± 0.33 <sup>d</sup>	12.00 ± 0.57 <sup>bc</sup>	12.66 ± 0.66 <sup>bc</sup>	12.66 ± 0.66 <sup>bc</sup>
	43,181	10.33 ± 0.33 <sup>f</sup>	12.33 ± 0.33 <sup>e</sup>	13.66 ± 0.33 <sup>d</sup>	14.66 ± 0.33 <sup>bc</sup>	15.33 ± 0.33 <sup>b</sup>	12.33 ± 0.33 <sup>e</sup>	14.00 ± 0.57 <sup>cd</sup>	15.33 ± 0.33 <sup>b</sup>	16.33 ± 0.33 <sup>a</sup>	16.66 ± 0.33 <sup>a</sup>
	42,269	R	R	R	R	R	R	R	R	R	R
	42,230	9.00 ± 0.57 <sup>e</sup>	10.66 ± 0.33 <sup>d</sup>	12.33 ± 0.33 <sup>c</sup>	13.33 ± 0.33 <sup>b</sup>	13.66 ± 0.33 <sup>b</sup>	10.00 ± 0.33 <sup>d</sup>	11.66 ± 0.33 <sup>c</sup>	13.33 ± 0.33 <sup>b</sup>	13.66 ± 0.33 <sup>b</sup>	14.33 ± 0.33 <sup>a</sup>
	43,546	0 <sup>d</sup>	0 <sup>d</sup>	0 <sup>d</sup>	8.33 ± 0.33 <sup>e</sup>	8.66 ± 0.33 <sup>e</sup>	0 <sup>d</sup>	0 <sup>d</sup>	8.66 ± 0.33 <sup>e</sup>	9.66 ± 0.33 <sup>e</sup>	10.33 ± 0.33 <sup>a</sup>
	43,230	13.33 ± 0.33 <sup>de</sup>	14.33 ± 0.33 <sup>cd</sup>	15.33 ± 0.33 <sup>abc</sup>	16 ± 0.57 <sup>ab</sup>	16.66 ± 0.33 <sup>a</sup>	12.66 ± 0.66 <sup>e</sup>	14.33 ± 0.88 <sup>cd</sup>	14.66 ± 0.88 <sup>bcd</sup>	16.33 ± 0.66 <sup>a</sup>	16.66 ± 0.33 <sup>a</sup>
	43,164	0 <sup>c</sup>	0 <sup>c</sup>	0 <sup>c</sup>	0 <sup>c</sup>	8.33 ± 0.33 <sup>b</sup>	0 <sup>c</sup>	0 <sup>c</sup>	0 <sup>c</sup>	8.33 ± 0.33 <sup>b</sup>	9.33 ± 0.33 <sup>a</sup>
	42,285	12.33 ± 0.33 <sup>e</sup>	13.66 ± 0.33 <sup>f</sup>	16 ± 0.57 <sup>de</sup>	17 ± 0.57 <sup>abcd</sup>	17.66 ± 0.33 <sup>ab</sup>	15.33 ± 0.33 <sup>e</sup>	15.66 ± 0.33 <sup>de</sup>	16.33 ± 0.33 <sup>bcde</sup>	17.33 ± 0.66 <sup>abc</sup>	18.66 ± 0.57 <sup>a</sup>
	43,571	11.66 ± 0.33 <sup>d</sup>	13.33 ± 0.33 <sup>c</sup>	15.33 ± 0.33 <sup>b</sup>	17.33 ± 0.33 <sup>a</sup>	17.66 ± 0.33 <sup>a</sup>	14.66 ± 0.66 <sup>bc</sup>	15.33 ± 0.88 <sup>b</sup>	16.33 ± 1.00 <sup>ab</sup>	17.33 ± 0.88 <sup>a</sup>	17.66 ± 0.66 <sup>e</sup>
	42,436	R	R	R	R	R	R	R	R	R	R
	43,529	0 <sup>e</sup>	0 <sup>e</sup>	8.33 ± 0.33 <sup>e</sup>	10 ± 0.57 <sup>d</sup>	10.66 ± 0.33 <sup>cd</sup>	9.66 ± 0.33 <sup>d</sup>	10.66 ± 0.33 <sup>cd</sup>	11.33 ± 0.66 <sup>bc</sup>	12.33 ± 0.57 <sup>b</sup>	13.66 ± 0.88 <sup>a</sup>
42,398	0 <sup>d</sup>	0 <sup>d</sup>	0 <sup>d</sup>	8.33 ± 0.33 <sup>b</sup>	8.66 ± 0.33 <sup>b</sup>	0 <sup>d</sup>	5.33 ± 2.66 <sup>c</sup>	9 ± 0.57 <sup>b</sup>	10.66 ± 0.33 <sup>a</sup>	10.66 ± 0.33 <sup>a</sup>	
43,280	R	R	R	R	R	R	R	R	R	R	
43,509	8.66 ± 0.33 <sup>f</sup>	10.33 ± 0.33 <sup>e</sup>	12.33 ± 0.33 <sup>cd</sup>	13.66 ± 0.66 <sup>ab</sup>	14.66 ± 0.88 <sup>a</sup>	0 <sup>i</sup>	8.66 ± 0.66 <sup>f</sup>	9.66 ± 0.33 <sup>ef</sup>	11.66 ± 0.33 <sup>d</sup>	13.33 ± 0.66 <sup>bc</sup>	
43,627	8.33 ± 0.33 <sup>f</sup>	8.33 ± 0.57 <sup>f</sup>	12.33 ± 0.66 <sup>d</sup>	13.66 ± 0.57 <sup>cd</sup>	14.66 ± 0.33 <sup>c</sup>	12.33 ± 0.66 <sup>d</sup>	13.33 ± 0.66 <sup>cd</sup>	14.66 ± 0.33 <sup>c</sup>	16.66 ± 0.33 <sup>b</sup>	18.33 ± 0.33 <sup>a</sup>	
42,006	0 <sup>c</sup>	8.66 ± 0.66 <sup>cd</sup>	11 ± 0.57 <sup>b</sup>	12 ± 0.57 <sup>a</sup>	12.33 ± 0.66 <sup>a</sup>	0 <sup>c</sup>	0 <sup>c</sup>	0 <sup>c</sup>	8 ± 0.33 <sup>cd</sup>	8.33 ± 0.33 <sup>cd</sup>	
42,369	8.33 ± 0.33 <sup>e</sup>	8.66 ± 0.33 <sup>d</sup>	10 ± 0.57 <sup>c</sup>	10.66 ± 0.33 <sup>c</sup>	10.66 ± 0.33 <sup>c</sup>	8.66 ± 0.33 <sup>d</sup>	10.33 ± 0.33 <sup>c</sup>	11.66 ± 0.33 <sup>b</sup>	12.66 ± 0.33 <sup>a</sup>	12.66 ± 0.33 <sup>a</sup>	
42,332	0 <sup>f</sup>	0 <sup>f</sup>	8.33 ± 0.33 <sup>e</sup>	8.66 ± 0.66 <sup>de</sup>	9.33 ± 0.33 <sup>cd</sup>	0 <sup>f</sup>	8.33 ± 0.33 <sup>e</sup>	9.66 ± 0.33 <sup>c</sup>	11.33 ± 0.3 <sup>b</sup>	12.33 ± 0.33 <sup>a</sup>	
42,313	8.33 ± 0.33 <sup>d</sup>	9.33 ± 0.57 <sup>cd</sup>	10.66 ± 0.33 <sup>b</sup>	12.33 ± 0.33 <sup>a</sup>	12.33 ± 0.33 <sup>a</sup>	0 <sup>f</sup>	0 <sup>f</sup>	8.33 ± 0.33 <sup>a</sup>	8.33 ± 0.33 <sup>a</sup>	9.66 ± 0.66 <sup>e</sup>	
<b>Microorganisms</b>											
Zone of inhibition (mm)											
Concentration (mg/cup) of in vivo plant extract											
Type	Isolate No	0.75	1.5	3.0	4.5	6.0	0.75	1.5	3.0	4.5	6.0
<b>(a) Pathogenic multidrug resistant urinary tract infecting bacterial strains</b>											
Pathogenic (multidrug resistant strains of urinary tract infecting bacteria)	42,571	0 <sup>h</sup>	6 ± 0.00 <sup>g</sup>	6.66 ± 0.66 <sup>g</sup>	6.66 ± 0.66 <sup>g</sup>	6.66 ± 0.66 <sup>g</sup>	6 ± 0.00 <sup>g</sup>	6.66 ± 0.66 <sup>g</sup>	8.33 ± 0.57 <sup>f</sup>	8.33 ± 0.57 <sup>f</sup>	9.00 ± 0.57 <sup>f</sup>
	42,423	0 <sup>h</sup>	6.66 ± 0.33 <sup>g</sup>	7.66 ± 0.33 <sup>ef</sup>	7.66 ± 0.33 <sup>ef</sup>	7.66 ± 0.33 <sup>ef</sup>	6.66 ± 0.33 <sup>g</sup>	7.66 ± 0.33 <sup>ef</sup>	8.66 ± 0.33 <sup>e</sup>	8.66 ± 0.33 <sup>e</sup>	10.33 ± 0.33 <sup>d</sup>
	43,181	0 <sup>i</sup>	6.00 ± 0.00 <sup>h</sup>	6.66 ± 0.33 <sup>h</sup>	6.66 ± 0.33 <sup>h</sup>	6.66 ± 0.33 <sup>h</sup>	6.00 ± 0.00 <sup>h</sup>	6.66 ± 0.33 <sup>h</sup>	8.66 ± 0.33 <sup>e</sup>	8.66 ± 0.33 <sup>e</sup>	11.00 ± 0.00 <sup>f</sup>
	42,269	R	R	R	R	R	R	R	R	R	R
	42,230	0 <sup>h</sup>	0 <sup>h</sup>	0 <sup>h</sup>	0 <sup>h</sup>	0 <sup>h</sup>	0 <sup>h</sup>	0 <sup>h</sup>	6.33 ± 0.33 <sup>g</sup>	7.66 ± 0.33 <sup>f</sup>	7.66 ± 0.33 <sup>f</sup>
	43,546	0 <sup>d</sup>	0 <sup>d</sup>	0 <sup>d</sup>	0 <sup>d</sup>	0 <sup>d</sup>	0 <sup>d</sup>	0 <sup>d</sup>	0 <sup>d</sup>	0 <sup>d</sup>	0 <sup>d</sup>
	43,230	0 <sup>j</sup>	6.00 ± 0 <sup>h</sup>	7.66 ± 0.33 <sup>g</sup>	8.00 ± 0 <sup>g</sup>	8.00 ± 0 <sup>g</sup>	6.00 ± 0 <sup>h</sup>	7.66 ± 0.33 <sup>g</sup>	8.00 ± 0 <sup>g</sup>	8.00 ± 0 <sup>g</sup>	10.00 ± 0.57 <sup>f</sup>
	43,164	0 <sup>c</sup>	0 <sup>c</sup>	0 <sup>c</sup>	0 <sup>c</sup>	0 <sup>c</sup>	0 <sup>c</sup>	0 <sup>c</sup>	0 <sup>c</sup>	0 <sup>c</sup>	0 <sup>c</sup>
	42,285	6.33 ± 0.33 <sup>ij</sup>	7.33 ± 0.33 <sup>ij</sup>	7.66 ± 0.33 <sup>ij</sup>	7.66 ± 0.33 <sup>ij</sup>	7.66 ± 0.33 <sup>ij</sup>	6.33 ± 0.33 <sup>ij</sup>	7.66 ± 0.33 <sup>ij</sup>	10.00 ± 0.57 <sup>h</sup>	10.00 ± 0.57 <sup>h</sup>	14.00 ± 0.57 <sup>f</sup>
	43,571	0 <sup>h</sup>	0 <sup>h</sup>	6.00 ± 0.00 <sup>g</sup>	6.66 ± 0.33 <sup>f</sup>	6.66 ± 0.33 <sup>f</sup>	0 <sup>h</sup>	6.00 ± 0.00 <sup>g</sup>	7.66 ± 0.33 <sup>f</sup>	7.66 ± 0.33 <sup>f</sup>	9.66 ± 0.33 <sup>e</sup>

Table 1 continued

Microorganisms		Zone of inhibition (mm)									
		Concentration (mg/cup) of in vivo plant extract									
Type	Isolate No	0.75	1.5	3.0	4.5	6.0	7.5	15.0	30.0	45.0	60.0
	42,436	R	R	R	R	R	R	R	R	R	R
	43,529	0 <sup>g</sup>	0 <sup>g</sup>	0 <sup>g</sup>	6.33 ± 0.33 <sup>f</sup>	7.66 ± 0.33 <sup>e</sup>	0 <sup>d</sup>	0 <sup>d</sup>	0 <sup>d</sup>	0 <sup>d</sup>	0 <sup>d</sup>
	42,398	0 <sup>d</sup>	0 <sup>d</sup>	0 <sup>d</sup>	0 <sup>d</sup>	0 <sup>d</sup>	0 <sup>d</sup>	0 <sup>d</sup>	0 <sup>d</sup>	0 <sup>d</sup>	0 <sup>d</sup>
	43,280	R	R	R	R	R	R	R	R	R	R
	43,509	0 <sup>i</sup>	0 <sup>i</sup>	0 <sup>i</sup>	6.00 ± 0.00 <sup>h</sup>	7.33 ± 0.33 <sup>g</sup>	0 <sup>i</sup>	0 <sup>i</sup>	0 <sup>i</sup>	0 <sup>i</sup>	0 <sup>i</sup>
	43,627	0 <sup>h</sup>	0 <sup>h</sup>	0 <sup>h</sup>	9.33 ± 0.33 <sup>f</sup>	10.66 ± 0.33 <sup>e</sup>	0 <sup>e</sup>	0 <sup>e</sup>	0 <sup>e</sup>	0 <sup>e</sup>	0 <sup>e</sup>
	42,006	0 <sup>e</sup>	0 <sup>e</sup>	0 <sup>e</sup>	6.33 ± 0.33 <sup>g</sup>	7.33 ± 0.33 <sup>f</sup>	0 <sup>f</sup>	0 <sup>f</sup>	0 <sup>f</sup>	0 <sup>f</sup>	0 <sup>f</sup>
	42,369	0 <sup>h</sup>	0 <sup>h</sup>	0 <sup>h</sup>	6.33 ± 0.33 <sup>e</sup>	7.33 ± 0.33 <sup>d</sup>	0 <sup>f</sup>	0 <sup>f</sup>	0 <sup>f</sup>	0 <sup>f</sup>	0 <sup>f</sup>
	42,332	0 <sup>f</sup>	0 <sup>f</sup>	0 <sup>f</sup>	6.33 ± 0.33 <sup>e</sup>	8.66 ± 0.33 <sup>cd</sup>	0 <sup>f</sup>	0 <sup>f</sup>	0 <sup>f</sup>	0 <sup>f</sup>	0 <sup>f</sup>
	42,313	0 <sup>f</sup>	0 <sup>f</sup>	0 <sup>f</sup>	6.33 ± 0.33 <sup>e</sup>	8.66 ± 0.33 <sup>cd</sup>	0 <sup>f</sup>	0 <sup>f</sup>	0 <sup>f</sup>	0 <sup>f</sup>	0 <sup>f</sup>
Microorganisms		Zone of inhibition (mm)									
		Concentration (mg/cup) of in vitro plant extract									
Type	Isolate No	0.75	1.5	3.0	4.5	6.0	7.5	15.0	30.0	45.0	60.0
(b) Against non-pathogenic laboratory standard strains (MTCC)											
Laboratory standard bacterial strain (MTCC)	MTCC 3160	13.66 ± 0.88 <sup>ef</sup>	15.66 ± 0.88 <sup>cd</sup>	17.00 ± 0.57 <sup>abc</sup>	17.66 ± 0.88 <sup>ab</sup>	18.33 ± 0.66 <sup>a</sup>	12.00 ± 0.57 <sup>fg</sup>	14.00 ± 0.57 <sup>de</sup>	16.33 ± 0.88 <sup>bc</sup>	18.00 ± 0.57 <sup>ab</sup>	18.66 ± 0.33 <sup>a</sup>
	MTCC 109	R	R	R	R	R	R	R	R	R	R
	MTCC 443	8.66 ± 0.33 <sup>c</sup>	11.66 ± 0.33 <sup>cd</sup>	13.33 ± 0.33 <sup>bc</sup>	14.33 ± 0.33 <sup>b</sup>	14.66 ± 0.33 <sup>b</sup>	11.33 ± 1.20 <sup>d</sup>	14.33 ± 1.20 <sup>b</sup>	17.00 ± 1.00 <sup>a</sup>	18.66 ± 0.88 <sup>a</sup>	18.66 ± 0.88 <sup>a</sup>
	MTCC 3542	10.00 ± 0.57 <sup>f</sup>	12.33 ± 0.33 <sup>de</sup>	14.00 ± 0.57 <sup>e</sup>	15.66 ± 0.66 <sup>ab</sup>	16.00 ± 0.57 <sup>ab</sup>	11.33 ± 0.33 <sup>e</sup>	12.66 ± 0.33 <sup>d</sup>	15.00 ± 0.57 <sup>bc</sup>	15.33 ± 0.33 <sup>ab</sup>	16.33 ± 0.33 <sup>a</sup>
	MTCC 441	9.66 ± 0.33 <sup>d</sup>	12 ± 0.57 <sup>c</sup>	13.66 ± 0.33 <sup>b</sup>	14.33 ± 0.33 <sup>ab</sup>	14.66 ± 0.33 <sup>ab</sup>	10.33 ± 0.57 <sup>d</sup>	12.00 ± 0.57 <sup>c</sup>	14.00 ± 1.00 <sup>ab</sup>	15.00 ± 0.57 <sup>ab</sup>	15.33 ± 0.66 <sup>a</sup>
	MTCC 3382	9.33 ± 0.88 <sup>e</sup>	11.33 ± 0.88 <sup>d</sup>	13.33 ± 1.88 <sup>e</sup>	14.33 ± 0.33 <sup>c</sup>	14.66 ± 0.33 <sup>c</sup>	13.33 ± 0.33 <sup>c</sup>	15.00 ± 0.57 <sup>c</sup>	17.33 ± 0.88 <sup>b</sup>	20.33 ± 0.88 <sup>a</sup>	21.00 ± 0.57 <sup>a</sup>
	MTCC 7621	7.66 ± 0.33 <sup>hi</sup>	9.00 ± 0.57 <sup>g</sup>	11.33 ± 0.33 <sup>f</sup>	13.66 ± 0.33 <sup>e</sup>	14.00 ± 0.37 <sup>e</sup>	15.33 ± 0.33 <sup>d</sup>	17.33 ± 0.33 <sup>c</sup>	19.33 ± 0.33 <sup>b</sup>	20.66 ± 0.88 <sup>a</sup>	21.33 ± 0.66 <sup>a</sup>
	MTCC 1972	0 <sup>i</sup>	8.33 ± 0.33 <sup>fg</sup>	10.66 ± 0.66 <sup>de</sup>	11.33 ± 0.33 <sup>d</sup>	11.33 ± 0.33 <sup>d</sup>	13.33 ± 0.88 <sup>c</sup>	14.66 ± 0.88 <sup>bc</sup>	16.00 ± 0.57 <sup>ab</sup>	16.66 ± 0.66 <sup>c</sup>	17.00 ± 0.57 <sup>a</sup>
Microorganisms		Zone of inhibition (mm)									
		Concentration (mg/cup) of in vivo plant extract									
Type	Isolate No	0.75	1.5	3.0	4.5	6.0	7.5	15.0	30.0	45.0	60.0
(b) Against non-pathogenic laboratory standard strains (MTCC)											
Laboratory standard bacterial strain (MTCC)	MTCC 3160	0 <sup>j</sup>	0 <sup>j</sup>	6.33 ± 0.33 <sup>i</sup>	8.33 ± 0.33 <sup>h</sup>	10.33 ± 0.33 <sup>g</sup>	13.33 ± 0.33 <sup>f</sup>	15.33 ± 0.33 <sup>e</sup>	18.33 ± 0.33 <sup>d</sup>	21.33 ± 0.33 <sup>c</sup>	24.33 ± 0.33 <sup>b</sup>
	MTCC 109	R	R	R	R	R	R	R	R	R	R
	MTCC 443	0 <sup>g</sup>	0 <sup>g</sup>	0 <sup>g</sup>	7.33 ± 0.33 <sup>f</sup>	8.00 ± 0.57 <sup>e</sup>	0 <sup>g</sup>	0 <sup>g</sup>	0 <sup>g</sup>	0 <sup>g</sup>	0 <sup>g</sup>
	MTCC 3542	0 <sup>h</sup>	0 <sup>h</sup>	0 <sup>h</sup>	6.33 ± 0.33 <sup>g</sup>	7.00 ± 0.57 <sup>de</sup>	0 <sup>h</sup>	0 <sup>h</sup>	0 <sup>h</sup>	0 <sup>h</sup>	0 <sup>h</sup>
	MTCC 441	0 <sup>f</sup>	0 <sup>f</sup>	0 <sup>f</sup>	6.00 ± 0.00 <sup>h</sup>	7.00 ± 0.57 <sup>de</sup>	0 <sup>f</sup>	0 <sup>f</sup>	0 <sup>f</sup>	0 <sup>f</sup>	0 <sup>f</sup>
	MTCC 3382	0 <sup>g</sup>	0 <sup>g</sup>	6.33 ± 0.33 <sup>f</sup>	7.33 ± 0.33 <sup>f</sup>	9.66 ± 0.33 <sup>de</sup>	11.00 ± 0.57 <sup>de</sup>	12.33 ± 0.33 <sup>cd</sup>	13.66 ± 0.33 <sup>bc</sup>	15.00 ± 0.57 <sup>ab</sup>	16.33 ± 0.33 <sup>b</sup>
	MTCC 7621	0 <sup>k</sup>	6.66 ± 0.33 <sup>j</sup>	7.33 ± 0.33 <sup>ij</sup>	8.00 ± 0.33 <sup>gh</sup>	9.33 ± 0.33 <sup>ef</sup>	10.66 ± 0.33 <sup>de</sup>	12.00 ± 0.33 <sup>cd</sup>	13.33 ± 0.33 <sup>bc</sup>	14.66 ± 0.33 <sup>ab</sup>	16.00 ± 0.33 <sup>a</sup>
	MTCC 1972	0 <sup>i</sup>	6.33 ± 0.33 <sup>h</sup>	7.66 ± 0.33 <sup>gh</sup>	9.33 ± 0.33 <sup>ef</sup>	11.00 ± 0.57 <sup>de</sup>	12.33 ± 0.33 <sup>cd</sup>	13.66 ± 0.33 <sup>bc</sup>	15.00 ± 0.57 <sup>ab</sup>	16.33 ± 0.33 <sup>b</sup>	17.66 ± 0.33 <sup>a</sup>

'R' = Resistant; The data were recorded after 24 h of culture. Each value represents the mean ± standard error. Mean followed by the same letters in each row are not significantly different at  $p \leq 0.05$  according to Tukey's multiple range tests

**Table 2** Minimum inhibitory concentration (MIC) and minimum bactericidal activity (MBC) of the methanolic leaf extract of in vitro and ex vitro plants of *Coleus forskohlii*

Bacteria	Isolate no	MIC (mg/ml)			MBC (mg/ml)		
		In vitro plant extract	Ex vitro plant extract	In vivo plant extract	In vitro plant extract	Ex vitro plant extract	In vivo plant extract
Pathogenic (Multi-drug resistant strains of urinary tract infecting bacteria)	42,571	1.25	0.75	2.75	1.75	1.25	3.50
	42,423	0.75	1.50	2.25	1.25	2.25	2.50
	43,181	1.00	0.75	2.25	1.75	1.50	2.75
	42,269	R	R	R	R	R	R
	42,230	1.50	1.25	3.00	2.25	2.00	3.75
	43,546	3.00	2.75	-	4.25	3.50	-
	43,230	1.25	1.00	-	1.75	1.75	-
	43,164	6.50	5.75	-	7.25	6.75	-
	42,285	1.00	0.75	2.00	1.75	1.50	2.50
	43,571	0.75	0.50	2.00	2.00	1.25	2.00
	42,436	R	R	R	R	R	R
	43,529	3.00	2.75	5.25	4.25	3.50	5.75
	42,398	4.75	4.25	-	6.25	5.50	-
	43,280	R	R	R	R	R	R
	43,509	2.25	3.00	5.75	3.25	4.25	6.50
	43,627	1.50	0.75	3.50	2.25	1.50	4.00
	42,006	3.25	6.25	-	4.75	7.50	-
	42,369	3.25	2.75	6.00	4.75	3.50	7.00
	42,332	4.50	4.25	-	5.25	4.75	-
	42,313	2.25	5.75	7.50	3.50	7.25	9.00
Laboratory standard bacterial strain (MTCC)	MTCC 3160	0.50	0.75	2.00	1.25	1.25	2.25
	MTCC 109	R	R	R	R	R	R
	MTCC 443	1.00	0.75	2.75	1.75	1.25	3.50
	MTCC 3542	0.75	0.75	1.75	1.50	1.50	2.00
	MTCC 441	1.25	1.00	2.75	2.25	1.75	3.50
	MTCC 3382	1.00	0.25	1.50	1.75	0.50	1.75
	MTCC 7621	1.50	0.25	2.75	2.25	0.50	3.25
MTCC 1972	1.75	0.50	3.00	2.25	0.75	4.00	

'R' = Resistant

### Gas Chromatography–Mass Spectroscopy

A total of 38 compounds were identified from in vitro plant extract and 35 compounds from ex vitro extract (Table 3) (Fig. 2a, b). Although a total of 27 compounds were detected in naturally grown plant extract, the major antimicrobial compound, found in the in vitro and ex vitro

extracts, were either missing or barely found in this. So, the data were not compared with those of vitro and ex vitro extracts. Common compounds identified in both in vitro and ex vitro extracts were 2–3 butanediol, Pentanoic acid, 6,7-Dimethyl triazolo (4,3 b) (1,2,4) triazine, Triazine, Furfuryl glycidyl ester, 2ethyl 2 hexen-1-ol, 5 methyl-3-heptyne, Ethylene glycol, Hexagol and many other

**Table 3** Important phytochemicals detected by GC–MS analysis of the methanolic leaf extract of micropropagated in vitro plants and field grown ex vitro plants of *Coleus forskohlii*

Sl. no	Chemical constituents	Molecular formula	In vitro plant			Ex vitro plant			Biological activities*
			Mol wt	Retention time	% Area	Mol wt	Retention time	% Area	
1	Isocyanic acid, methyl ester	C <sub>2</sub> H <sub>3</sub> NO	57	6.79	0.58	57	7.76	2.50	Effects on atherosclerosis, cataracts, rheumatoid arthritis
2	2–3 butanediol	C <sub>4</sub> H <sub>10</sub> O <sub>2</sub>	90	8.07	2.50	90	11.45	0.55	Used as liquid fuel and synthetic rubber
3	4-Ethyl-2-Hexynal	C <sub>8</sub> H <sub>12</sub> O	124	23.91	0.24	124	14.68	2.50	–
4	Thiophene- 2 carboxamide	C <sub>12</sub> H <sub>10</sub> N <sub>2</sub> O <sub>4</sub> S	278	15.18	2.50	–	–	–	Anti-allergic, antibacterial, antidiabetic, anti-inflammatory
5	Pentanoic acid	C <sub>5</sub> H <sub>10</sub> O <sub>2</sub>	102	15.67	1.57	102	15.81	1.75	Potential biofuel, used in cigarette to increase nicotine delivery
6	Acetamide derivative	C <sub>18</sub> H <sub>17</sub> N <sub>3</sub> O <sub>3</sub> S	355	16.57	2.50	–	–	–	Antioxidant, Anti-inflammatory
7	6,7- Dimethyl triazolo (4,3 b) (1,2,4) triazine	C <sub>6</sub> H <sub>7</sub> N <sub>5</sub>	149	17.67	1.00	149	29.32	0.45	Antifungal, antibacterial, anticancer, HIV, inflammatory
8	4 tetradecyne	C <sub>14</sub> H <sub>26</sub>	194	17.84	1.50	194	20.57	0.98	–
9	5-methyl-3-haptyne	C <sub>8</sub> H <sub>14</sub>	110	41.25	0.94	110	17.89	2.50	–
10	Neo Hexane	C <sub>6</sub> H <sub>14</sub>	66	17.99	2.50	66	40.59	1.48	Active against biological assay as probe molecule
11	Acetonitrile derivative	C <sub>4</sub> H <sub>6</sub> N <sub>2</sub>	82	18.43	2.50	82	15.66	1.28	Organic solvent for antioxidant
12	1 aminocyclopropanecarbonitrile	C <sub>4</sub> H <sub>6</sub> N <sub>2</sub>	82	18.78	2.50	–	–	–	Anxiolytic, anti-addictive, neuroprotective
13	Phthalic acid ester	C <sub>22</sub> H <sub>28</sub> C <sub>12</sub> O <sub>4</sub>	426	18.81	2.50	–	–	–	Carcinogen
14	2- pyrazoline	C <sub>8</sub> H <sub>16</sub> N <sub>2</sub>	–	–	–	140	19.07	3.75	Antibacterial, antifungal, anti-depression, anti-tumor
15	4- Aminopyrimidine	C <sub>4</sub> H <sub>5</sub> N <sub>3</sub>	95	19.34	2.50	–	–	–	Antibacterial activity
16	Cyclohexanol	C <sub>7</sub> H <sub>14</sub> O	144	19.52	2.50	–	–	–	Cytotoxic and antibacterial
17	2- Octyne	C <sub>8</sub> H <sub>14</sub>	110	19.57	2.50	–	–	–	–
18	S- triazine	C <sub>3</sub> H <sub>3</sub> N <sub>3</sub>	81	19.62	2.50	81	6.89	0.11	Antifungal, antibacterial, anti-protozoan
19	Furfuryl glycidal ester	C <sub>8</sub> H <sub>10</sub> O <sub>3</sub>	154	20.26	2.50	154	20.22	1.50	Antimicrobial activity
20	11 sulfanyl-1-undecanol	C <sub>11</sub> H <sub>24</sub> OS	204	20.31	1.75	–	–	–	–
21	1,3 Dioxolane, 2-tert-butyl-2-methyl	C <sub>8</sub> H <sub>16</sub> O <sub>2</sub>	–	–	–	144	20.47	7.25	Antibacterial and antifungal
22	1-Butene	C <sub>8</sub> H <sub>16</sub> O	–	–	–	128	20.95	2.50	–
23	Oxalic acid, dipropyl ester	C <sub>8</sub> H <sub>14</sub> O <sub>4</sub>	–	–	–	174	21.18	2.50	Processing agent
24	Cyclohexane Hexanoic acid	C <sub>13</sub> H <sub>22</sub> O <sub>3</sub>	226	21.58	7.50	–	–	–	–
25	Isopropyl derivative	C <sub>20</sub> H <sub>32</sub> O	288	21.74	7.50	288	21.74	7.50	Pharmacologically active
26	Thiophene	C <sub>8</sub> H <sub>16</sub> S	144	21.98	7.50	144	36.35	1.05	Antibacterial and anti-allergic
27	4-O-methyl-d-Arabinose	C <sub>6</sub> H <sub>12</sub> O <sub>5</sub>	–	–	–	164	22.05	5.00	–
28	2,4 Dimethyl – 3 Hexanone	C <sub>8</sub> H <sub>16</sub> O	128	34.08	1.15	128	22.29	7.50	Anti-germinative activity against <i>Clostridium botulinum</i> spores
29	Triethelene glycol	C <sub>10</sub> H <sub>18</sub> O <sub>6</sub>	234	22.68	1.25	234	22.74	7.50	Enhance protein stability
30	2H-Tetrazole	C <sub>6</sub> H <sub>10</sub> N <sub>4</sub> O <sub>2</sub>	–	–	–	170	23.28	1.75	–
31	Oxirane	C <sub>19</sub> H <sub>38</sub> O <sub>2</sub>	–	–	–	298	23.57	67.61	Antimicrobial
32	Propionic acid	C <sub>7</sub> H <sub>14</sub> O <sub>2</sub> S	162	24.91	32.39	162	24.91	1.25	Cosmetic, plastics and pharmaceutical industries
33	4-O-methyl-d-arabinose	C <sub>6</sub> H <sub>12</sub> O <sub>5</sub>	–	–	–	164	25.81	2.50	–
34	Hexagol	C <sub>12</sub> H <sub>26</sub> O <sub>7</sub>	282	26.09	2.50	–	–	–	–
35	Ethylene oxide cyclic hexamer	C <sub>12</sub> H <sub>24</sub> O <sub>6</sub>	–	–	–	264	27.23	7.50	–

**Table 3** continued

Sl. no	Chemical constituents	Molecular formula	In vitro plant			Ex vitro plant			Biological activities*
			Mol wt	Retention time	% Area	Mol wt	Retention time	% Area	
36	18,19-Dihydroxy 1,4,7,10,13,16 Hexaoxacycloeicosane	C <sub>14</sub> H <sub>28</sub> O <sub>8</sub>	324	31.25	0.25	324	27.93	3.75	Antibacterial activity
37	Propanoic acid	C <sub>10</sub> H <sub>22</sub> O <sub>3</sub> Si	82	28.88	5.75	82	28.18	2.50	Antifungal agent used in food safety
38	6,7-Dimethyl triazolo(4,3b)(1,2,4)-triazine	C <sub>6</sub> H <sub>7</sub> N <sub>5</sub>	149	29.32	0.45	149	29.32	0.45	–
39	3-Undecyne	C <sub>11</sub> H <sub>2</sub> O	152	29.93	0.73	152	24.26	0.73	–
40	Sulfurous acid	C <sub>19</sub> H <sub>40</sub> O <sub>3</sub> S	348	33.38	0.89	348	40.94	0.89	Antibacterial activity
41	11-Sulfanyl-1undecanol	C <sub>11</sub> H <sub>24</sub> OS	204	34.60	7.92	204	34.61	1.08	–
42	Sulfurous acid, butylheptadecylester	H <sub>2</sub> SO <sub>3</sub>	376	36.15	1.98	–	–	–	–
43	3-Undecan-5-yne	C <sub>11</sub> H <sub>18</sub>	–	–	–	150	37.41	0.35	–
44	Heptacosane	C <sub>27</sub> H <sub>56</sub>	380	38.66	2.02	–	–	–	–
45	Cetyl iodide	C <sub>16</sub> H <sub>33</sub> I	352	40.50	3.38	352	46.25	3.38	–
46	Methoxyacetic acid	C <sub>3</sub> H <sub>6</sub> O <sub>3</sub>	90	41.04	16.66	–	–	–	–
47	Isoxazole	C <sub>3</sub> H <sub>3</sub> NO	–	–	–	69	49.72	72.86	–
48	Hexaoxacyclononadeoane	C <sub>26</sub> H <sub>50</sub> O <sub>12</sub>	554	50.46	1.17	–	–	–	–
49	Silane	C <sub>3</sub> H <sub>14</sub> Si <sub>3</sub>	134	50.76	1.78	134	51.00	0.55	–

\*All biological activities are obtained from previously published literatures

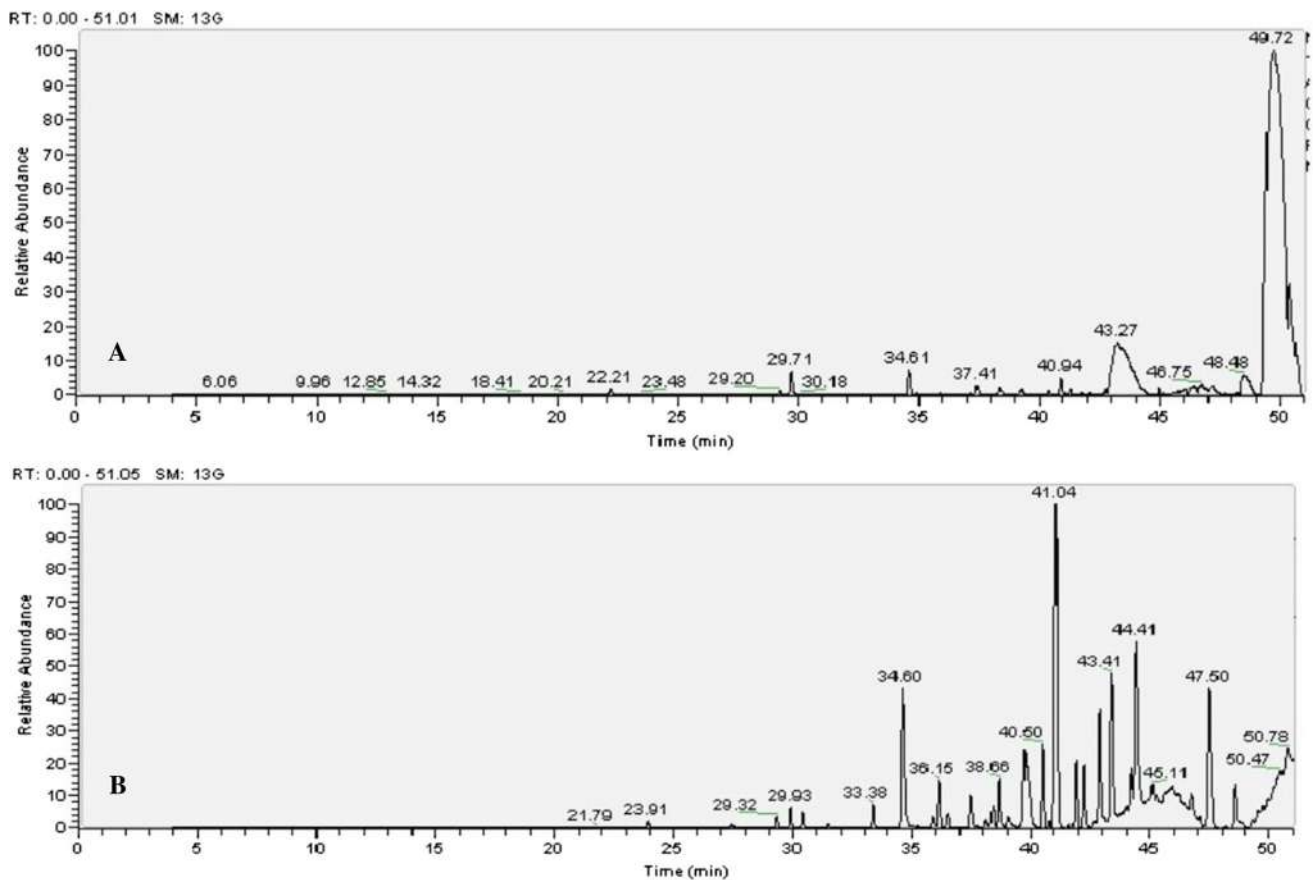


**Fig. 2** GC–MS chromatograph of methanolic extracts of the leaf of *Coleus forskohlii*. **a** In vitro plant extract, **b** ex vitro plant extract

derivatives. Some compounds like Isocyanic acid 4-ethyl-2-Hexanyl 1–3 dioxolane, Oxalic acid, Oxirane, Propanoic acid, Ethylene oxide cyclic Hexamer are present only in ex vitro extracts but not in the other. Likewise, some like Acetamide derivative, 1- tetradecyne, Neo Hexane, Acetonitrile derivative, 1 aminocyclopropanecarbonitrile, Phthalic acid ester, 2-Octyne, Isopropyl derivative, Thiophene are present exclusively in in vitro extracts. Almost all the compounds found recurrently in both the extracts have antimicrobial activity. High antimicrobial activity containing compounds like 6,7- Dimethyl triazolo, 2-Pyrazoline, S- triazine, furfuryl glycidyl ester were not detected in naturally grown plant extract. Compounds like 2–3 butanediol, 2ethyl 2 hexen-1-ol, Oxalic acid, Oxirane, and Propanoic acid were present in naturally grown extract as like ex vitro and in vitro extract. Absence of major antimicrobial compounds and presence of some compound in low amount proves naturally grown extract significantly low in activity against pathogen and non-pathogens. Gas chromatography–mass spectroscopy (GC–MS) of the root extracts of *C. forskohlii* was previously done by few researchers [24]. Availability of the leaf biomass is easier as compare to root, because collection of root is only possible by scarifying the plants whereas leaf could be collected throughout the years without scarifying the plants. GC–MS profiling of the leaf extract of *C. forskohlii* shows presence of different type of phyto-constituents, many of them having the ability to kill microbes and also have anti-inflammatory and anti-cancerous activity. Flavonoids are mostly active against bacteria by disrupting their enzyme system. Bacterial membrane disruption is also done by tannin groups through interfering with protein synthesis process [25]. Many compounds are present in the ex vitro extract but absent in the in vitro extract and vice versa regarding to comparative data. Most of the compounds, present both in in vitro and ex vitro extracts, are known to have antimicrobial properties. They may contribute cumulatively toward the antimicrobial potential of the extracts. Presence of some additional antimicrobial compounds in ex vitro extracts may be the cause of showing enhanced activity over that of in vitro. Similar findings has been described by few other researchers where ex vitro field grown plants exhibited more antimicrobial activity as compare to in vitro plants [7]. Protein that was present in the plant extract mostly was antimicrobial. Plants generate those peptide or protein for initial defense mechanism [26]. Furfuryl glycidyl ester commonly named furan, found in in vitro extracts, is also reported as an active compound against bacteria and fungi [27]. Propionic acid, a common compound present both in in vitro and ex vitro extracts, is active against the growth of bacteria and molds and commonly used in the food industries [28]. Phthalic acid ester, although present in small amount, is a

potent carcinogenic agent [29]. Pyrazoline is an active phyto-constituents present in the plant extract also having the antifungal antibacterial [30] activity.

## Conclusions

The leaf extracts of *C. forskohlii* (naturally grown source plants, tissue culture raised in vitro and ex vitro plants) found to be effective on some multi-drug resistant pathogenic ESBL positive bacterial strains collected from the urine samples of UTI patients. Specially, the ex vitro plant extract is significantly effective against multi-drug resistant UTI pathogens and can be produced through tissue culture throughout the year. Although root was previously subjected to similar experiments, the present study is the first attempt using leaves of *C. forskohlii* and seems extensive good pathogen-killing ability. Leaf biomass of a single plant is much higher than the root, additionally leaf could be collected round the years but roots once after completing the lifespan. Therefore, leaf is better choice than root for continuous supply of antimicrobial phytochemicals. Further investigation using various other pathogens would be very promising and according to the resulted data the compounds and extract can be used as alternative therapy in future medicine.

**Supplementary Information** The online version contains supplementary material available at <https://doi.org/10.1007/s40011-021-01285-4>.

**Acknowledgements** AC, SMH and BG thankful to Swami Kama-lasthananda, Principal, Ramakrishna Mission Vivekananda Centenary College, Rahara, Kolkata (India), for the facilities provided for the present study. SMH thankful to Dr. Sukla Hazra, Principal, East Calcutta Girls' College, Lake Town, Kolkata (India), for giving the permission to do research in collaboration with R.K.M.V.C. College. DD acknowledges technical and management support provided by Ashok Laboratory Clinical Testing Centre Private Limited, Kolkata.

## Declarations

**Conflict of interest** The authors declare that they have no conflict of interest.

## References

1. Shalayel MHF, Asaad AM, Qureshi MA, Elhusein AB (2017) Anti-bacterial activity of peppermint (*Mentha piperita*) extracts against some emerging multi-drug resistant human bacterial pathogens. *J Herb Med* 7:27–30
2. WHO (1998) Regulatory situation of herbal medicine: a World Wide Review. World Health Organization, Geneva
3. Efferth T, Zacchino S, Georgiev MI, Liu L, Wagner H, Panossian A (2015) Nobel Prize for artemisinin brings phytotherapy into the spotlight. *Phytomedicine* 22:A1–A3

4. Efferth T (2017) The road in front of us: phytomedicine research for the years to come. *Phytomedicine* 25:A1
5. Soni A, Sosa S (2013) Phytochemical analysis and free radical scavenging potential of herbal and medicinal plant extracts. *J Pharmacogn Phytochem* 2:22–29
6. Ulukanli Z, Cigremis Y, Ilcim A (2011) In vitro antimicrobial and antioxidant activity of acetone and methanol extracts from *Thymus leucotrichius* (Lamiaceae). *Eur Rev Med Pharmacol* 15:649–657
7. Haque SM, Chakraborty A, Dey D, Mukherjee S, Nayak S, Ghosh B (2017) Improved micropropagation of *Bacopa monnieri* (L.) Wettst. (Plantaginaceae) and antimicrobial activity of in vitro and ex vitro raised plants against multidrug-resistant clinical isolate of urinary tract infecting (UTI) and respiratory tract infecting (RTI) bacteria. *Clin Phytoscience* 3:17
8. Abejew AA, Denboba AA, Mekonnen AG (2014) Prevalence and antibiotic resistance pattern of urinary tract bacterial infections in Dessie area. North-East Ethiopia *BMC Res Notes* 7:687
9. Nikalje AP, Baheti S, Kamble S, Khan S, Sangshetti J (2017) Isolation of phyto constituents from the roots of *Coleus forskohlii* by column and flash chromatographic method. *Indo Am j pharm* 4:74–84
10. Kanne H, Burte NP, Prasanna V, Gujjula R (2015) Extraction and elemental analysis of *Coleus forskohlii* extract. *Pharmacogn Res* 7:237
11. Mothana RA, Khaled JM, El-Gamal AA, Noman OM, Kumar A, Alajmi MF, Al-Rehaily AJ, Al-Said MS (2019) Comparative evaluation of cytotoxic, antimicrobial and antioxidant activities of the crude extracts of three *Plectranthus* species grown in Saudi Arabia. *Saudi Pharm J* 27(2):162–170
12. Ganzera M, Choudhary MI, Khan IA (2003) Quantitative HPLC analysis of withanolides in *Withania somnifera*. *Fitoterapia* 74:68–76
13. Petersen M (1994) *Coleus* spp.: In vitro culture and the production of forskolin and rosmarinic acid. *Med Aoma Plants* 4:69–92
14. Murashige T, Skoog F (1962) A revised medium for rapid growth and bio assays with tobacco tissue cultures. *Physiol Plantarum* 15:473–497
15. Haque SM, Ghosh B (2013) High frequency micro cloning of *Aloe vera* and their true-to-type conformity by molecular cytogenetic assessment of two years old field growing regenerated plants. *Bot Stud* 54:46
16. Bayer AW, Kirby WM, Sherris JC, Turck M (1966) Antibiotic susceptibility testing by a standardized single disc method. *Am J Clin Pathol* 45(4):493–496
17. Deans SG, Ritchie G (1987) Antibacterial properties of plant essential oils. *Int J Food Microbiol* 5:165–180
18. Ericsson HM, Sherris JC (1971) Antibiotic sensitivity testing. Report of an international collaborative study. *Acta Pathologica et Microbiologica Scandinavica* (Suppl. 217)
19. Wadikar DD, Patki PE (2016) *Coleus aromatics*: a therapeutic herb with multiple potentials. *J Food Sci Technol* 53:2895–2901
20. Malleswari D, Bagyanarayana G, Hindumathi A (2013) Antibacterial activity of *Coleus forskohlii* extracts against some pathogenic bacteria. *J Nat Prod Plant Resour* 3:75–78
21. Mishra MP, Rath S, Swain SS, Ghosh G, Das D, Padhy RN (2015) In vitro antibacterial activity of crude extracts of 9 selected medicinal plants against UTI causing MDR bacteria. *J King Saud Univ Sci* 29:84–95
22. Rakholiya K, Chanda S (2012) In vitro interaction of certain antimicrobial agents in combination with plant extracts against some pathogenic bacterial strains. *Asian Pac J Trop Biomed* 2:S876–S880
23. Singh V, Jaryal M, Gupta J, Kumar P (2017) Antibacterial activity of medicinal plants against extended spectrum beta lactamase producing bacteria causing urinary tract infection. *Int J Drug Res Tech* 2:263–267
24. Rajkumar K, Malathi R (2015) Phytochemical investigation GC-MS analysis and in vitro antimicrobial activity of *Coleus forskohlii*. *Bangladesh J Pharmacol* 10:924–930
25. Cowan MM (1999) Plant products as antimicrobial agents. *Clin Microbiol Rev* 12:564–582
26. Vargas WA, Martín JMS, Rech GE, Rivera LP, Benito EP, Díaz-Mínguez JM, Thon MR, Sukno SA (2012) Plant defense mechanisms are activated during biotrophic and necrotrophic development of *Colletotricum graminicola* in maize. *Plant Physiol* 158:1342–1358
27. Alabi KA, Hassan GF (2014) Determination of minimum inhibitory concentrations of 2-(2-nitrovinyl) furan. *Academia J Microbiol Res* 2:028–032
28. Chen L, Guo G, Yuan X, Shimojo M, Yu C, Shao T (2014) Effect of applying molasses and propionic acid on fermentation quality and aerobic stability of total mixed ration silage prepared with whole-plant corn in Tibet. *Asian-Australas J Anim Sci* 27:349–356
29. Kluwe WM (1986) Carcinogenic potential of phthalic acid esters and related compounds: structure-activity relationships. *Environ Health Perspect* 65:271–278
30. Nauduri D, Reddy GBS (1998) Antibacterials and antimycotics: Part 1: synthesis and activity of 2-pyrazoline derivatives. *Chem Pharm Bull* 46:1254–1260

**Publisher's Note** Springer Nature remains neutral with regard to jurisdictional claims in published maps and institutional affiliations.





## Source details

[Feedback >](#) [Compare sources >](#)

### Proceedings of the National Academy of Sciences India Section B - Biological Sciences

Scopus coverage years: from 2008 to Present

Publisher: Springer Nature

ISSN: 0369-8211 E-ISSN: 2250-1746

Subject area: [Agricultural and Biological Sciences: General Agricultural and Biological Sciences](#) [Environmental Science: General Environmental Science](#)

Source type: Journal

[View all documents >](#)[Set document alert](#)[Save to source list](#)

CiteScore 2022

3.0



SJR 2022

0.314



SNIP 2022

0.627





## 5. In – Vitro Antibacterial Potentiality of Indian Medicinal Plant *Murraya Koenigii*

**Tanmay Ghosh**

*Department of Microbiology, Dinabandhu Andrews College, Baishnabghata, South 24 Parganas, Kolkata, West Bengal, India.*

### **ABSTRACT:**

*The aim of this study was to examine the antibacterial effects of curry leaves. After drying we grind the leaves to make powdery form. The powder was mixed with ethanol or methanol to make extract for examine antibacterial effect against some specific bacteria. The methanol extract of curry leaves more effective against *Streptococcus* sp., showed zone of inhibition  $38.0 \pm 2.0\text{mm}$  as compared to zone of inhibition of *Staphylococcus* sp. ( $34.1 \pm 1.0\text{mm}$ ) and *E. coli* ( $36.5 \pm 1.0\text{mm}$ ).*

### **KEYWORDS:**

*Murraya koenigii, Bacteria, Inhibition zone, Antimicrobial effects.*

### **Introduction:**

Curry leaves (*Murraya koenigii*) are well known spice for distinct aroma due to the presence of certain volatile oil and their ability to improve digestion. It is very common in Asian country for flavoring food. Even after drying it retains its slight pungent, better taste. It is very famous in traditional India for its medicinal properties. It is associated with Reactive Oxygen Species (ROS) like hydroxyl radicals, hydrogen peroxide and superoxide anion radicals. In case of stress our body produces high amount of ROS that cause cell injury, that cause nucleic acid damage, and damage of other cellular biomolecules. Although natural antioxidant use for treatment of various oxidative stress disease. It may be resisted by various multidrug resistant pathogens. This increase has made the use of broad spectrum antibiotics and immuno-suppressive agents indiscriminately. Synthetic drugs are not only expensive and inadequate for treatment of diseases but are often with serious side-effects. Essential oils are widely used secondary metabolites produced by aromatic plants due to their potent biological activities. *Murraya koenigii* leaves contain huge amount of proteins, carbohydrate, fiber, minerals, carotene, nicotinic acid, Vitamin C, Vitamin A, Calcium and Oxalic acid. It also contains crystalline glycosides, carbazole alkaloids, koenigin, girinimbine, iso-mahanimbine, koenine, koenidine and koenimbine. Triterpenoid alkaloids cyclomahanimbine, tetrahydromahanimbine are also present in the leaves. Murrayastine, murrayaline, pyrayafolinecarbazole alkaloids and many other chemicals have been isolated

from *Murraya koenigii* leaves. This leaves have properties to cure diarrhea, dysentery, can prevent vomiting tendency. Curry leaves as well as seeds are a source of essential oil used in soap and perfumery industry.

Leaves root and bark having other medicinal properties like relief from renal pain. Previous phytochemical investigations on this plant revealed the presence of carbazole alkaloids, and coumarins. The present study is aimed at preliminary phytochemical screening of the root extracts of *Murraya koenigii* and evaluation of the same for potential.

This study was undertaken to evaluate the antibacterial properties of the ethanol, methanol and aqueous extracts of curry leaves (*Murraya koenigii*) on selected clinically pathogenic bacteria isolates.

### **Materials and Methods:**

#### **Site of Experiments:**

The whole experiments were carried out in the lab room of Rabindra Mahavidyalaya, Champadanga, Hooghly, W.B, India.

#### **Collection of Microorganisms:**

The tested microorganism (*Staphylococcus* sp., *Streptococcus* sp., and *E. coli*.) bought together from MTCC Chandigarh, India.

#### **Collection of Plant Materials:**

The leaf of testing plant *Murraya koenigii* (Curry) was collected from the field of Champadanga, Hooghly, W.B, India.

#### **Methanol extraction:**

To make methanol extract, add 10gm of curry powder to 20ml of 70% aqueous methanol solution (w/v), then it cover by filter paper and keep on rotary shaker for 24hrs. Then keep in dark for 2-3 day at room temperature and then collect supernatant and solvent is evaporated by incubating at room temperature for 48hrs to make final volume 400mg/ml of curry leaves.

#### **Ethanol extraction:**

To make ethanol extract, add 10gm of curry powder to 20ml of ethanol and distilled water (8: 2 w/v), then it cover by filter paper and keep on rotary shaker for 24hrs.

Then keep in dark for 2-3 day at room temperature and then collect supernatant and solvent is evaporated by incubating at room temperature for 48hrs to make final volume 400mg/ml of curry leaves.

### **Aqueous extraction:**

To make aqueous extract, add 10gm of curry powder to 20ml of 70% aqueous solution (w/v), then it cover by filter paper and keep on rotary shaker for 24hrs.

Then keep in dark for 2-3 day at room temperature and then collect supernatant and solvent is evaporated by incubating at room temperature for 48hrs to make final volume 400mg/ml of curry leaves.

### **Determination of antimicrobial activity:**

Paper distinction method used to evaluate antibacterial activity of different extracts of curry leaves. The disc made by using filter paper with 66mm diameter that was soaked in methanol and ethanol solution (15ml in each disc) with concentration 400mg/ml 200mg/ml, 100mg/ml and 50mg/ml each extract.

### **Statistical Analysis:**

Each and every experiment was respected in triplicate sets and mean value of each set result were taken to represent the antibacterial activity of curry leaves extracts. All results were recorded as S (sensitive), I (intermediate sensitive) and R (resistant).

The results of sensitivity tests were expressed as (0) = (R) for no sensitivity, + for (below 6 mm) = (R) for low sensitivity, ++ (7- 12mm) = (I) for moderate sensitivity and +++ (13mm & above) = (S) for high sensitivity.

### **Result and Discussion:**

In comparing the inhibition zones of *Staphylococcus* sp., *Streptococcus* sp. and *E. coli* on nutrient agar, the curry leaves (methanol) extract was more effective with *Streptococcus* sp. in producing a maximum of  $38.0 \pm 2.0$ mm inhibition (table-1, Figure-1) zone as compared to a maximum of  $34.1 \pm 1.0$ mm inhibition (Table-2, Figure-2) zone for *Staphylococcus* sp. and to a maximum of  $36.5 \pm 1.0$ mm (Table-3, Figure-3) inhibition zone for *E. coli*.

The 400mg/ml concentration produced the maximum inhibition zones for both bacteria which progressively reduced with further dilutions from 200 mg/ml to 50 mg/ml.

**Table 1: Zone of inhibition (mm) for *Streptococcus* sp.**

Concentration	Methanol	Ethanol	Aqueous solution
400 mg/ml	$38.0 \pm 2.0$	$37.0 \pm 2.0$	$32.7 \pm 1.0$
200 mg/ml	$33.2 \pm 1.0$	$32.0 \pm 1.0$	$26.5 \pm 1.0$
100 mg/ml	$27.3 \pm 2.0$	$27.1 \pm 2.0$	$22.3 \pm 2.0$
50 mg/ml	$22.1 \pm 0.0$	$21.1 \pm 0.0$	$18.1 \pm 1.0$

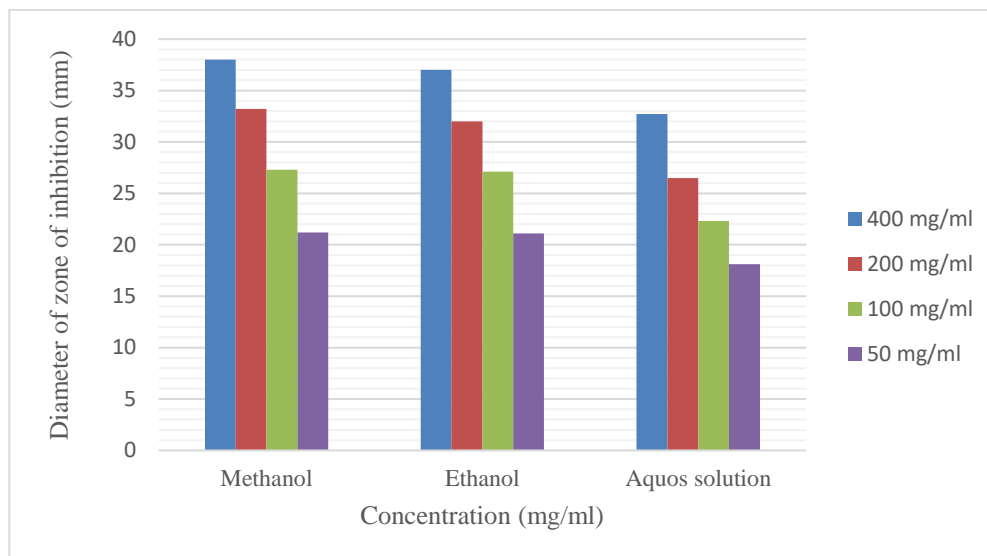


**Figure 1: Zone of inhibition (mm) for *Streptococcus* sp.**

**Table 2: Zone of inhibition (mm) for *Staphylococcus* sp.**

Concentration	Methanol	Ethanol	Aqueous solution
400mg/ml	34.1±1.0	32.3±1.0	27.5±1.0
200mg/ml	30.2±2.0	28.2±2.0	25.1±2.0
100mg/ml	26.4±1.0	24.1±1.0	22.5±1.0
50mg/ml	22.3±1.0	19.0±0.0	17.7±2.0

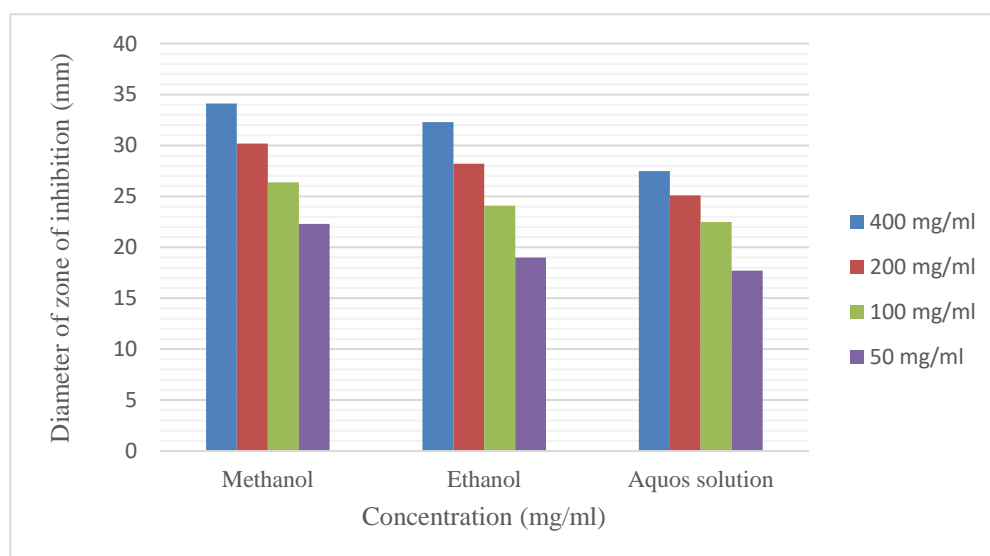


**Figure 2: Zone of inhibition (mm) for *Staphylococcus* sp.**

**Table 2: Zone of inhibition (mm) for *E.coli*.**

Concentration	Methanol	Ethanol	Aqueous solution
400mg/ml	36.5±1.0	33.1±1.0	29.1±1.0
200mg/ml	32.4±2.0	29.3±2.0	26.3±2.0
100mg/ml	27.1±1.0	25.1±1.0	23.5±1.0
50mg/ml	23.3±2.0	20.7±2.0	18.4±2.0

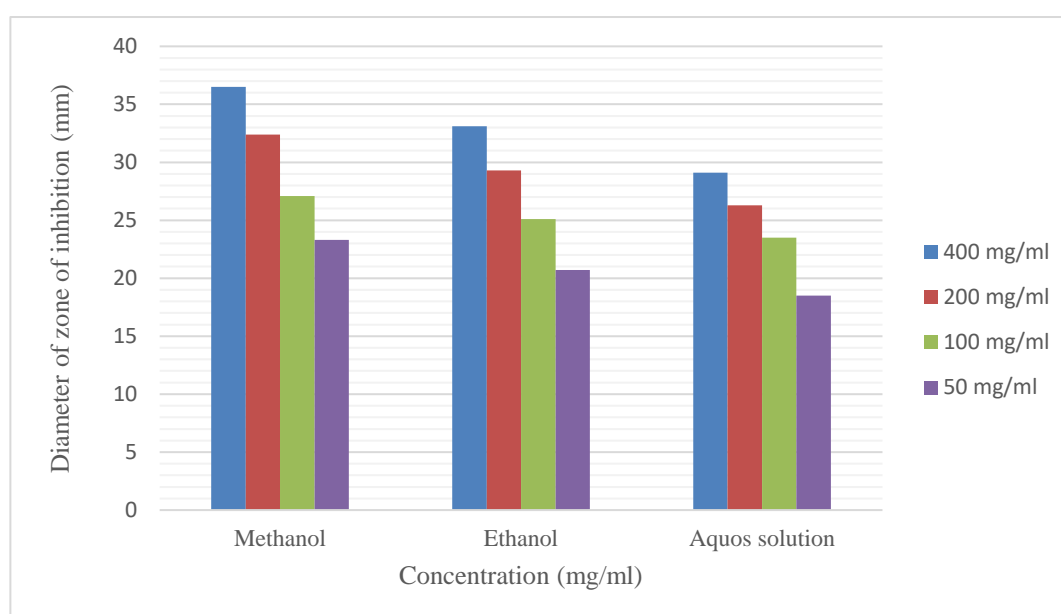


**Figure 2: Zone of inhibition (mm) for *E. coli*.**

### Conclusion:

After evaluating it is shown that curry leaves are effective on *E. coli*, *Staphylococcus*, and *Streptococcus* sp. The ethanol and methanol extracts of curry leaves were found to be effective on all strains, except *Klebsiella pneumonia* and *Pseudomonas aeruginosa*. Curry leaves have potential to use as antibiotic against tested microbes. So, it could be effectively used in everyday meal for its beneficial aspects. This plant can be a useful source of food industry and medicinal field. This research could be further extended to test the bioactive properties of curry leaves for therapeutic use.

### References:

1. Suman Singh A1, P. K. Omre B and Sandhya Madan Mohan C. Curry leaf (*Murraya koenigii*) a miracle plant. *Ind. J. Sci. Res.*, 2014; 4 (1): 46-52.
2. Krishnaiah D, Sarbatly R and Nithyanandam R, *Food Bioproducts Processing*, 2011, 89(3), 217–233; DOI:10.1016/j.fbp.2010.04.008.

3. Hippeli S and Elstner E F, *FEBS Lett.*,1999, 443, 1–7; DOI:10.1016/S0014-5793(98)01665-2
4. Maxwell S R J, *J Drugs.* 1995, 49, 345–361.
5. Bandow J E, Brotz H, Leichert L I O and Labsischinski H H M, *J Antimicrobial Agents Chemotherapy*, 2003, 47(3), 948-955; DOI:10.1128/AAC.47.3.948-955.2003
6. Gonzalez C E, Venzon D and Lee S Risk. *J Clin Infectious Diseases*, 1996, 23, 515-521.
7. Pattnaik S, Subramanyam V R, Bapaji M and Kole C R, *Microbios J.*, 1997, 89, 39-46.
8. Bhandari PR. Curry leaf (*Murraya koenigii*) or Cure leaf: Review of its curative properties. *J. Med. Nutr. Nutraceut*, 2012; 1: 92-97.
9. Adebajo A.C., Reisch J. Minor furocoumarins of *Murraya koenigii*. *Fitoterapia*. 2000; 71: 334–337.
10. Bhattacharya L., Roy S.K., Chakraborty D.P. Structures of the carbazole alkaloid isomurrayazoline from *Murraya koenigii*. *Phytochemistry*. 1982; 21:2432–2433.
11. Ito C., Thoyama Y., Omura M., Kajiura I., Furukawa H. Alkaloidal constituents of *Murraya koenigii*—isolation and structural elucidation of novel binary carbazole quinones and carbazole alkaloids. *Chem. Pharm. Bull.* 1993; 42: 2096–2100.
12. Kirtikar K.R., Basu B.D. *Indian Medicinal Plants*. Allahabad, India: Lalit Mohan Basu Publishing; 1993.
13. Nutan M.T. H., Hasan C. M., Rashid M. A. Bismurrayafoline E: a new dimeric carbazole alkaloid from *Murraya koenigii*. *Fitoterapia*. 1999; 70: 130–133.
14. Ramsewak R. S., Nair M.G., Strasburg G.M., Dewitt D.L., Nitiss J.L. Biologically active carbazole alkaloids from *Murraya koenigii*. *Agri. Food Chem.* 1999; 47:444–447.
15. Rao R.A.V., Rhide K. S., Mujumdar R.B. Mahanimbinol from *Murraya koenigii*. *Chem. Ind.* 1980; 17: 697–698.
16. Reisch J., Adebajo A.C., Kumar V., Aladesanmi A.J. Two carbazole alkaloids from *Murraya koenigii*. *Phytochemistry*. 1994; 36: 1073–1076.
17. Saha C., Chowdhury B.K. Carbazoquinones from *Murraya koenigii*. *Phytochemistry*. 1998; 48: 363–366.
18. Tachibana Y., Kikuzaki H., Lajis N.H., Nakatani N. Antioxidative activity of carbazoles from *Murraya koenigii*. *J. Agr. Food. Chem.* 2001; 49: 5589–5594.
19. Collee J.G., Miles R.S., Watt B. Tests for identification of bacteria. In: Collee J.G., Fraser A.G., Marmion B.P., Simmons A. (editors): *Mackie and McCartney Practical Medical Microbiology*, 14th edition. Churchill Livingstone, New York, 1996; 131-49.



## **4. Potential Natural Antioxidant and Other Health Benefits of Honey and its Possible Limitations**

**Tanmay Ghosh**

*Department of Microbiology, Dinabandhu Andrews College,  
Baishnabghata, South 24 Parganas, Kolkata, West Bengal, India.*

### **ABSTRACT**

*Honey is often called nectar. This honey is a sweet fluid made by honey bees and it's produced using the blossoms. Honey is hostile to bacterial, against viral and against contagious, and every one of these properties are utilized for wound recuperating. Because of the modest quantity of water it successfully dries the injuries and shields it. The rich sugar contents prevent microorganisms from development. Honey additionally contains a chemical that delivers the sanitizer  $H_2O_2$  when it contacts an injury like damp surface. People around the world have been appreciating the health benefits of honey for thousands of years. As a characteristic food supplement, honey has been linked to infectious and health effects. It has been set up as a potential restorative cell reinforcement specialist for different organic sicknesses. The process of dehydration of bees is frequent inside the bee. Honey contains an exceptionally unpredictable synthetic creation that fluctuates relying upon the wellspring of the plant. It has been utilized as food medication since antiquated occasions. So, it is totally healthy and nutritious nourishment for kids and grown-ups. Albeit not a bush, honey is created by a plant and is broadly utilized all throughout the planet. Madhu is a helpful compound to help staff and competitors defeat weakness and recover strength. Kids, youthful and old would all be able to eat nectar together with no bad results or side effects. Honey contains a multivitamin tonic and has antibacterial properties you can take honey alone or with milk and warm water in or out Practice a spot of cinnamon powder nectar; it will keep you sound.*

### **KEYWORDS**

*Medicinal, Honey, Biology, Microbiology, Nutritional science.*

### **Introduction:**

Honey is marvel in nature. Honey has been around for quite a while we actually know very less about it. It is just honey gathered from honey bees from numerous blossoms. Honey is a typical sweet and an amazing restorative device for a long time. In early human advancement the Sumerians were very much aware of guard and honey and it is to say that



protected to know to appreciate. This is the most straight forward and frequently the most ideal approach to lessen sore throat and it tends to be required some investment. Honey is finally called an ancient written archive of folk medicine. The specification of its use is completely inferior to the current therapy as a potential therapy. There is, however, a friendship among some researchers that offers a consistent proposal for the use of honey as a complement to natural products as a reflection of well-desirable current treatment therapy or combination antioxidant therapy. Antioxidants eating honey with one teaspoon of Tulsi (Tulsi) cures nausea, cough and runny nose. Leaf juice People with asthma can also benefit by consuming honey every day. Ayurveda recognizes honey as a great medicine that is able to provide life span. Osteoporosis is another situation that can be forestalled by ordinary nectar consumption. Modern research has shown that honey is effective against stomach and bone cancers by creating wonderful effects of honey. Eating 1 tablespoon of cinnamon powder and 1 teaspoon of honey 3 times in 1 day reduces the symptoms of cancer in a month. Honey contains several antioxidants, effective against the growth of cancer. Snazzy medication guarantees that honey is compelling in treating stomach ulcers and is a protected and delicate approach to manage this horrendous issue. Obviously in the body, honey has over and over again shown that it can clear the most profound injuries the most obstinate agony in certain spaces, where present day medication is exceptionally hard to obtain, honey is as yet being utilized to treat consumes and injuries. It is applying straight forwardly to the space, and covered with hygienic bandage or fabric. The fabric is taken out if new utilization of honey is required. The impact of the mending properties of Honey can be emotional. The blend of nectar shifts from blossom source to source. It shows a wide range of remedial properties like mitigating, antibacterial, against mutagenic, quick twisted recuperating, anti-toxin, antiviral, antifungal and antitumor impacts.

### **Chemical Composition of Natural Honey:**

It is composed of at least 181 elements of no small fame-honey. Its unique taste is the result of complex chemical processes, which is why sweet syrup alternatives simply cannot be compared. They cannot imitate the chemical knowledge of Mother Nature. Last year, bees in the United States alone produced a total of 158 million pounds of honey. It's a lot of chemistry.

- ❖ **Carbohydrates:** Shockingly, these contain the primary piece of honey – about 82%. The sugars present are monosaccharides such as glucose (30.45%) and fructose (39%), disaccharides (~8%) such as maltose, sucrose, furanose, isomaltose, cozymos and maltulose. There are additionally a few oligosaccharides (4.7%), including Illus, Thunderdose, and Panoz, which are framed from the inadequate breakdown of the greater saccharides presence in honey and hantide.
- ❖ **Vitamins and Minerals:** Honey is low in vitamin B, pantothenic acid, riboflavin, folic acid, niacin, and nutrient B6. It contains some vitamins like vitamin C and minerals like iron (Fe), potassium (K), calcium(Ca), zinc (Zn), phosphorus (P), chromium (Cr), magnesium (Mg), manganese (Mn) and selenium (Se).
- ❖ **Antioxidants:** The primary gatherings of cell reinforcements in honey are flavonoids, one of which, Pinocembrine, is remarkable to nectar and honey bee propolis. Ascorbic corrosive, catalase and selenium are additionally cancer prevention agents. All in all, the hazier the nectar, the more noteworthy its cancer prevention agent properties.

- ❖ **Proteins and amino acids:** Honey contains various chemicals, including invertase, which changes sucrose into glucose and fructose; Amylase, what separates starch into more modest units; Glucose oxidase, which changes glucose over to gluconolactone, coming about in gluconic corrosive and hydrogen peroxide; Catalysts, what separate peroxides framed by glucose oxidase into water and oxygen; and acid phosphorylation which eliminates inorganic phosphate from natural phosphate. Honey likewise contains eighteen free amino acids, the most plentiful of which is proline. The main amino amino is proline Honey ripe size measurements 71. Chronic components of ordinary injuries ought to be in excess of 210 mg/ kg. Value below 180 mg/ kg means honey is probably adulterated by adding sugar. Honeys proteins are mainly enzymes, reviewed by White 75 Bees add enzymes at different times honey ripening process. Digestive (amylase) digests starch from maltose and is heat and relatively stable Storage invertase (saccharin,  $\alpha$ -glucosidase), please convert mainly glucose and sucrose Fructose, however, converts many more sugars.
- ❖ **Others element:** Minor measures of nutrient riboflavin, niacin, folic corrosive, pantothenic corrosive, nutrient B6, and ascorbic corrosive. Different minor components incorporate Calcium, Iron, Zinc, Potassium, Phosphorus. Foras, Magnesium, Selenium, Chromium and Manganese a natural acids are other significant gatherings of machines, for instance, acidic, battery, citrus, succinic, lactic, malic and gluconic acids and a couple of other fragrant acids. The different catalysts present in nectar are glucose oxidase, sucrose diastase, catalysis and corrosive phosphatase. A portion of the distinguished flavonoids and phenolic compounds in the recognized honey incorporate campferol, quartcetin, chrysin, pinobexin, lutlin, epigenin, pinosembrin, genistein, hesperitin, p-viric corrosive, narcinid corrosive, glyxic corrosive, glycyrrhizin, Flavonoids and phenolic corrosive concentrates are known to be exclusively answerable for these cell reinforcements and opposite results of nectar.

**Average Composition in Honey:**

<b>Components</b>	<b>Average</b>
Water	17.2
Fructose	38.19
Glucose	31.28
Sucrose	1.71
Disaccharide calculated as maltose	3.71
Higher sugar	1.5
Free acid as gluconic	0.43
Lactone as gluconolatone	0.14
Total acid as gluconic	0.57
Ash	0.169
Nitrogen	0.041
Minerals	0.2

*Potential Natural Antioxidant and Other Health Benefits of Honey...*

<b>Components</b>	<b>Average</b>
Amino acid as protein	0.3
pH value	3.9

**Honey's Nutritional Value:**

Honey is mainly made up of fundamentally of carbohydrates and water. It contains a few follow sums minerals and nutrients. You can discover calcium, iron, magnesium, zinc, potassium, niacin and riboflavin in nectar additionally contain a combination of phenolic acid and flavonoids in honey.

These are cancer prevention agents that take out conceivably damaging free extremists in the human body. The USDA gives the accompanying data to 1 tablespoon (21 grams) of 100% unadulterated honey bee.

Calories	64mg
Fat	0mg
Sodium	0mg
Carbohydrates	17mg
Fiber	0mg
Sugars	17mg
Protein	0mg

**Medicinal Properties:**

1. Honey is made by thick, sweet fluid and Honey can be low in nutrients and minerals some plant compounds are high.
2. Honey contains various cancer prevention agents, including phenolics intensifies like flavonoids.
3. Some investigations have shown that nectar improves the heartRisk factors in individuals with diabetes. Notwithstanding, it additionally expands glucose levels - so it can't be viewed as Healthy for diabetics.
4. Eating honey can prompt moderate decrease Blood pressure is a huge danger factor for coronary illness.
5. Honey appears to positively affect Cholesterol levels. This prompts an unobtrusive decline altogether and "terrible" LDL Cholesterol when raising "great" HDL cholesterol.
6. Elevated fatty substances are a danger factor for this Heart infection and type 2 diabetes. A few examinations have shown that nectar can be diminished Triglyceride levels, particularly when utilized as a substitute for sugar.
7. Honey cans for babies over one year old go about as a characteristic and safe hack suppressant. A few examinations have shown that it is equal Cough is more powerful than medication.

8. Honey can be a piece of it when applied to the skin effective treatment plans for consumes, wounds and numerous other skin conditions It is especially viable for diabetic foot ulcers
9. Added to the cell antioxidants in honey beneficial consequences for heart wellbeing, including increasing your blood stream reduces the risk of heart and blood clusters.

### **Biological Activities of Honey:**

- ❖ **Antioxidants Activity:** Crude honey contains a variety of plant synthetic compounds that go about as cell antioxidants. A few kinds of honey contain cancer prevention agents like products of the soil. Cancer prevention agents help shield your body from cell harm because of free extremists. Free revolutionaries add to the maturing interaction can likewise add to the improvement of ongoing sicknesses like malignant growth and coronary illness. Studies have shown that the cell antioxidant agents in honey called polyphenols can assume a part in forestalling coronary illness.
- ❖ **Antibiotic activity:** Honey is one of the most seasoned known anti-toxins (antibiotics), following back to antiquate occasions. Egyptians often utilized honey as a characteristic anti-microbial and used as skin protectant. Nectar contains  $H_2O_2$  trusted source which may represent a portion of its antibacterial characters. Moreover, honey has a low pH contain. These attempts to pull dampness away from microbes, making the microscopic organisms get dried out and vanish.
- ❖ **Apoptotic activity:** Nectar makes apoptosis in numerous kinds of malignancy cells through depolarization of mitochondrial membranes Various tests were performed against the anti-sweetness movement Groups of tissue and disease cell lines, for example colorectal breast, endometrial, prostate, renal oral and cervical disease crude honey animates the activity of chemotherapeutic treatments as 5-fluorouracil and cyclophosphamide.
- ❖ **Anti-mutagenic Effects of Honey:** The capacity of mutagenicity to instigate hereditary transformation is interlinked with cancer-causing nature. Honey displays solid anti-mutagenic movement. The impact of honey on UV and gamma radiation uncovered Escherichia coli cells was researched to notice SOS reaction, which is a mistake inclined fix pathway adding to mutagenicity.
- ❖ **Anti-inflammatory and immune modulatory activities:** The immune modulatory activity of honey on invulnerable and cutaneous cells associated with wound mending. Honey can either invigorate or hinder the arrival of specific components (ROS, MMP-9, cytokine) from resistant and cutaneous cells relying upon wound condition. Honey builds T and B cells, eosinophils, antibodies, monocytes, neutrophils and normal executioner cells age during essential and auxiliary insusceptible reactions in tissue culture A sugar, nigero-oligosaccharides, present in honey has been seen to have immune potentiating impacts. Non sugar elements of nectar are likewise liable for immune modulation.
- ❖ **Antimicrobial activity:** In medicinal the helpful utilization of nectar necessitates that it should display predictable and normalized antimicrobial movement. Drug and natural researchers need to recognize the botanical species which give hostile to microbial qualities. Honey obtained high osmolarity and low pH joined through the enzymatic get together of  $H_2O_2$  applies an enemy of microbial outcomes.

### **Medicinal Effect of Honey:**

Honey has been known as a medication of nature for quite a long time. Ongoing medical researches there are many healing uses for honey. The benefits of on eyshadhi as natural and the use of honey Remedy.

1. **Burns:** Honeys have been utilized as a balm to mend consumes and forestall contaminations for millennia.
2. **Diabetes:** Honeys have a lower glycemic record than sugar, which implies it won't raise your glucose levels like sugar. It tastes sweeter than sugar and you can use fewer sweeteners in food. This makes nectar a preferred option over sugar. In one investigation, specialists found that substituting honey for unadulterated sugar was viable methods to keep glucose levels are stable.
3. **Cancer:** Nectar is commended for its cell antioxidant characters, which is the reason many are astounded in light of the fact that it can help forestall or treat malignant growth. A recent report from Iran shows how honey influences renal cell carcinoma, a kind of kidney malignant growth. Scientists have tracked down that nectar is viable in protecting malignancy cells from manifolds and they infer that it propels further investigation as a therapy for cancer.
4. **Wound care:** Topical use of medical-grade honey has been shown to promote wound healing, particularly in burns. Honey can sterilize wounds and promote healing, and also reduce pain, odour, and wound size.
5. **Psoriasis:** Psoriasis is a common skin condition that causes redness, blisters, itching and even sores. It is usually treated with topical creams that contain corticosteroids or vitamin D but honey can be more effective.
6. **Herpes:** Studies conducted in Dubai have shown that honey is an effective topical treatment for both oral and genital herpes. Honey can heal wounds from herpes just as quickly as those found in any pharmacy and it is even better to reduce itching.
7. **Cardiovascular Disease:** Cancer prevention agent (antioxidant) in Honey may be related with lessen hazard of coronary illness.
8. **Cough:** Studies have shown that eucalyptus honey, citrus honey and labiate honey can act as a reliable cough suppressant for upper respiratory tract infections and acute night cough in some people.
9. **Hair loss:** Those who suffer from hair loss or baldness can apply hot olive oil paste Table spoon or honey, one teaspoon cinnamon powder before bath and place it around 15 minutes and then wash the hair. It was kept for 5 minutes but it seemed very effective also.
10. **Cholesterol:** Two tablespoons of honey and three teaspoons of cinnamon powder mixed 16 If the cholesterol patient is given an ounce of tea water; It lowers cholesterol levels Body by 10% in 2 hours. As mentioned for arthritis patients, if taken 3 times a day Pure honey, according to information in the journal Chronic Cholesterol Healing Cholesterol complaints can be relieved by playing with food every day.
11. **Colds:** The individuals who experience the ill effects of normal or serious colds should be taken 1 teaspoon of hot honey with one-fourth teaspoon of cinnamon powder like clockwork. This interaction will be the most curable to clear chronic disease, runny nose and sinuses.

12. **Pimples:** Take 3 teaspoons of honey and 1 teaspoon of cinnamon powder glue. Apply this glue on the pimples prior to dozing and wash it next morning with warm water. Whenever done every day for about fourteen days, it eliminates pimples from the roots.
13. **Skin infections:** Applying cinnamon powder and honey in equivalent parts on the influenced parts for fixes dermatitis, ringworm and a wide range of skin contaminations.

### **Limitations of Honey:**

- ❖ **Allergic reactions:** Eating crude honey can cause gentle to direct sensitivities. It is the natural nectar of blossoms that can contain dust, pesticides, insect sprays and heaps of different synthetic substances. Its immediate intake may prompt the improvement of unfavorably susceptible manifestations like expanding, tingling, aggravation, rash, perspiring, asthma, coughing, honey side effects and honey application to the symptoms of the mouth and so on.
- ❖ **Weight gain:** Taking honey with gentle heated water or lemon juice advances weight reduction and assists with diminishing abundance calories and spread additional pounds in our body. In any case, it is significant that eating a lot of nectar or eating honey alone isn't so useful for our body weight and can make us fat. This is on the grounds that honey contains a great deal of sugar which can be handily ingested into our circulation system and can prompt weight gain and stoutness since it contains a ton of calories.
- ❖ **Nerve damage:** Crude honey contains a gathering of chemical called 'grayanotoxins' which are harmful to our sensory system. All in all, these poisons are excluded from food during its sanitization. Notwithstanding, when crude honey is devoured, it basically comes and damage our nerve cells. Accordingly, it meddles with the ordinary functioning of our sensory system.
- ❖ **Abdominal Discomfort:** Over consumed of honey may cause genuine stomach uneasiness. Being wealthy in fructose, it can intrude on the supplement assimilation limit of your small digestive tract. Now and again it likewise prompts intense conditions like looseness of the bowels or an annoyed stomach.
- ❖ **Risks of child botulism:**It is not safe to give honey to children under 12 months. Sweet bacterial spores can cause baby botulism, a rare but potentially fatal disease.

### **Conclusion:**

Honey is also known as Madhu in ayurvedic sacred texts is perhaps the main medications utilized in ayurveda. In ayurveda, honey is utilized for both inner and outside applications. Honey has a praiseworthy dietary benefit. Crude honey has astringent, anticonvulsant, anti-nociceptive and stimulant impacts and improves the oxidative state of the cerebrum. A few honey supplements consider have shown that nectar polyphenols have neuroprotective and nootropic impacts. Honey is an effective treatment for a range of oral ulcerative conditions Its natural immune-boosting capability. Quite possibly the main characteristic items is honey, which has been utilized for different lifeless purposes since antiquated occasions. The most notable impact of honey is its antibacterial action to reduce a variety of inflammatory, immune-regulating and estrogenic reactions. It can be concluded that bee honey is an invaluable natural ingredient with multiple uses. It is an effective medicine, a safe home remedy, cosmetics and a nutrient that can be used by people of all ages.

## **References:**

1. Medicinal uses and health benefits of Honey: An Overview K. P. Sampath Kumar\*<sup>1</sup>, Debjit Bhowmik<sup>2</sup>, Chiranjib<sup>2</sup>, Biswajit<sup>2</sup> and M.R.Chandira<sup>2</sup>.
2. Traditional and Modern Uses of Natural Honey in Human Diseases: A Review Tahereh Eteraf-Oskouei <sup>1,2</sup>, Moslem Najafi\*<sup>2</sup>.
3. Honey as a Potential Natural Antioxidant Medicine: An Insight into Its Molecular Mechanisms of Action Sarfraz Ahmed,<sup>1,2</sup> Siti Amrah Sulaiman,<sup>3</sup> Atif Amin Baig,<sup>4</sup> Muhammad Ibrahim,<sup>2</sup> Sana Liaqat,<sup>2</sup> Saira Fatima,<sup>2</sup> Sadia Jabeen,<sup>2</sup> Nighat Shamim,<sup>2</sup> and Nor Hayati Othman <sup>1</sup> Bell SG. The therapeutic use of honey. Neonatal Netw. 2007;26:247–51. [PubMed] [Google Scholar].
4. Honey and Health: A Review of Recent Clinical Research Saeed Samarghandian, Tahereh Farkhondeh, and Fariborz Samini Additional article information Traditional and Modern Uses of Natural Honey in Human Diseases: A Review Tahereh Eteraf-Oskouei and Moslem Najafi Additional article information.
5. Alvarez-Suarez JM, Tulipani S, Romandini S, Bertoli E, Battino M. Contribution of honey in nutrition and human health: a review. *Mediterr J Nutr Metab.* 2010;3:15–23. [Google Scholar].
6. Molan PC. Why honey is effective as a medicine. 2. The scientific explanation of its effects. *Bee World.* 2001;82(1):22–40. [Google Scholar].
7. Role of honey in modern medicine Author links open overlay panel Sultan Ayoub Meo<sup>a</sup> Saleh Ahmad Al Asiri<sup>b</sup> Abdul Latief Mahesar<sup>c</sup> Mohammad Javed Ansari<sup>d</sup>.
8. Article | Open Access Volume 2013 | Article ID 829070 | <https://doi.org/10.1155/2013/829070> Show citation Honey as a Potential Natural Anticancer Agent: A Review of Its Mechanisms.

See discussions, stats, and author profiles for this publication at: <https://www.researchgate.net/publication/356410483>

# Pathogenic variations and fungal metabolic, effect on Protein contents of Pulses

Article in *Annals of Plant Protection Sciences* · January 2021

DOI: 10.5958/0974-0163.2021.00048.3

---

CITATION

1

---

READS

33

2 authors:



**Tanmay Ghosh**

Dinabandhu Andrews College university of calcutta

74 PUBLICATIONS 211 CITATIONS

SEE PROFILE



**Mohan Kumar Biswas**

Visva Bharati University

118 PUBLICATIONS 521 CITATIONS

SEE PROFILE





## Pathogenic variations and fungal metabolic, effect on Protein contents of Pulses

Tanmay Ghosh and \*Mohan Kumar Biswas

Department of Microbiology, Dinabandhu Andrews College, Baishnabghata, South 24 Parganas, Kolkata – 700 084 (West Bengal); \*Department of Plant Pathology, Palli Siksha Bhavana, Visva-Bharati, Sriniketan – 731 236, Dst. Birbhum (West Bengal), India  
<tanmay.tanmay.ghosh780@gmail.com>

Date of Receipt: 09.08.2021; Accepted: 30.09.2021

### ABSTRACT

The nutritional value of the pulse crops are seemingly affected by the seed borne mycoflora of the seeds. In the pulse crops (Soya bean, cow pea, mung bean & lentil) many kind of seed borne mycoflora are found and reported. The mycoflora are responsible for the degradation of protein and causing the damage to seeds. The mycoflora include *Alternaria alternata*, *Fusarium oxysporum*, *Macrophomina phaseolina*, *F. moniliforme*, *A. raphani* and *Cercospora kikuchi*. The diminishing in the protein substance of the seeds. The decreases in protein content are Soya bean 135 mg/g, cow pea 110 mg/g, mung bean 125 mg/g and lentil 100 mg/g. The seed borne fungi usually reduce the protein and oil content of pulse seeds. As a result, the seed germination decreases. Some biochemical treatment can protect the seed from protein content loss.

**Key words:** Biotechnology, Microbiology, Mycoflora, Seed Biology.

Around 88% plant protein is consumed in India. Soya bean, cow pea, mung bean and lentil are more famous sources of protein. The protein content of pulse crops are proved as 45 g/100g for soya beans, 25g/100g for mung beans, 22g/100g for cow pea, and 26g/100g for lentil. The seed borne mycoflora include *Alternaria alternata*, *Fusarium oxysporum*, *Macrophomina phaseolina*, *F. moniliforme*, *A. raphani* and *Cercospora kikuchi* are found dominant upon the seeds of four pulse crops. The mycoflora damage the variety of crops (Ramanjineyulu 2018). Kashinath and Raha (2006) found that the degradation of protein cause the seed to disruption or decrease the health benefits of the crops and sometimes they cause the whole yield to be destroyed. The arhar seed disease are the results of the decrease of protein content caused by some soil mycoflora as *A. flavus*, *Fusarium*

*moniliforme*, *Aspergillus niger*, *Alternaria alternata*, *Fusarium oxysporum*, *Macrophomina phaseolina* (Ahlawat *et al.*, 2016). Causes the loss in seedling germination and growth of *Vigna radiata* L. (Maiti & Basu 2010). The mango pulp sugar content is also affected by the *Aspergillus niger*. So the point of the investigation was to find out the impact of the Seed borne mycoflora on the protein content of four pulse crops. The significant damage was observed in the pulse crops protein substance because of the seed borne mycoflora (Narayana & Manoharachary 2014). The damage of the pulse crops cases economical damage to the nation every year. And this Seed borne mycoflora also decrease the seed quality and affects the health status of the consumers. The seed borne mycoflora also decrease the germination rate of the seeds and damage the yield (Satyanarayana *et al.*, 2010).

Plus seeds are very important source of edible protein. They contain Protein approximately double than the protein content of cereals. Plus crops are also fixing atmospheric nitrogen as they are leguminous nitrogen fixing plants. They form the symbiotic relationship with the nitrogen fixing microbes. So they increase the fertility of the soil. They also help in agriculture by fertilizing the soil. About 90% of the mungbean is grown in irrigated areas in the District of Layah, Bhakhar, Mianwali and Jhang. Lentil needs more humidity and high rainfall area it is also grown in several parts of India. Thus the present study was under taken.

### **Materials and Methods**

Seed samples of soybean, mungbean, cowpeas and lentils were collected from field market near Champadanga, Hooghly by standard method technique. The fungal spore suspension of normal and prevailing seed borne fungi in pulse crop is prepared by mixing 10 ml of dissolved water and adding pure cultures of seed borne fungi in pulse crops and it is maintained by PDA agar slant at room temperature for 5-7 days.

Protein estimation is usually done using the Lowry's method where a spectrophotometer is used. A standard graph is prepared based on this method and the protein content estimation of every test pulse has been done. The reagents that have been used in this method are as follows: Folin ciocalteu reagent is commercially used with same volume of distilled water was mixed at a time. 2% Na<sub>2</sub>CO<sub>3</sub> in 0.1 N sodium hydroxide in 100 ml distilled water (Solution A). 0.5% CuSO<sub>4</sub>.5H<sub>2</sub>O in 1% sodium potassium tartarate in 100 ml distilled water (Solution B). Alkaline copper solution: 50 ml of solution A and 1ml of solution B. Standard protein solution: Here 20 mg gelatin is dissolved with 20 ml distilled water and then mixture was transferred into volumetric flask (100 ml) and 100 ml volume is made.

1g of each pulse seed like Mungbean, Cowpeas, Soybean and Lentils were taken and crushed through a grinder. The powder of every test pulse seed is removed independently and a mixture of

ethyl alcohol and petroleum ether in the ratio of 2:1 is prepared and left for a few minutes. Then the sediments were rinsed through ether solution and solvents of every pulse seeds were filtrate in conical flask. Then the filtrates and residue were collected separately. The collected pulse seeds residues are dried at room temperature and dissolved in 9 ml 20% TCA (Trichloro Acetic Acid) solution. Then the mixture was kept at 4°C temperature for 4 hrs and mixture was centrifuged at 10000 rpm for 5-10 minutes. As a result, of centrifugation a precipitation was observed which was dissolved between 50ml distilled water and 6 ml, 0.1N NaoH solution. 0.1 and 0.2 ml protein extract was taken between different test tubes and the same procedure is applied for each standard protein extract.

First five sterilized test tubes were prepared and the test tubes were serially numbered. From the protein stock solution 0.2, 0.4, 0.6, 0.8 and 1.0 ml pipetted and serially added to the test tube without blank. Then 1 ml of distilled water and 4 ml of copper solution was added every test tubes including blank tubes. Then the test tubes were shaken slowly and kept at room temperature for a time and 0.4 ml of Folin ciocalteu solution was added immediately. As a result, blue colour is produced in 30 minutes. Then we will measure optical density (OD) with the help of spectrophotometer at 640 nm and prepared standard graph with the help of OD. Similar results on biochemical changes in pigeon pea were reported by Kushwaha and Narain (2015), Gadgil & Chavan (2009).

### **Results and Discussion**

The result of Table 1 shows that common and dominant fungi show more or less reduction in protein content of different types of test pulse, where *Fusarium oxysporium* and *A. raphani* shows maximum reduction on the protein content of the following test pulse (Biligrami *et al.*, 1976): Mungbean, Cowpea and Lentil. *Alternaria alternata* and *Cercospora kikuchii* shows maximum reduction on the protein content of the Cowpea and Lentil test pulse. Minimum reduction on protein content was reported in Cowpea and Lentil by *Macrophomina phaseolina* and

**Table 1. The total protein content of pulses is affected by seed borne fungi**

Name of Fungi	Total protein contents of seeds (mg/g of seeds)			
	Soy-bean	Mung-bean	Cowpea	Lentil
<i>Alternaria alternata</i>	160	157	132	126
<i>Fusarium oxysporium</i>	176	108	120	100
<i>Macrophomina phaseolina</i>	154	154	125	131
<i>F. moniliforme</i>	173	161	134	120
<i>A. raphani</i>	153	109	128	137
<i>Cercospora kikuchii</i>	156	144	122	125
Control	180	166	136	144

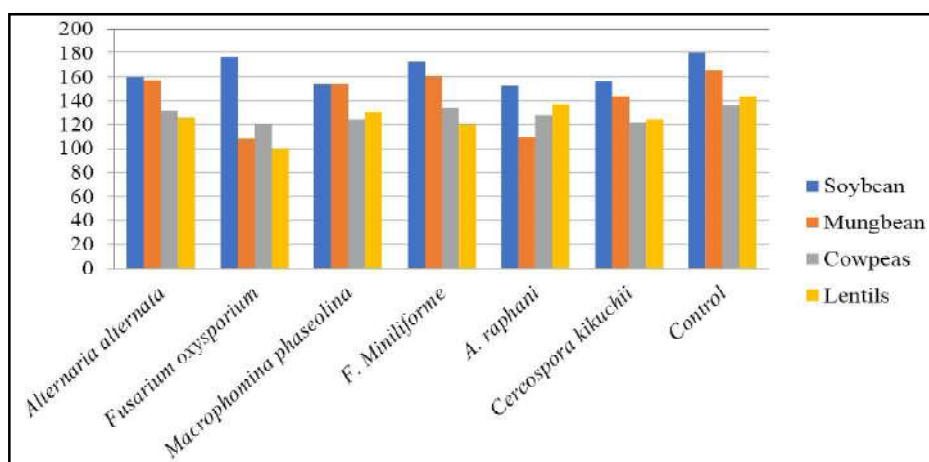
**Fig. 1. Seed Borne Fungi isolated form Pulse**

*F. moniliforme* and in soybean and Mungbean by *Cercospora kikuchii* (Table 1). During storage pulse seeds are adversely affected by seed borne fungi and result in loss of seed carbohydrates and protein. *Macrophomina phaseolina* is a common and dominant fungi those usually degrade the quality of seed protein, oil and carbohydrate (Fig. 1). Sambasivam and Girija (2006) reported almost similar results on Ginger.

Seed borne fungi are responsible for decreased seed protein content and as a result protein content reduction and the percentage of seed germination and seedlings are decreases. Some natural biochemical from seed borne fungi can be used to protect the seed (Shingare *et al.*, 2014).

### Conclusion

From the study we could easily conclude that the highest protein content was of soyabean infected by *Fusarium oxysporium* and the lowest protein content was of lentil affected by *Fusarium oxysporium*. The result clearly spots the light on the fact that the higher protein content were degraded due to the growth of seed borne mycoflora. The protein content was showing very much difference with the control one. All four beans Soya bean, cow pea, mung bean and lentils are highly affected by the seed borne mycoflora of the seed. Six isolated fungi (*Alternaria alternata*, *Fusarium oxysporium*, *Macrophomina phaseolina*, *F. moniliforme*, *A. raphani* and *Cercospora kikuchi*) have shown

**Fig. 2. The total protein content of pulses is affected by seed borne fungi**

more or less but significantly higher affects on the seeds. The highest damage was obtained in soybean and the lowest damage was obtained in cow pea.

## References

- Ahlawat, I.P.S., Purushottam Sharma, Ummed Singh (2016). Production, demand and import of pulses in India. *Indian J. Agronomy* **61**(4<sup>th</sup>): S33-S41.
- Biligrami, K.S., T. Prasad, Jamaluddin and A.K. Roy (1976). Studies on the deterioration of some Pulses by fungi. *Indian Phytopath.* **29**(3): 374-377.
- Gadgil, D.P. and A.M. Chavan (2009). Changes in sugar Contents of mango pulp due to different isolates of *Aspergillus niger*. *Geobios.* **36**: 211-212.
- Kashinath Bhattacharya and Subrata Raha (2006). Deteriorative changes in maize, groundnut and Soybean seeds by fungi in storage. *Mycopathologia.* **155**(3): 135-141.
- Kushwaha, K.P.S. and Udit Narain (2005). Biochemical changes in pigeon pea leaves infected with *Alternaria tenuissinia*. *Ann. Pl. Protec. Sci.* **15**(2): 287-290.
- Maiti, M.K. and A. Basu (2010). Quantitative estimation of chlorophyll, starch and total soluble sugar in potato cultivars infected with *Phytophthora infestans*. *Ann. Pl. Protec. Sci.* **18**(1): 167-171.
- Narayana, B., Bhadraiah and C. Manoharachary (2014). Biochemical changes due to fungal Infestation in stored seeds of some vegetable Crops. *Indian Phytopath.* **67**(2): 159-163.
- Ramanjineyulu, P., K. Viswanath, M. Reddi Kumar and P. Sumathi (2018). Incidence of pod rot of Groundnut (*Arachis hypogaea* L.) in Chittoor and Anantapur districts of Andhra Pradesh. *Ann. Pl. Protec. Sci.* **26**(2): 328-331.
- Sambasivam, P.K. and D. Girija (2006). Biochemical characterization of *Ralstonia solanacearum* infecting Ginger. *Ann. Pl. Protec. Sci.* **14**(2): 419-423.
- Satyanarayana, Ramachandra Rao, P. Arjuna Rao (2010). Incidence and management of *Spodoptera litura* on post rainy season of groundnut. *Ann. Pl. Protec. Sci.* **18**(1): 32-35.
- Sethumadhava Rao, S. Laxmi, B. Nrayana, Bhadraiah and C. Mohanachary (2014). Biochemical Changes due to fungal infestation in stored seeds of Some vegetable crops. *Indian Phytopath.* **67**(2): 159-163.
- Shingare Pawan and Ade Avinash (2014). Deterioration of protein in the diseased groundnut Kernels due to infection of fungi. National Conference on Plant Pathology, 2-3 March 2014, R. Shahu college, Latur, India.



Contents lists available at ScienceDirect

## Materials Today: Proceedings

journal homepage: [www.elsevier.com/locate/matpr](http://www.elsevier.com/locate/matpr)

## Towards application of various machine learning techniques in agriculture

Santosh T. Jagtap<sup>a,\*</sup>, Khongdet Phasinam<sup>b</sup>, Thanwamas Kassanuk<sup>c</sup>, Subhesh Saurabh Jha<sup>d</sup>, Tanmay Ghosh<sup>e</sup>, Chetan M. Thakar<sup>f</sup>

<sup>a</sup> Department of Computer Science, Prof. Ramkrishna More College, Pradhikaran, Pune, Maharashtra, India

<sup>b</sup> Faculty of Food and Agricultural Technology, Pibulsongkram Rajabhat University, Phitsanulok, Thailand

<sup>c</sup> School of Agricultural and Food Engineering, Faculty of Food and Agricultural Technology, Pibulsongkram Rajabhat University, Phitsanulok, Thailand

<sup>d</sup> Department of Botany, Institute of Sciences, Banaras Hindu University, India

<sup>e</sup> Department of Microbiology, Dinabandhu Andrews College, Baishnabghata, South 24 Parganas, Kolkata – 700084, West Bengal, India

<sup>f</sup> Department of Mechanical Engineering, Government College of Engineering, Karad, Maharashtra, India

### ARTICLE INFO

#### Article history:

Received 26 May 2021

Received in revised form 7 June 2021

Accepted 15 June 2021

Available online xxxx

#### Keywords:

Precision Agriculture

Machine learning

Feature Extraction

ICT

### ABSTRACT

Since the invention of the computer, all available information in every field has been digitized and made available to people who use computer resources. As a result, massive amounts of data are being generated in every domain at an alarming rate. Agriculture is one such area of interest for researchers. Machine learning is the process of extracting useful information from various types of data. The classification of objects is an important area within the field of data mining, and its application extends to a variety of areas, whether or not in the field of science. Although k-Nearest Neighbor classification is a simple and effective technique, it slows down the classification of each object. Furthermore, the classification's effectiveness suffers as a result of the uneven distribution of training data. The purpose of this paper is to look into the applicability of various machine learning techniques in agriculture.

© 2021 Elsevier Ltd. All rights reserved.

Selection and peer-review under responsibility of the scientific committee of the 1st International Conference on Computations in Materials and Applied Engineering – 2021.

### 1. Introduction

Indian agriculture [1] is in the early stages of adopting Information and Communication Technology (ICT) techniques for farm management and output improvement. ICT has the potential to benefit all farmers, including small landholders, who are the most vulnerable to crop losses. Agriculture is the most important part of the Indian economy and is critical to India's growth, employing more than 40% of the Indian population (directly or indirectly). ICT techniques can help vulnerable farmers, particularly small stakeholders, take appropriate preventive/mitigating actions in the event of crop diseases, adverse weather, or even soil health.

Machine Learning (and its subset deep learning) and Artificial Intelligence [2] have contributed to an explosive increase in the

application of computer science to previously thought-to-be-impossible complex science problems. The foundation of this thesis is machine learning, specifically Deep Learning and its subset, Convolutional Neural Networks (CNNs). Deep learning methods have been used successfully to solve problems that are simple for humans, such as game play or object recognition, but are difficult to describe mathematically or are computationally prohibitively expensive.

Image recognition, in particular, has undergone a paradigm shift, with use cases sprouting up all over the place. Machine Learning enables applications to predict outcomes with greater precision and accuracy without being explicitly programmed. It works by creating procedures that take input data and then predict an output based on statistical analysis of the data.

Machine learning [3] and data mining employ similar statistical analyses, both of which involve searching for patterns in data and updating outputs in response to new inputs. Furthermore, machine learning is powering virtual assistance technologies by combining several deep learning models to provide relevant context and to

\* Corresponding author.

E-mail addresses: [st.jagtap@gmail.com](mailto:st.jagtap@gmail.com) (S.T. Jagtap), [phasinam@psru.ac.th](mailto:phasinam@psru.ac.th) (K. Phasinam), [t.kassanuk@gmail.com](mailto:t.kassanuk@gmail.com) (T. Kassanuk), [subhesh.jha2@bhu.ac.in](mailto:subhesh.jha2@bhu.ac.in) (S.S. Jha), [tanmay.tanmay.ghosh780@gmail.com](mailto:tanmay.tanmay.ghosh780@gmail.com) (T. Ghosh), [cthakar12@gmail.com](mailto:cthakar12@gmail.com) (C. M. Thakar).

<https://doi.org/10.1016/j.matpr.2021.06.236>

2214-7853/© 2021 Elsevier Ltd. All rights reserved.

Selection and peer-review under responsibility of the scientific committee of the 1st International Conference on Computations in Materials and Applied Engineering – 2021.

interpret natural speech. Machine learning [4] is making it possible for us to live happier, healthier, and more productive lives.

Agriculture is critical to the country's economy since it feeds the whole population. In this way, it connects and interacts with all of the country's relevant companies. If a country has a reasonably big agricultural foundation, it is considered socially and economically wealthy. Agriculture is the principal source of employment in the majority of countries. Large farms frequently necessitate the hiring of additional personnel to assist with planting and farm animal care. The majority of these large farms have processing units nearby where their agricultural goods are finished and developed.

This article provides a comprehensive review of machine learning algorithms applicable in the area of agriculture. This will help future researchers to develop machine learning based solutions for agriculture sector to reduce agriculture waste, water irrigation etc.

## 2. Literature survey

This section contains literature review of various machine learning algorithms, which are applicable in agriculture domain for various tasks like- disease detection in crop, intelligent irrigation, and soil classification, monitoring and tracking.

### 2.1. Machine learning techniques

Machine learning (ML) is a new area of data mining that allows a computer program to become more accurate in predicting outcomes without being explicitly programmed. These ML algorithms are frequently classified as either supervised or unsupervised. For inference (classification, regression), supervised learning algorithms use labeled training data, whereas unsupervised learning algorithms use unlabeled data to discover hidden existing patterns (clustering).

Classification is the process of converting an input set of instances  $P$  into a unique set of attributes  $Q$ , also known as target attributes or labels. Various applications use classification techniques such as decision tree classifiers, bayesian classifiers, artificial neural networks, nearest neighbor classifiers, random forest, and support vector machines [5]. We'll talk about each of them briefly. Each technique operates on the basis of the learning algorithm it employs.

A decision tree is one of the most common and straightforward classifiers for solving classification problems. A decision tree is a graph in which instances are sorted based on their feature values to classify them. The decision tree is made up of nodes and branches, where each node represents a classification instance and each branch represents a value that the node can take on. In decision, instance classification begins at the root node, and instance sorting is based on their feature values.

In some applications, predicting the class label for a given set of input attributes is difficult. Furthermore, class variables are non-deterministic, even when using the given input attribute set values to match some of the attributes of the training data set. This is conceivable owing to the presence of some noisy data and puzzling aspects that are not taken into account during analysis. For example, predicting the likelihood of heart disease in a specific person based on the routine that person follows.

In this case, it is possible that most people who eat healthy foods and exercise regularly are at risk of developing heart disease due to other factors such as smoking, alcohol consumption, and possibly heredity. In such cases, the classification model is defined based on commonly known heart disease attributes, which cannot provide accurate information. There is a need to model probabilistic relationships between the attribute set and the class label in

such applications, and the Bayesian classifier is all about justifying such tasks [6].

The concept of an artificial neural network (ANN) is inspired by biological neural networks, which are used to construct animal brains. Because it is made up of interconnected nodes and directed links, ANN is also known as a connectionist system. Each connected link is given a weight and is in charge of transmitting a signal from one node to another. When a node receives a signal, it processes it before transmitting it to another node.

The signal at the connection between artificial neurons in common ANN implementations is essentially a real number, and the output of each neuron is calculated by a non-linear function of the sum of all its inputs. The strength of the signal increases or decreases as learning progresses due to the weights of artificial neurons and the connections between them [7].

There are two strategies for making a model learned in ML classification. One of them is that as soon as the training set is available, the model begins learning; such models are known as eager learners. Another model observes all training examples but performs classification only if the attributes of the test instance exactly match any one of the training instances. Such students are referred to as lazy students [8].

Each example is treated as a data point in a  $d$ -dimensional space by the Nearest Neighbour (NN) classifier, where  $d$  is the number of attributes. The distance between the given test example and all data points in the training set is calculated. The  $k$ -Nearest Neighbors of data point  $X$  are the  $k$  points closest to the  $X$ .

The data point is then classified based on its neighbors' class labels. If a data point has more than one class labeled neighbor, the data point is assigned the class label with the greatest number of class labels. The value of  $k$ 's nearest neighbors should be determined exactly. If the value of  $k$  is too small, it may misclassify due to the presence of noise in the training data. On the other hand, if the value of  $k$  is too large, there is a chance of misclassification because the set of nearest neighbors may contain data points that are located far away from the neighbourhood of the test attribute.

To begin, Random forest is a supervised machine learning algorithm that consists of a forest of decisions made by multiple decision trees generated using random vectors. This approach may be used to address classification difficulties as well as regression procedures. The result generated by the random forest is related to the number of trees it combines in the forest in such a way that as the number of trees in the forest increases, the possibility of obtaining greater accuracy increases. It is important to note that creating the forest is not the same as creating decision trees [8].

The primary distinction between decision trees and random forests is that in the case of random forest classification, finding the root node and splitting the feature nodes will occur at random. Because of its benefits, random forest classification is popular. One of them is that it can be used for classification as well as regression. Another advantage of this method is that if a sufficient number of trees are available, the problem of overfitting is avoided. In addition, a random forest classifier can handle missing values and can be modelled in the case of categorical values.

The random forest classifier has applications in medicine, banking, e-commerce, and the stock market. Random classifiers are used in banking to identify loyal and fraudulent customers. In medicine, Random Forest is used to identify the correct combination of medicines and to recognize the disease based on a patient's previous medical records. Random Forest classifier is used in the stock market to observe a stock's behavior and then identify the loss and profit. In the context of e-commerce, Random Forest may be used to forecast customer product recommendations.

The supervised learning model used for classification is the Support Vector Machine (SVM). It has gotten a lot of attention in the classification field. In the SVM model, instances of the distinct cat-

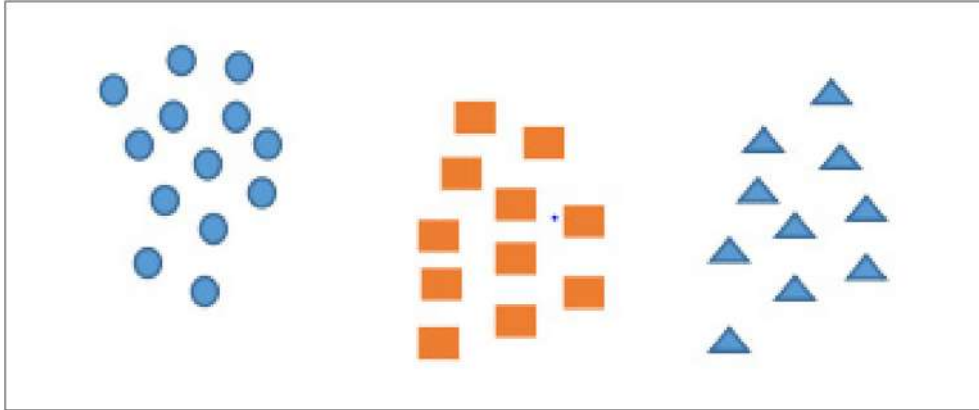


Fig. 1. Clustering.

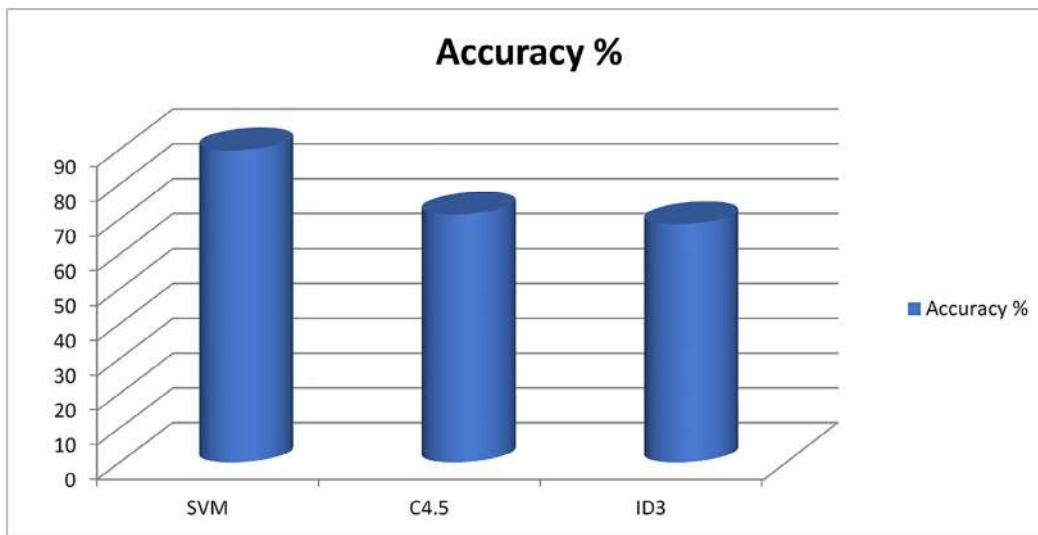


Fig. 2. Accuracy of Classifiers.

egories are separated in vector space by a visible gap. As soon as a new sample comes, it is mapped into the specific vector space, and its label is assigned to a category based on which side of the gap it falls [9]. Using the kernel trick, an SVM can perform non-linear classification efficiently.

Clustering, also known as cluster analysis, is the task of grouping a set of objects so that objects in one group are more similar to each other than objects in another, as illustrated in Fig. 1. The clustering would improve as the similarities between objects in one group and the dissimilarities between objects in different groups increased. Clustering is the foundation of data mining and can be applied in a variety of fields such as image processing, data compression, computer graphics, machine learning, and many others.

As shown in Fig. 1, clustering can be used in conjunction with other techniques for categorizing objects, such as classification, segmentation, and partitioning. When we compare Cluster analysis to classification, we can say that clustering is unsupervised learning. Cluster analysis differs from classification in that knowledge of classes is retained in classification, whereas knowledge of classes is not retained in clustering. Furthermore, in the case of classification, new samples are classified into known classes, whereas in the case of cluster analysis, groups are suggested based on data patterns [9].

Hierarchical clustering is popular for several reasons, including the following: 1) It does not require a specific value, as k-means

clustering does. 2) The generated tree contains meaningful taxonomy. 3) To compute the hierarchical clustering, only the distance matrix is required. There are two types of algorithms available for hierarchical clustering: an agglomerative algorithm that uses a bottom-up approach, and a divisive algorithm that uses a top-down approach.

## 2.2. Feature Extraction

Decock et al. [10] used mutual similarity relations in the domain of discourse to represent linguistic hedges (e.g., cool, warm) as fuzzy rough approximations.

In determining existing practices for the management of soil nutrients, the extent of those practices and perception of soil fertility changes, Pilbeam et al. [11] used triangulated data. According to the survey, the use of farm manure and chemical fertilizer are the two most important soil fertility maintenance practices (mainly urea and di-ammonium phosphate).

The comparison of various sensory types and instruments, including field-based electronic sensors, spectral radiometers, vision machines, multispectral and hyperspectral remote sensing, satellite imaging, thermal imaging and olfactors systems, was carried out by Lee et al. [12]. Lee et al. The study also examined and discussed how precision farming and crop management, especially with regard to specialty crops, can take place in these sensing tech-

nologies. The work relating to that impact on aspects such as accuracy, reliability and time-consuming, has been the imprecise or ambiguous character of information in decision-making.

In order to determine the membership and non Member Function of FUZZY System Reliability, Garg [13] proposed the hybridized technique called Particle Swarm Optimisation Vague Optimisation. The system uses regular arithmetic operations rather than flimsy arithmetic operations and particular swarm optimisation to prevent uncertainty. The system builds membership functions.

As a common approach to the representation and rationalisation of uncertainty, Sturlaugson and Sheppard illustrated a Bayesian network. When the complexities of the network increase, Bayesian is used as an intractable determinant with a large number of nodes and states.

Mueller et al. [14] have developed studies on soil structure relevance and how soil quality overall is preserved. Their findings indicate that for visual soil structure assessment, soil with a concentration in clay greater than 30%, i.e. unfavorable soil structure, was not reliably detected.

Chu et al. [15] aimed for a method of solving problems with pattern recognition based on measures of similarity using intuitionist fuzzy sets from Atanassov. In addition to the [16,17,18,19] convenience of computing and ranking processes, a computer interface decision support system has been developed to help decision-makers more efficiently make diagnoses. This helped a lot in crop monitoring, tracking, disease detection and freshwater saving.

### 3. Result and discussion

A data set of 500 images of crops was created for experimental study. In experimental analysis, three classification algorithms namely, SVM- Support Vector Machine, C 4.5 and ID3 classifiers are used. These machine learning algorithms classified different crop images. This will help in identifying diseases prediction in crop. It will result in reduction in crop waste. It is shown in Fig. 2:

### 4. Conclusion

Agricultural research has benefited from technological advancements, particularly by incorporating industrial advances into a sustainable agriculture production system. By electrifying every farming procedure, technology has transformed farming into a viable business. This saves the farmer money and eliminates the middleman who buys low from farmers and sells high to end consumers. Recent applications of computational intelligence techniques (such as evolutionary algorithms, neural networks, and so on) provide solutions to site-specific decision modeling problems in agricultural systems.

Agriculture is important to the country's economy since it feeds the whole population. It links and interacts with all of the country's relevant enterprises in this way. A country is considered socially and economically prosperous if it has a sufficiently large agricultural basis. In the majority of countries, agriculture is the primary source of employment. Large farms usually require the hiring of extra workers to help with planting and farm animal care. The bulk of these huge farms have close processing plants where their agricultural products are processed and developed.

Machine learning's adaptability, promotion, and reduced costs helps in assessing the complicated link between the input and output of agricultural systems utilizing analytical approaches that are characterized by non-linearity, time variable features, and numerous unknown elements. This paper provides a review of various machine learning-based algorithms that can be used in agriculture

for tasks such as crop disease detection, intelligent irrigation, soil classification, monitoring, and tracking.

### CRedit authorship contribution statement

**Santosh T. Jagtap:** Conceptualization, Methodology. **Khongdet Phasinam:** Data curation. **Thanwamas Kassanuk:** Visualization, Investigation. **Subhesh Saurabh Jha:** Writing - review & editing. **Tanmay Ghosh:** Validation. **Chetan M. Thakar:** Writing - original draft, Supervision.

### Declaration of Competing Interest

The authors declare that they have no known competing financial interests or personal relationships that could have appeared to influence the work reported in this paper.

### References

- [1] G. Gyarmati, T. Mizik, The present and future of the precision agriculture, in: 2020 IEEE 15th International Conference of System of Systems Engineering (SoSE), 2020, pp. 593–596. doi:10.1109/SoSE50414.2020.9130481.
- [2] R. Katarya, A. Raturi, A. Mehndiratta, A. Thapper, Impact of Machine Learning Techniques in Precision Agriculture, in: 2020 3rd International Conference on Emerging Technologies in Computer Engineering: Machine Learning and Internet of Things (ICETCE), 2020, pp. 1–6. doi:10.1109/ICETCE48199.2020.9091741.
- [3] A. Sharma, A. Jain, P. Gupta, V. Chowdary, Machine learning applications for precision agriculture: a comprehensive review, IEEE Access 9 (2021) 4843–4873. <https://doi.org/10.1109/ACCESS.2020.3048415>.
- [4] M.M. Anghelof, G. Suci, R. Craciunescu, C. Marghescu, Intelligent System for Precision Agriculture, in: 2020 13th International Conference on Communications (COMM), 2020, pp. 407–410. doi:10.1109/COMM48946.2020.9141981.
- [5] I. Khan, X. Zhang, M. Rehman, R. Ali, A literature survey and empirical study of meta-learning for classifier selection, IEEE Access 8 (2020) 10262–10281. <https://doi.org/10.1109/ACCESS.2020.2964726>.
- [6] S.P. Samuel, K. Malarvizhi, S. Karthik, S.G.M. Gowri, Machine Learning and Internet of Things based Smart Agriculture, in: 2020 6th International Conference on Advanced Computing and Communication Systems (ICACCS), 2020, pp. 1101–1106. doi:10.1109/ICACCS48705.2020.9074472.
- [7] B. Sharma, J.K.P.S. Yadav, S. Yadav, Predict Crop Production in India Using Machine Learning Technique: A Survey, in: 2020 8th International Conference on Reliability, Infocom Technologies and Optimization (Trends and Future Directions) (ICRITO), 2020, pp. 993–997. doi:10.1109/ICRITO48877.2020.9197953.
- [8] A. Muniasamy, Machine Learning for Smart Farming: A Focus on Desert Agriculture, in: 2020 International Conference on Computing and Information Technology (ICIT-1441), 2020, pp. 1–5, doi: 10.1109/ICIT-144147971.2020.9213759.
- [9] K.N. Bhanu, H.J. Jasmine, H.S. Mahadevaswamy, Machine learning Implementation in IoT based Intelligent System for Agriculture, in: 2020 International Conference for Emerging Technology (INCET), 2020, pp. 1–5. doi: 10.1109/INCET49848.2020.9153978.
- [10] M. Decock, A.M. Radzikowska, E.E. Kerre, A fuzzy-rough approach to the representation of linguistic hedges, in: *Technologies for Constructing Intelligent Systems*, Springer, Berlin, 2002, pp. 33–42.
- [11] C.J. Pilbeam, S.B. Mathema, P.J. Gregory, P.B. Shakya, Soil fertility management in the Mid-Hills of Nepal: practices and perceptions, *Agric. Hum. Values* 22 (2) (2005) 243–258.
- [12] W.S. Lee, V. Alchanatis, C. Yang, M. Hirafuji, D. Moshou, C. Li, Sensing technologies for precision specialty crop production, *Comput. Electron. Agric.* 74 (1) (2010) 2–33.
- [13] H. Garg, An approach for analyzing fuzzy system reliability using particle swarm optimization and Intuitionistic fuzzy set theory, *Multiple-Valued Logic and Soft Computing* 21 (3) (2013) 335–354.
- [14] L.E. Sturlaugson, J.W. Sheppard, Principal Component Analysis PreProcessing with Bayesian Networks for Battery Capacity Estimation. Conference in Instrumentation and Measurement Technology, IEEE, Minneapolis, 2013, pp. 98–101.
- [15] C.H. Chu, K.C. Hung, P. Julian, Complete pattern recognition approach under Atanassov's Intuitionistic Fuzzy Sets, *Knowl.-Based Syst.* 66 (2014) 36–45.
- [16] J. Gholap, A. Lngole, J. Gohil, Shailesh, V. Attar, Soil data analysis using classification techniques and soil attribute prediction, *Int. J. Comput. Sci.* 9 (3) (2012) 14.
- [17] S. Ghosh, S. Koley, Machine learning for soil fertility and plant nutrient management using back propagation neural networks, *Int. J. Recent Innov. Trends Comput. Commun.* 2 (2) (2014) 292–297.



- [18] S.S. Dahikar, V.S. Rode, Agricultural crop yield prediction using artificial neural network approach, *Int. J. Innov. Res. Elect. Electron. Instrum. Control Eng.* 2 (1) (2014) 683–686.
- [19] M. Kaur, H. Gulati, H. Kundra, Data mining in agriculture on crop price prediction: techniques and applications, *Int. J. Comput. Appl.* 99 (12) (2014) 975–988.



# Source details

[Feedback >](#) [Compare sources >](#)

## Materials Today: Proceedings

Scopus coverage years: 2005, from 2014 to 2023

E-ISSN: 2214-7853

Subject area: [Materials Science: General Materials Science](#)

Source type: Conference Proceeding

[View all documents >](#)

[Set document alert](#)

[Save to source list](#)

CiteScore 2022

3.2



SJR 2022

0.445



SNIP 2022

0.774



CiteScore

[CiteScore rank & trend](#)

[Scopus content coverage](#)



Contents lists available at ScienceDirect

## Materials Today: Proceedings

journal homepage: [www.elsevier.com/locate/matpr](http://www.elsevier.com/locate/matpr)

# Protein profiling of rice (Khas) and mustard (Jhumi) seeds before and after infected by seed borne mycoflora

Tanmay Ghosh<sup>a,\*</sup>, Mohan Kumar Biswas<sup>b</sup>, Kaustav Aikat<sup>c</sup>

<sup>a</sup> Department of Microbiology, Dinabandhu Andrews College, Baishnabghata, South 24 Parganas, Kolkata – 700084, West Bengal, India

<sup>b</sup> Department of Plant Pathology, Palli Siksha Bhavana, Visva-Bharati, Sriniketan, West Bengal 731236, India

<sup>c</sup> Department of Biotechnology, NIT Durgapur, Burdwan, West Bengal, India

## ARTICLE INFO

## Article history:

Received 25 May 2021

Received in revised form 1 June 2021

Accepted 15 June 2021

Available online xxxx

## Keywords:

Seed borne mycoflora

Microbiology

Biotechnology

Protein

Botany

## ABSTRACT

Rice and Mustard are the most important cereal and oilseed crops produced almost all over the world. Both Rice and Mustard contains several nutrients such as carbohydrates, protein, vitamin and etc. There are several seed borne mycoflora that infect rice and mustard seeds and effects it's worstly, impact on its purity and quality. Here we have detected several protein bands with suspected proteins. It has been observed that concentrations of proteins are decrease day by day. This is because several seed borne mycoflora has infects the oilseeds and cereal crops and used its nutrients for their own metabolism. The aim of this study is to analyze the effects of pathogenic microorganism on seeds in the aspects of its protein content.

© 2021 Elsevier Ltd. All rights reserved.

Selection and peer-review under responsibility of the scientific committee of the 1st International Conference on Computations in Materials and Applied Engineering – 2021.

## 1. Introduction

In poor storage conditions pathogens are the most important factors, which not only cause the seed ageing and deterioration during storage but also seed and seedling rotting, abnormal production of seed, seed necrosis.[1,2] The aim of our study is eco-friendly management of this seed borne mycoflora of rice (Khas) and mustard (Jhumi). Rice is the cereal crop seed belonging to grass species *Oryza sativa*. It is an important cereal grain that is use as widely consumed staple food in major part of the world, especially in Asia and Africa. [3,4]The mustard is the oilseed plant belongs to family *Brassicaceae*. It is used to make mustard oil and also used as spices. Rice has huge amount of protein and carbohydrate. [5]The main component of rice is carbohydrate but protein is also present. Mustard also contains vitamin as well as protein. In both rice and mustard, the amount of protein decreases due to the effect of seed borne mycoflora. Mustard contains coagulant protein, which may use for water treatment in drinking purpose [6]. Rice contains glutelins, which are classes of prolamin protein found in endosperm of rice.[7] Rice protein has high sulphur containing amino acid, cysteine.[8] On the other hand, Mustard has lower amount of cysteine and methionine and higher amount of lysine.[9,10] There are dif-

ferent size of protein band pattern present in rice and mustard. To analyze the protein qualitatively by denature its original form to linear peptide chain is a process called Sodium Dodecyl Sulphate Polyacrylamide Gel Electrophoresis [11]. It was observed that after infected by certain mycoflora the amount of protein decreased, it may be due to fungi utilized as a substrate for their growth. There was six fungi *Fusarium* sp., *Rhizopus* sp., *Alternaria* sp., *Rhizoctonia* sp., *Cochliobolus* sp. and *Aspergillus* sp. found associated with Rice and Mustard among which *Fusarium* sp. and *Rhizopus* sp. were more destructive. Farmers need a qualitative and quantitative food production. Hence, it is important to test seeds before shower in the field. An adverse aspect of seed borne pathogen is it will contaminate the areas which are disease free [10]. So, it is necessary to treat seed borne mycoflora by using various seed treatment method. [12]

## 2. Materials & methods

### 2.1. Lowry's method

This method was developed to determine the protein content of seeds. It is based on the principle of reduction of Phosphomolybdic-phosphotegenic components in Folin-ciocalteu reagent by using

\* Corresponding author.

E-mail address: [tanmay.tanmay.ghosh780@gmail.com](mailto:tanmay.tanmay.ghosh780@gmail.com) (T. Ghosh).

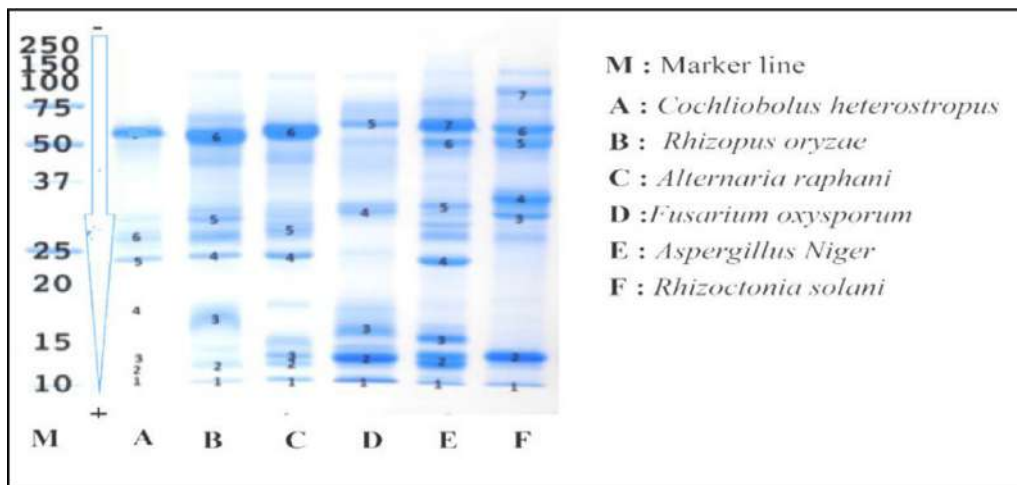


Fig. 1. Plate –8Protein profiling of fresh and infected Rice and Mustard seeds genotype at Plate no. 8.

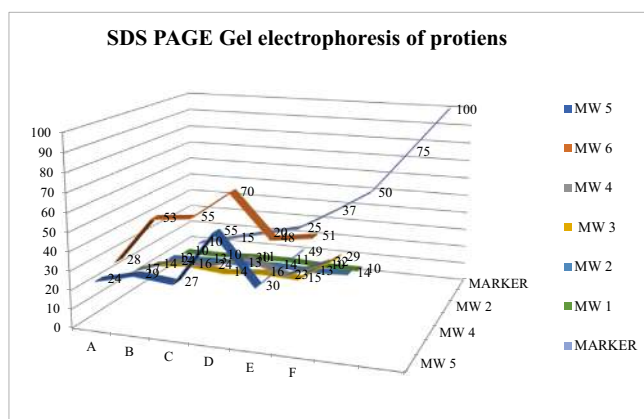


Fig. 2. SDS PAGE results of Proteins associated with the protein infection in seeds.

tyrosin and tryptophan that present in the protein with cupric tartate which is measured by Lowry’s method Figs. 1-4.

### 2.2. SDS-PAGE method

Polyacrylamide gel electrophoresis is a very common method used for quantitative study of protein mixture. It’s also helps to determine relative molecular mass of the protein. Soluble proteins were Electrophosphorised by 12% SDS polyacrylamide gel, here SDS is an anionic detergent that denatured the protein prior to leading. Protein separated by polyacrylamide gel treated with reducing agent like Mercapto-Ethanol (ME) or Dithiothreitol (DTT). SDS page disrupt the secondary, tertiary and quaternary structure of protein to linear polypeptide chain. Now it has a net uniform negative charge irrespected to its own negative charge. As a result, protein molecules migrate entirely according to their size.

### 2.3. UV-Visible spectrophotometer

It is a common analytic technique used to quantitative estimation of color. An estimated substance must be capable to addict the reagent. Color substance absorbs light according to its intensity.

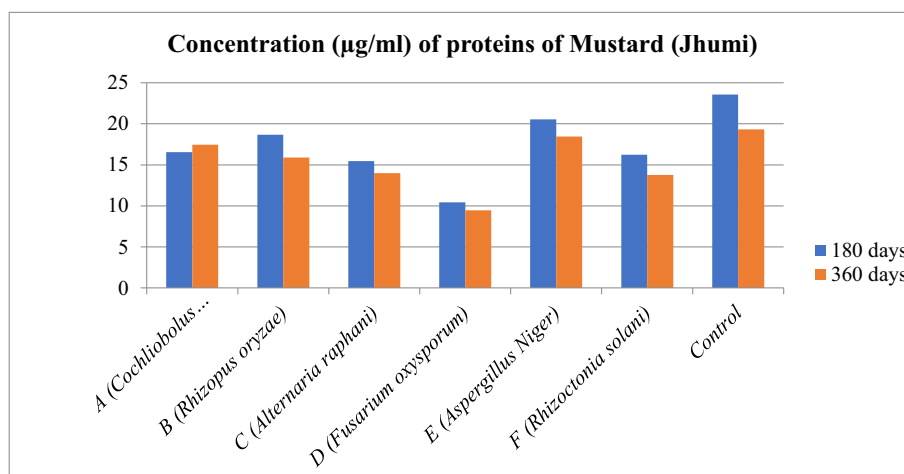


Fig. 3. Concentrations (µg/ml) of proteins estimated from UV Visible Spectrophotometer.

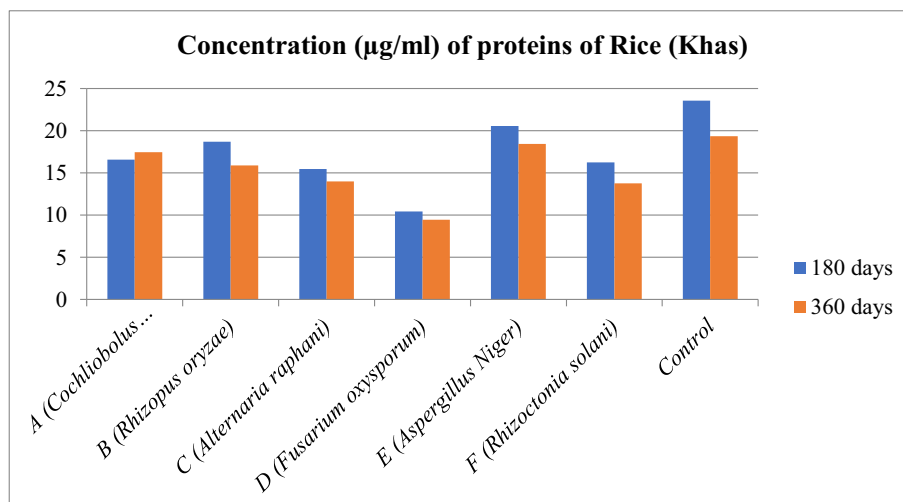


Fig. 4. Concentrations (µg/ml) of proteins estimated from UV Visible Spectrophotometer.

Intensity of color is proportional to the concentration of color substance. In related to color intensity some specific wavelength of light absorbed by passing monochromatic light passes through the colored solution. The instruments used in this method are colorimeter, photometer or absorptiometer.

#### 2.4. Chemical required

Tris base 2. Acrylamide and Bis acrylamide 3. Ammonium persulphate (APS) 4. TEMED 5. SDS 6. β-Mercaptoethanol 7. Glycerol 8. Bromophenol blue 9. Glycine 10. Brilliant blue R-250 11. Acetic acid 12. Methanol.

#### 2.5. Material required

Test tube 2. Micropipette 3. Eppendorf 4. Tips 5. Measuring cylinder.

#### 2.6. Instrument

Cooling centrifuge 2. Electrophoretic unit 3. Electronic balance.

#### 2.7. Different parts of colorimeter

Light source.

Filter (the device that selects the required wavelength).

Cuvette chamber (a beam of light is passed through the sample within cuvette to measure absorbance, fluorescence intensity of the sample).

Detector (photosensitive element which converts light signal to electrical signal).

Galvanometer (quantitatively measurement of electrical signal).

#### 2.8. Reagent preparation

Solution 1: Weighed 14.5 g Acrylamide and dissolved in minimum amount of water made 50 ml volume.

Solution 2: (1.5 (M) Tris - HCl, pH 8.8) – 9.086g Tris dissolved in 50 ml distilled water.

Solution 3: (1 (M) Tris - HCl, pH 6.8) - in 50 ml distilled water dissolved 6.057 g Tris.

To prepare 10% ammonium per sulphate dissolve 1 g of APS in 10 ml distilled water.

To prepare 10% SDS, 10 g SDS dissolve in 20 ml distilled water.

#### 2.9. 1X Tris glycine electrophoresis buffer

Tris 7.6 g, 47 g glycine dissolve in 450 ml of distilled water then add 50 ml of 10% SDS, mixed it properly.

#### 2.10. 1X SDS gel loading dye

Mixed 5 ml glycerol, Tris 2.5 ml (6.8 pH), β-Mercaptoethanol 10.394 ml, 10% SDS 10 ml, bromophenol blue 0.5 g in 50 µl, distilled water 32.106 ml.

#### 2.11. Staining solution

50 ml methanol, 10 ml acetic acid, glycerol, 0.05 g Coomassie brilliant blue and 40 ml distilled water, mixed properly.

#### 2.12. Destaining solution

Add 7 ml methanol with 5 ml acetic acid then add 88 ml distilled water.

#### 2.13. Sealing gel

ml of sol 1 + 50 µl APS + 9 µl

- To prepare 10% separating gel of 10 ml, add 4 ml distilled water into the 3.3 ml solution 1, 2.5 ml solution 2, 10% SDS 100 µl, 10% APS 100 µl and 100 µl and 4 µl TEMED.
- To prepare 5% stacking gel of 5 ml mixed 3.4 ml distilled water into 0.83 ml of solution 1, 0.63 ml of solution 2, 50 µl 10% SDS, 50 µl 10% APS and 4 µl TEMED.

### 3. Procedure

#### 3.1. Lowry's method

To make reagent A, mixed 2% sodium carbonate in 0.1 N sodium hydroxide reagent B was prepared by mixing 0.5% copper sulphate in 1% potassium tartate. Mixed 50 ml of reagent A with 1 ml of reagent B prior to use reagent C to make alkaline copper solution. Folin-Ciocalteu is used as reagent D. To make stock solution of protein mixed properly 50 mg of bovine serum albumin (fraction V) in distilled water and made up 50 ml in standard flask. A 10 ml of

**Table 1**  
Molecular weight of Proteins figured out from Plate No.8.

Name of Mycoflora	MW 5 (Molecular Weight - kD)
A ( <i>Cochliobolus heterostropus</i> )	24
B ( <i>Rhizopus oryzae</i> )	29
C ( <i>Alternaria raphani</i> )	27
D ( <i>Fusarium oxysporum</i> )	55
E ( <i>Aspergillus niger</i> )	30
F ( <i>Rhizoctonia solani</i> )	49

standard solution diluted by using 50 ml distilled water. Each 1 ml of solution contained 200 µg protein.

Freshly harvested, stored and fungal infected Rice and Mustard seeds were taken for protein extraction. For enzyme assay extraction was done by using buffer. Mixed 5–10 ml of phosphate buffer with 500 mg of each powdered solution. Then centrifuge the section and use the supernatant for protein estimation. Take standard solution of 0.2, 0.4, 0.6, 0.8 and 1 ml to a series of test tube by using pipette. From the other test tube pipette out 50 µl, 100 µl, 150 µl and 200 µl concentration extracts of each sample. Make a volume up to 1 ml in all test tubes. A tube filled with 1 ml of distilled water as the blank solution. Then 5 ml of alkaline copper solution were added to each tube including the blank. Then mixed all the solution well and allowed standing for 10 min. Made a mixture of 0.5 ml of Folin – Ciocalteu reagent and incubate the mixture at normal temperature for 30mins in dark condition. The development of blue color was observed. Taking the reading at 660 nm a standard graph was plotted and the calculation of amount of protein was done.

### 3.2. Sodium Dodecyl sulphate polyacrylamide gel electrophoresis (SDS-PAGE)

Take the glass plate according to manufacturer's instruction. It is an Erlenmeyer flask, pipette out proper volume of 12% separating resolving gel in desire concentration. Polymerization will begin with the addition of TEMED as soon as possible. Circulate the mixture very fast. Pure acrylamide gel between the glass plate and make sure that having space like the teeth length of comb plus 1 cm for staking gel. Overlay with water by using Pasteur pipette then places the gel at room temperature in vertical position. The polymerization process is complete within 30–40 min. It is observed those two distinct layers of gel and an overlay of water. Pipette out the overlay and release remaining water by filtering. Then prepare 5% staking gel and put it over the separating gel. Then put a clean Teflon comb into the staking gel solution, being careful to avoid trapping of air bubbles. Place the gel in a vertical position of room temperature for polymerization. Assembles the gel chamber, fill the buffer reservoir with 1 × Tris glycine electrophoresis buffer. After the completion of polymerization, remove Teflon comb carefully. Set the gel in the electrophoresis apparatus.

**Table 2**  
Concentrations (µg/ml) of proteins estimated from UV Visible Spectrophotometer.

Treatments	Total protein (µg/ml)		Mustard (Jhumi)			
	Genotypes Rice (Khas) Fresh seeds	180 days	360 days	Fresh seeds	180 days	360 days
A ( <i>Cochliobolus heterostropus</i> )	–	15.45	10.45	–	16.56	17.45
B ( <i>Rhizopus oryzae</i> )	–	16.68	14.25	–	18.68	15.89
C ( <i>Alternaria raphani</i> )	–	13.34	8.23	–	15.47	13.98
D ( <i>Fusarium oxysporum</i> )	–	9.34	6.34	–	10.44	9.46
E ( <i>Aspergillus niger</i> )	–	16.57	15.78	–	20.56	18.45
F ( <i>Rhizoctonia solani</i> )	–	15.23	14.9	–	16.23	13.78
Control	25.27	21.57	20.32	26.86	23.56	19.34

Removal air bubbles are caught below the gel between the glass plates. Load up to 50 µl of each sample according to the bottom of the walls with the help of a micro syringe, then wash with buffer from the lower reservoir after loading every sample. Load the equal volume of 1 × SDS gel loading buffer into the unused walls. The electrophoresis apparatus attached with the electricity then the pastier electrode have to be joined with lower buffer reservoir. Then about 8 V/cm voltage was applied to the gel. The voltage was increased about 15 V/cm after removal of the dye front into the resolving gel and run the gel bromophenol front reaches 0.5 cm from the lower edges of the gel. Detach this glass plates from electrophoresis apparatus the accommodation of the gel is marked by cutting a corner from the bottom of the gel that is closest to the left most well. Then fixed the gel and stained by protein after the completion of electrophoresis. The stain used is coomassie brilliant blue R-250 in methanol. Polypeptides are separated by SDS-PAGE can stained the coomassie brilliant blue R-250 fixed with methanol glacial acetic acid. Then immerse the gel in at 5 volumes of staining solution and rotate in a platform for 4 h at normal temperature. Then detach this stain and set aside that for later used. Destain the gel by socking in the destain solution of methanol, lactic acid on a slow soaking platform for 3–4 h. Change destain learning solution for 3–4 Times. The dye used each fairly sensitive and can detect up 100 µg of protein in an acrylamide gel. After destain store the gel in a sealed plastic bag without reducing the intensity of staining or it is also done by keeping the gel for 10mins under UV light in a laminar air flow and it can be stored in a sealed plastic bag at 4C.

### 3.3. UV-VISIBLE spectrophotometry method

Before starting the experiment the colorimeter calibrating is important that is done by applying standard solution with its known solute concentration. Then fill the standard solution in the cuvette and place it in the cuvette holder of colorimeter. A light ray of certain wavelength is specific for the assay in the direction of the solution. The light passes through a series of different lenses and filters. The color light navigate with the help of lenses, the filter helps to split a beam of light into different wavelength allowing only the required wavelength to pass through it and each the cuvette of the standard test solution. When the beam of light reaches cuvette, it is transmitted, reflected and absorbed by the solution. The transmitted ray falls on the photo detector system where it measures the intensity of transmitted light. It converts it into the electrical signals and sends it to the galvanometer. The electrical signals measured by the galvanometer are displayed in the digital form. There were several formulas use to determine protein concentration in test solution.

Several marker proteins were used which were Prolamin (10KD), Albumin (15KD) a Poaceae group protein, Basic Beta Glutinin with 20KD of protein band, Profilin (25KD), an acid Glutinin of

37KD protein bands, Tripsin (50KD), Gibberelin (17KD), Phosphorylase A possess 100KD protein band size, Lipomodulin (150KD) and 300KD protein banded Oculin susceptively.

#### 4. Results

#### 5. Discussion & conclusion

##### 5.1. Protein profiling of fresh and infested seeds

This study was carried out by UV-VISIBLE spectrophotometer (Table 2). The highest protein band was found for D (*Fusarium oxysporum*) stain and that is 55 kD and the rest of all bands are depicted followed by F (*Rhizoctonia solani*) was 49 kD, E (*Aspergillus niger*) was 30 kD, B (*Rhizopus oryzae*) was 29 kD, C (*Alternaria raphani*) was 27 kD and the lowest band found for A (*Cochliobolus heterostropus*) 24 kD.

For the Mustard seed the highest protein band was found for C (*Alternaria raphani*) was 55kD and the rest of all bands are depicted followed by D (*Fusarium oxysporum*) stain and that is 70 kD. B (*Rhizopus oryzae*) was 53 kD, F (*Rhizoctonia solani*) was 51 kD, E (*Aspergillus niger*) was 48 kD, and the lowest band found for A (*Cochliobolus heterostropus*) 28 kD.

As a result of protein by SDS – PAGE it can be conclude that the highest number of band was observed from fresh Rice and Mustard seeds. The presence or absence of band in protein profiling might be responsible for presence or absence of protein of that size.

##### 5.2. Change of concentration ( $\mu\text{g/ml}$ ) in protein content during different period of storage

Variation in the protein content was determined in both control and infested stored samples of Rice and Mustard seeds. Table 1-reveals that protein content was found to be decreased due to infestation of selected dominant seed borne mycoflora viz. *Cochliobolus heterostropus*, *Rhizopus oryzae*, *Alternaria raphani*, *Fusarium oxysporum*, *Aspergillus niger*, *Rhizoctonia solani* and increase in storage period. After 180 months, maximum protein content was observed in B (*Rhizopus oryzae*) (16.68  $\mu\text{g/ml}$ ) in Rice followed by E (*Aspergillus niger*) (20.56  $\mu\text{g/ml}$ ) in Mustard. In control (21.57  $\mu\text{g/ml}$ ) on Rice followed by (23.56  $\mu\text{g/ml}$ ) in Mustard. Minimum Protein content (9.34 and 10.44  $\mu\text{g/ml}$ ) was found in D (*Fusarium oxysporum*) infested seeds. Finally, after 360 months, maximum protein content was observed in B (*Rhizopus oryzae*) (14.25  $\mu\text{g/ml}$ ) in Rice followed by E (*Aspergillus niger*) (18.45  $\mu\text{g/ml}$ )

ml) in Mustard. In control (20.32  $\mu\text{g/ml}$ ) on Rice followed by (19.34  $\mu\text{g/ml}$ ) in Mustard. Minimum Protein content (6.34 and 9.46  $\mu\text{g/ml}$ ) was found in D (*Fusarium oxysporum*) infested seeds.

The decreases in crude fat are observed that is the cause of degradation of lipids by lipase enzyme by fungi. The slight moisture consumption might be due to the hydrolysis or breakdown of lipid, carbohydrate and protein and release of water molecule.

#### CRedit authorship contribution statement

**Tanmay Ghosh:** Investigation, Writing - original draft. **Mohan Kumar Biswas:** Investigation. **Kaustav Aikat:** Supervision.

#### Declaration of Competing Interest

The authors declare that they have no known competing financial interests or personal relationships that could have appeared to influence the work reported in this paper.

#### References

- [1] S.K. Diwakar, P.K. MadhuVajpeyi and Singh, Quality studies of some sesame (*Sesamum indicum* L.) seeds, oil, protein and fatty acids, Journal of Oilseed Research 19 (1) (2002) 71–72.
- [2] E.A. Iyayi, Changes in the cellulose, sugar and crude protein contents of agro-industrial by-products fermented with *Aspergillus niger*, *Aspergillus flavus* and *Penicillium* sp, African J. Biotech 3 (3) (2004) 186–188.
- [3] O.H. Lowry, N.J. Rosenbrough, A.L. Farr, R.J. Randall, Protein measurement with Folin-phenol reagent, J. Biol. Chem. 193 (1951) 265.
- [4] N. Saxena, D. Karan, Effect of seed borne fungi on protein and carbohydrate contents of sesame and sunflower seeds, Indian Phytopath 44 (1991) 134–136.
- [5] M. Weidenborner, H. Hindorf, Fungi isolated from protein enriched seeds and pods with special emphasis on the genus *Aspergillus*, Seed Science and Technology 17 (1989) 383–394.
- [6] M. Rusydi, M.R. Noraliza, C.W.A. Azrina, A. Zulkhairi, Nutritional changes in germinated legumes and rice varieties, International Food Research Journal 18 (2011) 705–713.
- [7] S. Sadasivam, A. Manickam, Biochemical Methods, (3rd ed.), New Age International (P) Limited, New Delhi, 2008.
- [8] M.J. Saleem, R. Bajwa, A. Hannan, T.A. Qaiser, Maize seed storage mycoflora in Pakistan and its chemical control, Pak. J. Bot 44 (2) (2011) 807–812.
- [9] V.R. Sangakkara, H.M. Somarante, Sources of storage conditions and quality of mungbean seeds for cultivars in Sri Lanka, Seed Sci. Tech 16 (1988) 5–10.
- [10] T. Agarwal, A. Malhotra, P.C. Trivedi, Fungi associated with chickpea, lentil and blackgram seeds of Rajasthan, International journal of pharma and bio sciences 2 (4) (2011) 478–483.
- [11] S.A. Ross, N.E. El-Keltawi, S.E. Megalla, Antimicrobial activity of some Egyptian aromatic plants, Fitoterapia 51 (1980) 201–205.
- [12] R.F. Chaudhary, R.L. Patel, S.M. Chaudhari, *In vitro* evaluation of different plant extracts against *Alternaria alternata* causing early blight of potato, J. Indian Potato Assoc 30 (1–2) (2003) 141–142.



# Source details

[Feedback >](#) [Compare sources >](#)

## Materials Today: Proceedings

Scopus coverage years: 2005, from 2014 to 2023

E-ISSN: 2214-7853

Subject area: [Materials Science: General Materials Science](#)

Source type: Conference Proceeding

[View all documents >](#)

[Set document alert](#)

[Save to source list](#)

CiteScore 2022

3.2



SJR 2022

0.445



SNIP 2022

0.774







Contents lists available at ScienceDirect

## Materials Today: Proceedings

journal homepage: [www.elsevier.com/locate/matpr](http://www.elsevier.com/locate/matpr)

## Biosorption of heavy metal by bacteria for sustainable crop production

Tanmay Ghosh<sup>a</sup>, Anirban Paul<sup>b</sup>, Sandipan Chatterjee<sup>b,\*</sup><sup>a</sup> Department of Microbiology, Dinabandhu Andrews College, Baishnabghata, South 24 Parganas, Kolkata 700084, West Bengal, India<sup>b</sup> Department of Botany, Suri Vidyasagar College, Suri, Birbhum 731101, West Bengal, India

## ARTICLE INFO

## Article history:

Received 27 April 2021

Received in revised form 12 May 2021

Accepted 26 May 2021

Available online xxxx

## Keywords:

Agricultural  
Heavy metal  
Enumeration  
Microbiology  
Environment

## ABSTRACT

In eco-system population several heavy metals play important roles those are spread from the domestic and industrial wastes, causing huge crop damage by damaging plant tissues. The collected heavy metal tolerance bacterial samples from agricultural lands of Durgapur zone, West Bengal, India against Molybdenum, Lead, Cobalt and Zinc are observed as *Proteus* sp. *Klebsiella* sp. and *Bacillus* sp. *Pseudomonas* sp. and *Staphylococcus* sp. as predominant. Demonstrated some confines displayed high protection from heavy metals with at least Minimum Inhibitory Concentration (MIC) for weighty metals as 80 µg/ml for Molybdenum, 160 µg/ml for Lead, 140 µg/ml for Cobalt and 1200 µg/ml for Zinc. In this study we noticed a relationship between substantial metal opposition and anti-microbial resistance in bacterial samples. The heavy metal free samples of *Triticum aestivum* showed batter results in root length and shoot length than the heavy metal contaminated samples.

© 2021 Elsevier Ltd. All rights reserved.

Selection and peer-review under responsibility of the scientific committee of the 1st International Conference on Computations in Materials and Applied Engineering – 2021.

## 1. Introduction

Globally, Environmental pollution brought about by weighty metals through anthropogenic and mechanical exercises has made significant unsalvageable harm the biological system. Among the various pollutants, heavy metals are released from the activity of industries such as smelting, mining, combustion of fossil fuel in soil and water [1,2]. In addition, agricultural activities such as application of agricultural land and sewage sludge in agricultural areas also add sufficient metals in the soil [3–5]. In addition, heavy metals such as Zinc, Cobalt, Lead and Molybdenum have been found to be the most toxic pollutants. The toxic metal pollution is a major concern, as these hazardous pollutants are accumulated in living organisms including microbes, plant, animal and human and are responsible for many physiological and metabolic disorders and in some cases plant tissues are damaged [6–8]. Substantial metal becomes poisonous when they aren't processed by the human body and collected in delicate tissue [9,10]. The increase in metallic toxicity is considered to be one of the main causes of limitation of plant growth. So, that's important to restore the heavy metal contaminated environments for both environmental and

economical sustainability. Among these it is imperative to consider local microbes on weighty metal tainted destinations [11,12]. Unnecessary collection of weighty metals on agrarian land through wastewater system can be sullied as well as can be substantial metals are take-up by harvests and accordingly influence food quality and wellbeing [13,14]. In the environment microorganism are usually affected by the discharge of heavy metals. Microbial ecosystem can drastically change the fate of metals inserted into aquatic or metallic soil environment [15]. Yeast, fungi, algae, bacteria and some aquatic plants have been shown to have the ability to thicken metals from dilute aqueous solution and to accumulate inside the cell structure. Many microorganisms have developed resistance to toxic metal ions to survive in heavy contaminated environment [16]. These mechanisms include: impermeability of the metal, active transport of the metal away from the cell organism, metal bypass mechanism, extracellular sequestration, enzymatic a less toxic form metal is unnecessary and decreasing the metallic sensitivity of cellular targets, which may be directed against one of the detoxifications processes a group of metals or chemically related metals. Besides, the detoxification process may vary depending on the variety of microorganism [17,18]. This transformation of pollutants is an incidental response is catalyzed by the enzymes present in the cell metabolic system [19,20]. In this work we are noticed that the heavy metals stress on bacteria,

\* Corresponding author.

E-mail address: [sandipanc787@gmail.com](mailto:sandipanc787@gmail.com) (S. Chatterjee).

isolated from contaminated site in Durgapur industrial zone and bioremediation assessment possibility of strain for better crop improvement (Fig. 1).

## 2. Materials and methods

### 2.1. Isolation and identification of bacteria

Soil sample were collected from the sedimented soil of the contaminated channel in Durgapur industrial area. The samples were then streaked on selective media with the help of calibrated loops and incubated at 37 °C for 24hrs to restore strong isolation. Morphological features to restored isolation, colony morphology (color, shape and surface) and cell morphology (shape, gram staining) is studied. Various biochemical tests were also performed to detect isolation.

### 2.2. Screening and determination of Minimum Inhibitory Concentration (MIC) of HMRB

Bacterial isolates were screened on heavy metal includes nutrient agar medium where bacterial isolates were grown. MIC of heavy metal resistant bacteria were gradually determined in the media where increase the concentration of heavy metals. Heavy metals used were  $\text{CoSO}_4 \cdot 7\text{H}_2\text{O}$ ,  $\text{NaMoO}_4 \cdot 2\text{H}_2\text{O}$ ,  $\text{Pb}(\text{NO}_3)_2$  and  $\text{Zn}^{2+}$  (Zinc metal powder) with starting concentration of 40  $\mu\text{g}/\text{ml}$ . The concentration of heavy metals were added to the nutrient agar plates each time until the strains on the plates failed to grow. The culture is growing the last concentration was transferred to

the higher concentration by streak on plate. MIC was noted when the isolates failed to grow on plates.

### 2.3. Antibiotic pattern of recovered isolates

All recovered isolates were identified for their resistant pattern by Kirby-Bauer disc diffusion and Double disc diffusion method. The most commonly used antibiotics are Ampicillin, Chloramphenicol, Amoxicillin, Cefalexin, Tetracycline and Methicillin. The recovered isolates were inoculated in Mueller Hinton Broth and Antibiotics the disc was placed flat on Mueller Hinton Agar (MHA) plate. Then incubation 24hrs at 37 °C, the resistance area was measured in mm and the results were explain using standard charts related to zone diameters to degree of microbial resistance.

### 2.4. Pot experiment

The pot was tested to determine the bioremediation of HMRB is likely to be isolated. Heavy metal contaminated soil collected from industrial area and coal-tar sites near paddy fields and are put in 2 different sets, each set containing 6 pots. The pots were coded as attached to the inoculums *Pseudomonas* sp. (Ps), *Staphylococcus* sp.(St), *Proteus* sp.(Pr), *Klebsiella* sp.(Kl) and all are compared with a control (c). The microorganisms showing the most noteworthy MIC were taken and vaccinated in supplement stock for the development of bio-compost. The stock was taken in rotator shaker hatchery 4-5 days at 37 °C. The seeds *Triticum aestivum* were splashed on petri plates containing sterile water for 24 hrs and appeared on every one of the 12 pots. In every day the bacterial

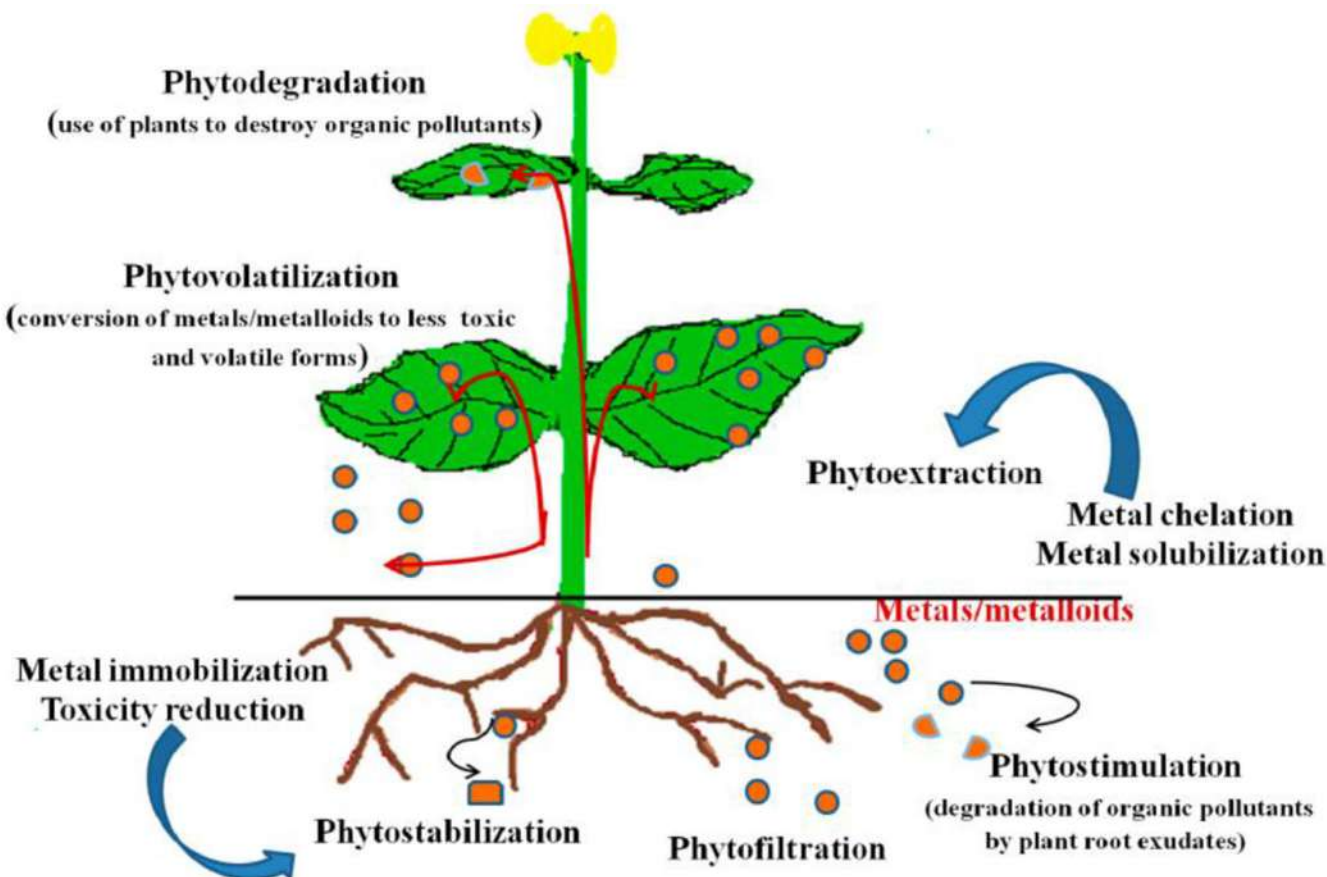


Fig. 1. Heavy Metal for Sustainable Crop Production.

**Table 1**

The pots are identified by the inoculums utilized, in each pots stock and refined water are added on a standard premise.

Pot labeling	Bacterial strains inoculated	Broth added (ml)	Distilled water added (ml)	Total volume (ml)
C	Control	–	100	100
Ps	<i>Pseudomonas</i> sp.	10	75	100
St	<i>Staphylococcus</i> sp.	10	75	100
Pr	<i>Proteus</i> sp.	10	75	100
KI	<i>Klebsiella</i> sp.	10	75	100

**Table 2**

Minimum Inhibitory Concentration (MIC) of potent isolates on respective heavy metals.

Bacterial isolates	Strain	Copper	Cobalt	Lead	Molybdenum
<i>Klebsiella</i> sp.	KI-1	55 µg/ml	NG	130 µg/ml	1300 µg/ml
<i>Proteus</i> sp.	Pr-2	NG	60 µg/ml	160 µg/ml	1300 µg/ml
<i>Pseudomonas</i> sp.	Ps-3	40 µg/ml	100 µg/ml	120 µg/ml	1600 µg/ml
<i>Bacillus</i> sp.	Bc-4	NG	NG	130 µg/ml	1250 µg/ml
<i>Staphylococcus</i> sp.	St-5	NG	90 µg/ml	130 µg/ml	1300 µg/ml

stock serving bio-composts and refined water were added each pot. The shoot height was estimated at 5 days intervals within 15<sup>th</sup> day.

### 3. Result and discussion

Microbial enrichment broths were taken as turbidity for primary indicators of microbial growth. There was an enriched culture streaked with the help of calibrated loop on nutrient agar and further on different selective media such as Mannitol salt agar, Starch agar, Phenylalanine agar, MacConkey agar and *Pseudomonas* isolation agar for isolation different bacteria from different soil samples. Total 62 separately isolates that were recovered from 10 soil samples (Table 1).

#### 3.1. Morphological and biochemical characterization of recovered isolates

62 types of bacteria were recovered from the soil samples and characterized by their colony features, Gram staining and biochemical testing and were identified as *Proteus* sp., *Klebsiella* sp., *Staphylococcus* sp., *Bacillus* sp. and *Pseudomonas* sp. The maximum spread was observed by *Pseudomonas* sp. (16%), *Staphylococcus* sp. (15%) and *Bacillus* sp. (29%) about 22% of the total isolation remains unidentified.

#### 3.2. MIC of the bacterial isolation against some selected heavy metal

All bacterial isolation was screened for heavy metals tolerance by growing them on media containing heavy metals. Out of which, 35 isolates showed heavy metal tolerance against Cu, Co, Pb and Mo with MIC ranging from 40 to 1600 µg/ml for different heavy metal resistant bacteria at contaminated sites. Heavy metal tolerance test indicated highest tolerance to Molybdenum by Ps-3 (1600 µg/ml), Copper by KI-1 and Ps-3 (40 and 55 µg/ml), Lead by Pr-2 (160 µg/ml) and Cobalt by Ps-3 (100 µg/ml). It was found that none of the *Proteus* sp. (Pr-2), *Bacillus* sp.(Bc-4) and *Staphylococcus* sp. (St-5) can tolerate the Copper stress at 40 µg/ml. In this

**Table 3**

Shoot height (in cm) of *Triticum aestivum* seedlings in substantial metal tainted modern (industrial) soil and inoculates with HMRB and control pot.

Bacterial strains	Shoot length (in cm) after 5 days	Shoot length (in cm) after 10 days	Shoot length (in cm) after 15 days
C	0	9	25
Ps	8	25	30
Pr	0	8	14
KI	0	2	15
St	3	18	27
All	5	23	31

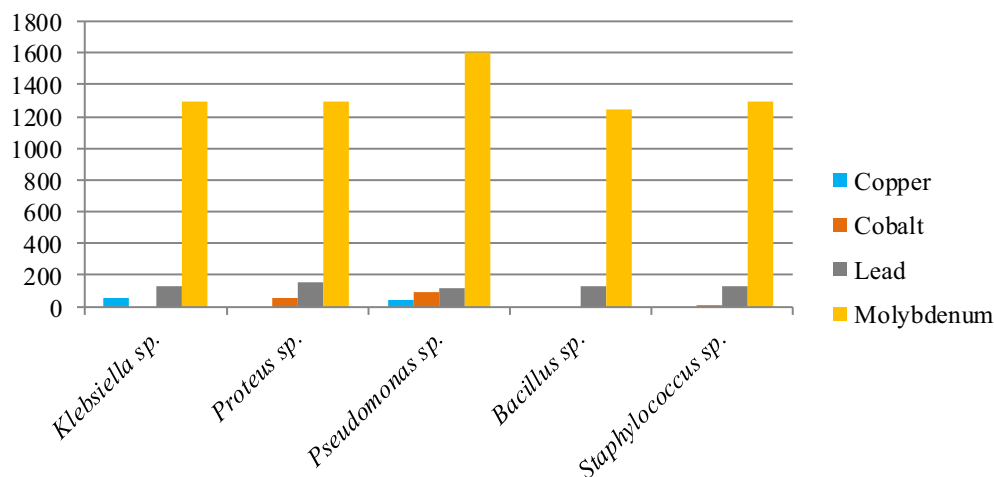


Fig. 2. Minimum Inhibitory Concentration (MIC) of potent isolates on respective heavy metals.

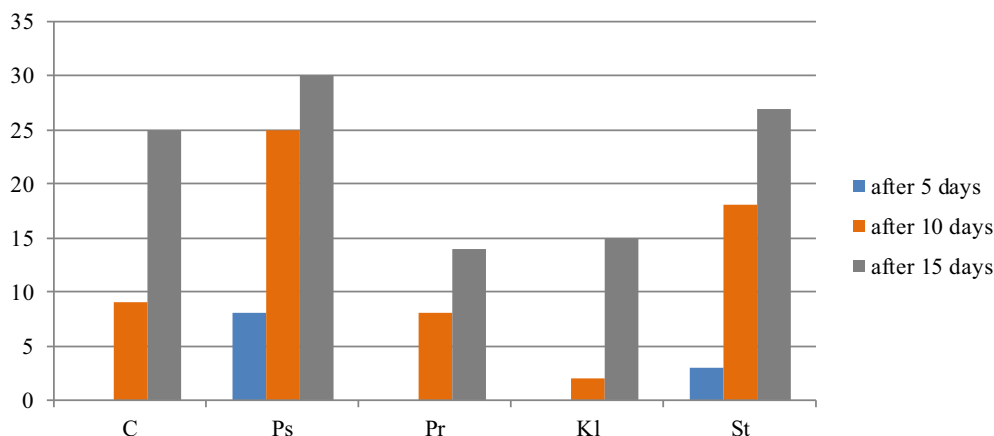


Fig. 3. Shoot height (in cm) of *Triticum aestivum* seedlings in substantial metal tainted modern (industrial) soil and inoculates with HMRB and control pot.

Table 4

Shoot height (in cm) of *Triticum aestivum* seedlings in substantial metal tainted coal-tar soil and inoculates with HMRB and control pot.

Bacterial strains	Shoot length (in cm) after 5 days	Shoot length (in cm) after 10 days	Shoot length (in cm) after 15 days
C	6	21	26
Ps	4	20	25
Pr	3	24	29
Kl	4	27	34
St	5	22	26
All	4	24	27

study we also fail to recover Cadmium resistant *Bacillus* sp. and *Klebsiella* sp. (Table 2 & Fig. 2).

### 3.3. Antibiotic tolerance and sensitivity

The vast majority of secludes in the current examination showed protection from different antibiotics against at least three heavy metals. 6 Strains of *Pseudomonas* sp. and 5 strains of *Staphylococcus* sp. showed one group of antibiotics had high resistance and many metal resistances. In this study we found a relationship between the resistance to high levels of heavy metals and antibiotics in the bacterial species. This reality was additionally settled by different scientists that exhibit high obstruction bacterial isolation to multiple metals towards a group of antibiotic resistance.

The present studied heavy metal and antibiotic resistance bacteria isolated are *Pseudomonas* sp., *Klebsiella* sp., *Proteus* sp. and *Staphylococcus* sp.

### 3.4. Impact of HMRB on the shoot development of *Triticum aestivum* inoculates in industrial soil

Impact of heavy metal resistant bacteria on *Triticum aestivum* shoots prolongation in modern (industrial) soil, which is gathered from paddy field close by paper industry. No development was seen in the initial two days, however after the third day shoots began to create in certain pots. On fifth day, development design was seen with the exception of the pots set apart as Kl, Pr and control. It has been seen that the pots set apart as Ps had an exceptional shoot development of 30 cm when contrasted and control pot with shoot height of 25 cm (Table 3 & Fig. 3).

### 3.5. Impact of HMRB on the shoot development of *Triticum aestivum* inoculates in coal-tar soil

The effectiveness of strong isolation was also tested on heavy metals contaminated coal-tar soil. Significantly shoot growth observed after the 3rd day inoculation all are compared with the control pot. Overall, control pots were added without any bacterial inoculums, showing a negligible difference inferring incompetence of HMRB as bio-fertilizers in coal-tar soil. On the 15th day, *Triticum aestivum* has been noticed among the highest growth on pots

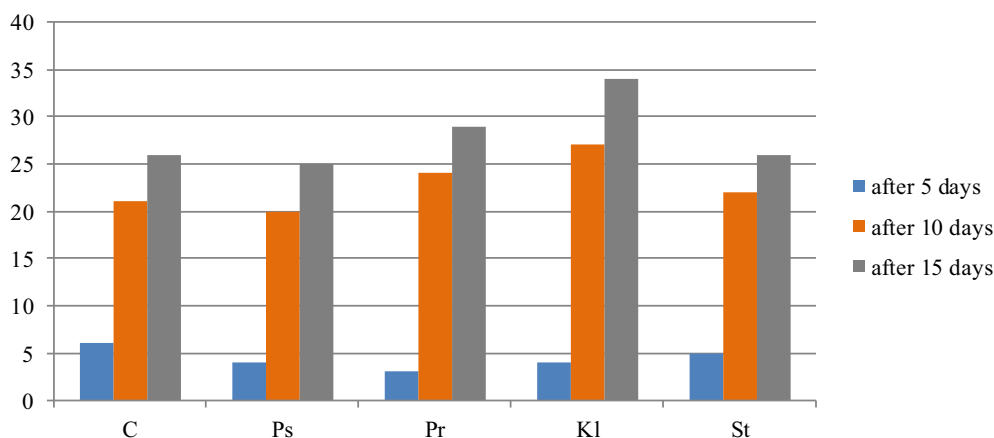


Fig. 4. Shoot height (in cm) of *Triticum aestivum* seedlings in substantial metal tainted coal-tar soil and inoculates with HMRB and control pot.

marked as Pr (29 cm) and Kl (34.0 cm) whereas the control pot grows up to 26 cm (Table 4 & Fig. 4).

Although several investigations have been exhibited the significance of bacterial immunization for plant development and weighty metal accumulate in contaminated conditions. This is proof by the current examination that the HMRB application is particularly adjusted as high concentration of substantial metals will build the capacity to remediate weighty metal defined soils.

#### 4. Conclusion

Bioremediation is a novel eco-friendly technology use to immobilize heavy metal. There are certain heavy metal resistances bacteria present in soil that helps to degrades heavy metal and promote agriculture production by enhancing soil quality. Collected heavy metal resistance bacteria were *Staphylococcus* sp., *Bacillus* sp. and *Klebsiella* sp. It has been observed that those bacteria can degrade and reduced heavy metal like Cr, Co, Zn and also antibiotic resistance. *Triticum aestivum* commonly called wheat plant can be easily cultivated in agricultural field after processed with heavy metal resistance bacteria. Production of wheat highly increases and root length, shoot length improved after applying these bacteria from outside to field. The use of heavy metal resistance bacteria in agricultural field nearby to industry is highly recommended.

#### CRedit authorship contribution statement

**Tanmay Ghosh:** Investigation, Writing - original draft. **Anirban Paul:** Conceptualization, Writing - review & editing, Supervision. **Sandipan Chatterjee:** Conceptualization, Writing - review & editing, Supervision.

#### Declaration of Competing Interest

The authors declare that they have no known competing financial interests or personal relationships that could have appeared to influence the work reported in this paper.

#### References

- [1] R.A.I. AbouShanab, J.S. Angle, T.A. Delorme, R.I. Chaney, P. Van Berkum, H. Moawad, K. Ghanem, H.A. Ghazlan, Rhizobacterial effects on nickel extraction From soil and uptake by *Alyssum murale*, *New Phytologist* 158 (2003) 219–224.
- [2] A.W. Bauer, W.M.M. Kirby, J.C. Sherris, M. Turck, Antibiotic susceptibility testing by a standardized single Disc method, *American Journal of Clinical Pathology* 45 (4) (1966) 493–496.
- [3] Brown, L.M., 1996. Removal of Heavy Metals from Water With Microalgal Resins 1: Process Development. Water Treatment Technology Program Report No. 74. US Department of the Interior Bureau of Reclamation.
- [4] M.R. Bruins, S. Kapil, F.W. Oehme, Microbial Resistance to metals in the environment, *Ecotoxicology And Environmental Safety* 45 (2000) 198–207.
- [5] J.J. Calomiris, J.L. Armstrong, R.J. Seidler, Association Of metal tolerance with multiple antibiotic resistance Of bacteria isolated from drinking water, *Applied and Environmental Microbiology* 47 (6) (1984) 238–242.
- [6] J.G. Cappuccino, N. Sherman, *Microbiology: A Laboratory Manual*, 7th Ed., Pearson Benjamin Cummings, San Francisco, 2005.
- [7] S.Z. Abbas, M. Rafatullah, N. Ismail, J. Lalung, Isolation, identification, characterization, and evaluation of cadmium removal capacity of Enterobacter species, *JBasicMicrob.* 54 (12) (2014) 1279–1287.
- [8] D. Alexander, D. Zuberer, Use of chrome azurol S reagents to evaluate siderophoreProduction by rhizosphere bacteria, *Biol. Fert. Soils* 12 (1) (1991) 39–45.
- [9] G. Baycu, D. Tolunay, H. Özden, S. Günebakan, Ecophysiological and seasonalVariations in Cd, Pb, Zn, and Ni concentrations in the leaves of urban deciduous treesIn Istanbul, *Environ Pollut.* 143 (3) (2006) 545–554.
- [10] Belimov, A., Hontzeas, N., Safronova, V., Demchinskaya, S., Piluzza, G., Bullitta, S., Glick,B., 2005. Cadmium-tolerant plant growth-promoting bacteria associated with theRoots of Indian mustard (*Brassica juncea* L. Czern.). *Soil Biol. Biochem.* 37 (2),241–250.
- [11] S.H. Abbas, I.M. Ismail, T.M. Mostafa, H. Abbas, A.H. Sulaymon, Biosorption of heavy metals: a review, *J ChemSciTechnol*3(4):74–102. (2014).
- [12] S.Z. Abbas, M. Rafatullah, N. Ismail, J. Lalung, Isolation, Identification, and characterization of cadmium resistant *Pseudomonas* sp. M3 from industrial wastewater, *J Waste Manag* 54 (12) (2014) 1279–1287.
- [13] H.K. Abicht, Y. Gonskikh, S.D. Gerber, M. Solioz, Non-enzymicCopper reduction by menaquinone enhances copper toxicity in*Lactococcuslactis* IL1403, *Microbiology* 159 (6) (2013) 1190–1197.
- [14] H. Abyar, A. Safahieh, H. Zolgharnein, I. Zamani, Isolation andIdentification of Achromobacterdenitrificans and evaluation ofIts capacity in cadmium removal, *Pol J Environ Study* 21 (6) (2012) 1523–1527.
- [15] S. AdebisiMusbaudeen, O. Adebowale Toba, O.II. AdeniyiAdewaleO, Bioaccumulation of heavy metals usingSelected heavy metal tolerant organisms isolated from dumpsiteLeachate, *Nat Sci* 12 (10) (2014) 101–106.
- [16] M. Ahemad, Implications of bacterial resistance against heavyMetals in bioremediation: a review, *IIOAB J* 3 (3) (2012) 39–46.
- [17] M. Ahemad, A. Malik, Bioaccumulation of heavy metals by zincResistant bacteria isolated from agricultural soils irrigated withWastewater, *Bacteriol J* 2 (1) (2012) 12–21.
- [18] I. Ahmad, S. Hayat, A. Ahmad, I.A. Samiullah, Effect of heavyMetal on survival of certain groups of indigenous soil microbialPopulation, *J ApplSci Environ Manag* 9 (1) (2005) 115–121.
- [19] J.G. Holt, R.N. Krieg, A.H.P. Sneath, T.J. Staley, T.S. Williams, *Bergey's Manual of Determinative Bacteriology*, 9th Edition., (International Edition), 1994.
- [20] R. Idris, R. Trifonova, M. Puschenreiter, W.W. Wenzel, A. Sessitsch, Bacterial communities associated With flowering plants of the Ni hyperaccumulator*ThaspiGoesingense*, *Applied and Environmental Microbiology* 70 (2004) 2667–2677.



# Source details

[Feedback >](#) [Compare sources >](#)

## Materials Today: Proceedings

Scopus coverage years: 2005, from 2014 to 2023

E-ISSN: 2214-7853

Subject area: [Materials Science: General Materials Science](#)

Source type: Conference Proceeding

[View all documents >](#)

[Set document alert](#)

[Save to source list](#)

CiteScore 2022

3.2



SJR 2022

0.445



SNIP 2022

0.774



CiteScore

[CiteScore rank & trend](#)

[Scopus content coverage](#)



### **3. A Study on the Antibacterial Activities and Medical Properties of Water Chestnut**

**Tanmay Ghosh**

*Department of Microbiology, Dinabandhu Andrews College, Baishnabghata,  
South 24 Parganas, Kolkata, West Bengal, India.*

**Joydip Ghosh**

*Department of Microbiology, Rabindra Mahavidyalaya, Champadanga,  
West Bengal, India.*

#### **ABSTRACT**

*Fruits and vegetables are generally known as very good and abundant sources of several vitamins and minerals, not only that but also they are very effective in increasing immunity power against several microbial infections.*

*In the matter of discussion of preventing bacterial infections the underwater vegetables are not staying back. One of the very effective and used under water vegetable is Water Chestnut. Water chestnut is not a nut at all, but it is a very useful aquatic vegetable that grows under Water in the mud. Eleocharis dulcis, belongs to family Cyperaceae, commonly called Chinese water chestnut. It was stem-like, its green leaves grow to about 1.5m.*

*The small, round forms have crisp. White stuff may be eaten fresh, boiled grilled and also used as pickled. Water Chestnuts are popular dishes in china. It also used for making many cake or delicious food. It is grown in many countries like Asia (china, India & Japan etc.), Africa, Australia, and Island. Water chestnut used in agricultural department. It also plays important role in medical Field to development medical science.*

*Its peels extracts, seed used for product many type of medicine. It showed a high-level antibacterial activity against some bacteria like Bacillus subtilis, Escherichia coli, Salmonella typhi etc. In medicinal field this plant use to cured many type of diseases like inflammation, urinary, discharges, fractures, leprosy, astringents, bad teeth and malaria.*

#### **KEYWORDS**

*Water Chestnut, Microbiology, Pharmaceutical Sciences, Biology.*

## **Introduction:**

Water chestnut is not a nut at all, but it is a very useful aquatic vegetable that grows under Water in the mud. *Eleocharis dulcis*, belongs to family Cyperaceae, commonly called Chinese water chestnut. It was stem-like, it's green leaves grow to about 1.5m.

The small, round forms have crisp. White stuff may be eaten fresh, boiled grilled and also used as pickled. Water Chestnuts are popular dishes in china. It also used for making many cake or delicious food. It is grown in many countries like Asia (china, India & Japan etc.), Africa, Australia, and Island. Water chestnut used in agricultural department. It also plays important role in medical Field to development medical science. Its peels extracts, seed used for product many type of medicine It showed a high-level antibacterial activity against some bacteria like *Bacillus subtilis*, *Escherichia coli*, *Salmonella typhi* etc.

In medicinal field this plant use to cured many type of diseases like inflammation, urinary, discharges, fractures, leprosy, astringents, bad teeth and malaria.



**Fig.1: Water Chestnut**

## **Taxonomy classification of Water Chestnut**

- Kingdom: Plantae
- Clade: Tracheophytes
- Clade: Angiosperms
- Clade: Monocots
- Clade: Commelinids
- Order: Poales
- Family: Cyperaceae
- Genus: *Eleocharis*
- Species: *E. dulcis*



## **Materials and Methods**

### **Collection of Plant**

The plant water chestnut was taken for study on its antimicrobial activity and antibacterial significance of water chestnut collected from Champadanga, Hooghly, and West Bengal.

### **Preparation of Plant Extract**

At first we washed the plant peels with distilled water and kept them for dry under shade, and grind them with the help of mixer grinder to a dust powder. And keep it in an air tight container at the room temperature in dark until used.

The powdered samples are extracted by the following methods.

- **Ether Extraction** To prepare the Ether extraction first, 5mg of dried of water chestnuts peel extract powder mixed with 25ml ether to each solution was stored at 4°C after collecting in sterile test tubes until use.
- **Hexane Extraction** About 5 gm of dried Water Chestnut peel extract powder taken, then dispersed in 25 ml of benzene solution and shaken in a rotary shaker for 10 minutes. Then closed with paper and tightened with a band few holes were made in the paper to facilitate air circulation and room temperature maintenance for 5 dates.
- **Benzene Extraction** About 5 gm of dried Water Chestnut peel extract powder taken, then dispersed in 25 ml of benzene solution and shaken in a rotary shaker for 10 minutes. Then closed with paper and tightened with a band. Few holes were made in the paper to facilitate air circulation and room temperature maintenance for 5 dates.
- **Chloroform Extraction** For making Chloroform extraction 5mg of dried of water chestnut peel extract powder mixed with 25ml Chloroform. Each solution was stored at 4°C after collecting in sterile test tubes until use.
- **Ethanol Extraction** First, 5mg of dried of water chestnut peel extract powder mixed with 25ml Ethyl Acetate. Each solution was stored at 4°C after collecting in sterile test tubes until use.
- **Ethanol Extraction** For preparing the Ethanol extraction, 5mg of dried of water chestnut peel extract powder mixed with 25ml ethanol. Each solution was stored at 4°C after collecting in sterile test tubes until use.
- **Medium** In this we use Mueller Hinton agar (MHA) is used as base medium for the screening of antibacterial activity and Mueller Hinton broth (MHB) is used for the preparation of inoculums.

### **Preparation of Extract Concentration**

Four concentrations were made 25, 50, 100, 200mg/ml from each of the four extract Ethanol, Benzene extract, Chloroform, Ethyl acetate and Ether. In every case 1gm of extract was mixed with 5ml DMSO to prepare 200mg/ml stock concentration. Other concentrations were made by adding extra DMSO with stock in other test tube.

## **Determination of Antibacterial Activity**

### **Bacterial Stains**

We take bacteria such as *Bacillus subtilis*, *Escherichia coli* and *Salmonella typhi* bacteria were selected for antibacterial activity test. The cultures of bacteria were maintained in their appropriate agar slants at 4°C throughout the study and used as stock cultures.

### **Preparation of Bacterial Inoculum**

Bacterial inoculums were prepared by 0.1 ml of cultures was transferred to the agar plates and incubated at 37°C for 4-5 hours.

### **Agar Diffusion Methods**

Agar well diffusion method is widely used to evaluate the antimicrobial activity of plant. This phenomenon forms the basis of the agar diffusion assay that is used to determine the susceptibility or resistance of a bacterial strain to an antibacterial agent. Disc diffusion method was carried on Mueller Hinton agar plates.

Petri plates were prepared by 20ml of Mueller Hinton agar and allowed to solidify for the use in susceptibility test against bacteria. Plates were dried and 0.1ml of inoculums was poured and spread and allow to dry. After the cork borer agar well made on agar plate and poured different concentration of extract into the well. The Penicillin is used as positive control and DMSO was used as negative or blind control. The plates were incubated at 37°C for 1 day.

The zone of inhibition were observed and measured. The agar plates were incubated at 4°C for 1 hour and were then incubated also at 37°C. After 24 to 48 hours of incubation, the antibacterial activity was evaluated by measuring the width of zone of inhibition of growth against the indicator organisms in comparison to a control of reference standards. The tests were study in triplicate.

### **Phytochemical Analysis**

Phytochemical analysis of all the evaporated solvent ex-tracts was conducted following the procedure of Indian Pharmacopoeia (1985).

- **Test For Alkaloids** For testing of alkaloids first we take 200 mg plant material in 10 ml methanol, (filtered) and a 2ml filtrate + 1% HCl + steam mixed and then 1 ml filtrate + 6 drops of Mayer's reagents or Wagner's reagent added then the creamish precipitate/brownish-red precipitate/orange precipitate found that indicated the presence of respective alkaloids.
- **Test For Tannins** For testing of tannins 200 mg plant material in 10 ml distilled water added (filtered), a 2 ml filtrate + 2 ml FeCl<sub>3</sub> mixed then blue-black precipitate that indicated found the presence of tannins.

- **Test For Flavonoids** For testing of flavonoids 200 mg plant material in 10 ml ethanol (filtered), a 2 ml filtrate + conc. HCl + magnesium mixed and then ribbon pink-tomato red color indicated the presence of flavonoids.
- **Test For Steroids** For testing of steroids we follow the Liebermann - Burchard reaction and there we take 200 mg plant material in 10 ml chloroform, (filtered), a 2 ml filtrate + 2 ml acetic anhydride + conc. H<sub>2</sub>SO<sub>4</sub> was added then the founded Blue-green ring indicated the presence of steroids.
- **Test For Phenols** For testing of phenols first 1ml of each solvent extracts dissolved in alcohol or water was separately treated with a few ml of neutral ferric chloride solution. The change in color indicated the presence of phenols.

**Table 1: Phytochemical Analysis**

No	Phytochemical	Method	Result
1	Tannin	Ferric chloride test	-
2	Flavonoid	Alkaline Reagent test	+
3	Phenol	Ferric chloride test	-
4	Carbohydrate	Molisch's test	+
5	Protein	Biuret test	+
6	Sapronin	Foam test	-
7	Starch	Iodine Test	+++

## Result

Antibacterial activity of water chestnut peel extract against bacterial culture of Escherichia coli, Bacillus subtilis, salmonella typhi etc. It help in to examine inhibition zone. Antibacterial activity of water chestnuts peels extract against many type potential of many extract. The extract of water chestnut showed antibacterial efficiency against many organisms like Bacillus subtilis, Escherichia coli, and Salmonella typhi. Pore efficiency was found against the Staphylococcus aureus.

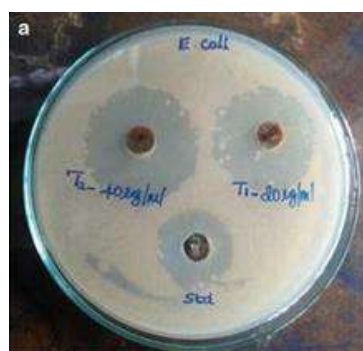


**Fig.2: Escherichia coli.**

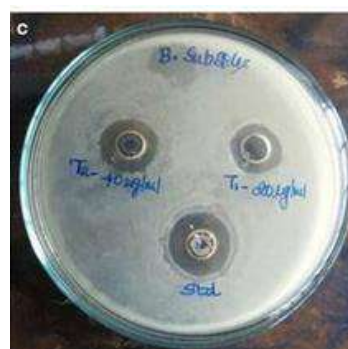


**Fig.3: Bacillus subtilis**

**Table-2: The antimicrobial activity of Chloroform extract against different bacteria**

Concentration (mg/ml)	Zone of inhibition (mm)			
	<i>Staphylococcus aureus</i>	<i>Escherichia coli</i>	<i>Bacillus subtilis</i>	<i>Salmonella typhi</i>
200 mg/ml	29.0±2	25.2±1	26.3±1	31.5±2
100 mg/ml	24.7±2	24.2±2	26.7±2	26.1±1
50 mg/ml	22.7±1	20.5±1	21.9±1	21.9±2
25 mg/ml	18.2±2	18.7±2	17.5±2	18.6±1

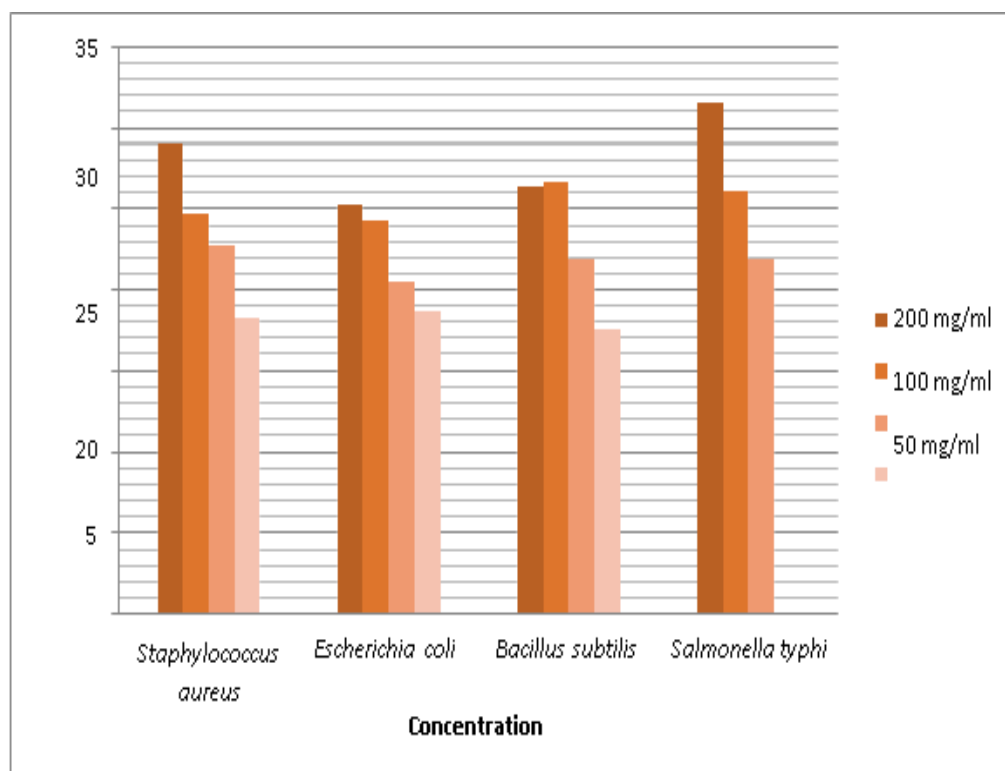


**Fig 4: The antimicrobial activity of chloroform extracts against different bacteria**

**Table-3: The antimicrobial activity of Ethanol extract against different bacteria**

Concentration (mg/ml)	Zone of inhibition (mm)			
	<i>Staphylococcus aureus</i>	<i>Escherichia coli</i>	<i>Bacillus subtilis</i>	<i>Salmonella typhi</i>
200 mg/ml	22.1±2	26.1±1	26.3±1	30.5±2
100 mg/ml	24.6±2	24.2±2	25.7±2	26.1±1
50mg g/ml	18.9±1	21.1±1	23.4±2	30.1±2
25m g/ml	17.2±2	22.9±2	17.5±2	19.1±1

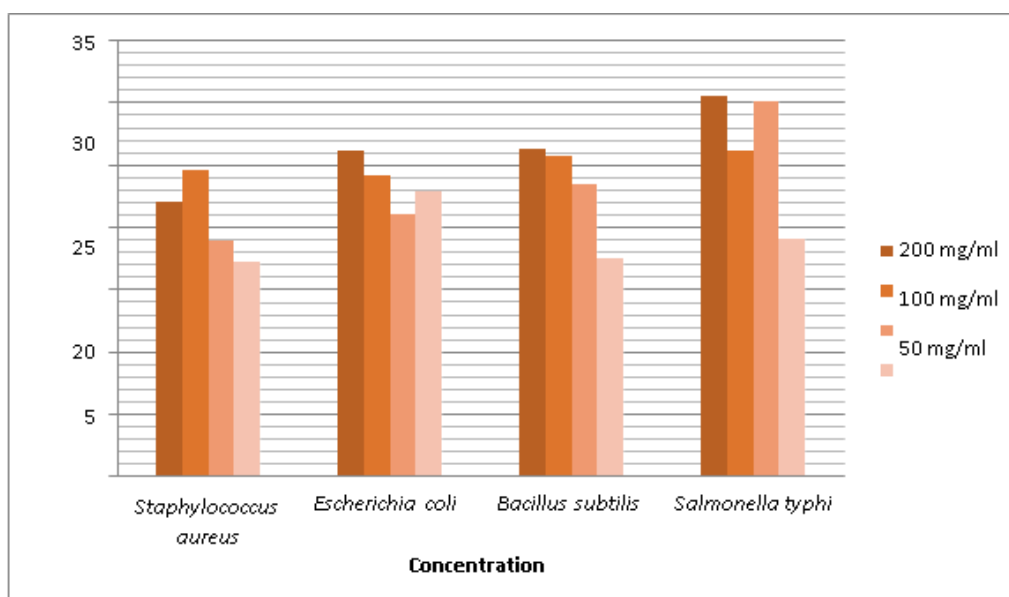


**Fig 5: The antimicrobial activity of Ethanol extract against different bacteria**

**Table-4: The antimicrobial activity of Ethanol extract against different bacteria**

Concentration (mg/ml)	Zone of inhibition (mm)			
	<i>Staphylococcus aureus</i>	<i>Escherichia coli</i>	<i>Bacillus subtilis</i>	<i>Salmonella typhi</i>
200mg/ml	22.1±2	26.1±1	26.3±1	30.5±2
100mg/ml	24.6±2	24.2±2	25.7±2	26.1±1
50mg/ml	18.9±1	21.1±1	23.4±2	30.1±2
25mg/ml	17.2±2	22.9±2	17.5±2	19.1±1

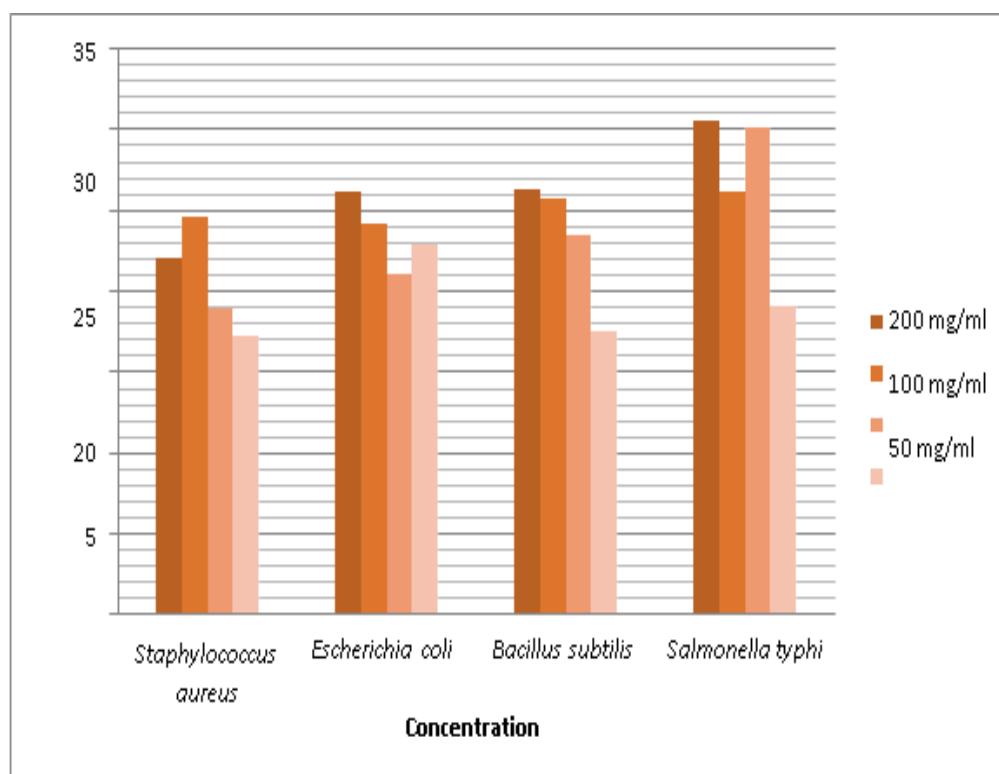


**Fig 6: The antimicrobial activity of Ethanol extract against different bacteria.**

**Table-5: The antimicrobial activity of Benzene extract against different bacteria**

Concentration (mg/ml)	Zone of inhibition (mm)			
	<i>Staphylococcus aureus</i>	<i>Escherichia coli</i>	<i>Bacillus subtilis</i>	<i>Salmonella typhi</i>
200mg/ml	26.9±2	27.4±1	25.8±1	28.5±2
100mg/ml	19.4±2	23.4±2	26.1±2	30.1±1
50mg/ml	22.4±1	22.9±1	24.3±2	31.2±2
25mg/ml	17.5±2	18.1±2	15.9±2	18.3±1

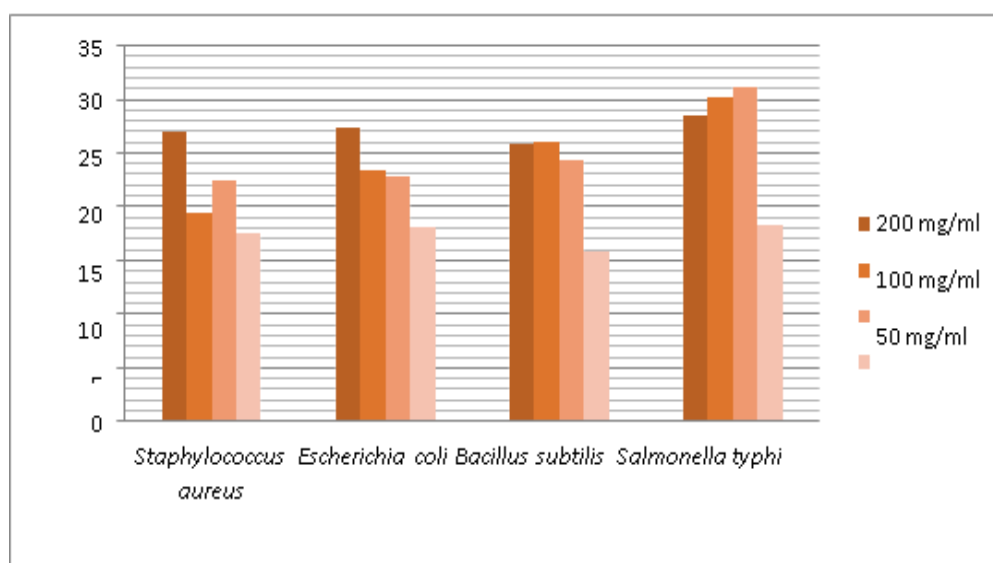


**Fig 7: The antimicrobial activity of Benzene extract against different bacteria**

## Discussion

The methanol extract of water chestnut fruit was found as very important antibacterial activity that inhibits both Gram positive and Gram negative bacteria. It helps to increase of antibacterial resistance of various microorganisms.

From result it seemed that water chestnut showed low antibacterial activity on staphylococcus aureus then other bacteria. Water chestnut showed high efficiency against *Bacillus subtilis*, *salmonella typhi* and *Escherichia coli*. Water chestnut play very important role in medical field to produce various type of medicines. It's effective process help to control infection of many diseases.

## Conclusion

In this paper we observed that phytochemical property of fruit to analyze their quality for their use. Hexane, Benzene, Chloroform, Ethanol extract physicochemical test showed positive result. It can be conclude that water chestnut showed antibacterial activity against many bacteria.

It helps to control infection of many diseases. This plant contains medicinally important compound that use in medical field for the treatment of various diseases. This plant helps in development medical field.

## References

1. Anonymous. The Wealth of India, A Dictionary of Indian Raw Materials and Industrial Products, Volume X. Council of Scientific Industrial Research, New Delhi, India, 1Hepatoprotective976, 274-277.
2. Kumar D, Rashid M, Singh AP. Evaluation of invitro anti-inflammatory, antimicrobial and antioxidant effects of *Trapa natans* (Linn.) leaves extract. *World Journal of Pharmacy and Pharmaceutical Sciences*. 2014; 3(2):1697-1710.
3. Dhiman AK. Sacred Plants and their Medicinal Uses. Daya Publishing House, New Delhi, 2003, 193.
4. Vhotracharcho C, Chironjib Banaushadhi. 4th edition, Calcutta India, Ananda Publishers Pvt. Ltd, 1987, 96-100.
5. Kang W, Li Y, Gu X, Huang X. activity of *Trapa acornis* shell extracts against CCl4-induced liver injury in rats. *Academic Journal of Pharmacy and Pharmacology*. 2012; 6(41):2856-2861.
6. Razvy MA, Faruk MO, Hoque MA. Environment friendly antibacterial activity of water chestnut fruits. *Journal of Biodiversity and Environmental Sciences*. (JBES). 2011; 1(1):26-34.
7. Stoicescu I, Sirbu R, Pirjol TN, Cocia M, Balaban DP, Camelia B. Invitro antioxidant and antibacterial activity of *Trapa natans* aquatic plant from Danube delta area. *Journal Academia Romana Rev Roum Chim*. 2012; 57(7-8):729-733.
8. Shukla AD, Gujrati A, Srivavasta N. In vitro analysis of anti-bacterial activity of *Trapa natans* Peel (Household paste). *International Journal of Pharmaceutical Research and Development (IJPRD)*. 2012; 3(1).
9. Mandal SM, Migliolo L, Franco OL, Ghosh AK. Identification of an antifungal peptide from *Trapa natans*fruits with inhibitory effects on *Candida tropicalis* biofilm formation. *Journal Elsevier Inc. Peptides*. 2011; 32(8):1741-1747.
10. Das PK, Bhattacharya S, Bhattacharya JN and Biswas M. Antidiabetic activity of *Trapa natans* fruit peel extract against streptozotocin induced diabetic rats. *Global Journal of Pharmacology*. 2011; 5(3):186-190.
11. Almeida, I. F., Valentao, P., Andrade, P. B., Seabra, R. M., Pereira, T. M., Amaral, M. H., Costa, P. C., and Bahia, M. F. 2008. In vivo skin irritation potential of a *Castanea sativa* (chestnut) leaf extract, a putative natural anti-oxidant for topical application. *Basic Clin. Pharmacol*. 103:461-467.
12. Anagnostakis, S. L. 1987. Chestnut blight—the classical problem of an introduced pathogen. *Mycologia* 79:23-37.



13. Basile, A., Sorbo, S., Giordano, S., Ricciardi, L., Ferrara, S., Montesano, D., Cobianchi, R. C., Vuotto, M. L., and Ferrara, L. 2000. Antibacterial and allelopathic activity of extract from *Castanea sativa* leaves. *Fitoterapia* 71:S110-S116.
14. Bounous, G. 2002. Inventory of Chestnut Research, Germplasm and References. FAO, Rome.
15. Bounous, G. The chestnut: a multipurpose resource for the new millennium. *Acta Hortic.* 693:33-40.

See discussions, stats, and author profiles for this publication at: <https://www.researchgate.net/publication/370583600>

# EVALUATION OF THE EFFECT OF DEADLY MUCORMYCOSIS IN POST COVID-19 PATIENTS

Article in *Türk Fizyoterapi ve Rehabilitasyon Dergisi/Turkish Journal of Physiotherapy and Rehabilitation* · May 2021

CITATION

1

READS

10

2 authors:



**Tanmay Ghosh**

Dinabandhu Andrews College university of calcutta

78 PUBLICATIONS 214 CITATIONS

SEE PROFILE



**Sandipan Chatterjee**

SURI VIDYASAGAR COLLEGE

21 PUBLICATIONS 372 CITATIONS

SEE PROFILE

# EVALUATION OF THE EFFECT OF DEADLY MUCORMYCOSIS IN POST COVID-19 PATIENTS

**Tanmay Ghosh<sup>1</sup>, Sandipan Chatterjee<sup>2</sup>**

<sup>1</sup>*Assistant Professor, Department of Microbiology, Dinabandhu Andrews College, Baishnabghata, South 24 Parganas, Kolkata – 700084, West Bengal, India.*

<sup>2</sup>*Assistant Professor, Department of Botany, SuriVidyasagar College, Suri, Birbhum - 731 101, West Bengal, India*

<sup>1</sup>*tanmay.tanmay.ghosh780@gmail.com, <sup>2</sup>chatterjeesandipan@rediffmail.com]*

## ABSTRACT

People of the entire world are fighting against the life-threatening disease COVID-19 during more than one year. In this microbiological war a large number of people have already lost their life, some fighter have won the war and many people have dedicated their life to take the human being to the door of victory in this war. In such a time of disaster another life-threatening disease appears recently, known as Mucormycosis. Mucormycosis, also known as “Black fungus” disease is playing the role of helping hand of COVID-19 to make it winner in this war because it is infecting the recovered or recovering COVID-19 patients. It mainly affects the people with suffering from some severe diseases as AIDS, cancer and mainly diabetes. Mucormycosis is a rare disease but the trending pandemic COVID-19 continues to welcome it to be the successor of next pandemic. It may fetal if it is untreated for long time and it also causes paralysis, seizure like disease. This disease is caused by inhalation of black fungal spore from air or it may occur in the wound skin. The aim of the discussion is to establish the interconnection between COVID-19 and Mucormycosis and giving awareness about the infection.

**Key-words:** Mucormycosis, Microbiology, Pathology, Pharmaceutical, Biology.

## I. INTRODUCTION

Coronavirus disease 2019 (COVID-19) pandemic was first flowed out in Wuhan, china in December 2019 and since then the frequency of bacterial growth and fungal coinfections has been continuously ascending. Flourishing record suggests that patients infected with severe acute respiratory syndrome coronavirus-2 (SARS Cov-2) may develop also in bacterial and fungal secondary infections. In this time, the chance of causing Invasive Pulmonary Aspergillosis (IPA) is high for post COVID-19 causes. It is caused by disclosure to *Mucormould* which is generally found in soil, plants, manure and decaying fruits and vegetables. It is also found in the nose, mucus of a healthy and normal people. Affects the sinuses, brain and lungs, life threatening in diabetes and cancer patients or people with HIV/ AIDS. Effects to the COVID-19 patients recovering after three weeks. Rhino- orbito- cerebral mucormycosis is considered as the most common manifestation. Here, we described with a patient with his uncontrolled diabetes who treated for COVID-19 but he was read mitted after three-week discharge with a diagnosis of rhinocerebralmucormycosis. COVID-19 patient has high risk of development of mucormycosis as because intake of widespread glucocorticoid to cure COVID-19. This glucocorticoid can lead to cause secondary fungal infection which is mucormycosis. This fungi mainly found in sinuses.



Fig-1: Microscopic view of Mucormycosis fungi

**Mucorales: causative agent of Mucormycosis:**

Mucorales are the largest group of zygomycete fungi. These fungi also known as pin molds or Black Fungi. Black fungi called because of its pigmentation. Mucorales are the order of fungi which are responsible for the disease mucormycosis.

**Scientific classification:**

Kingdom: Fungi

Sub kingdom: Eumycota

Division: Zygomycota

Sub division: Mucomycotina

Order: Mucorales

Family: Mucoraceae

Species: *Mucor* sp.

**II. MORPHOLOGY AND LIFE CYCLE OF MUCORALES**

Mucorales are the group of saprophytic aerobic fungi characterized by huge and rapidly growing mycelia. These are form in large quantity in anamorphic structure. The anamorphic sporangiospore are usually produced multiple spore, which are abundantly found in air. The spores are released, when it matured by disintegration of sporangium wall. The mature sporangiospore germinate to form haploid hyphae of a new mycelium. In case of heterothallic species of mucorales they reproduce by sexual mode of reproduction by formation of zygote. Haploid zygotes fuse to form diploid zygospore and then after meiosis within zygospore, new mycelium or sporangium are formed.



Fig-2: Mucorales

### III. SYMPTOMS

Warning signs include pain and redness around the eyes or nose, with fever, headache, coughing, shortness of breath, bloody vomits and altered mental status. According to the advisory, infection with mucormycosis should be suspected when there are:

- ❖ Sinusitis, nasal blockade or congestion, nasal discharge (blackish/bloody).
- ❖ Local pain in the cheek bone, one sided facial pain, numbness or swelling.
- ❖ Blackish discoloration over bridge of nose/palate.
- ❖ Loosening of teeth, jaw involvement.
- ❖ Blurred or double vision with pain.
- ❖ Thrombosis, necrosis, skin lesion.
- ❖ Chest pain, pleural effusion, worsening of respiratory symptoms.

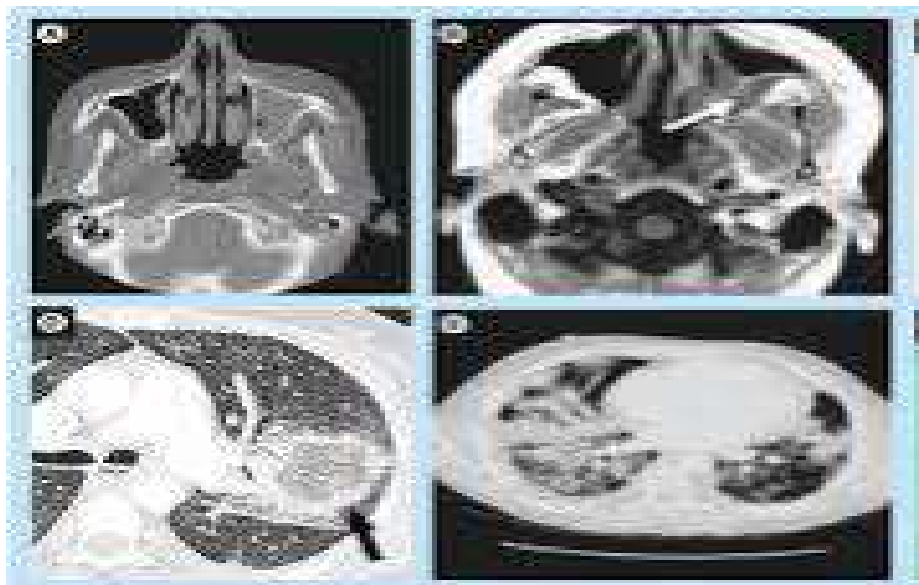


Fig 3: Sinus infection by mucormycosis

#### IV. CAUSE

Mucormycosis is caused by a group of moulds or saprophyte fungi, named mucormycota that normally grows in soil and decaying organic material such as rotten leaves, wood, fruits etc. It can be also found in mucus and nose of healthy people. To reduce the rate of mortality in the COVID-19 patients and to modulate their immune related lung injury, corticosteroids are using randomly to fulfill the need of respiratory supports and supplementary oxygen. This random use to mucormycosis that increase the rate of mortality. Its random use to the COVID-19 patients can increase the rate of mortality due to mucormycosis.

#### V. RELATION WITH COVID-19

There are no genetic relationship between coronavirus and mucormycosis but they are interconnected immunologically. When a patient become too much infected by COVID-19 and got hospitalized, his immunity power trying heart and soul to fight against coronavirus and in this case this patient is provided a huge amount of corticosteroid that act as a strong support of immune system in this war by reducing inflammation in lungs and repairing some damages that can happen for overdriving of immune system of body. But on the other hand, steroids reduce immunity power and increase blood sugar levels in both diabetic and non-diabetic patients. Patients suffering for COVID-19 disease are continuously use glucocorticoid. These types of steroid supported our own immune system, suppressed the activity of White Blood Cell (WBC). As WBC become inactive several fungal which are found in air, soil like mucor attack to the patient. Patient who is admitted in hospital for long time has high chance to cause this disease because of it low immune response. Generally, this black fungus naturally occurs in our environment. It may invade in our body lodge in the nasal passage and silently stay in our body, a symptomatically. When a patients fell sick, increase blood sugar levels, patients who unable to form neutrophils may victim to mucormycetes. Diabetic is very effective in lowering the immunity power. So in this situation if mucormycetes can able to enter into the body they can easily cause severe infection without any prevention and the patient have to accept death.

#### VI. TRANSMISSION

The causative agent of mucormycosis, Mucorales is a member of spore forming fungal group that have saclike fruiting structure (sporangia) and produced yellow or brown spores that is 3-11 micrometers in diameter and they are easily aerosolized. So they can enter into host by air flow. Staying in contact with rotten materials and dirty environment are the suitable way for their transmission. Mucormycosis also can be transmitted from the contaminated bandages, tongue depressors and other medical solutions or devices.

- ❖ It can spread by inhalation of fungal spore and it gets lodged into sinus and lungs.
- ❖ Low oxygen concentrations in blood help the fungi to replicate fast.

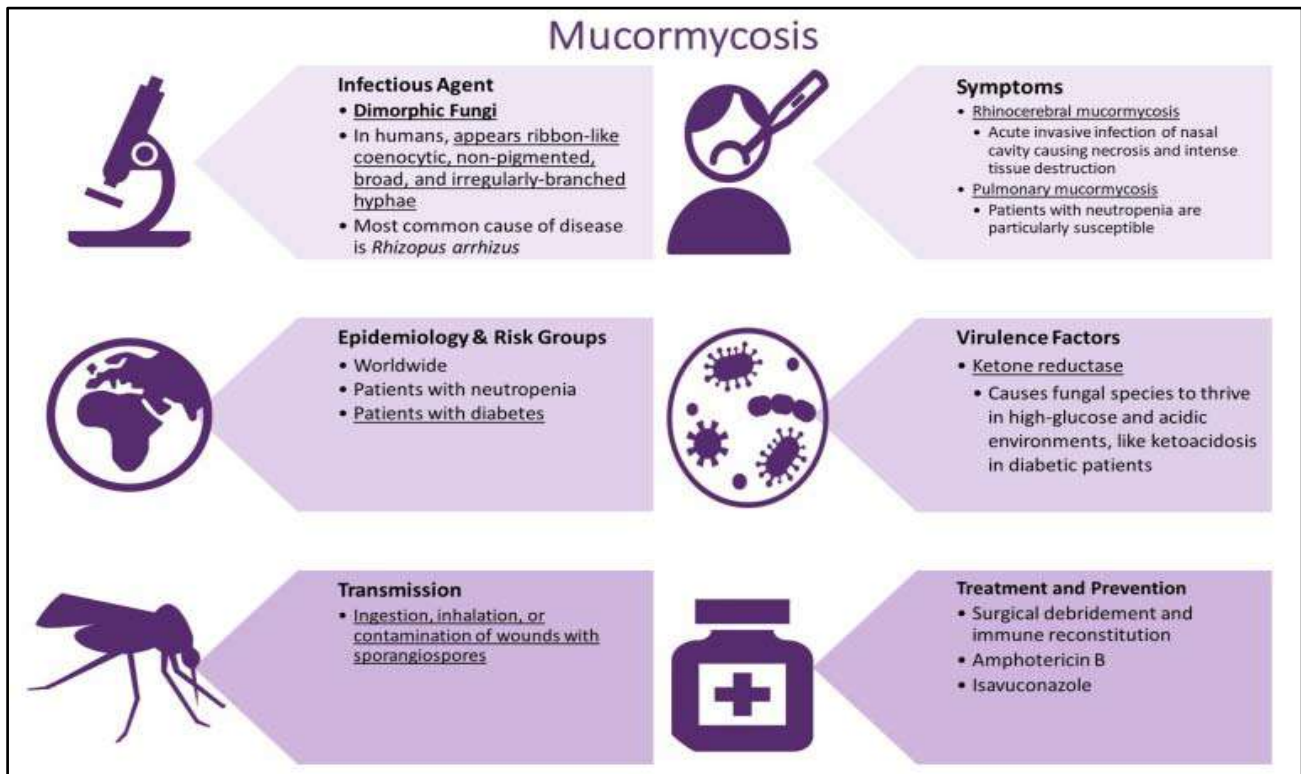


Fig 4: Overview of Mucormycosis

## VII. TREATMENT

A rare but serious fungal infection known as mucormycosis and colloquially as black fungus is being detected relatively frequently among COVID-19 patients in some states. The disease often manifests in the skin and affects the lungs and brain. While it is treated with antifungals, mucormycosis may eventually require surgery. Doctors have said that it is of at most importance to control diabetes, reduce steroids, and discontinue immune modulatory drugs. It is important to diagnose the disease as early as possible. The Mucormycetes medicine is costly enough. A six weeks dose of liposomal Amphotericin B is only a drug that can cure it. It is directly used on infection site. Experts in the task force have stressed the need to control hypercemia and monitor blood glucose levels after discharge following COVID-19 treatment and also diabetes. One should use steroids judiciously; correct timing, correct dose and duration are important.

In some cases, it can require surgery. It can lead to eventual loss of upper jaw and sometimes even an eye.

## VIII. PREVENTION

It is not possible to breath sincerely that no fungal spore enters in our body because the fungi of mucormycosis is very common in environment and the person with low immunity power has the great chance to get this infection. So people can protect themselves by protecting them from the environment and making yourself immunologically strong:

### Protection from Environment:

- ❖ Try to avoid the dusty and garbage area. If these areas can't be avoided then use face mask.
- ❖ Avoid direct contact with flood water, water damaged buildings, rotten things.
- ❖ In the outside of home try to wear long part, full sleeves shirts, shoes and wear gloves specially at the time of doing some outdoor or dusty activities.
- ❖ Always try to clean skin with soap.

### Antifungal Medication:

If someone feels to have lower immunity power and have the chance to get infected mucormycosis for his/her daily work, then he/she should consult with his/her medical practitioner and take some antifungal and immune booster medicines for advance protection.

## IX. CONCLUSION

During almost one and half year COVID-19 has made the world its kingdom of death and now it has been welcome mucormycosis to be its successor. This fungal infection is carrying the similar risk factor even its diagnosis become more challenging because of clinical suspicion and difficulty of isolating the causative fungi. Diabetes mellitus has been associated with SARS Cov-2 infection for the use of a large amount of steroid to the severe patients. Histopathology, direct examination and culture remain essential tools, although the molecular methods are improving and for this account molecular based methods and new fungal genetic are being explored.

## REFERENCES

- 1 Roden MM, Zaoutis TE, Buchanan WL, Knudsen TA, Sarkisova TA, Schaufele RL, et al. Epidemiology and outcome of zygomycosis: a review of 929 reported cases. *Clin Infect Dis*. 2005 Sep 1;41(5):634-53.
- 2 Petrikos G, Skiada A, Lortholary O, Roilides E, Walsh TJ, Kontoyiannis DP. Epidemiology and clinical manifestations of mucormycosis. *Clin Infect Dis*. 2012 Feb;54(Suppl 1):S23-34.
- 3 Walsh TJ, Gamaletsou MN, McGinnis MR, Hayden RT, Kontoyiannis DP. Early clinical and laboratory diagnosis of invasive pulmonary, extrapulmonary, and disseminated mucormycosis (zygomycosis). *Clin Infect Dis*. 2012 Feb;54(Suppl 1):S55-60.
- 4 Avery RK, Michaels MG. Strategies for safe living after solid organ transplantation. *Am J Transplant*. 2013 Mar;13(Suppl 4):304-10.
- 5 CDC. Guidelines for preventing opportunistic infections among hematopoietic stem cell transplant recipients. *MMWR Recomm Rep*. 2000 Oct;49(RR-10):1-125, CE1-7.
- 6 Davies BW, Smith JM, Hink EM, Durairaj VD. Increased incidence of rhino-orbital-cerebral mucormycosis after Colorado flooding. *Ophthalmic Plast Reconstr Surg*. 2017 May;33(3S Suppl 1):S148-S151.
- 7 Brizendine KD, Vishin S, Baddley JW. Antifungal prophylaxis in solid organ transplant recipients. *Expert Rev Anti Infect Ther*. 2011 May;9(5):571-81.
- 8 Rogers TR, Slavin MA, Donnelly JP. Antifungal prophylaxis during treatment for hematological malignancies: are we there yet? *Br J Haematol*. 2011 Jun;153(6):681-97.
- 9 Prenissl J, Jaacks LM, Mohan V, et al. Variation in health system performance for managing diabetes among states in India: a cross-sectional study of individuals aged 15 to 49 years. *BMC Med* 2019; 17:92.
- 10 Lim S, Bae JH, Kwon HS, et al. COVID-19 and diabetes mellitus: from pathophysiology to clinical management. *Nat Rev Endocrinol* 2021; 17:11-30.
- 11 Prakash H, Chakrabarti A. Global Epidemiology of Mucormycosis. *J Fungi (Basel)* 2019; 5:26.
- 12 Chakrabarti A, Kaur H, Savio J, et al. Epidemiology and clinical outcomes of invasive mould infections in Indian intensive care units (FISF study). *J Crit Care* 2019; 51:64-70.
- 13 Rudramurthy SM, Singh G, Hallur V et al. High fungal spore burden with predominance of *Aspergillus* in hospital air of a tertiary care hospital in Chandigarh. *Indian J Med Microbiol* 2016; 34:529-532.
- 14 Ibrahim AS, Spellberg B, Walsh TJ, et al. Pathogenesis of mucormycosis. *Clin Infect Dis* 2012; 54 (Suppl 1):S16-22.
- 15 Kathy H, Tony A, Matthew J, et al. A case of invasive pulmonary mucormycosis resulting from short courses of corticosteroids in a well-controlled diabetic patient. *Medical Mycology Case Reports* 2020; 29:22-24.





## Source details

[Feedback >](#) [Compare sources >](#)

### Turkish Journal of Physiotherapy and Rehabilitation

Scopus coverage years: from 2018 to 2023

Publisher: Turkish Physiotherapy Association

ISSN: 2651-4451 E-ISSN: 2651-446X

Subject area: [Medicine: Rehabilitation](#) [Health Professions: Physical Therapy, Sports Therapy and Rehabilitation](#) [Medicine: Orthopedics and Sports Medicine](#)

Source type: Journal

[View all documents >](#)[Set document alert](#)[Save to source list](#)

CiteScore 2022

0.3



SJR 2022

0.124



SNIP 2022

0.271



See discussions, stats, and author profiles for this publication at: <https://www.researchgate.net/publication/361037635>

# Utilization of Plant Probiotic Microorganisms for the Improvement of Agriculture

Article · August 2021

---

CITATIONS

0

---

READS

324

2 authors:



**Tanmay Ghosh**

Dinabandhu Andrews College university of calcutta

**74** PUBLICATIONS **211** CITATIONS

SEE PROFILE



**Mohan Kumar Biswas**

Visva Bharati University

**118** PUBLICATIONS **521** CITATIONS

SEE PROFILE



*Utilization of Plant Probiotic  
Microorganisms for the Improvement of  
Agriculture*

Tanmay Ghosh and Mohan Kumar Biswas

Research Journal of Agricultural Sciences  
An International Journal

P- ISSN: 0976-1675

E- ISSN: 2249-4538

Volume: 12

Issue: 04

Res Jr of Agril Sci (2021) 12: 1401–1407



 C A R A S

# Utilization of Plant Probiotic Microorganisms for the Improvement of Agriculture

Tanmay Ghosh\*<sup>1</sup> and Mohan Kumar Biswas<sup>2</sup>

Received: 09 May 2021 | Revised accepted: 18 Jul 2021 | Published online: 12 Aug 2021  
© CARAS (Centre for Advanced Research in Agricultural Sciences) 2021

## ABSTRACT

Pesticides and fertilizers are in intensive use due to agricultural push of needs in high productivity. This ruthless practice of chemical fertilizers negatively on humans' animals along with the natural properties as water soil etc. to reduce these environmental problems scientist studying on plant probiotic microorganisms in short PPM which are also known as bio-control Bio-protectants, Bio-stimulants and Bio-fertilizers that can by the microorganism to the plant and reduce environmental stress. The PPM mostly is engaged with a harmonious free-living relationship with the plant or they can work diversely in an unexpected way, now and again with explicit capacities to accomplish acceptable plant advancement. The study is about the PPM introduction, portrayal and several function and various ways of function with the application. A huge group that is named as plant growth promoting group or in short PGP. The group contains some bacterial and fungal species that stimulate plant growth and they can stimulate the growth through various mechanism. Many of the biogeochemical process are maintained by the soil borne microflora. Soil chemical fertilizers are needed to replace by an alternative. Scientist are studying on PPM to have it as the alternative as they don't provide with any environmental problems, they directly improve the nutrient supply. The species are truly organic. They have high role in biodegradation of pollutants. They also can decrease the chances of antibiotic-resistant bacteria and disease. The principle approaches are explained includes, the way of life subordinate methodology for the microorganisms contained in the plant material are additionally disengaged by refined and are distinguished by a blend of phenotypic and sub-atomic techniques and the refined free temperature microorganisms are recognized without developing them.

**Key words:** Cultivating, Microorganisms, Biodegradation, Decrease, PGP

It is said that the plants are never alone like human. They are always accompanied by microorganism known as plant probiotic microorganism with which they are involved with a symbiotic or symbiotic association. Humans and animals are strongly dependent upon the plant Kingdom activities for their survival. From the plant Kingdom activities agriculture and forestry are important for human survival throughout the whole history [1]. The high yield maintenance is now a problem for over countries due to population increase climate exchange soil degradation environmental contamination so we need high yield group that can feed the whole population [2-3].

For these problems as population increase we do

\* Tanmay Ghosh

✉ tanmay.tanmay.ghosh780@gmail.com

<sup>1</sup> Department of Microbiology, Dinabandhu Andrews College, Baishnabghata, South 24 Parganas, Kolkata - 700 084, West Bengal, India

<sup>2</sup> Department of Plant Pathology, Palli Siksha Bhavana, Visva - Bharti, Sriniketan, Birbhum, West Bengal, India

need high yield of edible crops so application of input such as pesticides fertilizers and become very compulsory in days to provide that yield. The chemical composts and pesticides have been negative impact on dirt (soil) contamination and water contamination and whole food chain is getting suffered for this. Scientist had also tried to reduce pesticide by selecting cultivars resistant to specific disease but in that case the resistance can cause dumping of crown rot root rot and many more diseases [4]. Therefore, the use of products based on PPM known as by a protected by chemicals by fertilizers by stimulated is a promising solution to overall the environment quietly and ecosystem that can maintain the equilibrium and reduce the excess cause of chemical fertilizers. The article is focusing upon the recent advantage of PPM. Plant culture improvement was also studied. Improvement stains are also studied in the study.



Fig 1 Microbes in soil

## MATERIALS AND METHODS

### PPM

Now a day what population is gradually increasing and some other problems are being faced by the humankind. The problems could be soil degradation environmental contamination climate change agriculture Hollister degrees which have critical for human activities and animal survival. So, the PPM is studied as the base product of alternative to Bio-fertilizers, Bio-pesticides or Phytoremediation. PPM is beneficial organism that can be found with plants in either symbiotic or free-living relationship. Primarily the association occurs in soil. Microalgae associate bacteria are also included to the types of PPM. There is a higher microbial presence of soil environments in the root system due to rhizodeposits and root exudates. Some of these germs can support their host which stimulates plant growth, reduces pathogen infection, increases yield, and reduces the pressure of biotic or abiotic plants as salt pressure. PPM are plant growth promoting microorganisms are consistent in soil microbial population plant disease suppressing bacteria fungi nitrogen fixing cyanobacteria as active member cities add toilet accident degrading microbes are also present in soil microflora. *Bacillus megaterium* or also a plant that causes the mutation of abscisic acid deficiency inhibition in the growth of mutant plants. *Bacillus* and *Pseudomonas* are the most predominant genera for the important PPM groups as plant growth promoting bacteria in short PGPB present in the soil. It is been believed that soil is the only source of PGP but some studies have shown that the bacteria are also associated with microalgae that stimulates the *Bacillus okhensis* case of growth. Aamantrit probiotic producing

bacteria are also considered as biocontrol for their activity against pathogenic microorganisms they can be lactic acid producing bacteria are generally recognized as safe GRAS status which is included in the FDA regulations in title 21 for code of federal regulations (21CFR). Another study to PPM the fungi is highly studied with important functions. For example, the endophytic fungi like *Exophiala* sp. Secrets the phytohormone that can improve the plant growth. *Trichoderma* strains have also studied for the identification of molecular mechanism of activation during in vitro interaction with tomatoes and *Trichoderma alongibrachiatum* MK1. The PPM interactions are influenced by crop rotation type and degree of fertilization toys of cultivation PPM performance and fields satisfactory etc.

### PGP

Plant growth promoters are microorganisms such as bacteria and fungi that stimulate plant growth through different mechanisms. Some direct PGP action mechanisms include nitrogen amelioration phosphorus or iron fixation and plant hormone production. Biomolecules as varied as antibiotics, enzymes and antimicrobial and pathogen inhibiting volatile compounds which can lower plant ethylene levels and induce systematic resistance are produced by PGP indirectly. PGP abilities can be presented by both Rhizosperic and endophytic soil bacteria. Rhizospere microbes are mainly found in the root inhibitors and endophytic bacteria are found with tissues of the plant itself or are free living. Food production systems are containing great importance to PGP as they are responsible for increasing the productivity.

Microorganism	Function
<i>Alcaligenesfaecalis</i> strain	Salt tolerance increase in <i>Arabidopsis thaliana</i>
<i>Bacillus subtilis</i>	Alleviates the adverse effects of soil salinity on wheat growth
<i>Arthrobacter</i> sp.	Promotes early plant growth
<i>Bacillus megaterium</i>	Increases plant biomass and the salt tolerance of rice
<i>Bacillus okhensis</i>	Inhibits abscisic acid (ABA) deficient mutant plants
<i>Fusarium culmorum</i> FcRed1	Promotes growth of a gibberellins (GAs)-deficient mutant cultivar and normal GAs biosynthesis cultivar rice seedlings
<i>Bacillus subtilis</i> GB03	Promotes early plant growth in <i>Sorghum bicolor</i> (L.) Moench
<i>Exophiala</i> sp.	Down-regulates expression of the high-affinity K <sup>+</sup> transporter (HKT1)
<i>Halomonas</i> sp.	Increases plant biomass and the salt tolerance of rice
<i>Lactobacillus plantarum</i> BY	Promotes early plant growth
<i>Novosphingobium</i> sp.	Reduces soft rot disease severity
<i>Penicillium minioluteum</i>	Metabolizes ABA in vitro
<i>Phomaglomerata</i>	Mitigates the adverse effects of salinity stress in various plants
<i>Penicillium</i> sp. LWL2	Promotes the growth of GAs-deficient dwarf mutant Waito-C and Dongjin-beyo rice
<i>Pseudomonas fluorescens</i>	Can help with the enrichment of proteins related to energy metabolism and cell division
<i>Sinorhizobium meliloti</i>	Produces Indole-3-acetic acid (IAA)
<i>Trichoderma longibrachiatum</i>	Promotes growth and/or increased biotic and abiotic tolerance to stresses

### Stress tolerance property

More than 30% of worldwide losses in crop production are due to the environmental stresses as soil salinization, soil solidification, and draught flooding soil pH UV light heavy metals environmental temperature abiotic stress. Primary signal such as change in ionic level so what are clauses and others and secondary signals as phytohormones as secondary metabolites releases are involved in the stressful conditions plant cascade which is responsible for such situations. Turgor pressure and mass production is affected by draught while the plants regulation cosmetic pressure ionic stress, oxidative stress. PGPR

interactions with other microorganisms and have effect on plant physiology [5]. Aminocyclopropane-1-carboxylic acid (ACC) deaminase is an enzyme present in the PGPR. Role of this enzyme is to regulate the hormone in plants. ACC deaminase is regulating ethylene, which is known as the stress hormone. The plant productions of these hormones are responsible for the roots acceleration that's response of abiotic and biotic process. The normal plant development, leaf abscission, senescence, follower wilting, chlorosis and low yield are inhibited by the high concentration of ACC deaminase. ACC deaminase containing bacteria inoculated plants have the increase in root height and biomass. This

happens for reduction in ethylene levels. Thus, they are beneficial for the plants in sense of stress tolerance.

#### Bioremediation

Due to the increase in industrial growth the environmental pollution are growing at a higher speed. Scientists are continuously trying to recover the contaminated soil. Due to the high cost and danger of the process of chemical cleanup for conventional hazards the study is becoming hard. Halogenated compounds like perchloroethylene, trichloroethylene, Pesticides like atrazine and bentazon, petroleum hydrocarbons, polycyclic aeromantic hydrocarbons, polychlorinated terphenyls are the main contaminants of soil. Primary inorganic contaminants are heavy metals (cadmium, chromium, lead, copper, zinc, nickel, mercury). For the remediation of polluted soil, the eco-friendly and cheaper ways are still being found. Phytoremediation is thought to be one of them as it includes plants that can accumulate heavy metals and recover the land. Another factor for the technique is to ensure the ability of microbe to tolerate heavy amount of contaminants. For the potential for metal bioaccumulation in polluted environment that is enhancing metal uptake and promote the plant growth the bio-fertilizers containing metal tolerant microorganisms (PGPR) is being studied. Soil decontamination and plant development is contributing the bioremediation which follows the mechanism of microbe plant interactions. Recently researchers have used PGPR availability to minimize arsenic toxicity on Malbec grape

seedlings. *M. luteus*, one of three tested species (*Micrococcus luteus*, *Bacillus lincheniformis* and *Pseudomonas fluorescens*) show high decrease in the arsenic toxicity and improving the biomass [6]. For another studies it was found that *Bacillus thuringiensis* improved metal accumulation and growth in the species *Alnus firma* in mine trailing soil. Inoculation of the microbe helped in root length increase, shoot height increase, plant biomass increase and heavy metal accumulation in inoculated plants of *Bacillus thuringiensis*.

#### Plant nutrition improvement

Plant growth production is favoured by different methods of soil fertilization such as chemical fertilization, organic fertilization and microorganism use for the macro and micro nutrients, mainly nitrogen and phosphorus. Bio-fertilization is having a definition as microbial usage for increase the supply of primary plant nutrition. Direct effects on nutrient availability, root growth enhancement, root pathogen antagonists, and soil detritus decomposition are included in nutrient improvement mechanism. Bacteria and fungi are among the microorganisms that can promote plant growth and have been identified as plant growth promoting *Rhizobacteria* as *Acinetobacter*, *Alcaligenes*, *Arthrobacter*, *Azospirillum*, *Azotobacter*, *Bacillus*, *Beijerinckia*, *Burkholderia*, *Enterobacter*, *Erwinia*, *Flavobacterium*, *Pseudomonas*, *Rhizobium*, *Serratia*, and *Arbuscularmycorrhizal* fungi [7-9].

PGP	Effect
<i>Trichoderma</i> spp.	Secondary metabolites produced by <i>Trichoderma</i> spp. affected the growth of tomato ( <i>Lycopersicon esculentum</i> ) and canola ( <i>Brassica napus</i> ) seedlings.
<i>Trichoderma harzianum</i>	<i>T. harzianum</i> caused effects on maize plant growth but only in combination with mineral fertilization and with disinfected soil as growth substrate.
<i>Pseudomonas</i> , <i>Ralstonia</i> , <i>Enterobacter</i> and <i>Pantoea</i>	Plant growth promotion was evaluated by screening for indoleacetic acid (IAA) production and mineral phosphate solubilisation in vitro.
<i>Bacillus velezensis</i>	Increased the growth of some tested plants (including beet, carrot, cucumber, pepper, potato, radish, squash, tomato, and turnip) at various levels in different plant parts.
<i>Azospirillum lipoferum</i>	Decreased plant water stress in maize ( <i>Zea mays</i> L.) with abscisic acid (ABA) and gibberellins (GAs) production by <i>Azospirillum lipoferum</i> .
Endophytic bacteria (217) and fungi (17) from coffee tissues.	Strains were evaluated for their potential to control coffee leaf rust ( <i>Hemileia vastatrix</i> ) and to promote coffee seedling growth. Bacterial strains named 85G ( <i>Escherichia fergusonii</i> ), 161G, 163G, 160G, 150G ( <i>Acinetobacter calcoaceticus</i> ), and 109G ( <i>Salmonella enterica</i> ) increased plant growth. 64R, 137G, 3F ( <i>Brevibacillus choshinensis</i> ), 14F ( <i>S. enterica</i> ), 36F ( <i>Pectobacterium carotovorum</i> ), 109G ( <i>Bacillus megaterium</i> ), 115G ( <i>Microbacterium testaceum</i> ), 116G, and 119G ( <i>Cedecea davisae</i> ) significantly reduced disease severity.

#### Plant growth promoting *Rhizobacteria* (PGPR)

PGPR has the greater contribution in enhancement of plant growth and yield because they are part of the rhizosphere biota that in association with plants, stimulates the host growth. PGPR are providing a large adaptability in a wide variety to the environment, enhances growth rate and biochemical versatility that allows them to metabolise a very wide range of natural and xenobiotic compounds. PGPR can be classified as rhizospheric and extracellular or and intracellular endophytic, according to the association between PGPR and the plant host. Extracellular PGPR in short e-PGPR are those PGPR that exists in the rhizosphere on the rhizoplane in the space between root cortex cells and intercellularly (i-PGPR) inside of the root cells mainly in nodular structure. Some examples of ePGPR are *Agrobacterium*, *Arthrobacter*, *Azotobacter*, *Azospirillum*, *Bacillus*, *Burkholderia*, *Caulobacter*, *Chromobacterium*,

*Erwinia*, *Flavobacterium*, *Micrococcus*, *Pseudomonas* and *Serratia* families. The examples of iPGPR are *Allorhizobium*, *Azorhizobium*, *Bradyrhizobium*, *Mesorhizobium*, and *Rhizobium* in rhizobiaceae family. The rhizobacteria are mostly belonging to the group are mainly Gram-negative rods. Sometimes they can be the gram-positive rods and sometimes may be cocci or pleomorphic. Intercellular PGPR or iPGPR are the bacteria that are colonizing in special root nodular structure and include bacteria that can fix atmospheric N<sub>2</sub> [10-13].

#### Arbuscularmycorrhizal fungi

Arbuscularmycorrhizal fungi or AMF can be enhancing solubility and availability of nutrients, including phosphorus and micronutrients, which are absorbed by the plant itself under many other different conditions. Phosphorus and nitrogen nutrition of *Medicago sativa* are

affected by AMF as well as carbon assimilation and water loss through modification of stomatal behaviour. The majority of plant roots are symbiotically associated with AMF. The AMF are *Glomeromycota*, family *Acaulosporaceae*, *Gigasporaceae* and *Glomaceae*. The interaction between AMF and bacteria may result in benefice impacts on plants. Fungal colonization in roots, interaction positivity influenced nitrogen and phosphorus enhancement was improved by PGPR. In improvement of availability of carbon and phosphorus compounds are improved by PHB (phosphate solubilizing bacteria) and AMF. AMF has important potential as Reforestation enhancement. Since the tropical forest are destroying at a high rate the investigation of AMF community in root structure and rhizospere soils of *Aquiliary crassna Pierre* ex *lec* and *Tectonsgrandis* lini. f. The field work was done on understanding weather the AMF vary to host plants. It was revealed that AMF community composition in *A. creassna*

and *T. grandis* were similar by the terminal restrictions fragment length polymorphism, complemented with clone libraries. Total 38 distinct terminal restriction fragments were found. 31 of them were share between *A. creassna* and *T. grandis*. Authors reported that TRF were attributed to *Claroideoglomeraceae*, *Divrrsisoraceae*, *Gigasporaceae*, and *Glomaceae*. The production of seedlings with high probability of survival required by Regengarating strands of valuable tropical hardwood tree species for sustainable harvest. Four families are being represented by the AME communities *Glomeraceae* (49%), *Acaulosporaceae* (24.9%), *Claroideoglomeraceae* (29.8%), and *Gigasporaceae* (4.8%). Which species were incubated in in vitro and colonized by all the study of a m f. in the results we find that the a.m. inoculated plants or taller than normal curated plants that suggest a high possibility of a MF symbiosis with both re forestation and important tree species productions in greenhouse studies [14-16].

Microorganism	Plant	Purpose	Bio-inoculation effects
<i>Rhizobial</i> strains		ACC deaminase production	ACC deaminase-producing organisms decrease plant ethylene levels that lead to plant growth inhibition or even death
<i>Staphylococcus</i> sp., <i>Bacillus</i> sp., <i>Curtobacterium</i> sp. M84, <i>Arthrobacter oxidans</i> BB1	<i>Arabidopsis thaliana</i>	To investigate pathogen resistance and salt stress tolerance	Strains BB1 and M84 showed the best performance under pathogen stress, and BB1 and L81 were better under salt tolerance
<i>Pseudomonas</i> spp.	<i>Zea mays</i> (maize)	To evaluate the potential of five <i>Pseudomonas</i> spp. in alleviating drought stress in maize	Bioinoculation with <i>Pseudomonas</i> spp. improved maize development under drought stress
<i>Agrobacterium tumefaciens</i> , <i>Zhinguelliella</i> , <i>Brachybacterium saurashtrense</i> , <i>Vibrio</i> , <i>Brevibacterium casei</i> , <i>Haererohalobacter</i>	<i>Arachis hypogaea</i>	To investigate the influence of these PRPGs in response of salinity	<i>A. hypogaea</i> development decreased in the control treatment under salt conditions. On the other hand, the presence of PGPR promoted plant growth and salt tolerance.
<i>Pseudomonas</i> GGRJ21	<i>Vignaradiata</i> (Mung bean)	To evaluate how the bacteria promote plant growth and alleviate drought stress.	The alleviation of drought stress in Mung beans by <i>Pseudomonas</i> is related to the production of antioxidant enzymes, cell osmolytes, hormones, and upregulation of stress-responsive genes in the host plant.
<i>Bacillus cereus</i> Pb25	<i>Vigna radiate</i> (Mung bean)	To evaluate the influence of bio-inoculation in Mung bean development under salt stress	<i>B. cereus</i> Pb25 showed an important role in mung bean plant protection due to increased production of its plant growth-promoting activity
<i>Bacillus amyloliquefaciens</i> RWL-1	<i>Oryza sativa</i> (Rice)	To investigate if the abscisic acid producer bacteria is able to protect rice crop from salinity stress	<i>B. amyloliquefaciens</i> was able to grow in different salt concentrations without affecting abscisic acid production and produced increased plant height, biomass, and total chlorophyll content.
PGPR isolated from <i>Hordeum secalinum</i> and <i>Plantago winteri</i>	<i>Hordeum vulgare</i> (Barley)	To isolate rhizobacteria associated with barley and <i>P. winteri</i> and evaluate the effect of bioinoculation on barley development under salt stress	The isolate E110 identified as <i>C. flaccumfaciens</i> was the most effective growth promoter and stress alleviator
<i>Azotobacter chroococcum</i> W5, <i>Mesorhizobium ciceri</i> F75, <i>Pseudomonas striata</i> P27, <i>Serratia marcescens</i> L11 and <i>Anabaena torulosa</i>	Wheat seeds	To evaluate the influence of phototroph heterotroph biofilm on wheat development	Soil treatment with biofilm led to an increase in soil chlorophyll, high concentrations of acetylene reduction activity using <i>Anabaena Serratia</i> biofilm, and <i>Anabaena-Pseudomonas</i> increased P-uptake
<i>Acetobacter</i> spp., <i>Azotobacter</i> spp., <i>Rhizobium</i> spp.,	<i>Camellia sinensis</i>	Soil recovery from excessive use of chemical	Lower chemical fertilization with biofilm improved soil microbiota and quality,

<i>Bradyrhizobium</i> spp., <i>Colletotrichum</i> spp. <i>Pseudomonas mendocina</i>	(Tea) <i>Lactuca sativa</i> (Lettuce)	fertilizers. To investigate the effect of interaction between PGPR and AMF in lettuce under salt stress.	favoring plant growth and Rhizoremediation <i>P. mendocina</i> was able to increase plant biomass under high salt level, while AMF were less effective in alleviating salt stress. Co-inoculation did not show an additive effect on plant growth
<i>Pseudomonas alcaligenes</i> , <i>Bacillus polymyxa</i> , <i>Mycobacterium phlei</i>	<i>Zea mays</i> (Maize)	To investigate the effects of Bio-inoculants on maize development in two types of soil.	The bio-inoculant stimulated the plant development and assimilation of N, P, and K in a low nutrient and saline soil.

#### Improvement of soil

Now days it is found that the increase in sustainable agriculture lead the necessity of new technological development for the reduction of environmentally harmful chemicals and fertilizers pesticides that are used by the agricultural people. Many other studies have put in light the plant probiotics as the alternative of soil fertilizers and their use as fertilizers in agriculture. Many of the studies have shown that they are used in agriculture improve the supply of management of nutrients in adverse conditions. They also took role in biochemical processes of plants with some specific effective natural substances and soil contaminated Bio-composts and antibiotic pressure tolerance [17].

#### Methods to study the microbial ecology of plants

It is important to study the plant associated microorganisms not only to understand the role in ecology and plant interactions also for the biochemical applications for those microorganisms in the management of the crops for high yield. Two different approaches are done upon the general knowledge of microbial community structure of different plants. Those two are culture dependent approach and culture independent approach. In culture dependent approach the isolated microorganism from plant material is cultivated and identified by a combination of molecular method and phenotype method from which their morphology and role can be studied. While in the other hand the culture independent approaches containing microorganism detected without cultivation based on extraction and DNA analysis through which their genetics can be easily studied. From there genetic library could be easily identified [18].

#### Methods that depends upon the culture

Mostly the methods that are depending upon the culture are used in determining the microbial ecology of plants. Most diverse plant systems have their diversity in microorganism too. Some diverse cleanser banana, strawberry, rice, potato, eucalyptus in wheat which has diverse variety of microorganisms. The method is based on growing after microbial cultures on agar plates or other nutrient plates and then characterizing and identifying them through various steps. Main lead identification is done by phenotype related identifications. Phenotype dependant identifications maybe morphological physiological or metabolic. Changes in growth condition and natural mutation can be changing these characters. So in this case such procedures may be insufficient for correct and reliable identification of the microorganisms that are cultured. In the other hand the procedure is time consuming and hard in laboratories. Recent recently many scientists have developed molecular method that can study microbial ecology and

overcome many limitations as we discussed in the field of understanding plant system microorganism diversity [19].

For the characterizing of plant growth promoting microorganism in short PGPR the sequence conservation regions of microbial DNA has been taken as a higher step. Generally, for investigation of bacterial community the 16 s rRNA gene is triggered for PCR amplification but 26 s and 18 s r RNA gene is normally targeted in eukaryotic commit investigation that is the major difference in investigation of community of eukaryotic and prokaryotic. Many other polyphasic approaches applied to identify and many endophytic bacteria isolated from maize and other crops. Biochemical applications were performed as growth in carbon sources intrinsic tolerance of antibiotics and biochemical test for catalase nitrate reductase and urease. Several genetic identifications are also performed as box PCR and sequencing of 16 s rRNA. Identifications revealed the presence of bacteria belonging to the genera *Pantoea*, *Bacillus*, *Burkholderia* and *Klebsiella*.

Further identification of groups and differentiation of microbial species in plant materials several methods applied such as BOX-PCR, REP-PCR, RAPD, RFLP, AFLP, ARDRA and PCR fingerprinting. The theory that the DNA varieties in microbial state that can be used for classification is proposed by all those methods we have done. It is hard to choose between many of the methods as a particular from the available literature as there are many other methods described in the literature. There are two main points depending on which the method or choosing one of them is microbial culture grouping priors to sequencing. And the other is microbial strain characterization within a species. In a study REP-PCR technique using the (GTG)<sup>5</sup> primer was employed for the bacterial endophytes isolation from strawberry fruits. In that particular study a cluster was found that was a total of 45 (GTG)<sup>5</sup> – REP-PCR cluster with the help of 16s rRNA sequencing of some microorganisms. Some of the microorganisms are *Bacillus subtilis*, *Bacillus* sp., *Enterobacter* sp., *Enterobacter ludwigii*, *Lactobacillus plantarum*, *Pseudomonas* sp, and *Pantoea* sp. It was evident that REP PCR techniques are a promising technique as a potential genotype tool for rapid and reliable detection of bacterial endophytes. Some other genetic tools are also finding successful for plaster plant microbial culture as ADRA-PCR in rice roots, BOX-PCR in maize and AFLP in banana roots [20-23].

#### Method that or not depending on culture

The method that are not dependent upon culture are extremely useful for understanding and isolating microorganisms but the microorganism cannot be cultivated because in this study physiological requirements not previously known so the microbial community composition



could be known but could not be cultivated in this process. It is started that plants grow in ecological niche and nutrient rich ecosystem. So, it is heart for selective media and culture conditions to full feel the requirements of reproduction of the ecological niche and relationships behind bacteria plant and bacteria interactions as there is a vast difference are known to us. The main principle of the method independent of culture based on amplification of PCR of the microorganism's RNA gene [24]. This technique is a valuable technique itself. Through this technique we can easily get instant info about the microorganisms specially the structure. The microorganisms who have in habitat in nutrient rich ecosystems whose growth conditions are very difficult to simulate can be easily identified through this technique. Potential to study the microphone quickly. That thing was just as equal to mi stone in this field. That has another impact economically and it lacks the time taking process. Sometimes the methods are done by denaturing gradient gel electrophoresis in short DGGE [25]. Through this method we can easily and directly profile the specific ecosystems microbial population through separating PCR products that have originated with universal primers. Mainly the Primus is based on the melting domain of specific DNA molecules. In the study of different plant species endophytic bacteria, the PCR-DGGE contains a greater potential as aiding [26]. It is confirmed by several authors that there is a difference between the naturally occurring species of plant growth promoting bacteria and the isolated bacteria. the indigenous bacterial flora diversity associated with potato plants essays to buy the use of both plating and PCR-DGGE. The results were very shocking to show that the PCR-DGGE analyzed sequences (*Telluria mixita*, *Caulobacter* sp., *Agromyces cerinus*, *Afipiageno* sp. and *Pseudomonas agarici*) did not matched from the isolated sequences. Get clearly suggest us about uncultivable or not yet cultural in the organisms that are detected in the DGGE analysis [27].

That clearly shows the importance of using both the culture dependent and culture independent methods for the understanding of ecological role of endophytic bacteria as well as its biochemical applications in agriculture. There are several techniques of culture independent methods as cloning and sequencing the whole communities rRNA sequence to explore the natural ecosystem microbial diversity [28]. Sequence of those RNA gene helps to let free the tools for gaining a more precise image of a given ecosystem diversity of species. Microbial diversity of plants is mainly discovered by the help of those liberates. Some scientist has reported the versatile and wild range of bacteria in the roots of rice [28-29]. The liberates are 16s rDNA which contains subclasses as alpha, beta, Gama, delta and epsilon subclasses of *Proteobacteria*, *Cytophaga*, *Flexibacteria*, bacteroids phyla, low G+C Gram positive bacteria, *Deinococcus thermus*, *Acidobacteria* and *Archaea*.

Scientist has found citrus grove bacterial community 16s rDNA Library. A total of 2062 clones were classified in to seven phyla, which are *Bacteroidetes*, *Dictyoglomi*, *proteobacteria*, *Actinobacteria*, *firmricutes*, *chlamydiae*, *verrucomicrobia*. Recently, for rare species detection and greater depth providing is done by some massive parallel sequencing platform as NGS (next gen sequencing). The NGC platform includes technology from 454 life sciences and solexa1G instruments. Another contender which is considered as serious, the name is ABI's solid platform. These techniques perform tens of thousands or more sequence reaction in single test tube. The new sequencing techs are highly impacting microbial study. In potato roots 454 pyrosequencing was examined. Scientist has detected several bacterial operational taxonomic units apparently 477 strains. The units are belonging to a total 238 genera of 15 phyla within banana roots [30-31]. Five of the endophytic potato plant microorganism's genera are *Rheinheimaea*, *Dyadobacter*, *Devosita*, *Pedobacter* and *Pseudoxanthomonas*. Other scientists have used 16 s rRNA illumina sequencing to access endophytic bacteria in Alovera. With a predominate of proteobacteria, Actinobacteria, firmricutes, Chlamydiae, found in the analysis. NGS technologies have power to capture microbial diversity in plant tissue [32]. This can easily improve the understanding between microbe's plant interactions. NGS platform use can quickly identify microbial candidates that can influence plant production and growth.

## CONCLUSION

From this study we could easily conclude that plant probiotic microorganisms in short PPM are very beneficial microorganisms which are associated with the plant to improve their growth. There is a high chance of the use of PPM as bio-fertilizer and bio-pesticides. In several studies it is also found that they can prevent several microbial diseases by secreting some molecules dangerous to other pathogens. There is a group in plant probiotic microorganisms which is called the plant growth promoters who can stimulate the plant growth through different mechanisms. The mechanisms can be nitrogen fixation Phosphorus fixation iron fixation production of plant hormones which can helps the growth and immunity of the plant. Bio-molecules antibody enzymes antimicrobial and pathogen inhabiting volatile compounds could be secreted by plant growth promoters or plant probiotic microorganisms. It is very important to molecular characterization and identifies plant associated microorganisms not only for the understanding of people logical role and plant interactions but also to enable the biochemical application of the cultures and to optimize the agricultural productivity.

## LITERATURE CITED

1. Ahemad M, Kibret M. 2014. Mechanisms and applications of plant growth promoting Rhizobacteria: Current perspective. *Jr. King Saud Univ-Sciences* 26: 1-20.
2. Antoun H, Prévost D. 2006. Ecology of plant growth promoting rhizobacteria. *In: (Eds) Siddiqui ZA. PGPR: Biocontrol and Biofertilization*, Dordrecht: Springer Netherlands. pp 1-38.
3. Brunner SM, Goos RJ, Swenson SJ. 2015. Impact of nitrogen fixing and plant growth-promoting bacteria on a phloem-feeding soybean herbivore. *Applied Soil Ecology* 86: 71-81.
4. Smith SE, Manjarrez M, Stonor R. 2015. Indigenous arbuscularmycorrhizal fungi Contribute to wheat phosphate uptake in a semi-arid field environment, shown by tracking with Radioactive phosphorus. *Applied Soil Ecology* 96: 68-74.

5. Mensah JA, Koch AM, Antunes PM. 2015. High functional diversity within species of Arbuscularmycorrhizal fungi is associated with differences in phosphate and nitrogen uptake and fungal phosphate metabolism. *Mycorrhiza* 25: 533-546.
6. Augé RM, Toler HD, Saxton AM. 2015. Arbuscularmycorrhizal symbiosis alters stomatal of host plants more under drought than under amply watered conditions: a meta-Analysis. *Mycorrhiza* 25: 13-24.
7. Schübler A, Schwarzott D, Walker C. 2001. A new fungal phylum, the Glomeromycota: Phylogeny and evolution. *Mycol. Research* 105: 1413-1421.
8. Dodd JC, Boddington CL, Rodriguez A. 2000. Mycelium of Arbuscular Mycorrhizal Fungi (AMF) from different genera: form, function and detection. *Plant Soil* 226: 131-151.
9. Artursson V, Finlay RD, Jansson JK. 2006. Interactions between arbuscularmycorrhizal fungi and bacteria and their potential for stimulating plant growth. *Environ Microbiology* 8: 1-10.
10. Miransari M. 2011. Interactions between arbuscularmycorrhizal fungi and soil bacteria. *Appl. Microbiol Biotechnology* 89: 917-930.
11. Zhang L, Xu M, Liu Y. 2016. Carbon and phosphorus exchange may enable cooperation between an arbuscularmycorrhizal fungus and a phosphate-solubilizing bacterium. *New Phytologist* 210: 1022-1032.
12. Chaiyasen A, Young JPW, Teamroong N. 2014. Characterization of arbuscular Mycorrhizal fungus communities of *Aquilariacrassna* and *Tectonagrandis* roots and soils in Thailand plantations. *Plos One* 9: e112591.
13. Chaiyasen A, Douds DD, Gavinlertvatan P. 2017. Diversity of arbuscularmycorrhizal Fungi in *Tectonagrandis* Linn.f. plantations and their effects on growth of micropropagated plantlets. *New Forest* 48: 547-562.
14. Brundrett MC, Bougher N, Dell B. 1996. *Working with Mycorrhizas in Forestry and Agriculture*. (Eds) Smith S, Read D (2008) *Mycorrhizal Symbiosis*, New York: Academic Press.
15. Porcel R, Ruiz-Lozano JM. 2004. Arbuscularmycorrhizal influence on leaf water potential, Solute accumulation, and oxidative stress in soybean plants subjected to drought stress. *Jr. Exp. Botany* 55: 1743-1750.
16. Doubková P, Vlasáková E, Sudová R. 2013. Arbuscularmycorrhizal symbiosis alleviates drought stress imposed on *Knautiaarvensis* plants in serpentine soil. *Plant Soil* 370: 149-161.
17. Azcón-Aguilar C, Barea JM. 1996. Arbuscular mycorrhizas and biological control of soil-Borne plant pathogens—an overview of the mechanisms involved. *Mycorrhiza* 6: 457-464.
18. Wright SF, Upadhyaya A. 1998. A survey of soils for aggregate stability and glomalin, a Glycoprotein produced by hyphae of arbuscularmycorrhizal fungi. *Plant Soil* 198: 97-107.
18. Khan UA, Rahman H, Qasim M, Hussain A, Azizillah A, Murad W, Khan Z, Anees M, Adnan M. 2015. Alkannatinctoria leaves extracts: a prospective remedy against Multidrug resistant human pathogenic bacteria. *BMC Complement Altern. Med.* 15: 127.
19. Kloepper JW, Schroth MN. 1981. Relationship of in vitro antibiosis of plant growth promoting rhizobacteria to plant growth and the displacement of root microflora. *Phytopathology* 71: 1020-1024.
20. Lee S, Flores-Encarnacion M, Contreras-Zentella M, Garcia-Flores L, Escamilla JE, Kennedy C. 2004. Indole-3-acetic acid biosynthesis is deficient in *Gluconacetobacter Diazotrophicus* strains with mutations in cytochrome C biogenesis genes. *Jr. Bacteriology* 186: 5384-5391.
21. Mahon CR, Lehman DC, Manuselis G. 2011. *Textbook of Diagnostic Microbiology*. 4<sup>th</sup> ed. W. B. Saunders Co, Philadelphia, PA.
22. Mia MAB, Hossain MM, Shamsuddin ZH, Islam MT. 2014. Plant-associated bacteria in nitrogen nutrition in crops, with special reference to rice and banana. In: (Eds) Maheshwari DK, Saraf M, Aeron A. *Bacteria in Agrobiology: Crop Productivity*. Springer, Heidelberg.
23. Mia MAB, Shamsuddin ZH, Mahmood M. 2012. Effects of rhizobia and plant growth promoting bacteria inoculation on germination and seedling vigor of lowland rice. *Afr. Jr. Biotechnology* 11: 3758-3765.
24. Mondal MMA, Malek MA, Puteh AB, Ismail MR, Ashrafuzzaman M, Naher L. 2012. Effect of foliar application of chitosan on growth and yield in okra. *Aust. Jr. Crop* 6: 918-921.
25. Naem M, Hassan A, Ahmed M, El-Sayed A. 2010. Radiation-induced degradation of Chitosan for possible use as a growth promoter in agricultural purposes. *Carbohydr. Polym.* 79: 555-562.
26. Perez AG, Olias R, Espeda J, Olias JM, Sanz C. 1997. Rapid determination of sugars, nonvolatile acids, and ascorbic acid in strawberry and fruits. *Jr. Agr. Food Chemistry* 45: 3545-3549.
27. Prince MFRK. 2014. Molecular characterization of novel environmental bacteria and their growth promoting effect on rice. *M. Sc. Thesis*, Department of Biotechnology, BSMRAU.
28. Riungu GM, Muthorni JW, Narla RD, Wagacha JM, Gathumbi JK. 2008. Management of fusarium head blight of wheat and deoxynivalenol accumulation using antagonistic microorganisms. *Plant Pathology Journal* 7(1): 13-19.
29. Ryan RP, Monchy S, Cardinale M, Taghavi S, Crossman L, Avison MB, Berg G, Van der Lelie D, Dow JM. 2009. The vrsality and adaptation of bacteria from the Genus *Stenotrophomonas*. *Nat. Rev. Microbiology* 7: 514-525.
30. Sabir AA. 2015. Molecular characterization of strawberry crown rot pathogen and enhancement of strawberry yield by plant probiotics. *M. Sc. Thesis*, Department of Biotechnology, BSMRAU.
31. Salachna P, Zawadzińska A. 2014. Effect of chitosan on plant growth, flowering and corms yield of potted *Freesia*. *Jr. Ecol. Engineering* 15(3): 97-102.
32. Siedlecka A, Krupa Z. 1996. Interaction between cadmium and iron and its effects on photosynthetic capacity of primary leaves of *Phaseolus vulgaris*. *Plant Physiology Biochemistry* 34: 841-883.



Home

○ UGC

🔍 Search



## UGC-CARE List

You searched for "0976-1675". Total Journals : 1

Search:

Sr.No.	Journal Title	Publisher	ISSN	E-ISSN	UGC-CARE coverage years	Details
1	Research Journal of Agricultural Sciences- An International Journal	Centre for Advanced Research in Agricultural Sciences	0976-1675	2249-4538	from September-2019 to Present	<a href="#">View</a>

Showing 1 to 1 of 1 entries

Previous

1

Next



## Maize sheath blight disease and its biological control

Dr. Harsha Sharma<sup>1</sup>, Mozammel Haque<sup>2</sup>, Dr. Anita Singh<sup>3</sup>, Dr. Tanmay Ghosh<sup>4</sup>,  
Ramengmawii<sup>5</sup>

<sup>1</sup>Assistant Professor, Department of Microbiology Faculty of Science, Motherhood University,  
Roorkee

<sup>2</sup>Department of Pharmacology, Bihar College of pharmacy, Bihar, Patna , 801503, India

<sup>3</sup>Assistant Professor, Chemistry, Career College Bhopal Madhya Pradesh-462023

<sup>4</sup>Assistant Professor, Department of Microbiology, Dinabandhu Andrews College,  
Baishnabghata, South 24 Parganas, Kolkata – 700084, West Bengal, India.

<sup>5</sup>Asst Professor , Govt. Hrangbana College

### **Abstract:**

One of the significant kharif crop of India is maize. It is unmistakably a summertime annual that needs extremely specific environmental conditions for healthy growth and development. It is grown all over the world in the temperate, subtropical, and tropical regions. Sheath blight, caused by *Rhizoctonia solani*, causes corn grain losses ranging from 11 to 40%, even up to 100% on some cultivars in some warm, humid locations, where the circumstances are suitable for the causative agent (Izhar and Chakrabarty 2013; Gao et.al., 2014). To gradually destroy this causative agent, a number of compounds are utilised. However, this same bacterium has also developed resistance to systemic fungicides like benomyl, carboxin, and thiophenate methyl as well as protectant organic fungicides like captan, maneb, and thiram. To manage this diseases, biological treatment options were tested in the current experiment. A biocontrol agent, *Trichoderma*, was tested in vitro against the pathogen *R. Solani* using several species. As a consequence of its ability to 80% effectively block the growth of pathogens, *T. harzianum* emerged as the most promising of the ten *Trichoderma* strains studied in this study. The pathogen was also exposed to certain botanicals (essential oils), and Neem oil (*Azadirachta* oil) showed the most promising results in thwarting the growth of the infection, followed by clove oil and mentha oil.

**Keywords:** Maize, Sheath Blight, *Rhizoctonia solani*, *Trichoderma*,

## INTRODUCTION

*Zea mays*, a significant Kharif crop, is crucial to the nutrition of Indians. After wheat, barley, and rice, corn is the fourth most common cereal crop in terms of area and output. The production of food accounts for 25% of GDP thanks to the main cereal grain. This crop grows quickly and tall yet has a limited lifespan. It may be used in a variety of goods, including industrial ones as well as animal and livestock feed. Andhra Pradesh, Karnataka, Rajasthan, Maharashtra, Uttar Pradesh, Bihar, Chhattisgarh, Madhya Pradesh, and Himachal Pradesh are the states with the largest corn acreage that account for more than 80% of corn output.

Out of the 112 corn diseases that have been recorded thus far from various regions of the world, 65 are known to exist in India (Singh and Shahi 2012; Asif 2013). The main ailments that affect the country's many agro-climatic areas include seed roll seedling blight, leaf blight, downy mildews, stalk rots, banded leaf and sheath blight, smuts, and rust, which cause yearly crop losses of 15% to 20%. The Corn Sheath Blight of Maize (*Thanatephorus sasakii* (Shirai) Tu and Kimbrough) is the Worse of These (Tu and Kimbrough 1978). Except for the tassel, all of the plant's aerial components exhibit diseases signs.

*Rhizoctonia solani* is a fungus that causes banded leaf and sheath blight, and it is a soil-borne disease. One of the most infamous, pervasive, harmful, and adaptable pathogens that can be found almost anywhere in the globe is the fungus (Divya Rani et al. 2013). Because *R. solani* is able to develop sclerotia that can survive in the soil for at least two years, control techniques can only be partially successful (Ou 1985).

Cultural, chemical, and biological techniques have all been proposed as ways to manage this illness. Chemical and cultural control techniques are time-consuming and insufficiently effective. Additionally, it harms the helpful bacteria in the soil, which causes ongoing issues (Monfil and Casas-Flores 2014). Therefore, a biological idea was proposed (Boukaew et al. 2013).

In the current study, biocontrol techniques are chosen because they pose less hazards to human health, have a targeted mode of action, enhance soil quality, don't interfere with the majority of helpful bacteria, and are sustainable from an agricultural standpoint. As a result, this approach can effectively control the *zea mays* sheath blight disease because the bio agent multiplies in the soil and provides protection throughout the crop's growth.

## Distribution

Germany, the United States, Nigeria, Venezuela, Sierra Leone, the Ivory Coast, and England have all recorded cases of this illness. In particular, sheath blight is acknowledged as a significant barrier to the development of maize in China, South Asia and Southeast Asia (Bangladesh, Sri Lanka, Indonesia, Cambodia) Philippines, Taiwan, Malaysia, Korea, Japan,

Thailand, Laos, Pakistan, Nepal, and Myanmar). Surprisingly, sheath blight has been blamed for yield losses in China that are close to 100%.

## Materials and methods

### Isolation and culture of the pathogen –

In order to identify the *Rhizoctonia solani* disease, samples from the local farms. The sample washed twice in double-distilled water after being surface sterilised with a 1 percent sodium hypochloride (NaOCl) solution. The sick material was crushed on sterile petri plates, and a little amount (size: 1-2 mm) of the infected area was transferred to a culture plate made up of PDA media under aseptic conditions. For five to seven days, inoculated plates were incubated at 25°C. Plates were continuously inspected for related microbial proliferation and growth. The fungus were sub-cultured for purification by choosing the desired colonies after five days of incubation. For subsequent research, isolated and purified cultures were kept alive by routine transfers in new PDA media and storage in a refrigerator at 4°C. A different batch of cultures was produced on paraffin-sealed slant and stored at -4°C. Growth pattern, colony diameter, and colour were evaluated as the fundamental identifying characteristics.

### In-vitro evaluation of biocontrol methods for the management of disease:

#### Isolation of *Trichoderma* strains

The places where the diseases brought on by *Rhizoctonia solani* was either very low or nonexistent in the presence of susceptible hosts are where the *Trichoderma* strains were identified from soil. The sample locations were at Gyanpur's experimental farms. At room temperature, air drying was done on the soil samples that were brought to the lab. On a selective medium, the *Trichoderma* species were isolated [(TSM) Elad, 1981]. Twenty millilitres of TSM medium were put onto Petri plates and let to harden. *Trichoderma* from soil samples was isolated using the serial dilution technique. 200 l aliquots of the soil suspension were then spread on TSM after one gramme of dried soil was added to nine ml of sterilised distilled water and serially diluted up to the dilution factor of 10<sup>4</sup>. At 25°C and 20°C, the plates were incubated. On to PDA were transferred the colonies that had formed on the medium. *Trichoderma* cultures were also kept at 40 C on PDA slants for future research. *Trichoderma* isolates were identified using Kubicek and Harman's taxonomic keys (1998).

#### Antagonistic efficacy of *Trichoderma* spp. against *R. solani*

By inoculating a 5 mm agar block of *Trichoderma* against *R. solani* on PDA medium, 3 cm apart from each other, antagonistic potential of *Trichoderma* species was in vitro screened. After 6 days of incubation at 25 2 0C, observations were taken on the inoculation plates. The approach outlined by Upadhyay and Rai was used to analyse the colony interaction in dual culture (1987). The parameter used for evaluation was the percentage of the pathogens' radial growth that was

inhibited, calculated using the formula  $100 (R1 - R2)/R1$  (Fokkema, 1976), where R1 represents the pathogen's radial growth towards the antagonist and R2 represents its radial growth towards the opposite side.

### Screening of essential oils against *R. solani*

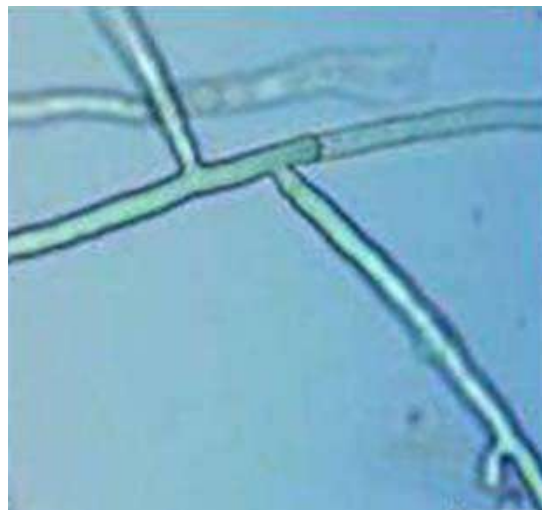
Using the poisoned food technique, the plant extract thus produced together with neem oil and lemon grass oil were evaluated against *R. solani*. Using the well method on a potato dextrose agar medium, the plant extracts lemon grass oil (0.2%), neem oil (0.1%), mentha oil (0.1%), basil oil (0.1%), and fenugreek oil (0.2%) were evaluated for their effectiveness against the pathogen *R. solani*. In the solidified medium, a well was made before it was placed onto 90 mm-diameter sterile petri dishes. The opposite side of the well cut in the petri plate was infected with a mycelial disc of 5 mm from a seven day old actively developing culture, and the well was then filled with test essential oil and incubated at 28 2 °C for seven days. Without any therapy, control was kept. Data were obtained 96 hours after inoculation and three replications were kept for each treatment.

The following formula may be used to calculate the percentage of mycelial growth inhibition: (Vardhan2020).

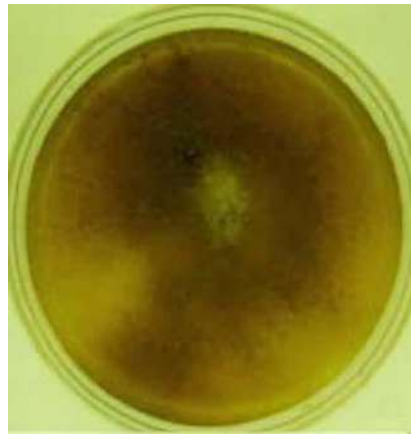
$I=C-T/TX100$ , Where, I = Percentage of mycelial growth inhibition C = Control's colony diameter (mm) T = Treatment for Colony Diameter (mm)

### Result:

#### Isolation of Pathogen:

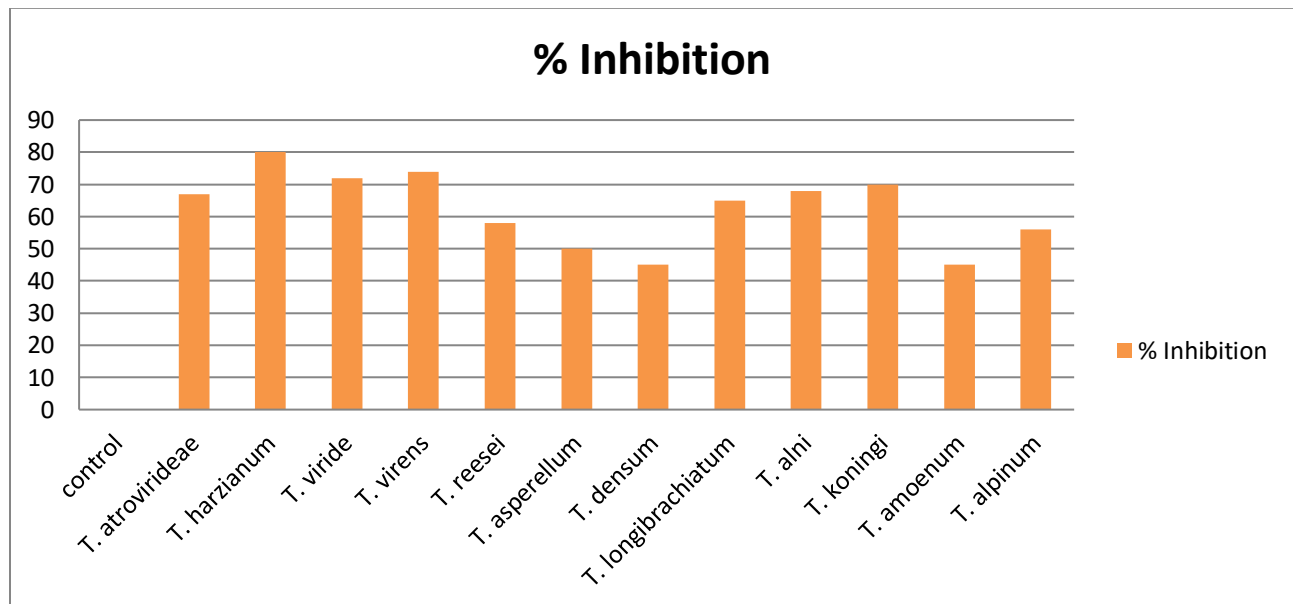


Hyphae of Pathogen



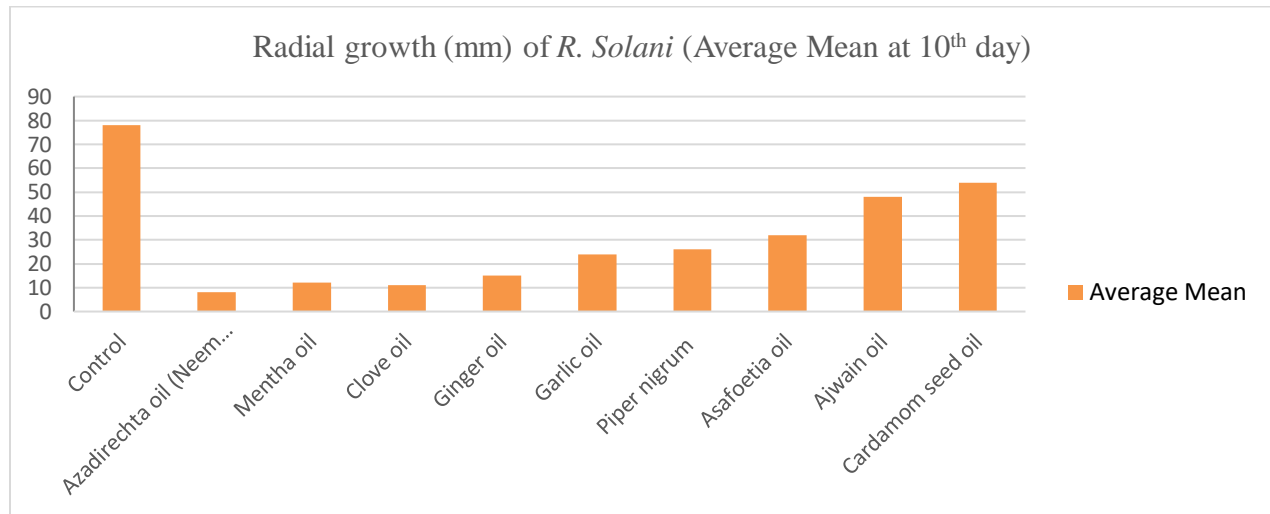
Pure culture of pathogen

Total 12 *Trichoderma* strain were used against *Rhizoctonia solani* in dual plate culture technique. The most effective strain found against *R.solani* are *T. harzianum* (80%) > *T. virens* (74) > *T. viride* (72%). Other strains were also able to prevent the growth of causal agent but at lesser extent (50 – 70) while *T. amoenum* were not found effective against *R. solani* (45%).



**Screening of essential oils against the Pathogen-** Out of 9 essential oils used against *R. solani* Neem oil (*Azadirachta* oil) shows most promising result in inhibiting the growth of pathogen followed by clove oil and mentha oil.





## Discussion-

Historically, efforts have been made to control *Rhizoctonia solani* populations by using fungicides (Du Plessis 1999; Stevenson 2000). To destroy this causative agent sequentially, many compounds are applied (Naz 2006). However, this same bacterium has also developed resistance to systemic fungicides like benomyl, carboxin, and thiophenate methyl as well as protectant organic fungicides like captan, maneb, and thiram (Van Bruggen and Arneson 1984). Additionally, non-selective chemical usage led to the development of disease resistance to some chemicals, unintended impacts on microbial proliferation in ecosystems, and dangerous natural phenomena (Prasad and Kumar 2011; Singh and Shahi 2012). As a result, alternative methods for the management of diseases in maize crops have taken the place of plant pathologists' care.

The current enquiry is a significant study that examines the potential for managing or controlling this condition by testing biological agents, namely *Trichoderma spp.* in dual culture. The results of the dual culture experiment showed that, in terms of the growth diameter of *R. solani*, each of the 12 *Trichoderma spp.* strains examined substantially varied from the control. However, compared to the other isolates, *T. harzianum* isolate demonstrated a stronger growth inhibition of *R. solani* (80%). Figure 2 shows antagonistic growth outpacing pathogen growth. An antagonist can overgrow when it has a greater growth rate, tolerance for the pathogens' metabolites, and the ability to manufacture antibiotics (Mathivanan et al., 2000). According to Chaudhary et al. (2020) and Abo-Elyousr et al. (2014), *Trichoderma*'s capacity to generate extracellular chitinase enzymes is correlated with mycoparasitism.

Essential oil effects were divided into three categories: weak (0.0-1.9 mm), moderate (2.0-3.9 mm), and powerful (4.0-5.9 mm and above). Neem oil had substantial fungicidal properties when

compared to the other essential oils tested against *R. Solani*, and its fungitoxic action may be caused by the presence of azadirachtin, which contains desactylimbin (Sehajpal et al., 2009)

Neem oil is used as a seed treatment, and spraying is the most effective and environmentally friendly way to manage this disease (Bunker et al. 2012) Divya et al.(2013) and Maravi K. K. (2016)

## Conclusion:

In order to maintain plant health and increase crop yield, a promising alternative strategy is the biological control of plant diseases. The findings of this investigation will also be applied to the field level control of this disease.

## Reference:

- Abo-Elyousr, K.A.M., S.I.I. Abdel-Hafez and I.R. Abdel-Rahim. (2014). Isolation of *Trichoderma* and evaluation of their antagonistic potential against *Alternaria porri*. J. Phytopathol., 162, 1e8
- Adams GC Jr, Butler EE, 1979. Serological relationship among anastomosis groups of *Rhizoctonia solani*. Phytopathol 69: 629-633
- Ahuja SC, Payak MM, 1982. Symptoms and signs of banded leaf and sheath blight in maize. Phytoparasitica. 10: 41-49
- Asea G, Vivek BS, Lipps PE, Pratt RC, 2012. Genetic gain and cost efficiency of marker-assisted selection of maize for improved resistance to multiple foliar pathogens. Mol Breeding 29: 515-527
- Akhtar.J, V. Kumar Jha, A. Kumar and H.C. Lal.(2009).Occurrence of Banded Leaf and Sheath Blight of Maize in Jharkhand with Reference to Diversity in *Rhizoctonia solani*. Asian Journal of Agricultural Sciences 1(2): 32-35, 2009.
- Asif, N. (2013). Threatening Diseases; banded leaf and sheath blight of maize. Ph.D Thesis. Kisan PG College, Bahraich (U.P), India. 256 p.
- Boukaew S, Klinmanee C, Prasertsan P. (2013). Potential for the integration of biological and chemical control of sheath blight disease caused by *Rhizoctonia solani* on rice. World Journal of Microbiology and Biotechnology, 29, 1885–1893
- Bunker, R.N., A. Trivedi and K. Mathur. (2012). Integrated management of banded leaf and sheath blight of maize caused by *Rhizoctonia solani* f.sp. sasakii. Journal of Mycology and Plant Pathology 42(3): 367-317.
- Chaudhary S., Sagar S., Lal M , Tomar A , Kumar V and Kumar M. (2020). Biocontrol and growth enhancement potential of *Trichoderma* spp. against *Rhizoctonia solani* causing sheath blight disease in rice. Journal of Environmental Biology.Vol.41. 1034-1045.

- Divya Rani, V., P. Narayan Reddy and G. Uma Devi. (2013). Banded leaf and sheath blight of maize incited by *Rhizoctonia solani* f.sp sasakii and its management. A Review. International journal of Applied Biology and Pharmaceutical Technology 4: 52-60.
- Gao, J., Chen, Z., Luo, M., Peng, H., Lin, H., Qin, C., Yuan, G., Shen, Y., Ding, H., Zhao, M., Pan, G. and Zhang, Z. (2014). Genome expression profile analysis of the maize sheath in response to inoculation to *R. solani*. Mol. Biol. Rep. 41: 2471-2483.
- Izhar, T., and Chakraborty, M. (2013). Genetic analysis of banded leaf and sheath blight resistance (*Rhizoctonia solani*) in maize. Journal of Pharmacognosy and Phytochemistry. 1: 1-5.
- K. K. Maravi (2016). Studies on banded leaf and sheath blight (*Rhizoctonia solani* Kuhn) Disease of maize. Thesis Deptt. Of Plantpathology, College of Agriculture, Indira Gandhi Krishi Vishwavidyalaya Raipur (C. G.).
- Madhavi, G.B., Bhattiprolu, S.L., Bharathi, S., Reddy, V.C. and Ankaiah, R. (2011). Studies on the management of banded leaf and sheath blight disease of maize (*Rhizoctonia solani* f. sp. sasakii) using fluorescent Pseudomonads. In: Proc. 2nd Asian PGPR Conference, Beijing P.R. China, pp 567-576
- Mahivanan, N., K. Srinivasan and S. Chelliah. (2000). Biological control of soilborne diseases of cotton, eggplant, okra and sunflower by *Trichoderma viride*. Journal of Plant Disease Protection. 107, 235-244.
- Monfil V O, Casas-Flores S. (2014). Molecular mechanisms of biocontrol in *Trichoderma* spp. and their applications in agriculture. In: Gupta V G, Schmoll M, Herrera-Estrella A, Upadhyay R S, Druzhinina I, Tuohy M, eds., Biotechnology and Biology of *Trichoderma* . Elsevier Press, Amsterdam. pp. 429–45.
- Ou SH (1985) Rice diseases, 2nd edn. Commonwealth Mycological Institute, Kew, p 380
- Sehajpal Anil Arora, Saroj and Kaur Parminder.(2009).Evaluation of plant extracts against *Rhizoctonia solani* causing sheath blight of rice. The Journal of Plant Protection Sciences, 1(1) : 25-30.
- Singh, A and J.P. Shahi. (2012). Banded leaf and sheath blight: an emerging disease of maize (*Zea mays* L). Review paper. Department of Genetics and Plant Breeding, Institute of Agricultural Sciences, Banaras Hindu University, Varanasi 221005, Uttar Pradesh, India. Maydica. 57p.
- Tu CC, Kimbrough JW (1978) Systematics and phylogeny of fungi in the *Rhizoctonia* complex. Bot Gaz 139:454–466

See discussions, stats, and author profiles for this publication at: <https://www.researchgate.net/publication/361037454>

# An in-vitro studies on the primary phytochemical estimation and antibacterial potentiality of the peel extract of *Musa acuminata* against *Pseudomonas aeruginosa*

Article · July 2021

CITATIONS

0

READS

283

2 authors:



**Tanmay Ghosh**

Dinabandhu Andrews College university of calcutta

74 PUBLICATIONS 211 CITATIONS

SEE PROFILE



**Mohan Kumar Biswas**

Visva Bharati University

118 PUBLICATIONS 521 CITATIONS

SEE PROFILE

## An *in-vitro* studies on the primary phytochemical estimation and antibacterial potentiality of the peel extract of *Musa acuminata* against *Pseudomonas aeruginosa*

Tanmay Ghosh<sup>1\*</sup>, Mohan Kumar Biswas<sup>2</sup>

<sup>1</sup> Department of Microbiology, Dinabandhu Andrews College, Baishnabghata, Kolkata, West Bengal, India

<sup>2</sup> Department of Plant Pathology, Palli Siksha Bhavana, Visva-Bharati, Sriniketan, West Bengal, India

### Abstract

By this research work, we know the phytochemical analysis and antibacterial activity of the peel extract of *Musa acuminata*. For this studies, ethanol, methanol and aqueous solvent of extraction are used. This work was done by using agar well diffusion method and we know the antibacterial activity of the banana peel extract. Four concentrations are used for this study, these are 12.5 mg/ml, 25mg/ml, 50mg/ml, and 100mg/ml. *Escherichia coli*, *Bacillus subtilis*, *Staphylococcus aureus*, *Klebsiella pneumoniae*, *Pseudomonas aeruginosa*, *Salmonella enteritidis* of these test microorganisms are used in this study and by which we know the antibacterial activity of the peel extract of *Musa acuminata*. To study the phytochemical analysis of the peel extract of *Musa acuminata*, flavonoids, terpenoids, quinines and alkaloids are present in ethanol, methanol and aqueous extracts. So, phytochemical screenings are revealed. From the result, we know that banana peels shows the antibacterial activity against this test microorganisms. Banana peels extract play a great importance role in public health. The yellow banana peel shows a good antibacterial activity against Gram (+) and Gram (-) and replace the synthetic medicine in this diseases caused by this bacteria. From the result, we can see that *Pseudomonas aeruginosa* shows the maximum zone of inhibition ( $31.7\pm 2.0$ ) in the highest concentration of 100 mg/ml concentration. *Staphylococcus aureus* shows the minimum zone of inhibition ( $25.0\pm 2.0$ ) in 100 mg/ml concentration of ethanol extract. In lowest concentration (12.5 mg /ml), *Bacillus subtilis* shows the maximum zone of inhibition ( $19.0\pm 2.0$ ) and *Staphylococcus aureus* shows the minimum zone of inhibition ( $15.5\pm 2.0$ ) in case of ethanol extract.

**Keywords:** phytochemicals, antibacterial, *Musa acuminata*, banana peel

### Introduction

*Musa acuminata* (banana) is a most important food crop in our country. It is developed in various countries and grown in 122 countries. It is available in our country. Banana peel extract contain in many types of vitamin viz -vitamin B6, vitamin C, vitamin E and malic acid. Mainly peel is the waste part of various fruit. But the banana peel have some antibacterial activity. In case of commercial application, peels might be due to their unknown benefit. The potential application of banana peel depends on it's chemical

composition. Fatty acids are present in the banana peel extract and it responsible for the antibacterial activity of the *Musaacuminata*. For this study, *Escherichia coli*, *Bacillus subtilis*, *Staphylococcus aureus*, *Klebsiella pneumoniae*, *Pseudomonas aeruginosa*, *Salmonella enteritidis* of this bacterial culture are used and to know the antibacterial activity. Methanol, ethanol and aqueous solvents are used. 100 mg/ml, 50mg/ml, 25mg/ml and 12.5mg/ml concentration are done in aqueous, ethanol and methanol extract and shows the zone of inhibition in each extracts.



Fig 1: *Musa acuminata* plant

## Material and method

### Collection of plant material

We are selected the fruit *Musa acuminata* for this study to know the antibacterial activity and phytochemical analysis. The fruit *Musa acuminata* was collected from our garden

beside our home at Kotalpara village. This specimen was identified in our Microbiology Department, Champadanga, Hooghly. After identified this fruit, peels are collected from the banana fruit.



**Fig 2:** *Musa acuminata* peels extract

### Preparation of the peel extract

At first, the collecting peels are washed in well with the hot water and cold water. Then it is dried in air. The dried peels are grinded in the blender machine. The mixture is collected in a closed jar for long storage.

### Preparation of aqueous extract

5g of peels powder is added in the 25 ml of distilled water and made aqueous solution. This solution is made in a conical flask. The conical flask is bounded with tissue paper and rubber band. Then, some pore are done in the surface of the tissue paper which that air are passes. The solutions are kept in room temperature at 37°C for 24 hours.

### Preparation of ethanol extract

5g of peels powder is added in 25 ml of ethanol and made ethanol extract. This extract is made in a conical flask. The conical flask is bound with tissue paper and rubber band. Some pores are done for air passes. Then it is kept in 37°C room temperature for 24 hours.

### Preparation of methanol extract

5g of peel powder is added in the 25 ml of methanol in a conical flask. The conical flask is covered with the tissue paper and rubber band. On their surfaces some pore are done for air passing. Then this flask is kept in room temperature at 37°C for 24 hours.

### Collection of test microorganisms

The test microorganisms are *Bacillus subtilis* (MTCC-441), *Staphylococcus aureus* (MTCC-737), *Klebsiella pneumonia* (MTCC-432), *Pseudomonas aeruginosa* (MTCC-424), *Escherichia coli* (MTCC-443), *Salmonella enteritidis* (MTCC -98) are collected. Those bacteria are grows on Muller Hinton ager and nutrients agar.

### Preparation of different concentration

100 mg/ml, 50mg/ml, 25mg/ml and 12.5mg/ml concentration are used for this study. 1g of peel mixture is measured and it added in 10 ml of DMSO and made 100 mg/ml concentration. This is called stock solution. For 50 mg /ml concentration, 1 ml stock solution and 1 ml of DMSO are taken in a appendops tube. 0.50 ml stock solution is added in 1.50 ml DMSO and prepare 25 mg/ml concentration. For 12.5 mg/ml concentration, 0.25 ml stock is added with 1.75 ml DMSO. Each concentration are kept in a 2ml volume of appendops tube. 6 nutrients ager plate are prepared and then it is inoculated with bacterial culture. 3 plates are taken for 1 bacterial culture and another 3 plates are taken for another bacterial culture. Well are done in each ager plate with the borar. 100 mg/ml and 12.5 mg/ml concentration are marked in two separate inoculated plate and given the concentration in the well from the particular tube. Another two inoculated plate are taken and then it is marked with 50 mg/ml and 25 mg/ml concentration and given concentration in the well from the particular tube. So, four plates are inoculated and given concentration. DMSO is given in another two plate.



**Fig 3:** A. Antibacterial activity of aqueous extract on *Klebsiella pneumoniae* b. Antibacterial activity aqueous extract on *Pseudomonas aeruginosa*

**Result**

Result obtained from this research

work are summarized in the tables below.

**Table 1:** Antibacterial activity of the *Musa acuminata* in different bacteria for aqueous extract in different concentration

Test microorganism	Concentration(mg/ml)			
	100 mg/ml	50 mg/ml	25 mg/ml	12.5 mg/ml
<i>Escherichia Coli</i>	27.25±2.0	22.25±2.0	18.25±2.0	17.25±2.0
<i>Bacillus Subtilis</i>	28.5±3.0	27.25±2.0	21.25±2.0	18.5±3.0
<i>Staphylococcus aureus</i>	36.1±3.0	27.4±3.0	23.7±2.0	20.0±2.0
<i>Klebsiellapneumoniae</i>	32.3±2.0	28.2±3.0	23.0±2.0	19.5±2.0
<i>Pseudomonas aeruginosa</i>	34.5±2.0	31.7±2.0	26.0±2.0	21.2±3.0
<i>Salmonella enterotitis</i>	29.0±2.0	26.2±3.0	23.1±2.0	19.4±3.0

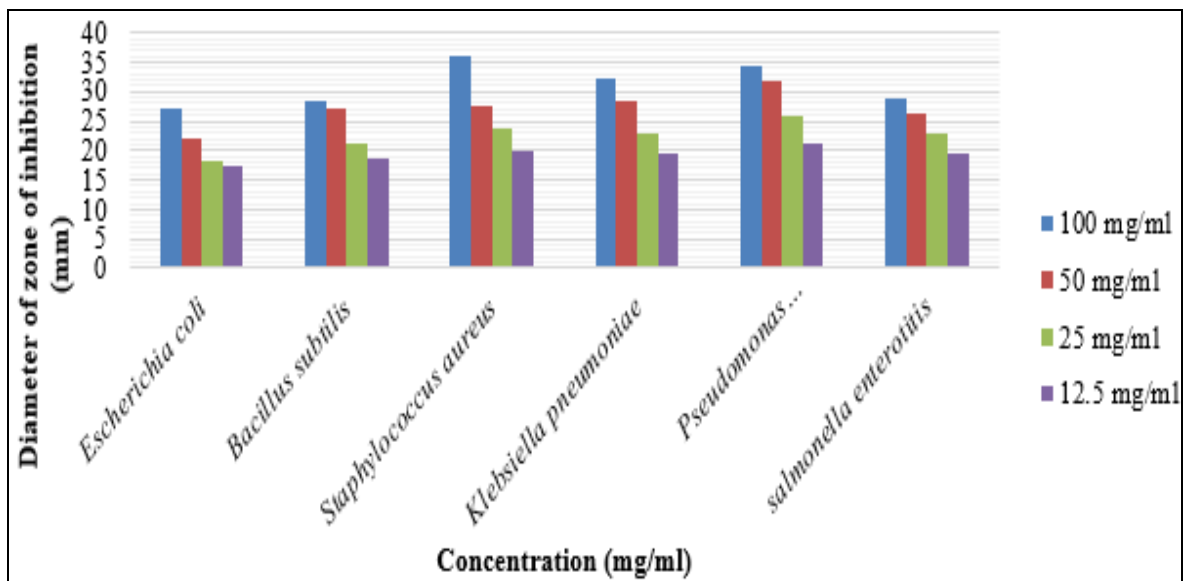


**Fig 4**

The antibacterial activity of *Musa acuminata* shows the highest zone of inhibition against *Pseudomonas aeruginosa*

and the lowest zone of inhibition against *Staphylococcus aureus*.

**Table 2:** The antibacterial activity (inhibition zones in cm) of the peel extract of *musa acuminata* against different bacteria for ethanolic extract in different concentration

Test microorganism	Concentration(mg/ml)			
	100 mg/ml	50 mg/ml	25 mg/ml	12.5 mg/ml
<i>Escherichia Coli</i>	31.6±3.0	27.5±2.0	23.0±2.0	18.2±2.0
<i>Bacillus Subtilis</i>	33.5±2.0	30.1±2.0	26.4±2.0	21.7±2.0
<i>Staphylococcus aureus</i>	29.4±2.0	25.7±2.0	21.3±2.0	18.0±2.0
<i>Klebsiellapneumoniae</i>	32.9±2.0	30.7±3.0	26.1±2.0	21.6±2.0
<i>Pseudomonas aeruginosa</i>	27.6±2.0	22.4±2.0	20.4±2.0	17.5±2.0
<i>Salmonella enteritidis</i>	30.0±2.0	27.4±3.0	24.5±2.0	18.7±3.0

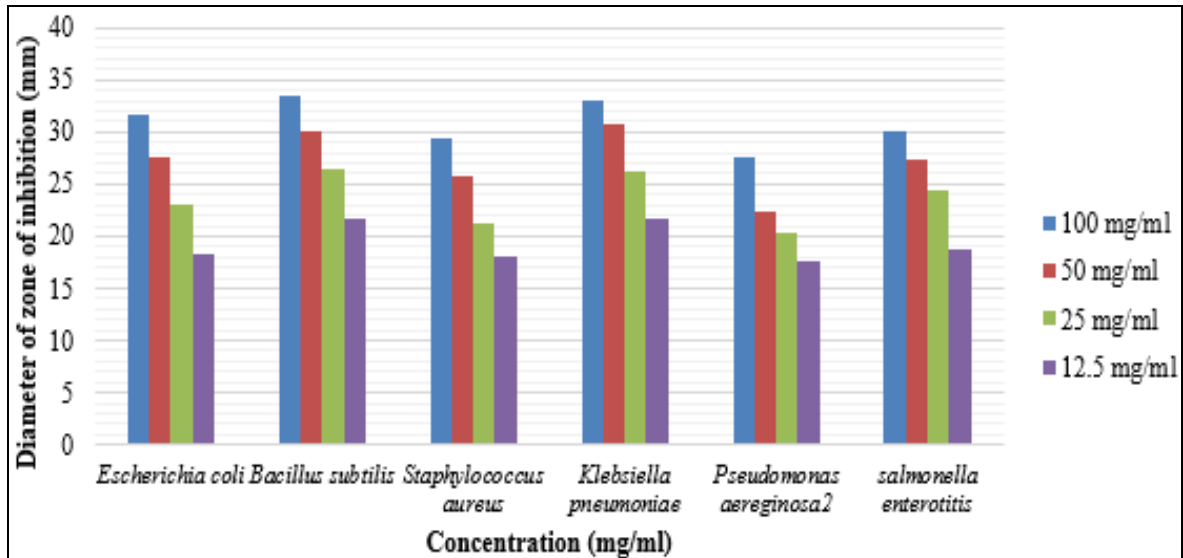


**Fig 5**

*Pseudomonas aeruginosa* shows the maximum zone of inhibition and *Escherichia coli* shows the minimum zone of inhibition.

**Table 3:** The antibacterial activity (inhibition zones in cm) of the peel extract of *musa acuminata* against different bacteria for methanolic extract in different concentration

Test microorganism	Concentration(mg/ml)			
	100 mg/ml	50 mg/ml	25 mg/ml	12.5 mg/ml
<i>Escherichia coli</i>	26.1±2.0	22.3±2.0	20.4±2.0	16.6±2.0
<i>Bacillus Subtilis</i>	29.3±2.0	26.7±2.0	23.4±3.0	19.0±2.0
<i>Staphylococcus aureus</i>	25.0±2.0	21.2±2.0	18.7±2.0	15.5±2.0
<i>Klebsiellapneumoniae</i>	29.4±2.0	25.0±2.0	21.5±2.0	16.2±2.0
<i>Pseudomonas aeruginosa</i>	31.7±2.0	24.5±2.0	20.3±3.0	17.0±2.0
<i>Salmonella enteritidis</i>	28.5±2.0	25.9±3.0	21.4±2.0	18.7±3.0

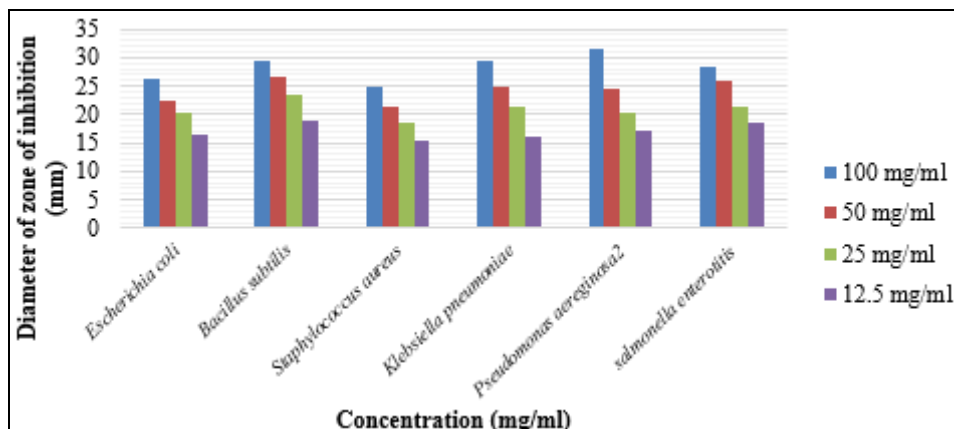


**Fig 6**



*Pseudomonas aeruginosa* shows the maximum zone of inhibition ( $31.7 \pm 2.0$ ) and *Staphylococcus aureus* shows the minimum zone of inhibition ( $15.5 \pm 2.0$ ).

### Discussion

Banana is cheap fruit and readily available that is consumed by different people around the world. Because it has high nutritional properties. In recent time, it had been reported that this peel is not altogether useless as many of the bioactive plant components reside in them. Therefore, the project work was done to ascertain the antimicrobial efficacy of banana peels against clinical isolates. From the phytochemicals analysis of ethanol and aqueous extracts of banana peel, we know that flavonoids, terpenoids, quinines and alkaloids are present in both ethanol and aqueous solvents, and tannins, saponins are absent in both solvents. Flavonoids are known as effective antimicrobial substances against a wide array of microorganisms. It is synthesized by the plant in response to microbial attack. Their activity is probably due to their ability to react with extracellular and soluble proteins and to complex with bacterial cell walls leading to the death of the bacteria. Tannins have various physiological effects like anti-irritant, antimicrobial and antiparasitic effects. Tannins containing plants are used to treat nonspecific diarrhoea, inflammation of the mouth and throat and slightly injured skins. From this research work, we found that which bacteria have a good antibacterial activity. We followed that *Staphylococcus aureus* is a susceptible bacterial species and its zones of inhibition is  $36.1 \pm 3$  in 100 mg/ml for aqueous extract. So, it shows a good antibacterial activity in highest concentration for aqueous extract. And lowest concentration (12.5 mg/ml) the zone of inhibition is  $20.0 \pm 2$ . *Pseudomonas aeruginosa* and *Klebsiella pneumoniae* is very sensitive in aqueous extract. In case of ethanol extract, *Bacillus subtilis* shows a good antibacterial activity in highest concentration. So, the range of zone inhibition is  $33.5 \pm 2.0$  in 100 mg/ml concentration. *Klebsiella pneumoniae* and *Escherichia coli* is very sensitive in ethanol extract and range of zone of inhibition are  $32.9 \pm 2.0$  and  $31.6 \pm 3.0$  in 100 mg/ml concentration. In methanolic extract, *Pseudomonas aeruginosa* the range of zone inhibition is  $31.7 \pm 2.0$  in 100 mg/ml. So, it shows a good antibacterial activity. *Bacillus subtilis* and *Klebsiella pneumoniae* is very sensitive in methanolic extract. The zone of inhibition are  $29.3 \pm 2.0$  and  $29.4 \pm 2.0$  in 100 mg/ml.

### Phytochemicals estimation

The peel extract of *Musa acuminata* were analysed for alkaloids, tannins, glycosides, steroids, flavonoids, saponins, volatile oil and resins using standard procedures.

### Test for Glycosides

To 1 ml of extract was taken, then it is mixed with 2 ml of acetic acid and then cooled in an ice bath at  $4^{\circ}\text{C}$ . 1 ml of sulfuric acid is added in drop wise to this mixture. An oil layer formation is seen on top of the solution that indicates the presence of glycosides.

### Test for alkaloids

1 ml of 1% HCL was added in 3 ml of the extract. Then, the mixture is treated with few drops of Meyer's reagent. If a creamy white precipitation is appeared so, we can identify the presence of alkaloids.

### Test for saponins

5 drops of olive oil was mixed in 2 ml of plant extract and this mixture shaken vigorously. A stable emulsion is formed that indicates the presence of saponins.

### Test for tannins

2 drops of 5% ferric chloride was added in 1 ml of the plant extract. A dirty green precipitate is appeared which indicated the presence of tannins.

### Test for flavonoids

To 1 ml of the extract was mixed in 3 drops of ammonia solution followed by 0.5 ml of concentrated HCL. A pale brown colour is formed in the mixture that indicated the presence of flavonoids.

### Test for steroids

1 ml of concentrated tetraoxo sulphate (vi) acid was added in 1 ml of the plant extract. A red colouration is formed that confirmed the presence of steroids.

### Test for Resins

To 5 ml of the extract was added in 5 ml of copper acetate solution. The mixture was shaken vigorously and allowed to separate. A reddish-brown precipitation is made and it indicates the presence of resins.

**Table 4:** Phytochemical analysis of ethanol and aqueous extracts of *Musa acuminata* peel

Phytochemicals	Solvents		
	Ethanol	Aqueous	Methanol
Flavonoids	+	+	+
Tannins	-	-	-
Terpenoids	+	+	+
Saponins	-	-	+
Quinines	+	+	-
Alkaloids	+	+	+

### Conclusion

In case of the ethanolic and aqueous extract of banana peels, the antibacterial properties have found to be considerably high in this research work. The test organisms were highly resistant to antibiotics and they were found to be susceptible in the banana peel extract. A yellow banana peel has a good antibacterial activity against both gram (+) and gram (-) and it is also known as a good antibacterial agent. We conclude that banana peel has a good antibacterial activity in public health. *Musa acuminata* the wild species of banana is a plant of the tropical and subtropical regions. All parts of the plant including fruit, peels, leaves, roots are used in the treatment of many diseases in traditional medicine. The pharmacological activities of *Musa acuminata* include antioxidant, antidiabetic, anticancer and antimicrobial especially anti-HIV activity. From phytochemicals study, we can know the traditional use of different parts of *Musa acuminata* in various diseases.

### References

- Lucky Egbuomwan, Ikechukwu Bright Jacob, Gift Onoriode Onodje, Chukwuka Emeka Patrick. "Evaluating the antibacterial activity of *Musa acuminata* (Banana) fruit peels against multi drug resistant bacterial isolates?". International journal of Novel research in life sciences, 2018;5(3):26-31.

2. Chanda S, Baravalia Y, Kaneria M, Rakholiy K. Fruit and vegetable peels-strong natural source of antimicrobics? *Journal of agricultural and food chemistry*2010:60121-126.
3. Nadkarni KM. *Indian MateriaMedica*, Vol-I, Bombay Popular Prakashan, second edition, reprint 1995, 595, 1927.
4. Mokbel Matook Saif, Hashinaga Fumio. Antimicrobial activity of Banana (Musa, AAA cv. Cavendish) Fruits Peel, *American Journal of Biochemistry and Biotechnology*,2005:1(3):125-13.
5. Fagbemi Josephine Ferdinand, Ugoji Esther, Adenipekun Tayo, Adelowotan Omotoyin. Banana (Musa sapientum L.), lemon grass (Cymbopogon citratus S.) and turmeric (Curcuma longa L.) on pathogens, *African Journal of Biotechnology*, 2009:8(7):13-19.
6. RathiBadal S, Thakurdesai Prasad A, Bodhankar Subhash L. Antimicrobial activity of aqueous extract of musasaientum flowers, *Indian J. nat.prod*, 2003:22(1):14.
7. Mukherji PK. *Quality Control of Herbal Drugs*, Business Horizon Publication, 1st, 2001, 183-219.
8. Kokate CK. *Practical Pharmacognosy*, Vallabh Prakashan, Delhi., 4th Edition, 1997, 107-111.8.
9. Dwivedi Sumeet, Dwivedi Sangeeta, Patel PC. Formulation, evaluation and antimicrobial activity of herbal lipstick, In *Recent Advances in Prospects and Potential of Medicinal Plants*, Ed. S. N. Dwivedi, Gayatri Publication, Rewa, 2009, 39-43.
10. Rabe T, Van J. Antibacterial activity of South African plants used for medicinal purposes. *J Ethnopharmacol*, 1997:56:81-87.
11. Fapohunda SO, Mmom JU, Fakeye F.? Proximate analyses, phytochemical screening and antibacterial potentials of bitter cola, cinnamon, ginger and banana peel?. *Academic Arena*,2012:4(8):8-15.
12. Idris S. Ndukwe GI, Gimba CE.? Preliminary phytochemical screening and antimicrobial activity of seed extract of persea Americana (avocado pear)". *Bayero Journal of Pure and Applied Science*, 2009(2)1:173-176.
13. Mumtaz J, Warsi MK, Khatoon F.? Concentration influence on antimicrobial activity of banana blossomextract-incorporated chitosan-polyethylene glycol (CS-PEG) blended film?. *Journal of Chemical and Pharmaceutical Research*,2010:2(5)373-378.
14. National Committee for Clinical Laboratory Standards NCCLS,? *Methods for Dilution antimicrobial susceptibility tests for bacteria that grow aerobically: approved standards- fifth edition*. NCCLS document M7-A5. NCCLS: Wayne, PA, USA, 2000.
15. Padam BS, Tin HS, Chye FY, Abdullah MI.? Antibacterial and antioxidative activities of the Various Solvent Extracts of Banana (Musa paradisiaca cv. Mysore) Inflorescences?. *Journal of Biological Sciences*,2012:12(2) 62-73.
16. Rao NM, Prasad SHKR, Jyothirmayi N.? Efficacy of Ripened and Unripened Fruit Extracts of Musa Paradisiaca L. (Bontha Cultivar) Against Human Pathogens?. *International Journal of Pharmacy and Pharmaceutical Sciences*,2012:4(1):455-460.
17. Sathya M.? Assaying the Antioxidant Activity of Banana Peel?. *American Journal of Biochemistry and Molecular Biology*,2014:6(5)1-6.
18. Sumathy V, Lachumy JS, Zakaria Z, Sasidharan S.? "*In Vitro* Bioactivity and Phytochemical Screening of Musa Acuminata Flower". *Pharmacologyonline*,2011:2:118-127,
19. Venkatesh VK, Kumar KG, Pradeepa K, Kumar SSR, Vijay K. "Anthelmintic Activity of Musa paradisiacal (L.). Puttabale". *International Journal of Pharmaceutical Sciences and Drug Research*,2013:5 (2)67-69.
20. Westendarp H. "Effects of tannins in animal nutrition". *Dtsch Tierarztl Wochenschr*, 2006:113(7):264-268.
21. Zafar IM, Saleha A, Mazumda MD, Hoque E, Sohail RM. Antimicrobial and Cytotoxic Properties of Different Extracts of Musa Sapientum L. Subsp Sylvestries". *International Research Journal of Pharmacy*,2011:2(8)62-65.



# Seasonal impact on the relationship between land surface temperature and normalized difference vegetation index in an urban landscape

Subhanil Guha & Himanshu Govil

To cite this article: Subhanil Guha & Himanshu Govil (2020): Seasonal impact on the relationship between land surface temperature and normalized difference vegetation index in an urban landscape, Geocarto International, DOI: [10.1080/10106049.2020.1815867](https://doi.org/10.1080/10106049.2020.1815867)

To link to this article: <https://doi.org/10.1080/10106049.2020.1815867>



Accepted author version posted online: 28 Aug 2020.  
Published online: 16 Sep 2020.



Submit your article to this journal [↗](#)



Article views: 14



View related articles [↗](#)



View Crossmark data [↗](#)



Citing articles: 1 View citing articles [↗](#)



# Seasonal impact on the relationship between land surface temperature and normalized difference vegetation index in an urban landscape

Subhanil Guha  and Himanshu Govil 

Department of Applied Geology, National Institute of Technology Raipur, Chhattisgarh, India

## ABSTRACT

The present study assesses the seasonal variation of land surface temperature (LST) and the relationship between LST and normalized difference vegetation index (NDVI) on different types of land use/land cover (LULC) in Raipur City of India using 119 Landsat images of pre-monsoon, monsoon, post-monsoon and winter seasons from 1988 to 2019. The results show that the highest LST is found in the bare lands and built-up areas, whereas the lowest LST is observed in the green vegetation. The LST-NDVI correlation is strong negative in the monsoon ( $-0.51$ ) and post-monsoon ( $-0.50$ ) seasons, moderate negative ( $-0.46$ ) in the pre-monsoon season and weak negative ( $-0.24$ ) in the winter season. The different LULC types largely influence the nature and strength of the LST-NDVI correlation. The correlation is strong negative ( $-0.60$ ) on green vegetation, moderate negative ( $-0.35$ ) on the built-up area and bare land and nonlinear on the water bodies.

## ARTICLE HISTORY

Received 16 March 2020  
Accepted 10 August 2020

## KEYWORDS

Landsat; land surface temperature (LST); land use/land cover (LULC); normalized difference vegetation index (NDVI)

## 1. Introduction

Thermal infrared (TIR) remote sensing has a huge impact on the land use/land cover (LULC) study in any natural or man-induced environment along with the visible and near-infrared (VNIR) and shortwave infrared (SWIR) remote sensing (Chen et al. 2006; Guha and Govil 2019; Alexander 2020). Land surface temperature (LST) is a major factor to assess the biogeochemical actions in the formation of land surface materials (Hao et al. 2016; Majumder et al. 2020). LST varies with the changes of tone, texture, pattern and association of the LULC types in any region (Hou et al. 2010). Generally, vegetation and water reduce the effect of LST, whereas a built-up area and bare earth surface enhance the effect of LST (Guha et al. 2018, 2019). Thus, a proper ecological planning and management system needs a sound knowledge and conception about LST and its relationship with various types of LULC (Li et al. 2017; Guha, Govil and Besoya 2020). Urban heat island and urban hot spots are a very common term in an urban environment and are indicated by the zone of very high LST inside the urban bodies (Guha et al. 2017). The most used spectral index in LST derivation is normalized difference vegetation index (NDVI) which is used in extracting green vegetation (Smith and Choudhury 1990; Yuan

et al. 2017; Guha, Govil, Dey, et al. 2020; Guha, Govil, Gill, et al. 2020). NDVI is directly used in the determination of land surface emissivity and thus is a significant factor for LST estimation (Carlson and Ripley 1997; Sobrino et al. 2004). The nature of LST-NDVI relationship is mainly inverse and it is regulated by several factors, such as dry or wet vegetation, the greenness of vegetation, air pollution, the moisture content in the air, heterogeneous man-made materials, dry or wet soil, etc. (Zhou et al. 2011; Qu et al. 2014).

Currently, the LST-NDVI relationship was constructed using TIR remote sensing technology (Li et al. 2016; Wen et al. 2017). LST-NDVI relationship was applied in most of the thermal remote sensing studies those were conducted with temporal discrete data sets on the urban environment, e.g. Shanghai (Yue et al. 2007), Bangkok (Estoque et al. 2017), Melbourne (Jamei et al. 2019), Shiraz (Fatemi and Narangifard 2019), Raipur (Guha and Govil 2020). In Monte Hermoso of Argentina, the LST-NDVI correlation was analyzed for urban planning (Ferrelli et al. 2018). Fewer studies are available on the long-term seasonal correlation among LST, NDVI and LULC in a tropical city. Thus, it is necessary to explore the seasonal LST-NDVI relationship in a tropical city.

A reverse relationship is built between LST and the concentration of green vegetation (Voogt and Oke 2003). Thus, NDVI is used as an important factor for determining LST in most of the LST retrieval methods (Gutman and Ignatov 1998; Goward et al. 2002; Govil et al. 2019; Govil et al. 2020a, 2020b; Guha and Govil 2020).

There are so many valuable research articles found on LST-NDVI relationships were conducted mainly in the Chinese landscape (Yao et al. 2017, 2018, Qu et al. 2018; Cui, Wang, Qu, Singh, Lai, Jiang, et al. 2019; Cui, Wang, Qu, Singh, Lai, Yao, et al. 2019; Gui et al. 2019; Yao et al. 2019; Qu et al. 2020; Yuan et al. 2020). Although some recent studies successfully analyzed the LST-NDVI correlation in some tropical Indian cities (Kumar and Shekhar 2015; Mathew et al. 2017; Singh et al. 2017; Mathew et al. 2018; Sannigrahi et al. 2018; Guha, Govil, Dey, et al. 2020; Guha, Govil and Diwan 2020; Guha, Govil, Gill, et al. 2020), the seasonal correlation analysis of LST and NDVI is rare. The variation of weather elements due to the seasonal changes has a great impact on the nature and strength of LST-NDVI correlation. Thus, to determine the characteristic features of seasonal variation of LST-NDVI correlation the Raipur City of India was selected as the location of this humid tropical city is not under any kind of severe climatic condition. Generally, the LST-NDVI correlation is negative on the tropical cities of similar environmental conditions of Raipur. But, the strength of the LST-NDVI relationship can change temporally, seasonally and spatially. The relationship is changed with time as the land surface materials change with time. The relationship also depends on the LULC types as vegetation, soil, water, or built-up area change the values of NDVI as well as LST. Different seasons also play a significant role in the LST-NDVI relationship as the growth of vegetation and increase of LST primarily depend on seasonal change. But, no specific conclusion can draw about the LST-NDVI correlation by using a small number of remotely sensed data or within a short duration of research. A strong conclusion on the LST-NDVI relationship can be drawn only after the analyses of the multi-temporal and multi-seasonal datasets. Thus, large Landsat datasets are necessary to obtain a reliable result on this relationship. The present study was an attempt to find the stable seasonal relationship between LST and NDVI by analyzing a large dataset of Landsat sensor for more than 30 years in a rapidly growing urban area for future environmental planning and management. The purpose of the study is to analyze the effect of different seasons and various LULC categories on estimated LST and LST-NDVI correlation.

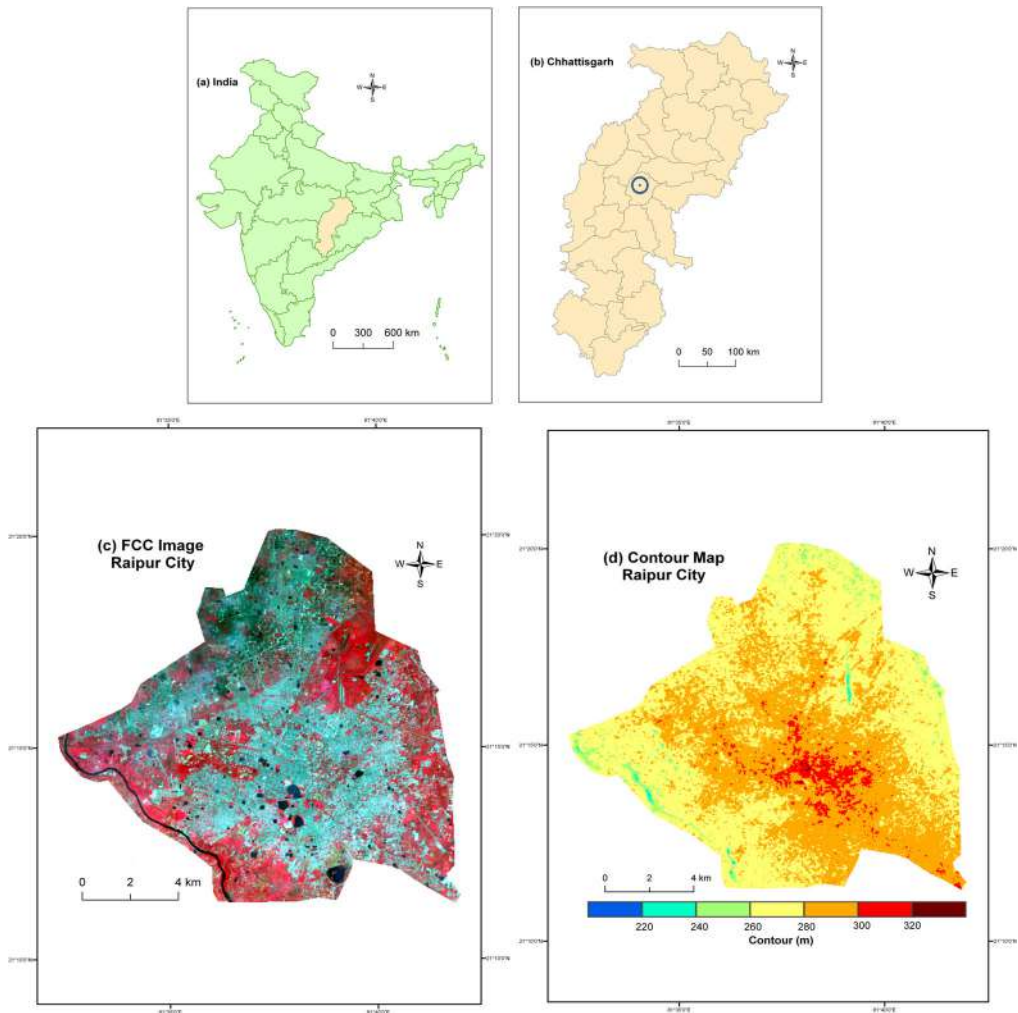


**Figure 1.** Location of Raipur City: (a) India, (b) Chhattisgarh, (c) FCC image of Raipur City, (d) Contour map of Raipur City.

## 2. Study area and data

Figure 1 shows the present study area (Raipur City of India) including map of India (Figure 1(a)), map of Chhattisgarh (Figure 1(b)), the false colour composite (FCC) image of the city (Figure 1(c)) and the contour map of the city (Figure 1(d)). Raipur is the most populous and the largest city of Chhattisgarh State of India. It is considered as one of the fastest-growing smart cities in India. The city extends from  $21^{\circ}11'22''\text{N}$  to  $21^{\circ}20'02''\text{N}$  and from  $81^{\circ}32'20''\text{E}$  to  $81^{\circ}41'50''\text{E}$  with an average elevation of 219–322 m. The total area of the city is  $165\text{ km}^2$  (approximately).

The area is under a tropical wet and dry climate with four typical seasons, i.e. pre-monsoon, monsoon, post-monsoon and winter (Source: India Meteorological Department (IMD)). A 30 years climatic data has been provided in Table 1 (Source: IMD). Pre-monsoon season extends from March to May. At that time weather conditions remain hot and dry. June to September (rainy months) is significantly considered under the monsoon season. The post-monsoon months (October and November) are characterized by

**Table 1.** Climate data for Raipur City (1981–2012) (Source: IMD).

Weather elements	January	February	March	April	May	June	July	August	September	October	November	December
Maximum temp (°C)	31.5	34.8	39.8	43.2	45.2	44.4	36.1	33.7	34.4	37.7	32.5	30.8
Minimum temp (°C)	8.6	11.3	15.7	19.7	22.2	21.6	21.2	21.7	21.3	16.8	11.6	8.9
Mean temp (°C)	20.7	23.4	28.9	32.3	34.7	31.7	27.8	27.2	27.8	27.6	23.1	20.3
Mean monthly rainfall (mm)	13.7	13.4	11.9	8.9	30.3	221.1	326.9	299.9	200.5	50.4	9.8	6.6
Average relative humidity (%)	47	35	28	22	27	52	76	79	73	59	51	49

low pollution, moderate temperature, and moisture content in plants and air, and a high percentage of green plants. In the winter season, cool and dry weather condition prevails in the city (Govil et al. 2019; Guha and Govil 2020). There are too many small patches of soil formed in the study area e.g. red sandy soil, Shallow black soil, red and yellow loamy soil, laterite soil, etc. The trees found in the study area are mostly tropical mixed deciduous types like bamboo, sal, teak, mahua, tendu, haura, etc. The total population of Raipur is 1,010,433 in which 518,611 are male and 491,822 are female (Source: Census of India 2011). The city has a widely diverse population that migrated from the different parts of the country. In the industrial sectors, the city achieves an exponential growth rate over recent years. Some basic and heavy industries (iron and steel, engineering and automobile) industries are developed along the periphery of the city. Some initial steps of social forestry are also being practiced along with the roadside and residential colonies that control the effect of LST in a certain range. There is also some government and private tree planting projects have been started to make the city green and less polluted.

A total of 119 Landsat satellite data of different sensors from 1988 to 2019 were selected and freely collected from the United States Geological Survey (USGS) Data Centre. These satellite images were taken between 10th and 25th day of each and every month to obtain the minimum range of deviation in LST values. Moreover, only a single data can obtain between 10th and 25th day of any month due to the 16 days temporal resolution of Landsat satellite sensors. Landsat 8 Operation Land Imager (OLI) and Thermal Infrared Sensor (TIRS) dataset have two TIR bands (bands 10 and 11). The TIR band 10 data (100 m resolution) was recommended for the present study due to better-calibrated certainty (Barsi et al. 2014). The TIR band of OLI/TIRS, TM and ETM+ data were resampled to 30 m × 30 m pixel size by the USGS Data Centre using cubic convolution method.

### 3. Methodology

NDVI calculation needs NIR and red bands, generation, while LST derivation needs red, NIR and TIR bands. In this study, the derived LST and NDVI of same season and same year were combined, e.g. the TM data of 21 March 2004, 22 April 2004 and 24 May 2004 – these three images were combined to obtain the final product of pre-monsoon image for 2004. If there was only one image found for a single season of a particular year, only this particular image was selected as the representative of the corresponding season of this particular year. Following these steps, all the combined images for four particular seasons of different years were generated. The following methods have been applied to perform the entire research work.

#### 3.1. Image pre-processing

The following steps are used for the atmospheric correction of Landsat data:

- i. Conversion of digital number (DN) into spectral reflectance:

$$\rho\lambda = M\rho XQcal + A\rho \quad (a)$$

where  $\rho\lambda$  is the spectral reflectance at top-of-atmosphere (TOA) without correction for solar angle (Unit less),  $Qcal$  is the level-1 pixel value in DN,  $M\rho$  is the reflectance multiplicative scaling factor for the VNIR and SWIR bands,  $A\rho$  is the reflectance additive scaling factor for the VNIR and SWIR bands.

- i. Correction of spectral reflectance at top-of-atmosphere ( $\rho\lambda$ ) with local sun elevation angle ( $\theta_s$ ):

$$\rho'\lambda = \rho\lambda / \sin(\theta_s) \quad (b)$$

For TIR bands of Landsat data, a similar calibration equation is used:

$$L\lambda = MLXQcal + AL \quad (c)$$

where  $L\lambda$  is the spectral radiance at TOA,  $Qcal$  is the level-1 pixel value in DN,  $ML$  is the radiance multiplicative scaling factor for the TIR bands and  $AL$  is the radiance additive scaling factor for the TIR bands.

### 3.2. Retrieving LST from the TIR bands of Landsat TM, ETM+ and OLI/TIRS data

In this study, LST was retrieved by using the mono-window algorithm (Qin et al. 2001). The entire methodology requires the following equations. Equation (1) is used to convert the digital number (DN) of TIR band to spectral radiance (Markham and Barker 1985):

$$L_\lambda = 0.0003342 * DN + 0.1 \quad (1a)$$

$$L_\lambda = 0.067087 * DN - 0.06709 \quad (1b)$$

$$L_\lambda = 0.055375 * DN + 1.18243 \quad (1c)$$

where  $L_\lambda$  is the spectral radiance in  $W\ m^{-2}\ sr^{-1}\ mm^{-1}$ . Equations (1a), (1b) and (1c) were applied for Landsat 8 OLI/TIRS, Landsat 7 ETM+ and Landsat 5 TM data, respectively.

Equation (2) is used to convert the spectral radiance to at-sensor brightness temperature (Wukelic et al. 1989; Chen et al. 2006):

$$T_b = \frac{K_2}{\ln\left(\frac{K_1}{L_\lambda} + 1\right)} \quad (2)$$

where  $T_b$  is the at-sensor brightness temperature (Kelvin);  $K_2$  and  $K_1$  are calibration constants. The land surface emissivity  $\varepsilon_s$  is estimated using the NDVI thresholds method (Sobrino et al. 2001, 2004). The fractional vegetation  $F_v$ , of each pixel, is determined from the NDVI using the following equation (Carlson and Ripley 1997):

$$F_v = \left(\frac{NDVI - NDVI_{\min}}{NDVI_{\max} - NDVI_{\min}}\right)^2 \quad (3)$$

where  $NDVI_{\min}$  is the minimum value (0.2) of NDVI for bare soil pixel and  $NDVI_{\max}$  is the maximum value (0.5) of NDVI for healthy vegetation pixel.

$d\varepsilon$  is the geometric distribution effect for the natural surface and internal reflection. The value of  $d\varepsilon$  may be 2% for mixed and elevated land surfaces (Sobrino et al. 2004).

$$d\varepsilon = (1 - \varepsilon_s)(1 - F_v)F\varepsilon_v \quad (4)$$



where  $\varepsilon_s$  is soil emissivity;  $F_v$  is fractional vegetation;  $F$  is a shape factor (0.55) (Sobrino et al. 2004);  $\varepsilon_v$  is vegetation emissivity.

$$\varepsilon = \varepsilon_v F_v + \varepsilon_s (1 - F_v) + d\varepsilon \quad (5)$$

where  $\varepsilon$  is land surface emissivity. The value of  $\varepsilon$  is determined by the following equation (Sobrino et al. 2004):

$$\varepsilon = 0.004 \times F_v + 0.986 \quad (6)$$

Water vapour content is determined by the following equation (Yang and Qiu 1996; Li 2006):

$$w = 0.0981 \times \left[ 10 \times 0.6108 \times \exp \left( \frac{17.27 \times (T_0 - 273.15)}{237.3 + (T_0 - 273.15)} \right) \times RH \right] + 0.1697 \quad (7)$$

where  $w$  is water vapour content ( $\text{g}/\text{cm}^2$ );  $T_0$  is near-surface air temperature (Kelvin);  $RH$  is relative humidity (%). These parameters of the atmospheric profile are obtained from the Meteorological Centre, Raipur. Atmospheric transmittance is determined for Raipur City using the following equation (Qin et al. 2001; Sun et al. 2010):

$$\tau = 1.031412 - 0.11536w \quad (8)$$

where  $\tau$  is the total atmospheric transmittance.

Raipur City is located in the tropical region. Thus, the following equation has been applied to compute the effective mean atmospheric transmittance of Raipur (Qin et al. 2001; Sun et al. 2010):

$$T_a = 17.9769 + 0.91715T_0 \quad (9)$$

LST is retrieved from TM, ETM+ and OLI/TIRS satellite data by using the following equations (Qin et al. 2001):

$$T_s = \frac{[a(1 - C - D) + (b(1 - C - D) + C + D)T_b - DT_a]}{C} \quad (10)$$

$$C = \varepsilon\tau \quad (11)$$

$$D = (1 - \tau)[1 + (1 - \varepsilon)\tau] \quad (12)$$

where  $T_a$  is mean atmospheric temperature;  $T_s$  is LST;  $a = -67.355351$ ,  $b = 0.458606$ .

### 3.3. Extraction of different types of LULC by using NDVI

Various land surface biogeochemical controlling factors are used in determining various land surface features (Chen et al. 2006). NDVI is a vegetation index which is frequently used in LULC and LST related studies (Tucker 1979; Purevdorj et al. 1998; Mondal et al. 2011; Ke et al. 2015) as it clearly distinguishes healthy vegetation from dead vegetation based on the chlorophyll content present in the plants. The lower and the upper limits of NDVI are  $-1$  and  $+1$ , respectively. Generally, the positive value of NDVI indicates green vegetation.  $\text{NDVI} > 0.5$  shows dense coverage of green and healthy vegetation. NDVI is also used to extract other LULC types, e.g. water bodies, built-up areas and bare lands (Chen et al. 2006). Generally, the post-monsoon images decrease the level of air pollution and these images also increase the greenness of an area. Thus, the post-monsoon images are generally considered for LULC mapping. LULC maps were generated by the threshold values of NDVI (Chen et al. 2006).  $\text{NDVI} > 0.2$  indicates green plants, whereas  $\text{NDVI} < 0$  reflects water bodies. The intermediate values ( $0-0.2$ ) of NDVI indicate the bare soil or

built-up area. In this study, suitable threshold limits (Chen et al. 2006) were used to identify different categories of LULC, and the results were validated by the maximum likelihood classification.

## 4. Results and discussion

This section focuses on the spatiotemporal and seasonal variation of LST distribution and the LST-NDVI relationship. To achieve this aim, the results are given in four main subsections including (i) accuracy assessment for LULC classification; (ii) spatiotemporal change of LULC types; (iii) spatiotemporal and seasonal variation in LST distribution; and (iv) seasonal variation on LST-NDVI relationship.

### 4.1. Accuracy assessment for LULC classification

As mentioned above, the NDVI threshold-based LULC classification map of Raipur City was validated by maximum likelihood classification algorithm. The extracted LULC data using the NDVI threshold method is used as the reference data. The overall accuracy of the seven-year LULC classification was 91.11%, 95.56%, 88.89%, 94.44%, 91.11%, 88.89% and 94.44% in 1988, 1993, 1999, 2004, 2009, 2014 and 2019, respectively. The kappa coefficient for the seven-year classification was 0.86, 0.93, 0.80, 0.90, 0.85, 0.78 and 0.88 in 1988, 1993, 1999, 2004, 2009, 2014 and 2019, respectively. The kappa coefficient value of more than 0.75 indicates that the classification data and the reference data are compatible with each other (Nigatu et al. 2014). In the present study, the average overall accuracy and average kappa coefficient for seven different years are 92.06% and 0.86, respectively. Thus, the NDVI threshold method based LULC classification is significantly validated by the maximum likelihood classification method.

### 4.2. Spatiotemporal change of LULC types

The total area under different LULC categories has been shown in Table 2. Water bodies were decreased at an alarming rate (58% during the entire time) than green vegetation. Green vegetation was also decreased in a very significant amount (80.10 km<sup>2</sup>) from 1988 to 2019. On the other hand, the built-up area and bare land were increased at a very high rate (81.77 km<sup>2</sup> in 32 years) due to rapid land conversion.

In 1988, built-up areas and bare lands were mostly found in the middle part of the Raipur City. The northwest portion of the city was rapidly urbanized between 1988 and 2004 due to the conversion of urban vegetation into the built-up area. After 2004, the green areas were reduced at an alarming rate due to the large conversion of vegetation into the built-up area. Only the eastern and the south-western parts are covered by urban vegetation.

**Table 2.** Total area (km<sup>2</sup>) under different types of LULC in Raipur City from 1988 to 2019.

Date of acquisition	Green vegetation	Built-up area and bare land	Water bodies
19-October-1988	143.28	18.16	2.79
18-November-1993	131.62	30.33	2.28
11-November-1999	117.75	44.59	1.89
15-October-2004	112.41	49.68	2.14
13-October-2009	90.69	71.59	1.95
12-November-2014	81.63	81.28	1.32
10-November-2019	63.18	99.93	1.12

Steady and significant growth of the built-up area and bare land was noticed inside the city area during the full period of the study (12.17 km<sup>2</sup> between 1988 and 1993, 14.26 km<sup>2</sup> between 1993 and 1999, 5.09 km<sup>2</sup> between 1999 and 2004, 21.91 km<sup>2</sup> between 2004 and 2009, 9.69 km<sup>2</sup> between 2009 and 2014 and 18.65 km<sup>2</sup> between 2014 and 2019). On the other hand, the gradual decay of urban vegetation was also noticed during the study (11.66 km<sup>2</sup> between 1988 and 1993, 13.87 km<sup>2</sup> between 1993 and 1999, 5.34 km<sup>2</sup> between 1999 and 2004, 21.72 km<sup>2</sup> between 2004 and 2009, 9.06 km<sup>2</sup> between 2009 and 2014 and 18.45 km<sup>2</sup> between 2014 and 2019).

#### **4.3. Spatiotemporal and seasonal variation in LST distribution**

Table 3 shows a clear observation of seasonal change in the mean LST values. In this table, the mean LST of each image is shown. The mean LST of every month was also determined. Each month was categorized under a separate season. In this way, the mean LST for four different seasons were presented. The mean LST of pre-monsoon season for the whole period was estimated from the mean LST values of March (13 data), April (11 data) and May (17 data). Following the same procedure, the mean LST of monsoon, post-monsoon and winter seasons were also determined. Four multi-date images each from June and September were used to determine the mean LST of the monsoon season. The mean LST of post-monsoon was estimated by using the mean LST of 28 satellite data (13 from October and 15 from November). A total of 42 (11 from January, 15 from February and 16 from December) Landsat satellite data were used to quantify the mean LST of the winter season. The lowest mean LST (24.83 °C) and the highest mean LST (35.90 °C) was found in the winter and pre-monsoon seasons, respectively. The mean LST of monsoon and post-monsoon season was 30.87 °C and 26.48 °C, respectively. The highest and the lowest mean LST was noticed in April (38.79 °C) and January (23.01 °C), respectively. The mean LST was increased from 1988 to 2019.

The pre-monsoon season (Figure 2) reflects the highest mean LST during the study period followed by monsoon (Figure 3), post-monsoon (Figure 4) and winter (Figure 5) season. The northwest and southeast parts of the city (mainly built-up area and bare land) experience high LST. The area with high LST values corresponds to the area with low NDVI and vice-versa.

It is seen from Figure 2 that >90% area of the city was above 32 °C mean LST in the pre-monsoon season of 1992, 2001–02, 2004–05, 2008–11, 2013, 2016–17 and 2019. In the monsoon season of 2005, 2006 and 2009 have mean LST values more than the earlier or later years (Figure 3). The scenario was completely different in the post-monsoon (Figure 4) and winter season (Figure 5), where <10% area of the city was above 32 °C LST. Figure 6(a–c) presents the seasonal variation of LST distribution based on monthly and annual LST estimation. April (38.79 °C mean LST), May (36.65 °C mean LST), June (34.56 °C mean LST) and March (32.11 °C mean LST) – these four months have an average value of >30 °C mean LST throughout the entire period of study. February (27.88 °C mean LST), October (27.23 °C mean LST), September (27.18 °C mean LST) and November (25.83 °C mean LST) – these four months have an average value of 25–28 °C mean LST throughout the entire time. Only December (23.76 °C mean LST) and January (23.01 °C mean LST) months have an average value of <24 °C mean LST for the entire period. The highest average LST from 1988 to 2019 was found in the pre-monsoon season, followed by the monsoon, post-monsoon and winter season.

**Table 3.** Temporal and seasonal variation of mean LST from 1988 to 2019.

March	LST (°C)	April	LST (°C)	May	LST (°C)
1989-Mar-12	28.14	1990-Apr-16	40.87	1991-May-21	36.63
1990-Mar-15	30.96	1992-Apr-21	41.19	2002-May-11	40.92
1991-Mar-18	29.50	1995-Apr-14	34.63	2004-May-24	40.74
1992-Mar-20	32.84	2001-Apr-22	41.34	2005-May-11	38.72
2003-Mar-11	29.49	2002-Apr-25	38.85	2006-May-14	28.43
2004-Mar-21	36.48	2003-Apr-12	31.28	2007-May-17	36.20
2007-Mar-14	27.57	2004-Apr-22	36.80	2008-May-19	38.36
2009-Mar-19	33.79	2009-Apr-20	39.74	2009-May-22	33.20
2014-Mar-17	31.68	2010-Apr-23	40.63	2010-May-25	36.11
2015-Mar-20	32.83	2016-Apr-23	42.97	2011-May-12	39.80
2016-Mar-22	37.00	2017-Apr-10	38.37	2013-May-17	40.28
2017-Mar-25	37.06	Mean	38.79	2014-May-20	34.91
2018-Mar-12	30.09			2015-May-23	36.42
Mean	32.11			2016-May-25	37.22
				2017-May-12	33.33
				2018-May-15	31.42
				2019-May-18	40.21
				Mean	36.64
Mean LST value of pre-monsoon season is 35.90 °C					
June	LST (°C)	September	LST (°C)		
2005-Jun-12	38.66	1996-Sep-23	24.09		
2006-Jun-15	35.43	2001-Sep-21	26.13		
2009-Jun-23	33.05	2002-Sep-16	28.81		
2018-Jun-16	31.08	2014-Sep-25	29.67		
Mean	34.56	Mean	27.18		
Mean LST value of monsoon season is 30.87 °C					
October	LST (°C)	November	LST (°C)		
1988-Oct-19	28.86	1988-Nov-20	24.27		
1991-Oct-12	24.98	1989-Nov-23	25.16		
1992-Oct-14	24.61	1991-Nov-13	23.64		
1996-Oct-25	22.56	1993-Nov-18	24.47		
2001-Oct-15	30.12	1996-Nov-10	23.15		
2001-Oct-23	26.85	1999-Nov-11	29.16		
2004-Oct-15	27.56	2004-Nov-16	28.45		
2006-Oct-21	26.30	2005-Nov-19	26.72		
2009-Oct-13	27.10	2006-Nov-22	26.40		
2011-Oct-19	28.30	2008-Nov-11	27.38		
2015-Oct-14	27.61	2013-Nov-25	26.09		
2016-Oct-16	30.02	2014-Nov-12	23.47		
2018-Oct-22	29.01	2016-Nov-17	27.18		
Mean	27.22	2017-Nov-20	26.28		
		2019-Nov-10	25.60		
		Mean	25.83		
Mean LST value of post-monsoon season is 26.48 °C					
January	LST (°C)	February	LST (°C)	December	LST (°C)
1988-Jan-21	24.52	1989-Feb-24	28.31	1988-Dec-22	23.96
1990-Jan-10	24.42	1990-Feb-11	25.26	1992-Dec-17	22.34
1992-Jan-16	21.33	1991-Feb-14	23.98	1994-Dec-23	18.55
1993-Jan-18	23.41	1992-Feb-17	25.30	1995-Dec-10	21.49
1996-Jan-27	22.08	1993-Feb-19	28.42	2000-Dec-15	26.81
2005-Jan-19	22.08	2002-Feb-20	30.39	2002-Dec-21	27.09
2007-Jan-25	26.37	2004-Feb-18	26.64	2004-Dec-18	25.76
2009-Jan-14	17.15	2006-Feb-23	32.95	2006-Dec-24	23.35
2011-Jan-20	23.03	2009-Feb-15	31.01	2008-Dec-13	25.71
2015-Jan-15	23.49	2010-Feb-18	22.67	2009-Dec-16	23.59
2018-Jan-23	25.26	2015-Feb-16	29.75	2010-Dec-19	22.31
Mean	23.01	2016-Feb-19	24.60	2013-Dec-11	24.62
		2017-Feb-21	32.45	2016-Dec-19	24.60
		2018-Feb-24	31.05	2017-Dec-22	24.02
		2019-Feb-11	25.37	2018-Dec-25	21.17
		Mean	27.88	2019-Dec-12	24.74
				Mean	23.76
Mean LST value of winter season is 24.83 °C					

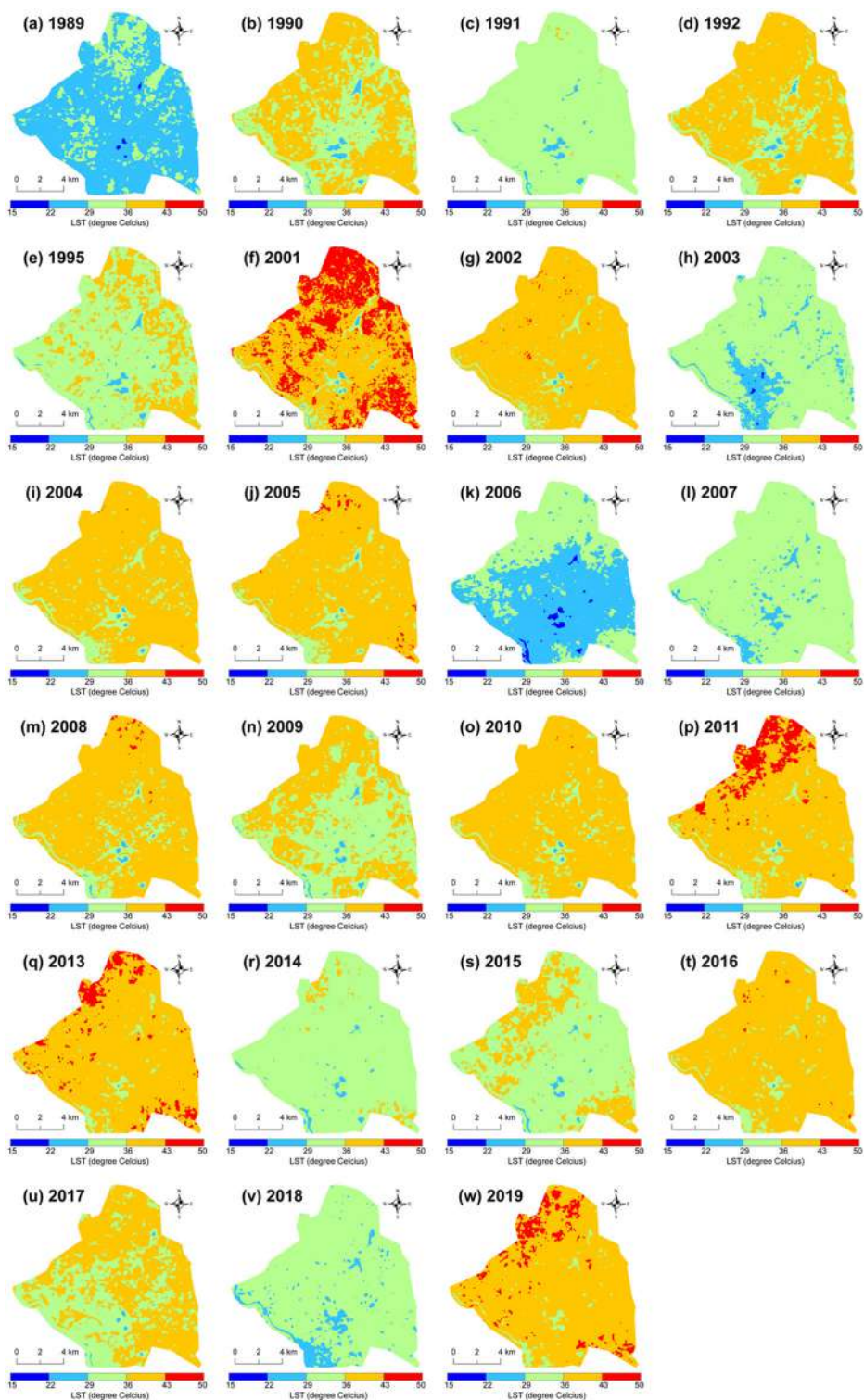


**Figure 2.** LST maps in pre-monsoon season: (a) 1989, (b) 1990, (c) 1991, (d) 1992, (e) 1995, (f) 2001, (g) 2002, (h) 2003, (i) 2004, (j) 2005, (k) 2006, (l) 2007, (m) 2008, (n) 2009, (o) 2010, (p) 2011, (q) 2013, (r) 2014, (s) 2015, (t) 2016, (u) 2017, (v) 2018, (w) 2019.

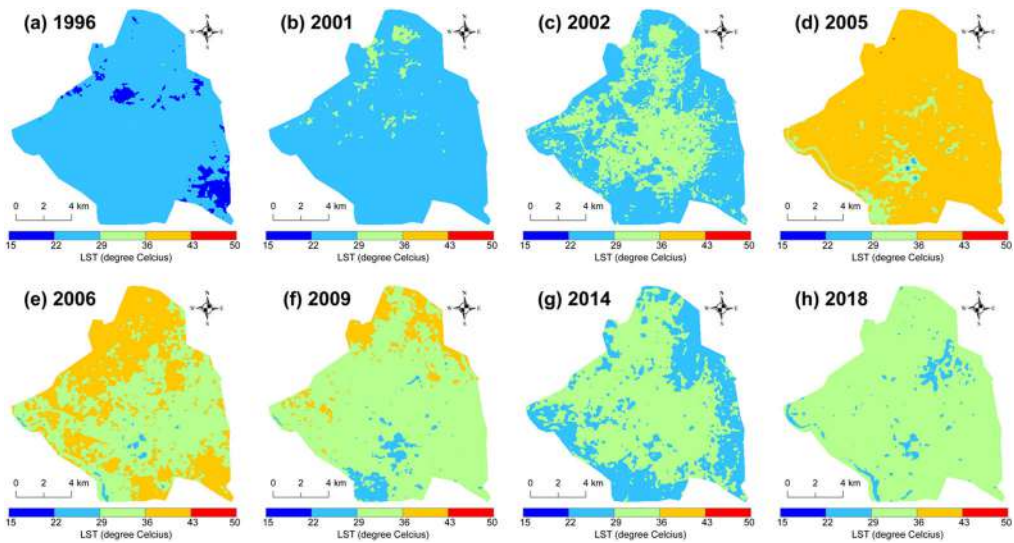


**Figure 3.** LST maps in monsoon season: (a) 1996, (b) 2001, (c) 2002, (d) 2005, (e) 2006, (f) 2009, (g) 2014, (h) 2018.

#### **4.4. Temporal and seasonal change in mean LST (°C) on different types of LULC**

Generally, the land of the study area was mainly converted into the built-up area or bare land from the other types of LULC, e.g. vegetation or water bodies. The percentage of the built-up area and bare land was increased, whereas vegetation and water bodies were decreased significantly. Land conversion has a great impact on the seasonal change of mean LST of the city. [Figure 7](#) presents a clear picture of the changing pattern of mean LST from 1988 to 2019. There was a significant change in LST observed in the converted LULC types ([Table 4](#)). The mean LST of the converted built-up area from the other land was increased (16.12 °C in the pre-monsoon season, 8.44 °C in monsoon season, 4.59 °C in post-monsoon season and 1.32 °C in winter season).

A moderate change in mean LST was also noticed in the unchanged LULC types. The unchanged built-up area and bare land have witnessed an increase in mean LST during the entire time (7.29 °C in the pre-monsoon season, 5.92 °C in monsoon season, 3.03 °C in post-monsoon season and 1.07 °C in winter season). The mean LST was also increased (7.47 °C in the pre-monsoon season, 5.79 °C in monsoon season, 3.25 °C in post-monsoon season and 0.93 °C in winter season) in the unchanged green vegetation during the period. An increase in mean LST was also found in the water bodies (6.36 °C in the pre-monsoon season, 5.80 °C in monsoon season, 2.78 °C in post-monsoon season and 0.91 °C in winter season). Hence, the results significantly indicate the trend of climate change. The maximum increase in mean LST for any type of LULC was noticed during the second (1993–1999) and third (1999–2004) phases of the entire time.

In Raipur, the high LST zones are mainly centralized in the northwest and southeast sectors. The northwest sector (Urla Industrial Complex, Birgaon, etc.) is a bare land where a group of factories and power plants are located along the Birgaon Main Road, Urla Road and Ring Road Number 2. Some of the well-known industrial factories are Maa Kudargarhi Steel, Akash Ispat Pvt. Ltd., Sambhav Warehouse, Jyoti Structures Ltd., Ganpati Ispat Pvt., Sheela Steel and Furnitures, Mahamaya Steel Industries Ltd., Balaji Corrugating Industries, Chhattisgarh Steel Products, Harshad Thermit Industries Pvt.

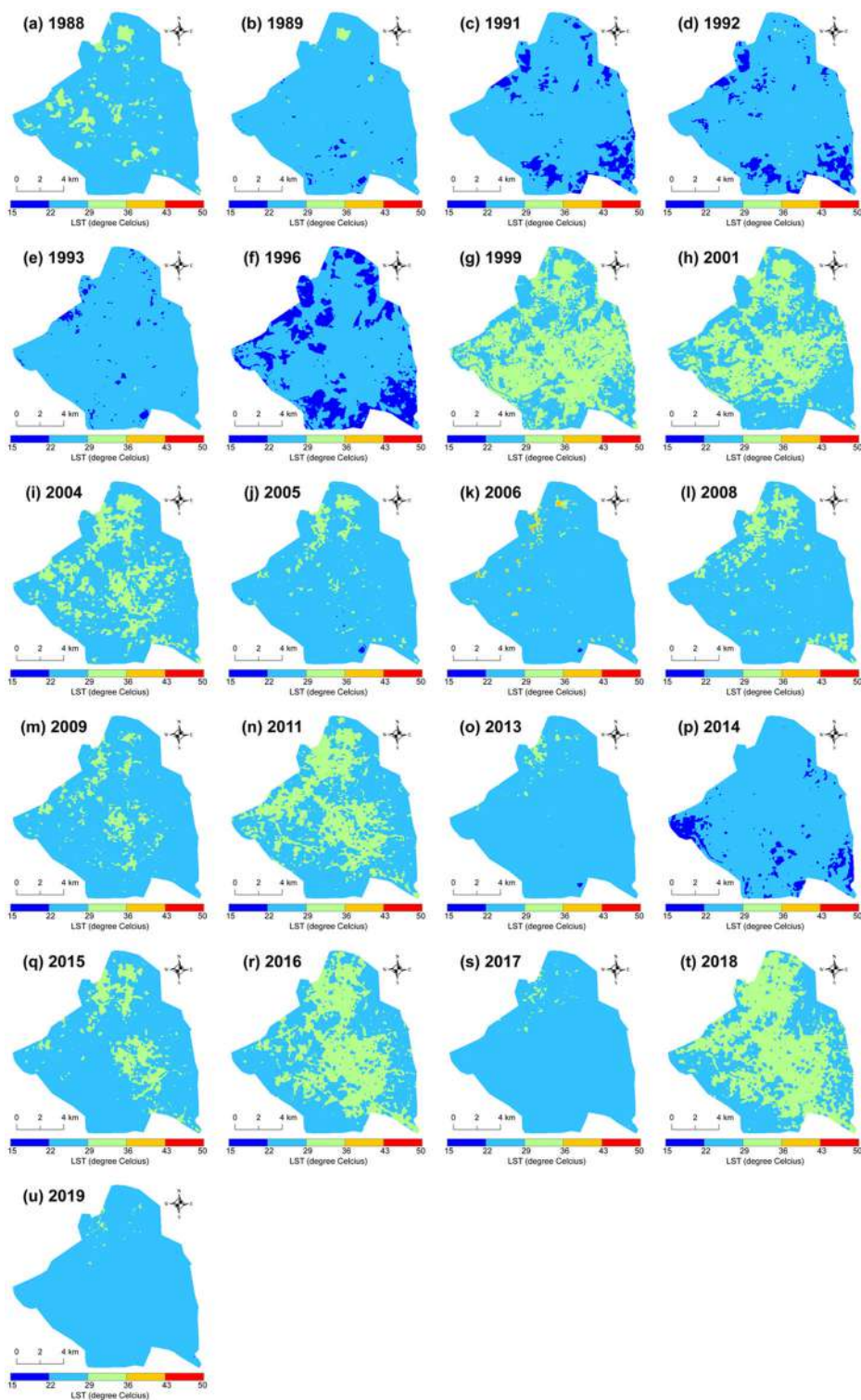


**Figure 4.** LST maps in post-monsoon season: (a) 1988, (b) 1989, (c) 1991, (d) 1992, (e) 1993, (f) 1996, (g) 1999, (h) 2001, (i) 2004, (j) 2005, (k) 2006, (l) 2008, (m) 2009, (n) 2011, (o) 2013, (p) 2014, (q) 2015, (r) 2016, (s) 2017, (t) 2018), (u) 2019.

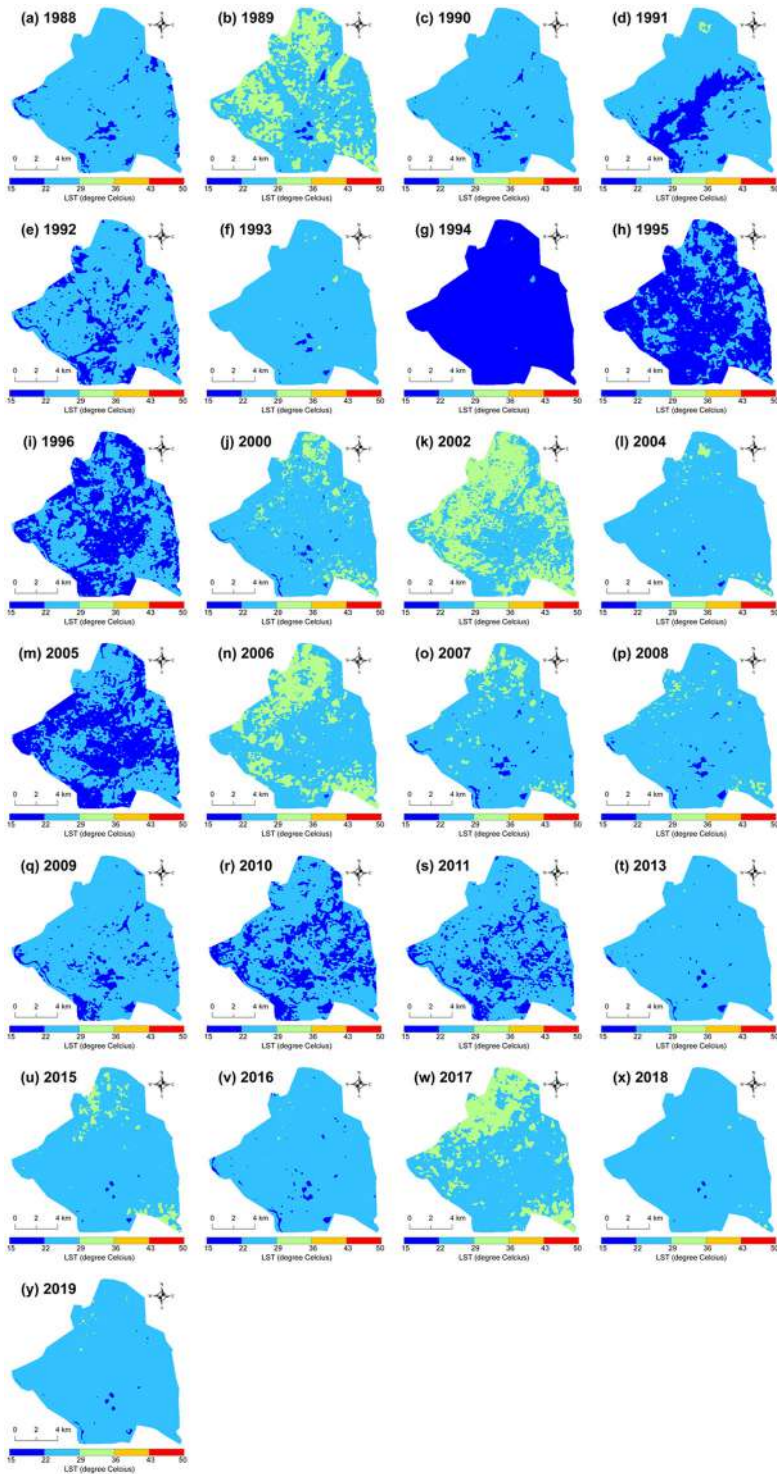


**Figure 5.** LST maps in winter season: (a) 1988, (b) 1989, (c) 1990, (d) 1991, (e) 1992, (f) 1993, (g) 1994, (h) 1995, (i) 1996, (j) 2000, (k) 2002, (l) 2004, (m) 2005, (n) 2006, (o) 2007, (p) 2008, (q) 2009, (r) 2010, (s) 2011, (t) 2013, (u) 2015, (v) 2016, (w) 2017, (x) 2018, (y) 2019.



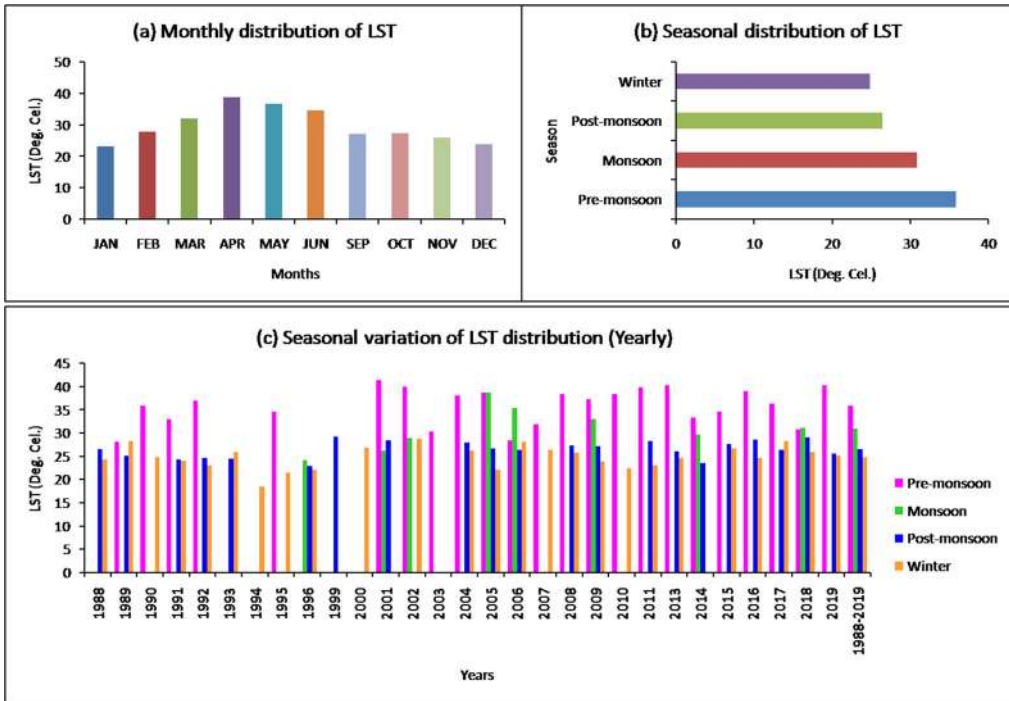


Figure 6. Variation of LST distribution (1988–2019): (a) monthly distribution, (b) overall seasonal distribution, (c) yearly seasonal distribution.

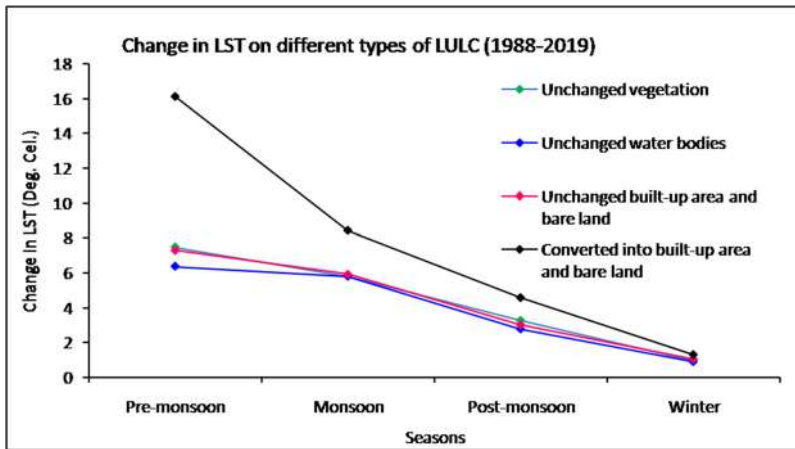


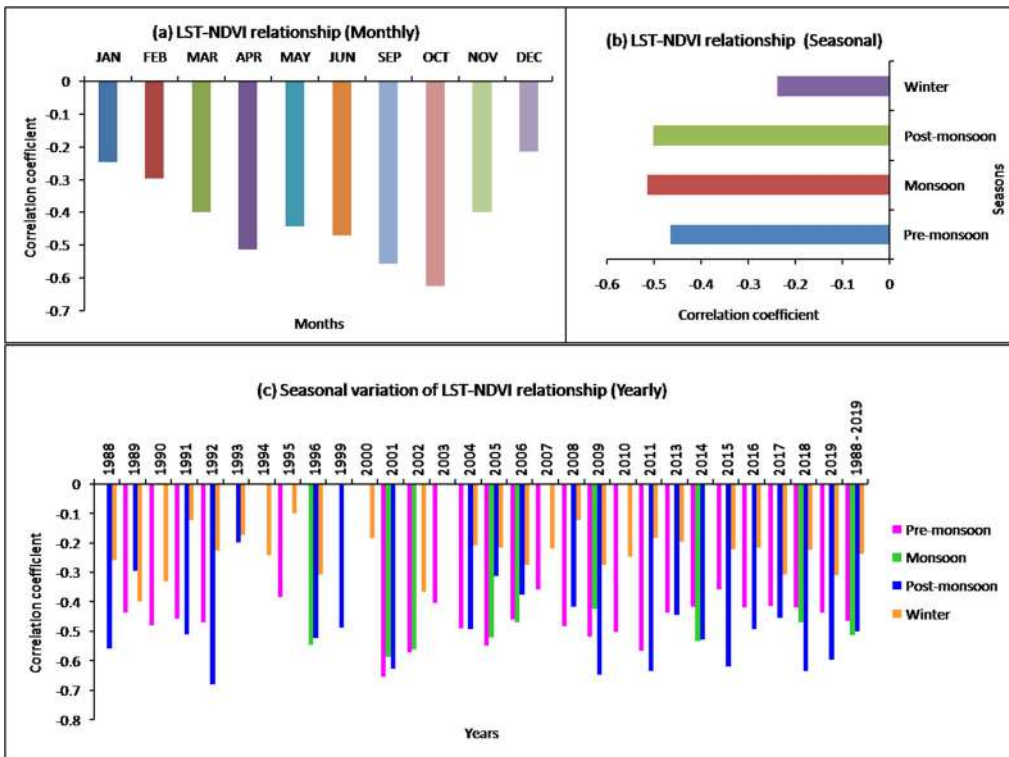
Figure 7. Change in mean LST on different types of LULC between 1988 and 2019.

Table 4. Seasonal variation in mean LST (°C) for different LULC during the study.

	Unchanged green vegetation	Unchanged water bodies	Unchanged built-up area and bare land	Other land changed into built-up area
Pre-monsoon	7.47	6.36	7.29	16.12
Monsoon	5.79	5.80	5.92	8.44
Post-monsoon	3.25	2.78	3.03	4.59
Winter	0.93	0.91	1.07	1.32

**Table 5.** Seasonal variation of LST-NDVI correlation coefficient from 1988 to 2019 (significant at 0.05 level).

March	LST (°C)	April	LST (°C)	May	LST (°C)
1989-Mar-12	-0.43	1990-Apr-16	-0.52	1991-May-21	-0.43
1990-Mar-15	-0.43	1992-Apr-21	-0.53	2002-May-11	-0.56
1991-Mar-18	-0.40	1995-Apr-14	-0.38	2004-May-24	-0.46
1992-Mar-20	-0.40	2001-Apr-22	-0.65	2005-May-11	-0.54
2003-Mar-11	-0.41	2002-Apr-25	-0.57	2006-May-14	-0.46
2004-Mar-21	-0.49	2003-Apr-12	-0.39	2007-May-17	-0.33
2007-Mar-14	-0.38	2004-Apr-22	-0.51	2008-May-19	-0.48
2009-Mar-19	-0.54	2009-Apr-20	-0.56	2009-May-22	-0.44
2014-Mar-17	-0.42	2010-Apr-23	-0.52	2010-May-25	-0.47
2015-Mar-20	-0.36	2016-Apr-23	-0.46	2011-May-12	-0.56
2016-Mar-22	-0.40	2017-Apr-10	-0.51	2013-May-17	-0.43
2017-Mar-25	-0.43	Mean	-0.51	2014-May-20	-0.41
2018-Mar-12	-0.37			2015-May-23	-0.34
Mean	-0.40			2016-May-25	-0.38
				2017-May-12	-0.29
				2018-May-15	-0.45
				2019-May-18	-0.43
				Mean	-0.44
Mean LST-NDVI correlation coefficient value of pre-monsoon season is -0.46					
June	LST (°C)	September	LST (°C)		
2005-Jun-12	-0.51	1996-Sep-23	-0.54		
2006-Jun-15	-0.46	2001-Sep-21	-0.58		
2009-Jun-23	-0.42	2002-Sep-16	-0.56		
2018-Jun-16	-0.46	2014-Sep-25	-0.53		
Mean	-0.47	Mean	-0.55		
Mean LST-NDVI correlation coefficient value of monsoon season is -0.51					
October	LST (°C)	November	LST (°C)		
1988-Oct-19	-0.69	1988-Nov-20	-0.41		
1991-Oct-12	-0.63	1989-Nov-23	-0.29		
1992-Oct-14	-0.68	1991-Nov-13	-0.38		
1996-Oct-25	-0.64	1993-Nov-18	-0.19		
2001-Oct-15	-0.66	1996-Nov-10	-0.40		
2001-Oct-23	-0.58	1999-Nov-11	-0.48		
2004-Oct-15	-0.63	2004-Nov-16	-0.35		
2006-Oct-21	-0.51	2005-Nov-19	-0.31		
2009-Oct-13	-0.64	2006-Nov-22	-0.23		
2011-Oct-19	-0.63	2008-Nov-11	-0.41		
2015-Oct-14	-0.61	2013-Nov-25	-0.44		
2016-Oct-16	-0.53	2014-Nov-12	-0.52		
2018-Oct-22	-0.63	2016-Nov-17	-0.44		
Mean	-0.62	2017-Nov-20	-0.45		
		2019-Nov-10	-0.59		
		Mean	-0.39		
Mean LST-NDVI correlation coefficient value of post-monsoon season is -0.50					
January	LST (°C)	February	LST (°C)	December	LST (°C)
1988-Jan-21	-0.31	1989-Feb-24	-0.39	1988-Dec-22	-0.20
1990-Jan-10	-0.36	1990-Feb-11	-0.38	1992-Dec-17	-0.15
1992-Jan-16	-0.35	1991-Feb-14	-0.12	1994-Dec-23	-0.24
1993-Jan-18	-0.38	1992-Feb-17	-0.29	1995-Dec-10	-0.09
1996-Jan-27	-0.30	1993-Feb-19	-0.37	2000-Dec-15	-0.18
2005-Jan-19	-0.21	2002-Feb-20	-0.44	2002-Dec-21	-0.29
2007-Jan-25	-0.21	2004-Feb-18	-0.30	2004-Dec-18	-0.10
2009-Jan-14	-0.25	2006-Feb-23	-0.31	2006-Dec-24	-0.23
2011-Jan-20	-0.18	2009-Feb-15	-0.36	2008-Dec-13	-0.12
2015-Jan-15	-0.27	2010-Feb-18	-0.24	2009-Dec-16	-0.20
2018-Jan-23	-0.15	2015-Feb-16	-0.16	2010-Dec-19	-0.24
Mean	-0.24	2016-Feb-19	-0.21	2013-Dec-11	-0.19
		2017-Feb-21	-0.30	2016-Dec-19	-0.21
		2018-Feb-24	-0.28	2017-Dec-22	-0.30
		2019-Feb-11	-0.21	2018-Dec-25	-0.22
		Mean	-0.29	2019-Dec-12	-0.40
				Mean	-0.21
Mean LST-NDVI correlation coefficient value of winter season is -0.24					



**Figure 8.** Variation of LST-NDVI relationship (1988–2019): (a) average monthly variation, (b) average seasonal variation, (c) yearly seasonal variation (significant at 0.05 level).

Ltd., Roger Power Technologies Ltd., Vinayak Ispat Udyog, etc. The satellite image always reflects a very dark tone when it passes over the northwest industrial sector of Raipur due to the presence of concentrated industrial smoke. The smoke causes severe air pollution and affects the surrounding areas. LST remains high in this particular industrial belt due to the presence of metal roof and concrete structure. The southeast sector also suffers from high LST values due to its dryness and bareness. In this part of city very little shadow effect is observed due to the low density of high-rise buildings.

#### 4.5. Seasonal variation on LST-NDVI relationship

Table 5 and Figure 8(a–c) represent a generalized view of the overall seasonal variation of LST-NDVI relationships for the whole study area based on the monthly and annual correlation analysis. The relationship is negative, irrespective of any season. A two-tailed test at 0.05 significance level was performed to determine the Pearson's linear correlation coefficient between LST and NDVI at different circumstances. October (−0.62), September (−0.55) and April (−0.51) months build a strong negative correlation. June (−0.47), May (−0.44), March (−0.44) and November (−0.39) months have a moderate negative correlation. A weak negative correlation was found in February (−0.29), January (−0.24) and December (−0.21) months. Overall it can be said that in the winter season, the average LST-NDVI correlation is weak negative (−0.24). The pre-monsoon season has a moderate negative correlation (−0.46). In monsoon (−0.51) and post-monsoon (−0.50) seasons, the average LST-NDVI correlation is a strong negative. The main reason behind the strong

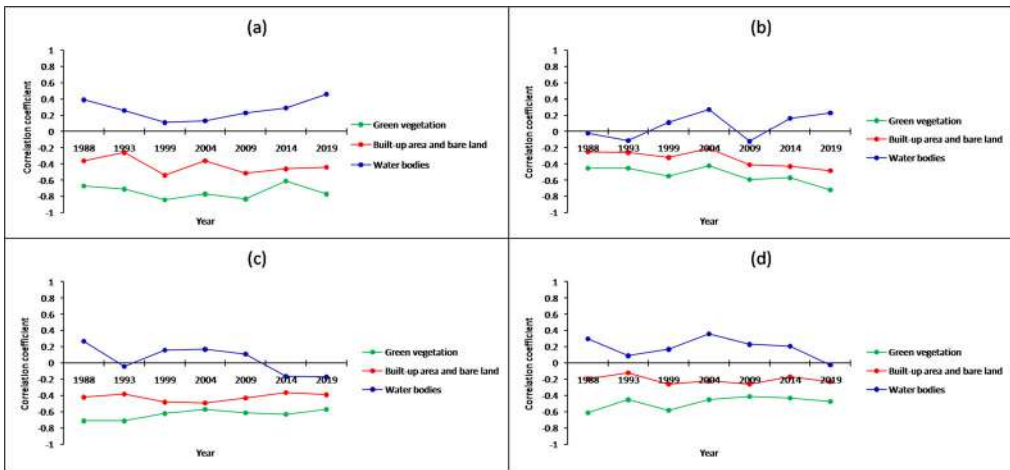


**Figure 9.** Seasonal variation on the LST-NDVI correlation on different types of LULC: (a) pre-monsoon, (b) monsoon, (c) post-monsoon, (d) winter (significant at 0.05 level).

LST-NDVI correlation in the monsoon and post-monsoon season is the presence of high intensity of moisture and chlorophyll content in green vegetation. Dry months reduce the strength of correlation, while the wet months raise the strength of the LST-NDVI correlation.

Figure 9(a–d) shows the seasonal variation of LST-NDVI relationships on different LULC types in winter, pre-monsoon, monsoon and post-monsoon season, respectively. Here, only three types of LULC were considered, i.e. (1) vegetation, (2) water bodies and (3) built-up area and bare land. On the vegetation, the LST-NDVI correlation is a strong negative (−0.60), irrespective of any season. On the water bodies, the relationship is not significant. On the built-up area and bare land, the correlation is moderate negative (−0.35) as the surface materials become more heterogeneous.

Liang et al. (2012), Ghobadi et al. (2015) and Govil et al. (2019) presented similar results (negative correlation) for LST-NDVI relationships. A nonlinear LST-NDVI relationship was found in Shanghai City, while a significant positive linear LST-NDVI relationship was found between LST and NDVI (Cao et al. 2011). In high latitudes, positive LST-NDVI relationships have been observed (Karnieli et al. 2006). Yue et al. (2007) showed that the LST-NDVI relationship in Shanghai City, China was negative and was different in different LULC types. Sun and Kafatos (2007) stated that the LST-NDVI correlation was positive in the winter season while it was negative in the summer season. This relationship was also negative in Mashhad, Iran (Gorgani et al. 2013). The relationship was strong negative in Berlin City for any season (Marzban et al. 2018). This correlation tends to be more negative with the increase of surface moisture (Moran et al. 1994; Lambin and Ehrlich 1996; Prehodko and Goward 1997; Sandholt et al. 2002). The present study also found that the LST-NDVI correlation is negative, irrespective of any season. The value of the correlation coefficient is inversely related to the surface moisture content, i.e. the negativity of the relationship increases with the increase of surface moisture content.

## 5. Conclusions

The present study estimates the temporal and seasonal variation of LST distribution in Raipur City, India using 119 Landsat datasets of four different seasons (winter, pre-

monsoon, monsoon and post-monsoon) from 1988 to 2019. The mean LST of the study area was increased between 1988 and 2019. The LST is directly related to the land conversion. The unchanged land also heated significantly. The results significantly present the influence of climate change in Raipur City. Moreover, the study also reflects the increasing trend of the heated land surface with the expansion of urban areas which can be a serious threat for plants, animals and human health systems.

The present study also assesses the temporal and seasonal correlation of LST and NDVI in Raipur City. The results show that LST is inversely related to NDVI, irrespective of any season. In the monsoon ( $-0.51$ ) and post-monsoon ( $-0.50$ ) season, the correlation is a strong negative, whereas it is found weak negative in winter ( $-0.24$ ). A moderate range of negativity ( $-0.46$ ) was noticed in the pre-monsoon season. The presence of healthy green plants and humid weather is the main responsible factors for strong negativity. The LST-NDVI correlation varies for specific LULC types. The green area presents a strong negative correlation ( $-0.60$ ), whereas the built-up area and bare land present a moderate negative regression ( $-0.35$ ). The correlation is non-linear on water bodies. In the monsoon and post-monsoon season, the LST-NDVI correlation is strong negative on vegetation.

## Acknowledgements

The author is indebted to the United States Geological Survey (USGS), India Meteorological Department (IMD) and Census of India. This study was supported by National Institute of Technology Raipur, Government of India, Grant No./NITRR/Dean (R & C)/2017/8301.

## Disclosure statement

No potential conflict of interest was reported by the author(s).

## ORCID

Subhanil Guha  <http://orcid.org/0000-0002-2967-7248>

Himanshu Govil  <http://orcid.org/0000-0002-3433-8355>

## References

- Alexander C. 2020. Normalised difference spectral indices and urban land cover as indicators of land surface temperature (LST). *Int J Appl Earth Obs Geoinf.* 86:102013.
- Barsi J, Schott J, Hook S, Raqueno N, Markham B, Radocinski R. 2014. Landsat-8 thermal infrared sensor (TIRS) vicarious radiometric calibration. *Remote Sens.* 6(11):11607–11626.
- Cao L, Hu HW, Meng XL, Li JX. 2011. Relationships between land surface temperature and key landscape elements in urban area. *Chin J Ecol.* 30:2329–2334.
- Carlson TN, Ripley DA. 1997. On the relation between NDVI, fractional vegetation cover, and leaf area index. *Remote Sens Environ.* 62(3):241–252.
- Chen XL, Zhao HM, Li PX, Yi ZY. 2006. Remote sensing image-based analysis of the relationship between urban heat island and land use/cover changes. *Remote Sens Environ.* 104(2):133–146.
- Cui L, Wang L, Qu S, Singh RP, Lai Z, Jiang L, Yao R. 2019. Association analysis between spatiotemporal variation of vegetation greenness and precipitation/temperature in the Yangtze River Basin (China). *Environ Sci Pollut Res Int.* 25(22):21867–21878.
- Cui L, Wang L, Qu S, Singh RP, Lai Z, Yao R. 2019. Spatiotemporal extremes of temperature and precipitation during 1960–2015 in the Yangtze River Basin (China) and impacts on vegetation dynamics. *Theor Appl Climatol.* 136(1–2):675–692.

- Estoque RC, Murayama Y, Myint SW. 2017. Effects of landscape composition and pattern on land surface temperature: an urban heat island study in the megacities of Southeast Asia. *Sci Total Environ.* 577: 349–359.
- Fatemi M, Narangifard M. 2019. Monitoring LULC changes and its impact on the LST and NDVI in District 1 of Shiraz City. *Arab J Geosci.* 12(4):127.
- Ferrelli F, Huamantincó MA, Delgado DA, Piccolo MC. 2018. Spatial and temporal analysis of the LST-NDVI relationship for the study of land cover changes and their contribution to urban planning in Monte Hermoso. *Doc Anàl Geogr.* 64 (1):25–47.
- Ghobadi Y, Pradhan B, Shafri HZM, Kabiri K. 2015. Assessment of spatial relationship between land surface temperature and land use/cover retrieval from multi-temporal remote sensing data in South Karkheh Sub-basin, Iran. *Arab J Geosci.* 8(1):525–537.
- Gorgani SA, Panahi M, Rezaie F. 2013. The relationship between NDVI and LST in the urban area of Mashhad, Iran. International Conference on Civil Engineering Architecture and Urban Sustainable Development; November; Tabriz, Iran.
- Govil H, Guha S, Dey A, Gill N. 2019. Seasonal evaluation of downscaled land surface temperature: a case study in a humid tropical city. *Heliyon.* 5(6):e01923.
- Govil H, Guha S, Diwan P, Gill N, Dey A. 2020a. Evaluation of ASTER TIR data-based lithological indices in parts of Madhya Pradesh and Chhattisgarh state, India. In: Sharma N, Chakrabarti A, Balas V, editors. *Data management, analytics and innovation.* Singapore: Springer; p. 161–169. (Advances in intelligent systems and computing; vol. 1042).
- Govil H, Guha S, Diwan P, Gill N, Dey A. 2020b. Analyzing linear relationships of LST with NDVI and MNDISI using various resolution levels of Landsat 8 OLI and TIRS data. In: Sharma N, Chakrabarti A, Balas V, editors. *Data management, analytics and innovation.* Singapore: Springer, p. 171–184. (Advances in intelligent systems and computing; vol. 1042).
- Goward SN, Xue YK, Czajkowski KP. 2002. Evaluating land surface moisture conditions from the remotely sensed temperature/vegetation index measurements: an exploration with the simplified simple biosphere model. *Remote Sens Environ.* 79(2–3):225–242.
- Guha S, Govil H. 2020. An assessment on the relationship between land surface temperature and normalized difference vegetation index. *Environ Dev Sustain.*
- Guha S, Govil H, Besoya M. 2020. An investigation on seasonal variability between LST and NDWI in an urban environment using Landsat satellite data. *Geomat Nat Haz Risk* 11(1): 1319–1345. <https://doi.org/10.1080/19475705.2020.1789762>
- Guha S, Govil H, Dey A, Gill N. 2018. Analytical study of land surface temperature with NDVI and NDBI using Landsat 8 OLI and TIRS data in Florence and Naples city, Italy. *Eur J Remote Sens.* 51(1): 667–678.
- Guha S, Govil H, Dey A, Gill N. 2020. A case study on the relationship between land surface temperature and land surface indices in Raipur City, India. *Geogr Tidsskr.* 120(1): 35–50.
- Guha S, Govil H, Diwan P. 2019. Analytical study of seasonal variability in land surface temperature with normalized difference vegetation index, normalized difference water index, normalized difference built-up index, and normalized multiband drought index. *J Appl Remote Sens.* 13(2):024518.
- Guha S, Govil H, Diwan P. 2020. Monitoring LST-NDVI Relationship Using Premonsoon Landsat Datasets. *Adv Meteorol* 2020: 4539684. <https://doi.org/10.1155/2020/4539684>
- Guha S, Govil H, Gill N, Dey A. 2020. Analytical study on the relationship between land surface temperature and land use/land cover indices. *Ann GIS.* 26(2): 201–216.
- Guha S, Govil H, Mukherjee S. 2017. Dynamic analysis and ecological evaluation of urban heat islands in Raipur city. *J Appl Remote Sens.* 11(3):036020.
- Gui X, Wang L, Yao R, Yu D, Li C. 2019. Investigating the urbanization process and its impact on vegetation change and urban heat island in Wuhan, China. *Environ Sci Pollut Res Int.* 26(30):30808–30825.
- Gutman G, Ignatov A. 1998. The derivation of the green vegetation fraction from NOAA/AVHRR data for use in numerical weather prediction models. *Int J Remote Sens.* 19(8):1533–1543.
- Hao X, Li W, Deng H. 2016. The oasis effect and summer temperature rise in arid regions – case study in Tarim Basin. *Sci Rep.* 6:35418.
- Hou GL, Zhang HY, Wang YQ, Qiao ZH, Zhang ZX. 2010. Retrieval and spatial distribution of land surface temperature in the middle part of Jilin Province based on MODIS data. *Sci Geogr Sin.* 30: 421–427.
- Jamei Y, Rajagopalan P, Sun QC. 2019. Spatial structure of surface urban heat island and its relationship with vegetation and built-up areas in Melbourne, Australia. *Sci Total Environ.* 659:1335–1351.
- Karnieli A, Bayasgalan M, Bayarjargal Y, Agam N, Khudulmur S, Tucker CJ. 2006. Comments on the use of the Vegetation Health Index over Mongolia. *Int J Remote Sens.* 27(10):2017–2024.

- Ke YH, Im J, Lee J, Gong HL, Ryu Y. 2015. Characteristics of Landsat 8 OLI-derived NDVI by comparison with multiple satellite sensors and in-situ observations. *Remote Sens Environ.* 164:298–313.
- Kumar D, Shekhar S. 2015. Statistical analysis of land surface temperature-vegetation indexes relationship through thermal remote sensing. *Ecotoxicol Environ Saf.* 121:39–44.
- Lambin EF, Ehrlich D. 1996. The surface temperature-vegetation index space for land use and land cover change analysis. *Int J Remote Sens.* 17(3):463–487.
- Li J. 2006. Estimating land surface temperature from Landsat-5 TM. *Remote Sens Technol Appl.* 21: 322–326.
- Li WF, Cao QW, Kun L, Wu JS. 2017. Linking potential heat source and sink to urban heat island: heterogeneous effects of landscape pattern on land surface temperature. *Sci Total Environ.* 586:457–465.
- Li ZN, Duan SB, Tang BH, Wu H, Ren HZ, Yan GJ, Tang RL, Leng P. 2016. Review of methods for land surface temperature derived from thermal infrared remotely sensed data. *J Remote Sens.* 20:899–920.
- Liang BP, Li Y, Chen KZ. 2012. A research on land features and correlation between NDVI and land surface temperature in Guilin City. *Remote Sens Tech Appl.* 27:429–435.
- Majumder A, Kingra PK, Setia R, Singh SP, Pateriya B. 2020. Influence of land use/land cover changes on surface temperature and its effect on crop yield in different agro-climatic regions of Indian Punjab. *Geocarto Int.* 35(6):663–686.
- Markham BL, Barker JK. 1985. Spectral characteristics of the LANDSAT thematic mapper sensors. *Int J Remote Sens.* 6(5):697–716.
- Marzban F, Sodoudi S, Preusker R. 2018. The influence of land-cover type on the relationship between LST-NDVI and LST-T<sub>air</sub>. *Int J Remote Sens.* 39(5):1377–1398.
- Mathew A, Khandelwal S, Kaul N. 2017. Investigating spatial and seasonal variations of urban heat island effect over Jaipur city and its relationship with vegetation, urbanization and elevation parameters. *Sustain Cities Soc.* 35:157–177.
- Mathew A, Khandelwal S, Kaul N. 2018. Spatio-temporal variations of surface temperatures of Ahmedabad city and its relationship with vegetation and urbanization parameters as indicators of surface temperatures. *Remote Sens Appl Soc Environ.* 11:119–139.
- Mondal A, Guha S, Mishra PK, Kundu S. 2011. Land use/land cover changes in Hugli Estuary using Fuzzy CMean algorithm. *Int J Geomat Geosci.* 2(2):613–626.
- Moran MS, Clarke TR, Inoue Y, Vidal A. 1994. Estimating crop water-deficit using the relation between surface air-temperature and spectral vegetation index. *Remote Sens Environ.* 49(3):246–263.
- Nigatu W, Dick ØB, Tveite H. 2014. GIS based mapping of land cover changes utilizing multi-temporal remotely sensed image data in Lake Hawassa Watershed, Ethiopia. *Environ Monit Assess.* 186(3): 1765–1780.
- Prehodko L, Goward SN. 1997. Estimation of air temperature from remotely sensed surface observations. *Remote Sens Environ.* 60: 335–346.
- Purevdorj TS, Tateishi R, Ishiyama T, Honda Y. 1998. Relationships between percent vegetation cover and vegetation indices. *Int J Remote Sens.* 19(18):3519–3535.
- Qin Z, Karnieli A, Berliner P. 2001. A mono-window algorithm for retrieving land surface temperature from Landsat TM data and its application to the Israel-Egypt border region. *Int J Remote Sens.* 22(18): 3719–3746.
- Qu C, Ma JH, Xia YQ, Fei T. 2014. Spatial distribution of land surface temperature retrieved from MODIS data in Shiyang River Basin. *Arid Land Geogr.* 37:125–133.
- Qu S, Wang L, Lin A, Yu D, Yuan M, Li C. 2020. Distinguishing the impacts of climate change and anthropogenic factors on vegetation dynamics in the Yangtze River Basin, China. *Ecol Indic.* 108: 105724.
- Qu S, Wang L, Lin A, Zhu H, Yuan M. 2018. What drives the vegetation restoration in Yangtze River basin, China: climate change or anthropogenic factors? *Ecol Indic.* 90:438–450.
- Sandholt I, Rasmussen K, Andersen J. 2002. A simple interpretation of the surface temperature/vegetation index space for assessment of surface moisture status. *Remote Sens Environ.* 79(2–3):213–224.
- Sannigrahi S, Bhatt S, Rahmat S, Uniyal B, Banerjee S, Chakraborti S, Jha S, Lahiri S, Santra K, Bhatt A. 2018. Analyzing the role of biophysical compositions in minimizing urban land surface temperature and urban heating. *Urban Clim.* 24:803–819.
- Singh P, Kikon N, Verma P. 2017. Impact of land use change and urbanization on urban heat island in Lucknow city, Central India. A remote sensing based estimate. *Sustain Cities Soc.* 32:100–114.
- Smith RCG, Choudhury BJ. 1990. On the correlation of indices of vegetation and surface temperature over south-eastern Australia. *Int J Remote Sens.* 11(11):2113–2120.
- Sobrino JA, Jimenez-Munoz JC, Paolini L. 2004. Land surface temperature retrieval from Landsat TM5. *Remote Sens Environ.* 90(4):434–440.

- Sobrino JA, Raissouni N, Li Z. 2001. A comparative study of land surface emissivity retrieval from NOAA data. *Remote Sens Environ.* 75(2):256–266.
- Sun D, Kafatos M. 2007. Note on the NDVI-LST relationship and the use of temperature-related drought indices over North America. *Geophys Res Lett.* 34:L24406.
- Sun Q, Tan J, Xu Y. 2010. An ERDAS image processing method for retrieving LST and describing urban heat evolution: a case study in the Pearl River Delta Region in South China. *Environ Earth Sci.* 59(5): 1047–1055.
- Tucker CJ. 1979. Red and photographic infrared linear combinations for monitoring vegetation. *Remote Sens Environ.* 8(2):127–150.
- Voogt JA, Oke TR. 2003. Thermal remote sensing of urban climates. *Remote Sens Environ.* 86(3): 370–384.
- Wen L, Peng W, Yang H, Wang H, Dong L, Shang X. 2017. An analysis of land surface temperature (LST) and its influencing factors in summer in western Sichuan Plateau: a case study of Xichang City. *Remote Sens Land Res.* 29(2):207–214.
- Wukelic GE, Gibbons DE, Martucci LM, Foote HP. 1989. Radiometric calibration of Landsat Thematic Mapper thermal band. *Remote Sens Environ.* 28:339–347.
- Yang J, Qiu J. 1996. The empirical expressions of the relation between precipitable water and ground water vapor pressure for some areas in China. *Sci Atmos Sin.* 20:620–626.
- Yao R, Cao J, Wang L, Zhang W, Wu X. 2019. Urbanization effects on vegetation cover in major African cities during 2001–2017. *Int J Appl Earth Obs.* 75:44–53.
- Yao R, Wang L, Huang X, Chen J, Li J, Niu Z. 2018. Less sensitive of urban surface to climate variability than rural in Northern China. *Sci Total Environ.* 628–629:650–660.
- Yao R, Wang L, Huang X, Niu Z, Liu F, Wang Q. 2017. Temporal trends of surface urban heat islands and associated determinants in major Chinese cities. *Sci Total Environ.* 609:742–754.
- Yuan M, Wang L, Lin A, Liu Z, Li Q, Qu S. 2020. Vegetation green up under the influence of daily minimum temperature and urbanization in the Yellow River Basin, China. *Ecol Indic.* 108:105760.
- Yuan X, Wang W, Cui J, Meng F, Kurban A, De Maeyer P. 2017. Vegetation changes and land surface feedbacks drive shifts in local temperatures over. *Sci Rep.* 7(1):3287.
- Yue W, Xu J, Tan W, Xu L. 2007. The relationship between land surface temperature and NDVI with remote sensing. Application to Shanghai Landsat 7 ETM+ data. *Int J Remote Sens.* 28(15):3205–3226.
- Zhou Y, Shi TM, Hu YM, Liu M. 2011. Relationships between land surface temperature and normalized difference vegetation index based on urban land use type. *Chin J Ecol.* 30:1504–1512.





## Source details

[Feedback >](#) [Compare sources >](#)

### Geocarto International

Open Access [i](#)

Scopus coverage years: from 1986 to Present

Publisher: Taylor & Francis

ISSN: 1010-6049 E-ISSN: 1752-0762

Subject area: [Social Sciences: Geography, Planning and Development](#) [Environmental Science: Water Science and Technology](#)

Source type: Journal

[View all documents >](#)

[Set document alert](#)

[Save to source list](#)

CiteScore 2022

4.3



SJR 2022

0.655



SNIP 2022

1.260





# Seasonal variability of LST-NDVI correlation on different land use/land cover using Landsat satellite sensor: a case study of Raipur City, India

Subhanil Guha<sup>1</sup> · Himanshu Govil<sup>1</sup>

Received: 24 March 2020 / Accepted: 4 September 2021 / Published online: 21 September 2021  
© The Author(s), under exclusive licence to Springer Nature B.V. 2021

## Abstract

The modern cities of the world are characterized by continuous warming status. Land surface temperature (LST) is a very important part of the environmental status of mixed urban land and it is intimately associated with normalized difference vegetation index (NDVI). The current study makes an attempt on the seasonal fluctuation of LST-NDVI relation on diversified land surface material in Raipur City of India by using a large Landsat dataset for different seasons from 1991–92 to 2018–19. The results present the considerable rising trend of mean LST (1.6 °C, 5.3 °C, 4.8 °C, and 1.1 °C in the pre-monsoon, monsoon, post-monsoon, and winter, respectively) during the study period. The LST and NDVI produce a strong negative correlation (−0.74, −0.54, −0.63, and −0.49 in these four seasons) on plants; a moderate negative correlation (−0.42, −0.34, −0.42, and −0.21 in the four aforesaid seasons) on the barren land and urban settlement; and an insignificant correlation (0.27, 0.08, 0.05, and 0.19 in the four abovementioned seasons) on water bodies. This study is helpful in future planning for the ecological development of a city in tropical environment.

**Keywords** Landsat sensor · LST · NDVI · Raipur · Seasonal variability

## 1 Introduction

Presently, the expansion of urban areas with newly converted land surfaces accelerates the land surface temperature (LST) in almost every modern city (Fu & Weng, 2016; Peng et al., 2018). Different spectral bands produce different remote sensing indices that are used in the delineation of different land surface features (Chen et al., 2006). Normalized difference vegetation index (NDVI) is invariably used in identifying live vegetation (Das et al., 2013; Du et al., 2016; Govil et al., 2019; Gui et al., 2019; Mondal et al., 2011). The LST-NDVI correlation is an important part of the environmental monitoring of a city (Goward et al., 2002; Guha et al., 2020; Kikon et al., 2016). NDVI can play a key role in land use/

---

✉ Subhanil Guha  
subhanilguha@gmail.com

<sup>1</sup> Department of Applied Geology, National Institute of Technology, Raipur, India



## Source details

[Feedback](#) > [Compare sources](#) >

### Environment, Development and Sustainability

Scopus coverage years: from 1999 to Present

Publisher: Springer Nature

ISSN: 1387-585X E-ISSN: 1573-2975

Subject area: [Social Sciences: Geography, Planning and Development](#) [Economics, Econometrics and Finance: Economics and Econometrics](#)  
[Environmental Science: Management, Monitoring, Policy and Law](#)

Source type: Journal

[View all documents](#) >[Set document alert](#)[Save to source list](#)

CiteScore 2022

7.2



SJR 2022

0.835




SNIP 2022

1.291





# Dynamic status of land surface temperature and spectral indices in Imphal city, India from 1991 to 2021

Arun Mondal<sup>a</sup>, Subhanil Guha<sup>b</sup>  and Sananda Kundu<sup>c</sup>

<sup>a</sup>School of Earth, Ocean and Environment, University of South Carolina, Columbia, SC, USA;

<sup>b</sup>Department of Applied Geology, National Institute of Technology Raipur, Rajpur, India; <sup>c</sup>Department of Geography, Manipur University, Imphal, India

## ABSTRACT

The thermal status of northeast Indian cities has a great impact on the sustainability of these places. To meet the research gap in this area, a study is performed in Imphal city, India by investigating the relationship between land surface temperature (LST) and four spectral indices in the summer and winter seasons from 1991 to 2021. The mean LST of the city increases at >1% rate per decade in both seasons. The urban heat island (UHI) develops mostly along the central Imphal. A considerable difference in the mean LST between UHI and non-UHI in summer (3.05 °C in 1991, 2.46 °C in 2001, 3.13 °C in 2011, and 2.49 °C in 2021) and winter (2.01 °C in 1991, 2.63 °C in 2001, 2.64 °C in 2011, and 2.57 °C in 2021) reflects the continuous warming status of the city. Some urban hot spots develop inside the UHI of the central and north Imphal. The dynamic nature of the relationships of spectral indices with LST (moderate negative for MNDWI and NDVI, strongly positive for NDBI, and moderate negative for NDBal) will be helpful for proper sustainable urban planning. Urban thermal field variance index map shows that the south Imphal attains more ecological comfort than the rest of the parts.

## ARTICLE HISTORY

Received 12 July 2021

Accepted 14 November 2021

## KEYWORDS

Imphal; land surface temperature; urban heat island; urban hot spots; urban thermal field variance index

## 1. Introduction

The process of urbanization enhances the thermal stress of an area by global or local warming (Grimm et al. 2008; Fu and Weng 2016). The continuous conversion process of land surface accelerates the warming status of today's urban atmosphere (Zhou et al. 2018 ; Guha et al. 2020). Land surface temperature (LST) determined from various satellite sensors is considerably used in the demarcation of the heat islands and thermal stressed zones inside the urban area (Weng 2009; Tomlinson et al. 2011; Fu and Weng 2016; Hao et al. 2016; Tran et al. 2017). The variation of LST in the heterogeneous urban landscape is largely influenced by the land use/land cover (LULC) categories (Li et al. 2016; Estoque et al. 2017; Guha et al. 2020).

CONTACT Subhanil Guha  [subhanilguha@gmail.com](mailto:subhanilguha@gmail.com)

© 2021 The Author(s). Published by Informa UK Limited, trading as Taylor & Francis Group.

This is an Open Access article distributed under the terms of the Creative Commons Attribution License (<http://creativecommons.org/licenses/by/4.0/>), which permits unrestricted use, distribution, and reproduction in any medium, provided the original work is properly cited.

Satellite remote sensing techniques are applied to detect the changed land surface zones by using their visible to near-infrared (VNIR) and shortwave infrared (SWIR) bands (Chen et al. 2006). Moreover, thermal infrared (TIR) bands are also used to create some spectral indices (Kalnay and Cai 2003; Du et al. 2016; Berger et al. 2017; He et al. 2019). The most popular index for vegetation in LST estimation is the normalized difference vegetation index (NDVI) (Carlson and Ripley 1997; Sobrino et al. 2004). In mixed urban land, high LST is related to low vegetated area (Voogt and Oke 2003). Many studies are based on the LST-NDVI correlation (Gutman and Ignatov 1998; Guha and Govil 2021) are available to explore the pattern of LST. Modified normalized difference water index (MNDWI) is one of the most used water indices and it is considerably used in LST-related research works (Essa et al. 2012; Guha et al. 2017). Normalized difference built-up index (NDBI) is the most popular built-up index that is invariably used in LST-related studies (Zha et al. 2003; Guha et al. 2020). Normalized difference bareness index (NDBaI) is an index for bare land identification (Zhao and Chen 2005; Chen et al. 2006; Guha and Govil 2021).

Urban hot spots (UHS) develop mainly inside the urban heat island (UHI) due to heavy construction and manufacturing activities. These UHS are the most severely heated surface of the area (Chen et al. 2006; Coutts et al. 2016; Feyisa et al. 2016; Ren et al. 2016; Lopez et al. 2017; Pearsall 2017). The detection of UHS for prioritization is very significant to maintain the thermal status of a city.

Several research works introduced some ecological comfort indices (Matzarakis et al. 1999; Kakon et al. 2010; Willett and Sherwood 2012) among which urban thermal field variance index (UTFVI) is the most popular index for ecological evaluation as it is directly related to LST (Nichol 2005; Liu and Zhang 2011; Mackey et al. 2012; Guha et al. 2017).

Recently, there are some research materials available on the relationship between LST and different spectral indices in South Asia. Ramaiah et al. (2020) attempted to quantify the influence of urban factors on LST in the Panaji and Tumkur of India. Dissanayake (2020) investigated the spatiotemporal changes of LULC and its impact on LST in Galle City, Sri Lanka. Halder (2021) evaluated the impact of climate change on UHI based on LST and geospatial indicators in Kolkata, India. Shukla and Jain (2021) analyzed the impact of changing landscape patterns and dynamics on LST in Lucknow city, India. Dissanayake et al. (2019) assessed the changes in LULC and their impact on surface UHI in Kandy City, Sri Lanka. Ranagalage et al. (2018) showed the spatial changes of UHI formation in Colombo District, Sri Lanka for sustainable planning.

Imphal is an ecological smart city which is expanding rapidly in recent decades. It has agricultural fields, water bodies, wetlands, and green vegetation inside and outside the city area. The city can be representative of moderately populated Indian cities under humid subtropical climates. Kalota (2017) analyzed the LST of Manipur State with some selected built-up, vegetation, and topographical variables. The present study is perhaps the first significant attempt to evaluate the relationship built between LST and the spectral indices in Imphal city for the summer and winter seasons. The prime objectives of this study are: (1) to analyze the spatial, temporal, and seasonal changes of LST in UHI and non-UHI of Imphal city; (2) to identify the UHS inside the UHI; (3) to correlate

LST with the different spectral indices for the whole city and inside the UHI and UHS; and (4) to measure the ecological comfort level by UTFVI.

## 2. Study area and data

The present study was performed over Imphal, the capital city of Manipur, and its surrounding area. It is a humid subtropical landlocked mountainous city and is one of the important cities in northeast India. Imphal is the second round winner for the selection of Smart Cities Mission under the Ministry of Urban Development. The study area (Imphal city and its surroundings) extends from  $24^{\circ}53'47''\text{N}$  to  $24^{\circ}41'43''\text{N}$  and from  $93^{\circ}51'00''\text{E}$  to  $94^{\circ}01'00''\text{E}$  (Figure 1). The study area covers approximately  $419.62\text{ km}^2$  area. It has an average elevation of around 800 m. Imphal city is divided into Imphal West and Imphal East districts. Imphal, Kongba, and Iril are the main rivers of the city those are flowing from north to south direction. Nambul is another river that flows from west to east. The city has a humid subtropical (Cwa) type of climate characterized by cool dry winter and warm wet summer. The summer season extends from April to August while December, January, and February are considered as the winter months. The average annual range of temperature is  $14^{\circ}\text{C}$ – $27^{\circ}\text{C}$  and the average annual precipitation is 145 cm. July is the rainiest month.

A total of eight (four from summer and four from winter season) multi-temporal cloud-free Landsat satellite imageries (<http://earthexplorer.usgs.gov/>) of Imphal from 1991 to 2021 were used in this study (Table 1). The simple description of four used remote sensing spectral indices in the current study have been shown in Table 2. Shuttle Radar Topographic Mission (SRTM) Digital Elevation Model (DEM) data of 23 September 2014 (<http://earthexplorer.usgs.gov/>) were also used to determine the elevation value of the study area. The spatial information of Imphal city was obtained from the Imphal Municipal Corporation (<https://imc.mn.gov.in/>). High-resolution Google Earth Image (<https://earth.google.com/web/>) was used for LULC identification.

## 3. Methodology

The entire methodology of the present study needs to determine the four mentioned spectral indices and to estimate the LST of the study area for each Landsat dataset. Apart from these, UHI, UHS, and UTFVI of the study area for different seasons have also been quantified. In below, these methods have been described briefly.

### 3.1. Description of NDVI, MNDWI, NDBI, and NDBaI

Many remote sensing indices are regularly used for the identification of different types of landscapes (Guha et al. 2017). Here, NDBaI (Zhao and Chen 2005), NDBI (Zha et al. 2003), NDVI (Tucker 1979), and MNDWI (Xu 2006) and were used for determining the relationship with LST. The band combinations of these spectral indices were given in Table 1. The value of any normalized difference spectral index is ranged between  $-1.0$  and  $+1.0$ . Generally, the positive value of NDBaI, NDBI,

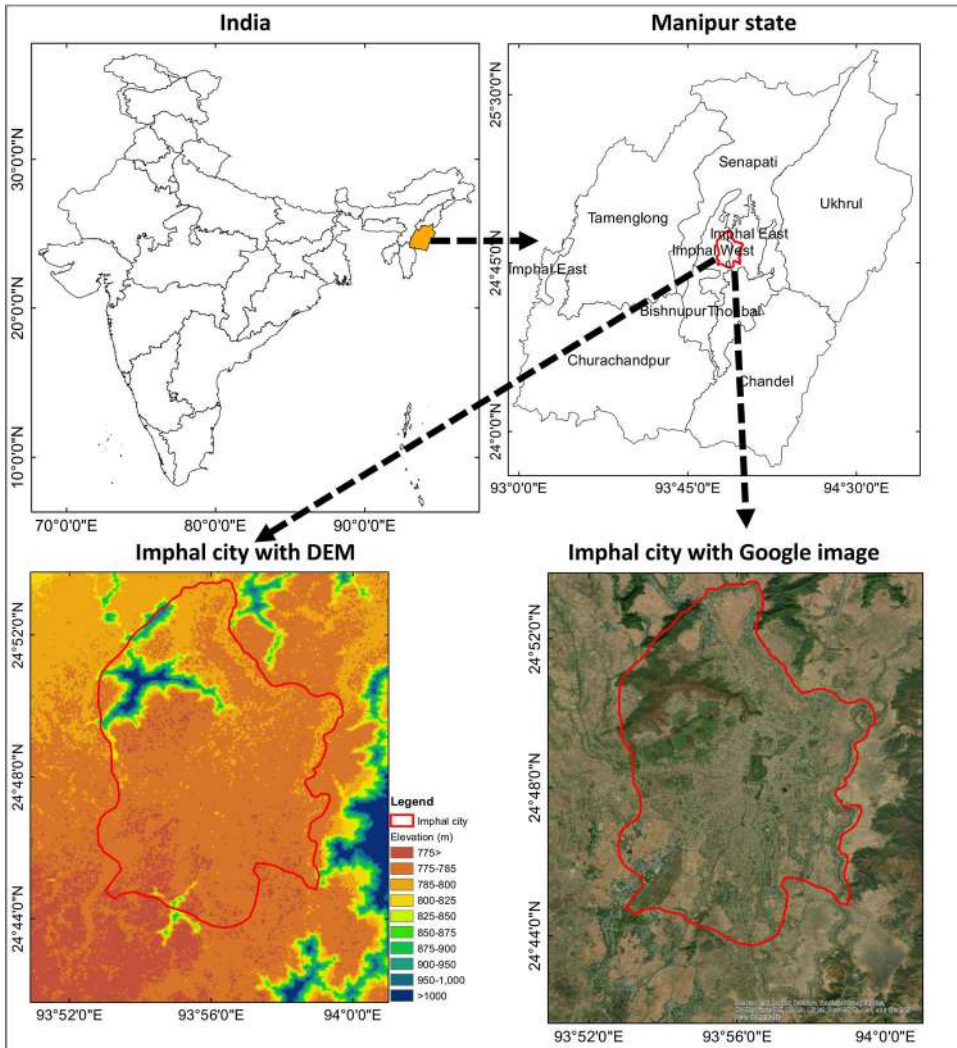


**Figure 1.** Imphal city was shown on Manipur state, DEM, and Google image. The SRTM DEM (30 m spatial resolution) was used for this study (source: <http://earthexplorer.usgs.gov/>).

NDVI, and MNDWI indicate the bare land, built-up, vegetation, and water surface, respectively (Chen et al. 2006).

### 3.2. LST estimation using landsat TIR band

LST is estimated from the TIR band of Landsat satellite sensor by Equation (1) (Artis and Carnahan 1982):

$$L_{\lambda} = \text{RadianceMultiBand} \times DN + \text{RadianceAddBand} \quad (1)$$

$L_{\lambda}$  = the spectral radiance in  $\text{Wm}^{-2}\text{sr}^{-1}\text{mm}^{-1}$ .

**Table 1.** Specification of satellite images.

Landsat scene ID	Date of acquisition	Time (UTC)*	Path/Row	Sun elevation (°)	Sun azimuth (°)	Cloud cover (%)	Earth-Sun distance (astronomical unit)	Resolution of VNIR bands (m)	Resolution of TIR bands (m)
Summer season									
LT51350431991108BK00	18-Apr-91	03:34:00	135/043	56.09	108.42	7.00	1.00	30	120
LT51350432001135BK01	15-May-01	03:52:12	135/043	64.13	97.29	5.00	1.01	30	120
LT51350432011099BK01	09-Apr-11	04:01:51	135/043	59.68	119.96	0.00	1.00	30	120
LC8135043202110LGN00	20-Apr-21	04:11:42	135/043	64.64	116.66	9.64	1.00	30	100
Winter season									
LT51350431991028IS00	28-Jan-91	03:32:37	135/043	34.42	137.09	1.00	0.98	30	120
LT51350432001039BK00	08-Feb-01	03:52:05	135/043	39.76	138.59	0.00	0.99	30	120
LT51350432011035BK00	04-Feb-11	04:02:01	135/043	40.21	142.28	0.00	0.99	30	120
LC81350432021014LGN00	14-Jan-21	04:12:14	135/043	37.97	149.60	7.94	0.98	30	100

\*IST = UTC + 05:30 (IST = Indian standard time, UTC = Coordinated universal time)



At-sensor brightness temperature is estimated by Equation (2).

$$T_B = \frac{K_2}{\ln((K_1/L_\lambda) + 1)} \quad (2)$$

Where,  $T_B$  = brightness temperature in Kelvin (K),  $L_\lambda$  = spectral radiance in  $\text{Wm}^{-2}\text{sr}^{-1}\text{mm}^{-1}$ ;  $K_2$  and  $K_1$  = calibration constants,.

Fractional vegetation is calculated by Equation (3) (Carlson and Ripley 1997).

$$F_v = \left( \frac{NDVI - NDVI_{min}}{NDVI_{max} - NDVI_{min}} \right)^2 \quad (3)$$

Where,  $NDVI_{min}$  = minimum NDVI,  $NDVI_{max}$  = maximum NDVI.  $F_v$  = fractional vegetation.

Land surface emissivity  $\varepsilon$ , is calculated by Equation (4) (Sobrino et al. 2001, 2004):

$$\varepsilon = 0.004 * F_v + 0.986 \quad (4)$$

Where,  $\varepsilon$  = surface emissivity.

Finally, LST is estimated by Equation (5) (Weng et al. 2004):

$$LST = \frac{T_B}{1 + (\lambda\sigma T_B / (hc)) \ln \varepsilon} \quad (5)$$

Where,  $\lambda$  = effective wavelength,  $\sigma$  = Boltzmann constant ( $1.38 \times 10^{-23}$  J/K),  $h$  = Plank's constant ( $6.626 \times 10^{-34}$  Js),  $c$  = velocity of light in a vacuum ( $2.998 \times 10^8$  m/sec),  $\varepsilon$  = emissivity.

### 3.3. Mapping UHI

UHI and non-UHI zones are demarcated using the following equations (Guha et al. 2017):

$$LST > \mu + 0.5 * \sigma \quad (6)$$

$$0 < LST \leq \mu + 0.5 * \sigma \quad (7)$$

Where,  $\mu$  and  $\sigma$  are the mean and standard deviation of LST in the study area, respectively.

### 3.4. Delineating the urban hot spots (UHS)

The UHS were delineated by the following equation (Guha et al. 2017):

$$LST > \mu + 2 * \sigma \quad (8)$$

**Table 2.** Description of the remote sensing spectral indices.

Acronym	Description	Formulation	References
NDVI	Normalized difference vegetation index	$\text{NIR-Red}/(\text{NIR} + \text{Red})$	Tucker 1979
MNDWI	Modified normalized difference water index	$\text{Green-SWIR1}/(\text{Green} + \text{SWIR1})$	Xu 2006
NDBI	Normalized difference built-up index	$\text{SWIR1-NIR}/(\text{SWIR1} + \text{NIR})$	Zha et al. 2003
NDBaI	Normalized difference bareness index	$\text{SWIR1-TIR}/(\text{SWIR1} + \text{TIR})$	Zhao and Chen 2005

### 3.5. The urban thermal field variance index (UTFVI)

UTFVI was determined using the following equation (Liu and Zhang 2011):

$$\text{UTFVI} = \frac{T_s - T_{\text{mean}}}{T_{\text{mean}}} \quad (9)$$

Where, *UTFVI* = Urban Thermal Field Variance Index

$T_s$  = LST (°C)

$T_{\text{mean}}$  = Mean LST (°C)

This methodology used in Imphal city can also be used in similar types of the study area with Landsat data as the process of LST derivation and spectral indices determination remains the same. In different geographical locations, some methods may be modified to obtain a logical output.

## 4. Results and discussion

### 4.1. Spatial, temporal, and seasonal dynamics of different spectral indices

Figure 2 present the spatial distribution (1991–2021) of NDVI (Figure 2A) and MNDWI (Figure 2B) for the summer and winter seasons whereas Figure 3 shows the same for NDBI (Figure 3A) and NDBaI (Figure 3B) for both seasons. The maximum NDVI values gradually decrease in the region due to the loss of vegetation. North-western parts and south-eastern peripheries indicate a concentrated vegetal cover. Most of the water bodies are found in the southwest portions of the study area where MNDWI values are greater. High NDBI values are observed mainly along the outskirts of the central city. In the whole area, NDBI increases at an alarming rate that indicates a positive trend of LST. NDBaI values generally increase with time and the eastern part of the city is characterized by high NDBaI values compared to the western side because of the high proportion of bare lands.

Table 3 shows the dynamic nature of LST and these spectral indices. The mean NDVI values are gradually decreasing from 1991 to 2021 and the values of summer mean NDVI is slightly higher than winter mean NDVI. It indicates the exploitation of parks and green spaces inside the city. The summer and winter mean MNDWI values show a steady decrease throughout the periods that reflect an increase of water bodies and wetlands in the study area. The mean MNDWI values are a little bit more in the summer season due to wet conditions. Despite the increase of built-up surface,

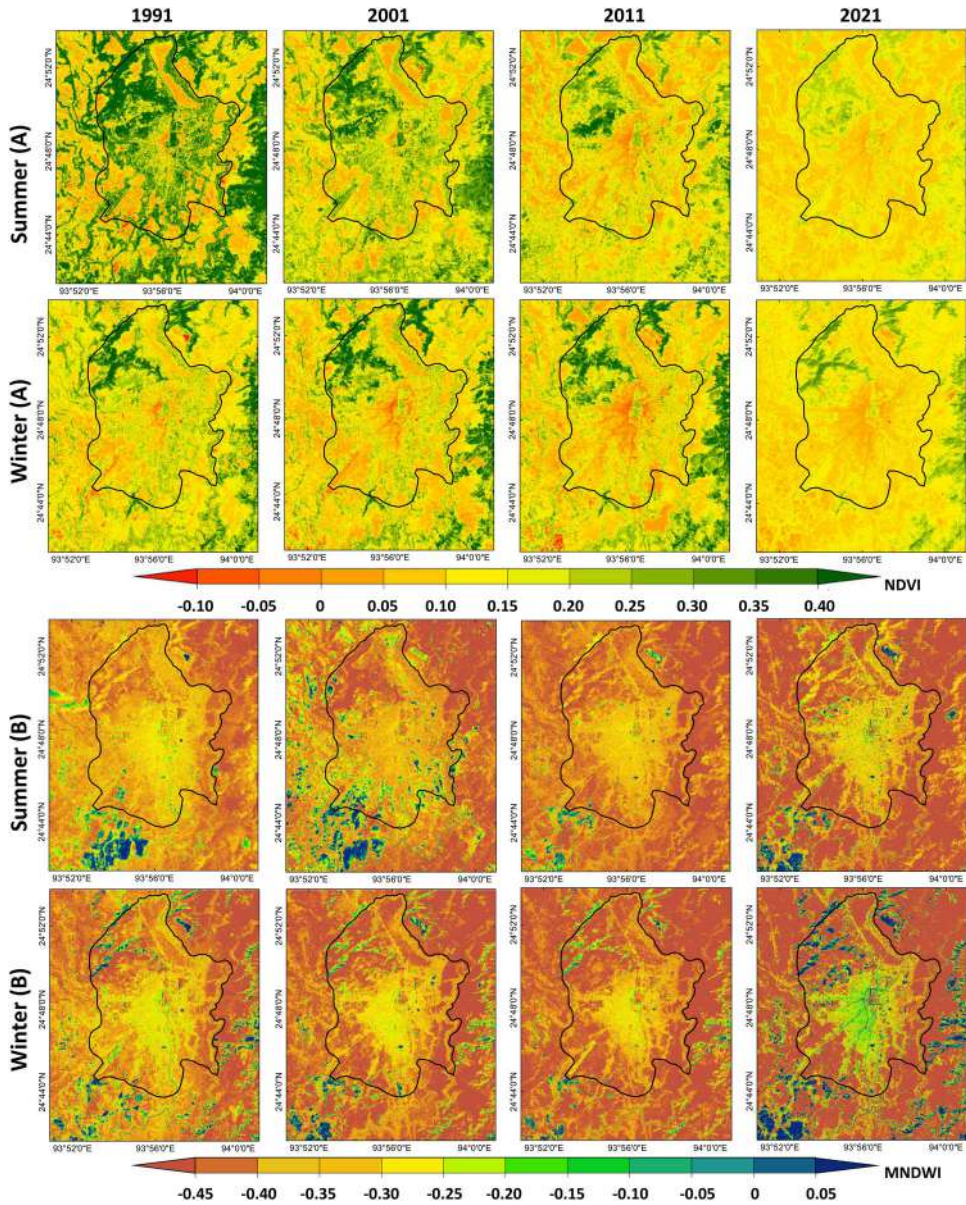


**Figure 2.** Distribution of NDVI and MNDWI in summer and winter season in 1991, 2001, 2011, and 2021 in Imphal city (A = NDVI, B = MNDWI, Black line = city boundary).

the mean NDBI values show low variability due to the heterogeneity of built-up surface. The mean NDBI is continuously increasing and it always remains higher in the winter season due to dry weather. A steady increase in mean NDBaI reflects the increase of bare land during the span. The mean NDBaI of the summer season always reflects a higher value. These bare lands can enhance the ecological status of Imphal city through proper environmental planning. Mean LST increases considerably from 1991 to 2021 and the summer season always provides a high mean LST (more than 9°C) than the winter one.

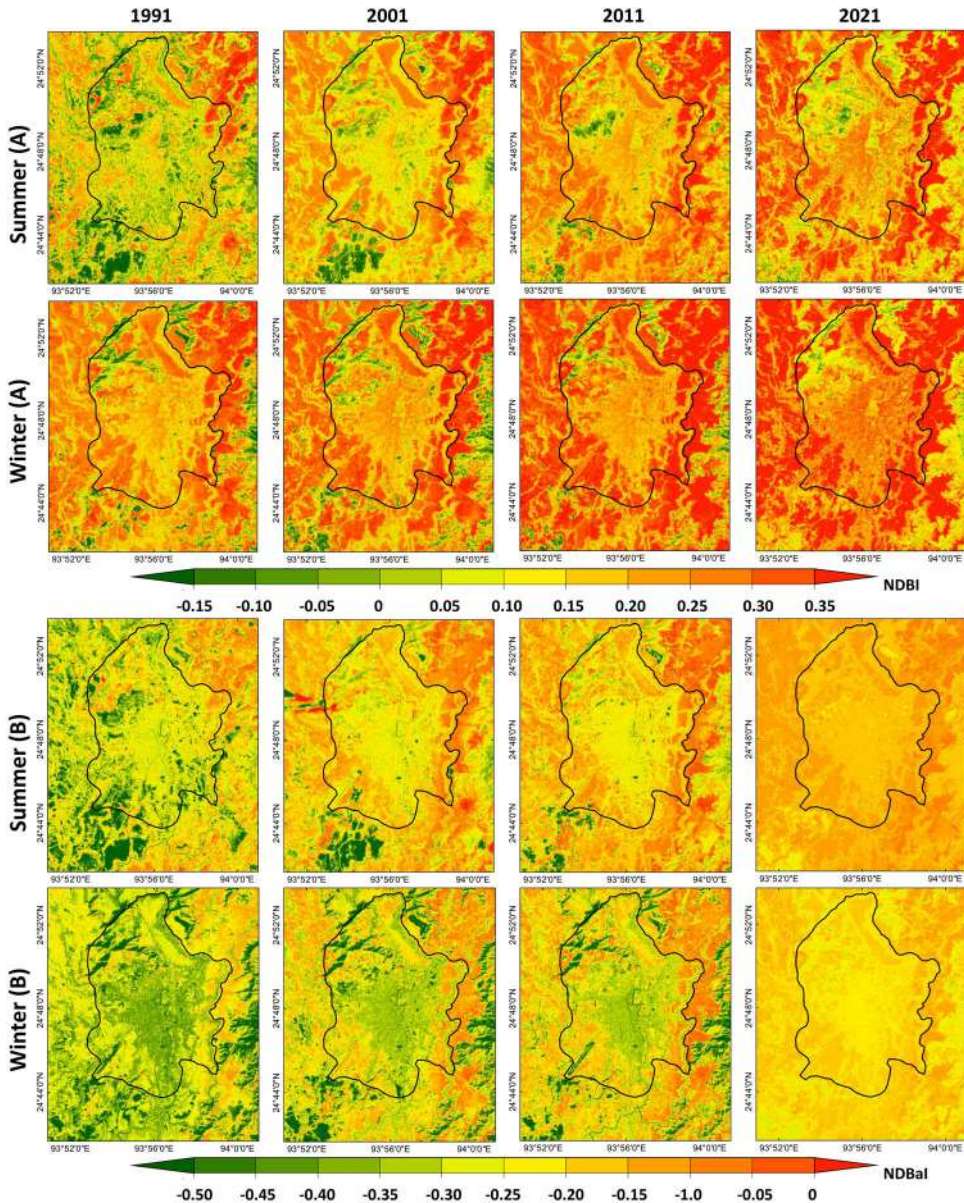


Figure 3. Distribution of NDBI and NDBal in summer and winter season in 1991, 2001, 2011, and 2021 in Imphal city (A = NDBI, B = NDBal, Black line = city boundary).

#### 4.2. Changing pattern of LST

A significant LST distribution trend was noticed during the last three decades (Figure 4A). A gradual increase of LST is noticed in the minimum, maximum, mean, and standard deviation values due to the change in LULC types. The green and water surfaces are decreased while the built-up surfaces are increased and this LULC change reflects in the LST distribution. North-eastern and central parts of the city receive more LST in every decade. Table 4 shows the temporal distribution of LST in Imphal

**Table 3.** Descriptive statistics of MNDWI, NdaBI, NDBI, and NDVI (1991–2021).

MNDWI	Summer				Winter			
	Min	Max	Mean	Std	Min	Max	Mean	Std
1991	-0.60	0.36	-0.34	0.09	-0.67	0.73	-0.35	0.12
2001	-0.68	0.66	-0.35	0.13	-0.62	0.57	-0.39	0.10
2011	-0.61	0.38	-0.39	0.08	-0.66	0.65	-0.41	0.12
2021	-0.64	0.28	-0.43	0.06	-0.69	0.26	-0.46	0.07
NDBal	Min	Max	Mean	Std	Min	Max	Mean	Std
1991	-0.70	0.33	-0.28	0.10	-0.91	0.22	-0.32	0.13
2001	-0.88	0.28	-0.19	0.13	-0.86	0.15	-0.26	0.12
2011	-0.73	0.25	-0.17	0.09	-0.89	0.27	-0.22	0.13
2021	-0.62	0.23	-0.14	0.07	-0.63	0.35	-0.19	0.07
NDBI	Min	Max	Mean	Std	Min	Max	Mean	Std
1991	-0.34	0.46	0.10	0.10	-0.74	0.52	0.20	0.12
2001	-0.61	0.46	0.17	0.13	-0.53	0.48	0.21	0.11
2011	-0.49	0.53	0.22	0.10	-0.67	0.53	0.26	0.12
2021	-0.36	0.38	0.18	0.08	-0.30	0.42	0.23	0.07
NDVI	Min	Max	Mean	Std	Min	Max	Mean	Std
1991	-0.60	0.41	0.23	0.10	-0.68	0.44	0.17	0.10
2001	-0.72	0.44	0.18	0.16	-0.65	0.33	0.16	0.09
2011	-0.57	0.44	0.14	0.08	-0.64	0.34	0.15	0.11
2021	-0.54	0.40	0.12	0.07	-0.42	0.29	0.12	0.06

city from 1991 to 2021. It is noticed that the minimum, maximum, and mean values of LST increase at a significant rate of 62.73%, 7.02%, and 14.39% in the summer season for the last three decades. In winter, the minimum, maximum, and mean values of LST increase at a rate of 42.19%, 8.63%, and 19.67% for the last 30 years.

Figure 4B shows the LST change over Imphal city. A little LST change is found in this span. The central part gets warmer than the cooler periphery regions. However, the picture changes in 2001–2011. In that time, the periphery receives more LST than the middle portions. In the next decade, the central parts become warmer than the previous decade and some outskirts of the city also experience a negative change in LST. Overall, the central and southern parts of Imphal city have significantly heated ( $>5^{\circ}\text{C}$  increase in mean LST) in the summer season of the last three decades. In the winter season, the whole city becomes warmer ( $>2\text{--}3^{\circ}\text{C}$  increase in mean LST) except in some patches of the northwest portions. The city is constantly heated due to rapid urbanization and land conversion.

#### 4.3. Dynamic scenario of UHI effect

A significant increase in the mean LST between UHI and non-UHI for summer ( $3.05^{\circ}\text{C}$  in 1991,  $2.46^{\circ}\text{C}$  in 2001,  $3.13^{\circ}\text{C}$  in 2011, and  $2.49^{\circ}\text{C}$  in 2021) and winter ( $2.01^{\circ}\text{C}$  in 1991,  $2.63^{\circ}\text{C}$  in 2001,  $2.64^{\circ}\text{C}$  in 2011, and  $2.57^{\circ}\text{C}$  in 2021) seasons of different decades is observed from the estimated LST (Table 5). For the UHI, A straight 12.14% and 19.35% mean LST is increased in summer and winter season respectively from 1991 to 2021. For the non-UHI, these temporal estimations are 16.05% and 18.2% for the summer and winter seasons, respectively. The standard deviation values of LST in the UHI zones for the summer and winter seasons are  $<0.98$  and  $<1.07$ , respectively for each year indicate a very little variation in LST. The ranges of the

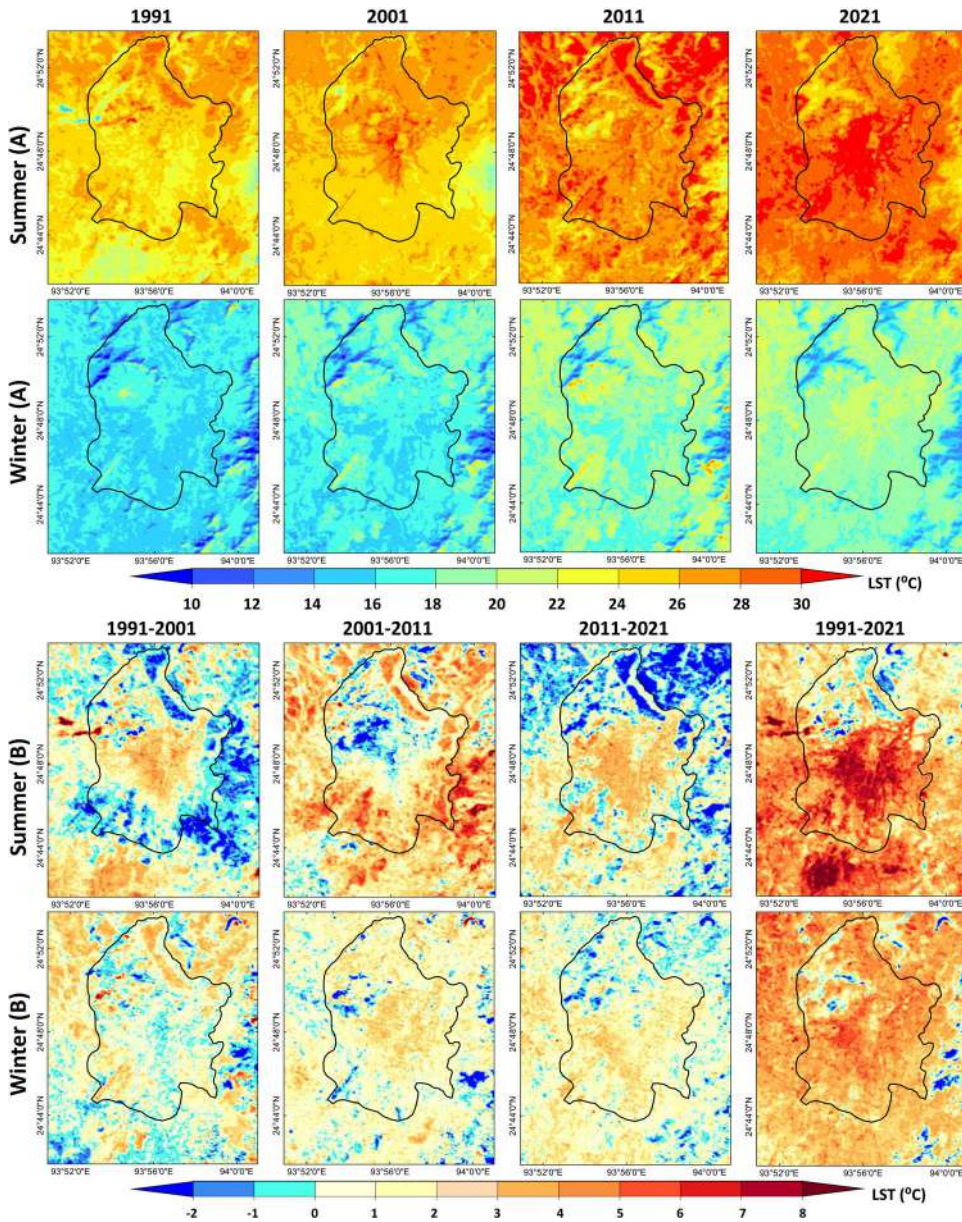


**Figure 4.** (A) Distribution of LST in summer and winter seasons in 1991, 2001, 2011, and 2021 in Imphal city. (B) Temporal changes in LST difference in the Imphal city from 1991-2001, 2001-2011, 2011-2021, and 1991-2021. (Black line = city boundary).

standard deviation for UHI and non-UHI are 0.18 and 0.19 in the summer season while these ranges of standard deviation are 0.40 and 0.39 in the winter season. It reflects that the summer season has more consistent LST values in UHI and non-UHI compared to the winter season.

In Imphal, the UHI zones are consistently concentrated in the northern part in the first two decades and the central part in the last decade (Figure 5A). The northern

**Table 4.** Temporal distribution of LST (°C) in Imphal city.

Summer						
Year	LST(Min)	LST(Max)	LST(Mean)	LST(Std)	Threshold LST for UHI	Threshold LST for UHS
1991	13.31	32.47	24.80	1.85	25.83	28.78
2001	17.02	32.05	25.59	1.55	26.67	28.76
2011	20.62	35.26	27.77	1.94	28.78	31.65
2021	21.66	34.75	28.37	1.64	29.19	31.65
Winter						
Year	LST(Min)	LST(Max)	LST(Mean)	LST(Std)	Threshold LST for UHI	Threshold LST for UHS
1991	8.01	27.95	15.71	1.44	16.58	18.85
2001	9.97	30.44	19.09	1.99	20.19	23.27
2011	9.39	27.08	17.80	1.78	18.76	21.43
2021	11.39	30.36	18.80	1.80	19.70	22.40

part is an area of the dry bare land surface while the central part of the city is mainly the built-up area with commercial and residential blocks. The north-western and eastern portions are the area with high vegetal coverage space and come under the non-UHI. Some urban vegetation has been planted in the north-western and eastern parts of the city to reduce the pollution level. Most of the numerous water bodies are found in the southwestern corner of the study area.

The UHI estimated from different satellite imageries occupies some common areas. These common UHI experience a constant increase in LST (Figure 5B). Here, the black colour shows the area under non-UHI. The analysis derived from Figures 5A and 5B depicts that the highest LST values exist in the built-up and bare lands. Change in mean LST for common UHI was represented in Figure 5B. UHI received more surface temperature with time. During 1991–2021, 3–8 °C mean LST was increased in most of the portions of common UHI.

Figure 6 presents some randomly selected points in Imphal city from the 20 April 2021 image. Points 1, 2, 3, 4, 5, and 6 falls inside the UHI whereas points 7, 8, 9, 10, 11, and 12 falls inside the non-UHI. Points 1-6 are mainly concentrated in the central built-up area of the city where the high density of population and commercial buildings is directly responsible for high LST generation. Point 1 is located in the Lamlong Bazar area, point 2 is located in the Yengkhom Leirak area, point 3 is located near Manipur Rural Bank, point 4 is located in Kangjabi Leirak locality, point 5 is located near Leiningthow Khanglamba area, and point 6 is located in Sanakhwa Yaima Kollup locality. Points 7 to 12 are mainly scattered along the area outside the central built-up area that is a part of a vegetation-covered area or a water body. Point 7 is located in a water body near NIT Manipur sports ground, point 8 is located in dense vegetation near Cheirao Ching Garden, point 9 is located in a zone surrounded by vegetation and water body near Imphal City Sewage Treatment Plant, point 10 is located in a water body in Kakwa Pat area, point 11 is located in RMS Equestrian Ground, and point 12 is located in a water body near Khurai Lamlong Baptist Church in the north-eastern part of the city. These particular areas have low LST values. The LST of the above location strongly validates the results.

**Table 5.** Temporal variation of LST (°C) in UHI and Non-UHI (summer and winter).

Summer LST								
Year	Min		Max		Mean		Std	
	UHI	Non-UHI	UHI	Non-UHI	UHI	Non-UHI	UHI	Non-UHI
1991	25.83	13.31	32.46	25.41	26.85	23.80	0.84	1.31
2001	26.66	17.01	32.04	26.24	27.36	24.90	0.79	1.18
2011	28.77	20.62	35.26	28.35	29.83	26.70	0.97	1.37
2021	29.19	21.65	34.75	29.19	30.11	27.62	0.82	1.30
Winter LST								
Year	Min		Max		Mean		Std	
	UHI	Non-UHI	UHI	Non-UHI	UHI	Non-UHI	UHI	Non-UHI
1991	16.57	8.01	27.94	16.11	17.21	15.20	1.06	1.17
2001	17.65	8.72	26.61	17.26	18.46	15.83	0.89	1.37
2011	18.76	9.39	30.35	18.31	19.53	16.89	0.82	1.45
2021	19.70	11.39	27.07	19.70	20.54	17.97	0.66	1.56

#### 4.4. Delineation of UHS

In this study, UHS has been delineated for continuous monitoring of the most vulnerable heat zones. These small pockets are developed inside the UHI. UHS is more abundant over the bare land areas and the highly commercial and industrial zones. The UHS is mainly identified in the northern, eastern, and central parts of the city (Figure 7A). In 2021, the UHS is identified by a threshold value of 31.65 °C in summer and 22.40 °C in winter (Table 4). Bare earth surfaces, parking zones, metalled roads, metal roofs, and industrial factories are the most common places of UHS.

#### 4.5. Relationship of LST with four spectral indices

Table 6 shows the dynamic analysis of the correlation of LST with MNDWI, NDVI, NDBI, and NDBaI for the whole Imphal city, for the UHI of Imphal city, and the UHS of Imphal city during the period. MNDWI gives a moderate negative correlation with LST for the entire study area in both seasons. However, for UHI, the LST-MNDWI relationship becomes weak negative in both seasons. For UHS, the correlation is weak negative in winter and insignificant in summer. NDVI also builds a moderate negative correlation with LST for the whole Imphal city in both seasons. For UHI, the strength of the relationship becomes weak negative in summer and insignificant in winter. For UHS, the correlation is insignificant in both seasons. The result indicates that areas with very high LST give a weak negative correlation with NDVI. In summer and winter, NDBI presents a strong positive correlation with LST for the whole Imphal city. However, in UHI, the value of the correlation coefficient becomes very weak positive in both seasons. UHS presents an insignificant correlation in summer and a weak positive correlation in winter. It is mainly due to the complex landscape composition. NDBaI reflects a moderate positive correlation with LST in the whole city in both the seasons which becomes insignificant for UHI and UHS. It indicates that a wide area with high LST values generates a moderate to a strong positive relationship with NDBI and NDBaI whereas the corresponding area builds a moderate negative correlation with NDVI and MNDWI. However, the strength tends to be weak with the increase of LST concentrated in a small area. It happens because



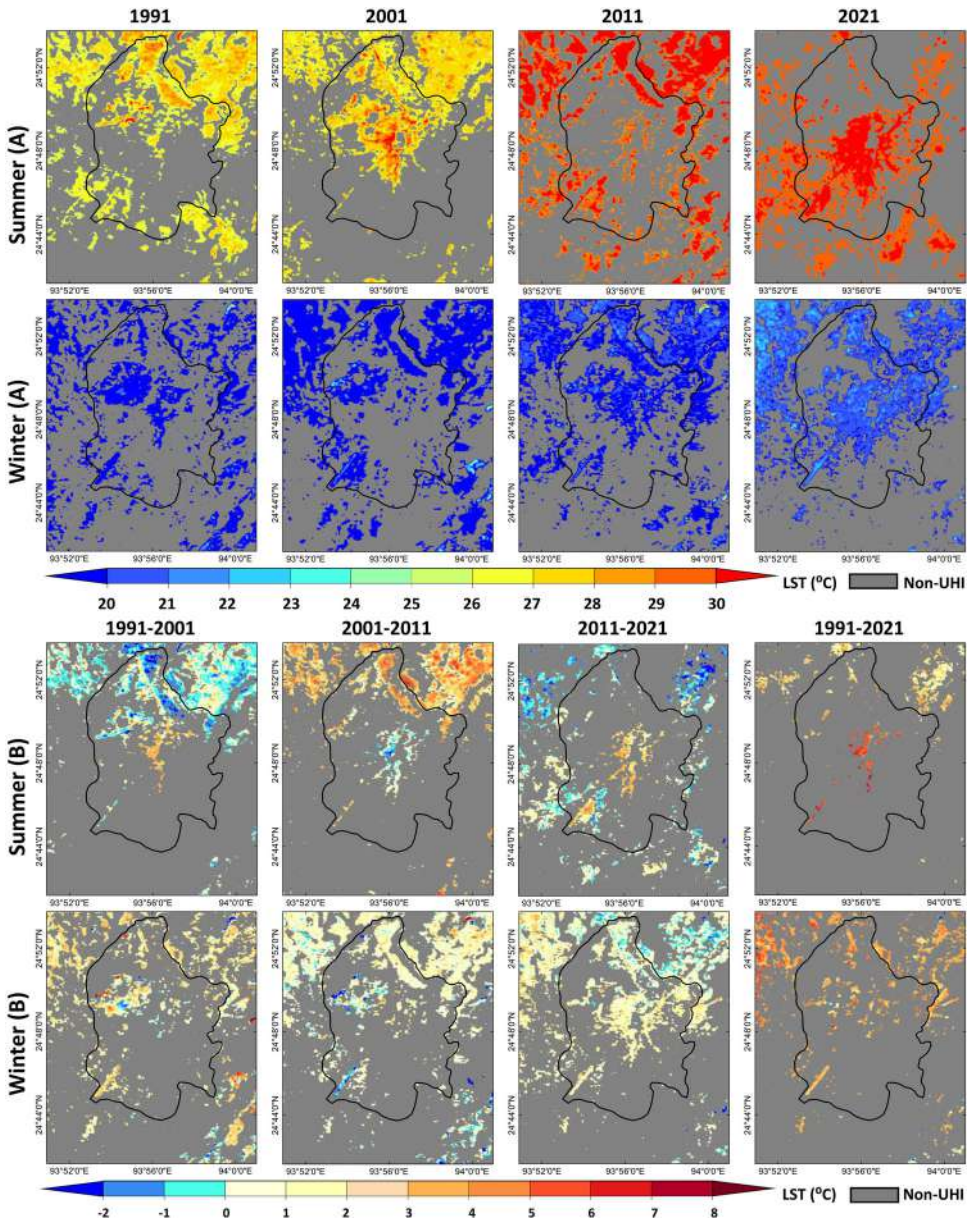


**Figure 5.** (A) Spatial and temporal distribution of LST in the UHI area (1991, 2001, 2011, and 2021). (B) Temporal changes in LST for the common UHI (1991-2001, 2001-2011, 2011-2021, and 1991-2021).

a small mixed land area does not generate a homogeneous surface that is very much responsible for the strong correlation between surface temperature and surface material.

The study presents a good output regarding the relationship. Halder et al. (2021) showed that LST builds a negative relation with NDVI and SAVI ( $R^2$  values are 0.20 and 0.15, respectively), positive relation with NDBI and UI ( $R^2$  values are 0.61 and

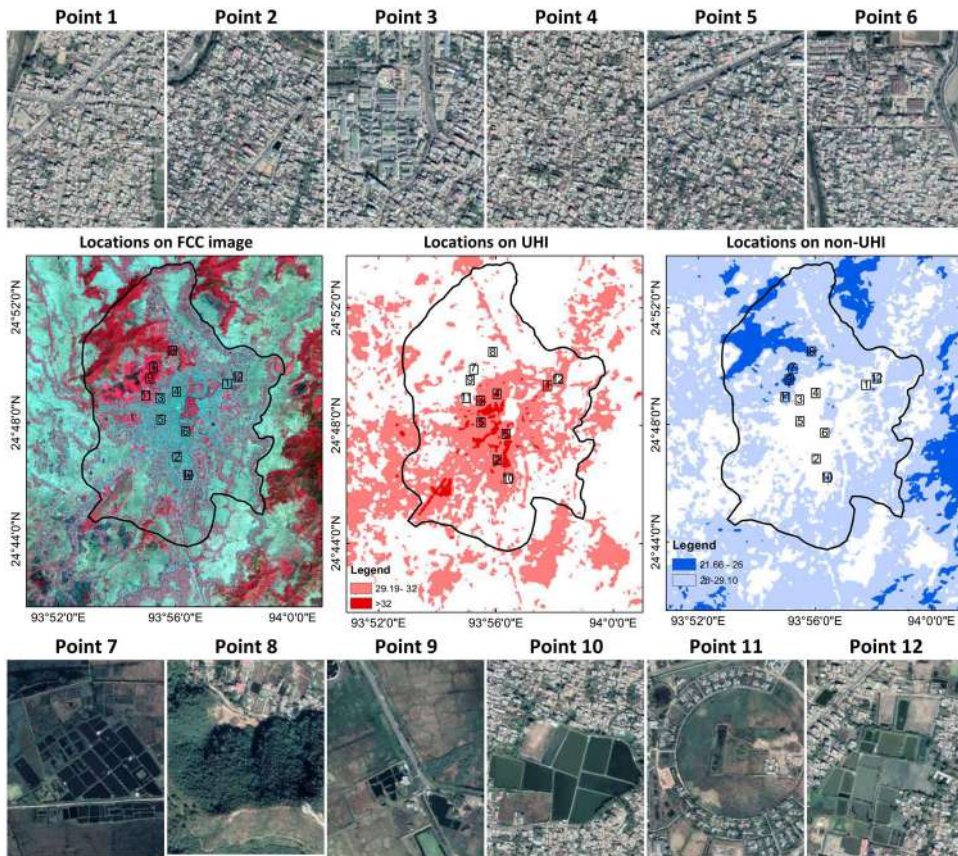


**Figure 6.** Random selection of locations in UHI ( $>32^{\circ}\text{C}$ ) and non-UHI ( $<26^{\circ}\text{C}$ ) of Imphal city. The number of locations was selected as 12 (UHI = 6 and non-UHI = 6), which shows on False Colour Composite (FCC) on April 20, 2021. The locations (12 points) were zoomed on Google image to show the actual landscape.

0.27, respectively), and an insignificant relation with MNDWI and NDBaI ( $R^2$  values are 0.0003 and 0.04, respectively) in Kolkata, India. Ramaiah et al. (2020) also presented the fact that LST is positively correlated to EBBI and negatively correlated to SAVI and MNDWI in a study performed in Panaji and Tumkur City of India and these relationships become weak in the UHI zones as the heterogeneity of land surface is increased. Guha and Govil (2021) also observed that LST builds a positive correlation with NDBI, NDBaI, and NDWI (0.65, 0.30, and 0.19, respectively), and a negative correlation with NMDI, MNDWI, and NDVI (0.54, 0.38, and 0.38, respectively) in a 30 years long study conducted on Raipur City, India. These results support the output of the present study.

#### 4.6. Ecological evaluation of imphal city using UTFVI

Table 7 shows the six different ecological evaluation indices for Imphal city based on the UTFVI values in both seasons from 1991-2021. Figure 7B presents the spatial distribution maps of UTFVI of the city during the entire study period.

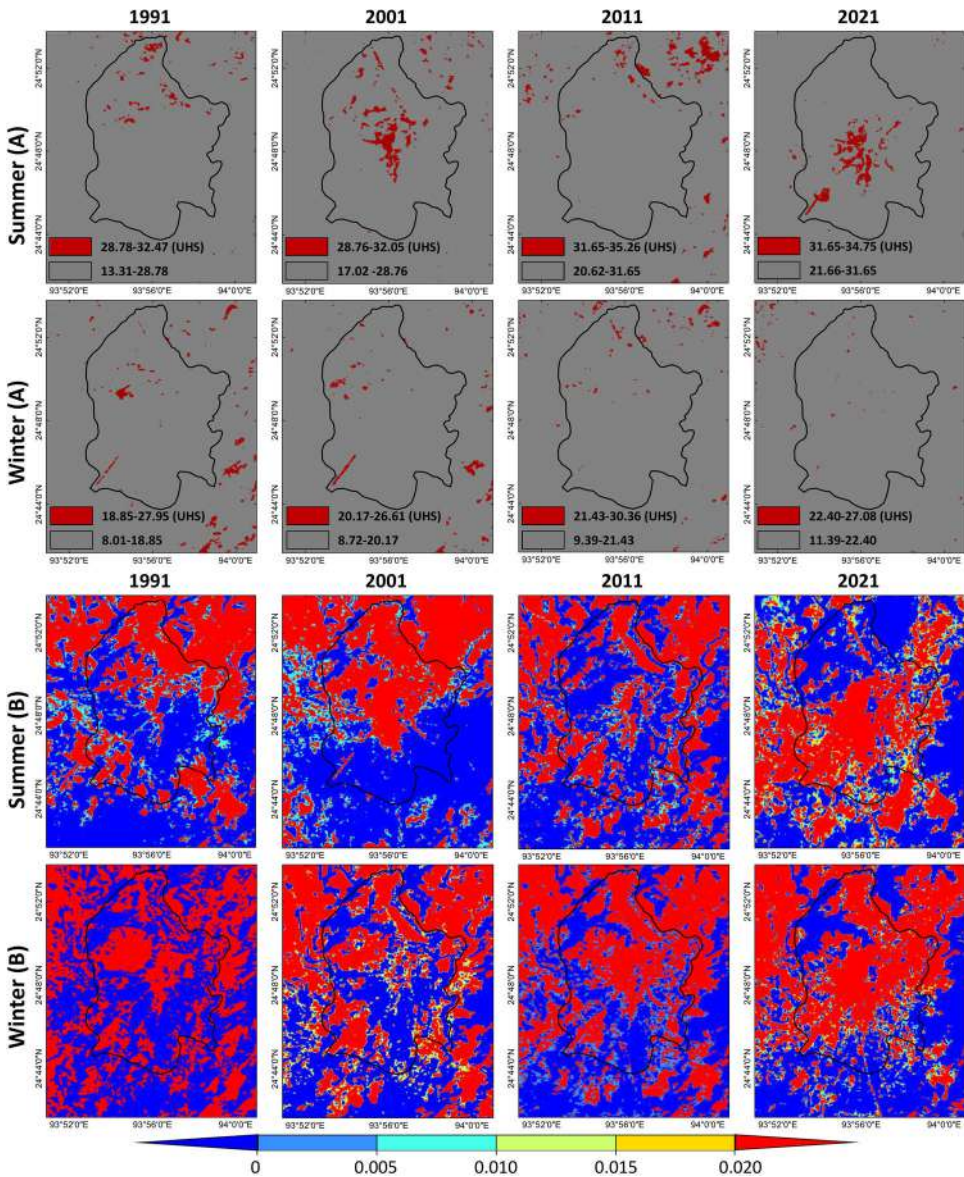


**Figure 7.** (A) The concentration of UHS in Imphal city in different periods (1991, 2001, 2011, and 2021). (B) Ecological evaluation index of Imphal city according to UTFVI (1991, 2001, 2011, and 2021).

It is clear from **Figure 7B** and **Table 7** that most of the areas of Imphal (>44% in summer and >39% in winter throughout the entire time) having excellent thermal conditions (i.e., UTFVI < 0). The percentage of the area under this excellent category is gradually decreasing from 1991 to 2021. Here the concentration of water bodies and vegetation is more. Mainly the southern portions experience such thermal conditions. However, the worst category (i.e., UTFVI > 0.020) of the ecological evaluation index also exists in a large portion (>37% in summer and >42% in winter throughout the entire time) of the city. The northern and some of the central parts fall under

**Table 6.** Correlation coefficient values of LST with different indices for whole Imphal city, UHI, and UHS (1991-2021).

	Summer				Winter			
	(whole Imphal city)							
	1991	2001	2011	2021	1991	2001	2011	2021
MNDWI	-0.50	-0.15	-0.49	-0.24	-0.50	-0.54	-0.46	-0.45
NDBal	0.48	0.20	0.60	0.36	0.56	0.58	0.59	0.49
NDBI	0.68	0.38	0.75	0.56	0.52	0.66	0.66	0.69
NDVI	-0.40	-0.26	-0.61	-0.54	-0.20	-0.41	-0.46	-0.48
	(UHI)							
	1991	2001	2011	2021	1991	2001	2011	2021
MNDWI	-0.12	-0.04	-0.24	-0.30	-0.24	-0.01	-0.17	-0.08
NDBal	0.06	0.13	0.13	-0.34	0.12	-0.20	0.13	0.05
NDBI	0.35	0.05	0.38	-0.07	0.01	-0.05	0.18	0.09
NDVI	-0.29	-0.02	-0.22	-0.23	0.17	0.06	-0.07	-0.04
	(UHS)							
	1991	2001	2011	2021	1991	2001	2011	2021
MNDWI	0.10	0.23	-0.15	-0.05	-0.22	-0.12	-0.33	-0.08
NDBal	-0.46	-0.17	-0.07	-0.05	0.17	-0.01	0.17	0.06
NDBI	-0.12	0.10	0.01	0.17	0.28	0.32	0.22	0.17
NDVI	0.13	-0.30	0.18	-0.07	-0.12	-0.15	0.02	-0.01

the worst category where most of the lands are impervious. The good ( $0 < UTFVI < 0.005$ ) and normal ( $0.005 < UTFVI < 0.010$ ) thermal conditions are found in some small patches surrounding the areas under excellent condition while the bad ( $0.010 < UTFVI < 0.015$ ) and worse ( $0.015 < UTFVI < 0.020$ ) conditions exist around the areas of the worst condition. The area under the excellent category slightly decreases from 50.05% in 1991 to 44.53% in 2021 (summer) and from 52.69% in 1991 to 43.33% in 2021 (winter) due to loss of vegetation and increase of built-up area. Some eco-environmental strategies like social forestry or wetland preservation can reduce the severe UHI effects.

Table 8 shows the correlation matrix of the UTFVI values among the summer and winter seasons of 1991, 2001, 2011, and 2021. The results show a strong positive correlation in the winter season while it is moderate positive in the summer season. In summer, the UTFVI of 1991 and 2001 has a correlation coefficient value of 0.52 which becomes 0.45 between the UTFVI of 2001 and 2011. This value remains almost similar (0.48) for the 2011 and 2021 UTFVI values. In winter, the correlation becomes stronger. The correlation coefficient values are 0.76, 0.81, and 0.82 between 1991-2001, 2001-2011, and 2011-2021, respectively. The correlation matrix of UTFVI indicates that the effect of UHI is more consistent in the winter season while it is much variable in the summer. This correlation matrix validates the result that comes from the UTFVI analysis.

The specific strengths of this research work are the LST-spectral indices relationship. It clearly describes the nature of the thermal status of the city and also helps to delineate the ecologically most vulnerable zones of the city. The UHSs are the most severely heated surface of the study area where special attention must be paid to developing better environmental condition. However, there are also some specific weaknesses of the study. LST also depends on wind speed, surface moisture,

**Table 7.** The threshold of ecological evaluation index of Imphal city (1991–2021).

UTFVI	UHI phenomenon	Ecological evaluation index	Summer season				Winter season			
			Percentage of Area (%)				Percentage of Area (%)			
			1991	2001	2011	2021	1991	2001	2011	2021
<0.000	None	Excellent	50.05	49.53	48.70	44.53	52.69	46.60	39.72	43.33
0.000–0.005	Weak	Good	—	—	—	3.59	4.72	—	12.52	2.72
0.005–0.010	Middle	Normal	10.00	11.07	9.09	4.99	—	—	—	2.67
0.010–0.015	Strong	Bad	—	—	—	4.64	—	10.69	—	2.66
0.015–0.020	Stronger	Worse	—	—	—	4.59	—	—	—	2.62
>0.020	Strongest	Worst	39.95	39.40	42.19	37.66	47.31	42.71	47.76	46.00

humidity, and intensity of solar radiation which have not been considered in the present study. Further, the analysis might be more authentic if it assessed the nighttime LST data. However, Landsat data does not provide nighttime LST. Furthermore, the results may be validated with a high-resolution LST product but it is a costly and time-taking task. Thus, the results should be considered in light of these limitations.

## 5. Conclusion

In this article, multi-temporal Landsat satellite images of the summer and winter seasons in 1991, 2001, 2011, and 2021 are used to evaluate the dynamic correlation between LST and different LULC indices in Imphal city and surroundings, India.

UHI zones are identified through LST which are mainly distributed in the north-eastern and south-central parts of Imphal. LST of the specified UHI has been significantly increased from 1991 to 2021. During the study period, the LST of the city increases at 14.39% and 19.67% rates in summer and winter, respectively. The southern part of the city is less warm compared to the rest of the parts due to the concentration of vegetation and water bodies. Some UHS were also delineated inside the zone of UHI, characterized by high concentrated LST.

Furthermore, the relationship of LST to NDVI, MNDWI, NDBI, and NDBaI was quantitatively interpreted by Pearson's correlation coefficient method. For the whole Imphal city, LST shows a moderate negative correlation with NDVI and MNDWI, a strong positive correlation with NDBI, and a moderate positive correlation with NDBaI. The winter season indicates a more consistent relationship. The relationship becomes weaker or even tends to be an inverse for UHI zones and urban hot spots. It may be due to the heterogeneous landscape in the urban area.

In addition, the spatial, temporal, and seasonal dynamics of the ecological evaluation index of Imphal were measured by the UTFVI. Most of the lands (44–50% in summer and 39–52% in winter) are under excellent condition although the percentage is declined. A high proportion of land (37–42% in summer and 42–47% in winter) also comes under the worst category. It indicates that the non-UHI zones remain almost unchanged. The ecological condition of the city can be developed by converting the bad category lands into the good category.

It can be recommended from the present study that a proper arrangement of LULC features is the most essential part of sustainable urban management planning. Urban land is always built over a small area and therefore a space-saving modern

**Table 8.** Correlation matrix of UTFVI values for 1991, 2001, 2011, and 2021 (summer and winter).

Year	Summer				Year	Winter			
	1991	2001	2011	2021		1991	2001	2011	2021
1991	1.00	0.52	0.61	0.28	1991	1.00	0.76	0.71	0.59
2001	0.52	1.00	0.45	0.40	2001	0.76	1.00	0.81	0.70
2011	0.61	0.45	1.00	0.48	2011	0.71	0.81	1.00	0.82
2021	0.28	0.40	0.48	1.00	2021	0.59	0.70	0.82	1.00

planning and management system is required. The built-up area should be expanded without reducing the concentration of green areas, water bodies, and wetlands.

The study was an attempt to simply correlate LST with four spectral indices in a humid subtropical landlocked mountainous urban area using Landsat data for summer and winter seasons. There are some limitations of the study. Such as, the results should be compared with other satellite data of different spatial resolutions (e.g., IKONOS (1 m), Quickbird (0.6 m), ASTER (15 m), Sentinel-2A (10 m), MODIS (1000 m), etc.). Besides, the seasonal variation of the correlation coefficients can be monitored for one or two years. Moreover, some other spectral indices (e.g., urban index, built-up index, soil and vegetation index, normalized difference mud index, normalized multi-band drought index, etc.) can be investigated to find a better correlation with LST. Apart from these, the results can be examined in different environments with large physical varieties. In addition to these, some other statistical methods and algorithms (Spearman rank correlation coefficient, Kendall correlation coefficient, etc.) can also be applied to estimate the correlation between LST and different spectral indices.

## Acknowledgment

The authors are indebted to USGS server (<http://earthexplorer.usgs.gov/>) and Manipur Municipal Corporation (<https://imc.mn.gov.in/>).

## Disclosure statement

No potential conflict of interest was reported by the authors.

## ORCID

Subhanil Guha  <http://orcid.org/0000-0002-2967-7248>

## Data availability statement

The data that support the findings of this study are openly available in the earth explorer website of USGS at <https://earthexplorer.usgs.gov/>.

## References

Artis DA, Carnahan WH. 1982. Survey of emissivity variability in thermography of urban areas. *Remote Sens Environ.* 12(4):313–329.

- Berger C, Rosentreter J, Voltersen M, Baumgart C, Schmullius C, Hese S. 2017. Spatio-temporal analysis of the relationship between 2D/3D urban site characteristics and land surface temperature. *Remote Sens Environ.* 193:225–243.
- Carlson TN, Ripley DA. 1997. On the relation between NDVI, fractional vegetation cover, and leaf area index. *Remote Sens Environ.* 62(3):241–252. [https://doi.org/10.1016/S0034-4257\(97\)00104-1](https://doi.org/10.1016/S0034-4257(97)00104-1).
- Chen XL, Zhao HM, Li PX, Yi ZY. 2006. Remote sensing image-based analysis of the relationship between urban heat island and land use/cover changes. *Remote Sens Environ.* 104(2): 133–146. <https://doi.org/10.1016/j.rse.2005.11.016>.
- Coutts AM, White EC, Tapper NJ, Beringer J, Livesley SJ. 2016. Temperature and human thermal comfort effects of street trees across three contrasting street canyon environments. *Theor Appl Climatol.* 124(1-2):55–68. [doi.org/10.1007/s00704-015-1409-y](https://doi.org/10.1007/s00704-015-1409-y).
- Dissanayake D. 2020. Land use change and its impacts on land surface temperature in Galle City, Sri Lanka. *Climate.* 8(5):65. <https://doi.org/10.3390/cli8050065>.
- Dissanayake D, Morimoto T, Ranagalage M, Murayama Y. 2019. Land-use/land-cover changes and their impact on surface urban heat islands: Case study of Kandy City, Sri Lanka. *Climate.* 7(8):99. <https://doi.org/10.3390/cli7080099>.
- Du S, Xiong Z, Wang Y, Guo L. 2016. Quantifying the multilevel effects of landscape composition and configuration on land surface temperature. *Remote Sens Environ.* 178:84–92.
- Essa W, Verbeiren B, Van der Kwast J, Van de Voorde T, Batelaan O. 2012. Evaluation of the DisTrad thermal sharpening methodology for urban areas. *Int J Appl Earth Obs Geoinf.* 19: 163–172. <https://doi.org/10.1016/j.jag.2012.05.010>.
- Estoque RC, Murayama Y, Myint SW. 2017. Effects of landscape composition and pattern on land surface temperature: An urban heat island study in the megacities of Southeast Asia. *Sci Total Environ.* 577:349–359.
- Feyisa GL, Meilby H, Jenerette GD, Pauliet S. 2016. Locally optimized separability enhancement indices for urban land cover mapping: Exploring thermal environmental consequences of rapid urbanization in Addis Ababa, Ethiopia. *Remote Sens Environ.* 175:14–31. <https://doi.org/10.1016/j.rse.2015.12.026>.
- Fu P, Weng Q. 2016. A time series analysis of urbanization induced land use and land cover change and its impact on land surface temperature with landsat imagery. *Remote Sens Environ.* 175:205–214.
- Grimm NB, Faeth SH, Golubiewski NE, Redman CL, Wu J, Bai X, Briggs JM, Grimm N. 2008. Global change and the ecology of cities. *Science.* 319(5864):756–760.
- Guha S, Govil H. 2021. Annual assessment on the relationship between land surface temperature and six remote sensing indices using Landsat data from 1988 to 2019. *Geocarto Int.* :1–20. <https://doi.org/10.1080/10106049.2021.1886339>.
- Guha S, Govil H, Dey A, Gill N. 2020. A case study on the relationship between land surface temperature and land surface indices in Raipur City, India. *Geogr Tidsskr.* 120(1):35–50. <https://doi.org/10.1080/00167223.2020.1752272>.
- Guha S, Govil H, Mukherjee S. 2017. Dynamic analysis and ecological evaluation of urban heat islands in Raipur city, India. *J Appl Remote Sens.* 11(03):1.
- Gutman G, Ignatov A. 1998. The derivation of the green vegetation fraction from NOAA/AVHRR data for use in numerical weather prediction models. *Int J Remote Sens.* 19(8): 1533–1543.
- Halder B, Bandyopadhyay J, Banik P. 2021. Evaluation of the climate change impact on urban heat island based on land surface temperature and geospatial indicators. *Int J Environ Res.* 15(5):819–835. <https://doi.org/10.1007/s41742-021-00356-8>.
- Hao X, Li W, Deng H. 2016. The oasis effect and summer temperature rise in arid regions — case study in Tarim Basin. *Sci Rep.* 6:35418. <https://doi.org/10.1038/srep35418>.
- He BJ, Zhao ZQ, Shen LD, Wang HB, Li LG, He BJ. 2019. An approach to examining performances of cool/hot sources in mitigating/enhancing land surface temperature under different temperature backgrounds based on Landsat 8 image. *Sustain Cities Soc.* 44:416–427.

- Kakon AN, Nobuo M, Kojima S, Yoko T. 2010. Assessment of thermal comfort in respect to building height in a high-density city in the tropics. *Am J Eng Appl Sci.* 3(3):545–551.
- Kalnay E, Cai M. 2003. Impact of urbanization and land-use change on climate. *Nat Cell Biol.* 423(6939):528–531.
- Kalota D. 2017. Exploring relation of land surface temperature with selected variables using geographically weighted regression and ordinary least square methods in Manipur State, India. *Geocarto Int.* 32(10):1105–1119. <https://doi.org/10.1080/10106049.2016.1195883>.
- Li ZN, Duan SB, Tang BH, Wu H, Ren HG, Yan GJ. 2016. Review of methods for land surface temperature derived from thermal infrared remotely sensed data. *J Remote Sens.* 20: 899–920.
- Liu L, Zhang Y. 2011. Urban heat island analysis using the landsat TM data and ASTER data: A case study in Hong Kong. *Remote Sens.* 3(7):1535–1552.
- Lopez JMR, Heider K, Scheffran J. 2017. Frontiers of urbanization: Identifying and explaining urbanization hot spots in the south of Mexico City using human and remote sensing. *Appl Geogr.* 79:1–10.
- Mackey CW, Lee X, Smith RB. 2012. Remotely sensing the cooling effects of city scale efforts to reduce urban heat island. *Build Environ.* 49:348–358.
- Matzarakis A, Mayer H, Iziomon MG. 1999. Applications of a universal thermal index: physiological equivalent temperature. *Int J Biometeorol.* 43(2):76–84.
- Nichol JE. 2005. Remote sensing of urban heat islands by day and night. *Photogram Eng Remote Sens.* 19:1639–1649.
- Pearsall H. 2017. Staying cool in the compact city: Vacant land and urban heating in Philadelphia. Pennsylvania. *Appl Geogr.* 79:84–92. <http://dxdoi.org/10.1016/j.apgeop.2016.12.010>.
- Ramaiah M, Avtar R, Rahman MM. 2020. Land cover influences on LST in two proposed smart cities of India: Comparative analysis using spectral indices. *Land.* 9(9):292. <https://doi.org/10.3390/land9090292>.
- Ranagalage M, Estoque RC, Zhang X, Murayama Y. 2018. Spatial changes of urban heat island formation in the Colombo District, Sri Lanka: Implications for sustainability planning. *Sustainability.* 10(5):1367. <https://doi.org/10.3390/su10051367>.
- Ren Y, Deng LY, Zuo SD, Song XD, Liao YL, Xu XD, Chen Q, Hua LZ, Li ZW. 2016. Quantifying the influences of various ecological factors on land surface temperature of urban forests. *Environ Pollut.* 216:519–529.
- Sobrino JA, Jimenez-Munoz JC, Paolini L. 2004. Land surface temperature retrieval from Landsat TM5. *Remote Sens Environ.* 90(4):434–440.
- Sobrino JA, Raissouni N, Li Z. 2001. A comparative study of land surface emissivity retrieval from NOAA data. *Remote Sens Environ.* 75(2):256–266. [https://doi.org/10.1016/S0034-4257\(00\)00171-1](https://doi.org/10.1016/S0034-4257(00)00171-1).
- Shukla A, Jain K. 2021. Analyzing the impact of changing landscape pattern and dynamics on land surface temperature in Lucknow city, India. *Urban for Urban Green.* 58:126877. <https://doi.org/10.1016/j.ufug.2020.126877>.
- Tomlinson CJ, Chapman L, Thornes JE, Baker C. 2011. Remote sensing land surface temperature for meteorology and climatology: a review. *Met Apps.* 18(3):296–306.
- Tran DX, Pla F, Latorre-Carmona P, Myint SW, Caetano M, Kieu HV. 2017. Characterizing the relationship between land use land cover change and land surface temperature. *ISPRS J Photogramm Sens.* 124:119–132.
- Tucker CJ. 1979. Red and photographic infrared linear combinations for monitoring vegetation. *Remote Sens Environ.* 8(2):127–150.
- Voogt JA, Oke TR. 2003. Thermal remote sensing of urban climates. *Remote Sens Environ.* 86(3):370–384.
- Weng Q. 2009. Thermal infrared remote sensing for urban climate and environmental studies: methods, applications, and trends. *ISPRS J Photogramm Sens.* 64(4):335–344.
- Weng QH, Lu DS, Schubring J. 2004. Estimation of land surface temperature–vegetation abundance relationship for urban heat island studies. *Remote Sens Environ.* 89(4):467–483.



- Willett KM, Sherwood S. 2012. Exceedance of heat index thresholds for 15 regions under a warming climate using the wet-bulb globe temperature. *Int J Climatol.* 32(2):161–177.
- Xu H. 2006. Modification of normalized difference water index (NDWI) to enhance open water features in remotely sensed imagery. *Int J Remote Sens.* 27(14):3025–3033.
- Zha Y, Gao J, Ni S. 2003. Use of normalized difference built-up index in automatically mapping urban areas from TM imagery. *Int J Remote Sens.* 24(3):583–594. <https://doi.org/10.1080/01431160304987>.
- Zhao HM, Chen XL. 2005. Use of normalized difference bareness index in quickly mapping bare areas from TM/ETM+. *Geosci Remote Sens Symp.* 3(25–29): 1666–1668. <https://doi.org/10.1109/IGARSS.2005.1526319>.
- Zhou D, Xiao J, Bonafoni S, Berger C, Deilami K, Zhou Y, Frohling S, Yao R, Qiao Z, Sobrino JA. 2018. Satellite remote sensing of surface urban heat islands: progress, challenges, and perspectives. *Remote Sens.* 11(1):48.



# Source details

[Feedback >](#) [Compare sources >](#)

## Geomatics, Natural Hazards and Risk

Open Access [i](#)

Scopus coverage years: from 2010 to Present

Publisher: Taylor & Francis

ISSN: 1947-5705 E-ISSN: 1947-5713

Subject area: [Earth and Planetary Sciences: General Earth and Planetary Sciences](#) [Environmental Science: General Environmental Science](#)

Source type: Journal

[View all documents >](#)

[Set document alert](#)

[Save to source list](#)

CiteScore 2022

7.3



SJR 2022

0.813



SNIP 2022

1.184



See discussions, stats, and author profiles for this publication at: <https://www.researchgate.net/publication/348442749>

# Relationship between land surface temperature and normalized difference water index on various land surfaces: A seasonal analysis

Article · January 2021

CITATIONS

13

READS

193

2 authors:



**Subhanil Guha**

National Institute of Technology Raipur

69 PUBLICATIONS 1,353 CITATIONS

[SEE PROFILE](#)



**Himanshu Govil**

National Institute of Technology Raipur

130 PUBLICATIONS 2,195 CITATIONS

[SEE PROFILE](#)



## Relationship between land surface temperature and normalized difference water index on various land surfaces: A seasonal analysis

Subhanil Guha<sup>\*1</sup>  Himanshu Govil<sup>1</sup> 

<sup>1</sup>National Institute of Technology Raipur, Department of Applied Geology, Raipur, India

### Keywords

Landsat  
Land surface  
LST  
NDWI  
Raipur

### ABSTRACT

The present study examines the seasonal relationship between land surface temperature (LST) and normalized difference water index (NDWI) on various land surfaces in Raipur City of India by using a series of Landsat images for four specific seasons since 1991-92. The LST is retrieved using the mono-window algorithm technique. The results show that the LST of the study area is noticeably affected by surface composition. The best correlation (correlation coefficient  $r = 0.42$ ) between the LST and NDWI is achieved in the post-monsoon season, followed by the monsoon season ( $r = 0.33$ ), pre-monsoon season ( $r = 0.25$ ), and winter season ( $r = 0.04$ ). There is a moderate negative correlation ( $r = -0.49, -0.33, -0.31, \text{ and } -0.25$  in the pre-monsoon, monsoon, post-monsoon, and winter season, respectively) generated between the LST and NDWI on water bodies. On green vegetation, this LST-NDWI correlation is moderate positive ( $r = 0.67, 0.43, 0.50, \text{ and } 0.25$  in the pre-monsoon, monsoon, post-monsoon, and winter season, respectively). On human settlement and barren land surface, the correlation is weak positive ( $r = 0.24, 0.21, 0.27, \text{ and } 0.15$  in the pre-monsoon, monsoon, post-monsoon, and winter season, respectively). The output of the research work can be used in the town planning section of any urban agglomeration.

## 1. INTRODUCTION

Land surface temperature (LST) is a significant factor for investigating the biogeochemical processes of the land surface (Tomlinson et al. 2011; Hao et al. 2016). A variation on LST is due to the variation in land surface configuration (Hou et al. 2010). Generally, green vegetation and water bodies present low LST, whereas built-up area, bare rock surface or dry soil reflects high LST (Guha et al. 2020a). Thus, LST related studies are very important in urban land use planning and development (Li et al. 2017). Urban heat island and urban hot spots are a very common term in an urban environment and are indicated by the zone of very high LST inside the urban bodies (Guha et al. 2017). Normalized difference water index (NDWI) is the most popular index for water surface extraction and it is invariably used in LULC and LST related studies (McFeeters 1996; Chen et al. 2006; Essa et al. 2012;

Yuan et al. 2017; Guha et al. 2020b). Generally, the nature of LST-NDWI relationship in an urban area is insignificant which is controlled by several factors, such as humidity, vegetation, wetland, bare land, air pollution, rock surface, dry or wet soil, heterogeneous man-made materials, etc. (McFeeters 1996; Ghobadi et al. 2014; Guha et al. 2020c).

In many current research articles, the relationship between LST and NDWI was constructed using thermal infrared remote sensing. However, the seasonal analysis of the LST-NDWI relationship in tropical India is rare. The nature of LST and NDWI is changed due to the seasonal changes of evaporation, precipitation, moisture content, air temperature, etc. The LST-NDWI relationship was performed on Raipur City of Chhattisgarh State in Central India as it is not influenced by the humid maritime or dry extreme climatic condition. The study examines the nature and trend of

### \*Corresponding Author

<sup>\*</sup>(subhanilguha@gmail.com) ORCID ID 0000-0002-2967-7248  
(himgeo@gmail.com) ORCID ID 0000-0002-3433-8355

### Cite this article

Guha S & Govil H (2021). Relationship between land surface temperature and normalized difference water index on various land surfaces: A seasonal analysis. International Journal of Engineering and Geosciences, 6(3), 165-173

the effect of LST on NDWI and the LST-NDWI relation on various land surfaces and their seasonal variation. The main focus of the study is to explore the long-term seasonal analysis of LST-NDWI correlation on various land surfaces. The study will be effective for the future town and country planners for better environmental planning.

## 2. MATERIALS AND METHOD

### 2.1. Study area

The Raipur City of India was selected as the study area for the entire research work (Fig. 1). It is the capital and the largest city of Chhattisgarh State of India (URL-1). Raipur is one of the fastest-growing smart cities in India in terms of the urban area and urban population. Fig. 1(a) presents the outline map of India where Chhattisgarh State is located in the middle part (URL-2). Fig. 1(b) presents the outline map of Chhattisgarh State with districts (URL-2). Fig. 1(c) presents the false colour composite (FCC) image of Raipur City from recent Landsat 8 data (Date: 7 November 2018). Fig. 1(d) presents the digital elevation model (Date: 11 October 2011) of Raipur City (URL-3). The total study area extends between 21°11'22"N to 21°20'02"N and

81°32'20"E to 81°41'50"E with an average elevation of 219m to 322m (Fig. 1(d)). The Mahanadi River flows to the east of the city of Raipur, and the southern side has dense forests. The Maikal Hills rise on the northwest of Raipur; on the north, the land rises and merges with the Chota Nagpur Plateau, which extends northeast across Jharkhand state. On the south of Raipur lies the Deccan Plateau. The area is under a tropical wet and dry climate with four typical seasons (pre-monsoon, monsoon, post-monsoon, and winter). Hot and dry pre-monsoon season extends from March to May (Govil et al. 2019). June to September (rainy months) is significantly considered under the monsoon season. October and November months are often considered as the post-monsoon season, characterised by low pollution, moderate temperature, and moderate moisture content in plants and air, and a high percentage of green plants. December to February months (winter season) experience a cool and dry climate. The study area is also characterised by tropical mixed deciduous vegetation and mixed red soil (Govil et al. 2020). The total population of the city is over 1 million, and the sex ratio is 945 (URL-1). The city has an 86.90% total literacy rate (URL-1).

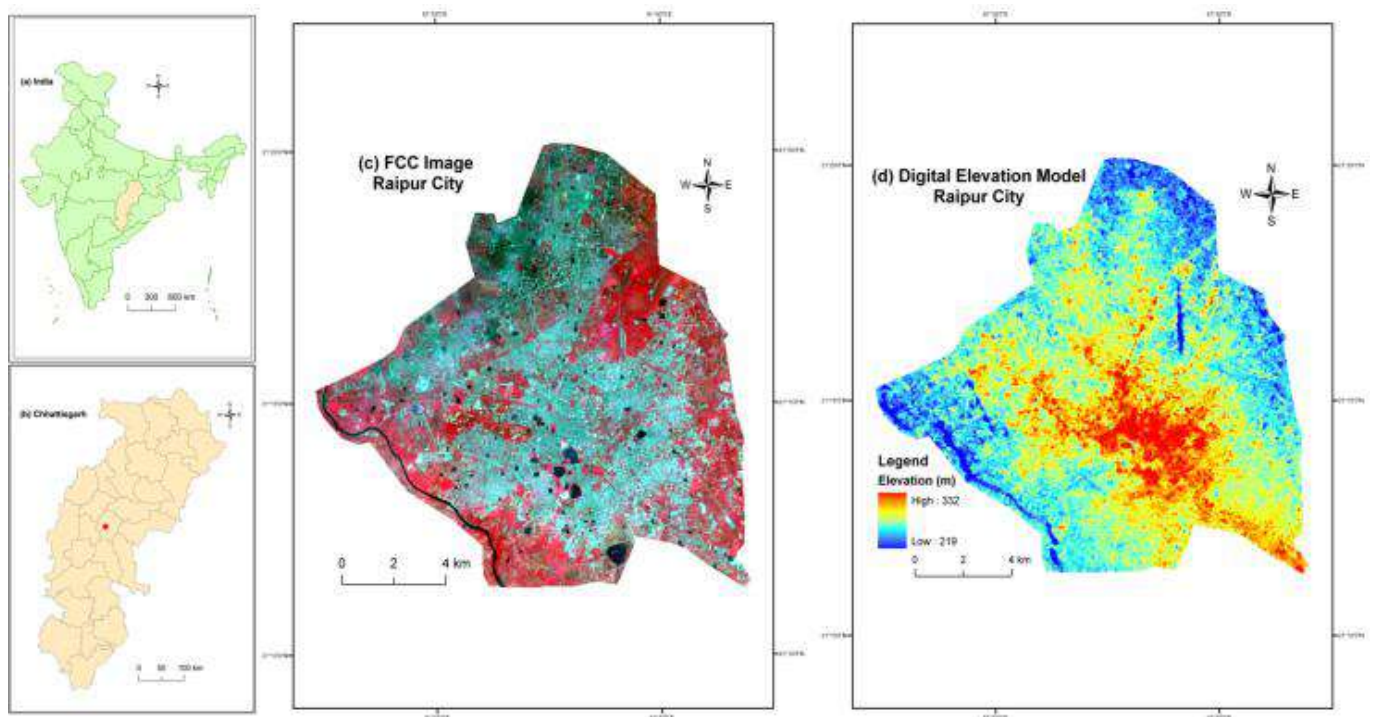


**Figure 1.** Location of the study area: (a) India (b) Chhattisgarh (c) FCC image of Raipur City (d) DEM of Raipur City

### 2.2. Data

Table 1 shows the specification of Landsat data of different sensors. Landsat 8 thermal infrared sensors (TIRS) dataset has two TIR bands (bands 10 and 11) in which band 11 has a larger calibration uncertainty. Thus, only TIR band 10 data (100 m resolution) was recommended for the present study (Barsi et al. 2014). Landsat 5 thematic mapper (TM) data has only one TIR band (band 6) of 120 m resolution. Landsat 7 enhanced

thematic mapper plus (ETM+) data has a TIR band (band 6) of 60 m resolution. The TIR bands of all the Landsat sensors were resampled to 30 m pixel size by the data provider (URL-3) as the spatial resolution of visible to near-infrared (VNIR) and shortwave infrared (SWIR) bands of the three types of Landsat sensors is 30 m. All the raster calculations were processed in the environment of ArcGIS 9.3 and ERDAS IMAGINE 9.1 software.

**Table 1.** Specification of Landsat data sets

Date of acquisition	Time (UTC)	Cloud cover (%)	Resolution of TIR bands (m)
18-Mar-91	04:17:34	0	120
03-Apr-91	04:17:46	0	120
21-May-91	04:18:39	1	120
26-Sep-91	04:20:03	13	120
12-Oct-91	04:20:12	6	120
13-Nov-91	04:20:19	1	120
16-Jan-92	04:20:22	3	120
01-Feb-92	04:20:27	0	120
17-Feb-92	04:20:15	4	120
14-Apr-95	04:05:06	0	120
10-Dec-95	03:56:47	0	120
27-Jan-96	04:00:14	0	120
23-Sep-96	04:14:16	2	120
09-Oct-96	04:15:07	0	120
25-Oct-96	04:15:55	5	120
10-Nov-96	04:16:41	7	120
11-Nov-99	04:49:00	0	60
30-Jan-00	04:48:55	0	60
03-Apr-00	04:48:35	0	60
05-May-00	04:48:20	0	60
26-Sep-00	04:46:33	6	60
15-Dec-00	04:46:31	0	60
21-Mar-04	04:35:14	0	120
22-Apr-04	04:36:01	1	120
24-May-04	04:36:54	0	120
09-Jun-04	04:37:23	9	120
29-Sep-04	04:40:16	9	120
15-Oct-04	04:40:36	4	120
16-Nov-04	04:41:11	0	120
02-Dec-04	04:41:33	0	120
18-Dec-04	04:41:52	0	120
19-Jan-05	04:42:17	0	120
04-Feb-05	04:42:29	0	120
03-Mar-09	04:42:22	0	120
19-Mar-09	04:42:44	2	120
04-Apr-09	04:43:05	0	120
20-Apr-09	04:43:24	0	120
06-May-09	04:43:42	0	120
22-May-09	04:44:00	1	120
23-Jun-09	04:44:35	0	120
13-Oct-09	04:46:12	0	120
29-Oct-09	04:46:20	0	120
16-Dec-09	04:46:44	1	120
17-Jan-10	04:46:55	6	120
02-Feb-10	04:46:59	0	120
18-Feb-10	04:47:02	7	100
17-Mar-14	04:56:36	0	100
02-Apr-14	04:56:19	0	100
20-May-14	04:55:38	5	100
05-Jun-14	04:55:45	0	100
12-Nov-14	04:56:21	7	100
30-Dec-14	04:56:09	0	100
15-Jan-15	04:56:09	0	100
31-Jan-15	04:56:04	0	100
16-Feb-15	04:55:55	0	100
12-Mar-18	04:55:43	2	100
28-Mar-18	04:55:36	0	100
15-May-18	04:55:08	0	100
16-Jun-18	04:55:01	2	100
06-Oct-18	04:55:53	0	100
22-Oct-18	04:55:59	0	100
07-Nov-18	04:56:03	0	100
25-Dec-18	04:55:59	0	100
11-Feb-19	04:55:52	0	100
27-Feb-19	04:55:48	4	100

### 2.3. Retrieving LST from Landsat Data

In this study, the mono-window algorithm was applied to retrieve LST from multi-temporal Landsat satellite sensors (Qin et al. 2001) where three necessary parameters are ground emissivity, atmospheric

transmittance, and effective mean atmospheric temperature. At first, the original TIR bands (100 m resolution for Landsat 8 OLI/TIRS data, 120 m resolution for Landsat 5 TM data, and 60 m resolution for Landsat 7 ETM+ data) were resampled into 30 m by USGS data centre for further application.

The TIR pixel values are firstly converted into radiance from digital number (DN) values (Markham & Barkar 1985). Radiance for TIR band of Landsat 5 TM data and Landsat 7 ETM+ data is obtained using Eq. (1) (URL-3):

$$L_{\lambda} = \left[ \frac{L_{MAX\lambda} - L_{MIN\lambda}}{QCAL_{MAX} - QCAL_{MIN}} \right] * [QCAL - QCAL_{MIN}] + L_{MIN\lambda} \quad (1)$$

where,  $L_{\lambda}$  is Top of Atmosphere (TOA) spectral radiance ( $Wm^{-2}sr^{-1}mm^{-1}$ ),  $QCAL$  is the quantized calibrated pixel value in DN,  $L_{MIN\lambda}$  ( $Wm^{-2}sr^{-1}mm^{-1}$ ) is the spectral radiance scaled to  $QCAL_{MIN}$ ,  $L_{MAX\lambda}$  ( $Wm^{-2}sr^{-1}mm^{-1}$ ) is the spectral radiance scaled to  $QCAL_{MAX}$ ,  $QCAL_{MIN}$  is the minimum quantized calibrated pixel value in DN and  $QCAL_{MAX}$  is the maximum quantized calibrated pixel value in DN.  $L_{MIN\lambda}$ ,  $L_{MAX\lambda}$ ,  $QCAL_{MIN}$ , and  $QCAL_{MAX}$  values are obtained from the metadata file of Landsat TM and ETM+ data. Radiance for Landsat 8 TIR band is obtained from Eq. (2) (Zanter 2019):

$$L_{\lambda} = M_L \cdot QCAL + A_L \quad (2)$$

where,  $L_{\lambda}$  is the TOA spectral radiance ( $Wm^{-2}sr^{-1}mm^{-1}$ ),  $M_L$  is the band-specific multiplicative rescaling factor from the metadata,  $A_L$  is the band-specific additive rescaling factor from the metadata,  $QCAL$  is the quantized and calibrated standard product pixel values (DN). All of these variables can be retrieved from the metadata file of Landsat 8 data.

For Landsat 5 and 7 data, the reflectance value is obtained from radiances using Eq. (3) (URL-3):

$$\rho_{\lambda} = \frac{\pi \cdot L_{\lambda} \cdot d^2}{ESUN_{\lambda} \cdot \cos \theta_s} \quad (3)$$

where,  $\rho_{\lambda}$  is unitless planetary reflectance,  $L_{\lambda}$  is the TOA spectral radiance ( $Wm^{-2}sr^{-1}\mu m^{-1}$ ),  $d$  is Earth-Sun distance in astronomical units,  $ESUN_{\lambda}$  is the mean solar exo-atmospheric spectral irradiances ( $Wm^{-2}\mu m^{-1}$ ) and  $\theta_s$  is the solar zenith angle in degrees.  $ESUN_{\lambda}$  values for each band of Landsat 5 and 7 can be obtained from the handbooks of the related mission.  $\theta_s$  and  $d$  values can be attained from the metadata file (Coll et al. 2010).

For Landsat 8 data, reflectance conversion can be applied to DN values directly as in Eq. (4) (Zanter 2019):

$$\rho_{\lambda} = \frac{M_p \cdot QCAL + A_p}{\sin \theta_{SE}} \quad (4)$$

where,  $M_p$  is the band-specific multiplicative rescaling factor from the metadata,  $A_p$  is the band-specific additive rescaling factor from the metadata,  $Q_{CAL}$  is the quantized and calibrated standard product pixel values (DN) and  $\theta_{SE}$  is the local sun elevation angle from metadata file.

Eq. (5) is used to convert the spectral radiance to at-sensor brightness temperature (Wukelic et al. 1989; Chen et al. 2006):

$$T_b = \frac{K_2}{\ln\left(\frac{K_1}{L_\lambda} + 1\right)} \quad (5)$$

where,  $T_b$  is the brightness temperature in Kelvin (K),  $L_\lambda$  is the spectral radiance in  $Wm^{-2}sr^{-1}mm^{-1}$ ;  $K_2$  and  $K_1$  are calibration constants. For Landsat 8 data,  $K_1$  is 774.89,  $K_2$  is 1321.08 ( $Wm^{-2}sr^{-1}mm^{-1}$ ). For Landsat 7 data,  $K_1$  is 666.09,  $K_2$  is 1282.71 ( $Wm^{-2}sr^{-1}mm^{-1}$ ). For Landsat 5 data,  $K_1$  is 607.76,  $K_2$  is 1260.56 ( $Wm^{-2}sr^{-1}mm^{-1}$ ).

The land surface emissivity  $\varepsilon$ , is estimated from Eq. (6) using the NDVI Thresholds Method (Sobrino et al. 2001, 2004; Vlassova et al. 2014).

$$\varepsilon = \varepsilon_v F_v + \varepsilon_s (1 - F_v) + d\varepsilon \quad (6)$$

where,  $\varepsilon$  is land surface emissivity,  $\varepsilon_v$  is vegetation emissivity,  $\varepsilon_s$  is soil emissivity,  $F_v$  is fractional vegetation,  $d\varepsilon$  is the effect of the geometrical distribution of the natural surfaces and internal reflections that can be expressed by Eq. (7):

$$d\varepsilon = (1 - \varepsilon_s)(1 - F_v)F\varepsilon_v \quad (7)$$

where,  $\varepsilon_v$  is vegetation emissivity,  $\varepsilon_s$  is soil emissivity,  $F_v$  is fractional vegetation,  $F$  is a shape factor whose mean is 0.55, the value of  $d\varepsilon$  may be 2% for mixed land surfaces (Sobrino et al. 2004).

The fractional vegetation  $F_v$ , of each pixel, is determined from the NDVI using Eq. (8) (Carlson & Ripley 1997):

$$F_v = \left( \frac{NDVI - NDVI_{min}}{NDVI_{max} - NDVI_{min}} \right)^2 \quad (8)$$

where, (a)  $NDVI < 0.2$  for bare soil; (b)  $NDVI > 0.5$  for vegetation; (c)  $0.2 \leq NDVI \leq 0.5$  for mixed land with bare soil and vegetation; (d)  $NDVI < 0$  for water body (Sobrino et al. 2001, 2004; Vlassova et al. 2014).

Finally, the land surface emissivity  $\varepsilon$  can be expressed by Eq. (9):

$$\varepsilon = 0.004 * F_v + 0.986 \quad (9)$$

where,  $\varepsilon$  is land surface emissivity,  $F_v$  is fractional vegetation.

Water vapour content is estimated by Eq. (10) (Yang & Qiu 1996; Li 2006):

$$w = 0.0981 * \left[ 10 * 0.6108 * \exp\left(\frac{17.27 * (T_0 - 273.15)}{237.3 + (T_0 - 273.15)}\right) * RH \right] + 0.1697 \quad (10)$$

where,  $w$  is the water vapour content ( $g/cm^2$ ),  $T_0$  is the near-surface air temperature in Kelvin (K),  $RH$  is the relative humidity (%). These parameters of atmospheric profile are the average values of 14 stations around Raipur which are obtained from the Meteorological Centre, Raipur (URL-4) and the Regional Meteorological Centre, Nagpur (URL-5). Atmospheric transmittance is determined for Raipur City using Eq. (11) (Qin et al. 2001; Sun et al. 2010):

$$\tau = 1.031412 - 0.11536w \quad (11)$$

where,  $\tau$  is the total atmospheric transmittance,  $w$  is the water vapour content ( $g/cm^2$ ).

Raipur City is located in the tropical region. Thus, Eq. (12) is applied to compute the effective mean atmospheric transmittance of Raipur (Qin et al. 2001; Sun et al. 2010):

$$T_a = 17.9769 + 0.91715T_0 \quad (12)$$

LST is retrieved from Landsat 5 TM, Landsat 7 ETM+, and Landsat 8 OLI/TIRS satellite data by using Eq. (13-15) (Qin et al. 2001):

$$T_s = \frac{[a(1-C-D) + (b(1-C-D) + C + D)T_b - DT_a]}{C} \quad (13)$$

$$C = \varepsilon\tau \quad (14)$$

$$D = (1-\tau)[1 + (1-\varepsilon)\tau] \quad (15)$$

where,  $\varepsilon$  is the land surface emissivity,  $\tau$  is the total atmospheric transmittance,  $C$  and  $D$  are internal parameters based on atmospheric transmittance and land surface emissivity,  $T_b$  is the at-sensor brightness temperature,  $T_a$  is the mean atmospheric temperature,  $T_0$  is the near-surface air temperature,  $T_s$  is the land surface temperature,  $a = -67.355351$ ,  $b = 0.458606$ .

#### 2.4. Extraction of Different Types of land surface by Using NDWI

Various land surface biophysical parameters were applied to specify different types of land surface features (Govil et al. 2019, 2020). In this study, special emphasis was given on NDWI (McFeeters 1996, 2013) for determining the relationship with LST. NDWI is determined by the green and NIR bands. For, Landsat 5 TM and Landsat 7 ETM+ data, band 2 is used as the green band and band 4 is used as the NIR band, respectively. For Landsat 8 OLI/TIRS data, band 3 and band 5 are used as the green and NIR bands, respectively (Table 2). The value of NDWI is ranged between -1 and +1. Generally, the negative value of NDWI indicates the built-up area and bare land that

have no water surfaces (Table 2). The dryness increases with the increase of the negativity of NDWI. NDWI value ranges between 0 to 0.3 shows the water bodies (McFeeters 2013), whereas NDWI > 0.3 shows the vegetation with water surfaces (McFeeters 1996, 2013; Chen et al. 2006; Guha et al. 2017). Generally, the post-monsoon images reduce the level of air pollution due to the presence of high moisture content in the air and these images also enhance the greenness of an area. Thus, the post-monsoon images are generally considered for the generation of land use/land cover (LULC) maps. LULC maps were generated using the aforesaid threshold limits of NDWI (McFeeters 1996, 2013; Chen et al. 2006; Guha et al. 2017) and the result was validated by the maximum likelihood classification. The average calculated values of the kappa coefficient and overall accuracy for all the images were 0.87 and 92.14%, respectively.

**Table 2.** Description of NDWI

Acronym	Description	Formulation	References
NDWI	Normalized difference water index	$\frac{Green - NIR}{Green + NIR}$	McFeeters 1996

### 3. RESULTS AND DISCUSSION

#### 3.1. Extraction of LULC Types Using NDWI

The total area under different LULC categories was shown in Table 3. Water bodies were the most stable LULC type in the study area. Green vegetation was decreased in a very significant amount (76.80 km<sup>2</sup>) from 1991-92 to 2018-19. On the other hand, the built-up area and bare land were increased at a very high rate (78.37 km<sup>2</sup> in 27 years) due to rapid land conversion. In 1991-92, the built-up area and bare land were mainly found in the central part of the Raipur City. The northwest portion of the city was urbanised rapidly from 1991-92 to 2004-05 as the percentage of urban vegetation was declined due to the conversion into built-up areas. After 2004-05, the green areas were reduced at an alarming rate as most of the parts of the city were converted into bare land and built-up area. Only the eastern and the south-western parts were covered by urban vegetation.

**Table 3.** Total area (km<sup>2</sup>) under different types of LULC

Year	Green vegetation	Built-up area and bare land	Water bodies
1991-92	140.38	21.16	2.69
1995-96	130.23	31.72	2.29
1999-00	117.74	44.59	1.89
2004-05	112.41	49.68	2.14
2009-10	90.69	71.59	1.95
2014-15	81.63	81.28	1.32
2018-19	63.58	99.53	1.12

#### 3.2. Characteristics of the Spatial Distribution of LST and NDWI

There is a prominent seasonal variation of different periods that occurred in mean and standard deviation (STD) values of LST (Table 4). The winter season indicates the lowest mean LST values for all the years, whereas the highest mean LST values were found in the

pre-monsoon seasons during the entire time. From 1991-92 to 2018-19, the mean LST increased in every season. The post-monsoon season has the mean LST value nearer to the winter season, while monsoon season has a slightly high value of mean LST than the post-monsoon season. The average values of LST and the correlation coefficient of LST and NDWI from 1991-92 to 2018-19 were shown in grey shades inside the Table 4.

Fig. 2 shows the seasonal contrast in the distribution of LST from 1991-92 to 2018-19. The pre-monsoon season has the maximum values of mean LST followed by monsoon, post-monsoon, and winter season. The northwest and southeast parts of the study area exhibit high LST. These parts also have a low percentage of urban vegetation and a high percentage of built-up area and bare land. It shows that the proportion of vegetation has been reduced and the built-up area was increased significantly with time. The Pearson's correlation coefficient (*r*) values between the LST and NDWI for the entire period were moderate positive to weak negative. The post-monsoon season has the best mean correlation coefficient value (0.42), followed by the monsoon (0.34), pre-monsoon (0.25), and winter (0.04) season.

**Table 4.** Temporal and seasonal variation of LST values and Pearson's correlation coefficient values of LST-NDWI relationship (significant at 0.05 level).

Season	Year of acquisition	LST (°C)				Correlation coefficients for LST-NDWI relationship
		Min.	Max.	Mean	Std.	
Pre-monsoon	1991-92	23.81	36.27	31.54	1.52	0.13
	1995-96	24.54	41.07	34.64	1.89	0.12
	1999-00	26.36	42.23	36.38	1.93	0.33
	2004-05	26.95	44.07	38.01	2.19	0.29
	2009-10	28.81	46.48	39.60	2.54	0.26
	2014-15	31.93	48.22	41.28	1.75	0.29
	2018-19	33.46	51.11	43.74	1.75	0.35
	<b>Average</b>	<b>27.98</b>	<b>44.21</b>	<b>37.88</b>	<b>1.94</b>	<b>0.25</b>
Monsoon	1991-92	19.87	30.83	25.74	1.41	0.26
	1995-96	21.21	33.01	26.50	1.33	0.36
	1999-00	22.76	35.91	27.81	1.34	0.48
	2004-05	24.17	36.20	31.32	1.33	0.38
	2009-10	25.94	38.38	33.06	2.40	0.31
	2014-15	27.74	40.15	34.87	1.68	0.33
	2018-19	30.59	41.98	37.30	1.13	0.36
	<b>Average</b>	<b>24.61</b>	<b>36.64</b>	<b>30.94</b>	<b>1.52</b>	<b>0.34</b>
Post-monsoon	1991-92	19.72	29.56	24.32	1.72	0.35
	1995-96	20.42	30.33	25.12	1.34	0.45
	1999-00	22.41	33.47	26.84	1.91	0.26
	2004-05	23.03	35.25	28.01	1.71	0.34
	2009-10	24.62	37.91	30.26	1.60	0.47
	2014-15	26.24	38.22	31.68	1.12	0.49
	2018-19	28.92	41.28	33.70	1.34	0.55
	<b>Average</b>	<b>23.62</b>	<b>35.15</b>	<b>28.56</b>	<b>1.53</b>	<b>0.42</b>
Winter	1991-92	18.22	28.33	23.29	1.22	0.05
	1995-96	20.08	28.68	24.40	1.04	-0.03
	1999-00	20.44	32.80	25.21	1.81	-0.08
	2004-05	21.08	33.21	26.47	1.25	-0.03
	2009-10	22.06	34.36	27.98	1.23	0.11
	2014-15	22.80	36.21	28.90	1.39	0.03
	2018-19	24.31	38.36	30.46	1.37	0.21
	<b>Average</b>	<b>21.28</b>	<b>33.14</b>	<b>26.67</b>	<b>1.33</b>	<b>0.57</b>

It is seen from Fig. 2 that in 2018-19, more than 90% of the area in the pre-monsoon season was above 38°C LST. The result is different in the winter season, where no area of the city was above 38°C LST. In 1991-92, almost 90% of the area was below 24°C LST in the



winter season. Monsoon and post-monsoon seasons indicate a moderate range of LST. The mean LST of the study area was gradually increased between 1991-92 and 2018-19. The conversion of other lands into the built-up area and bare land influences a lot on the mean LST of the city. Both the changed and unchanged built-up area and bare land suffer from the increasing trend of LST. These results significantly present the influence of climate shift in Raipur City.

Fig. 3 shows the seasonal variation in the spatial distribution of NDWI from 1991-92 to 2018-19. The high and low NDWI regions were seasonally stable since the 1991-92 sessions. Only the values of NDWI were changed, whereas the overall distributional pattern of NDWI remains almost unchanged. The central part of the city always presents a higher NDWI value. A lower NDWI value is seen throughout the periphery of the city.

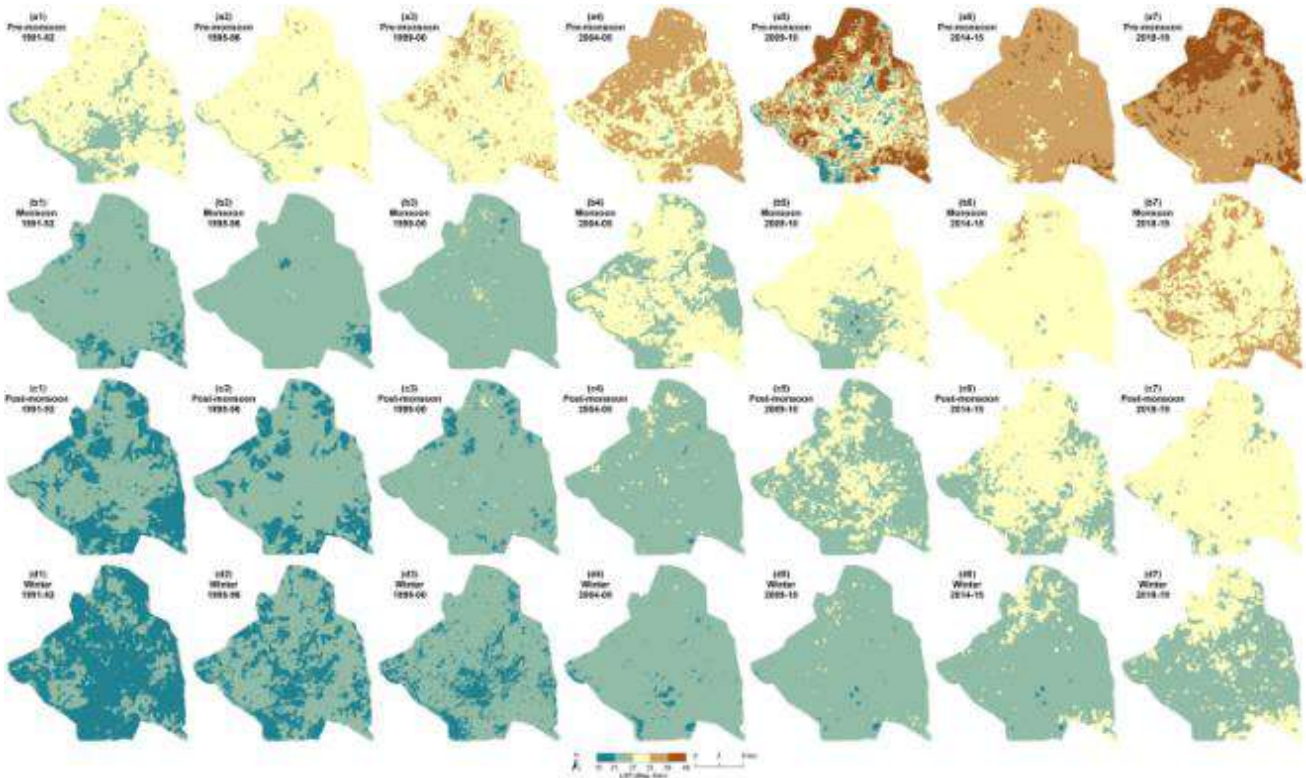


**Figure 2.** Spatial distribution of LST from 1991-92 to 2018-19: (a1-a7) pre-monsoon season (b1-b7) monsoon season (c1-c7) post-monsoon season (d1-d7) winter season

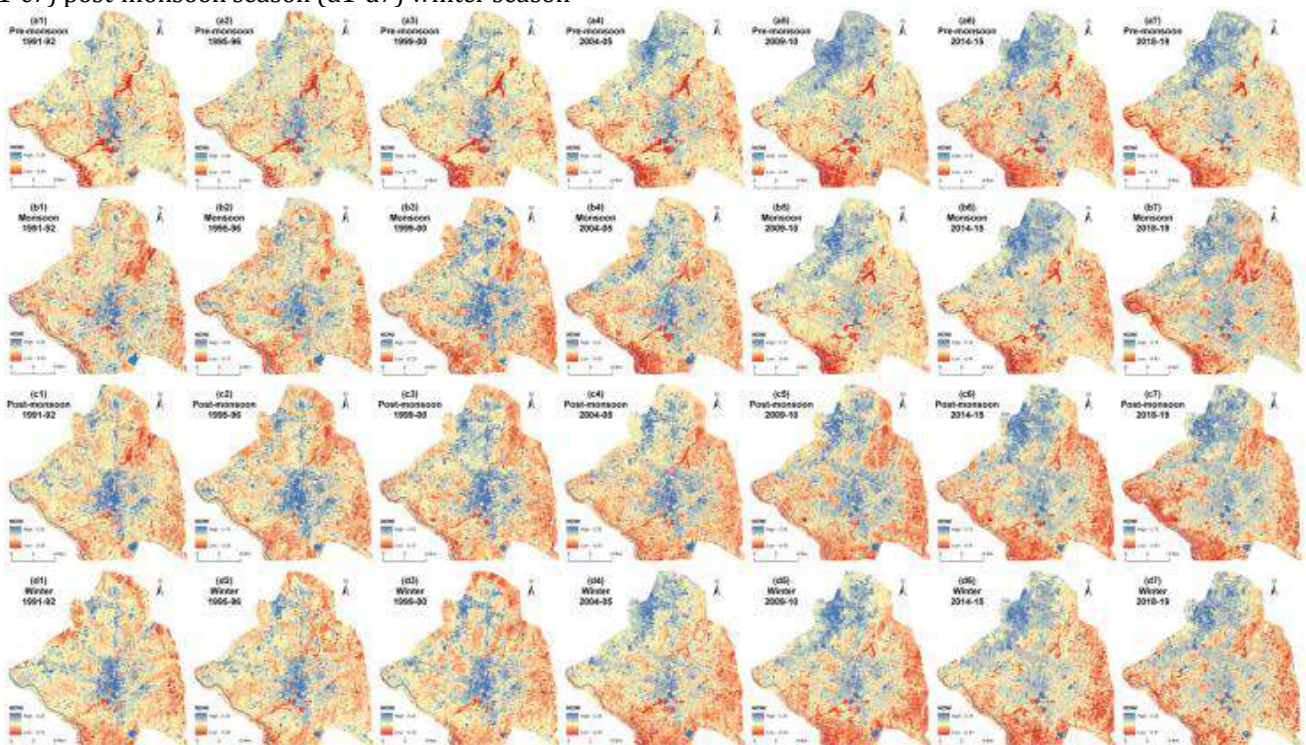


**Figure 3.** Spatial distribution of NDWI from 1991-92 to 2018-19: (a1-a7) pre-monsoon season (b1-b7) monsoon season (c1-c7) post-monsoon season (d1-d7) winter season

### 3.3. Relationship between LST and various types of LULC

The LST of the study area significantly depends upon the LULC types. Generally, the area with green vegetation has low LST value; the built-up areas and bare lands have moderate to high LST value, and the water bodies are characterised by a low to moderate range of LST. In the pre-monsoon season, the built-up area and bare land have comparatively high LST than the other LULC types. But in the winter season, these areas have comparatively low to moderate LST due to low emissivity. Green areas and water areas are characterised by a relatively stable range of low LST values.

Fig. 4 presents the temporal changes of LST on various categories of LULC. Vegetation and water surface increases the LST, while bare land/built-up surface decreases LST. Most of the converted lands are built-up or bare land. Consequently, the built-up/bare land surfaces increase, while vegetation and water surface decrease in a significant amount. Land conversion is the main responsible factor for the seasonal change of mean LST. As a result, the mean LST significantly increased (1.60°C in pre-monsoon, 5.34°C in monsoon, 4.76°C in post-monsoon, and 1.08°C in winter season) from 1991-92 to 2018-19.

### 3.4. Seasonal contrast on LST-NDWI relationship

Table 5 shows the seasonal contrast of LST-NDWI relationships on different LULC types in winter, pre-monsoon, monsoon, and post-monsoon season, respectively. Here, only three types of LULC were considered, i.e., (1) vegetation, (2) water bodies, and (3) built-up area and bare land. On water bodies, the LST-NDWI relationship is moderate negative for any season. NDWI is a water index that is frequently used in water body extraction. On the bare land and built-up area of the study area, the correlation is a weak positive for all four seasons. On green vegetation, the relationship is strong positive (pre-monsoon) to moderate positive (monsoon and post-monsoon), and weak moderate positive (winter). The pre-monsoon season has a strong positive LST-NDWI correlation on the green vegetation (0.67), a weak positive correlation on the bare land and built-up area (0.24), and a moderate negative correlation on green vegetation (-0.49). In the monsoon season, the correlation is moderate positive on green vegetation (0.43), weak positive (0.21) on bare land and built-up area, whereas the correlation is moderate negative (-0.43) on water bodies. The post-monsoon season has a moderate to strong positive correlation (0.50) on green vegetation, a weak positive correlation (0.27) on the bare land and built-up area, and has a moderate negative correlation (-0.31) on water bodies. In winter season, the LST-NDWI correlation is weak positive (0.25) on green vegetation, weak positive (0.15) on built-up area and bare lands. Water bodies have a moderate negative (-0.45) correlation in the winter season.

Fig. 5 represents a generalised view of the overall seasonal variation of LST-NDWI relationships for the

whole of the study area. The relationship was positive in the three seasons except for the winter, where it was mostly negative along with some positive values. It can be concluded from Fig. 5 that the post-monsoon season reveals the best correlation, followed by the monsoon and pre-monsoon seasons. There was practically no such relationship found in the winter season. It was mainly due to the high intensity of moisture content in the air. Dry seasons (winter and pre-monsoon) reduce the strength of the correlation, while the wet seasons (post-monsoon and monsoon) enhance the strength of the LST-NDWI correlation.

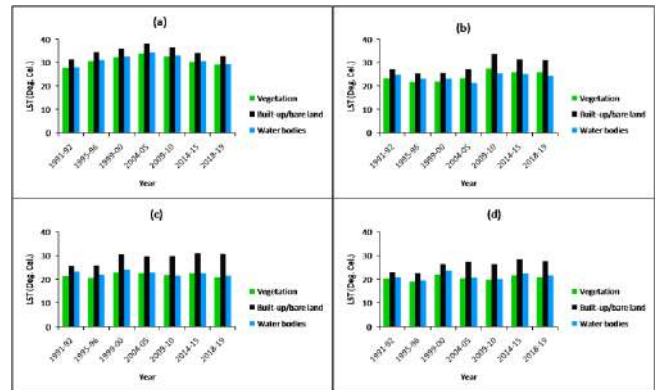


**Figure 4.** Seasonal variability of mean LST on various categories of LULC: (a) pre-monsoon (b) monsoon (c) post-monsoon (d) winter

**Table 5.** Seasonal contrast in the LST-NDWI relationship on different types of LULC (significant at 0.05 level).

Year	Pre-monsoon			Monsoon		
	Vegetation	Built-up/bare land	Water bodies	Vegetation	Built-up/bare land	Water bodies
1991-92	0.57	0.08	-0.55	0.23	0.11	-0.41
1995-96	0.60	0.14	-0.49	0.25	0.10	-0.31
1999-00	0.76	0.31	-0.51	0.37	0.29	-0.28
2004-05	0.70	0.14	-0.40	0.33	0.07	-0.35
2009-10	0.73	0.35	-0.46	0.59	0.30	-0.31
2014-15	0.61	0.33	-0.46	0.56	0.34	-0.28
2018-19	0.70	0.35	-0.59	0.65	0.27	-0.42
	0.67	0.24	-0.49	0.43	0.21	-0.33
Year	Post-monsoon			Winter		
	Vegetation	Built-up/bare land	Water bodies	Vegetation	Built-up/bare land	Water bodies
1991-92	0.55	0.19	-0.26	0.39	0.16	-0.49
1995-96	0.57	0.23	-0.22	0.23	0.14	-0.46
1999-00	0.51	0.34	-0.27	0.23	0.10	-0.43
2004-05	0.48	0.28	-0.38	0.19	0.14	-0.55
2009-10	0.49	0.27	-0.45	0.25	0.21	-0.47
2014-15	0.46	0.26	-0.32	0.22	0.11	-0.39
2018-19	0.44	0.32	-0.28	0.26	0.18	-0.34
	0.50	0.27	-0.31	0.25	0.15	-0.45

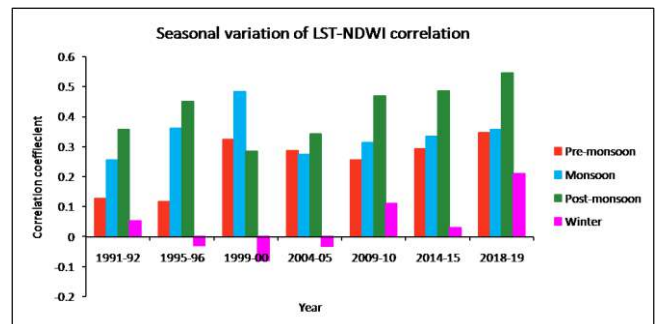


**Figure 5.** Seasonal contrast on the LST-NDWI relationship for the whole of the study area (significant at 0.05 level)

The present study indicates that LST builds an insignificant correlation with NDWI in Raipur City, India

from 1991-92 to 2018-19 in four different seasons (pre-monsoon, monsoon, post-monsoon, and winter). The result is reliable and significant compared to the other similar studies using Landsat data conducted on the cities from different parts of the world in recent years. NDWI and LST built an insignificant correlation when considering the whole urban area in Wuhan City of China (Wu et al. 2019). Choudhury et al. (2019) showed a negative correlation of the LST-NDWI relationship on the water bodies in the Asansol-Durgapur Development Region, India. LST and NDWI produced a negative correlation on the water bodies of Nanchang City, China (Zhang et al. 2017). A significant negative relationship was found between LST and NDWI on the water bodies in Shenzhen City, China (Chen et al. 2006). The present result shows a significant and stable negative correlation (-0.49, -0.34, -0.31, and -0.45 in pre-monsoon, monsoon, post-monsoon, and winter seasons, respectively) between LST and NDWI on the water bodies throughout the period.

#### 4. CONCLUSION

The present study investigates the temporal and seasonal relationship of LST and NDWI in Raipur City, India using sixty-four Landsat datasets of four different seasons (pre-monsoon, monsoon, post-monsoon, and winter) for 1991-92, 1995-96, 1999-00, 2004-05, 2009-10, 2014-15, and 2018-19. In general, the results show that the relationship between LST and NDWI is insignificant. The correlation is moderate positive in the post-monsoon (0.42) and monsoon (0.34) seasons, whereas it is found weak positive in pre-monsoon (0.25) and winter (0.03). The presence of high moisture content in the air and plants is the main responsible factor for high positivity. The LST-NDWI relationship varies for specific LULC types. The water bodies reflect a moderate negative correlation of LST-NDWI in all the four seasons (-0.49 in pre-monsoon, -0.34 in monsoon, -0.31 in post-monsoon, and -0.45 in winter). On green vegetation, this LST-NDWI correlation is also strong positive in pre-monsoon (0.67), moderate positive in monsoon (0.43) and post-monsoon (0.50), weak positive in winter (0.25). The built-up area and bare land build a weak positive correlation of LST-NDWI in all the four seasons (0.24 in pre-monsoon, 0.21 in monsoon, 0.27 in post-monsoon, and 0.15 in winter). All the four seasons have an insignificant correlation for all LULC types (0.14 in pre-monsoon, 0.10 in monsoon, 0.15 in post-monsoon, and -0.02 in winter). The high percentage of urban vegetation and urban water bodies can promote the ecological health of a rapidly growing city like Raipur. Thus, this research work can be an effective one for the future town and country planners.

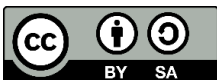
#### ACKNOWLEDGEMENT

The authors are indebted to the United States Geological Survey (URL-3).

#### REFERENCES

- Barsi J, Schott J, Hook S, Raqueno N, Markham B & Radocinski R (2014). Landsat-8 thermal infrared sensor (TIRS) vicarious radiometric calibration. *Remote Sensing*, 6(11), 11607-11626.
- Carlson T N & Ripley D A (1997). On the Relation between NDVI, Fractional Vegetation Cover, and Leaf Area Index. *Remote Sensing of Environment*, 62, 241-252. [https://doi.org/10.1016/S0034-4257\(97\)00104-1](https://doi.org/10.1016/S0034-4257(97)00104-1)
- Chen X L, Zhao H M, Li P X & Yi Z Y (2006). Remote sensing image-based analysis of the relationship between urban heat island and land use/cover changes. *Remote Sensing of Environment*, 104(2), 133-146. <https://doi.org/10.1016/j.rse.2005.11.016>
- Choudhury D, Das K, & Das A (2019). Assessment of land use land cover changes and its impact on variations of land surface temperature in Asansol-Durgapur Development Region. *Egyptian Journal of Remote Sensing and Space Sciences*, 22(2), 203-218. <https://doi.org/10.1016/j.ejrs.2018.05.004>
- Coll C, Galve J M, Sanchez J M & Caselles V. 2010. Validation of Landsat-7/ETM+ thermal-band calibration and atmospheric correction with ground-based measurements. *IEEE Transactions on Geoscience and Remote Sensing*, 48(1), 547-555. <https://doi.org/10.1109/TGRS.2009.2024934>
- Essa W, Verbeiren B, Van der Kwast J, Van de Voorde T & Batelaan O (2012). Evaluation of the DisTrad thermal sharpening methodology for urban areas. *International Journal of Applied Earth Observation and Geoinformation*, 19, 163-172. <https://doi.org/10.1016/j.jag.2012.05.010>
- Ghobadi Y, Pradhan B, Shafri H Z M & Kabiri K (2014). Assessment of spatial relationship between land surface temperature and land use/cover retrieval from multi-temporal remote sensing data in South Karkheh Sub-basin, Iran. *Arabian Journal of Geosciences*, 8(1), 525-537. <https://doi.org/10.1007/s12517-013-1244-3>.
- Govil H, Guha S, Dey A & Gill N (2019). Seasonal evaluation of downscaled land surface temperature: A case study in a humid tropical city. *Heliyon*, 5(6), e01923. <https://doi.org/10.1016/j.heliyon.2019.e01923>
- Govil H, Guha S, Diwan P, Gill N & Dey A (2020). Analyzing Linear Relationships of LST with NDVI and MNDISI Using Various Resolution Levels of Landsat 8 OLI and TIRS Data. *Data Management, Analytics and Innovation. Advances in Intelligent Systems and Computing*, 1042. Springer, Singapore, 171-184. [https://doi.org/10.1007/978-981-32-9949-8\\_13](https://doi.org/10.1007/978-981-32-9949-8_13)
- Guha S, Govil H & Besoya M (2020c). An investigation on seasonal variability between LST and NDWI in an urban environment using Landsat satellite data. *Geomatics, Natural Hazards and Risk*, 11(1), 1319-1345. <https://doi.org/10.1080/19475705.2020.1789762>
- Guha S, Govil H & Mukherjee S (2017). Dynamic analysis and ecological evaluation of urban heat islands in Raipur city, India. *Journal of Applied Remote Sensing*, 11(3), 036020. <https://doi.org/10.1117/1.JRS.11.036020>
- Guha S, Govil H, Dey A & Gill N (2020a). A case study on the relationship between land surface temperature and land surface indices in Raipur City, India.

- Geografisk Tidsskrift-Danish Journal of Geography, 120(1), 35-50. <https://doi.org/10.1080/00167223.2020.1752272>
- Guha S, Govil H, Gill N & Dey A (2020b). Analytical study on the relationship between land surface temperature and land use/land cover indices. *Annals of GIS*, 26(2), 201-216. <https://doi.org/10.1080/19475683.2020.1754291>
- Hao X, Li W & Deng H (2016). The oasis effect and summer temperature rise in arid regions-case study in Tarim Basin. *Scientific Reports*, 6, 35418. <https://doi.org/10.1038/srep35418>
- Hou G L, Zhang H Y, Wang Y Q, Qiao Z H & Zhang Z X (2010). Retrieval and Spatial Distribution of Land Surface Temperature in the Middle Part of Jilin Province Based on MODIS Data. *Scientia Geographica sinica*, 30, 421-427.
- Li J (2006). Estimating land surface temperature from Landsat-5 TM. *Remote Sensing Technology and Application*, 21, 322-326.
- Li W F, Cao Q W, Kun L, & Wu J S (2017). Linking potential heat source and sink to urban heat island: Heterogeneous effects of landscape pattern on land surface temperature. *Science of the Total Environment*, 586, 457-465. <https://doi.org/10.1016/j.scitotenv.2017.01.191>
- Markham B L & Barker J K (1985). Spectral characteristics of the LANDSAT thematic mapper sensors. *International Journal of Remote Sensing*, 6(5), 697-716. <https://doi.org/10.1080/01431168508948492>
- McFeeters S K (1996). The use of the Normalized Difference Water Index (NDWI) in the delineation of open water features. *International Journal of Remote Sensing*, 17(7), 1425-1432. <https://doi.org/10.1080/01431169608948714>
- McFeeters S K (2013). Using the Normalized Difference Water Index (NDWI) within a Geographic Information System to Detect Swimming Pools for Mosquito Abatement: A Practical Approach. *Remote Sensing*, 5(7), 3544-3561. <https://doi.org/10.3390/rs5073544>
- Qin Z, Karnieli A & Barliner P (2001). A Mono-Window Algorithm for Retrieving Land Surface Temperature from Landsat TM Data and Its Application to the Israel-Egypt Border Region. *International Journal of Remote Sensing*, 22(18), 3719-3746. <https://doi.org/10.1080/01431160010006971>
- Sobrino J A, Jimenez-Munoz J C & Paolini L (2004). Land surface temperature retrieval from Landsat TM5. *Remote Sensing of Environment*, 9, 434-440. <https://doi.org/10.1016/j.rse.2004.02.003>
- Sobrino J A, Raissouni N & Li Z (2001). A comparative study of land surface emissivity retrieval from NOAA data. *Remote Sensing of Environment*, 75(2), 256-266. [https://doi.org/10.1016/S0034-4257\(00\)00171-1](https://doi.org/10.1016/S0034-4257(00)00171-1)
- Sun Q, Tan J & Xu Y (2010). An ERDAS image processing method for retrieving LST and describing urban heat evolution: A case study in the Pearl River Delta Region in South China. *Environmental Earth Science*, 59, 1047-1055.
- Tomlinson C J, Chapman L, Trones J E & Baker C (2011). Remote sensing land surface temperature for meteorology and climatology: a review. *Meteorological Application*, 118, 296-306. <https://doi.org/10.1002/met.287>
- URL-1: <https://censusindia.gov.in/2011>  
 URL-2: <http://www.surveyofindia.gov.in>  
 URL-3: <https://www.earthexplorer.usgs.gov>  
 URL-4: <http://www.imdraipur.gov.in>  
 URL-5: <http://www.imdnagpur.gov.in>
- Vlassova L, Perez-Cabello F, Nieto H, Martín P, Riaño D, & De La Riva J (2014). Assessment of methods for land surface temperature retrieval from Landsat-5 TM images applicable to multiscale tree-grass ecosystem modeling. *Remote Sensing*, 6(5), 4345-4368.
- Wu C, Li J, Wang C, Song C, Chen Y, Finka M & Rosa D L (2019). Understanding the relationship between urban blue infrastructure and land surface temperature. *Science of the Total Environment*, 694, 133742. <https://doi.org/10.1016/j.scitotenv.2019.133742>
- Wukelic G E, Gibbons D E, Martucci L M & Foote H P (1989). Radiometric calibration of Landsat Thematic Mapper thermal band. *Remote Sensing of Environment*, 28, 339-347. [https://doi.org/10.1016/0034-4257\(89\)90125-9](https://doi.org/10.1016/0034-4257(89)90125-9)
- Yang J & Qiu J (1996). The empirical expressions of the relation between precipitable water and ground water vapor pressure for some areas in China. *Scientia Atmospherica Sinica*, 20, 620-626.
- Yuan X, Wang W, Cui J, Meng F, Kurban A & De Maeyer P (2017). Vegetation changes and land surface feedbacks drive shifts in local temperatures over Central Asia. *Scientific Reports*, 7(1), 3287. <https://doi.org/10.1038/s41598-017-03432-2>
- Zanter K (2019). *Landsat 8 (L8) Data Users Handbook*; EROS: Sioux Falls, SD, USA.
- Zhang X, Estoque R C & Murayama Y (2017). An urban heat island study in Nanchang City, China based on land surface temperature and social-ecological variables. *Sustainable Cities and Society*, 32, 557-568. <https://doi.org/10.1016/j.scs.2017.05.005>



## **A seasonal relationship between land surface temperature and normalized difference bareness index**

Subhanil Guha<sup>1</sup> and Himanshu Govil

Department of Applied Geology, National Institute of Technology Raipur, India  
<sup>1</sup> subhanilguha@gmail.com

DOI: <http://dx.doi.org/10.4314/sajg.v10i2.12>

### **Abstract**

*The present study analyzes the seasonal variability of the relationship between the land surface temperature (LST) and normalized difference bareness index (NDBaI) on different land use/land cover (LULC) in Raipur City, India by using sixty-five Landsat images of four seasons (pre-monsoon, monsoon, post-monsoon, and winter) of 1991-1992, 1995-1996, 1999-2000, 2004-2005, 2009-2010, 2014-2015, and 2018-2019. The results show that the post-monsoon season indicates the best correlation (0.59), followed by the monsoon (0.56), pre-monsoon (0.47), and winter (0.44) season. The water bodies reflect a strongly positive correlation in all the four seasons (0.65 in pre-monsoon, 0.51 in monsoon, 0.53 in post-monsoon, and 0.62 in winter). On green vegetation, this correlation is also strongly positive in monsoon (0.57), post-monsoon (0.62), and winter (0.55), whereas it is moderate positive in pre-monsoon (0.37) season. The built-up area and bare land build a moderate positive correlation in all the four seasons (0.35 in pre-monsoon, 0.43 in monsoon, 0.48 in post-monsoon, and 0.39 in winter). Among the four seasons, the post-monsoon season builds the best correlation for all LULC types, whereas the pre-monsoon season has the least correlation. This research work is beneficial for land use and environmental planning of any city under similar climatic conditions.*

**Keywords:** *Landsat; Land surface temperature (LST); Land use/land cover (LULC); Normalized difference bareness index (NDBaI).*

### **1. Introduction**

Land surface temperature (LST) is a significant factor in analyzing the bio-geochemical functions of the land surface features (Tomlinson et al. 2011; Hao et al. 2016; Guha 2017). Green plants, wetlands, and water bodies generate low LST, whereas human settlement, and bare land surface produce high LST in the summer season of tropical areas (Chen et al. 2006; Guha et al. 2020). Thus, LST related studies are quite important in the ecological planning of the recent urban agglomerations (Li et al. 2016). Normalized difference bareness index (NDBaI) is the most popular index for bare land extraction that is invariably used in LULC and LST related studies (Zhao and Chen 2005; Chen

et al. 2006; Weng and Quattrochi 2006; Essa et al. 2012; Chen et al. 2013; Guha et al. 2019; Yuan et al. 2017).

Several research articles presented the LST-NDBaI relationship in different parts of the world. As-Syakur et al. (2012) investigates various bareness indices for bare land mapping in Denpasar of Bali, Indonesia. Ahmed (2013) used NDBaI along with other LULC indices to simulate the land surface changes and their impact on LST in Dhaka, Bangladesh. Sharma et al. (2013) examined the relationship between LST and NDBaI in Surat City of India. Guo et al. (2014) estimated sub-pixel LST and built a relationship between LST and NDBaI in Guangzhou core urban area of China. Ali et al. (2017) compared the relationship of LST with NDBaI and other LULC indices in London and Baghdad cities. Macarof et al. (2017) investigated the relationship between LST and NDBaI in Iași Municipality Area of eastern Romania from 2013 to 2016 by using Landsat 8 data. Alibakshi et al. (2019) investigated the relationship between NDBaI and LST from 2001 to 2015 in Tehran and its satellite cities in Iran by the geographically weighted regression model using Landsat 7 data. Alexander (2020) evaluated the LST-NDBaI relationship in Aarhus City of Denmark by using Landsat 8 data. Jain et al. (2020) investigated the LST-NDBaI relationship in Nagpur City, India from 2000 to 2015 by using Landsat data.

The nature of LST and NDBaI changes due to the seasonal changes of various atmospheric components. Thus, to reveal the characteristics of seasonal variation of the LST-NDBaI relationship in a tropical city, we have selected the Raipur City of Chhattisgarh State in India. The main aim of the study is to determine the seasonal variation of LST-NDBaI relationship on different LULC types. The study will be a beneficial one ecological planning and management. The seasonal LST-NDBaI relationship means the relationship between LST and NDBaI in different seasons like pre-monsoon, monsoon, post-monsoon, and winter. It is determined by using a number of Landsat satellite data of these four aforesaid seasons from 1991-92 to 2018-19. The study tries to establish a long-term relationship between LST and NDBaI for various seasons and also on different types land use/land cover. No such type of study has been conducted on this city before the work. The study is beneficial for ecological planning because it focuses on the LST-NDBaI relationship on different LULC types.

## **2. Study area and data**

Figure 1 shows the geographical location of Raipur city of India which extends from 21°11'22"N to 21°20'02"N and from 81°32'20"E to 81°41'50"E. The city covers an area of around 165 km<sup>2</sup>. The upper left corner of the figure presents the outline map of India where Chhattisgarh State is located in the middle part (<http://www.surveyofindia.gov.in>). The lower left corner of the figure presents the outline map of Chhattisgarh State with districts (<http://www.surveyofindia.gov.in>). The upper right corner of the figure represents the false colour composite (FCC) image of Raipur city (<https://raipur.gov.in>) from recent Landsat 8 OLI/TIRS data of 22 October 2018 (<https://www.earthexplorer.usgs.gov>). The lower right corner of the figure indicates the digital

elevation map (DEM) of Raipur city produced by the ArcGIS software using the last available ASTER DEM data of 11 October 2011 (<https://www.earthexplorer.usgs.gov>). The city is characterised by the tropical dry and wet type of climate (<http://www.imdraipur.gov.in>). The mean monthly temperature ranges from 12°C to 42°C. May presents the highest average temperature (35°C), while December presents the lowest average temperature (20°C). The highest average rainfall (327 mm) is observed in July. March, April, and May are considered as the summer or pre-monsoon months.

Table 1 shows the Landsat data sets used in this study. LST was retrieved through the TIR bands of Landsat data sets [band 6 for Landsat 5 Thematic Mapper (TM) and Landsat 7 Enhanced Thematic Mapper Plus (ETM+) data, whereas band 10 for Landsat 8 Operational Land Imager (OLI)/ Thermal Infrared Sensors (TIRS) data]. The whole study was performed by using ArcGIS 9.3 software. Landsat 8 TIRS dataset has two TIR bands (bands 10 and 11) in which band 11 has a larger calibration uncertainty. Thus, only TIR band 10 data (100 m resolution) has been recommended for the present study (Barsi et al. 2014). The TIR band of Landsat 5 TM data and Landsat 7 ETM+ data is band 6. The TIR bands of each Landsat sensors have been resampled to 30 m x 30 m pixel size by the data provider (EROS) using the cubic convolution resampling method.

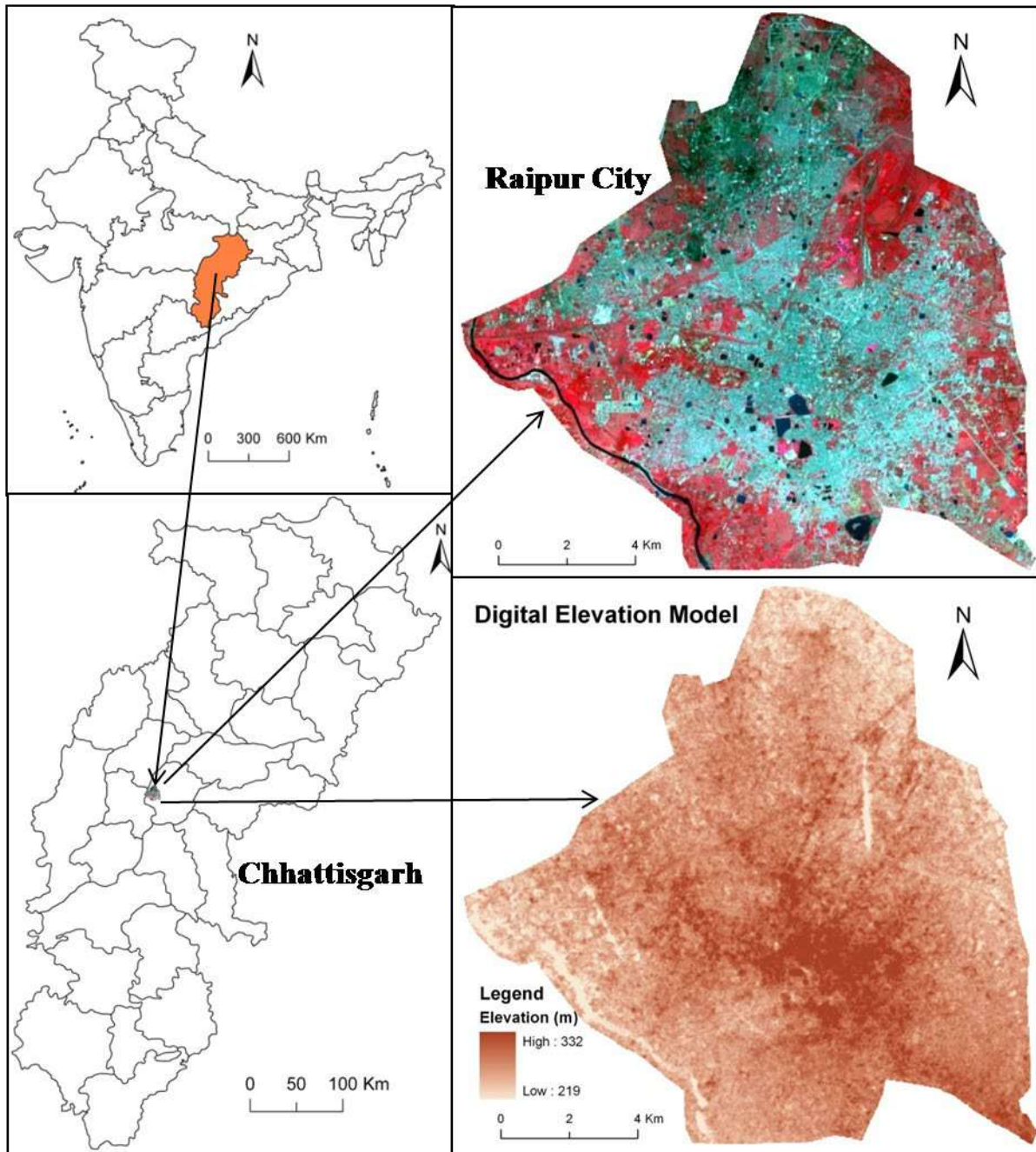


Figure 1. Location of the study area.



Table 1: Specification of Landsat data sets.

Landsat scene ID	Date of acquisition	Time (UTC)	Sun elevation (°)	Sun azimuth (°)	Cloud cover (%)	Earth-Sun distance (astronomical unit)	Resolution of TIR bands (m)
LT51420451991077ISP00	18-Mar-91	04:17:34	48.58	118.92	0	0.99	120
LT51420451991093ISP00	03-Apr-91	04:17:46	53.04	111.64	0	0.99	120
LT51420451991141ISP00	21-May-91	04:18:39	59.93	87.09	1	1.01	120
LT51420451991269ISP01	26-Sep-91	04:20:03	52.47	123.30	13	1.00	120
LT51420451991285BKT02	12-Oct-91	04:20:12	42.22	131.85	6	0.99	120
LT51420451991317ISP00	13-Nov-91	04:20:19	41.53	142.35	1	0.99	120
LT51420451992016ISP00	16-Jan-92	04:20:22	35.26	139.03	3	0.98	120
LT51420451992032BKT01	01-Feb-92	04:20:27	37.41	135.03	0	0.98	120
LT51420451992048ISP00	17-Feb-92	04:20:15	40.89	130.26	4	0.98	120
LT51420451995104ISP01	14-Apr-95	04:05:06	52.75	103.75	0	1.00	120
LT51420451995344BKT00	10-Dec-95	03:56:47	33.01	139.15	0	0.98	120
LT51420451996027ISP00	27-Jan-96	04:00:14	33.31	132.27	0	0.98	120
LT51420451996267ISP00	23-Sep-96	04:14:16	51.81	120.64	2	1.00	120
LT51420451996283ISP00	09-Oct-96	04:15:07	48.92	129.53	0	0.99	120
LT51420451996299ISP00	25-Oct-96	04:15:55	45.37	136.48	5	0.99	120
LT51420451996315ISP00	10-Nov-96	04:16:41	41.61	141.11	7	0.99	120
LE71420451999315SGS00	11-Nov-99	04:49:00	45.72	149.96	0	0.99	60
LE71420452000030SGS00	30-Jan-00	04:48:55	41.46	142.31	0	0.98	60
LE71420452000094SGS00	03-Apr-00	04:48:35	59.72	118.62	0	1.00	60
LE71420452000126SGS00	05-May-00	04:48:20	65.97	98.50	0	1.00	60
LE71420452000270SGS00	26-Sep-00	04:46:33	57.21	131.59	6	1.00	60
LE71420452000350SGS00	15-Dec-00	04:46:31	38.94	150.22	0	0.98	60
LT51420452004081BKT00	21-Mar-04	04:35:14	53.26	121.40	0	0.99	120
LT51420452004113BKT00	22-Apr-04	04:36:01	61.43	104.47	1	1.00	120
LT51420452004145BKT00	24-May-04	04:36:54	64.25	86.72	0	1.00	120
LT51420452004161BKT00	09-Jun-04	04:37:23	63.98	81.78	9	1.01	120
LT51420452004273BKT00	29-Sep-04	04:40:16	55.47	131.40	9	1.00	120
LT51420452004289BKT00	15-Oct-04	04:40:36	51.63	139.65	4	0.99	120
LT51420452004321BKT00	16-Nov-04	04:41:11	43.41	148.58	0	0.98	120
LT51420452004337BKT00	02-Dec-04	04:41:33	40.14	149.58	0	0.98	120
LT51420452004353BKT00	18-Dec-04	04:41:52	38.12	148.74	0	0.98	120
LT51420452005019BKT00	19-Jan-05	04:42:17	38.92	143.21	0	0.98	120
LT51420452005035BKT00	04-Feb-05	04:42:29	41.74	139.16	0	0.98	120
LT51420452009062KHC01	03-Mar-09	04:42:22	49.04	130.64	0	0.99	120
LT51420452009078KHC00	19-Mar-09	04:42:44	54.10	124.40	2	0.99	120
LT51420452009094BKT00	04-Apr-09	04:43:05	58.86	116.70	0	1.00	120
LT51420452009110BKT00	20-Apr-09	04:43:24	62.67	107.39	0	1.00	120
LT51420452009126BKT00	06-May-09	04:43:42	65.03	97.25	0	1.00	120
LT51420452009142KHC00	22-May-09	04:44:00	65.88	88.22	1	1.00	120
LT51420452009174KHC00	23-Jun-09	04:44:35	64.96	80.76	0	1.00	120
LT51420452009286KHC00	13-Oct-09	04:46:12	53.04	140.48	0	0.99	120
LT51420452009302BKT00	29-Oct-09	04:46:20	48.72	146.41	0	0.99	120
LT51420452009350KHC00	16-Dec-09	04:46:44	38.90	150.21	1	0.99	120
LT51420452010017KHC00	17-Jan-10	04:46:55	39.27	144.86	6	0.99	120
LT51420452010033KHC00	02-Feb-10	04:46:59	41.92	140.89	0	0.98	120
LT51420452010049KHC00	18-Feb-10	04:47:02	45.89	136.27	7	0.98	100
LC81420452014076LGN01	17-Mar-14	04:56:36	55.95	129.38	0	0.99	100
LC81420452014092LGN01	02-Apr-14	04:56:19	60.91	121.72	0	0.99	100
LC81420452014140LGN01	20-May-14	04:55:38	68.56	90.40	5	1.01	100
LC81420452014156LGN01	05-Jun-14	04:55:45	68.38	83.30	0	1.01	100
LC81420452014316LGN01	12-Nov-14	04:56:21	46.22	152.46	7	0.98	100
LC81420452014364LGN01	30-Dec-14	04:56:09	39.34	150.83	0	0.98	100
LC81420452015015LGN01	15-Jan-15	04:56:09	40.22	147.71	0	0.98	100
LC81420452015031LGN01	31-Jan-15	04:56:04	42.76	143.86	0	0.98	100
LC81420452015047LGN01	16-Feb-15	04:55:55	46.67	139.41	0	0.98	100
LC81420452018071LGN00	12-Mar-18	04:55:43	54.19	131.16	2	0.99	100
LC81420452018087LGN00	28-Mar-18	04:55:36	59.29	124.07	0	0.99	100
LC81420452018135LGN00	15-May-18	04:55:08	68.27	93.32	0	1.01	100
LC81420452018167LGN00	16-Jun-18	04:55:01	67.74	81.10	2	1.01	100
LC81420452018279LGN00	06-Oct-18	04:55:53	56.39	140.40	0	0.99	100
LC81420452018295LGN00	22-Oct-18	04:55:59	51.96	147.33	0	0.99	100
LC81420452018311LGN00	07-Nov-18	04:56:03	47.49	151.56	0	0.99	100
LC81420452018359LGN00	25-Dec-18	04:55:59	39.40	151.57	0	0.98	100
LC81420452019042LGN00	11-Feb-19	04:55:52	45.33	140.84	0	0.98	100
LC81420452019058LGN00	27-Feb-19	04:55:48	49.94	135.93	4	0.99	100

### 3. Methodology

#### 3.1. Retrieving LST from Landsat data

In this study, the mono-window algorithm was applied to retrieve LST from multi-temporal Landsat satellite sensors where three necessary parameters are ground emissivity, atmospheric transmittance, and effective mean atmospheric temperature (Qin et al. 2001; Weng et al. 2004; Wang et al. 2016; Sekertekin and Bonafoni 2020). At first, the original TIR bands (100 m resolution for Landsat 8 OLI/TIRS data, 120 m resolution for Landsat 5 TM data and Landsat 7 ETM+ data) were resampled into 30 m by USGS data centre for further application.

The TIR pixel values are firstly converted into radiance from digital number (DN) values. Radiance for TIR band of Landsat 5 TM data and Landsat 7 ETM+ data is obtained using equation [1] (USGS):

$$L_{\lambda} = \left[ \frac{L_{MAX\lambda} - L_{MIN\lambda}}{QCAL_{MAX} - QCAL_{MIN}} \right] * [QCAL - QCAL_{MIN}] + L_{MIN\lambda} \quad [1]$$

where,  $L_{\lambda}$  is Top of Atmosphere (TOA) spectral radiance ( $Wm^{-2}sr^{-1}mm^{-1}$ ),  $QCAL$  is the quantized calibrated pixel value in DN,  $L_{MIN\lambda}$  ( $Wm^{-2}sr^{-1}mm^{-1}$ ) is the spectral radiance scaled to  $QCAL_{MIN}$ ,  $L_{MAX\lambda}$  ( $Wm^{-2}sr^{-1}mm^{-1}$ ) is the spectral radiance scaled to  $QCAL_{MAX}$ ,  $QCAL_{MIN}$  is the minimum quantized calibrated pixel value in DN and  $QCAL_{MAX}$  is the maximum quantized calibrated pixel value in DN.  $L_{MIN\lambda}$ ,  $L_{MAX\lambda}$ ,  $QCAL_{MIN}$ , and  $QCAL_{MAX}$  values are obtained from the metadata file of Landsat TM and ETM+ data. Radiance for Landsat 8 TIR band is obtained from equation [2] (Zanter 2019):

$$L_{\lambda} = M_L \cdot QCAL + A_L \quad [2]$$

where,  $L_{\lambda}$  is the TOA spectral radiance ( $Wm^{-2}sr^{-1}mm^{-1}$ ),  $M_L$  is the band-specific multiplicative rescaling factor from the metadata,  $A_L$  is the band-specific additive rescaling factor from the metadata,  $QCAL$  is the quantized and calibrated standard product pixel values (DN). All of these variables can be retrieved from the metadata file of Landsat 8 data.

For Landsat 5 data, the reflectance value is obtained from radiances using equation [3] (USGS):

$$\rho_{\lambda} = \frac{\pi \cdot L_{\lambda} \cdot d^2}{ESUN_{\lambda} \cdot \cos \theta_s} \quad [3]$$

where,  $\rho_{\lambda}$  is unitless planetary reflectance,  $L_{\lambda}$  is the TOA spectral radiance ( $Wm^{-2}sr^{-1}\mu m^{-1}$ ),  $d$  is Earth-Sun distance in astronomical units,  $ESUN_{\lambda}$  is the mean solar exo-atmospheric spectral irradiances ( $Wm^{-2}\mu m^{-1}$ ) and  $\theta_s$  is the solar zenith angle in degrees.  $ESUN_{\lambda}$  values for each band of Landsat 5 and 7 data can be obtained from the handbooks of the related mission.  $\theta_s$  and  $d$  values can be attained from the metadata file.

For Landsat 8 data, reflectance conversion can be applied to DN values directly as in equation [4] (Zanter 2019):

$$\rho_{\lambda} = \frac{M_{\rho} \cdot Q_{CAL} + A_{\rho}}{\sin \theta_{SE}} \quad [4]$$

where,  $M_{\rho}$  is the band-specific multiplicative rescaling factor from the metadata,  $A_{\rho}$  is the band-specific additive rescaling factor from the metadata,  $Q_{CAL}$  is the quantized and calibrated standard product pixel values (DN) and  $\theta_{SE}$  is the local sun elevation angle from the metadata file.

Equation [5] is used to convert the spectral radiance to at-sensor brightness temperature (Wukelic et al. 1989; Chen et al. 2006):

$$T_b = \frac{K_2}{\ln\left(\frac{K_1}{L_{\lambda}} + 1\right)} \quad [5]$$

where,  $T_b$  is the brightness temperature in Kelvin (K),  $L_{\lambda}$  is the spectral radiance in  $Wm^{-2}sr^{-1}mm^{-1}$ ;  $K_2$  and  $K_1$  are calibration constants. For Landsat 8 data,  $K_1$  is 774.89,  $K_2$  is 1321.08 ( $Wm^{-2}sr^{-1}mm^{-1}$ ). For Landsat 7 data,  $K_1$  is 666.09,  $K_2$  is 1282.71 ( $Wm^{-2}sr^{-1}mm^{-1}$ ). For Landsat 5 data,  $K_1$  is 607.76,  $K_2$  is 1260.56 ( $Wm^{-2}sr^{-1}mm^{-1}$ ).

The land surface emissivity  $\varepsilon$ , is estimated from equation [6] using the NDVI Thresholds Method (Sobrino et al. 2001; 2004).

$$\varepsilon = \varepsilon_v F_v + \varepsilon_s (1 - F_v) + d\varepsilon \quad [6]$$

where,  $\varepsilon$  is land surface emissivity,  $\varepsilon_v$  is vegetation emissivity,  $\varepsilon_s$  is soil emissivity,  $F_v$  is fractional vegetation,  $d\varepsilon$  is the effect of the geometrical distribution of the natural surfaces and internal reflections that can be expressed by equation [7]:

$$d\varepsilon = (1 - \varepsilon_s)(1 - F_v)F\varepsilon_v \quad [7]$$

where,  $\varepsilon_v$  is vegetation emissivity,  $\varepsilon_s$  is soil emissivity,  $F_v$  is fractional vegetation,  $F$  is a shape factor whose mean is 0.55, the value of  $d\varepsilon$  may be 2% for mixed land surfaces (Sobrino et al. 2004).

The fractional vegetation  $F_v$ , of each pixel, is determined from the NDVI using equation [8] (Carlson and Repley 1997):

$$F_v = \left( \frac{NDVI - NDVI_{min}}{NDVI_{max} - NDVI_{min}} \right)^2 \quad [8]$$

where, (a)  $NDVI < 0.2$  for bare soil; (b)  $NDVI > 0.5$  for vegetation; (c)  $0.2 \leq NDVI \leq 0.5$  for mixed land with bare soil and vegetation (Sobrino et al. 2001; 2004).

Finally, the land surface emissivity  $\varepsilon$  can be expressed by equation [9]:

$$\varepsilon = 0.004 * F_v + 0.986 \quad [9]$$

where,  $\varepsilon$  is land surface emissivity,  $F_v$  is fractional vegetation.

Water vapour content is estimated by equation [10] (Yang and Que 1996; Li 2006):

$$w = 0.0981 * \left[ 10 * 0.6108 * \exp \left( \frac{17.27 * (T_0 - 273.15)}{237.3 + (T_0 - 273.15)} \right) * RH \right] + 0.1697 \quad [10]$$

where,  $w$  is the water vapour content ( $\text{g}/\text{cm}^2$ ),  $T_0$  is the near-surface air temperature in Kelvin (K),  $RH$  is the relative humidity (%). These parameters of atmospheric profile are obtained from the Meteorological Centre, Raipur (<http://www.imdraipur.gov.in>). Atmospheric transmittance is determined for Raipur City using equation [11] (Qin 2001; Sun 2010):

$$\tau = 1.031412 - 0.11536w \quad [11]$$

where,  $\tau$  is the total atmospheric transmittance,  $w$  is the water vapour content ( $\text{g}/\text{cm}^2$ ).

Raipur City is located in the tropical region. Thus, equation [12] is applied to compute the effective mean atmospheric transmittance of Raipur (Qin 2001; Sun 2010):

$$T_a = 17.9769 + 0.91715T_0 \quad [12]$$

LST is retrieved from Landsat 5 TM and Landsat 8 OLI/TIRS satellite data by using equations [13-15] (Qin 2001):

$$T_s = \frac{[a(1-C-D) + (b(1-C-D) + C + D)T_b - DT_a]}{C} \quad [12]$$

$$C = \varepsilon\tau \quad [13]$$

$$D = (1 - \tau)[1 + (1 - \varepsilon)\tau] \quad [14]$$

where,  $\varepsilon$  is the land surface emissivity,  $\tau$  is the total atmospheric transmittance,  $C$  and  $D$  are internal parameters based on atmospheric transmittance and land surface emissivity,  $T_b$  is the at-sensor brightness temperature,  $T_a$  is the mean atmospheric temperature,  $T_0$  is the near-surface air temperature,  $T_s$  is the land surface temperature,  $a = -67.355351$ ,  $b = 0.458606$ .

### **3.2. Extraction of different types of LULC by using NDBaI**

In this study, special emphasis has been given on NDBaI for determining the relationship with LST (Chen et al. 2006; Zhao and Chen 2005). NDBaI is determined by the short wave infrared (SWIR) and thermal infrared (TIR) bands. For, Landsat 5 TM and Landsat 7 ETM+ data, band 5 is used as the SWIR band and band 6 is used as TIR band, respectively. For Landsat 8 OLI and TIRS data, band 6 and band 10 are used as the TIR bands, respectively (Table 2). The value of NDBaI is ranged between  $-1$  and  $+1$ . Generally, the positive value of NDBaI indicates the bare land (Table 2). The bareness increases with the increase of the positive NDBaI. NDBaI value ranges between  $-0.2$  to  $0$  shows the built-up area, whereas  $\text{NDBaI} > 0$  shows the bare land [3]. NDBaI is also used to extract other LULC types, e.g., vegetation ( $\text{NDBaI} < -0.25$ ), and water bodies ( $\text{NDBaI} < -0.65$ ). LULC maps have been generated using the aforesaid threshold limits of NDBaI and the results have been validated

by the maximum likelihood classification. The average calculated values of the Kappa coefficient and overall accuracy for all the images are 0.91 and 92.19%, respectively.

Table 2. Description of NDBaI and its threshold values used for extracting the various types of LULC.

Acronym	Description	Formulation	References	Threshold limits of NDBaI for extracting different LULC types			
				Vegetation	Water bodies	Built-up area	Bare land
NDBaI	Normalized difference bareness index		Zhao and Chen 2005; Chen et al. 2006	< -0.25	< -0.65	-0.2 - 0	> 0

## 4. Results and discussion

### 4.1. Extraction of LULC types using NDBaI

Figure 2 shows the LULC maps of the post-monsoon Landsat images of different years. LULC maps have been generated using the threshold limits of NDBaI. In 1991-92, the built-up area and bare land were mainly found in the central part of the Raipur City. The northwest portion of the city has been urbanized rapidly from 1991-92 to 2004-05 as the percentage of urban vegetation has been declined due to the conversion into built-up areas. After 2004-05, the green areas have been reduced at an alarming rate as most of the parts of the city have been converted into bare land and built-up area. Only the east and the southwest parts were covered by urban vegetation. Water bodies are the most stable LULC type in the study area. Green vegetation has been decreased in a very significant amount (76.80 km<sup>2</sup>) from 1991-92 to 2018-19. On the other hand, the built-up area and bare land have been increased at a very high rate (78.37 km<sup>2</sup> in 27 years) due to rapid land conversion.

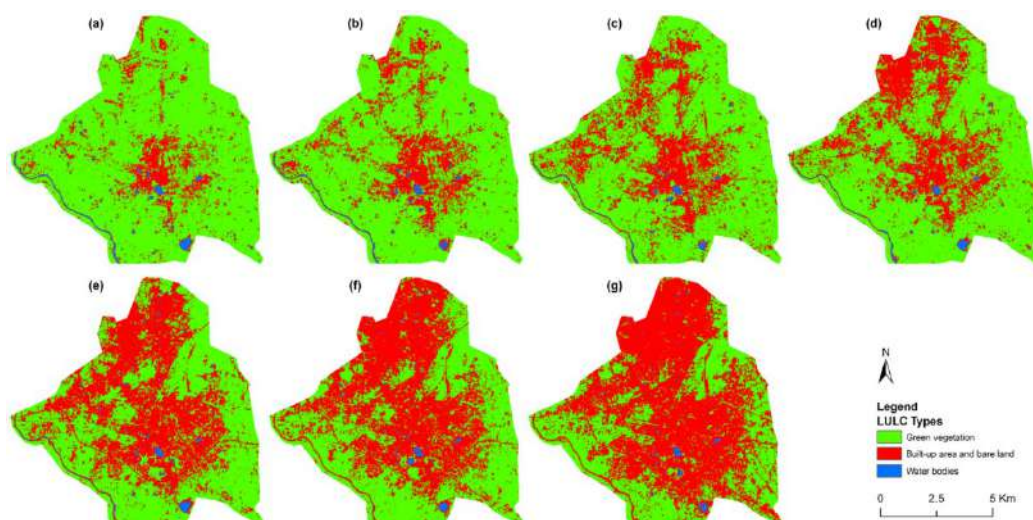


Figure 2. LULC maps of the study area for the following years: (a) 1991-92 (b) 1995-96 (c) 1999-00 (d) 2004-05 (e) 2009-10 (f) 2014-15 (g) 2018-19.

#### 4.2. Characteristics of the spatial distribution of LST and NDBaI

There is a prominent seasonal variation of different periods that occurred in mean and standard deviation (STD) values of LST (Table 3). The winter season indicates the lowest mean LST values for all the years, whereas the highest mean LST values are found in the pre-monsoon seasons during the entire span. From 1991-92 to 2018-19, the mean LST has increased in every season. The post-monsoon season has the mean LST value nearer to the winter season, while monsoon season has a slightly high value of mean LST than the post-monsoon season. The average values of LST and the correlation coefficient of LST and NDBaI from 1991-92 to 2018-19 have been shown in grey shades inside Table 3.

Table 3. Temporal and seasonal variation of LST values and Pearson's correlation coefficient values of LST-NDBaI relationship (significant at 0.05 level).

Season	Year of acquisition	LST (°C)				Correlation coefficients for LST-NDBaI relationship
		Min.	Max.	Mean	Std.	
Pre-monsoon	1991-92	23.81	36.27	31.54	1.52	0.58
	1995-96	24.54	41.07	34.64	1.89	0.51
	1999-00	26.36	42.23	36.38	1.93	0.49
	2004-05	26.95	44.07	38.01	2.19	0.48
	2009-10	28.81	46.48	39.60	2.54	0.43
	2014-15	31.93	48.22	41.28	1.75	0.41
	2018-19	33.46	51.11	43.74	1.75	0.40
	<b>Average</b>	<b>27.98</b>	<b>44.21</b>	<b>37.88</b>	<b>1.94</b>	<b>0.47</b>
Monsoon	1991-92	19.87	30.83	25.74	1.41	0.66
	1995-96	21.21	33.01	26.50	1.33	0.54
	1999-00	22.76	35.91	27.81	1.34	0.53
	2004-05	24.17	36.20	31.32	1.33	0.54
	2009-10	25.94	38.38	33.06	2.40	0.56
	2014-15	27.74	40.15	34.87	1.68	0.50
	2018-19	30.59	41.98	37.30	1.13	0.55
	<b>Average</b>	<b>24.61</b>	<b>36.64</b>	<b>30.94</b>	<b>1.52</b>	<b>0.56</b>
Post-monsoon	1991-92	19.72	29.56	24.32	1.72	0.69
	1995-96	20.42	30.33	25.12	1.34	0.59
	1999-00	22.41	33.47	26.84	1.91	0.57
	2004-05	23.03	35.25	28.01	1.71	0.56
	2009-10	24.62	37.91	30.26	1.60	0.58
	2014-15	26.24	38.22	31.68	1.12	0.56
	2018-19	28.92	41.28	33.70	1.34	0.57
	<b>Average</b>	<b>23.62</b>	<b>35.15</b>	<b>28.56</b>	<b>1.53</b>	<b>0.59</b>
Winter	1991-92	18.22	28.33	23.29	1.22	0.53
	1995-96	20.08	28.68	24.40	1.04	0.48
	1999-00	20.44	32.80	25.21	1.81	0.46
	2004-05	21.08	33.21	26.47	1.25	0.44
	2009-10	22.06	34.36	27.98	1.23	0.42
	2014-15	22.80	36.21	28.90	1.39	0.41
	2018-19	24.31	38.36	30.46	1.37	0.37
	<b>Average</b>	<b>21.28</b>	<b>33.14</b>	<b>26.67</b>	<b>1.33</b>	<b>0.44</b>

The pre-monsoon season has the maximum values of mean LST (31.54°C in 1991-92, 34.64°C in 1995-96, 36.38°C in 1999-00, 38.01°C in 2004-05, 39.60°C in 2009-10, 41.28°C in 2014-15, and 43.74°C in 2018-19) (Figure 3), followed by monsoon (Figure 4), post-monsoon (Figure 5), and

winter (Figure 6) season. At the macro-level, the areas with high LST values show the urban heat island phenomenon. These areas have relatively high NDBaI values. At the micro-level, the high peaks of LST also presented the high peaks of NDBaI. The correlation coefficient values of Pearson's linear correlation between the LST and NDBaI are positive (for any year or season). The post-monsoon season has the best mean (mean value of 1991-92, 1995-96, 1999-00, 2004-05, 2009-10, 2014-15, and 2018-19) correlation coefficient value (0.59), followed by the monsoon (0.56), pre-monsoon (0.48), and winter (0.44) season. It is seen from Figure 3 that in 2018-19, more than 90% of the area in the pre-monsoon season was above 40°C LST. The picture is different in the winter season, where no area of the city was above 40°C LST. In 1991-92, almost 90% of the area was below 25°C LST in the winter season (Figure 6). The monsoon (Figure 4) and post-monsoon (Figure 5) seasons indicate a moderate range of LST. The mean LST of the study area has been gradually increased between 1991-92 and 2018-19. The conversion of other lands into the built-up area and bare land influences a lot on the mean LST of the city. Both the changed and unchanged built-up area and bare land suffer from the increasing trend of LST. These results significantly present the influence of climate change in Raipur City.

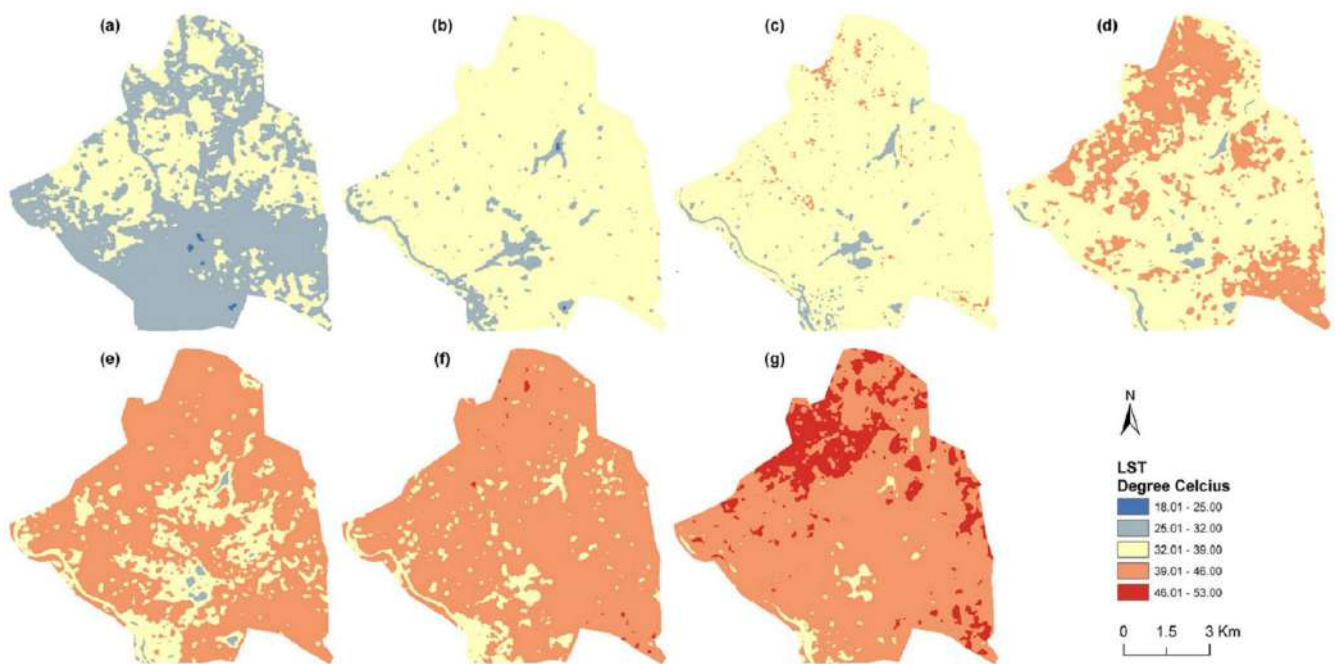


Figure 3. Spatial distribution of LST in pre-monsoon season for the following years: (a) 1991-92 (b) 1995-96 (c) 1999-00 (d) 2004-05 (e) 2009-10 (f) 2014-15 (g) 2018-19 2004-05 (e1-e4) 2009-10 (f1-f4) 2014-15 (g1-g4) 2018-19.

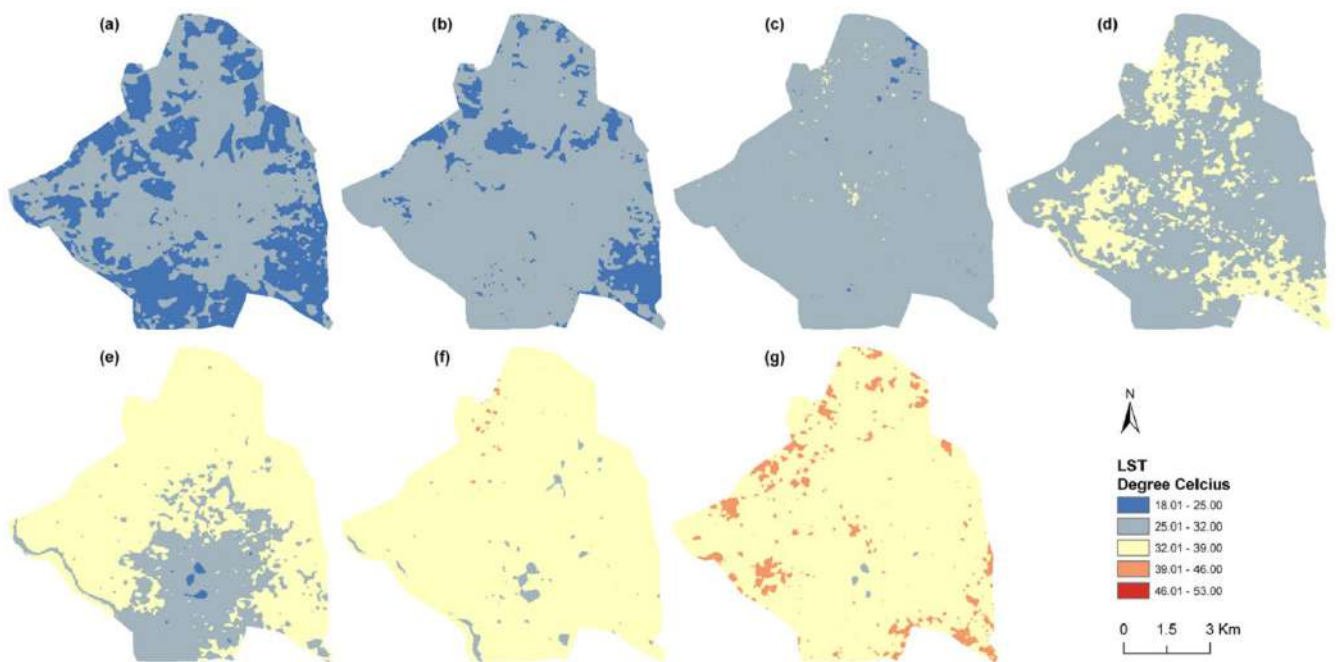


Figure 4. Spatial distribution of LST in monsoon season for the following years: (a) 1991-92 (b) 1995-96 (c) 1999-00 (d) 2004-05 (e) 2009-10 (f) 2014-15 (g) 2018-19 2004-05 (e1-e4) 2009-10 (f1-f4) 2014-15 (g1-g4) 2018-19.

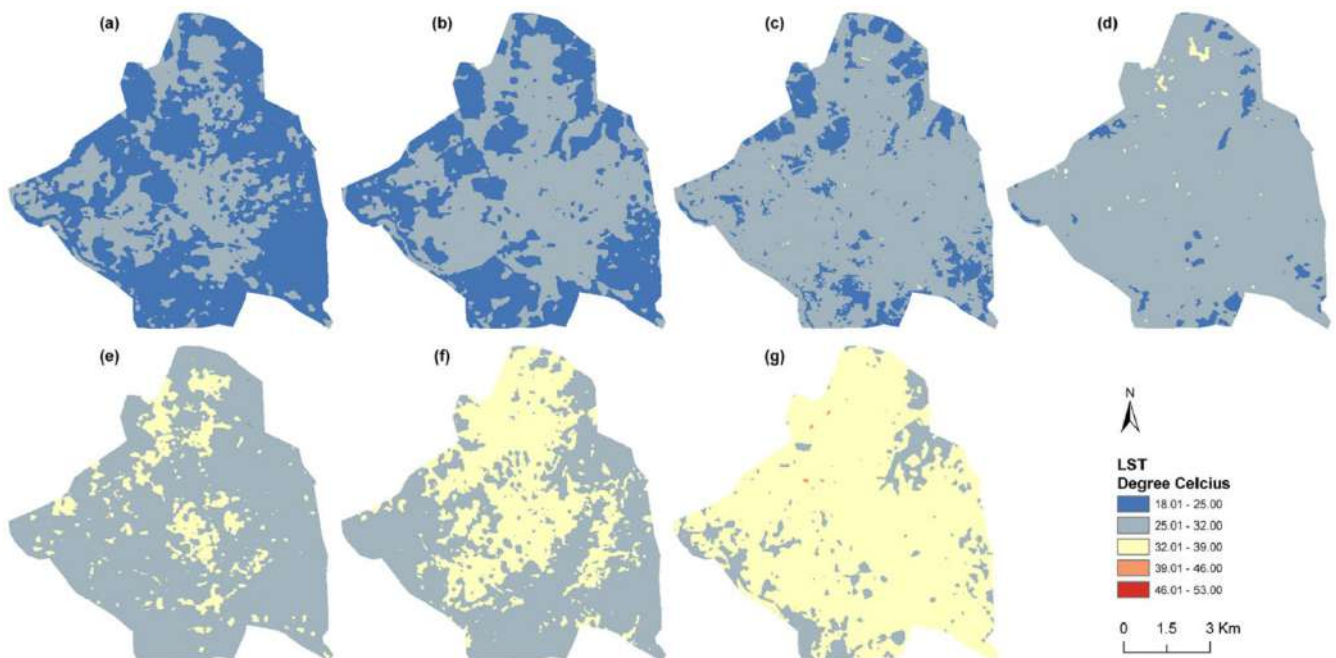


Figure 5. Spatial distribution of LST in post-monsoon season for the following years: (a) 1991-92 (b) 1995-96 (c) 1999-00 (d) 2004-05 (e) 2009-10 (f) 2014-15 (g) 2018-19 2004-05 (e1-e4) 2009-10 (f1-f4) 2014-15 (g1-g4) 2018-19.



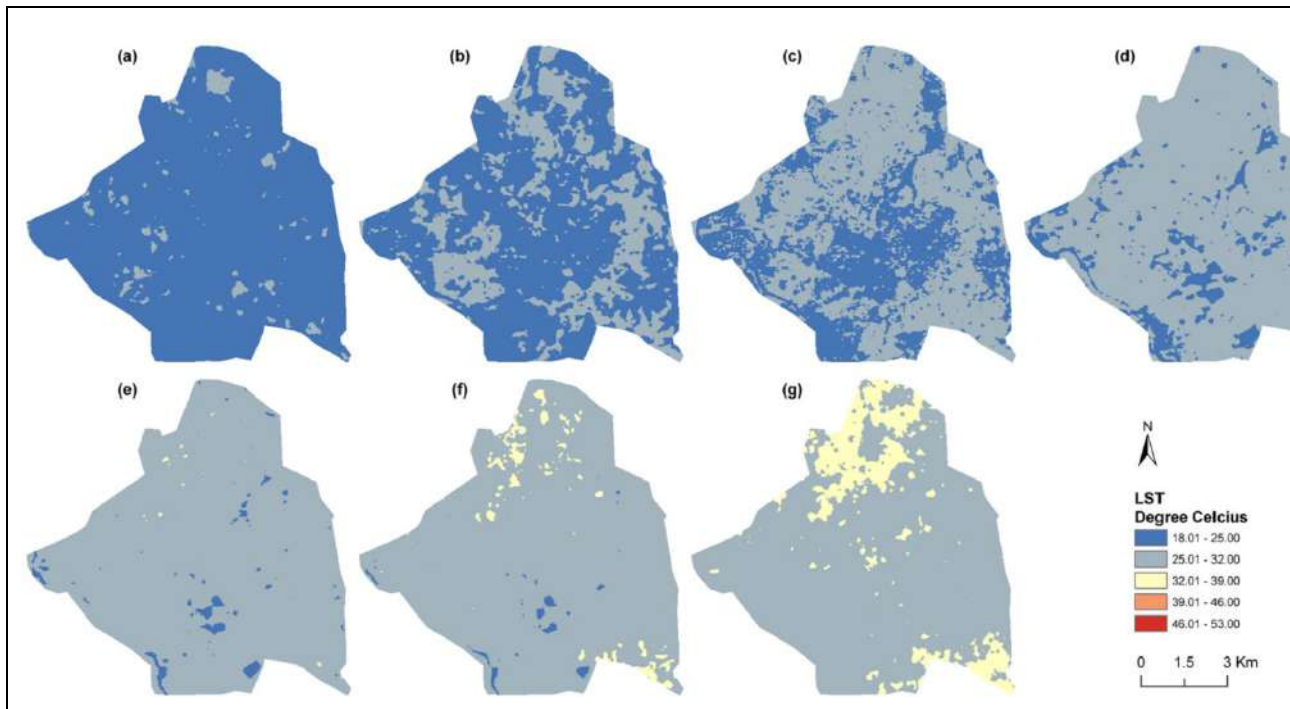


Figure 6. Spatial distribution of LST in winter season for the following years: (a) 1991-92 (b) 1995-96 (c) 1999-00 (d) 2004-05 (e) 2009-10 (f) 2014-15 (g) 2018-19 2004-05 (e1-e4) 2009-10 (f1-f4) 2014-15 (g1-g4) 2018-19.

### 4.3. Seasonal variation on LST-NDBaI relationship

Figure 7 (a-d) shows the seasonal variation of LST-NDBaI relationships on different LULC types in winter, pre-monsoon, monsoon, and post-monsoon season, respectively. Here, only three types of LULC are considered, i.e., (1) vegetation, (2) water bodies, and (3) built-up area and bare land. On water bodies, the LST-NDBaI relationship is strongly positive for any season. NDBaI is a bareness index that is frequently used in bare land extraction. On the bare land and built-up area of the study area, the correlation is a moderate positive for all four seasons. On green vegetation, the relationship is strong (monsoon, post-monsoon, and winter) to moderate (pre-monsoon) positive. The pre-monsoon season (Figure 7 (a)) has a strong positive LST-NDBaI correlation on the water bodies (0.65) and a moderate positive correlation on green vegetation (0.37), bare land, and built-up area (0.35). In the monsoon season, the correlation is strongly positive on green vegetation (0.56) and water bodies (0.51), whereas the correlation is moderate positive (0.43) on bare land and built-up area (Figure 7 (b)). The post-monsoon season has a stable and strong positive correlation (correlation coefficient  $> 0.48$ ) for any LULC categories throughout the period (Figure 7 (c)). The best correlation has been built on green vegetation (0.62), followed by the water bodies (0.53), bare land and built-up area (0.48). In winter (Figure 7 (d)), the LST-NDBaI correlation is strongly positive on water bodies (0.62) and green vegetation (0.54). Bare lands and built-up areas reflect the moderate positive (0.39) correlation in the winter season because at that time dry soil, exposed rock surface, and building materials get cooler than green vegetation and water bodies. Figure 7 (e) represents a generalized

view of the overall seasonal variation of LST-NDBaI relationships for the whole of the study area. The relationship is positive, irrespective of any season. It can be concluded from Figure 7 (e) that the post-monsoon season reveals the best correlation among all the four seasons. It is mainly because of the high intensity of moisture content in the air. Dry seasons (winter and pre-monsoon) reduce the strength of the correlation, while the wet seasons (post-monsoon and monsoon) enhance the strength of the LST-NDBaI correlation.

The present study indicates that LST builds a stable and strong to moderate positive correlation with NDBaI in Raipur City, India throughout the study period. The result is comparable to the recently conducted other similar studies on the different urban agglomerations in the world. Essa et al (2012) have shown that NDBaI builds a positive correlation (0.39) with LST in the Greater Dublin region, Ireland. Chen and Zhang (2017) have shown the strong positive nature of the correlation coefficient of the LST-NDBaI relationship in a study performed in Kunming, China. A weak positive correlation between LST and NDBaI has been presented in London (0.086) and Baghdad (0.469) by Ali et al. (2017). This relationship was also positive (0.458) in Kolkata Metropolitan Area, India. The LST and NDBaI have built a weak negative correlation (-0.11) in Guangzhou, China. This correlation was weak positive (0.06) in Harare Metropolitan City, Zimbabwe. Sharma and Joshi (2016) have shown the moderate positive nature of LSI-NDBaI correlation in the National Capital Region of India. The present study shows that the average correlation coefficient between LST and NDBaI of all the four seasons from 1991-92 to 2018-19 is moderate positive (0.052), which can be considered as a very stable and authentic relationship between the two variables.

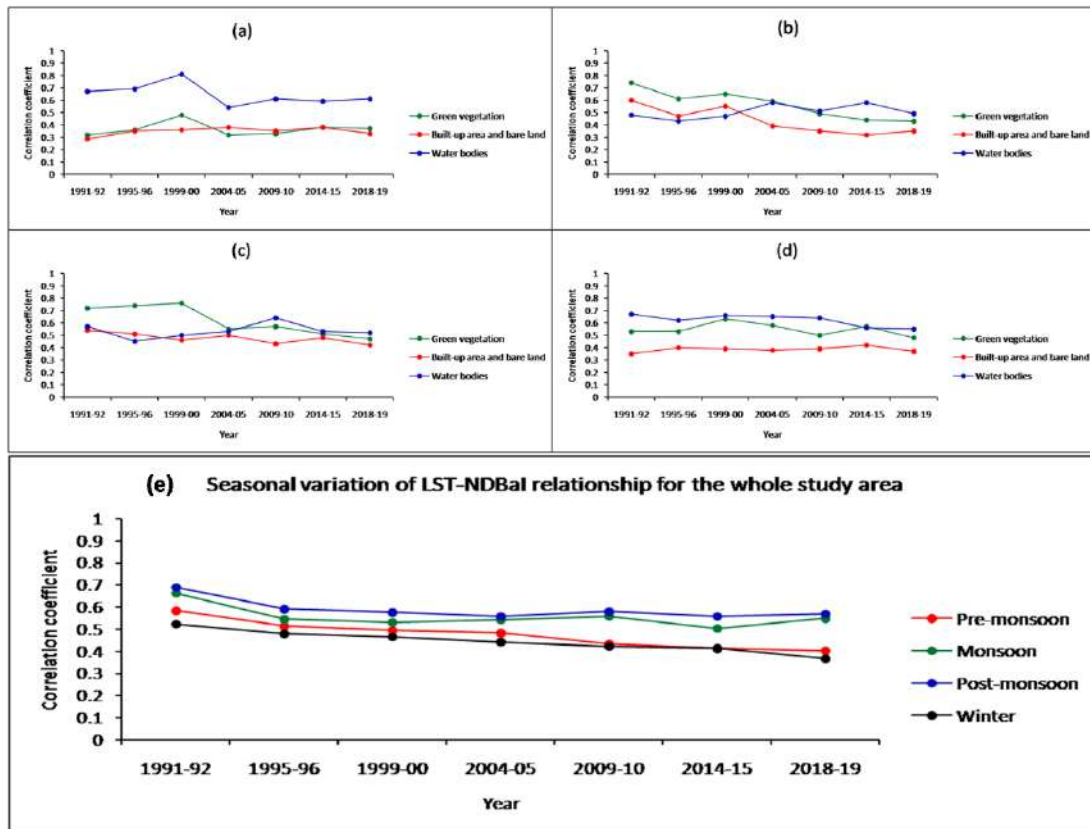


Figure 7. (a-d) Seasonal variation of the LST-NDBaI relationship on different types of LULC: (a) Pre-monsoon (b) Monsoon (c) Post-monsoon (d) Winter; (e) Seasonal variation of the LST-NDBaI relationship for the whole of the study area (significant at 0.05 level).

#### 4. Conclusion

The present study analyzed the temporal and seasonal relationship of LST and NDBaI in Raipur City, India using sixty-five Landsat data sets of four different seasons (pre-monsoon, monsoon, post-monsoon, and winter) for different years. The main expectation was the relationship should be positive between LST and NDBaI across seasons. Moreover, another expectation was that the strength of the relationship should tend to be weaker with time. Another one is that the relationship should be stronger in comparatively wet season. The results support the expectations.

In general, the results show that LST is positively related to NDBaI, irrespective of any season. In the post-monsoon (0.59) and monsoon (0.56) seasons, the correlation is strongly positive, whereas it is found moderate positive in pre-monsoon (0.47) and winter (0.44). The LST-NDBaI relationship varies for specific LULC types. The water bodies reflect a strong positive correlation of LST-NDBaI in all the four seasons (0.65 in pre-monsoon, 0.51 in monsoon, 0.53 in post-monsoon, and 0.62 in winter). On green vegetation, this LST-NDBaI correlation is also strongly positive in monsoon (0.57), post-monsoon (0.62), and winter (0.55), whereas it is moderate positive in pre-monsoon (0.37) season. The built-up area and bare land build a moderate positive correlation of LST-NDBaI in all the four seasons (0.35 in pre-monsoon, 0.43 in monsoon, 0.48 in post-monsoon, and 0.39 in winter).

Among the four seasons, the post-monsoon season builds the best LST-NDBaI correlation for all LULC types, whereas the pre-monsoon season has the least correlation. Among the various LULC categories, the water bodies present the best positive LST-NDBaI correlation (0.65 in pre-monsoon, 0.51 in monsoon, 0.53 in post-monsoon, and 0.62 in winter), irrespective to any season. Green vegetation shows strong positive (0.57 in monsoon, 0.62 in post-monsoon, and 0.55 in winter) to moderate positive (0.37 in pre-monsoon) correlation between LST and NDBaI. On the other hand, the bare land and built-up area present a moderate positive correlation (0.35 in pre-monsoon, 0.43 in monsoon, 0.48 in post-monsoon, and 0.39 in winter). Among the four seasons, the post-monsoon season builds the best LST-NDBaI correlation for all LULC types, whereas the pre-monsoon season has the least correlation. The high ratio of green plants and water surface can enhance the ecological health. Thus, this research work can be beneficial for the environmental planners.

## 5. Acknowledgment

The author is indebted to the United States Geological Survey (USGS).

## 6. Disclosure statement

No potential conflict of interest was reported by the author.

## References

- Ahmed B, Kamruzzaman M, Zhu X, Rahman MS, Choi K. Simulating Land Cover Changes and Their Impacts on Land Surface Temperature in Dhaka, Bangladesh. *Remote Sens.* 2013;5(11):5969-5998. <https://doi.org/10.3390/rs5115969>
- Alexander C. Normalised difference spectral indices and urban land cover as indicators of land surface temperature (LST). *Int. J. Appl. Earth Obs. Geoinf.* 2020;86:102013. <https://doi.org/10.1016/j.jag.2019.102013>
- Alibakhshi Z, Ahmadi M, Farajzadeh Asl M. Modeling Biophysical Variables and Land Surface Temperature Using the GWR Model: Case Study—Tehran and Its Satellite Cities. *J. Indian Soc. Remote Sens.* 2020;48:59–70. <https://doi.org/10.1007/s12524-019-01062-x>
- Ali JM, Marsh SH, Smith MJ. A comparison between London and Baghdad surface urban heat islands and possible engineering mitigation solutions. *Sustain. Cities Soc.* 2017;29:159-168. <https://doi.org/10.1016/j.scs.2016.12.010>
- As-syakur AR, Adnyana IWS, Arthana IW, Nuarsa IW. Enhanced Built-Up and Bareness Index (EBBI) for Mapping Built-Up and Bare Land in an Urban Area. *Remote Sens.* 2012;4(10):2957-2970. <https://doi.org/10.3390/rs4102957>
- Barsi J, Schott J, Hook S, Raqueno N, Markham B, Radocinski R. Landsat-8 thermal infrared sensor (TIRS) vicarious radiometric calibration. *Remote Sens.* 2014;6(11):11607-11626.
- Carlson TN, Ripley DA. On the Relation between NDVI, Fractional Vegetation Cover, and Leaf Area Index. *Remote Sens. Environ.* 1997;62:241-252. [https://doi.org/10.1016/S0034-4257\(97\)00104-1](https://doi.org/10.1016/S0034-4257(97)00104-1)

- Chen XL, Zhao HM, Li PX, Yi ZY. Remote sensing image-based analysis of the relationship between urban heat island and land use/cover changes. *Remote Sens. Environ.* 2006;104(2):133–146. <https://doi.org/10.1016/j.rse.2005.11.016>
- Chen X, Zhang Y. Impacts of urban surface characteristics on spatiotemporal pattern of land surface temperature in Kunming of China. *Sustain. Cities Soc.* 2017;32:87-99. <https://doi.org/10.1016/j.scs.2017.03.013>
- Essa W, Verbeiren B, Van der Kwast J, Van de Voorde T, Batelaan O. Evaluation of the DisTrad thermal sharpening methodology for urban areas. *Int. J. Appl. Earth Obs. Geoinf.* 2012;19:163-172. <https://doi.org/10.1016/j.jag.2012.05.010>
- Guha S, Govil H, Diwan P. Analytical study of seasonal variability in land surface temperature with normalized difference vegetation index, normalized difference water index, normalized difference built-up index, and normalized multiband drought index. *J. Appl. Remote Sens.* 2019;13(2): 024518. <https://doi.org/10.1016/j.jrs.2019.02.018>
- Guha S, Govil H, Gill N, Dey A. Analytical study on the relationship between land surface temperature and land use/land cover indices. *Ann. GIS.* 2020;26(2): 201-216. <https://doi.org/10.1080/19475683.2020.1754291>
- Guha S, Govil H, Mukherjee S. Dynamic analysis and ecological evaluation of urban heat islands in Raipur city, India. *J. Appl. Remote Sens.* 2017;11(3): 036020. <https://doi.org/10.1016/j.jrs.2017.03.020>
- Guo G, Wu Z, Chen Y. Estimation of subpixel land surface temperature using Landsat TM imagery: A case examination over a heterogeneous urban area. Third International Workshop on Earth Observation and Remote Sensing Applications
- Hao X, Li W, Deng H. The oasis effect and summer temperature rise in arid regions-case study in Tarim Basin. *Sci. Rep.* 2016;6:35418. <https://doi.org/10.1038/srep35418>
- Jain S, Sannigrahi S, Sen S, Bhatt S, Chakraborti S, Rahmat S. Urban heat island intensity and its mitigation strategies in the fast-growing urban area. *J. Urban Manage.* 2020;9(1):54-66. <https://doi.org/10.1016/j.jum.2019.09.004>
- Li J. Estimating land surface temperature from Landsat-5 TM. *Remote Sens. Technol. Appl.* 2006;21:322-326.
- Li ZN, Duan SB, Tang BH, Wu H, Ren HG, Yan GJ. Review of methods for land surface temperature derived from thermal infrared remotely sensed data. *J. Remote Sens.* 2016;20:899–920.
- Macarof P, Bîrlăcă IC, Stătescu F. Investigating the relationship between land surface temperature and urban indices using landsat-8: a case study of Iași. *Lucrările Seminarului Geografic Dimitrie Cantemir* 2017;45:81-88. <https://doi.org/10.15551/lsgdc.v45i0.07>
- Mushore TD, Odindi J, Dube T, Mutanga O. Prediction of future urban surface temperatures using medium resolution satellite data in Harare metropolitan city, Zimbabwe. *Build. Environ.* 2017;122:397-410. <https://doi.org/10.1016/j.buildenv.2017.06.033>
- Nimish G, Bharath HA, Lalitha A. Exploring temperature indices by deriving relationship between land surface temperature and urban landscape. *Remote Sens. Appl. Soc. Environ.* 2020;18:100299. <https://doi.org/10.1016/j.rsase.2020.100299>
- Qin Z, Karnieli A, Barliner P. A Mono-Window Algorithm for Retrieving Land Surface Temperature from Landsat TM Data and Its Application to the Israel-Egypt Border Region. *Int. J. Remote Sens.* 2001;22(18):3719-3746. <https://doi.org/10.1080/01431160010006971>
- Sharma R, Joshi PK. Mapping environmental impacts of rapid urbanization in the National Capital Region of India using remote sensing inputs. *Urban Clim.* 2016;15:70-82. <https://doi.org/10.1016/j.uclim.2016.01.004>

- Yuan X, Wang W, Cui J, Meng F, Kurban A, De Maeyer. Vegetation changes and land surface feedbacks drive shifts in local temperatures over Central Asia. *Sci. Rep.* 2017;(1):3287. <https://doi.org/10.1038/s41598-017-03432-2>
- Sekertekin A, Bonafoni S. Land surface temperature retrieval from landsat 5, 7, and 8 over rural areas: assessment of different retrieval algorithms and emissivity models and toolbox implementation. *Remote Sens.* 2020;12(2):294. <https://doi.org/10.3390/rs12020294>
- Sharma R, Ghosh A, Joshi PK. Mapping environmental impacts of rapid urbanization in the National Capital Region of India using remote sensing inputs. *Geocarto Int.* 2013;28(5):420-438. <https://doi.org/10.1080/10106049.2012.715208>
- (EORSA), Changsha, 2014. p. 304-308. <https://doi.org/10.1109/EORSA.2014.6927900>
- Sobrino JA, Raissouni N, Li Z. A comparative study of land surface emissivity retrieval from NOAA data. *Remote Sens. Environ.* 2001;75(2):256–266. [https://doi.org/10.1016/S0034-4257\(00\)00171-1](https://doi.org/10.1016/S0034-4257(00)00171-1)
- Sobrino JA, Jimenez-Munoz JC, Paolini L. Land surface temperature retrieval from Landsat TM5. *Remote Sens. Environ.* 2004;9:434–440. <https://doi.org/10.1016/j.rse.2004.02.003>
- Sun Q, Tan J, Xu Y. An ERDAS image processing method for retrieving LST and describing urban heat evolution: A case study in the Pearl River Delta Region in South China. *Environ. Earth Sci.* 2010;59:1047-1055.
- Tomlinson CJ, Chapman L, Trones JE, Baker C. Remote sensing land surface temperature for meteorology and climatology: a review. *Meteorol. Appl.* 2011;118:296–306. <https://doi.org/10.1002/met.287>
- Wang J, Qingming Z, Guo H, Jin Z. Characterizing the Spatial Dynamics of Land Surface temperature–impervious Surface Fraction Relationship. *Int. J. Appl. Earth Obs. Geoinf.* 2016;45:55–65.
- Weng QH, Lu DS, Schubring J. Estimation of Land Surface Temperature–Vegetation Abundance Relationship for Urban Heat Island Studies. *Remote Sens. Environ.* 2004;89:467-483. <https://doi.org/10.1016/j.rse.2003.11.005>
- Weng Q, Quattrochi DA. Thermal remote sensing of urban areas: An introduction to the special issue. *Remote Sens. Environ.* 2006;104(2):119-122. <https://doi.org/10.1016/j.rse.2006.05.002>
- Wukelic GE, Gibbons DE, Martucci LM, Foote HP. Radiometric calibration of Landsat Thematic Mapper thermal band. *Remote Sens. Environ.* 1989;28:339–347. [https://doi.org/10.1016/0034-4257\(89\)90125-9](https://doi.org/10.1016/0034-4257(89)90125-9)
- Yang J, Que J. The empirical expressions of the relation between precipitable water and ground water vapor pressure for some areas in China. *Sci. Atmos. Sin.* 1996;20:620-626.
- Zanter K. Landsat 8 (L8) Data Users Handbook; EROS: Sioux Falls, SD, USA. 2019.
- Zhao HM, Chen XL. Use of normalized difference bareness index in quickly mapping bare areas from TM/ETM+. *Geoscience and Remote Sensing Symposium.* 2005;3(25–29):p.1666–1668. <https://doi.org/10.1109/IGARSS.2005.1526319>



## Source details

[Feedback >](#) [Compare sources >](#)

### International Journal of Engineering and Geosciences

Scopus coverage years: from 2019 to Present

Publisher: Murat Yakar

E-ISSN: 2548-0960

Subject area: Environmental Science: Environmental Science (miscellaneous)

Source type: Journal

[View all documents >](#)

[Set document alert](#)

[Save to source list](#)

SJR



SNIP



See discussions, stats, and author profiles for this publication at: <https://www.researchgate.net/publication/351484110>

# Estimating the seasonal relationship between land surface temperature and normalized difference bareness index using Landsat data series

Article in *International Journal of Engineering and Geosciences* · January 2021

DOI: 10.26833/ijeg.833260

CITATIONS

8

READS

114

2 authors:



**Himanshu Govil**

National Institute of Technology Raipur

130 PUBLICATIONS 2,195 CITATIONS

[SEE PROFILE](#)



**Subhanil Guha**

National Institute of Technology Raipur

69 PUBLICATIONS 1,353 CITATIONS

[SEE PROFILE](#)





## Estimating the seasonal relationship between land surface temperature and normalized difference bareness index using Landsat data series

Subhanil Guha\*<sup>1</sup> , Himanshu Govil<sup>1</sup> 

<sup>1</sup>National Institute of Technology Raipur, Department of Applied Geology, Raipur, India

### Keywords

Landsat  
LST  
LULC  
NDBaI  
Raipur

### ABSTRACT

The present study analyzes the seasonal variability of the relationship between the land surface temperature (LST) and normalized difference bareness index (NDBaI) on different land use/land cover (LULC) in Raipur City, India by using sixty-five Landsat images of four seasons (pre-monsoon, monsoon, post-monsoon, and winter) of 1991-1992, 1995-1996, 1999-2000, 2004-2005, 2009-2010, 2014-2015, and 2018-2019. The mono-window algorithm was used to retrieve LST and Pearson's correlation coefficient was used to generate the LST-NDBaI relationship. The post-monsoon season builds the best correlation (0.59) among the four seasons. The water bodies builds a moderate to strong positive correlation (>0.50) in all the four seasons. On green vegetation, this correlation is moderate to strong positive (>0.54) in the three seasons, except the pre-monsoon season. The built-up area and bare land generate a moderate positive correlation (>0.34) in all the four seasons. Among the four seasons, the post-monsoon season builds the best correlation for all LULC types, whereas the pre-monsoon season has the least correlation. This research work is useful for environmental planning of other cities with similar climatic conditions.

## 1. INTRODUCTION

Land surface temperature (LST) is an indispensable parameter in analyzing the bio-geochemical functions of the earth surface features (Tomlinson et al. 2011; Hao et al. 2016; Guha et al. 2020a). Green plants, wetlands, and water bodies generate low LST, whereas human settlement, and bare land surface produce high LST in the summer season of tropical areas (Chen et al. 2006). Thus, LST and normalized difference spectral indices related studies are quite important in the ecological planning of the recent urban agglomerations (Sekertekin et al. 2016; Li et al. 2016; Guha et al. 2020b). Normalized difference bareness index (NDBaI) is one of the most popular indices for bare land extraction that is often used in LULC and LST related studies (Zhao and Chen 2005; Chen et al. 2006; Essa et al. 2012; Guha et al. 2017).

Several research articles presented the LST-NDBaI relationship in recent years. As-Syakur et al. (2012) investigates various bareness indices for bare land mapping in Denpasar of Bali, Indonesia. Ahmed et al. (2013) used NDBaI along with other LULC indices to simulate the land surface changes and their impact on

LST in Dhaka, Bangladesh. Sharma et al. (2013) examined the relationship between LST and NDBaI in Surat City of India. Guo et al. (2014) estimated sub-pixel LST and built a relationship between LST and NDBaI in Guangzhou core urban area of China. Ali et al. (2017) compared the relationship of LST with NDBaI and other LULC indices in London and Baghdad cities. Macarof et al. (2017) investigated the relationship between LST and NDBaI in Iasi Municipality Area of eastern Romania from 2013 to 2016 by using Landsat 8 data. Alibakshi et al. (2020) investigated the relationship between NDBaI and LST from 2001 to 2015 in Tehran and its satellite cities in Iran by the geographically weighted regression model using Landsat 7 data. Alexander (2020) evaluated the LST-NDBaI relationship in Aarhus City of Denmark by using Landsat 8 data. Jain et al. (2020) investigated the LST-NDBaI relationship in Nagpur City, India from 2000 to 2015 by using Landsat data.

The LST and NDBaI values vary due to the seasonal variation of various atmospheric components. Thus, to estimate the characteristics of seasonal variation of the LST-NDBaI relationship in Indian context, Raipur City of Chhattisgarh has been chosen. The main aim of the study is to estimate the seasonal variation of LST-NDBaI

### \*Corresponding Author

\*(subhanilguha@gmail.com) ORCID ID 0000-0002-2967-7248  
(himgeo@gmail.com) ORCID ID 0000-0002-3433-8355

### Cite this article

Guha S & Govil H (2022). Estimating the seasonal relationship between land surface temperature and normalized difference bareness index using Landsat data series. International Journal of Engineering and Geosciences, 7(1), 09-16

relationship on different categories of LULC. The study will be a beneficial one for ecological planning and management in an urban environment.

## 2. STUDY AREA AND DATA

Figure 1 shows the geographical location of Raipur city of India which extends from 21°11'22"N to 21°20'02"N and from 81°32'20"E to 81°41'50"E. The city covers an area of around 165 km<sup>2</sup>. Figure 1(a) presents the outline map of India (URL-1). Figure 1(b) presents the outline map of Chhattisgarh State (URL-1). Figure 1(c) represents the false colour composite (FCC) image of Raipur City (URL-2) from recent Landsat 8 data of 07 November 2018(URL-3). Figure 1(d) shows the digital elevation map (DEM) of Raipur City produced by the ArcGIS software using the last available ASTER DEM data of 11 October 2011 (URL-3). The city is characterised by the tropical dry and wet type of climate (URL-4). The mean monthly temperature ranges from 12°C to 42°C. May presents the highest average temperature (35°C), while December presents the lowest average temperature (20°C). The highest average rainfall (327 mm) is observed in July. March, April, and May are considered as the summer or pre-monsoon months. June, July, August, and September are the monsoon months. The post-monsoon months are October and November, when the weather remains pleasant. The winter months are December, January, and February, when the temperature falls significantly.

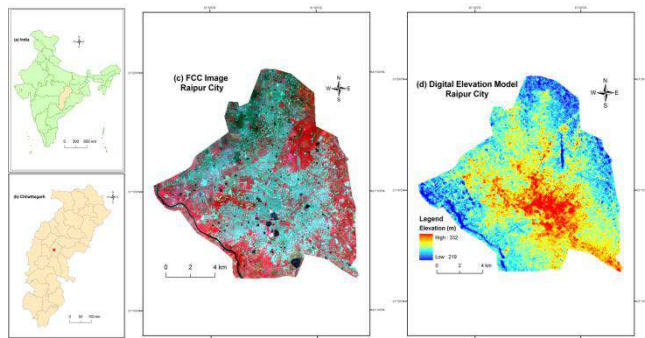


**Figure 1.** Location of the study area: (a) India highlighting Chhattisgarh; (b) Chhattisgarh highlighting Raipur City; (c) False colour composite image of Raipur; (d) Digital elevation model of Raipur.

Table 1 shows the specification of Landsat data of different sensors. The band 10 of Landsat 8 thermal infrared sensors (TIRS) dataset was used as the only TIR band in the present study due to a larger calibration certainty (Barsi et al. 2014). Landsat 5 thematic mapper (TM) data has only one TIR band (band 6) of 120 m resolution. Landsat 7 enhanced thematic mapper plus (ETM+) data has a TIR band (band 6) of 60 m resolution. The TIR bands of all the Landsat sensors were resampled to 30 m pixel size by the data provider (USGS) as the spatial resolution of visible to near-infrared (VNIR) and shortwave infrared (SWIR) bands of the three types of Landsat sensors is 30 m. All the raster calculations were processed in the environment of ArcGIS 9.3 and ERDAS IMAGINE 9.1 software.

**Table 1.** Specification of the used Landsat data

Date of acquisition	Time (UTC)	Cloud cover (%)	Resolution of TIR bands (m)
18-Mar-91	04:17:34	0	120
03-Apr-91	04:17:46	0	120
21-May-91	04:18:39	1	120
26-Sep-91	04:20:03	13	120
12-Oct-91	04:20:12	6	120
13-Nov-91	04:20:19	1	120
16-Jan-92	04:20:22	3	120
01-Feb-92	04:20:27	0	120
17-Feb-92	04:20:15	4	120
14-Apr-95	04:05:06	0	120
10-Dec-95	03:56:47	0	120
27-Jan-96	04:00:14	0	120
23-Sep-96	04:14:16	2	120
09-Oct-96	04:15:07	0	120
25-Oct-96	04:15:55	5	120
10-Nov-96	04:16:41	7	120
11-Nov-99	04:49:00	0	60
30-Jan-00	04:48:55	0	60
03-Apr-00	04:48:35	0	60
05-May-00	04:48:20	0	60
26-Sep-00	04:46:33	6	60
15-Dec-00	04:46:31	0	60
21-Mar-04	04:35:14	0	120
22-Apr-04	04:36:01	1	120
24-May-04	04:36:54	0	120
09-Jun-04	04:37:23	9	120
29-Sep-04	04:40:16	9	120
15-Oct-04	04:40:36	4	120
16-Nov-04	04:41:11	0	120
02-Dec-04	04:41:33	0	120
18-Dec-04	04:41:52	0	120
19-Jan-05	04:42:17	0	120
04-Feb-05	04:42:29	0	120
03-Mar-09	04:42:22	0	120
19-Mar-09	04:42:44	2	120
04-Apr-09	04:43:05	0	120
20-Apr-09	04:43:24	0	120
06-May-09	04:43:42	0	120
22-May-09	04:44:00	1	120
23-Jun-09	04:44:35	0	120
13-Oct-09	04:46:12	0	120
29-Oct-09	04:46:20	0	120
16-Dec-09	04:46:44	1	120
17-Jan-10	04:46:55	6	120
02-Feb-10	04:46:59	0	120
18-Feb-10	04:47:02	7	100
17-Mar-14	04:56:36	0	100
02-Apr-14	04:56:19	0	100
20-May-14	04:55:38	5	100
05-Jun-14	04:55:45	0	100
12-Nov-14	04:56:21	7	100
30-Dec-14	04:56:09	0	100
15-Jan-15	04:56:09	0	100
31-Jan-15	04:56:04	0	100
16-Feb-15	04:55:55	0	100
12-Mar-18	04:55:43	2	100
28-Mar-18	04:55:36	0	100
15-May-18	04:55:08	0	100
16-Jun-18	04:55:01	2	100
06-Oct-18	04:55:53	0	100
22-Oct-18	04:55:59	0	100
07-Nov-18	04:56:03	0	100
25-Dec-18	04:55:59	0	100
11-Feb-19	04:55:52	0	100
27-Feb-19	04:55:48	4	100

## 3. METHODOLOGY

### 3.1. Retrieving LST from Landsat Data

In this study, the mono-window algorithm was applied to retrieve LST from multi-temporal Landsat satellite sensors (Qin et al. 2001) where three necessary

parameters are ground emissivity, atmospheric transmittance, and effective mean atmospheric temperature. At first, the original TIR bands (100 m resolution for Landsat 8 OLI/TIRS data, 120 m resolution for Landsat 5 TM data, and 60 m resolution for Landsat 7 ETM+ data) were resampled into 30 m by USGS data centre for further application.

The TIR pixel values are firstly converted into radiance from digital number (DN) values (Markham & Barkar 1985). Radiance for TIR band of Landsat 5 TM data and Landsat 7 ETM+ data is obtained using Eq. (1) (URL-3):

$$L_{\lambda} = \left[ \frac{L_{MAX\lambda} - L_{MIN\lambda}}{QCAL_{MAX} - QCAL_{MIN}} \right] * [Q_{CAL} - QCAL_{MIN}] + L_{MIN\lambda} \quad (1)$$

where,  $L_{\lambda}$  = Top of Atmosphere (TOA) spectral radiance ( $Wm^{-2}sr^{-1}mm^{-1}$ ),  $Q_{CAL}$  = quantized calibrated pixel value in DN,  $L_{MIN\lambda}$  ( $Wm^{-2}sr^{-1}mm^{-1}$ ) = spectral radiance scaled to  $QCAL_{MIN}$ ,  $L_{MAX\lambda}$  ( $Wm^{-2}sr^{-1}mm^{-1}$ ) = spectral radiance scaled to  $QCAL_{MAX}$ ,  $QCAL_{MIN}$  = minimum quantized calibrated pixel value in DN and  $QCAL_{MAX}$  = maximum quantized calibrated pixel value in DN.  $L_{MIN\lambda}$ ,  $L_{MAX\lambda}$ ,  $QCAL_{MIN}$ , and  $QCAL_{MAX}$  values are obtained from the metadata file of Landsat TM and ETM+ data. Radiance for Landsat 8 TIR band is obtained from Eq. (2) (Zanter 2019):

$$L_{\lambda} = M_L \cdot Q_{CAL} + A_L \quad (2)$$

where,  $L_{\lambda}$  = TOA spectral radiance ( $Wm^{-2}sr^{-1}mm^{-1}$ ),  $M_L$  = band-specific multiplicative rescaling factor from the metadata,  $A_L$  = band-specific additive rescaling factor from the metadata,  $Q_{CAL}$  = quantized and calibrated standard product pixel values (DN). All of these variables can be retrieved from the metadata file of Landsat 8 data.

For Landsat 5 and 7 data, the reflectance value is obtained from radiances using Eq. (3) (URL-3):

$$\rho_{\lambda} = \frac{\pi \cdot L_{\lambda} \cdot d^2}{ESUN_{\lambda} \cdot \cos \theta_s} \quad (3)$$

where,  $\rho_{\lambda}$  = unitless planetary reflectance,  $L_{\lambda}$  = TOA spectral radiance ( $Wm^{-2}sr^{-1}\mu m^{-1}$ ),  $d$  = Earth-Sun distance in astronomical units,  $ESUN_{\lambda}$  = mean solar exo-atmospheric spectral irradiances ( $Wm^{-2}\mu m^{-1}$ ) and  $\theta_s$  = solar zenith angle in degrees.  $ESUN_{\lambda}$  values for each band of Landsat 5 and 7 can be obtained from the handbooks of the related mission.  $\theta_s$  and  $d$  values can be attained from the metadata file (Coll et al. 2010).

For Landsat 8 data, reflectance conversion can be applied to DN values directly as in Eq. (4) (Zanter 2019):

$$\rho_{\lambda} = \frac{M_{\rho} \cdot Q_{CAL} + A_{\rho}}{\sin \theta_{SE}} \quad (4)$$

where,  $M_{\rho}$  = band-specific multiplicative rescaling factor from the metadata,  $A_{\rho}$  = band-specific additive rescaling factor from the metadata,  $Q_{CAL}$  = quantized and calibrated standard product pixel values (DN) and  $\theta_{SE}$  = local sun elevation angle from metadata file.

Eq. (5) is used to convert the spectral radiance to at-sensor brightness temperature (Wukelic et al. 1989; Chen et al. 2006):

$$T_b = \frac{K_2}{\ln\left(\frac{K_1}{L_{\lambda}} + 1\right)} \quad (5)$$

where,  $T_b$  = brightness temperature in Kelvin (K),  $L_{\lambda}$  = spectral radiance in  $Wm^{-2}sr^{-1}mm^{-1}$ ;  $K_2$  and  $K_1$  = calibration constants. For Landsat 8 data,  $K_1 = 774.89$ ,  $K_2 = 1321.08$  ( $Wm^{-2}sr^{-1}mm^{-1}$ ). For Landsat 7 data,  $K_1 = 666.09$ ,  $K_2 = 1282.71$  ( $Wm^{-2}sr^{-1}mm^{-1}$ ). For Landsat 5 data,  $K_1 = 607.76$ ,  $K_2 = 1260.56$  ( $Wm^{-2}sr^{-1}mm^{-1}$ ).

The land surface emissivity  $\varepsilon$ , is measured from Eq. (6) using the NDVI Thresholds Method (Sobrino et al. 2001, 2004; Vlassova et al. 2014).

$$\varepsilon = \varepsilon_v F_v + \varepsilon_s (1 - F_v) + d\varepsilon \quad (6)$$

where,  $\varepsilon$  = land surface emissivity,  $\varepsilon_v$  = vegetation emissivity,  $\varepsilon_s$  = soil emissivity,  $F_v$  = fractional vegetation,  $d\varepsilon$  = effect of the geometrical distribution of the natural surfaces and internal reflections that can be expressed by Eq. (7):

$$d\varepsilon = (1 - \varepsilon_s)(1 - F_v)F\varepsilon_v \quad (7)$$

where,  $\varepsilon_v$  = vegetation emissivity,  $\varepsilon_s$  = soil emissivity,  $F_v$  = fractional vegetation,  $F$  = a shape factor whose mean is 0.55, the value of  $d\varepsilon$  may be 2% for mixed land surfaces (Sobrino et al. 2004).

The fractional vegetation  $F_v$ , of each pixel, is estimated from the NDVI using Eq. (8) (Carlson & Ripley 1997):

$$F_v = \left( \frac{NDVI - NDVI_{min}}{NDVI_{max} - NDVI_{min}} \right)^2 \quad (8)$$

where, (a)  $NDVI < 0.2$  for bare soil;  
 (b)  $NDVI > 0.5$  for vegetation;  
 (c)  $0.2 \leq NDVI \leq 0.5$  for mixed land with bare soil

and vegetation; (d)  $NDVI < 0$  for water body (Sobrino et al. 2001, 2004; Vlassova et al. 2014).

Finally, the land surface emissivity  $\varepsilon$  can be expressed by Eq. (9):

$$\varepsilon = 0.004 * F_v + 0.986 \quad (9)$$

where,  $\varepsilon$  = land surface emissivity,  $F_v$  = fractional vegetation.

Water vapour content is calculated by Eq. (10) (Yang and Qie 1996; Li 2006):

$$w = 0.0981 * \left[ 10 * 0.6108 * \exp \left( \frac{17.27 * (T_0 - 273.15)}{237.3 + (T_0 - 273.15)} \right) * RH \right] + 0.1697 \quad (10)$$

where,  $w$  = water vapour content ( $\text{g}/\text{cm}^2$ ),  $T_0$  = near-surface air temperature in Kelvin (K),  $RH$  = relative humidity (%). These parameters of atmospheric profile are obtained from the Meteorological Centre, Raipur (<http://www.imdraipur.gov.in>). Atmospheric transmittance is estimated for Raipur City using Eq. (11) (Qin et al. 2001; Sun et al. 2010):

$$\tau = 1.031412 - 0.11536w \quad (11)$$

where,  $\tau$  = total atmospheric transmittance,  $w$  = water vapour content ( $\text{g}/\text{cm}^2$ ).

Raipur City is located in the tropical region. Thus, Eq. (12) is applied to calculate the effective mean atmospheric transmittance of Raipur (Qin et al. 2001; Sun et al. 2010):

$$T_a = 17.9769 + 0.91715T_0 \quad (12)$$

LST is retrieved from Landsat 5, Landsat 7, and Landsat 8 satellite data by using Eq. (13-15) (Qin et al. 2001):

$$T_s = \frac{[a(1-C-D) + (b(1-C-D) + C + D)T_b - DT_a]}{C} \quad (13)$$

$$C = \varepsilon\tau \quad (14)$$

$$D = (1-\tau)[1 + (1-\varepsilon)\tau] \quad (15)$$

where,  $\varepsilon$  = land surface emissivity,  $\tau$  = total atmospheric transmittance,  $C$  and  $D$  = internal parameters based on atmospheric transmittance and land surface emissivity,  $T_b$  = at-sensor brightness temperature,  $T_a$  = mean atmospheric temperature,  $T_0$  = near-surface air temperature,  $T_s$  = land surface temperature,  $a = -67.355351$ ,  $b = 0.458606$ .

### 3.2. Retrieving Extraction of Different Types of LULC by Using NDBaI

The study emphasized NDBaI for determining the relationship with LST (Zhao and Chen 2005; Chen et al.

2006). NDBaI is determined by the SWIR and TIR bands. For, Landsat 5 and Landsat 7 data, band 5 and band 6 are used as the SWIR and TIR band, respectively. For Landsat 8 data, band 6 and band 10 are used as the SWIR and TIR bands, respectively (Table 2). The value of NDBaI ranges between  $-1$  and  $+1$ . Generally, the positive value of NDBaI indicates the bare land. The bareness increases with the increase of the positive NDBaI. NDBaI value ranges between  $-0.2$  to  $0$  shows the built-up area,  $NDBaI > 0$  shows the bare land,  $NDBaI < -0.25$  presents the vegetation, and  $NDBaI < -0.65$  presents the water bodies (Chen et al. 2006). LULC maps have been generated using the aforesaid threshold limits of NDBaI and the results have been validated by the maximum likelihood classification. The average calculated values of the Kappa coefficient and overall accuracy for all the images are  $0.91$  and  $92.19\%$ , respectively.

**Table 2.** General description of NDBaI

Acronym	Description	Formulation	References
NDBaI	Normalized difference bareness index	$\frac{SWIR1 - TIR}{SWIR1 + TIR}$	Zhao and Chen 2005; Chen et al. 2006

### 3.3. LST-NDBaI relationship generation on different types of LULC

LST-NDBaI correlation develops on the following LULC categories, i.e., green plants, water bodies, human settlement, and bare lands. The study also evaluates the seasonal and temporal variability of the LST-NDBaI correlation.

## 4. RESULTS AND DISCUSSION

### 4.1. Extraction of LULC Types Using NDBaI

Figure 2 shows the classified LULC maps from the post-monsoon data, prepared by the threshold limits of NDBaI and these maps have been validated by applying the maximum likelihood classification method. In the earlier period, the built-up area and bare land were developed along the middle portion of the city. The northwest part has been rapidly urbanized till 2004-05. Most of the vegetation covered areas of this area were converted into the built-up areas. However, in the last phase of the study period, most of the remaining vegetated areas were decreased due to quick conversion into bare land and built-up area. These conversions were mainly by the anthropogenic activities, although some natural desertification process was also responsible in the semi-arid parts. Conversion of the water bodies is lesser than the vegetation. On the other hand, a high increasing rate was observed for the settlement and bare earth surface (approximately  $3 \text{ km}^2$  area annually).

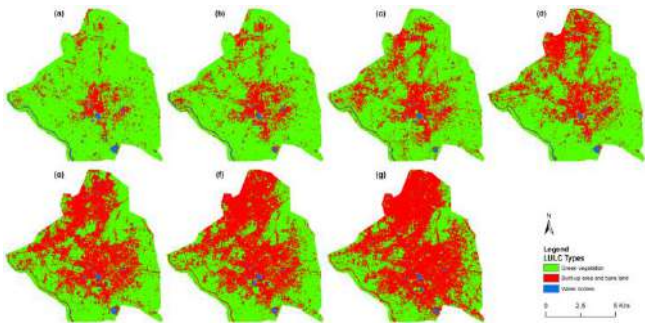


**Figure 2.** LULC maps of the study area: (a) 1991-1992; (b) 1995-1996; (c) 1999-2000; (d) 2004-2005; (e) 2009-2010; (f) 2014-2015; (g) 2018-2019.

**4.2. Seasonal Distribution of LST and NDBaI**

A prominent seasonal variation in the minimum, maximum, mean and standard deviation values of LST is noticed in Table 3. The average values of LST and the Pearson's correlation coefficient between LST-NDBaI relationship from 1991-92 to 2018-19 have been shown in italic font text inside Table 3.

**Table 3.** Seasonal variation of LST and LST-NDBaI relationship (0.05 level of significance).

Season	Year of acquisition	LST (°C)				Correlation coefficients for LST-NDBaI relationship
		Min.	Max.	Mean	Std.	
Pre-monsoon	1991-92	23.81	36.27	31.54	1.52	0.58
	1995-96	24.54	41.07	34.64	1.89	0.51
	1999-00	26.36	42.23	36.38	1.93	0.49
	2004-05	26.95	44.07	38.01	2.19	0.48
	2009-10	28.81	46.48	39.60	2.54	0.43
	2014-15	31.93	48.22	41.28	1.75	0.41
	2018-19	33.46	51.11	43.74	1.75	0.40
	<i>Average</i>	<i>27.98</i>	<i>44.21</i>	<i>37.88</i>	<i>1.94</i>	<i>0.47</i>
Monsoon	1991-92	19.87	30.83	25.74	1.41	0.66
	1995-96	21.21	33.01	26.50	1.33	0.54
	1999-00	22.76	35.91	27.81	1.34	0.53
	2004-05	24.17	36.20	31.32	1.33	0.54
	2009-10	25.94	38.38	33.06	2.40	0.56
	2014-15	27.74	40.15	34.87	1.68	0.50
	2018-19	30.59	41.98	37.30	1.13	0.55
	<i>Average</i>	<i>24.61</i>	<i>36.64</i>	<i>30.94</i>	<i>1.52</i>	<i>0.56</i>
Post-monsoon	1991-92	19.72	29.56	24.32	1.72	0.69
	1995-96	20.42	30.33	25.12	1.34	0.59
	1999-00	22.41	33.47	26.84	1.91	0.57
	2004-05	23.03	35.25	28.01	1.71	0.56
	2009-10	24.62	37.91	30.26	1.60	0.58
	2014-15	26.24	38.22	31.68	1.12	0.56
	2018-19	28.92	41.28	33.70	1.34	0.57
	<i>Average</i>	<i>23.62</i>	<i>35.15</i>	<i>28.56</i>	<i>1.53</i>	<i>0.59</i>
Winter	1991-92	18.22	28.33	23.29	1.22	0.53
	1995-96	20.08	28.68	24.40	1.04	0.48
	1999-00	20.44	32.80	25.21	1.81	0.46
	2004-05	21.08	33.21	26.47	1.25	0.44
	2009-10	22.06	34.36	27.98	1.23	0.42
	2014-15	22.80	36.21	28.90	1.39	0.41
	2018-19	24.31	38.36	30.46	1.37	0.37
	<i>Average</i>	<i>21.28</i>	<i>33.14</i>	<i>26.67</i>	<i>1.33</i>	<i>0.44</i>

The mean LST of the city was increased gradually. The pre-monsoon season always creates high mean LST values (31.54°C in 1991-92, 34.64°C in 1995-96, 36.38°C in 1999-00, 38.01°C in 2004-05, 39.60°C in 2009-10, 41.28°C in 2014-15, and 43.74°C in 2018-19) (Figure 3). In the urban heat island zones, the LST-NDBaI relationship is direct or high LST areas have high NDBaI values. Moreover, at the micro-level analysis, the high peaks of LST also presented the high peaks of NDBaI. The correlation coefficient values between the LST and NDBaI are positive throughout the span. In the post-monsoon season, the best mean correlation coefficient value (0.59) is found, followed by the monsoon (0.56), pre-monsoon (0.48), and winter (0.44) seasons. Hence,

it can be concluded that wet weather produce a better LST-NDBaI relationship.

Figure 3 shows that in the summer season of 2018-19, the LST for most of the places (>90%) have >40°C. In winter, LST of the whole city is less than 40°C. A moderate LST values are noticed in the monsoon and post-monsoon seasons. The mean LST of the study area has been gradually increased between 1991-92 and 2018-19. The converted bare land and built-up area produce high LST value compared to the other LULC categories. The low LST value is found in the unchanged vegetation covered area. The moderate LST value is observed in the unchanged water bodies, wetland, or settlement with homestead orchard.

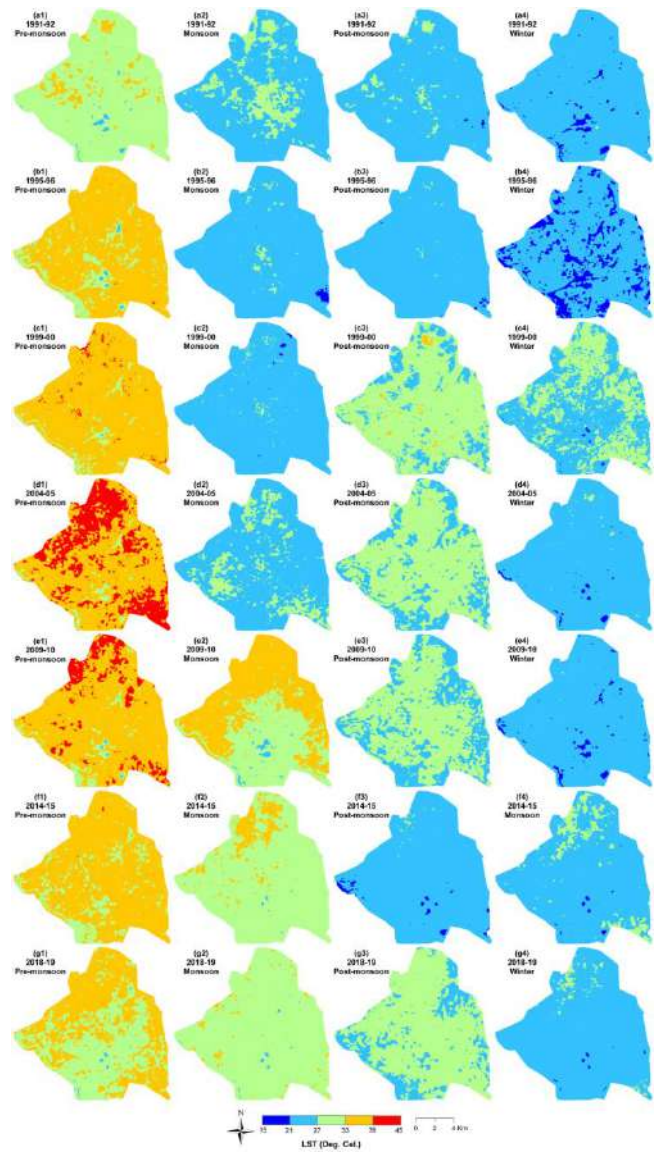


**Figure 3.** Seasonal distribution of LST: (a1,a2,a3,a4) 1991-1992; (b1,b2,b3,b4) 1995-1996; (c1,c2,c3,c4) 1999-2000; (d1,d2,d3,d4) 2004-2005; (e1,e2,e3,e4) 2009-2010; (f1,f2,f3,f4) 2014-2015; (g1,g2,g3,g4) 2018-2019.

Figure 4 shows the seasonal change in the spatial distribution of NDBaI from 1991-92 to 2018-19. The high and low NDBaI regions were seasonally stable since the 1991-92 sessions. The change was observed

only in the values of the NDBaI, not in the distributional pattern. The central part and the periphery of the city show the reverse value of the NDBaI.

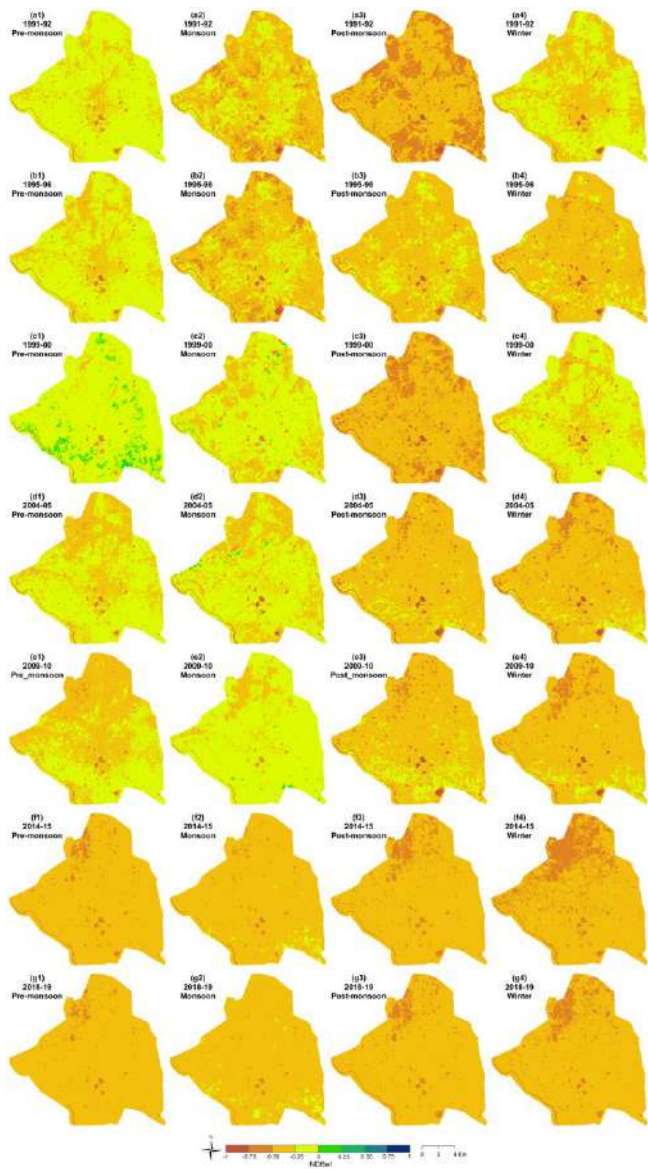


**Figure 4.** Seasonal distribution of NDBaI: (a1,a2,a3,a4) 1991-1992; (b1,b2,b3,b4) 1995-1996; (c1,c2,c3,c4) 1999-2000; (d1,d2,d3,d4) 2004-2005; (e1,e2,e3,e4) 2009-2010; (f1,f2,f3,f4) 2014-2015; (g1,g2,g3,g4) 2018-2019.

**4.3. Seasonal Variation on LST-NDBaI Relationship**

Figure 5 (a-d) shows the seasonal variation of LST-NDBaI relationships on different categories of LULC. This relationship is strongly positive on water bodies and wetland, strong to moderate positive on vegetation covered area, and moderate positive on the bare land/built-up area. The pre-monsoon season (Figure 5(a)) has a strong positive LST-NDBaI correlation on the water bodies (0.65) and a moderate positive correlation on green vegetation (0.37), bare land, and built-up area (0.35). In the monsoon season, the correlation is strongly positive on green vegetation (0.56) and water bodies (0.51), whereas it is moderate positive (0.43) on bare land and built-up area (Figure 5(b)). In the post-

monsoon season, the best correlation has been built on green vegetation (0.62), followed by the water bodies (0.53), bare land and built-up area (0.48) (Figure 5(c)). In winter (Figure 5(d)), the LST-NDBaI correlation is strongly positive on water bodies (0.62) and green vegetation (0.54), whereas it is moderate positive (0.39) on the bare lands and built-up areas.

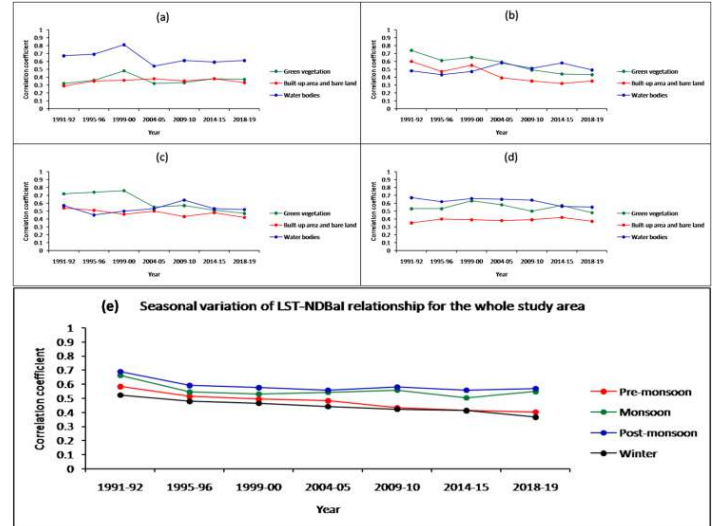


**Figure 5.** (a-d) Seasonal variation of the LST-NDBaI relationship on various categories of LULC: (a) Pre-monsoon; (b) Monsoon; (c) Post-monsoon; (d) Winter; (e) Seasonal variation of the LST-NDBaI relationship for the whole of the study area (0.05 level of significance).

Figure 5(e) represents the seasonal variation of LST-NDBaI relationships for the whole of the study area. The relationship is positive, for each season. The post-monsoon season presents the best correlation. The results also shows that the dry climate decreases the strength of the regression, while the moist climate increases the strength.

The study shows that LST builds a stable and strong to moderate positive correlation with NDBaI in Raipur City, India throughout the period. The result is comparable to the recently conducted other similar studies on the different urban agglomerations in the world. Essa et al. (2012) have shown that NDBaI generates a positive correlation (0.39) with LST in the Greater Dublin region, Ireland. A study conducted in Kunming of China shows that NDBaI and LST generate strong positive correlation (Chen and Zhang 2017). A weak positive correlation between LST and NDBaI has been presented in London (0.086) and Baghdad (0.469) by Ali et al. (2017). This relationship was also positive (0.458) in Kolkata Metropolitan Area, India (Nimish et al. 2020). The LST and NDBaI have built a weak negative correlation (-0.11) in Guangzhou, China (Guo et al. 2015). This correlation was weak positive (0.06) in Harare Metropolitan City, Zimbabwe (Mushore et al. 2017). Sharma and Joshi (2016) have shown the moderate positive nature of LSI-NDBaI correlation in the National Capital Region of India. The present study shows that the average correlation coefficient between LST and NDBaI of all the four seasons from 1991-92 to 2018-19 is moderate positive (0.052), which can be

considered as a very stable and authentic relationship between the two variables.

The present study is useful for the urban and environmental planning. The bare or fallow lands can be converted into road vegetation, park, wetland, or water bodies to resist the increasing rate of LST, at least to some extent.

## 5. CONCLUSION

The present study deals with the seasonal estimation of the relation between NDBaI and LST in Raipur City. It is seen that LST is directly correlated to NDBaI for all the seasons. This relationship varies in accordance with the variation of LULC. This correlation remains strong on the water bodies, irrespective of any season. On green vegetation, this correlation is moderate in pre-monsoon season and strong in the other three seasons. The barren land and settlement produce a moderate correlation for all the four seasons. Among the four seasons, the post-monsoon season builds the best LST-NDBaI correlation for all LULC types, whereas the pre-monsoon season has the least correlation. Among the various LULC categories, the water bodies present the best positive LST-NDBaI correlation, irrespective to any season. The high ratio of green plants and water surface can enhance the ecological health. Thus, this research work can be beneficial for the environmental planners. It is also suitable for the land use scientist and geographers. The study can be further expanded by the remote sensing scientist by apply the same methods on other satellite sensors and for different physical environment.

## ACKNOWLEDGEMENT

The author is indebted to the United States Geological Survey (URL-3).

## REFERENCES

Ahmed B, Kamruzzaman M, Zhu X, Rahman M S & Choi K (2013). Simulating Land Cover Changes and Their Impacts on Land Surface Temperature in Dhaka, Bangladesh. *Remote Sensing*, 5(11), 5969-5998. <https://doi.org/10.3390/rs5115969>

Alexander C (2020). Normalised difference spectral indices and urban land cover as indicators of land surface temperature (LST). *International Journal of Applied Earth Observation and Geoinformation*, 86, 102013. <https://doi.org/10.1016/j.jag.2019.102013>

Alibakhshi Z, Ahmadi M& Farajzadeh Asl M (2020). Modeling Biophysical Variables and Land Surface Temperature Using the GWR Model: Case Study— Tehran and Its Satellite Cities. *Journal of Indian Society of Remote Sensing*,48, 59-70. <https://doi.org/10.1007/s12524-019-01062-x>

Ali J M, Marsh S H& Smith M J (2017). A comparison between London and Baghdad surface urban heat islands and possible engineering mitigation solutions. *Sustainable Cities and Society*, 29, 159-168. <https://doi.org/10.1016/j.scs.2016.12.010>

As-syakur A R, Adnyana I W S, Arthana I W & Nuarsa I W (2012). Enhanced Built-Up and Bareness Index

(EBBI) for Mapping Built-Up and Bare Land in an Urban Area. *Remote Sensing*, 4(10), 2957-2970. <https://doi.org/10.3390/rs4102957>

Barsi J, Schott J, Hook S, Raqueno N, Markham B& Radocinski R (2014). Landsat-8 thermal infrared sensor (TIRS) vicarious radiometric calibration. *Remote Sensing*, 6(11), 11607-11626.

Carlson T N& Ripley D A (1997). On the Relation between NDVI, Fractional Vegetation Cover, and Leaf Area Index. *Remote Sensing of Environment*, 62, 241-252. [https://doi.org/10.1016/S0034-4257\(97\)00104-1](https://doi.org/10.1016/S0034-4257(97)00104-1)

Chen X L, Zhao H M, Li P X& Yi Z Y (2006). Remote sensing image-based analysis of the relationship between urban heat island and land use/cover changes. *Remote Sensing of Environment*, 104(2), 133-146. <https://doi.org/10.1016/j.rse.2005.11.016>

Chen X& Zhang Y (2017). Impacts of urban surface characteristics on spatiotemporal pattern of land surface temperature in Kunming of China. *Sustainable Cities and Society*, 32, 87-99. <https://doi.org/10.1016/j.scs.2017.03.013>

Essa W, Verbeiren B, Van der Kwast J, Van de Voorde T& Batelaan O (2012). Evaluation of the DisTrad thermal sharpening methodology for urban areas. *International Journal of Applied Earth Observation and Geoinformation*, 19, 163-172. <https://doi.org/10.1016/j.jag.2012.05.010>

Guha S, Govil H, Dey A & Gill N (2020a). A case study on the relationship between land surface temperature and land surface indices in Raipur City, India. *Geografisk Tidsskrift-Danish Journal of Geography*, 120(1), 35-50. <https://doi.org/10.1080/00167223.2020.1752272>

Guha S, Govil H, Gill N & Dey A (2020b). Analytical study on the relationship between land surface temperature and land use/land cover indices. *Annals of GIS*, 26(2), 201-216. <https://doi.org/10.1080/19475683.2020.1754291>

Guha S, Govil H & Mukherjee S (2017). Dynamic analysis and ecological evaluation of urban heat islands in Raipur city, India. *Journal of Applied Remote Sensing*, 11(3), 036020. <https://doi.org/10.1117/1.JRS.11.036020>

Guo G, Wu Z& Chen Y (2014). Estimation of subpixel land surface temperature using Landsat TM imagery: A case examination over a heterogeneous urban area. *Third International Workshop on Earth Observation and Remote Sensing Applications (EORSA)*, Changsha, p. 304-308. <https://doi.org/10.1109/EORSA.2014.6927900>

Guo G, Wu Z, Xiao R, Chen Y, Liu X& Zhang X (2015). Impacts of urban biophysical composition on land surface temperature in urban heat island clusters. *Landscape and Urban Planning*, 135, 1-10. <https://doi.org/10.1016/j.landurbplan.2014.11.007>

Hao X, Li W& Deng H (2016). The oasis effect and summer temperature rise in arid regions-case study in Tarim Basin. *Scientific Reports*, 6, 35418. <https://doi.org/10.1038/srep35418>

Jain S, Sannigrahi S, Sen S, Bhatt S, Chakraborti S& Rahmat S (2020). Urban heat island intensity and its mitigation strategies in the fast-growing urban area.

- Journal of Urban Management, 9(1), 54-66.  
<https://doi.org/10.1016/j.jum.2019.09.004>
- Li J (2006). Estimating land surface temperature from Landsat-5 TM. *Remote Sensing Technology and Application*, 21, 322-326.
- Li Z N, Duan S B, Tang B H, Wu H, Ren H G & Yan G J (2016). Review of methods for land surface temperature derived from thermal infrared remotely sensed data. *Journal of Remote Sensing*, 20, 899-920.
- Macarof P, Bîrlica I C & Stătescu F (2017). Investigating the relationship between land surface temperature and urban indices using landsat-8: a case study of Iași. *Lucrările Seminarului Geografic Dimitrie Cantemir*, 45, 81-88.  
<https://doi.org/10.15551/lsgdc.v45i0.07>
- Mushore T D, Odindi J, Dube T & Mutanga O (2017). Prediction of future urban surface temperatures using medium resolution satellite data in Harare metropolitan city, Zimbabwe. *Building and Environment*, 122, 397-410.  
<https://doi.org/10.1016/j.buildenv.2017.06.033>
- Nimish G, Bharath H A & Lalitha A (2020). Exploring temperature indices by deriving relationship between land surface temperature and urban landscape. *Remote Sensing Application: Society and Environment*, 18, 100299.  
<https://doi.org/10.1016/j.rsase.2020.100299>
- Qin Z, Karnieli A & Barliner P (2001). A Mono-Window Algorithm for Retrieving Land Surface Temperature from Landsat TM Data and Its Application to the Israel-Egypt Border Region. *International Journal of Remote Sensing*, 22(18), 3719-3746.  
<https://doi:10.1080/01431160010006971>
- Sekertekin A, Kutoglu SH & Kaya S (2016). Evaluation of spatio-temporal variability in Land Surface Temperature: A case study of Zonguldak, Turkey. *Environmental Monitoring and Assessment*, 188, 30.  
<https://doi.org/10.1007/s10661-015-5032-2>
- Sharma R, Ghosh A & Joshi P K (2013). Mapping environmental impacts of rapid urbanization in the National Capital Region of India using remote sensing inputs. *Geocarto International*, 28(5), 420-438.  
<https://doi.org/10.1080/10106049.2012.715208>
- Sharma R & Joshi P K (2016). Mapping environmental impacts of rapid urbanization in the National Capital Region of India using remote sensing inputs. *Urban Climate*, 15, 70-82.  
<https://doi.org/10.1016/j.uclim.2016.01.004>
- Sobrino J A, Raissouni N & Li Z (2001). A comparative study of land surface emissivity retrieval from NOAA data. *Remote Sensing of Environment*, 75(2), 256-266.  
[https://doi.org/10.1016/S0034-4257\(00\)00171-1](https://doi.org/10.1016/S0034-4257(00)00171-1)
- Sobrino J A, Jimenez-Munoz J C & Paolini L (2004). Land surface temperature retrieval from Landsat TM5. *Remote Sensing of Environment*, 9, 434-440.  
<https://doi:10.1016/j.rse.2004.02.003>
- Sun Q, Tan J & Xu Y (2010). An ERDAS image processing method for retrieving LST and describing urban heat evolution: A case study in the Pearl River Delta Region in South China. *Environmental Earth Science*, 59, 1047-1055.
- Tomlinson C J, Chapman L, Trones J E & Baker C (2011). Remote sensing land surface temperature for meteorology and climatology: a review. *Meteorological Application*, 118, 296-306.  
<https://doi.org/10.1002/met.287>
- URL-1: <http://www.surveyofindia.gov.in>  
 URL-2: <http://www.raipur.gov.in>  
 URL-3: <https://www.earthexplorer.usgs.gov>  
 URL-4: <http://www.imdraipur.gov.in>
- Vlassova L, Perez-Cabello F, Nieto H, Martín P, Riaño D, & De La Riva J (2014). Assessment of methods for land surface temperature retrieval from Landsat-5 TM images applicable to multiscale tree-grass ecosystem modeling. *Remote Sensing*, 6(5), 4345-4368.
- Wukelic G E, Gibbons D E, Martucci L M & Foote H P (1989). Radiometric calibration of Landsat Thematic Mapper thermal band. *Remote Sensing of Environment*, 28, 339-347.  
[https://doi.org/10.1016/0034-4257\(89\)90125-9](https://doi.org/10.1016/0034-4257(89)90125-9)
- Yang J & Que J (1996). The empirical expressions of the relation between precipitable water and ground water vapor pressure for some areas in China. *Scientia Atmospherica Sinica*, 20, 620-626.
- Zanter K (2019). *Landsat 8 (L8) Data Users Handbook*; EROS: Sioux Falls, SD, USA.
- Zhao H M & Chen X L (2005). Use of normalized difference bareness index in quickly mapping bare areas from TM/ETM+. *Geoscience and Remote Sensing Symposium*. 3 (25-29), p.1666-1668.  
<https://doi.org/10.1109/IGARSS.2005.1526319>



© Author(s) 2021.

This work is distributed under <https://creativecommons.org/licenses/by-sa/4.0/>





## Source details

[Feedback >](#) [Compare sources >](#)

### International Journal of Engineering and Geosciences

Scopus coverage years: from 2019 to Present

Publisher: Murat Yakar

E-ISSN: 2548-0960

Subject area: Environmental Science: Environmental Science (miscellaneous)

Source type: Journal

[View all documents >](#)

[Set document alert](#)

[Save to source list](#)

SJR



SNIP





# A long-term monthly assessment of land surface temperature and normalized difference vegetation index using Landsat data

*Uma avaliação mensal de longo prazo da temperatura da superfície da terra e índice de vegetação de diferença normalizada usando dados Landsat*

Subhanil Guha<sup>[a]</sup> 

<sup>[a]</sup> National Institute of Technology Raipur, Department of Applied Geology, Raipur, India

**How to cite:** Guha, S. (2021). A long-term monthly assessment of land surface temperature and normalized difference vegetation index using Landsat data. *urbe. Revista Brasileira de Gestão Urbana*, v.13, e20200345. <https://doi.org/10.1590/2175-3369.013.e20200345>

## Abstract

The present study assesses the monthly variation of land surface temperature (LST) and the relationship between LST and normalized difference vegetation index (NDVI) in Raipur City of India using one hundred and eighteen Landsat images from 1988 to 2019. The results show that a monthly variation is observed in the mean LST. The highest mean LST is found in April (38.79°C), followed by May (36.64°C), June (34.56°C), and March (32.11°C). The lowest mean LST is observed in January (23.01°C), followed by December (23.76°C), and November (25.83°C). A moderate range of mean LST is noticed in September (27.18°C), October (27.22°C), and February (27.88°C). Pearson's linear correlation method is used to correlate LST with NDVI. The LST-NDVI correlation is strong negative in October (-0.62), September (-0.55), and April (-0.51). The moderate negative correlation is developed in March (-0.40), May (-0.44), June (-0.47), and November (-0.39). A weak negative correlation is observed in December (-0.21), January (-0.24), and February (-0.29). The change in weather elements and variation in land surface characteristics contribute to the monthly fluctuation of mean LST and LST-NDVI correlation. The study will be an effective one for the town and country planners for their future estimation of land conversion.

**Keywords:** Landsat. Land surface. Land surface temperature. Normalized difference vegetation index. Raipur.

## Resumo

*O presente estudo avalia a variação mensal da temperatura da superfície terrestre (LST) e a relação entre LST e o índice de vegetação de diferença normalizado (NDVI) na cidade de Raipur, na Índia, utilizando cento e dezoito imagens landsat de 1988 a 2019. Os resultados mostram que uma variação mensal é observada no LST médio. O LST médio mais elevado é encontrado em abril (38,79oC), seguido por maio (36.64oC), junho (34.56oC) e março (32.11oC). O LST médio mais baixo é observado em janeiro (23.01oC), seguido por dezembro (23.76oC) e novembro (25,83oC). Uma gama moderada de LST médio é notada em setembro (27.18oC), outubro (27.22oC) e fevereiro (27.88oC). O método linear de correlação de Pearson é usado para correlacionar LST com NDVI. A correlação LST-NDVI é fortemente negativa em outubro (-0,62), setembro (-0,55) e abril (-0,51). A correlação negativa moderada é desenvolvida em março (-0,40), maio (-0,44), junho (-0,47) e novembro (-0,39). Uma correlação negativa fraca é observada em dezembro (-0,21), janeiro (-0,24) e fevereiro (-0,29). A alteração dos elementos meteorológicos e a variação das características da superfície terrestre contribuem para a flutuação mensal da correlação média LST e LST-NDVI. O estudo será eficaz para os planejadores da cidade e do país para a sua futura estimativa da conversão de terras.*

**Palavras-chave:** Landsat. Superfície de terra. Temperatura da superfície do terreno. Índice de vegetação de diferença normalizado. O Raipur.

## Introduction

The thermal infrared (TIR) region of the electromagnetic spectrum has a huge potential in determining the nature and characteristics of land surface dynamics in any natural environment along with the visible and near-infrared (VNIR) and shortwave infrared (SWIR) regions (Chen et al., 2006; Ghobadi et al., 2014; Guha et al., 2018; Guha & Govil, 2020; Guha & Govil, 2021a; Guha & Govil, 2019; Alexander, 2020). Land surface temperature (LST) is a major factor to assess the biogeochemical actions in the formation of land surface materials and it is the most essential parameter to evaluate the ecological condition of rural or urban areas (Tomlinson et al., 2011; Hao et al., 2016). LST varies with the changes of tone, texture, pattern, and association of the land surface types in any region (Hou et al., 2010). Generally, green vegetation and water bodies present low LST, whereas a built-up area, bare rock surface, or dry soil reflects high LST (Guha et al., 2019). Thus, LST-related studies are very important in urban and land use planning and development (Li et al., 2017; Guha, Govil & Besoya, 2020; Guha, Govil, Gill & Dey, 2020a). Urban heat islands and urban hot spots are very common term in an urban environment and are indicated by the zone of very high LST inside the urban bodies (Guha et al., 2017). The most popular spectral index is the normalized difference vegetation index (NDVI) which is used in extracting green vegetation (Yuan et al., 2017; Guha & Govil, 2021b; Mondal et al., 2011; Guha, 2016; Guha, Govil, Gill & Dey, 2020b; Guha, Govil, Dey et al., 2020; Guha, Govil, Gill & Dey, 2020c; Guha, Govil & Diwan, 2020). NDVI is directly used in the determination of land surface emissivity and thus is a significant factor for LST estimation (Sobrino et al., 2004; Carlson & Ripley, 1997).

Currently, the relationship between LST and NDVI was constructed using thermal infrared remote sensing technology and only some satellite sensors have the thermal bands like Landsat, MODIS, and ASTER (Wen et al., 2017; Guha et al., 2017). The required wavelength of these thermal bands is 8-14  $\mu\text{m}$  for LST determination. An infrared thermometer instrument is used to validate the derived LST values (Li et al., 2017; Guha, Govil & Besoya, 2020; Guha, Govil, Gill & Dey, 2020a; Guha et al., 2017). LST-NDVI relationship was applied in most of the thermal remote sensing studies that were conducted with temporal discrete data sets on the urban environment, e.g., Tokyo, Melbourne, Shiraz, Raipur (Shigeto, 1994; Jamei et al., 2019; Fatemi & Narangifard, 2019; Guha & Govil, 2021c). Ferelli et al. (2018) correlate LST with NDVI in Monte Hermoso of Argentina. Fewer studies are available on the long-term and continuous seasonal correlation among LST, NDVI, and LULC in a tropical city.

A reverse relationship is built between LST and the concentration of green vegetation and thus, NDVI is used as an important factor for determining LST in most of the LST retrieval methods (Voogt & Oke, 2003; Gutman & Ignatov, 1998; Goward et al., 2002; Govil et al., 2019; Guha, 2021; Govil et al., 2020).

There are so many valuable research articles found on LST-NDVI relationships that were conducted mainly in the Chinese landscape (Gui et al., 2019; Qu et al., 2020; Qu et al., 2018; Cui, Wang, Qu, Singh, Lai, Jiang & Yao, 2019; Cui, Wang, Qu, Singh, Lai & Yao, 2019; Yao, Cao et al., 2019; Yao, Wang, Gui et al., 2017; Yao, Wang, Huang, Chen et al., 2018; Yao, Wang et al., 2019; Yao, Wang, Huang et al., 2017; Yao, Wang, Huang, Zhang et al., 2018; Yuan et al., 2020). Some recent studies successfully analyze the LST-NDVI correlation in some tropical Indian cities (Kikon et al., 2016; Kumar & Shekhar, 2015; Mathew et al., 2018; Mathew et al., 2017; Sannigrahi et al., 2018; Singh et al., 2017). The nature of LST and NDVI varies due to the seasonal change of evaporation, precipitation, moisture content, air temperature, etc. But, time-series analysis of the monthly variation in the LST-NDVI relationship in a tropical Indian city is rare.

It is a necessary task to build a month-wise LST-NDVI correlation for the sustainable development of town and country planning. Thus, to determine the characteristic features of monthly variation of LST-NDVI correlation, Raipur City of India was selected as it is not under any kind of extreme climatic condition and it is a smart city with a rapid land conversion. Generally, the LST-NDVI correlation is negative on the tropical cities of similar environmental conditions of Raipur. But, the strength of the LST-NDVI relationship can change temporally, seasonally, and spatially. The relationship is changed with time as the land surface materials change with time. Elevation and slope are two main physiographic influencing factors that generate a negative correlation with LST. Wind speed and humidity are two climatic factors that create a negative relationship with LST. The relationship also depends on the LULC types as vegetation, soil, water, or built-up area change the values of NDVI as well as LST. Different seasons also play a significant role in the LST-NDVI relationship as the growth of vegetation and increase of LST primarily depend on seasonal change. But, no specific conclusion can draw between LST and NDVI by using a small number of remotely sensed data or within a short duration of research. A strong conclusion on the LST-NDVI relationship can be drawn only after the analyses of the multi-temporal and multi-seasonal data sets for a long-term continuous timeframe. Thus, large Landsat data sets are necessary to obtain a reliable result on this relationship. The present study analyzes the nature, strength, and trend of the effect of LST on NDVI and the LST-NDVI correlation on different types of LULC and their seasonal variation from 1988 to 2019. Thus, the new direction of the study is the long-term monthly change of LST-NDVI correlation analysis using the time-series data of Landsat sensors. The objective of the current research is to analyze the response of mean LST and LST-NDVI correlation in different months.

## **Study area and data**

Figure 1 shows the research place (Raipur City of India) of the present research work. Figure 1(a) presents the outline map of India where Chhattisgarh State is located in the middle part (Source: Survey of India). Figure 1(b) presents the outline map of Chhattisgarh State with districts (Source: Survey of India). Figure 1(c) represents the false colour composite (FCC) image of Raipur City from recent Landsat 8 data (Date: 7 November 2018) where blue, green, and red bands of the image are filtered by the green, red, and infrared bands, respectively. False colour composite images are the combination of bands other than visible red, green, and blue as the red, green, and blue components of the display. These images are useful to allow us to distinguish various types of land surface materials that are difficult to identify by the naked eye or true colour composite image. Figure 1(d) indicates the contour map (Date: 11 October 2011) of the city from Advanced Spaceborne Thermal Emission and Reflection Radiometer (ASTER) Digital Elevation Model (DEM) data (Source: USGS). The city extends from 21°11'22"N to 21°20'02"N and from 81°32'20"E to 81°41'50"E. The total area of the city is approximately 164.23 km<sup>2</sup>. The only big river in the area is Mahanadi. The south of the city is covered by dense forests. Geologically the city is very stable and no such major geological hazards are seen in the area. The central

part of the city has a higher elevation compared to the periphery area. According to India Meteorological Department (IMD), Raipur is under the savannah type of climate. Table 1 presents the climatic data of Raipur from 1981-2012 (Source: IMD). May is the hottest month followed by April, June, and March. July is the rainiest month followed by August, June, and September. October and November are the post-monsoon months that experience pleasant weather conditions. December (the coldest month), January, and February are the winter months. The pre-monsoon and winter months (including November) remain dry compared to the monsoon and post-monsoon months.

**Table 1** –Climate data for Raipur City (1981–2012)

Weather Elements	January	February	March	April	May	June	July	August	September	October	November	December
Maximum Temp (°C)	31.5	34.8	39.8	43.2	45.2	44.4	36.1	33.7	34.4	37.7	32.5	30.8
Minimum Temp (°C)	8.6	11.3	15.7	19.7	22.2	21.6	21.2	21.7	21.3	16.8	11.6	8.9
Mean Temp (°C)	20.7	23.4	28.9	32.3	34.7	31.7	27.8	27.2	27.8	27.6	23.1	20.3
Mean Monthly Rainfall (mm)	13.7	13.4	11.9	8.9	30.3	221.1	326.9	299.9	200.5	50.4	9.8	6.6
Average Relative Humidity (%)	47	35	28	22	27	52	76	79	73	59	51	49

Source: IMD (2020).

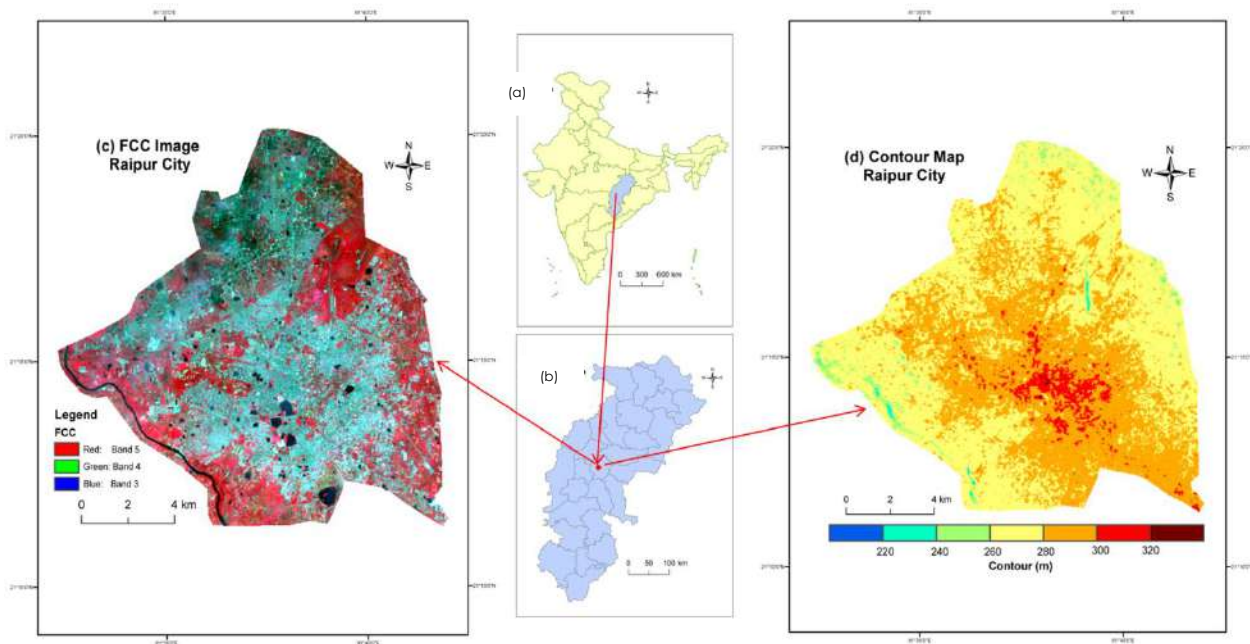


**Figure 1** – Location of the study area (a) India (b) Chhattisgarh (c) FCC image of Raipur (d) Contour Map of Raipur showing the contours of 220 m, 240 m, 260 m, 280 m, 300 m, and 320 m. Source: Authors (2020).

Table 2 shows the resolution and wavelength information visible to near-infrared (VNIR) bands, shortwave infrared (SWIR) bands, and thermal infrared (TIR) bands of different types of Landsat satellite sensors.

**Table 2** – Band and wavelength information about various types of Landsat sensors

Landsat 5 TM			Landsat 7 ETM+			Landsat 8 OLI/TIRS		
Bands	Wavelength (µm)	Resolution (m)	Bands	Wavelength (µm)	Resolution (m)	Bands	Wavelength (µm)	Resolution (m)
Band1-Blue	0.45-0.52	30	Band1-Blue	0.45-0.52	30	Band1-Ultra Blue	0.435-0.451	30
Band2-Green	0.52-0.60	30	Band2-Green	0.52-0.60	30	Band2-Blue	0.452-0.512	30
Band3-Red	0.63-0.69	30	Band3-Red	0.63-0.69	30	Band3-Green	0.533-0.590	30
Band4-NIR	0.76-0.90	30	Band4-NIR	0.77-0.90	30	Band4-Red	0.636-0.673	30
Band5-SWIR1	1.55-1.75	30	Band5-SWIR1	1.55-1.75	30	Band5-NIR	0.851-0.879	30
Band6-TIR	10.40-12.50	120*(30)	Band6-TIR	10.40-12.50	60**(30)	Band6-SWIR1	1.566-1.651	30
Band7-SWIR2	2.08-2.35	30	Band7-SWIR2	2.09-2.35	30	Band7-SWIR2	2.107-2.294	30
			Band8-Pan	0.52-0.90	15	Band8-Pan	0.503-0.676	15
						Band9-Cirrus	1.363-1.384	30
						Band10-TIR1	10.60-11.19	100***(30)
						Band11-TIR2	11.50-12.51	100***(30)

Note: \*TM band 6 was acquired at 120 m resolution, but products are resampled by USGS to 30 m pixels. \*\*ETM+ band 6 is acquired at 60 m resolution, but products are resampled by USGS to 30 m pixels. \*\*\*TIRS bands 10 and 11 are acquired at 100 m resolution, but products are resampled by USGS to 30 m pixels. Source: USGS.

One hundred and eighteen available cloud-free Landsat TM, ETM+, and OLI/TIRS data from 1988 to 2019 were freely downloaded from the USGS Data Centre (Table 2) to conduct the whole study. OLI/TIRS dataset has two TIR bands (bands 10 and 11). This large dataset was prepared by taking eleven data from January, fifteen from February, thirteen from March, ten from April, seventeen from May, four from June, four from September, thirteen from October, fifteen from November, and sixteen from December. There are very few cloud-free data sets available in the wet season (June-September), and this phenomenon could have an impact on the result of the retrieved LST. These Landsat data sets passed over the Raipur City every day between 10:00 AM to 10:30 AM. Hence, there is a scope to retrieve the LST of the study area at a specific time every day. The TIR band 10 data (100 m resolution) was applied for the current research due to better-calibrated certainty (Guha et al., 2018). The TIR band 10 data was resampled to 30 m x 30 m pixel size by the USGS data centre. TM data has only one TIR band (band 6) of 120 m resolution that was also resampled to 30 m x 30 m pixel size by the USGS data centre. ETM+ data has a TIR band (band 6) of 60 m resolution, and it was again resampled to 30 m x 30 m pixel size by the USGS data centre. The spatial resolution of the VNIR bands of the three types of Landsat sensors is 30 m.

Table 3 – Specification of TM, ETM+, and OLI/TIRS data used in the present study

Landsat scene ID	Date of acquisition	Time (UTC)	Path/Row	Sun elevation (°)	Sun azimuth (°)	Cloud cover (%)	Earth-Sun distance (astronomical unit)	Resolution of VNIR bands (m)	Resolution of TIR bands (m)
LT51420451988021BKT00	21-Jan-88	04:25:17	142/044	36.59	139.02	0.00	0.98	30	120
LT51420451990010BKT02	10-Jan-90	04:18:43	142/044	34.63	139.85	0.00	0.98	30	120
LT51420451992016ISPO0	16-Jan-92	04:20:22	142/044	35.26	139.03	3.00	0.98	30	120
LT51420451993018ISPO0	18-Jan-93	04:17:47	142/044	35.14	137.86	0.00	0.98	30	120
LT51420451996027ISPO0	27-Jan-96	04:00:14	142/044	33.31	132.27	0.00	0.98	30	120
LT51420452005019BKT00	19-Jan-05	04:42:17	142/044	38.92	143.21	0.00	0.98	30	120
LT51420452007025BKT00	25-Jan-06	04:51:03	142/044	40.86	143.96	0.00	0.98	30	120
LT51420452009014BKT01	14-Jan-09	04:41:09	142/044	38.24	144.11	0.00	0.98	30	120
LT51420452011020BKT00	20-Jan-11	04:46:03	142/044	39.52	144.02	0.00	0.98	30	120
LC81420452015015LGN01	15-Jan-15	04:56:09	142/044	40.22	147.71	0.01	0.98	30	100
LC81420452018023LGN00	23-Jan-18	04:56:05	142/044	41.34	145.80	0.14	0.98	30	100
LT51420451989055BKT00	24-Feb-89	04:25:59	142/044	43.93	128.98	0.00	0.98	30	120
LT51420451990042BKT00	11-Feb-90	04:17:45	142/044	39.09	131.39	0.00	0.98	30	120
LT51420451991045ISPO0	14-Feb-91	04:16:55	142/044	39.64	130.41	0.00	0.98	30	120
LT51420451992048ISPO0	17-Feb-92	04:20:15	142/044	40.89	130.26	4.00	0.98	30	120
LT51420451993050BKT00	19-Feb-93	04:18:04	142/044	41.21	128.89	0.00	0.98	30	120
LE71420452002051BKT00	20-Feb-02	04:44:56	142/044	46.09	135.11	0.00	0.98	30	60
LT51420452004049BKT00	18-Feb-04	04:35:03	142/044	43.76	133.39	0.00	0.98	30	120
LT51420452006054BKT00	23-Feb-06	04:46:49	142/044	47.31	134.66	0.00	0.98	30	120
LT51420452009046KHC01	15-Feb-09	04:41:59	142/044	44.35	135.85	0.00	0.98	30	120
LT51420452010049KHC00	18-Feb-10	04:47:02	142/044	45.89	136.27	7.00	0.98	30	120
LC81420452015047LGN01	16-Feb-15	04:55:55	142/044	46.67	139.41	0.01	0.98	30	100
LC81420452016050LGN01	19-Feb-16	04:56:00	142/044	47.48	138.61	0.10	0.98	30	100
LC81420452017052LGN00	21-Feb-17	04:56:01	142/044	48.28	137.76	0.00	0.98	30	100
LC81420452018055LGN00	24-Feb-18	04:55:51	142/044	49.09	136.84	0.07	0.98	30	100
LC81420452019042LGN00	11-Feb-19	04:55:52	142/044	45.33	140.84	0.00	0.98	30	100
LT51420451989071BKT00	12-Mar-89	04:25:33	142/044	48.55	123.00	0.00	0.99	30	120
LT51420451990074BKT02	15-Mar-90	04:16:41	142/044	47.52	119.81	0.00	0.99	30	120
LT51420451991077ISPO0	18-Mar-91	04:17:34	142/044	48.58	118.92	0.00	0.99	30	120
LT51420451992080ISPO0	20-Mar-91	04:20:18	142/044	49.87	118.28	0.00	0.99	30	120
LE71420452003070SGS01	11-Mar-03	04:44:52	142/044	51.76	128.43	4.00	0.99	30	60
LT51420452004081BKT00	21-Mar-04	04:35:14	142/044	53.26	121.40	0.00	0.99	30	120
LT51420452007073BKT00	14-Mar-07	04:51:04	142/044	53.78	128.95	2.00	0.99	30	120
LT51420452009078KHC00	19-Mar-09	04:42:44	142/044	54.10	124.40	2.00	0.99	30	120
LC81420452014076LGN01	17-Mar-14	04:56:36	142/044	55.95	129.38	0.00	0.99	30	100
LC81420452015079LGN01	20-Mar-15	04:55:41	142/044	56.69	127.93	0.02	0.99	30	100
LC81420452016082LGN01	22-Mar-16	04:55:53	142/044	57.61	126.77	0.00	0.99	30	100
LC81420452017084LGN00	25-Mar-17	04:55:44	142/044	58.46	125.46	0.00	0.99	30	100
LC81420452018071LGN00	12-Mar-18	04:55:43	142/044	54.19	131.16	2.10	0.99	30	100
LT51420451992112BKT00	21-Apr-92	04:20:02	142/044	57.53	102.14	0.00	1.00	30	120
LT51420451995104ISPO1	14-Apr-95	04:05:06	142/044	52.75	103.75	0.00	1.00	30	120
LE71420452001112SGS00	22-Apr-01	04:46:12	142/044	63.60	106.77	0.00	1.00	30	60
LE71420452002115SGS01	25-Apr-02	04:44:53	142/044	63.79	104.70	0.00	1.00	30	60
LE71420452003102BKT00	12-Apr-03	04:44:52	142/044	61.11	112.94	0.00	1.00	30	60
LT51420452004113BKT00	22-Apr-04	04:36:01	142/044	61.43	104.47	1.00	1.00	30	120
LT51420452009110BKT00	20-Apr-09	04:43:24	142/044	62.67	107.39	0.00	1.00	30	120
LT51420452010113KHC00	23-Apr-10	04:46:58	142/044	63.95	106.44	0.00	1.00	30	120
LC81420452016114LGN01	23-Apr-16	04:55:38	142/044	65.99	108.18	0.00	1.00	30	100
LC81420452017084LGN00	10-Apr-17	04:55:44	142/044	58.46	125.46	0.00	0.99	30	100
LT51420451991141ISPO0	21-May-91	04:18:39	142/044	59.92	87.09	1.00	1.01	30	120
LE71420452002131SGS00	11-May-02	04:44:54	142/044	65.61	94.50	5.00	1.00	30	60
LT51420452004145BKT00	24-May-04	04:36:54	142/044	64.25	86.72	0.00	1.00	30	120
LT51420452005131BKT00	11-May-05	04:43:22	142/044	65.34	94.16	0.00	1.00	30	120
LT51420452006134BKT00	14-May-06	04:48:12	142/044	66.63	93.11	6.00	1.01	30	120
LT51420452007137BKT00	17-May-07	04:50:37	142/044	67.20	91.75	0.00	1.01	30	120
LT51420452008140BKT01	19-May-08	04:44:32	142/044	65.93	89.64	0.00	1.01	30	120
LT51420452009142KHC00	22-May-09	04:44:00	142/044	65.88	88.22	1.00	1.00	30	120
LT51420452010145BKT01	25-May-10	04:46:51	142/044	66.53	87.12	0.00	1.00	30	120
LT51420452011132KHC00	12-May-11	04:45:42	142/044	65.90	94.11	0.00	1.00	30	120
LC81420452013137LGN02	13-May-13	04:58:06	142/044	69.04	92.30	2.54	1.01	30	100
LC81420452014140LGN01	20-May-14	04:55:38	142/044	68.56	90.40	5.46	1.01	30	100
LC81420452015143LGN01	23-May-15	04:55:10	142/044	68.48	88.84	9.84	1.01	30	100
LC81420452016146LGN01	25-May-16	04:55:44	142/044	68.61	87.48	0.26	1.01	30	100
LC81420452017132LGN00	12-May-17	04:55:30	142/044	68.25	95.17	0.28	1.01	30	100
LC81420452018135LGN00	15-May-18	04:55:08	142/044	68.27	93.32	0.30	1.01	30	100
LC81420452019138LGN00	18-May-19	04:55:43	142/044	68.51	91.70	0.00	1.01	30	100
LT51420452005163BKT00	12-Jun-05	04:43:39	142/044	65.27	81.43	0.00	1.00	30	120
LT51420452006166BKT00	15-Jun-06	04:48:42	142/044	66.32	81.13	4.00	1.01	30	120
LT51420452009174KHC00	23-Jun-09	04:44:35	142/044	64.96	80.76	0.00	1.00	30	120
LC81420452018167LGN00	16-Jun-18	04:55:01	142/044	67.74	81.10	2.31	1.01	30	100
LT51420451996267ISPO0	23-Sep-96	04:14:16	142/044	51.81	120.64	2.00	1.00	30	120
LT51420452001264SGI00	21-Sep-01	04:36:11	142/044	56.36	125.04	1.00	1.00	30	120
LE71420452002259SGS00	16-Sep-02	04:43:55	142/044	58.78	123.87	1.00	1.00	30	60
LC81420452014268LGN01	25-Sep-14	04:56:11	142/044	59.21	134.18	0.81	1.00	30	100
LT51420451988293BKT00	19-Oct-88	04:26:40	142/044	48.50	137.09	4.00	0.99	30	120
LT51420451991285BKT02	12-Oct-91	04:20:12	142/044	42.22	131.85	6.00	0.99	30	120
LT51420451992288BKT00	14-Oct-92	04:17:37	142/044	48.16	132.43	0.00	0.99	30	120
LT51420451996299ISPO0	25-Oct-96	04:15:55	142/044	45.37	136.48	5.00	0.99	30	120
LE71420452001288SGS00	15-Oct-01	04:44:20	142/044	52.23	140.69	6.00	0.99	30	60
LT51420452001296SGI00	23-Oct-01	04:35:57	142/044	48.90	141.22	0.00	0.99	30	120
LT51420452004289BKT00	15-Oct-04	04:40:36	142/044	51.63	139.65	4.00	0.99	30	120
LT51420452006294BKT01	21-Oct-06	04:50:19	142/044	51.50	144.97	0.00	0.99	30	120
LT51420452009286KHC00	13-Oct-09	04:46:12	142/044	53.04	140.48	0.00	0.99	30	120
LT51420452011292KHC00	19-Oct-11	04:44:07	142/044	51.29	142.15	1.00	0.99	30	120
LC81420452015287LGN01	14-Oct-15	04:56:07	142/044	54.32	144.18	0.99	0.99	30	100
LC81420452016290LGN01	16-Oct-16	04:56:27	142/044	53.58	145.43	0.00	0.99	30	100
LC81420452018295LGN00	22-Oct-18	04:55:59	142/044	51.96	147.33	0.02	0.99	30	100
LT51420451988325BKT01	20-Nov-88	04:26:43	142/044	40.65	145.10	0.00	0.98	30	120
LT51420451989327BKT00	23-Nov-89	04:20:05	142/044	39.18	143.73	0.00	0.98	30	120
LT51420451991317ISPO0	13-Nov-91	04:20:19	142/044	41.53	142.35	1.00	0.99	30	120
LT51420451993322ISPO0	18-Nov-93	04:18:01	142/044	39.98	142.68	1.00	0.98	30	120
LT51420451996315ISPO0	10-Nov-96	04:16:41	142/044	41.61	141.11	7.00	0.99	30	120
LE71420451999315SGS00	11-Nov-99	04:49:00	142/044	45.72	149.96	0.00	0.99	30	60
LT51420452004321BKT00	16-Nov-04	04:41:11	142/044	43.41	148.58	0.00	0.98	30	120
LT51420452005323BKT01	19-Nov-05	04:44:37	142/044	43.18	149.85	2.00	0.98	30	120
LT51420452006326BKT01	22-Nov-06	04:50:37	142/044	43.19	151.69	0.00	0.98	30	120
LT51420452008316BKT00	11-Nov-08	04:39:17	142/044	44.41	147.38	1.00	0.98	30	120
LC81420452013329LGN01	25-Nov-13	04:57:43	142/044	43.28	153.97	0.00	0.98	30	100
LC81420452014316LGN01	12-Nov-14	04:56:21	142/044	46.22	152.46	7.59	0.98	30	100
LC81420452016322LGN01	17-Nov-16	04:56:27	142/044	44.87	153.13	0.00	0.98	30	100
LC81420452017324LGN01	20-Nov-17	04:56:20	142/044	44.22	153.32	1.75	0.98	30	100
LC81420452019314LGN00	10-Nov-19	04:56:29	142/044	46.82	152.20	0.64	0.99	30	100
LT51420451988357BKT00									

## Methodology

### Retrieving LST from Landsat data

In this study, the mono-window algorithm was applied to retrieve LST from multi-temporal Landsat satellite sensors where three necessary parameters are ground emissivity, atmospheric transmittance, and effective mean atmospheric temperature (Qin et al., 2001; Wang et al., 2016; Wang et al., 2019; Sekertekin & Bonafoni, 2020). At first, the original TIR bands (100 m resolution for Landsat 8 OLI/TIRS data, 60 m resolution for Landsat 7 ETM+ data, and 120 m resolution for Landsat 5 TM data) were resampled into 30 m by the USGS data centre for further application.

The TIR pixel values are firstly converted into radiance from digital number (DN) values. Radiance for TIR band of Landsat 5 TM data and Landsat 7 ETM+ data is obtained using Eq. (1) (USGS):

$$L_{\lambda} = \left[ \frac{L_{MAX\lambda} - L_{MIN\lambda}}{QCAL_{MAX} - QCAL_{MIN}} \right] * [QCAL - QCAL_{MIN}] + L_{MIN\lambda} \quad (1)$$

where,  $L_{\lambda}$  is Top of Atmosphere (TOA) spectral radiance ( $Wm^{-2}sr^{-1}mm^{-1}$ ),  $QCAL$  is the quantized calibrated pixel value in DN,  $L_{MIN\lambda}$  ( $Wm^{-2}sr^{-1}mm^{-1}$ ) is the spectral radiance scaled to  $QCAL_{MIN}$ ,  $L_{MAX\lambda}$  ( $Wm^{-2}sr^{-1}mm^{-1}$ ) is the spectral radiance scaled to  $QCAL_{MAX}$ ,  $QCAL_{MIN}$  is the minimum quantized calibrated pixel value in DN and  $QCAL_{MAX}$  is the maximum quantized calibrated pixel value in DN.  $L_{MIN\lambda}$ ,  $L_{MAX\lambda}$ ,  $QCAL_{MIN}$ , and  $QCAL_{MAX}$  values are obtained from the metadata file of Landsat TM and ETM+ data. Radiance for Landsat 8 TIR band is obtained from Eq. (2) (Zanter, 2019):

$$L_{\lambda} = M_L \cdot QCAL + A_L \quad (2)$$

where,  $L_{\lambda}$  is the TOA spectral radiance ( $Wm^{-2}sr^{-1}mm^{-1}$ ),  $M_L$  is the band-specific multiplicative rescaling factor from the metadata,  $A_L$  is the band-specific additive rescaling factor from the metadata,  $QCAL$  is the quantized and calibrated standard product pixel values (DN). All of these variables can be retrieved from the metadata file of Landsat 8 OLI/TIRS data.

For Landsat 5 TM data and Landsat 7 ETM+ data, the reflectance value is obtained from radiances using Eq. (3) (USGS):

$$\rho_{\lambda} = \frac{\pi \cdot L_{\lambda} \cdot d^2}{ESUN_{\lambda} \cdot \cos \theta_s} \quad (3)$$

where,  $\rho_{\lambda}$  is unitless planetary reflectance,  $L_{\lambda}$  is the TOA spectral radiance ( $Wm^{-2}sr^{-1}\mu m^{-1}$ ),  $d$  is Earth-Sun distance in astronomical units,  $ESUN_{\lambda}$  is the mean solar exo-atmospheric spectral irradiances ( $Wm^{-2}\mu m^{-1}$ ) and  $\theta_s$  is the solar zenith angle in degrees.  $ESUN_{\lambda}$  values for each band of Landsat 5 can be obtained from the handbooks of the related mission.  $\theta_s$  and  $d$  values can be attained from the metadata file.

For Landsat 8 OLI/TIRS data, reflectance conversion can be applied to DN values directly as in Eq. (4) (Zanter, 2019):



$$\rho_{\lambda} = \frac{M_{\rho} \cdot Q_{CAL} + A_{\rho}}{\sin \theta_{SE}} \quad (4)$$

where,  $M_{\rho}$  is the band-specific multiplicative rescaling factor from the metadata,  $A_{\rho}$  is the band-specific additive rescaling factor from the metadata,  $Q_{CAL}$  is the quantized and calibrated standard product pixel values (DN) and  $\theta_{SE}$  is the local sun elevation angle from the metadata file.

Eq. (5) is used to convert the spectral radiance to at-sensor brightness temperature (Wukelic et al., 1989).

$$T_b = \frac{K_2}{\ln\left(\frac{K_1}{L_{\lambda}} + 1\right)} \quad (5)$$

where,  $T_b$  is the brightness temperature in Kelvin (K),  $L_{\lambda}$  is the spectral radiance in  $Wm^{-2}sr^{-1}mm^{-1}$ ;  $K_2$  and  $K_1$  are calibration constants. For Landsat 8 data,  $K_1$  is 774.89,  $K_2$  is 1321.08 ( $Wm^{-2}sr^{-1}mm^{-1}$ ). For Landsat 7 data,  $K_1 = 666.09$ ,  $K_2 = 1282.71$  ( $Wm^{-2}sr^{-1}mm^{-1}$ ). For Landsat 5 data,  $K_1$  is 607.76,  $K_2$  is 1260.56 ( $Wm^{-2}sr^{-1}mm^{-1}$ ).

The land surface emissivity  $\varepsilon$ , is estimated using the NDVI Thresholds Method (Sobrino et al., 2004). The fractional vegetation  $F_v$ , of each pixel, is determined from the NDVI using the following equation (Carlson & Ripley, 1997):

$$F_v = \left( \frac{NDVI - NDVI_{min}}{NDVI_{max} - NDVI_{min}} \right)^2 \quad (6)$$

where,  $NDVI_{min}$  is the minimum NDVI value (0.2) for bare soil pixel and  $NDVI_{max}$  is the maximum NDVI value (0.5) for healthy vegetation pixel.

$d\varepsilon$  is the effect of the geometrical distribution of the natural surfaces and internal reflections. For mixed and elevated land surfaces, the value of  $d\varepsilon$  may be 2% (Sobrino et al., 2004).

$$d\varepsilon = (1 - \varepsilon_s)(1 - F_v)F\varepsilon_v \quad (7)$$

where,  $\varepsilon_v$  is vegetation emissivity,  $\varepsilon_s$  is soil emissivity,  $F_v$  is fractional vegetation,  $F$  is a shape factor whose mean is 0.55 (Sobrino et al., 2004).

$$\varepsilon = \varepsilon_v F_v + \varepsilon_s (1 - F_v) + d\varepsilon \quad (8)$$

where,  $\varepsilon$  is the land surface emissivity that is determined by the following equation (Sobrino et al., 2004):

$$\varepsilon = 0.004 * F_v + 0.986 \quad (9)$$

Water vapour content is estimated by the following equation (Li, 2006; Yang & Qiu, 1996):

$$w = 0.0981 * \left[ 10 * 0.6108 * \exp\left(\frac{17.27 * (T_0 - 273.15)}{237.3 + (T_0 - 273.15)}\right) * RH \right] + 0.1697 \quad (10)$$

where,  $w$  is the water vapour content ( $\text{g}/\text{cm}^2$ ),  $T_0$  is the near-surface air temperature in Kelvin (K),  $RH$  is the relative humidity (%). These parameters of the atmospheric profile are obtained from the Meteorological Centre, Raipur (<http://www.imdraipur.gov.in>). Atmospheric transmittance is determined for Raipur City using the following equation (Qin et al., 2001; Sun et al., 2010):

$$\tau = 1.031412 - 0.11536w \quad (11)$$

where,  $\tau$  is the total atmospheric transmittance,  $\varepsilon$  is the land surface emissivity.

Raipur City is located in the tropical region. Thus, the following equations are applied to compute the effective mean atmospheric transmittance of Raipur (Qin et al., 2001; Sun et al., 2010):

$$T_a = 17.9769 + 0.91715T_0 \quad (12)$$

LST is retrieved from Landsat 5 TM, Landsat 7 ETM+, and Landsat 8 OLI/TIRS satellite data by using the following equations (Qin et al., 2001):

$$T_s = \frac{[a(1-C-D) + (b(1-C-D) + C + D)T_b - DT_a]}{C} \quad (13)$$

$$C = \varepsilon\tau \quad (14)$$

$$D = (1-\tau)[1 + (1-\varepsilon)\tau] \quad (15)$$

where,  $\varepsilon$  is the land surface emissivity,  $\tau$  is the total atmospheric transmittance,  $T_b$  is the at-sensor brightness temperature,  $T_a$  is the mean atmospheric temperature,  $T_0$  is the near-surface air temperature,  $T_s$  is the land surface temperature,  $a = -67.355351$ ,  $b = 0.458606$ .

Figure 2 shows the flowchart of methodology of the present study which clearly presents the steps of the LST retrieval process.

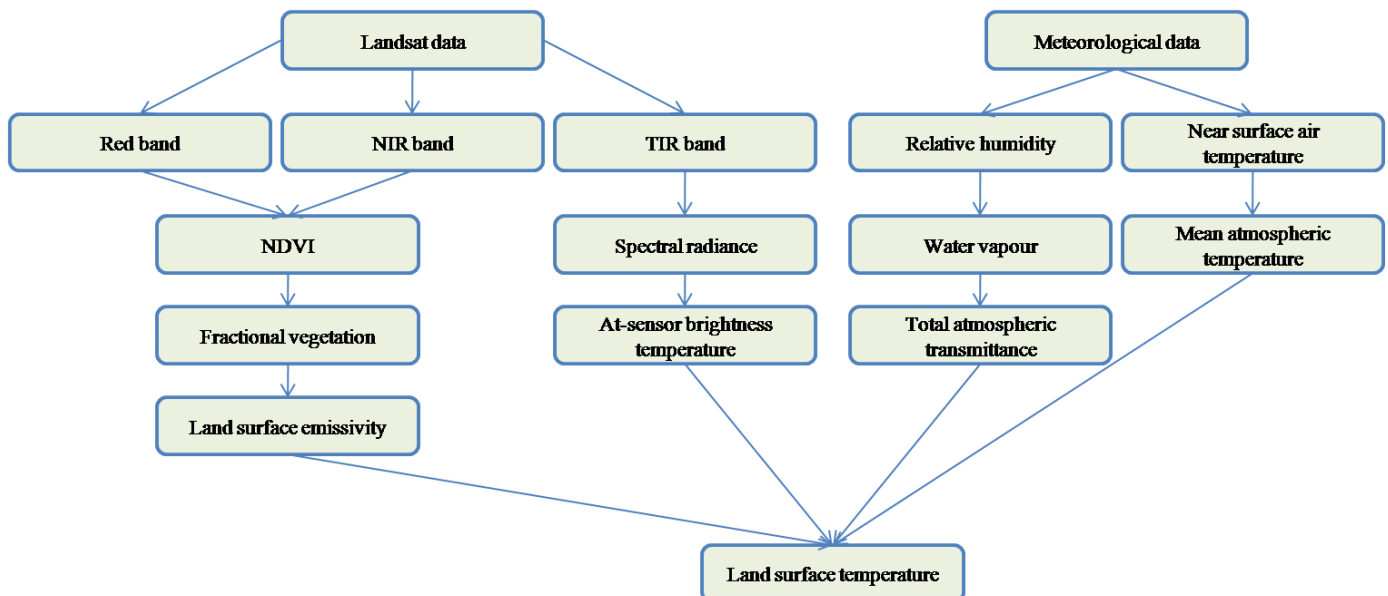


Figure 2 – Flowchart showing the methodology of the present study. Source: Author (2021).

## Determination of NDVI

Here, NDVI was selected as a normalized difference spectral index in the research work (Tucker, 1979). NDVI is determined by the red and NIR bands. For TM and ETM+ data, band 3 is used as a red band and band 4 is used as a NIR band, respectively. For OLI/TIRS data, band 4 and band 5 are used as red and NIR bands, respectively (Table 4). The value of NDVI ranges between -1 and +1. Generally, the negative value of NDVI indicates the water surfaces. Positive NDVI shows vegetation surface. The increasing positive value of NDVI indicates the increase of greenness in plants.

**Table 4** – Description of normalized difference vegetation index (NDVI)

Acronym	Description	Formulation	References
NDVI	Normalized difference vegetation index	$\frac{NIR - Red}{NIR + Red}$	Tucker 1979

Source: Author (2020).

## Results and discussion

### Monthly variation in LST distribution

Table 5 shows a clear observation of monthly change in the mean LST values. In this table, the mean LST of each image is shown. The mean LST of every month was also determined. In this way, the mean LST values for ten months (no cloud-free data was available for July and August) were presented.

It is seen from Table 5 that the mean LST of the city was above 32°C mean LST for all the months from March-May of 1992, 2001-02, 2004-05, 2008-11, 2013, 2016-17, and 2019. June and September of 2005, 2006, and 2009 have more mean LST values than the earlier and later years. The scenario was completely different from October to February, where that the mean LST of the city was below 28°C LST. April (38.79°C mean LST), May (36.65°C mean LST), June (34.56°C mean LST), and March (32.11°C mean LST) - these four months have an average value of > 35°C mean LST throughout the entire period of study. February (27.88°C mean LST), October (27.23°C mean LST), September (27.18°C mean LST), and November (25.83°C mean LST) - these four months have an average value of 25-28°C mean LST throughout the entire time. Only December (23.76°C mean LST) and January (23.01°C mean LST) months have an average value of < 24°C mean LST for the period. The average value of the highest and the lowest mean LST from 1988 to 2019 is observed in April and January, respectively. The northwest and southeast parts of the study area exhibit high LST. These parts also have a low percentage of urban vegetation and a high percentage of built-up areas and bare land. It shows that the proportion of vegetation reduced significantly with time.

Figure 3 shows the line graph of LST in different months from 1988 to 2019. October, November, and December present an almost similar pattern of LST distribution. January and February show an almost similar trend in their LST graph. A similarity also has been seen in the mean LST graph of March, April, and May. The LST graph of June shows a negative trend, while September shows a positive trend.

**Table 5 – Monthly distribution of mean LST (°C) for the entire Raipur City from 1988 to 2019**

<b>January</b>	<b>LST (°C)</b>	<b>February</b>	<b>LST (°C)</b>	<b>March</b>	<b>LST (°C)</b>	<b>April</b>	<b>LST (°C)</b>	<b>May</b>	<b>LST (°C)</b>
1988-Jan-21	24.52	1989-Feb-24	28.31	1989-Mar-12	28.14	1990-Apr-16	40.87	1991-May-21	36.63
1990-Jan-10	24.42	1990-Feb-11	25.26	1990-Mar-15	30.96	1992-Apr-21	41.19	2002-May-11	40.92
1992-Jan-16	21.33	1991-Feb-14	23.98	1991-Mar-18	29.50	1995-Apr-14	34.63	2004-May-24	40.74
1993-Jan-18	23.41	1992-Feb-17	25.30	1992-Mar-20	32.84	2001-Apr-22	41.34	2005-May-11	38.72
1996-Jan-27	22.08	1993-Feb-19	28.42	2003-Mar-11	29.49	2002-Apr-25	38.85	2006-May-14	28.43
2005-Jan-19	22.08	2002-Feb-20	30.39	2004-Mar-21	36.48	2003-Apr-12	31.28	2007-May-17	36.20
2007-Jan-25	26.37	2004-Feb-18	26.64	2007-Mar-14	27.57	2004-Apr-22	36.80	2008-May-19	38.36
2009-Jan-14	17.15	2006-Feb-23	32.95	2009-Mar-19	33.79	2009-Apr-20	39.74	2009-May-22	33.20
2011-Jan-20	23.03	2009-Feb-15	31.01	2014-Mar-17	31.68	2010-Apr-23	40.63	2010-May-25	36.11
2015-Jan-15	23.49	2010-Feb-18	22.67	2015-Mar-20	32.83	2016-Apr-23	42.97	2011-May-12	39.80
2018-Jan-23	25.26	2015-Feb-16	29.75	2016-Mar-22	37.00	2017-Apr-10	38.37	2013-May-17	40.28
		2016-Feb-19	24.60	2017-Mar-25	37.06			2014-May-20	34.91
		2017-Feb-21	32.45	2018-Mar-12	30.09			2015-May-23	36.42
		2018-Feb-24	31.05					2016-May-25	37.22
		2019-Feb-11	25.37					2017-May-12	33.33
		1989-Feb-24	28.31					2018-May-15	31.42
								2019-May-18	40.21
<i>Mean</i>	<i>23.01</i>	<i>Mean</i>	<i>27.88</i>	<i>Mean</i>	<i>32.11</i>	<i>Mean</i>	<i>38.79</i>	<i>Mean</i>	<i>36.64</i>
<b>June</b>	<b>LST (°C)</b>	<b>September</b>	<b>LST (°C)</b>	<b>October</b>	<b>LST (°C)</b>	<b>November</b>	<b>LST (°C)</b>	<b>December</b>	<b>LST (°C)</b>
2005-Jun-12	38.66	1996-Sep-23	24.09	1988-Oct-19	28.86	1988-Nov-20	24.27	1988-Dec-22	23.96
2006-Jun-15	35.43	2001-Sep-21	26.13	1991-Oct-12	24.98	1989-Nov-23	25.16	1992-Dec-17	22.34
2009-Jun-23	33.05	2002-Sep-16	28.81	1992-Oct-14	24.61	1991-Nov-13	23.64	1994-Dec-23	18.55
2018-Jun-16	31.08	2014-Sep-25	29.67	1996-Oct-25	22.56	1993-Nov-18	24.47	1995-Dec-10	21.49
				2001-Oct-15	30.12	1996-Nov-10	23.15	2000-Dec-15	26.81
				2001-Oct-23	26.85	1999-Nov-11	29.16	2002-Dec-21	27.09
				2004-Oct-15	27.56	2004-Nov-16	28.45	2004-Dec-18	25.76
				2006-Oct-21	26.30	2005-Nov-19	26.72	2006-Dec-24	23.35
				2009-Oct-13	27.10	2006-Nov-22	26.40	2008-Dec-13	25.71
				2011-Oct-19	28.30	2008-Nov-11	27.38	2009-Dec-16	23.59
				2015-Oct-14	27.61	2013-Nov-25	26.09	2010-Dec-19	22.31
				2016-Oct-16	30.02	2014-Nov-12	23.47	2013-Dec-11	24.62
				2018-Oct-22	29.01	2016-Nov-17	27.18	2016-Dec-19	24.60
						2017-Nov-20	26.28	2017-Dec-22	24.02
						2019-Nov-10	25.60	2018-Dec-25	21.17
								2019-Dec-12	24.74
<i>Mean</i>	<i>34.56</i>	<i>Mean</i>	<i>27.18</i>	<i>Mean</i>	<i>27.22</i>	<i>Mean</i>	<i>25.83</i>	<i>Mean</i>	<i>23.76</i>

Source: Author (2021).

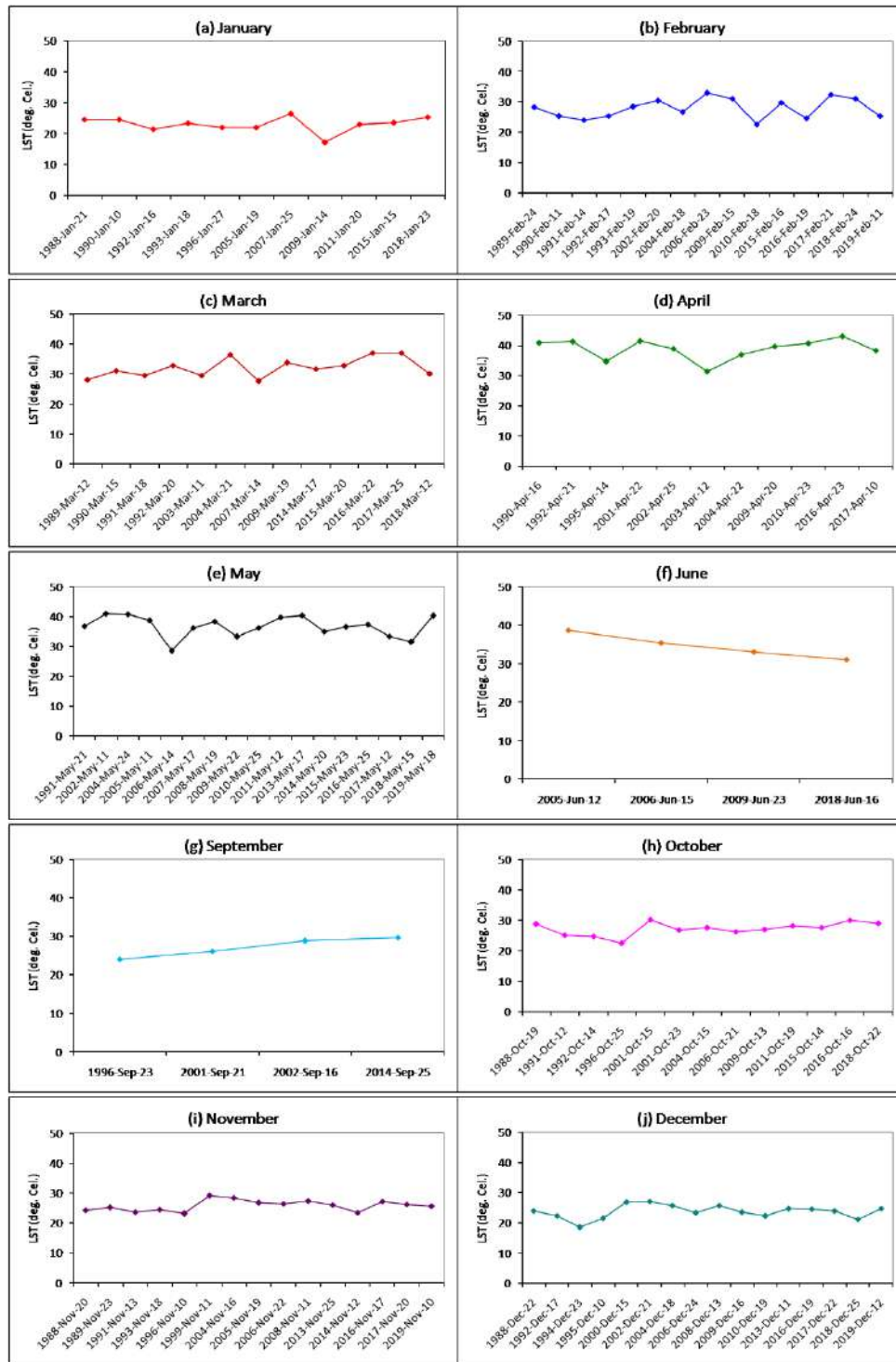


Figure 3 – Line graphs for monthly variation of LST (°C) from 1988 to 2019: (a) January (b) February (c) March (d) April (e) May (f) June (g) September (h) October (i) November (j) December. Source: Author (2021).

Monthly variation on LST-NDVI relationship

**Table 6** – Monthly variation of LST-NDVI correlation coefficient(1988-2019) (significant at 0.05 level)

January	Correlation coefficient	February	Correlation coefficient	March	Correlation coefficient	April	Correlation coefficient	May	Correlation coefficient
1988-Jan-21	-0.31	1989-Feb-24	-0.39	1989-Mar-12	-0.43	1990-Apr-16	-0.52	1991-May-21	-0.43
1990-Jan-10	-0.36	1990-Feb-11	-0.38	1990-Mar-15	-0.43	1992-Apr-21	-0.53	2002-May-11	-0.56
1992-Jan-16	-0.35	1991-Feb-14	-0.12	1991-Mar-18	-0.40	1995-Apr-14	-0.38	2004-May-24	-0.46
1993-Jan-18	-0.38	1992-Feb-17	-0.29	1992-Mar-20	-0.40	2001-Apr-22	-0.65	2005-May-11	-0.54
1996-Jan-27	-0.30	1993-Feb-19	-0.37	2003-Mar-11	-0.41	2002-Apr-25	-0.57	2006-May-14	-0.46
2005-Jan-19	-0.21	2002-Feb-20	-0.44	2004-Mar-21	-0.49	2003-Apr-12	-0.39	2007-May-17	-0.33
2007-Jan-25	-0.21	2004-Feb-18	-0.30	2007-Mar-14	-0.38	2004-Apr-22	-0.51	2008-May-19	-0.48
2009-Jan-14	-0.25	2006-Feb-23	-0.31	2009-Mar-19	-0.54	2009-Apr-20	-0.56	2009-May-22	-0.44
2011-Jan-20	-0.18	2009-Feb-15	-0.36	2014-Mar-17	-0.42	2010-Apr-23	-0.52	2010-May-25	-0.47
2015-Jan-15	-0.27	2010-Feb-18	-0.24	2015-Mar-20	-0.36	2016-Apr-23	-0.46	2011-May-12	-0.56
2018-Jan-23	-0.15	2015-Feb-16	-0.16	2016-Mar-22	-0.40	2017-Apr-10	-0.51	2013-May-17	-0.43
		2016-Feb-19	-0.21	2017-Mar-25	-0.43			2014-May-20	-0.41
		2017-Feb-21	-0.30	2018-Mar-12	-0.37			2015-May-23	-0.34
		2018-Feb-24	-0.28					2016-May-25	-0.38
		2019-Feb-11	-0.21					2017-May-12	-0.29
		1989-Feb-24	-0.39					2018-May-15	-0.45
								2019-May-18	-0.43
Mean	-0.24	Mean	-0.29	Mean	-0.40	Mean	-0.51	Mean	-0.44
June	Correlation coefficient	September	Correlation coefficient	October	Correlation coefficient	November	Correlation coefficient	December	Correlation coefficient
2005-Jun-12	-0.51	1996-Sep-23	-0.54	1988-Oct-19	-0.69	1988-Nov-20	-0.41	1988-Dec-22	-0.20
2006-Jun-15	-0.46	2001-Sep-21	-0.58	1991-Oct-12	-0.63	1989-Nov-23	-0.29	1992-Dec-17	-0.15
2009-Jun-23	-0.42	2002-Sep-16	-0.56	1992-Oct-14	-0.68	1991-Nov-13	-0.38	1994-Dec-23	-0.24
2018-Jun-16	-0.46	2014-Sep-25	-0.53	1996-Oct-25	-0.64	1993-Nov-18	-0.19	1995-Dec-10	-0.09
				2001-Oct-15	-0.66	1996-Nov-10	-0.40	2000-Dec-15	-0.18
				2001-Oct-23	-0.58	1999-Nov-11	-0.48	2002-Dec-21	-0.29
				2004-Oct-15	-0.63	2004-Nov-16	-0.35	2004-Dec-18	-0.10
				2006-Oct-21	-0.51	2005-Nov-19	-0.31	2006-Dec-24	-0.23
				2009-Oct-13	-0.64	2006-Nov-22	-0.23	2008-Dec-13	-0.12
				2011-Oct-19	-0.63	2008-Nov-11	-0.41	2009-Dec-16	-0.20
				2015-Oct-14	-0.61	2013-Nov-25	-0.44	2010-Dec-19	-0.24
				2016-Oct-16	-0.53	2014-Nov-12	-0.52	2013-Dec-11	-0.19
				2018-Oct-22	-0.63	2016-Nov-17	-0.44	2016-Dec-19	-0.21
						2017-Nov-20	-0.45	2017-Dec-22	-0.30
						2019-Nov-10	-0.59	2018-Dec-25	-0.22
								2019-Dec-12	-0.40
Mean	-0.47	Mean	-0.55	Mean	-0.62	Mean	-0.39	Mean	-0.21

Source: Author (2021).

Table 6 represents a monthly variation of Pearson's linear correlation method between LST and NDVI significant at 0.05 level. On average, October (-0.62), September (-0.55), and April (-0.51) months build a strong negative correlation. June (-0.47), May (-0.44), March (-0.44), and November (-0.39) months have a moderate negative correlation. A weak negative correlation was found in February (-0.29), January (-0.24), and December (-0.21) months. The main reason behind the strong to moderate LST-NDVI correlation in March-November is the presence of high intensity of moisture and chlorophyll content in green vegetation. Dry months reduce the strength of regression, while wet months enhance the strength of the LST-NDVI regression. Hence, the climatic condition and surface material influence the LST-NDVI correlation analysis.

A long-term monthly assessment of land surface temperature and normalized difference vegetation index using Landsat data

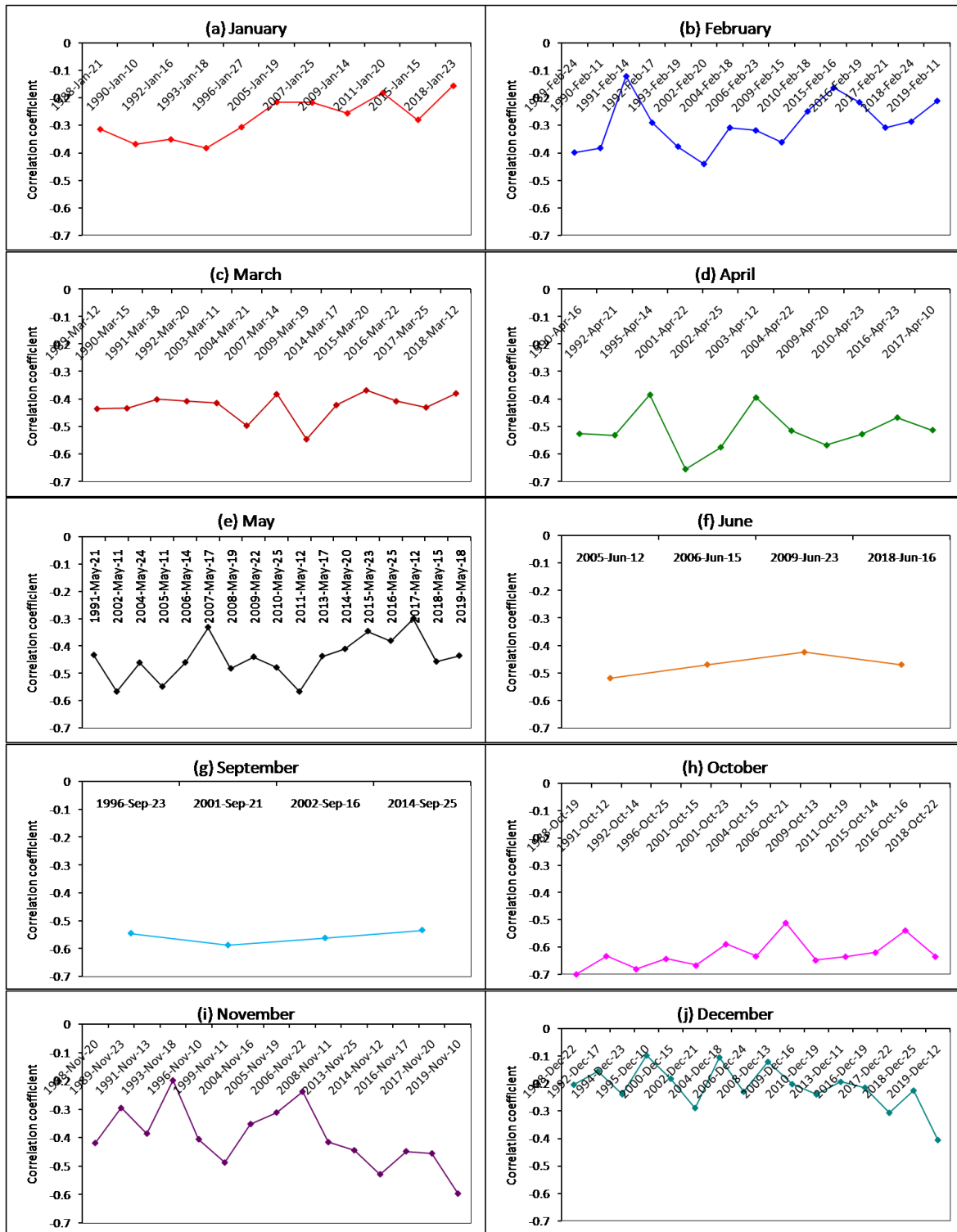


**Figure 4** – Line graphs for monthly variation of LST-NDVI relationship (1988-2019): (a) January (b) February (c) March (d) April (e) May (f) June (g) September (h) October (i) November (j) December. Source: Author (2021).

Figure 4 shows the line graphs for monthly variation of LST-NDVI relationships. June and September months show a smooth convex and concave trend, respectively due to wet weather. The line graphs of October, November, and December show more fluctuation due to more differences in atmospheric components. The line graphs of January and March look almost similar. February, April, and May present similar trends of LST.

Liang et al. (2012) presented similar types of negative NDVI-LST correlation in Guilin City, China. In high latitudes, positive LST-NDVI relationships have been observed as the presence of vegetation increases the value of LST in high latitudes where the winter season is severe (Karnieli et al., 2006). Yue et al. (2007) showed that the LST-NDVI relationship in Shanghai City, China was negative and was different in different LULC types like the relationship was strong negative on vegetation. Sun and Kafatos (2007) stated that the LST-NDVI correlation was positive in the winter season while it was negative in the summer season as the winter season produces the lowest LST on the rock surface and dry soil and vice-versa in the summer season. This relationship was also negative in Mashhad, Iran as it is a dry tropical city (Gorgani et al., 2013). The relationship was strongly negative in Berlin City for any season (Marzban et al., 2018). This correlation tends to be more negative with the increase of surface moisture as in the wet season more green and healthy vegetation is produced (Moran et al., 1994; Lambin & Ehrlich, 1996; Prehodko & Goward, 1997; Sandholt et al., 2002). The present study also found a negative LST-NDVI correlation for all the months as it is a humid tropical city. The value of the correlation coefficient is inversely related to the surface moisture content, i.e., the negativity of the relationship increases with the increase of surface moisture content.

## Conclusions

The present study estimates the monthly variation of LST distribution in Raipur City, India using one hundred and eighteen Landsat datasets from 1988 to 2019. April, May, June, and March present higher LST values than the rest of the months. The present study also assesses the monthly correlation of LST and NDVI in Raipur City. In general, the results show that LST is inversely related to NDVI, irrespective of any month. From March to November, the correlation is strong to moderate negative, whereas it is found weak negative in the winter season (December to February). The presence of healthy green plants and high moisture content in the air is the main responsible factors for strong negativity. The study is useful for the environmentalists and urban planners for future ecological planning from several points of view. Special attention may be taken in March, April, May, and June to increase the negativity of the relationship by plantation. Simultaneously, more trees can be planted in December, January, and February for generating pleasant weather. Moreover, some commercial activities may be decreased in the winter months as at that time the city remains dry and more polluted. Special emphasis should be taken on the transport and industrial sectors as these sectors are mainly responsible for generating high LST. Mass transport system must be encouraged instead of the private transport system. The area under the park, urban vegetation, water bodies, and wetland must be increased at any cost as these changes can bring ecological comfort to the city. The unused fallow lands should be converted into vegetation and water area. It will be beneficial to the residents if any public and private initiatives have to be taken on seasonal plantation programmes along the roadways and barren lands.

## References

- Alexander, C. (2020). Normalised difference spectral indices and urban land cover as indicators of land surface temperature (LST). *Int J Appl Earth Obs Geoinf*, 86, 102013. <https://doi.org/10.1016/j.jag.2019.102013>.
- Carlson, T. N., & Ripley, D. A. (1997). On the Relation between NDVI, Fractional Vegetation Cover, and Leaf Area Index. *Remote Sens Environ*, 62(3), 241-252. [https://doi.org/10.1016/S0034-4257\(97\)00104-1](https://doi.org/10.1016/S0034-4257(97)00104-1).
- Chen, XL, Zhao, HM, Li, PX, & Yi, ZY. (2006). Remote sensing image-based analysis of the relationship between urban heat island and land use/cover changes. *Remote Sens Environ*, 104(2), 133-146. <https://doi.org/10.1016/j.rse.2005.11.016>
- Cui, L., Wang, L., Qu, S., Singh, R. P., Lai, Z., & Yao, R. (2019). Spatiotemporal extremes of temperature and precipitation during 1960-2015 in the Yangtze River Basin (China) and impacts on vegetation dynamics. *Theor Appl Climatol*, 136(1-2), 675-692. <https://doi.org/10.1007/s00704-018-2519-0>.



- Cui, L., Wang, L., Qu, S., Singh, R. P., Lai, Z., Jiang, L., & Yao, R. (2019). Association analysis between spatiotemporal variation of vegetation greenness and precipitation/temperature in the Yangtze River Basin (China). *Environ Sci Pollut Res*, 25(22), 21867–21878. <https://doi.org/10.1007/s11356-018-2340-4>.
- Fatemi, M., & Narangifard, M. (2019). Monitoring LULC changes and its impact on the LST and NDVI in District 1 of Shiraz City. *Arab J Geosci*, 12, 127. <https://doi.org/10.1007/s12517-019-4259-6>.
- Ferrelli, F., Huamantincó, M. A., Delgado, D. A., & Piccolo, M. C. (2018). Spatial and temporal analysis of the LST-NDVI relationship for the study of land cover changes and their contribution to urban planning in Monte Hermoso, Argentina. *Doc Anal Geogr*, 64(1), 25-47. <https://doi.org/10.5565/rev/dag.355>.
- Ghobadi, Y., Pradhan, B., Shafri, H. Z. M., & Kabiri, K. (2014). Assessment of spatial relationship between land surface temperature and land use/cover retrieval from multi-temporal remote sensing data in South Karkheh Sub-basin, Iran. *Arab J Geosci*, 8(1), 525–537. <https://doi.org/10.1007/s12517-013-1244-3>.
- Gorgani, S. A., Panahi, M., & Rezaie, F. (2013). The relationship between NDVI and LST in the Urban area of Mashhad, Iran. In *International Conference on Civil Engineering Architecture and Urban Sustainable Development*. November, Tabriz, Iran.
- Govil, H., Guha, S., Dey, A., & Gill, N. (2019). Seasonal evaluation of downscaled land surface temperature: A case study in a humid tropical city. *Heliyon*, 5(6), e01923. <https://doi.org/10.1016/j.heliyon.2019.e01923>.
- Govil, H., Guha, S., Diwan, P., Gill, N., & Dey, A. (2020). Analyzing Linear Relationships of LST with NDVI and MNDISI Using Various Resolution Levels of Landsat 8 OLI/TIRS Data. In Sharma N., Chakrabarti A., Balas V. (Eds.), *Data Management, Analytics and Innovation. Advances in Intelligent Systems and Computing* (Vol. 1042, p. 171-184). Singapore: Springer. [https://doi.org/10.1007/978-981-32-9949-8\\_13](https://doi.org/10.1007/978-981-32-9949-8_13)
- Goward, S. N., Xue, Y. K., & Czajkowski, K. P. (2002). Evaluating Land Surface Moisture Conditions from the Remotely Sensed Temperature/Vegetation Index Measurements: An Exploration with the Simplified Simple Biosphere Model. *Remote Sens Environ*, 79, 225-242. [https://doi.org/10.1016/S0034-4257\(01\)00275-9](https://doi.org/10.1016/S0034-4257(01)00275-9).
- Guha, S. (2016). Capability of NDVI technique in detecting mangrove vegetation. *Int J Adv Biol Res*, 6(2), 253-258.
- Guha, S. (2021). Dynamic seasonal analysis on LST-NDVI relationship and ecological health of Raipur City, India. *Ecosyst Health Sustain*. 7(1): 1927852. <https://doi.org/10.1080/20964129.2021.1927852>.
- Guha, S., & Govil, H. (2019). Evaluation of ASTER TIR data-based lithological indices in Malanjkhand Copper Mines of Madhya Pradesh, India. *Appl Earth Sci*, 129(1), 3-8. <https://doi.org/10.1080/25726838.2019.1684018>.
- Guha, S., & Govil, H. (2020). Seasonal impact on the relationship between land surface temperature and normalized difference vegetation index in an urban landscape. *Geocarto Int*. <https://doi.org/10.1080/10106049.2020.1815867>.
- Guha, S., & Govil, H. (2021a). Annual assessment on the relationship between land surface temperature and six remote sensing indices using Landsat data from 1988 to 2019. *Geocarto Int*. <https://doi.org/10.1080/10106049.2021.1886339>.
- Guha, S., & Govil, H. (2021b). COVID-19 lockdown effect on land surface temperature and normalized difference vegetation index. *Geomat Nat Haz Risk*, 12(1): 1082-1100. <https://doi.org/10.1080/19475705.2021.1914197>.
- Guha, S., & Govil, H. (2021c). An assessment on the relationship between land surface temperature and normalized difference vegetation index. *Environ Dev Sustain*, 23(2): 1944-1963. <https://doi.org/10.1007/s10668-020-00657-6>.
- Guha, S., Govil, H., & Besoya, M. (2020). An investigation on seasonal variability between LST and NDVI in an urban environment using Landsat satellite data. *Geomat Nat Haz Risk*, 11(1), 1319-1345. <https://doi.org/10.1080/19475705.2020.1789762>.
- Guha, S., Govil, H., & Diwan, P. (2019). Analytical study of seasonal variability in land surface temperature with normalized difference vegetation index, normalized difference water index, normalized difference built-up index, and normalized multiband drought index. *J Appl Remote Sens*, 13(2), 024518. <https://doi.org/10.1117/1.JRS.13.024518>.
- Guha, S., Govil, H., & Diwan, P. (2020). Monitoring LST-NDVI Relationship Using Premonsoon Landsat Datasets. *Adv Meteorol*, 2020, 4539684. <https://doi.org/10.1155/2020/4539684>.

- Guha, S., Govil, H., & Mukherjee, S. (2017). Dynamic analysis and ecological evaluation of urban heat islands in Raipur city, India. *J Appl Remote Sens*, 11(3), 036020. <https://doi.org/10.1117/1.JRS.11.036020>.
- Guha, S., Govil, H., Dey, A., & Gill, N. (2018). Analytical study of land surface temperature with NDVI and NDBI using Landsat 8 OLI/TIRS data in Florence and Naples city, Italy. *Eur J Remote Sens*, 51(1), 667-678. <https://doi.org/10.1080/22797254.2018.1474494>.
- Guha, S., Govil, H., Dey, A., & Gill, N. (2020). A case study on the relationship between land surface temperature and land surface indices in Raipur City, India. *Geogr Tidsskr*, 120(1), 35-50. <https://doi.org/10.1080/00167223.2020.1752272>.
- Guha, S., Govil, H., Gill, N., & Dey, A. (2020a). A long-term seasonal analysis on the relationship between LST and NDBI using Landsat data. *Quatern Int*. 575-576: 249-258. <https://doi.org/10.1016/j.quaint.2020.06.041>
- Guha, S., Govil, H., Gill, N., & Dey, A. (2020b). Analysing the Capability of NCI Technique in Change Detection Using High-and Medium-Resolution Multispectral Data. In S. Sahdev, R. B. Singh, & M. Kumar (Eds.), *Geoecology of Landscape Dynamics* (p. 133-147). Springer, Singapore. [https://doi.org/10.1007/978-981-15-2097-6\\_10](https://doi.org/10.1007/978-981-15-2097-6_10).
- Guha, S., Govil, H., Gill, N., & Dey, A. (2020c). Analytical study on the relationship between land surface temperature and land use/land cover indices. *Ann GIS*, 26(2), 201-216. <https://doi.org/10.1080/19475683.2020.1754291>.
- Gui, X., Wang, L., Yao, R., Yu, D., & Li, C. (2019). Investigating the urbanization process and its impact on vegetation change and urban heat island in Wuhan, China. *Environ Sci Pollut Res*, 26(30), 30808-30825. <https://doi.org/10.1007/s11356-019-06273-w>.
- Gutman, G., & Ignatov, A. (1998). The Derivation of the Green Vegetation Fraction from NOAA/ AVHRR Data for Use in Numerical Weather Prediction Models. *Int J Remote Sens*, 19(8), 1533-1543. <https://doi.org/10.1080/014311698215333>.
- Hao, X., Li, W., & Deng, H. (2016). The oasis effect and summer temperature rise in arid regions-case study in Tarim Basin. *Sci Rep*, 6, 35418. <https://doi.org/10.1038/srep35418>.
- Hou, G. L., Zhang, H. Y., Wang, Y. Q., Qiao, Z. H., & Zhang, Z. X. (2010). Retrieval and Spatial Distribution of Land Surface Temperature in the Middle Part of Jilin Province Based on MODIS Data. *SciGeogr Sin*, 30, 421-427.
- Jamei, Y., Rajagopalan, P., & Sun, Q. C. (2019). Spatial structure of surface urban heat island and its relationship with vegetation and built-up areas in Melbourne, Australia. *Sci Total Environ*, 659, 1335-1351. <https://doi.org/10.1016/j.scitotenv.2018.12.308>.
- Karnieli, A., Bayasgalan, M., Bayarjargal, Y., Agam, N., Khudulmur, S., & Tucker, C. J. (2006). Comments on the use of the Vegetation Health Index over Mongolia. *Int J Remote Sens*, 27(10), 2017-2024. <https://doi.org/10.1080/01431160500121727>.
- Kikon, N., Singh, P., Singh, S. K., & Vyas, A. (2016). Assessment of urban heat islands (UHI) of Noida City, India using multi-temporal satellite data. *Sustain Cities Soc*, 22, 19-28. <https://doi.org/10.1016/j.scs.2016.01.005>.
- Kumar, D., & Shekhar, S. (2015). Statistical analysis of land surface temperature-vegetation indexes relationship through thermal remote sensing. *Ecotox Environ Safe*, 121, 39-44. <https://doi.org/10.1016/j.ecoenv.2015.07.004>.
- Lambin, E. F., & Ehrlich, D. (1996). The Surface Temperature-Vegetation Index Space for Land Use and Land Cover Change analysis. *Int J Remote Sens*, 17, 463-487. <https://doi.org/10.1080/01431169608949021>.
- Li, J. (2006). Estimating land surface temperature from Landsat-5 TM. *Remote Sens Technol Appl*, 21, 322-326.
- Li, W. F., Cao, Q. W., Kun, L., & Wu, J. S. (2017). Linking potential heat source and sink to urban heat island: Heterogeneous effects of landscape pattern on land surface temperature. *Sci Total Environ*, 586, 457-465. <https://doi.org/10.1016/j.scitotenv.2017.01.191>.
- Liang, B. P., Li, Y., & Chen, K. Z. (2012). A Research on Land Features and Correlation between NDVI and Land Surface Temperature in Guilin City. *Remote Sens Tech Appl*, 27, 429-435.
- Marzban, F., Sodoudi, S., & Preusker, R. (2018). The influence of land-cover type on the relationship between LST-NDVI and LST-T<sub>air</sub>. *Int J Remote Sens*, 39(5), 1377-1398. <https://doi.org/10.1080/01431161.2017.1462386>.
- Mathew, A., Khandelwal, S., & Kaul, N. (2017). Investigating spatial and seasonal variations of urban heat island effect over Jaipur city and its relationship with vegetation, urbanization and elevation parameters. *Sustain Cities Soc*, 35, 157-177. <https://doi.org/10.1016/j.scs.2017.07.013>.

- Mathew, A., Khandelwal, S., & Kaul, N. (2018). Spatio-temporal variations of surface temperatures of Ahmedabad city and its relationship with vegetation and urbanization parameters as indicators of surface temperatures. *Remote Sens Appl Soc Environ*, 11, 119-139. <https://doi.org/10.1016/j.rsase.2018.05.003>.
- Mondal, A., Guha, S., Mishra, P. K., & Kundu, S. (2011). Land use/Land cover changes in Hugli Estuary using Fuzzy CMean algorithm. *Int J Geomat Geosci*, 2(2), 613-626.
- Moran, M. S., Clarke, T. R., Inouie, Y., & Vidal, A. (1994). Estimating Crop Water-Deficit using the Relation between Surface Air-Temperature and Spectral Vegetation Index. *Remote Sens Environ*, 49, 246-263. [https://doi.org/10.1016/0034-4257\(94\)90020-5](https://doi.org/10.1016/0034-4257(94)90020-5).
- Prehodko, L., & Goward, S. N. (1997). Estimation of Air Temperature from Remotely Sensed Surface Observations. *Remote Sens Environ*, 60, 335-346. [https://doi:10.1016/S0034-4257\(96\)00216-7](https://doi:10.1016/S0034-4257(96)00216-7).
- Qin, Z., Karnieli, A., & Barliner, P. (2001). A Mono-WindowAlgorithm for Retrieving Land Surface Temperature from Landsat TM Data and Its Application to the Israel-Egypt Border Region. *Int J Remote Sens*, 22(18), 3719-3746. <https://doi:10.1080/01431160010006971>.
- Qu, S., Wang, L., Lin, A., Yu, D., Yuan, M., & Li, C. (2020). Distinguishing the impacts of climate change and anthropogenic factors on vegetation dynamics in the Yangtze River Basin, China. *Ecol Indic*, 108, 105724. <https://doi.org/10.1016/j.ecolind.2019.105724>.
- Qu, S., Wang, L., Lin, A., Zhu, H., & Yuan, M. (2018). What drives thevegetation restoration in Yangtze River basin, China: Climate change or anthropogenic factors? *Ecol Indic*, 90, 438-450. <https://doi.org/10.1016/j.ecolind.2018.03.029>.
- Sandholt, I., Rasmussen, K., & Andersen, J. (2002). A simple interpretation of the Surface Temperature/Vegetation Index Space for Assessment of Surface Moisture Status. *Remote Sens Environ*, 79, 213-224. [https://doi.org/10.1016/s0034-4257\(01\)00274-7](https://doi.org/10.1016/s0034-4257(01)00274-7).
- Sannigrahi, S., Bhatt, S., Rahmat, S., Uniyal, B., Banerjee, S., Chakraborti, S., Jha, S., Lahiri, S., Santra, K., & Bhatt, A. (2018). Analyzing the role of biophysical compositions in minimizing urban land surface temperature and urban heating *Urban Climate*, 24, 803-819. <https://doi.org/10.1016/j.uclim.2017.10.002>.
- Sekertekin, A., & Bonafoni, S. (2020). Land surface temperature retrieval from landsat 5, 7, and 8 over rural areas: assessment of different retrieval algorithms and emissivity models and toolbox implementation. *Remote Sens*, 12(2), 294.
- Shigeto, K. (1994). Relation between vegetation, surface temperature, and surface composition in the Tokyo region during winter. *Remote Sens Environ*, 50(1), 52-60. [https://doi.org/10.1016/0034-4257\(94\)90094-9](https://doi.org/10.1016/0034-4257(94)90094-9)
- Singh, P., Kikon, N., & Verma, P. (2017). Impact of land use change and urbanization on urban heat island in Lucknow city, Central India. A remote sensing based estimate. *Sustain Cities Soc*, 32, 100-114. <https://doi.org/10.1016/j.scs.2017.02.018>.
- Sobrino, J. A., Jimenez-Munoz, J. C., & Paolini, L. (2004). Land surface temperature retrieval from Landsat TM5. *Remote Sens Environ*, 90(4), 434-440. <https://doi.org/10.1016/j.rse.2004.02.003>.
- Sun, D., & Kafatos, M. (2007). Note on the NDVI-LST Relationship and the Use of Temperature-Related Drought Indices over North America. *Geophys Res Lett*, 34(24), L24406. <http://doi.org/10.1029/2007GL031485>.
- Sun, Q., Tan, J., & Xu, Y. (2010). An ERDAS image processing method for retrieving LST and describing urban heat evolution: A case study in the Pearl River Delta Region in South China. *Environ Earth Sci*, 59, 1047-1055. <https://doi.org/10.1007/s12665-009-0096-3>.
- Tomlinson, C. J., Chapman, L., Trones, J. E., & Baker, C. (2011). Remote sensingland surface temperature for meteorology and climatology: a review. *Meteorol Appl*, 18, 296-306. <https://doi.org/10.1002/met.287>.
- Tucker, C. J. (1979). Red and photographic infrared linear combinations for monitoring vegetation. *Remote Sens Environ*, 8(2), 127-150.
- USGS: Science for a Changing World. *EarthExplorer*. Retrieved from <https://www.earthexplorer.usgs.gov>
- Voogt, J. A., & Oke, T. R. (2003). Thermal Remote Sensing of Urban Climates. *Remote Sens Environ*, 86, 370-384. [https://doi.org/10.1016/S0034-4257\(03\)00079-8](https://doi.org/10.1016/S0034-4257(03)00079-8).

- Wang, J., Qingming, Z., Guo, H., & Jin, Z. (2016). Characterizing the spatial dynamics of land surface temperature–impervious surface fraction relationship. *Int J Appl Earth Obs Geoinf*, 45, Part-A, 55–65. <https://doi.org/10.1016/j.jag.2015.11.006>.
- Wang, L., Lu, Y., & Yao, Y. (2019). Comparison of three algorithms for the retrieval of land surface temperature from Landsat 8 images. *Sensors*, 19(22), 5049.
- Wen, L., Peng, W., Yang, H., Wang, H., Dong, L., & Shang, X. (2017). An analysis of land surface temperature (LST) and its influencing factors in summer in western Sichuan Plateau: A case study of Xichang City. *Remote Sens Land Res*, 29(2), 207–214. <https://doi.org/10.6046/gtzyyg.2017.02.30>.
- Wukelic, G. E., Gibbons, D. E., Martucci, L. M., & Foote, H. P. (1989). Radiometric calibration of Landsat Thematic Mapper thermal band. *Remote Sens Environ*, 28, 339–347.
- Yang, J., & Qiu, J. (1996). The empirical expressions of the relation between precipitable water and ground water vapor pressure for some areas in China. *Sci Atmos Sinica*, 20, 620-626.
- Yao, R., Cao, J., Wang, L., Zhang, W., & Wu, X. (2019). Urbanization effects on vegetation cover in major African cities during 2001-2017. *Int J Appl Earth Obs*, 75, 44-53. <https://doi.org/10.1016/j.jag.2018.10.011>.
- Yao, R., Wang, L., Gui, X., Zheng, Y., Zhang, H., & Huang, X. (2017). Urbanization Effects on Vegetation and Surface Urban Heat Islands in China’s Yangtze River Basin. *Remote Sens*, 9(6), 540. <https://doi.org/10.3390/rs9060540>.
- Yao, R., Wang, L., Huang, X., Chen, J., Li, J., & Niu, Z. (2018). Less sensitive of urban surface to climate variability than rural in Northern China. *Sci Total Environ*, 628-629, 650-660. <https://doi.org/10.1016/j.scitotenv.2018.02.087>.
- Yao, R., Wang, L., Huang, X., Chen, X., & Liu, Z. (2019). Increased spatial heterogeneity in vegetation greenness due to vegetation greening in mainland China. *Ecol Indic*, 99, 240-250. <https://doi.org/10.1016/j.ecolind.2018.12.039>.
- Yao, R., Wang, L., Huang, X., Niu, Z., Liu, F., & Wang, Q. (2017). Temporal trends of surface urban heat islands and associated determinants in major Chinese cities. *Sci Total Environ*, 609, 742-754. <https://doi.org/10.1016/j.scitotenv.2017.07.217>.
- Yao, R., Wang, L., Huang, X., Zhang, W., Li, J., & Niu, Z. (2018). Interannual variations in surface urban heat island intensity and associated drivers in China. *J Environ Manage*, 222, 86-94. <https://doi.org/10.1016/j.jenvman.2018.05.024>.
- Yuan, M., Wang, L., Lin, A., Liu, Z., & Qu, S. (2020). Vegetation green up under the influence of daily minimum temperature and urbanization in the Yellow River Basin, China. *Ecol Indic*, 108, 105760. <https://doi.org/10.1016/j.ecolind.2019.105760>.
- Yuan, X., Wang, W., Cui, J., Meng, F., Kurban, A., & De Maeyer, P. (2017). Vegetation changes and land surface feedbacks drive shifts in local temperatures over Central Asia. *Sci Rep*, 7(1), 3287. <https://doi.org/10.1038/s41598017034322>.
- Yue, W., Xu, J., Tan, W., & Xu, L. (2007). The Relationship between Land Surface Temperature and NDVI with Remote Sensing. Application to Shanghai Landsat 7 ETM+ data. *Int J Remote Sens*, 28, 3205–3226. <https://doi.org/10.1080/01431160500306906>.
- Zanter, K. (2019). *Landsat 8 (L8) Data Users Handbook*. EROS, Sioux Falls, SD, USA.

---

**Editor:** Fábio Duarte

Received: Sep. 25<sup>th</sup>, 2020

Approved: Jun. 30<sup>th</sup>, 2021



# Source details

[Feedback >](#) [Compare sources >](#)

## Urbe

Open Access [i](#)

Scopus coverage years: from 2015 to 2023

Publisher: Editora Champagnat

E-ISSN: 2175-3369

Subject area: [Engineering: Architecture](#) [Social Sciences: Urban Studies](#) [Social Sciences: Geography, Planning and Development](#)

Source type: Journal

[View all documents >](#)

[Set document alert](#)

[Save to source list](#)

CiteScore 2022

0.7



SJR 2022

0.177



SNIP 2022

0.302



CiteScore

[CiteScore rank & trend](#)

[Scopus content coverage](#)



## A long-term monthly analytical study on the relationship of LST with normalized difference spectral indices

Subhanil Guha & Himanshu Govil

To cite this article: Subhanil Guha & Himanshu Govil (2021) A long-term monthly analytical study on the relationship of LST with normalized difference spectral indices, European Journal of Remote Sensing, 54:1, 487-511, DOI: [10.1080/22797254.2021.1965496](https://doi.org/10.1080/22797254.2021.1965496)

To link to this article: <https://doi.org/10.1080/22797254.2021.1965496>



© 2021 The Author(s). Published by Informa UK Limited, trading as Taylor & Francis Group.



Published online: 30 Aug 2021.



Submit your article to this journal [↗](#)





View related articles [↗](#)



View Crossmark data [↗](#)

## A long-term monthly analytical study on the relationship of LST with normalized difference spectral indices

Subhanil Guha  and Himanshu Govil 

Department of Applied Geology, National Institute of Technology Raipur, Raipur, Chhattisgarh, India

### ABSTRACT

This study analyzes the long-term monthly variation of land surface temperature (LST) and its relationship with normalized difference vegetation index (NDVI), normalized difference water index (NDWI), normalized difference built-up index (NDBI), and normalized difference bareness index (NDBal) in the Raipur City of India using one hundred and twenty-three Landsat images from 1988–2020. In terms of LST, the warmest month is April (38.49°C) and the coldest month is January (23.04°C). The standard deviation in LST is noticed as 1.1022°C throughout the period. The growth pattern of LST is increasing in the earlier stage while it is steady and decreasing in the later stage. The mean linear regression coefficients for LST-NDVI is -0.42, LST-NDBI are 0.68, LST-NDWI is 0.27, and LST-NDBal is 0.32. It indicates that the high ratio of green vegetation and water bodies resist the raise of LST, whereas the bare rock surface and built-up land accelerate the LST. The value of the spectral indices and LST varies with the change of month due to the physical change of the land surface materials. Hence, the study will be an effective one for the town and country planners for their future estimation of land conversion.

### ARTICLE HISTORY

Received 14 December 2020  
Revised 24 May 2021  
Accepted 4 August 2021

### KEYWORDS

Land surface temperature (LST); normalized difference bareness index (NDBal); normalized difference built-up index (NDBI); normalized difference vegetation index (NDVI); normalized difference water index (NDWI)

### Introduction

Urbanization accelerates the ecological stress by warming the local or global cities for a large extent (Foley et al., 2005; Fu & Weng, 2016; Grimm et al., 2008; Liu et al., 2018; Peng et al., 2018a). Presently, many urban areas are suffering with a huge land conversion and resultant new heat zones (Huang et al., 2009; Patz et al., 2005; Zhou et al., 2019). Remote sensing techniques are significantly effective in detecting the land use/land cover (LULC) change and its consequences (Guha et al., 2018). Apart from the conventional LULC classification algorithms, some spectral indices are used in detecting specific land features. Recently, thermal infrared (TIR) bands are used by generating some indices for different types of LULC extraction (Kalnay & Cai, 2003; Peng et al., 2018b; X-L. Chen et al., 2006). These remote sensing indices are used significantly in various application fields like rocks and mineral mapping, forest mapping, agricultural monitoring, LULC mapping, hazard mapping, urban heat island mapping, and monitoring (Berger et al., 2017; Chen et al., 2006; Du et al., 2016; He et al., 2019; Peng et al., 2016).

Land surface temperature (LST) retrieved from various remotely-sensed data is widely used in the detection of urban heat island and ecological comfort zone (Fu & Weng, 2015; Hao et al., 2016; Tomlinson et al., 2011; Tran et al., 2017; Weng, 2009). LST can be changed significantly in a vast homogeneous land

surface or even inside a relatively small heterogeneous urban area (Hou et al., 2010; X-L. Chen et al., 2006). Different types of LULC response differently in TIR band and consequently LST largely varies in an urban environment (Estoque et al., 2017; Ghobadi et al., 2014; Li et al., 2016; Shigeto, 1994; Stroppiana et al., 2014; Yue et al., 2007). The LULC types are mainly changed by land conversion process. Thus, time is an important factor in LST monitoring. These spatial and temporal data of LST is also varied with the seasonal changes as sun elevation and sun azimuth are changed with seasons. Hence, the seasonal variation of LST is quite important in any LULC related study.

Most popular index for vegetation is normalized difference vegetation index (NDVI) that is invariably used in LST-related studies from the very beginning (Tucker, 1979; Smith & Choudhury, 1990; Hope & McDowell, 1992; Julien, ; Yuan et al., 2017). NDVI is directly used in the determination of land surface emissivity and thus is a significant factor for LST estimation (Carlson & Ripley, 1997; Sobrino et al., 2004). Generally, the nature of LST–NDVI relationship in a region is negative and is controlled by a number of factors, such as, dry or wet vegetation, greenness of vegetation, air pollution, moisture content in air, heterogeneous man-made materials, dry or wet soil, etc. (Ghobadi et al., 2014; Qu et al., 2014; Zhou et al., 2011). In mixed urban land, high LST is related to low vegetal covered area (Voogt & Oke,

2003). NDVI depends on the method that computes LST (e.g., NDVI threshold method) (Goward et al., 2002) and many studies based on the LST-NDVI correlation (Gutman & Ignatov, 1998; Weng et al., 2004) are available to explore the pattern of LST. There are so many valuable research articles found on LST-NDVI relationships were conducted mainly in the Indian and Chinese landscape (Guha et al., 2020; Gui et al., 2019; Kikon et al., 2016; Kumar & Shekhar, 2015; Qu et al., 2020; Yuan et al., 2020). Normalized difference water index (NDWI) is the most popular index for extraction of water bodies and it is considerably used in LULC and LST related studies (Essa et al., 2012; McFeeters, 1996; X-L. Chen et al., 2006; Yuan et al., 2017). Generally, the nature of LST-NDWI relationship in an urban area is insignificant which is controlled by several factors, such as humidity, vegetation, wetland, bare land, air pollution, rock surface, dry or wet soil, heterogeneous man-made materials, etc. (Ghobadi et al., 2014; McFeeters, 1996, 2013). Normalized difference built-up index (NDBI) is the most popular built-up index which is invariably used in LST-related studies (Chen et al., 2013; Yuan et al., 2017; Zha et al., 2003). Generally, the nature of LST-NDBI relationship in a region is positive and is controlled by several factors, such as humidity, vegetation, air pollution, rock surface, dry or wet soil, heterogeneous man-made materials, etc. (Ghobadi et al., 2014). Normalized difference bareness index (NDBaI) is the most popular index for bare land extraction that is invariably used in LULC and LST-related studies as it builds a positive relationship in tropical environment (Essa et al., 2012; L Chen et al., 2013; X-L. Chen et al., 2006; Weng & Quattrochi, 2006; Yuan et al., 2017; Zhao & Chen, 2005). Moreover, the dependence on LST of different land covers and the relation of LST with different indices has also been discussed together in some previous works (Bala et al., 2020, 2021).

However, these abovementioned research works mostly performed on temporal or seasonal analysis of the relationship. Number of research works conducted on monthly analysis of LST-spectral indices relationship is rare in any physical environment. Hence, it is a necessary task to build month-wise LST-spectral indices correlation for the sustainable development of town and country planning as the values of the LST and spectral indices change with the change of months due to the different climatic and biophysical factors. The study was conducted on Raipur City of India as it is a smart growing city with a moderate climatic condition. However, the strength of the LST-spectral indices relationship can change temporally, seasonally, and spatially. The relationship is changed with time as the land surface materials change with time. The relationship also depends on

the LULC types as vegetation, soil, water, or built-up area change the values of spectral indices as well as LST. Different seasons also play a significant role in the LST-spectral indices relationship as the growth of vegetation and increase of LST primarily depend on seasonal change. However, no specific conclusion can be drawn on LST-spectral indices relationship for a small number of remotely-sensed data. Thus, long-term Landsat data sets are necessary to obtain a reliable result on this relationship. The present study analyzes the nature, strength, and trend of the effect of LST on NDVI, NDWI, NDBI, and NDBaI.

### Study area and data

Raipur City is located in between 21°11'22"N to 21°20'02"N and 81°32'20"E to 81°41'50"E (Figure 1). Figure 1(a) presents the outline map of India where Chhattisgarh State is located in the middle part (Source: Survey of India). (Figure 1(b)) presents the outline map of Chhattisgarh State with districts (Source: Survey of India). (Figure 1(c)) represents the false colour composite (FCC) image of Raipur City from recent Landsat data. (Figure 1(d)) indicates the contour map of Raipur (Date: 11 October 2011) of Raipur City (Source: USGS). The total area covers around 165 km<sup>2</sup>. The southern part of the city is covered by dense forests. The Mahanadi River flows along the western side of the city. The elevation is higher in the middle part of the city compared to the outer part. The climate of the city is considered as dry and wet savannah climate (source: India Meteorological Department (IMD)). Four types of seasons are observed in Raipur, i.e., monsoon (June–September), pre-monsoon (March–May), post-monsoon (October–November), and winter (December–February). The mean annual temperature ranges from 12°C (December) to 42°C (May). The temperature often rises above 45°C in April and May. November to April remains almost dry (average rainfall <50 mm) compared to the June to September (average rainfall >200 mm). The study area is also characterized by tropical mixed deciduous vegetation and mixed red soil. The city has a widely diverse population that migrated from the different parts of the country. The city is considered as one of the fastest-growing smart cities in India.

A total of 123 cloud-free (<10% cloud coverage) Landsat TM, ETM+, and OLI/TIRS data from 1988 to 2020 were freely downloaded from the USGS Data Centre to conduct the whole study (<https://www.earthexplorer.usgs.gov>). These satellite images were taken between 10th and 25th day of each and every month to obtain the minimum range of deviation in LST values. Moreover, only a single image can obtain between



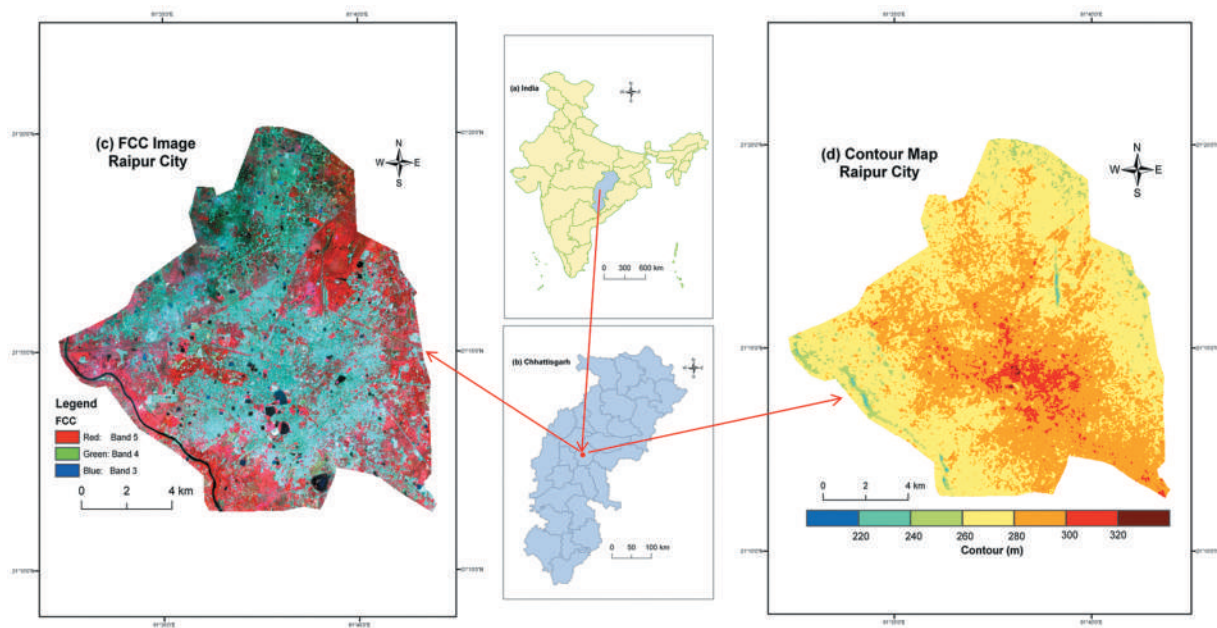


**Figure 1.** The study area: (a) Chhattisgarh state in India (b) Raipur city in Chhattisgarh (c) FCC image of raipur (d) contour map of raipur.

10th and 25th day of any month due to the 16 days temporal resolution of Landsat satellite sensors. These satellite images have been radiometrically and geometrically corrected. All the TIR bands of OLI/TIRS, TM, and ETM+ data were resampled to 30 m resolution by USGS data centre using cubic convolution resampling method.

## Methodology

### LST estimation from Landsat satellite sensors

Many LST retrieval methods are applicable for different satellite sensors. The mono-window algorithm (García-Santos et al., 2018; Gui et al., 2019; Qin et al., 2001; Sekertekin and Bonafoni, 2020; Yang et al., 2014), single-channel algorithm (Jiménez-Muñoz and Sobrino, 2003; Jiménez-Muñoz et al., 2009; Coll et al., 2010; Chatterjee et al., 2017), split-window algorithm (McMillin, 1975; Price, 1984; Becker and Li, 1990), and radiative transfer equation (C Qu et al., 2014) are the main well-known LST retrieval algorithms using Landsat thermal bands (Weng, 2001; Weng et al., 2004; Zhang et al., 2016). Despite giving a good result, the radiative transfer algorithm cannot be applicable without *in situ* parameters of atmospheric profile at the satellite pass. The actual measurement with infrared thermometer has not been applied to verify the results of the study due to some unavoidable circumstances. Although the split-window algorithm gives the accurate result, it was not used in the study as only band 10 of Landsat 8 OLI/TIRS data was selected for LST generation due to its better calibration (Barsi et al., 2014). The mono-window algorithm and single-channel algorithm also

provide good results. In this study, the mono-window algorithm was applied to retrieve LST from multi-temporal Landsat satellite images. Ground emissivity, atmospheric transmittance, and effective mean atmospheric temperature – these three parameters are needed to derive the LST using the mono-window algorithm. At first, the original TIR bands (100 m resolution for Landsat 8 OLI/TIRS data, 120 m resolution for Landsat 5 TM data, and 60 m resolution for Landsat 7 ETM+ data) were resampled into 30 m by USGS data centre for further application.

The TIR pixel values are firstly converted into radiance from digital number (DN) values. Band 10 of Landsat 8 data was used as TIR band for its better calibration (Barsi et al., 2014). Radiance for TIR bands of Landsat 5 TM data and Landsat 7 ETM+ data are obtained using Eq. (1) (USGS):

$$L_{\lambda} = \left[ \frac{L_{MAX\lambda} - L_{MIN\lambda}}{QCAL_{MAX} - QCAL_{MIN}} \right] * [QCAL - QCAL_{MIN}] + L_{MIN\lambda} \quad (1)$$

where  $L_{\lambda}$  is Top of Atmosphere (TOA) spectral radiance ( $Wm^{-2}sr^{-1}mm^{-1}$ ),  $QCAL$  is the quantized calibrated pixel value in DN,  $L_{MIN\lambda}$  ( $Wm^{-2}sr^{-1}mm^{-1}$ ) is the spectral radiance scaled to  $QCAL_{MIN}$ ,  $L_{MAX\lambda}$  ( $Wm^{-2}sr^{-1}mm^{-1}$ ) is the spectral radiance scaled to  $QCAL_{MAX}$ ,  $QCAL_{MIN}$  is the minimum quantized calibrated pixel value in DN and  $QCAL_{MAX}$  is the maximum quantized calibrated pixel value in DN.  $L_{MIN\lambda}$ ,  $L_{MAX\lambda}$ ,  $QCAL_{MIN}$ , and  $QCAL_{MAX}$  values are obtained from the metadata file of Landsat 5 TM data and Landsat 7 ETM+ data. Radiance for Landsat 8 TIR band is obtained from Eq. (2) (Zanter, 2019):

$$L_\lambda = M_L \cdot Q_{CAL} + A_L \quad (2)$$

where  $L_\lambda$  is the TOA spectral radiance ( $\text{Wm}^{-2}\text{sr}^{-1}\text{mm}^{-1}$ ),  $M_L$  is the band-specific multiplicative rescaling factor from the metadata,  $A_L$  is the band-specific additive rescaling factor from the metadata,  $Q_{CAL}$  is the quantized and calibrated standard product pixel values (DN). All of these variables can be retrieved from the metadata file of Landsat 8 data.

For Landsat 5 and Landsat 7 data, the reflectance value is obtained from radiances using Eq. (3) (USGS):

$$\rho_\lambda = \frac{\pi \cdot L_\lambda \cdot d^2}{ESUN_\lambda \cdot \cos \theta_s} \quad (3)$$

where  $\rho_\lambda$  is unitless planetary reflectance,  $L_\lambda$  is the TOA spectral radiance ( $\text{Wm}^{-2}\text{sr}^{-1}\mu\text{m}^{-1}$ ),  $d$  is Earth-Sun distance in astronomical units,  $ESUN_\lambda$  is the mean solar exo-atmospheric spectral irradiances ( $\text{Wm}^{-2}\mu\text{m}^{-1}$ ) and  $\theta_s$  is the solar zenith angle in degrees.  $ESUN_\lambda$  values for each band of Landsat 5 and Landsat 7 data can be obtained from the handbooks of the related mission.  $\theta_s$  and  $d$  values can be attained from the metadata file.

For Landsat 8 data, reflectance conversion can be applied to DN values directly as in Eq. (4) (Zanter, 2019):

$$\rho_\lambda = \frac{M_p \cdot Q_{CAL} + A_p}{\sin \theta_{SE}} \quad (4)$$

where  $M_p$  is the band-specific multiplicative rescaling factor from the metadata,  $A_p$  is the band-specific additive rescaling factor from the metadata,  $Q_{CAL}$  is the quantized and calibrated standard product pixel values (DN) and  $\theta_{SE}$  is the local sun elevation angle from the metadata file.

Eq. (5) is used to convert the spectral radiance to at-sensor brightness temperature (Wukelic et al., 1989; X-L. Chen et al., 2006):

$$T_b = \frac{K_2}{\ln\left(\frac{K_1}{L_\lambda} + 1\right)} \quad (5)$$

where  $T_b$  is the brightness temperature in Kelvin (K),  $L_\lambda$  is the spectral radiance in  $\text{Wm}^{-2}\text{sr}^{-1}\text{mm}^{-1}$ ;  $K_2$  and  $K_1$  are calibration constants. For Landsat 8 data,  $K_1$  is 774.89,  $K_2$  is 1321.08 ( $\text{Wm}^{-2}\text{sr}^{-1}\text{mm}^{-1}$ ). For Landsat 7 data,  $K_1$  is 666.09,  $K_2$  is 1282.71 ( $\text{Wm}^{-2}\text{sr}^{-1}\text{mm}^{-1}$ ). For Landsat 5 data,  $K_1$  is 607.76,  $K_2$  is 1260.56 ( $\text{Wm}^{-2}\text{sr}^{-1}\text{mm}^{-1}$ ).

The land surface emissivity  $\varepsilon$ , is estimated from Eq. (6) using the NDVI Thresholds Method (Sobrino et al., 2004, 2001).

$$\varepsilon = \varepsilon_v F_v + \varepsilon_s (1 - F_v) + d\varepsilon \quad (6)$$

where,  $\varepsilon$  is land surface emissivity,  $\varepsilon_v$  is vegetation emissivity,  $\varepsilon_s$  is soil emissivity,  $F_v$  is fractional vegetation,  $d\varepsilon$  is the effect of the geometrical distribution of

the natural surfaces and internal reflections that can be expressed by Eq. (7):

$$d\varepsilon = (1 - \varepsilon_s)(1 - F_v)F\varepsilon_v \quad (7)$$

where  $\varepsilon_v$  is vegetation emissivity,  $\varepsilon_s$  is soil emissivity,  $F_v$  is fractional vegetation,  $F$  is a shape factor whose mean is 0.55, the value of  $d\varepsilon$  maybe 2% for mixed land surfaces (Sobrino et al., 2004).

The fractional vegetation  $F_v$ , of each pixel, is determined from the NDVI using Eq. (8) (Carlson & Ripley, 1997):

$$F_v = \left( \frac{NDVI - NDVI_{min}}{NDVI_{max} - NDVI_{min}} \right)^2 \quad (8)$$

where (a)  $NDVI < 0.2$  for bare soil; (b)  $NDVI > 0.5$  for vegetation; (c)  $0.2 < NDVI < 0.5$  for mixed land with bare soil and vegetation (Sobrino et al., 2004, 2001).

Finally, the land surface emissivity  $\varepsilon$  can be expressed by Eq. (9):

$$\varepsilon = 0.004 * F_v + 0.986 \quad (9)$$

where  $\varepsilon$  is land surface emissivity,  $F_v$  is fractional vegetation.

Water vapour content is estimated by Eq. (10) (X-L. Chen et al., 2006; Yang & Qiu, 1996):

$$w = 0.0981 * \left[ 10 * 0.6108 * \exp\left(\frac{17.27 * (T_0 - 273.15)}{237.3 + (T_0 - 273.15)}\right) * RH \right] + 0.1697 \quad (10)$$

where  $w$  is the water vapour content ( $\text{g/cm}^2$ ),  $T_0$  is the near-surface air temperature in Kelvin (K),  $RH$  is the relative humidity (%). These parameters of atmospheric profile are obtained from the Meteorological Centre, Raipur (<http://www.imdraipur.gov.in>). Atmospheric transmittance is determined for Raipur City using Eq. (11) and Table 2 (Qin et al., 2001; Sun et al., 2010):

$$\tau = 1.031412 - 0.11536w \quad (11)$$

where  $\tau$  is the total atmospheric transmittance,  $w$  is the water vapour content ( $\text{g/cm}^2$ ).

Raipur City is located in the tropical region. Thus, Eq. (12) is applied to compute the effective mean atmospheric transmittance of Raipur (Qin et al., 2001; Sun et al., 2010):

$$T_a = 17.9769 + 0.91715T_0 \quad (12)$$

LST is retrieved from Landsat 5 TM and Landsat 8 OLI/TIRS satellite data by using Eq. (13–15) (Qin et al., 2001):

$$T_s = \frac{[a(1-C-D) + (b(1-C-D) + C + D)T_b - DT_a]}{C} \tag{13}$$

$$C = \epsilon\tau \tag{14}$$

$$D = (1 - \tau)[1 + (1 - \epsilon)\tau] \tag{15}$$

where  $\epsilon$  is the land surface emissivity,  $\tau$  is the total atmospheric transmittance,  $C$  and  $D$  are internal parameters based on atmospheric transmittance and land surface emissivity,  $T_b$  is the at-sensor brightness temperature,  $T_a$  is the mean atmospheric temperature,  $T_0$  is the near-surface air temperature,  $T_s$  is the LST,  $a = -67.355351$ ,  $b = 0.458606$ .

**Determination of NDVI, NDWI, NDBI, and NDBaI**

In this study, special emphasis was given on NDVI (Ke et al., 2015; Purevdorj et al., 1998; Tucker, 1979), NDWI (McFeeters, 1996, 2013), NDBI (Zha et al., 2003), and NDBaI (Zhao & Chen, 2005) for determining the relationship with LST. NDVI is a vegetation index used in LULC-related study and the determination of fractional vegetation. NDWI is a water index used to distinguish the water bodies from the wetland and moist soil. NDBI is a built-up index used in detecting the built-up areas and it is frequently used by the urban geographers in land use study. NDBaI is a bareness index used to differentiate the bare

**Table 1.** Description of NDVI, NDWI, NDBI, and NDBaI.

Acronym	Description	Formulation	References
NDVI	Normalized difference vegetation index	$\frac{NIR - Red}{NIR + Red}$	Tucker, 1979
NDWI	Normalized difference water index	$\frac{Green - NIR}{Green + NIR}$	McFeeters, 1996
NDBI	Normalized difference built-up index	$\frac{SWR1 - NIR}{SWR1 + NIR}$	Zha et al., 2003
NDBaI	Normalized difference bareness index	$\frac{SWR1 - TIR}{SWR1 + TIR}$	Zhao & Chen, 2005

lands from semi-bare lands and other LULC types. The band combinations of these spectral indices were given in Table 1. The value of any normalized difference spectral index is ranged between -1 and +1. Various types of LULC can be estimated by using the threshold limits of these normalized difference spectral indices (Table 1). Generally, in the tropical city, the positive value of NDVI, NDWI, NDBI, and NDBaI indicates the vegetation surface, water surface, built-up surface, and bare land surface, respectively (X-L. Chen et al., 2006).

**Results and discussion**

**Monthly variation in LST distribution**

Table 2 shows a clear observation of monthly change in the mean LST values. April (38.49°C) shows the highest mean monthly temperature while January

**Table 2.** Monthly distribution of LST (°C) from 1988 to 2020.

January	LST (°C)	February	LST (°C)	March	LST (°C)	April	LST (°C)	May	LST (°C)
1988-Jan-21	24.52	1989-Feb-24	28.31	1989-Mar-12	28.14	1990-Apr-16	40.87	1991-May-21	36.63
1990-Jan-10	24.42	1990-Feb-11	25.26	1990-Mar-15	30.96	1992-Apr-21	41.19	2002-May-11	40.92
1992-Jan-16	21.33	1991-Feb-14	23.98	1991-Mar-18	29.50	1995-Apr-14	34.63	2004-May-24	40.74
1993-Jan-18	23.41	1992-Feb-17	25.30	1992-Mar-20	32.84	2001-Apr-22	41.34	2005-May-11	38.72
1996-Jan-27	22.08	1993-Feb-19	28.42	2003-Mar-11	29.49	2002-Apr-25	38.85	2006-May-14	28.43
2005-Jan-19	22.08	2002-Feb-20	30.39	2004-Mar-21	36.48	2003-Apr-12	31.28	2007-May-17	36.20
2007-Jan-25	26.37	2004-Feb-18	26.64	2007-Mar-14	27.57	2004-Apr-22	36.80	2008-May-19	38.36
2009-Jan-14	17.15	2006-Feb-23	32.95	2009-Mar-19	33.79	2009-Apr-20	39.74	2009-May-22	33.20
2011-Jan-20	23.03	2009-Feb-15	31.01	2014-Mar-17	31.68	2010-Apr-23	40.63	2010-May-25	36.11
2015-Jan-15	23.49	2010-Feb-18	22.67	2015-Mar-20	32.83	2016-Apr-23	42.97	2011-May-12	39.80
2018-Jan-23	25.26	2015-Feb-16	29.75	2016-Mar-22	37.00	2017-Apr-10	38.37	2011-May-17	40.28
2020-Jan-13	23.24	2016-Feb-19	24.60	2017-Mar-25	37.06	2020-Apr-18	33.47	2014-May-20	34.91
		2017-Feb-21	32.45	2018-Mar-12	30.09			2015-May-23	36.42
		2018-Feb-24	31.05	2020-Mar-17	27.66			2016-May-25	37.22
		2019-Feb-11	25.37					2017-May-12	33.33
		1989-Feb-24	28.31					2018-May-15	31.42
		2020-Feb-14	27.58					2019-May-18	40.21
<i>Mean</i>	<i>23.04</i>	<i>Mean</i>	<i>27.86</i>	<i>Mean</i>	<i>31.80</i>	<i>Mean</i>	<i>38.49</i>	<i>Mean</i>	<i>36.64</i>
June	LST (°C)	September	LST (°C)	October	LST (°C)	November	LST (°C)	December	LST (°C)
2005-Jun-12	38.66	1996-Sep-23	24.09	1988-Oct-19	28.86	1988-Nov-20	24.27	1988-Dec-22	23.96
2006-Jun-15	35.43	2001-Sep-21	26.13	1991-Oct-12	24.98	1989-Nov-23	25.16	1992-Dec-17	22.34
2009-Jun-23	33.05	2002-Sep-16	28.81	1992-Oct-14	24.61	1991-Nov-13	23.64	1994-Dec-23	18.55
2018-Jun-16	31.08	2014-Sep-25	29.67	1996-Oct-25	22.56	1993-Nov-18	24.47	1995-Dec-10	21.49
				2001-Oct-15	30.12	1996-Nov-10	23.15	2000-Dec-15	26.81
				2001-Oct-23	26.85	1999-Nov-11	29.16	2002-Dec-21	27.09
				2004-Oct-15	27.56	2004-Nov-16	28.45	2004-Dec-18	25.76
				2006-Oct-21	26.30	2005-Nov-19	26.72	2006-Dec-24	23.35
				2009-Oct-13	27.10	2006-Nov-22	26.40	2008-Dec-13	25.71
				2011-Oct-19	28.30	2008-Nov-11	27.38	2009-Dec-16	23.59
				2015-Oct-14	27.61	2013-Nov-25	26.09	2010-Dec-19	22.31
				2016-Oct-16	30.02	2014-Nov-12	23.47	2013-Dec-11	24.62
				2018-Oct-22	29.01	2016-Nov-17	27.18	2016-Dec-19	24.60
						2017-Nov-20	26.28	2017-Dec-22	24.02
						2019-Nov-10	25.60	2018-Dec-25	21.17
								2019-Dec-12	24.74
<i>Mean</i>	<i>34.56</i>	<i>Mean</i>	<i>27.18</i>	<i>Mean</i>	<i>27.22</i>	<i>Mean</i>	<i>25.83</i>	<i>Mean</i>	<i>23.76</i>

(23.04°C) shows the lowest mean monthly temperature from 1988 to 2020.

(Figure 2–11)) show the spatial distribution maps of Raipur City in different months from 1988 to 2020. It is seen from (Figure 2–11)) that >90% area of the city was above 32°C mean LST in March–May of 1992, 2001–2002, 2004–2005, 2008–2011, 2013, 2016–2017, and 2019 (Figure 2–4)). In June and September, 2005, 2006, and 2009 have mean LST values more than the earlier or later years (Figure 5–6)). The scenario was completely different in October to February (Figure 7–11)), where <10% area of the city was above 32°C LST. April (38.49°C mean LST), May (36.65°C mean LST), June (34.56°C mean LST), and March (31.80°C mean LST) – these four months have an average value of >30°C mean LST throughout the entire period of study. February (27.86°C mean LST), October (27.23°C mean LST), September (27.18°C mean LST), and November (25.83°C mean LST) – these four months have an average value of 25–28°C mean LST throughout the entire time. Only December (23.76°C mean LST) and January (23.04°C mean LST) months have an average value of <24°C mean LST for the entire period. The average value of the highest and the lowest mean LST from 1988 to 2020 is observed in April and January, respectively. The northwest and southeast parts of the study area exhibit

high LST. These parts also have a low percentage of urban vegetation and a high percentage of built-up area and bare land. It shows that the proportion of vegetation was reduced significantly with time.

Figure 12 shows the line graph of LST in different months from 1988 to 2019. October, November, and December present almost similar pattern of LST distribution. January and February show almost similar trend in their LST graph. A similarity also has been seen in the mean LST graph of March, April, and May. The LST graph of June shows a negative trend, while September shows a positive trend.

Figure 13 shows the mean monthly variation of LST (°C) during the study. The mean LST graph is sharply rising from January to April. After that, the graph is gently falling from April to June. A sharp fall is also noticed from June to September. One fact should be remembered that there was no data available for July and August; otherwise the falling trend might be gentle. From September to December the LST graph falls continuously.

### Monthly analysis on LST–spectral indices relationship

Table 3 represents a monthly variation of Pearson's linear correlation method between LST and NDVI. In

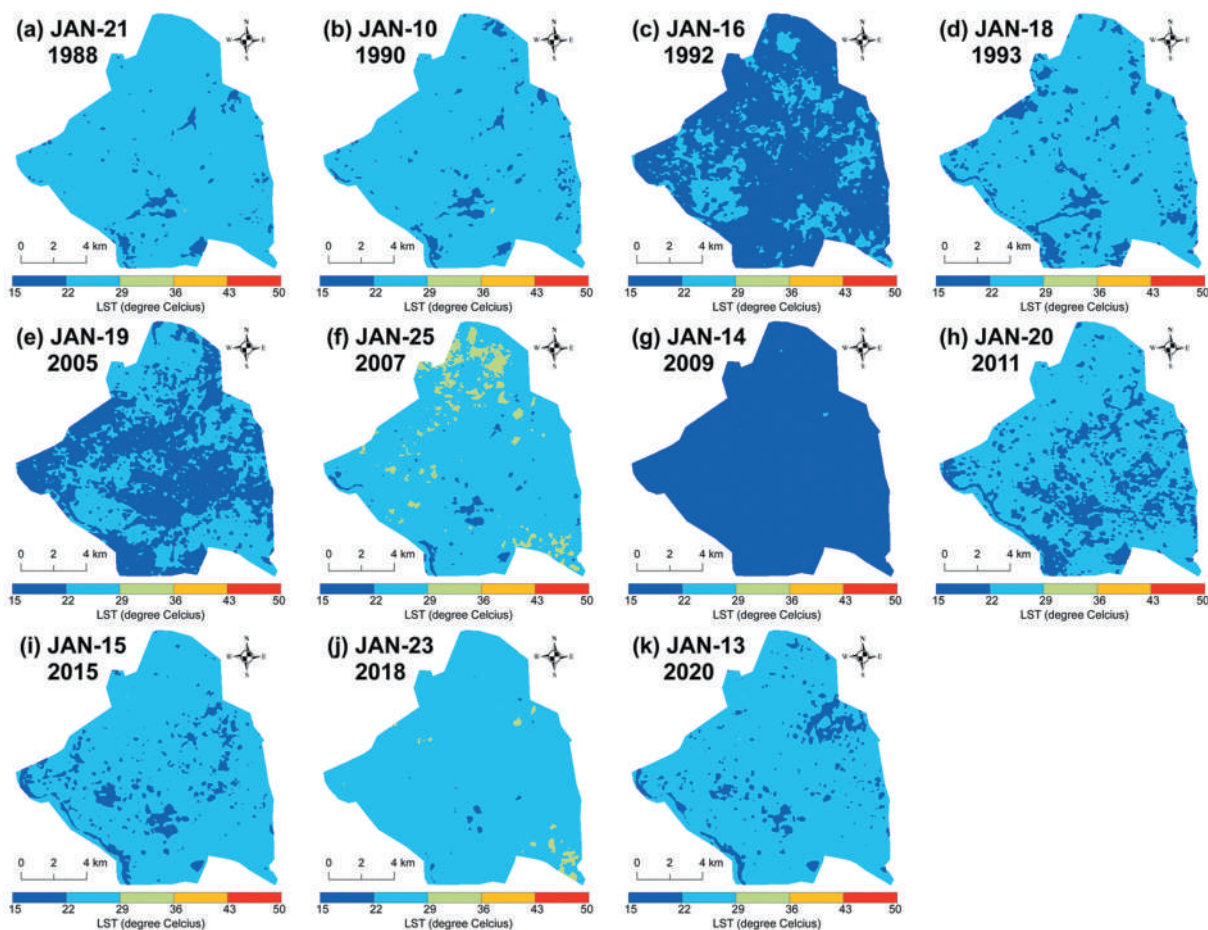
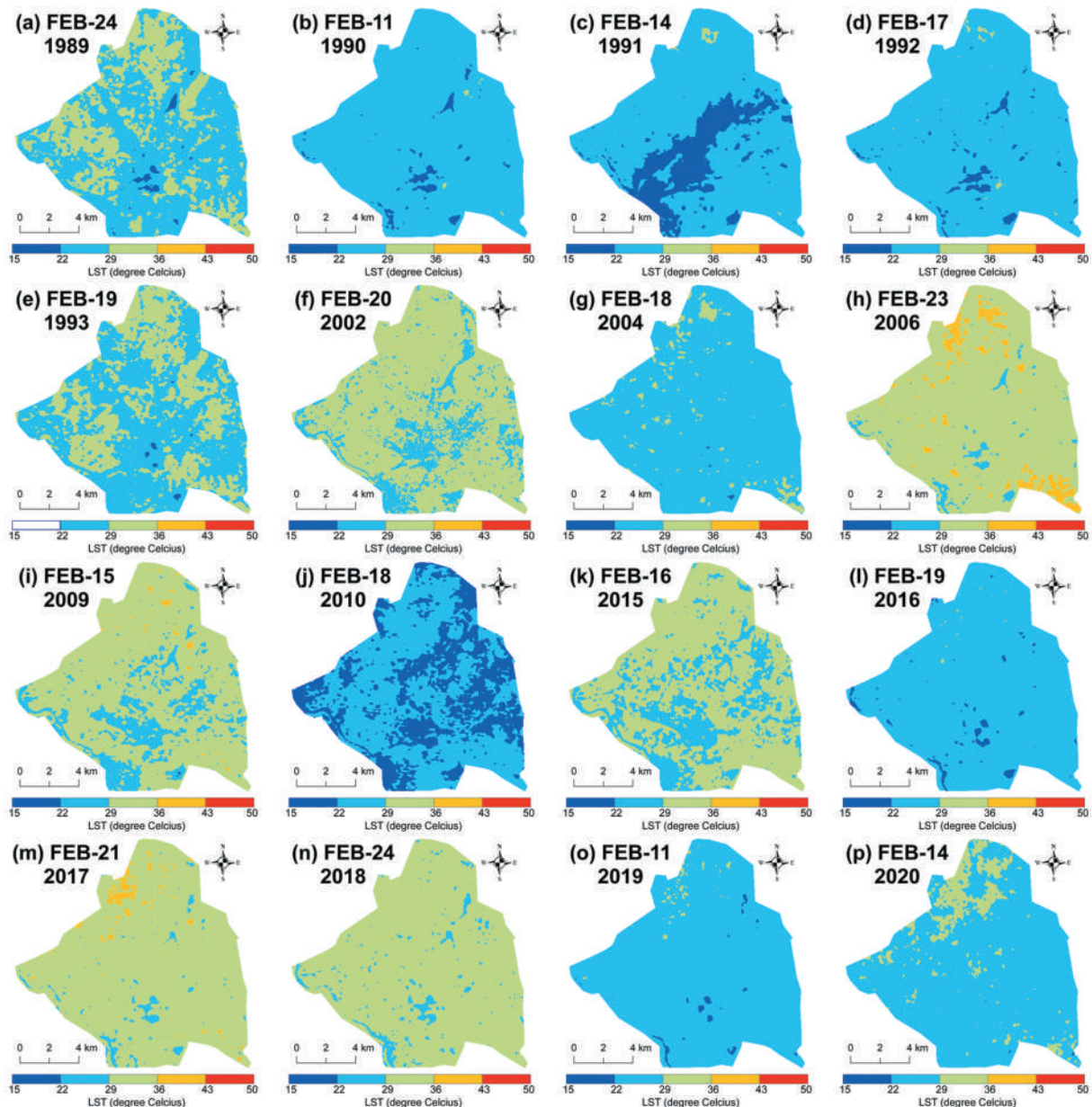


Figure 2. Mean LST in January: (a) 21 January 1988 (b) 10 January 1990 (c) 16 January 1992 (d) 18 January 1993 (e) 17 January 1996 (f) 19 January 2005 (g) 25 January 2007 (h) 14 January 2009 (i) 20 January 2011 (j) 15 January 2015 (k) 23 January 2018 (l) 13 January 2020.



**Figure 3.** Mean LST in February: (a) 24 February 1989 (b) 11 February 1990 (c) 14 February 1991 (d) 17 February 1992 (e) 19 February 1993 (f) 20 February 2002 (g) 18 February 2004 (h) 23 February 2006 (i) 15 February 2009 (j) 18 February 2010 (k) 16 February 2015 (l) 19 February 2016 (m) 21 February 2017 (n) 24 February 2018 (o) 11 February 2019 (p) 14 February 2020.

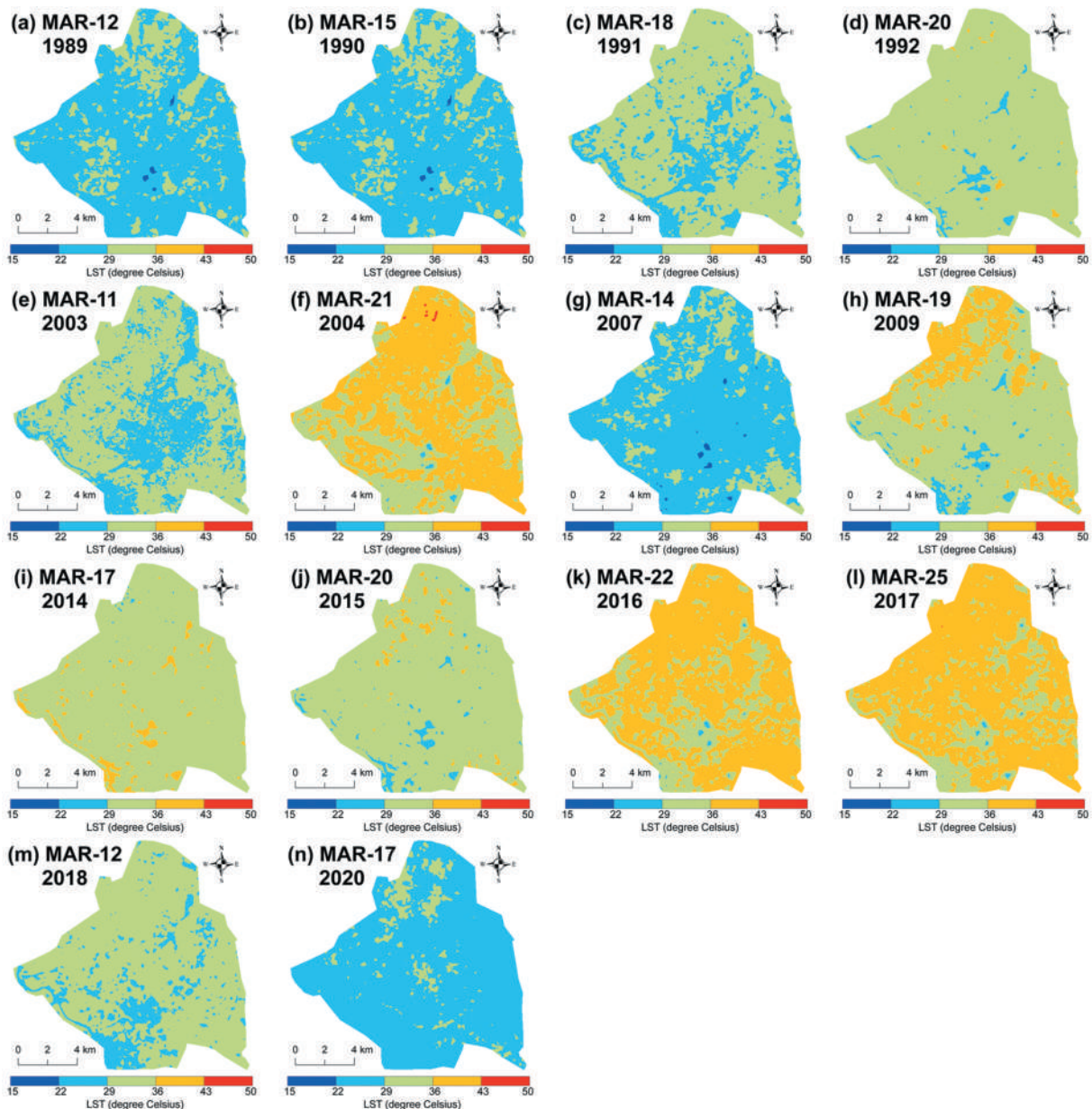
average, October ( $-0.62$ ), September ( $-0.55$ ), April ( $-0.51$ ), June ( $-0.47$ ), May ( $-0.44$ ), March ( $-0.44$ ), and November ( $-0.39$ ) months have a moderate negative correlation. A weak negative correlation was found in February ( $-0.29$ ), January ( $-0.24$ ), and December ( $-0.21$ ) months. The main reason behind the moderate LST–NDVI correlation in March–November is the presence of high intensity of moisture and chlorophyll content in green vegetation. Dry months reduce the strength of regression, while the wet months enhance the strength of the LST–NDVI regression.

Table 4 represents a monthly variation of Pearson’s linear correlation method between LST and NDBI. In average, October (0.80), September (0.76), April (0.73), and May (0.71) months build a strong positive correlation. March (0.69), June (0.68), November

(0.66), February (0.63), January (0.61), and November (0.52) months have a moderate to strong positive correlation. The strength of correlation increases with the increase of wetness.

Table 5 represents a monthly variation of Pearson’s linear correlation method between LST and NDWI. In average, October (0.49), September (0.40), June (0.33), and April (0.33) months build a moderate positive correlation. November (0.29), May (0.27), and March (0.23) months have a weak positive correlation. There is no such linear correlation found in February (0.09), December (0.04), and January (0.02). Here again, dryness of the season reflects low correlation.

Table 6 represents a monthly variation of Pearson’s linear correlation method between LST and NDBaI. In average, October (0.48) and September (0.47) months



**Figure 4.** Mean LST in March: (a) 12 March 1989 (b) 15 March 1990 (c) 18 March 1991 (d) 20 March 1992 (e) 11 March 2003 (f) 21 March 2004 (g) 14 March 2007 (h) 19 March 2009 (i) 17 March 2014 (j) 20 March 2015 (k) 22 March 2016 (l) 25 March 2017 (m) 12 March 2018 (n) 17 March 2020.

build a moderate positive correlation. January (0.36), February (0.32), November (0.31), and March (0.30) months have a moderate to weak positive correlation. A weak positive correlation is found in April (0.29), December (0.28), June (0.22), and May (0.21) months. Thus, the pre-monsoon and winter months indicate low correlation compared to the monsoon and post-monsoon months.

Figure 14 shows the line graphs for monthly variation of LST–spectral indices relationships. The LST–NDVI correlation is always negative, whereas the LST–NDBI correlation and the LST–NDBaI correlation are always positive. From 1988 to 2000 a slightly falling trend is observed for LST–NDBI and LST–NDBaI correlation. The trend of LST–NDWI

correlation is slightly rising or neutral. There is also no such variation in LST–NDVI correlation and the trend is almost neutral. LST–spectral indices build a stronger correlation between March and November.

Figure 15 presents a comparison between LST and four aforesaid spectral indices. Average correlation coefficient was used to compare the monthly assessment of these relationships. LST builds the least correlation with NDVI, NDBI, and NDWI from November to February. Pre-monsoon months have the least correlation between LST and NDBaI as the dry soil and open land absorbs a lot of heat in the summer months. Humidity accelerates the strength of the correlation while dry weather reduces the correlation coefficient values.

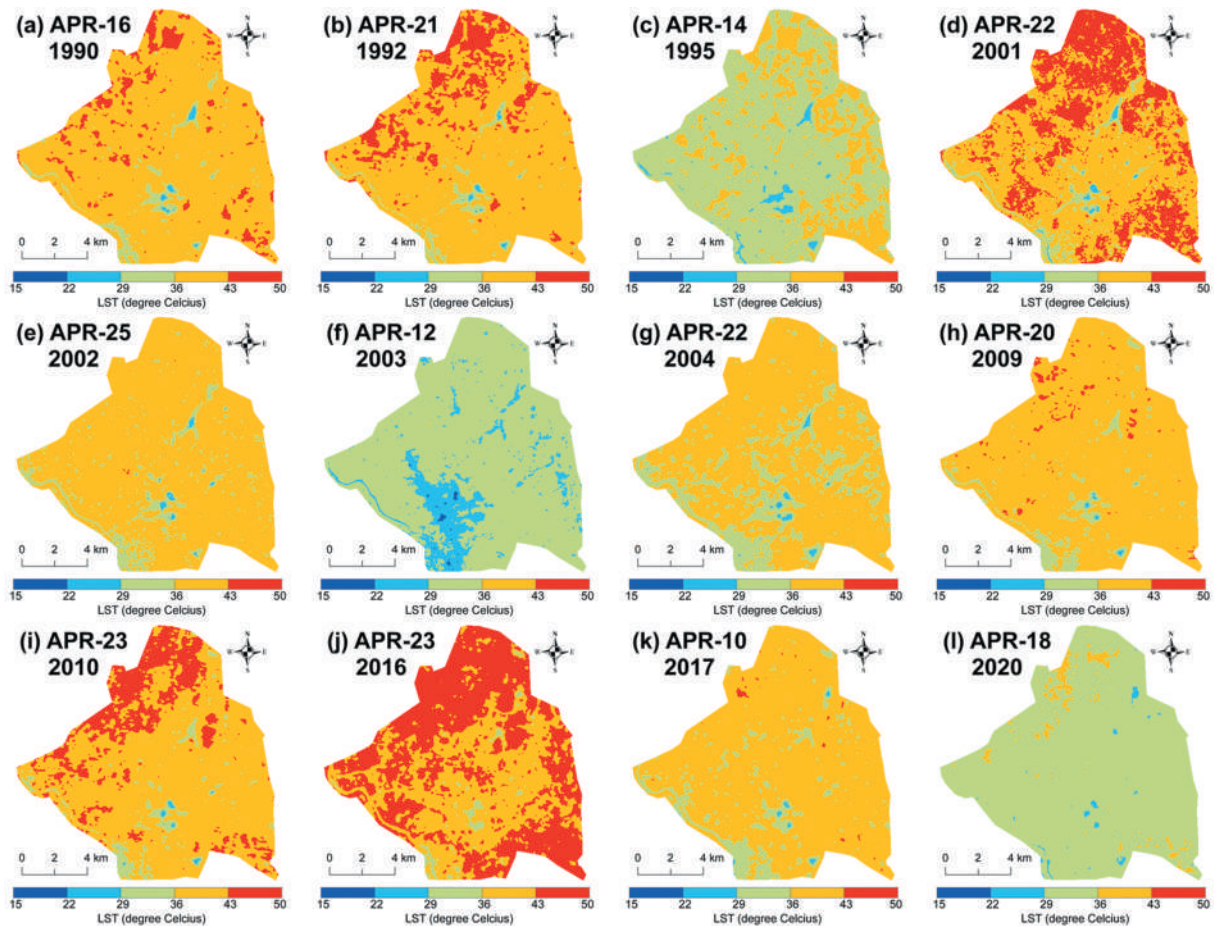


**Figure 5.** Mean LST in April: (a) 21 April 1992 (b) 16 April 1990 (c) 14 April 1995 (d) 22 April 2001 (e) 25 April 2002 (f) 12 April 2003 (g) 22 April 2004 (h) 20 April 2009 (i) 23 April 2010 (j) 23 April 2016 (k) 10 April 2017 (l) 18 April 2020.

This LST–NDVI correlation tends to be more negative with the increase of surface moisture (Lambin & Ehrlich, 1996; Moran et al., 1994; Sandholt et al., 2002). In high latitudes, positive LST–NDVI relationships have been observed (Karnieli et al., 2010) as the heat capacity of vegetation and water is more than the bare rock surface. Sun and Kafatos (2007) stated that the LST–NDVI correlation was positive in the winter season as vegetation retains temperature in winter; while it was negative in the summer season because presence of vegetation helps in cooling in summer. Yue et al. (2007) showed that the LST–NDVI relationship in Shanghai City, China was negative and was different in different LULC types. Liang et al. (2012) presented similar types of negative NDVI–LST correlation. This relationship was also negative in Mashhad, Iran (Gorgani et al., 2013). The relationship was strong negative in Berlin City for any season (Marzban et al., 2018). The present study also found the negative LST–NDVI correlation for all the months (average correlation coefficient value is  $-0.42$  from 1988 to 2020). The value of the correlation coefficient is inversely related to the surface moisture content, i.e., the negativity of

the relationship increases with the increase of surface moisture content.

The LST–NDBI correlation found in the present study is strong positive for each and every month. The strongest correlation was noticed in October (0.80) and September (0.76), whereas the least correlation was found in December (0.52) and January (0.61). Moist climate intensifies the strength of the correlation. The result of this study is comparable with the other LST–NDBI related studies conducted in the other cities. LST and NDBI built a strong correlation in Fuzhou City of China (Zhang et al., 2009). L Chen et al. (2013) established a strong positive correlation between LST and NDBI in Wuhan City, China (0.639, 0.717, 0.807, and 0.762 in spring, summer, autumn, and winter, respectively). A strong positive LST–NDBI correlation was also observed in Kunming of China (Chen & Zhang, 2017). A strong positive correlation between LST and NDBI was noticed in Vila Velha, ES, Brazil (Dos Santos et al., 2017). In Melbourne City of Australia, LST and NDBI built a moderate to strong positive correlation (Jamei et al., 2019). Balew and Korme (2020) noticed a positive correlation in Bahir

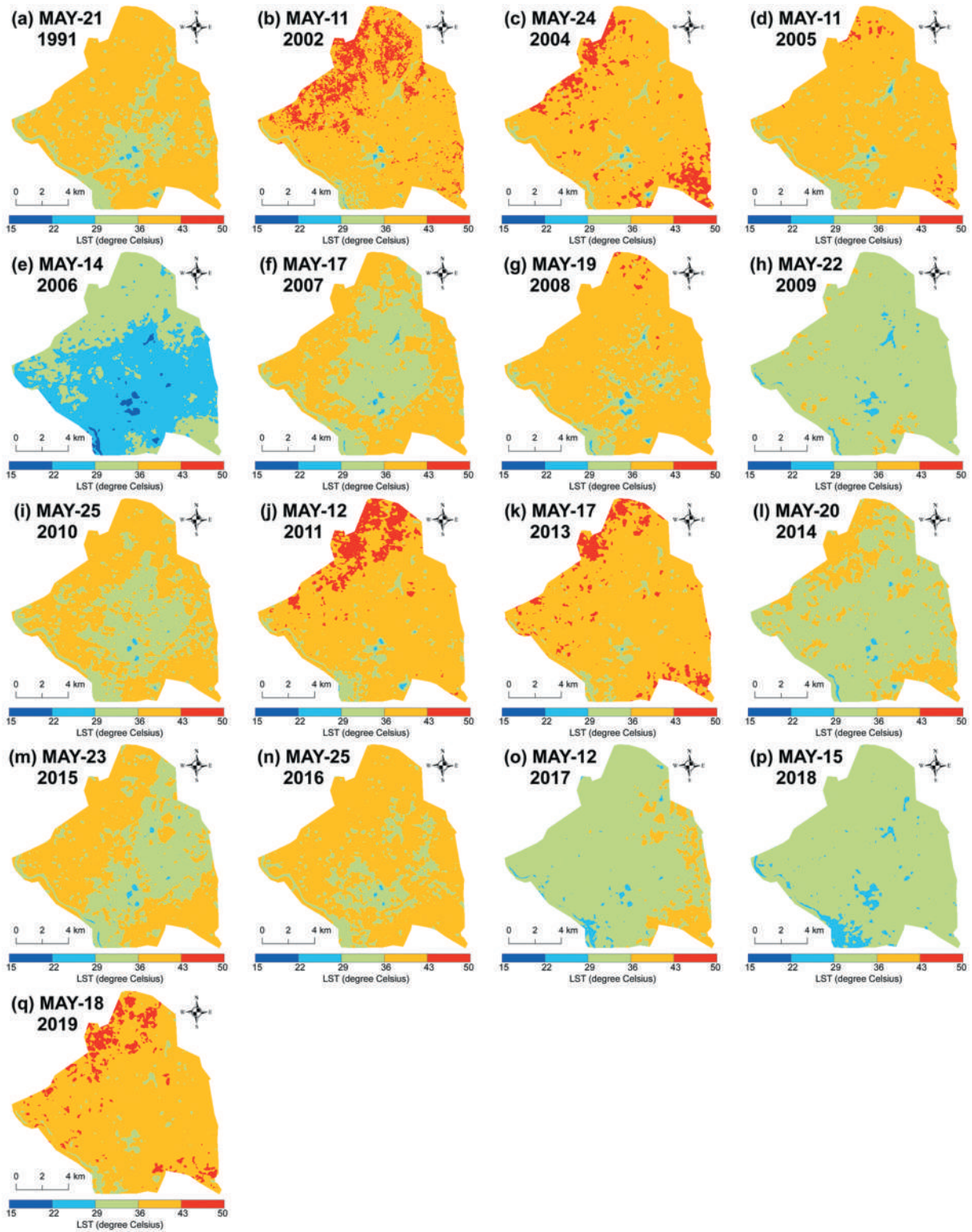


Figure 6. Mean LST in May: (a) 21 May 1991 (b) 11 May 2002 (c) 24 May 2004 (d) 11 May 2005 (e) 14 May 2006 (f) 17 May 2007 (g) 19 May 2008 (h) 22 May 2009 (i) 25 May 2010 (j) 12 May 2011 (k) 17 May 2013 (l) 20 May 2014 (m) 23 May 2015 (n) 25 May 2016 (o) 12 May 2017 (p) 15 May 2018 (q) 18 May 2019.

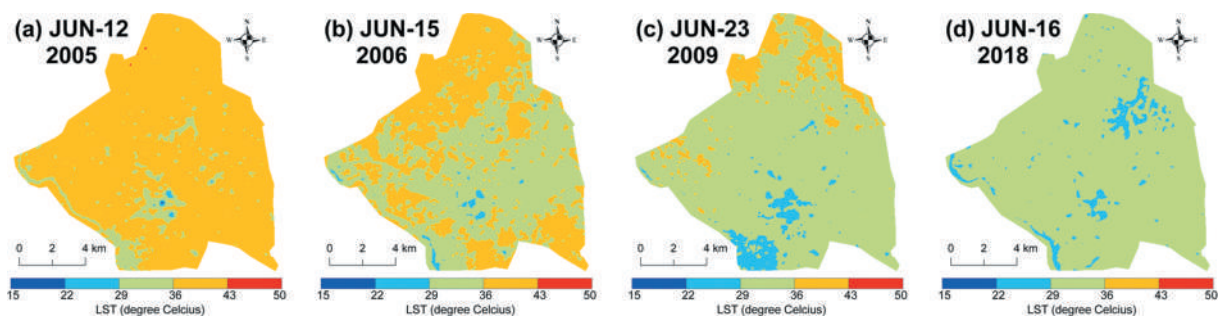


Figure 7. Mean LST in June: (a) 12 June 2005 (b) 15 June 2006 (c) 23 June 2009 (d) 16 June 2018.



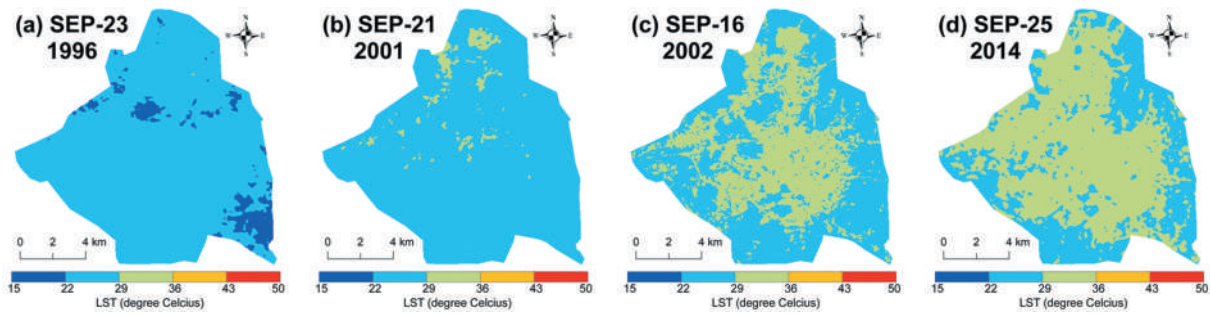


Figure 8. Mean LST in September: (a) 23 September 1996 (b) 21 September 2001 (c) 16 September 2002 (d) 25 September 2014.

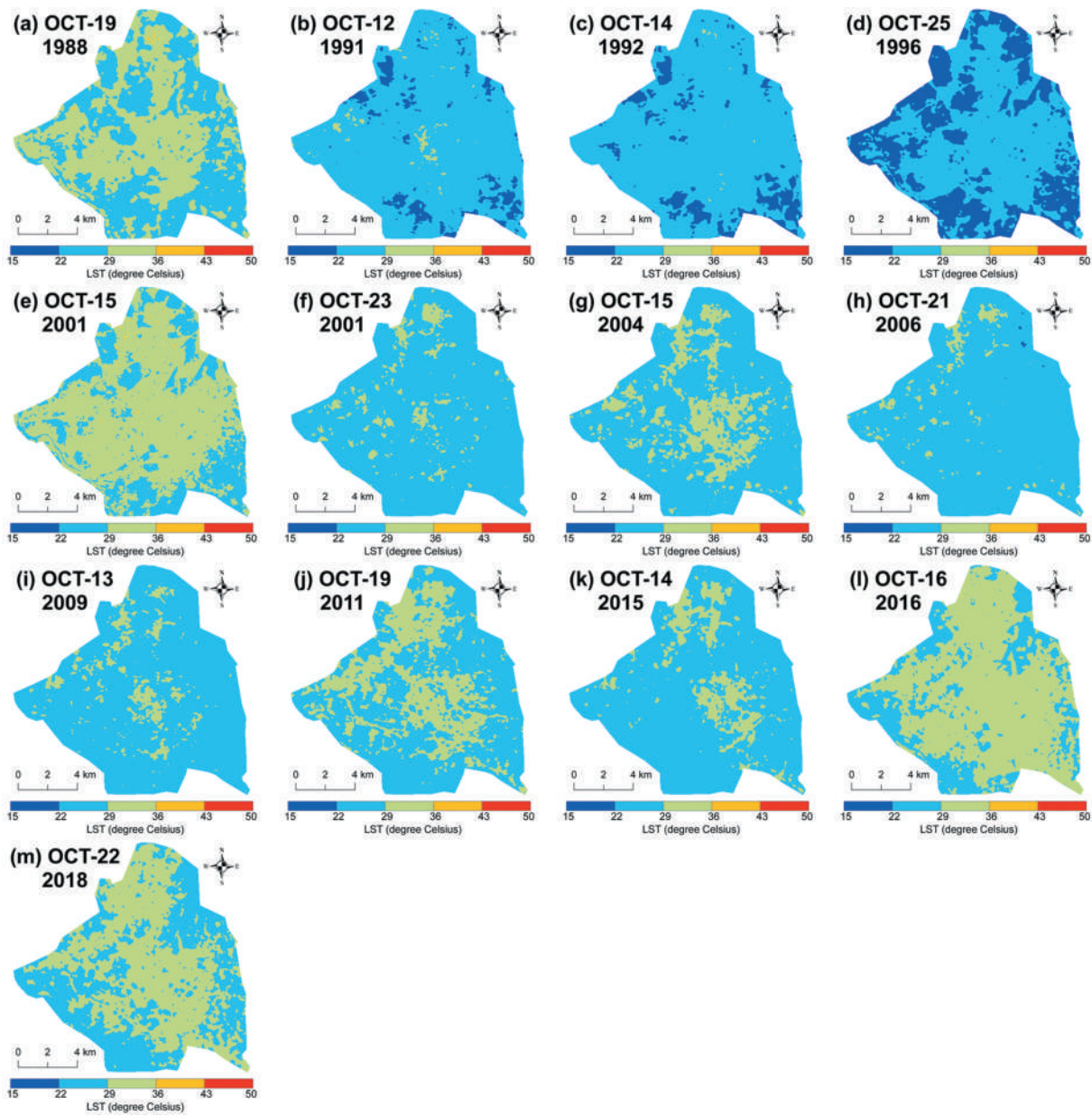
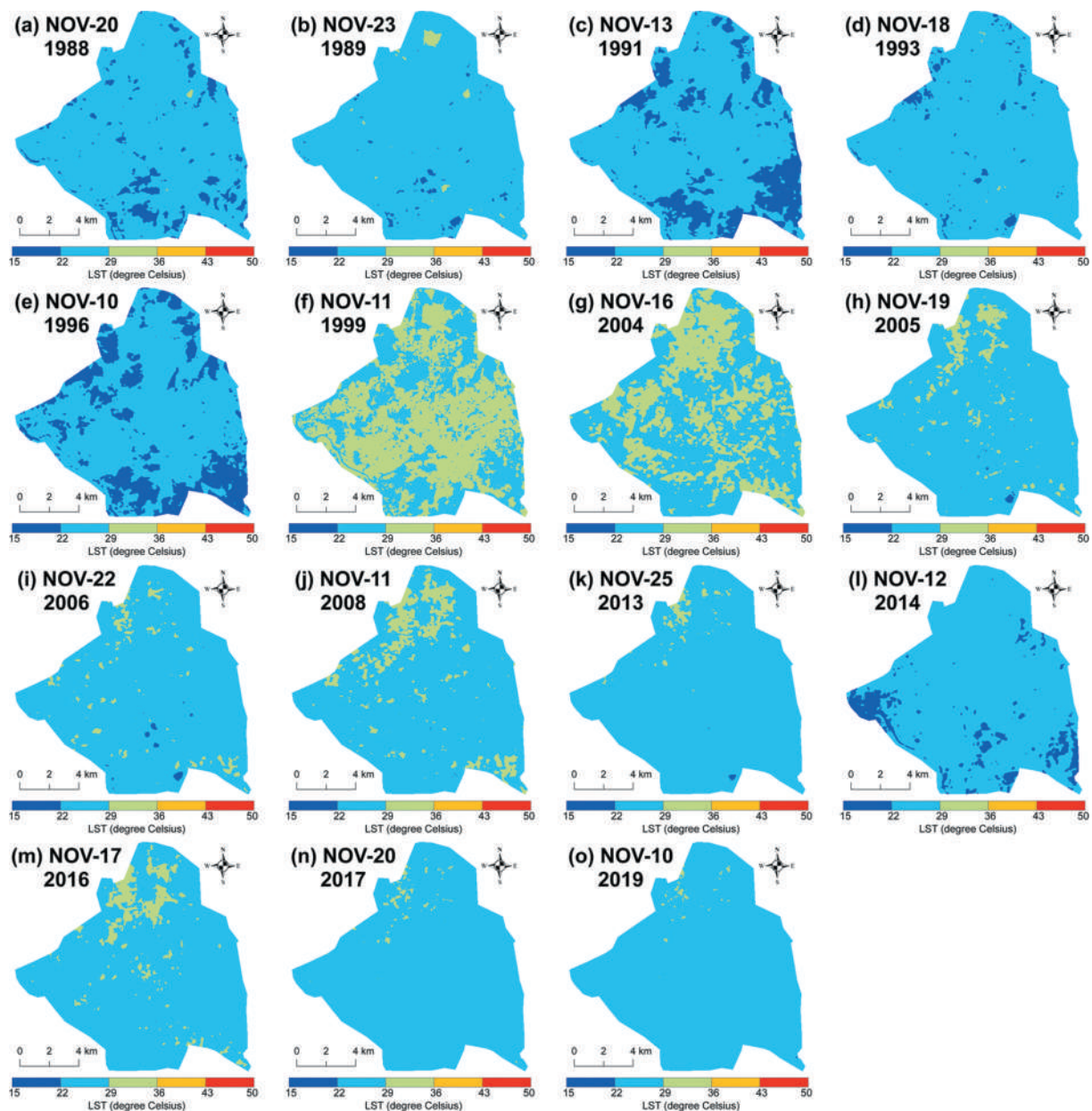
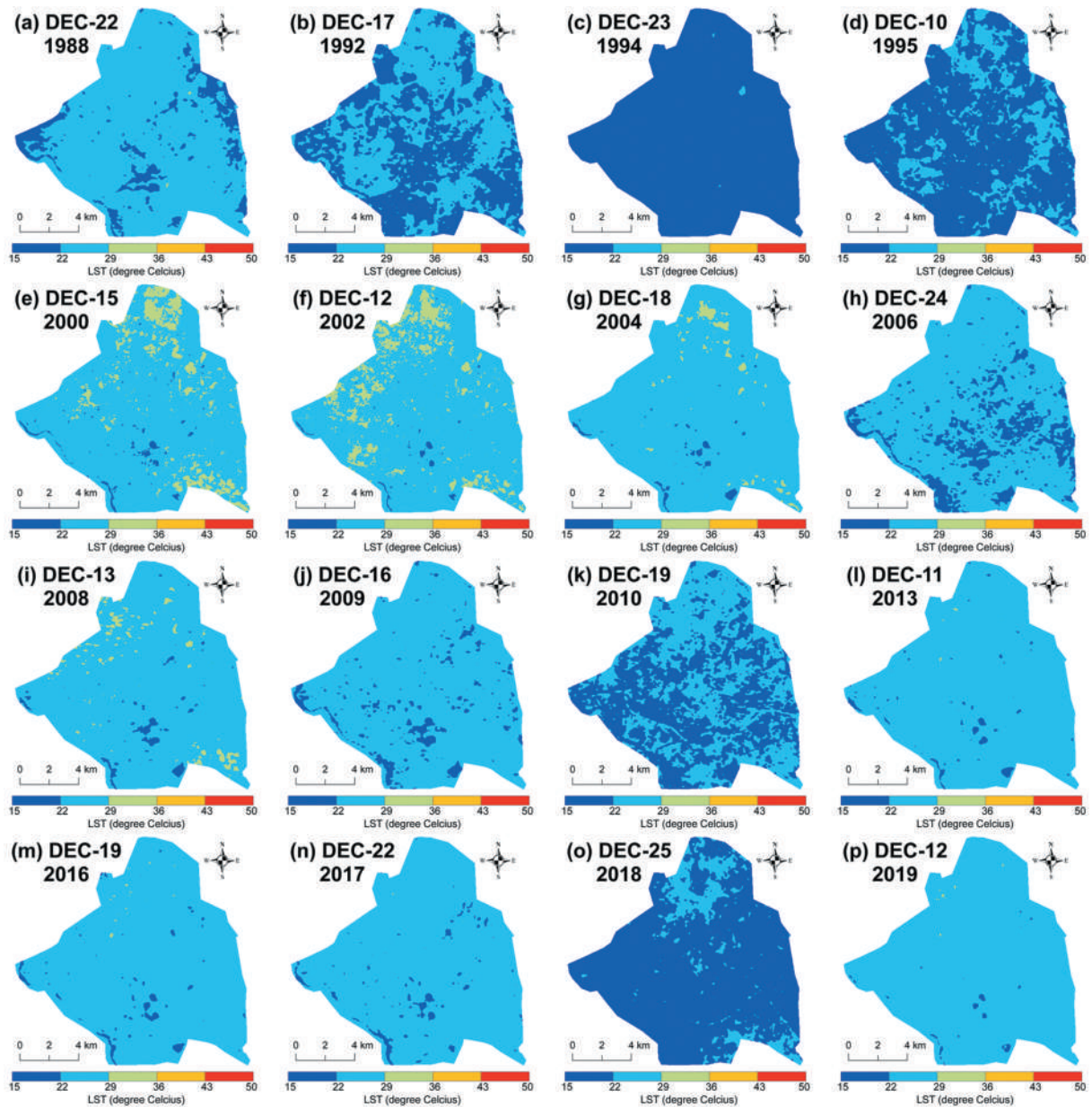


Figure 9. Mean LST in October: (a) 19 October 1988 (b) 12 October 1991 (c) 14 October 1992 (d) 25 October 1996 (e) 15 October 2001 (f) 23 October 2001 (g) 15 October 2004 (h) 21 October 2006 (i) 13 October 2009 (j) 19 October 2011 (k) 14 October 2015 (l) 16 October 2016 (m) 22 October 2018.



**Figure 10.** Mean LST in November: (a) 20 November 1988 (b) 23 November 1989 (c) 13 November 1991 (d) 18 November 1993 (e) 10 November 1996 (f) 11 November 1999 (g) 16 November 2004 (h) 19 November 2005 (i) 22 November 2006 (j) 11 November 2008 (k) 25 November 2013 (l) 12 November 2014 (m) 17 November 2016 (n) 20 November 2017 (o) 10 November 2019.



**Figure 11.** Mean LST in December: (a) 22 December 1988 (b) 17 December 1992 (c) 23 December 1994 (d) 10 December 1995 (e) 15 December 2000 (f) 21 December 2002 (g) 18 December 2004 (h) 24 December 2006 (i) 13 December 2008 (j) 16 December 2009 (k) 19 December 2010 (l) 11 December 2013 (m) 19 December 2016 (n) 22 December 2017 (o) 25 December 2018 (p) 12 December 2019.

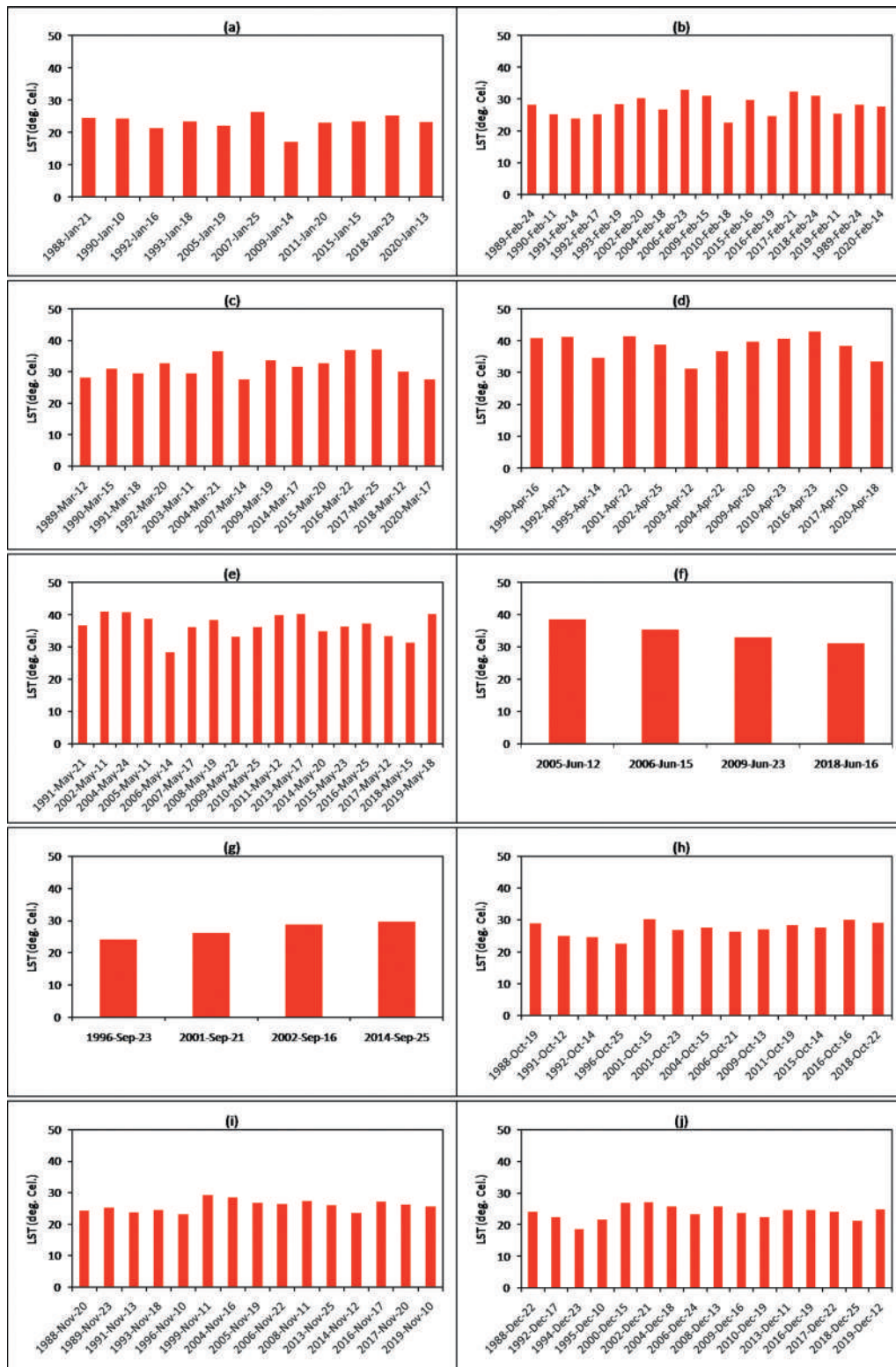


Figure 12. Monthly assessment of mean LST (°C) from 1988 to 2020: (a) January (b) February (c) March (d) April (e) May (f) June (g) September (h) October (i) November (j) December.

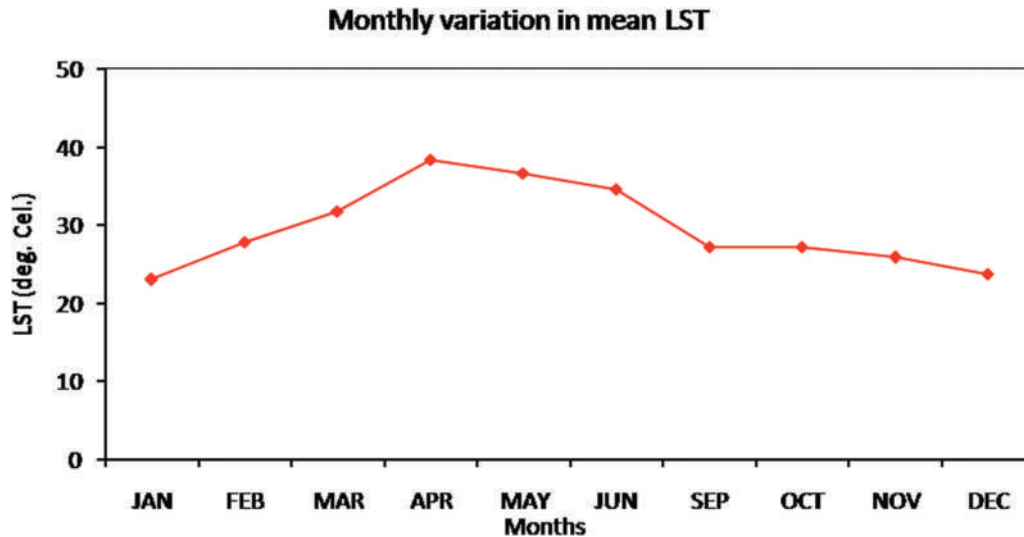


Figure 13. Monthly variation in LST (°C) from 1988 to 2020.

Dar City of Ethiopia. Using a long term Landsat series data in Chattogram Metropolitan Area of Bangladesh, Roy et al. (2020) showed that NDBI is positively correlated to LST. Son et al. (2020) showed that the LST–NDBI relationship was also strong positive (0.85) in San Salvador City of El Salvador in last 30 years. These aforesaid examples of LST–NDBI positive correlations are simply based on the fact that the building and road construction materials like rock, cement, brick, concrete, tar, sand, stone chips, etc. produce high LST values. This result is very much similar to the result of the present study (mean correlation coefficients between LST and NDBI is 0.68 during the entire period).

The result is quite authentic with respect to the other LST–NDWI related studies in recent years. A study performed in Shenzhen City of China showed a significant negative LST–NDWI correlation on the water bodies (X-L. Chen et al., 2006). LST and NDWI built a negative correlation in desert landscape in Kuwait (Uddin et al., 2010). In Nanchang City of China, LST and NDWI develop a negative correlation on the water bodies (Zhang et al., 2017). In Asansol-Durgapur Development Region of India, a negative LST–NDWI correlation was found in the water bodies (Choudhury et al., 2019). Das (Choudhury et al., 2019) presented a dynamic negative LST–NDWI correlation in the dry bare land of Northwest India and the surrounding places of Pakistan, where different types of rock compositions influence the values of LST and NDWI. LST and NDWI built a negative linear correlation in Banda Aceh City of Indonesia in the last 30 years (Achmad & Zainuddin, 2019). An insignificant correlation was found in Wuhan City of China. The current analysis showed an insignificant and weak positive correlation (average value of 0.27 for all the months during the study period) between LST and

NDWI. These results are based on the fact that LST reduces significantly in water bodies or wetland, but other surface materials have an insignificant relationship because different materials have different water or moisture content ratio.

The LST–NDBaI correlation is positive, irrespective of any season. The post-monsoon season reveals the best correlation among all the four seasons. The present study indicates that LST builds a stable strong to a moderate positive correlation with NDBaI in Raipur City, India from 1988 to 2020. Essa et al. (2012) presented a moderate positive LST–NDBaI correlation (0.39) in Greater Dublin region, Ireland. The LST and NDBaI have built a weak negative correlation (–0.11) in Guangzhou, China (Guo et al., 2015) as the bare earth surface was less. Sharma and Joshi (2016) showed the moderate positive nature of LSI–NDBaI correlation in the National Capital Region of India. A weak positive correlation between LST and NDBaI was presented in London (0.086) and Baghdad (0.469) by Ali et al. (2017). Chen and Zhang (2017) noticed the strong positive nature of the correlation coefficient of the LST–NDBaI relationship in a study performed in Kunming, China due to the presence of high bare land ratio. This correlation was weak positive (0.06) in Harare Metropolitan City, Zimbabwe (Mushore et al., 2017). This relationship was also positive (0.458) in Kolkata Metropolitan Area, India (Nimish et al., 2020). The present study shows that the average correlation coefficient between LST and NDBaI for all the months from 1988 to 2020 is moderate positive (0.32). LST will obviously be increased if the ratio of the bare rock surface, sand, or dry soil is high. However, in many modern cities, percentage of barren land is low that promotes a moderate positive LST–NDBaI relationship. From

**Table 3.** Monthly variation of LST-NDVI correlation coefficient (1988–2020).

Year	Correlation coefficient	February	Correlation coefficient	March	Correlation coefficient	April	Correlation coefficient	May	Correlation coefficient
1988-Jan-21	-0.31	1989-Feb-24	-0.39	1989-Mar-12	-0.43	1990-Apr-16	-0.52	1991-May-21	-0.43
1990-Jan-10	-0.36	1990-Feb-11	-0.38	1990-Mar-15	-0.43	1992-Apr-21	-0.53	2002-May-11	-0.56
1992-Jan-16	-0.35	1991-Feb-14	-0.12	1991-Mar-18	-0.40	1995-Apr-14	-0.38	2004-May-24	-0.46
1993-Jan-18	-0.38	1992-Feb-17	-0.29	1992-Mar-20	-0.40	2001-Apr-22	-0.65	2005-May-11	-0.54
2005-Jan-19	-0.21	1993-Feb-19	-0.37	2003-Mar-11	-0.41	2002-Apr-25	-0.57	2006-May-14	-0.46
2007-Jan-25	-0.21	2002-Feb-20	-0.44	2004-Mar-21	-0.49	2003-Apr-12	-0.39	2007-May-17	-0.33
2009-Jan-14	-0.25	2004-Feb-18	-0.30	2007-Mar-14	-0.38	2004-Apr-22	-0.51	2008-May-19	-0.48
2011-Jan-20	-0.18	2006-Feb-23	-0.31	2009-Mar-19	-0.54	2009-Apr-20	-0.56	2009-May-22	-0.44
2015-Jan-15	-0.27	2009-Feb-15	-0.36	2014-Mar-17	-0.42	2010-Apr-23	-0.52	2010-May-25	-0.47
2018-Jan-23	-0.15	2010-Feb-18	-0.24	2015-Mar-20	-0.36	2016-Apr-23	-0.46	2011-May-12	-0.56
2020-Jan-13	-0.17	2015-Feb-16	-0.16	2016-Mar-22	-0.40	2017-Apr-10	-0.51	2013-May-17	-0.43
		2016-Feb-19	-0.21	2017-Mar-25	-0.43	2020-Apr-18	-0.53	2014-May-20	-0.41
		2017-Feb-21	-0.30	2018-Mar-12	-0.37			2015-May-23	-0.34
		2018-Feb-24	-0.28	2020-Mar-17	-0.55			2016-May-25	-0.38
		2019-Feb-11	-0.21					2017-May-12	-0.29
		1989-Feb-24	-0.39					2018-May-15	-0.45
		2020-Feb-14	-0.31					2019-May-18	-0.43
<i>Mean</i>	-0.27	<i>Mean</i>	-0.30	<i>Mean</i>	-0.44	<i>Mean</i>	-0.51	<i>Mean</i>	-0.44
June	Correlation coefficient	September	Correlation coefficient	October	Correlation coefficient	November	Correlation coefficient	December	Correlation coefficient
2005-Jun-12	-0.51	1996-Sep-23	-0.54	1988-Oct-19	-0.69	1988-Nov-20	-0.41	1988-Dec-22	-0.20
2006-Jun-15	-0.46	2001-Sep-21	-0.58	1991-Oct-12	-0.63	1989-Nov-23	-0.29	1992-Dec-17	-0.15
2009-Jun-23	-0.42	2002-Sep-16	-0.56	1992-Oct-14	-0.68	1991-Nov-13	-0.38	1994-Dec-23	-0.24
2018-Jun-16	-0.46	2014-Sep-25	-0.53	1996-Oct-25	-0.64	1993-Nov-18	-0.19	1995-Dec-10	-0.09
				2001-Oct-15	-0.66	1996-Nov-10	-0.40	2000-Dec-15	-0.18
				2001-Oct-23	-0.58	1999-Nov-11	-0.48	2002-Dec-21	-0.29
				2004-Oct-15	-0.63	2004-Nov-16	-0.35	2004-Dec-18	-0.10
				2006-Oct-21	-0.51	2005-Nov-19	-0.31	2006-Dec-24	-0.23
				2009-Oct-13	-0.64	2006-Nov-22	-0.23	2008-Dec-13	-0.12
				2011-Oct-19	-0.63	2008-Nov-11	-0.41	2009-Dec-16	-0.20
				2015-Oct-14	-0.61	2013-Nov-25	-0.44	2010-Dec-19	-0.24
				2016-Oct-16	-0.53	2014-Nov-12	-0.52	2013-Dec-11	-0.19
				2018-Oct-22	-0.63	2016-Nov-17	-0.44	2016-Dec-19	-0.21
						2017-Nov-20	-0.45	2017-Dec-22	-0.30
<i>Mean</i>	-0.47	<i>Mean</i>	-0.55	<i>Mean</i>	-0.62	<i>Mean</i>	-0.39	2018-Dec-25	-0.22
								2019-Dec-12	-0.40
								<i>Mean</i>	-0.21

Table 4. Monthly variation of LST-NDBI correlation coefficient (1988–2020).

January	Correlation coefficient	February	Correlation coefficient	March	Correlation coefficient	April	Correlation coefficient	May	Correlation coefficient
1988-Jan-21	0.67	1989-Feb-24	0.69	1989-Mar-12	0.70	1990-Apr-16	0.79	1991-May-21	0.75
1990-Jan-10	0.69	1990-Feb-11	0.73	1990-Mar-15	0.73	1992-Apr-21	0.74	2002-May-11	0.76
1992-Jan-16	0.70	1991-Feb-14	0.68	1991-Mar-18	0.76	1995-Apr-14	0.76	2004-May-24	0.76
1993-Jan-18	0.69	1992-Feb-17	0.69	1992-Mar-20	0.75	2001-Apr-22	0.82	2005-May-11	0.73
2005-Jan-19	0.61	1993-Feb-19	0.72	2003-Mar-11	0.79	2002-Apr-25	0.82	2006-May-14	0.69
2007-Jan-25	0.60	2002-Feb-20	0.76	2004-Mar-21	0.69	2003-Apr-12	0.70	2007-May-17	0.80
2009-Jan-14	0.55	2004-Feb-18	0.64	2007-Mar-14	0.72	2004-Apr-22	0.72	2008-May-19	0.82
2011-Jan-20	0.55	2006-Feb-23	0.62	2009-Mar-19	0.61	2009-Apr-20	0.71	2009-May-22	0.71
2015-Jan-15	0.52	2009-Feb-15	0.58	2014-Mar-17	0.63	2010-Apr-23	0.63	2010-May-25	0.73
2018-Jan-23	0.50	2010-Feb-18	0.65	2015-Mar-20	0.64	2016-Apr-23	0.68	2011-May-12	0.69
2020-Jan-13	0.48	2015-Feb-16	0.58	2016-Mar-22	0.69	2017-Apr-10	0.69	2013-May-17	0.69
		2016-Feb-19	0.48	2017-Mar-25	0.64	2020-Apr-18	0.66	2014-May-20	0.70
		2017-Feb-21	0.56	2018-Mar-12	0.67			2015-May-23	0.63
		2018-Feb-24	0.64	2020-Mar-17	0.65			2016-May-25	0.65
		2019-Feb-11	0.51					2017-May-12	0.63
		1989-Feb-24	0.49					2018-May-15	0.61
		2020-Feb-14	0.69					2019-May-18	0.65
<i>Mean</i>	0.61	<i>Mean</i>	0.63	<i>Mean</i>	0.69	<i>Mean</i>	0.73	<i>Mean</i>	0.71
June	Correlation coefficient	September	Correlation coefficient	October	Correlation coefficient	November	Correlation coefficient	December	Correlation coefficient
2005-Jun-12	0.69	1996-Sep-23	0.74	1988-Oct-19	0.85	1988-Nov-20	0.69	1988-Dec-22	0.56
2006-Jun-15	0.71	2001-Sep-21	0.75	1991-Oct-12	0.87	1989-Nov-23	0.68	1992-Dec-17	0.49
2009-Jun-23	0.63	2002-Sep-16	0.77	1992-Oct-14	0.85	1991-Nov-13	0.75	1994-Dec-23	0.50
2018-Jun-16	0.69	2014-Sep-25	0.78	1996-Oct-25	0.82	1993-Nov-18	0.63	1995-Dec-10	0.47
				2001-Oct-15	0.83	1996-Nov-10	0.74	2000-Dec-15	0.59
				2001-Oct-23	0.78	1999-Nov-11	0.78	2002-Dec-21	0.64
				2004-Oct-15	0.79	2004-Nov-16	0.68	2004-Dec-18	0.52
				2006-Oct-21	0.77	2005-Nov-19	0.64	2006-Dec-24	0.49
				2009-Oct-13	0.78	2006-Nov-22	0.60	2008-Dec-13	0.50
				2011-Oct-19	0.77	2008-Nov-11	0.60	2009-Dec-16	0.48
				2015-Oct-14	0.76	2013-Nov-25	0.59	2010-Dec-19	0.45
				2016-Oct-16	0.74	2014-Nov-12	0.63	2013-Dec-11	0.52
				2018-Oct-22	0.74	2016-Nov-17	0.58	2016-Dec-19	0.48
						2017-Nov-20	0.56	2017-Dec-22	0.49
						2019-Nov-10	0.66	2018-Dec-25	0.47
<i>Mean</i>	0.68	<i>Mean</i>	0.76	<i>Mean</i>	0.80	<i>Mean</i>	0.66	2019-Dec-12	0.54
								<i>Mean</i>	0.52

Table 5. Monthly variation of LST-NDWI correlation coefficient (1988–2020).

Year	Correlation coefficient	February	Correlation coefficient	March	Correlation coefficient	April	Correlation coefficient	May	Correlation coefficient
1988-Jan-21	0.03	1989-Feb-24	0.03	1989-Mar-12	0.12	1990-Apr-16	0.28	1991-May-21	0.15
1990-Jan-10	0.08	1990-Feb-11	0.07	1990-Mar-15	0.21	1992-Apr-21	0.27	2002-May-11	0.34
1992-Jan-16	0.08	1991-Feb-14	-0.04	1991-Mar-18	0.13	1995-Apr-14	0.11	2004-May-24	0.24
1993-Jan-18	0.10	1992-Feb-17	0.01	1992-Mar-20	0.07	2001-Apr-20	0.46	2005-May-11	0.36
2005-Jan-19	-0.03	1993-Feb-19	0.05	2003-Mar-11	0.13	2002-Apr-25	0.31	2006-May-14	0.34
2007-Jan-25	0.01	2002-Feb-20	0.19	2004-Mar-21	0.30	2003-Apr-12	0.23	2007-May-17	0.05
2009-Jan-14	0.10	2004-Feb-18	-0.09	2007-Mar-14	0.15	2004-Apr-22	0.31	2008-May-19	0.29
2011-Jan-20	0.06	2006-Feb-23	0.06	2009-Mar-19	0.22	2009-Apr-20	0.39	2009-May-22	0.22
2015-Jan-15	-0.01	2009-Feb-15	0.17	2014-Mar-17	0.30	2010-Apr-23	0.38	2010-May-25	0.31
2018-Jan-23	-0.28	2010-Feb-18	0.08	2015-Mar-20	0.23	2016-Apr-23	0.31	2011-May-12	0.45
2020-Jan-13	0.08	2015-Feb-16	0.02	2016-Mar-22	0.26	2017-Apr-10	0.38	2013-May-17	0.29
		2016-Feb-19	0.11	2017-Mar-25	0.29	2020-Apr-18	0.42	2014-May-20	0.25
		2017-Feb-21	0.17	2018-Mar-12	0.29			2015-May-23	0.20
		2018-Feb-24	0.16	2020-Mar-17	0.46			2016-May-25	0.22
		2019-Feb-11	0.13					2017-May-12	0.16
		1989-Feb-24	0.22					2018-May-15	0.39
		2020-Feb-14	0.03					2019-May-18	0.31
Mean	0.02	Mean	0.09	Mean	0.23	Mean	0.33	Mean	0.27
June	Correlation coefficient	September	Correlation coefficient	October	Correlation coefficient	November	Correlation coefficient	December	Correlation coefficient
2005-Jun-12	0.34	1996-Sep-23	0.36	1988-Oct-19	0.47	1988-Nov-20	0.22	1988-Dec-22	-0.16
2006-Jun-15	0.31	2001-Sep-21	0.44	1991-Oct-12	0.43	1989-Nov-23	0.09	1992-Dec-17	-0.02
2009-Jun-23	0.31	2002-Sep-16	0.35	1992-Oct-14	0.49	1991-Nov-13	0.28	1994-Dec-23	0.051
2018-Jun-16	0.35	2014-Sep-25	0.44	1996-Oct-25	0.50	1993-Nov-18	0.32	1995-Dec-10	-0.08
				2001-Oct-15	0.53	1996-Nov-10	0.27	2000-Dec-15	-0.21
				2001-Oct-23	0.45	1999-Nov-11	0.28	2002-Dec-21	-0.03
				2004-Oct-15	0.49	2004-Nov-16	0.18	2004-Dec-18	-0.09
				2006-Oct-21	0.35	2005-Nov-19	0.18	2006-Dec-24	0.09
				2009-Oct-13	0.53	2006-Nov-22	0.06	2008-Dec-13	0.01
				2011-Oct-19	0.53	2008-Nov-11	0.27	2009-Dec-16	0.10
				2015-Oct-14	0.53	2013-Nov-25	0.34	2010-Dec-19	0.15
				2016-Oct-16	0.44	2014-Nov-12	0.48	2013-Dec-11	0.06
				2018-Oct-22	0.55	2016-Nov-17	0.35	2016-Dec-19	0.11
						2017-Nov-20	0.38	2017-Dec-22	0.23
						2019-Nov-10	0.53	2018-Dec-25	0.13
Mean	0.33	Mean	0.40	Mean	0.49	Mean	0.29	Mean	0.04



**Table 6.** Monthly variation of LST-NDBal correlation coefficient (1988–2020).

Year	Correlation coefficient	February	Correlation coefficient	March	Correlation coefficient	April	Correlation coefficient	May	Correlation coefficient
1988-Jan-21	0.54	1989-Feb-24	0.44	1989-Mar-12	0.47	1990-Apr-16	0.42	1991-May-21	0.44
1990-Jan-10	0.53	1990-Feb-11	0.57	1990-Mar-15	0.47	1992-Apr-21	0.38	2002-May-11	0.34
1992-Jan-16	0.53	1991-Feb-14	0.12	1991-Mar-18	0.52	1995-Apr-14	0.47	2004-May-24	0.32
1993-Jan-18	0.49	1992-Feb-17	0.49	1992-Mar-20	0.51	2001-Apr-22	0.46	2005-May-11	0.28
2005-Jan-19	0.42	1993-Feb-19	0.48	2003-Mar-11	0.56	2002-Apr-25	0.51	2006-May-14	0.19
2007-Jan-25	0.21	2002-Feb-20	0.51	2004-Mar-21	0.22	2003-Apr-12	0.22	2007-May-17	0.45
2009-Jan-14	0.14	2004-Feb-18	0.37	2007-Mar-14	0.41	2004-Apr-22	0.29	2008-May-19	0.17
2011-Jan-20	0.14	2006-Feb-23	0.30	2009-Mar-19	0.12	2009-Apr-20	0.12	2009-May-22	0.20
2015-Jan-15	0.11	2009-Feb-15	0.09	2014-Mar-17	0.11	2010-Apr-23	0.15	2010-May-25	0.17
2018-Jan-23	0.34	2010-Feb-18	0.34	2015-Mar-20	0.09	2016-Apr-23	0.16	2011-May-12	0.11
2020-Jan-13	0.22	2015-Feb-16	0.19	2016-Mar-22	0.17	2017-Apr-10	0.14	2013-May-17	0.10
		2016-Feb-19	0.25	2017-Mar-25	0.14	2020-Apr-18	0.13	2014-May-20	0.11
		2017-Feb-21	0.23	2018-Mar-12	0.15			2015-May-23	0.10
		2018-Feb-24	0.24	2020-Mar-17	0.17			2016-May-25	0.10
		2019-Feb-11	0.21					2017-May-12	0.15
		1989-Feb-24	0.14					2018-May-15	0.11
		2020-Feb-14	0.44					2019-May-18	0.10
<i>Mean</i>	0.36	<i>Mean</i>	0.32	<i>Mean</i>	0.30	<i>Mean</i>	0.29	<i>Mean</i>	0.21
June	Correlation coefficient	September	Correlation coefficient	October	Correlation coefficient	November	Correlation coefficient	December	Correlation coefficient
2005-Jun-12	0.13	1996-Sep-23	0.54	1988-Oct-19	0.67	1988-Nov-20	0.41	1988-Dec-22	0.51
2006-Jun-15	0.23	2001-Sep-21	0.53	1991-Oct-12	0.81	1989-Nov-23	0.34	1992-Dec-17	0.35
2009-Jun-23	0.25	2002-Sep-16	0.56	1992-Oct-14	0.66	1991-Nov-13	0.42	1994-Dec-23	0.26
2018-Jun-16	0.24	2014-Sep-25	0.21	1996-Oct-25	0.60	1993-Nov-18	0.32	1995-Dec-10	0.38
				2001-Oct-15	0.52	1996-Nov-10	0.43	2000-Dec-15	0.51
				2001-Oct-23	0.48	1999-Nov-11	0.57	2002-Dec-21	0.48
				2004-Oct-15	0.44	2004-Nov-16	0.24	2004-Dec-18	0.29
				2006-Oct-21	0.39	2005-Nov-19	0.19	2006-Dec-24	0.11
				2009-Oct-13	0.36	2006-Nov-22	0.29	2008-Dec-13	0.19
				2011-Oct-19	0.31	2008-Nov-11	0.17	2009-Dec-16	0.15
				2015-Oct-14	0.38	2013-Nov-25	0.21	2010-Dec-19	0.19
				2016-Oct-16	0.30	2014-Nov-12	0.26	2013-Dec-11	0.17
				2018-Oct-22	0.31	2016-Nov-17	0.21	2016-Dec-19	0.25
						2017-Nov-20	0.23	2017-Dec-22	0.24
						2019-Nov-10	0.24	2018-Dec-25	0.20
<i>Mean</i>	0.22	<i>Mean</i>	0.47	<i>Mean</i>	0.48	<i>Mean</i>	0.31	2019-Dec-12	0.19
								<i>Mean</i>	0.28

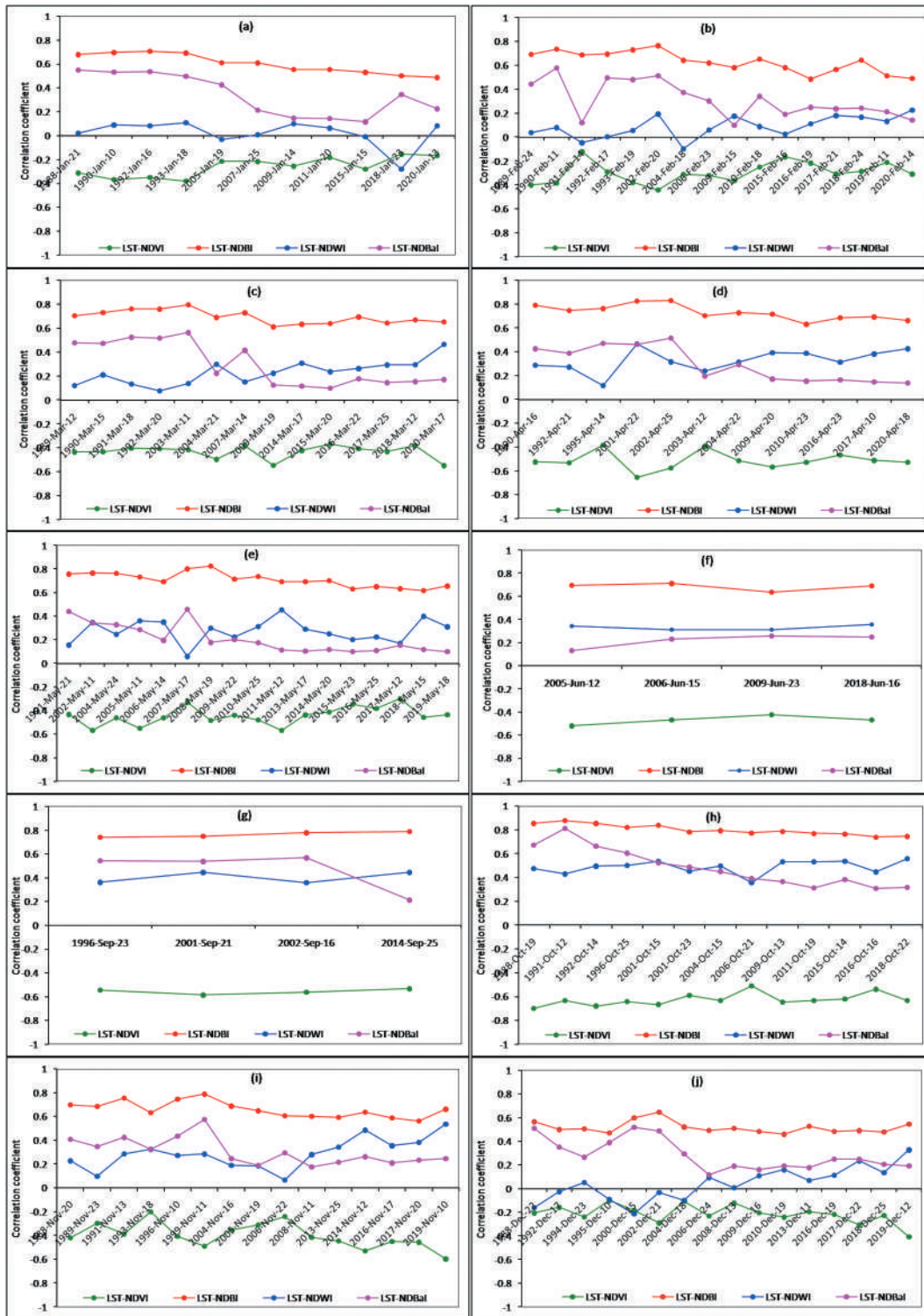


Figure 14. Monthly assessment of LST-spectral indices relationship (1988–2020): (a) January (b) February (c) March (d) April (e) May (f) June (g) September (h) October (i) November (j) December (significant at 0.05 level).

the above examples, it is clear that the relationship between LST and the four spectral indices is consistent and reliable with respect to the other previous similar types of research works.

The study reflects the relationship between LST and normalized difference spectral indices to take new action in environmental planning and management of any city. The area has a positive correlation promotes the LST whereas the area with a negative correlation

reduces the LST. Hence, the environmental planners should take special attention in conversion of the barren or fallow lands into vegetation, water bodies, and wetland to control the rising trend of LST. In this way, the fallow or barren lands can be converted into parks, wetlands, or artificial water bodies. Forest or dense vegetation must be protected and social forestry can be introduced at a large scale. Most of the industrial and commercial activities must be restrained in

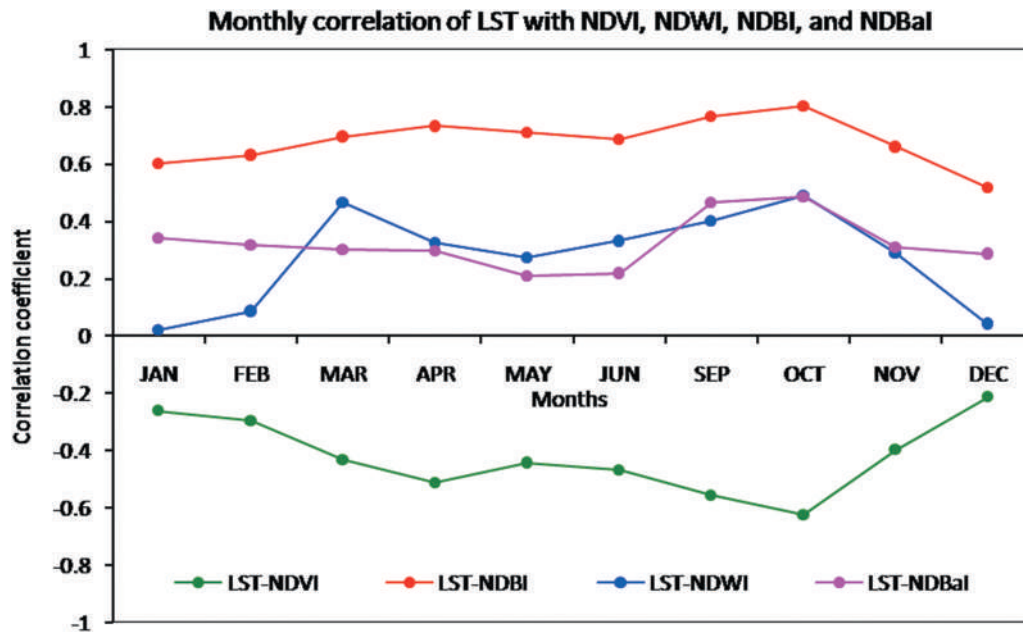


Figure 15. Monthly correlation of LST–spectral indices relationship (1988–2020) (significant at 0.05 level).

particular areas located far away from the dense residential places. A specific area of the city should be allotted as wasteland. Thus, the correlation between LST and the spectral indices significantly determines the vulnerable area of the city and the ecological health of the city could be improved by converting these vulnerable places into vegetation and water bodies.

## Conclusion

The present study estimates the monthly variation of LST distribution in Raipur City, India using 123 Landsat images from 1988 to 2020. April, May, June, and March present higher LST value than the rest of the months. The present study also assesses the monthly correlation of LST and spectral indices in Raipur City. The results show that LST is inversely related to NDVI, and positively related to NDBI and NDBaI, irrespective of any month. NDWI does not generate significant correlation with LST. LST builds strong to moderate correlation with NDVI, NDBI, and NDWI between March and November, whereas it is found weak negative in the winter months (December to February). For LST–NDBaI correlation, the strength is reduced in the summer and winter months. The growth of vegetation depends on the climatic component and soil condition those are largely changed in different months. The LST is directly controlled by the ratio of green vegetation in a city. The value of the spectral indices and LST varies with the change of month. Thus, the study is useful for the environmentalist and urban planner for the future ecological planning.

There is obviously some limitations and future scope of the present study. First, LST can be derived by using other algorithms or from other satellite sensors to compare with the present result. Downscaling technique can be applied to get the LST with high pixel values. Secondly, the *in situ* measurement can be used to validate the result significantly. Third, some new spectral indices can be used for different land surface features to compare the result with the existing indices. Fourth, some other robust statistical techniques and diagrams can be applied to present these relationships. Finally, the entire method may be applied in other study areas with different climatic and physiographic regions.

## Acknowledgments

The authors are indebted to the United States Geological Survey (USGS). This study was supported by National Institute of Technology Raipur, Government of India, Grant No./NITRR/Dean(R&C)/2017/8301.

## Data availability statement

All the used data sets are freely downloadable from the official website of earth explorer (<http://earthexplorer.USGS.gov>).

## Disclosure statement

No potential conflict of interest was reported by the author(s).

## ORCID

Subhanil Guha  <http://orcid.org/0000-0002-2967-7248>

Himanshu Govil  <http://orcid.org/0000-0002-3433-8355>

## References

- Achmad, A., & Zainuddin, M. M. (2019). The relationship between land surface temperature and water index in the urban area of a tropical city. *IOP Conference Series: Earth and Environmental Science*, 365, 012013. <https://doi.org/10.1088/1755-1315/365/1/012013>
- Ali, J. M., Marsh, S. H., & Smith, M. J. (2017). A comparison between London and Baghdad surface urban heat islands and possible engineering mitigation solutions. *Sustain Cities Soc*, 29, 159–168. <https://doi.org/10.1016/j.scs.2016.12.010>
- Bala, R., Prasad, R., & Yadav, V. P. (2020). A comparative analysis of day and night land surface temperature in two semi-arid cities using satellite images sampled in different seasons. *Advances in Space Research*, 66(2), 412–425. <https://doi.org/10.1016/j.asr.2020.04.009>
- Bala, R., Prasad, R., & Yadav, V. P. (2021). Quantification of urban heat intensity with land use/land cover changes using Landsat satellite data over urban landscapes. *Theoretical and Applied Climatology*, 145(1–2), 1–12. <https://doi.org/10.1007/s00704-021-03610-3>
- Balew, A., & Korme, T. (2020). Monitoring land surface temperature in Bahir Dar city and its surrounding using Landsat images. *Egypt J Remote Sens Space Sci*. <https://doi.org/10.1016/j.ejrs.2020.02.001>
- Barsi, J., Schott, J., Hook, S., Raqueno, N., Markham, B., Radocinski, R. (2014). Landsat-8 thermal infrared sensor (TIRS) vicarious radiometric calibration. *Remote Sens*, 6(11), 11607–11626. <https://doi.org/10.3390/rs6111607>
- Becker, F and Li, ZL. (1990). Towards a local split window method over land surfaces. *Int J Remote Sens* 11(3), 369–393. <https://doi.org/10.1080/01431169008955028>
- Berger, C., Rosentreter, J., Voltersen, M., Baumgart, C., Schmillius, C., & Hese, S. (2017). Spatio-Temporal analysis of the relationship between 2D/3D Urban Site characteristics and land surface temperature. *Remote Sensing of Environment*, 193, 225–243. <https://doi.org/10.1016/j.rse.2017.02.020>
- Carlson, T. N., & Ripley, D. A. (1997). On the relation between NDVI, fractional vegetation cover, and leaf area index. *Remote Sensing of Environment*, 62(3), 241–252. [https://doi.org/10.1016/S0034-4257\(97\)00104-1](https://doi.org/10.1016/S0034-4257(97)00104-1)
- Chatterjee RS, Singh N, Thapa S, Sharma D, Kumar D. (2017). Retrieval of land surface temperature (LST) from landsat TM6 and TIRS data by single channel radiative transfer algorithm using satellite and ground-based inputs. *Int J Appl Earth Obs Geoinf*, 58, 264–277. <https://doi.org/10.1016/j.jag.2017.02.017>
- Chen, L., Li, M., Huang, F., & Xu, S. (2013). Relationships of LST to NDBI and NDVI in Wuhan City based on Landsat ETM+ image. *2013 6th International Congress on Image and Signal Processing (CISP)*, Hangzhou, pp. 840–845. <https://doi.org/10.1109/CISP.2013.6745282>
- Chen, X., & Zhang, Y. (2017). Impacts of urban surface characteristics on spatiotemporal pattern of land surface temperature in Kunming of China. *Sustain Cities Soc*, 32, 87–99. <https://doi.org/10.1016/j.scs.2017.03.013>
- Chen, X.-L., Zhao, H.-M., Li, P.-X., & Yi, Z.-Y.. (2006). Remote sensing image-based analysis of the relationship between urban heat island and land use/cover changes. *Remote Sensing of Environment*, 104(2), 133–146. <https://doi.org/10.1016/j.rse.2005.11.016>
- Choudhury, D., Das, K., & Das, A. (2019). Assessment of land use land cover changes and its impact on variations of land surface temperature in Asansol-Durgapur development region. *Egypt J Remote Sens Space Sci*, 22(2), 203–218. <https://doi.org/10.1016/j.ejrs.2018.05.004>
- Coll C, Galve JM, Sanchez JM, Casseles V (2010) Validation of Landsat-7/ETM+ thermal-band calibration and atmospheric correction with ground-based measurements. *IEEE Trans Geo sci Remote Sens* 48(1), 547–555. <https://doi.org/10.1109/TGRS.2009.2024934>
- Dos Santos, A. R., de Oliveira, F. S., Da Silva, A. G., Gleriani, J. L., Gonçalves, W., Moreira, G. L., Silva, F. G., Branco, E. R. F., Moura, M. M., Da Silva, R. G., Juvanhol, R. S., de Souza, K. B., Rebeiro, C. A. A. S., de Queiroz, V. T., Costa, A. V., Lorenzon, A. S., Domingues, G. F., Marcatti, G. E., De Castro, N. L. M., Resende, R. T., ... PHS, M. (2017). Spatial and temporal distribution of urban heat islands. *The Science of the Total Environment*, 605-606, 946–956. <https://doi.org/10.1016/j.scitotenv.2017.05.275>
- Du, S., Xiong, Z., Wang, Y., & Guo, L. (2016). Quantifying the multilevel effects of landscape composition and configuration on land surface temperature. *Remote Sensing of Environment*, 178, 84–92. <https://doi.org/10.1016/j.rse.2016.02.063>
- Essa, W., Verbeiren, B., Van der Kwast, J., Van de Voorde, T., & Batelaan, O. (2012). Evaluation of the DisTrad thermal sharpening methodology for urban areas. *International Journal of Applied Earth Observation and Geoinformation : ITC Journal*, 19, 163–172. <https://doi.org/10.1016/j.jag.2012.05.010>
- Estoque, R. C., Murayama, Y., & Myint, S. W. (2017). Effects of landscape composition and pattern on land surface temperature: An urban heat island study in the megacities of Southeast Asia. *The Science of the Total Environment*, 577, 349–359. <https://doi.org/10.1016/j.scitotenv.2016.10.195>
- Foley, J. A., DeFries, R., Asner, G. P., Barford, C., Bonan, G., Carpenter, S. R., Chapin, F. S., Coe, M. T., Daily, G. C., Gibbs, H. K., et al. (2005). Global Consequences of Land Use. *Science*, 309(5734), 570–574. <https://doi.org/10.1126/science.1111772>
- Fu, P., & Weng, Q. (2015). Temporal dynamics of land surface temperature from landsat TIR time series images. *IEEE Geosci Sens Lett*, 12, 1–5.
- Fu, P., & Weng, Q. (2016). A time series analysis of urbanization induced land use and land cover change and its impact on land surface temperature with landsat imagery. *Remote Sensing of Environment*, 175, 205–214. <https://doi.org/10.1016/j.rse.2015.12.040>
- García-Santos V, Cuxart J, Martínez-Villagrana D, Jiménez MA, Simó G (2018) Comparison of Three Methods for Estimating Land Surface Temperature from Landsat 8-TIRS Sensor Data. *Remote Sens* 10(9), 1450. <https://doi.org/10.3390/rs10091450>
- Ghobadi, Y., Pradhan, B., Shafri, H. Z. M., & Kabiri, K. (2014). Assessment of spatial relationship between land surface temperature and land use/cover retrieval from multi-temporal remote sensing data in South Karkheh Sub-basin, Iran. *Arab J Geosci*, 8(1), 525–537. <https://doi.org/10.1007/s12517-013-1244-3>
- Gorgani, S. A., Panahi, M., & Rezaie, F. (2013). *The relationship between NDVI and LST in the Urban area of Mashhad, Iran. International Conference on Civil Engineering Architecture and Urban Sustainable Development. November, Tabriz, Iran.*

- Goward, S. N., Xue, Y. K., & Czajkowski, K. P. (2002). Evaluating land surface moisture conditions from the remotely sensed temperature/vegetation index measurements: An exploration with the simplified simple biosphere model. *Remote Sensing of Environment*, 79(2–3), 225–242. [https://doi.org/10.1016/S0034-4257\(01\)00275-9](https://doi.org/10.1016/S0034-4257(01)00275-9)
- Grimm, N. B., Faeth, S. H., Golubiewski, N. E., Redman, C. L., Wu, J., Bai, X., Briggs, J. M., & Grimm, N. (2008). Global change and the ecology of cities. *Science*, 319(5864), 756–760. <https://doi.org/10.1126/science.1150195>
- Guha, S., Govil, H., Dey, A., & Gill, N. (2018). Analytical study of land surface temperature with NDVI and NDBI using Landsat 8 OLI/TIRS data in Florence and Naples city, Italy. *Eur J Remote Sens*, 51(1), 667–678. <https://doi.org/10.1080/22797254.2018.1474494>
- Guha, S., Govil, H., Dey, A., & Gill, N. (2020). A case study on the relationship between land surface temperature and land surface indices in Raipur City, India. *Geografisk Tidsskrift / udgivet af Bestyrelsen for Det Kongelige danske geografiske selskab*, 120(1), 35–50. <https://doi.org/10.1080/00167223.2020.1752272>
- Gui, X., Wang, L., Yao, R., Yu, D., & Li, C. (2019). Investigating the urbanization process and its impact on vegetation change and urban heat island in Wuhan, China. *Environ Sci Pollut Res*, 26(30), 30808–30825. <https://doi.org/10.1007/s11356-019-06273-w>
- Guo, G., WGuo, G., Wu, Z., Xiao, R., Chen, Y., Liu, X., & Zhang, X. (2015). Impacts of urban biophysical composition on land surface temperature in urban heat island clusters. *Landscape and Urban Planning*, 135, 1–10. <https://doi.org/10.1016/j.landurbplan.2014.11.007>
- Gutman, G., & Ignatov, A. (1998). The derivation of the green vegetation fraction from NOAA/ AVHRR data for use in numerical weather prediction models. *International Journal of Remote Sensing*, 19(8), 1533–1543. <https://doi.org/10.1080/014311698215333>
- Hao, X., Li, W., & Deng, H. (2016). The oasis effect and summer temperature rise in arid regions-case study in Tarim Basin. *Scientific Reports*, 6(1), 35418. <https://doi.org/10.1038/srep35418>
- He, B. J., Zhao, Z. Q., Shen, L. D., Wang, H. B., Li, L. G., & He, B. J. (2019). An approach to examining performances of cool/hot sources in mitigating/enhancing land surface temperature under different temperature backgrounds based on landsat 8 image. *Sustain Cities Soc*, 44, 416–427. <https://doi.org/10.1016/j.scs.2018.10.049>
- Hope, A. S., & McDowell, T. P. (1992). The relationship between surface temperature and a spectral vegetation index of a tall grass prairie: Effects of burning and other landscape controls. *International Journal of Remote Sensing*, 13(15), 2849–2863. <https://doi.org/10.1080/01431169208904086>
- Hou, G. L., Zhang, H. Y., Wang, Y. Q., Qiao, Z. H., & Zhang, Z. X. (2010). Retrieval and spatial distribution of land surface temperature in the middle part of Jilin Province based on MODIS data. *Sci Geogr Sin*, 30, 421–427. [http://en.cnki.com.cn/Article\\_en/CJFDTOTAL-DLKX201003017.htm](http://en.cnki.com.cn/Article_en/CJFDTOTAL-DLKX201003017.htm)
- Huang, S., Taniguchi, M., Yamano, M., & Wang, C. H. (2009). Detecting urbanization effects on surface and subsurface thermal environment — A case study of Osaka. *The Science of the Total Environment*, 407(9), 3142–3152. <https://doi.org/10.1016/j.scitotenv.2008.04.019>
- Jamei, Y., Rajagopalan, P., & Sun, Q. C. (2019). Spatial structure of surface urban heat island and its relationship with vegetation and built-up areas in Melbourne, Australia. *The Science of the Total Environment*, 659, 1335–1351. <https://doi.org/10.1016/j.scitotenv.2018.12.308>
- Jiménez-Muñoz JC, Cristóba J, Sobrino JA, Soria G, Ninyerola M, Pons X (2009) Revision of the single-channel algorithm for land surface temperature retrieval from Landsat thermal-infrared data. *Photogram Eng Remote Sens* 47(1), 339–349. <http://dx.doi.org/10.1109/TGRS.2008.2007125>
- Jiménez-Muñoz JC, Sobrino JA (2003) A generalized single channel method for retrieving land surface temperature from remote sensing data. *J Geophys Res*, 108(D22), 4688. <http://dx.doi.org/10.1029/2003JD003480>
- Julien, Y. Sobrino JA Verhoef W (2006) Changes in land surface temperatures and NDVI values over Europe between 1982 and 1999. *Remote Sensing of Environment*, 103(1), 43–55. <https://doi.org/10.1016/j.rse.2006.03.011>
- Kalnay, E., & Cai, M. (2003). Impact of urbanization and land-use change on climate. *Nat Cell Biol*, 423, 528–531.
- Karnieli A, Agam N, Pinker RT, Anderson M, Imhoff ML, Gutman GG, Panov N, Goldberg A (2010) Use of NDVI and land surface temperature for drought assessment: Merits and limitations. *J Clim* 23(3), 618–633. doi:10.1175/2009JCLI2900.1
- Ke, Y. H., Im, J., Lee, J., Gong, H. L., & Ryu, Y. (2015). Characteristics of landsat 8 oli-derived NDVI by comparison with multiple satellite sensors and in-situ observations. *Remote Sensing of Environment*, 164, 298–313. <https://doi.org/10.1016/j.rse.2015.04.004>
- Kikon, N., Singh, P., Singh, S. K., & Vyas, A. (2016). Assessment of urban heat islands (UHI) of Noida City, India using multi-temporal satellite data. *Sustain Cities Soc*, 22, 19–28. <https://doi.org/10.1016/j.scs.2016.01.005>
- Kumar, D., & Shekhar, S. (2015). Statistical analysis of land surface temperature-vegetation indexes relationship through thermal remote sensing. *Ecotox Environ Safe*, 121, 39–44. <https://doi.org/10.1016/j.ecoenv.2015.07.004>
- Lambin, E. F., & Ehrlich, D. (1996). The surface temperature-vegetation index space for land use and land cover change analysis. *International Journal of Remote Sensing*, 17(3), 463–487. <https://doi.org/10.1080/01431169608949021>
- Li ZN, Duan SB, Tang BH, Wu H, Ren HG, Yan GJ. (2016). Review of methods for land surface temperature derived from thermal infrared remotely sensed data. *J Remote Sens*, 20, 899–920.
- Liang, B. P., Li, Y., & Chen, K. Z. (2012). A research on land features and correlation between NDVI and land surface temperature in Guilin City. *Remote Sens Tech Appl*, 27, 429–435.
- Liu, Y., Peng, J., & Wang, Y. (2018). Efficiency of landscape metrics characterizing urban land surface temperature. *Landscape and Urban Planning*, 180, 36–53. <https://doi.org/10.1016/j.landurbplan.2018.08.006>
- Marzban, F., Sodoudi, S., & Preusker, R. (2018). The influence of land-cover type on the relationship between LST-NDVI and LST-Tair. *International Journal of Remote Sensing*, 39(5), 1377–1398. <https://doi.org/10.1080/01431161.2017.1462386>
- McFeeters, S. K. (1996). The use of the Normalized Difference Water Index (NDWI) in the delineation of open water features. *International Journal of Remote Sensing*, 17(7), 1425–1432. <https://doi.org/10.1080/01431169608948714>
- McFeeters, S. K. (2013). Using the Normalized Difference Water Index (NDWI) within a geographic information system to detect swimming pools for mosquito

- abatement: A practical approach. *Remote Sens*, 5(7), 3544–3561. <https://doi.org/10.3390/rs5073544>
- McMillin, L.M. (1975). Estimation of sea surface temperatures from two infrared window measurements with different absorption. *J Geophys Res* 80, 80–82. <https://doi.org/10.1029/JC080i036P05113>
- Moran, M. S., Clarke, T. R., Inouie, Y., & Vidal, A. (1994). Estimating crop water-deficit using the relation between surface air-temperature and spectral vegetation index. *Remote Sensing of Environment*, 49(3), 246–263. [https://doi.org/10.1016/0034-4257\(94\)90020-5](https://doi.org/10.1016/0034-4257(94)90020-5)
- Mushore, T. D., Odindi, J., Dube, T., & Mutanga, O. (2017). Prediction of future urban surface temperatures using medium resolution satellite data in Harare metropolitan city, Zimbabwe. *Building and Environment*, 122, 397–410. <https://doi.org/10.1016/j.buildenv.2017.06.033>
- Nimish, G., Bharath, H. A., & Lalitha, A. (2020). Exploring temperature indices by deriving relationship between land surface temperature and urban landscape. *Remote Sens Appl Soc Environ*, 18, 100299. <https://doi.org/10.1016/j.rsase.2020.100299>
- Patz, J. A., Campbell-Lendrum, D., Holloway, T., & Foley, J. A. (2005). Impact of regional climate change on human health. *Nat Cell Biol*, 438, 310–317. <https://doi.org/10.1038/nature04188>
- Peng, J., Jia, J., Liu, Y., Li, H., & Wu, J. (2018a). Seasonal contrast of the dominant factors for spatial distribution of land surface temperature in urban areas. *Remote Sensing of Environment*, 215, 255–267. <https://doi.org/10.1016/j.rse.2018.06.010>
- Peng, J., Ma, J., Liu, Q., Liu, Y., Hu, Y., Li, Y., & Yue, Y. (2018b). Spatial-temporal change of land surface temperature across 285 cities in china: An urban-rural contrast perspective. *The Science of the Total Environment*, 635, 487–497. <https://doi.org/10.1016/j.scitotenv.2018.04.105>
- Peng, J., Xie, P., Liu, Y., & Ma, J. (2016). Urban thermal environment dynamics and associated landscape pattern factors: a case study in the Beijing metropolitan region. *Remote Sensing of Environment*, 173, 145–155. <https://doi.org/10.1016/j.rse.2015.11.027>
- Price, J.C. (1984). Land surface temperature measurements from the split window channels of the NOAA 7 Advanced Very High Resolution Radiometer. *J Geophys Res Atmos* 89, 231–237. <https://doi.org/10.1029/JD089iD05p07231>
- Purevdorj, T. S., Tateishi, R., Ishiyama, T., & Honda, Y. (1998). Relationships between percent vegetation cover and vegetation indices. *International Journal of Remote Sensing*, 19(18), 3519–3535. <https://doi.org/10.1080/014311698213795>
- Qin, Z., Karnieli, A., & Barliner, P. (2001). A mono-window algorithm for retrieving land surface temperature from landsat TM data and its application to the Israel-Egypt border region. *International Journal of Remote Sensing*, 22(18), 3719–3746. <https://doi.org/10.1080/01431160010006971>
- Qu, C., Ma, J. H., Xia, Y. Q., & Fei, T. (2014). Spatial distribution of land surface temperature retrieved from MODIS data in Shiyang River Basin. *Arid Land Geogr*, 37, 125–133.
- Qu, S., Wang, L., Lin, A., Yu, D., Yuan, M., & Li, C. (2020). What drives the vegetation restoration in Yangtze River basin, China: Climate change or anthropogenic factors? *Ecological Indicators*, 108, 105724. <https://doi.org/10.1016/j.ecolind.2019.105724>
- Roy, S., Pandit, S., Eva, E. A., Bagmar, M. S. H., Papia, M., Banik, L., Dube, T., Rahman, F., & Razi, M. A. (2020). Examining the nexus between land surface temperature and urban growth in Chattogram Metropolitan Area of Bangladesh using long term Landsat series data. *Urban Clim*, 32, 100593. <https://doi.org/10.1016/j.uclim.2020.100593>
- Sandholt, I., Rasmussen, K., & Andersen, J. (2002). A simple interpretation of the surface temperature/vegetation index space for assessment of surface moisture status. *Remote Sensing of Environment*, 79(2–3), 213–224. [https://doi.org/10.1016/s0034-4257\(01\)00274-7](https://doi.org/10.1016/s0034-4257(01)00274-7)
- Sekertekin, A and Bonafoni, S. (2020). Land surface temperature retrieval from landsat 5, 7, and 8 over rural areas: assessment of different retrieval algorithms and emissivity models and toolbox implementation. *Remote Sens* 12 (2): 294. <https://doi.org/10.3390/rs12020294>
- Shigeto, K. (1994). Relation between vegetation, surface temperature, and surface composition in the Tokyo region during winter. *Remote Sensing of Environment*, 50(1), 52–60. [https://doi.org/10.1016/0034-4257\(94\)90094-9](https://doi.org/10.1016/0034-4257(94)90094-9)
- Smith, R. C. G., & Choudhury, B. J. (1990). On the correlation of indices of vegetation and surface temperature over south-eastern Australia. *International Journal of Remote Sensing*, 11(11), 2113–2120. <https://doi.org/10.1080/01431169008955164>
- Sobrino, J. A., Jimenez-Munoz, J. C., & Paolini, L. (2004). Land surface temperature retrieval from Landsat TM5. *Remote Sensing of Environment*, 90(4), 434–440. <https://doi.org/10.1016/j.rse.2004.02.003>
- Sobrino, J. A., Raissouni, N., & Li, Z. (2001). A comparative study of land surface emissivity retrieval from NOAA data. *Remote Sensing of Environment*, 75(2), 256–266. [https://doi.org/10.1016/S0034-4257\(00\)00171-1](https://doi.org/10.1016/S0034-4257(00)00171-1)
- Son, N. T., Chen, C. F., & Chen, C. R. (2020). Urban expansion and its impacts on local temperature in San Salvador, El Salvador. *Urban Clim*, 32, 100617. <https://doi.org/10.1016/j.uclim.2020.100617>
- Stroppiana, D., Antoninetti, M., & Brivio, P. A. (2014). Seasonality of MODIS LST over Southern Italy and correlation with land cover, topography and solar radiation. *Eur J Remote Sens*, 47(1), 133–152. <https://doi.org/10.5721/EuJRS20144709>
- Sun, D., & Kafatos, M. (2007). Note on the NDVI-LST relationship and the use of temperature-related drought indices over North America. *Geophysical Research Letters*, 34. <http://doi.org/10.1029/2007GL031485>
- Sun, Q., Tan, J., & Xu, Y. (2010). An ERDAS image processing method for retrieving LST and describing urban heat evolution: A case study in the Pearl River Delta Region in South China. *Environ Earth Sci*, 59(5), 1047–1055. <https://doi.org/10.1007/s12665-009-0096-3>
- Tomlinson, C. J., Chapman, L., Trones, J. E., & Baker, C. (2011). Remote sensing land surface temperature for meteorology and climatology: A review. *Meteorol Appl*, 18(3), 296–306. <https://doi.org/10.1002/met.287>
- Tran, D. X., Pla, F., Latorre-Carmona, P., Myint, S. W., Caetano, M., & Kieu, H. V. (2017). Characterizing the relationship between land use land cover change and land surface temperature. *ISPRS J Photogramm Sens*, 124, 119–132. <https://doi.org/10.1016/j.isprsjprs.2017.01.001>
- Tucker, C. J. (1979). Red and photographic infrared linear combinations for monitoring vegetation. *Remote Sensing of Environment*, 8(2), 127–150. [https://doi.org/10.1016/0034-4257\(79\)90013-0](https://doi.org/10.1016/0034-4257(79)90013-0)
- Uddin S, Al Ghabban AN, Al Dousari A, Al Murad, M. Al Shamroukh D (2010) A Remote Sensing Classification for Land-Cover Changes and Micro-Climature in Kuwait. *Int J Sustain Dev Plann* 5, 367–377. <https://doi.org/10.2495/SDP-V5-N4-367-377>

- Voogt, J. A., & Oke, T. R. (2003). Thermal remote sensing of urban climates. *Remote Sensing of Environment*, 86(3), 370–384. [https://doi.org/10.1016/S0034-4257\(03\)00079-8](https://doi.org/10.1016/S0034-4257(03)00079-8)
- Weng, Q. (2001). A remote sensing-GIS evaluation of urban expansion and its impact on surface temperature in Zhujiang Delta, China. *Int J Remote Sens* 22(10), 1999–2014. <https://doi.org/10.1080/713860788>
- Weng, Q. H. (2009). Thermal infrared remote sensing for urban climate and environmental studies: Methods, applications, and trends. *ISPRS J Photogramm Sens*, 64(4), 335–344. <https://doi.org/10.1016/j.isprsjprs.2009.03.007>
- Weng, Q. H., Lu, D. S., & Schubring, J. (2004). Estimation of land surface temperature–vegetation abundance relationship for urban heat island studies. *Remote Sensing of Environment*, 89(4), 467–483. <https://doi.org/10.1016/j.rse.2003.11.005>
- Weng, Q. H., & Quattrochi, D. A. (2006). Thermal remote sensing of urban areas: An introduction to the special issue. *Remote Sensing of Environment*, 104(2), 119–122. <https://doi.org/10.1016/j.rse.2006.05.002>
- Wukelic, G. E., Gibbons, D. E., Martucci, L. M., & Foote, H. P. (1989). Radiometric calibration of landsat thematic mapper thermal band. *Remote Sensing of Environment*, 28, 339–347. [https://doi.org/10.1016/0034-4257\(89\)90125-9](https://doi.org/10.1016/0034-4257(89)90125-9)
- Yang, J., & Qiu, J. (1996). The empirical expressions of the relation between precipitable water and ground water vapor pressure for some areas in China. *Sci Atmos Sinica*, 20, 620–626.
- Yang L, Cao YG, Zhu XH, Zeng SH, Yang GJ, He JY, Yang XC (2014). Land surface temperature retrieval for arid regions based on Landsat-8 TIRS data: a case study in Shihezi, Northwest China. *J Arid Land* 6, 704–716. <https://doi.org/10.1007/s40333-014-0071-z>
- Yuan, F., & Bauer, M. E. (2007). Comparison of impervious surface area and normalized difference index as indicators of surface urban heat island effects in Landsat imagery. *Remote Sensing of Environment*, 106(3), 375–386. <https://doi.org/10.1016/j.rse.2006.09.003>
- Yuan, M., Wang, L., Lin, A., Liu, Z., & Qu, S. (2020). Vegetation green up under the influence of daily minimum temperature and urbanization in the Yellow River Basin, China. *Ecological Indicators*, 108, 105760. <https://doi.org/10.1016/j.ecolind.2019.105760>
- Yuan X, Wang W, Cui J, Meng F, Kurban A, De Maeyer P. (2017). Vegetation changes and land surface feedbacks drive shifts in local temperatures over Central Asia. *Sci Rep* 7(1), 3287. <https://doi.org/10.1038/s41598017034322>
- Yue, W., Xu, J., Tan, W., & Xu, L. (2007). The relationship between land surface temperature and NDVI with remote sensing. application to shanghai landsat 7 ETM+ data. *International Journal of Remote Sensing*, 28(15), 3205–3226. <https://doi.org/10.1080/01431160500306906>
- Zanter, K. (2019). *Landsat 8 (L8) Data Users Handbook*; EROS: Sioux Falls, SD, USA.
- Zha, Y., Gao, J., & Ni, S. (2003). Use of normalized difference built-up index in automatically mapping urban areas from TM imagery. *International Journal of Remote Sensing*, 24(3), 583–594. <https://doi.org/10.1080/01431160304987>
- Zhang X, Estoque RC, Murayama Y. (2017). An urban heat island study in Nanchang City, China based on land surface temperature and social-ecological variables. *Sustain Cities Soc* 32, 557–568. <https://doi.org/10.1016/j.scs.2017.05.005>
- Zhang, Y., Odeh, I. O. A., & Han, C. (2009). Bi-temporal characterization of land surface temperature in relation to impervious surface area, NDVI and NDBI, using a sub-pixel image analysis. *International Journal of Applied Earth Observation and Geoinformation : ITC Journal*, 11(4), 256–264. <https://doi.org/10.1016/j.jag.2009.03.001>
- Zhang Z, He G, Wang M, Long T, Wang G, Zhang X, Jiao W. (2016). Towards an operational method for land surface temperature retrieval from Landsat 8 data. *Remote Sens Lett* 7(3), 279–288. <http://doi.org/10.1080/215704X.2015.1130877>
- Zhao, H. M., & Chen, X. L. (2005). Use of normalized difference bareness index in quickly mapping bare areas from TM/ETM+. *Geoscience and Remote Sensing Symposium*, 3(25–29), 1666–1668. <https://doi.org/10.1109/IGARSS.2005.1526319>
- Zhou, D., Xiao, J., Bonafoni, S., Berger, C., Deilami, K., Zhou, Y., Froking, S., Yao, R., Qiao, Z., & Sobrino, J. A. (2019). Satellite remote sensing of surface urban heat Islands: Progress, challenges, and perspectives. *Remote Sens*, 11(1), 48. <https://doi.org/10.3390/rs11010048>
- Zhou, Y., Shi, T. M., Hu, Y. M., & Liu, M. (2011). Relationships between land surface temperature and normalized difference vegetation index based on urban land use type. *Chin J Ecol*, 30, 1504–1512.
- Sharma R, Joshi PK. (2016). Mapping environmental impacts of rapid urbanization in the National Capital Region of India using remote sensing inputs. *Urban Clim* 15, 70–82. <https://doi.org/10.1016/j.uclim.2016.01.004>



# Source details

[Feedback >](#) [Compare sources >](#)

## European Journal of Remote Sensing

Formerly known as: [Italian Journal of Remote Sensing / Rivista Italiana di Telerilevamento](#)

[Open Access](#)

Scopus coverage years: from 2012 to Present

Publisher: Taylor & Francis

E-ISSN: 2279-7254

Subject area: [Mathematics: Applied Mathematics](#) [Earth and Planetary Sciences: Computers in Earth Sciences](#)  
[Environmental Science: General Environmental Science](#) [Earth and Planetary Sciences: Atmospheric Science](#)

Source type: Journal

[View all documents >](#)[Set document alert](#)[Save to source list](#)

CiteScore 2022

7.0



SJR 2022

0.660



SNIP 2022

1.131

[CiteScore](#)[CiteScore rank & trend](#)[Scopus content coverage](#)